



ISFA2016

ISSN 1349-113X
JAXA-SP-16-008E

宇宙航空研究開発機構特別資料

May 15-17 2016 Tokyo, JAPAN

Flutter

Proceedings of the First International Symposium on Flutter and its Application



©Mitsui Engineering & Shipbuilding Co.,Ltd.

©Honsu-Shikoku Bridge Expressway Co.,Ltd.

PREFACE

On behalf of the organizing committee of the First International Symposium on Flutter and its Application (ISFA2016), we would like to welcome all attendees to ISFA2016. Thank you very much for your coming over to Tokyo and joining us.

During these three days, we have here a pool of distinguished researchers with a proper balance between academia and industry as well as between senior and junior researchers including students, from 16 countries in the world. Experts of concerned disciplines will address more than 100 themes in plenary and technical sessions.

The objectives of this symposium are to investigate the integration of traditional and fundamental technologies of flutter in a multidisciplinary research environment, involving aerospace engineering, mechanical engineering, civil engineering, architecture and biological engineering, and to establish new areas such as energy conversion, explorations of bio-flight mechanisms and propulsions through analytical and experimental concept of flutter phenomena.

We believe that ISFA2016 will provide a momentum toward future to extend scholarly collaborations and to disseminate innovative ideas and technologies by making possible international joints.

ISFA2016 is hosted by Japan Research Association on Flutter and is also a collaborative endeavor among 12 academic societies and associations in Japan. The organizing committee would like to appreciate all partners and sponsors for their contributions to hold this symposium in a good circumstance.

Please enjoy ISFA2016 and Tokyo.

May 15, 2016



Dr. Jiro NAKAMICHI
Chair
Organizing Committee
First International Symposium of Flutter and its application (ISFA2016)

OPENING ADDRESS

(given by Prof. Isogai at the opening ceremony of ISFA2016 on May 16,2016)

Ladies and gentlemen,

It is a great honor for me to take a role to declare the opening of the First International Symposium on Flutter and its Applications 2016. Hereby I cordially and formally do it.

I would like to welcome the persons from all over the world to exchange the technical information and to work together for a few days on exciting field of flutter and their applications.

As was introduced by the chairperson, I'm the president of the Japan Research Association on Flutter, which is a domestic consolidation body of aeroelasticians from a variety of engineering fields in Japan. This is the mother body of ISFA 2016 organizing committee which is affiliated to design this symposium.

On behalf of JRAF, I wish to extend our warm appreciation to the responsible committee for their excellent arrangements for ISFA2016. We have the privilege of holding this symposium in a good circumstance.

My thanks will also reach all of the domestic communities which allowed us to solve all difficult issues including the financial problems to hold this symposium.

Thank you very much.

Prof. Koji Isogai
President, Japan Research Association on Flutter
General Co-Chairs, ISFA 2016

INTRODUCTION ADDRESS

(given by Prof. Matsumoto at the opening ceremony of ISFA2016 on May 16, 2016)

Dear distinguished guests,

I would like to welcome all attendees to ISFA2016. Thank you very much for your coming over to Tokyo and joining us.

I'm pleased indeed to be here at the opening ceremony of ISFA2016 today and I appreciate long-term efforts of all members of the organizing committee to implement this challenging event.

Our conference is entitled: "First International symposium on Flutter and its Application". Allow me to explain the motivation of this symposium a little further.

It is sometimes mentioned that the research activities of flutter are reaching a certain status that marks a transition to maturity and another development.

We have definitely to warm and appreciate the classical achievements developed by a lot of outstanding pioneers. But it must be confirmed that we have now responsibilities to explore a new field for flutter.

The objectives of this symposium are to investigate the integration of traditional and fundamental technologies of flutter in a multidisciplinary research environment, involving aerospace engineering, mechanical engineering, civil engineering, architecture and biological engineering, and to establish new areas such as energy conversion, explorations of bio-flight mechanisms and propulsions through analytical and experimental concept of flutter phenomena.

I am talking about an integrated research approach of flutter not only in terms of contributing to the design technology of machines, aircraft, bridges and buildings, but also in terms of applying that technology to inventing innovation way, for example, to take out a new energy from nature. I firmly believe that it is now to set up the circumstances to do so.

We would greatly appreciate if you could give useful suggestions for realization of our intention and we would like to ask you to give us your greatest consideration and assistance to make the symposium successful.

Thank you very much.

Prof. Masaru Matsumoto
Vice President, Japan Research Association on Flutter
General Co-Chairs, ISFA2016

First International Symposium on Flutter and its Application (ISFA2016)

May 15-17 2016, Mielparque-tokyo, Tokyo, Japan

- Organized by Japan Research Association on Flutter (JRAF)
- Co-organized by Japan Aerospace Exploration Agency (JAXA)
- Sponsored by Association for Disaster Prevention Research
 Japan Aerospace Exploration Agency (JAXA)
 Nippon Kaiji Kyokai (ClassNK)
 The Kajima Foundation
- Supported by Architectural Institute of Japan
 International Association for Wind Engineering
 Japan Wind Energy Association
 Japan Association for Wind Engineering
 Japanese Society of Steel Construction
 Japan Society of Civil Engineers
 Society of Aero Aqua Bio-Mechanisms
 The Japan Society for Aeronautical and Space Sciences
 The Japan Society of Fluid Mechanics
 The Japan Society of Mechanical Engineers
 The Japan Society of Naval Architects and Ocean Engineers
 The Visualization Society of Japan

ISFA2016 Committee Members

General Co-Chairs:

Prof. Emeritus Koji Isogai (Kyushu University, Japan)
Prof. Emeritus Masaru Matsumoto (Kyoto University, Japan)

Organizing Committee:

Chair: Dr. Jiro Nakamichi (Japan Aerospace Exploration Agency, Japan)
Prof. Hiroshi Katsuchi (Yokohama National University, Japan)
Prof. Emeritus Hiromasa Kawai (Kyoto University, Japan)
Dr. Hiroshi Ishizaki (SE Corporation, Japan)

Advisor Mr. Hiroo Inoue (NIPPON KAIJI KYOKAI, Japan)

International Advisory Committee:

Co-Chair: Prof. Emeritus Masaru Matsumoto (Kyoto University, Japan)
Co-Chair: Prof. Katsuhisa Fujita (Osaka City University, Japan)
Prof. Emeritus Michael P. Païdoussis (McGill University, Canada)
Prof. David S. Weaver (McMaster University, Canada)
Dr. Olivier Flamand (Scientific and Technical Centre for Building (CSTB), France)
Prof. Gregory A. Kopp (West University, Canada)
Prof. Huosheng Hu (University of Essex, UK)
Dr. Sanjay Sharma (Plymouth University, UK)
Prof. Forng-Chen Chiu (National Taiwan University, Taiwan)
Prof. Carlos E. S. Cesnik (University of Michigan, USA)
Dr. Günter Schewe (German Aerospace Center (DLR), Germany)

Academic Committee

Chair: Prof. Emeritus Koji Isogai (Kyushu University, Japan)
Vice Chair: Prof. Emeritus Masaru Matsumoto (Kyoto University, Japan)
Manager: Dr. Yasuaki Ito (Shimizu Corporation, Japan)
Prof. Masahiro Watanabe (Aoyama Gakuin University, Japan)
Prof. Katsuhisa Fujita (Osaka City University, Japan)
Mr. Kazumasa Okubo (Kajima Technical Research Institute, Japan)

Conference Venue and Tour Committee

- Co-Chair: Dr. Hiroshi Ishizaki (SE Corporation, Japan)
Co-Chair: Prof. Emeritus Hiromasa Kawai (Kyoto University, Japan)
Manager: Dr. Hitoshi Arizono (Japan Aerospace Exploration Agency, Japan)
Mr. Shiro Kawakita (Hanshin Expressway Co. Ltd., Japan)
Mr. Hiroo Inoue (NIPPON KAIJI KYOKAI, Japan)
Mr. Takuya Murakami (JFE Steel Corp., Japan)
Prof. Hiromichi Shirato (Kyoto University, Japan)
Mr. Hiroshi Kamitsuji (INGÉROSEC Corp., Japan)

Public Relations and Outreach Committee

- Chair: Prof. Hiroshi Katsuchi (Yokohama National University, Japan)
Manager: Dr. Hisato Matsumiya (Central Research Institute of Electric Power Industry, Japan)
Dr. Taku Iwase (Hitachi Ltd., Japan)
Prof. Fumiaki Nagao (Tokushima University, Japan)
Prof. Minoru Noda (Tokushima University, Japan)
Mr. Kazumasa Okubo (Kajima Technical Research Institute, Japan)

Finance Committee

- Chair: Dr. Jiro Nakamichi (Japan Aerospace Exploration Agency, Japan)
Manager: Dr. Hitoshi Arizono (Japan Aerospace Exploration Agency, Japan)
Mr. Hiroo Inoue (NIPPON KAIJI KYOKAI, Japan)
Dr. Kenichi Saitoh (Japan Aerospace Exploration Agency, Japan)
Prof. Tomomi Yagi (Kyoto University, Japan)
Prof. Masahiro Watanabe (Aoyama Gakuin University, Japan)

Secretariat

- General: Dr. Kenichi Saitoh (Japan Aerospace Exploration Agency, Japan)
Dr. Hitoshi Arizono (Japan Aerospace Exploration Agency, Japan)

CONTENTS

KeyNote

- ISFA-1K01 DYNAMICS OF TUBULAR CYLINDRICAL STRUCTURES IN AXIAL FLOW 19
 Michael P. Païdoussis
 McGill University, Canada
- ISFA-1K02 SOME APPLICATIONS OF AN OPTIMUM DESIGN TECHNIQUE TO FLAPPING WING
 DESIGNS 33
 Koji Isogai
 Kyushu University, Japan

Invited

- ISFA-1I01 STALL-TYPE GALLOPING OF BLUFF BODIES 45
 Masaru Matsumoto⁺¹, Hiroshi Ishizaki⁺²
⁺¹Kyoto University, Japan; ⁺²SE Corporation, Japan
- ISFA-1I02 SOME CONFIRMATIONS RELATED WITH PRANDTL'S LIFTING LINE THEORY 55
 Jiro Nakamichi
 Japan Aerospace Exploration Agency, Japan

Flutter (Various Structures)

- ISFA-1R01 NONLINEAR SINGLE-MODE PANEL FLUTTER AT CONTINUOUSLY VARYING FLIGHT
 SPEED 59
 Anastasia Shishaeva⁺¹, Vasily Vedenev⁺¹, Andrey Aksenov⁺²
⁺¹Lomonosov Moscow State University, Russia; ⁺²Tesis LTD, Russia
- ISFA-1R03 PASSIVE AND ACTIVE PIEZOELECTRIC EFFECTS ON FLUTTER SUPPRESSION OF
 HIGHLY FLEXIBLE WINGS 67
 Natsuki Tsushima, Weihua Su
 University of Alabama, USA
- ISFA-1R04 ANALYTICAL AND NUMERICAL EVALUATION OF COUPLED GALLOPING OF
 SLENDER TOWERS 77
 Liang Wu, Delong Zuo
 Texas Tech University, USA
- ISFA-1R06 EFFECT OF MODELING ON DYNAMIC STABILITY OF A FLEXIBLE CANTILEVERED
 PLATE SUBJECTED TO A PARALLEL FLOW 87
 Katsuhisa Fujita, Keiji Matsumoto
 Osaka City University, Japan

ISFA-1R08	EFFECT OF VIBRATION DATA PREPROCESSING FOR FLUTTER MARGIN PREDICTION	97
	Masato Tamayama, Kenichi Saitoh, Norio Yoshimoto, Hitoshi Arizono Japan Aerospace Exploration Agency, Japan	
ISFA-1R10	STRUCTURAL DESIGN OF MORPHING CONTROL SURFACE USING CORRUGATED PANELS	105
	Keigo Sato, Tomohiro Yokozeki University of Tokyo, Japan	
ISFA-1R11	EIGEN-FREQUENCY CONTROL DESIGN OF CFRP STRUCTURES USING AN EMBROIDERY MACHINE	111
	Tadashige Ikeda, Kosuke Oka, Tatsuya Nishida Nagoya University, Japan	
ISFA-1R12	FLUTTER ANALYSIS OF PIEZOELECTRIC BEAMS IN MEMS	121
	Raffaele Ardito, Rocco Musci Politecnico di Milano, Italy	
ISFA-1R14	EXTENTION OF DISCRETE-TIME FLUTTER PREDICTION METHOD TO A HIGHER-MODE SYSTEM	131
	Hiroshi Torii Meijo University, Japan	
ISFA-1R15	EXPERIMENTAL STUDY ON TURBULENCE PARTIAL SIMULATION FOR BLUFF BODY	141
	Hiroshi Katsuchi, Hitoshi Yamada Yokohama National University, Japan	
ISFA-1R16	EXPERIMENTS ON THE PFLÜGER COLUMN: FLUTTER FROM FRICTION	151
	Davide Bigoni ⁺¹ , Oleg Kirillov ⁺² , Diego Misseroni ⁺¹ , Giovanni Noselli ⁺³ , Mirko Tommasini ⁺¹ ⁺¹ University of Trento, Italy; ⁺² Steklov Mathematical Institute, Russia; ⁺³ International School for Advanced Studies, Italy	
ISFA-1R21	WING FLUTTER COMPUTATION USING SPECTRAL VOLUME METHOD FOR HYBRID UNSTRUCTURED MESH	157
	Yuta Sawaki, Seiya Tateoka, Keisuke Sawada Tohoku University, Japan	
ISFA-3R14	EFFECTS OF MASS UNBALANCE AND HIGH LEVELS OF EXTERNAL DAMPING ON THE POST- CRITICAL FLUTTER OF A FLAT PLATE	169
	Luca Pigolotti, Claudio Mannini, Gianni Bartoli University of Florence, Italy	
ISFA-3R15	POD AND DMD OF FLOW NEAR SIDE SURFACE OF 2-D BLUFF BODY	179
	Hiromichi Shirato, Yusuke Taniguchi, Ikuma Tsukamae, Mai Shimonishi Kyoto University, Japan	

- ISFA-3R16 EXPERIMENTAL STUDY ON THE EFFECTS OF FREQUENCY RATIO ON IN-LINE OSCILLATION OF TWO SQUARE CYLINDERS IN TANDEM ARRANGEMENT 189
Kazutoshi Matsuda⁺¹, Kusuo Kato⁺¹, Itsuki Aratsu⁺¹, Yoko Tashiro⁺¹
⁺¹Kyushu Institute of Technology, Japan
- ISFA-3R17 EFFECTS OF VERTICAL PLATES ON THE UNSTEADY PRESSURE CHARACTERISTICS OF RECTANGULAR CYLINDERS 199
Cristiano Augusto Trein, Hiromichi Shirato, Masaru Matsumoto
Kyoto University, Japan
- ISFA-3R18 CORRELATION OF FLUCTUATING VELOCITY IN THE WAKE OF AN OSCILLATING SQUARE CYLINDER WITH OPENINGS OR APPENDAGES 209
Seiji Nakato
Kanto-gakuin University, Japan

Flutter (Bridges)

- ISFA-2R01 STUDY ON IDENTIFICATION OF BRIDGE DECK FLUTTER DERIVATIVES BY GUST RESPONSE 217
Hoang Trong Lam, Hiroshi Katsuchi, Hitoshi Yamada
Yokohama National University, Japan
- ISFA-2R03 THE ROLE OF HORIZONTAL AERODYNAMIC DERIVATIVES IN BRIDGE FLUTTER ANALYSIS 227
Allan Larsen
COWI Consulting Engineers, Denmark
- ISFA-2R04 NONLINEAR PHENOMENA OF COUPLED FLUTTER RESPONSES AND SELF-EXCITED FORCES OF A FLAT CLOSED-BOX BRIDGE DECK 237
Ledong Zhu⁺¹, Guangzhong Gao⁺¹, Hao Wu⁺²
⁺¹Tongji University, China; ⁺²China Resources Land (Shanghai) Co. Ltd, China
- ISFA-2R06 MULTI-SCALE EXPERIMENTAL COMPARISONS OF AERODYNAMIC VIBRATIONS OF A SUSPENSION BRIDGE 247
Haotian Dong, Yaojun Ge, Yongxin Yang
Tongji University, China
- ISFA-2R08 EXPERIMENTAL FLUTTER SUPPRESSION OF A LONG-SPAN SUSPENSION BRIDGE SECTION 257
Kevin Gouder⁺¹, Xiaowei Zhao⁺², David Limebeer⁺³, Michael R. Graham⁺¹
⁺¹Imperial College, UK; ⁺²University of Warwick, UK; ⁺³University of Oxford, UK
- ISFA-2R10 ENERGY CONVERSION MECHANISM OF AERODYNAMIC FLUTTER OF A BOX GIRDER 267
Yaojun Ge⁺¹, Zujun Liu⁺², Yongxin Yang⁺¹
⁺¹Tongji University, China; ⁺²North China University of Water Resources and Electric Power, China

Vortex Flow

- ISFA-3R01 ON THE HISTORICAL MISTAKES OF CLASSIC FLUID DYNAMICS THEORY 279
 Baku M. Nagai
 Okinawa Peace Club, Japan

FIV (Various Structures)

- ISFA-3R04 LES OF AERODYNAMIC INSTABILITY OF A THREE-DIMENSIONAL SQUARE
 CYLINDER IN TURBULENT BOUNDARY LAYER 283
 Yoshiyuki Ono⁺¹, Tetsuro Tamura⁺²
⁺¹Obayashi Corporation, Japan; ⁺²Tokyo Institute of Technology, Japan
- ISFA-3R06 PARAMETRIC MODEL REDUCTION FOR UNSTEADY FLOW ABOUT AIRFOIL
 BASED ON COMPRESSIBLE CFD SOLVER 293
 Zhao Xiang, Taehyoun Kim
 National University of Singapore, Singapore

Flapping Wing

- ISFA-3R07 STRUCTURAL DESIGN OF AEROELASTIC FLAPPING WING 303
 Hiroto Nagai⁺¹, Shunsuke Nakamura⁺², Masahiko Murozono⁺¹, Kosei Ono⁺¹, Nobuhide Uda⁺¹
⁺¹Kyushu University, Japan; ⁺²Toyota Motor Corporation, Japan
- ISFA-3R08 ANALYSIS OF KINEMATICS OF FLAPPING WING MAV USING OPTITRACK
 SYSTEMS 313
 Matthew NG Rongfa⁺¹, Teppatat Pantuphag⁺², Sutthiphong Srigrarom⁺¹,
 Chinnapat Thipyopas⁺²
⁺¹University of Glasgow Singapore, Singapore; ⁺²Kasetsart University, Thailand
- ISFA-3R09 ORNITHOPTER TYPE FLAPPING WINGS FOR AUTONOMOUS MICRO AERIAL
 VEHICLES 321
 Sutthiphong Srigrarom⁺¹, Woei Leong Chan⁺²
⁺¹University of Glasgow Singapore, Singapore; ⁺²National University of Singapore, Singapore

Flexible Tube

- ISFA-3R10 DYNAMIC STABILITY OF PIPES SUBJECTED TO INTERNAL FLOW AND
 ANNULAR AXIAL FLOW SIMULTANEOUSLY 331
 Katsuhisa Fujita, Akinori Moriasa
 Osaka City University, Japan
- ISFA-3R11 FLUTTER IN COLLAPSIBLE TUBES AT TURBULENT AND LAMINAR FLOW
 REGIMES 341
 Julia Zayko, Vladimir Yushutin, Vasily Vedeneev
 Lomonosov Moscow State University, Russia

VIV (Circular & Rectangular Cylinder)

- ISFA-4R01 HIGH-SPEED COMPUTATION AND EXPERIMENT ON ADDED-MASS AND VISCOUS-DAMPING FORCES ACTING ON VARIOUS OSCILLATING 3D OBJECTS..... 349
 Ryuta Tanaka⁺¹, Hajime Onishi⁺¹, Hideki Shimohara⁺², Hirochika Tanigawa⁺³,
 Katsuya Hirata⁺¹
⁺¹Doshisha University, Japan; ⁺²Doshisha International High School, Japan;
⁺³NIT, Maizuru College, Japan
- ISFA-4R02 PROPERTIES OF WAKE EXCITATION OF CIRCULAR CYLINDER 359
 Fumiaki Nagao⁺¹, Minoru Noda⁺¹, Masahiro Inoue⁺², Shota Matsukawa⁺³, Akihiro Shitamori⁺⁴
⁺¹Tokushima University, Japan; ⁺²Chuden Plant Co., Ltd., Japan;
⁺³Anan Technical High School, Japan; ⁺⁴Graduate School of Tokushima University, Japan
- ISFA-4R04 STUDY ON SPATIAL CORRELATION STRUCTURE OF FLUCTUATING PRESSURE ACTING ON A CIRCULAR CYLINDER 367
 Minoru Noda⁺¹, Shinya Onishi⁺², Fumiaki Nagao⁺¹
⁺¹Tokushima University, Japan; ⁺²Graduate school of Tokushima University, Japan
- ISFA-4R05 AERODYNAMIC FORCES ON A SQUARE PRISM IN CONTROLLED MOTION: A PHENOMENOLOGICAL DISCUSSION 375
 Luigi Carassale, Lorenzo Banfi, Andrea Freda
 University of Genova, Italy
- ISFA-4R06 VIBRATION OF MULTIPLE CIRCULAR CYLINDERS IN TANDEM ALIGNMENT 385
 Takashi Nomura⁺¹, Nariaki Saegusa⁺², Hiroshi Hasebe⁺¹
⁺¹Nihon University, Japan; ⁺²Ohmoto Gumi, Co. Ltd., Japan

Flutter (Fundamentals)

- ISFA-4R07 TOPICS ON VARIATIONAL PRINCIPLES IN ENGINEERING 393
 Jiro Nakamichi
 Japan Aerospace Exploration Agency, Japan
- ISFA-4R10 DEVELOPMENT OF A SURGICAL INSTRUMENT USING AN ELASTIC VIBRATION WING MECHANISM 403
 Ren Ota, Ikuyo Yamamoto, Murray John Lawn, Takeshi Nagayasu, Naoya Yamasaki, Keitaro Matsumoto
 Nagasaki University, Japan
- ISFA-4R12 FLUTTER INHIBITION IN ANIMAL WINGS 407
 Yoshinobu Inada, Ryoya Saito
 Tokai University, Japan
- ISFA-4R13 DEVELOPMENT OF FLUTTER ANALYSIS TOOL USING NEXT-GENERATION CFD (COMPUTATIONAL FLUID DYNAMICS) ALGORITHMS 413
 Takaaki Yumitori⁺¹, Katsutoshi Ishikawa⁺¹, Keizo Takenaka⁺¹, Toshihiko Azuma⁺²
⁺¹Mitsubishi Heavy Industries, Ltd., Japan;
⁺²Japan Aircraft Development Corporation/ Churyo Engineering Co., Ltd., Japan

ISFA-4R15	NUMERICAL SIMULATION TECHNIQUE FOR AEROELASTIC RESPONSE USING INVERSE FOURIER TRANSFORM	421
	Tetsuhiko Ueda ⁺¹ , Kenichi Saitoh ⁺²	
	⁺¹ Nagoya University, Japan; ⁺² Japan Aerospace Exploration Agency, Japan	
ISFA-4R16	FLUTTER PREDICTION IN MODERN AIRCRAFT ENGINES AND GAS TURBINES	431
	Mikhail Kolotnikov ⁺¹ , Pavel Makarov ⁺² , Farrukh Abdukhakimov ⁺¹ , Vasily Vedenev ⁺¹	
	⁺¹ Lomonosov Moscow State University, Russia;	
	⁺² Gas Turbine Engineering Research and Production Center “Salut”, Russia	
ISFA-4R17	FLUTTER ANALYSIS AND EXPERIMENTS OF A RECTANGULAR SHEET NEAR SIDE WALLS	441
	Keiichi Hiroaki, Chihiro Kumakura, Masahiro Watanabe	
	Aoyama Gakuin University, Japan	
ISFA-4R19	LOW SPEED FLUTTER AND POST-CRITICAL BEHAVIOUR OF FLAT PLATE AND NACA0018 SECTION MODELS IN A WIND TUNNEL	447
	Xavier Amandolese	
	Ecole Polytechnique-CNRS, France	
ISFA-4R21	NUMERICAL STUDY ON ADAPTIVE WING STRUCTURE USING LEADING AND TRAILING EDGE FLAPS FOR REDUCTION OF BENDING MOMENT	457
	Kanata Fujii ⁺¹ , Tomohiro Yokozeki ⁺¹ , Hitoshi Arizono ⁺² , Masato Tamayama ⁺²	
	⁺¹ The University of Tokyo, Japan; ⁺² Japan Aerospace Exploration Agency, Japan	
ISFA-4R22	FLAT-PLATE HIGH-FREQUENCY SMALL THRUSTER ON A FREE SURFACE	467
	Yutaka Terao	
	Tokai University, Japan	
ISFA-4R23	AN EXAMPLE OF LANDING GEAR SHIMMY EXPERIENCE ON SMALL JET AIRCRAFT	475
	Kohei Inoue	
	Sumitomo Precision Products Co., LTD, Japan	

Energy Harvest

ISFA-5R01	BETZ ANALYSIS OF A SINGLE FLAPPING FOIL POWER GENERATOR	485
	John Young, Fang-Bao Tian, Joseph C.S. Lai	
	University of New South Wales, Australia	
ISFA-5R02	EFFECT OF ANGLE OF ATTACK ON VIBRATION CHARACTERISTICS OF A CANTILEVERED PRISM FOR ENERGY HARVEST	495
	Takahiro Kiwata, Aguri Nakajima, Shunichi Mizukami, Toshiyuki Ueno, Takaaki Kono	
	Kanazawa University, Japan	

ISFA-5R03	AEROELASTIC AND PERFORMANCE BASELINE ANALYSIS OF PIEZO-AEROELASTIC WING SECTION FOR ENERGY HARVESTER	505
	Harijono Djojodihardjo The Institute for the Advancement of Aerospace Science and Technology, Indonesia	
ISFA-5R04	PIEZOELECTRIC ENERGY HARVESTING FROM AEROELASTIC VIBRATION WITH COMPOSITE PLATE WINGS	517
	Masaki Kameyama ⁺¹ , Kanjuro Makihara ⁺² ⁺¹ Shinshu University, Japan; ⁺² Tohoku University, Japan	
ISFA-5R05	PENDULUM WITH HOOP-TYPE FLOW ENERGY CONVERTER SYSTEM	525
	Yutaka Terao Tokai University, Japan	
ISFA-5R06	A STUDY ON NUMERICAL SIMULATION OF WAVE ENERGY CONVERTER CONSIDERING NONLINEAR WAVE INTERACTION USING BEM	535
	Takeshi Kamio, Makoto Iida, Chuichi Arakawa The University of Tokyo, Japan	
ISFA-5R07	GALLOPING OSCILLATIONS OF PRISMS AND ENERGY HARVESTING IN WIND TUNNEL	545
	Pascal Hémon ⁺¹ , Xavier Amandolese ⁺¹ , Thomas Andrianne ⁺² ⁺¹ LadHyX, Ecole Polytechnique-CNRS, France; ⁺² University of Liège, Belgium	
ISFA-5R08	ENERGY RECOVERY CONCEPTS IN ACTIVELY CONTROLLED LCO INSTABILITIES CAUSED BY FREE-PLAY INDUCED AEROELASTIC FLUTTER	555
	Atul G. Kelkar ⁺¹ , Prachi Deshpande ⁺¹ , Jerald Vogel ⁺² ⁺¹ Iowa State University, USA; ⁺² VSI Aerospace, Inc., USA	
ISFA-5R09	RECENT FINDINGS ON STREAM-WISE FLUIDELASTIC INSTABILITY AND ITS APPLICATION	565
	Tomomichi Nakamura ⁺¹ , Njuki Mureithi ⁺² ⁺¹ Osaka Sangyo University, Japan; ⁺² Polytechnique Montreal, Canada	

Wind Turbine

ISFA-5R11	DYNAMIC BEHAVIOR OF PARKED WIND TURBINE AT EXTREME WIND SPEED	575
	Yoshitaka Totsuka ⁺¹ , Hiroshi Imamura ⁺¹ , Anders Yde ⁺² ⁺¹ Wind Energy Institute of Tokyo Inc., Japan; ⁺² Technical University of Denmark, Denmark	
ISFA-5R12	FIELD MEASUREMENT OF BLADE TIP RESPONSE OF A MEDIUM SIZE WIND TURBINE IN OPERATION	585
	Kichiro Kimura ⁺¹ , Hiroshi Torikai ⁺¹ , Masao Hosomi ⁺² , Eijiro Yukoku ⁺² ⁺¹ Tokyo University of Science, Japan; ⁺² KOMAIHALTEC Inc., Japan	

Galloping (Basic Sections)

- ISFA-2R13 LOW-SPEED GALLOPING FOR RECTANGULAR CYLINDERS WITH SIDE RATIOS LARGER THAN UNITY 591
 Claudio Mannini, Antonino M. Marra, Tommaso Massai, Gianni Bartoli
 University of Florence, Italy
- ISFA-2R14 LARGE AMPLITUDE AERODYNAMIC VIBRATION OF RECTANGULAR CYLINDER WITH A SIDE RATIO OF TWO 601
 Tomomi Yagi⁺¹, Hisato Matsumiya⁺², Masaaki Hamano⁺¹, Yuta Sasaki⁺¹, Takashi Nishihara⁺²
⁺¹Kyoto University, Japan; ⁺²Central Research Institute of Electric Power Industry, Japan

Galloping (Cables)

- ISFA-2R17 VIBRATIONS AND COUNTERMEASURES FOR CABLE STRUCTURE OF HONSHU-SHIKOKU BRIDGES 611
 Shigeki Kusuhara
 Honshu-Shikoku Bridge Expressway, Japan
- ISFA-2R19 AN OBSERVATION OF DRY GALLOPING AT CRITICAL REYNOLDS NUMBER IN NORMAL WIND 621
 Qingkuan Liu, Wenyong Ma, Xiaobing Liu
 Shijiazhuang Tiedao University, China
- ISFA-2R20 DRY GALLOPING OF SURFACE MODIFICATION CABLE IN LOW SCRUTON NUMBER RANGE 629
 Duy Hung Vo, Hiroshi Katsuchi, Hitoshi Yamada
 Yokohama National University, Japan
- ISFA-2R22 DRY GALLOPING CHARACTERISTIC AND VIBRATION CONTROL OF INCLINED STAY CABLE 639
 Tomo Tanaka⁺¹, Masaru Matsumoto⁺², Hiroshi Ishizaki⁺¹, Hiroshi Kibe⁺¹
⁺¹SE Corporation, Japan; ⁺²Kyoto University, Japan
- ISFA-2R23 COMPARATIVE ANALYSIS OF BRIDGE CABLES WITH CONCAVE FILLETS 649
 Celeste Burlina⁺¹, Christos T. Georgakis⁺¹, Søren V. Larsen⁺², Philipp Egger⁺³
⁺¹Technical University of Denmark, Denmark; ⁺²FORCE Technology, Denmark;
⁺³VSL International Ltd., Switzerland

VIV (Proto-Type Structures)

- ISFA-3R19 INFLUENCE OF NATURAL WIND TURBULENCE ON VORTEX SHEDDING EXCITATION, FROM REAL STRUCTURE EXPERIENCE 659
 Olivier Flamand⁺¹, Akis Panagis⁺², Aris Stathopoulos-Vlamiis⁺²
⁺¹CSTB, France; ⁺²GEFYRA, Greece

- ISFA-3R20 EFFECTS OF GAP DISTANCE ON VIV OF A PARALLEL CABLE-STAYED BRIDGE 665
 Jin Park, Ho-Kyung Kim
 Seoul National University, Korea
- ISFA-3R22 STUDY ON AERODYNAMIC VIBRATIONS OF A BRACING MEMBER WITH
 A RECTANGULAR CROSS SECTION OF A LONG-SPANDED TRUSS BRIDGE 669
 Kentaro Suda⁺¹, Kazutoshi Matsuda⁺¹, Kusuo Kato⁺¹, Yusuke Tamai⁺²
⁺¹Kyushu Institute of Technology, Japan; ⁺²Hitachi, Ltd., Japan

Wind Turbine

- ISFA-5R13 TIME-DOMAIN AEROELASTIC LOADS AND RESPONSE OF WIND TURBINE
 BLADES IN GUSTY WIND: PREDICTION AND EXPERIMENTAL VALIDATION 679
 Heather Scot Sauder, Partha P. Sarkar
 Iowa State University, USA
- ISFA-5R14 PRELIMINARY INVESTIGATION OF A FLAPPING VERTICAL AXIS WIND TURBINE 689
 Yutaka Terao
 Tokai University, Japan
- ISFA-5R16 FIELD MEASUREMENT OF THE MAIN SHAFT DYNAMIC LOADINGS ON A
 FIXED-SPEED ACTIVE STALL CONTROLLED 1MW WIND TURBINE 697
 Sho Oh
 ClassNK, Japan
- ISFA-5R17 AEROELASTIC STABILITY ANALYSIS OF OFFSHORE WIND TURBINE BLADES
 AT STANDSTILL CONDITION CONSIDERING UNSTEADY AERODYNAMICS 705
 Koji Fukami, Kai Karikomi, Akihiro Honda, Masaaki Shibata
 Mitsubishi Heavy Industries, Ltd., Japan
- ISFA-5R18 DYNAMIC ANALYSIS OF THE TWO-BLADED HORIZONTAL AXIS WIND TURBINE 711
 Shigemitsu Aoki, Tetsuya Kogaki, Kenichi Sakurai
 National Institute of Advanced Industrial Science and technology, Japan
- ISFA-5R19 NUMERICAL ANALYSIS OF THE EFFECTS OF A WIND TURBINE'S ROTATING
 BLADES ON THE AERODYNAMIC FORCES ON THE TOWER 723
 Takaaki Kono⁺¹, Satoshi Nebucho⁺¹, Tetsuya Kogaki⁺², Takahiro Kiwata⁺¹, Shigeo Kimura⁺¹,
 Nobuyoshi Komatsu⁺¹
⁺¹Kanazawa University, Japan;
⁺²National Institute of Advanced Industrial Science and Technology, Japan
- ISFA-5R20 EFFECTS OF MULTIDIRECTIONAL SEA STATES AND FLEXIBLE FOUNDATION
 ON DYNAMIC RESPONSE OF FLOATING OFFSHORE WIND TURBINE SYSTEM 729
 Shining Zhang, Takeshi Ishihara
 The University of Tokyo, Japan

- ISFA-5R22 WIND LOADS ON A BOTTOM-MOUNTED OFFSHORE WIND TURBINE TOWER 739
Kazumasa Okubo⁺¹, Manabu Yamamoto⁺¹, Yukinari Fukumoto⁺², Takeshi Ishihara⁺³
⁺¹Kajima Technical Research Institute, Japan;
⁺²Tokyo Electric Power Company Research & Development Center, Japan;
⁺³The University of Tokyo, Japan
- ISFA-5R23 TWO-DIMENSIONAL AEROELASTIC ANALYSIS OF A BRIMMED-DIFFUSER
SHROUD WITH COMPOSITE MATERIAL FOR A WIND TURBINE 747
Taeyoung Kim, Hiroto Nagai, Kousei Ono, Nobuhide Uda, Yuji Ohya
Kyushu University, Japan

DYNAMICS OF TUBULAR CYLINDRICAL STRUCTURES IN AXIAL FLOW

Michael P. Païdoussis

Department of Mechanical Engineering, McGill University, Montreal, QC, Canada

e-mail: michael.paidoussis@mcgill.ca

The dynamics of slender cylinders in axial flow subject to conventional boundary conditions is recalled first. This is followed by brief reviews and discussion of new developments in (i) the dynamics of unconventionally supported cylinders, e.g. cylinders free at the upstream end and supported at the downstream one, (ii) the dynamics of cylinders subject to both internal and external flow for applications in oil and gas drilling and production, as well as hydrocarbon storage in salt-mined caverns, and (iii) the peculiar dynamics of very long cylinders, such as acoustic streamers used in underwater oil and gas exploration.

Keywords: Cylinders in axial flow; dynamics; static divergence; single- and coupled-mode flutter; unconventionally supported cylinders; cylinders with both internal and external flow; very long cylinders.

1. DYNAMICS OF CYLINDERS IN AXIAL FLOW

Consider a cylinder, modelled as a beam, in axial flow. At low flow velocities, the cylinder is subject to flow-induced damping. At higher flow velocities, however, it may become subject to static and/or dynamic fluidelastic instabilities.

Let the cross-sectional area of the cylinder be A , its length L , diameter D , mass per unit length m , and flexural rigidity EI ; let also the mean axial flow velocity be U . For a horizontal system, neglecting pressurization and gravity effects as well as dissipative forces, the simplest form of the equation of motion is

$$EI \frac{\partial^4 y}{\partial x^4} + MU^2 \frac{\partial^2 y}{\partial x^2} + 2MU \frac{\partial^2 y}{\partial x \partial t} + \frac{1}{2} \rho DU^2 C_T (L-x) \frac{\partial^2 y}{\partial x^2} + \rho D^2 U^2 C_b \frac{\partial^2 y}{\partial x^2} + \frac{1}{2} \rho DUC_N \left(\frac{\partial y}{\partial t} + U \frac{\partial y}{\partial x} \right) + \frac{1}{2} \rho DC_D \frac{\partial y}{\partial t} + (M+m) \frac{\partial^2 y}{\partial t^2} = 0, \quad (1)$$

where $M = \rho A$ is the virtual or added mass per unit length for lateral motions in unconfined flow, ρ being the fluid density. C_N and C_T are the coefficients of the viscous forces acting on the cylinder in the normal and longitudinal direction, respectively, and C_D is the lateral force coefficient for zero axial flow; C_b is the base drag coefficient in case of a free end. The form above supposes that the downstream end can slide axially or is entirely free; more generally, $L-x$ above must be replaced by $[(1-\frac{1}{2}\delta)L-x]$ and C_b by $(1-\delta)C_b$, where $\delta = 0$ if the downstream end is free to slide axially or totally free, and $\delta = 1$ if the supports are fixed and do not allow any extension.

Comparing equation (1) to equation (A.1) for a cylinder or pipe with internal flow, we note that, apart from the terms associated with viscous forces, there is complete correspondence in the first, second and third terms, as well as the last one. Here, however, M is not a physical mass, but an equivalent mass of the external fluid flow according to the slender body approximation.

If the cylinder is subjected to an externally applied tension \bar{T} and pressurization \bar{p} , then a term equal to $-\{\delta [\bar{T} + (1-2\nu)\bar{p}A] (\partial^2 y / \partial x^2)\}$ would have to be added in the equation of motion, where ν is the Poisson ratio. Also, if the cylinder is vertical instead of horizontal, gravity and hydrostatic effects have to be taken into account.

Moreover, if the flow past the cylinder is laterally confined by proximity to the flow-containing channel or by the presence of adjacent structures, the added mass M is no longer equal to ρA but to $\chi \rho A$, where $\chi = [(D_{ch}^2 + D^2) / (D_{ch}^2 - D^2)] > 1$, in which D_{ch} is the diameter of the flow channel; for unconfined flow, $D_{ch} \rightarrow \infty$ and $\chi = 1$.

Taking these effects into account [refer to Païdoussis^(1),2)] and now considering a vertical geometry with the cylinder hanging in downward flow, the nondimensional version of the equation of motion may be written as

$$\begin{aligned} & \frac{\partial^4 \eta}{\partial \xi^4} + \{\chi u^2 - \delta [\Gamma + (1 - 2\nu)\Pi] - [\frac{1}{2}\varepsilon c_T u^2(1+h) + \gamma] [(1 - \frac{1}{2}\delta) - \xi] \\ & - \frac{1}{2}(1 - \delta)c_b u^2\} \frac{\partial^2 \eta}{\partial \xi^2} + 2\chi\beta^{1/2}u \frac{\partial^2 \eta}{\partial \xi \partial \tau} + [\frac{1}{2}\varepsilon c_N u^2(1+h) + \gamma] \frac{\partial \eta}{\partial \xi} \\ & + \left[\frac{1}{2}\varepsilon c_N \beta^{1/2} u + \frac{1}{2}\varepsilon c \beta^{1/2} \right] \frac{\partial \eta}{\partial \tau} + [1 + (\chi - 1)\beta] \frac{\partial^2 \eta}{\partial \tau^2} = 0, \end{aligned} \quad (2)$$

where

$$\xi = x/L, \quad \eta = y/L, \quad \tau = \{EI/(m + \rho A)\}^{1/2} t/L^2 \quad (3)$$

and

$$\begin{aligned} \beta &= \frac{\rho A}{\rho A + m}, \quad \gamma = \frac{(m - \rho A)g L^3}{EI}, \quad \Gamma = \frac{\bar{T}L^2}{EI}, \\ \varepsilon &= \frac{L}{D}, \quad u = \left(\frac{\rho A}{EI}\right)^{1/2} UL, \quad \Pi = \frac{\bar{p}AL^2}{EI}, \quad h = \frac{D}{D_h}, \\ c_N &= \frac{4}{\pi}C_N, \quad c_T = \frac{4}{\pi}C_T, \quad c_b = \frac{4}{\pi}C_b, \quad c = \frac{4}{\pi} \left(\frac{\rho A}{EI}\right)^{1/2} LC_D. \end{aligned} \quad (4)$$

The approximation $c_N = c_T = c_f$ is sometimes used, as in the calculations for some of the figures to be discussed next.

Additional parameters need to be introduced for cantilevered cylinders, presumed to be terminated by an ogival end-piece, notably f which is a measure of how well streamlined the free end is. The simplest free-end boundary conditions are that at $\xi = 1$ the bending moment is zero and the shear force is

$$\frac{\partial^3 \eta}{\partial \xi^3} + \chi f u^2 \frac{\partial \eta}{\partial \xi} + \chi f \beta^{1/2} u \frac{\partial \eta}{\partial \tau} - \{1 + (\chi f - 1)\beta\} \chi_e \frac{\partial^2 \eta}{\partial \tau^2} = \frac{\partial^2 \eta}{\partial \xi^2} = 0, \quad (5)$$

in which $f \rightarrow 1$ for a well-streamlined end, and $f \rightarrow 0$ for a blunt one; $\chi_e = (1/AL) \int_{L-l}^L A(x)dx$, l being the length of the end-piece.

In this paper, the dynamics is discussed with the aid of Argand diagrams of the dimensionless complex eigenfrequencies of the system, ω_j , as a function of the dimensionless axial flow velocity, u . A typical such diagram for a pinned-pinned cylinder in axial flow is shown in Figure 1. The imaginary components of the first- and second-mode eigenfrequencies, $\mathcal{I}m(\omega_j)$, $j = 1$ and 2, are plotted versus the real parts, $\mathcal{R}e(\omega_j)$, as a function of u . Here,

$$\omega_j = [(\rho A + m)/EI]^{1/2} \Omega_j L^2, \quad (6)$$

and Ω_j the j th radian eigenfrequency; u is defined in (4).

Displacements of the cylinder in the j th mode are expressed as $\eta_j(\xi, \tau) = F(\xi) \exp(i\omega_j \tau)$, where $\xi = x/L$ and $\omega_j = \mathcal{R}e(\omega_j) + i\mathcal{I}m(\omega_j)$; τ is the dimensionless time. Thus, $\eta(\xi, \tau) \propto \exp[-\mathcal{I}m(\omega_j)] \exp[i\mathcal{R}e(\omega_j)\tau]$. If $\mathcal{I}m(\omega_j) > 0$, motions are damped, whereas if $\mathcal{I}m(\omega_j) < 0$ they are amplified. In the latter case, if $\mathcal{R}e(\omega_j) \neq 0$, the amplified motions are oscillatory, and hence the instability is termed *flutter*; if $\mathcal{R}e(\omega_j) = 0$, we have nonoscillatory amplified motion, i.e. a *static divergence* — or simply *divergence*, for short.

Thus, in Figure 1, oscillations in the first mode are damped for $u < \pi$ approximately. For $u > 3.1406$, $\mathcal{R}e(\omega_1) = 0$ is reached, and the locus of the first mode bifurcates on the $\mathcal{I}m(\omega)$ -axis; one branch crosses the origin at slightly higher u , say $u = u_{cd}$. Thereafter, $\mathcal{R}e(\omega_1) = 0$, and $\mathcal{I}m(\omega_1) < 0$ for that branch of the solution, indicating that a static divergence has occurred at u_{cd} .

At higher u , the first-mode locus which had split into two, as shown in the diagram on the left of the figure, recombines on the $\mathcal{I}m(\omega)$ -axis and then leaves it, such that $\mathcal{I}m(\omega_1) < 0$ while $\mathcal{R}e(\omega_1) > 0$,

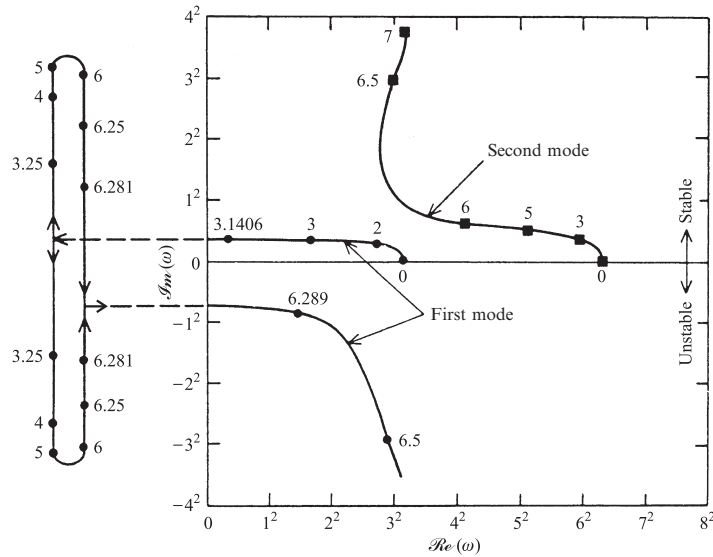


Figure 1: Argand diagram of complex frequencies, ω , of the lowest two modes of a pinned-pinned cylinder in unconfined axial flow, as functions of u for $\beta = 0.48$, $\varepsilon c_f = 0.25$ ($c_f = c_T = c_N$), $\delta = \chi = 1$, $c = h = \gamma = \Gamma = 0$; Ref 23).

indicating amplified oscillation (flutter) at a value of u a little higher than $u \simeq 6.281$.^{*} The second-mode locus is always stable in this case, indicating damped oscillation in that mode throughout.

The flutter in Figure 1, which arises from a statically unstable state, is nowadays commonly referred to as a *Païdoussis coupled-mode flutter*, as originally christened by Done & Simpson^{3),4)}, in contradistinction to classical coupled-mode flutter.^{5),6)}

The dynamics of a cantilevered system is illustrated in Figure 2. Here it is seen that the system loses stability by static divergence in its first mode at a value of u a little higher than $u = 2$; it then regains stability in that mode at $u \simeq 5$. For $u \simeq 5.2$, however, stability is lost in the second mode by single-mode flutter via a Hopf bifurcation. Stability is regained in that mode at $u \simeq 8.6$, but meanwhile flutter in the third mode has occurred at $u \simeq 8.25$.

Changing the system parameters, e.g. β or εc_f , alters the dynamics, but the qualitative behaviour generally remains the same. In the case of a cantilevered cylinder, two parameters have a profound effect on the dynamics: f , the free-end streamlining parameter ($f \rightarrow 1$ for a well-streamlined free end, and $f \rightarrow 0$ for a blunt end), and c_b , a form drag coefficient at the free end. For a sufficiently blunt end ($f \rightarrow 0$, $c_b > 0$) a cantilevered cylinder remains stable, no matter how high u becomes.

It is of considerable interest that for systems subject to a sequence of instabilities as predicted by linear analysis and as shown in Figures 1 and 2, the nonlinear dynamics is not radically different; i.e. the second and higher instabilities predicted by linear theory actually materialize in the nonlinear realm, as they do in the experiments, though the sequence of the bifurcations involved may not be quite the same. In this regard, the routes to instability and the dynamics are quite different from that of the kindred system of a pipe conveying fluid^{4),5)}.

The behaviour of tapered cylinders in axial flow may also be quite different from that just described, because the boundary layer around the cylinder can become quite thick, thus creating an ‘insulating effect’ *vis-à-vis* the mean flow.

^{*}Although this flutter is generated by coalescence of branches of the same mode, we still call it a *coupled-mode flutter* — as would be the normal notation if the coalescing branches belonged to two different modes.

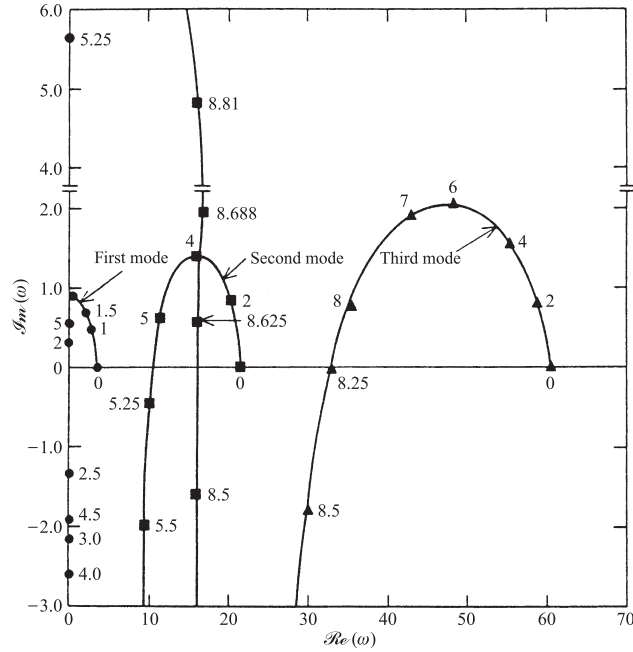


Figure 2: Argand diagram of the complex frequencies, ω , of the lowest three modes of a solitary cantilevered cylinder with a tapered free end in unconfined axial flow, as functions of u , for $\beta = 0.5$, $\varepsilon c_f = 1$, $\delta = 0$, $\chi = 1$, $f = 0.8$, $\chi_e = 0.01$, $c_b = \gamma = 0$; Ref²³⁾.

2. UNCONVENTIONALLY SUPPORTED CYLINDERS IN AXIAL FLOW

The dynamics of ‘aspirating cantilevered pipes’, i.e. with the flow entering at the free end and exiting at the clamped end, was first studied by Païdoussis in the 1960s as a curiosity and then in 1985 in a simplistic, as it turned out in retrospect, analysis related to ocean mining applications. Later, a number of more elaborate models by Kuiper & Metrikine and Païdoussis *et al.* predicted that the system is unstable either at very low (infinitesimal in the absence of dissipation) flow velocities, or never, with the pendulum of predictions swinging to and fro¹⁾. The latest is that, for high enough flow velocities, a very weak form of flutter may arise, depending on the fine details of the flow at inlet; refer to Giacobbi *et al.*⁷⁾ and section 4.3 of Païdoussis⁵⁾.

In the process, this ‘reverse flow’ problem was related to another, namely that of the reverse (aspirating) sprinkler which has exercised the Physics community from the time of Richard Feynman on, with the same reverses of opinion, as to whether it would rotate or not, and in what sense, as for the potential flutter of the aspirating pipe; refer to Jenkins⁸⁾.

Indeed, the study of fluid-structure interactions involving ‘reverse flow’ has become fashionable. Rinaldi & Païdoussis⁹⁾ studied the dynamics of ‘free-clamped’ cylinders in axial flow; i.e. with the upstream end free and the downstream end clamped, both experimentally and theoretically. For relatively low flow velocities ($U \simeq 5$ m/s, $u \simeq 0.36$), flutter-like oscillatory motions of very small amplitude A_{rms} were observed, such that $A_{\text{rms}}/D \sim \mathcal{O}(10^{-3})$, of first-mode frequency and cylinder shape. The oscillation was quite unsteady, with maximum amplitudes 2.5 times the r.m.s. values, similarly to observations for aspirating pipes. Beyond a certain flow velocity, the oscillation amplitude decreased, while a steady bow in the pipe developed and grew, following the classical route to divergence. Thus the system displayed flutter-like oscillations at low flow velocities, and divergence at higher flow velocities. The effect of the upstream-end shape was surprisingly weak.

The flutter-like motions occurred at $u = 0.3 - 0.4$, which is consistent with the predicted behaviour (very small, marginally positive $\mathcal{I}m(\omega_1)$) in Figure 3. However, the discrepancy between the experimental critical flow velocity for divergence, $u_{cd} \simeq 1.1 - 1.7$, and the theoretical $u_{cd} > 2.4$ is rather larger than

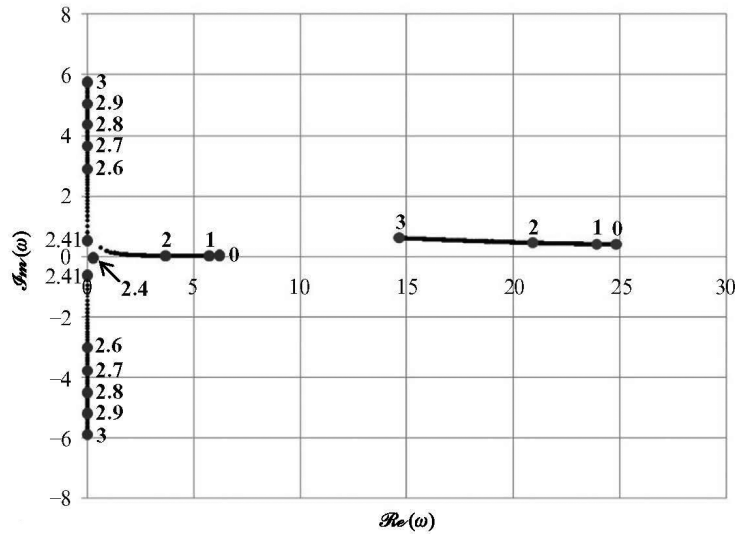


Figure 3: Argand diagram of the lowest two complex eigenfrequencies of a free-clamped cylinder in axial flow for $f = 0.80$ and $c_b = 0.60$, as functions of u ; $\beta = 1.14 \times 10^{-3}$, $\gamma = 17.6$, $\varepsilon = 25.3$, $h = 0.455$, $\chi = 1.22$, $\chi_e = 0.00792$, $c_N = 0.010$, $c_T = 0.0125$, and dissipative coefficients $\bar{\alpha}^* = 0.0003$, $\bar{\mu}^* = 0.0358$; Ref⁹⁾.

what could comfortably be attributed to the effect of imperfections; rather, suggesting imperfections in the theory!

The dynamics of pinned-free cylinders was long considered to be not particularly interesting, because the system was thought to be quite similar to a cantilevered one. The problem was re-studied recently by Kheiri & Païdoussis¹⁰⁾, considering a flexibly supported cylinder, as shown in Figure 4, with varying stiffnesses at the support. The pinned-free system was simulated by taking a large value for the transla-

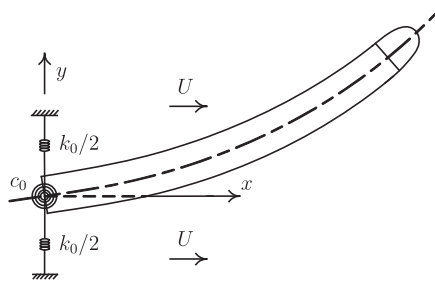


Figure 4: A flexible cylinder subjected to axial flow and supported only at the upstream end by a translational and a rotational spring of stiffnesses k_0 and c_0 , respectively.

tional spring stiffness k_0 and zero for the rotational spring stiffness c_0 . It was found that the cylinder is unstable from essentially zero flow velocity, the instability being in the form of stationary yawing, as seen in Figure 5; here $\varepsilon^* = \frac{1}{2}\varepsilon c_f$. At higher flow velocities, static/dynamic instabilities in the first and higher modes of the system may occur. It was also found that, by increasing the length of the cylinder while keeping all other parameters constant, the critical flow velocities for various instabilities asymptotically approach constant values; in other words, increasing the length of the cylinder beyond a certain value affects the stability of the system only weakly. Moreover, it was shown numerically and confirmed analytically that there is a limiting value for the length of the cylinder, dependent only on the shape of the tapering end, below which a zero-flow instability may not occur.

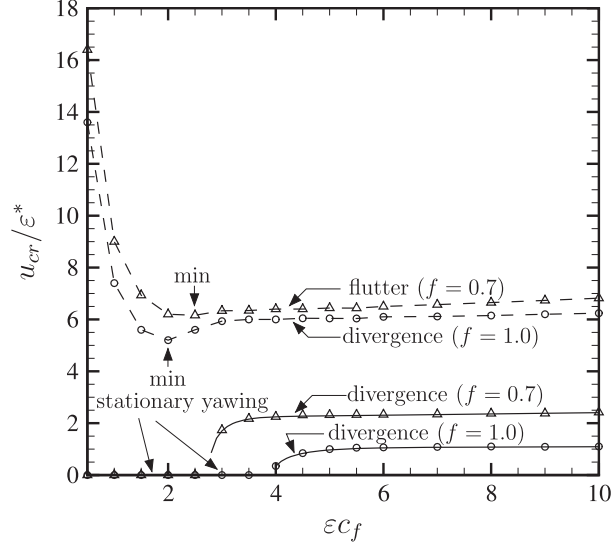


Figure 5: Variation of the critical flow velocity u_{cr}/ε^* , where $\varepsilon^* = \frac{1}{2}\varepsilon c_f$, for static and dynamic instability of a flexible neutrally buoyant (i.e. $\beta = 0.5$) pinned-free cylinder as a function of εc_f ($\varepsilon c_f = \varepsilon c_N = \varepsilon c_T$), in the case of $c_b = 1 - f$; Ref ¹⁰).

Additional insights into the dynamics is afforded from consideration of the related problem of a pipe conveying fluid, spring-supported at the upstream end by a translational and a rotational spring; refer to Kheiri *et al.*¹¹). It is found that there are ranges in which the critical flow velocity does not change with varying either of the spring stiffnesses. It is also shown that, as the stiffnesses are reduced to low values, the system behaviour approaches that of a free-free pipe: the critical flow velocity is diminished and finally approaches zero.

3. CYLINDERS WITH BOTH INTERNAL AND EXTERNAL FLOW

The dynamics of this system was first studied by Cesari & Curioni¹²) and Hannover & Paidoussis¹³) for its own sake and for applications in axial-flow heat exchangers. The two flows (the fluids and flow velocities) are independent of each other. Later studies were motivated by applications to the drill-string system used in oil and gas drilling pipes; in this case, the internal flow in a vertical pipe, after exiting the drill-bit at the bottom, reverses direction and carries the drilled-out debris upward around the drill-pipe; thus, the internal and external flows are related. This system was first studied by Luu¹⁴) and Paidoussis, Luu & Prabhakar¹⁵).

Argand diagrams for a realistic large-scale drill-string system ($L = 1000$ m) and a bench-top system ($L = 0.443$ m) display qualitatively similar dynamics. Here the dimensionless flow velocities of the internal and external flows, u_i and u_o respectively, are related, depending on $\alpha = D_i/D_o$ and $\alpha_{ch} = D_{ch}/D_o$, where D_i and D_o are the inside and outside diameters of the pipe, and D_{ch} is the diameter of the drilled-out channel. In this case we define two dimensionless flow velocities:

$$u_i = (\rho A_i/EI)^{1/2} U_i L \quad \text{and} \quad u_o = (\rho A_o/EI)^{1/2} U_o L, \quad (7)$$

where A_i is the cross-sectional flow area of the internal flow, U_i the internal flow velocity, and u_o is the same as u_i in equations (4) with $A \equiv A_o$ and $U \equiv U_o$.

For a wide channel ($\alpha_{ch} = 20$), the dynamics is controlled by the internal flow, as u_i is three orders of magnitude larger than u_o . For small enough u_i , the effect of flow is stabilizing, but for higher u_i it becomes destabilizing (in this case at $u_i \simeq 100$). Similar behaviour is obtained for $\alpha_{ch} = 2$, even though in this case $u_o = 0.3u_i$. For $\alpha_{ch} = 1.1$, however, where $u_o = 4.28u_i$, the external flow plays the dominant role, destabilizing the system and precipitating flutter at $u_i = 0.96$.

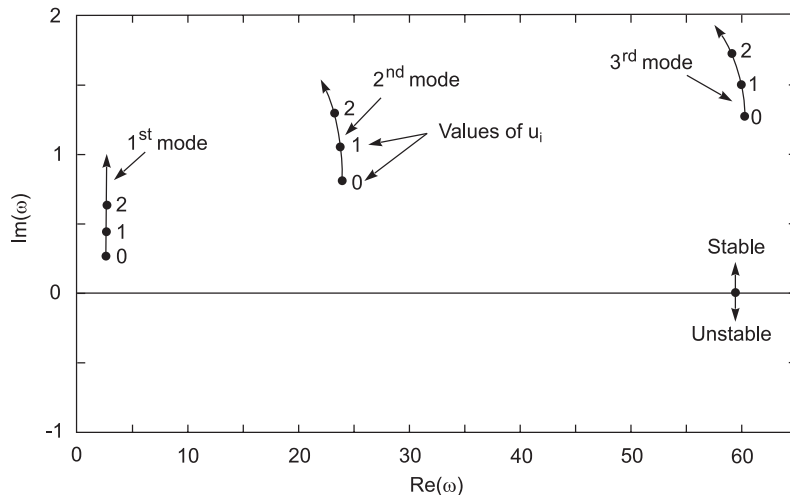


Figure 6: Argand diagram of the complex dimensionless eigenfrequencies of the bench-top-size drill-string-like system, ω_i , $i = 1, 2, 3$ as a function of the dimensionless flow velocity u_i for $\alpha_{ch} = 2.0$.

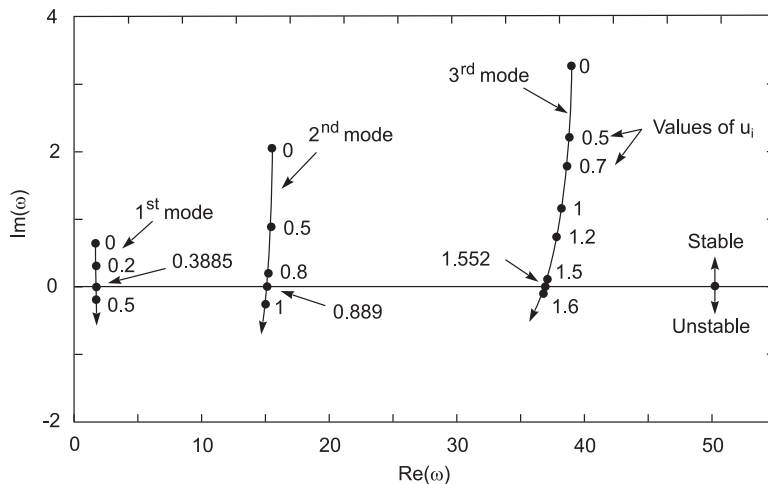


Figure 7: Argand diagram of the complex dimensionless eigenfrequencies of the bench-top-size drill-string-like system, ω_i , $i = 1, 2, 3$ as a function of the dimensionless flow velocity u_i for $\alpha_{ch} = 1.2$.

Similar behaviour is obtained for the bench-top system. As seen in Figure 6 for $\alpha_{ch} = 2.0$, the system is stabilized with increasing flow, as indicated by the increasing positive $\mathcal{I}m(\omega)$ in all the three modes shown. However, for large enough u_i the effect of flow becomes destabilizing; the loci of the second and third modes begin to bend, a preamble to the locus eventually crossing to $\mathcal{I}m(\omega) < 0$ (cf. Figure 2). In this case, the critical flow velocity is $u_{ic} = 6.8$ (not shown).

In Figure 7, on the other hand, where $\alpha_{ch} = 1.2$, the effect of the flow is destabilizing for all u_i . The system loses stability by flutter in the first mode at $u_i \simeq 0.39$. Thus, for large α_{ch} the dynamics is controlled by the internal flow, whereas for small enough α_{ch} it is the external flow which determines stability.

It should finally be remarked that the dimensionless critical flow velocities, u_{ic} , for both the large-scale and bench-top systems are similar, despite large differences in the parameters, particularly L , because the dimensional critical flow velocities for the longer system are proportionately smaller. Thus u_i is a successful scaling parameter.

Further work on this topic has recently been done, related to yet another application: the dynamics of the kilometer long pipe-strings used in salt-mining applications (Ratigan¹⁶); Moditis *et al.*¹⁷); Païdoussis²) for storing and later retrieving hydrocarbons in solution-mined caverns. Pumping fresh water into underground salt deposits dissolves the salt, generating brine-filled caverns. If the brine is pumped out, there remains a cavern which may be used for storage of liquid or gaseous hydrocarbons. In this case the pipe-string is partly surrounded by a cylindrical tube, creating an annular region. Brine may be pumped into the cavern via the central pipe, forcing the stored hydrocarbon out through the annulus, or *vice versa*. The dynamics is both intricate and quite interesting.

4. VERY LONG CYLINDERS AND STRINGS IN AXIAL FLOW

If the cylinder is sufficiently long and slender, flow-induced tension effects become very important, while the flexural rigidity loses its dominance as the principal restoring force. Thus, the cylinder may be modelled as a taut string, rather than a beam, which also results in a mathematically simpler system.

Here the reader is encouraged to refer to the Doaré & de Langre¹⁸) study of very long hanging pipes conveying fluid, showing the existence of asymptotic regimes in the dynamics, a paradigm for understanding the behaviour of long systems subjected to nonconservative forces.

Towed arrays of hydrophones housed in very long, neutrally buoyant hollow cylinders are the premier example making such systems of practical, as well as academic, interest. In some cases, the existence of a towrope is neglected, and the system is modelled as a cylindrical string supported at its upstream end and free downstream. The dynamics of this latter system is discussed here, while that of towed systems in chapter 4 of Païdoussis²).

Several analytical studies on the dynamics of this system have been published, unfortunately some based on the equations of motion in Païdoussis¹⁹), containing an error in the viscous forces, which becomes significant for long cylinders, and in other papers with other errors, e.g. Ortloff & Ives²⁰).

An important study on this system has been done by Triantafyllou & Chrystostomidis²¹) with the corrected equations of motion^{22,23}) in a very elegant analysis, resulting in a remarkably simple stability diagram. The flexural forces are neglected, and tension becomes the main restoring force. The nondimensional equation of motion is

$$[1 - p - \varepsilon^*(1 - \xi)] \frac{\partial^2 \eta}{\partial \xi^2} + 2 \frac{\partial^2 \eta}{\partial \xi \partial \tau} + \varepsilon^* \left(\frac{\partial \eta}{\partial \tau} + \frac{\partial \eta}{\partial \xi} \right) + (1 + \mu) \frac{\partial^2 \eta}{\partial \tau^2} = 0, \quad (8)$$

subject to boundary conditions

$$\eta(0, \tau) = 0, \quad [(p - f)(\partial \eta / \partial \xi) - f(\partial \eta / \partial \tau)]_{\xi=1} = 0, \quad (9)$$

where

$$\xi = \frac{x}{L}, \quad \eta = \frac{y}{L}, \quad \tau = \left(\frac{U}{L} \right) t, \quad p = \frac{T_0}{MU^2}, \quad \varepsilon^* = \frac{1}{2} \varepsilon c_f \quad \text{and} \quad \mu = \frac{m}{M} = \frac{1 - \beta}{\beta}; \quad (10)$$

here m is the mass of the cylinder and M the virtual (added) mass per unit length, f is a streamlining parameter, as in equation (5), such that $f \rightarrow 1$ for a well-streamlined end and $f \rightarrow 0$ for a blunt one, T_0 is the free-end tension as in Figure 8, e.g. due to a drogue, but constant rather than flow-velocity dependent.

The stability diagram is shown in Figure 9. Thus, for $\varepsilon^* > 1$ the system is predicted to be unconditionally stable. In the dimensional form of equation (8), the first term is $[MU^2 - T_0 - \frac{1}{2} \rho DU^2 C_f (L - x)] (\partial^2 y / \partial x^2)$. Hence, in the range $1 - \varepsilon^* < p < 1$ the total tension, $T(x) = T_0 + \frac{1}{2} \rho DU^2 C_f (L - x)$, becomes equal to MU^2 somewhere along the long string. From thereon there is no tensile restoring force,[†] and the neglected flexural forces, even if vanishingly small, become important and may have a destabilizing effect on the string.

The stability analysis leading to Figure 9 explicitly presumes the instability to be flutter, since static divergence for a string is not possible, as it would imply the existence of negative tension (compression)

[†]No self-respecting string can exist without tension, for it is then indistinguishable from a limp strand of overcooked spaghetti.

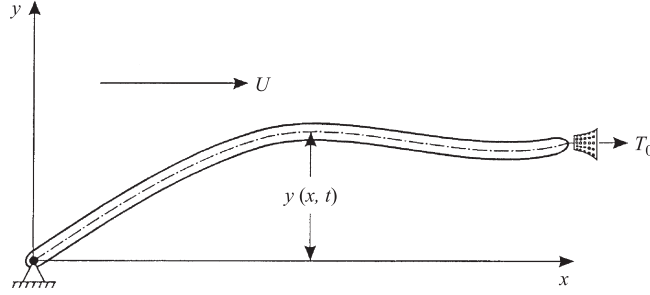


Figure 8: The pinned-free cylinder in axial flow considered by Triantafyllou & Chryssostomidis²¹⁾, with a drogue added which generates a tension T_0 at the free end.

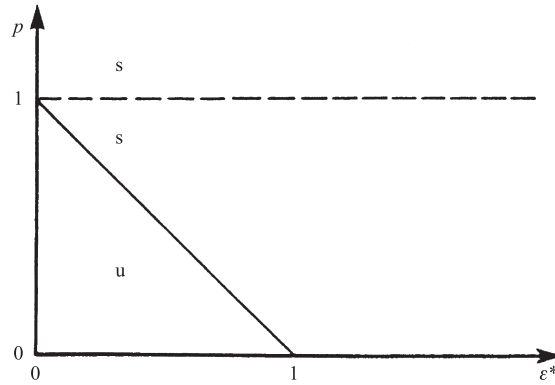


Figure 9: Stability diagram for a pinned-free cylinder in axial flow in terms of the modified slenderness parameter ε^* and the tension parameter p . Stable regions are denoted by s, and the unstable one by u; Ref²¹⁾.

over some portion of the string. It is therefore necessary to take into account the flexural restoring forces even for long cylinders, as done by de Langre *et al.*²⁴⁾.

Placing the origin for $\xi = x/L$ at the downstream end of the cylinder, the analysis is conducted by means of a slightly different form of the equation of motion,

$$\begin{aligned} \frac{\partial^4 \eta}{\partial \xi^4} + \frac{\partial}{\partial \xi} \left[u^2 \left(1 - \frac{1}{2} c_b + \frac{1}{2} \varepsilon c_T \xi \right) \frac{\partial \eta}{\partial \xi} \right] + \frac{1}{2} \varepsilon c_T \left(\frac{c_N}{c_T} - 1 \right) u^2 \frac{\partial \eta}{\partial \xi} \\ + \frac{1}{2} \varepsilon c_T \left(\frac{c_N}{c_T} \right) \beta^{1/2} u \frac{\partial \eta}{\partial \tau} + 2\beta^{1/2} u \frac{\partial^2 \eta}{\partial \xi \partial \tau} + \frac{\partial^2 \eta}{\partial \tau^2} = 0, \end{aligned} \quad (11)$$

and simplified boundary conditions,

$$\begin{aligned} \eta(-1) = \frac{\partial \eta}{\partial \xi}(-1) = 0, \\ \left[\frac{\partial^2 \eta}{\partial \xi^2} \right]_{\xi=0} = \left[\frac{\partial^3 \eta}{\partial \xi^3} + f u \left(\beta^{1/2} \frac{\partial \eta}{\partial \tau} + u \frac{\partial \eta}{\partial \xi} \right) \right]_{\xi=0} = 0. \end{aligned} \quad (12)$$

It is clear that in (11) there generally exists a location $\xi_c = -L_c/L = -(2 - c_b)/\varepsilon c_T$, where the flow-induced tension vanishes; this location is referred to as the *neutral point*. Downstream of that point the cylinder is *in compression*. This at-first-sight surprising statement becomes perfectly understandable by reference to the similar system of a pipe conveying fluid [refer to Appendix A].

The analysis is pursued in terms of the above equations, but also in terms of similar but significantly different ones in which the scaling length is not L but L_c ; thus,

$$z = x/L_c, \quad v = (\rho A/EI)^{1/2} U L_c = u/l, \quad l = L/L_c, \quad (13)$$

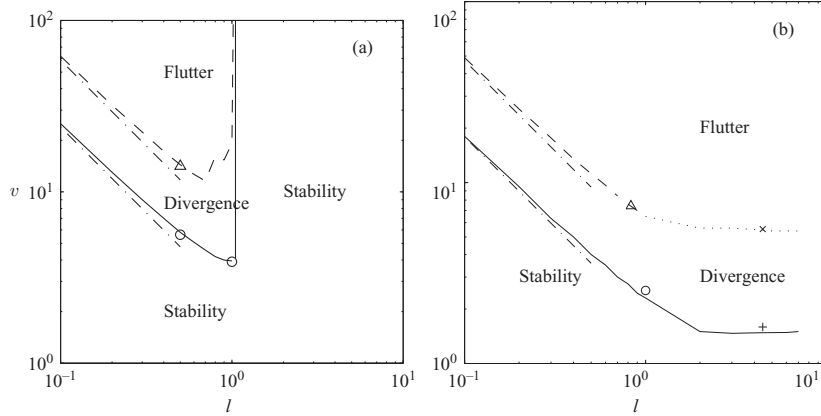


Figure 10: Effect of length on the stability of a cylinder, (a) for a system stable at high enough l , with $f = 0.5$, (b) for a system unstable at high l , with $f = 0.8$: —, critical flow velocity for divergence; - - -, critical value for flutter by Hopf bifurcation; · · ·, critical value for Païdoussis-type flutter; - · - ·, critical value for divergence and flutter of short cylinders; o, Δ , for cylinders of intermediate length; \times , +, for long cylinders; Ref ²⁴).

etc. Numerical results are obtained via the Galerkin method^{4),1)} and a finite difference scheme²⁵⁾. Interesting new results are obtained, supplemented by some determined earlier by Semler *et al.*²⁶⁾, as shown in Figure 10.

For a fairly blunt end ($f = 0.5$), it is seen in Figure 10(a) that both divergence and flutter cease to exist for $l \geq 1$. In terms of dependence on length, Semler *et al.*²⁶⁾ find that divergence occurs at $u = 2.39/l$, which compares well with the Semler *et al.* results. Similarly, $v = 5.87/l$ for flutter, which again gives results consistent with those of Semler *et al.*

For a well-streamlined end, $f = 0.8$, on the other hand, both divergence and flutter persist to $l \simeq 10$ (Figure 10(b)) and beyond, in both cases reaching a plateau for $l \geq 2$ approximately. For small l the flutter is via a Hopf bifurcation, while for $l > 1$ it is of the Païdoussis coupled-mode type.

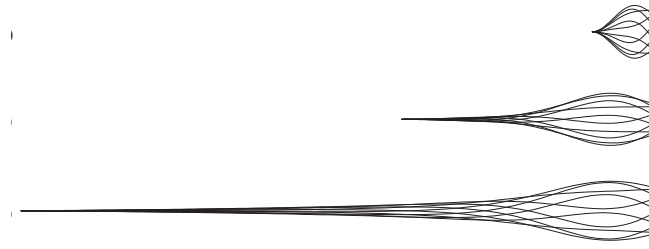


Figure 11: Modal shapes of the flutter modes for $f = 0.8$: and, top to bottom, $l = 0.5, 2$ and 5 , respectively; Ref ²⁴).

In Figure 11 we see the shape of the unstable mode for several values of l . The flutter mode shape is evaluated at $v \simeq 1.1v_c$, neglecting the imaginary component of the frequency (the growth rate) for clarity. These results confirm the existence of limit regimes for long cylinders where both divergence and flutter exist, with the motion confined to a downstream portion of the cylinder, typically of size L_c .

The existence of flutter for very long cylinders contradicts previous predictions of the dynamics by Triantafyllou & Chryssostomidis²¹⁾ and Dowling²⁷⁾. Below, we discuss how this has come about, despite all analyses being free of error.

In the Triantafyllou & Chryssostomidis analysis, the cause of instability is related to the disappearance of tension, i.e. the absence of any stiffness in the system. However, in the de Langre *et al.*²⁴⁾ analysis it is shown that the presence of even a small bending rigidity is sufficient to stabilize the system for small enough f . Therefore, the string model is inappropriate for assessing stability of cylinders of small bending stiffness.

The reason why flutter is not predicted in the Dowling analysis is simpler. For long cylinders, flutter is of the Païdoussis type, emanating from a static divergence solution, which we know does exist (Triantafyllou & Cryssostomidis²⁸). In the Dowling analysis divergence is excluded, as it implies the existence of negative tension, and thereby so is flutter.

The most important findings of this work are that (i) long cylinders with a streamlined free end are not immune to flutter and (ii) the dynamics of long cylinders may be approximated by that of cylinders of length L_c .

CONCLUSION

The dynamics of tubular cylindrical structures in axial flow has been reviewed briefly in this paper, focusing on new developments, as discussed in Sections 2-4. Several other facets of the system have been explored over the past 10-15 years, but are not discussed in this paper, for example (i) flexible cylinders being extruded or deployed in dense fluid, (ii) self-propelled articulated cylinders modelling trains going through tunnels, pipelines towed underwater for installation farther afield, propulsion of autonomous underwater vehicles and aquatic drones, including a great deal of new work on fish locomotion. The interested reader is referred to chapters 3 and 4 of Païdoussis²).

APPENDIX A: DYNAMICS OF A PIPE CONVEYING FLUID

As discussed in Païdoussis^{4,5)} at length, the simplest form of the equation of motion of a pipe conveying fluid is

$$EI \frac{\partial^4 y}{\partial x^4} + MU^2 \frac{\partial^2 y}{\partial x^2} + 2MU \frac{\partial^2 y}{\partial x \partial t} + (M + m) \frac{\partial^2 y}{\partial t^2} = 0, \quad (\text{A.1})$$

where all the symbols have the same meaning as in the main text of this paper, except that M here is the mass of the conveyed fluid per unit length. The first term is the flexural restoring force, the third is the Coriolis force, and the second is the follower compressive force term; cf. the equation of motion of a beam subject to a compressive force P ,

$$EI(\partial^4 y / \partial x^4) + P(\partial^2 y / \partial x^2) + m(\partial^2 y / \partial t^2) = 0. \quad (\text{A.2})$$

The viscous frictional terms in (1) do not exist for internal flow.

For a cantilevered cylinder in axial flow, we also have a tension due to traction. As discussed in Section 4, beyond the neutral point, the flow-induced tension vanishes, and the cylinder is under compression. The system loses stability by static divergence, and at higher flow velocities by Païdoussis-type coupled-mode flutter. For a short cylinder, however, flutter can arise via a Hopf bifurcation, as in Figure 2.

ACKNOWLEDGEMENT

Support of this research by the Natural Sciences and Engineering Research Council of Canada (NSERC), the Salt Mining Research Institute (SMRI) and Pipeline Research Council International (PRCI) is gratefully acknowledged.

REFERENCES

- 1) Païdoussis, M.P.: *Fluid-Structure Interactions: Slender Structures and Axial Flow*, Volume 2. London: Elsevier Academic Press, 2004.
- 2) Païdoussis, M.P.: *Fluid-Structure Interactions: Slender Structures and Axial Flow*, Volume 2, 2nd edition. London: Elsevier Academic Press, 2016.
- 3) Done, G.T.S., Simpson, A.: Dynamic stability of certain conservative and non-conservative systems. *I.Mech.E. J. Mech. Eng. Sci.*, Vol. 19, pp. 251-263, 1977.

- 4) Païdoussis, M.P.: *Fluid-Structure Interactions: Slender Structures and Axial Flow*, Volume 1. London: Academic Press, 1998.
- 5) Païdoussis, M.P.: *Fluid-Structure Interactions: Slender Structures and Axial Flow*, Volume 1, 2nd edition. London: Elsevier Academic Press, 2014.
- 6) Païdoussis, M.P., Price, S.J., de Langre, E.: *Fluid-Structure Interactions: Cross-Flow-Induced Instabilities*. Cambridge: Cambridge University Press, 2011.
- 7) Giacobbi, D.B., Rinaldi, S., Semler, C., Païdoussis, M.P.: The dynamics of a cantilevered pipe aspirating fluid studied by experimental, numerical and analytical methods. *J. Fluids Struct.*, Vol. 30, pp. 73-96, 2012
- 8) Jenkins, A.: Sprinkler head revisited: momentum, forces and flows in Machian propulsion. *Eur. J. Physics*, Vol. 32, pp. 1213-1226, 2011.
- 9) Rinaldi, S., Païdoussis, M.P.: Theory and experiments on the dynamics of a free-clamped cylinder in confined axial air-flow. *J. Fluids Struct.* Vol. 28, pp. 167-179, 2012.
- 10) Kheiri, M., Païdoussis, M.P.: Dynamics and stability of a flexible pinned-free cylinder in axial flow. *J. Fluids Struct.*, Vol. 55, pp. 204-217, 2015.
- 11) Kheiri, M., Païdoussis, M.P., Amabili, M.: An experimental study of dynamics of towed flexible cylinders. *J. Sound Vib.*, Vol. 348, pp. 149-166, 2015.
- 12) Cesari, F., Curioni, S.: Buckling instability in tubes subject to internal and external axial fluid flow. In *Proc. 4th Conf. on Dimensioning*, Budapest: Hungarian Academy of Science, pp. 301-311, 1971.
- 13) Hannoyer, M.J., Païdoussis, M.P.: Instabilities of tubular beams simultaneously subjected to internal and external axial flows. *ASME J. Mech. Design*, Vol. 100, pp. 328-336, 1978.
- 14) Luu, T.P.: On the dynamics of three systems involving tubular beams conveying fluid. M.Eng. Thesis, Dept. Mech. Eng., McGill University, Montreal, Québec, Canada, 1983.
- 15) Païdoussis, M.P., Luu, T.P., Prabhakar, S.: Dynamics of a long tubular cantilever conveying fluid downwards, which then flows upwards around the cantilever as a confined annular flow. *J. Fluids Struct.*, Vol. 24, pp. 111-128, 2008.
- 16) Ratigan, J.: Brine string integrity and model simulation. *Proc. 2nd SMRI Tech. Conf.*, Galveston/Austin, TX, USA, pp. 273-293, 2008.
- 17) Moditis, K., Païdoussis, M.P., Ratigan, J.: Dynamics of a partially-confined, discharging, cantilever pipe with reverse external flow, *J. Fluids Struct.*, under review, 2015.
- 18) Doaré, O., de Langre, E.: The flow-induced instability of long hanging pipes. *Eur. J. Mechanics A/Solids*, Vol. 21, pp. 857-867, 2002.
- 19) Païdoussis, M.P.: Dynamics of flexible slender cylinders in axial flow. Part 1: theory. Part 2: experiments. *J. Fluid Mech.*, Vol. 26, pp. 717-736 and pp. 737-751, 1966.
- 20) Ortloff, C.R., Ives, J.: On the dynamic motion of a thin flexible cylinder in a viscous stream. *J. Fluid Mech.*, Vol. 38, pp. 713-720, 1969.
- 21) Triantafyllou, G.S., Chryssostomidis, C.: Stability of a string in axial flow. *ASME J. Energy Res. Tech.*, Vol. 107, pp. 421-425, 1985.
- 22) Païdoussis, M.P.: Dynamics of submerged towed cylinders. *Eighth Symp. Naval Hydrodynamics: Hydrodynamics in the Ocean Environment*. U.S. ONR, ARC-179, pp. 981-1016, 1970.
- 23) Païdoussis, M.P.: Dynamics of cylindrical structures subjected to axial flow. *J. Sound Vib.*, Vol. 29, pp. 365-385, 1973.
- 24) de Langre, E., Païdoussis, M.P., Doaré, O., Modarres-Sadeghi, Y.: Flutter of long flexible cylinders in axial flow. *J. Fluid Mech.*, Vol. 571, pp. 371-389, 2007.
- 25) Sugiyama, Y., Kawagoe, H.: Vibration and stability of elastic columns under the combined action of uniformly distributed vertical and tangential forces. *J. Sound Vib.*, Vol. 38, pp. 341-355, 1975.
- 26) Semler, C., Lopes, J.-L., Augu, N., Païdoussis, M.P.: Linear and nonlinear dynamics of cantilevered cylinders in axial flow. Part 3: Nonlinear dynamics. *J. Fluids Struct.* Vol. 16, pp. 739-759, 2002.

- 27) Dowling, A.P.: The dynamics of towed flexible cylinders. Part 1: neutrally buoyant elements. *J. Fluid Mech.*, Vol. 187, pp. 507-532, 1988.
- 28) Triantafyllou, G.S., Chryssostomidis, C.: Analytic determination of the buckling speed of towed slender cylindrical beams. *ASME J. Energy Res. Tech.*, Vol. 106, pp. 246-249, 1984.

Prof. Emeritus

Michael P. Païdoussis(McGill University, Canada)



Michael P. Païdoussis was born in Cyprus in 1935, and was educated in the Greek Schools of Egypt, McGill University and the University of Cambridge, receiving his B.Eng. in Mechanical Sciences (with honours) in 1958 and his Ph.D. (Cantab) in Engineering in 1963. He has been Overseas Fellow at GEC in Britain (1958-60) and Research Officer at Atomic Energy of Canada Ltd (Applied Physics Division, 1963-67) in Chalk River, Canada. He joined the Department of Mechanical Engineering of McGill University in 1967. Promoted to Professor in 1976, he served as Chairman of the Department from 1977 to 1986, and now is the Thomas Workman Professor Emeritus. Since 1960, he has worked on various aspects of fluid-structure interactions and flow-induced vibrations and instabilities. He is the author of "Fluid-Structure Interactions: Slender Structures and Axial Flow", Vol. 1 (1998, 2nd edition 2014, Academic Press, London), Vol. 2 (2004, Elsevier Academic Press, London), and co-author of "Fluid-Structure Interactions: Cross-Flow-Induced Instabilities", (2011, Cambridge University Press). He has published 215 papers in refereed journals and 136 full papers in refereed conference proceedings. He has received a British Association Medal for High Distinction in Mech. Engineering (1958), the George Stephenson Prize from the Institution of Mechanical Engineers (IMechE) in 1975, the CANCAM Prize in 1995, and the ASME 1999 Fluids Engineering Award. He is Fellow of IMechE, ASME, CSME, the American Academy of Mechanics, the Royal Society of Canada (Academy of Science), and the Canadian Academy of Engineering. He has served as Chairman of Division III of IAHR (1981-87), and has been active in various committees of the Pressure Vessels and Piping, Fluids Engineering and Applied Mechanics Divisions of ASME; he was the ASME Calvin Rice Lecturer for 1992, and was elevated to Life Fellow. He is the founding Editor (1986) of the Journal of Fluids and Structures (Academic Press, now Elsevier).

SOME APPLICATIONS OF AN OPTIMUM DESIGN TECHNIQUE TO FLAPPING WING DESIGNS

Koji Isogai[†]

Professor Emeritus, Kyushu University, Fukuoka, Japan

Flapping wing has been utilized in many engineering fields such as power generation, micro aerial vehicles, under water vehicles, etc.. As is well known, flapping wing motion is governed by many parameters such as frequency, heaving amplitude, pitching (or feathering) amplitude, phase difference between heaving and pitching motions for rigid wing and additional parameters such as bending and torsion rigidity, mass distribution, etc. for elastic wings. Therefore, the application of optimum design technique plays crucial role for the design of high performance devices/vehicles using flapping wing. In this paper, some applications of an optimization technique to the flapping wing designs that the present author has studied during last fifteen years of his career are outlined. They are a flutter power generation system, a micro aerial vehicle and its use for the estimation of the propulsive performance of dolphin.

Keyword: power generation, flapping wing MAV, propulsive efficiency of dolphin, optimum design

1. ELASTICALLY SUPPORTED FLAPPING WING POWER GENERATOR¹⁾

In this section, the application of an optimization technique to a power generation system utilizing an elastically supported flapping wing power generator is explained. As shown in Fig. 1, a rigid rectangular wing is supported elastically in heaving oscillation while the pitching oscillation of the whole wing is mechanically driven by an electric motor with a prescribed frequency and amplitude. The basic idea of this system is that the lift induced by the pitching oscillation does work to the heaving oscillation while the phase angle between the two motions is automatically adjusted to the optimum value by aeroelastic response as shown later. (It can also be shown later that the work consumed by the forced pitching oscillation is less than 1% of the total energy generated by wind.)

1.1. METHOD OF ANALYSIS

The governing equation of motion of this system can easily be derived as follows:

$$M_h d^2 H / dT^2 + \omega_h^2 M_h (1 + ig) H = L + M_w (X_{cg} - A) d^2 \alpha / dT^2 \quad (1)$$

where T is time, H is the vertical displacement of the wing (positive up), α is the displacement (positive nose-up) of the forced pitching oscillation, M_h is the total mass relating to the heaving oscillation (including wing, electric motor, etc.), ω_h is the natural circular frequency of heaving oscillation, g is the artificial structural damping coefficient added to the system to maintain harmonic oscillation with constant amplitude, A is the location of the axis of pitch, X_{cg} is the location of the center of mass of the wing, M_w is the wing mass, and L is the lift (positive up). We assume here that the wing is designed so that the center of mass of the wing

[†]koji.isogai@nifty.com

coincides with the axis of pitch, namely, $X_{cg}=A$. With this assumption, the second term of the right hand side of Eq. (1) can be removed, which from our experience gives unfavorable effects on the power generation.

If we assume the aspect-ratio of the present rectangular wing is large, we can employ 2D unsteady (potential) aerodynamic forces, for that the analytical solutions are given, for solving Eq. (1). As a system of wind power generator, the designer should give the following parameters, those are, semi-chord length b , wing span l , the nominal free-stream velocity U and the amplitude of forced pitching oscillation α_o . From the dimensionless form of Eq. (1), it can be easily identified that the aeroelastic response of the system is also governed by the following five non-dimensional parameters: reduced frequency k ($b\omega/U$, ω : circular frequency of the forced pitching oscillation), g , ω_h/ω , mass ratio μ ($=M_w/(\pi\rho b^2l)$), and a ($=A/b$). Once these parameters are given, it is easy to obtain, with the assumption of simple harmonic motion of the wing, the analytical solution of Eq. (1), namely, the amplitude and phase angle (with respect to the forced pitching oscillation) of the heaving oscillation. Then, it is easy to estimate the time averaged work done by the aerodynamic forces, namely, the wind energy extracted from the system. The problem is, however, how we can determine those parameters (five dimensionless parameters described previously) that give the highest power generation efficiency. The power generation efficiency η_p is defined by

$$\eta_p = W / ((1/2)\rho U^3 (2H_s)l(16/27)) \quad (2)$$

where W is the rate of work, the coefficient, $16/27$, is referred as the Betz coefficient, and H_s is the amplitude of the leading or trailing edges, either of which is larger than the other. We employ an optimization algorithm ‘‘Complex Method’’, which is originally proposed by Box²⁾, to determine the five dimensionless parameters that attain the maximum efficiency.

1.2. APPLICATION OF OPTIMIZATION TECHNIQUE

We applied the Complex Method to the rectangular wing of aspect ratio 10 ($b=0.5m$ and span $l=10m$) with $\alpha_o=50$ deg in the nominal wind speed of 15 m/s. The Complex Method is one of the optimization methods that do not depend on the derivatives of objective and constraint functions, and it can handle the multiple constraints. In the present study, the objective function is the power generation efficiency η_p , while the design variables are the five dimensionless parameters, namely, k , g , ω_h/ω , μ , and a . (It should be noted that x_{cg} is assumed to be equal to a .) We have imposed the following constraints to this problem:

$$k < 0.30, \quad 0.5 < \mu < 200.0, \quad -1.0 < a < 1.0, \quad 0.5 < \omega_h/\omega < 1.5, \\ 0.5 < H_o/b < 2.0, \quad 100 \text{ deg} < \phi < 150 \text{ deg}, \quad g > 0.0, \quad W > 1 \text{ kW}, \quad W_2 < 0.0$$

where H_o is the amplitude of the heaving oscillation, ϕ is the phase delay angle of the heaving oscillation with

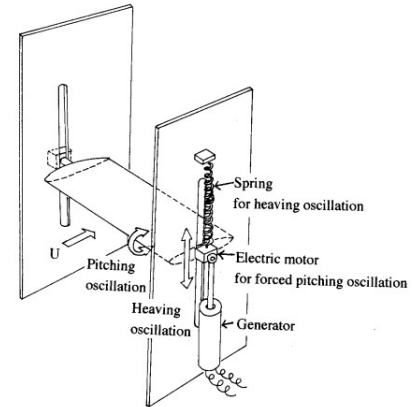


Figure 1 : Concept of elastically supported flapping wing power generator.

respect to the forced pitching oscillation, and W is the total power generated which is the sum of W_1 and W_2 , where W_1 is the work done by lift and W_2 is the work done by pitching moment. Among these constraints, those imposed to μ , a , ω_h/ω and H_o/b are for that these variables should be within the practical range. The constraints imposed to k , ϕ and W_2 need some explanation. These constraints are imposed so that the dynamic stall phenomenon gives favorable effects on the power generation. According to our numerical simulations using a Navier-Stokes (NS) code, the dynamic stall phenomenon reduces both the efficiency and the power considerably if these constraints were not imposed. By applying these constraints to k , ϕ and W_2 , it is guaranteed, as shown in Ref. 1, that the dynamic stall phenomenon increases both the efficiency and the power beyond those predicted by the present optimization code which employs the potential aerodynamics. What we have obtained by applying the present optimization code to the model system with the constraints described above is as follows:

$$\eta_p=49\%, \quad W=6.99\text{ kW}, \quad W_1=6.99\text{ kW}, \quad W_2=-0.014\text{ kW}$$

The detailed values of other parameters obtained at this optimum condition are as follows: $k=0.30$, $g=0.472$, $\omega=9.0\text{ rad/s}$, $\omega_h=8.06\text{ rad/s}$, $a=0.412$,

$$\mu=23.8, \quad H_o=0.471\text{ m}, \quad \phi=110\text{ deg}$$

It should be noted, however, that the maximum effective angle of attack for this case becomes about 34 deg , which is far beyond the static stalling angle (NACA0012 airfoil section is assumed). Therefore, we also have performed the aeroelastic response computation of the present elastic system by using a 2D compressible Navier-Stokes code which have been developed by one of the present authors (see further details in Ref. 1).

1.3. EFFECT OF PLANFORM ON EFFICIENCY AND POWER

When the lift in Eq. (1) is replaced by that computed by 3D potential theory, namely, by doublet lattice method (DLM), we can evaluate the effect of the plan-form of the flapping wing. In this section, the comparison of the power and efficiency of the two different plan-forms, namely, a plan-form of a caudal fin of

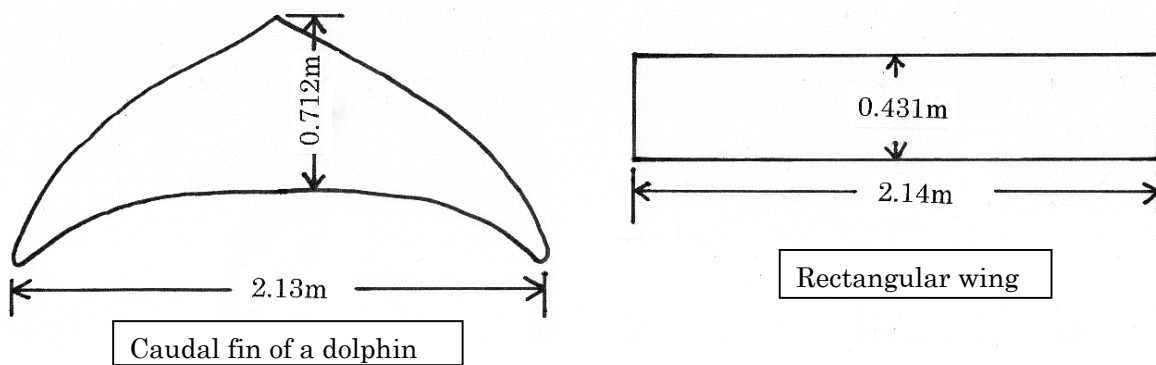


Figure 2 : Plan-forms used for the study of the flapping wing power generator.

a dolphin and a rectangular wing are discussed. The plan-forms are shown in Fig. 2. As shown in Fig. 2, the caudal-fin of dolphin has the root chord length of 0.712 m, the full span length of 2.13 m and the wing area of 0.922 m² and the aspect-ratio of 4.96. The rectangular wing has the same wing area and aspect ratio as those of the dolphin tail. The both wing has the same wing section of NACA0015 and are assumed to be operated in

the water with velocity of 2 m/s. The same optimization technique discussed in section 1.2 is applied to these systems to determine the elastic and mass properties of each system to obtain the maximum efficiency. As a result, the power and efficiency obtained for the caudal fin of the dolphin are 984 W and 20 %, respectively, with $k=0.30$, $H_0=0.37$ m, $\theta_0=50$ deg and $\phi=89$ deg, and the power and efficiency for the rectangular wing are 1,009 W and 34 %, respectively, with $k=0.30$, $H_0=0.224$ m, $\theta_0=50$ deg and $\phi=90$ deg. From these results we can conclude that the rectangular wing shows better performance than the dolphin type plan-form. To examine the effect of viscosity, the numerical simulations for the same optimized systems using the 3D Navier-Stokes code were conducted. As the results, the power and efficiency of the dolphin type plan-form are 726 W and 14.7 %, respectively while those of the rectangular wing are 1,070 W and 36.1 %, respectively. Therefore, the power and efficiency of the rectangular wing are increased by the viscous effect, namely, the dynamic stall effect, while those of the dolphin type plan-form is decreased from those predicted by the potential theory. Therefore as far as we concern about the flapping wing power generator, we can conclude that the rectangular plan-form is superior compared with the dolphin type plan-form.

1.4. EXAMPLES OF A 2 DIMENSIONAL MULTI-WING CASCADE CONFIGURATION³⁾

The analytical method for two-dimensional (2D) multi-wing cascade configuration of the elastically supported flapping wing power generator was also developed (details of the analysis using the doublet lattice method should be referred to Ref. 3). The same optimization technique as used for a single wing configuration described in section 1.2 is applied to the middle wing of a 2D three wing cascade configuration. The following assumptions are made for a design study: wing chord is 1 m; wing distance between the adjacent wings is 2.0 m; amplitude of the forced pitching oscillation is 50 deg; oscillation mode is anti-phase; wind speed is 8 m/s. The results of optimization are as follows: power is 132 W/m, $\eta_p=50.3$ % ($C_p=0.30$). The power and efficiency of the outer two wings are 111 W/m, $\eta_p=42.6$ % ($C_p=0.25$). Therefore the total power of three wings of span 10 m is 3.54 kW. (C_p is defined as power coefficient.)

1.5. EXAMPLES OF A 3 DIMENSIONAL MULTI-WING CASCADE CONFIGURATION

The analytical method for a rectangular multi-wing cascade configuration of the elastically supported flapping wing power generator was also developed (details of the analysis using the doublet lattice method should be referred to Ref. 4). The same optimization technique as used for a single wing configuration described in section 1.2 is applied to the middle wing of a rectangular three wing cascade configuration which is assumed to be used in the water channel. The following assumptions are made for a design study: wing chord is 0.431 m; full span is 2.14 m; area is 0.922 m²; aspect ratio is 4.96; wing distance between the adjacent wings is 0.65 m; amplitude of the forced pitching oscillation is 50 deg; oscillation mode is anti-phase; water velocity is 2 m/s. The results of optimization are as follows: power of the middle wing is 1.45 kW, $\eta_p=41.2$ % ($C_p=0.244$). The power and efficiency of the outer two wings are 1.30 kW, $\eta_p=36.7$ % ($C_p=0.217$). Therefore the total power of three wings is 3.85 kW. Therefore, total power generated during one month for this system becomes $3.85 \times 0.80 \times 24 \times 30 = 2,219$ kWh/month. Since the average power needed for one standard family is about 373.5 kWh, the present hydro-power generator of 3 wing configuration can supply the power needed by about 6 standard families.

2. APPLICATION OF OPTIMIZATION TECHNIQUE TO RESONANCE TYPE FLAPPING WING⁵⁾

In this section, the application of the optimization technique to a resonance type flapping wing for a dragonfly-type micro aerial vehicle, which shows high performance in spite of its simple structure and light weight, is briefly explained. Figure 3 shows the planform and structure of the present resonance type flapping wing. The experimental and numerical studies (using a 3D NS code) on the single/tandem wing configurations using this original resonance type

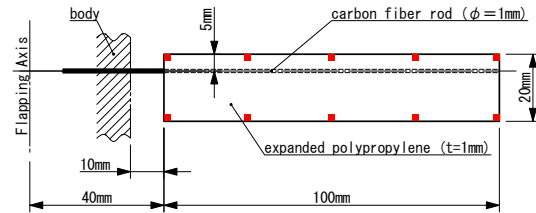


Figure 3 : Planform, arrangement and structure of resonance type flapping wing.

flapping wing have been conducted. Figure 4 shows the arrangement of tandem wing configuration. Figure 5 shows the variation of lift under hovering condition with respect to the oscillation frequency. As seen in Fig. 5, the agreement between the numerical and experimental results is very good for a single wing configuration in the frequency range between 35 Hz to 50 Hz. In Fig. 5, the results obtained using the 3D NS code for the tandem wing configuration are also shown. In this case, the phase difference ψ between the flapping wing motions of the fore- and hind-wings is assumed to be zero. As seen in the figure, the lifts generated by the fore- and hind-wings increase about 25 % at $f=50\text{Hz}$ compared with that of the single wing configuration. It is clear that this increase of lift is due to the flow interaction between the two wings. The efficiency \bar{P}/\bar{L}

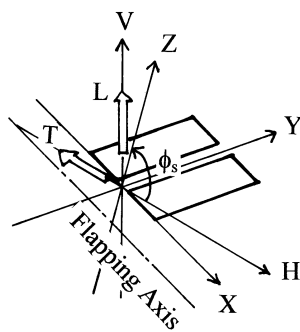


Figure 4 : Arrangement of tandem wing configuration.

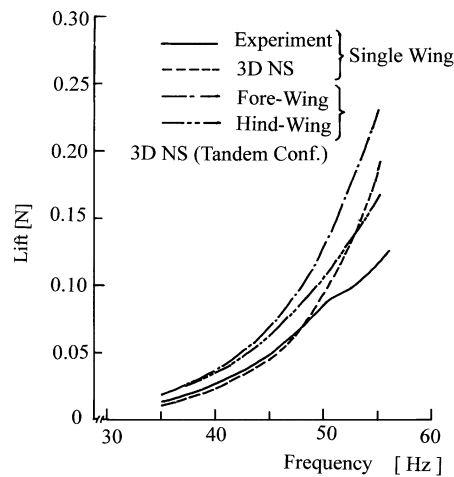


Figure 5 : Lift vs. frequency characteristics.

(necessary power per unit lift) at $f=50\text{ Hz}$ for the tandem wing configuration is 22.0 W/N. The original structure of the resonance type flapping wing shown in Fig.3 is not necessarily the optimum structure which gives the highest efficiency. Therefore we try to determine the optimum diameter of the CFRP rod and the thickness of the EPP plate of the present resonance type flapping wing. The planform and the arrangement of the CFRP rod and the EPP plate are assumed to be same as the original wing (see Fig. 3). For this purpose, we have developed the optimization code which couples the optimization algorithm, vibration analysis code and

the 3D NS code. As to the optimization algorithm, the Complex Method²⁾, which is one of the direct search method without recourse to the derivatives, is also employed. The objective function of the present problem is the efficiency, namely, \bar{P}/\bar{L} . We have employed total five design variables, that are, the diameter of the CFRP rod (d), the thickness of the EPP plate (h), the flapping amplitude (ϕ_0), the reduced frequency (k) and the stroke-plane angle (ϕ_s). The constraint is that the time mean lift (\bar{L}) should be larger than the weight of the MAV. The weight of the MAV is assumed to be 0.392 N (40 gf). Since the number of the design variables is only five, we have obtained the converged solution after 8 iteration steps. The results of the optimization are as follows: $\bar{P}/\bar{L}=10.8$ W/N ($\bar{L}=0.460$ N, $\bar{P}=4.97$ W), $d=1.93$ mm, $h=1.16$ mm, $k=0.541$ ($f=52.42$ Hz), $\phi_s=-4.5$ deg. The theoretical natural frequencies of the optimized wing are $f_1=83.0$ Hz, $f_3=115$ Hz and $f_5=3,788$ Hz. The efficiency of the present optimized wing, namely, $\bar{P}/\bar{L}=10.8$ W/N is the improvement of 51% over the 22.0 W/N of the original wing. The theoretical values of d and h of the original wing are $d=1.65$ mm and $h=1.95$ mm. (It should be noted that these values of d and h of the original wing are adjusted so that the theoretical natural frequencies match with those of the ground vibration test data.) When we compare the values of d and h of the optimized wing with those of the original wing, it is identified that the stiffness of the CFRP rod is increased while the stiffness of the EPP plate is reduced considerably for the optimized wing compared with those of the original wing. This fact enables the larger feathering displacement of the optimized wing than that of the original wing as confirmed in Figs. 6, which show the aeroelastic responses at the tip stations of the fore- and hind-wings in hovering condition.

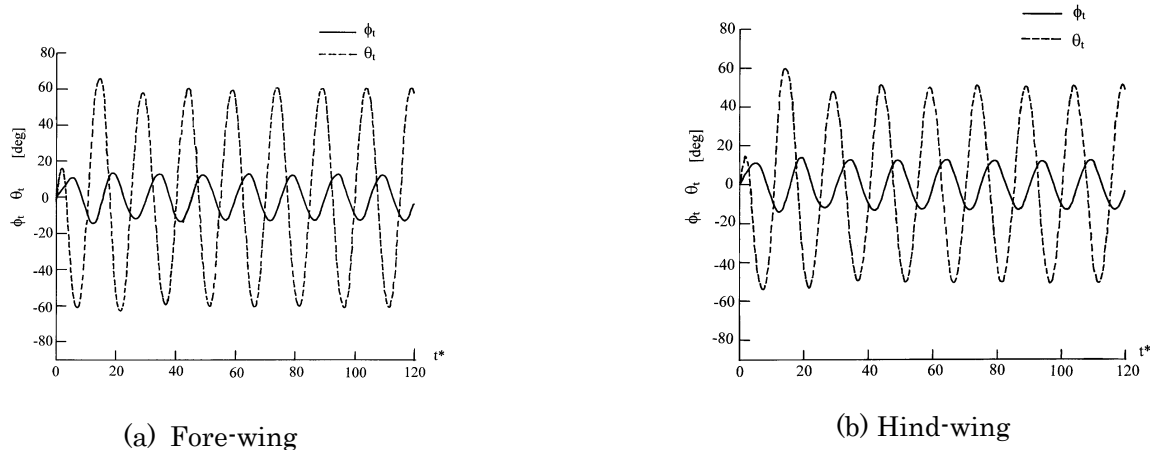


Figure 6 : Aeroelastic responses for optimized fore- and hind-wings.

3. PROPULSIVE PERFORMANCE OF DOLPHINE

In this section, the application of an optimization technique to the analysis of propulsive performance of dolphins is outlined. (Details of the analyses should be referred to Ref. 6 and 7.) In a paper published in 1936, Gray⁸⁾ pointed out that the power generation capability of a dolphin's muscle is seven times larger than that of a terrestrial mammal. This conclusion was derived on the basis of the assumptions that the maximum speed of

the dolphin is 20 knots (10 m/s), that the friction drag of the body can be estimated by assuming that the boundary layer around the body is turbulent and that the propulsive efficiency is 100%. If these assumptions are correct, the conclusion he derived is contradictory to the fact that the dolphin is a mammal. Therefore, it is called “Gray’s paradox.” Gray also pointed out in the same paper that the power generation capability of a dolphin’s muscle might be equivalent to that of other types of mammalian muscle if the boundary layer around the body is laminar. Numerous studies have been made on the nature of the boundary layer since then (see the extensive review by Fish and Rohr⁹). However, Fish¹⁰ concluded, by examining the numerous studies on the nature of the boundary layer, that there is no special mechanism for drag reduction and dolphins appear to maintain a turbulent boundary layer. Fish computed the thrust, efficiency and power using a potential theory from the experimental data of the fin motion read from video footage of several trained dolphins swimming horizontally. Then he computed the drag coefficient from the computed power. However, the value of the drag coefficient and the power thus derived show considerable scatter depending on the data of the individual dolphin used for the analyses, making the accurate determination of the power generation capability of dolphins difficult. (The power thus determined around the maximum speed of 6 m/s was scattered from 1,900 W to 7,600 W.) On the other hand, there is no such uncertainty for the standing swimming performance shown in aquariums where the body (in the air) is supported by the caudal fin in the water (see Fig. 7). It is clear that the thrust generated by the fanning motion of the caudal fin is equal to the body weight, which can be measured accurately. Therefore, an accurate estimation of the power generation capability could be possible without having to include the body drag if we can analyze the standing swimming. An analysis of standing swimming is only possible using a numerical simulation technique which takes into account the effect of viscosity, since the flow around the caudal fin becomes an unsteady viscous flow with large scale flow separation. As the first step, we determine the power necessary for the standing swimming using a three-dimensional Navier–Stokes (3D NS) code. To the best of our knowledge, no analysis of standing swimming has been published to date. As the next step, we estimate the maximum speed in water based on the power generation capability thus determined. For the analysis of the second step, we employ a 3D modified doublet lattice method (MDLM) (modification of the doublet lattice method taking into account leading edge suction) coupled with an optimization technique. As will be discussed later, the optimization method is used to find the optimum fin motion which attains the maximum propulsive efficiency.

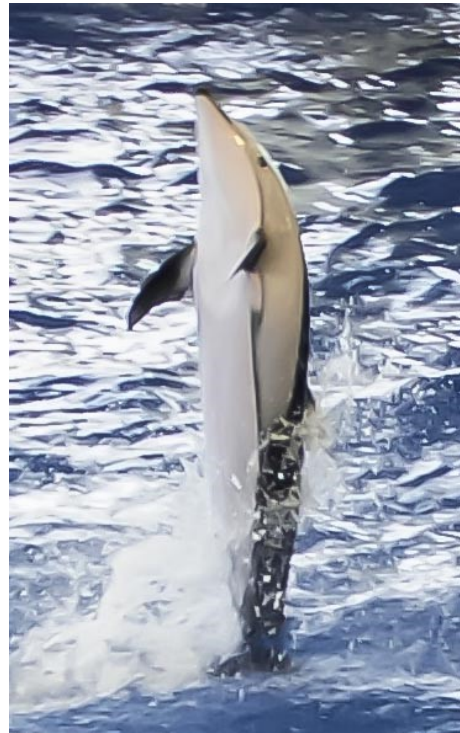


Figure 7 : Standing swimming of a dolphin.

3.1 MOEL DOLPHIN AND METHOD OF ANALYSIS

In the present analysis, we consider one of the bottlenose dolphins (*Tursiops truncatus*) studied by Nagai¹¹) for the analytical model. The length (l), mass (M) and fineness ratio (l/d , d : maximum diameter of body) of the model dolphin are 2.3 m, 138 kg and 5.38, respectively. Figure 8 shows the planform of the caudal fin. The root chord length is 0.144 m, the full span length is 0.432 m and the area of the fin is 0.0377 m². The aspect ratio is 4.96. The airfoil section of the fin is assumed to be NACA0021. In this analysis, the flexibility of the caudal fin is also taken into account.

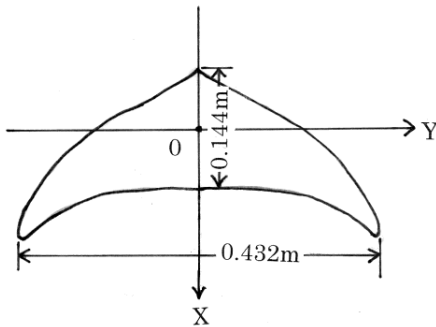


Figure 8 : Plan form of caudal fin.

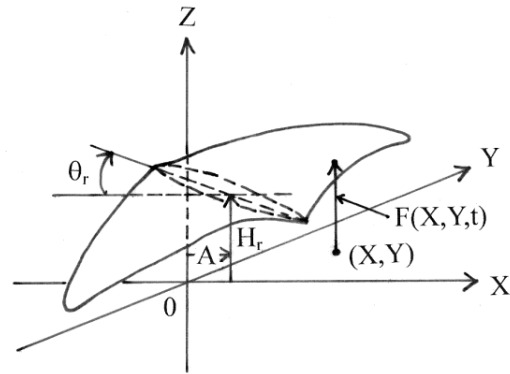


Figure 9 : Definitions of coordinate and fin motion.

The elastic property of the fin such as Young's modulus is taken from the data reported by Sun et al.¹²). For hydro-elastic response computations, we apply the modal approach used in Ref. 5. Figure 9 shows the definitions of the coordinates and the fin motion. In the modal approach, the displacement of the fin mean surface $F(X, Y, t)$ in the Z direction is expressed using nine mode shapes as

$$F(X, Y, t) = F_r(X, Y, t) + \sum_{i=1}^9 \phi_i(X, Y) q_i(t) \quad (3)$$

where $F_r(X, Y, t)$ is the rigid displacement due to the forced oscillation, $\phi_i(X, Y)$ is the i -th natural vibration mode of the fin and q_i is the unknown generalized coordinate of the elastic deformation. The rigid displacement $F_r(X, Y, t)$ of the fin can be expressed as

$$F_r(X, Y, t) = H_r - (X-A)\theta_r \quad (4)$$

where H_r and θ_r are the heaving and pitching displacements, respectively, and they are given as

$$H_r = H_o \sin(\omega t) \quad (5)$$

$$\theta_r = \theta_o \sin(\omega t + \phi) \quad (6)$$

where H_o and θ_o are the amplitudes of the heaving and pitching oscillations, respectively, ω is the circular frequency of forced oscillation and ϕ is the phase advance angle of the pitching oscillation ahead of the heaving oscillation. Using Lagrange's equations of motion, we obtain the ordinary differential equations of motion to determine q_i as follows.

$$M_i (d^2 q_i / dt^2) + (\omega_i^2 / \omega) g M_i dq_i / dt + \omega_i^2 M_i q_i =$$

$$- \iint_S m(X, Y) \phi_i(X, Y) (d^2 F_r / dt^2) dX dY$$

$$+ \iint_S \Delta P(X, Y, t) \phi_i(X, Y) dX dY$$

$$\text{for } i=1, \dots, 9 \quad (7)$$

where M_i is generalized mass, ω_i is the i -th natural circular frequency, $m(X,Y)$ is mass per unit area of fin, $\Delta P(X,Y,t)$ is the pressure difference between the upper and lower surfaces of the fin and g is the damping coefficient which is equivalent to the structural damping coefficient. Equations (3)–(7) are the basic equations for computing hydro-elastic deformation of the flexible fin, those are used both for the NS simulations including the standing swimming and the horizontal swimming.

3.2 RESULTS OF STANDING SWIMMING

For the numerical simulation of the standing swimming, the 3D NS equations are solved with Eq. (7). The 3D NS code used in the present study is a Reynolds averaged Navier–Stokes (RANS) code originally developed by Isogai. (See Ref. 7 for further details of the analysis.)

In Fig. 10, the flow pattern (stream lines) around the 52% semispan at the typical phase of oscillation is shown. As seen in the figure, large-scale flow separation around the leading edge region is observed. As the result of the numerical simulation, we obtain the time-averaged thrust of 1,352 N (138 kgf) which can sustain the body weight of 138 kgf with the necessary power of 8,582 W. These results give power-mass-ratio (PMR: power per unit mass of body) of 62.2 W/kg which is 2.6 times larger than that of a human athlete and it is an approximately 11% reduction compared with 70.2 W/kg which was obtained under the assumption of the rigid fin⁶.

It is of great interest to determine the maximum swimming speed of the present model dolphin when the power predicted by the standing swimming is used for horizontal swimming in water. This analysis is presented in the next section.

3.3 RESULTS OF HORIZONTAL SWIMMING

In this section, the propulsive performance of horizontal swimming of the present model dolphin is estimated using the MDLM coupled with an optimization technique²). The optimization technique is used to find the optimum fin motion which attains the maximum propulsive efficiency. As the result of optimization, the thrust, power, propulsive efficiency and PMR at the optimum condition are determined. In order to evaluate the effect of the viscosity, especially the effect of flow separation, on the performance thus determined using the MDLM, the numerical simulations using the 3D NS code are also conducted. (Details of the procedure of computing the performance of horizontal swimming should be referred to Ref. 6 and 7.)

The propulsive performance of the horizontal swimming at the speeds of $V=6.5$ m/s, 9.43 m/s, 11 m/s and 12 m/s is shown in Fig. 11, where the results obtained using the MDLM are shown by the solid line and the results obtained using the 3D NS code are shown by the solid circles. As seen in the figure, the PMR predicted by the 3D NS code is larger; namely, approximately 16% for $V=6.5$ m/s and 21% for $V=12$ m/s, than that

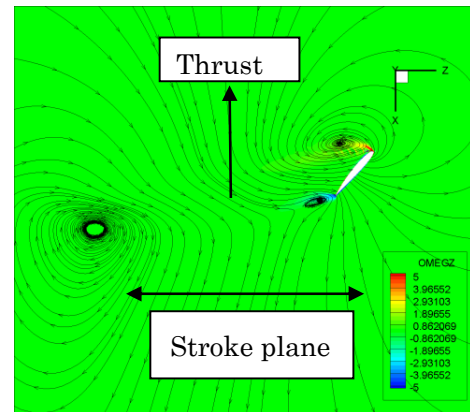


Figure 10 : Flow pattern around the 52% semispan for the standing swimming condition.

predicted by the MDLM. These discrepancies between the two can be attributed to the effect of flow separation observed at the tip region.

From Fig. 11, it is identified that the maximum speed of horizontal swimming is estimated as 12 m/s. Note that the PMR of the maximum speeds of dolphins observed in the aquariums, namely, 6.5-9.5 m/s, are in the range 10–30 W/kg, far below the PMR of 62.2 W/kg estimated from the analysis of the standing swimming.

REFERENCES

- 1) Isogai, K, Yamamoto, M., Matsubara, M. and Asaoka, T. : Design study of elastically supported slapping wing power generator, International Forum on Aeroelasticity and Structural Dynamics, Amsterdam, 2003.
- 2) Box, M. J. : A new method of constrained optimization and a comparison with other methods”, *Computer Journal*, Vol. 8, pp. 42-52, 1965.
- 3) Isogai, K. and Abiru, H. : Study of multi-wing configurations of elastically supported flapping wing power generator, *Trans. Jpn. Soc. Aeronaut. Space Sci.*, 55, No. 2, pp. 133-142, 2012.
- 4) Isogai, K. and Abiru, H. : Lifting-surface theory for multi-wing configurations of elastically supported flapping wing power generator, *Trans. Jpn. Soc. Aeronaut. Space Sci.*, 55, No. 3, pp. 157-165, 2012.
- 5) Isogai, K. and Nagai, H. : Experimental and numerical study of resonance type flapping wings for micro aerial vehicles, APISAT 2009, Nov. 4-6, 2009.
- 6) Isogai, K. : Propulsive performance of dolphins –Estimation from analysis of standing swimming-, *Trans. Jpn. Soc. Aeronaut. Space Sci.*, 56, No. 2, pp. 90-95, 2013.
- 7) Isogai, K. : Effect of flexibility of the caudal fin on the propulsive performance of dolphins, *Jpn. Soc. Aeronaut. Space Sci.*, 57, No. 1, pp. 21-30, 2014.
- 8) Gray, J. : Studies in animal locomotion. VI. The propulsive powers of the dolphin, *J. of Experimental Biology* **13**, pp.192-199, 1936.
- 9) Fish, F. E. and Rohr, J. J. : Review of dolphin hydrodynamics and swimming performance, *SSC San Diego*, Technical Report 1801, 1999.
- 10) Fish, F. E. : Power output and propulsive efficiency of swimming bottlenose dolphin (*Tursiops truncatus*), *Journal of Experimental Biology*, **185** , pp. 179-193, 1993.
- 11) Nagai, M. : *Thinking fluid dynamics with dolphins*, Ohmsha Press, 2002.
- 12) Sun, Q., Morikawa, H., Kobayashi, S., Ueda, K., Miyahara, H. and Nakajima, M. : Structure and mechanical properties on tail flukes of dolphin, *J. of Aero Aqua Bio-Mechanisms*, **1**, No. 1, 2011.

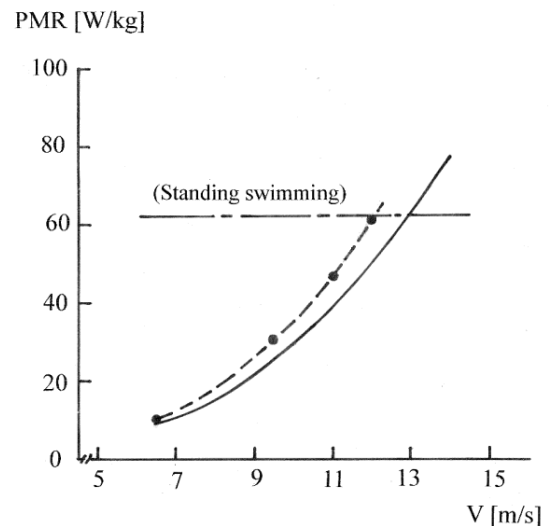


Figure 11 : Variation of PMR with respect to horizontal speed.

(3D NS: ● , MDLM: —).

Prof. Emeritus

Koji Isogai (Kyushu University, Japan)



Koji Isogai graduated the graduate course of the Department of Aeronautics of Kyushu University, Japan in 1965. He entered the National Aerospace Laboratory (Japan) in 1965, where he conducted the research works on the aeroelasticity and unsteady aerodynamics of aircraft for 28 years. He moved to the Department of Aeronautics and Astronautics of Kyushu University in 1993, then he moved to the Department of Aeronautics and Astronautics of Nippon Bunri University in 2004 and he retired in 2010. He is now Professor emeritus of Kyushu University. He is the honorary member of The Japan Society for Aeronautics and Space Sciences and the Associate Fellow of American Institute of Aeronautics and Astronautics. He has published about 90 papers in refereed journals and in full paper conference proceedings. His research fields are the transonic aeroelasticity of aircraft, flapping wing power generator, unsteady fluid dynamics of bird, insect and fish, and micro aerial vehicle (MAV).

STALL-TYPE GALLOPING OF BLUFF BODIES

1st Masaru Matsumoto⁺¹, 2nd Hiroshi Ishizaki⁺²

⁺¹Kyoto University, Professor Emeritus, Kyoto, Japan

⁺²SE Corporation, Vice President, Tokyo, Japan

Keyword: stall, stall-type galloping, flow separation, flow reattachment, separation bubble

The “stall-type galloping(STG)” of bluff bodies is studied in contrast with the well-known conventional “reattachment type pressure distribution flow Galloping (RPDFG)”. STG can be excited by unsteady switching of a generation of the separated bubble(SB) on a side face of a body generated by a flow reattachment on a side face and destruction of SB, because of a flow-change to a separated type from reattachment type. Some bluff bodies similarly show the peculiar characteristics the “stall” with an airfoil at the critical stalling angle, those are a drastic change of a drag, a drastic change Strouhal number, appearance of a negative slope of the lift associated with a pitching angle, and a significant low frequency fluctuation of the flow and the lift force. The “stall” of bluff bodies appears mostly associated to the angle of attack to the flow similarly with an airfoil, but the “stall” of a circular, observed at a range of critical Reynolds number is a particular case. STG would be excited by an unsteady generation/destruction of SB, in consequence, STG would not be explained by the quasi-steady theory, and it might be characterized by a low frequency flow/vortex produced by the “stall”. Some bluff bodies such as, a circular cylinder with protuberance(s), a yawed circular cylinder, a circular cylinder with a splitter plate in a wake, a snow-accreted transmission line, a rectangular cylinder with B/D=2.8, a circular cylinder at the critical Reynolds number and so on show STG.

1. INTRODUCTION

Numerous former studies on stall and related to the “stall” of airfoils in the field of the Aeronautical engineering have significantly contributed on verification of the generation mechanism and its characteristics of the “stall”. However the detail generation-mechanism of low frequency flow field during the “stall” still remains unclear. On the generation low frequency unsteady flow at the stall of stationary airfoil has been studied, the large-scale vortex caused by the unsteady bi-stable flow is shedded at changing from the long-separation bubble to the short-separation bubble at the “leading edge stall”. (Rinoie[1]). The low frequency flow/vortex during the stall of an airfoil should be generated in relation to the “Kelvin-Helmholtz instability” (K-H instability) and the “Tommlin-Schlichting Wave instability” (T-S Wave instability) of the separated shear flow forming the separation bubble on body surface.(Rinoie[2],Zhou[3]).Furthermore, the lift force variation with a pitching angle, drastic/ discontinuous decrease, significant decrease and gradual/smooth decrease has been observed at the case of leading edge stall, trailing edge stall and thin-airfoil stall, respectively. (Hirose[4]) In particular, the sudden change of separation bubble from the short-bubble to the long bubble should be the “bubble-burst”, which means disappearance of the bubble, causes the sudden decrease of the lift force.(Rinoie[1]). This bubble change by the bubble-burst is expressed by flow change from the reattachment-flow to the separated-flow/non-reattached flow. On the dynamic instability caused by the “stall”, the torsional flutter has been well known. On the torsional flutter/ the stall-flutter, it has been clarified that the dynamic stall vortex generated by the pitching motion of airfoil plays an essentially important role on the torsional flutter or the stall flutter.(McAlister, Carr[5], Wang[6]). On the other hand, E.K. Armstrong et al. (1960[7]) reported the fatigue of the

⁺¹isfa0001@jaxa.jp, ⁺²isfa0002@company.com, ⁺³isfa0003@univ.ac-u.jp

blade of the compressor of aircraft caused by the flexural mode. Their report must be thought to imply appearance of the flexural oscillation by the stall of blade. This flexural oscillation can be thought to be the galloping caused by the negative slope of lift force associated to the pitching angle. It is significantly interesting that taking into account of the lift force property in terms of angle of attack, the characteristics of the low frequency fluctuation of lift and wake velocity, the flow property around the body, some bluff bodies must show the similar stall with an airfoil described above, and the cross-flow fluid-dynamic instability related to the “stall”. Those are a circular cylinder with a protuberance at the particular location, a yawing circular cylinder with 45° to the flow and a circular cylinder at the range of critical Reynolds number (Matsumoto[8]), a snow accreted conductor(Matsumiya[9]) and a rectangular cylinder with the side-ratio(B/D) of 2.8.(Itou[10]) In particular, Schewe[11] studied based on the precise wind tunnel tests on the aerostatic characteristics, including time-averaged lift and drag forces, fluctuating lift force and Strouhal number, at the range of critical Reynolds number. He indicated the peculiar low frequency property of fluctuating lift force when the non-zero time-averaged lift force suddenly appears or disappears at the specified Reynolds number. Taking into account of recent studies on the airfoil-stall described above, these aerostatic characteristics of a circular cylinder at the critical Reynolds number must be related to the “stall”.

2. CONTRAST BETWEEN THE CONVENTIONAL GALLOPING OF BLUFF BODIES AND THE STALL-TYPE GALLOPING

Conventional galloping of bluff bodies, such as rectangular cylinders with the side-ratios between $B/D=0.8$ to $B/D=2.8$, is generated by the particular flow around bluff body, so called as “reattachment-type pressure distribution flow”. (Nakamura[12]) It should be noted that this particular time-averaged flow generating the galloping, never reattaches on body-side face. Den Hartog condition has been often used for judgement of galloping instability, that is when $dCF_y/d\alpha=dCL/d\alpha+CD<0$, galloping can be excited. This particular flow making $dCF_y/d\alpha<0$ is observed at the lower face of a body at the positive angle of attack. In consequence, the time average lift force is down-ward, it means the negative lift, at the range of positive pitching angle. In contrast, the negative slope of lift, $dCF_y/d\alpha=dCL/d\alpha+CD<0$, regarding the stall-type galloping, can be characterized by the separation bubble formation/ disappearance at the upper side face of body when angle of attack of the flow is positive. Therefore, the time-average lift force should be positive. Also the flow substantially reattaches on the upper side face to produce a separation bubble. In conclusion, the “stall” provides $dCF_y/d\alpha<0$. The “separated bubble” plays, in consequence, definitely important role to excite the “stall-type galloping”.

3. WIND-INDUCED VIBRATION OF STAY CABLES OF CABLE-STAYED BRIDGES

Recent the main-span length of cable-stayed bridges become more longer than 1,000m, including the Sutong Bridge(1088m China), the Stone cutters Bridge (1018m China) and the Russky Island Bridge(1104m Russia). Their length of the stay cables is more than 600m. The stay cables are extremely low frequency- and low damped- structures, in consequence, they are sensitively excited

by the wind. Since Hikami[13]'s finding, in 1986, of the peculiar wind-induced vibration under the condition of the precipitation. He named this cable-vibration as the "rain-wind induced vibration(RWIV)". Nowadays RWIV of the stay cables of many cable stayed bridges have been observed in the world. Because of serious damages caused by their large amplitudes and frequent occurrence, RWIV become the crucial issues in the design of cable-stayed bridges. Moreover, the violent cable vibration has been observed at the some cable-stayed bridges without rain. This kind of cable vibration has been named as "Dry Galloping (DG)". (Larose[14], Macdonald[15]) How to suppress RWIV and DG of stay cables must be substantial issue for safety design of cable stayed bridges. Based on many field observations of RWIV, the occurrence conditions of RWIV have been mostly summarized as (1) Polyethylene lapped cable, (2) wind direction to the cable-plane: at the range of yawing angle of $30^{\circ}\sim 60^{\circ}$ (measured from cable plane) (3)wind velocity range ; at the range of $5\text{m/s}\sim 30\text{m/s}$ (4) cable vibration frequency; at the range of $0.5\text{Hz}\sim 3\text{Hz}$ (5) low turbulent wind: low intensity of turbulence; $I_u < 10\%$, (6) low structural damping of cables; $\delta < 0.01$. The sequential studies on cable wind induced vibration clarified that major factors of RWIV and DG are (1) formation of the upper rivulet on cable surface at particular position determined by the balance of wind pressure, cable surface roughness, tensile force of water on cable surface and water-rivulet gravity. (2) the axial flow, that is secondary flow along the cable-axis, generated in the near wake, (3) the critical Reynolds number effect on cable aerodynamic properties. Matsumoto.[16to25], Vervue[26], MacDonald[15], Larose[14], Chen[27], Katsuchi[28], Kimura[29], Georgakis[30], Liu[31], Flamand and Benidir[32]) Matsumoto [8], Jakobsen[14]. The major countermeasures to suppress RWIV are installation of dampers, cross-tie and helical fin or indented cable surface. Particular attention should pay that the Scruton number ($Sc=2m\delta/\rho D^2$: m:mass of cable unit length, δ : logarithmic damping decrement of cable, ρ :air density, D:cable diameter) is no effect on DG suppression by Macdonald[15] and Kimura[29]. The clarification of the generation mechanism of RWIV and DG is absolutely expected to establish more reasonable and effective countermeasures for safety maintenance and design of existed and to be constructed cable stayed bridges, respectively.

4. THE "STALL" AND THE "STALL-TYPE GALLOPING" OF BLUFF BODIES

(1) Non-yawed ($\beta=0^{\circ}$) circular cylinder with protuberance(s)

In order to clarify the effect of the water rivulet on RWIV, A protuberance with rectangular shape, $w/D=0.064$ in width and $t=0.032D$ in thickness (D:cylinder diameter(0.05m)) is installed to simulate a water rivulet on the face of a stationary circular cylinder. The protuberance position, θ , was changed from 0° to 180° , measured from the front stagnation point .

Time-averaged Lift force coefficient, CL , and the time-averaged drag force coefficient, CD , the fluctuating lift force, LF' caused by the vortex and Strouhal number, $St(=f_vrD/V$: f_vr :vortex shedding frequency, D: cylinder diameter, V: mean wind velocity)of the stationary circular cylinder with a protuberance associated with protuberance position, θ , measured in smooth flow and at the

subcritical Reynolds number, are shown in Fig.1. These C_L , C_D , Lfl' and St sensitively varies with θ , in particular, at near critical stalling angle of $\theta_{cr}=50^\circ$. The Flow around cylinder affected by the protuberance position would be characterized mainly based on these, as follows:

$\theta < 30^\circ$: The almost effect of protuberance, and the flow is fundamentally separated-type.

$30^\circ < \theta < 50^\circ$: Separation bubble behind a protuberance gradually grows with increase of θ , and the flow is reattached-type. FL' gradually decrease with increase of θ , since the flow becomes more intensively reattached-type.

$\theta = 50^\circ$: the most intensive separation bubble (short bubble) is formed behind a protuberance, and, the flow shows the bi-stable flow, those are a separated-type and a reattached-type.(based on St - θ diagram)

$50^\circ < \theta < 54^\circ$: The intensive “bubble-burst” appears following with drastic decrease of C_L with increase of θ . The flow mainly is mainly a separated-type affected by the intensive “bubble-burst”.

$54^\circ < \theta < 70^\circ$: the weak “bubble-burst” continues following with gradual decrease of C_L with increase of θ . Comparatively large value of FL' corresponds on the low frequency vortex caused by the “bubble-burst”. The flow is fundamentally a separated-type, but affected by a separated-type, because of small value of St .

$70^\circ < \theta < 100^\circ$: The flow gradually becomes the one affected by a protuberance. The flow, in consequence, is a separated type.

$100^\circ > \theta$: The almost effect of protuberance, and the flow is fundamentally separated-type.

As summary on the effect of protuberance on circular cylinder, the “bubble burst” can be observed near at $\theta=50^\circ$, then the low frequency flow /vortex appears. The bubble-burst at $\theta=50^\circ$ can be successfully visualized by CFD analysis by Liu[33] as shown in Fig.2.

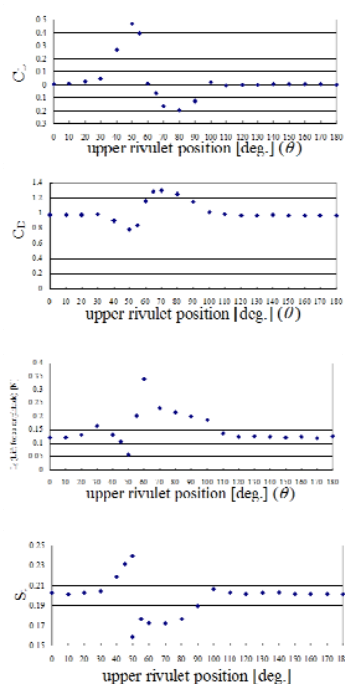


Fig.1 Lift coefficient, CL (top), Drag coefficient, CD(second), Fluctuating lift, FL'(third) and Strouhal number, St(bottom) of a circular cylinder with a protuberance

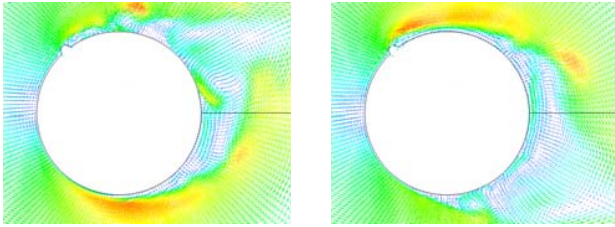


Fig.2 Unsteady flow around a stationary circular cylinder with a protuberance at stalling angle of $\theta=50^\circ$. Appearance of the “bubble-burst(left) “and reattachment flow during stall(right)(CFD analysis by Liu[33])

Fig.3 shows the PSD diagrams of fluctuating lift force measured at the condition of $V=8\text{m/s}$, $D=0.05\text{m}$ non-yawed circular cylinder /without with a protuberance at the range of $\theta =0^\circ$ and 90° are shown in Fig.4. The multiple-peaks are particularly found, in the one at $\theta=50^\circ$, which is critical stalling angle. The low frequency slight peak arises at of $\theta=55^\circ$ and $\theta=60^\circ$, corresponding on the

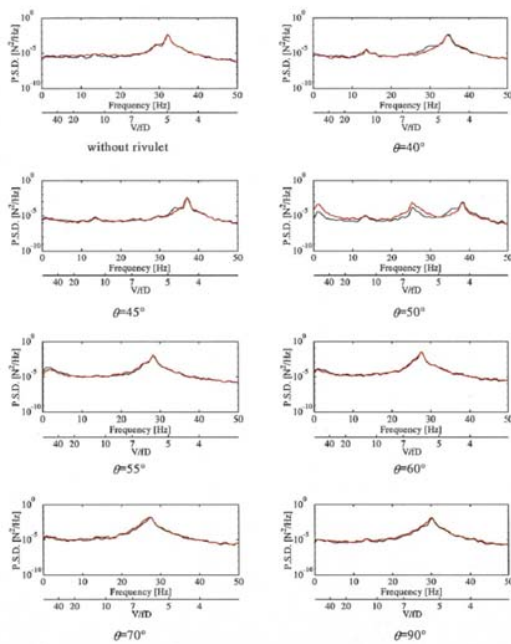


Fig.3 PSD of fluctuating lift force of non-yawed circular cylinder with a protuberance. ($V=8\text{m/s}$)

Fig.4 shows the PSD of lift force of a non-yawed circular cylinder with symmetrical double and same size protuberances, measured at the conditions of $V=6\text{m/s}$, $D=0.05$ in smooth flow and at $\theta=50^\circ$. The low frequency fluctuation of flow/lift force can be observed similarly with the case of a single protuberance. The aerostatic properties of a non-yawed circular cylinders with symmetrical double protuberances are precisely studied by Hori[34]. Their drag and fluctuating lift and Strouhal number associated to protuberance position are interestingly similar with the ones with the case of a single protuberance explained above, exceptionally the results of lift force. Because of symmetrical shape, lift force shows zero exceptionally $\theta=50^\circ$. Which means the separation bubble is formed at

the critical stalling angle, $\theta=50^\circ$, on one side face of cylinder, then the asymmetrical flow appears and the sequential aerostatic properties, including the appearance of bi-stable flow and the low frequency flow/vortex, caused by the “bubble-burst”. The flow thought to be “bubble-burst” calculated by CFD is shown in Fig.6.(Hori[34]) The significant asymmetrical flow and the intensive vortex shedding in a near wake can be observed. The cross-flow vibration of the non-yawed cylinder with symmetrical protuberances and a single protuberance at $\theta=50^\circ$ and $\theta=54^\circ$, respectively. In summary, the stall galloping can be excited in relation to the “bubble-burst” of the “stall”, the bubble burst can produce the low frequency flow/ vortex similarly with the case of airfoil.

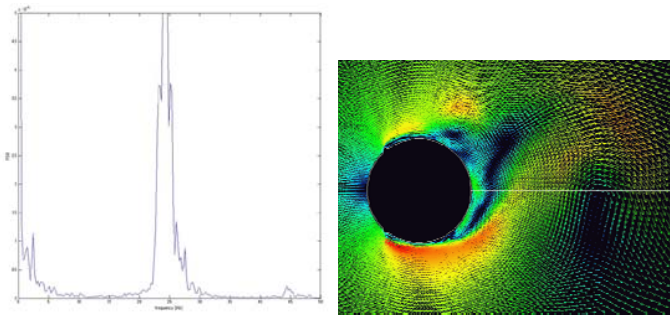
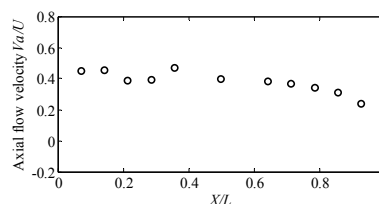
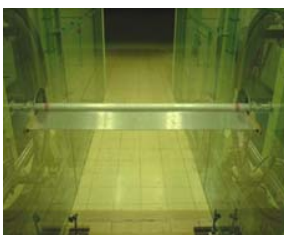


Fig.4 the PSD of lift force of a non-yawed circular cylinder with symmetrical double and same size protuberances, measured at the conditions of $V=6\text{m/s}$, $D=0.05$ in smooth flow and at $\theta=50^\circ$ (top left) and the Unsteady and instant flow visualized at $\theta=50^\circ$.(top left) (Hori[34])

(2) Yawed smooth circular cylinder with yawed angle of 45° and non-yawed cylinder with a perforated splitter plate

An intensive axial flow with the velocity of around 20% to 50% of the one of approaching flow is generated at a near wake of a stationary yawed ($\beta=45^\circ$) circular cylinder. The intensity of axial flow velocity varies in the axial direction, X/L (X is distance from the upstream end of the yawed cylinder, L : cylinder length) as shown in Fig.5 (top right). In the PSD of the lift measured at $V=4\text{m/s}$, the low frequency peak is observed additionally the peak at the Strouhal number of the yawed cylinder with $\beta=45^\circ$, $St \approx 0.14$. Both cases, yawed ($\beta=45^\circ$) state and with a perforated splitter plate, the galloping instabilities are observed, moreover as in Fig.5(bottom right and left), Their PSD diagrams of lift force show significantly similar, including the low frequency peak. In consequence, both of their galloping are thought to be the “stall-type galloping”.



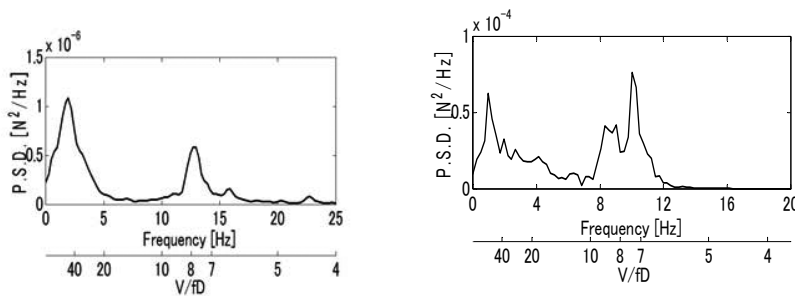


Fig.5 non-yawed cylinder with a separately installed splitter plate with 30% perforation and the length of 4D(top left), the axial flow intensity along yawed($\beta=45^\circ$) cylinder measured in a wake positioned at vertically cylinder center and 1D in along wind (top right), PSD of lift of nonyawed cylinder with a 30%perforated splitter plate, and the one of yawed($\beta=45^\circ$) cylinder, (bottom left and bottom right , respectively)

(3) A circular cylinder at the critical Reynolds number

As described before, Schewe[11] reported the detail information on the aerostatic properties of non-yawed circular cylinder at the critical Reynolds number, in particular on the appearance of non-zero stationary lift and low frequency lift during the drag-crisis. The non-zero stationary lift was measured at the range of the critical Reynolds number by Larose[14], Liu[31], Matsumoto[16] and Flamand[32]. Furthermore, Liu[31] reported the appearance of the velocity-restricted cross-flow response of non-yawed circular cylinder corresponding to the specified velocity where the stationary lift appears and disappears. It has been known that the laminar separation bubble is formed on the one-side of cylinder face at the critical Reynolds number(Sato[35], Basu[36], Jakobsen[14]). The aerostatic characteristics affected by the cylinder surface roughness have been studied by (Georgakis[30]). The cross-flow response characteristics have been studied by Kimura[29] and Katsuchi[28]. It can be said that almost recent these studies are to understand more clearly the complex generation mechanism of the “Dry Galloping (DG)” of inclined stay cables. Furthermore, Saito[37] and Kimura[29] have experimentally reported significantly important cross-flow response property of the yawed cylinder with $\beta=45^\circ$, those are first divergent-type response starts at the reduced velocity ($V_r=V/fD$) of around 40 till up to the critical Reynolds number. At this critical Reynolds number, the responsive amplitude becomes small, but the second divergent-type response continuously starts. Taking into account of the existence of the axial flow in a near wake formation at the sub-critical Reynolds range and formation of the laminar separation bubble at the critical Reynolds number, these cross-flow vibration should be excited in relation to the “stall”, in another expression, both of their first and second responses must be the “stall-type galloping”. On the DG of cable related the critical Reynolds number, Macdonald[15] and Kimura[29] pointed the less/non effect of the Scruton number, Sc , on their galloping. The authors evaluate their view-points as follows: 1. The separation bubble is formed at around $130^\circ(230^\circ)$ from the front stagnation point evaluated from the pressure distribution on cylinder surface (Flamand[32]), therefore the stationary lift appears at this point. Based on the quasi-steady theory, when a cylinder moves downward, the quasi-steady lift can be expressed as follows;

$$LFDy=L\sin(\theta+\alpha r_e)=L\sin\theta+L\cos\theta\sin(dy/dt)\cos\theta\approx L\sin\theta+L\cos\theta(dy/dt)$$

Where L :stationary lift at the critical Reynolds number (upward positive), y :displacement of a cylinder (down ward positive) and θ is central position of the laminar separation bubble measured from the front stagnation point. Based on this hypothesis, the term of $L\cos\theta(dy/dt)$ is the quasi-steady damping term, then it can excite a cylinder because of $\theta\approx 130^\circ$ or $\theta=230^\circ$. Therefore if the effect of this term would mainly play, Sc must make significant effect on the cross-flow vibration of a cylinder at the critical Reynolds number, which is contradictory to the view-points by

Macdonald[15] and Kimura[29].

On the other hand, taking account of separated flow caused the cross-flow vibration, when a cylinder moves downwards, it can be easily evaluated that the separated flow tends to move far away from the cylinder face, and contrary the one of from down side of cylinder tends to approach. In consequence, if a laminar separated bubble would be formed on upper-side of cylinder, it would be easily destructed or significantly weakened. On the contrary, when a cylinder moves upwards, the separation bubble should be amplified because of promotion of reattaching of the separated flow. Which means the lift force must be always produced in the same direction of the cylinder movement. In the case of formation of separated bubble is formed on the down-side of cable surface, the same role of the cylinder motion on the intensity of the separation bubble is easily confirmed. These cases are thought to be excited by the displacement, y , plays definitely play an important role, instead of displacement velocity, (dy/dt) . Based on the discussions explained, the later effect might be more effectively on the excitation of the “stall-type galloping”.

5. THE LOW FREQUENCY FLOW/VORTEX IN RELATION TO THE “STALL”

The reason of the appearance of the low frequency flow/vortex has been mainly reported to be in relation of H-S Instability and T-S Wave Instability in the field of the aeronautical engineering field. However its detail remains not clear. The authors investigate that the generation of the low frequency flow/vortex during the “stall” of bluff body as follows: The flow changes from the separated-type to the reattached-type at the “stall”. The Karman vortex, in consequence, must be drastically suppressed/ mitigated. The Karman vortex in a wake of bluff body is also stabilized vortex of separated shear layer instability in relation to K-H instability. In another words, the stabilized Karman vortex might interrupt the stabilization of another vortices from the shear layer with various frequencies. In the case of the “stall” of the bluff bodies, including the circular cylinders under the various conditions described above, because of mitigation of the Karman-vortex, the low frequency flow/vortex might be produced in original and latent Strouhal numbers-property, like the “DNA”, of the bluff body. The fluctuating flow in relation to the latent Strouhal numbers might be amplified by certain stimulation to the shear layer, when the Karman Vortex is sufficiently mitigated. In order to verify this scenario of appearance of the low frequency flow/vortex by mitigation of Karman vortex, regarding to the “stall” of a circular cylinder, the Karman vortex is mitigated by the splitter plate installed separately from a cylinder with the gap length between cylinder and the splitter plate of 0.1D, the length of 18D and 70% and 10% perforated plate. The fluctuating lift by the Karman vortex is mitigated into be almost 10% and almost 0% by these splitter plates respectively. The longitudinal and sinusoidal fluctuating-flow, with the extremely slight amplitude, that is u/U , of 0.67% can be generated by the sinusoidal generator, which is composed by two rotators installed on a perforated plate at the wind tunnel-outlet, by changing the air-volume at the wind tunnel outlet. The wake velocity was measured at 1.5D along-wind and 1D cross-wind from cylinder center in a wake. Fig.6 shows the diagrams of the PSD of wake velocity-frequency-fluctuating flow frequency measured at 6m/s. The enhanced flows/vortices at the peculiar frequencies are observed in these diagrams corresponding to the characteristic Strouhal numbers, in particular, significantly low frequency, in another expression significantly lower Strouhal number than $St=0.2$, such as $St=0.05, 0.025, 0.0125, \dots$. Thus, the hypothesis of the role of mitigation of Karman vortex caused by “the stall” explained above might be thought to be supported.

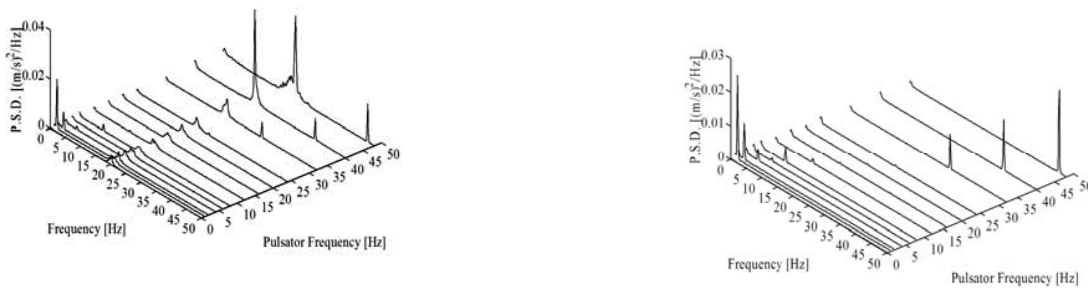


Fig.6 the PSD diagrams of wake velocity of non-yawed circular cylinder with perforated splitter plate in a wake, affected by the longitudinal fluctuating flow measured at 6m/s. (70% perforated splitter plate(left) and 10% perforated splitter plate(right))

6.CONCLUSIONS

The conclusions of this study are as follows:

1. The galloping of bluff body can be excited by the stall. This kind of galloping is called as the “stall-type galloping”.
2. The “stall” should be related to the “bubble-burst/ destruction” similarly with an airfoil stall.
3. Significantly low frequency flow/vortex can be generated by the “stall” of bluff bodies, similarly with the case of airfoil.
4. The “stall” of bluff bodies can be characterized by following factors :1. Negative slope of lift slope associated to pitching angle, 2.mitigation of Karman vortex, 3. Unsteady appearance of bi-stable flows, those are separated f-type and reattached-type flows, 4. Appearance of low frequency flow/vortex and 5. Appearance of cross-flow vibration.
5. RWIV (rain wind induced vibration) and DG(dry galloping), induced by the water-rivulet formation, the axial flow in a near wake and the critical Reynolds number, of stay cables of the cable stay bridges must be kinds of the “stall-type galloping”.
6. The low frequency flow/vortex caused by the “stall” of bluff bodies might be related to the mitigation of Karman vortex caused by the “stall”

ACKNOWLEDFEMENT

The wind tunnel tests and CFD analyses related to this study definitely rely on many persons who graduated from, the Bridge Engineering Lab. of Kyoto University. The authors have to express their sincere gratitude to Mr.C.Izumi, Dr.Y.Kim, Mr.J.Aoki, Mr.M.Tsujii, Mr.Y.Sano, Mr.S.Hirai, Mr.K.Katsura, D.Tsushima, Mr.S.Sakai, Mr.J.Ohya, Mr.T.Okada, Mr.T.Ohishi, Mr. Y.Adachi, Mr.Hatsuda, Mr.Shima, Mr.Tanaka, Ms. H.Naito, Dr.Q.Liu, K.Hori. Furthermore, The authors would like to express their special thanks to Prof. J.Macdonalds, Dr. O.Flamand, Dr.A.Benidir, Prof. H.Shirato, Prof. T.Yagi, Dr. Y.Ito, Dr.H.Matsumiya, Dr. Q. Liu, Dr.K.Hori for their valuable personal communications.

REFERENCES

1. K.Rinoue, , NAGARE(Fluid) 22, pp15-22, 2003(in Japanese)
2. K.Rioie, Aeronautical and Space, Japan, Vol.61, No.3, 2013 (in Japanese)
3. Y.Zhou. Graduate theses and dissertation, Iowa Univ. 2011
4. N.Hirose. NAGARE(Fluid) 22, pp23-228, 2003(in Japanese)
5. McAlister K, Pucci S, McCroskey W, Carr L. vol. 2. NASA, Technical Memorandum 84245; 1982.
6. S.Wang, D.B.Ingham, L.Ma, M.Pourkashanian, Z.Tao, Computer and Fluids, Vol.39, pp.1529-1541, 2010
7. E.K.Armstrong, and R.E.Stevenson.J.Royal Aeronautical Society,Vol.64, No.591,1960

8. M. Matsumoto, T. Yagi, Y. Adachi, H. Hatsuda, T. Shima, , Proc. of the 12th International Conference of Wind Engineering, pp.175-182, 2007
9. H.Matsumiya.Civil Engineering Research Lab. Rep.No.N11031, CRIEPI, 2009
10. Y.Ito. Dr. Dissertation, Kyoto University, 2014
11. G.Schewe. J . Fluid Mech., vol. 133, pp. 265-285, 1983
12. Y. Nakamura, K.Hirata, , Trans. of the Japan Soc. for Aeronautical and Space Science, Vol.36, No.114, pp.257-269, 1994
13. Y. Hikami (1986), Journal of Wind Eng. JAWE, No.27, (in Japanese)
14. T.L.Andersen, J.B. Jakoben, J.H.G. Macdonald, N.Nikitas, G/L.Larose, M.G.Savage, B.R.Mcauliffe.Proc. of ISCD, pp341-348
15. J.G. Macdonald(2005), Proc. of 6th ISCD, Charleston, South Carolina, , 435-442
16. M.Matsumoto,N.Shiraishi,M.Kitazawa,T.Saito(1989), Proc. of Structural Congress '89, ASCE,
17. M. Matsumoto,N.Shiraishi, H.Shirato(1992), , JWEIA, 41-44, pp.2011-2022,
18. M.Matsumoto,Y.Hikami,M.Kitazawa, Proc. of International Conference of Cable Stayed and Suspension Bridges, Deauville, IABSE, 1994
19. .M.Matsumoto(1998) , Bridge Aerodynamics, in Proceedings of the International Symposium on Advances in Bridge Aerodynamics, Copenhagen, Denmark, May, 1998, pp.189-211
20. M.Matsumoto, H. Shirato, T. Yagi, M. Goto, S. Sakai and J. Ohya(2003), , JWEIA, Vol. 91, No.1-2, pp.13-26
21. M. Matsumoto, T.Yagi, Q.Liu, T.Ohishi, Y.Adachi(2005), Proceedings of 6th International Symposium on Cable Dynamics, Charleston, South Carolina, U.S.A.,247-254
22. .M. Matsumoto, Proceedings of Wind Induced Vibration of Cable Stay Bridges Workshop, St. Louis, Missouri, U.S.A.2006
23. M.Matsumoto, Proceedings of ASME 2010 3rd Joint US-European Fluids Engineering Summer Meeting, FEDSM-ICNMM2010 Montreal,
24. M.Matsumoto, T.Yagi, H.Hatsuda, T.Shima, M.Tanaka, H.Naito(2010), JWEIA, 98, pp317-327
25. M.Matsumoto(2011), Proceedings of the 9th ISCDI, Shanghai
26. C. Vervue(1998), Proceedings of Bridge Aerodynamics, Larsen & Esdahl(eds), Balkema
27. S.Cheng , P.A. Irwin., J.B. Jakobsen, J.Lankin, G.L.Larose, M.G. Savage, ,H.Tanaka and H., C. Zurell, Proceedings of 5th ISCD, 2003Santa Margherita Ligure, 271-278
28. H. Katsuchi, H.Yamada, Proc. of 8th ISCD, 2009, Paris
29. K. Kimura, K.Kato , Y.Kubo, Y.Ohashi, , Proc. of 8th ISCD, 2009,Paris
30. G.Matteoni,C.Georgakis, "Aerodynamic coefficients of dry inclined cables in smooth flow" Proc. of the 9th ISCD, 2011, Shanghai
31. Q.Liu, Y.Wang, Y.Cheng, W.Ma, , Proc. of the 9th ISCD, 2011, Shanghai
32. Q.K.Liu, (2005), Doctor Dissertation of Kyoto University (in Japanese)
33. Q.Liu, Y.Wang, Y.Cheng, W.Ma, , "Reynolds number effect on wind induced vibration of stay cables", Proc. of the 9th ISCD, 2011, Shanghai
34. K.Hori, Kyoto University,2007, (in Japanese)
35. M.Sato, H.Kanda, H.Suenaga, N.Sudani, M.Shigemi, ,Technical Report of National Aerospace Laboratory, ISSN 0452-2982, 1999
36. R.I. Basu, 1985, JWEIA, 21, 1985, pp-273-294
37. T.Saito : personal communication

SOME CONFIRMATIONS RELATED WITH PRANDTL'S LIFTING LINE THEORY

Jiro Nakamichi^{† 1}

Japan Aerospace Exploration Agency, Tokyo, Japan

The Lifting Line Theory is based upon the fact that the local lift at a wing section depends not only on the local section angle of attack but also on the downwash induced by the trailing vortices shed from the next segments of the wing. It predicts quantitatively the spanwise lift distributions of 3D wing, the induced drag and the load distribution of minimum-drag 3D wing. It is also well consistent with the momentum theory about 3D wing. There are two puzzles for the engineers in the aeronautics, especially for aeroelasticians and aerodynamicians in the world. (i) the collocation point for the numerical solution of lifting surface theory (DLM or VLM) must be at the 3-quarter-chord point of each element. Why? (ii) in the momentum theory about 3D wing, what should be the reference mass to exactly explain the lift and drag? In the present note, the two points are clarified with the help of some mathematical manipulations, using the models of an isolated horseshoe vortex and an elliptically load distributed bound vortex with a trailing vortex sheet.

Keyword: lifting line theory, induced drag, momentum theory

1. INTRODUCTION¹⁻⁵⁾

Since the earlier times than the first flight of powered aircraft, wing theories have been rigorously developed. Prandtl's lifting line theory developed in 1918 is one of the greatest achievements in the history of the aeronautics. It is a simple but a great theoretical interpretation of physical phenomena around lifting surface, which properly explains the relationships among the lift and the induced drag as well as the momentum theory about 3D wing. It was also the first step toward the sophisticated lifting surface theory established in 1950's.

There are two facts which are well known among aeroelasticians and aerodynamicians, those are;

- i) The collocation point must be specified at the 3-quarter-chord point in divided each wing panel when we employ the DLM(Doublet Lattice Method) or VLM(Vortex Lattice Method) for the solution of lifting surface theory.
- ii) When we apply the momentum theory to 3D wing, the reference mass should be the mass of the air which flows through a circle with a diameter of the wing span.

The theoretical explanations on the above two points are given in the present note by further studying the lifting line theory.

1. OUTLINE OF LIFTING LINE THEORY^{3,4)}

The mathematical model of the lifting line theory consists of a bound vortex $\Gamma(y)$ supposed to be on the wing surface and trailing vortices $d\Gamma/d\eta$ shed from the bound vortex depending on the variations in its magnitude. Introducing the concept of the Kutta-Joukowski Theorem and the relation between lift and downwash (the angle-of-attack) at a wing section y , we obtain an integral-differential equation with respect to the distributed circulation $\Gamma(y)$ in a form as

$$\rho U \Gamma(y) = \frac{1}{2} \rho U^2 a_0 C(y) \left[\alpha(y) - \frac{1}{4\pi U} \oint_{-l}^{+l} \frac{d\Gamma}{d\eta} \frac{d\eta}{y-\eta} \right] \quad (1)$$

where l is a half-span length of the 3D wing; $\alpha(y)$ is local angle of attack; $a_0 (= 2\pi)$ is the theoretical

^{†1}nakamichi.jiro@jaxa.jp

value of lift-curve slope of 2D wing; $C(y)$ is the local chord-length, respectively.

The second term in the right-hand side of Eq.1 is the downwash induced by trailing vortexes. It describes mathematically that the local lift at a wing section is determined not only due to the section local angle-of- attack but also due to the influence of the trailing vortexes shed from the next segments of the wing. The spanwise lift distributions on 3D wing can be predicted by solving Eq.1 and 2 with boundary condition at every spanwise section. The Eq.1 can be rewritten as a relationship among the boundary condition, the downwashes due to bound vortex and the trailing vortex at a section y as

$$U\alpha(y) = \frac{1}{2\pi} \frac{\Gamma(y)}{\frac{1}{2}c(y)} + \frac{1}{4\pi} \oint_{-l}^{+l} \frac{d\Gamma}{d\eta} \frac{d\eta}{y-\eta} \quad (2)$$

$$w_{3/4}^{(B)} = \frac{1}{2\pi} \frac{\Gamma(y)}{\frac{1}{2}c(y)} \quad , \quad w_{1/4}^{(T)} = \frac{1}{4\pi} \oint_{-l}^{+l} \frac{d\Gamma}{d\eta} \frac{d\eta}{y-\eta} \quad (3), (4)$$

The bound vortex should be located at the quarter-chord point since that is the location of the aerodynamic center of a thin flat plate airfoil. The right-side term of Eq.3 is identical with the downwash at a half-chord downstream from the bound vortex, that means the downwash at the 3-quarter-chord point of the section. On the other hand, the integral term in Eq.4 expresses the totally integrated downwash at a quarter-chord-point due to the trailing vortex sheet.

If we let the angle-of-attack at the 3-quarter-chord point represent the angle-of-attack of the section, there is a small difference in evaluation points between $w_{3/4}^{(B)}$ and $w_{1/4}^{(T)}$. However, in the case of high-aspect-ratio wing, the difference is small enough because

$$|y - \eta| \gg |c(y)| \quad (5)$$

is true in most part over the 3D wing¹⁾.

3. INDUCED VELOCITY DISTRIBUTION BY A HORSESHOE VORTEX^{1,2)}

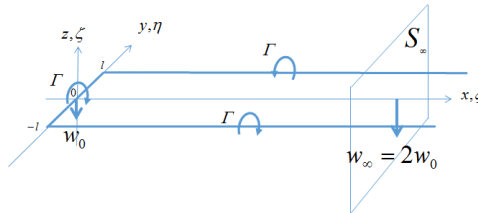


Figure 1: Schematic View of a Horseshoe Vortex

A horseshoe vortex is one of the simplest models of wing circulation system. The coordinates system used here is defined as is shown in Fig.1. It assumes that a bound vortex of which magnitude is Γ is located along y -axis and the trailing vortexes from tips are modeled as is show in Fig.1. The spatial distributions of the induced velocity due to the horseshoe vortex are calculated by use of the law of Biot-Savart. The downwash at a point (x,y,z) becomes

$$w(x, y, z) = \frac{\Gamma}{4\pi} \left[\frac{x}{x^2+y^2} \left(\frac{l+y}{r_+} + \frac{l-y}{r_-} \right) + \frac{l+y}{(l+y)^2+z^2} \left(\frac{x}{r_+} + 1 \right) + \frac{l-y}{(l-y)^2+z^2} \left(\frac{x}{r_-} + 1 \right) \right] \quad (6)$$

where $r_{\pm} = \sqrt{x^2 + (l \pm y)^2 + z^2}$.

From Eq.1, the downwashes at the origin and at an infinite downstream point are evaluated as,

$$w_0 = w_{x=0,y=0,z=0} = \frac{\Gamma}{2\pi l} \quad \text{and} \quad w_\infty = w_{x=\infty,y=0,z=0} = \frac{\Gamma}{\pi l} \quad (7)$$

respectively. Though w_0 and w_∞ are not constant in the yz -plane, if we consider them as the representative magnitudes of the downwash at $x = 0$ and $x = \infty$, then the well-known relationship between w_0 and w_∞ of

$$w_\infty = 2w_0 \quad (8)$$

is maintained.

The change in the z -direction velocity components of the upstream and the downstream is related to the change in the z -direction momentum of the total flow which is passing through a yz plane per unit time. The total change of the z direction momentum of the flow can be counted by integrating the downwash $w(\infty,y,z)$ in the plane S_∞ and if we use w_∞ (Eq.7) as a representative velocity at $x = \infty$,

$$\rho U \int_{S_\infty} w(\infty,y,z) dydz = \rho U (2\pi l^2) w_\infty \quad (9)$$

is obtained. Therefore the total mass of the air which changes the flow direction is apparently to be

$$S_B = \rho U (2\pi l^2) \quad . \quad (10)$$

This is recognized as the total mass flow which passes per unit time through a circular with diameter $2\sqrt{2}l$.

4. INDUCED VELOCITY BY AN ELLIPTICALLY LOAD DISTRIBUTED BOUND VORTEX^{1,3)}

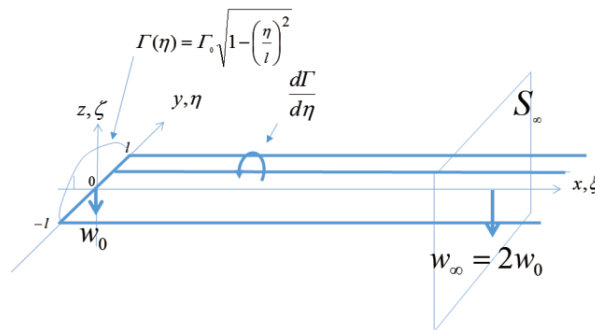


Figure 2: Schematic View of an Elliptically Load Distributed Bound Vortex

Elliptically load distributed bound vortex of which strength is defined by

$$\Gamma(\eta) = \Gamma_0 \sqrt{1 - \left(\frac{\eta}{l}\right)^2} \quad (11)$$

is considered. In this case, accounting the influence from the trailing vortex, the spatial distribution of the downwash behind the wing is derived by the Law of Biot-Savart and is obtained in a form of

$$w(x,y,z) = \frac{1}{4\pi} \frac{\Gamma(\eta)}{d\eta} \left[\frac{y-\eta}{(y-\eta)^2+z^2} \left(\frac{x}{r} + 1 \right) \right] \int_{-l}^{+l} d\eta + \frac{1}{4\pi} \Gamma(\eta) \frac{z}{r^3} \int_{-l}^{+l} d\eta \quad (12)$$

where $r = \sqrt{x^2 + (y - \eta)^2 + z^2}$.

Performing the integration in Eq.12 with respect to η at $x = 0$ and $x = \infty$, w_0 and w_∞ are obtained as

$$w_0 = w_{x=0,-l \leq y \leq l, z=0} = \frac{\Gamma_0}{4l}, \quad w_\infty = w_{x=\infty,-l \leq y \leq l, z=0} = \frac{\Gamma_0}{2l} \quad -l \leq y \leq l, \quad (13)$$

respectively. It is noted here that in the $z = 0$ plane which includes the wing surface, the magnitudes of

the downwash do not depend on y .

The relationship between w_0 and w_∞ ,

$$w_\infty = 2w_0 \quad (14)$$

is also maintained here.

The momentum change of mass flow in z -direction can be counted in a similar manner to the previous case and leads

$$\rho U \int_{S_\infty} w_\infty(y, z) dy dz = \rho U \left[\frac{1}{2} \pi l \Gamma_0 \right] = \rho U (\pi l^2) w_\infty \quad (15)$$

Therefore the total mass which is used in the momentum theory about 3D wing becomes apparently to be

$$S_B = \rho U (\pi l^2) \quad (16)$$

This is the total mass of the air which flows per unit time through a circular with diameter $2l$. This is the reference mass which is usually used in the momentum theory about 3D wing and is well consistent with the related wing theories developed so far.

5. FINAL COMMENTS

Through the present study, followings are led.

(i) For the solutions of the lifting surface theory, the collocation point should be at a half-chord downstream from the assumed concentrated vortex. The bound vortex should be located at the quarter-chord point since that is the location of the aerodynamic center of a thin flat plate airfoil. It leads that the collocation point should be at the 3 quarter-chord point, where there is consistency between relationships of lift-circulation and lift-downwash.

(ii) In the momentum theory about lifting surface, reference mass exactly “the mass of air that goes through a circle per unit time, of which diameter equals the wing span length, in the case of 3D wing elliptically loaded in spanwise.

We hope the two points mentioned above are useful for those who analyze flutter or the unsteady aerodynamics to understand the basic theoretical backgrounds of DLM and VLM which are installed in the NASTRAN and other aerodynamic analyses tools.

REFERENCES

- 1) Bisplinghoff, R.L., Ashley, H., R.L. Halfman : *Aeroelasticity*, 2nd ed. Addison-Wesley Publishing Company, 1957.
- 2) Rodden, W.P. : The Development of the Doublet-Lattice Method, International Forum on Aeroelasticity and Structural Dynamics, June 1997.
- 3) Anderson, J.D., : *Fundamentals of Aerodynamics*, 4th ed., McGraw-Hill, New York NY, 2007.
- 4) Moriya, T., *Aerodynamics*, (written in Japanese), Bifukan, Tokyo, 1959.
- 5) Toda, N. : private communications, 2015.

NONLINEAR SINGLE-MODE PANEL FLUTTER AT CONTINUOUSLY VARYING FLIGHT SPEED

Anastasia Shishaeva⁺¹, Vasily Vedenev⁺², and Andrey Aksenov⁺³
^{+1,2}Lomonosov Moscow State University, Moscow, Russia
^{+1,3}Tesis LTD, Moscow, Russia

Instability of elastic plate in unsteady sub- and supersonic flow is studied. The observe various limit cycle oscillations of the plate for different rates of increase and decrease of the flow speed. A number of the limit cycles bifurcations is detected and analysed.

Keyword: panel flutter, single mode flutter, internal resonance, nonlinear oscillations.

1. INTRODUCTION

Aeroelastic instability of skin panels, known as panel flutter, has been intensively studied over decades [1-6]. At high supersonic speeds the coupled-mode panel flutter occurs, while at low supersonic speeds the single-mode flutter is dominating. The coupled-mode flutter was investigated in details in the 1960th [1-2]. The single-mode flutter was studied during last ten years [7-12]. Recent nonlinear study [13] has shown that at small supersonic flight speeds, different limit cycles can coexist at the same flight conditions, which is caused by linear growth mechanism and nonlinear interaction between growing eigenmodes. Some of the limit cycles include internal resonance between natural modes. Switches of panel oscillations from one limit cycles to another is accompanied by bifurcation of the aeroelastic dynamic system. In the present paper we study such bifurcations by continuously changing the flow speed at various rates, and watching the panel response. This approach gives an explicit way to note the bifurcations in the limit cycles and reveals additional bifurcations not noticed before.

2. PROBLEM FORMULATION

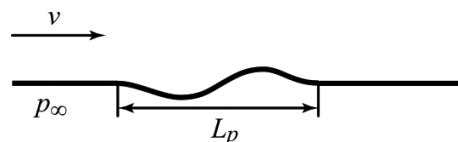


Figure 1. Plate in a gas flow

The formulation of the problem is as follows. The elastic plate of length $L_p = 0.3$ m and thickness $h_p = 0.001$ m is mounted into a rigid plane (Figure 1). The plate is made of steel with Young's modulus $E = 2 \times 10^{11}$ Pa, Poisson coefficient $\nu = 0.3$ and density $\rho_m = 7800$ kg/m³. In dimensionless terms, the plate stiffness and length are:

$$D = D_p / (a^2 \rho_m h^3) = 21.4, \quad L = L_p / h_p = 300,$$

Where $D_p = Eh^3 / (12(1 - \nu))$ is the dimensional plate stiffness, and $a = 331$ m/s is the speed of sound in the air. Similar values of dimensionless parameters correspond to other metal materials (e.g., aluminium and titanium). The plate is governed by the nonlinear Mindlin plate model, where elastic strains are calculated through Koiter–Sanders shell theory.

⁺¹anastasiashishaeva@rambler.ru, ⁺²vasily@vedeneev.ru, ⁺³andrey@tesis.com.ru

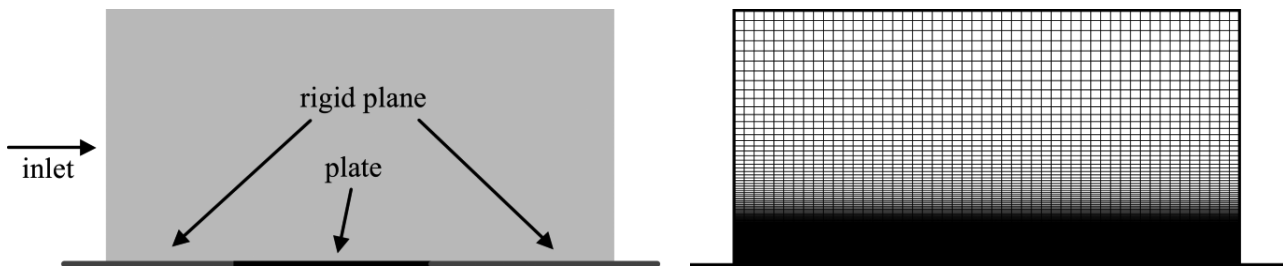


Figure 2. Simulation domain (a) and computational grid (b) in FlowVision

The simulation domain of the gas flow is a rectangular 0.6×0.3 m (Figure 2a). We consider inviscid perfect gas with air properties assigned. Gas flows over one side of the plate with varying Mach number $M(t)$. At the other side of the plate, a pressure equal to the undisturbed flow pressure is specified, such that the undisturbed pressure difference along the plate is zero. Linear increase and decrease of M between 0.7 and 1.7 during 2.5 s, 5 s, 7.5 s and 10 s is considered. In all simulation, a slight sinusoidal disturbing force is applied to the plate in order to excite each bifurcation of limit cycle oscillation.

Subsequent plate-flow interaction is calculated using two coupled codes, Abaqus for simulating the plate, and FlowVision for simulating the gas flow. Abaqus is a finite-element commercial code originally developed for stress analysis. FlowVision is a finite-volume commercial code developed by Tesis LTD for aero/hydrodynamic applications. Interaction between the codes is organized through direct coupling mechanism along the surface of the deformed plate [14-15]. Both codes are executed in turns; exchanges occur at each time step according to conventional. The displacements and velocities of the plate points are sent from Abaqus to FlowVision, whereas the pressure distribution along the plate surface is sent back from FlowVision to Abaqus. Mesh properties used in the simulation are as follows. The Abaqus plate model consists of hexahedral finite elements, with 60 elements along the chordwise direction. The FlowVision flow model consists of 50×494 (length \times height) finite volumes. The vertical size of finite volumes varies from 0.0001 m near the plate to 0.01 m in the far field of the simulation domain (see Figure 2a).

It is convenient to analyze plate behavior by watching deflection y of a reference point plotted versus time. The reference point is located at 0.22 m downstream of the leading edge of the elastic plate, which is approximately $3/4$ of the plate length. Fourier analysis is used to calculate the spectra of limit cycles observed.

Investigation of grid, time and domain convergence, testing of the model on coupled and single mode flutter at constant flow speed are described in [13].

3. RESULTS

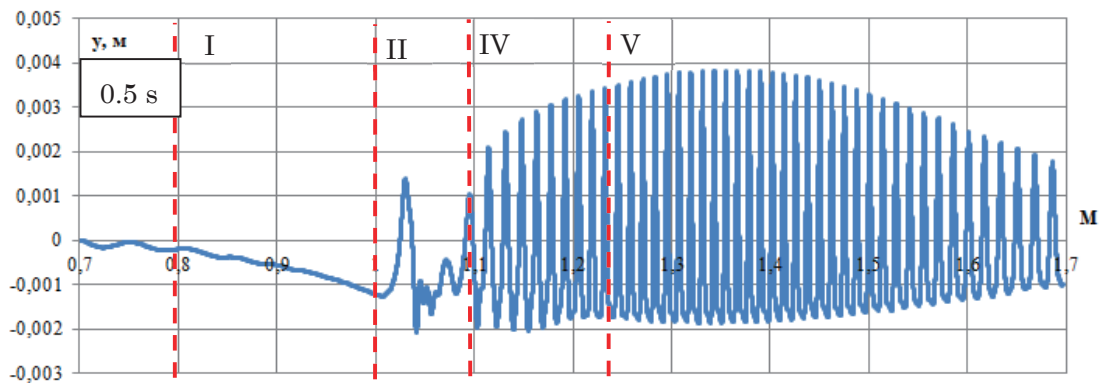
Our previous investigation of is described in [13]. We investigated plate instability at constant flow speed. We obtained eight bifurcations. They are shown in Table 1 for comparison.

Two series of calculation have been considered in our present investigation. The first corresponds to increase of M , the second corresponds to decrease of M . Results are shown in Table 1, Figure 3 and Figure 4. Nine bifurcations were detected. Here bifurcation sequence corresponds to acceleration. I - pitchfork bifurcation is a static plate divergence. II - Hopf bifurcation is a limit cycle occurrence. We detected first mode limit cycle with freezing. Freezing is a short stop of oscillation during the limit cycle. III - first mode limit cycle without freezing. IV - transition from non-resonant to resonant limit cycle. V - minor bifurcation of resonant limit cycles, VI - transition from resonant limit cycle to high-frequency non-periodic oscillations, VII - transition from high-frequency non-periodic oscillations to third-mode limit cycle, VIII - transition from third-mode limit cycle to first-mode limit cycle, IX - transition to stability. The number and positions of bifurcations vary with intensity and direction of M changing (Table 1). We can see that bifurcations II and III are the same for all accelerations and for constant speed. Bifurcation IV depends on acceleration direction but not on acceleration intensity. Bifurcations VI, VII, VIII, IX are the most sensitive for direction and intensity of acceleration.

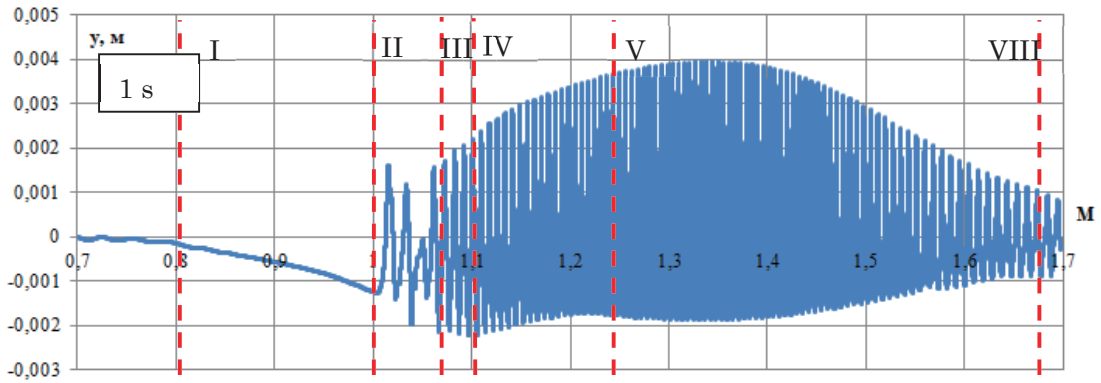
Table 1. The list of bifurcation.

	Increase of M						Decrease of M				M = const [13]
	0,5 s	1 s	2,5 s	5 s	7,5 s	10 s	2,5 s	5 s	7,5 s	10 s	
I	0,79	0,79	0,79	0,79	0,8	0,8	0,83	0,83	0,83	0,821	0,7
II	1	1	1	1	1	1	0,97	0,97	0,993	0,993	1
III	-	1,07	1,07	1,07	1,06	1,06	1,07	1,07	1,07	1,07	1,05
IV	1,1	1,1	1,1	1,1	1,1	1,1	1,09	1,09	1,09	1,09	1,12
V	1,24	1,24	1,24	1,23	1,23	1,22	1,17	1,2	1,25	1,165	-
VI	-	-	-	1,45	1,41	1,4	1,19	1,22	1,28	1,27	1,33
VII	-	-	-	-	1,53	1,53	1,2	1,31	1,36	1,36	1,42
VIII	-	1,68	1,6	1,58	1,63	1,63	1,23	1,34	1,37	1,38	1,44
IX	-	-	-	-	1,68	1,68	1,5	1,5	1,46	1,46	1,67

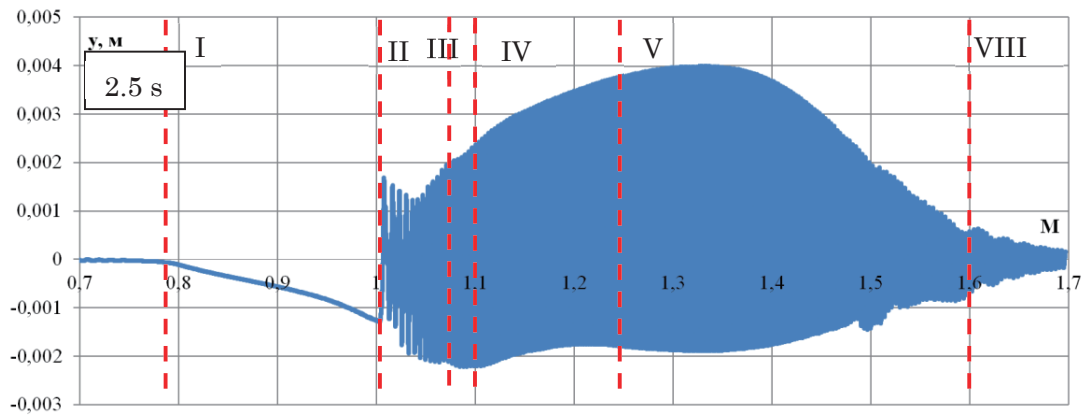
For faster increase of M, some of the limit cycles are not formed, since the formation period is too large. For example, for $\Delta M=1$ during 0.5 s, 1 s and 2.5 s we have only divergence, first mode limit cycles, resonant limit cycle, though more dangerous high-frequency or non-periodic oscillations are missed (see Figure 3a-Figure 3c). For $\Delta M=1$ during 5 s we have the same behavior as in the previous case almost in whole interval, except a small area $1.45 < M < 1.58$, where a high-frequency non-periodic oscillations are formed (see Figure 3d). For $\Delta M=1$ during 7.5 s we have a similar behavior in a low Much number as in previous cases. But for $M > 1.4$ we have a completely difference results. There is a long segment of non-periodic oscillations ($1.41 < M < 1.53$) and third-mode limit cycle ($1.53 < M < 1.63$) (see Figure 3e). Then, for smaller increase of M ($\Delta M=1$ during 10 s) we have a very similar behavior as in the previous case in the whole interval. Only positions of some bifurcation are slightly different (see Figure 3f).



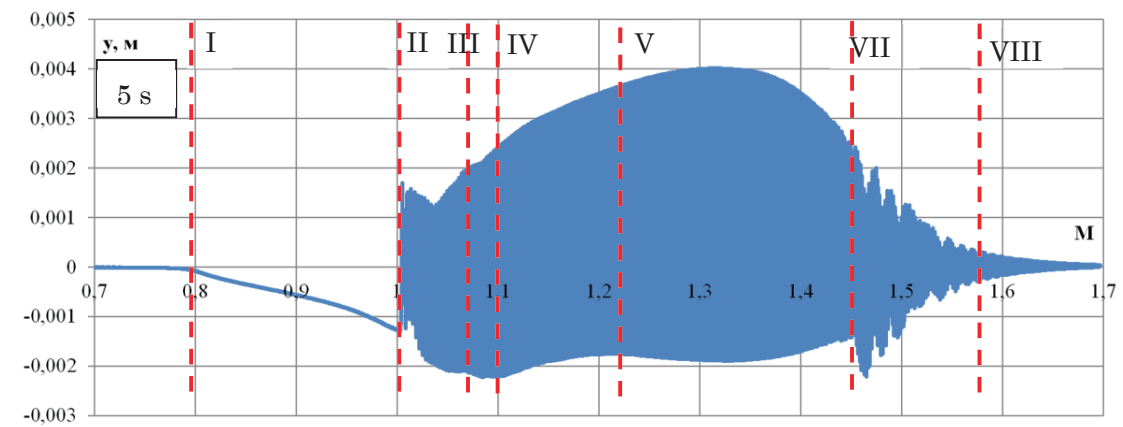
a



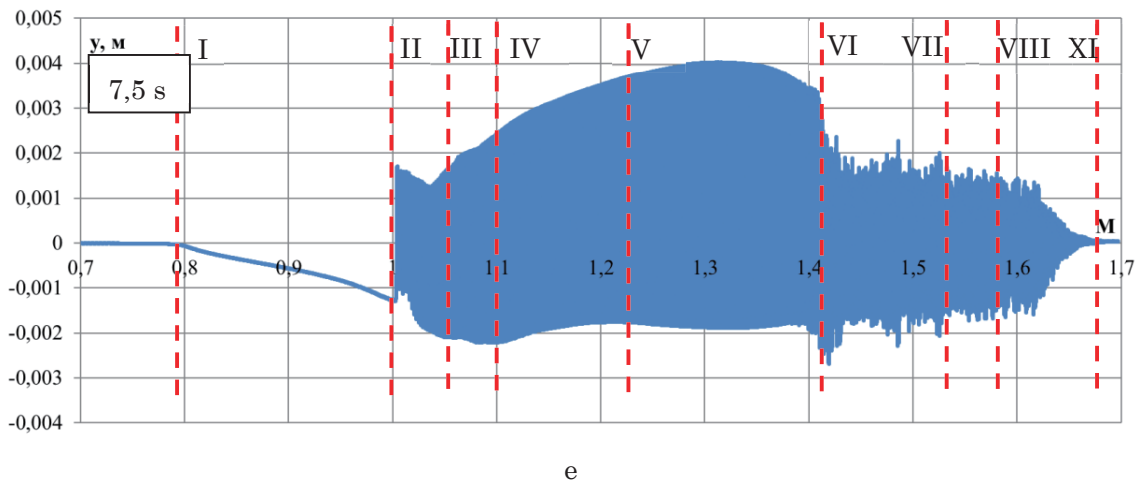
b



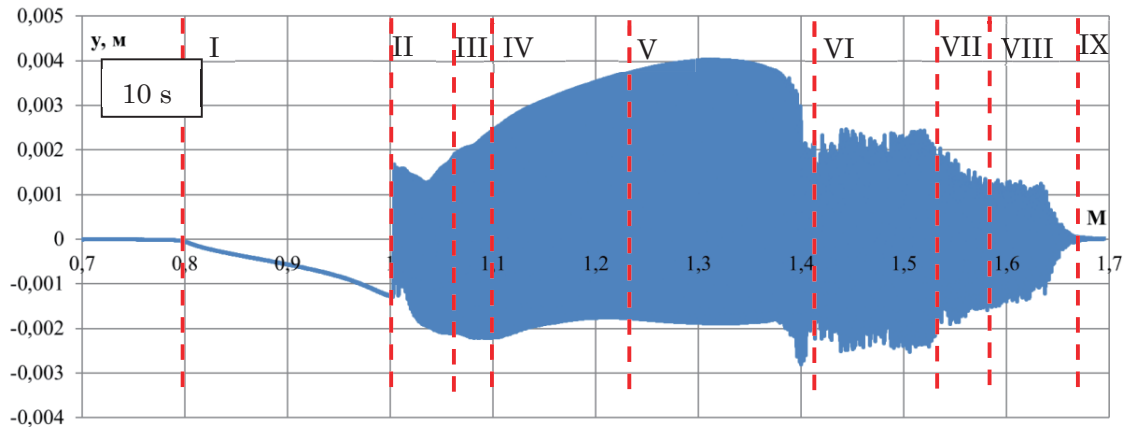
c



d



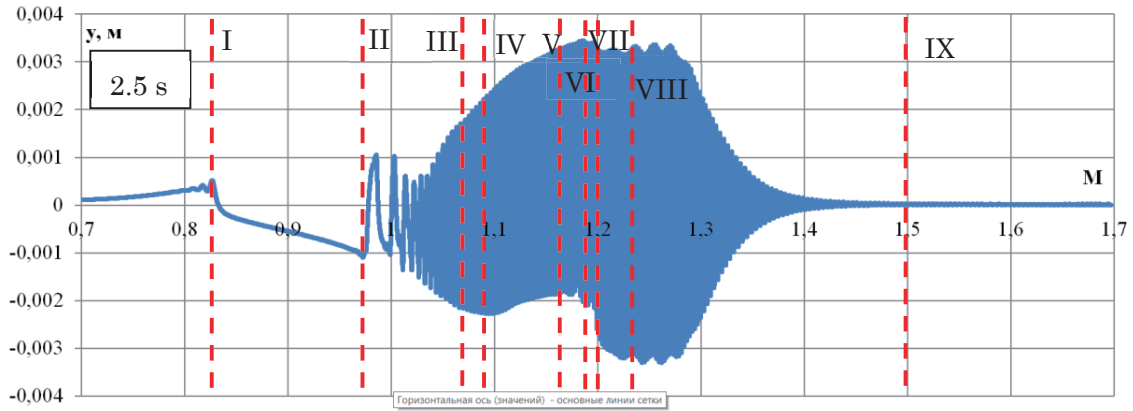
e



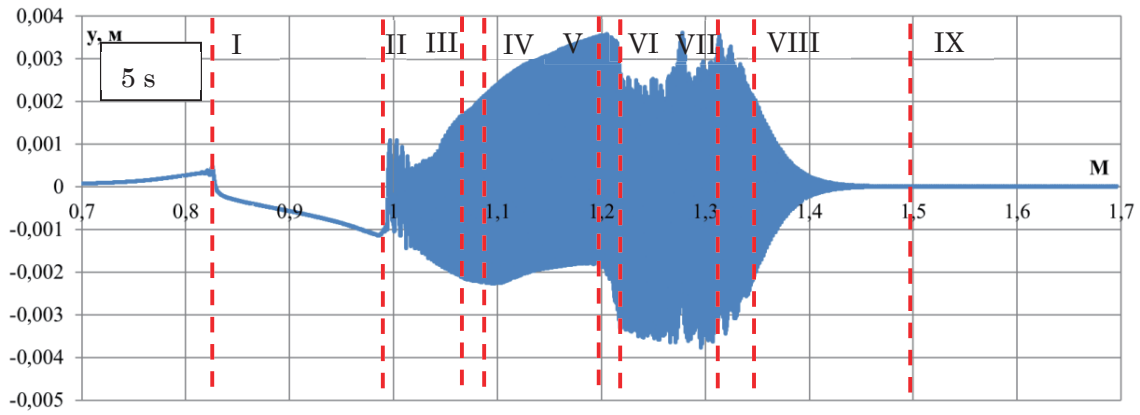
f

Figure 3: Vertical deflection of a plate point vs M in the case of acceleration from $M=0.7$ to $M=1.7$ during 0.5 s (a), 1 s (b), 2.5 s (c), 5 s (d), 7.5 s (e), 10 s (f), red lines represent bifurcations of the limit cycle.

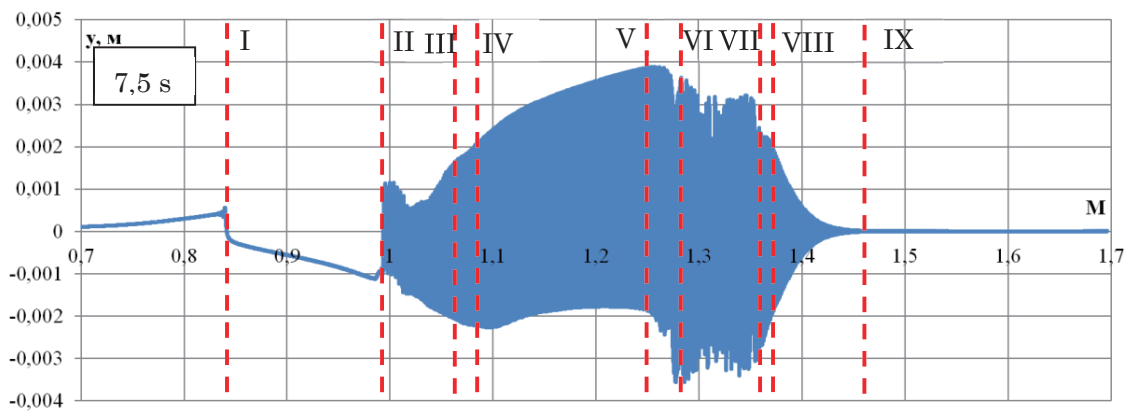
Plate instability is significantly different for increase and decrease of M . Thus, in all cases of decrease instability occurs if $M < 1.5$ and may take place till $M = 0.8$, whereas in the case of increase plate become unstable then $M > 0.8$ and can be unstable till $M = 1.7$ (see Figure 4). Also there is a significant difference between corresponding rates of increasing and decreasing with the same module of acceleration. For example, for decreasing of M during 2.5 s there is a small area of high-frequency non-periodic oscillations (see Figure 4a) ($1.19 < M < 1.2$), while for increasing of M during 2.5 s there are no high-frequency non-periodic oscillations (see Figure 3a). Further all cases of decrease of M are significantly different from each other for $M > 1.2$ (see Figure 4). Thus, for decreasing of M during 2.5 s there is a big area of first mode limit cycle ($1.23 < M < 1.5$) and small areas of non-periodic oscillations and third mode limit cycle ($1.19 < M < 1.2$, $1.2 < M < 1.23$) (see Figure 4a), while for decreasing during 5 s there is a big area of non-periodic oscillations ($1.22 < M < 1.31$) and shifted area of third mode limit cycle ($1.31 < M < 1.34$) (see Figure 4b). For decreasing during 7.5 s the area of non-periodic oscillations is shifted to the high M ($1.28 < M < 1.36$), also the region of resonant limit cycle is bigger than in previous cases ($1.09 < M < 1.25$) (see Figure 4c). For decreasing during 10 s there is a large region of transition from resonant limit cycle to non-periodic oscillations ($1.165 < M < 1.27$) (see Figure 4d).



a



b



c

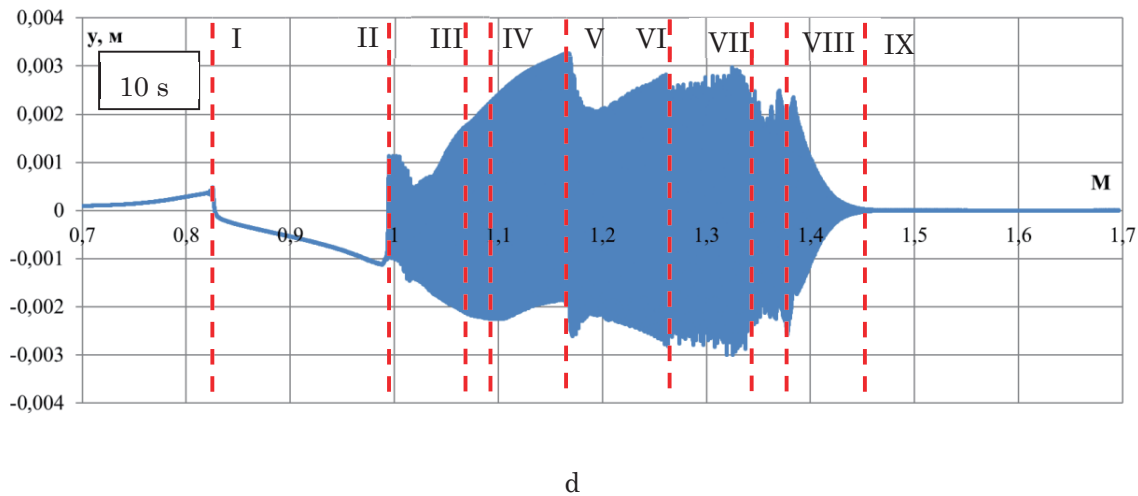


Figure 4: Vertical deflection of a plate point vs M in the case of deceleration from $M=1.7$ to $M=0.7$ during 2.5 s (a), 5 s (b), 7.5 s (c), 10 s (d), red lines represent bifurcations of the limit cycle.

Summary, we have shown that plate behavior is significantly different in the cases of increase and decrease of a flow speed. We can conclude that hysteresis areas near bifurcation are detected. Beside that, we have obtained that fast increase and decrease of a flow allow avoiding the most dangerous types of flutter, such as high frequency non-periodic flutter or third mode flutter, while slow increase or decrease allows investigating instability area in details. Also, we have obtained that instability occurs at all considered accelerations.

4. CONCLUSIONS

Numerical study of a plate instability in an unsteady flow has been conducted. Ten different rates of the increase and decrease of the flow speed have been investigated. A series of bifurcations for each case is detected. It is shown that fast increase and decrease of a flow speed allows avoiding the most dangerous types of flutter, namely high frequency non-periodic flutter or third mode flutter. However, first mode flutter is not suppressed even for very high accelerations.

ACKNOWLEDGMENT

The work is supported by grant MK-5514.2016.1 and grant MD-4544.2015.1.

REFERENCES

- 1) Movchan, A.A.: On stability of a panel moving in a gas. *Prikladnaya Matematika i Mekhanika*, Vol. 21 (2), pp. 231–243, 1957 (in Russian); translated in NASA RE 11-22-58 W, 1959.
- 2) Bolotin, V.V.: *Nonconservative Problems of the Theory of Elastic Stability*, Pergamon Press, Oxford, 1963.
- 3) Dowell, E.H.: *Aeroelasticity of Plates and Shells*. Noordhoff International Publishing, Leyden. 1974.
- 4) Dugundji, J.: Theoretical considerations of panel flutter at high supersonic Mach numbers, *AIAA Journal* Vol. 4 (7), pp. 1257–1266, 1966.
- 5) Grigolyuk, E.I., Lamper, R.E., Shandarov, L.G.: Flutter of plates and shells, *Itogi nauki. Mekhanika*. 1963, VINITI, Moscow, pp. 34–90 (in Russian), 1965.
- 6) Mei, C., Abdel-Motagaly, K., Chen, R.R.: Review of nonlinear panel flutter at supersonic and hypersonic speeds, *Applied Mechanics Reviews*, Vol. 10, pp. 321–332, 1999.
- 7) Vedenev, V.V.: Flutter of a wide strip plate in a supersonic gas flow, *Fluid Dynamics* Vol. 5, 805–817,

2005.

- 8) Vedenev, V.V.: Nonlinear high-frequency flutter of a plate, *Fluid Dynamics* Vol. 5, 858–868, 2007.
- 9) Vedenev, V.V., Guvernyuk, S.V., Zubkov, A.F., Kolotnikov, M.E., Experimental observation of single mode panel flutter in supersonic gas flow, *Journal of Fluids and Structures*, Vol. 26, 764–779, 2010.
- 10) Vedenev, V.V.: Panel flutter at low supersonic speeds, *Journal of Fluids and Structures* Vol. 29, pp. 79–96, 2012.
- 11) Vedenev, V.V.: Effect of damping on flutter of simply supported and clamped panels at low supersonic speeds, *Journal of Fluids and Structures* Vol. 40, pp. 366–372, 2013.
- 12) Vedenev, V.V.: Limit oscillatory cycles in the single mode flutter of a plate. *Journal of Applied Mathematics and Mechanics*, Vol 77 (3), pp. 257–267, 2013.
- 13) Shishaeva, A.S., Vedenev, V.V., Aksenov A.A.: Nonlinear single-mode and multi-mode panel flutter oscillations at low supersonic speeds, *Journal of fluids and structures*, Vol. 56, pp. 205-223, 2015.
- 14) Aksenov, A.A., Dyadkin, A.A., Pokhilko, V.I.: Overcoming of barrier between CAD and CFD by modified finite volume method. Proceedings of 1998, ASME Pressure Vessels and Piping Division Conference, San Diego, 377-2, pp. 79–86, 1998.
- 15) Aksenov, A.A, Korenev, D.V, Shishaeva, A.S., Vucinic, D., Mravak, Z.: Drop-Test FSI simulation with Abaqus and FlowVision based on the direct 2-way coupling approach. Proceedings of Abaqus Users' Conference, Newport, Rhode Island, pp. 611–624, 2008.

Passive and Active Piezoelectric Effects on Flutter Suppression of Highly Flexible Wings

Natsuki Tsushima⁺¹, Weihua Su⁺²

^{+1, +2} University of Alabama, Tuscaloosa, AL, USA

The paper addresses both active and passive flutter suppression for highly flexible wings using piezoelectric transduction. The piezoelectric effect is included in a strain-based geometrically nonlinear beam formulation. The resulting structural dynamic equations for multifunctional beams are then coupled with a finite-state unsteady aerodynamic formulation, allowing for piezoelectric energy harvesting and actuation with the nonlinear aeroelastic system. With the development, it is possible to provide an integral aeroelastic and electromechanical solution of concurrent active piezoelectric control on and energy harvesting from wing vibrations, with the consideration of the geometrical nonlinear effects of the slender multifunctional wings. The energy harvesting system can provide an additional damping effect on the wing as well as its harvesting capability. In this paper, an LQG controller is developed for the active control of wing limit-cycle oscillations due to the onset of flutter instability. The controller demonstrates effective flutter control capability. Furthermore, a concurrent active vibration control and energy harvesting can also be realized for the multifunctional wing system with embedded piezoelectric materials.

Keyword: Flutter, Multifunctional structure, Active control, Energy harvesting, Slender wing

1. Introduction

With an increase of demands for high-performance aircraft, nonlinear aeroelasticity has been one of the most important and interested fields nowadays. With the application of flexible structures to reach the desired high performance, aeroelastic instabilities including flutter and LCOs may reduce the aircraft flight performance and lead to structural problems such as fatigue on the structures. There have been extensive literatures regarding aeroelasticity.¹ Especially, Dowell et al.² provided a good summary of nonlinear aeroelasticity studies, especially for flutter and limit cycle oscillations (LCOs) at the time.

High-altitude long-endurance (HALE) UAVs have been developed for several applications such as Intelligence, Surveillance, and Reconnaissance (ISR) and environmental researches. They feature high aspect-ratio slender wings with low structural weight. Due to the nature of the slender wings, they may undergo large deformations with normal operation conditions, which lead to geometrically-nonlinear behaviors.³⁻⁵ Therefore, geometrical nonlinearity must be taken into account in the aeroelastic modeling of these vehicles.^{3, 6, 7}

Recently, wing morphing has also become a dynamic research field that is hoped to improve the flight performance under different flight conditions where traditional control surfaces are less effective, or to provide extra control in poor flight conditions. Although an early concept of wing warping was employed in the aircraft system built by the Wright brothers, the technique was later replaced by discrete control surfaces due to the lack of the structural stiffness. In recent studies of the active aeroelastic wing (AAW) technology,⁸ a set of control surfaces was used to induce aeroelastic deformations on the wing so that the reshape of the wing can provide optimum performance instead of directly generating the maneuver loads. The studies showed promising benefits of AAW technology in weight and performance perspectives. At the same time, multifunctional structural technologies⁹ are being developed, which may bring revolutionary changes to aircraft structures. These structures are capable of performing multiple primary functions and can potentially improve aircraft performance through consolidation of subsystem materials and functions.^{9, 10} The

⁺¹ntsushima@crimson.ua.edu, ⁺²suw@eng.ua.edu

employment of the wing morphing concept and multifunctional structural technologies may create new aircraft platforms with enhanced effectiveness and improved capability of operation.

The growth of active material technologies including anisotropic piezo-composite actuators (APA)¹¹ may facilitate the applications of multifunctional structures. In fact, one may take advantage of piezoelectric transducers to fulfill the dual functions of actuation and energy harvesting.¹² To explore the approaches to model the electromechanical behavior of piezoelectric transducing, many research groups from different fields have developed various prediction models. Early studies of piezoelectric transducing have modeled the piezoelectric transducer using a simplified lumped model with bending vibrations.¹³ Even though the approach was effective, the lumped model came with some disadvantages, such as the over simplification of the real physics. To improve the accuracy, some distributed models have been applied in the subsequent studies. For example, Bilgen et al.¹⁴ modeled the cantilever beam with embedded piezoelectric materials using the linear Euler-Bernoulli beam theory, and applied this approach to the piezoelectric transducing and gust alleviation of a small UAV.¹⁵ Sodano et al.¹⁶ developed a model of the piezoelectric power harvesting device based on works of Hagood et al.¹⁷ and Crawley and Anderson.¹⁸ They used energy methods to develop the constitutive equations of a bimorph piezoelectric cantilever beam. The model was solved with the Rayleigh-Ritz procedure. More recently, Anton et al.¹⁰ presented the investigation of a multifunctional wing spar for UAVs.

On the other hand, the piezoelectric actuation was implemented for aerospace applications in many ways. For example, Bent et al.¹⁹ developed the actuator equations for piezoelectric fiber composites with a conventional poling condition. They applied the Classical Laminated Plate Theory (CLPT) for the anisotropic composites force calculations. Wilkie et al.²⁰ employed this approach to find the piezoelectric induced stress and to calculate the resultant moment on a rectangular, thin-walled, closed-section structure with the piezoelectric twist actuation. Cesnik and Ortega-Morales²¹ used an energy approach for the actuation equations for a composite wing. They compared their model capability with preceding studies in the literature.²² Furthermore, an integrated structure of active actuation and energy harvesting may be designed by utilizing piezoelectric materials. Such a structure may work with one of the two functions of piezoelectric materials, which can be either actuated for wing morphing and/or vibration control, replacing the traditional control surfaces, or used as an energy harvester.

Finally, control algorithms are required to properly actuate the active wing structures to achieve the desired aircraft performance. In a modern aircraft control system, there are multiple variables that need to be controlled simultaneously. To satisfy the mission requirement and achieve the desired flight performance, an optimal feedback strategy should be implemented. In a simple control problem, Linear Quadratic Regulator (LQR) or more practical Linear Quadratic Gaussian (LQG) regulator may be selected as the starting point. These regulators are popular due to their capability to obtain the optimal control configurations. A lot of literatures²³ have provided detailed discussions on these controllers.

In summary, as a study on the aforementioned integrated system, this paper will model both active piezoelectric actuation and energy harvesting in a strain-based geometrically nonlinear aeroelastic formulation. Numerical studies will be performed to explore the concurrent piezoelectric energy harvesting and wing flutter control of the multifunctional system.

2. THEORETICAL FORMULATION

The theoretical formulation used in the current study is introduced in this section, where a slender wing with piezoelectric actuation is modeled using a strain-based geometrically-nonlinear beam formulation. The strain-based beam²⁴ and aeroelastic^{4,5} formulations have been introduced in the literature. The finite-state inflow theory²⁵ is incorporated for aerodynamic loads on lifting surfaces. Piezoelectric actuation is considered as an additional external load to the system.

(1) Multifunctional wing structure

Fig. 1 illustrates a multifunctional beam with both energy harvesting and actuation capabilities, using piezoelectric materials. The current work is an extension to the piezoelectric actuation based on the previous

work on the modeling of the piezoelectric energy harvesting.²⁶ For simplicity, the piezoelectric energy harvesting works in the flap bending direction.

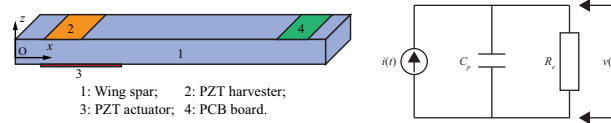


Figure 1: Multifunctional beam and equivalent circuit for energy harvesting subsystem.

The constitutive equation for piezoelectric materials is given as

$$\begin{Bmatrix} \bar{\boldsymbol{\sigma}} \\ \bar{\mathbf{B}} \end{Bmatrix} = \begin{bmatrix} \bar{\mathbf{D}} & -\mathbf{e}^T \\ \mathbf{e} & \zeta \end{bmatrix} \begin{Bmatrix} \bar{\boldsymbol{\varepsilon}} \\ \mathbf{E} \end{Bmatrix} \quad (1)$$

where $\bar{\boldsymbol{\sigma}}$ is the material stress, $\bar{\mathbf{B}}$ is the electric displacement, $\bar{\mathbf{D}}$ is the piezoelectric material stiffness matrix, \mathbf{e} is the piezoelectric coupling, ζ is the permittivity, $\bar{\boldsymbol{\varepsilon}}$ is the material strain, and \mathbf{E} is the electric field, which is obtained from the gradient of the electric voltage v across the piezoelectric layer. The coupled electromechanical effect of piezoelectric material will be considered when deriving the equations of motion.

(2) Fundamental wing modeling description

A cantilever beam is defined in a fixed frame B . A local beam frame (w) is built within the B frame (see Fig. 2), which is used to define the position and orientation of each node along the beam reference line. Vectors $\mathbf{w}_x(s, t)$, $\mathbf{w}_y(s, t)$, and $\mathbf{w}_z(s, t)$ are bases of the beam frame w , whose directions are pointing along the beam reference axis, toward the leading edge, and normal to the beam (wing) surface, respectively, resolved in the B frame. The curvilinear beam coordinate s provides the nodal location within the body frame.

To model the elastic deformation of slender beams, a new nonlinear beam element was developed in the work of Ref. [24, 27]. Each of the elements has three nodes and four local strain degrees of freedom, which are extension, twist, flap bending rate (κ_y), and edge bending rate (κ_z), respectively, of the beam reference line:

$$\boldsymbol{\varepsilon}^T(s) = \{\varepsilon_x(s) \quad \kappa_x(s) \quad \kappa_y(s) \quad \kappa_z(s)\} \quad (2)$$

which is not to be confused with the strain of the materials ($\bar{\boldsymbol{\varepsilon}}$) in Eq. 1, even though they are related.

Positions and orientations of each node along the beam are determined by a vector consisting of 12 components, and the derivative and variation dependent variable \mathbf{h} are derived from those of the independent variable $\boldsymbol{\varepsilon}$ using the Jacobians \mathbf{J} which are obtained from kinematics.^{6, 24}

(3) Equations of motion

The equations of motion can be derived by following the principle of virtual work. The detailed derivation, where the electromechanical coupling effect was not considered, can be found in Su and Cesnik.^{4, 24} The electromechanical coupling effect was further discussed and studied for energy harvesting.²⁶ By putting internal and external virtual works together, the total virtual work on a beam can be obtained.²⁸ Because the variations of the strain and the voltage are arbitrary, the electromechanical system's equations of motion is

$$\begin{aligned} \mathbf{M}_{FF} \ddot{\boldsymbol{\varepsilon}} + \mathbf{C}_{FF} \dot{\boldsymbol{\varepsilon}} + \mathbf{K}_{FF} \boldsymbol{\varepsilon} &= \mathbf{R}_F \\ \mathbf{B}_{vh}^T \boldsymbol{\varepsilon} + C_p v + Q_e &= 0 \quad \text{or} \quad \mathbf{B}_{vh}^T \dot{\boldsymbol{\varepsilon}} + C_p \dot{v} + v / R_e = 0 \end{aligned} \quad (3)$$

where the generalized inertia, damping, stiffness matrices and generalized force vector are

$$\begin{aligned} \mathbf{M}_{FF}(\boldsymbol{\varepsilon}) &= \mathbf{J}_{he}^T \mathbf{M}_s \mathbf{J}_{he} & \mathbf{C}_{FF}(\boldsymbol{\varepsilon}, \dot{\boldsymbol{\varepsilon}}) &= \mathbf{C}_s + \mathbf{J}_{he}^T \mathbf{M}_s \dot{\mathbf{J}}_{he} & \mathbf{K}_{FF} &= \mathbf{K}_s \\ \mathbf{R}_F &= \mathbf{K}_{FF} \boldsymbol{\varepsilon}_0 + \mathbf{J}_{he}^T \mathbf{N} \mathbf{g} + \mathbf{J}_{pe}^T \mathbf{B}^F \mathbf{F}^{\text{dist}} + \mathbf{J}_{0e}^T \mathbf{B}^M \mathbf{M}^{\text{dist}} + \mathbf{J}_{pe}^T \mathbf{F}^{\text{pt}} + \mathbf{J}_{0e}^T \mathbf{M}^{\text{pt}} + (\mathbf{B}_{va} + \mathbf{B}_{vh}) v \end{aligned} \quad (4)$$

in which $\boldsymbol{\varepsilon}_0$ is the initial strain of the beam. \mathbf{B}_{va} and \mathbf{B}_{vh} are the electromechanical coupling matrix for the piezoelectric actuator and harvester. \mathbf{g} , \mathbf{F}^{dist} , \mathbf{M}^{dist} , \mathbf{F}^{pt} , and \mathbf{M}^{pt} are the gravity field, distributed forces, distributed moments, point forces, respectively. \mathbf{N} , \mathbf{B}^F , and \mathbf{B}^M are the influence matrices for

the gravitational force, distributed forces, and distributed moments, which come from the numerical integration. In addition, Q_e is the total charge accumulated over the electrodes, whose time derivative is the current. The coupling matrix \mathbf{B}_{va} will be derived in the next discussion while \mathbf{B}_{vh} and C_p are from the cross-sectional value:

$$\begin{aligned}\mathbf{B}_{vh} &= [0 \quad 0 \quad B_{vh} \quad 0]^T \\ B_{vh} &= B_{vh}^{cs} s_p = s_p \int_A -(z_p e_{31} / t_p) dA \\ C_p &= \zeta b_p s_p / t_p\end{aligned}\quad (5)$$

in which A is the cross-sectional area of the piezoelectric layer. z_p is the distance between the elastic axis of the beam and the piezoelectric layer (see Fig. 3). Quantities b_p , t_p , and s_p are the width, thickness, and length of the piezoelectric layer, respectively. As shown in Eq. 4, the generalized force vector involves the effects from initial strains $\boldsymbol{\varepsilon}_0$, gravitational field \mathbf{g} , distributed forces \mathbf{F}^{dist} , distributed moments \mathbf{M}^{dist} , point forces \mathbf{F}^{pt} , point moments \mathbf{M}^{pt} , and the electric field v . The aerodynamic forces and moments are considered as distributed loads.

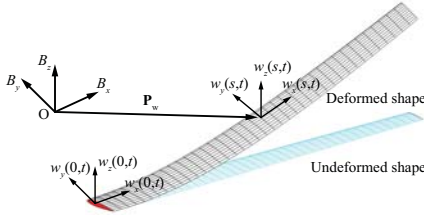


Figure 2: Beam references frames.

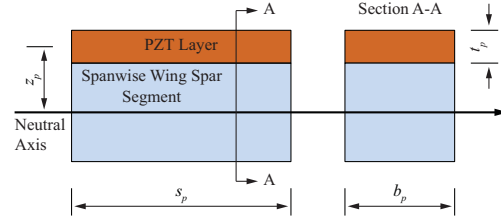


Figure 3: Spanwise segment and cross-section of multifunctional wing spar.

(4) Piezoelectric actuation of bending and torsion deformation

The multifunctional wing with embedded piezoelectric materials is also considered as a piezoelectric actuation device, in addition to the energy harvesting function. Bent et al.¹⁹ developed the anisotropic actuator equations using the conventional poling, which are followed in the current development of the structural dynamic equations of the multifunctional wing. With the in-plane structural anisotropy in the piezoelectric material, a transformation between a piezoelectric material and beam coordinate, and the assumption of plane stress ($T_3=T_4=T_5=0$), the reduced piezoelectric constitutive relations are obtained.²⁸ The electric field and displacement are assumed to be along the 3-direction for simplicity. Piezoelectric induced stresses can be

$$\bar{\boldsymbol{\sigma}}_{pe} = -\mathbf{T}_s^T \tilde{\mathbf{e}}^T E_3 \quad (6)$$

Resultant forces and moments can be calculated from the piezoelectric induced terms. Bent et al.¹⁹ developed the forces and moments on thin-walled anisotropic composites using the Classical Laminated Plate Theory (CLPT). The detailed discussion of the CLPT can be found in Ref. [29]. On the other hand, if a composite structure is a simple rectangular thin-walled section, one may choose an approach using the piezoelectric induced stresses to calculate the induced bending and torsional moments as in Ref. [20].

The coupling matrix \mathbf{B}_{va} is related to the resultant piezoelectric forces and moments as

$$\{B_{va1} \quad B_{va2} \quad B_{va3} \quad B_{va4}\}^T v = \{F_{1a} \quad M_{1a} \quad M_{2a} \quad M_{3a}\}^T \quad (7)$$

where F_{1a} is a piezoelectric induced extensional force, and M_{1a} , M_{2a} , M_{3a} are piezoelectric induced moments about 1, 2, 3 axes, respectively. In this paper, the 1, 2, 3 axes are oriented so that the coordinate aligned with the wing beam coordinate axes x , y , z .

(5) Unsteady aerodynamics

The distributed loads, \mathbf{F}^{dist} and \mathbf{M}^{dist} in Eq. 4 are divided into aerodynamic loads and user-supplied loads. The unsteady aerodynamic loads used in the current study are based on the two dimensional (2-D) finite-state inflow theory, provided in Peters and Johnson.²⁵ The theory calculates aerodynamic loads on a thin

airfoil section undergoing large motions in an incompressible inviscid subsonic flow. The lift, moment, and drag of a thin 2-D airfoil section about its midchord are given by

$$\begin{aligned} l_{mc} &= \pi\rho b^2(-\ddot{z} + \dot{y}\dot{\alpha} - d\ddot{\alpha}) + 2\pi\rho b\dot{y}^2[-\dot{z}/\dot{y} + (b/2 - d)\dot{\alpha}/\dot{y} - \lambda_0/\dot{y}] \\ m_{mc} &= 2\pi\rho b^2(-\dot{y}\dot{z}/2 - d\dot{y}\dot{\alpha}/2 - \dot{y}\lambda_0/2 - b^2\ddot{\alpha}/16) \\ d_{mc} &= -2\pi\rho b(\dot{z}^2 + d^2\dot{\alpha}^2 + \lambda_0^2 + 2d\dot{\alpha}\dot{z} + 2d\dot{\alpha}\lambda_0) \end{aligned} \quad (8)$$

where b is the semichord, and d is the distance of the mid-chord in front of the reference axis. The quantity $-\dot{z}/\dot{y}$ is the angle of attack that consists of the contribution from both the steady state angle of attack and the unsteady plunging motion of the airfoil. The different velocity components are shown in Fig. 4. The inflow velocity λ_0 accounts for induced flow due to free vorticity, which is the weighted summation of the inflow states λ as described Peters and Johnson²⁵ and governed by

$$\dot{\lambda} = \mathbf{F}_1\ddot{\epsilon} + \mathbf{F}_2\dot{\epsilon} + \mathbf{F}_3\lambda \quad (9)$$

The aerodynamic loads about the midchord center are transferred to the wing elastic axis and rotated into the fixed B frame for the solution of equations of motion.

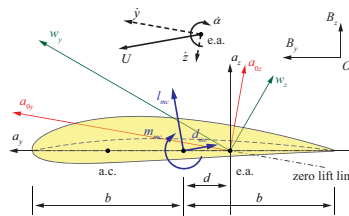


Figure 4: Airfoil coordinate system and velocity components.

(6) LQR and LQG feedback controllers

Linear Quadratic Regulator (LQR)²³ (see Fig. 5) is commonly used in traditional aircraft control studies. To apply the linear control theory, the linearization of the system equations about a nonlinear equilibrium state is performed.²⁸ The structural Jacobians are assumed to be constant when the system is perturbed, while this assumption holds for small perturbations to the system. It helps to simplify the linearization process by making the generalized mass matrices independent of the state variables. The nonlinear aeroelastic equations of the cantilever wing is rewritten with the small perturbation about the nonlinear equilibrium state, which yields

$$\begin{aligned} \bar{\mathbf{M}}_{FF}\ddot{\epsilon} + \bar{\mathbf{C}}_{FF}\dot{\epsilon} + \bar{\mathbf{K}}_{FF}\epsilon - \mathbf{R}_{F/\lambda_0}^{\text{aero}}\lambda - \mathbf{B}_v\mathbf{v} &= \mathbf{0} \\ \dot{\lambda} - \mathbf{F}_1\ddot{\epsilon} - \mathbf{F}_2\dot{\epsilon} - \mathbf{F}_3\lambda &= \mathbf{0} \end{aligned} \quad (10)$$

where $\bar{\mathbf{M}}$, $\bar{\mathbf{C}}$, and $\bar{\mathbf{K}}$ are the linearized general inertia, damping, and stiffness matrices. $\mathbf{R}_{F/\lambda_0}^{\text{aero}}$ is the derivative of the aerodynamic load vector with respect to the inflow states. Eq. 10 is put into the state-space form:

$$\begin{aligned} \dot{\mathbf{x}} &= \mathbf{A}\mathbf{x} + \mathbf{B}\mathbf{u} \\ \mathbf{x} &= \{\epsilon^T \quad \dot{\epsilon}^T \quad \lambda^T\}^T \quad \mathbf{u} = \{\mathbf{v}^T\}^T \end{aligned} \quad (11)$$

where \mathbf{v} is the inputs of piezoelectric actuation. The associated quadratic performance index is defined as

$$J = \int_0^\infty (\mathbf{x}^T\mathbf{Q}\mathbf{x} + \mathbf{u}^T\mathbf{R}\mathbf{u}) dt \quad (12)$$

where \mathbf{R} and \mathbf{Q} are positive-definite penalty matrices. The optimal control and associated Riccati-equation are

$$\begin{aligned} \mathbf{u} &= -\mathbf{K}\mathbf{x} \\ \mathbf{K} &= \mathbf{R}^{-1}\mathbf{B}^T\mathbf{S} \\ \mathbf{A}^T\mathbf{S} + \mathbf{S}\mathbf{A} - \mathbf{S}\mathbf{B}\mathbf{R}^{-1}\mathbf{B}^T\mathbf{S} + \mathbf{Q} &= \mathbf{0} \end{aligned} \quad (13)$$

The LQR results in a robust closed-loop system. However, the LQR design assumes all the states of the system are available for feedback. In most practical systems, it is not possible to obtain all the state. The

Linear Quadratic Gaussian regulator (LQG) provides the compensation to the limitation of state variable availability. The LQG consists of an LQR and a Kalman filter which gives state estimations (see Fig. 5). The state-space model describing the problem is now

$$\begin{aligned}\dot{\mathbf{x}} &= \mathbf{Ax} + \mathbf{Bu} + \mathbf{Gw} \\ \mathbf{y} &= \mathbf{Cx} + \mathbf{Du} + \mathbf{Hw} + \mathbf{n}\end{aligned}\quad (14)$$

where \mathbf{x} is the state vector, \mathbf{u} is the control input to the system plant, \mathbf{w} is the process noise, and \mathbf{n} is the sensor noise. The noises \mathbf{w} and \mathbf{n} are zero-mean white noises. The Kalman filter provides an estimated $\hat{\mathbf{x}}$ of \mathbf{x} with

$$\begin{aligned}\dot{\hat{\mathbf{x}}} &= \mathbf{A}\hat{\mathbf{x}} + \mathbf{Bu} + \mathbf{L}(\mathbf{y} - \mathbf{C}\hat{\mathbf{x}} - \mathbf{Du}) \\ \mathbf{y} &= \mathbf{Cx} + \mathbf{Du} + \mathbf{Hw} + \mathbf{n} \\ \mathbf{L} &= \mathbf{PC}^T\mathbf{R}^{-1} \\ \mathbf{AP} + \mathbf{PA}^T + \mathbf{Q}_n - \mathbf{PC}^T\mathbf{R}_n^{-1}\mathbf{CP} &= \mathbf{0}\end{aligned}\quad (15)$$

where \mathbf{Q}_n and \mathbf{R}_n are the covariance matrices of noise \mathbf{w} and \mathbf{n} , and \mathbf{L} is the filter gain. The control input to the original model can be obtained as

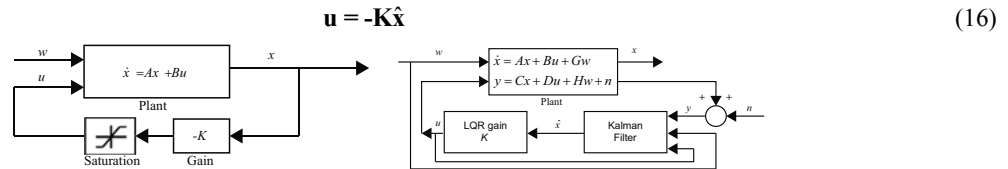


Figure 5: LQR (left) and LQG (right) feedback control diagram.

The linear quadratic controllers minimize a certain performance index by applying penalties on both state variables and control inputs. Different combinations of penalties may result in different control system performances. It may reduce the excess wing deformations with large control power, while it may allow a certain level of wing vibration, saving the excess power consumption. Therefore, it is important to establish a way to evaluate the trade-off and find a cost effective controller setting.

One good way to evaluate the performance is to normalize the cost function and to split them into two components for state variables and control inputs, which can be defined as the state cost J_s and the control cost J_c .³⁰ The objective cost function defined in the Eq. 12 can be rewritten with an additional weighting term r :

$$J = \int_0^{\infty} (\mathbf{x}^T\mathbf{Q}\mathbf{x} + r\mathbf{u}^T\mathbf{R}\mathbf{u}) dt\quad (17)$$

As a preliminary design, the balanced penalty point, cost effective point in other words, can be found at the vertex of the hyperbolic curve of state and control cost.²⁸

3. NUMERICAL STUDIES

In this section, nonlinear active aeroelastic analysis results are presented for a slender wing, which are obtained by using the derived electro-aeroelastic formulation. Passive and active suppressions of the wing flutter are also discussed. Particularly, concurrent active piezoelectric actuation and energy harvesting with a LQG controller are explored with different multifunctional wing configurations.

(1) Multifunctional wing

The multifunctional wing model in Ref. [28] is used for the study of flutter suppression. The detailed wing properties can be found in Ref. [30]. The wing model is divided into 10 elements. Some of the elements are “designated” as active actuators for the vibration control, while others are “designated” as energy harvesters. The system resistance load is set to be 1 MΩ. Fig. 6 is the wing geometry and the lay-up of the cross-section. The model applies Active Fiber Composites (AFC) for bending twist actuation and it is tapered through 75% of the wing. There is a single wing spar at 40% chord, and element IDs are assigned from the wing root to the tip, ranging from 1 to 10. Although the studies in Ref. [30] covered different actuator

orientations from 0° to $\pm 45^\circ$, only the case with the actuation oriented at $\pm 22^\circ$ is performed in the current study to have the balanced bending and torsional actuation capability.

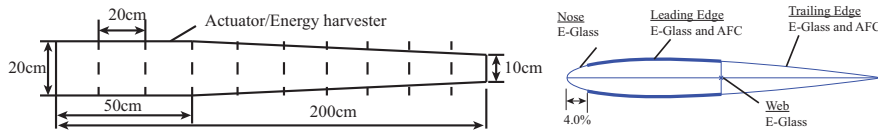


Figure 6: Wing model dimensions and lay-up of the cross-section.

(2) Stability analysis and flutter boundary

A stability analysis⁴ is performed to properly understand the wing aeroelastic stability characteristics. To evaluate the impacts of gravity and angle of attack (AOA) α on the flutter boundary of the wing, several conditions with and without a gravity load at different AOAs are investigated as shown in Fig. 7. The flutter speed U_F and the frequency ω_F depend on the AOA, but the gravity effect seems to be negligible for the wing and it will not be considered in the following analysis for simplicity. To consider a specific case for flutter, $\alpha = 8^\circ$ is chosen, and the flight altitude is set as sea level in the following studies. The stability analysis yields $U_F = 71.4$ m/s and $\omega_F = 22.3$ Hz. The flutter behavior of the wing with the condition is then simulated in the time-domain. Fig. 8 shows the wing tip vertical deflection at $U_\infty = 89.25$ m/s which is 25% above the flutter speed, which will be used in the following flutter control studies.

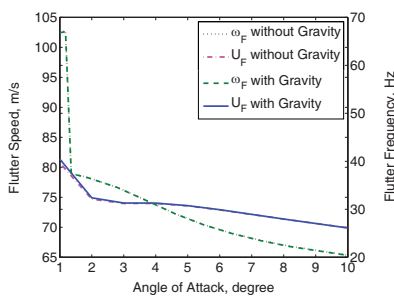


Figure 7: Flutter speed and frequency.

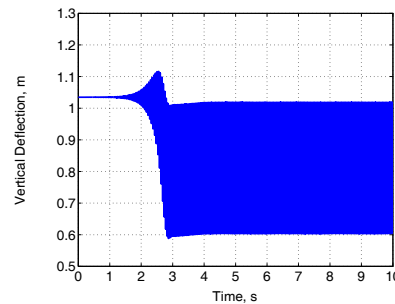


Figure 8: Wing tip vertical deflection at $U_\infty = 89.25$ m/s and $\alpha = 8^\circ$.

(3) Passive damping with energy harvesting

Energy harvesting has an additional damping effect,²⁶ so called shunt damping, associated to its harvesting function, which is studied in this section. To focus on the damping effect due to the energy harvesting, all the multifunctional wing elements are activated as harvesters in this section. Fig. 9 shows the wing tip vertical deflections of two aeroelastically neutral cases, while impacted by the energy harvesting subsystem. In the first one $\alpha = 2^\circ$ and $U_\infty = 76$ m/s, while the second has $\alpha = 8^\circ$ and $U_\infty = 73.75$ m/s. Since the passive damping magnitude from this system is not so large, it cannot provide a large flutter suppression effect all the time. However, it can suppress the small vibration as can be seen in the first case.

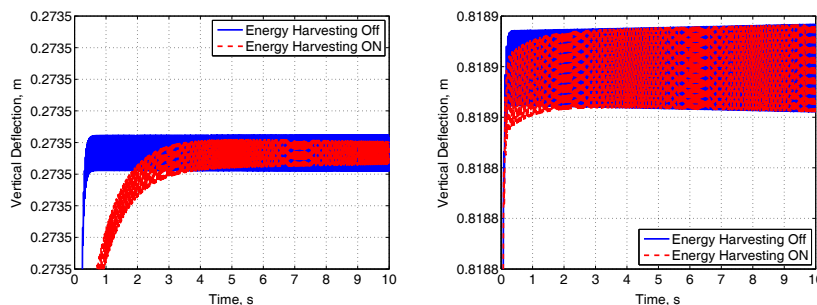


Figure 9: Wing tip vertical deflection at $\alpha = 2^\circ$ and $U_\infty = 76$ m/s (left), $\alpha = 8^\circ$ and $U_\infty = 73.75$ m/s (right) with and without energy harvesting.

(4) Active control analysis

A LQG controller is then investigated for flutter control. Because the LQG estimates the states through the Kalman filter, the filter setting is very important for the feedback control design. The Kalman filter is configured based on the flight condition at $U_\infty = 89.25$ m/s. Even though the controller will not be fully optimized, the filter is designed to give the feasible estimation (Fig. 10) for an effective control of the wing. The controller setting is chosen based on the result in Ref. [28]. To suppress the flutter, wing vibrations should be constrained. Therefore, a strong vibration penalty is used in this analysis by using a higher weighting term r . Fig. 11 shows the vertical wing tip deflection without and with LQG controller. It can be seen that the LQG provides a very good stability control when the flow speed is above the flutter boundary.

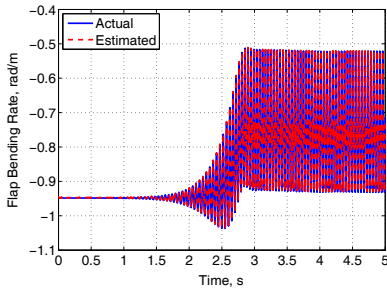


Figure 10: Estimated and actual flap bending rate.

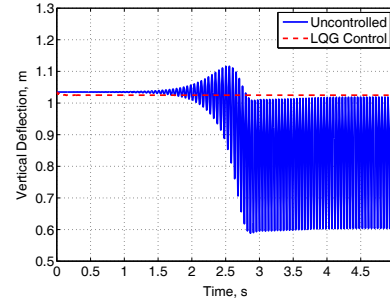


Figure 11: Wing tip vertical deflection at $U_\infty = 89.25$ m/s and $\alpha = 8^\circ$ without and with LQG.

(5) Concurrent active control and energy harvesting system

A parametric study of concurrent active control and energy harvesting is performed in this section. Based on the vibration mode, positions closer to the wing root have higher bending rates. Thus, it is more efficient to place controllers closer to the wing root for the flutter control. The rest of the elements can be used as energy harvesters to scavenge some energy. Starting with the multifunctional configuration in which all the wing element are designated as actuator, various configurations are tested as shown in Tab. 1. Fig. 12 shows the wing tip vertical deflection with each multifunctional configuration. Cases 5 and 6 have a limit cycle oscillation with 1 cm and 0.5 cm, respectively. Cases 7 to 9 settle back to an almost stable deflection, but Case 10 cannot provide any flutter control capability. Tab. 2 lists the output and input voltages from each harvester and actuator in the different configurations. Cases 5 to 7 can provide a certain amount of harvesting energy while controlling flutter with small vibration allowed. Cases 8 and 9 show an excellent flutter control effectiveness with some harvesting outputs. The result is due to the combination of active control of actuator and passive damping from harvester.

Table 1: Multifunctional wing configurations for each simulation case.

Simulation case	1	2	3	4	5	6	7	8	9	10
Actuator element ID	1 - 10	1 - 9	1 - 8	1 - 7	1 - 6	1 - 5	1 - 4	1 - 3	1 - 2	1
Harvester element ID	-	10	9 - 10	8 - 10	7 - 10	6 - 10	5 - 10	4 - 10	3 - 10	2 - 10

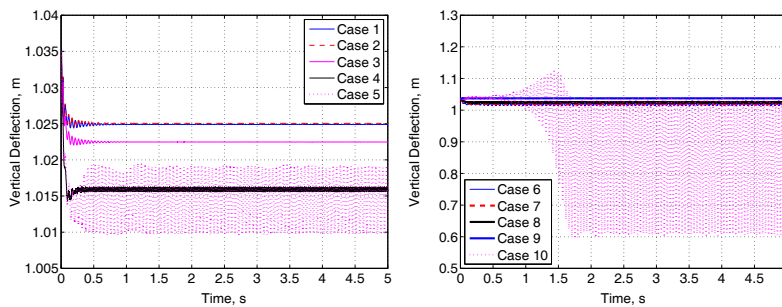


Figure 12: Wing tip vertical deflection at $U_\infty = 89.25$ m/s with each multifunctional configuration.

Table 2: Root mean square voltage output/input (V_{rms} , V) with typical wing cases.

Case	V_{rms} , V	Element ID (from root)										Total
		1	2	3	4	5	6	7	8	9	10	
1	Harvest output	-	-	-	-	-	-	-	-	-	-	-
	Actuation input	1318.9	480.6	1497.7	1997.9	1998.4	1998.8	1998.9	1849.5	753.2	29.2	13922.9
5	Harvest output	-	-	-	-	-	-	6.226	6.310	5.562	6.132	24.230
	Actuation input	1614.6	1973.1	1999.4	1999.4	1999.4	1999.2	-	-	-	-	11585.1
9	Harvest output	-	-	1.211	0.932	0.811	0.767	0.683	0.555	0.365	0.156	5.479
	Actuation input	1724.3	1180.0	-	-	-	-	-	-	-	-	2904.2
10	Harvest output	-	261.075	186.858	189.158	203.085	209.275	180.086	132.267	83.701	31.251	1476.745
	Actuation input	1999.1	-	-	-	-	-	-	-	-	-	1999.1

4. CONCLUSION

An approach for studying the flutter suppression using the active and passive piezoelectric effects was introduced in the paper. The strain-based geometrically nonlinear beam formulation, which makes no approximation to the deformation of beam reference line, was coupled with electromechanical model of the piezoelectric effect. For aeroelastic analysis, the finite-state unsteady subsonic aerodynamic loads are coupled to the wing surface. The coupled electro-aeroelastic model enables the prediction of the transient electric outputs and the mechanical deformations of the electro-aeroelastic system. The nonlinear electro-aeroelastic formulation is suitable for both the active piezoelectric actuation and energy harvesting studies for highly flexible wings. Based on the formulation, a LQG controller was applied to regulate piezoelectric actuation.

A multifunctional wing having bending/torsional actuation capability was considered for active control and energy harvesting with flutter. Flutter characteristics of the wing were investigated, and it yielded $U_F = 71.4$ m/s and $\omega_F = 22.3$ Hz at $\alpha = 8^\circ$. Time-domain simulations proved the frequency-domain stability analysis results and also provided actual temporal wing behavior. The shunt damping effects from energy harvesting function on the flutter was then investigated. The energy harvesting could provide an additional passive damping effect and was helpful to achieve the aeroelastic stability in some case, yet not being very efficient. A LQG controller was also designed by setting to have the cost-effective control of vibration, allowing for the active flutter suppression. The designed controller showed good flutter control capability.

Finally, the concurrent active piezoelectric actuation control and energy harvesting were studied for the multifunctional wing. Several device placements of the multifunctional wing were tested to perform parametric study of multifunctional system performance on flutter. Most of the dual-functional wings provided its flutter control capability, while one of them could not suppress the flutter. The interesting point was that it showed that, for efficient flutter suppression, the multifunctional wing could be designed with a combination of the active control and passive piezoelectric damping. They also successively scavenged energy from the controlled vibration, which would otherwise be wasted without the energy harvesting subsystem.

REFERENCES

- 1) Bisplinghoff, R. L., Ashley, H., and Halfman, R. L.: Aeroelasticity, Boston, MA, Addison-Wesley, 1955.
- 2) Dowell, E., Edwards, J., and Strganac, T.: Nonlinear aeroelasticity, *Journal of Aircraft*, Vol. 40, No. 5, pp. 857-874, 2003.
- 3) Patil, M. J., Hodges, D. H., and Cesnik, C. E. S.: Nonlinear Aeroelasticity and Flight Dynamics of High-Altitude Long-Endurance Aircraft, *Journal of Aircraft*, Vol. 38, No. 1, pp. 88-94, 2001.
- 4) Su, W., and Cesnik, C. E. S.: Nonlinear Aeroelasticity of a Very Flexible Blended-Wing-Body Aircraft, *Journal of Aircraft*, Vol. 47, No. 5, pp. 1539-1553, 2010.
- 5) Su, W., and Cesnik, C. E. S.: Dynamic Response of Highly Flexible Flying Wings, *AIAA Journal*, Vol. 49, No. 2, pp. 324-339, 2011.
- 6) Cesnik, C. E. S., and Brown, E. L.: Modeling of High Aspect Ratio Active Flexible Wings for Roll Control, *43rd AIAA/ASME/ASCE/AHS Structures, Structural Dynamics, and Materials Conferences*. AIAA Paper 2002-1719, Denver, CO, 2002.
- 7) Chang, C.-S., Hodges, D. H., and Patil, M. J.: Flight Dynamics of Highly Flexible Aircraft, *Journal of*

- Aircraft*, Vol. 45, No. 2, pp. 538-545, 2008.
- 8) Pendleton, E., Flick, P., Paul, D., Voracek, D. F., Reichenbach, E., and Griffin, K.: The X-53 A Summary of the Active Aeroelastic Wing Flight Research Program, *48th AIAA/ASME/ASCE/AHS/ASC Structures, Structural Dynamics and Materials Conference and Exhibit*. AIAA Paper 2007-1855, Honolulu, Hawaii, Apr. 23-26, 2007.
 - 9) Christodoulou, L., and Venables, J. D.: Multifunctional Material Systems: The First Generation, *Journal of the Minerals Metals & Materials Society*, Vol. 55, No. 12, pp. 39-45, 2003.
 - 10) Anton, S. R., Erturk, A., and Inman, D. J.: Multifunctional Unmanned Aerial Vehicle Wing Spar for Low-Power Generation and Storage, *Journal of Aircraft*, Vol. 49, No. 1, pp. 292-301, 2012.
 - 11) Williams, R. B., Park, G., Inman, D. J., and Wilkie, W. K.: An Overview of Composite Actuators with Piezoceramic Fibers, *20th International Modal Analysis Conference*. Vol. 4753, Los Angeles, CA, pp. 421-427, Feb. 4-7, 2002.
 - 12) Erturk, A., and Inman, D. J.: *Piezoelectric Energy Harvesting*, Hoboken, NJ, John Wiley & Sons, 2011.
 - 13) Roundy, S., and Wright, P. K.: A Piezoelectric Vibration Based Generator for Wireless Electronics, *Smart Materials and Structures*, Vol. 13, No. 5, pp. 1131-1142, 2004.
 - 14) Bilgen, O., Wang, Y., and Inman, D. J.: Electromechanical Comparison of Cantilevered Beams with Multifunctional Piezoceramic Devices, *Mechanical Systems and Signal Processing*, Vol. 27, No. 1, pp. 763-777, 2012.
 - 15) Wang, Y., and Inman, D. J.: Simultaneous energy harvesting and gust alleviation for a multifunctional composite wing spar using reduced energy control via piezoceramics, *Journal of Composite Materials*, Vol. 47, No. 1, pp. 125-146, 2013.
 - 16) Sodano, H. A., Park, G., and Inman, D. J.: Estimation of Electric Charge Output for Piezoelectric Energy Harvesting, *Strain*, Vol. 40, No. 2, pp. 49-58, 2004.
 - 17) Hagood, N. W., Chung, W. H., and von Flotow, A.: Modelling of Piezoelectric Actuator Dynamics for Active Structural Control, *Journal of Intelligent Material Systems and Structures*, Vol. 1, No. 3, pp. 327-354, 1990.
 - 18) Crawley, E. F., and Anderson, E. H.: Detailed Models of Piezoceramic Actuation of Beams, *Journal of Intelligent Material Systems and Structures*, Vol. 1, No. 1, pp. 4-25, 1990.
 - 19) Bent, A. A., Hagood, N. W., and Rodgers, J. P.: Anisotropic Actuation with Piezoelectric Fiber Composites, *Journal of Intelligent Material Systems and Structures*, Vol. 6, No. 3, pp. 338-349, 1995.
 - 20) Wilkie, W. K., Belvin, W. K., and Park, K. C.: Aeroelastic Analysis of Helicopter Rotor Blades Incorporating Anisotropic Piezoelectric Twist Actuation, *ASME 1996 World Congress and Exposition*. Vol. 52, pp. 423-434, 1996.
 - 21) Cesnik, C. E. S., and Ortega-Morales, M.: Active Beam Cross-sectional Modeling, *Journal of Intelligent Material Systems and Structures*, Vol. 12, No. 7, pp. 483-496, 2001.
 - 22) Du Plessis, A. J.: Modeling and Experimental Testing of Twist Actuated Single Cell Composite Beams for Helicopter Blade Control. M.S. thesis, Massachusetts Institute of Technology, Cambridge, MA, 1996.
 - 23) Lewis, F. L., and Syrmos, V. L.: *Optimal Control*, New York, NY, John Wiley & Sons, 1995.
 - 24) Su, W., and Cesnik, C. E. S.: Strain-Based Geometrically Nonlinear Beam Formulation for Modeling Very Flexible Aircraft, *International Journal of Solids and Structures*, Vol. 48, No. 16-17, pp. 2349-2360, 2011.
 - 25) Peters, D. A., and Johnson, M. J.: Finite-State Airloads for Deformable Airfoils on Fixed and Rotating Wings, *Symposium on Aeroelasticity and Fluid Structure Interaction Problems, ASME Winter Annual Meeting*. Vol. 44, New York, NY, pp. 1-28, 1994.
 - 26) Tsushima, N., and Su, W.: Modeling of Highly Flexible Multifunctional Wings for Energy Harvesting, *Journal of Aircraft*, In Press.
 - 27) Cesnik, C. E. S., and Brown, E. L.: Active Warping Control of a Joined-Wing Airplane Configuration, *44th AIAA/ASME/ASCE/AHS/ASC Structures, Structural Dynamics, and Material Conference*. Norfolk, VA, Apr. 7-10, 2003.
 - 28) Tsushima, N., and Su, W.: Concurrent Active Piezoelectric Control and Energy Harvesting of Highly Flexible Multifunctional Wings, *Journal of Aircraft*, Under Review.
 - 29) Jones, R. M.: *Mechanics of Composite Materials*, New York, NY, McGraw-Hill, 1975.
 - 30) Ortega-Morales, M.: Modeling and Control of the Aeroelastic Response of Highly Flexible Active Wings. Ph.D. Thesis, Massachusetts Institute of Technology, Cambridge, MA, 2000.

ANALYTICAL AND NUMERICAL EVALUATION OF COUPLED GALLOPING OF SLENDER TOWERS

Liang Wu and Delong Zuo

Department of Civil, Environmental and Construction Engineering, Texas Tech University
Lubbock, TX, USA

ABSTRACT: Many previous studies have been conducted to study galloping of slender structures or structural components. While some recent studies have investigated the problem of coupled galloping involving the across-wind and along-wind vibrations, few of these investigations focused on the prediction of the steady-state amplitudes of coupled galloping oscillations. This paper presents a state-space formulation of the equations of motion for the analysis of coupled translational galloping of full-scale structures under the quasi-steady assumption. A numerical procedure based on the Fourth-order Runge-Kutta method is used to solve these equations of motion and predict coupled galloping amplitudes. A full-scale tower which has been observed to exhibit coupled galloping is used as an example structure to illustrate the application of the proposed analytical-numerical formulation.

Keyword: Slender tower, coupled galloping, state-space formulation.

1. INTRODUCTION

Galloping is a type of wind-induced low-frequency oscillation due to negative aerodynamic damping that can reach high-amplitudes. This type of vibration frequently occurs for slender structures with cylindrical structural members of bluff cross-sections. For example, iced power transmission lines, highway lighting poles, and bridge hangers have been observed to gallop at excessive amplitudes in natural winds.

Early study of the galloping phenomenon focused on the across-wind vibration and neglected the oscillation in the along-wind direction as well as torsional motion. Based on the quasi-steady assumption, Den Hartog [1] introduced a criterion for across-wind galloping that specifies the condition under which a conductor will gallop. This criterion has been widely used to assess the propensity of a variety of cross-sectional shapes to gallop in the across-wind direction (e.g., [2-6]) based on force coefficients obtained from wind tunnel tests. To predict the across-wind galloping amplitude of bluff cylinders, Parkinson and Smith [7] formulated a nonlinear differential equation that governs the across-wind galloping motion of a single-degree-of-freedom oscillator by expressing the aerodynamic force coefficients as polynomial functions of the vibration velocity. They solved this equation for the steady-state vibration amplitude using the Krylov-Bogoliubov method. On the basis of this formulation, Novak [8] investigated the influence of the slope of the lateral force coefficient at zero angle of attack (i.e., positive, zero and negative) on the galloping response, revealing the possibility of the translational galloping even when the Den Hartog criterion is not satisfied. Using an example of a prism that is stable in smooth flow but unstable in turbulent flow, he also pointed out that the effect of turbulence on the galloping instability should not be neglected. Subsequently, Richardson [9, 10] proposed an alternative method for the prediction of across-wind galloping amplitude. Although this method is still based on the principle of energy balance, it expresses the lateral force coefficient as a Fourier series instead of a polynomial function.

Following the early studies of across-wind galloping, more recent studies have taken into account vibrations in more than one direction. Jones [11] derived a coupled galloping criterion for a two-degree-of-freedom system with oscillations in both the across-wind and along-wind directions. However, Jones's study only addressed the situation where the along-wind direction coincides with one of the principal axes of the structure and the natural frequencies of the modes in the directions of the two principal axes are identical. Liang et al. [12] developed a seemingly more general formula to calculate the onset wind velocity for coupled

⁺¹isfa0001@jaxa.jp, ⁺²isfa0002@company.com, ⁺³isfa0003@univ.ac-u.jp

translational galloping without the restriction of the wind direction., Li et al. [13] further extended the formulation by Liang et al. [12] to enable the prediction of steady-state amplitudes of coupled translational galloping. However, these studies incorrectly asserted that the translational oscillations in the two orthogonal directions are in phase. This led to the erroneous conclusion that coupled translational galloping occurs only when the natural frequencies of a structure in the two principal translational directions are the same.

In a recent investigation, Nikitas and Macdonald [14] conducted a comprehensive review of the galloping instability criteria and modeled coupled translational galloping without restrictions on the natural frequencies and the wind direction. They further investigated the effect of detuning between the natural frequencies of a structure in the principal directions on the trajectory of the galloping oscillation. However, this investigation of the vibration trajectory is trivial because the formulation of coupled galloping model was based on the linearization of the aerodynamic force coefficients and thereby is only suitable for small vibration amplitude, which is often not of interest. In order to accurately predict the steady-state trajectory of the galloping oscillation, the nonlinear aerodynamic damping has to be properly modeled.

In this paper, the aerodynamic damping in the two translational directions are expressed as polynomial functions of the velocities, and the equations of motion for coupled translational galloping are formulated in a state-space form under the quasi-steady assumption. Then the steady-state amplitudes of the coupled galloping oscillations are evaluated by solving the state-space equations of motion with the Fourth-order Runge-Kutta method. As an illustration, the proposed approach is used to assess the galloping oscillation of a slender tower.

2. ANALYTICAL-NUMERICAL FORMULATION

For slender structures under wind excitation, the torsional response can be neglected. In this situation, with the quasi-steady assumption, the instantaneous flow and displacement quantities for a section of unit length can be represented by Figure 1. In this graph, \bar{U} is the mean along-wind speed, u and v are the along-wind and across-wind components of the turbulence, \bar{r}_x and \bar{r}_y are the mean displacements of the section in the directions of the principal axes, r_x and r_y are the corresponding dynamic displacements, D and L are the drag and lift forces, respectively, $\bar{\alpha}$ is the angle of incidence of the mean wind component defined relative to the principle axis x , $\Delta\alpha$ is the increment of the angle of incidence of the total horizontal wind speed relative to the cross-section, the magnitude of which is U_{rel} , and α is the total angle of incidence of the relative wind speed.

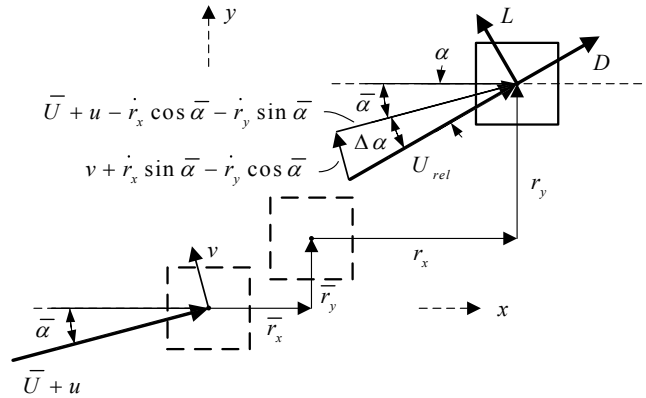


Figure 1 Instantaneous wind and displacements in two translational degrees of freedom

The instantaneous drag and lift forces acting on the segment of unit length can be expressed as

$$\begin{bmatrix} D & L \end{bmatrix}^T = \begin{bmatrix} \frac{1}{2} \rho U_{rel}^2 B C_D(\alpha) & \frac{1}{2} \rho U_{rel}^2 B C_L(\alpha) \end{bmatrix}^T \quad (1)$$

in which $C_D(\alpha)$ and $C_L(\alpha)$ are the drag and lift force coefficients measured at the angle of incidence α .

The attack-angle-dependent force coefficients can be approximated by polynomials of the attack angle as:

$$[C_D(\alpha) \quad C_L(\alpha)]^T = \left[\sum_{j=1}^m A_j \alpha^j \quad \sum_{j=1}^n B_j \alpha^j \right]^T \quad (2)$$

in which A_j and B_j are the coefficients of the polynomials approximating the drag and lift force coefficients, respectively.

Since $u \ll \bar{U}$ and $v \ll \bar{U}$, $\Delta\alpha$ and U_{rel}^2 in Figure 1 and equation (1) can be expressed as

$$\Delta\alpha = \arctan \left(\frac{v + \dot{r}_x \sin \bar{\alpha} - \dot{r}_y \cos \bar{\alpha}}{\bar{U} + u - \dot{r}_x \cos \bar{\alpha} - \dot{r}_y \sin \bar{\alpha}} \right) \quad (3)$$

$$U_{rel}^2 = [(\bar{U} + u) \cos \bar{\alpha} - \dot{r}_x - v \sin \bar{\alpha}]^2 + [(\bar{U} + u) \sin \bar{\alpha} - \dot{r}_y + v \cos \bar{\alpha}]^2 \quad (4)$$

$$\approx \bar{U}^2 + 2u\bar{U} - 2[(\bar{U} + u) \cos \bar{\alpha} - v \sin \bar{\alpha}] \dot{r}_x - 2[(\bar{U} + u) \sin \bar{\alpha} + v \cos \bar{\alpha}] \dot{r}_y + \dot{r}_x^2 + \dot{r}_y^2$$

The drag and lift forces can be decomposed into the components along the principal axes, the resultants of which are

$$\begin{bmatrix} f_x \\ f_y \end{bmatrix} = \begin{bmatrix} \cos \alpha & -\sin \alpha \\ \sin \alpha & \cos \alpha \end{bmatrix} \begin{bmatrix} D \\ L \end{bmatrix} \quad (5)$$

Substituting equation (1) into equation (5), the equations of motion of a segment of unit length can be expressed as

$$\mathbf{m}\ddot{\mathbf{r}} + \mathbf{c}\dot{\mathbf{r}} + \mathbf{m}\Omega^2\mathbf{r} = \mathbf{f} \quad (6)$$

where,

$$\mathbf{r} = \begin{bmatrix} r_x & r_y \end{bmatrix}^T; \quad \mathbf{f} = \begin{bmatrix} f_x & f_y \end{bmatrix}^T = \frac{1}{2} \rho U_{rel}^2 B [C_D \cos \alpha - C_L \sin \alpha \quad C_D \sin \alpha + C_L \cos \alpha] \quad (7)$$

$$\mathbf{m} = \begin{bmatrix} m & 0 \\ 0 & m \end{bmatrix}; \quad \mathbf{c} = \begin{bmatrix} c_{xx} & 0 \\ 0 & c_{yy} \end{bmatrix}; \quad \Omega^2 = \begin{bmatrix} \omega_x^2 & 0 \\ 0 & \omega_y^2 \end{bmatrix} \quad (8)$$

Assuming that the vibration of a slender tower is dominated by one mode each in the directions of the principle axes, the translational displacements of a slender tower at a height of z above ground can be expressed as

$$\mathbf{r} = \Phi(z)\mathbf{q}(t) \quad (9)$$

in which the modal matrix and the generalized coordinate vector are

$$\Phi(z) = \begin{bmatrix} \phi_x(z) & 0 \\ 0 & \phi_y(z) \end{bmatrix}; \quad \mathbf{q}(t) = \begin{bmatrix} q_x(t) \\ q_y(t) \end{bmatrix} \quad (10)$$

With equation (9), the generalized equations of motion for a slender tower of height h take the form

$$\mathbf{M}\ddot{\mathbf{q}} + \mathbf{C}\dot{\mathbf{q}} + \mathbf{M}\Omega^2\mathbf{q} = \mathbf{F} \quad (11)$$

where,

$$\mathbf{M} = \int_0^h (\Phi^T \mathbf{m} \Phi) dz = \begin{bmatrix} M_x & 0 \\ 0 & M_y \end{bmatrix} \quad (12)$$

$$\mathbf{C} = \int_0^h (\Phi^T \mathbf{c} \Phi) dz = \begin{bmatrix} C_{xx} & 0 \\ 0 & C_{yy} \end{bmatrix} \quad (13)$$

$$\mathbf{F} = \int_0^h (\Phi^T \mathbf{f}) dz = \left[\int_0^h \phi_x f_x dz \quad \int_0^h \phi_y f_y dz \right]^T = \begin{bmatrix} F_x & F_y \end{bmatrix}^T \quad (14)$$

The elements of the above matrices are given by

$$M_x = \int_0^h m(z) \phi_x^2(z) dz; \quad M_y = \int_0^h m(z) \phi_y^2(z) dz \quad (15)$$

$$C_{xx} = \int_0^h c_{xx} \phi_x^2(z) dz = 2M_x \omega_x \zeta_x; \quad C_{yy} = \int_0^h c_{yy} \phi_y^2(z) dz = 2M_y \omega_y \zeta_y \quad (16)$$

$$F_x = \int_0^h \frac{1}{2} \rho U_{rel}^2 B \phi_x (C_D \cos \alpha - C_L \sin \alpha) dz; \quad F_y = \int_0^h \frac{1}{2} \rho U_{rel}^2 B \phi_y (C_D \sin \alpha + C_L \cos \alpha) dz \quad (17)$$

in which ζ_x and ζ_y are the damping ratios of the two modes considered.

Ignoring the buffeting forces for the galloping analysis, $\Delta\alpha$ and U_{rel}^2 in equations (3) and (4) can be further simplified as

$$\Delta\alpha = \frac{\phi_x \dot{q}_x \sin \bar{\alpha} - \phi_y \dot{q}_y \cos \bar{\alpha}}{\bar{U} - \phi_x \dot{q}_x \cos \bar{\alpha} - \phi_y \dot{q}_y \sin \bar{\alpha}} \quad (18)$$

$$U_{rel}^2 = \bar{U}^2 - 2\phi_x \dot{q}_x \bar{U} \cos \bar{\alpha} - 2\phi_y \dot{q}_y \bar{U} \sin \bar{\alpha} + \phi_x^2 \dot{q}_x^2 + \phi_y^2 \dot{q}_y^2 \quad (19)$$

Because C_D and C_L are functions of α and $\alpha = \bar{\alpha} + \Delta\alpha$, the generalized equations of motion (11) are nonlinearly coupled differential equations with the generalized coordinates in the denominator. In the following, a numerical method is used to evaluate the amplitudes of coupled galloping oscillations.

First, the generalized equations of motion (11) are rewritten in a state-space form

$$\dot{\boldsymbol{\eta}} = \mathbf{A}\boldsymbol{\eta} + \mathbf{B}\mathbf{F}_b \quad (20)$$

where

$$\boldsymbol{\eta} = [q_x \quad q_y \quad \dot{q}_x \quad \dot{q}_y]^T; \quad \mathbf{F}_b = [0 \quad 0 \quad F_x \quad F_y]^T \quad (21)$$

$$\mathbf{A} = \begin{bmatrix} 0 & 0 & 1 & 0 \\ 0 & 0 & 0 & 1 \\ -\omega_x^2 & 0 & -2\omega_x \zeta_x & 0 \\ 0 & -\omega_y^2 & 0 & -2\omega_y \zeta_y \end{bmatrix}; \quad \mathbf{B} = \begin{bmatrix} 0 & 0 & 0 & 0 \\ 0 & 0 & 0 & 0 \\ 0 & 0 & 1/M_x & 0 \\ 0 & 0 & 0 & 1/M_y \end{bmatrix} \quad (22)$$

The fourth-order Runge-Kutta method is used to solve the above system of first-order differential equations. Because the differential equations are coupled, the solution for the coupled galloping oscillations is obtained iteratively. The general form of equation (20) can be expressed as

$$\dot{\boldsymbol{\eta}} = \mathbf{f}(t, \boldsymbol{\eta}^T) \quad (23)$$

in which,

$$\mathbf{y} = \boldsymbol{\eta} = [\eta_1 \quad \eta_2 \quad \eta_3 \quad \eta_4]; \quad \mathbf{f} = [f_1(t, \boldsymbol{\eta}^T) \quad f_2(t, \boldsymbol{\eta}^T) \quad f_3(t, \boldsymbol{\eta}^T) \quad f_4(t, \boldsymbol{\eta}^T)]^T \quad (24)$$

The iterative steps of the fourth-order Runge-Kutta method for solving equation (20) are as follows

$$\mathbf{K}_1 = h\mathbf{f}(t_i, \boldsymbol{\eta}_i^T) \quad (25)$$

$$\mathbf{K}_2 = h\mathbf{f}(t_i + 0.5h, (\boldsymbol{\eta}_i + 0.5\mathbf{K}_1)^T) \quad (26)$$

$$\mathbf{K}_3 = h\mathbf{f}(t_i + 0.5h, (\boldsymbol{\eta}_i + 0.5\mathbf{K}_2)^T) \quad (27)$$

$$\mathbf{K}_4 = h\mathbf{f}(t_i + h, (\boldsymbol{\eta}_i + \mathbf{K}_3)^T) \quad (28)$$

$$\boldsymbol{\eta}_{i+1} = \boldsymbol{\eta}_i + \frac{1}{6}(\mathbf{K}_1 + 2\mathbf{K}_2 + 2\mathbf{K}_3 + \mathbf{K}_4) \quad (29)$$

where i is the iteration step, and

$$h = t_{i+1} - t_i; \quad \boldsymbol{\eta}_i = [\eta_{1i} \quad \eta_{2i} \quad \eta_{3i} \quad \eta_{4i}]^T \quad (30)$$

$$\mathbf{K}_j = [K_{1j} \quad K_{2j} \quad K_{3j} \quad K_{4j}]^T, \quad j = 1, 2, 3, 4 \quad (31)$$

The analytical-numerical solution of the coupled galloping problem will be illustrated by a full-scale application example in the following section.

3. EXAMPLE APPLICATION

As an illustrative example, the analytical-numerical method developed herein is used to evaluate the galloping oscillation of a full-scale slender tower at the field testing site at Texas Tech University.

Figure 2 shows the tower consisting of a base tube and a swing tube, both being rectangular Hollow Structural Steel sections. The base tube is rigidly connected to the foundation, and the swing tube pivots about the top of the base tube. When in the upright position, the swing tube is pinned to the base tube approximately 0.9 m above the foundation. Also shown in Figure 2 are the coordinate system for describing wind-induced

vibration of the tower. \bar{U} and $\bar{\alpha}$ in this system are the wind speed and wind angle of incidence, respectively. Overbar represents time averaging.

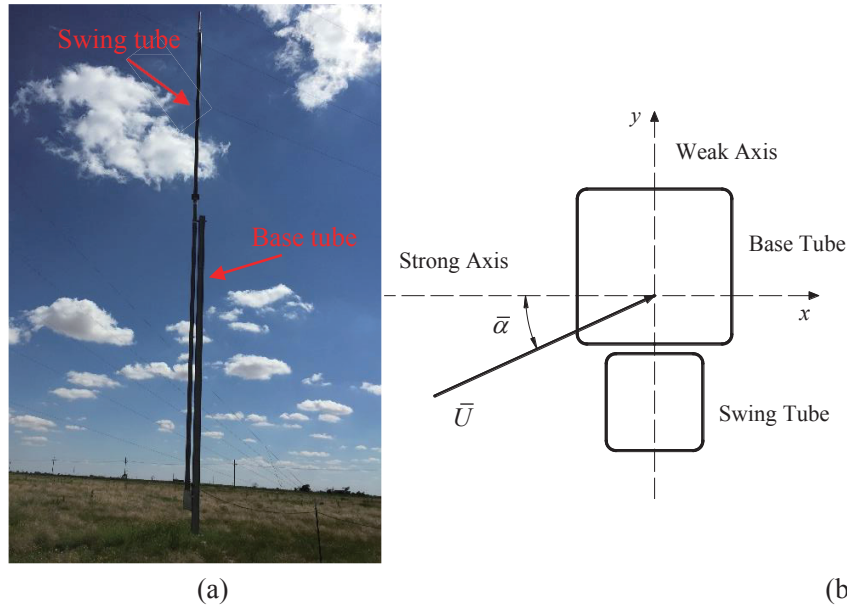


Figure 2 (a) A tilt tower for positive train control and (b) coordinate system for description of wind and vibration

The major structural properties of the tower are given in Table 1. Based on measurements of the ambient vibration of the tower using accelerometers, the fundamental frequencies of the structure about the weak and strong axes are approximately 0.62 Hz and 0.7 Hz, respectively, and the damping ratios of the fundamental modes about these two axes are approximately 1.5% and 1.4%, respectively.

Table 1 Dimensions of the structural members of the tower instrumented for vibration measurements

	Width (cm)	Wall Thickness (cm)	Corner Radius/Width	Length (m)
Base Tube	21.0	0.74	0.07	9.3
Swing Tube	12.7	0.59	0.09	16.5

Assessment of the galloping stability of the tower requires information about the mode shapes of the structure, the mean wind speed profile along the height, as well as the drag and lift force coefficients of the cross-sections. For this illustrative example, only the fundamental modes in the two principal axes are considered. The shapes of these two modes are estimated through a finite-element model of the structure using the commercial software ANSYS. These numerically obtained mode shapes are then fitted to two third-order polynomial functions, the results of which are

$$\phi_x(z) = 1.102 \times 10^{-4} z^3 - 6.253 \times 10^{-4} z^2 + 0.0274z; \quad \phi_y(z) = 7.777 \times 10^{-4} z^3 + 1.5399 \times 10^{-4} z^2 + 0.0241z \quad (32)$$

The mean wind speed profile at the site of the tower is assumed to follow the power law

$$\bar{U}(z) = \bar{U}_{ref} \left(\frac{z}{z_{ref}} \right)^\beta \quad (33)$$

in which \bar{U}_{ref} is the mean wind speed at the reference height z_{ref} , chosen at the top of the tower; β is the power law exponent. According the wind speed measurements at heights of 2.44 m, 10 m and 18 m by anemometers on an adjacent tower, the mean value of the power exponent β at this site is approximately 0.2.

The drag and lift force coefficients of the different segments of the tower are taken as the drag and lift force coefficients of the corresponding section models tested in a series of wind tunnel experiments described in [15]. Since the wind tunnel experiments suggest that the wind loading of the tower segments is not significantly affected by the Reynolds number, the force coefficients obtained at a test wind speed of 10 m/s are

used herein. Using a formulation described in [16], it is determined that for this structure, galloping instability can occur only when $0^\circ < |\bar{\alpha}| < 9^\circ$ or $81^\circ < |\bar{\alpha}| < 90^\circ$. The largest $\Delta\alpha$ during vibration is assumed to be smaller than 9° . Then in the ranges of $-18^\circ < \alpha < 18^\circ$, $-99^\circ < \alpha < -72^\circ$ and $72^\circ < \alpha < 99^\circ$, the aerodynamic force coefficients are approximated by 5th order polynomials of the wind angle of incidence.

As an illustration, Figure 3 shows drag and lift force coefficients of the section of the tower consisting of both the base tube and the swing tube (C_{D1} and C_{L1}) and the those of the section of the tower consisting of only the swing tube (C_{D2} and C_{L2}) as well as the polynomial approximations of these coefficients. It can be seen that the force coefficients of the swing tube section are well approximated by the corresponding polynomials. However, the polynomial fit for the force coefficients of the section consisting of both the base and swing tubes are not very satisfactory near some wind angles of incidence. However, the effect of this misfit is expected to be insignificant as the wind speeds over this section of the tower is lower than those over the section consisting of the swing tube only and for the mode shapes of interest, the displacement of the lower section is smaller than that of the upper section.

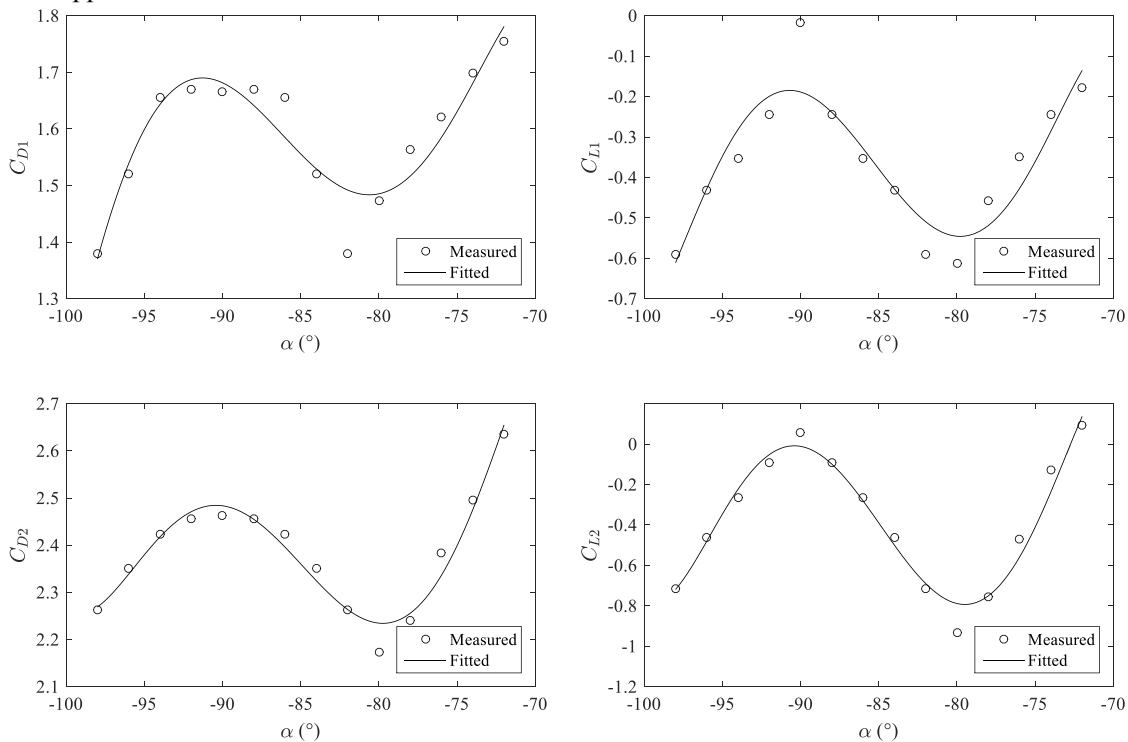


Figure 3 Aerodynamic force coefficients of the slender tower sections

Using the analytical-numerical formulation described above, the responses of the tower to winds of various speeds and angles of incidence are evaluated. As an example, Figure 4 shows the displacement time histories at the top of the slender tower for a mean wind speed of $\bar{U} = 18$ m/s at the top of the tower and a mean angle of incidence of $\bar{\alpha} = -85^\circ$. The initial conditions used in the numerical evaluations are 0.01 m dynamic displacements and zero velocities at the top of the tower in the directions of both the weak and the strong axes, and the time step used in the numerical evaluation is 0.01 s. It can be seen that under this wind condition, the coupled galloping vibration is dominated by the component about the weak axis (i.e., in the x -direction), but vibration of significant amplitude also occurred about the strong axis (i.e., in the y -direction).

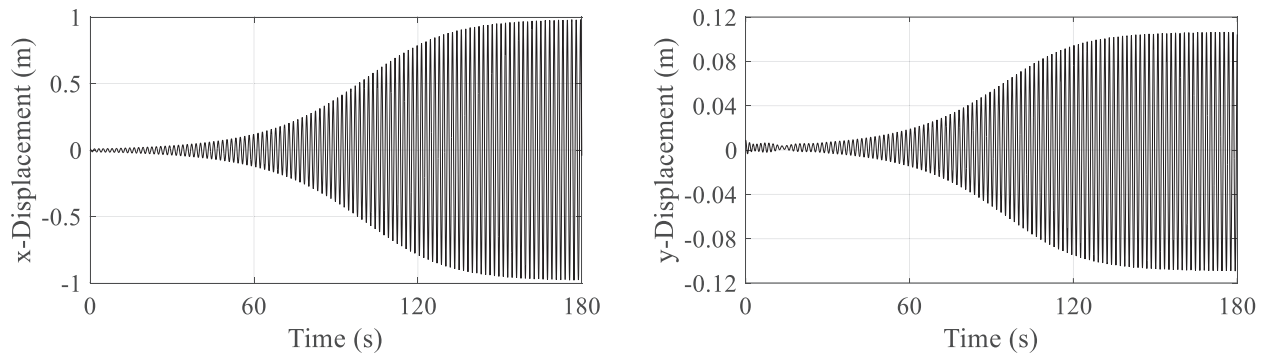


Figure 4 Simulated time histories of coupled galloping oscillation at $\bar{U} = 18 \text{ m/s}$ and $\bar{\alpha} = -85^\circ$

The coupling between the vibration components about the weak and strong axes also manifests itself in the vibration frequencies of these components. Figure 5 shows the frequencies of the vibration components depicted in Figure 4, which are estimated by identifying the peaks in the wavelet scalograms of the displacements [17] computed using the complex Morlet wavelet. It is evident that while the frequencies of the components about the principal axes are distinct at the beginning, when the vibration amplitudes are small, they quickly converge and become essentially identical when the vibration amplitude about the weak axis becomes large. This feature of the coupled galloping oscillation has also been observed in the recorded oscillation of the full-scale tower. For example, Figure 6 shows the displacement time histories of the full-scale tower dominated by the component about the weak axis and the corresponding time histories of the instantaneous dominant vibration frequencies, which are also estimated by identifying the peaks in the wavelet scalograms of the displacements. As in the case of the numerical simulation, the frequencies of the two vibration components are distinct when the amplitude of the vibration about the weak axis is small but converge when the amplitude of the vibration about the weak axis is large.

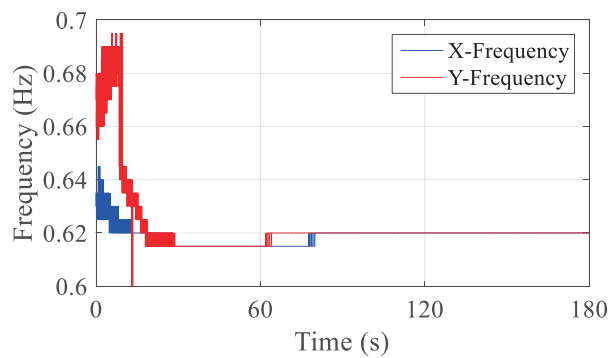


Figure 5 Evolution of vibrations frequencies of simulated coupled galloping oscillation

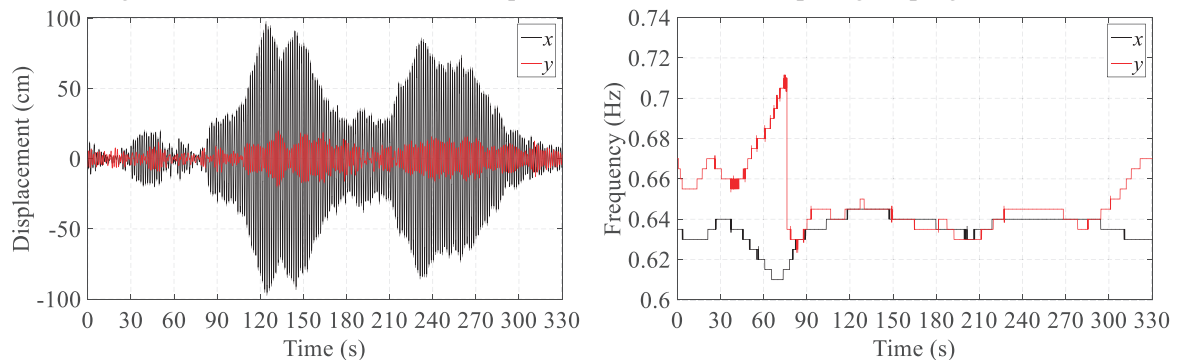


Figure 6 Evolution of vibration frequencies with displacement amplitudes for vibration of full-scale tower dominated by the component about the weak axis

In addition to producing results that reveal characteristics of the coupled galloping similar to those

observed in the full-scale data, the analytical-numerical formulation is also able to effectively predict the overall dynamic behavior of the tower at a given combination of wind speed and wind angle of incidence. Figure 7 shows the steady-state amplitudes of the coupled galloping oscillation of the full-scale tower predicted using the analytical-numerical formulation over ranges of mean wind speed and angle of incidence, and Figure 8 shows the measured 10-min maximum displacements of the tower about its principal axes over corresponding mean wind speed and direction. It can be seen that the analytical-numerical model successfully predicts the wind speed and direction range over which large-amplitude coupled galloping occurs. Direct comparison of the predicted vibration amplitudes to the measured vibration amplitudes is challenging because full-scale winds are often nonstationary with changing mean wind speed and direction. However, according to Figure 7 and Figure 8, the analytical-numerical method can indeed approximately predict some largest-amplitude oscillations (e.g., those at wind angles of incidence of about 90°).

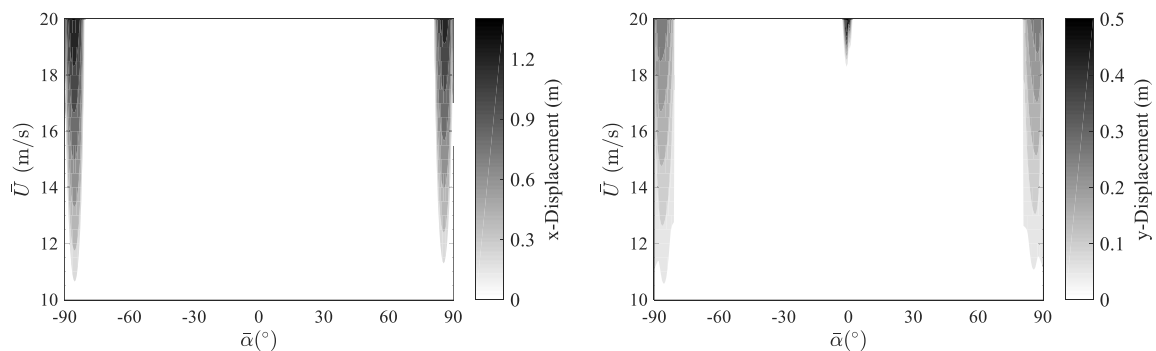


Figure 7 Numerically predicted vibration amplitudes

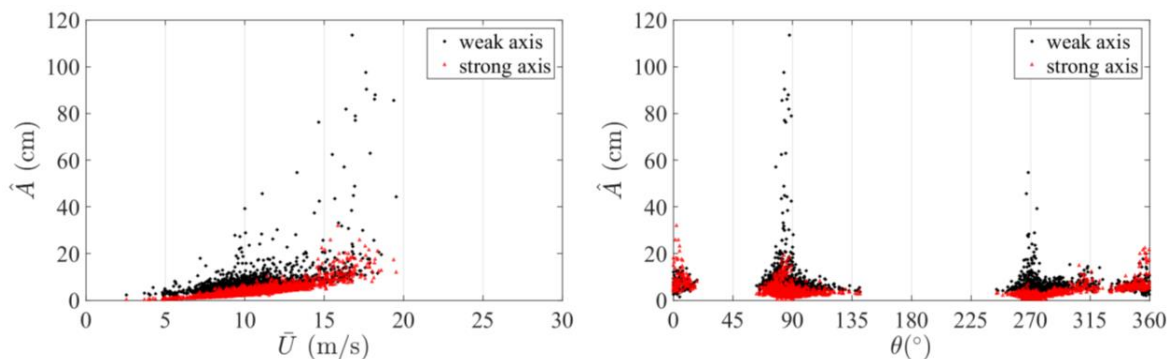


Figure 8 Measured maximum displacements

4. Conclusion

Under excitation from wind, slender towers with certain cross-sectional shapes can be susceptible to galloping oscillations. This paper presents the formulation of an analytical model in terms of a state-space equation that can be used to evaluate coupled galloping of a slender tower. Because the equation of motion involves nonlinear coupling, the Runge-Kutta method is used to yield numerical solutions. For illustration, the proposed method is used to evaluate the coupled galloping of a full-scale tower. Comparison between the numerical results and the measured vibrations of the full-scale tower suggests that the proposed method can effectively capture the essential characteristics of the full-scale coupled oscillations.

REFERENCES

- 1) Den Hartog, J.P., *Transmission line vibration due to sleet*. transactions of the american institute of electrical engineers, 1932. 51(4): p. 1074–1086.
- 2) Novak, M., H. Tanaka, and A.G. Davenport, *Vibration of towers due to galloping of iced cables*. ASCE Journal of the Engineering Mechanics Division, 1978. 104(2): p. 457-473.

- 3) Nigol, O. and P.G. Buchan, *Conductor Galloping Part I - Den Hartog Mechanism*. Power Apparatus and Systems, IEEE Transactions on, 1981. PAS-100(2): p. 699-707.
- 4) Norberg, C., *Flow around rectangular cylinders: Pressure forces and wake frequencies*. Journal of Wind Engineering and Industrial Aerodynamics, 1993. 49(1-3): p. 187-196.
- 5) Reuther, J.J., et al., *Constrained multipoint aerodynamic shape optimization using an adjoint formulation and parallel computers, Part 1*. Journal of Aircraft, 1999. 36(1): p. 51-60.
- 6) Reuther, J.J., et al., *Constrained multipoint aerodynamic shape optimization using an adjoint formulation and parallel computers, Part 2*. Journal of Aircraft, 1999. 36(1): p. 61-74.
- 7) Parkinson, G.V. and J.D. Smith, *The Square Prism as an Aeroelastic Non-linear Oscillator*. Quarterly Journal of Mechanics and Applied Mathematics, 1964. XVII Pt. 2: p. 225-239.
- 8) Novak, M., *Galloping Oscillations of Prismatic Structures*. ASCE Journal of the Engineering Mechanics Division, 1972. 98(EM1): p. 27-46.
- 9) Richardson, A., *Predicting Galloping Amplitudes: II*. Journal of Engineering Mechanics, 1988. 114(11): p. 1945-1952.
- 10) Richardson, A., *Predicting Galloping Amplitudes*. Journal of Engineering Mechanics, 1988. 114(4): p. 716-723.
- 11) Jones, K.F., *Coupled vertical and horizontal galloping*. Journal of Engineering Mechanics, ASCE, 1992. 118(1): p. 92-107.
- 12) Liang, S., et al., *An evaluation of onset wind velocity for 2-D coupled galloping oscillations of tower buildings*. Journal of Wind Engineering and Industrial Aerodynamics, 1993. 50(0): p. 329-339.
- 13) Li, Q.S., J.Q. Fang, and A.P. Jeary, *Evaluation of 2D coupled galloping oscillations of slender structures*. Computers & Structures, 1998. 66(5): p. 513-523.
- 14) Nikitas, N. and J. Macdonald, *Misconceptions and Generalizations of the Den Hartog Galloping Criterion*. Journal of Engineering Mechanics, 2014. 140(4): p. 04013005.
- 15) Zuo, D., D.A. Smith, and S.M. Morse, *Coupled galloping of a slender tower with distinct natural frequencies in two orthogonal directions: experimental study*, in *14th International Conference on Wind Engineering*. 2015: Porto Alegre, Brazil.
- 16) Wu, L. and D. Zuo. *Coupled galloping of a slender tower with distinct natural frequencies in two orthogonal directions: analytical study*. in *14th International Conference on Wind Engineering*. 2015. Porto Alegre, Brazil.
- 17) Kijewski, T. and A. Kareem, *Wavelet Transforms for system identification in civil engineering*. Computer-aided Civil and Infrastructure Engineering, 2003. 18: p. 339-355.

EFFECT OF MODELING ON DYNAMIC STABILITY OF A FLEXIBLE CANTILEVERED PLATE SUBJECTED TO A PARALLEL FLOW

Katsuhisa Fujita⁺¹ and Keiji Matsumoto⁺²

^{+1,2}Mechanical & Physical Engineering, Graduate School of Engineering, Osaka City University
3-3-138, Sugimoto, Sumiyoshi-ku, Osaka, 558-8585, Japan

The stability of a flexible cantilevered plate subjected to an axial flow is investigated. As the flexible flat plates, the papers in a high speed printing machine, the thin plastic and metal films, the fluttering flag are enumerated. The fluid is assumed to be treated as an ideal fluid in a subsonic domain, and the fluid pressure is calculated using the velocity potential theory. The coupled equation of motion of a flexible cantilevered plate is derived taking into consideration with the added mass, added damping and added stiffness respectively. The complex eigenvalue analysis is performed for the stability analysis. In order to consider the accuracy of dynamic stability analysis, three stability analysis methods are performed. Firstly, the analysis method based on boundary conditions in the half space surrounded by the leading edge and the trailing edge of a plate is performed. Hereafter, let's call it the coupled solution. Secondly, the analysis method based on the non circulatory aerodynamic theory is performed. Let's call it the non circulatory solution. Thirdly, the analysis method which fulfills the Kutta's condition is performed. Let's call it the circulatory solution. The following matters are clarified through the comparison of three solutions. When the mass ratio of a fluid system for a structure system is small, the flutter of the lower mode such as a second mode become predominant. And, when the mass ratio is large, the higher mode flutter appears. The critical flow velocity of the circulatory solution becomes lower than those of the coupled solution and the non circulatory solution when the mass ratio becomes low. On the other hand, the critical flow velocity of the circulatory solution becomes higher than those of the coupled solution and the non circulatory solution when the mass ratio becomes high.

Keyword: flutter, flow-induced vibration, self-excited vibration, panel flutter, parallel flow

1. INTRODUCTION

The energy-related machine and structure often show the performance through fluid and heat. The destructive vibration was activated to a machine and a structure by fluid flow, and it has been often experienced that it led to a great accident. Here, our attention is paid to the dynamic stability of a relatively flexible flat plate subjected to a parallel flow, namely flutter. For example, here, the vibrations of the paper in a high speed printing machine, the vibrations of the thin plastic and metal films, and in addition, the vibrations of turbo-machineries and the components of nuclear power plant are considered to be a problem.

There are already many studies in this field. For example, as a representative example of a flexible structure, Chang and Moretti^{1), 2)} reported the experiment and the analysis about the instability of a paper. In addition, the study on the stability of the stationary flat plate subjected to a water power reported by Weaver and Unny³⁾, and the study on stability of the cantilevered rectangular plate in the non-viscous passage flow reported by Guo and Paidoussis⁴⁾ have been included. Moreover, many research papers such as Bidkar et al.⁵⁾, Howell et al.⁶⁾ and Eloy et al.⁷⁾ have been reported. Also, the authors have reported the flutter and divergence of the stationary simply supported flexible plate subjected to a parallel flow and the simply supported plate moving through the stagnant fluid by Fujita and Imai⁸⁾, Fujita⁹⁾. Successively to these, in this paper, we propose three kinds of analysis modelings on the dynamic stability of the flexible cantilevered plate subjected to a parallel flow from a simplified modeling to a more exact modeling.

⁺¹fujita@mech.eng.osaka-cu.ac.jp

Three stability analysis methods are as follows. Firstly, the analysis method based on boundary conditions in the half space surrounded by the leading edge and the trailing edge of a flexible flat plate is performed as reported by Fujita and Imai⁸⁾. Hereafter, let's call it the coupled solution. Secondly, Kornecki et al.¹⁰⁾ derived the unsteady velocity potential by applying the non circulatory steady aerodynamics theory, and proposed the fluid pressure acting on a flexible plate. Using this proposal, the stability analysis is performed. Let's call it the non circulatory solution. We have already reported the first method and the second method by Fujita and Matsumoto¹¹⁾. In order to study more, the third method is proposed and discussed.

Thirdly, the velocity potential is derived by using the circulatory aerodynamics theory explained in the book by Bisplinghoff et al.¹²⁾. Assuming the continuous vortex sheet from the trailing edge to the backward direction, the velocity potential based on the vortex sheet is obtained. And then, the circulatory solution is obtained by superposing this velocity potential based on the vortex sheet on the non circulatory velocity potential so that the Kutta's condition is satisfied at the trailing edge of a flat plate. Let's call it the circulatory solution. Comparing the three numerical results, the effect of analysis modeling on the dynamic stability of a cantilevered plate are discussed.

2. THEORY

Figure 1 shows the analysis model. x is the coordinate of a flowing direction, y is the coordinate parallel to a plate surface and perpendicular to a flowing direction, and z is the coordinate perpendicular to the plate. The plate is subjected to a parallel flow with the fluid density ρ_f , and the lateral deflection w to z direction of the plate is induced by an uniform flow velocity U . The width of a plate is assumed to be infinite. The leading edge of $x = 0$ is assumed to be fixed, and the trailing edge of $x = l$ is free. h_p is the thickness of a plate, and l is the length of a plate.

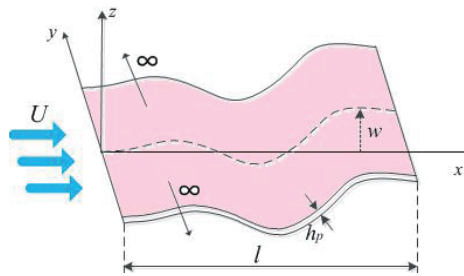


Figure 1: Analysis model in coupled solution and non-circulatory solution.

(1) Governing equation

As reported by Fujita and Imai⁸⁾, Fujita and Matsumoto¹¹⁾, the equation of motion of a stationary flexible flat plate subjected to a parallel flow is obtained in the following expression.

$$\rho_p h_p \frac{\partial^2 w}{\partial t^2} + D \frac{\partial^4 w}{\partial x^4} + (p_U - p_L) = 0, \quad (1)$$

where, ρ_p is the mass per unit area of a plate. D is the bending rigidity of a plate, t is time. $(p_U - p_L)$ shows the difference between the pressure acting at upper surface and the one at lower surface. When a fluid is assumed to be inviscid, the unsteady Bernoulli's equation is given on the $z = 0$ plane of a plate as follows.

$$p_U - p_L = -2\rho_f \left(\frac{\partial \phi}{\partial t} + U \frac{\partial \phi}{\partial x} \right)_{z=0}, \quad (2)$$

where ϕ is a two dimensional velocity potential.

The following dimensionless parameters is introduced. The subscript p shows a plate, subscript f shows a fluid, and $*$ shows a dimensionless system. Moreover, μ means the ratio of a fluid density for a plate density including the effect of l and h_p , let's call it the mass ratio.

$$\begin{aligned} x^* &= x/l, \quad z^* = z/l, \quad w^*(x^*, t^*) = w(x, t)/l, \quad \mu = \rho_f l / \rho_p h_p \\ t^* &= t \sqrt{D / \rho_p h_p} / l^2, \quad U^* = Ul \sqrt{\rho_p h_p / D}, \quad \phi^* = \phi \sqrt{\rho_p h_p / D}, \quad p^* = pl^3 / D. \end{aligned} \quad (3)$$

Using the dimensionless parameters system, Eqs. (1), (2) and the Laplace equation in which ϕ is satisfied can be obtained in the dimensionless form as follows. Besides, $*$ is deleted for a simplicity of description only in this section.

$$\frac{\partial^2 w}{\partial t^2} + \frac{\partial^4 w}{\partial x^4} + (p_U - p_L) = 0. \quad (4)$$

$$(p_U - p_L) = -2\mu \left(\frac{\partial \phi}{\partial t} + U \frac{\partial \phi}{\partial x} \right)_{z=0}. \quad (5)$$

$$\frac{\partial^2 \phi}{\partial x^2} + \frac{\partial^2 \phi}{\partial z^2} = 0. \quad (6)$$

The solution of $w(x, t)$ of equation (4) is assumed to be given by superposing the modes function in a vacuum.

$$w(x, t) = \sum_k w_k(x) q_k(t), \quad (7)$$

where $q_k(t)$ is the time function. $w_k(x)$ is the uncoupled k -th mode of a cantilevered plate.

The equation of motion of a plate is described by Eqs. (4) ~ (6) and Eq. (7). When the fluid force given by Eq. (5) is substituted into Eq. (4), the coupled equation of motion of a flexible cantilevered plate is derived in consideration of the added mass, added damping and added stiffness, respectively. As it is necessary to formulate the velocity potentials, let's explain the three kinds of solutions in the following 3 sections.

(2) Solution based on the boundary condition in the half-space

Firstly, the solution based on the boundary condition in the half-space is explained, that is the coupled solution. The analysis model shown in Fig. 1 is utilized. When the Laplace equation (6) is resolved by the variable separation method, and the boundary condition that the velocity potential must converge to zero at the infinity point of z direction is applied, the velocity potential ϕ can be obtained.

The boundary conditions at the ends of $x = 0, 1$ is considered. The unsteady fluid velocity in x direction is equal to the unsteady velocity of a plate in x direction. As the plate is fixed at $x = 0$, the unsteady fluid velocity becomes zero. On the other hand, the free edge can move freely. However, although there is the component of x direction generated by the movement of the free edge, it is assumed to be small as a second order. Therefore, as for the boundary condition of x direction at the free edge of $x = 1$, the unsteady fluid velocity in x direction can be assumed to be also equal to the unsteady velocity of a plate in x direction. Therefore, the following equation is given.

$$\left. \frac{\partial \phi}{\partial x} \right|_{z=0} = 0 \quad \text{for } x = 0, 1. \quad (8)$$

And, as for the boundary condition in z direction for $0 \leq x \leq L$, the flow velocity on the plate in z direction can be expressed in the following equation by Lighthill¹³⁾ when the steady flow velocity is U .

$$\left. \frac{\partial \phi}{\partial z} \right|_{z=0} = \frac{\partial w}{\partial t} + U \frac{\partial w}{\partial x}. \quad (9)$$

When Eq. (7) can be applied for $w(x, t)$, the velocity potential ϕ is determined by using the boundary conditions of Eqs. (8) and (9) as follows.

$$\phi(x, z, t) = \sum_k \sum_{i=1}^{\infty} \left[\left(-\frac{2}{i\pi} \right) \exp(-i\pi z) \cos(i\pi x) \times \left\{ \int_0^1 w_k(x) \cos(i\pi x) dx \cdot \dot{q}_k(t) + \int_0^1 \frac{dw_k(x)}{dx} \cos(i\pi x) dx \cdot U q_k(t) \right\} \right]. \quad (10)$$

The fluid pressure ($p_U - p_L$) can be determined by using Eq. (5). Here this solution is called as the coupled solution.

(3) Solution based on the non circulatory aerodynamic theory

Secondarily, the solution based on the non circulatory aerodynamic theory is explained. Similarly, the analysis model shown in Fig. 1 is utilized. As shown in Fig. 2, $H(\xi, t)$ is the intensity per unit length of local source or sink on the small length $d\xi$ of a flexible flat plate which carries out an unsteady motion. The velocity potential at the location (x, ξ) can be derived by using the local source and sink as follows.

$$d\phi = \frac{1}{4\pi} H(\xi, t) \ln\{(x - \xi)^2 + z^2\} d\xi. \quad (11)$$

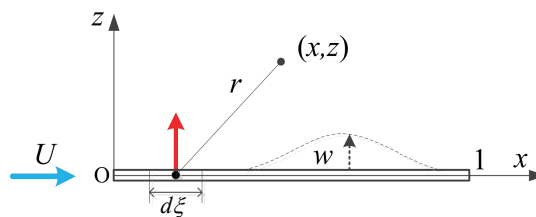


Figure 2: Local strength of source or sink at the microelement of a plate.

In general, the flow around the object subjected to an uniform flow can be expressed by a combination of source and sink. The unsteady velocity potential can be obtained by putting the source line along the chord of airfoil. That is, it is given by integrating Eq. (11) along the chord of airfoil in the following.

$$\phi(x, z, t) = \frac{1}{4\pi} \int_0^1 H(\xi, t) \ln\{(x - \xi)^2 + z^2\} d\xi. \quad (12)$$

It is confirmed easily that this velocity potential satisfies the Laplace equation (6). When $H(\xi, t)$ is determined so that Eq. (12) satisfies the boundary condition Eq. (9) on the range $0 < x < 1$ of a plate, the following equation is obtained.

$$\phi(x, z, t) = \frac{1}{2\pi} \int_0^1 \left\{ \frac{\partial w(\xi, t)}{\partial t} + U \frac{\partial w(\xi, t)}{\partial \xi} \right\} \ln\{(x - \xi)^2 + z^2\} d\xi. \tag{13}$$

The fluid pressure ($p_U - p_L$) is derived by putting this velocity potential into Eq. (5). Here this solution is called as the non circulatory solution.

(4) Solution based on the circulatory aerodynamic theory

As the third solution, the solution based on circulatory aerodynamic theory is explained. In general, the unsteady fluid velocity becomes infinite at the trailing edge of a plate in the flow field with the velocity potential which is obtained by assuming an ideal fluid. However, as it is not a practical flow to become infinite, the solution is obtained using the velocity potential which satisfies the Kutta's condition, that is, "the value of flow velocity is finite at the trailing edge of a plate". In order to get the velocity potential by using the Joukowski transformation, the analysis model shown in Fig. 3 is utilized instead of Fig. 1. Similarly, x is the coordinate of a flowing direction, y is the coordinate parallel to a plate surface and perpendicular to a flowing direction, and z is the coordinate perpendicular to a plate. The leading edge of $x = -b$ is assumed to be fixed, and the trailing edge of $x = b$ is free, and $2b$ is the length of a plate. Besides, in the analysis model of Fig. 3, the representative length l must be replaced by $2b$ for the dimensionless system of Eq. (3).

When the flow field around a flat plate is replaced with the flow field around a circle, the analysis handling becomes convenient. By using the Joukowski transform, the flow field around a plate in the orthogonality coordinate system of Fig. 4 (a) is rewritten to the flow field around a circle in the polar coordinates system of Fig. 4 (b), and then the velocity potential is formulated by the polar coordinate system.

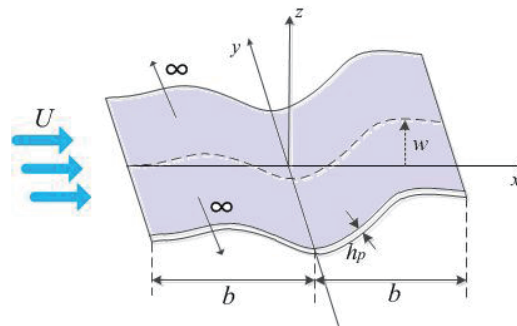
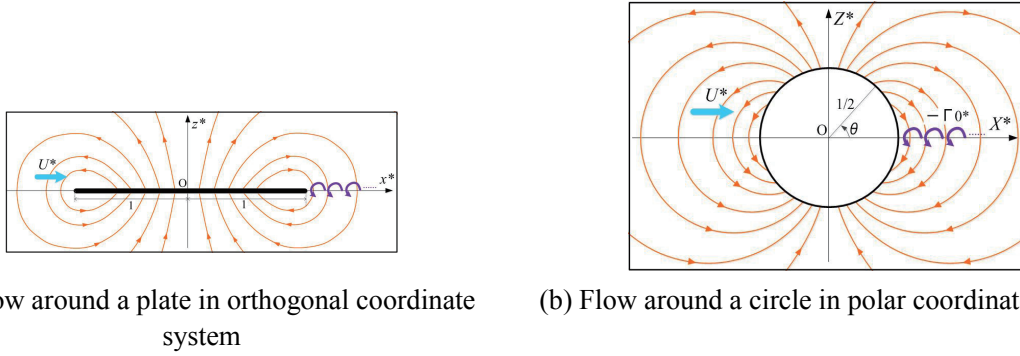


Figure 3: Analysis model in circulatory solution. U is a uniform flow velocity, w is the deflection of a plate, $2b$ is the length and h_p is the thickness.

Concerning the flow field around a circle, the continuous distribution of source is assumed to be on upper half circumference and that of sink is assumed to be on lower half circumference. Deriving the velocity potential from these source and sink, the velocity potential which is equivalent with the non circulatory velocity potential shown in Eq. (13) can be formulated in the polar coordinate system as follows.



(a) Flow around a plate in orthogonal coordinate system (b) Flow around a circle in polar coordinate system

Figure 4: Joukowski transformation. * shows a dimensionless system as shown in Eq. (3). U is an uniform velocity, Γ_0 is the circulation per unit length.

$$\phi_U(\theta, t) = -\frac{1}{\pi} \int_0^\pi \int_0^\pi \frac{w_a \sin^2 \phi d\phi}{(\cos \phi - \cos \theta)} d\theta, \quad (14)$$

where ϕ , θ is the argument in the circumference, w_a is equal with the righthand side of Eq. (9). ϕ_U is the velocity potential on upper half circumference, and has a different relation on the plus and minus with the velocity potential in the lower half circumference each other. The fluid pressure which is caused by the non circulatory velocity potential can be obtained substituting Eq. (14) into Eq. (5) in the following.

$$(p_U - p_L)_{NC} = \frac{2\mu}{\pi} \left[\int_0^\pi \left\{ \int_0^\pi \frac{(\partial w_a / \partial t) \sin^2 \phi d\phi}{(\cos \phi - \cos \theta)} \right\} d\theta + \frac{U}{\sin \theta} \int_0^\pi \frac{w_a \sin^2 \phi d\phi}{(\cos \phi - \cos \theta)} \right], \quad (15)$$

where the subscript NC means the non circulatory. As shown in Fig. 4, the velocity potential can be derived by assuming the existence of the continuous vortex sheet from the trailing edge of a plate to the flow behind from it. Similarly, the following equation is given by formulating it in the polar coordinate system.

$$\phi_U^{all\Gamma_0}(\theta, t) = -\frac{1}{\pi} \int_1^\infty \gamma_w(\xi, t) \times \tan^{-1} \left[\frac{(\xi - 1)(1 + \cos \theta)}{(\xi + 1)(1 - \cos \theta)} \right] d\xi, \quad (16)$$

where ξ is the variable which denotes the location from the trailing edge of a plate to the flow behind from it ($1 \leq \xi < \infty$), $\gamma_w(\xi, t)$ is the intensity of circulation per unit length at the location ξ . And, the subscript $all\Gamma_0$ denotes the total of the circulation Γ_0 per unit length. Substituting Eq. (16) into Eq. (5), the following fluid pressure is obtained.

$$(p_U - p_L)_{all\Gamma_0} = \frac{\mu U}{\pi \sin \theta} \int_1^\infty \left\{ \frac{\xi}{\sqrt{\xi^2 - 1}} (1 - \cos \theta) + \sqrt{\frac{\xi + 1}{\xi - 1}} \cos \theta \right\} \gamma_w(\xi, t) d\xi. \quad (17)$$

The velocity potential of Eq. (14) and that of Eq. (16) are superposed so that the Kutta's condition is satisfied. Concerning the relationship between the unsteady flow velocity on a plate and that on a circumference, the condition that the flow velocity at the trailing edge must be finite introduces the following equation.

$$Q = \frac{1}{\pi} \int_0^{\pi} \frac{w_a \sin^2 \phi d\phi}{(\cos \phi - 1)} = -\frac{1}{2\pi} \int_1^{\infty} \sqrt{\frac{\xi+1}{\xi-1}} \gamma_w(\xi, t) d\xi. \quad (18)$$

Using Eq. (18), the fluid pressure of Eq. (17) can be rewritten. As a result, the total fluid pressure, that is the sum of Eq. (15) and Eq. (17) which is rewritten, is given as follows.

$$(p_U - p_L)_C = \frac{2\mu}{\pi} \left[\int_{\theta}^{\pi} \left\{ \int_0^{\pi} \frac{(\partial w_a / \partial t) \sin^2 \phi d\phi}{(\cos \phi - \cos \theta)} \right\} d\theta + \frac{U}{\sin \theta} \int_0^{\pi} \frac{w_a \sin^2 \phi d\phi}{(\cos \phi - \cos \theta)} \right] - 2\mu U Q \left\{ \cot \theta + \left[\frac{1 - \cos \theta}{\sin \theta} \right] C(k) \right\}, \quad (19)$$

where the subscript C means a circulation. Using the Hankel functions of the second kind $H_0^{(2)}$, $H_1^{(2)}$, $C(k)$ is shown in the following.

$$C(k) = F(k) + iG(k) = \frac{H_1^{(2)}(k)}{H_1^{(2)}(k) + iH_0^{(2)}(k)}, \quad (20)$$

where $C(k)$ is the Theodorsen function, it has a variable of the reduced frequency k . k is given by a dimensionless natural circular frequency ω and a dimensionless flow velocity U as follows.

$$k = \frac{\omega}{U}. \quad (21)$$

Here this solution is called as the circulatory solution.

(5) Fluid-structure coupled equation of motion

Substituting the fluid pressure into the equation of motion of a plate shown by Eq. (4), the fluid-structure coupled equation of motion can be derived. Truncating the mode number k as n , and then multiplying $w_j(x)$ ($j = 1, 2, \dots, n$) on the both sides of the fluid-structure coupled equation of motion, it is integrated from 0 to 1 as for x using the orthogonal characteristics. When the order of expressions is arranged further, the equation of motion can be obtained.

Changing the fluid velocity U , the complex eigenvalue analysis is performed and the root locus is obtained. When the real part $\Re(\lambda)$ of the eigenvalue λ is positive and the imaginary part $\Im(\lambda)$ is not zero, the system becomes flutter. And, when $\Re(\lambda)$ is positive and $\Im(\lambda)$ is zero, the system is divergence. Besides, $\Re(\lambda)$ means the growth rate of vibration, and $\Im(\lambda)$ means the coupled frequency.

3. ANALYSIS RESULTS AND CONSIDERATIONS

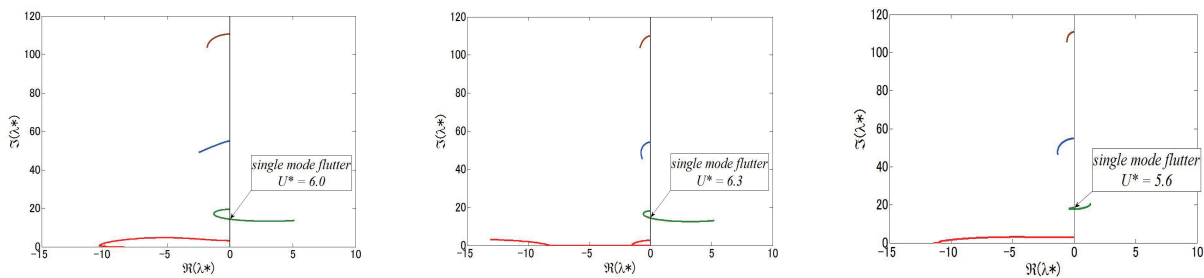
(1) Numerical analysis results on the stability of a cantilevered plate

Firstly, the numerical analysis results on the stability of a cantilevered flexible plate by performing the complex eigenvalue analysis. The solution depends on the dimensionless fluid velocity U^* and the dimensionless parameter μ . This μ means the ratio of the density of a fluid for the density of a structure as shown in Eq. (3), and it is called as a mass ratio here. When μ is small, the system of a structure governs the stability, and when it is large, the system of a fluid governs the stability. Here, changing μ , the comparison among the coupled solution, the non circulatory solution, and the circulatory solution is performed.

Besides, as the Theodorsen function is included in the circulatory solution due to the Kutta's condition, the reduced frequency k^* is a variable in the numerical calculation. Therefore, the iteration calculation is performed by using the relationship $k_{cr}^* = \omega_{cr}^* / U_{cr}^*$ in order to get the converged solution. Besides, * shows a dimensionless system.

a) Root locus

Figure 5 shows the root loci of the coupled solution, the non circulatory solution, and the circulatory solution, respectively. Besides, the fluid velocity U^* is changed from 0 to 10.0. As the eigenvalues are investigated from 1st mode to 4th mode. The red color shows 1st mode, green color shows 2nd mode, blue color shows 3rd mode, and brown color shows 4th mode, respectively.



(a) Coupled solution

(b) Non circulatory solution

(c) Circulatory solution

Figure 5: Root locus at $\mu = 1$. μ is the mass ratio of a fluid density for a plate density.

In all of the coupled solution, the non circulatory solution and the circulatory solution, the real part of the first mode which means the growth rate of vibration is negative. So, it is found to be always stable.

Next, concerning with the 2nd mode in all of the coupled solution, the non circulatory solution and the circulatory solution, the growth rate and the frequency decrease gently increasing the flow velocity. However, the growth rate begins to increase when the flow velocity surpasses a certain value, and the coupled solution, non circulatory solution and circulatory solution become a single mode flutter at $U^* = 6.0$, $U^* = 6.3$, and $U^* = 5.6$, respectively. Further, increasing the flow velocity, they move to the more unstable side.

The 3rd mode and 4th mode of the coupled solution, the non circulatory solution and the circulatory solution are stable, respectively.

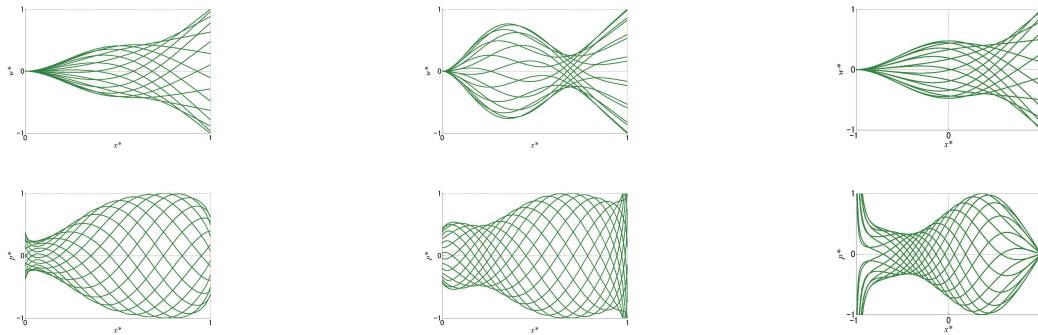
The mode number at which a flutter generates and the characteristics of a root locus show considerably a good agreement among three solutions qualitatively, although the critical flow velocities show a little differences quantitatively.

b) Vibration modes and fluid pressure distribution

Figure 6 shows the vibration mode and the fluid pressure distribution just after the outbreak of a flutter is investigated. These figures show the 2nd mode of the coupled solution, the non circulatory solution and the circulatory solution for $\mu = 1$, respectively. The upper row shows the vibration mode, and the lower row shows the fluid pressure distribution.

When the flow velocity increases, the fluid pressure of the non circulatory solution at the trailing edge is found to become very large. On the other hand, that of the circulatory solution converges to zero. This difference is thought to be due to the Kutta's condition which is applied to the circulatory solution, not to the non circulatory solution. That is, a fluid flowing along the upper surface of a plate and that along the lower surface become the same velocity, and then flow backward smoothly due to the Kutta's condition.

Moreover, at the leading edge, the fluid pressure of the circulatory solution is found to be very large comparing with the non circulatory solution. In the circulatory solution, it is thought that the flow field in which the leading edge becomes a stagnant point is formed strongly.



(a) Coupled solution, $U^* = 6.0$ (b) Non circulatory solution, $U^* = 6.3$ (c) Circulatory solution, $U^* = 5.6$

Figure 6: Vibration mode and fluid pressure distribution just after flutter at $\mu = 1$.

(2) Relationship between mass ratio and critical velocity

Figure 7 shows the relationship of the critical velocity versus the mass ratio. The horizontal axis of Fig. 7 means the mass ratio, and the vertical axis of Fig. 7 shows the dimensionless critical flow velocity. Here, changing the dimensionless velocity from 0 to 20.0, the dimensionless critical velocity is determined.

The dotted line is the coupled solution, the one-dotted line is the non circulatory solution, and the solid line is the circulatory solution, respectively. It is found that the critical velocities of the coupled solution, the non circulatory solution, and the circulatory solution change as the mass ratio μ change. When the mass ratio becomes smaller, it is found that the critical flow velocity of the circulatory solution becomes lowest. When the mass ratio becomes about 1, three solutions approach to the same value. When the mass ratio increases from 1 to 10, the circulatory solution is found to be most stable, other two solutions show the stability of same degree. Furthermore, the step-like phenomena appear in three critical curves. When the mass ratio is small, the flutter of the lower mode such as a second mode become predominant. And, when the mass ratio is large, the higher mode appears. The step-like phenomena express the change of the flutter mode from the lower mode to the higher mode. As for the value of the mass ratio μ where the mode changes, it is found to be different among the coupled solution, the non circulatory solution, and the circulatory solution.

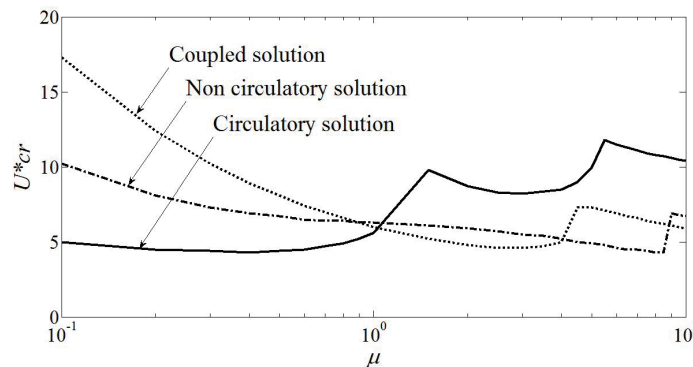


Figure7: Critical velocity versus mass ratio. μ is mass ratio.

In the range of $\mu \leq 1$ where the 2nd mode flutter generates, the critical velocity of the circulatory solution is smaller than those of the coupled solution and the non circulatory solution. And, in the range of $\mu > 1$ where the 3rd mode flutter generates, the critical velocity of the circulatory solution is larger than those of the coupled solution and the non circulatory solution. A cause of such a difference is thought to include the Kutta's condition. As the flow at the trailing edge becomes smooth by considering the Kutta's condition in the

circulatory solution, the stability at this region is thought to become good. When the mass ratio becomes large, the effect of a fluid increases relatively and the fluctuation at the neighborhood of the trailing edge is apt to be active. In such situation that the fluctuation of the neighborhood of the trailing edge is large, the effect considering the Kutta's condition is activated more, and as a result, it is thought that the critical velocity increase. Therefore, the critical flow velocity is thought to become larger in the case that the Kutta's condition is considered when the mass ratio increases.

4. CONCLUSIONS

Being common to three solutions, the flutter of the lower mode such as 2nd mode occurs when the mass ratio is small. And, the flutter of the higher mode such as 3rd mode and 4th mode occurs when the mass ratio is large. The critical flow velocity of the circulatory solution becomes lower than those of the coupled solution and the non circulatory solution when the mass ratio becomes low. On the other hand, the critical flow velocity of the circulatory solution becomes higher than those of the coupled solution and the non circulatory solution when the mass ratio becomes high. The reason why such a difference generates is that the Kutta's condition is considered.

REFERENCES

- 1) Chang, Y. B., Fox, S. J., Lilley, D. G. and Moretti, P. M. : Aerodynamics of moving belts, tapes and webs, *Proceedings of the ASME 1991 Machinery Dynamics and Element Vibrations Conference*, DE-Vol. 36, pp.33-40, 1991.
- 2) Chang, Y. B. and Moretti, P. M. : Interaction of fluttering webs with surrounding air, *Tappi Journal*, pp.231-236, 1991.
- 3) Weaver, D. S. and Unny, T. E. : The hydroelastic stability of a flat plate, *Journal of Applied Mechanics*, Vol.37, pp.823-827, 1970.
- 4) Guo, C. Q. and Paidoussis, M. P. : Stability of rectangular plates with free side-edges in two-dimensional inviscid channel flow, *Journal of Applied Mechanics*, Vol. 67, pp.171-176, 2000.
- 5) Bidkar, R. A., Raman, A. and Bajaj, A. K. : Aeroelastic stability of wide webs and narrow ribbons in cross flow, *Transactions of the American Society of Mechanical Engineers, Journal of Applied Mechanics*, Vol. 75, pp.041023-1-041023-9, 2008.
- 6) Howell, R. M., Lucey, A. D., Carpenter, P. W. and Pitman, M. W. : Interaction between a cantilevered-free flexible plate and ideal flow, *Journal of Fluids and Structures*, 25, pp.544-566, 2009.
- 7) Eloy, C., Souilliez, C. and Schouveiler, L. : Flutter of a rectangular cantilevered plate, *Proceedings of the ASME 2006 Pressure Vessels & Piping Division Conference*, PVP2006-ICPVT-11-93837 in CD-ROM, 2006.
- 8) Fujita, K. and Imai, T. : Dynamic stability analysis of a flexible plate moving in a parallel flow, *Transactions of the Japan Society of Mechanical Engineers*, Series C, Vol.79, No.801, pp.1336-1347, 2013 (in Japanese).
- 9) Fujita, K. : Dynamic stability analysis of a flexible plate moving in a parallel flow, *Proceedings of the ASME 2013 Pressure Vessels & Piping Division Conference*, PVP2013-97132 in CD-ROM, 2013.
- 10) Kornecki, A., Dowell, E. H. and O'Brien, J. : On the aeroelastic instability of two-dimensional panels in uniform incompressible flow, *Journal of Sound and Vibration*, 47(2), pp.163-178, 1976.
- 11) Fujita, K. and Matsumoto, K. : Stability of a stationary flexible cantilevered plate in an axial flow, *Proceedings of the ASME 2014 Pressure Vessels & Piping Division Conference*, PVP2014-28147 in CD-ROM, 2014.
- 12) Bisplinghoff, R. L., Ashley, H. and Halfman, R. L. : *Aeroelasticity*, Reading, Massachusetts: Addison-Welsey, 1955.
- 13) Lighthill, M. J. : Note on the swimming of slender fish, *Journal of Fluid Mechanics*, pp.305-317, 1960.

EFFECT OF VIBRATION DATA PREPROCESSING FOR FLUTTER MARGIN PREDICTION

Masato TAMAYAMA⁺¹, Kenichi SAITOH⁺¹, Norio YOSHIMOTO⁺¹ and Hitoshi ARIZONO⁺¹
⁺¹Japan Aerospace Exploration Agency, JAXA, Tokyo, JAPAN

Although airplane's model certification must be proved by showing enough damping margin at every flight condition, the damping is not a reliable index to conduct flight tests safely, i.e. it might change drastically against the flight condition. Flight tests should stand on much more reliable index rather than damping. In this study, the Discrete Flutter Margin is used. Whichever index is used during the flight test, the accuracy of index might be influenced by the original vibration data of structures. For this purpose, two methods are taken in this study: the Random Decrement (RDD) method and the Natural Excitation Technique (NExT), each of which can effectively reduce the structural response caused by a random noise. By applying each of the RDD and the NExT processing methods to the original data, the resultant signal becomes the structural quasi-step or quasi-impulse responses. For the method to identify the system model from step and impulse responses, the Eigen-system Realization Algorithm (ERA) suits well. In this study, two sets of system identification procedures are applied to the wind tunnel experimental data: one is the combination of the RDD and the ERA, and another is the combination of the NExT and the ERA. The wind tunnel model is the half-spanned wing model of Super Sonic Transport (SST) Airplane. The test data are acquired in the JAXA's 0.6m×0.6m Transonic Flutter Wind Tunnel. The resultant Discrete Flutter Margin values acquired from both sets of procedures are compared.

Keyword: Flutter Prediction, System Identification

1. INTRODUCTION

Flight tests are definitely required in the Aeroelastic stability requirements of airworthiness regulations such as the Federal Aviation Administration Regulations, FAR. The flight tests are conducted by exploring in more severe test conditions in level flight. At every moment, therefore, the safety flight is required. Airplane's model certification must be proved by having enough damping margin in every flight condition, and damping, therefore, should be monitored to see the aeroelasticity instability. On the other hand, the damping is not a reliable index to conduct flight tests safely, i.e. it might change drastically against the flight condition. Flight tests should stand on much more reliable index rather than damping. For this purpose, the Discrete Flutter Margin, F_z , was proposed by Torii¹⁾ utilizing a system identification technique: the Auto-Regressive Moving Average (ARMA) modeling was used in his research. Whichever index is monitored in flight tests, the accuracy of index might be influenced by the original vibration data of flying airplane. The Random Decrement (RDD) method and the Natural Excitation Technique (NExT) are introduced independently to improve the prediction accuracy of aeroelasticity instability. Each of both methods can effectively reduce the structural response caused by a random noise. By applying each of the RDD and the NExT processing to the original data, the resultant signals become the structural quasi-step and quasi-impulse responses respectively. For the method to identify the system model from step and impulse responses, the Eigen-system Realization Algorithm (ERA) suits well.

In this study, two combinations of system identification procedures, {RDD and ERA} and {NExT and ERA}, were applied to the wind tunnel experimental data. The resultant F_z values were compared from a viewpoint of flutter prediction accuracy.

Most of the description, figures and tables shown in this paper is referring to the Ref.2.

⁺¹masato@chofu.jaxa.jp

2. PROCESSING METHOD

In this section, the processing methods used in this study are explained. In our study, the processes are conducted in the discrete time domain.

(1) Random Decrement Method: RDD

The RDD process proposed by Cole³⁾ is referred in this study. Suppose structural vibration data history, $\{y\}$, as shown in Fig.1 (a), which is usually measured with accelerometers or strain gauges. An offset $-y_s$ is applied to $\{y\}$, and $\{y_0\}$ is generated as follows:

$$y_0 = y - y_s \quad (1)$$

If $-y_s$ is taken appropriately, $\{y_0\}$ crossing $y_0=0$ exists at the time series $\{t_n \mid n=1 \sim N\}$. Here, both points on the time history showing plus and minus slopes are picked up. The next process is to extract a certain length data beginning from t_n as shown in Fig.1 (b). The RDD signal, $\{D\}$, is acquired by simply taking an average of these N sets of data:

$$D(m) = \frac{1}{N} \sum_{n=1}^N y_0(t_n + m - 1), \quad m = 1, 2, \dots, L \quad (2)$$

where, L is the number of data samples captured in one data set. If the structure is linear against external forces, $\{D\}$ approaches the structure's response against the external step force of $-y_s$ height. In the ERA processing, the system model must be identified based on an impulse response. To meet this requirement, $\{D\}$ is differentiated as follows:

$$\left. \begin{aligned} \hat{Y}(0) &= 0 \\ \hat{Y}(m) &= \frac{D(m+1) - D(m)}{-y_s}, \quad m = 1, 2, \dots, L-1 \end{aligned} \right\} \quad (3)$$

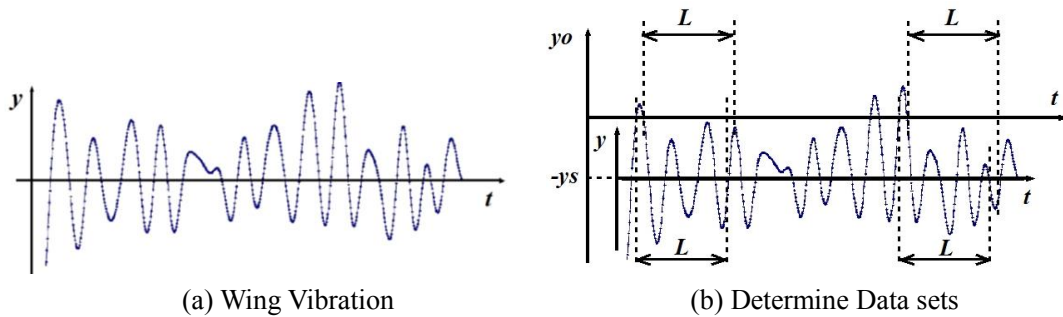


Figure 1: Time History Extraction in RDD processing

(2) Natural Excitation Technique: NExT

The mathematical background of NExT was given by James et al.⁴⁾ Consider the cross-correlation function of vibration data under a white noise excitation, $R_{ij}(t)$, between two different points of a structure, e.g. points i and j . $R_{ij}(t)$ satisfies the homogeneous equation of motion of the corresponding vibration system, and, therefore, the system characteristics can be identified from $R_{ij}(t)$. For the ERA processing, $R_{ij}(t)$ can be used directory instead of the system impulse response.

(3) Eigen-system Realization Algorithm: ERA

The Linear Time-Invariant state-space model in discrete time domain is written as follows:

$$\left. \begin{aligned} X(n+1) &= A \cdot X(n) + B \cdot u(n) \\ Y(n) &= C \cdot X(n) + D \cdot u(n) \end{aligned} \right\} \quad n = 0, 1, 2, \dots \quad (4)$$

An impulse input at zero state will cause the response known as the Markov parameter $\{Y\}$:

$$Y(n) = C \cdot A^{n-1} \cdot B \quad (5)$$

The Hankel matrix is constructed by windowing $\{Y\}$ and piling it in the row direction:

$$H_{rs}^{n-1} = \begin{bmatrix} Y(n) & \cdots & Y(n+s-1) \\ Y(1+n) & \cdots & Y(1+n+s-1) \\ \vdots & \ddots & \vdots \\ Y(r-1+n) & \cdots & Y(r-1+n+s-1) \end{bmatrix} \quad (6)$$

where 's' is the windowing length and 'r' is the number of time steps to shift the data window. In the system identification process, the Markov parameter is replaced by measured time-series data, $\{\hat{Y}\}$:

$$\hat{H}_{rs}^{n-1} = \begin{bmatrix} \hat{Y}(n) & \cdots & \hat{Y}(n+s-1) \\ \hat{Y}(1+n) & \cdots & \hat{Y}(1+n+s-1) \\ \vdots & \ddots & \vdots \\ \hat{Y}(r-1+n) & \cdots & \hat{Y}(r-1+n+s-1) \end{bmatrix} \quad (7)$$

Then, singular value decomposition is applied to \hat{H}_{rs}^0 :

$$\hat{H}_{rs}^0 = \hat{U}\hat{\Sigma}\hat{V}^T \quad (8)$$

The state-space realization is obtained by using the one step time-shifted Hankel matrix \hat{H}_{rs}^1 :

$$A = \hat{\Sigma}^{-1/2}\hat{U}^T\hat{H}_{rs}^1\hat{V}\hat{\Sigma}^{-1/2}, \quad B = \hat{\Sigma}^{1/2}\hat{V}^TE_m, \quad C = E_p^T\hat{U}\hat{\Sigma}^{1/2}, \quad D = \hat{Y}(0) \quad (9)$$

where, for the SISO system, E_m and E_p are $\{1,0,\dots,0\}^T$ sized $s \times 1$ and $\{1,0,\dots,0\}^T$ sized $r \times 1$ respectively. ' $\hat{\Sigma}$ ' is the matrix in which all of diagonal elements are non-zero and the others are zero. For the case of considering N_m structural modes, $\hat{\Sigma}$ can be truncated into the square matrix sized $2N_m \times 2N_m$. In this study, N_m was set to 3. The characteristic equation of state-space model is constructed from the eigenvalue analysis of the system state equation. The eigenvalues of discrete system, $\{\lambda_j, \lambda_j^* \mid j=1 \sim N_m\}$, where '*' indicates complex conjugate transpose, are also used to calculate modal frequencies, $\{f_j \mid j=1 \sim N_m\}$, and damping ratios, $\{\zeta_j \mid j=1 \sim N_m\}$:

$$f_j = \frac{|\lambda_{Cj}|}{2\pi}, \quad \zeta_j = -\frac{\text{real}(\lambda_{Cj})}{|\lambda_{Cj}|} \quad j=1,2,\dots,N_m \quad : \quad \lambda_{Cj} = \frac{\ln(\lambda_j)}{\Delta t} \quad (10)$$

where Δt is the sampling time interval.

(4) Discrete Flutter Margin

The discrete flutter margin was proposed by Torii.¹⁾ Consider the system characteristic equation in discrete time domain:

$$G(z) = A_6z^6 + A_5z^5 + A_4z^4 + A_3z^3 + A_2z^2 + A_1z + A_0 \quad (11)$$

where the order of equation is 6, and the equation have 3 conjugate pairs of poles. For this system, the Jury's stability criteria is expressed as follows:

$$\left. \begin{aligned} G(1) &= A_6 + A_5 + A_4 + A_3 + A_2 + A_1 + A_0 > 0 \\ G(-1) &= A_6 - A_5 + A_4 - A_3 + A_2 - A_1 + A_0 > 0 \end{aligned} \right\} \quad (12)$$

and also,

$$\left. \begin{aligned} F_1^+ &\equiv A_6 + A_0 > 0, & F_1^- &\equiv A_6 - A_0 > 0 \\ F_5^+ &\equiv \det(S+T) > 0, & F_5^- &\equiv \det(S-T) > 0 \end{aligned} \right\} \quad (13)$$

$$S = \begin{bmatrix} A_6 & A_5 & A_4 & A_3 & A_2 \\ 0 & A_6 & A_5 & A_4 & A_3 \\ 0 & 0 & A_6 & A_5 & A_4 \\ 0 & 0 & 0 & A_6 & A_5 \\ 0 & 0 & 0 & 0 & A_6 \end{bmatrix}, \quad T = \begin{bmatrix} A_4 & A_3 & A_2 & A_1 & A_0 \\ A_3 & A_2 & A_1 & A_0 & 0 \\ A_2 & A_1 & A_0 & 0 & 0 \\ A_1 & A_0 & 0 & 0 & 0 \\ A_0 & 0 & 0 & 0 & 0 \end{bmatrix} \quad (14)$$

Then the Discrete Flutter Margin, F_z , is constructed with the parameters acquired in Eq. (13):

$$F_z \equiv \frac{F_5^-}{(F_1^-)^2} = \frac{d e (S - T)}{(A_6 - A_0)^2} \tag{15}$$

3. RESULTS AND DISCUSSIONS

The experimental model is the low aspect ratio semi-spanned wing with an engine nacelle. Figure 2 shows the planform of model. The airfoil shape is NACA0006 at every span section. Four strain gauges, #1 through #4, are attached at the locations shown in Fig.2. The wing’s first three structural eigen-modes are shown in Tab.1 accompanied with their natural frequencies. The tests were conducted at the Transonic Flutter Wind Tunnel in JAXA, whose specification is shown in Tab.2. The bottom graph in Fig.3 shows the time history of strain gauge. The test was conducted at the nominal Mach number of 0.90: the time history of free stream Mach number is also shown in Fig.3. The dynamic pressure, q , was changed by sweeping the total pressure, P_0 , with the speed of 6 kPa/s from 200 kPa to 300 kPa, and then 3 kPa/s from 300 kPa. Strain data were sampled at a frequency of 5 kHz after 1 kHz low pass filtering. The flutter occurred at $q = 109$ kPa with a mild vibration. Figure 4 shows the spectrogram of strain gauge signal. The 1st structural mode increases its frequency as q increases.

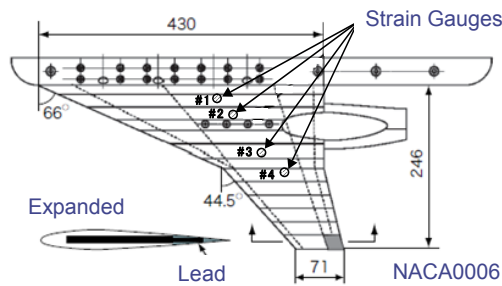


Figure 2: Plan View of Wing Model

Table 1: Eigen-modes and frequencies (Vibration Tests)

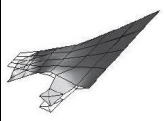
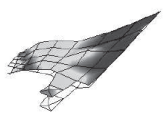
1st Mode	2nd Mode	3rd Mode
77[Hz]	126[Hz]	196[Hz]
		

Table 2: Specification of Wind Tunnel

Type	Blow Down
Operation Range	M : 0.5 ~ 1.2 Po : 150 ~ 400 kPa Re : ~ 6.0x10 ⁷ /m Dynamic Pressure : 22 ~ 166 kPa
Test Section	0.6m x 0.6m
Test Period	~ about 120 s
Mass Flow Rate	~ 320kg/s

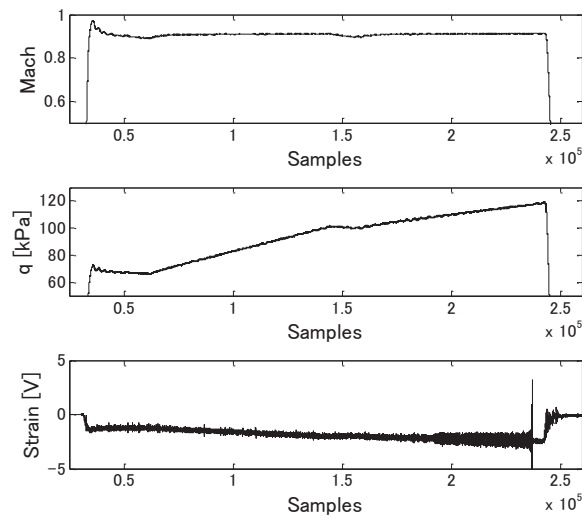


Figure 3: Results of Wind Tunnel Tests

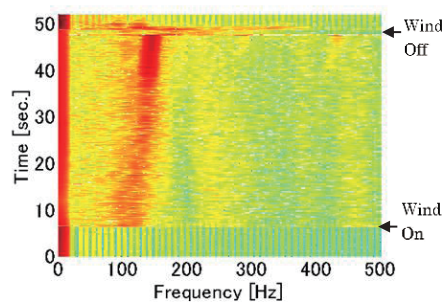


Figure 4: Spectrogram of Strain Gauge Signal

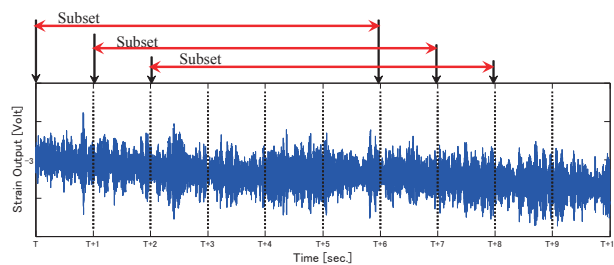


Figure 5: Data 'Subset' in the RDD Processing

(1) Application of RDD and NExT

The RDD and NExT were applied to the vibration signals of 6 sec. period, which is named here as 'subset.' As shown in Fig.5, each subset starts 1 sec. delayed from the former subset. The threshold level, y_s , was set to $1.4\sigma_m$: σ_m is the standard deviation of the corresponding subset signal. In order to include only 3 structural modes in the vibration signal, the measured signal was applied with digital band-pass filtering designed with Butterworth filter; from 100 Hz through 260 Hz for the RDD, and from 100 Hz through 280 Hz for the NExT. Although there is a discrepancy of the upper pass frequencies between each method, these values gave the best result in this study. Figure 6 (b) shows the example processed with the subset indicated in Fig.6 (a). Both results of the RDD and the NExT show almost the same decaying time histories. Figure 6 (c) is the power spectrums of both processed results. The RDD processing shows high values for higher structural

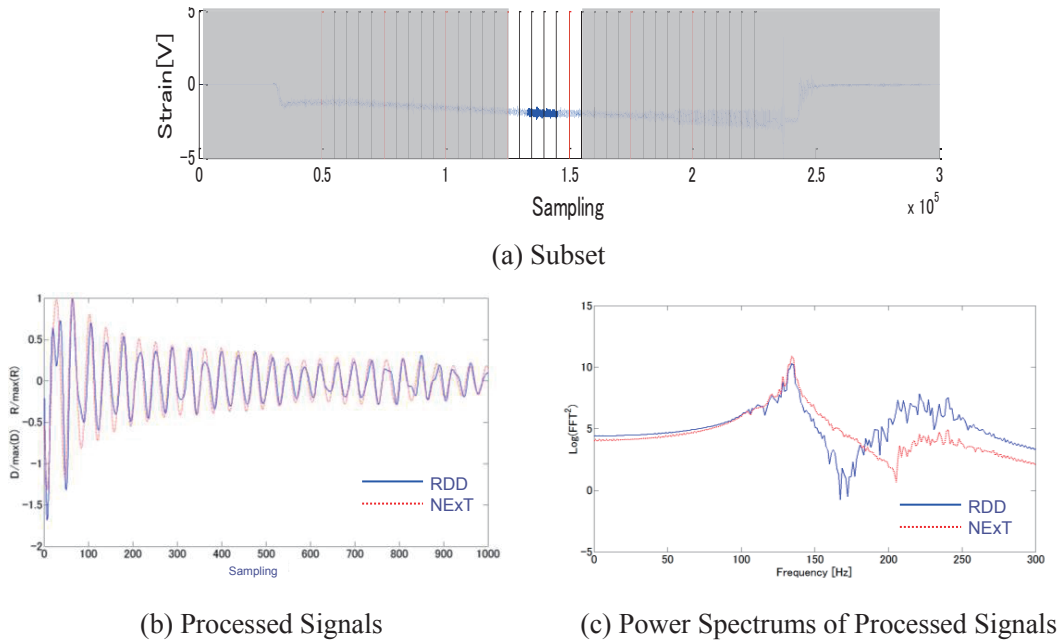


Figure 6: Example of RDD and NExT Processing

modes comparing to the NExT processing.

(2) System Identification by ERA

The size of Hankel matrix was set to 10×150 referring to Tamayama et al.⁵⁾ Figure 7 shows the Modal Amplitude Coherence (MAC) to see the accuracy of system identification by the ERA. The MAC for the *i* th mode is defined as the coherence between the measured modal amplitude history and the identified one.⁶⁾ The former one for the *i* th mode, \bar{q}_i , is calculated directly from the decomposition of Hankel matrix. The latter one, \hat{q}_i , is calculated from the initial modal amplitudes, which is also presented by the decomposition of Hankel matrix, and the eigenvalues of identified state matrix. The MAC is defined by the following equation:

$$MAC_i = \frac{|\bar{q}_i^* \cdot \hat{q}_i|}{\left((\bar{q}_i^* \cdot \bar{q}_i) \cdot (\hat{q}_i^* \cdot \hat{q}_i) \right)^{1/2}} \tag{16}$$

where ' * ' indicates complex conjugate transpose. The MAC takes a value between 0 and 1. The more accurate the system identification was performed, the more the MAC value becomes close to 1. From Fig.7, the MAC for both methods of RDD and NExT gives over 0.96. The hatched area is supercritical condition and out of consideration in this research. The ERA identification is considered to have been properly conducted for both of RDD and NExT processed signals.

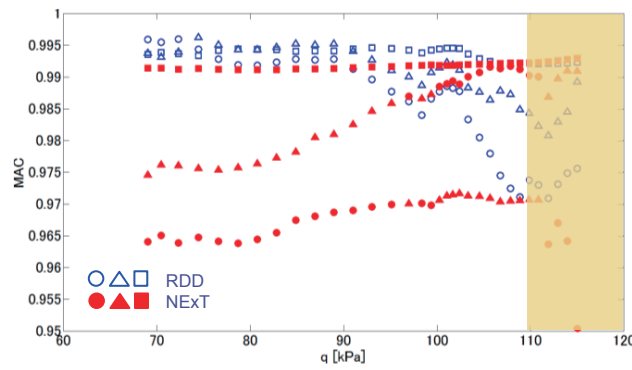


Figure 7: Modal Amplitude Coherence (MAC) ○●:1st Mode, ▲△:2nd Mode, □■:3rd Mode

Figures 8(a) and (b) show the change of modal characteristics as q increases. The modal frequencies of 1st and 3rd modes show good agreement between the RDD and the NExT results. The 2nd mode frequency shows larger decrease for the NExT result than the RDD one. The modal damping ratio of 1st mode decreases suddenly beyond $q = 100$ kPa for both of the RDD and the NExT results.

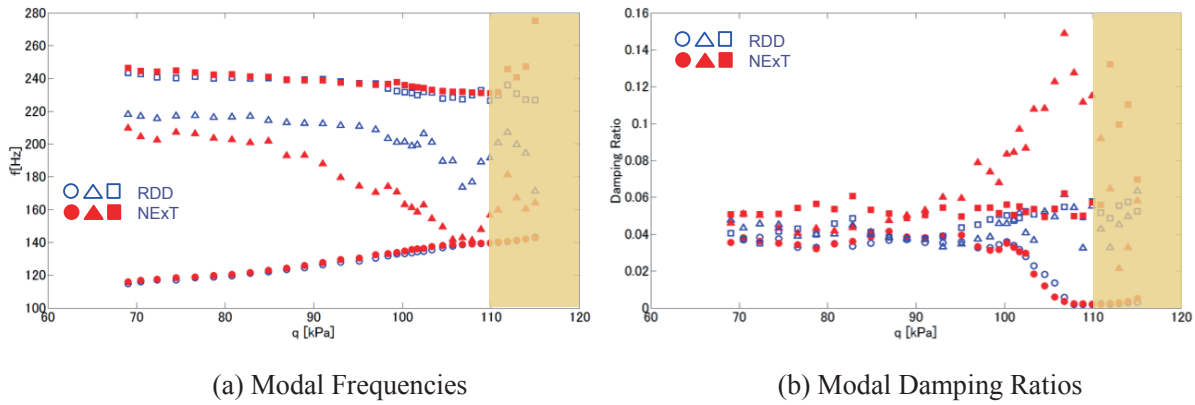


Figure 8: Modal Characteristics ○●:1st Mode, ▲▲:2nd Mode, □■:3rd Mode

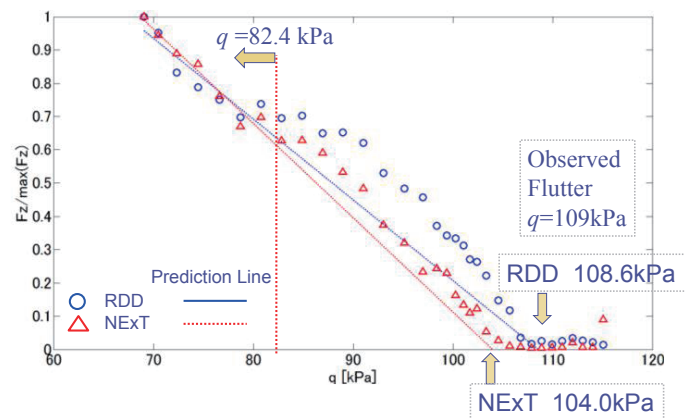


Figure 9: Flutter Condition Prediction

(3) Discrete Flutter Margin and Flutter Condition Prediction

Figure 9 shows F_z distribution against q . The lines in the figure show the linear fittings drawn from F_z calculated below $q = 82.4$ kPa, which is correspond with the 15% velocity margin from the experimentally observed flutter speed. In order to compare the values calculated from different methods, the vertical axis is normalized by the maximum values for each method. Prediction with the RDD shows closer prediction to the actual flutter dynamic pressure than that with the NExT. The standard deviations around the prediction line were calculated for each of the RDD and the NExT; 0.0717 for the RDD and 0.0428 for the NExT. The linearity of F_z is well for the NExT than the RDD.

4. CONCLUDINGS

The demonstration of flutter prediction from the Discrete Flutter Margin was presented in this study. The prediction was conducted by identifying the system model by the ERA. This identification method needs an impulse response of the corresponding structure. For this requirement, two different methods were compared in this study. One is the RDD, and another is the NExT. Followings are presented as the conclusions:

- (1) The RDD seems to have stronger signal at higher frequencies comparing to the NExT,

- (2) The ERA seems to have identified the system model appropriately for each of the RDD and the NExT considering from the Modal Amplitude Coherence, MAC,
- (3) Prediction with the NExT shows more linear relationship against the dynamic pressure than the RDD.

REFERENCES

- 1) Torii, H. : Application of Discrete-Time Flutter Prediction Method to a Three-Mode System, *the International Forum on Aeroelasticity and Structural Dynamics 2011*.
- 2) Tamayama, M. : Comparison between Random Decrement Method and Natural Excitation Technique as a Preprocessor of Flutter Margin Prediction Program, *the International Conference in Nonlinear Problems in Aviation and Aerospace 2014*.
- 3) Cole, H. A., Jr. : On-line Failure Detection and Damping Measurement of Aerospace Structures by Random Decrement Signatures, *NASA CR-2205*, 1973.
- 4) James, G. H., Carrie, T. G. and Lauffer, J. P. : The Natural Excitation Technique (NExT) for Modal Parameter Extraction From Operating Wind Turbines, *SANDIA REPORT*, SAND92-1666, 1993.
- 5) Tamayama, M., Arizono, H., Saitoh, K. and Yoshimoto, N. : Flutter Margin Prediction by Combination of Random Decrement Method and Eigen-system Realization Algorithm, *the International Forum on Aeroelasticity and Structural Dynamics 2013*.
- 6) Juang, J. N. and Pappa, R. S. : An Eigensystem Realization Algorithm for Modal Parameter Identification and Modal Reduction, *Journal of Guidance, Control, and Dynamics*, Vol.8, No.5, p.p.620-627, 1985.

STRUCTURAL DESIGN OF MORPHING CONTROL SURFACE USING CORRUGATED PANELS

Sato Keigo⁺¹ and Yokozeki Tomohiro⁺²
^{+1, +2}University of Tokyo, Tokyo, Japan

Morphing wings are anticipated as a way to improve efficiency over a wider range of flight conditions, but it is difficult to realize morphing because there are two conflicting demands, i.e. stiffness for aerodynamic forces and flexibility for morphing. Super-anisotropy of the corrugated panels is a solution to satisfy those demands. In this paper, in order to realize morphing control surface, the model which has corrugated panels driven by skins is proposed. The deformation analysis and the aerodynamic analysis are conducted. The parametric study showed the efficiency of this model compared with the plain flap.

Keyword: morphing, corrugated panel, Super-anisotropy, control surface, lift-drag ratio

1. INTRODUCTION

With the restricted environmental regulation and increasing fuel prices, airplanes are requested to be more efficient. One way of achieving this is improving aerodynamic efficiency, and morphing wings are anticipated as a way to improve efficiency over a wider range of flight conditions. Traditional wings are made by stiff materials and only few wing sections can be realized in a flight. Wing design is mainly considered to optimize efficiency at cruising. When the plane is lifting, landing and maneuvering, airfoil is changed by using either high-lift devices or control surfaces. However, the traditional high-lift devices and control surfaces have some gaps such as hinges, leading to decrease in aerodynamic performance and induction of noise. Morphing technology can realize a seamless deformation of wing section, optimized deformation at each flight condition and integrate those devices. These advantages will lead to improve aerodynamic efficiency and weight. Morphing wing is researched enthusiastically all over the world and various forms of morphing wing are discussed¹⁾. Camber morphing wing is one type of morphing wing which is well discussed²⁾⁻⁴⁾. However, two conflicting characteristics are required for camber morphing wing: stiffness for aerodynamic forces and flexibility for shape change ability. Super-anisotropy of corrugated panels is one of the feasible solutions to satisfy these conflicting characteristics (Fig. 1). The corrugated panel is stiff along the corrugation direction, but flexible in the transverse direction. Our previous works suggested that the corrugated panels have the potential to be applied to camber morphing wings consisting of morphing leading edge and trailing edge for high-lift devices⁵⁾. In previous research, using film at intrados, wrinkles leading to reduce aerodynamic efficiency were observed. Also, this model can move downwards only. In this paper, aircraft wing with morphing control surfaces enabling the leading edge to move upwards and downwards flexibility is focused on. Morphing mechanism and deformation estimation are investigated using FEM analysis (Marc) combined with aerodynamic analysis (XFLR5). The parametric studies are carried out to maximize the lift-drag ratio (L/D) at the one engine inoperative take-off condition.

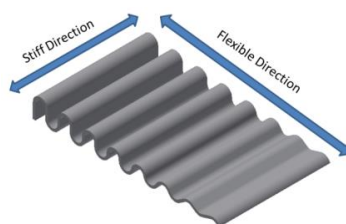


Figure 1: Super-anisotropic corrugated structures

⁺¹sato@aastr.t.u-tokyo.ac.jp, ⁺²yokozeki@aastr.t.u-tokyo.ac.jp

2. MODEL of MORPHING WING

(1) Airfoil

Symmetric airfoil, NACA64A010, is chosen considering deformation upwards and downwards and expecting to adopt as a vertical tail plane. Chord length of airfoil is 1000 mm considering wing tunnel test for future.

(2) Way of actuation

The part of morphing (corrugation) is from 65% chord length to 90% chord length. It is necessary to avoid skin buckling because intrados skin will be compressed as increasing camber. Morphing skin is one of the main problems for realization morphing wing⁶⁾. Many ideas about morphing skin are proposed, for example, using corrugated panel⁷⁾, compliant mechanism⁸⁾, or pneumatic muscle fibers⁹⁾ for skin. In this paper, the skin is made of flexible sheet and corrugated panel is actuated by winding it. The intrados skin is drawn in while both side skins have tension.

(3) Detail of model

To keep symmetry, the corrugated panels are arranged symmetrically and there is a rib which transfers the reaction force at the center line. There are also guides to generate bending moment and prevent skins from separating from airfoil (Fig. 2)

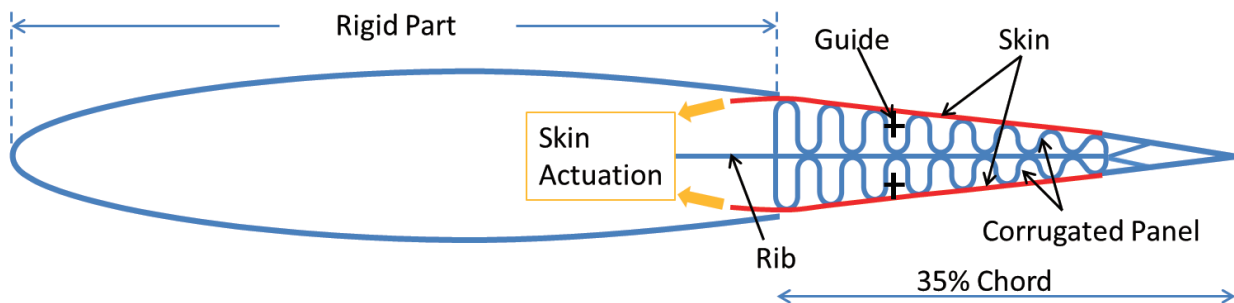


Figure 2: Schematic model of morphing control surface

3. NUMERICAL ANALYSIS

(1) FEM analysis

Deformation analysis and airfoil analysis were conducted to validate this model. Morphing mechanism and deformation estimation are investigated using FEM analysis (Marc). Focusing on two-dimensional deformation in airfoil cross section, plain strain was assumed. Element length was about 1 mm or smaller at curved area and near load area. Solid element was adapted to skin, and beam element was adapted to other parts. The geometric parameters and material properties of each part are given in Tab .1 and Tab. 2, respectively. The properties of CFRP were from JAXA Advanced Composites Database System¹⁰⁾. The contact was defined between all parts.

Table 1: Geometric parameters of the model

Baseline airfoil	NACA64A010
Chord (c) [mm]	1000
Span (b) [mm]	1000
Start of morph [mm]	$0.65c = 650$
End of morph [mm]	$0.9c = 900$
Number of corrugation	7.5
Corrugate thickness [mm]	1
Skin thickness [mm]	0.186
Rib thickness [mm]	1.5
Guide thickness [mm]	1
Rigid part thickness [mm]	2.2

Table 2: Material properties

Part		Material	E (GPa)	ν
Corrugated panel, Rigid part and Guide		Aluminum 2024	74	0.34

Part	Material	E_1 (GPa)	E_2 (GPa)	E_3 (GPa)	ν_{12}	ν_{23}	ν_{31}	G_{12} (GPa)	G_{23} (GPa)	G_{31} (GPa)
Rib	UD CFRP	153	8	8	0.34	0.3	0.02	4.03	3.07	4.03
Skin	Stain CFRP	74	74	8	0.05	0.34	0.037	12	4.03	4.03

UD CFRP: Unidirectional CFRP

Front rigid part and the first line of corrugation were fixed for all degrees of freedom. The end of the rib was fixed for only displacements. Displacement boundary condition was applied at end of the skins to simulate skin winding. Another end of the skins sheared nodes with the corrugated panel. Non-linear analysis for large displacement was conducted.

(2) Airfoil analysis

The deformation data derived by FEM was inputted and two-dimensional airfoil aerodynamic analysis was conducted by XFLR5. Aerodynamic load case assumes one engine inoperative condition which is a critical case at take-off. Tab. 3 shows this condition. Because morphing wing deforms the whole structure of morphing part, the rudder angle cannot be defined by using rotation angle around hinge like traditional rudder. In reference to previous work⁵⁾, morphing rudder angle is defined as a rotation angle of plain flap whose hinge is the same position of the start of the morph and trailing edge coincides with morphing trailing edge (Fig. 3). As the performance index of wing, each aerodynamic coefficient, i.e. lift coefficient (C_L), drag coefficient (C_D) and moment coefficient (C_M) were obtained. The case of a plain flap whose hinge line is 65% chord was also calculated to show the efficiency of this mode.

Table 3: Condition of aerodynamic analysis

Re (Reynolds number)	M (Mach number)	Angle of attack (deg)	Morphing angle (deg)
2.0×10^7	0.3	0	30

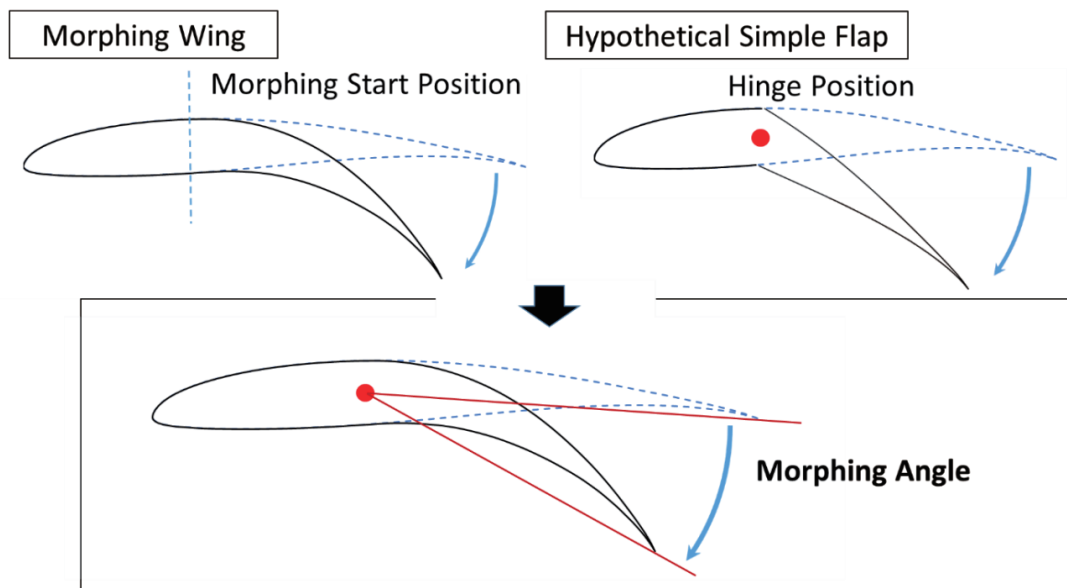


Figure 3: Definition of morphing angle⁵⁾

(3) Parametric study

The configuration of corrugated panel or the number and the position of guide will affect the final deformation of morphing and then the aerodynamic coefficients. Therefore, the parametric study was conducted. Parameters were corrugated pitch rate and the number and position of guide. Corrugated pitch rate means a common ratio of two adjoining circles of radius. An example of different corrugate pitch rate shows in Fig. 4. The guides were inserted in the rear five openings because deformation of corrugation will be too large if there are guides in other openings. The expression of the position of the guide is as follows. 1 means a guide and 0 means no guide in an opening and for example, the position of guide in Fig. 5 expresses as from front opening 0011010. The objective function is maximum lift to drag ratio (L/D).



Figure 4: Corrugated pitch rate

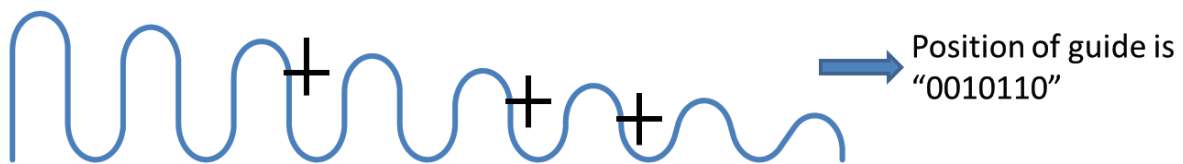


Figure 5: Example of position of guide

4. RESULT and DISUCUSSION

The best configuration is that corrugated pitch rate is 0.90 and the position of guide is 0011100. Fig. 6, Fig. 7 and Tab. 4 show wing section after 60% chord, pressure distribution and aerodynamic coefficients compared with plain flap, respectively.

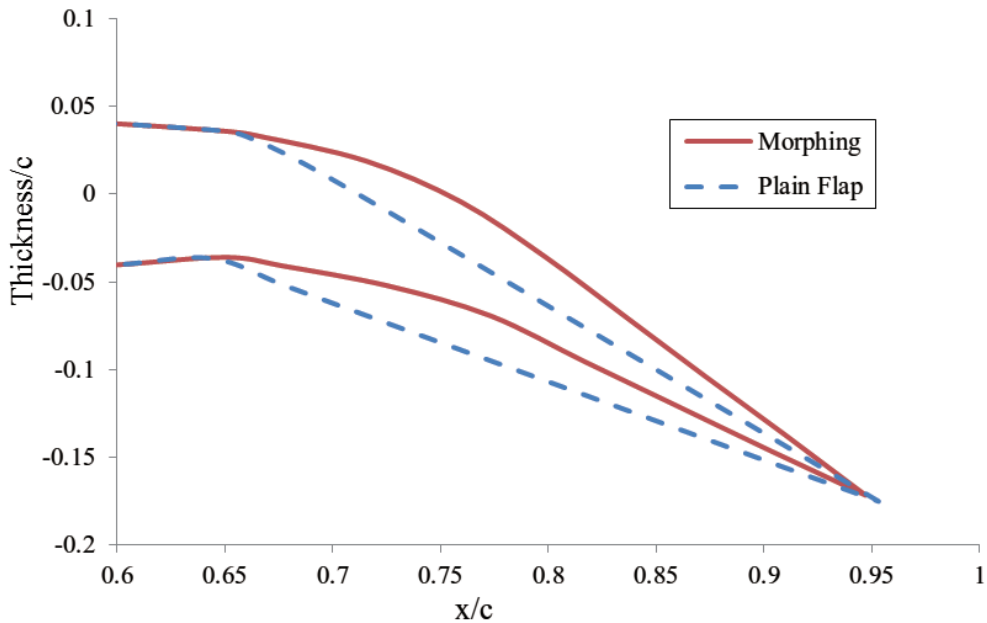


Figure 6: Comparison of wing section after 60% chord

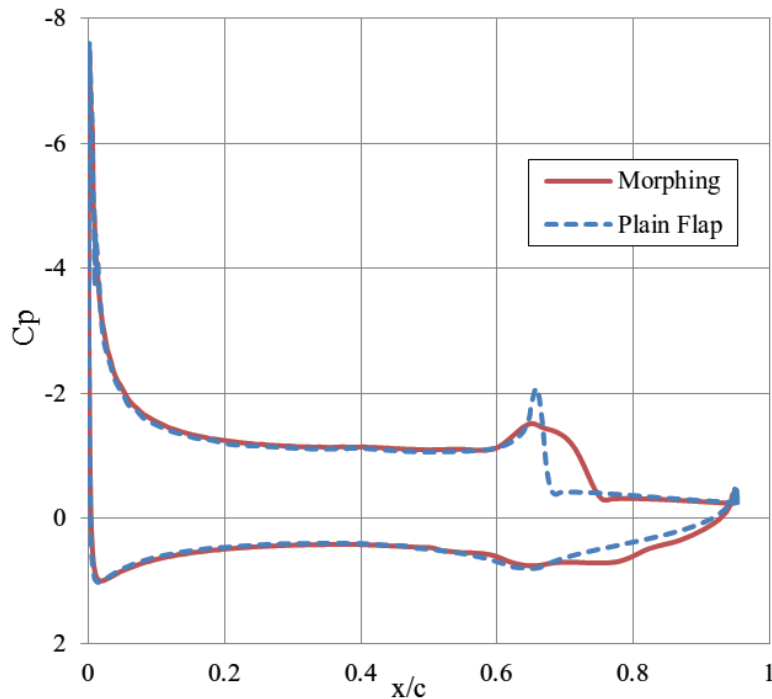


Figure 7: Comparison of pressure distribution

Table 4: Comparison of aerodynamic analyses

	Morphing	Plain flap	Ratio
C_L	1.58	1.49	1.07
C_D	0.0523	0.0593	0.0881
C_M	-0.214	-0.177	1.21
L/D	30.3	25	1.21

The morphing model exhibits 20% higher L/D than the plain flap. This is mainly because of the reduction of drag coefficient. In this case, the deformation of airfoil becomes sharper as approaching to the trailing edge (see Fig. 6) and this mitigates the flow separation (see Fig. 7). In XFLR5, the drag coefficient was obtained by measuring the momentum thickness at downstream infinity. This means that drag coefficient was calculated by reduction of momentum, thus mitigation of the flow separation leads to the reduction of wake, which translates into decreasing reduction of momentum and then drag. It also produces longer area of negative pressure at upper surface and improvement of lift. From Fig. 7, the peak of pressure also becomes blunting which could translate into weight saving.

5. CONCLUSION

As a result of comparison of two cases, the morphing model performs higher L/D than the plain flap, meaning that the aerodynamic efficiency can be improved by using morphing control. This property results from the smooth deformation which mitigates the flow separation. The parametric study shows that shape deformation of airfoil can be changed by altering the corrugated panel configuration and the position of guide. The results demonstrated that morphing control surfaces are realized using corrugated panels, and applicable to the high-performance rudder structure.

In this study, deformation analysis was conducted under no aerodynamic forces and optimized deformation shape by skin actuation was obtained. The possibility of obtaining this shape by this morphing model is shown. However, it is necessary to combine aerodynamic effects and structural elastic effect. This

could be the aim of future study.

ACKNOWLEDGEMENT

This study was conducted under the financial support of Grant-in-Aid for Scientific Research (No.15K06598) by Japan Society for the Promotion of Science.

6. REFERENCES

- 1) Solfa, A. Y. N., Meguid, S. A., Tan, K. T., Yeo, W. K. : Shape morphing of aircraft wing: Status and Challenges, *Materials and Design*, Vol. 31, pp.1284-1292, 2010.
- 2) Lyu, Z., Martins, R. R., Joaquim, A. : Aerodynamic shape optimization of an adaptive morphing trailing edge, *15th AIAA/ISSMO Multidisciplinary Analysis and Optimization Conference*, Atlanta, USA, June 16-20, 2014.
- 3) Kota, S., Osborn, R., Ervin, G., Maric, D. : Mission adaptive compliant wing - design, fabrication and flight test, *RTO Applied Vehicle Technology Panel (AVT) Symposium*, RTO-MP-AVT-168, 2009.
- 4) Woods, K. S. B., Bilgen, O., Friswell, I. M. : Wind tunnel testing of the fish bone active camber morphing concept, *Journal of Intelligent Material Systems and Structures*, Vol.25, No.7, pp.772-785, 2014.
- 5) Yokozeki, T., Takahashi, H., Hirano, Y. : Variable camber morphing wing using corrugated composites. *26th International Conference on Adaptive Structures and Technologies*, Kobe, Japan, October 14-16, 2015
- 6) Thill, C., Etches, J., Bond, I., Ptter, K., Weaver, P. : Morphing skins, *The Aeronautical Journal*, Vol.112, No.1129, pp.117-139, 2008.
- 7) Dayyani, I., Khodaparast, H. H., Woods, K. S. B., Friswell, I. M. : The design of a coated composite corrugated skin for the camber morphing airfoil, *Journal of Intelligent Material Systems and Structures*, Vol.26, No.13, pp. 1592-1608, 2015.
- 8) Berglind, A. L., , Summers, D. J. : Direct displacement synthesis method for shape morphing skins using compliant mechanisms, *International Design Engineering Technical Conferences & Computers and Information in Engineering Conference*, Montreal, Canada, August 15-18, 2010.
- 9) Fenf, N., Liu, L., Liu, Y., Leng, J. : A bio-inspired, active morphing skin for camber morphing structures, *Smart Materials and Structures*, Vol.24, No.3, 035023, 2015.
- 10) Advanced Composite Database System: JAXA-ACDS; Ver.06-1 <http://www.jaxa-acdb.com/>

EIGEN-FREQUENCY CONTROL DESIGN OF CFRP STRUCTURES USING AN EMBROIDERY MACHINE

Tadashige Ikeda⁺¹, Kosuke Oka⁺² and Tatsuya Nishida⁺³

⁺¹⁻³Department of Aerospace Engineering, Nagoya University, Nagoya, Japan

To raise the flutter speed of an airplane wing, increase in frequency margin between its fundamental torsional and bending modes is effective. Recently fiber reinforced plastic (FRP) laminates came to be widely used as the primary structures of airplanes, which can control the mechanical properties and the eigen-frequencies by the laminate stacking sequence, ply orientation, and so on. Moreover, if curved paths of the fibers can be allowed, the structure can be designed more lightly and accordingly the airplane can show higher performances. To this end a tailored fiber placement (TFP) method using an embroidery machine was suggested. In this paper, feasibility of the TFP with the embroidery machine was examined for the eigen-frequency control of a cantilever rectangular laminate plate as a preliminary study of applications of the TFP method to the flutter problems. First, the method to estimate material constants of a TFP layer and substrate layers was proposed according to the classical laminate theory. Then, using the obtained material constants an optimal fiber bundle path was calculated for the cantilever rectangular laminate plate with a size of 150mm×100mm×2mm so that the frequency margin between the fundamental torsional and bending modes was maximized keeping the fundamental frequency of the bending mode more than 80 Hz. Experimental verification was also performed. The prediction agreed well with the experiment, differing by approximately 10% due to the manufacturing error and the assumptions. Next to design further light structures a method that the stiffening fiber bundles were locally placed was proposed. The optimization result of the local TFP showed it had a comparable performance yet less than a half of weight of the reinforcing fiber bundles compared to the global TFP. These results indicate feasibility of application of the TFP to the aeroelastic problems.

Keyword: eigen-frequency, CFRP, tailored fiber placement, embroidery, flutter.

1. INTRODUCTION

Raising flutter speed is one of the challenges of aircraft design since the flutter leads to reduction of operational safety and durability of the aircraft structure. According to the classical theory of aeroelasticity, it is known that large frequency margin between the fundamental torsional and the fundamental bending modes is effective to raise the flutter speed of an airplane wing. With respect to the airplane structures, recently fiber reinforced plastics (FRPs) came to be used as the primary structures because of their high specific strength and corrosion resistance. However, the strength and stiffness of FRP plates significantly depend on the angle between the fiber and load direction. If the direction of the loads is different from the fiber by 5°, the strength reduces by more than 60% for instance. Because of such anisotropic properties, the mechanical properties of the laminates can be controlled by arranging the stacking sequence and ply orientation. The aeroelastic properties can be also improved by this arrangement. This technology is referred to as the aeroelastic tailoring and have been studied actively since 1970's, although the first patent was filed in 1949¹⁾ according to Ref. 2. The state-of-art for aeroelastic tailoring and related research were well overviewed in Ref. 3 published recently.

In the traditional aeroelastic tailoring, the stacking sequence and ply orientation of prepregs with unidirectional fibers are arranged. If the fibers can be placed along a desired path, not only straight but also curved, the laminates can be designed more lightly and more optimally. To this end tailored fiber placement

⁺¹ikeda@nuae.nagoya-u.ac.jp, ⁺²oka@smart.nuae.nagoya-u.ac.jp, ⁺³nishida.tatsuya@g.nagoya-u.jp

(TFP) methods⁴⁻¹⁰⁾ can be suggested. However, the TFP methods have been still hardly applied to the aeroelastic problems¹¹⁾. With respect to the TFP itself, some researchers use prepreg tows for processing the laminates^{4,5)}, while others use dry tows, in which the dry tows are placed on a substrate by using an embroidery machine and impregnated with resin⁶⁻¹⁰⁾. The former method uses costly prepregs, freezers to store them, and autoclaves to harden them, while the latter method does not use such materials and facilities. Accordingly the composites processed by the latter method are expected to be lower-cost. Hence we have studied the embroidery-based TFP. Oka et al.¹²⁾ proposed a design method for the embroidery-based TFP and verified its availability for a static bending-torsion problem of a cantilever plate. Then, Nishida et al.¹³⁾ and Oka et al.¹⁴⁾ applied this method to a dynamic problem of controlling eigen-frequencies of the cantilever plate. In this paper, these results are introduced as a preliminary study for application of the embroidery-based TFP method to the aeroelastic problems.

2. EMBROIDERY-BASED TFP

In this study the embroidery-based TFP method was applied. The embroidery machine used here is shown in Fig. 1 (Tajima, TCWM-101). When a desired path of the carbon fiber bundle was input to the embroidery machine, the machine placed a continuous reinforcement fiber bundle on the desired path on a substrate and processed a dry preform. A pair of the preforms were symmetrically put together as shown in Fig. 3, and impregnated with resin by using the vacuum assisted resin transfer molding method (VaRTM). Here a carbon fiber bundle (Toho Tenax, HTA40-12K) was used as the reinforcement fiber, plain woven carbon fabrics (Toho Tenax, W3101) with a stacking sequence of (45°/0°) were used as the substrate, and epoxy resin (Nagase Chemtex, XNR/H6815) was used as the resin.

3. ESTIMATION OF ELASTIC MODULI OF EACH LAYER¹³⁾

Stiffness of the TFP layer is affected by the embroidery effects of not only holes opened by a needle and the threads included but also interval between neighboring fiber bundle paths and thickness variation due to the variation of the interval. The interval, d , and the thickness, t , are related to the fiber bundle direction, θ , in the applied embroidery-based TFP.

$$d = d_0 \cos \theta, \quad (1)$$

where d_0 is the interval between the neighboring fiber bundle paths along the reference direction defined as $\theta = 0^\circ$ here, as shown in Fig. 2.

To predict the mechanical properties and to design the laminate structures having TFP layers precisely, the embroidery effects must be involved in the stiffness matrix of each layer. The stiffness matrix and the thickness of the TFP layer must be given by functions of the fiber bundle angle, θ , or the interval, d , and accordingly they must vary during the optimization design process.

The stacking sequence of the TFP laminate plates considered here was [TFPL/45°/0°]_s. TFPL represents the TFP layer, a pair of square brackets represent the laminates stitched together by the threads, and the subscript S represents that a pair of the stitched preforms are symmetrically put together. Accordingly, the TFP laminate plates were comprised of a pair of TFP layers with the threads in the transversal direction and in-plane direction, a pair of plain woven layers in 45° direction with the threads in the transverse direction, and a pair of plain woven layers in 0° direction with the threads in the transverse direction and in-plane direction. These three kinds of layers are referred to as TFPL, PW_{mid}, and PW_{in}, respectively, as shown in Fig. 3.

To obtain the mechanical properties including the embroidery effects in each layer, [TFPL0°/45°/0°(d)]_s, [0°/0°(d)], [0°/0°(d)]_s, [0°/45°/0°(d)]_s were processed and the mechanical properties of the laminate plates were measured by tensile tests. TFPL0° represents the TFP layer with fiber bundles placed in the 0° direction on the substrate, d represents the interval between neighboring fiber bundle paths, and (d) represents that their mechanical properties are functions of the interval. Although the interval should be related to the fiber bundle angle, θ , with Eq. (1) in the practical TFP laminate plates, only the interval was varied keeping the fiber bundle angle at 0° here. This is because it was assumed that the angle between the direction

of the fiber bundles and the substrate did not affect the mechanical properties of the TFP layer and the substrate layers. The mechanical properties of each layer against the interval were calculated by using the classical laminate theory. In this study, the relationship between resultant forces and in-plane strains becomes

$$\begin{Bmatrix} N_x \\ N_y \\ N_{xy} \end{Bmatrix} = \begin{bmatrix} A_{11} & A_{12} & 0 \\ A_{12} & A_{22} & 0 \\ 0 & 0 & A_{66} \end{bmatrix} \begin{Bmatrix} \varepsilon_x \\ \varepsilon_y \\ \gamma_{xy} \end{Bmatrix}, \quad (2)$$

where

$$A_{ij} = \sum_{k=1}^N (Q_{ij})_k t_k, \quad (Q_{11})_k = \frac{E_{x,k}}{1 - \nu_{xy,k} \nu_{yx,k}}, \quad (Q_{12})_k = \frac{\nu_{yx,k} E_{x,k}}{1 - \nu_{xy,k} \nu_{yx,k}}, \quad (Q_{22})_k = \frac{E_{y,k}}{1 - \nu_{xy,k} \nu_{yx,k}},$$

$$(Q_{66})_k = \frac{1}{\frac{4}{E_{45,k}} - \frac{1}{E_{x,k}} - \frac{1}{E_{y,k}} + \frac{2\nu_{xy,k}}{E_{x,k}}}.$$

E and ν denote Young's modulus and Poisson ratio, respectively, and the subscripts k , x , y , and 45 represent the material constants in k -th layer, and those in the x , y , and 45° direction, respectively. N , ε , and γ denote the resultant force, in-plane normal strain, and in-plane shearing strain.

The specimens [TFPL0°/45°/0°(d)]_s, [0°/0°(d)], [0°/0°(d)]_s, [0°/45°/0°(d)]_s are referred to as TFP, PW₂, PW₄, and PW₆, respectively. Here it was assumed that the thickness and the material constants for the corresponding layer were consistent in PW₂, PW₄, PW₆, and TFP. More specifically, it was assumed that PW₂ consisted of (PW_{sur})_s, PW₄ consisted of (PW_{sur}/PW_{in})_s, PW₆ consisted of (PW_{sur}/PW_{mid}/PW_{in})_s, and TFP consisted of (TFPL0°_o/PW_{mid}/PW_{in})_s. PW_{sur} represents the plain woven layer in 0° direction with the threads in the transverse direction and in-plane direction on the surface, and it was distinguished from PW_{in} because PW_{sur} had irregular surface due to the peel ply and the distribution medium for VaRTM. The mechanical properties of PW_{sur}(d) can be obtained from those of PW₂(d), the mechanical properties of PW_{in}(d) can be obtained from those of PW₄(d) and PW_{sur}(d), the mechanical properties of PW_{mid}(d) can be obtained from those of PW₆(d), PW_{sur}(d), and PW_{in}(d), and the mechanical properties of TFPL0°(d) can be obtained from those of TFP(d), PW_{in}(d), and PW_{mid}(d).

The tensile tests were carried out with a universal testing machine (Shimadzu, AG-5000B) following JIS K7164. The specimen size was 250mm×25mm. The 50mm regions of the both ends were clamped through sandpapers (#180) used as friction tabs. The displacement rate was 1.0mm/min. The strain was measured by strain gauges. The test was performed at room temperature of 23°C. The tensile moduli were calculated within the range between 500μ ε and 2500μ ε . The intervals, d , of the specimens were set to 2.0mm, 1.7mm, 1.4mm, 1.2mm, and 1.0mm, which corresponded to $\theta = 0^\circ, 30^\circ, 45^\circ, 53^\circ$, and 60° , respectively, because d_0 was set to 2.0mm. Four specimens for each in the 0°, 45°, and 90° direction were cut out from the TFP plates, while four specimens for each in the 0° and 45° direction were cut out from the PW₂, PW₄, and PW₆ plates because the properties in the 90° direction was assumed to be the same as those in the 0° direction.

Fig. 4 shows the elastic moduli for each laminate plate. Closed symbols, error bars, and lines represent mean, standard deviation, and approximation line, respectively. The properties for PW₂, PW₄, and PW₆ can be assumed to be independent of the intervals, that is, amount of the holes and threads. The properties for TFP can be approximated by liner functions of the interval. The elastic modulus of TFP in the 0° direction decreases with increase in the interval, while the elastic moduli in the 45° and 90° direction increase with increase in the interval. The latter is attributed to the fact that the volume fraction of the TFP layer decreases and the volume fraction of the fibers in the 45° and 90° direction increases as the interval increases.

Substituting the obtained approximation values into the classical lamination theory, Eq. (2), the

material constants in the longitudinal and transversal direction of the fiber were estimated. They are listed in Table 1. The subscript L and T represent the longitudinal and transverse direction of the fiber, G and ρ denote the shearing modulus and the density, respectively. The material constants of TFPL were assumed to be a linear function again.

Open symbols in Fig. 4(d) represent the elastic moduli recalculated with the estimated material constants for each layer listed in Table 1. The recalculated moduli are seen to be in good agreement with the measured values and that indicates the validity of the assumption.

4. EIGEN-FREQUENCY CONTROL BY GLOBAL FIBER PLACEMENT¹³⁾

(1) Formulation

To raise the flutter speed of an airplane wing, increase in frequency margin between its fundamental torsional and bending modes is effective. Hence here we considered a problem of finding an optimal fiber bundle path so that the frequency margin between the first and second modes of a $[TFP/45^\circ/0^\circ]_S$ laminate cantilever plate was maximized yet the first eigen-frequency was kept more than a certain frequency to maintain a certain level of bending stiffness. The size of cantilever plate was assumed to be 150mm by 100mm and the first eigen-frequency was kept more than 80Hz. This problem is specifically formulated as

$$\begin{aligned}
 \text{Design variables:} \quad & \boldsymbol{\theta} = [\theta_1, \dots, \theta_{15}] \\
 \text{which minimalizes:} \quad & f(\boldsymbol{\theta}) = -(Freq2 - Freq1); \\
 \text{subject to constrains:} \quad & -60^\circ \leq \theta_i \leq 60^\circ \quad (i = 1, \dots, 15), \\
 & |\theta_j - \theta_{j-1}| \leq 15^\circ \quad (j = 2, \dots, 15), \\
 & Freq1 \geq 80\text{Hz}.
 \end{aligned} \tag{3}$$

The cantilever plate was divided by 15 elements along the longitudinal direction as shown in Fig. 5. θ_i , $Freq1$, and $Freq2$ denote the fiber bundle angle in the i -th element, the first, and the second eigen-frequency of the plate, respectively. The fiber bundle angle θ_i was limited within $\pm 60^\circ$ and the difference in fiber bundle angle between the neighboring elements was limited within $\pm 15^\circ$. The subproblem approximation method built in ANSYS ver. 12 and a kind of sweeping methods were applied to optimize the fiber bundle path of the TFP layer.

(2) Results and discussions

The optimal path for this problem is shown in Fig. 6 and the first and the second eigen-frequency in this case are listed in Table 2. The eigen-frequencies of the plates having TFP layers with a uniform fiber bundle angle of 0° , 45° , and 60° were also calculated. Of course, the eigen-frequencies were not controlled in these cases.

The first vibration mode was bending and the second vibration mode was twisting. It is seen from Fig. 6 that the fiber bundle angle became close to 0° around the root and 50° around the middle of the plate. The former may affect increasing the first eigen-frequency and the latter may affect increasing the second eigen-frequency. It is seen that the constraint of the first eigen-frequency equal or more than 80 Hz is not satisfied for the plates with uniform fiber directions of 45° and 60° , and that the plate with the optimal placement of fibers is surely optimized for the objective function under the constraints. The validity of the predicted results was verified by comparing to experimental results. A specimen was clamped by a vice. Vibration was generated by giving an impact with a hammer. The vibration was measured by a strain gauge. The obtained eigen-frequencies are also listed in Table 2.

The measured eigen-frequencies agree well with calculated ones, which have a margin of error of approximately 10% due to manufacturing errors of the plates for the example problem and for measurement of the material constants, the assumption for estimation of the material constants, and so on. Considering the errors, the calculated optimal fiber path is approximately optimal in the experiment, although the constraint of the first eigen-frequency is not satisfied. The first eigen-frequency cannot be known before the experiment.

Such a value might not be adequate to be included in the constraints because experiments involve errors. Nevertheless, when a structural optimization must be carried out with such constraints, the error margin should be considered.

5. EIGEN-FREQUENCY CONTROL BY LOCAL FIBER PLACEMENT¹⁴⁾

(1) Formulation

In the previous section the reinforcing fiber bundles were placed over the whole substrate. However, if the fiber bundles could be placed locally, the weight could be reduced and the performance could be improved more. Therefore here the local fiber placement is considered for the same objective in the previous section that is the frequency margin between the first and second modes was maximized yet the first eigen-frequency was kept more than 80Hz. This problem is specifically formulated as

$$\begin{aligned} \text{Design variables:} \quad & \mathbf{t} = [t_1, \dots, t_N] \\ \text{which minimalizes:} \quad & f(\mathbf{t}) = -(Freq2 - Freq1); \\ \text{subject to constrains:} \quad & Freq1 \geq 80\text{Hz}, \\ & m_f \leq m_{f \max}. \end{aligned} \quad (4)$$

Here, i is the element ID, t_i is the thickness of the i -th element, N is the number of the elements, m_f is the mass fraction of a TFPL to the TFPL filled with fiber bundles in the 0° -direction, and $m_{f \max}$ is the maximum value of m_f , which were assumed to be 0.3, 0.4, and 0.5 here. In this optimization problem, the fiber bundle angle in TFPL was fixed at 0° and the thickness distribution was optimized for the objective.

(2) Results and discussions

The first eigen-frequency and the frequency margin between the first and the second eigen-frequencies are listed in Table 3 for the three $m_{f \max}$. For reference those of the global TFP are also listed for the optimal fiber bundle path and 0° fiber bundle path. Figure 7 shows an optimal thickness distribution and assumed fiber paths for the local TFP that was optimized under the constraint $m_{f \max} = 0.4$. From Table 3, the largest margin between the first and the second eigen-frequency is the one for the global TFP with the optimal fiber bundle path. The mass fraction of this case is 1.0 or more value, because the density of TFPL depends on a fiber bundle angle and $m_f = 1.0$ was defined for the TFPL filled with fiber bundles in the 0° -direction. On the other hand, the result for the local TFP shows comparable performance yet with less than a half of the mass fraction of the global TFP. From the three results of the local TFP, the margin between the two eigen-frequencies reduces as the mass fraction decreases. The constraint about the mass fraction should be determined from the trade-off between the performance and the weight. There are three thick regions in TFPL as shown in Fig. 7. Two are located near the fixed edge and one is located from the center to the tip. It is considered that two thick regions near the fixed edge are effective to increase the first and the second eigen-frequencies by increasing the stiffness for the both the bending and twisting modes, and that another thick region from the center to the tip is effective to decrease the first eigen-frequency without decreasing the second eigen-frequency by increasing the inertia for the bending mode.

5. CONCLUSIONS

A TFP method using an embroidery machine was suggested to raise the flutter speed of an airplane wing by controlling eigen-frequencies of the structure. This method was verified by a preliminary example problem of controlling eigen-frequencies of a cantilever plate. First, the method to estimate material constants of a TFP layer and substrate layers was proposed according to the classical laminate theory. Then, using the obtained material constants an optimal fiber bundle path was calculated for the cantilever plate so that the frequency margin between the fundamental torsional and bending modes was maximized with a constrain of the fundamental frequency of the bending mode kept more than a certain frequency value. A desired result could be obtained by an optimization calculation. The carbon fiber bundles were placed along the desired path

on plain woven carbon fabrics by an embroidery machine and the preform was impregnated by using VaRTM method. The eigen-frequencies of the laminate plate agreed well with the calculated results with an error of approximately 10%. Accordingly, it was found that the error margin should be considered when an optimization result is realized. Next a local TFP method was proposed to reduce the weight more. The optimization result of the local TFP showed it had a comparable performance yet less than a half of weight of the reinforcing fiber bundles compared to the global TFP. This result indicates that the local TFP is more effective to design high performance yet light laminates.

In this paper a passive eigen-frequency control with the TFP was introduced as a preliminary study for the aeroelastic problems by placing passive carbon fiber bundles on a substrate optimally. Furthermore a method to place shape memory alloy wires on a TFP layer has been also proposed in our laboratory¹⁵⁾. Combining such an active material with the passive materials must expand the limitations of not only aeroelastic problems but also aerodynamic and structural problems.

ACKNOWLEDGMENT

A part of this study was supported by JSPS KAKENHI Grant Number 22560781 and 26420811.

REFERENCES

- 1) Munk, M.: Propeller containing diagonally disposed fibrous material, *U.S. Patent* 2,484,308,1111, 1949.
- 2) Shirk, M., Hertz, T., and Weisshaar, T.: Aeroelastic tailoring – theory, practice, promise, *J. Aircraft*, Vol. 23, No. 1, pp. 6-18, 1986.
- 3) Jutte, C. V. and Stanford, B. K.: Aeroelastic tailoring of transport aircraft wings: State-of-the-art and potential, *NASA/TM-2014-218252*, pp. 1-29, 2014.
- 4) Tatting, B. F. and Gürdal, Z.: Design and manufacture of elastically tailored tow placed plates, *NASA/CR*, 211919, 2002.
- 5) Gürdal, Z. and Tatting, B. F.: Tow-placement technology and fabrication issues for laminated composite structures, *Proc. 46th AIAA/ASME/ASCE/AHS/ASC SDM Conf.*, Austin, U.S.A., AIAA 2005-2017, pp. 1-18, 2005.
- 6) Crothers, P. J., Drechsler, K., Feltn, D., Herszberg, I., and Kruckenberg, T.: Tailored fiber placement to minimise stress concentrations, *Composites Part A*, Vol. 28A, pp. 619-625, 1997.
- 7) Mattheij, P., Gliesche, K., and Feltn, D.: 3D reinforced stitched carbon/epoxy laminates made by tailored fibre placement, *Composites Part A*, Vol. 31, pp. 571-581, 2000.
- 8) Temmen, H., Degenhardt, R., and Raible, T.: Tailored fibre placement optimization tool, *Proc. 25th ICAS*, Hamburg, Germany, ICAS2006-4.8.3, pp. 1-10, 2006.
- 9) Hazra, K., Saverymuthapulle, M., Hawthorne, M., Stewart, D. L., Weaver, P., and Potter, K.: Investigation of mechanical properties of tow steered CFRP panels, *Proc. ICCM17*, Edinburgh, Scotland, D11-5, pp. 1-11, 2009.
- 10) Panesar, A. S., Hazra, K., and Weaver, P. M.: Investigation of thermally induced bistable behaviour for tow-steered laminates, *Composites Part A*, Vol. 43, pp. 926-934, 2012.
- 11) Haddadpour, H. and Zamani, Z.: Curvilinear fiber optimization tools for aeroelastic design of composite wings, *J. Fluids Struct.*, Vol. 33, pp. 180-190, 2012.
- 12) Oka, K., Ikeda, T., Senba, A., and Ueda, T.: Design of CFRP with fibers placed by using an embroidery machine, *Proc. ICCM18*, Jeju Island, Korea, M32-2, pp. 1-5, 2011.
- 13) Nishida, T., Ikeda, T., and Senba, A.: Optimal fiber placement including effects of embroidery, *Proc. ICCM19*, Montreal, Canada, pp. 3865-3872, 2013.
- 14) Oka, K., Ikeda, T., and Senba, A.: Optimal placement design of fibers partially set by an embroidery machine, *Proc. APISAT-2013*, Takamatsu, 07-03-3, pp. 1-4, 2013.
- 15) Torii, N., Oka, K., and Ikeda, T.: Creation of smart composites using an embroidery machine, *Proc. SPIE*, Vol. 9800, Las Vegas, U.S.A, 2016.



Figure 1: Embroidery machine. Tajima TCWM-101.

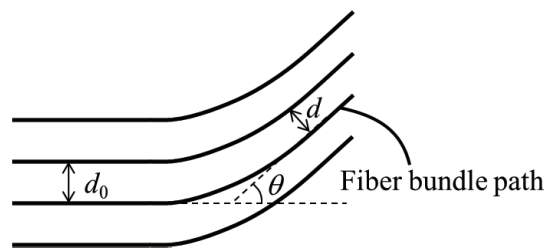


Figure 2: Variation of interval between the neighboring fiber bundle paths due to the fiber bundle angle.

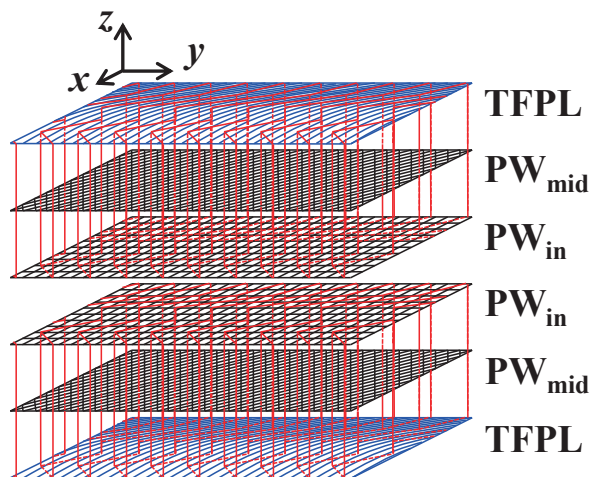


Figure 3: Schematic diagram of the laminate with stacking sequence $[TFPL/45^{\circ}/0^{\circ}]_s$. Red lines represent the stitched threads.

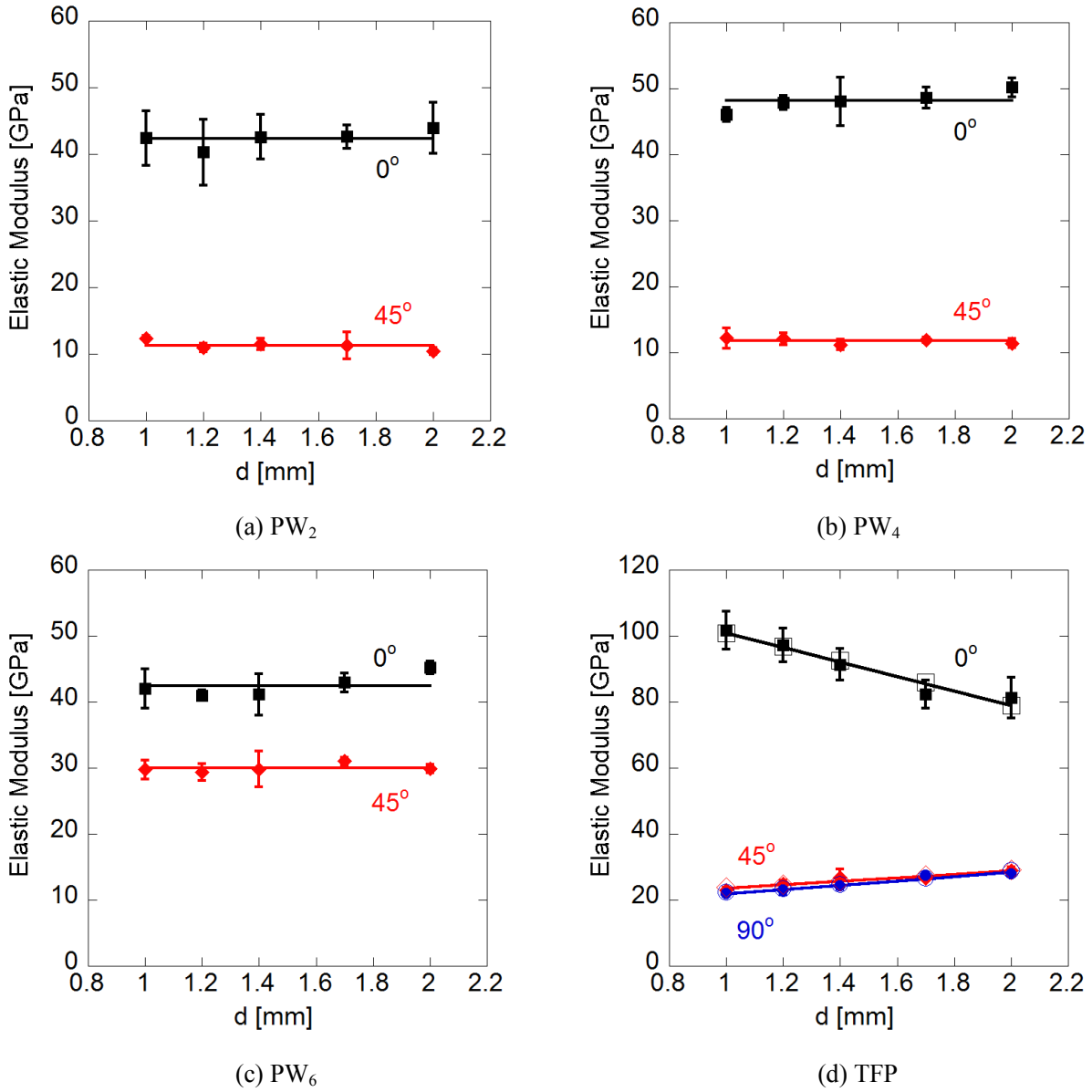


Figure 4: Elastic moduli of the various laminate plates¹³⁾.

Closed symbols, error bars, and lines represent mean, standard deviation, and approximation line, respectively.

Open symbols in (d) represent the elastic moduli recalculated by using the estimated material constants for each layer listed in Table 1.

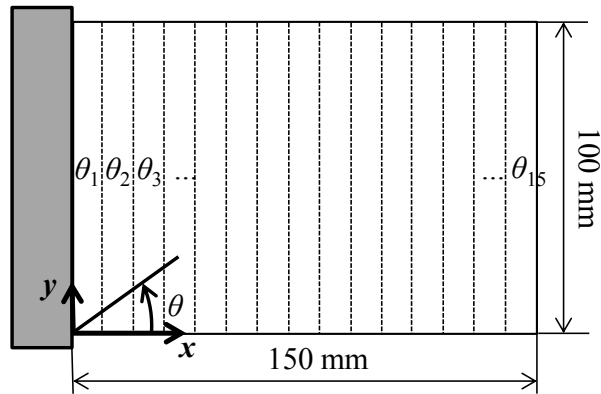


Figure 5: Cantilever plate of the example problem.

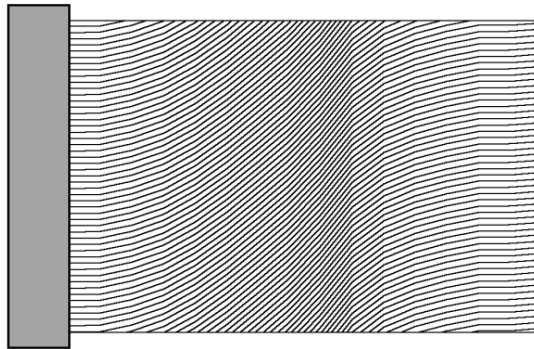


Figure 6: Optimal fiber bundle path¹³⁾.

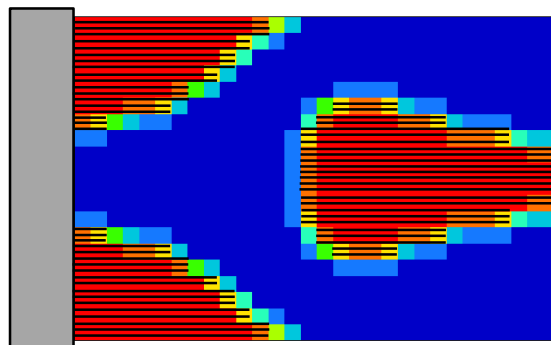


Figure 7: Thickness distribution and assumed fiber path of the local TFP ($m_{fmax} = 0.4$)¹⁴⁾.

Table 1: Estimated material constants for each layer¹³⁾.

	PW _{in}	PW _{mid}	TFPL(<i>d</i> [mm])
E_L [GPa]	54.5	59.7	$-14.2d+154.5$
E_T [GPa]	-	-	$1.9d+4.7$
ν_{LT}	0.08	0.12	$0.02d+0.34$
ν_{TL}	-	-	$0.008d+0.009$
G_{LT} [GPa]	3.6	5.2	$0.4d+3.8$
t [mm]	0.26	0.23	$-0.3d+1.1$
ρ [g/cm ³]	1.4	1.3	$-0.09d+1.69$

Table 2: Calculated and measured first eigen-frequency and margin between the first and the second eigen-frequencies in Hz for various fiber bundle paths¹³⁾.

Fiber bundle angle		0°	45°	60°	Optimal
Calculation	Freq1	110	58	49	80
	Freq2-Freq1	94	194	177	180
Experiment	Freq1	101	52	54	72
	Freq2-Freq1	83	172	182	158

Table 3: Optimization results of the global TFP and the local TFP¹⁴⁾.

	Global TFP	Local TFP			
		$m_{fmax} = 0.30$	$m_{fmax} = 0.40$	$m_{fmax} = 0.50$	
Fiber bundle angle	Optimal	0°			
m_f	$\geq 1.0^*$	1.0	0.30	0.40	0.45
Freq1	80	110	80	80	80
Freq2-Freq1	180	94	148	154	154

FLUTTER ANALYSIS OF PIEZOELECTRIC BEAMS IN MEMS

Raffaele Ardito⁺¹ and Rocco Musci⁺¹

⁺¹ Department of Civil and Environmental Engineering, Politecnico di Milano, Milan, Italy

Micro-electro-mechanical systems (MEMS) represent a huge class of devices characterized by the smart coupling between electronics and mechanics, in order to obtain microscopic sensors and actuators. The use of piezoelectric materials in MEMS is steadily increasing, considering both the “direct effect”, e.g. in energy harvesters, and the “indirect effect”, for the cases of resonators, micropumps and other actuators. This paper is devoted to the study of piezoelectric laminate beams in the presence of aeroelastic effects due to the interaction of the structure with a fluid flow, as it may happen if the MEMS is embedded in a fluidic system. More specifically, the analytical conditions for the onset of flutter instability are studied, with the purpose of providing a sound basis for further studies focused on energy harvesting from fluid flows.

Keyword: micro-electro-mechanical systems, fluid-structure interaction, aeroelasticity, piezoelectric behavior, energy harvesting.

1. INTRODUCTION

The world of micro-electro-mechanical systems (MEMS) is currently expanding by means of the inclusion of piezoelectric materials, which can be embedded in the manufacturing process in the form of thin films¹⁾. The conversion of mechanical energy into electrical one can be used in order to harvest (or scavenge) small amounts of energy from ambient vibrations²⁾. A scavenged power of the order of microWatts can be sufficient to feed MEMS sensors, with the aim of eliminating batteries or complex wiring in microsystems, thus moving a step closer towards battery-less, autonomous sensors systems and networks which recover on-site the energy they need to fulfill their tasks.

For MEMS energy harvesters, piezoelectric transduction is the most appropriate scenario since standard MEMS thin-film processes are available for many piezoelectric materials assuring high efficiency, high energy density and scalability. Operating frequency, frequency bandwidth, excitation level, power density and size are the key design function requirements. Cantilever laminated beams with thin films of lead zirconate titanate $\text{Pb}(\text{Zr,Ti})\text{O}_3$ (PZT) have been widely used as linear resonating harvesters achieving high power generation. The multi-physics simulation of piezoelectric effect can be obtained by considering that the structural members are represented by a laminate composite with piezoelectric and silicon layers; the piezoelectric material is then attached to an external circuitry, which reproduces the device employed for the power management.

The energy source for MEMS harvester is commonly represented by ambient vibration: in that case, the micro-device is basically an inertial transducer, endowed with a large mass in order to emphasize the kinetic energy³⁾. Such systems are characterized by a severe discrepancy between the natural frequency and the excitation frequency, so that some specific provisions should be introduced in order to force a resonating behaviour (frequency-up-conversion). In this paper, a different scenario is considered: the possibility of energy harvesting from fluid flow is explored, with the exploitation of aeroelastic phenomena (such as the vortex induced vibration, thoroughly studied in our previous work⁴⁾). This paper is specifically focused on the theoretical and computational analysis of Flutter Instability (FI⁵⁾) for piezoelectric beams in MEMS, with the main purpose of establishing the solution procedure and achieving some preliminary results. In view of its ability to reduce the dissipative component, flutter behavior can be exploited for the energy harvesting purpose, joining this aeroelastic phenomenon with another type of excitation, like an inertial forcing.

In our multi-physics simulations, the structural members are represented by laminate composites with

⁺¹raffaele.ardito@polimi.it, muscirocco@gmail.com

piezoelectric and silicon layers, the active layer being attached to an external circuitry. The sectional behavior of the beam is studied through the Classical Lamination Theory (CLT, specifically modified in order to introduce the piezoelectric coupling⁶⁾) and a reduced order model is built through separation of time and space variables. The theoretical study has been based on reduced order models, obtained by applying the Rayleigh-Ritz method. The preliminary simulations, carried out in the present study, allow for a deeper understanding of energy harvesting from fluid flow at the micro-scale. The achieved results will be used, in future works, in order to obtain optimized devices, possibly endowed with different and more complex shapes with respect to the simple cantilever considered herein.

The paper is organized as follows. Section 2 contains a detailed explanation of the mechanical model for a piezoelectric composite beam subject to aeroelastic effects. Section 3 is devoted to the description of the simple device, which is studied as a paradigm of a class of realistic MEMS. Section 4 contains the main results in terms of the assessment of FI and Section 5 is referred to the possible application in the field of energy harvester. Some conclusive remarks and future prospects are drawn in Section 6.

2. MULTI-PHYSICS MODEL OF LAYERED PIEZOELECTRIC BEAMS

(1) Mechanical and electrical model

The paper deals with layered piezoelectric beams, such as the simple cantilever shown in Fig. 1. It is worth noting that realistic piezoelectric beams include many different layers, among which the upper and the lower electrodes for the active layer. In view of the limited thickness of ancillary layers, in this preliminary study a simplified geometry is considered, with a structural layer (e.g. made of silicon) and a piezoelectric layer (e.g. made of PZT). In what follows, l is the length, t is the total thickness and t_p is the thickness of PZT layer, b is the width. The origin of the reference system is located on the clamped-in edge, in correspondence of the neutral axis of the cross-section.

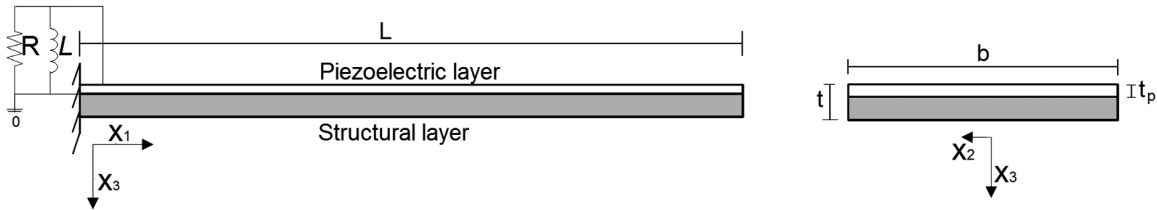


Figure 1: Schematic views of the considered beam: lateral view, along with the external RL circuit, and cross-section view.

The piezoelectric layer is polarized in the vertical direction (i.e. along the x_3 axis) and it works in the so-called “d31-mode” when the beam vibrates: this means that the deformation along x_1 axis causes an electric field along the x_3 axis. In order to implement the d31-mode, the electrodes span both upper and lower surfaces of PZT thin film.

Considering that the structural member is represented by a laminate composite, the sectional behavior of the beam is studied through the Classical Lamination Theory specifically modified in order to introduce the piezoelectric coupling⁷⁾. The beam is sufficiently thin and slender, so that Bernoulli’s assumptions can be adopted: the rotation of the cross section is the derivative of the vertical displacement (w_3) and the horizontal displacement (s_1) and strain (S_{11}) read (in the standard notation for piezoelectricity⁸⁾):

$$s_1(x_1, x_3) = -x_3 \frac{\partial w_3(x_1)}{\partial x_1} \quad S_{11}(x_1, x_3) = -x_3 \frac{\partial^2 w_3(x_1)}{\partial x_1^2} \quad (1)$$

The electric potential is constant over the electrodes: the potential value is assigned on the bottom electrode (grounded electrode) and it is free to change on the upper one (v). According to the piezoelectric constitutive law, the electric field is proportional to strain, which is linear across the piezoelectric layer thickness. Consequently, the electric potential across the thickness of the piezoelectric layer, denoted by $\phi(x_3)$,

should be a quadratic function of x_3 . However, as long as the piezoelectric layer is thin, a linear approximation of the potential can be adopted, so that the electric field E_3 turns out to be constant:

$$\phi(x_3) = -\frac{x_3^*}{t_p}v \quad E_3(x_1, x_3) = -\frac{\partial\phi(x_3)}{\partial x_3} = \frac{v}{t_p} \quad (2)$$

where the axis x_3^* axis has the same direction as x_3 but its origin is located on the interface between the two layers. A piezoelectric constitutive law is employed herein to describe strain-stress relation; the fully-coupled law for d31-mode reads:

$$T_{11} = c_1 S_{11} - e_{31} E_3 \quad D_3 = e_{31} S_{11} + \epsilon_3^s E_3 \quad (3)$$

In Eq. 3, T_{11} and S_{11} are the stress and strain components along the axis x_1 ; D_3 and E_3 are the electric displacement and the electric field components along the axis x_3 and c_1 , e_{31} and ϵ_3^s are the elastic, piezoelectric and dielectric constant, respectively.

By considering the integration across the thickness, one obtains the generalized parameters in terms of stiffness, piezoelectric coupling coefficient and electrical capacitance⁹). In order to describe the beam deflection, the Rayeigh-Ritz method is adopted. The deformed shape is governed by a single parameter, namely the tip displacement $w(t)$:

$$w_3(x_1, t) = w(t)\psi_w(x_1) \quad (4)$$

The accuracy of this approximate method will be discussed in the next Section.

Through the principle of virtual power and using the assumptions herein adopted, the dynamic equilibrium equations of the coupled system results:

$$\begin{cases} m\ddot{w} + c\dot{w} + kw - \Theta v = f \\ C_E v + \Theta w = q \end{cases} \quad (5)$$

The above equation describes the dynamic behavior of the linear piezoelectric beam. The coefficients are evaluated by integrating the shape functions and the generalized constitutive coefficients on the area of the beam: m is the total mass, k is the linear elastic stiffness, C_E is the internal capacitance of PZT and Θ is the linear coupling coefficient.

The electric charge collected by the electrodes is managed by an external electric circuit. Two kinds of circuits are analyzed: a purely resistive solution (RC) and a resistive-inductive one (RLC)¹⁰). The resistor and the inductor are governed by the laws:

$$i_R = \dot{q} = -\frac{v}{R} \quad \frac{d(i_L)}{dt} = \ddot{q} = -\frac{\dot{v}}{L} \quad (6)$$

Therefore, the second expression in Eq. (5) becomes, for RC case:

$$C_E \dot{v} + \Theta \dot{w} + \frac{v}{R} = 0 \quad (7)$$

and for RLC case:

$$C_E \ddot{v} + \Theta \ddot{w} + \frac{\dot{v}}{R} + \frac{v}{L} = 0 \quad (8)$$

where R and L are the value of load resistance and inductance, respectively.

(2) Aeroelastic model

In this paper, the so-called classical flutter instability is analyzed. In a simple mechanical model, this aeroelastic phenomenon is characterized by two degrees of freedom, rotation and vertical translation, coupled in a flow-driven, unstable oscillation. According to the features of the instability mechanisms, the motion of the structure will either decay or diverge according to whether the energy of motion extracted from the flow is less than or exceeds the energy dissipated by the system through mechanical damping. The border that divides these two conditions is eventually recognized as the critical flutter condition.

When a piezoelectric beam is considered, the equations of motion should include also the effect of the

electric potential in the piezoelectric layer. In the specific configuration that is considered herein, the torsional degree of freedom is not influenced by the electric field, and vice-versa. The complete set of aeroelastic equations of the piezoelectric beam reads:

$$\begin{cases} m\ddot{w} + c\dot{w} + kw - \Theta v = L_w \\ I_g \ddot{\mathcal{G}} + c_g \dot{\mathcal{G}} + k_g \mathcal{G} = M_g \\ C_E v + \Theta w = q \end{cases} \quad (9)$$

Eq. 9 contains the torsional mechanical parameters, namely the torsional inertia I_g , the torsional damping c_g and the torsional stiffness k_g , which have been obtained by introducing a suitable shape function for the torsional rotation:

$$\varphi_1(x_1, t) = \mathcal{G}(t) \psi_g(x_1) \quad (10)$$

The self-excited aerodynamic lift and moment components are computed on the basis of the Scanlan's expressions⁵⁾:

$$l_w = \frac{1}{2} \rho_f U^2 b \left(KH_1^* \frac{\dot{w}}{U} + KH_2^* \frac{\dot{\mathcal{G}}}{U} + K^2 H_3^* \mathcal{G} + K^2 H_4^* \frac{w}{b} \right) \quad (11)$$

$$m_g = \frac{1}{2} \rho_f U^2 b^2 \left(KA_1^* \frac{\dot{w}}{U} + KA_2^* \frac{\dot{\mathcal{G}}}{U} + K^2 A_3^* \mathcal{G} + K^2 A_4^* \frac{w}{b} \right) \quad (12)$$

where $K = b\omega/U$ is the reduced circular frequency, U is the velocity of the fluid flow, ω is the circular frequency of the piezoelectric beam, H_i^* and A_i^* are the flutter derivatives, expressed as dimensionless functions of K .

In order to evaluate the instability condition of the system and the correspondence critical velocity, the following assumption on the governing field is introduced:

$$w = w^* e^{\lambda t}, \quad \mathcal{G} = \mathcal{G}^* e^{\lambda t}, \quad v = v^* e^{\lambda t} \quad (13)$$

so that Eq. 9 is transformed into a quadratic eigenvalue problem (QEP):

$$(\lambda^2 \bar{M} + \lambda \bar{C} + \bar{K}) X^* = 0 \quad X^* = \begin{pmatrix} w^* & \mathcal{G}^* & v^* \end{pmatrix}^T \quad (14)$$

In Eq. 14, \bar{M} , \bar{C} and \bar{K} are the mass, viscous damping and stiffness matrices, respectively. The electro-mechanical coupling is introduced through Eqs. 7 and 8, according to the type of electric external circuit adopted. For RC circuit, by dividing the damping (d) and the stiffness (k) contributions of aeroelastic forces, one finds:

$$\bar{M} = \begin{bmatrix} m & 0 & 0 \\ 0 & I_g & 0 \\ 0 & 0 & 0 \end{bmatrix} \quad \bar{C} = \begin{bmatrix} c - L_w^d & 0 & 0 \\ 0 & c_g - M_g^d & 0 \\ \Theta & 0 & C_E \end{bmatrix} \quad \bar{K} = \begin{bmatrix} k - L_w^k & 0 & -\Theta \\ 0 & k_g - M_g^k & 0 \\ 0 & 0 & 1/R \end{bmatrix} \quad (15)$$

Conversely, for RLC circuit:

$$\bar{M} = \begin{bmatrix} m & 0 & 0 \\ 0 & I_g & 0 \\ \Theta & 0 & C_E \end{bmatrix} \quad \bar{C} = \begin{bmatrix} c - L_w^d & 0 & -\Theta \\ 0 & c_g - M_g^d & 0 \\ 0 & 0 & 1/R \end{bmatrix} \quad \bar{K} = \begin{bmatrix} k - L_w^k & 0 & 0 \\ 0 & k_g - M_g^k & 0 \\ 0 & 0 & 1/L \end{bmatrix} \quad (16)$$

The problem is solved by transforming (QEP) into an equivalent standard eigenvalue problem (SEP)¹¹⁾. The real part of eigenvalues λ stands for the damping component of the system, therefore the flutter instability occurs when this term becomes negative, and the corresponding velocity is the Critical Flutter Velocity.

It is worth noting that, in the case of beams with microscopic size, the Reynolds number attains very low value: Bruno and Fransos¹²⁾ have computed, through CFD simulations, the flutter derivatives for a flat plate even for $Re = 10$. Those functions, reported in Figure 2, are adopted in the present paper.

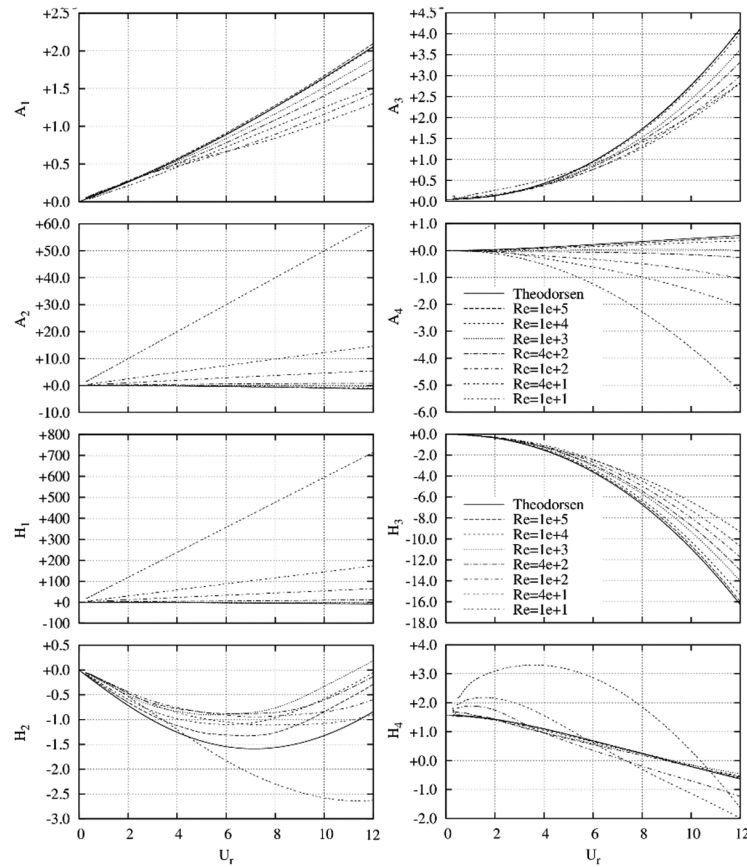


Figure 2: Flutter derivatives computed by Bruno and Fransos for flat plates (adapted from the original paper¹²).

The effects of Reynolds number on aeroelastic behavior of the structure is clear: indeed, when one assumes very small values for Re , the difference from the Theodorsen's theory is more marked. According to the trend of the flutter derivatives in Fig. 2, it is possible to make some preliminary considerations on the FI mechanism. For $Re = 10$, the coefficients H_1^* and A_2^* weigh more than the other ones, especially H_1^* ; this means that probably the instability occurs according to the transverse degree of freedom. It is important to verify the magnitude of Reynolds number after calculating the critical velocity, as a matter of fact for a variation in the values of Re the FI mechanism may change significantly, assuming possibly a coupled translational-torsional behavior.

3. FEATURES OF THE CONSIDERED BEAM

The procedure described in Sec. 2 is applied to a simple cantilever beam, subject to a transverse fluid flow that induces FI. The geometric and constitutive parameters are summarized in Tab. 1. Such a model, which represents a paradigm of realistic devices used as energy harvesters, is used with the purpose of evidence the basic behavior of FI in piezoelectric beams.

The Young's moduli of silicon and PZT are used in order to build the stiffness coefficient of the layered beam; in a similar way, the densities are used for obtaining the mass coefficient; the parameter e_{31} represents the piezoelectric coupling and is adopted in order to obtain Θ ; finally, the relative permittivity of PZT, ϵ_r , is used for computing the capacitance C_E of the piezoelectric layer. The intrinsic bending and torsional damping ratios are assumed, respectively, equal to: $\zeta_w = 0.01$ and $\zeta_\theta = 0.005$. The resistance R and the inductance L of the external circuit are parametrically varied in order to assess their effect on the flutter critical velocity and on the performance of the energy harvester. It is well known from the theory of piezoelectric beams that a non-monotonic effect of the electric parameters is expected⁽⁶⁾¹⁰, with the presence of optimal values which entails the maximum conversion of elastic energy into electric energy.

Table 1: Constitutive and geometric features of the beam studied in this paper.

Parameter	Value	Parameter	Value
$\rho_{sil} [kg/mm^3]$	$2.23 \cdot 10^{-6}$	$E_{sil} [MPa]$	$1.6 \cdot 10^5$
$\rho_{PZT} [kg/mm^3]$	$7.83 \cdot 10^{-6}$	$E_{PZT} [MPa]$	$1 \cdot 10^5$
$e_{31,PZT} [N/(mmV)]$	$9.33 \cdot 10^{-3}$	$\epsilon_{r,PZT}$	2400
$l [\mu m]$	200	$b [\mu m]$	25
$t [\mu m]$	8	$t_p [\mu m]$	2

In order to set up the governing system summarized in Eq. 9, the approximating functions for the Rayleigh-Ritz method are defined in this way:

$$\psi_w = \frac{3}{2} \left(\frac{x_1}{L} \right)^2 - \frac{1}{2} \left(\frac{x_1}{L} \right)^3 \quad \psi_s = \frac{x_1}{L} \quad (17)$$

The cubic approximation, used for the transverse displacement, yields excellent results in terms of the corresponding natural frequency. A very refined, three-dimensional finite element (FE) model has been adopted for establishing a reliable value of the natural frequency for the electro-mechanical system. The one-DOF model adopted herein provide an excellent estimate of the first natural frequency, with a relative error w.r.t the FE solution of less than 0.1%. It is interesting to realize that the 1-DOF model shows a slightly lower frequency than the one for the FE mode, thus suggesting a more compliant behavior. That strange result can be explained by considering that the FE model encompasses three-dimensional effects of piezoelectric behavior, which has the final outcome of increasing the electro-mechanical coupling and, consequently, the natural frequency. For what concerns the torsional vibration frequency, the simple linear model shown in Eq. 17 is not the best option, since it is endowed with a 26.7% relative error w.r.t. the FE model. The situation would be by far better (4% relative error) by considering a cubic function also for the torsional DOF. Nevertheless, in view of the fact that the FI involves the bending DOF only in the present case, the simple approximation of Eq. 17 is retained, because the error on the torsional frequency has no effect on the flutter behavior.

4. CRITICAL FLUTTER VELOCITY

First of all, the case of standard beam, in the absence of piezoelectric coupling, is considered in order to provide the reference value of the critical flutter velocity. In that way, it is possible to give a precise assessment of the effect of piezoelectric coupling for different external circuitry. By considering the first and the second equations in Eq. 9 and by setting to zero the coefficient Θ , one can easily obtain the critical flutter velocity:

$$\bar{U}_{cr} = 3.3 \text{ m/s} \quad (18)$$

The barred symbol stands for the reference value, in the absence of piezoelectric coupling. Account taken of the kinematic viscosity of air ($\nu = 15.35 \cdot 10^{-6} \text{ m}^2/\text{s}$), one finds that the critical velocity corresponds to the Reynolds number $Re = 1.72$. That number is lower than the minimum value considered in the flutter derivatives, so we have been forced to keep valid the flutter derivatives given for $Re = 10$: this is an important limitation of the present study, even though the final considerations are not largely affected by that fact.

(1) Case of RC circuitry

The electric parameter of the external circuitry has a strong influence on the final damping of the system. Taking into account the damping for the first flexural mode, one finds that the final damping is a non-monotonic function of the parameter $\alpha = \omega_w R C_E$, where $(R C_E)$ is the time constant of charge for the RC circuit. The maximum damping is attained for $\alpha \approx 1$, with a 60% increase w.r.t. the initial value of purely mechanical damping. This means that the condition $R \approx 1/(\omega_w C_E) \approx 30 \Omega$ should hold in order to obtain, for

the considered beam, the optimal external circuit. In Fig. 3 the real and imaginary part of the eigenvalues for the cantilever are plotted. The analyses are performed considering three different values of load resistance. In all the cases the instability occurs for the transverse degree of freedom. The trend of damping ratio follows that obtained in the purely mechanical case, related to the H_I^* coefficient. The load resistance does not affect the natural frequency of the structure, which remains almost constant (as it happens in the absence of electro-mechanical coupling). Tab. 2 shows the electro-mechanical damping ratio and the critical fluid velocity. It can be seen a substantial increase in both quantities w.r.t. the absence of electro-mechanical coupling. That behavior is expected, since the piezoelectric effect entails an increase of damping, due to the conversion of mechanical energy into electrical one, so that the fluid velocity to reach FI is increased. When $R = 30 \Omega$ the damping and the flutter speed achieve their maximum.

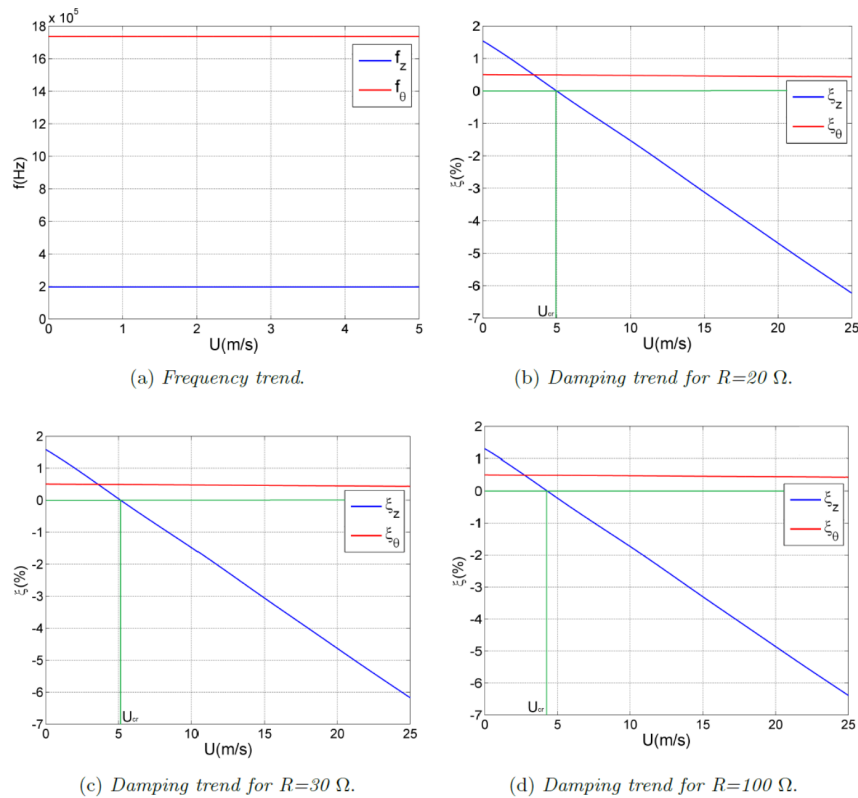


Figure 3: Results of FI analyses for the considered cantilever, RC circuitry with various load resistances.

Table 2: Synopsis of the results and comparison with no electro-mechanical coupling (RC circuitry).

R [Ω]	ζ_w [-]	$\Delta\zeta_w$	U_{cr} [m/s]	ΔU_{cr}	Re_{cr}
20	0.0154	54%	5.0	52%	2.61
30	0.0160	60%	5.1	54%	2.66
100	0.0131	31%	4.3	30%	2.24

(2) Case of RLC circuitry

In this case, there is also the complex eigenvalue associated to the voltage field, in agreement with the non-singularity of the matrix of the masses. Like for the RC circuit the influence of electric parameters on the transverse damping ratio is evaluated. The results show a maximum at the condition $\eta = 1$, where $\eta = \omega_w^2 L C_E$; this means that the damping is amplified when the mechanical part of the system is synchronized with electric one. On the other hand, the effect of resistance shows a different peak in function of the value of

inductance and of the electro-mechanical coupling coefficient. In general, one can notice that the increase of damping for RLC circuitry is by far larger than in the previous case: the final damping is up to 8 times larger than the initial mechanical damping.

Fig. 4 shows the evolution of frequency and damping for each field, by introducing the aeroelastic component. The value of inductance is taken in order to match the circular natural frequency of the mechanical part to the frequency of the electrical circuitry ($L = 0.024$ mH), so that the mechanical damping is maximized. The analysis is performed for three different load resistances, see Tab. 3. As expected, the magnitude of equivalent damping for $U=0$ is much larger compared to the RC circuit and this aspect is reflected in the magnitude of flutter velocity, which considerably increases. In the considered cantilever ζ_w assumes its maximum for $R = 100 \Omega$, but U_{cr} is higher for $R = 150 \Omega$, achieving values much larger than the purely mechanical case. It is interesting to notice that in this case the damping ratio shows a different decay w.r.t. to what happens for the RC circuit and the simple mechanical problem. This behavior is more accentuated for $R = 100 \div 150 \Omega$. The plot in Fig. 4 presents an initial velocity range in which the electrical and mechanical damping follow the same trend, then, by increasing the fluid speed, the slope of electrical response changes sign in contrast to the mechanical response. The order of magnitude of Reynolds number, in agreement with the increase of critical flutter velocity, is higher, reaching for $R = 100 \div 150 \Omega$, suitable values in order to consider appropriate the set of flutter derivatives assumed in this analysis.

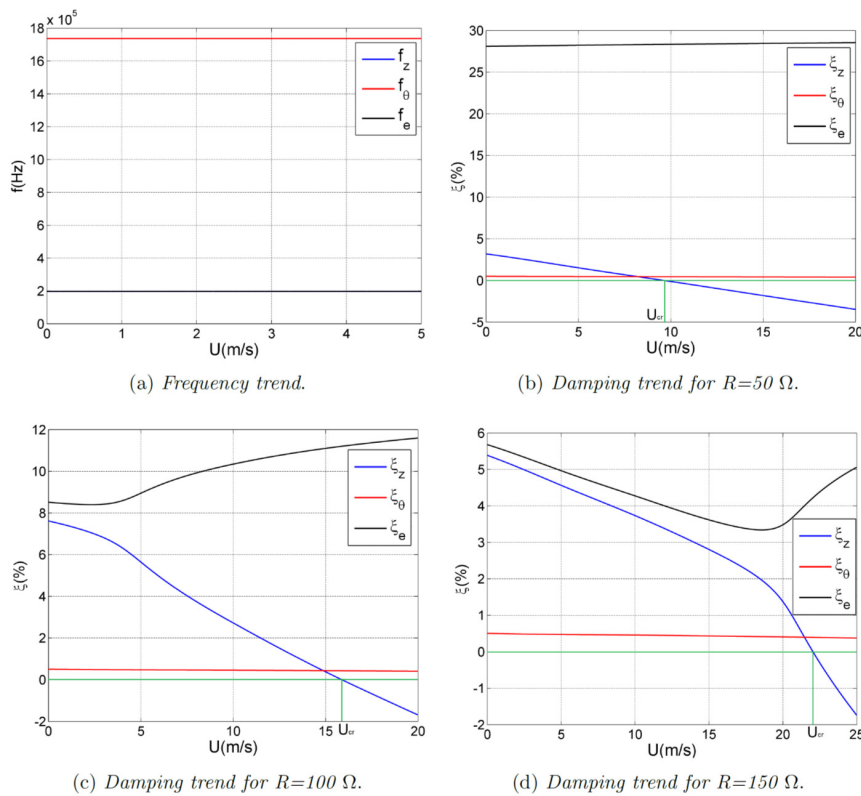


Figure 4: Results of FI analyses for the considered cantilever, RLC circuitry with various load resistances.

Table 3: Synopsis of the results and comparison with no electro-mechanical coupling (RLC circuitry).

R [Ω]	ζ_w [-]	$\Delta\zeta_w$	U_{cr} [m/s]	ΔU_{cr}	Re_{cr}
50	0.0320	220%	9.6	190%	5.00
100	0.0762	662%	15.9	381%	8.28
150	0.0540	440%	22.0	567%	11.47

5. APPLICATION TO ENERGY HARVESTING

In this chapter, the possibility to exploit aeroelastic effects for energy harvesting purposes is evaluated. However, being flutter essentially an unstable phenomenon, it is necessary to integrate another exciting component that ensures a continuous supply of energy, e.g. an inertial system. In order to understand how FI affects the behavior of the energy harvesting system, the time-variant evolution is computed for the cantilever subject to the fluid flow and to an initial tip displacement equal to the thickness of the beam. In this way, we consider the dynamic response to an impulsive excitation of the beam. Such a situation is quite common if the energy harvester is used in conjunction with a frequency-up conversion device¹³⁾. The structure is studied considering the two different electric circuit, with resistance and inductance that maximize the mechanical damping. This means, for RC circuitry, that $R = 30 \Omega$ and for RLC circuit that $L = 0.024 \text{ mH}$ and $R = 100 \Omega$. The aeroelastic effect is included by considering a fluid speed slightly smaller than the critical value computed in Sec. 4: RC circuit $U = 5 \text{ m/s}$; RLC circuit $U = 15 \text{ m/s}$.

(1) Case of RC circuitry

The aeroelastic mechanism affects significantly the response of the system. According to the magnitude of coefficient A_2^* , the torsional rotation is not affected by the aeroelastic behavior. On the other hand the tip displacement presents a much less damped response considering the fluid effect. This aspect is reflected on the voltage due to the electro-mechanical coupling and consequently on the harvested power trend (see Fig. 5). The reduction of damping, however, does not affect the peak amplitude of the harvested power, that remains practically the same, contrary to what happens for RLC circuit as discussed in the following section. It is important to mention that the overall harvested energy is largely increased, because of the slow oscillation decay.

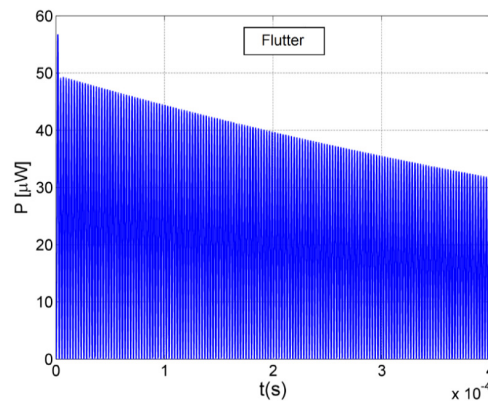


Figure 5: Dynamic response of the cantilever, RC circuit, $R = 30 \Omega$, $U = 5 \text{ m/s}$.

(2) Case of RLC circuitry

Also in this case, the dynamic response is largely affected by the aeroelastic effect, showing larger oscillation amplitude. Compared to the purely resistive solution, in this case the harvested power achieves an amount much larger: the peak power is on orders of magnitude higher than in the RC circuit (see Fig. 6). We can conclude that, for RLC circuitry, the reduction of the mechanical damping affects not only the decay of the response (i.e. the overall harvested energy), but also the maximum amplitude (i.e. the peak power).

5. CONCLUSIONS

In the present paper, we show the application of flutter analysis to piezoelectric beams in MEMS, with the main purpose of exploring the possible application of energy harvesting in the presence of aeroelastic effects. The results, computed on the basis of the dynamic solution of the fully coupled problem, demonstrate the possibility to exploit the flutter mechanism to improve an energy harvesting device. The advantages are linked to the considerable reduction of the mechanical damping. The relatively small critical velocities make it possible to adopt these devices anywhere in the surrounding environment. As previously mentioned, it is

necessary to point out that the device must still integrate another exciting source, as the flutter is just an instability mechanism.

One important aspect for MEMS is the low Reynolds number. Despite the increase of the flutter critical speed for piezoelectric coupling, the magnitude of the Reynolds number still fails to achieve the value $Re = 10$, which is the minimum value for the flutter derivatives in literature. For this reason, the results could be slightly altered. To comply with this problem it would be better to evaluate, through CFD analyses¹⁴⁾, a more accurate set of aerodynamic coefficient, applicable to this particular structure.

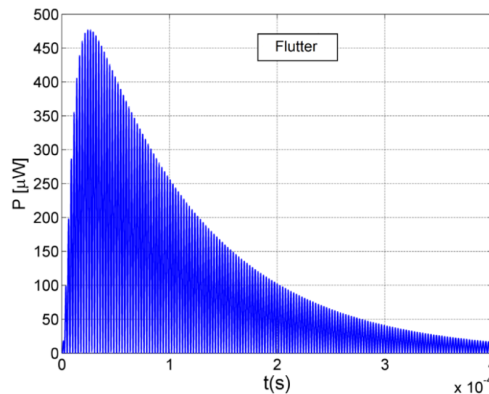


Figure 6: Dynamic response of the cantilever, RLC circuit, $L = 0.024$ mH, $R = 100$ Ω , $U = 15$ m/s.

REFERENCES

- 1) Jacobsen, H., Prume, K., Wagner, B., Ortner, K., and Jung, T. : High-rate sputtering of thick PZT thin films for MEMS. *J. of Electroceramics*, Vol. 25, pp. 198-202, 2010.
- 2) Kim, S.-G., Priya, S., and Kanno, I. : Piezoelectric MEMS for energy harvesting. *MRS Bulletin*, Vol. 37, pp. 1039-1050, 2012.
- 3) Jeon, Y., Sood, R., Jeong, J.-H., and Kim, S.-G. : MEMS power generator with transverse mode thin film PZT. *Sens. Act., A: Phys.*, Vol. 122, pp. 16-22, 2005.
- 4) Ardito R., and Musci R.: MEMS energy harvesters based on aeroelastic phenomena, *Proc. of the 11th World Congress on Computational Mechanics (WCCM)*, Barcelona, Spain, 2014
- 5) Scanlan, R.H., and Simiu, E. : *Wind effects on Structures*, John Wiley and Sons Inc., 3rd edition, 1996.
- 6) Gafforelli, G., Corigliano, A., and Ardito, R.: Improved one-dimensional model of piezoelectric laminates for energy harvesters including three dimensional effects. *Compos. Struct.*, Vol. 127, pp. 369-381, 2015.
- 7) Ballhause, D., D'Ottavio, M., Kröplin, B., and Carrera, E.: A unified formulation to assess multilayered theories for piezoelectric plates. *Computers & Struct.*, Vol. 83, pp. 1217-1235, 2005.
- 8) IEEE Standard on Piezoelectricity. *The institute of Electrical and Electronics Engineers*, 1987.
- 9) Ardito, R., Bertarelli, E., Corigliano, A., and Gafforelli, G. On the application of piezolaminated composites to diaphragm micropumps. *Compos. Struct.*, Vol. 99, pp. 231-240, 2013.
- 10) Renno, J.M., Daqaq, M.F., and Inman, D.J.: On the optimal energy harvesting from a vibration source. *J. Sound Vibr.*, Vol. 320, pp. 386-405, 2009.
- 11) Ardito, R., Comi, C., Corigliano, A., and Frangi, A.: Solid damping in micro electro mechanical systems. *Meccanica*, Vol. 43, pp. 419-428, 2008.
- 12) Bruno, L., and Fransos, D.: Evaluation of the Reynolds number effects on the flutter derivatives of a flat plate by means of a new computational approach, *J. Fluid Struct.*, Vol. 24, pp. 1058-1076, 2008.
- 13) Ardito, R., Corigliano, A., Gafforelli, G, Valzasina, C., Procopio, F., and Zafalon, R.: Advanced model for fast assessment of piezoelectric micro energy harvesters. *Frontiers in Materials*, in press, 2016.
- 14) Le Maître, O.P., Scanlan, R.H., and Knio, O.M.: Estimation of the flutter derivatives of an NACA airfoil by means of Navier-Stokes simulations, *J. Fluid Struct.*, Vol. 17, pp. 1-28, 2003.

EXTENSION OF DISCRETE-TIME FLUTTER PREDICTION METHOD TO A HIGHER-MODE SYSTEM

Hiroshi Torii⁺¹
Meijo University, Nagoya, Japan

Conventionally flutter boundaries have been predicted based on the modal damping. However, the accurate estimation of damping is difficult and, in some cases, the damping coefficient is not necessarily an appropriate measure for the flutter prediction. To overcome the defect of the damping method, authors proposed an alternative parameter, the flutter margin for discrete-time systems (FMDS), which is approximately equivalent to Zimmermann's flutter margin, and has suitable properties as the flutter prediction parameter. Since it was applicable only to the binary flutter, we have attempted to extend the FMDS so as to be applicable to a higher-mode system. In this paper we give an overview of FMDS and attempt its extension to a higher-mode system.

Keyword: flutter prediction, flight testing, ARMA model, flutter margin

1. INTRODUCTION

Since flutter is the self excited vibration which causes a fatal damage to an airfoil, we have to pay utmost attention to the occurrence of flutter in the airplane design and development. At the final stage of airplane development, therefore, wind tunnel and flight tests are conducted to check that flutter does not occur in the flight envelop, and to evaluate the flutter boundary speed. Since the flutter tests are generally carried out in the safety range far below the critical point to avoid structural damage during the tests, the flutter boundary is predicted from the behavior of some stability criteria plotted against flight speed or dynamic pressure as shown in Fig.1. The stability margin has been conventionally evaluated by damping of aeroelastic modes. For a reliable prediction of flutter, it is quite significant to measure the modal damping as accurate as possible from flight test data. However an accurate evaluation of damping of a wing in an airstream is not necessarily an easy task, so that lots of works on the flutter prediction have been directed to improve the accuracy or

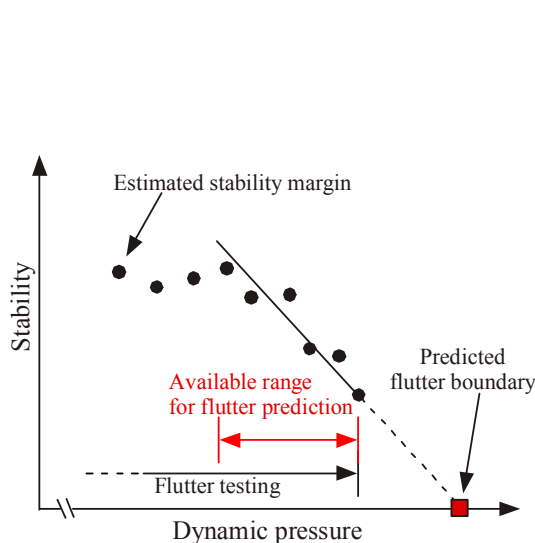


Figure 1: Flutter prediction

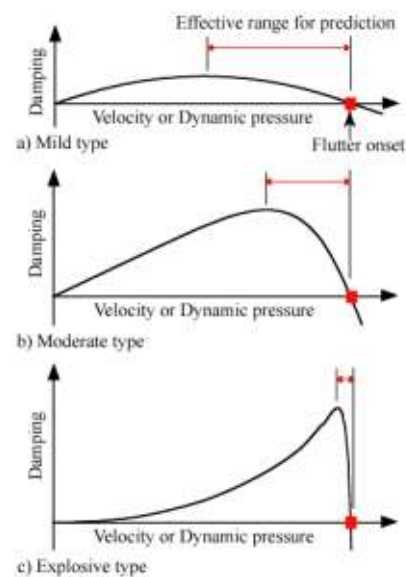


Figure 2: Behavior of damping

⁺¹htorii@meijo-u.ac.jp

efficiency of damping estimation. It is pointed out, however, that damping is not always an appropriate index to predict the flutter boundary¹⁾. Figure 2 depicts the behavior of damping against the dynamic pressure for three types of flutter. For the explosive type of flutter, it shows that damping gives no sign of instability up to the neighborhood of the critical speed.

As an alternative approach, Zimmerman and Weissenburger¹⁾ attempted to propose a more suitable parameter for the flutter prediction than damping, and introduced "Flutter Margin". It is derived from Routh's stability test, which is a method to check the stability of system based on the characteristic equation. The parameter decreases almost monotonically toward zero as the dynamic pressure increases. This is a very favorable property for the flutter prediction. However, it is applicable only to binary-flutter. The extension to a three-mode system was attempted by Price and Lee²⁾.

Since the Flutter Margin is defined based on the continuous-time system, it is not convenient for digital processing. In the discrete-time domain, Matsuzaki and Ando³⁾ proposed to use Jury's stability parameters as the indicator of stability margin, which is stability criteria for the discrete-time system and are calculated from the discrete-time characteristic equation. Jury's stability parameter starts to decrease at lower speed range than damping, but it is sensitive to the noise and filter setting. Then authors⁴⁾ modified Jury's parameters and introduced the new indicator called "Flutter Margin for the Discrete-time System (FMDS)". We showed that it was approximately equivalent to Zimmerman's Flutter Margin, so that it decreases almost monotonically as the dynamic pressure increases for the simple two-dimensional wing model. Though the FMDS has superior properties as the flutter prediction parameter, it is applicable to the data which include only two coupling modes similarly to Flutter Margin. This limitation should be relaxed to make FMDS method practicable to the flutter tests. Bae et al.⁵⁾ attempted the extension of the FMDS to the multimode system. As mentioned by McNamara and Friedmann⁶⁾, however, a mathematical foundation or a theoretical consideration of the parameter introduced is not given in Ref.5, and furthermore it is not consistent with the FMDS for the two-mode system. Therefore the extension of the FMDS is still an open problem.

The purpose of this work is to extend the FMDS to the three-mode system. A new flutter prediction parameter is proposed based on Jury's stability determinant method. The properties of the parameter are investigated using wing models with three- and four-modes. Then to check the feasibility for an actual data we show the application results to the wind tunnel flutter test data which are measured under the stationary and non-stationary conditions.

2. REVIEW OF FLUTTER PREDICTION METHODS

In this section we will review Zimmermann's Flutter Margin¹⁾, Jury's stability parameter method³⁾, and FMDS⁴⁾.

(1) Flutter Margin

From the modal damping and frequency, we can obtain the characteristic roots of the j -th mode.

$$s_j = \alpha_j + i\beta_j, \quad s_j^* = \alpha_j - i\beta_j$$

The equation corresponding to the roots, s_j and s_j^* , is expressed as follows.

$$(s - s_1)(s - s_1^*)(s - s_2)(s - s_2^*) = 0$$

The expansion of it gives the following characteristic equation.

$$s^4 + P_3s^3 + P_2s^2 + P_1s + P_0 = 0 \quad (1)$$

Combining Routh's stability parameters for Eq.1, Zimmermann defined the flutter margin:

$$F = -\left(\frac{P_1}{P_3}\right)^2 + P_2\left(\frac{P_1}{P_3}\right) - P_0 \quad (2)$$

The value of F indicates the stability margin, that is, F is positive in the subcritical speed range and becomes zero at the flutter boundary. Using the relation between roots and coefficients of equation, Eq.2 is also expressed as follows.

$$F = \left\{ \left(\frac{\beta_2^2 - \beta_1^2}{2} \right) + \left(\frac{\alpha_2^2 - \alpha_1^2}{2} \right) \right\}^2 + 4\alpha_1\alpha_2 \left\{ \left(\frac{\beta_2^2 + \beta_1^2}{2} \right) + 2 \left(\frac{\alpha_2^2 + \alpha_1^2}{2} \right) \right\} - \left\{ \left(\frac{\alpha_2 - \alpha_1}{\alpha_2 + \alpha_1} \right) \left(\frac{\beta_2^2 - \beta_1^2}{2} \right) + 2 \left(\frac{\alpha_2^2 + \alpha_1^2}{2} \right) \right\}^2$$

This is a convenient expression to evaluate the value of F from the aeroelastic characteristics estimated at the experiments. Moreover, from the analysis using a two-dimensional wing model with a quasi-steady aerodynamics, the Flutter Margin is shown to be a quadratic function of the dynamic pressure q .

$$F = C_2 (C_{L_\alpha} q)^2 + C_1 (C_{L_\alpha} q) + C_0 \quad (3)$$

(2) Jury's stability parameter

Nowadays we generally acquire and treat data at a digital form. Since the Flutter Margin, however, is defined in the continuous-time domain, it is not adequate to cope with such a digital system. In Ref.3 Matsuzaki proposed to use Jury's stability criteria to measure the stability margin.

Using the time-series analysis method, sampled data $\{y_1, y_2, y_3, \dots\}$ can be identified by the following Autoregressive Moving Average (ARMA(n, m)) model.

$$y_t + \alpha_1 y_{t-1} + \alpha_2 y_{t-2} + \dots + \alpha_n y_{t-n} = e_t + \beta_1 e_{t-1} + \beta_2 e_{t-2} + \dots + \beta_{t-m} e_{t-m}$$

where y_t is the data observed at time t , e_t a white noise. The order n of AR part (the left hand side) is twice the number of vibration modes M , that is, $n=2M$, and the order m of MA part (the right hand side) is less than n . Generally the optimal order n and m are decided by the Akaike Information Criteria (AIC). The AR part corresponds to the following characteristic polynomial of the discrete-time system.

$$G(z) = z^{2M} + \alpha_1 z^{2M-1} + \dots + \alpha_{2M-1} z + \alpha_{2M} = \sum_{i=1}^M (z - z_i)(z - z_i^*)$$

where z_i is the characteristic root of the i -th mode, and the root with a superscript * is the complex conjugate.

According to Jury's stability test (determinant method), the system is stable if and only if all the following conditions are satisfied.

$$\begin{aligned} G(1) &= 1 + \alpha_1 + \dots + \alpha_{2M-1} + \alpha_{2M} > 0 \\ G(-1) &= 1 - \alpha_1 + \dots - \alpha_{2M-1} + \alpha_{2M} > 0 \\ F_k^+ &= \det(X_k + Y_k) > 0, \quad (k = 1, 3, \dots, 2M-1) \\ F_k^- &= \det(X_k - Y_k) > 0, \quad (k = 1, 3, \dots, 2M-1) \end{aligned}$$

where matrices X_k and Y_k are

$$X_k = \begin{pmatrix} 1 & \alpha_1 & \cdots & \alpha_{k-1} \\ 0 & 1 & \ddots & \vdots \\ \vdots & \ddots & \ddots & \alpha_1 \\ 0 & \cdots & 0 & 1 \end{pmatrix}, \quad Y_k = \begin{pmatrix} \alpha_{n-k,1} & \cdots & \alpha_{n-1} & \alpha_n \\ \vdots & \ddots & \alpha_n & 0 \\ \alpha_{n-1} & \ddots & \ddots & \vdots \\ \alpha_n & 0 & \cdots & 0 \end{pmatrix}$$

In the flutter test, the system is stable at the subcritical speed range, so that all the above conditions are satisfied. At the flutter boundary the system becomes unstable, and one of the values reaches zero. Among them, parameter F_{2M-1}^- is expressed as follows⁷⁾.

$$F_{2M-1}^- = \prod_{i < j}^{2M} (z - z_i z_j) = \prod_{i < j}^M (1 - |z_i|^2) \times f(z_1, \dots, z_{2M}) \quad (4)$$

where $z_{M+i} = z_i^*$ for $i=1, 2, \dots, M$, and $f(z_1, \dots, z_{2M})$ includes the remaining terms, which does not become zero at the flutter boundary. Because of the first factor in the right hand side of Eq.4, this parameter becomes zero when one of z_i reaches a unit circle, that is, the occurrence of flutter. Therefore we can use F_{2M-1}^- for the flutter prediction, and this is Jury's stability parameter proposed in Ref.3

(3) Flutter Margin for the Discrete-time System (FMDS)

After preprocessing through the band-pass filter so as to include only the coupling mode which causes flutter, sampled data is identified by the ARMA(4, m) model

$$y_t + \alpha_1 y_{t-1} + \alpha_2 y_{t-2} + \alpha_3 y_{t-3} + \alpha_4 y_{t-4} = e_t + \beta_1 e_{t-1} + \beta_2 e_{t-2} + \beta_{t-m} e_{t-m} \quad (5)$$

where the order m is less than 4 and is determined by AIC. From the left hand side the following characteristic equation of the system is obtained.

$$G(z) = z^4 + \alpha_1 z^3 + \alpha_2 z^2 + \alpha_3 z + \alpha_4 = \prod_{i=1}^2 (z - z_i)(z - z_i^*)$$

Jury's stability parameter for this system is

$$F_3^- = \det(X_3 - Y_3)$$

where

$$X_3 = \begin{pmatrix} 1 & \alpha_1 & \alpha_2 \\ 0 & 1 & \alpha_1 \\ 0 & 0 & 1 \end{pmatrix}, \quad Y_3 = \begin{pmatrix} \alpha_2 & \alpha_3 & \alpha_4 \\ \alpha_3 & \alpha_4 & 0 \\ \alpha_4 & 0 & 0 \end{pmatrix}$$

and $\alpha_1 \sim \alpha_4$ are the coefficients of Eq.5.

Instead of F_3^- , however, we construct the following parameter combining the stability parameters.

$$F_z = \frac{F_3^-}{(F_1^-)^2} = \frac{\det(X_3 - Y_3)}{(1 - \alpha_4)^2} \quad (6)$$

The denominator is always positive at and below the flutter speed, and the numerator is Jury's stability parameter, so that F_z is positive in the subcritical range and becomes zero at flutter boundary.

The analysis using a two-dimensional wing model shows that Eqs.2 and 6 have approximately the relation

$$F_z \approx T^4 F = T^4 \left[C_2 (C_{L\alpha} q)^2 + C_1 (C_{L\alpha} q) + C_0 \right]$$

where T is a sampling interval. Therefore the parameter F_z has a similar property to the flutter margin, that is, the value of F_z decreases monotonically and almost linearly toward zero in the subcritical range with the increase of the dynamic pressure.

3. EXTENSION OF FLUTTER PREDICTION METHOD

Though the FMDS has a superior property for the flutter prediction, it is applicable only to the two-mode system as shown in the definition. In this section, we attempt to extend it to the three-mode system.

The data having three modes is identified by the following ARMA(6, m) model instead of Eq.5.

$$y_t + \alpha_1 y_{t-1} + \alpha_2 y_{t-2} + \dots + \alpha_6 y_{t-6} = e_t + \beta_1 e_{t-1} + \dots + \beta_{t-m} e_{t-m} \tag{7}$$

Therefore, we obtain the characteristic equation

$$G(z) = z^6 + \alpha_1 z^5 + \dots + \alpha_5 z + \alpha_6 = \prod_{i=1}^3 (z - z_i)(z - z_i^*)$$

Here we propose a new flutter prediction parameter using Jury's stability criteria

$$F_z^{(3)} = \frac{F_5^-}{(F_1^-)^3} = \frac{\det(X_5 - Y_5)}{(1 - \alpha_6)^3} \tag{8}$$

where X_5 and Y_5 are matrices whose elements consists of the coefficients of Eq.7.

$$X_5 = \begin{pmatrix} 1 & \alpha_1 & \alpha_2 & \alpha_3 & \alpha_4 \\ 0 & 1 & \alpha_1 & \alpha_2 & \alpha_3 \\ 0 & 0 & 1 & \alpha_1 & \alpha_2 \\ 0 & 0 & 0 & 1 & \alpha_1 \\ 0 & 0 & 0 & 0 & 1 \end{pmatrix}, \quad Y_5 = \begin{pmatrix} \alpha_2 & \alpha_3 & \alpha_4 & \alpha_5 & \alpha_6 \\ \alpha_3 & \alpha_4 & \alpha_5 & \alpha_6 & 0 \\ \alpha_4 & \alpha_5 & \alpha_6 & 0 & 0 \\ \alpha_5 & \alpha_6 & 0 & 0 & 0 \\ \alpha_6 & 0 & 0 & 0 & 0 \end{pmatrix}$$

We can express the denominator of Eq.8 using the characteristic roots z_i as

$$1 - \alpha_6 = 1 - |z_1|^2 |z_2|^2 |z_3|^2$$

If the system is stable, the absolute value of the root is less than 1, so that the above equation has a positive value at and below the critical speed. The numerator of Eq.8 is expressed as

$$\begin{aligned} \det(X_5 - Y_5) &= \prod_{1 \leq i < j \leq 6} (1 - z_i z_j) \\ &= (1 - z_1^2)(1 - z_2^2)(1 - z_3^2) \\ &\quad \times |1 - z_1 z_2|^2 |1 - z_1 z_3|^2 |1 - z_2 z_3|^2 |1 - z_1 z_2^*|^2 |1 - z_1 z_3^*|^2 |1 - z_2 z_3^*|^2 \end{aligned}$$

where $z_4 = z_1^*$, $z_5 = z_2^*$ and $z_6 = z_3^*$. Therefore, it has a positive value as long as all roots locate in a unit circle, and becomes zero when one of the roots reaches a unit circle. In the flutter prediction, this means that the parameter $F_z^{(3)}$ is positive in the subcritical range and becomes zero at the speed of flutter onset.

4. ANALYSIS AND SIMULATION USING TWO-DIMENSIONAL WING MODEL

To study the property of $F_z^{(3)}$, we carry out the analysis using a three-degree-of-freedom wing model illustrated in Fig. 3. The values used in this model are $a = -0.4$, $c = 0.6$, $\mu = m / (\pi \rho b^2) = 40$, $S_\alpha / (mb) = 0.2$, $S_\beta / (mb) = 0.0125$, $r_\alpha^2 = I_\alpha / (mb^2) = 0.25$, $r_\beta^2 = I_\beta / (mb^2) = 0.00625$, $\omega_h = \sqrt{K_h / m} = 50$ (rad/sec), $\omega_\alpha = \sqrt{K_\alpha / I_\alpha} = 100$ (rad/sec) and $\omega_\beta = \sqrt{K_\beta / I_\beta}$. Here we compare the property of damping, Jury's stability parameter F_5^- and 3 mode FMDS $F_z^{(3)}$. For this purpose, we use two different values for ω_β , that is, (model 1) $\omega_\beta = 200$ (rad/sec), and (model 2) $\omega_\beta = 170$ (rad/sec). These models cause the different type of flutter.

The results of damping, Jury's stability parameter, and FMDS for 3-mode system $F_z^{(3)}$ are depicted in Figs. 4-6, respectively. In these figures the horizontal axis gives normalized dynamic pressure q/q_F , that is, the flutter boundary is $q/q_F=1$. As shown in Fig. 4, for model 1 the first and second mode are coupling and the first mode damping become unstable, whereas the third mode damping causes flutter for model 2. Model 1 is a moderate type of flutter, and model 2 is a mild type. These figures show that the critical mode can change, and the type of flutter also can change with a slight deference of the wing configuration. The critical mode damping of model 1 starts to decrease around $q/q_F=0.8$, so that the available range for the flutter prediction is higher than $q/q_F=0.8$.

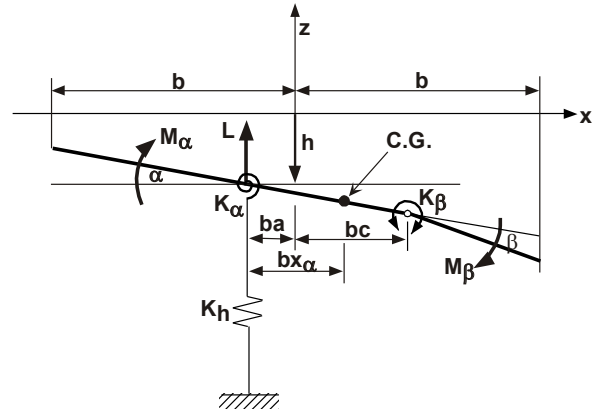


Figure 3: Two-dimensional wing model

The curve of Jury's stability parameter F_5^- for both models have a similar pattern as shown in Fig. 5 and the value starts to decrease around $q/q_F=0.5$. Figure 6 shows that also the values of the parameter $F_z^{(3)}$ has a similar pattern for both models, but unlike damping and Jury's stability parameter, $F_z^{(3)}$ decreases monotonically in the whole subcritical range. From this analysis, we can use all data in the subcritical range to predict flutter boundary by $F_z^{(3)}$. These results demonstrate that if we use $F_z^{(3)}$ as the flutter prediction parameter, we can make an accurate and reliable prediction of flutter in comparison with the method using modal damping or Jury's stability parameter.

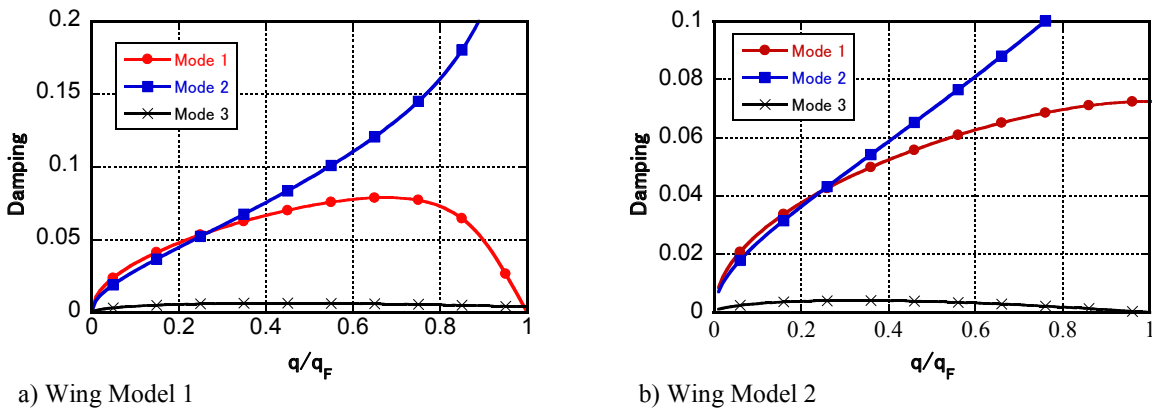


Figure 4: Damping of the wing model

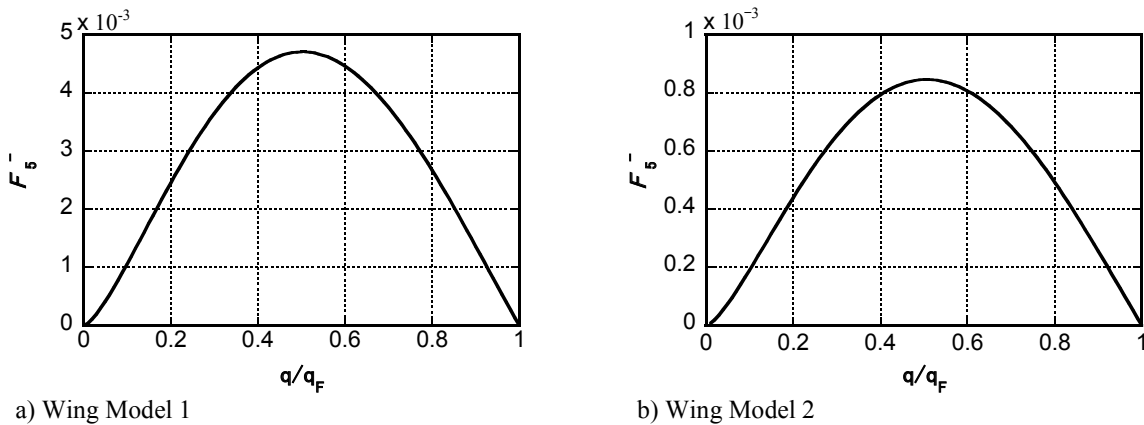


Figure 5: Jury's stability parameter F_5^- of the wing model

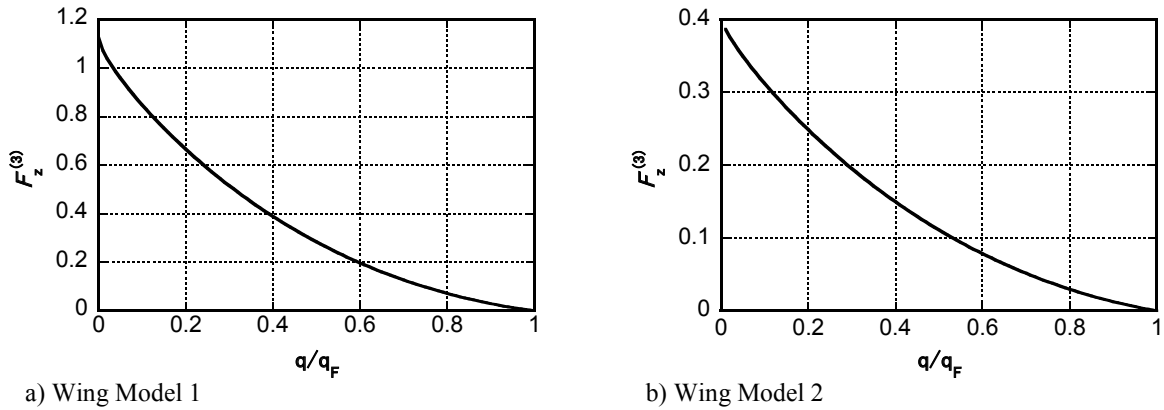


Figure 6: Parameter $F_z^{(3)}$ of the wing model

As the next analysis we use the wing model given in Ref.8, which is used for a quaternary flutter analysis of the wing of a large transport aircraft. It has four vibration mode, 1) fundamental wing bending, 2) first overtone wing bending, 3) fundamental wing torsion, and 4) aileron deflexion. Figures 7 and 8 show modal frequencies and damping, respectively. The second mode is critical and starts to decrease around $q/q_F=0.5$ as shown in Fig. 8. Here we chose 3 modes to calculate $F_z^{(3)}$, in which the second mode should be included. Figure 9 depicts the value of $F_z^{(3)}$ obtained from the lowest 3 modes, and Fig. 10 is the result obtained from 2nd to 4th mode. The value decreases monotonically toward zero for both cases. Therefore, it is obvious that $F_z^{(3)}$ is superior to damping for the flutter prediction.

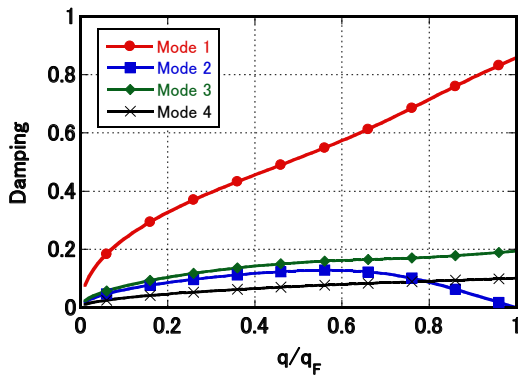


Figure 7: Modal frequencies

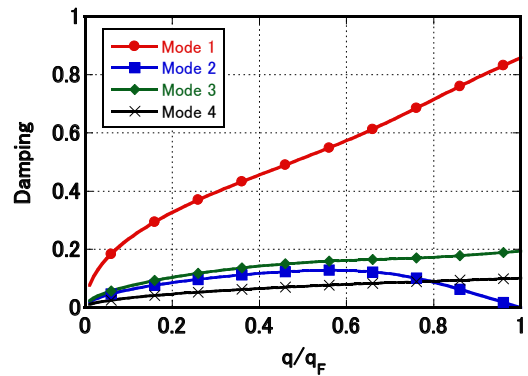


Figure 8: Modal damping

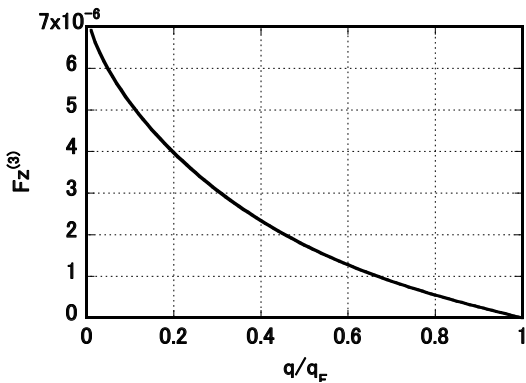


Figure 9: $F_z^{(3)}$ obtained from 1-3 modes

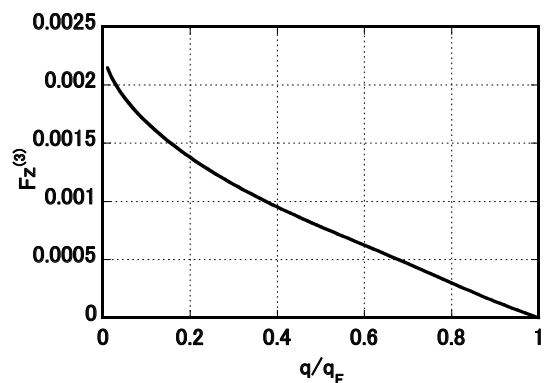


Figure 10: $F_z^{(3)}$ obtained from 2-4 modes

5. APPLICATION TO FLUTTER TEST DATA

To check the feasibility of this method in an actual situation, we apply it to the wind tunnel flutter test data. Figure 11 is the planform of a wing model, which is made of aluminum alloy flat plate of 2 mm thickness, and has a double-wedge at the leading and trailing edges. The response to flow turbulence is measured by strain gauge stuck on the surface of the wing.

The lowest three natural frequencies measured by the vibration test and the FEM analysis are given in Table 1. The power spectral density at $q = 75.7$ kPa depicted in Fig. 12 shows that the data have strong noise in the lower frequency than 25 Hz. Figure 13 is the modal frequencies of the lowest 4 modes at each dynamic pressure. To include the lowest three modal frequencies and cut the low frequency noise, we apply the digital highpass filter with a cut off frequency 30 Hz.

The Mach number is fix at $M = 2.51$ for all tests. The data are sampled at an interval $T = 2$ ms from the analog data recorder. The flutter boundary observed by the experiment is $q_f = 113.5$ kPa, where flutter occurs by a coupling of the first and the second modes, and the second mode becomes unstable.

Wind tunnel tests are conducted (1) under the stationary condition and (2) the non-stationary condition. In the stationary tests, the data are measured at 11 points of dynamic pressure from $q = 75.7$ to 99.4 kPa and the number of data used is $N = 6000$, which corresponds to the measurement of 12 sec. In the non-stationary test, the dynamic pressure is swept from $q = 76.0$ to 116.6 kPa at a rate of 2.6 kPa/sec.

Table 1 Modal frequency of wing model (Hz)

Mode No.	FEM	Vibration test
1	27.9	27.2
2	145.7	142.0
3	207.1	192.3

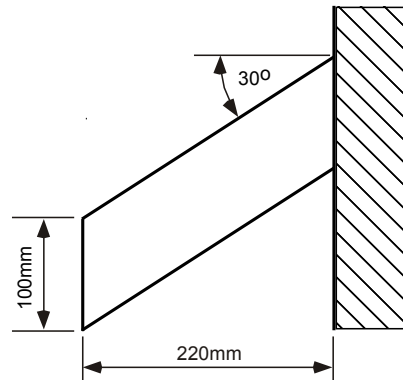


Figure 11: Planform of wing model

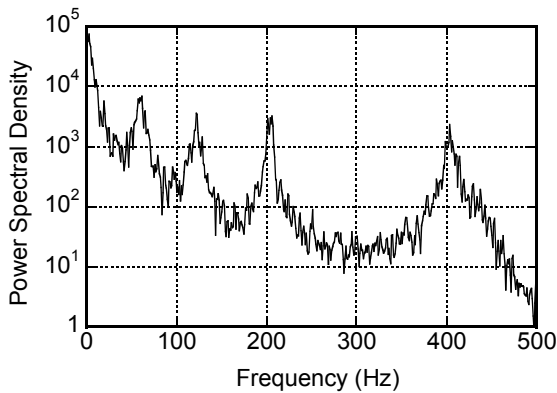


Figure 12: Power spectral density of data at $q=75.5$

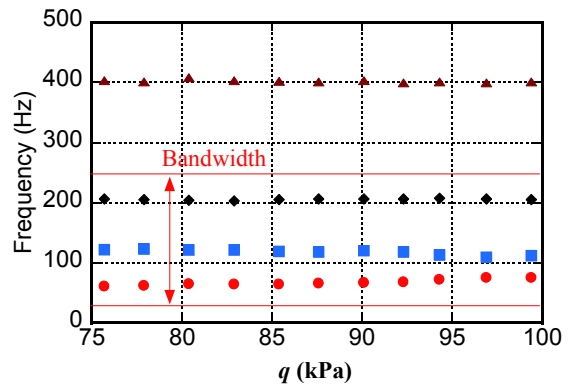


Figure 13: Modal frequencies

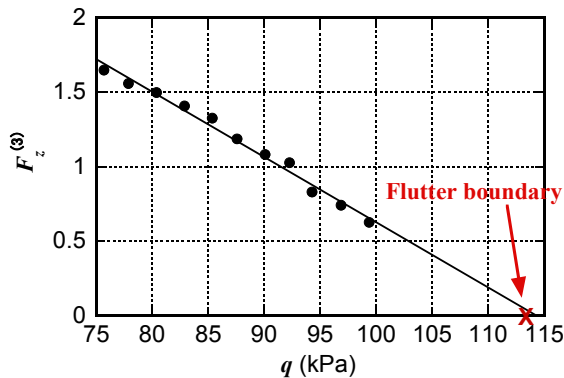


Figure 14: Estimated $F_z^{(3)}$ and the flutter prediction

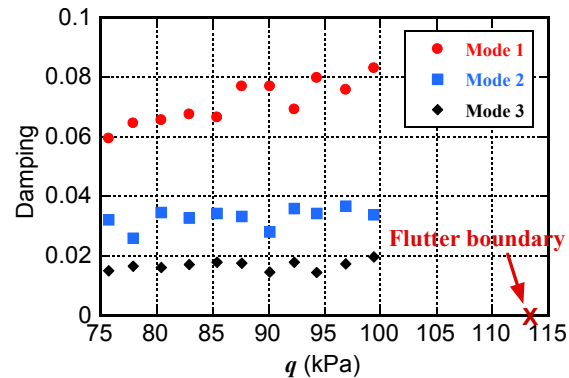


Figure 15: Estimated modal damping

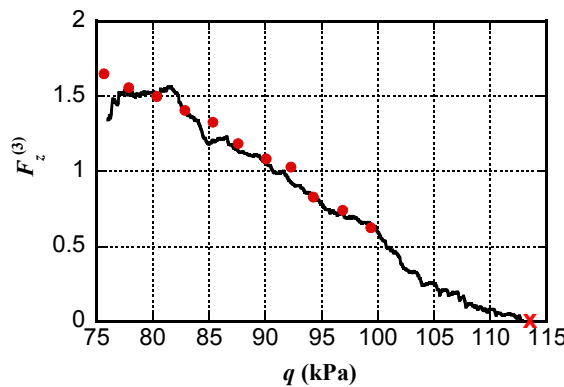


Figure 16: Estimated $F_z^{(3)}$

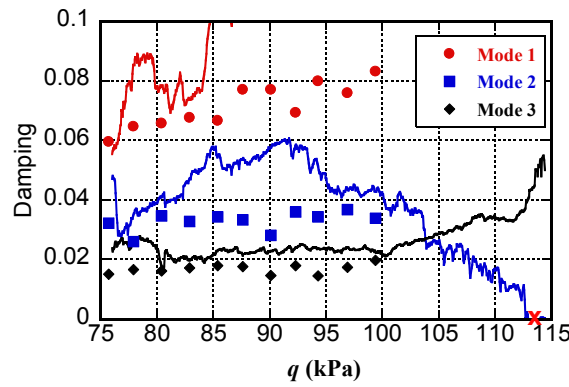


Figure 17: Estimated modal damping

(1) Results of stationary tests

Figure 14 depicts the estimated value of $F_z^{(3)}$ plotted against the dynamic pressure. These values decrease almost linearly as the dynamic pressure increases. Therefore a linear fitting drawn by a solid straight line gives a good prediction of flutter boundary q_F . The actual flutter boundary observed in the experiment is marked by a symbol 'x'. The regression analysis for these estimated data gives the straight line shown in Fig.14. The intersection of this line with the horizontal axis gives the prediction of the flutter boundary, that is, $\hat{q}_F = 114.3$ kPa, which is 0.7% higher than the actual value. The goodness of fit for this regression line is $R^2 = 0.986$. This means that the linear fitting is reasonable.

In Fig.15 the estimated values of modal damping are depicted. The first mode has a little upward trend, and the other two modes show no trend in evidence from the tests in this range. Therefore, it is impossible to predict the flutter boundary, the point shown by 'x', based on these estimated values. We need to conduct the tests at higher dynamic pressure than this to predict the flutter boundary based on the modal damping.

(2) Results of non-stationary test

For non-stationary data, we use a recursive identification procedure to estimate the parameters in real time, in which the coefficients of the ARMA model are updated at every sampling instance, and the value of $F_z^{(3)}$ and the modal damping is also renewed. The estimation result of $F_z^{(3)}$ is given in Fig.16, where circle symbols are the values estimated in the stationary tests. This figure shows that the values estimated recursively on a real-time procedure are the similar as the one of the stationary case, and decreases almost linearly toward zero. From this result, $F_z^{(3)}$ is an effective parameter to monitor the stability margin using with

the a real-time estimation method, and gives a accurate and reliable prediction of flutter based on the recursively estimated values.

The real-time estimation of modal damping, however, gives quite different values from the results of the stationary tests as shown in Fig.17, which shows that the estimation of damping is sensitive to noise or test condition. Though the accuracy of values estimated is not clear, the second mode damping starts to decline around $q=90$ kPa. But we are not sure that these estimations are reliable or not.

6. CONCLUDING REMARKS

A new flutter prediction parameter applicable to the three-mode system was proposed. The analysis using wing models with three- and four-degrees of freedom showed that the value decreased monotonically and became zero at the flutter speed. Depend on a wing configuration, the critical mode changes, while $F_z^{(3)}$ was not affected. Furthermore, the feasibility for actual flutter tests was examined by the analysis of the wind tunnel test data under the stationary and non-stationary conditions, whereas damping method did not work for the same test data.

For the two-mode FMDS, we have derived approximately the relation between F_z and the dynamic pressure q through Zimmerman's Flutter Margin. However, we have no such relation for the parameter $F_z^{(3)}$ in this moment, and that is a problem we have to solve from now on. Also we need to consider how to expand FMDS to the system higher than 3-mode based on the framework of Jury's stability criterion.

REFERENCES

- 1) Zimmerman, N. and Weissenburger, J. : Prediction of Flutter Onset Speed Based on Flight Testing at Subcritical Speeds, *J. Aircraft*, Vol. 1, No. 4, pp 190-202, 1964.
- 2) Price, S. and Lee, B. : Evaluation and Extension of the Flutter Margin Method for Flight Flutter Prediction, *J. Aircraft*, Vol.30, No.3, pp.395-402, 1993.
- 3) Matsuzaki, Y. and Ando, Y. : Estimation of Flutter Boundary from Random Responses due to Turbulence at Subcritical Speeds, *J. Aircraft*, Vol.18, No.10, pp.862-868, 1981.
- 4) Torii, H. and Matsuzaki, Y. : Flutter Margin Evaluation for Discrete-Time Systems, *J. Aircraft*, Vol. 38, No. 1, pp 42-47, 2001.
- 5) Bae, J. et al. : Extension of Flutter Prediction Parameter for Multimode Flutter Systems, *J. Aircraft*, Vol.42, No.1, pp.285-288, 2005.
- 6) McNamara, J. and Friedmann, P. : Flutter-Boundary Identification for Time-Domain Computational Aeroelasticity, *AIAA Journal*, Vol.45, No.7, pp.1546-1555, 2007.
- 7) Jury, I. E. Pavlidis, T. :Stability and aperiodicity constraints for system design, *Trans. Circuit Theory*, Vol.10, pp.137-141, 1963.
- 8) Collar, A. R. and Simpson, A. :Matrices and Engineering Dynamics, Ellis Horwood Ltd., London, 1987.

EXPERIMENTAL STUDY ON TURBULENCE PARTIAL SIMULATION FOR BLUFF BODY

Hiroshi Katsuchi⁺¹ and Hitoshi Yamada⁺²

⁺¹Yokohama National University, Yokohama, Japan

⁺²Yokohama National University, Yokohama, Japan

Wind-induced response/vibration of a bridge deck is governed by the surrounding flow field including flow separation and reattachment. It was also pointed out that the flow field is strongly affected by a small-scale turbulence component in an approaching flow. In wind-tunnel testing, in order to simulate turbulence effects, turbulence intensity is usually simulated. However the simulation of the power spectral density (PSD) of a small-scale turbulence component (high-frequency sub-inertia range), the so-called “turbulence partial simulation” may be a more rational way. In fact, past studies suggested that the turbulence partial simulation could give a better explanation for bridge deck vortex-induced vibration response between full scale and wind-tunnel test. In this study, using “reduced turbulence intensity”, the turbulence partial simulation was experimentally investigated for bluff-body structures. Results showed that reduced turbulence intensity could represent turbulence effects to the same degree as could turbulence intensity do. In addition, it was observed that a small-scale turbulence component governed the flow field around a bluff body.

Keyword: turbulence partial simulation, bluff body, small-scale turbulence, wind-tunnel test

1. INTRODUCTION

Wind-induced response/vibration of a bridge deck is governed by the surrounding flow field including flow separation and reattachment. It was also pointed out that the flow field is strongly affected by a small-scale turbulence component in an approaching flow¹⁾. In wind-tunnel testing, in order to simulate turbulence effects, simulation of turbulence intensity is practically adopted. However the simulation of the power spectral density (PSD) of a small-scale turbulence component (high-frequency sub-inertia range), the so-called “turbulence partial simulation” may be a more rational way. In fact, Irwin et al. suggested that the turbulence partial simulation could give a better explanation for bridge deck vortex-induced vibration response between full scale and wind-tunnel test^{2,3,4)}.

In this study, using “reduced turbulence intensity”, the turbulence partial simulation was experimentally investigated for bluff-body structures. For that purpose, more than 10 different turbulent flows with different intensity and integral scale were generated by grids. Then wind-tunnel tests were conducted for the following items. Measurement results were examined in terms of turbulence intensity, integral scale and reduced turbulence intensity.

- 1) Base pressure of rectangular cylinder ($B/D = 0.26 - 0.98$)
- 2) Surface pressure and static coefficient of bridge deck ($B/D = 5$ and 7.5)
- 3) Surface pressure and PIV test of rectangular cylinder ($B/D = 2$ and 3)

where B/D is slenderness ratio of bluff bodies.

2. TURBULENCE PARTIAL SIMULATION

Turbulence flow can be perfectly simulated in a wind tunnel if its PSD is simulated over all frequency range. However, due particularly to the wind-tunnel size, the turbulence scale generated in a wind tunnel is usually much smaller than that of full-scale turbulence. Therefore, it is very difficult to simulate the low-frequency part of that (large-scale turbulence) in a wind tunnel.

⁺¹katsuchi@ynu.ac.jp, ⁺²y-yamada@ynu.ac.jp

Small-scale turbulence affects flow fields around a bluff body and therefore it governs characteristics of cross-sectional aerodynamics. On the other hand, large-scale turbulence will decrease span-wise correlation and change mean wind speed, which will decrease the amplitude and probability of wind-induced vibration. Disregard of large-scale turbulence effects will therefore be practically conservative. Considering these, one can suggest that the simulation of PSD in a high-frequency part might give a good explanation of the full-scale behavior in a wind-tunnel test.

Assuming the Karman-type PSD function (Eq. 1) and considering the simulation of a high-frequency part of it, Eq. 1 is transformed to Eq. 2.

$$\frac{fS_u}{\sigma_u^2} = \frac{4(fL_u^x/U)}{(1 + 70.8(fL_u^x/U)^2)^{5/6}} \tag{1}$$

$$\frac{fS_u}{U^2} \equiv I_u^2 \left(\frac{f}{U}\right)^{-2/3} (L_u^x)^{-2/3} \tag{2}$$

where f is frequency, U is wind speed, I_u is turbulence intensity and L_u^x is turbulence scale.

Quantity f/U has an inverse dimension of length, then replacing f/U by $1/D$ (D : representative length) transforms Eq. 2 to Eq. 3. Therefore, simulating or equating a reduced PSD yields a similarity law as in Eq. 4.

$$\frac{fS_u}{U^2} = \left[\frac{I_u}{(L_u^x/D)^{1/3}} \right]^2 \tag{3}$$

$$\left(\frac{I_u}{I_u}\right)_m = \left(\frac{(L_u^x/D)_m}{(L_u^x/D)_p}\right)^{1/3} \tag{4}$$

where subscripts m and p represent model and prototype (full scale), respectively.

From Eq. 4, if a turbulence scale ratio to the structural dimension in a wind tunnel $(L_u^x/D)_m$ is by one order smaller than that in the full scale, the similarity requirement for the turbulence intensity in the wind tunnel will be about half of that in the full scale, as shown in Fig. 1. This turbulence similarity requirement (referred to turbulence partial simulation) was suggested by Irwin^{2, 4)} and pointed out that the full-scale measurement by Macdonald et al.³⁾ might prove this.

Based on Eq. 4, a new similarity parameter “reduced turbulence intensity” calculated by turbulence intensity divided by the cubic root of the turbulence scale ratio (L_u^x/D) is introduced as shown in Eq. 5. It is understood that the similitude of reduced turbulence intensity represents the turbulence partial simulation.

$$I_r = \frac{I_u}{(L_u^x/D)^{1/3}} \tag{5}$$

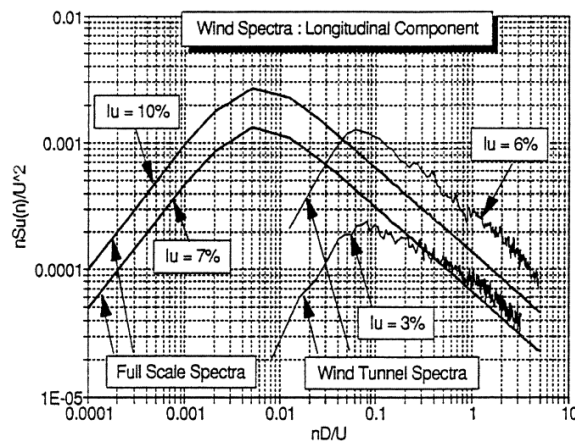


Figure 1: Turbulence partial simulation²⁾

3. BASE PRESSURE OF RECTANGULAR CYLINDER⁵⁾

(1) Base pressure coefficient

Wind-induced response of a bluff body is governed by the flow field around the body and it was thought that base pressure rather than the response would be sensitive to the change of the flow field and that base pressure coefficient would be a good indicator to judge whether the partial simulation is satisfied or not. Base pressure was compared under various combinations of turbulence properties (intensity and scale).

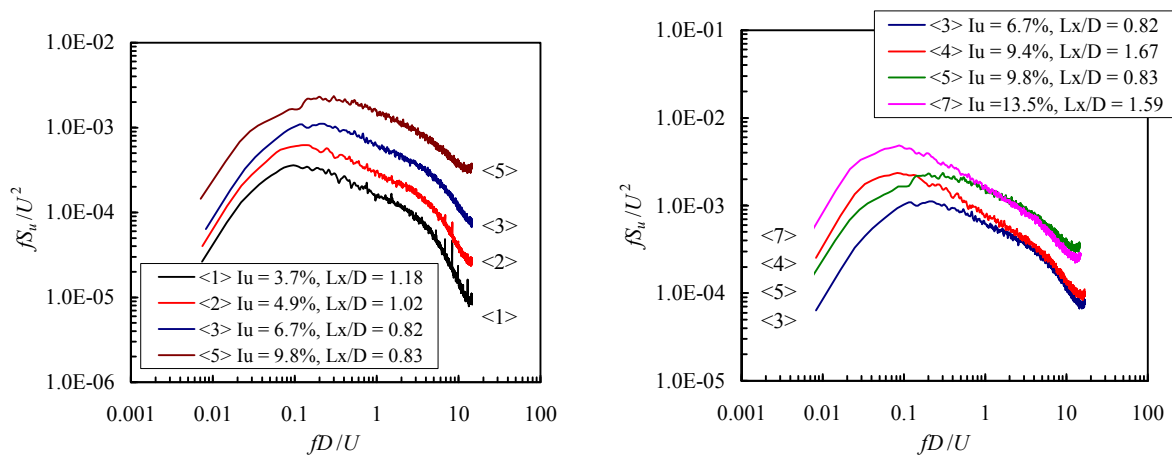
Table 1 shows the turbulence properties generated and Fig. 2 shows their PSD. Three different size of a rectangular cylinder (projection height $D = 3, 6$ and 9 cm) was used in order to cover the wide range of the turbulence scale ratio to the model size. Of those combinations with the different turbulences and model sizes in Table 1, two series of combinations were chosen to investigate the small-scale turbulence simulation. First series are different turbulence-intensity flows, PSDs of which do not coincide with each other as shown in Fig. 2(a). Second series are turbulence flows with the same PSD in a high-frequency part as shown in Fig. 2(b). After all, comparisons were made in model cases of $D = 9$ cm as shown in Table 1.

The base pressure was measured at a 100Hz sampling frequency for 300 seconds. The Reynolds number at the measurement was approximately 3.7×10^4 with respect to the model height D . In order to correct the wind-tunnel blockage effect, correction factors were obtained from the base-pressure measurement results of the different model size at each B/D ratio based on Ref. 6). For the sake of brevity, the base-pressure coefficient represents the corrected one hereinafter.

Table 1: Properties of turbulence generated

Turbulence intensity I_u (%)	Turbulence scale L_x (cm)	Ratio of turbulence scale and model scale (L_x / D)		
		$D = 3$ cm	$D = 6$ cm	$D = 9$ cm
3.7	10.6	3.53	1.77	1.18 <1>
4.9	9.2	3.07	1.53	1.02 <2>
6.7	7.4	2.47	1.23	0.82 <3>
9.4	15.0	5.0	2.50	1.67 <4>
9.8	7.5	2.50	1.25	0.83 <5>
10.8	16.6	5.53	2.77	1.84 <6>
13.5	14.3	4.77	2.38	1.59 <7>
Smooth	—	—	—	—

* The number in < > is referred to in Fig. 1.



(a) Different turbulence intensity series

(b) Small-scale turbulence simulation series

Figure 2: Power spectral density of wind-tunnel turbulence

Fig. 3 shows the comparisons of C_{pb} in turbulent flows with different turbulence intensities but close turbulence scale together with that in a smooth flow. Negative peak of C_{pb} at around 5.5 of B/D can be seen as pointed out by past studies^{7, 8)}. It can be seen that C_{pb} for B/D less than the critical value is not so much different but that C_{pb} at and larger than the critical value becomes large (to positive value) as the turbulence intensity becomes large. This may result from the enhancement of interaction of shear layers with small eddies around the cylinder by the increase of turbulence intensity. In addition, the critical slenderness ratio of B/D moves to lower B/D as the turbulence intensity increases.

Fig. 4 shows the comparisons of C_{pb} for partially simulated turbulences. As shown in Fig.2 (b), turbulences <3> and <4>, and <5> and <7> are pairs of turbulences with PSD simulated in a high-frequency part. These two pairs hold the relationship of Eq. 4. It can be seen that C_{pb} at and larger than the critical slenderness ratio of B/D is almost identical for the partially simulated turbulences. This fact proves that flow patterns around a rectangular cylinder can be simulated if turbulence is simulated in a high-frequency part, in other word, the turbulence partial simulation can be achieved. However C_{pb} in Figs. 3 and 4 covers B/D ranging from 0.26 to 0.98 which is much smaller than a typical value of a bridge deck ($B/D > 3$).

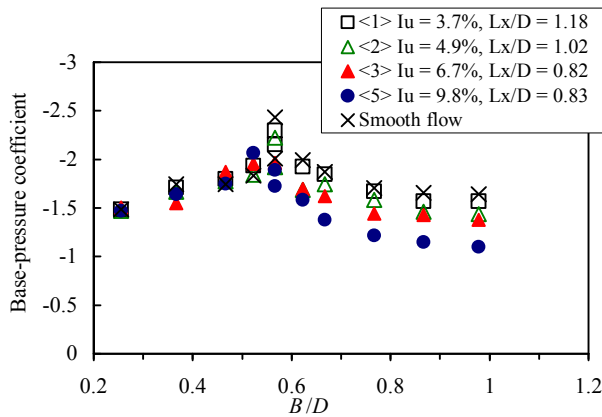


Figure 3: Comparison of C_{pb} in different turbulence intensity

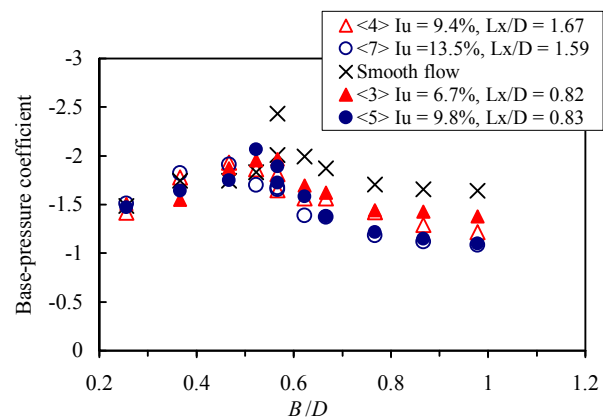


Figure 4: Comparison of C_{pb} in partially-simulated turbulence

(2) Reduced turbulence intensity

In order to investigate turbulence partial simulation quantitatively, base pressure of rectangular cylinders was measured similarly to the previous section (1) and examined by reduced turbulence intensity. PSDs of turbulences (1, 2 & 3), (4, 5 & 6) and (7 & 8) in a high-frequency part coincide as shown in Fig. 5 and they are partially simulated turbulence groups. Table 2 shows the reduced turbulence intensity for those turbulences. It can be recognized that reduced turbulence intensities for partially simulated turbulence groups have close values and therefore it can be an index of turbulence partial simulation.

Fig. 6 shows C_{pb} measured vs. slenderness ratios. It can be seen again that C_{pb} for partially simulated turbulence pairs fairly agree in a large slenderness ratio range. Fig. 7 shows C_{pb} vs. the reduced turbulence intensity where broken lines are linear regression lines. Results for the slenderness ratio greater than the critical value are only shown. It can be seen that C_{pb} changes linearly against the reduced turbulence intensity. It was also checked that C_{pb} has a linear relationship with turbulence intensity and turbulence scale as shown in Figs. 8 and 9, respectively. However, the degree of linear regression in cases of turbulence intensity and turbulence scale is less than the case of reduced turbulence intensity. Based on these observations, the effects of turbulence on the base pressure can be represented by reduced turbulence intensity and in turn the flow field around a rectangular cylinder can be simulated by the turbulence partial simulation method.

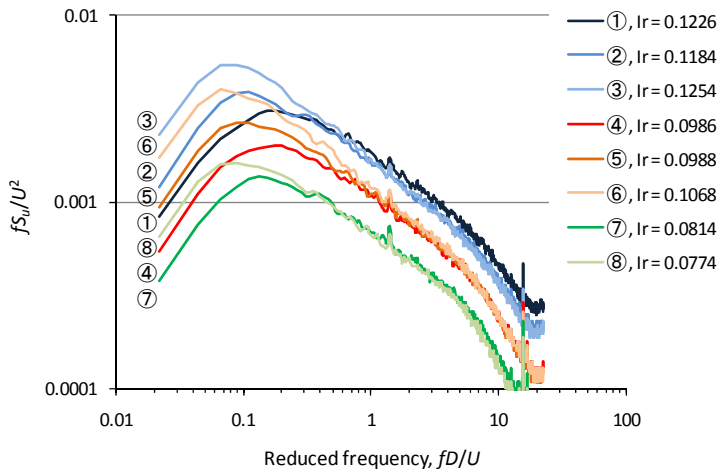


Figure 5: PSD of wind-tunnel turbulences

Table 2: Properties of turbulence flows

No.	I_u (%)	L_u^x (m)	I_r
①	11.11	0.067	0.1226
②	11.84	0.090	0.1184
③	13.76	0.119	0.1254
④	8.85	0.065	0.0986
⑤	9.99	0.093	0.0988
⑥	11.76	0.120	0.1068
⑦	7.23	0.063	0.0814
⑧	7.96	0.098	0.0774

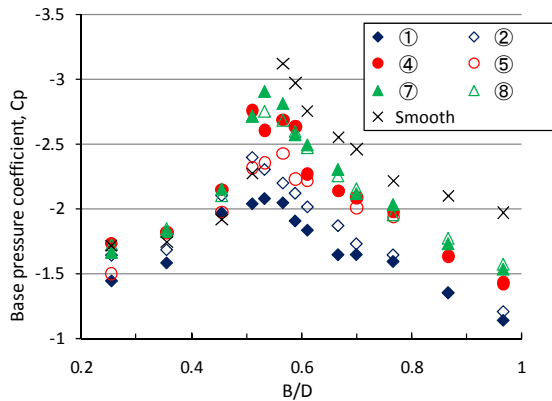


Figure 6: Base pressure coefficients vs. slenderness ratio

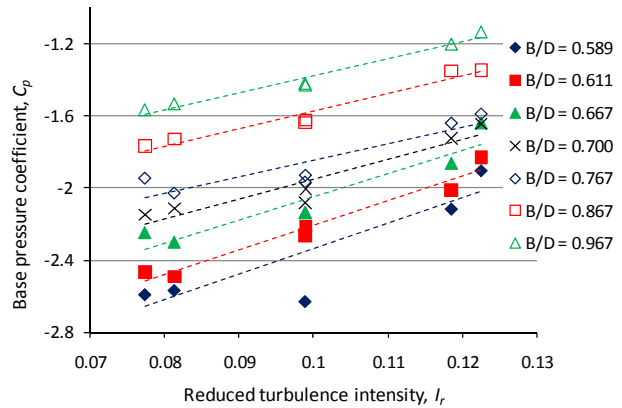


Figure 7: Base pressure coefficients vs. reduced turbulence intensity

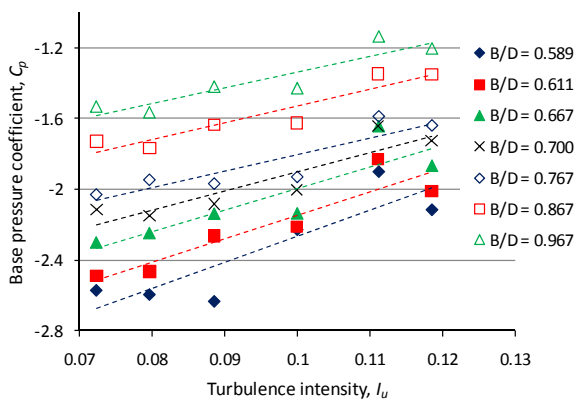


Figure 8: Base pressure coefficients vs. turbulence intensity

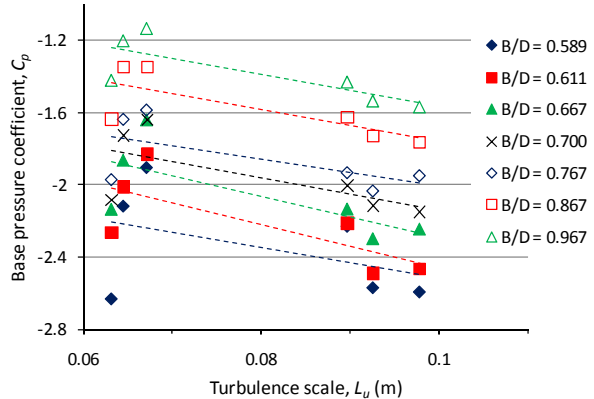


Figure 9: Base pressure coefficients vs. turbulence scale

4. SURFACE PRESSURE AND STATIC COEFFICIENT OF BRIDGE DECK⁹⁾

Turbulence partial simulation was also checked using a hexagonal bridge deck model as shown in Fig. 10. Two slenderness ratio models ($B/D = 5$ and 7.5 , $B = 0.3$ m) were tested. Surface pressures at 38 points were measured at a wind speed of 10 m/s in partially simulated turbulences as shown in Table 2 and Fig. 5. Fig. 8 shows the distribution of mean surface pressure coefficients for $B/D = 7.5$ model at 0 degree angle of

attack. Negative peak pressure was produced at just after the leading edge on the upper and lower surfaces. In addition, mean pressure coefficients are not so much different on leeward surfaces among different turbulence flows.

The negative peak pressure coefficients are plotted by reduced turbulence intensity, turbulence intensity and turbulence scale for $B/D = 7.5$ and 5 in Figs. 11 and 12, respectively. This is because the negative peak pressure represents a flow separation intensity, separation flow width and wind excitation force intensity. It can be seen that the negative peak pressure coefficients have the best linear relationship with reduced turbulence intensity. This implies that the flow field around the bridge deck can be simulated by the turbulence partial simulation, and that reduced turbulence intensity can be a simulation index.

Secondly, lift and pitching moment coefficients were calculated by integrating the surface pressures over the deck cross section in order to estimate the aerodynamic characteristics pseudo-dynamically. Figs. 13 and 14 show the slopes of lift and pitching moment coefficients at 0-degree angle of attack with reduced turbulence intensity, turbulence intensity and turbulence scale for $B/D = 7.5$ and 5 , respectively. The slope was calculated as an average slope between -4 to $+4$ degrees. The slope of pitching moment coefficient is insensitive to turbulences while that of lift coefficient has a weaker linear relationship with each turbulence parameter. However, there is no significant difference among three turbulence parameters. This may be due to the fact that surface pressure distribution is not so different except for neighborhood of the separation point. Contrarily to the negative peak pressure, superiority of reduced turbulence intensity to turbulence intensity or turbulence scale was not observed. However it can be understood that the reduced turbulence intensity as well as turbulence intensity will be an index of turbulence simulation.

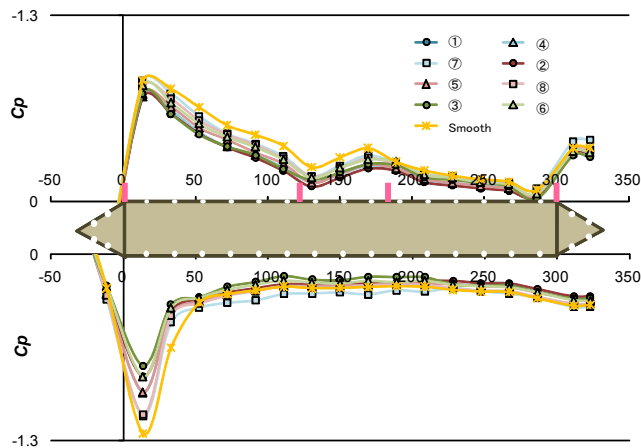


Figure 10: Bridge deck model and mean pressure distribution of $B/D = 7.5$

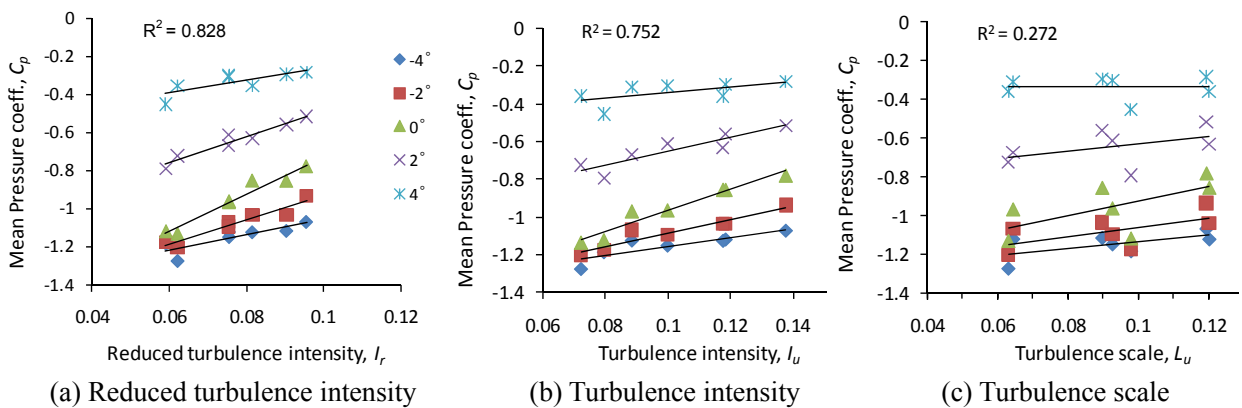
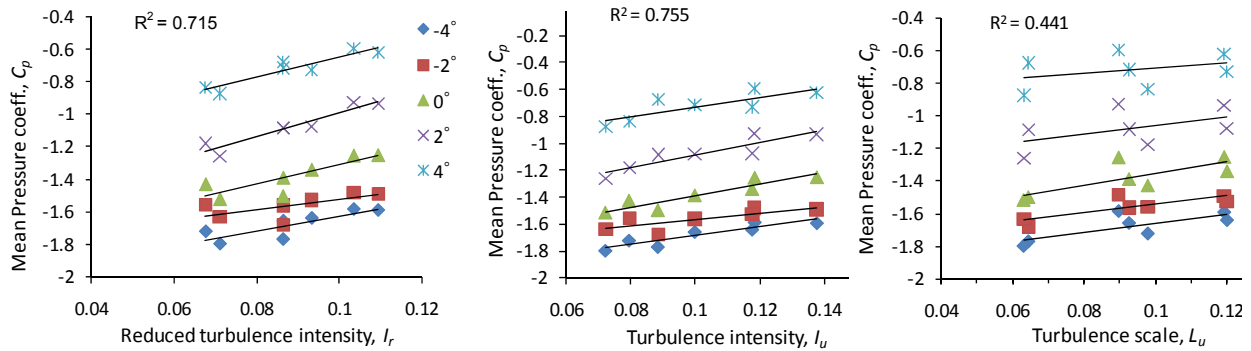
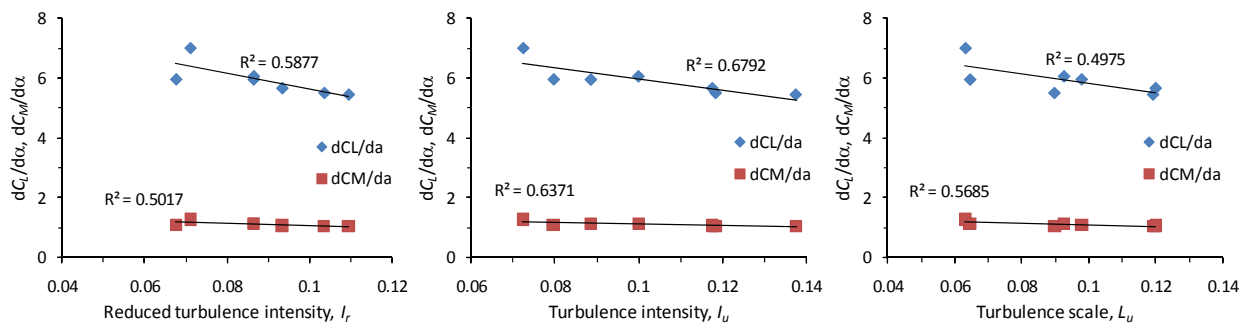


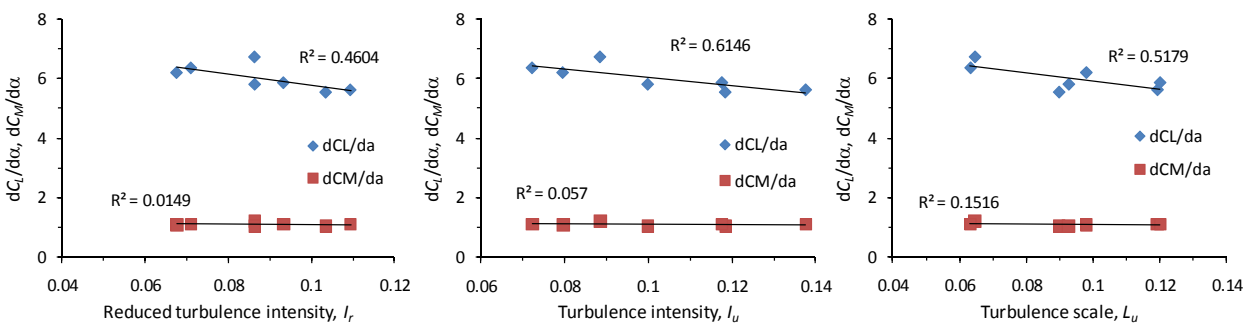
Figure 11: Negative peak pressure coefficient at separation point of lower surface for $B/D = 7.5$



(a) Reduced turbulence intensity (b) Turbulence intensity (c) Turbulence scale
 Figure 12: Negative peak pressure coefficient at separation point of lower surface for $B/D = 5$



(a) Reduced turbulence intensity (b) Turbulence intensity (c) Turbulence scale
 Figure 13: Slope of lift and pitching moment coefficient for $B/D = 7.5$



(a) Reduced turbulence intensity (b) Turbulence intensity (c) Turbulence scale
 Figure 14: Slope of lift and pitching moment coefficient for $B/D = 5$

5. SURFACE PRESSURE AND PIV TEST OF RECTANGULAR CYLINDER^{10, 11)}

(1) Surface pressure

In order to understand more clearly the effects of the turbulence parameters on flow field around bluff bodies, surface pressures of rectangular cylinders of $B/D = 2$ and 3 were measured in various turbulent flows. Results were examined by focusing on the reduced turbulence intensity. Measurement was taken at wind speeds of 6 and 9 m/s, which is equivalent to Reynolds number of $40,000$ and $60,000$, respectively.

Figs. 15 and 16 show mean surface pressure coefficient around rectangular cylinder of $B/D = 2$ and 3 , respectively. Surface pressures at the leading edge generally become smaller as the reduced turbulence intensity increases. On the other hand, surface pressures at the trailing edge become larger as the reduced turbulence intensity increases. This suggests that reattachment of the flow to the side surface is enhanced by turbulence. In addition, larger reduced turbulence intensity which is equivalent to larger small scale turbulence

enhances the reattachment trend. Furthermore, peak location of the mean surface pressure coefficient was identified by fitting a sixth order polynomial equation. The peak locations on both top and bottom surfaces shift to the leading edge as the reduced turbulence intensity increases. Therefore, reduced turbulence intensity might be the better representative index of flow field around a rectangular cylinder.

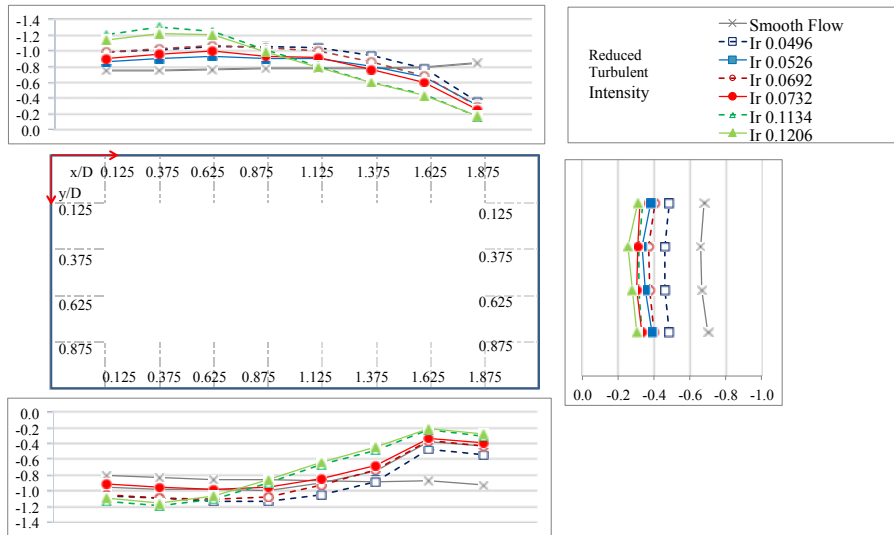


Figure 15: Mean surface pressure coefficients around a rectangular cylinder of $B/D = 2$

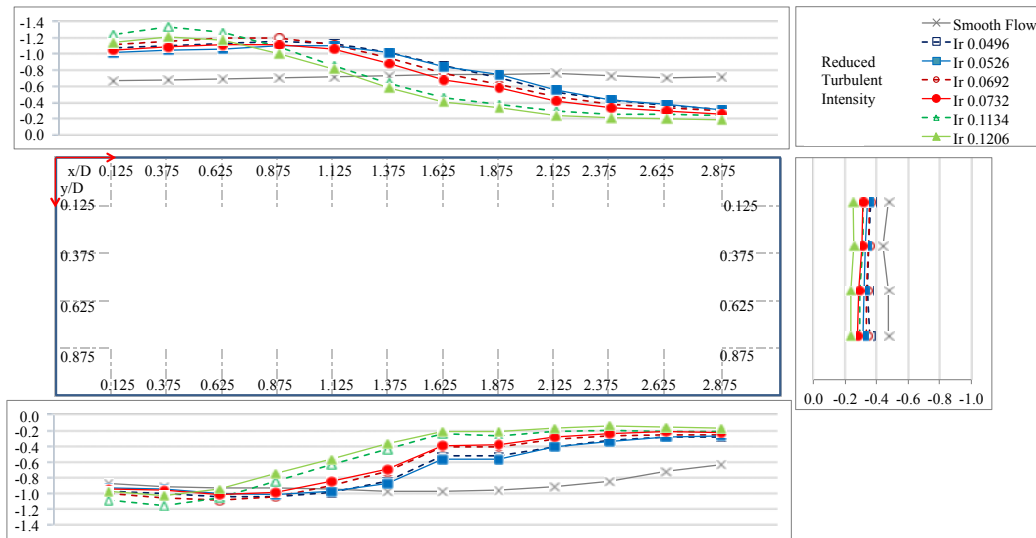


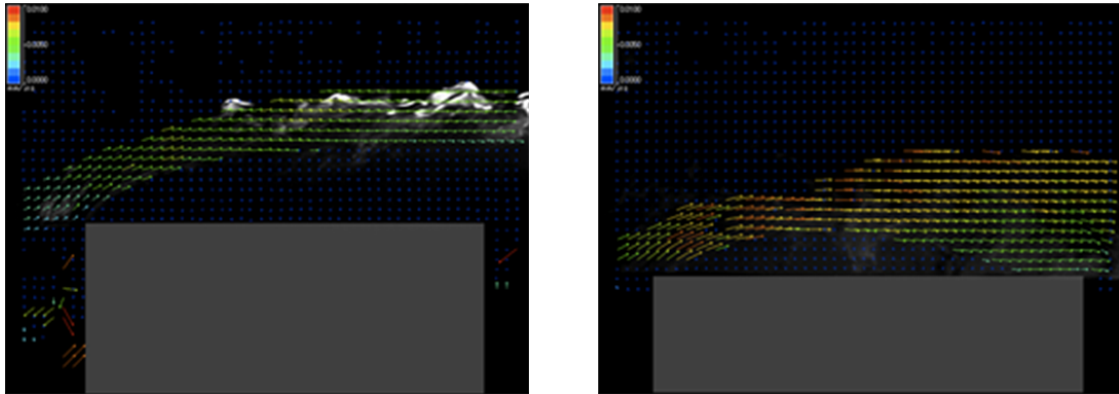
Figure 16: Mean surface pressure coefficients around a rectangular cylinder of $B/D = 3$

(2) PIV test

A PIV test was conducted to illustrate effects of small-scale turbulence on flow field around a rectangular cylinder. Measurement was done at wind speeds of 5 – 7 m/s, which is equivalent to Reynolds number of 52,500 – 73,500, respectively. Fig. 17 shows time-average velocity vector fields for a rectangular cylinder of $B/D = 3$. It can be seen that flow separates at the leading edge and does not reattach in a smooth flow case while flow reattaches at the trailing edge in a turbulent flow case.

Using this PIV test results, wind velocity data was taken and PSD was analyzed. Fig. 18 shows the peak frequency in PSD along the shear layer (shown by red circles) for different turbulent flows. Generally peak frequency increases near the leading edge while it decreases toward the trailing edge. Clear trend among

different turbulent flows is not observed, larger reduced turbulence intensity shows lower peak frequency, however. It can also be understood that higher frequency component of turbulence (small-scale turbulence) enhances flow reattachment near the leading edge.



(a) Smooth flow at 5m/s (b) Reduced turbulence intensity of 0.1206 at 6m/s

Figure 17: Time-average velocity vector field for rectangular cylinder of $B/D = 3$

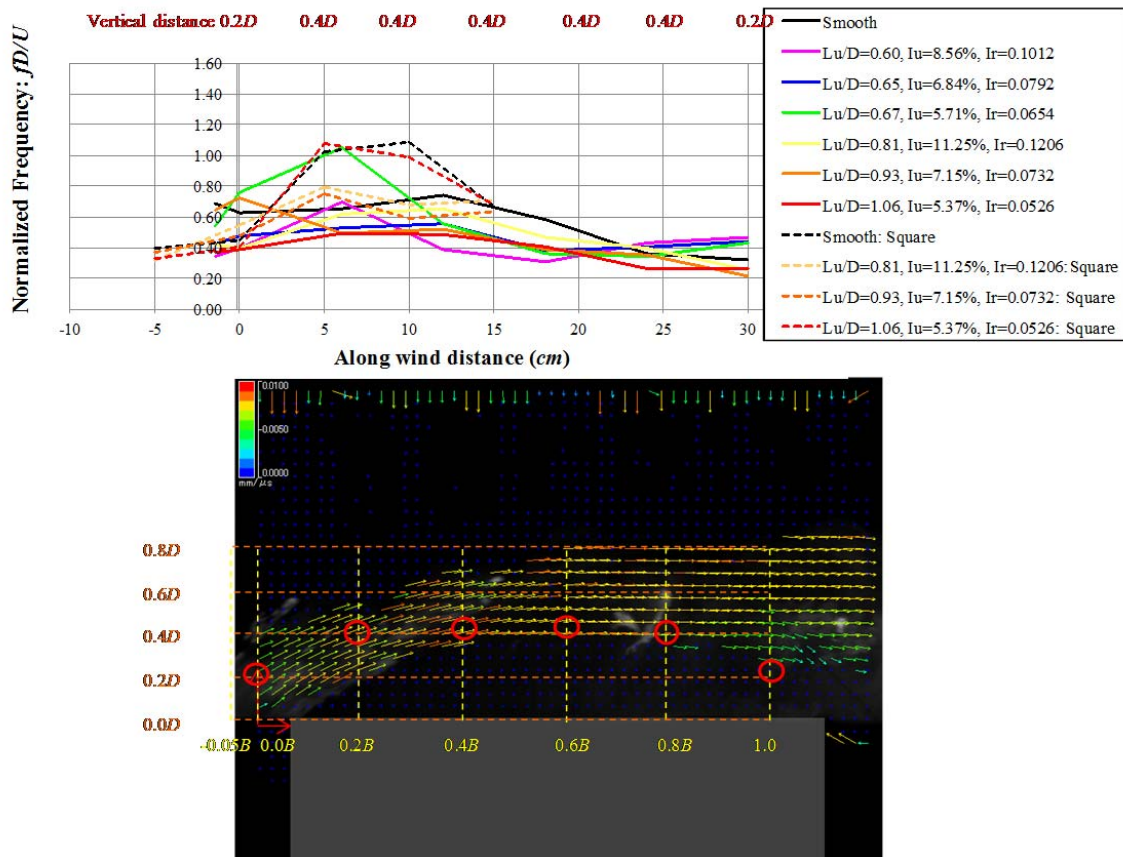


Figure 18: Variation of peak frequency in PSD of shear layer along-wind speed fluctuation

6. CONCLUSIONS

In this study, the turbulence partial simulation was experimentally investigated for three different bluff-body structures from the view point of “reduced turbulence intensity”. Results obtained are as follows:

Base pressure measurement of rectangular cylinder ($B/D = 0.26 - 0.98$) showed that the base pressure coefficients of a rectangular cylinder with and larger than the critical slenderness ratio fairly agree in partially-simulated turbulences.

Measurement of surface pressure and static coefficients of bridge deck ($B/D = 5$ and 7.5) showed that reduced turbulence intensity as well as turbulence intensity can represent a negative peak pressure of a hexagonal bridge deck. On the other hand, turbulence scale cannot represent it as can the reduced turbulence intensity do. Reduced turbulence intensity can also represent the slopes of static force coefficients of the bridge deck model as can turbulence intensity and turbulence scale do.

Surface pressure measurement and PIV test of rectangular cylinder ($B/D = 2$ and 3) showed that reattachment of the flow to the side surface is enhanced by turbulence. In addition, larger reduced turbulence intensity which is equivalent to larger small scale turbulence enhances the reattachment trend. It can also be understood from PIV test that higher frequency component of turbulence (small-scale turbulence) enhances flow reattachment near the leading edge.

Based on these observations, further study on reduced turbulence intensity should be conducted.

ACKNOWLEDGMENT

Wind-tunnel tests were carried out with great help by graduate students of those days. They are Mr. Yasuhiro Takaoka (Nippon Koei Co., Ltd.), Mr. Keisuke Takano (Kajima Corporation), Mr. Yasunori Aoki (Oriental Consultant Co., Ltd.), Dr. Panpipat Sangchuwong (Norciv Engineering). They are greatly appreciated.

REFERENCES

- 1) Nakamura, Y., Ohya, Y. and Watanabe, K., The effects of turbulence on the aerodynamic characteristics of two-dimensional rectangular cylinders, *Proc. of 8th National Symposium on Wind Engineering*, pp.249-254, 1984 (in Japanese).
- 2) Irwin, P. A., The role of wind tunnel modeling in the prediction of wind effects on bridges, *Proc. of the Int. Symp.: Advances in Bridge Aerodynamics*, Balkema, pp.99-117, 1998.
- 3) Macdonald, J. H. G., Irwin, P. A. and Fletcher, M. S., Vortex-induced vibrations of the Second Severn Crossing cable-stayed bridge – full scale and wind tunnel measurements, *Proc. of the ICE: Structures and Buildings*, SB152(2), 2002.
- 4) Irwin, P. A., Bluff body aerodynamic in wind engineering, *Proc. of BBAA V*, Ottawa, Canada, pp.51-57, 2004.
- 5) Yamada, H. and Katsuchi, H., Wind-tunnel study on effects of small-scale turbulence on flow patterns around rectangular cylinder, *Proc. of VI International Colloquium on Bluff Body Aerodynamics & Applications*, pp.64-67, Milano, Italy, 2008.
- 6) Nakamura, Y. and Ohya, Y., The effects of turbulence on the mean flow past two-dimensional rectangular cylinders, *J. Fluid Mechanics*, 149, pp.255-273, 1984.
- 7) Nakaguchi, H., Hashimoto, K. and Muto, S., An experimental study on aerodynamic drag of rectangular cylinders, *J. of Japan Society of Aero. Space Science*, 16, pp.1-5, 1968 (in Japanese).
- 8) Bearman, P. W. and Trueman, D. M., An investigation of the flow around rectangular cylinders, *Aeronautical Quarterly*, 23, pp.229-237, 1972.
- 9) Katsuchi, H. and Yamada, H., Study on turbulence partial simulation for wind-tunnel testing of bridge deck, *Proc. of 13th International Conference on Wind Engineering (CD-ROM)*, Amsterdam, 2011.7.
- 10) Panpipat Sangchuwong, Hitoshi Yamada, Hiroshi Katsuchi, Study on turbulence effects on flow fields around sharp-edged bluff bodies, *J. of Structural Engineering*, Vol.59A, JSCE, pp.627-636, 2013.3.
- 11) Sangchuwong, P., Yamada, H. and Katsuchi, H., Flow visualization study on effect of small-scale turbulence on flow fields around sharp-edge bluff bodies, *Proc. of 12th America Conference on Wind Engineering*, No.34.2, Seattle, USA, 2013.6.

EXPERIMENTS ON THE PFLÜGER COLUMN: FLUTTER FROM FRICTION

Davide Bigoni¹, Oleg Kirillov², Diego Misseroni¹, Giovanni Noselli³, Mirko Tommasini¹

¹DICAM, University of Trento, Trento, Italy

²Russian Academy of Sciences, Steklov Mathematical Institute, Moscow, Russia

³SISSA, International School for Advanced Studies, Trieste, Italy

Flutter and divergence instabilities are theoretically and experimentally analyzed in elastic structures with internal and external damping. Despite of the fact that only the former (and not the latter) was believed to be a destabilizing effect, it is theoretically demonstrated that the external damping plays a role similar to internal damping, so that both yield a pronounced destabilization paradox (in the Ziegler sense).

This finding and other features of the Beck and Pflüger columns are substantiated by an experimental campaign in which the follower forces are obtained via dry friction with a newly designed experimental apparatus.

Keyword: Pflüger column, Beck column, Ziegler destabilization paradox, damping, follower force

1. INTRODUCTION

Flutter and divergence instabilities may occur in elastic structures subject to tangential follower loads and well-known examples are the Ziegler double pendulum and the Beck¹⁾ and Pflüger²⁾ columns. A key point in these mechanical frameworks is the realization of the follower force, which has been long debated and often considered of impossible practical realization, as discussed in detail by Elishakoff³⁾.

The controversy about the realization of the force was definitively solved by Bigoni and Noselli⁴⁾, who showed how to realize a follower tangential force in the Ziegler pendulum via Coulomb friction. Their idea, sketched in Fig. 1, was to provide the follower force through a wheel of negligible mass mounted at the end of the Ziegler double pendulum and constrained to slide against a frictional plane.

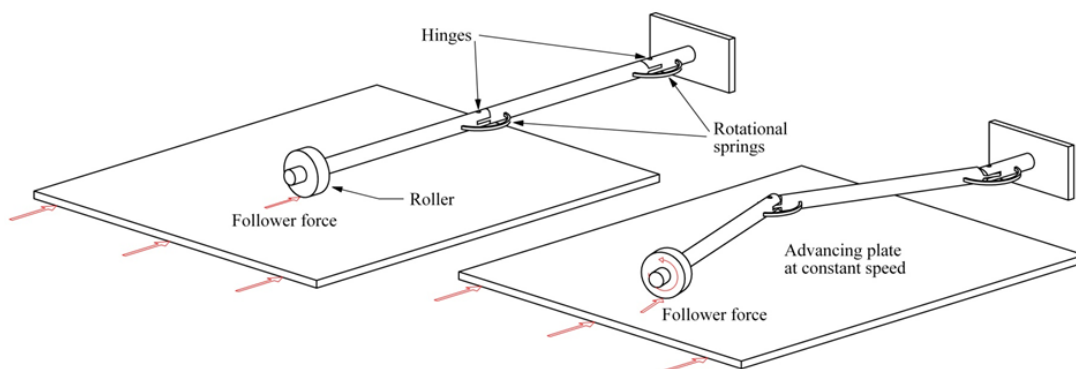


Figure 1: Sketch of the experiment set-up to realize a follower tangential force in the Ziegler double pendulum (figure adapted from [4]).

2. ZIEGLER'S PARADOX DUE TO INTERNAL AND EXTERNAL DAMPING

The linearized equations of motion for the Ziegler pendulum, made up of two rigid bars of length l , loaded by a follower force P , when both the internal and external damping are present, have the form⁵⁾

$$\mathbf{M}\ddot{\mathbf{x}} + c_i \mathbf{D}_i \dot{\mathbf{x}} + c_e \mathbf{D}_e \dot{\mathbf{x}} + \mathbf{K}\mathbf{x} = 0, \quad (1)$$

where a superimposed dot denotes time derivative and c_i and c_e are the coefficients of internal and external damping, respectively, in front of the corresponding matrices \mathbf{D}_i , \mathbf{D}_e

$$\mathbf{D}_i = \begin{pmatrix} 2 & -1 \\ -1 & 1 \end{pmatrix}, \quad \mathbf{D}_e = \frac{l^3}{6} \begin{pmatrix} 8 & 3 \\ 3 & 2 \end{pmatrix}, \quad (2)$$

and \mathbf{M} and \mathbf{K} are respectively the mass and the stiffness matrices, defined as

$$\mathbf{M} = \begin{pmatrix} m_1 l^2 + m_2 l^2 & m_2 l^2 \\ m_2 l^2 & m_2 l^2 \end{pmatrix}, \quad \mathbf{K} = \begin{pmatrix} -Pl + 2k & Pl - k \\ -k & l \end{pmatrix}, \quad (3)$$

in which k is the elastic stiffness of both viscoelastic springs acting at the hinges. Assuming a time-harmonic solution to the Eq. (1) in the form $\mathbf{x} = \mathbf{u} e^{\sigma t}$ and introducing the non-dimensional parameters

$$\lambda = \frac{\sigma l}{k} \sqrt{km_2}, \quad E = c_e \frac{l^2}{\sqrt{km_2}}, \quad B = \frac{c_i}{l\sqrt{km_2}}, \quad F = \frac{Pl}{k}, \quad \mu = \frac{m_2}{m_1}, \quad (4)$$

an eigenvalue problem is obtained, which eigenvalues λ are the roots of the characteristic polynomial.

In the undamped case, when $B = 0$ and $E = 0$, the pendulum is stable, if $0 \leq F \leq F_u^-$, unstable by flutter, if $F_u^- \leq F \leq F_u^+$, and unstable by divergence, if $F > F_u^+$, where

$$F_u^\pm(\mu) = \frac{5}{2} + \frac{1}{2\mu} \pm \frac{1}{\sqrt{\mu}} \quad (5)$$

In the case when only internal damping is present ($E = 0$) the Routh-Hurwitz criterion yields the flutter threshold as

$$F_i(\mu, B) = \frac{25\mu^2 + 6\mu + 1}{4\mu(5\mu + 1)} + \frac{1}{2} B^2. \quad (6)$$

The limit for vanishing internal damping is

$$\lim_{B \rightarrow 0} F_i(\mu, B) = F_i^0(\mu) = \frac{25\mu^2 + 6\mu + 1}{4\mu(5\mu + 1)}. \quad (7)$$

Let us evaluate the difference between the flutter onset in the absence of damping and that in the limit of vanishing internal damping: $\Delta_i = F_u^- - F_i^0$. We find that for all non-negative values of μ

$$\Delta_i = \frac{1}{4} \frac{\mu(5\sqrt{\mu} - 2)^2 + (2\sqrt{\mu} - 1)^2 + 6\mu}{\mu(5\mu + 1)} > 0. \quad (8)$$

Hence, the critical flutter load in the limit of vanishing internal damping is smaller than that of the undamped system for all physically possible mass distributions⁵. For instance, at $\mu = 0.5$ corresponding to the original Ziegler problem⁴, the drop in the critical load is

$$\Delta_i = \frac{57}{28} - \sqrt{2} \approx 0.622. \quad (9)$$

The discrepancy between the flutter onset in the ideal (undamped system) and in the dissipative system with the vanishing internal damping is known as the Ziegler destabilization paradox. Since its discovery, it is widely believed that such a dissipation-induced destabilization is a privilege of internal damping only⁵.

In a route similar to the above, by employing the Routh-Hurwitz criterion, the critical flutter load of the Ziegler pendulum with the external damping $F_e^0(\mu, E)$ can be found and its limit calculated when $E \rightarrow 0$, which provides the result

$$F_e^0(\mu) = \frac{122\mu^2 - 19\mu + 5 - (2\mu + 1)\sqrt{112\mu^2 + (13\mu - 5)^2}}{5\mu(8\mu - 1)}. \quad (10)$$

Calculating the discrepancy $\Delta_e = F_u^- - F_e^0$, we establish that at $\mu \geq 0$

$$\Delta_e = \frac{2(2\mu + 1)\sqrt{112\mu^2 + (13\mu - 5)^2} - (11\mu - 5)(4\mu - 3)}{10\mu(8\mu - 1)} - \frac{1}{\sqrt{\mu}} \geq 0. \quad (11)$$

For instance, $\Delta_e = (\sqrt{281} - 11)/20 \approx 0.288$ in the limit $\mu \rightarrow \infty$, corresponding to $m_2 = 0$, $m_1 \neq 1$. Consequently, the external damping yields destabilization and a finite drop in the critical flutter load for all mass distributions except a finite number of mass distributions at which $\Delta_e = 0$. Therefore, both internal and external damping leads to the qualitatively the same Ziegler's destabilization paradox for almost all physically plausible mass distributions, in contrast to the common belief. The same result is valid for the continuous analogue of the Ziegler pendulum – the Pflüger column loaded by the follower force⁸⁾.

2. THE EXPERIMENTAL REALIZATION OF THE BECK COLUMN

The experimental realization by Bigoni and Noselli was found unsuitable for the analysis of the Beck and the Pflüger columns, because if the ellipse of inertia of the cross-section of the rod to be tested is elongated, lateral torsional buckling occurs and if the ellipse of inertia of the cross-section of the rod is a circle, flexure involves large deformation, too large to produce the force necessary to flutter. Therefore, a new apparatus has been designed, following the scheme reported in Fig. 2 and realized.

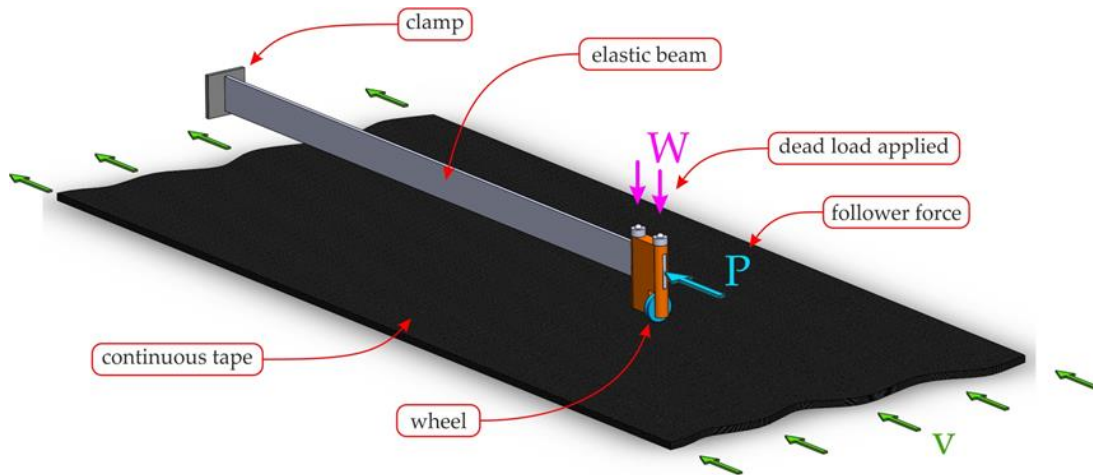


Figure 2: Sketch of the experimental setup to realize a follower tangential force in the Pflüger column.

The elastic structure is installed over a continuous tape that can move with a fixed velocity v . The force P is transmitted to the free end of the beam with a dead load W . The friction of the wheel with the tape generates the tangential follower force, as in the Ziegler model.

The new experimental setup allows the first realization of follower tangential forces on elastic structures and allows a systematic investigation of flutter, divergence, and dissipation-induced instabilities^{6,7)} changing the dead weight, the mass ratio or the velocity of the plane. In these experiments, internal and external damping (respectively the viscosity of the material and the air drag for instance) play a chief role, so that the effects associated to these two types of damping have been thoroughly investigated. From theoretical

point of view it is shown that external damping plays a destabilizing role qualitatively similar to internal damping⁸⁾, a feature previously not believed⁵⁾, and which is now also experimentally confirmed.

In Fig. 3 are shown the discrete system (Ziegler pendulum) and the continuous one (Pflüger column) mounted on the new testing machine realized.

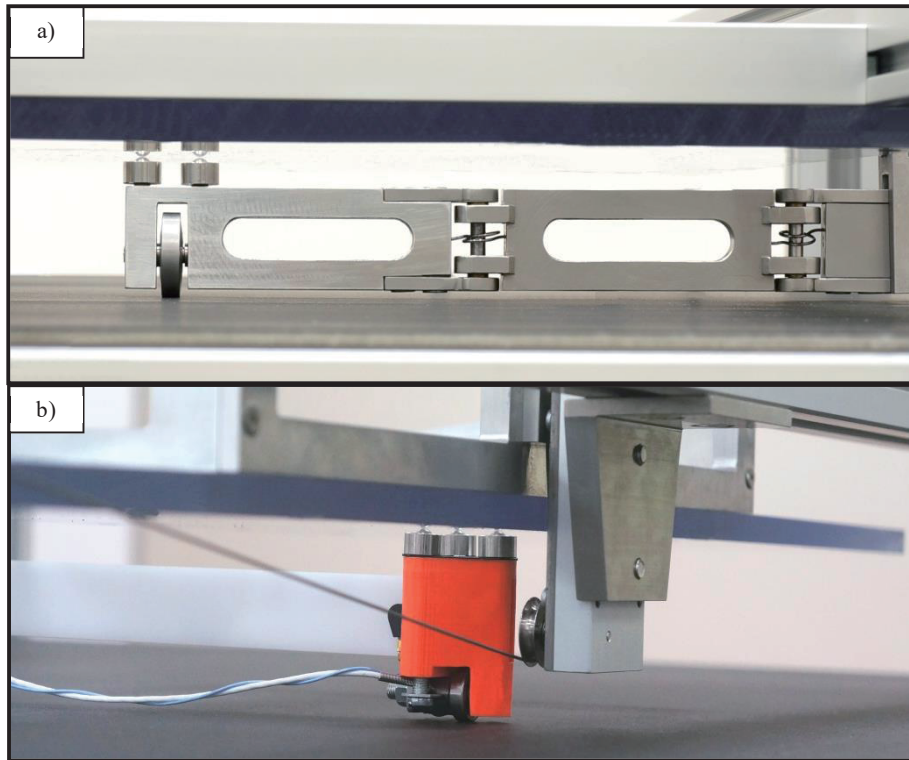


Figure 3: a) Ziegler column mounted on the experimental device, b) detail of the free end of the Pflüger column realized in the laboratory.

The Fig. 4 is a frame taken from a test with the new device. The beam shows clearly a flutter instability for a certain amount of load, and the amplitude of the motion depends on the velocity of the plane under the structure.



Figure 4: Deformed shape of the Pflüger column in flutter condition.

4. CONCLUSION

A theoretical framework and an experimental setup have been proposed for the investigation of flutter and divergence instabilities in elastic continuous structures, in the presence of internal and external damping. Results confirm recent a classical theoretical findings that were never experimentally verified and pave the way to the realization of self-oscillating mechanisms of completely new design.

ACKNOWLEDGEMENT

The authors gratefully acknowledge financial support from the ERC Advanced Grant ‘Instabilities and nonlocal multiscale modelling of materials’ FP7-PEOPLE-IDEAS-ERC-2013-AdG (2014-2019).

REFERENCES

- 1) Beck, M. Die Knicklast des einseitig eingespannten, tangential gedrückten Stabes. *Z. angew. Math. Phys.* 3:225, 1952.
- 2) Pflüger, A. Zur Stabilität des tangential gedrückten Stabes. *Z. angew. Math. Mech.* 35:191, 1955.
- 3) Elishakoff, I. Controversy associated with the so-called “follower force”: critical overview. *Appl. Mech. Rev.* 58:117-142, 2005.
- 4) Bigoni, D., Noselli, G. Experimental evidence of flutter and divergence instabilities induced by dry friction. *J. Mech. Phys. Solids* 59:2208–2226, 2011.
- 5) Panovko, Ya.G., Sorokin, S.V. Quasi-stability of viscoelastic systems with tracking forces. *Mech. Solids.* 22: 128-132, 1987.
- 6) Krechetnikov, R. Marsden, J.E. Dissipation-induced instabilities in finite dimensions. *Rev. Modern. Phys.* 79:519-553, 2007.
- 7) Kirillov, O.N. *Nonconservative stability problems of modern physics*. De Gruyter, Berlin/ Boston, 2013.
- 8) Tommasini, M., Kirillov, O., Misseroni, D., Bigoni, D. The destabilizing effect of external damping: Singular flutter boundary for the Pflüger column with vanishing external. *Submitted*.

WING FLUTTER COMPUTATION USING SPECTRAL VOLUME METHOD FOR HYBRID UNSTRUCTURED MESH

Yuta Sawaki⁺¹, Seiya Tateoka⁺² and Keisuke Sawada⁺³

Tohoku University, Sendai, Japan

Toward accurate prediction of transonic wing flutter phenomenon, an implicit spectral volume method is extended to employ the ALE formulation for moving and deforming grid, and unstructured hybrid meshes for higher computational efficiency. The developed aeroelastic analysis code is applied to compute the transonic flutter of the AGARD 445.6 wing and a rectangular unswept wing. In this study, modal structure analysis is employed. The eigen frequencies and mode shapes of each mode in a reference are employed for the AGARD 445.6 wing flutter analysis. For the rectangular wing flutter analysis, we make the structure plate model using NASTRAN. It is shown that the computed flutter speed index and flutter frequency agree well with the experimental data at subsonic freestream condition, and considering viscous effects improve the computed results in supersonic freestream regime for the AGARD 445.6 wing. In the rectangular flutter case, the flutter speed index at transonic dip cannot be obtained quantitatively. Accounting for viscous effects slightly improve the flutter speed index. On the other hand, the flutter frequency is significantly improved by solving RANS equations at the transonic dip condition compared with that obtained by Euler computation. The cause for this improvement is under consideration.

Keyword: CFD, Unstructured Mesh, Fluid-Structure Interaction

1. INTRODUCTION

Wing flutter is an aeroelastic phenomenon where excitation and deformation of wing become significant due to coupling of aerodynamic, elastic, and inertial forces¹⁾. Due to the strong demands for environmentally friendly aircrafts, new technologies, such as high-aspect-ratio wings and high-bypass geared turbofan engines are employed to realize low fuel burn, low noise and low emission. These heavier engines may cause flutter in combination with high-aspect-ratio wings because of low bending and torsional stiffness. Because flutter can lead to destruction of wing, accurate aeroelastic analyses of wing flutter are very important for design of recent commercial airplanes which fly through transonic flow regime where dynamic pressure is large.

In numerical analyses of wing flutter, the doublet-lattice method (DLM)²⁾ coupled with structural code is efficiently employed but it provides poor accuracy in transonic flowfields where shock waves emerge. Use of high fidelity CFD methods in aeroelastic analyses is really desired to take the nonlinear effects into account so far as the computational cost remains acceptable for aircraft design routines.

Arizono et al.³⁾ conducted experiments and numerical analyses of flutter for wing-pylon-nacelle configuration. They used Euler solver in numerical analyses and rough trends of flutter boundaries are estimated. Morino et al.⁴⁾ also calculated flutter for wing-pylon-nacelle configuration using reduced-order model (ROM) compared with full-order inviscid CFD. These researches show the two types of flutter trend for wing-pylon-nacelle configuration; mild flutter (hump mode) observed in transonic regime including transonic dip and hard flutter observed in high Mach number. These trends should be accurately predicted for real aircraft development, so higher spatial accuracy and geometrical flexibility are important for flutter computations around such complicated real configuration. Unstructured CFD methods surely provide geometrical flexibility, but generally their spatial accuracy seems insufficient.

In a couple of decades, a lot of high-order unstructured mesh methods are developed and improved.

⁺¹sawaki@cfm.mech.tohoku.ac.jp, ⁺²tateoka@cfm.mech.tohoku.ac.jp, ⁺³sawada@cfm.mech.tohoku.ac.jp

Discontinuous Galerkin (DG) method⁵⁾ is the most widely used high-order numerical method employing finite element discretization. Spectral Volume (SV) method⁶⁾ is based on the idea of subdividing each computational cell into sub-cells employing finite volume discretization. Flux Reconstruction (FR) method⁷⁾ is the latest high-order numerical method amounts to evaluating the straightforward derivative of a piecewise polynomial with correction at the cell interface employing finite difference discretization. In this study, we employ SV method because hierarchical cell structure can be utilized for h -adaptive strategy and sub-cell-based shock capturing⁸⁾. In flutter analyses, the level of flutter boundary and transonic dip depends on the shock wave location, so numerically capturing the shock wave has great significance. In the conventional SV method, for a second-order of spatial accuracy, as many as four degrees of freedom (DOFs) are introduced into a tetrahedral cell to reconstruct a linear polynomial of dependent variables. A tetrahedral cell volume is divided into four sub-cells and the conservative variables in these sub-cells correspond the DOFs. The time evolution of these DOFs in each cell is computed. For high Reynolds number flowfields, thin boundary layer needs to be resolved. In order to reduce the number of computational cells and also to retain the spatial accuracy of the conventional finite volume methods, it is customary to employ prismatic cell layers on the solid wall. Although the spatial accuracy of the second-order SV method is strictly retained even for skewed tetrahedral computational cells, we proposed to formulate the SV discretization for prismatic computational cells to reduce the total number of computational cells in the boundary layer region⁹⁾. Moreover, in flutter analyses, we need to compute flowfields using moving and deforming meshes. The arbitrary Lagrangian-Eulerian (ALE) method solving the geometric conservation law (GCL)¹⁰⁾ is implemented in the present SV code.

In section 2, the details of the present aeroelastic analysis code based on the spectral volume discretization is described. In section 3, the computed results using the developed aeroelastic code are shown for the AGARD 445.6 wing flutter and the rectangular wing flutter. Finally we summarize the present study in section 4.

2. NUMERICAL METHOD

(1) Arbitrary Lagrangian-Eulerian (ALE) form

The unsteady, three-dimensional, compressible Navier-Stokes equations in the conservative form can be expressed as

$$\frac{\partial \mathbf{Q}}{\partial t} + \nabla \cdot \mathbf{F}(\mathbf{Q}) - \nabla \cdot \mathbf{F}_v(\mathbf{Q}, \nabla \mathbf{Q}) = 0, \quad (1)$$

where \mathbf{Q} represents the vector of conservative variables, \mathbf{F} the vectors of inviscid fluxes, and \mathbf{F}_v the vectors of viscous fluxes. Integration of Eq. 1 over a moving and deforming control volume $\Omega(t)$ yields

$$\int_{\Omega} \frac{\partial \mathbf{Q}}{\partial t} dV + \int_{\partial \Omega} (\mathbf{F} - \mathbf{F}_v) \cdot \mathbf{n} dS = 0. \quad (2)$$

Applying the differential identity to the time derivative term gives

$$\frac{\partial}{\partial t} \int_{\Omega} \mathbf{Q} dV = \int_{\Omega} \frac{\partial \mathbf{Q}}{\partial t} dV + \int_{\partial \Omega} \mathbf{Q} \{\dot{\mathbf{x}} \cdot \mathbf{n}\} dS, \quad (3)$$

where $\dot{\mathbf{x}}$ and \mathbf{n} denote the grid velocity and the unit normal vector of the surface, respectively. Substituting Eq. 3 into Eq. 2, we obtain

$$\frac{\partial}{\partial t} \int_{\Omega} \mathbf{Q} dV + \int_{\partial \Omega} (\mathbf{F} - \mathbf{F}_v - \mathbf{Q}\dot{\mathbf{x}}) \cdot \mathbf{n} dS = 0. \quad (4)$$

Assuming that $\bar{\mathbf{Q}}$ represents the cell-averaged values, Eq. 4 becomes

$$\frac{\partial}{\partial t} (V\bar{\mathbf{Q}}) = - \int_{\partial \Omega} (\mathbf{F} - \mathbf{F}_v - \mathbf{Q}\dot{\mathbf{x}}) \cdot \mathbf{n} dS, \quad (5)$$

$$\frac{\partial \bar{\mathbf{Q}}}{\partial t} V + \frac{\partial V}{\partial t} \bar{\mathbf{Q}} = - \int_{\partial \Omega} (\mathbf{F} - \mathbf{F}_v - \mathbf{Q} \dot{\mathbf{x}}) \cdot \mathbf{n} dS, \quad (6)$$

$$\frac{\partial \bar{\mathbf{Q}}}{\partial t} + \frac{\partial V}{\partial t} \frac{\bar{\mathbf{Q}}}{V} = \mathbf{R}, \quad (7)$$

where we define the residual operator

$$\mathbf{R} = - \frac{1}{V} \int_{\partial \Omega} (\mathbf{F} - \mathbf{F}_v - \mathbf{Q} \dot{\mathbf{x}}) \cdot \mathbf{n} dS \quad (8)$$

for convenience.

(2) Geometric Conservation Law (GCL)

Assuming that \mathbf{Q} is constant over the entire domain, we obtain

$$\frac{\partial V}{\partial t} = \int_{\partial \Omega} (\dot{\mathbf{x}} \cdot \mathbf{n}) dS. \quad (9)$$

This relation indicates the geometric conservation law¹⁰⁾ in which the time derivative of cell volume is coincides with the surface integral of projected grid velocity. In the finite volume discretization, in order to satisfy Eq. 9, the projected grid velocity at each cell interface is evaluated by

$$\dot{\mathbf{x}} \cdot \mathbf{n} = \left(\frac{\partial V}{\partial t} \right) / S, \quad (10)$$

where S represents the area of cell interface and $\partial V / \partial t$ the volume extruded by the surface in Δt .

(3) Spectral volume formulation

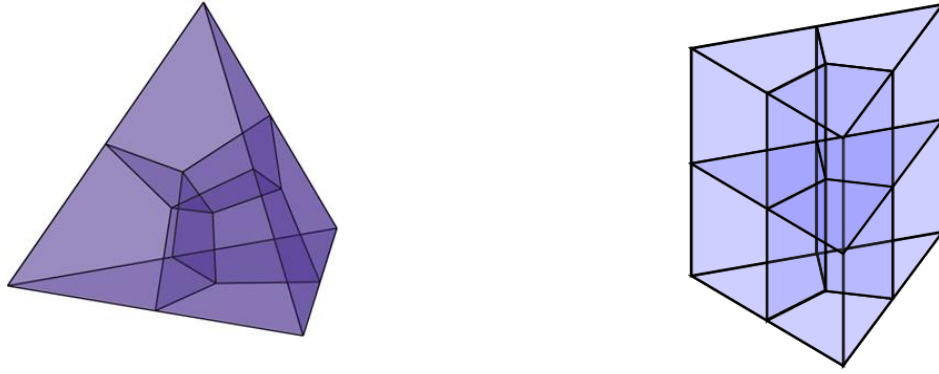
In the SV method, a computational cell referred to as the SV cell is partitioned into a set of sub-cells referred to as the control volume (CV) cells. The conservative variables in these CV cells correspond to the degrees of freedom (DOFs) in the spectral volume formulation. When a second-order scheme is considered, four CV cells in a tetrahedral cell¹¹⁾ and six CV cells in a prismatic cell⁹⁾ are used to reconstruct a linear distribution of the dependent variables in a SV cell. The partitions of the tetrahedral cell and prismatic cell are shown in Fig. 1. Let us denote the CV cell-averaged conservative variables in j -th CV cell within a SV cell as $\bar{\mathbf{Q}}_j$. The reconstructed variables in an arbitrary location within a SV cell can be expressed by

$$\mathbf{Q}(\vec{r}, t) = \sum_{j=1}^N L_j(\xi, \eta, \zeta) \bar{\mathbf{Q}}_j(t), \quad (11)$$

where L_j denotes the shape function for j -th CV cell, and N the number of CV cells in each SV cell. This shape function satisfies the following orthogonal relations

$$\frac{1}{V_j} \int_{CV_j} L_k(\xi, \eta, \zeta) dV = \delta_{j,k} \quad (j, k = 1, \dots, N), \quad (12)$$

where $\delta_{j,k}$ represents the Kronecker's delta function. Because \mathbf{Q} in Eq. 11 are cell-wise polynomials, they become discontinuous at the SV cell interface. The numerical flux functions at the cell interface are determined by an approximate Riemann solver. In this study, we employ SLAU scheme¹²⁾ which is one of the AUSM-family. When the computational meshes are moving and deforming, a modified SLAU scheme¹³⁾ taking the grid velocity into account is utilized. Viscous flux functions are computed using BR2 formulation by Bassi and Rebay¹⁴⁾. Flux functions at the interface of two adjacent CV cells inside a SV cell are analytically obtained because reconstructed variables are continuous there.



(a) Tetrahedral SV

(b) Prismatic SV

Figure 1: Partitions of tetrahedral and prismatic SV cells.

(4) LU-SGS implicit method

The lower-upper symmetric Gauss-Seidel (LU-SGS) implicit method¹⁵⁾ is employed in the time integration. From Eq. 7, the first-order fully implicit scheme is expressed as

$$\frac{\bar{Q}_c^{n+1} - \bar{Q}_c^n}{\Delta t} + \frac{V^{n+1} - V^n}{\Delta t} \frac{\bar{Q}_c^{n+1}}{V^{n+1}} = \mathbf{R}_c(\bar{Q}^{n+1}), \quad (13)$$

where the subscript c denotes the current SV cell. In Eq. 13, $\partial V/\partial t$ is evaluated in first-order. We note that the number of components of vectors \bar{Q}_c and \mathbf{R}_c is given as the product of the number of dependent variables and the number of DOFs in a SV. Because \mathbf{R}_c depends not only on \bar{Q}_c but also on \bar{Q}_{nb} in the neighbor cells through the numerical fluxes, a linearization of the residual yields

$$\mathbf{R}_c(\bar{Q}^{n+1}) \approx \mathbf{R}_c(\bar{Q}^n) + \frac{\partial \mathbf{R}_c}{\partial \bar{Q}_c} \Delta \bar{Q}_c + \sum_{nb \neq c} \frac{\partial \mathbf{R}_c}{\partial \bar{Q}_{nb}} \Delta \bar{Q}_{nb}. \quad (14)$$

Substituting Eq. 14 into Eq. 13 gives

$$\left(\dot{V}_{\text{ratio}} + \frac{I}{\Delta t} - \frac{\partial \mathbf{R}_c}{\partial \bar{Q}_c} \right) \Delta \bar{Q}_c - \sum_{nb \neq c} \frac{\partial \mathbf{R}_c}{\partial \bar{Q}_{nb}} \Delta \bar{Q}_{nb} = \mathbf{R}_c(\bar{Q}^n) - \dot{V}_{\text{ratio}} \bar{Q}_c^n, \quad (15)$$

where \dot{V}_{ratio} denotes the ratio of time derivative of cell volume $\partial V/\partial t$ to the latest cell volume. In order to avoid storing the Jacobian matrices for the “nb” cells, inner iterations are further introduced. Equation 13 can be rewritten using inner sweep number k as

$$\frac{\bar{Q}_c^{k+1} - \bar{Q}_c^k}{\Delta t} + \frac{V^{k+1} - V^k}{\Delta t} \frac{\bar{Q}_c^{k+1}}{V^{k+1}} = \mathbf{R}_c(\bar{Q}^{k+1}). \quad (16)$$

Linearization of the residual in terms of the current cell yields

$$\mathbf{R}_c(\bar{Q}^{k+1}) = \mathbf{R}_c(\bar{Q}_c^{k+1}, \bar{Q}_{nb}^{k+1}) \approx \mathbf{R}_c(\bar{Q}_c^k, \bar{Q}_{nb}^{k+1}) + \frac{\partial \mathbf{R}_c}{\partial \bar{Q}_c} (\bar{Q}_c^{k+1} - \bar{Q}_c^k). \quad (17)$$

Substituting Eq. 17 into Eq. 16, we obtain

$$\begin{aligned} \left(\dot{V}_{\text{ratio}} + \frac{I}{\Delta t} - \frac{\partial \mathbf{R}_c}{\partial \bar{Q}_c} \right) (\bar{Q}_c^{k+1} - \bar{Q}_c^k) &= \mathbf{R}_c(\bar{Q}_c^k, \bar{Q}_{nb}^{k+1}) - \frac{\bar{Q}_c^k - \bar{Q}_c^n}{\Delta t} - \dot{V}_{\text{ratio}} \bar{Q}_c^n \\ &\approx \mathbf{R}_c(\bar{Q}_c^k, \bar{Q}_{nb}^*) - \frac{\bar{Q}_c^k - \bar{Q}_c^n}{\Delta t} - \dot{V}_{\text{ratio}} \bar{Q}_c^n, \end{aligned} \quad (18)$$

in which we replace \bar{Q}_{nb}^{k+1} by the latest solution \bar{Q}_{nb}^* in the neighbor cells. The solutions are updated with multiple symmetric forward and backward sweeps in the domain. If a higher-order time accuracy is needed, the second-order backward difference formula (BDF2) is employed to evaluate $\partial Q/\partial t$ and $\partial V/\partial t$.

3. FLUTTER ANALYSES AND DISCUSSIONS

(1) AGARD 445.6 wing

The AGARD 445.6 weakened model flutter cases are computed using the developed aeroelastic SV code accounting for hybrid unstructured meshes and fluid-structure interaction. A tightly coupling method is employed in which the temporal evolution of the flowfield and structural deformation of the wing are alternately solved with several inner iterations within one time step. The computational conditions follow those of experiment described by Yates¹⁶⁾. The angle of attack is 0 [deg]. The freestream Mach numbers are 0.499, 0.678, 0.901, 0.960, 1.072, and 1.141. The Reynolds number based on the mean aerodynamic chord (MAC) length is about one million. The structure model of Yates¹⁶⁾ having 10×10 elements shown in Fig. 2 is used in which three bending modes and two twisting modes of the wing are considered in the modal analysis. This model is a plate model. The eigen frequencies of this model are summarized in Tab. 1. In the structural calculation, the eigen frequencies of each modes and modal shape data at all grid points of each modes are needed.

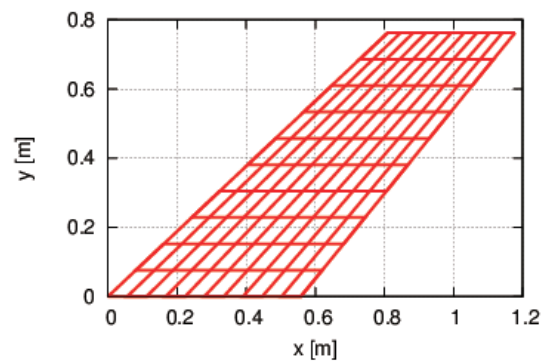
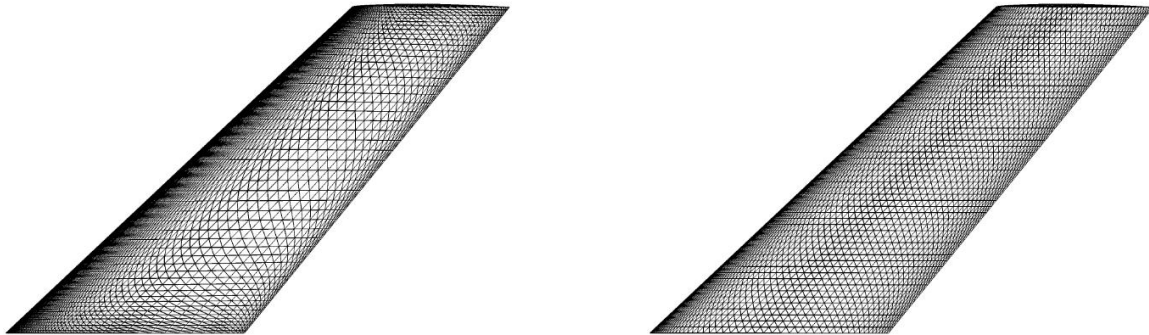


Figure 2: Structure model for the AGARD 445.6 wing by Yates¹⁶⁾.

Table 1: Eigen frequencies used in calculations and experimental data for the AGARD 445.6 wing.

Mode		1st (Bending)	2nd (Torsion)	3rd (Bending)	4th (Torsion)	5th (Bending)
Eigen frequency [Hz]	Yates's model ¹⁶⁾	9.6	38.2	48.3	91.5	118.1
	Experiment	9.6	38.1	50.7	98.5	–

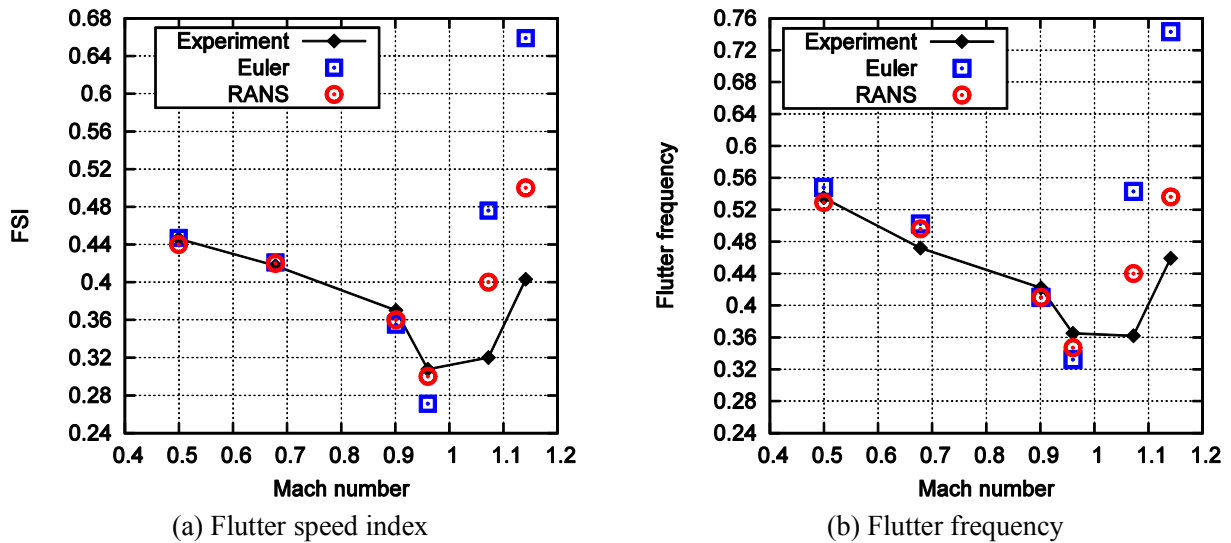
The computational surface meshes are shown in Fig. 3. In the Euler computation, 193,068 tetrahedral cells are used. In the RANS calculation, 178,278 tetrahedral cells and 310,464 prismatic cells (24 layers) are employed in which the minimum grid spacing on the wall satisfies $y^+ \leq 2$ for all flow conditions. The Spalart-Allmaras turbulence model¹⁷⁾ (SA noft2) is used in the RANS computation. The outer boundary of the computational domain is located at 30 MAC length from the wing surface. In the present aeroelastic calculations, the computational mesh moves and deforms according to the structure displacement. Mesh deformation at each iteration is accomplished by using interpolation method utilizing the inverse distance weighting function. In the implicit time integration, the BDF2 is employed. The inner iterations are continued till the L1 norm of density computed by using all residuals in the entire domain less than 10^{-7} . The number of inner iterations is typically eight when Δt is 0.005 in the Euler computation. In the RANS computation, the number of inner iterations is less than 30 for Δt of 0.05. The unsteady flow calculation starts from the steady flowfield solution with a small oscillation enforced in the first bending mode.



(a) Mesh for Euler computations

(b) Mesh for RANS computations

Figure 3: Computational surface meshes for the AGARD 445.6 wing.



(a) Flutter speed index

(b) Flutter frequency

Figure 4: Flutter boundary values for the AGARD 445.6 wing.

The flutter boundaries computed in this study are shown with experimental data in Fig. 4. The horizontal axis represents the freestream Mach number and the vertical axis the flutter speed index (FSI) in Fig. 4(a), and the flutter frequency in Fig. 4(b), respectively. The FSI is expressed by

$$FSI = \frac{U_\infty}{b_s \omega_a \sqrt{\mu}} \quad (19)$$

where U_∞ denotes the freestream velocity, b_s the half root chord length, ω_a the eigen angular frequency of the first torsion, and μ the fluid-to-structure mass ratio. The flutter frequency is expressed by ω/ω_a where ω denotes the frequency at the flutter boundary point. The calculated flutter boundary shows good agreements with experimental data in the Euler computation as well as the RANS computation so far as the

freestream is subsonic and no shock wave appears on the wing surface. The “transonic dip” is successfully obtained in which the shock wave appears. However, some distinctions between the computed flutter boundary values and those of experiment become evident at supersonic freestream conditions. We note that results in RANS computations give closer agreements with experimental data than those in Euler computations. This implies that the distinctions seen in the supersonic freestream cases are caused by possible shock boundary layer interaction near the trailing edge, which the Euler calculation cannot account for. The pressure coefficient contours obtained by steady inviscid simulations are plotted on the wing surface as shown in Fig. 5.

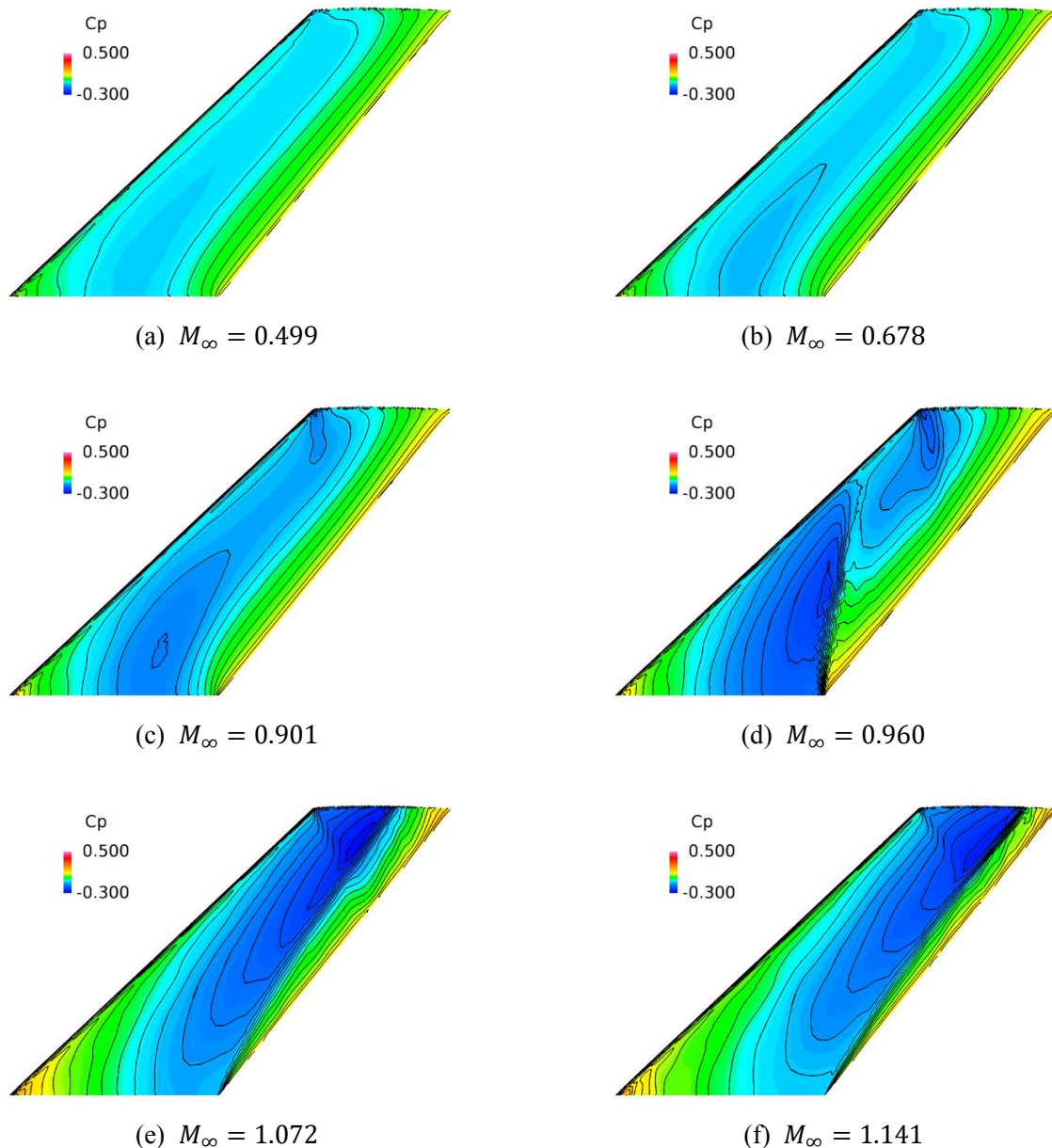


Figure 5: Pressure coefficient contours for steady inviscid flowfields over the AGARD 445.6 wing.

When the freestream Mach number becomes 0.96 or higher, a strong shock wave appears on the wing which moves toward the trailing edge as the freestream Mach number increases. The pressure coefficients at several spanwise cross-sections computed by both the Euler and the RANS calculations are plotted in Fig. 6. The difference in C_p distribution between these simulations becomes apparent when a shock wave emerges in the

freestream Mach number above 0.96 where significant shock boundary layer interaction begins to take place. Indeed, the pressure coefficients show smooth profiles at the shock location when viscous effects are taken into account in the simulation.

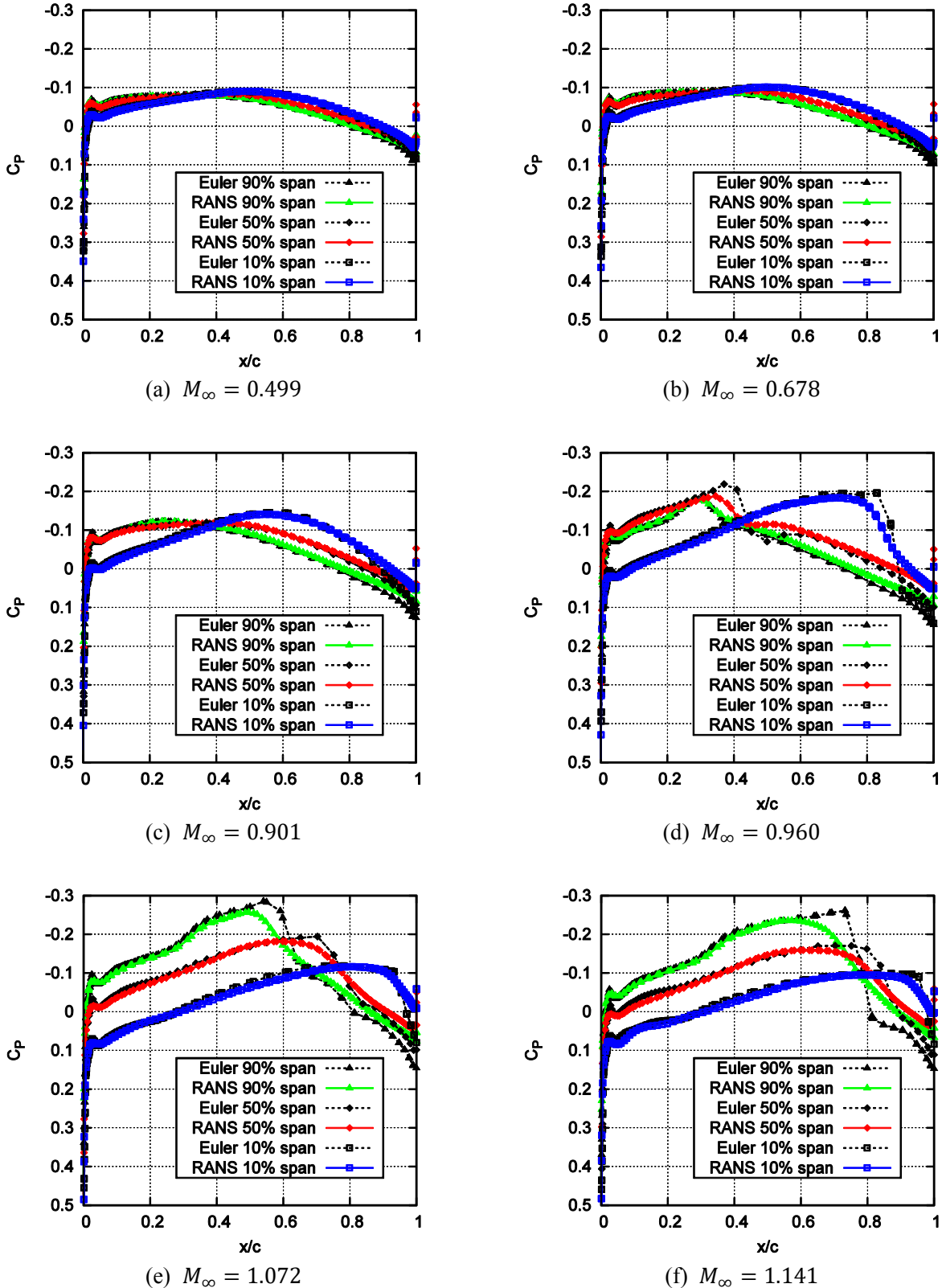
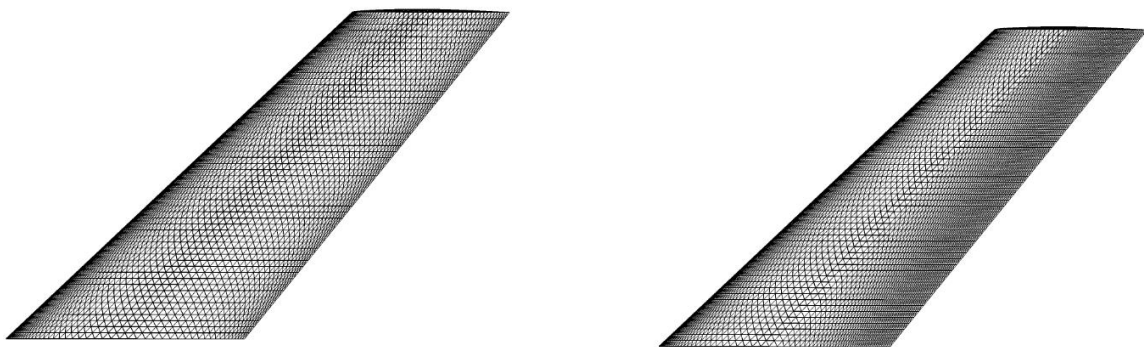


Figure 6: Pressure coefficients at several spanwise cross-sections over the AGARD 445.6 wing.

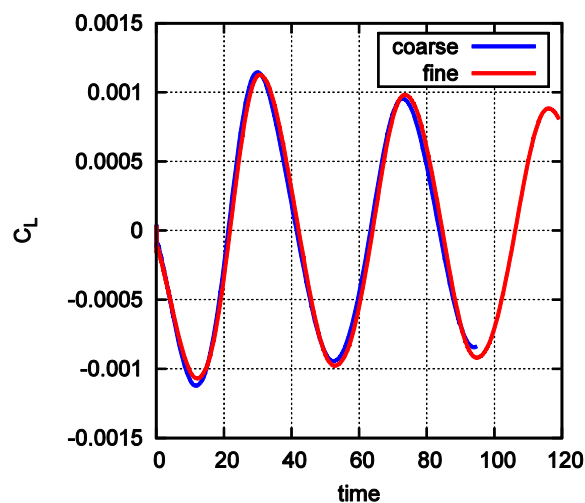
Gan et al.¹⁸⁾ used delayed detached eddy simulation (DDES) on structured meshes for supersonic cases of the AGARD 445.6 wing flutter and computed flutter boundaries show excellent agreements with experimental data even for supersonic freestream regime. For better agreements with experiment, it seems to be necessary to resolve accurately the shock boundary layer interaction in high Mach number condition. In order to investigate effects of the grid resolution in this study, the coarse mesh and fine mesh are prepared as shown in Fig. 7. The coarse mesh is same as the mesh in Fig. 3 (b). In the fine mesh, grids near the shock wave on the wing surface are refined, and wall-normal grid distribution is same as the coarse mesh. Figure 8 shows the corresponding computed C_L histories. These cases on the coarse mesh and the fine mesh are computed using the SA model in the Mach number of 1.141 and FSI of 0.45 above the experimental flutter point. The history employing the fine mesh shows slightly improved trend of oscillation but an expected flutter boundary point will be still higher than that of experiment.



(a) Coarse mesh

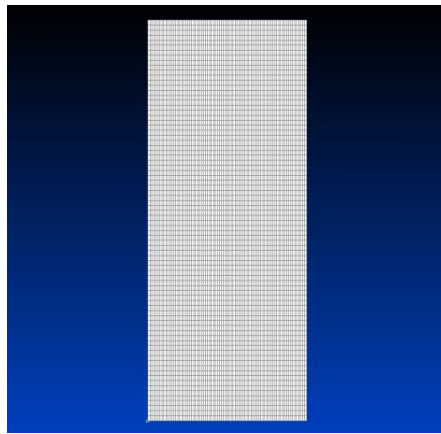
(b) Fine mesh

Figure 7: Computational surface meshes in RANS computations for the AGARD 445.6 wing.

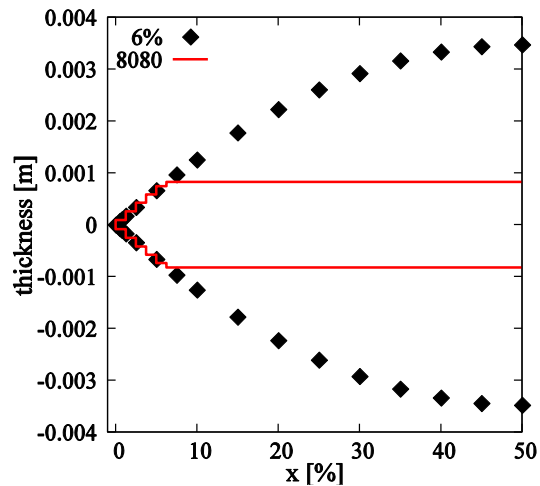
Figure 8: C_L histories using the coarse mesh and the fine mesh in $M_\infty = 1.141$ and $FSI = 0.45$.

(2) Rectangular wing

In the second flutter analysis case, a wing having a rectangular and unswept plan form with a circular-arc airfoil section is employed. This wing has a 6% thickness to the chord length, taper ratio of 1, and aspect ratio of 2.5. The computational conditions follow those of experiment described by Doggett et al.¹⁹⁾ The angle of attack is 0 [deg]. The freestream Mach numbers are 0.715, 0.814, 0.851, 0.913, 0.956, and 1.017. The Reynolds number based on the MAC length is about one million. In these cases, we make a structure model using Femap with NX NASTRAN. In the experiment, a 0.065-inch-thick aluminum alloy plate of the desired plan form was covered with a lightweight flexible plastic foam to make a circular-arc airfoil section. In the reference¹⁹⁾, it is noted that the foam added comparatively little mass and stiffness to that of the aluminum alloy. Therefore, we regard effects of the foam as negligible, and only aluminum core plate is modeled. The plate model has 80 × 80 elements is shown in Fig. 9. As shown in Fig. 9 (b), thickness of elements at the leading edge and the trailing edge is adjusted in tune with the circular-arc airfoil section. In this model, three bending modes and two twisting modes of the wing are considered in the modal analysis. The eigen frequencies of this model are summarized in Tab. 2. It is confirmed that 80 × 80 elements is enough number in terms of frequencies of each modes by comparing with other models having different number of elements.



(a) Wing surface of 80 × 80 plate model



(b) Cross-section

Figure 9: Structure model for the rectangular wing.

Table 2: Eigen frequencies used in flutter computations for the rectangular wing.

Mode		1st (Bending)	2nd (Torsion)	3rd (Bending)	4th (Torsion)	5th (Bending)
Eigen frequency [Hz]	Present model	14.35	77.75	89.34	246.4	250.6
	Experiment	14.29	80.41	89.80	–	–

The computational surface mesh which is same in both Euler and RANS mesh is shown in Fig. 10. In the Euler computation, 209,534 tetrahedral cells are used. In the RANS calculation, 369,878 tetrahedral cells and 252,540 prismatic cells (24 layers) are employed in which the minimum grid spacing on the wall satisfies $y^+ \leq 1$ for all flow conditions. The outer boundary of the computational domain is located at 30 MAC length from the wing surface.

The computed flutter boundaries are shown with experimental data in Fig. 11. When the freestream Mach number is less than 0.913, good agreements with experiment are obtained in both the *FSI* and the flutter frequency. However, the computed *FSI* values are overestimated in high Mach number regime where the shock wave emerges. Considering viscous effects did not improve significantly the *FSI* boundary values. On the other hand, the flutter frequency values at the $M_\infty = 0.913$ is particularly improved by accounting for viscous effects. The cause for this improvement is under consideration.

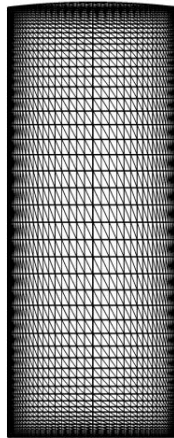


Figure 10: Surface mesh in Euler and RANS computations for the rectangular wing.

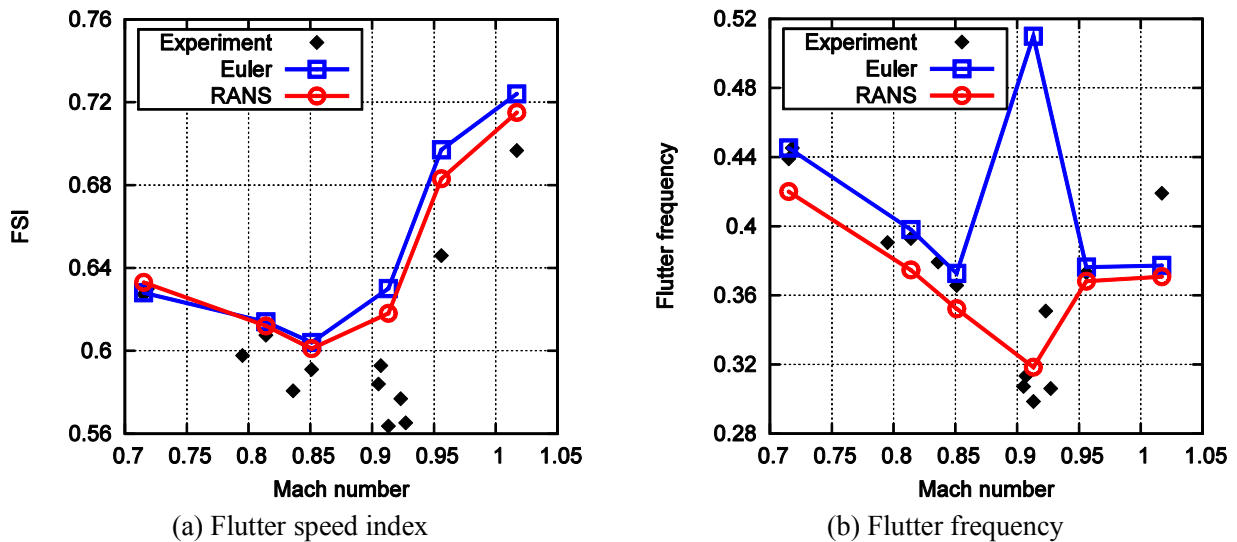


Figure 11: Flutter boundary values for the rectangular wing.

4. CONCLUSIONS

Two flutter cases are computed using the present aeroelastic code based on the spectral volume discretization for aerodynamic analysis and on the modal structure analysis. In the AGARD 445.6 wing flutter case, the transonic dip is well reproduced. Considering viscous effects improve the flutter boundary values at the supersonic freestream regime. In the rectangular wing flutter case, the transonic dip in the *FSI* boundaries cannot be reproduced well. Accounting for viscous effects does not improve significantly the *FSI* boundary values in high Mach number condition but improve particularly the flutter frequency.

REFERENCES

- 1) Nakamichi, J., "Coupling Dynamics in Flutter Analysis," *Japan Computational Fluid Dynamics Journal*, Vol. 9, No. 4, pp. 116–121, 2001.
- 2) Rodden, W. P., Taylor, P. F., and McIntosh, S. C., "Improvement to the Doublet-Lattice Method in MSC/NASTRAN."
- 3) Arizono, H. and Nakamichi, J., "Transonic Flutter Wind Tunnel Tests and Simulations for Twin-Jet Commercial Aircraft," *Japan Computational Fluid Dynamics Journal*, Vol. 26, No. 4, pp. 267–272, 2007.
- 4) Morino, H., "Multi-Objective Design Exploration and Aeroelastic Analysis for Next-Generation Regional

- Jet Development,” PhD thesis, Tohoku University, 2013.
- 5) Cockburn, B., “Discontinuous Galerkin Methods,” *School of Mathematics*, pp. 1–25, 2003.
 - 6) Wang, Z. J., “Spectral (finite) volume method for conservation laws on unstructured grids: Basic formulation,” *Journal Computational Physics*, Vol. 178, No. 1, pp. 210–251, 2002.
 - 7) Huynh, H. T., “A flux reconstruction approach to high-order schemes including discontinuous Galerkin methods,” AIAA paper 2007-4079, 2007.
 - 8) Wang, Z. J., Zhang, L., and Liu, Y., “Spectral (finite) volume method for conservation laws on unstructured grids IV: Extension to two-dimensional systems,” *Journal Computational Physics*, Vol. 194, No. 2, pp. 716–741, 2004.
 - 9) Sawaki, Y., Haga, T., Ogino, Y., Kawai, S., and Sawada, K., “Improved Spectral Volume Method (SV⁺ Method) for Hybrid Unstructured Mesh,” AIAA paper 2016-1327, 2016.
 - 10) Mavriplis, D. J., and Yang, Z., “Achieving Higher-order Time Accuracy for Dynamic Unstructured Mesh Fluid Flow Simulations: Role of the GCL,” AIAA paper 2005-5114, 2005.
 - 11) Liu, Y., Vinokur, M., and Wang, Z. J., “Spectral (finite) volume method for conservation laws on unstructured grids V: Extension to three-dimensional systems,” *Journal Computational Physics*, Vol. 212, No. 2, pp. 454–472, 2006.
 - 12) Shima, E. and Kitamura, K., “On New Simple Low-Dissipation Scheme of AUSM-Family for All Speeds,” AIAA paper 2009-136, 2009.
 - 13) Sawaki, Y., Haga, T., Ogino, Y., and Sawada, K., “Wing Flutter Computation Using Modified Spectral Volume Method for Hybrid Unstructured Mesh,” AIAA paper 2015-0768, 2015.
 - 14) Bassi, F. and Rebay, S., “GMRES discontinuous Galerkin solution of the compressible Navier-Stokes equations,” In *Discontinuous Galerkin Methods*, pp. 197–208, Springer, 2000.
 - 15) Jameson, A. and Yoon, S., “Lower-upper implicit scheme with multiple grids for the Euler equations,” *AIAA Journal*, Vol. 25, No. 7, pp. 929–935, 1987.
 - 16) Yates, E. C. Jr., “AGARD Standard Aeroelastic Configuration for Dynamic Response I—Wing 445.6,” NASA TM 100492, 1987.
 - 17) Spalart, P. R. and Allmaras, S. R., “A one-equation turbulence model for aerodynamic flows,” *La Recherche Aérospatiale*, Vol. 1, pp. 5–21, 1994.
 - 18) Gan, J.-y., Im, H.-S., Chen, X.-y., Zha, G.-C., and Pasilio, C. L., “Prediction of Wing Flutter Boundary Using High Fidelity Delayed Detached Eddy Simulation,” AIAA paper 2015-0442, 2015.
 - 19) Doggett, R. V. Jr., Rainey, A. G., and Morgan, H. G., “An Experimental Investigation of Aerodynamic Effects of Airfoil Thickness on Transonic Flutter Characteristics,” NASA TM X-79, Technical report, 1959.

EFFECTS OF MASS UNBALANCE AND HIGH LEVELS OF EXTERNAL DAMPING ON THE POST-CRITICAL FLUTTER OF A FLAT PLATE

Luca Pigolotti⁺¹, Claudio Mannini⁺² and Gianni Bartoli⁺³

^{+1,2,3} CRIACIV/Department of Civil and Environmental Engineering, University of Florence, Italy

The post-critical flutter regime is still an open issue, despite the interest for its applications in the field of energy harvesting, where the knowledge of the self-sustained motion at large amplitudes is of crucial importance. In the paper, the experimental approach has been followed to investigate this issue. The role of some governing parameters, mainly the mass centre position and the damping level in the translational degree of freedom, were investigated through wind tunnel tests, evaluating their effects on the critical condition and subsequent oscillatory regime. Linear analyses supported the identification of the instability threshold. Downstream mass eccentricity of about 0.05 times the section chord significantly anticipated the critical onset velocity and modified the motion characteristics, in terms of ratio between translational and rotation amplitudes and their phase difference. External damping was introduced, up to a ratio-to-critical value of 18%, and the consequent reduction of the motion amplitudes was clearly shown. In particular, even if the amplitude-velocity diagrams always maintained the same qualitative features, a non-linear dependence on the damping level of its slopes was apparent. In addition, a theoretically stable configuration with large damping was found to perform self-sustained motion if triggered by large initial conditions.

Keyword: Flutter, Wind Tunnel Tests, Post-critical Behaviour, Sub-critical Bifurcation.

1. INTRODUCTION

In the common practice of wind and aeronautical engineering, dynamic fluid-structure interaction is a dangerous phenomenon and the design of structures prone to flow-induced vibrations usually aims at limiting any flow-induced vibration. Nevertheless, the aeroelastic phenomena are characterized by important nonlinear effects that produce Limit Cycles of Oscillation (LCO). In some cases, LCO is restricted to a limited range of flow velocities, as in the case of vortex-induced vibrations, or flow-velocity-unrestricted oscillations can be observed after a critical threshold, as in the case of galloping and flutter. From a different perspective, recent studies on alternative energy sources showed the possibility of exploiting fluid-elastic instabilities and the consequent large steady-state oscillations to capture energy from the flow and generate electricity through suitable energy conversion apparatus¹⁾. Some authors have preliminarily explored aero/hydro-elastic generators based on: vortex-induced vibrations²⁾; transverse³⁾ and torsional^{4),5)} galloping; wake-galloping⁶⁾; flapping^{7),8),9)} and fluttering¹⁰⁾ wings.

From the literature analysis one can conclude that flutter-based solutions are the most promising ones^{8),10)} and the actual capability of performing self-sustained large-amplitude motion in the post-critical regime is a fundamental requirement for any flutter-based generator. Nevertheless, only very few scientific works have been developed so far on the flutter post-critical regime, due to the limited interest for conventional civil/aeronautical structures. Reliable predictive models for the post-critical behaviour are still missing and CFD investigations are hardly applicable due to the very large-amplitude oscillations. Following an experimental approach, aeroelastic setups can be developed to observe the post-critical response¹¹⁾, but they require specific and complex design solutions.

In the classical flutter¹²⁾ involving two Degrees of Freedom (DoFs), the system is excited by aerodynamic lift and moment forces depending on its motion. The energy transfer between airstream and structure relies on the elastic and/or aerodynamic coupling between two modes, generally with components on

⁺¹luca.pigolotti@dicea.unifi.it, ⁺²claudio.mannini@dicea.unifi.it, ⁺³gianni.bartoli@unifi.it

both DoFs, as well as on the phase lag between the displacement and its aerodynamic reaction. This interaction generates phase adjustment and loss of damping in one of the modes, which leads to the instability and drives the growth of the motion. Then, when the cross-flow displacements and rotations are no longer small, nonlinearities occur in the self-excited loads. Particularly important are those due to the massive flow separation encountered for large angles of attack, beyond the dynamic stall angle of the section. The subsequent amplitude-velocity path manifests large amplitudes in both degrees of freedom that generally increase with the flow velocity, after a steep initial jump.

Unlike the availability of semi-empirical predictive models about the dynamic-stall flutter mechanism^(13),14),15), due to the importance for wings operating at high angles of attack^(16),17),18),19),20), the research on post-critical oscillations due to classical flutter is not so extensive. In addition, the physical sources of nonlinearity still represent an open issue, since the literature studies often focused on classical flutter LCOs under specific nonlinear mechanical boundary conditions^(21),22),23). Hence, further research is required on reliable mathematical models and experimental setups allowing for large oscillations to deal with the classical-flutter post-critical behaviour.

This work concentrates on wind tunnel tests on a sectional model with elongated rectangular cross section (width-to-depth ratio of 25:1, with the smaller dimension of 4 mm facing the flow). The developed setup allowed motion in two DoFs), namely vertical (heaving, η , maximum ± 100 mm) and rotational (pitching, α , maximum $\pm 150^\circ$) oscillations, with linear mechanical features in the tested range. Magnetic dampers were used to introduce linear viscous damping into the heaving degree of freedom, up to a ratio-to-critical value of about 20%. Linear aeroelastic models were preliminary used to parametrically explore the flutter boundaries.

The main objective of the paper is to improve the understanding of the influence of some of the governing parameters on the system response⁽²⁴⁾, such as the position of the mass centre, the ratio of pitching to heaving frequency and the still-air heaving damping. The latter, in the context of flutter-based energy generators, can be assumed to simulate the energy extraction process⁽²⁵⁾, as it pumps out energy from the fluid-structure system.

2. METHODOLOGY

(1) Analytical linear model

The stability of the system is investigated by means of linearized models, arranged for the 2-DoF problem, within the assumption of small perturbations around the equilibrium position. The self-excited loads are given by Theodorsen's model⁽¹²⁾, which derives from potential flow theory applied to a theoretical flat plate in conjunction with the Kutta condition. The investigated width-to-depth ratio of the cross section is 25:1 and it is large enough for the oscillation body to be idealized as a flat plate⁽²⁶⁾.

The 2-DoF flutter problem (Figure 1) and the governing equations are reported in a non-dimensional form in Eqs. 1-2, assuming the heaving and pitching DoFs in the form $\eta(t) = \eta^* e^{i(2\pi n t)}$ and $\alpha(t) = \alpha^* e^{i(2\pi n t - \phi^*)}$, where n and ϕ^* are respectively the frequency of oscillation and phase difference at flutter onset:

$$\begin{cases} \mu \left\{ \left[(1 + i g_{\eta 0}) \frac{X}{\gamma_n^2} - 1 \right] \frac{\eta(t)}{B} - x_m \alpha(t) \right\} = \bar{L}_{\eta,j}(\eta, \alpha, K, x_e, t) \\ \mu r_\alpha^2 \left\{ [(1 + i g_{\alpha 0}) X - 1] \alpha(t) - \frac{x_m \eta(t)}{r_\alpha^2 B} \right\} = \bar{M}_{\alpha,j}(\eta, \alpha, K, x_e, t) \end{cases} \quad (1)$$

$$\bar{L}_{\eta,T}(t) = - \left[-\frac{\pi}{2} + i C'_L \frac{C(k)}{K} \right] \frac{\eta(t)}{B} - \left\{ \left[\frac{\pi x_e}{2} + C'_L \frac{C(k)}{K^2} \right] + i \left[\frac{\pi}{2K} + C'_L \frac{C(k)}{K} \left(\frac{1}{4} - x_e \right) \right] \right\} \alpha(t); \quad (2)$$

$$\bar{M}_{\alpha,T}(t) = \left[-\frac{\pi x_e}{2} + i C'_M \frac{C(k)}{K} \right] \frac{\eta(t)}{B} + \left\{ \left[\pi \left(\frac{1}{64} + \frac{x_e^2}{2} \right) + C'_M \frac{C(k)}{K^2} \right] + i \left[-\frac{\pi}{2K} \left(\frac{1}{4} - x_e \right) + C'_M \frac{C(k)}{K} \left(\frac{1}{4} - x_e \right) \right] \right\} \alpha(t).$$

The heaving amplitude is normalized with the plate chord (width) $B = 2b$. $g_{\eta 0}$ and $g_{\alpha 0}$ are the coefficients

of rate-independent damping¹²⁾ for the heaving and pitching DoFs, as obtained through free-vibration decays of the mechanically uncoupled system in still air, and they are used here instead of the ratio-to-critical damping $\xi_{\eta 0} = \xi_{\eta 0,S} + \xi_{\eta 0,E}$ and $\xi_{\alpha 0} = \xi_{\alpha 0,S}$. Concerning the notation of $\xi_{\eta 0}$ and $\xi_{\alpha 0}$, the subscript ‘S’ stands for the structural damping, while ‘E’ for the external damping that can be varied with the electromagnetic dampers. The parameters C_L' and C_M' in Eq. 2 are the slopes of the lift and moment aerodynamic coefficients, which for a flat plate are equal respectively to 2π and $2\pi(1/4 + x_e)$, while $C(k)$ is Theodorsen’s circulatory function¹²⁾ depending on $k = \omega b/U = K/2$. The other dimensionless parameters playing a role in the flutter problem are: x_e and x_m , non-dimensional position respectively of the centre of elasticity and of the centre of mass; μ , proportional to the ratio of the mass of the model to the mass of the moved air; r_α , non-dimensional radius of polar inertia; γ_n , frequency ratio in still air of the uncoupled modes; X , unknown non-dimensional flutter frequency; $U_{R\alpha}$, reduced flow velocity or $K_{R\alpha}$ reduced frequency:

$$x_e = \frac{e}{B}; \quad x_m = \frac{S_\alpha}{I_\eta B} = \frac{a}{B}; \quad \mu = \frac{2I_\eta}{\rho B^2 S}; \quad r_\alpha = \sqrt{\frac{I_\alpha}{I_\eta B^2}}; \quad \gamma_n = \frac{n_{\alpha 0}}{n_{\eta 0}}; \quad X = \left(\frac{n_{\alpha 0}}{n}\right)^2; \quad U_{R\alpha} = \frac{U}{n_{\alpha 0} B} = \frac{2\pi}{K_{R\alpha}} \quad (3)$$

In Eq. 3: ρ is the flow density; I_η and I_α are the inertiae in the heaving and pitching DoFs, respectively; S_α is the static mass unbalance; S denotes the span of the model.

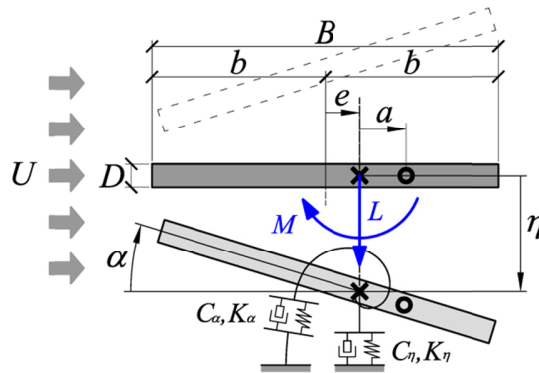


Figure 1: Sketch of the flutter problem of a two-degree-of-freedom, two-dimensional flat plate.

(2) Experimental campaign

The experimental campaign was conducted in the open-circuit, boundary layer wind tunnel of CRIACIV, in Prato, Italy. The facility is about 22 m long and the geometry of the test section is $2.41 \times 1.60 \text{ m}^2$ (width×height). The 156 kW fan, placed downstream the test section, allows continuously varying the flow speed up to 30 m/s through an inverter and/or controlling the pitch angle of the rotor blades.

The aeroelastic setup (Figure 2) was specifically designed to allow large amplitudes of oscillation with linear mechanical behavior. The stiffness of the heaving DoF was controlled through the free length (1004 mm) of two pairs of aluminium beams (or blade-springs, 50 mm wide and 3 mm thick). Each pair was arranged to provide a frame with shear-type deformation thanks to a Vierendeel girder connecting the free ends of the beams, while the other ends are clamped by fixed supports. Two linear springs (the top one having a stiffness of 195 N/m and the bottom one of 95 N/m), placed outside the test section, were linked to the free ends of each frame through steel cables, in order to compensate the static deflection and contribute to the heaving stiffness. Each frame was equipped with a clock spring (with a rotational stiffness of 2.057 Nm/rad). Moreover, the model axis was connected to the elastic supporting frames by means of radial ball bearings, in order to decouple the two degrees of freedom. In addition, the connection of the flat plate to the end tube allowed to control the position of the elastic centre, while two rocker arms fixed to the model axis were devised to vary the mass centre by adding calibrated masses. Damping devices, based on the eddy-current dissipation generated on an aluminium plate (5 mm thick) moving between a pair of circular permanent magnets (neodymium N45, 35×20 mm) at close distance, were installed to introduce linear viscous damping in the heaving DoF.

The heaving motion was recorded through two analogic laser displacement transducers (measuring range of 200 mm), pointing the ends of the shear-type frames, so enabling also the monitoring of the possible rolling motion. A third laser transducer was pointing directly the model to check for a possible mean pitching rotation with increasing flow speed. Two miniaturized accelerometers were installed at the ends of one of the rocker arms to record the pitching motion up to large amplitudes. The sampling frequency during the tests was 2000 Hz.



Figure 2: Frontal view of the aeroelastic setup (top); close-ups of the damping devices (bottom-left) and of the Vierendeel girder with clock spring and hooking system for the elastic/mass centre control (bottom-right).

The suspension system was sheltered from the flow by means of two screens having a nose following the geometry of a NACA0020 profile, limiting both the disturbances produced by the setup to the incident flow and the unwanted aeroelastic effects of the oscillating supporting elements (mainly the blade-springs). Circular aluminium end-plates, 400 mm large and 1.5 mm thick, were also provided to the model ends to ensure time-averaged two-dimensional flow conditions.

The steel model had a rectangular cross section with sharp edges and it was 100 mm wide (B) and 4 mm deep (D), the smaller dimension being the one facing the wind. The free span of the model (S) was 541 mm, calculated as the distance between end-plates. The model was arranged with a nose-up angle of about 0.43° to compensate the vertical incidence of the flow in the test section. Much attention was paid to arrange the whole setup as symmetric as possible with respect to the along-wind centreline of the model in order to limit the unwanted rolling motion. The blockage ratio, calculated in a vertical plane crossing the model in the rest position, was about 0.25%. This value increased up to 6.25% when the model experienced pitching amplitudes around 90° .

The tests were conducted in smooth flow conditions with a free-stream turbulence intensity of about 0.7%. The mean flow speed was measured by means of a Prandtl tube installed upstream the model and corrected through known flow maps to infer the velocity at the model centreline. The Reynolds number (defined as $Re = UB/\nu$, with $\nu = 15 \text{ mm}^2/\text{s}$) during the tests was in the range 33,000 to 107,000.

The stiffness linearity of the aeroelastic setup, both in the pitching and heaving degrees of freedom, was verified through static tests (Figure 3), measuring static displacements for different known loads. The effective inertia of the oscillating system in the heaving and pitching motions, I_η and I_α , were calculated from the previously estimated stiffness and the corresponding frequency of oscillation in still air. Dynamic tests, in which the frequencies were measured for different additional inertias, confirmed the results. Moreover, for each configuration, several free decay tests (Figure 4) were performed in still air for different initial conditions, in order to evaluate the natural frequencies of oscillation ($n_{\eta 0}$, $n_{\alpha 0}$) and the ratio-to-critical damping coefficients ($\xi_{\eta 0}$, $\xi_{\alpha 0}$). Higher levels of $\xi_{\eta 0}$ were reached through the electromagnetic system, up to a value of about 18%. The static unbalance, S_α , was estimated by measuring the frequencies of oscillation of the system during coupled pitching-heaving motion²⁷. Table 1 summarises the characteristics of the tested configurations.

Table 1. Parameters of the configurations tested during the experimental campaign.

Configuration	ρ [kg/m ³]	I_η [kg]	I_α [kg·m ²]	S_α [kg·m]	$n_{\eta 0}$ [Hz]	$n_{\alpha 0}$ [Hz]	$\xi_{\eta 0}$ [%]	$\xi_{\alpha 0}$ [%]	x_e [-]	x_m [-]	μ [-]	r_α [-]	γ_n [-]
#1	1.15	8.058	0.03147	0.073	1.886	1.820	0.05	1.67	0.00	0.091	2708.9	0.625	0.965
#2	1.17	7.867	0.03165	0.045	1.731	1.814	0.04	1.24	"	0.057	2604.7	0.634	1.048
#2a	1.16	"	"	"	"	"	9.52	"	"	"	2615.4	"	"
#2b	1.17	"	"	"	"	"	18.13	"	"	"	2605.3	"	"
#3	1.16	7.872	0.02902	0.000	1.731	1.895	0.05	1.23	"	0.000	2617.1	0.607	1.095
#3a	1.15	"	"	"	"	"	9.52	"	"	"	2660.6	"	"
#4	1.16	"	0.03165	0.045	"	1.814	0.05	1.24	"	0.057	2627.6	0.634	1.048

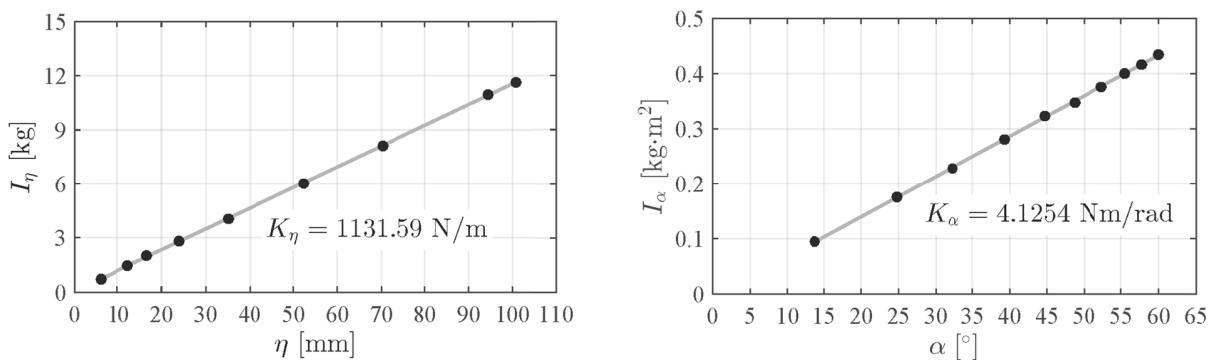


Figure 3: Static measurements to verify the linearity of heaving (left) and pitching (right) stiffnesses.

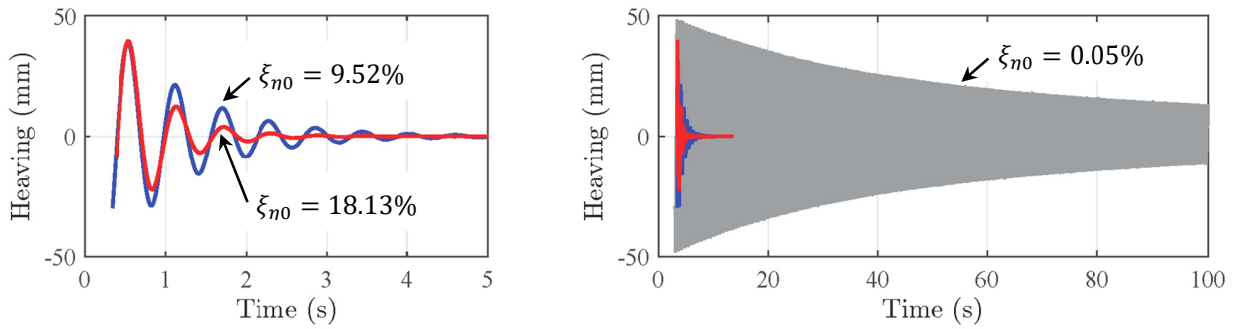


Figure 4: Example of free-decay tests for high levels of heaving damping (left) and comparison with the free-decay oscillation in the case of structural damping only (right).

3. RESULTS

The experiments were conducted in a systematic way. For each configuration, the estimation of the critical condition was theoretically conducted on the basis of the governing parameters, as obtained from the system identification, and then compared with those experimentally observed. Several initial conditions with different amplitudes were released for some flow velocities close to the theoretical flutter boundary, in order to get information on the unstable branch position, separating up to the critical threshold the stable rest position and the stable subcritical branch of the amplitude-velocity path. Indeed, as a general result, all configurations featured an instability mechanism with sub-critical bifurcation. After the flutter onset, the build-up of the oscillation was registered (Figure 5), identifying a transition regime in which the system markedly adjusts its response with respect to the nonlinear aeroelastic loads due to the large-amplitude motion. The following amplitude-velocity path was recorded for a time long enough (about 200 s) both to allow the stabilisation of the LCO amplitudes and to achieve a frequency resolution in the spectra to correctly detect the frequency peaks even at close distance. Amplitude-velocity points with increasing and decreasing flow speed were observed, up to the end of the sub-critical branch when the oscillation died out.

As predicted by the linear theory, the instability threshold is significantly anticipated in the case of small positive mass eccentricity (Figure 6). Moreover, comparing configurations #3 and #2, the sole modification of x_m importantly changes the characteristics of the motion. The phase ϕ^* varies from 12° to 152° , moving the region in which the motion centre of rotation lies from upstream to downstream the midchord. The motion components are strongly modified as well, producing larger pitching-heaving amplitude ratios $B\alpha^*/\eta^*$. Considering also configuration #1, the ratio $B\alpha^*/\eta^*$ seems to be importantly affected by the frequency ratio (Figure 6). In fact, in the case of $\gamma_n < 1$, the centre of rotation lies in a small region downstream the midchord, as suggested by the increase of the phase angle to about 164° , and the heaving component is enhanced.

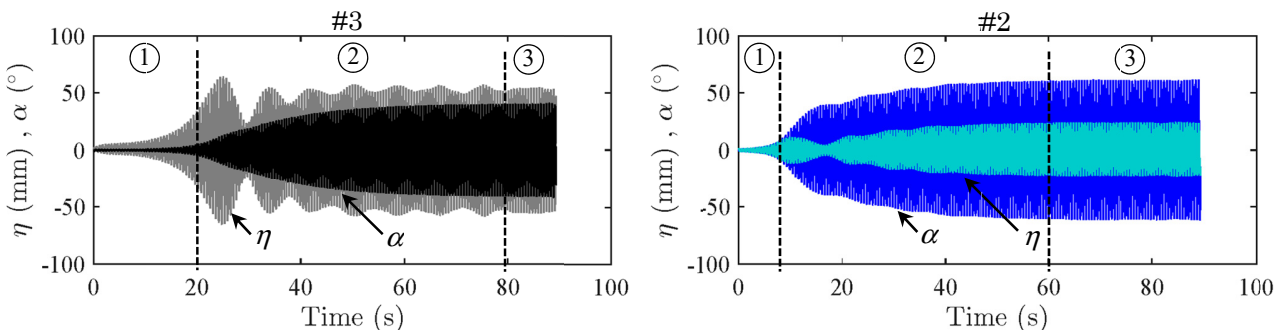


Figure 5: Build-up of flutter oscillations for symmetric (left) and mass-unbalanced (right) configurations having low heaving damping. Three phases are highlighted: 1) exponentially growing motion according to linear theory; 2) transition regime due to the activation of nonlinearities of self-excited loads and phase adjustment; 3) steady-state LCO amplitudes.

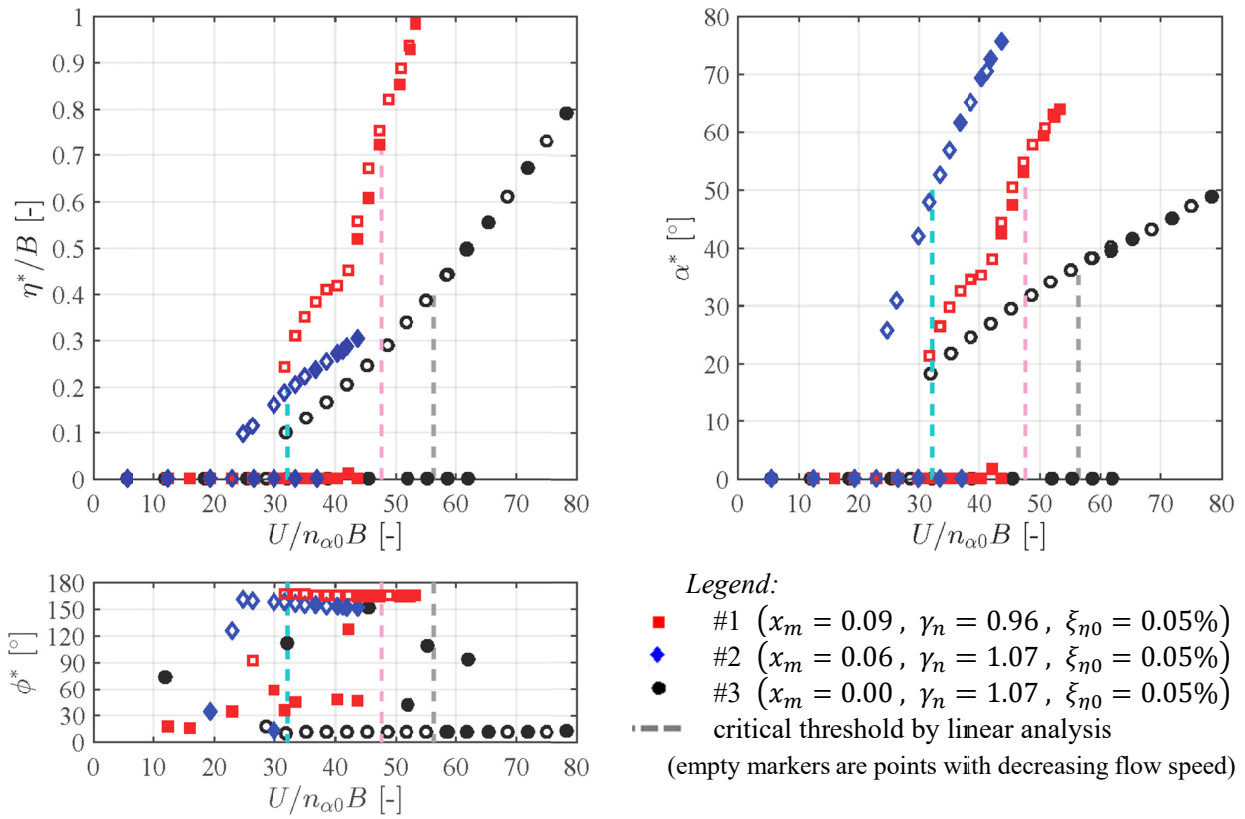


Figure 6: Comparison of amplitude-velocity diagrams for heaving and pitching components and their phase difference for the configurations with low heaving damping.

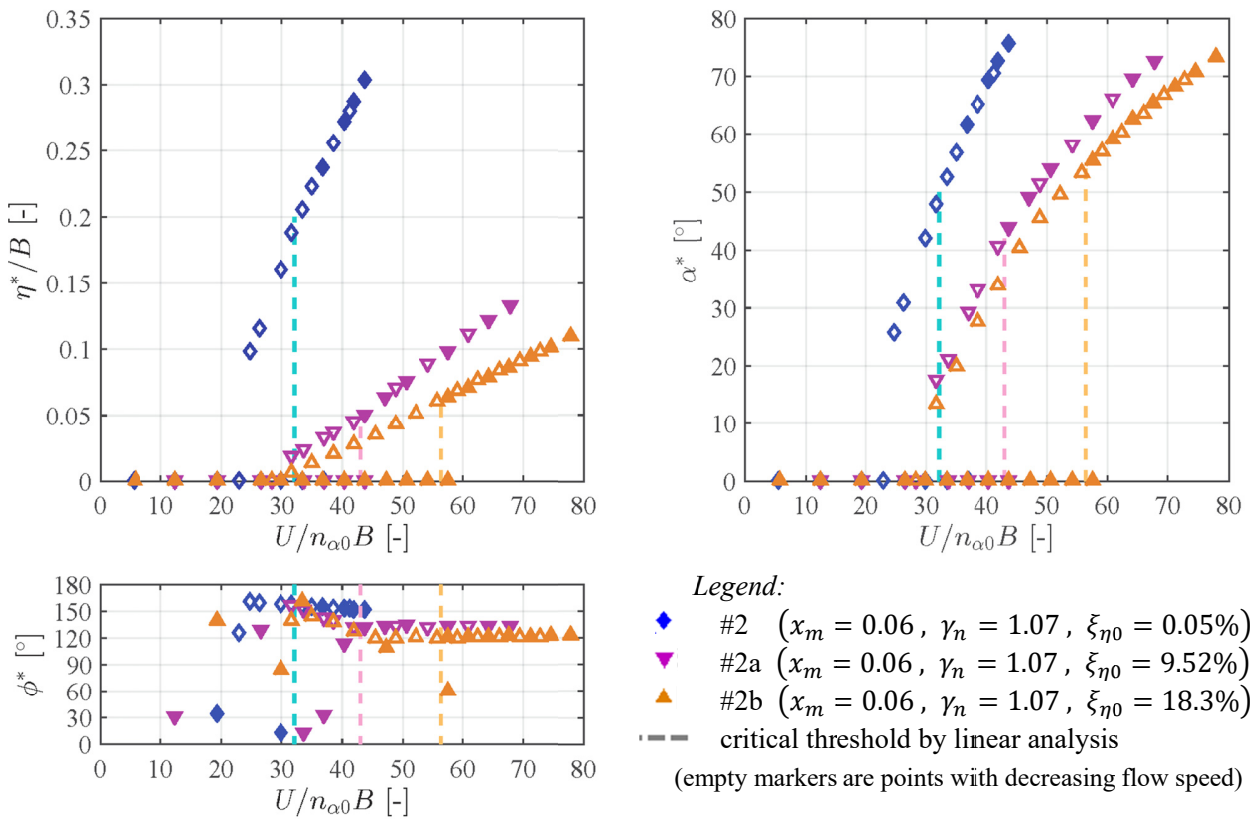


Figure 7: Effects of high levels of heaving damping on the mass unbalanced configuration.

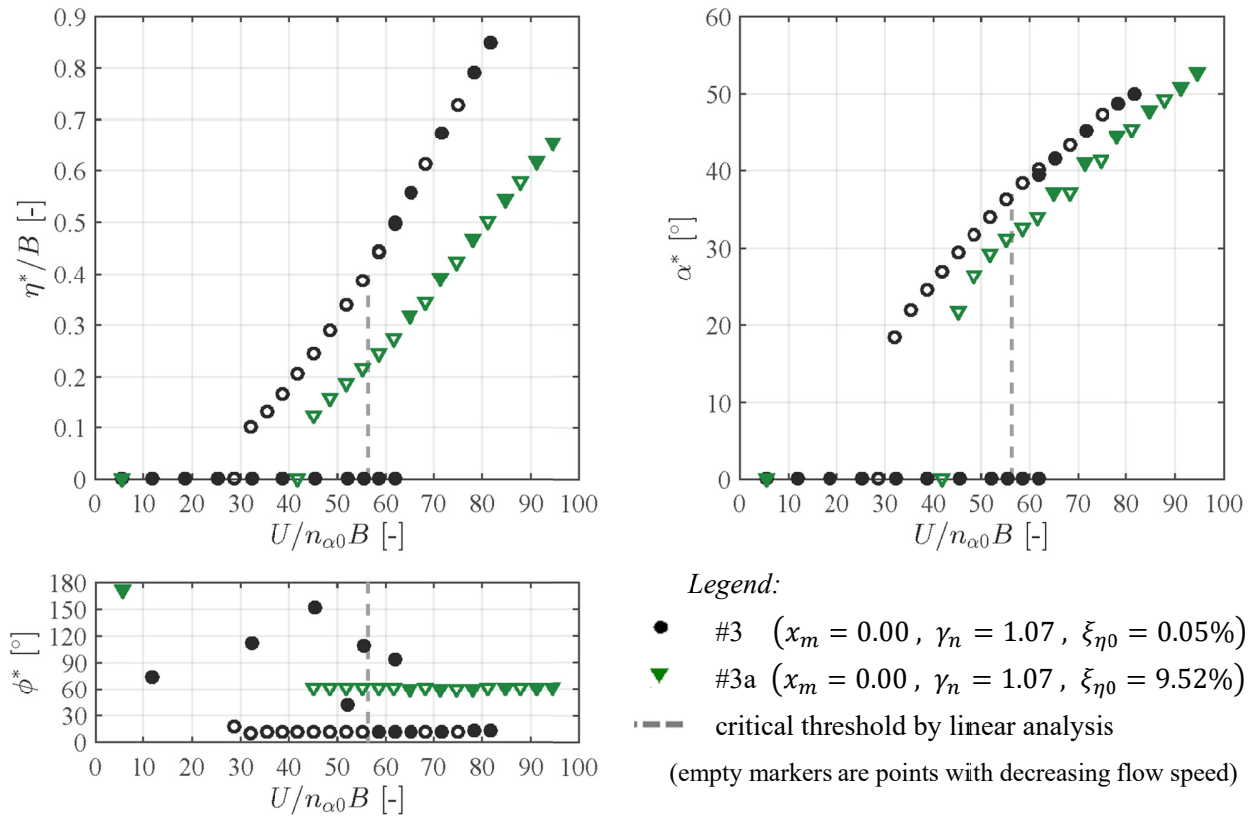


Figure 8: Effects of high level of heaving damping on the symmetric configuration. It is worth remarking that configuration #3a is stable according to the linear theory but it exhibits steady-state oscillations, if triggered by the release of large initial conditions.

In general, the increase of heaving damping nonlinearly modifies the amplitude-velocity diagrams, as shown in Figure 7. In particular, for the specific case of configuration #2, it is clear that the pitching and even more the heaving amplitudes first significantly reduce for an increment of the heaving damping from 0.05% to 9.5%. By contrast, a further increase of the damping, up to 18.3%, does not produce any dramatic reduction of the oscillation amplitude. In addition, the critical condition is postponed but the amplitude-velocity paths preserve the main qualitative features, such as the sudden jump at the instability threshold and the drop-down at the lower bound of the subcritical branch, or the nearly linear evolution with the flow speed of the sub-critical and post-critical branches.

According to the linear theory, the increase of external damping in the case of the symmetric configuration #3 fully stabilizes the system. Therefore, although configuration #3a is theoretically not prone to flutter instability, steady-state oscillations were achieved, as shown in Figure 8, provided that the system was artificially disturbed through large initial conditions, so that an amplitude-velocity diagram was obtained anyway. This result highlights the differences between the self-excited loads that dominate the steady-state regime and those responsible for the incipient classical flutter instability. In particular, while this last relies on the aeroelastic coupling between structural modes and respective fluid-dynamic reactions that leads to phase adjustment and loss of damping, when massive flow separation occurs at high angles of attack due to dynamic stall¹²⁾, the motion is governed by hysteresis loops in the nonlinear fluid-dynamic loads.

In the case of small mass unbalance (Figure 7), the phase ϕ^* decreases from about 152° for low heaving damping ($\xi_{\eta 0} = 0.05\%$) to about 133° for $\xi_{\eta 0} = 9.52\%$ and to about 121° for $\xi_{\eta 0} = 18.13\%$. By contrast, for the symmetric configuration (Figure 8) the phase angle starts from about 12° and increases up to about 61° if the heaving damping is equal to 9.52%. In general, the phase difference between pitching and heaving motions seems to tend to 90° for very high heaving damping, suggesting that the system adjusts the motion to an optimal condition while exhibiting self-sustained oscillations in the case of very high mechanical dissipation.

In all the tested configurations, the theoretical and experimental critical conditions are in good agreement. Moreover, the instability threshold always lies close to the change of slope between the sub-critical and the post-critical branch, probably suggesting a slightly different excitation mechanism in the two ranges. It is also worth noting that, even though the increase of heaving damping stabilises the system, mainly through a reduction of the motion amplitudes, the unstable branch gets closer to the rest position, so that smaller perturbations can be sufficient to foster the steady-state motion in the sub-critical range.

4. CONCLUSIONS

A systematic experimental approach was used to explore the behaviour of a flat plate model with rectangular 25:1 width-to-depth cross section prone to two-degree-of-freedom classical flutter. Analytical linear models supported the investigation of the flutter critical condition. Wind tunnel tests on a spring-mounted sectional model were conducted to verify the critical condition and to investigate the large amplitude oscillations in the post-critical regime for several dynamic configurations. The key role played by the position of the mass centre and by the damping in the translational degree of freedom was mainly studied.

A small mass unbalance significantly anticipates the instability threshold and modifies the characteristics of the motion in terms of ratio of pitching to heaving components and phase difference. For the investigated set of configurations, the introduction of high levels of heaving damping reduces the motion amplitude and postpones the instability threshold. The amplitude-velocity diagrams are not distorted by increasing the external damping, maintaining a linear evolution with the flow speed of the sub-critical and post-critical branches. By contrast, the slopes of these branches nonlinearly depend on the damping. Steady-state oscillations were found also for a configuration theoretically stable with large damping provided that the motion is artificially triggered through a large enough initial condition

The present results can form the basis for the development of numerical nonlinear models to predict large-amplitude post-critical oscillations that are triggered by the classical-flutter instability but whose evolution to the steady state is mainly driven by the dynamic-stall mechanism.

In the near future, the investigation will be extended to other dynamic parameters governing the flutter problem, in order to achieve a more complete knowledge of their influence on the post-critical flutter regime.

5. ACKNOWLEDGMENT

The authors gratefully acknowledge the contribution of Mikel Ogueta during the experimental tests.

REFERENCES

- 1) S. Roundy, "On the effectiveness of vibration-based energy harvesting", *J. Intel. Mat. Syst. Str.*, vol. 16, no. 10, pp. 809-823, 2005.
- 2) M. M. Bernitsas, K. Raghavan, Y. Ben-Simon and E. M. H. Garcia, "VIVACE (Vortex Induced Vibration Aquatic Clean Energy): A New Concept in Generation of Clean and Renewable Energy From Fluid Flow," *J. Offshore Mech. Arct.*, vol. 130, no. 4, pp. 041101 (1-15), 2008.
- 3) A. Barrero-Gil, G. Alonso and A. Sanz-Andres, "Energy harvesting from transverse galloping", *J. Sound Vib.*, vol. 329, no. 14, pp. 2873-2883, 2010.
- 4) G. Ahmadi, "An oscillatory wind energy convertor", *Wind Energy*, vol. 18, pp. 115-120, 1978.
- 5) L. Caracoglia, "Feasibility assessment of a leading-edge-flutter wind power generator", *J. Wind Eng. Ind. Aerod.*, vol. 98, no. 10-11, pp. 679-686, 2010.
- 6) H.-J. Jung and S.-W. Lee, "The experimental validation of a new energy harvesting system based on the wake galloping phenomenon", *Smart Mater. Struct.*, vol. 20, no. 5, pp. 055022 (1-11), 2011.
- 7) W. McKinney and J. De Laurier, "The Wingmill: An Oscillating-Wing Windmill", *J. Energy*, vol. 5, no. 2, pp. 106-115, 1981.
- 8) K. Isogai, M. Yamasaki, M. Matsubara and T. Asaoka, "Design study of elastically supported

- flapping wing power generator”, in Int. Forum on Aeroelasticity and Structural Dynamics, Amsterdam, 2003.
- 9) Q. Zhu, M. Haase and C. H. Wu, “Modeling the capacity of a novel flow-energy harvester”, *Appl. Math. Model.*, vol. 33, no. 5, pp. 2207–2217, 2009.
 - 10) M. Bryant and E. Garcia, “Modeling and Testing of a Novel Aeroelastic Flutter Energy Harvester”, *J. Vib. Acoustics*, vol. 133, no. 1, pp. 011010 (1-11), 2011.
 - 11) X. Amandolese, S. Michelin and M. Choquel, “Low speed flutter and limit cycle oscillations of a two-degree-of-freedom flat plate in a wind tunnel”, *J. Fluid. Struct.*, vol. 43, pp. 244-255, 2013.
 - 12) Y. Fung, *An Introduction to the Theory of Aeroelasticity*, New York: John Wiley and Sons, Inc., 1955.
 - 13) J. Larsen, S. Nielsen and S. Krenk, “Dynamic stall model for wind turbine airfoils”, *J. Fluids Struct.*, vol. 23, pp. 959-982, 2007.
 - 14) J. Leishman and T. Beddoes, “A semi-empirical model for dynamic stall”, *J. Am. Helicopter Soc.*, vol. 34, no. 3, pp. 3-17, 1989.
 - 15) D. Petot, “Modélisation du décrochage dynamique par équations différentielles”, *La Recherche Aérospatiale*, vol. 5, pp. 59-72, 1989.
 - 16) E. Dowell, R. Clark, D. Cox, H. Curtiss, J. Edwards, D. Peters, R. Scanlan, E. Simiu, F. Sisto, K. Hall and T. W. Strganac, *A Modern Course in Aeroelasticity (Solid Mechanics and Its Applications)*, 4th ed., Kluwer, USA: Springer, 2004.
 - 17) S. Bhat and R. Govardhan, “Stall flutter of NACA0012 airfoil at low Reynolds numbers”, *J. Fluids Struct.*, vol. 41, p. 166–174, 2013.
 - 18) W. McCroskey, “Unsteady airfoils”, *Annu. Rev. Fluid Mech.*, vol. 14, p. 285–311, 1982.
 - 19) S. Sarkar and H. Bijl, “Nonlinear aeroelastic behavior of an oscillating airfoil during stall induced vibration”, *J. Fluids Struct.*, vol. 24, p. 757–777, 2008.
 - 20) N. Razak, T. Andrianne and G. Dimitriadis, “Flutter and stall flutter of a rectangular wing in a wind tunnel”, *J. AIAA*, vol. 49, no. 10, p. 2258–2271, 2011.
 - 21) C. W. Emory, “Prediction of Limit Cycle Oscillation in an Aeroelastic System using Nonlinear Normal Modes”, Blacksburg, Virginia, 2010.
 - 22) A. Abdelkefi, R. Vasconcellos, F. D. Marques and M. R. Hajj, “Modeling and identification of freeplay nonlinearity”, *J. Sound Vib.*, vol. 331, no. 8, pp. 1898-1907, 2012.
 - 23) P. Dunn and J. Dugundji, “Nonlinear stall flutter and divergence analysis of cantilevered graphite/epoxy wings”, *J. AIAA*, vol. 30, no. 1, p. 153–162, 1992.
 - 24) L. Pigolotti, C. Mannini, G. Bartoli and K. Thiele, “Wind tunnel tests on elongated rectangular plates under flutter motion: limit-cycle oscillations and preliminary energy harvesting considerations”, in Proc. of 14th Int. Conf. on Wind Engineering, Porto Alegre, Brazil, June 21-26, 2015.
 - 25) M. Karami, M. Amin and J. Daniel, “Equivalent damping and frequency change for linear and nonlinear hybrid vibrational energy harvesting systems”, *J. Sound Vib.*, vol. 330, no. 23, pp. 5583-5597, 2011.
 - 26) M. Matsumoto, “Aerodynamic damping of prisms”, *J. Wind. Eng. Ind. Aerod.*, vol. 59, pp. 159-175, 1996.
 - 27) R. Bisplinghoff and H. Ashley, *Principles of Aeroelasticity*, New York: John Wiley and Sons, Inc., 1962

POD AND DMD OF FLOW NEAR SIDE SURFACE OF 2-D BLUFF BODY

Hikomichi Shirato, Yusuke Taniguchi, Ikuma Tsukamae and Mai Shimonishi
Department of Civil and Earth Resources Engineering, Kyoto University, Kyoto, Japan

Proper Orthogonal Decomposition (POD) and Dynamic Mode Decomposition (DMD) are to be applied to the flow near the leading edge and wake of a 2-D rectangular prism. Flow around 2-D rectangular prisms with $B/D=1$ and 8 are visualized by PIV and its 2-D velocity vector field is decomposed by POD and DMD. The prism is set in still condition in smooth flow and in grid turbulence in wind tunnel. Flow field in xy or xz plane (x : chord-wise, y : span-wise, z : vertical (normal to side surface) directions) is visualized using laser sheet and smoke under $Re=2.5$ to $3.75e3$ with respect to D . DMD was applied to the wake behind a 2-D square prism at first examined. The periodicity in wake is clearly extracted by POD and DMD. Flow in a separation bubble is then observed through POD and DMD, which illuminate 3-dimensional flow characteristics and may connect with the increase of span-wise correlation of aerodynamic force.

Keyword: Wake, Separation bubble, POD, DMD.

1. INTRODUCTION

The conventional buffeting analysis proposed by Davenport¹⁾ is widely accepted in the wind loading codes for engineering structures including long span bridges and high-rise buildings. The analysis assumes that the span-wise coherence of aerodynamic force due to wind turbulence, gust force, is identical to that of oncoming wind velocity fluctuations. On the other hand, previous study reports that pressure fluctuations on a side surface of a still rectangular prism and resulting buffeting force shows higher span-wise coherence than that of oncoming flow²⁾⁻⁹⁾. Its mechanism has been understood as the distortion of approaching turbulent eddies at the leading edge and their elongation along span-wise direction^{2), 9)}, by the flow separation which has higher uniformity along span-wise direction⁵⁾⁻⁷⁾, or due to 2-D like shedding vortices behind a bluff body for relatively smaller side ratio B/D (B : chord length, D : depth of cross section)⁸⁾. The authors' group has been investigating spatial correlation of surface pressure on the side surface of rectangular prisms in grid turbulence. In addition to the aforementioned higher span-wise correlation than the approaching wind, it was known that the surface pressure shows most correlated where the rms of pressure fluctuation reaches the maximum, then decreases near the reattaching point. Even in the region downstream from the reattaching point, the span-wise correlation has a tendency to increase again. The spatial correlation of the shear flow being separated from the leading edge was also discussed in wind tunnel experiments. Span-wise and chord-wise coherence of surface pressure were obtained for rectangular prisms for various side ratio B/D in three different grid turbulence. Based on these coherence data, a generalized frequency transfer function was proposed, which is equivalent to the multiple of joint mode acceptance and aerodynamic admittance¹⁰⁾. Surface pressure correlation between at the reference point near the leading edge and at the other point demonstrates more correlated tendency if the other location is not at along just downstream from the reference point but at along skewed direction from the main flow.

In this study, a new approach to capture the flow which enhances the span-wise correlation in the separation bubble on a rectangular prism with $B/D=1$ and 8 is attempted by implementing POD and DMD analysis to the time dependent PIV data of wind velocity field within the plane parallel to the side surface of a prism near the leading edge. In some POD modes, a ridge which expresses similar harmonic motion is recognized as expanding with a skew angle to the main flow direction. This implies cross momentum transport, that is transport of u -momentum towards span-wise direction by v -component and of v -momentum

⁺¹isfa0001@jaxa.jp, ⁺²isfa0002@company.com, ⁺³isfa0003@univ.ac-u.jp

towards chord-wise direction by u -component, respectively. And this may create higher correlation of surface pressure at two locations with oblique angle to the main flow. Some DMD modes indicate little decaying rate and demonstrates enough sustainability. These modes may also an indication to provoke the cross momentum transport nature, since the domain of similar harmonic motion was observed with an oblique angle.

2. EXPERIMENTAL SETUP AND DATA DECOMPOSITION

(1) Wind Tunnel Experiment

A flat rectangular prism with $B/D=8.0$ ($B=300\text{mm}$, $D=37.5\text{mm}$ and span length $l=900\text{mm}$) and a square prism ($B/D=1$) are focused in this study. The separating shear layer is expected to completely reattach to the side surface for $B/D=8$ and periodic Karman vortex shedding will be obtained for $B/D=1$. The prism is set horizontally and in still condition in the working section of wind tunnel. On the side surface of $B/D=8$ prism, 20 pressure taps are installed in one row along chord-wise direction and 13 rows are arranged in span-wise direction. Surface pressures are led to both ends of the prism through interior tubes in the model. The arrangement of pressure taps on the side surface is shown in Figure 1. Pressure signals are detected by 32ch multiple pressure transducers (ZOC17, Scanivalve) and stored in PC through A/D converter (DF-3422, Pavec) by 1kHz sampling rate.

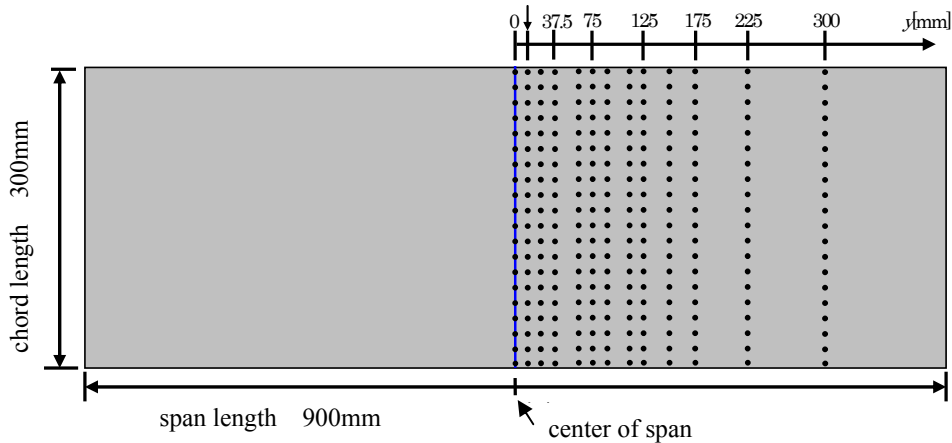


Figure 1: pressure tap arrangement of $B/D=8$ prism

The working section of the wind tunnel has 1000mm in width and 1800mm in height. Wind velocity is controlled over 0.5 to 25m/s continuously by adjusting constant rotation rate of fan. A grid consists of a bar 40mm in width (facing to main wind direction) with 160mm x 160mm square opening is installed at 2600mm ($=8.67B$) upstream from the prism to generate turbulent flow. Basic turbulence properties are summarized in Table 1. The scale of turbulence was evaluated by integrating the autocorrelation coefficient of longitudinal and vertical wind velocity fluctuation component. Wind velocity is measured by a hot-wire anemometer (model 1011, model 1013, Kanomax) with X-type probe (model 0252-T5, Kanomax) Figure 2 shows the experimental setup in wind tunnel.

Flow visualization is also carried out using laser sheet (PIV Laser 2000m/G-KD, Kato Koken) and smoke (model 8384, Kanomax) in order to obtain time dependent PIV data of wind velocity field within the plane parallel to the side surface of a prism near the leading edge. A PIV camera (Fastcam 1024PCI model 1K, Photron) is used to capture the visualized image. The area to be visualized is 62.5mm in width (ly) and 150mm in length (lx) in xy plane (being horizontal and parallel to the side surface of a prism). The distance between side surface and the laser sheet is kept to 5mm ($0.13D$). Since the visualized area is immersed in the separation bubble, the smoke has to be supplied directly to the interior of the bubble. In this study, another identical prism as shown in Figure 3 is prepared, which has small slit near the leading edge so as to discharge the smoke. Wind velocity, U , is adjusted to 1.0m/s ($Re_D=UD/\nu=2500$) and 1.5m/s ($Re_D=3750$) in order to have

enough smoke density. As for the prism with $B/D=1$, $B=D=37.5\text{mm}$ and the slit to emit smoke near the leading edge is installed on both sides. (See Figure 3)

Table 1: Basic properties of grid turbulence

Item	Component	Unit	Quantity
Intensity of turbulence	Longitudinal	[%]	10.5
	Vertical	[%]	9.0
Scale of turbulence	Longitudinal	[mm]	95.0
	Vertical	[mm]	45.0
Bar width		[mm]	60.0
Spacing distance		[mm]	160.0
Opening ratio		[%]	64.0

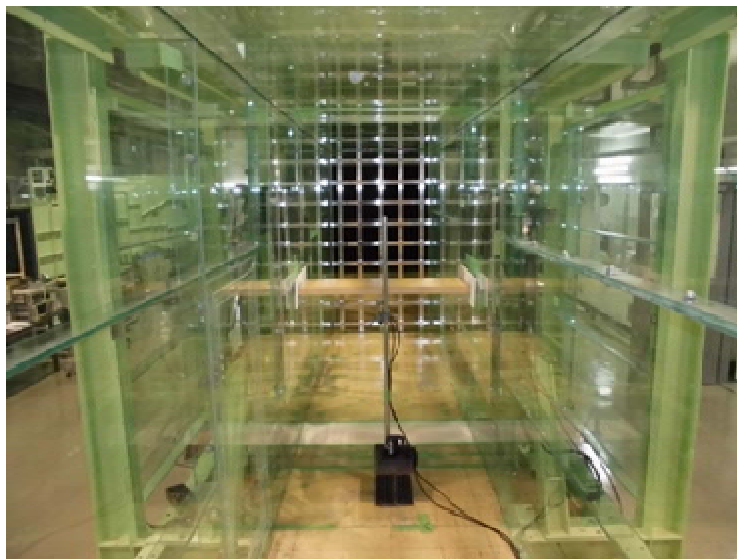


Figure 2: Experimental setup of a rectangular prism in grid turbulence

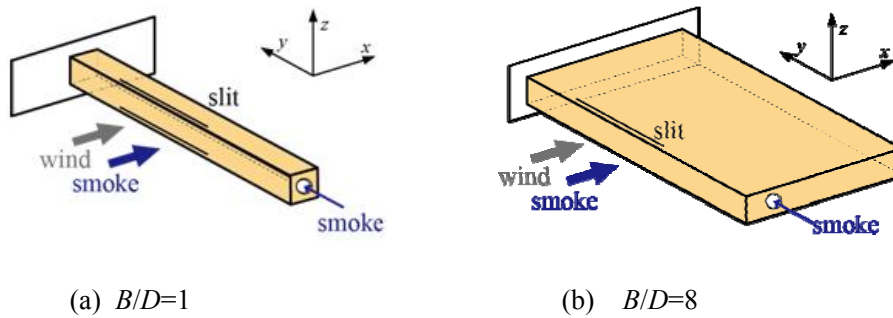


Figure 3: 2-D rectangular prism for flow visualization

(2) Mode Decomposition of Multivariate Time Series

a) POD

POD is widely used to extract dominating modes $\{\phi_r(\mathbf{x})\}$ ($r=1, \dots, n$) of n -dof from m set of time series data (or m snap shots of image) of fluctuating components in a physical quantity $\{v_t(\mathbf{x})\}$ ($t=0, \Delta t, 2\Delta t, \dots, (m-1)\Delta t$), where Δt is constant sampling interval [sec]. A vector \mathbf{x} denotes a certain location in n -dimensional space (or index of a certain node in 2-D plane), such as a velocity component at the location \mathbf{x} ¹¹⁻¹⁴. A POD mode represents a principal steady flow structure fluctuating with its natural frequency. POD modes are determined by solving the eigenvalue problem of covariance matrix $[C]$ of $\{v_t(\mathbf{x})\}$, where the normalized eigenvectors of $[C]$ correspond the orthogonal POD modes and each eigenvalue represents energy contribution of a mode to the overall data. That is,

$$[C] \{\phi_r(\mathbf{x})\} = \lambda_r \{\phi_r(\mathbf{x})\} \quad (1)$$

$$\sum_{r=1}^n \int_0^{(m-1)\Delta t} [\{\phi_r(\mathbf{x})\} \{\phi_r(\mathbf{x})\}^T \{v_t(\mathbf{x})\}]^2 dt = \sum_{r=1}^n \lambda_r \quad (2)$$

where, $[C]$: covariance matrix of time series data $\{v_t(\mathbf{x})\}$,

$$[C] = \frac{1}{T} \int_0^{(m-1)\Delta t} \{v_t(\mathbf{x})\} \{v_t(\mathbf{x})\}^T dt \quad (3)$$

$\{\phi_r(\mathbf{x})\}$: r -th POD mode ($r=1, \dots, n$) and $\{\phi_i(\mathbf{x})\} \{\phi_j(\mathbf{x})\}^T = \delta_{ij}$ (Kronecker's delta), T : data length [sec].

b) DMD

DMD is able to extract temporal variation in the flow fields¹⁴) and gives temporal and spatial evolution of flow pattern. Phase information of velocity component at different location is also contained in DMD modes, whereas the ordinary POD loses it¹⁵). DMD assumes that time sequence of physical quantity, $\{v_t(\mathbf{x})\}$ to $\{v_{t+\Delta t}(\mathbf{x})\}$, can be expressed by a linear mapping,

$$[A] \{v_t(\mathbf{x})\} = \{v_{t+\Delta t}(\mathbf{x})\} \quad (4)$$

where, $[A]$ is a matrix and not a function of time t .

An m set of time series data, $[\mathbf{X}]_0^{(m-1)\Delta t}$, can be converted to $[\mathbf{X}]_{\Delta t}^{m\Delta t}$ by using $[A]$,

$$\begin{aligned} [A] [\mathbf{X}]_0^{(m-1)\Delta t} &= [[A]\{v_0(\mathbf{x})\}, [A]\{v_{\Delta t}(\mathbf{x})\}, [A]\{v_{2\Delta t}(\mathbf{x})\}, \dots, [A]\{v_{(m-1)\Delta t}(\mathbf{x})\}] \\ &= [\mathbf{X}]_{\Delta t}^{m\Delta t} \end{aligned} \quad (5)$$

where, $[\mathbf{X}]_0^{(m-1)\Delta t} = [\{v_0(\mathbf{x})\}, \{v_{\Delta t}(\mathbf{x})\}, \{v_{2\Delta t}(\mathbf{x})\}, \dots, \{v_{(m-1)\Delta t}(\mathbf{x})\}]$.

DMD modes are eigenvectors of the matrix $[A]$. Instead of solving eigenvalue problem of $[A]$ directly, the mathematical approach called singular value decomposition (SVD) will be used because of saving time to solve large-scale eigenvalue analysis and the SVD gives more robust result^{14), 15)}. By SVD, the matrix $[\mathbf{X}]_0^{(m-1)\Delta t}$ can be decomposed into three matrices $[U]$, $[\Sigma]$ and $[W]$, as

$$[\mathbf{X}]_0^{(m-1)\Delta t} = [U][\Sigma][W]^* \quad (6)$$

where, $[U]$ and $[W]$ are unitary matrices, $[]^*$ is the transposed taking conjugate of each element.

Substituting equation (6) into equation (5), the matrix $[S]$ can be obtained after rearranging,

$$[S] = [U]^*[A][U] = [U]^* [\mathbf{X}]_{\Delta t}^{m\Delta t} [W][\Sigma]^{-1} \quad (7)$$

All matrices in the right hand side of equation (7) can be calculated or available, the matrix $[S]$ is determined. Since the matrix $[A]$ contains the POD modes of the data sequence $[\mathbf{X}]_0^{(m-1)\Delta t}$, the above operation amounts to a projection of the linear operator $[A]$ onto a POD basis [15]. Eigenvectors of $[A]$, DMD modes, are calculated from eigenvectors of the matrix $[S]$ as

$$\{\xi_r\} = [U]\{y_r\} \tag{8}$$

where, $\{\xi_r\}$: r -th DMD mode, $\{y_r\}$: r -th eigenvector of $[S]$, i.e. $[S]\{y_r\} = \kappa_r\{y_r\}$.

The data $\{v_{m\Delta t}(\mathbf{x})\}$ can be expressed as:

$$\{v_{m\Delta t}(\mathbf{x})\} = [A]^{m-1}\{v_0(\mathbf{x})\} = \sum_{r=1}^n c_r \kappa_r^{m-1} \{\xi_r\} \tag{9}$$

where, c_r is the coefficient decided for each mode and has a dimension of focused physical quantity (velocity [m/s] in this study).

The coefficient c_r is not a function of time (but degree of contribution), and only the part κ_r^{m-1} in equation (9) is dependent on time [14]. The norm of κ_r determines amplification of flow structures in the DMD mode, while the characteristic frequency of the DMD mode can be obtained by argument of κ_r as:

$$f_r = \arg[\kappa_r]/2\pi/\Delta t \tag{10}$$

where, f_r : frequency of r -th DMD mode [Hz], $\arg[\]$: argument of complex number ($\arg[\] = \tan^{-1}(\text{Im}(\)/\text{Re}(\))$).

Figure 4 compares the energy distribution of DMD modes determined by eq. (11) and PSD of vertical velocity (w -) component in the wake behind the $B/D=1$ prism.

$$F_{midr} = c_{midr}^2 = (c_r|\kappa_r|^{m/2})^2 \tag{11}$$

where, F_{midr} : energy of r -th DMD mode at $t=m\Delta t/2$ assuming the data consists of m snap shots with sampling interval of Δt .

It is known that the energy distribution of F_{mid} is similar to PSD and the frequency at the peak in the figure corresponds well to the vortex shedding frequency. Figure 5 shows the time evolution of a DMD mode of wake behind the $B/D=1$ prism, whose characteristic frequency is the same as that of vortex shedding. The organization with alternating sign is moving toward downstream and this mode captures well the dominating periodic flow. And DMD is one of the powerful tools to extract dominating and sustainable modes from complex flow pattern.

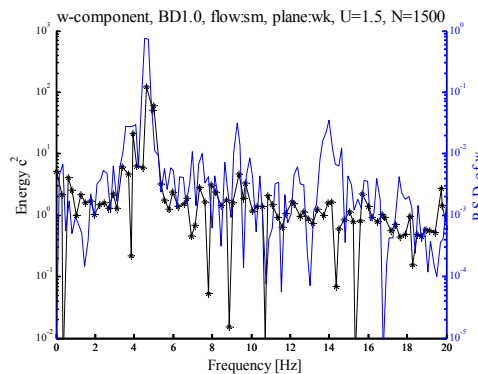


Figure 4 Comparison of energy distribution of DMD mode and PSD of w -component in wake ($B/D=1$).

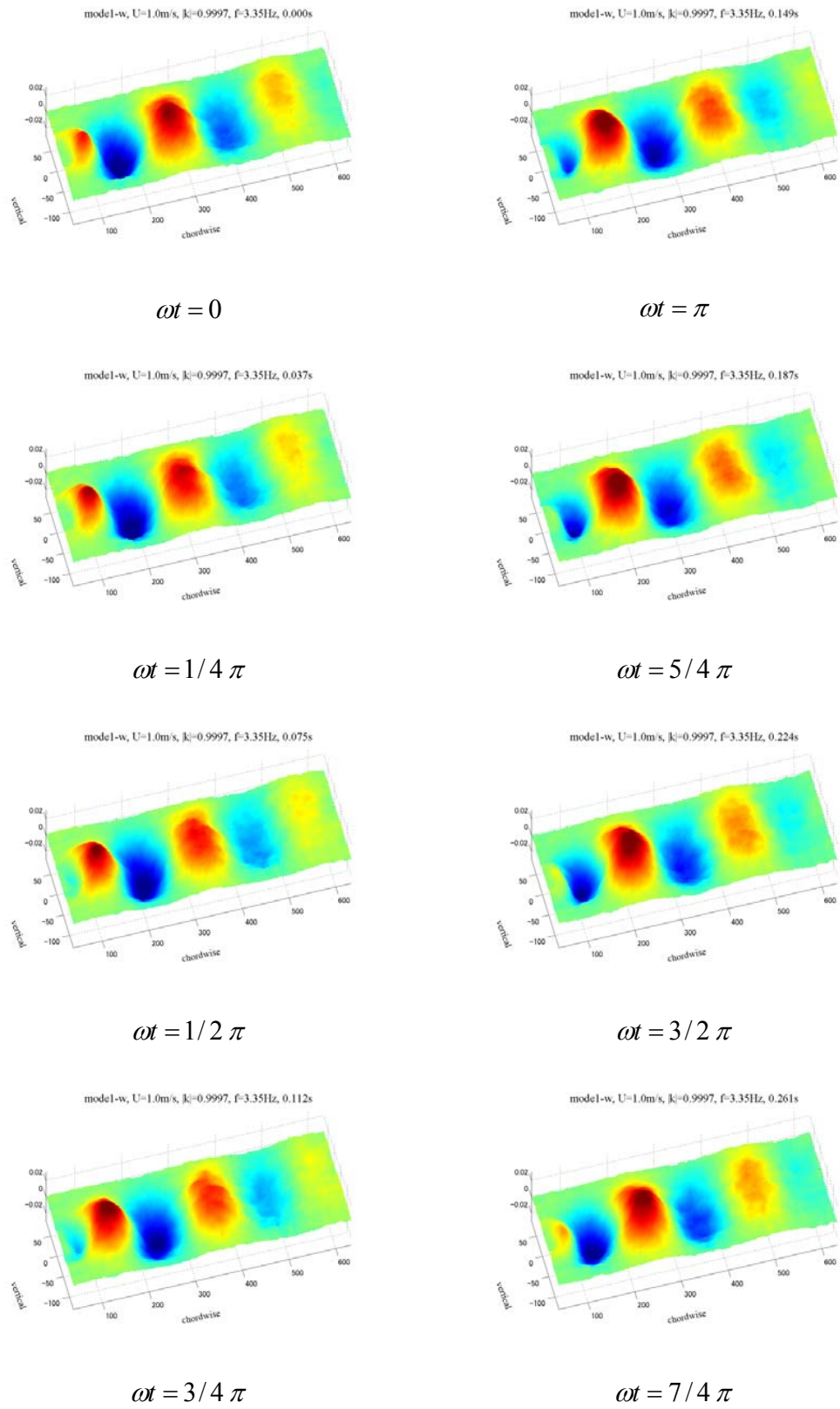


Figure 5 time evolution of DMD mode in wake ($B/D=1$).

3. RESULTS AND DISCUSSION

(1) Pressure fields of side surface

Time averaged and *rms* of pressure coefficients, C_{p_bar} and C_{p_tilde} , at each pressure tap on the side surface are shown in Figure 6. The reattaching point of separating flow is presumed to be at around $x/D=1.8$ to 2.6, by taking an indication of “a bit downstream from C_{p_tilde} peak and a bit upstream of C_{p_bar} ” by the literature.

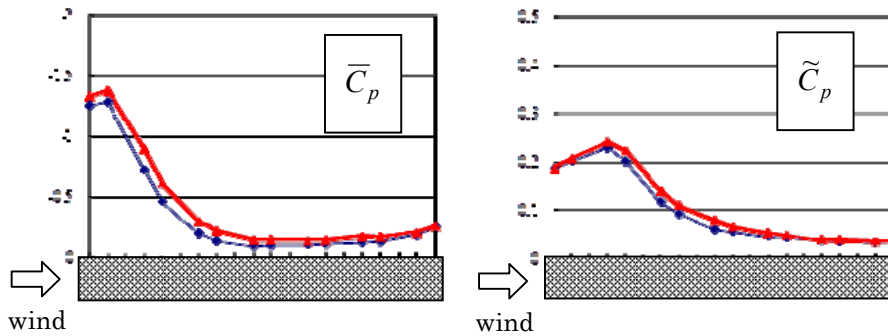


Figure 6: Time average and rms of pressure coefficient ($B/D=8.0$ rectangular prism in grid turbulence)

Figure 7 shows spatial distribution of cross correlation coefficient of surface pressure fluctuation between two locations on the side surface. Reference point is chosen at the most upstream pressure tap in the span center of the prism (indicated by red solid circle in the figure). Cross correlation coefficient $\rho_p(x,y)$ is calculated by the following equation:

$$\rho_p(x, y) = E[p(x_0, y_0; t)p(x, y; t)] / [\{E[p(x_0, y_0; t)^2]\}^{1/2}\{E[p(x, y; t)^2]\}^{1/2}] \quad (11)$$

where, $E[f(t)g(t)] = \frac{1}{T} \int_0^T f(t)g(t)dt$, T : data length [sec], $p(x_0, y_0; t)$: time series of pressure fluctuation at the reference point [Pa], $p(x, y; t)$: time series of pressure fluctuation at location (x, y) [Pa].

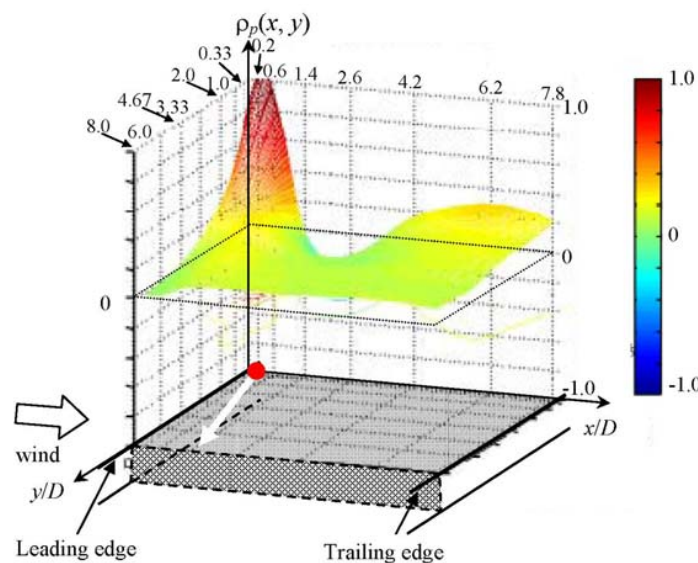


Figure 7: Spatial distribution of cross correlation coefficient $\rho_p(x/D, y/D)$
 (● : reference point, $(x_0/D, y_0/D)=(0.2, 0)$. White arrow indicates relatively more correlated domain.)

The cross correlation coefficient takes negative value at about $x/D=1.4$ to 3.5 and just downstream from the reference point. This region is presumed to be near the reattaching point. This negative correlation means that the pressure in this region fluctuates out of phase from those at the reference point. If the location of reattaching point is assumed to move back and forth, the separation bubble will undergo shrink and elongation. Pressure level in the separation bubble will be up and down alternatively. When the bubble shrinks, the reattaching point must move to upstream and pressure level in the bubble will decrease. Therefore, pressure at the reference point being always in the bubble will be more negative, while pressure at near the reattaching point will be out from the bubble which makes pressure reduced (relatively more positive).

It is known that the pressure near the leading edge and being apart from the reference point more than $4.67D$ shows almost non-correlated. However, along the line parallel to x axis at $y/D=8.0$, the coefficient starts from zero near the leading edge but seems to increase and slightly more positive value. It seems that the distribution of cross correlation coefficient displays more correlated domain along the white arrow as shown in the figure. The existence of this skewed correlated domain was confirmed for other rectangular prisms with different B/D as shown in Figure 8 and in other grid turbulence.

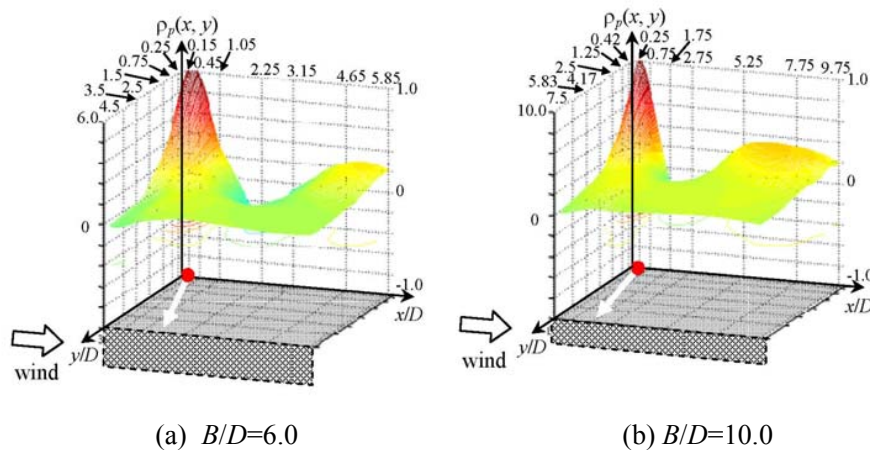


Figure 8: Spatial distribution of cross correlation coefficient $\rho_p(x/D, y/D)$

(2) Velocity fields on side surface

Figure 9 shows the 1st and 2nd POD modes for u and v components in xy plane. For both components, the 1st mode looks to be relatively uniform along span-wise direction, whereas the non-uniform pattern dominates in the 2nd mode. The energy ratio of the 1st mode to the 2nd is about 3 for u - and 2 for v -component, where the participation of the 1st mode to the overall variance is 6% for u - and 4% for v -component. Therefore, the entire velocity field cannot be well described by the 1st mode only, and the 2nd or higher mode plays an important role. Larger u -component appears in $x/D=2.5$ to 3.5 , which is just behind the reattaching point at around $x/D=1.8$ to 2.6 presumed in the last sub-section, (1). This area invokes the longitudinal movement of the reattaching point in back and forth manner.

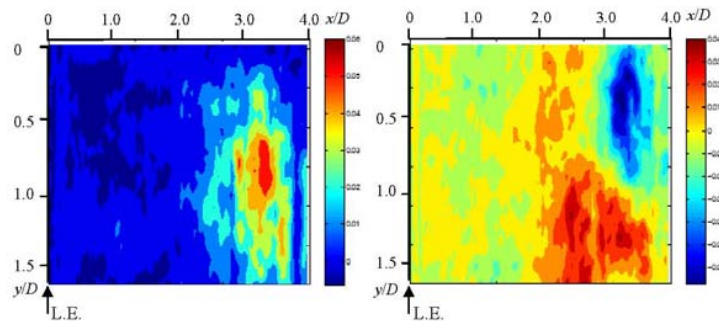
It may be pointed out that there is a skewed ridge configuration in the 2nd mode and more typical in v -component, in this case. The u -momentum in the ridge may be transported towards span-wise direction by v -component and of v -momentum towards chord-wise direction by u -component. This cross momentum transport will enhance the mixing of flow and will contribute to the increase of span-wise correlation of velocity components as well as surface pressure.

Figure 10 is obtained by DMD. Since each DMD mode (eigenvector) consists of complex number elements, it is not easy to catch an image of dynamic flow patterns from DMD modes by displaying real part or norm (absolute value) of each element of an eigenvector. The figures indicated below are displaying phase lag between at the reference point at the leading edge (at bottom left by black circle) and each location in the domain, which is determined by:

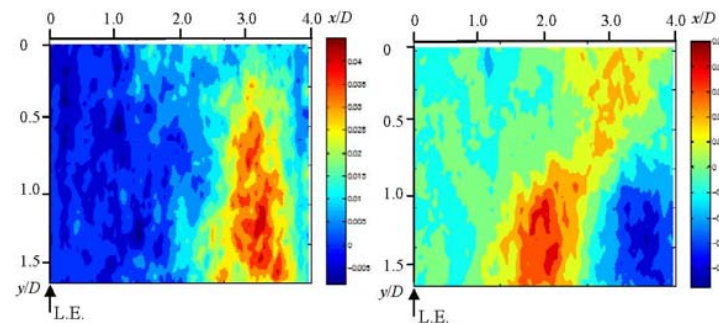
$$\psi_r(x, y) = \arg[\{\xi_r\}_i] - \arg[\{\xi_r\}_{ref}] \tag{12}$$

where, $\psi_r(x, y)$: phase lag of the r -th DMD mode at (x, y) , $\{\xi_r\}_i$: the i -th element of the r -th DMD eigenvector which corresponds to the location at (x, y) , $\{\xi_r\}_{ref}$: the element corresponding to the reference point.

The two modes (4th and 32nd) are selected under the condition of small enough decaying rate ($|\kappa_r|=0.972$ for 4th, 0.995 for 32nd) and low natural frequency ($f_r=3.67$ [Hz] for 4th, 8.80[Hz] for 32nd). Small decaying rate, $|\kappa_r|$ being nearly equal to 1.0, represents enough sustainability of these modes. As for the 4th DMD mode, wide area having the same phase lag is scattered at $x/D=2.8$ to 4.0 (within the broken line in the figure), where larger velocity component was observed in the POD 1st mode as shown in Figure 8. Furthermore, the skewed area of the same phase lag is obtained in the 32nd DMD mode within the broken line. This may be again an indication of the cross momentum transport and the increase of span-wise correlation.



(a) u -component



(b) v -component

Figure 9: POD modes for u - and v -velocity components (left: 1st mode, right: 2nd mode, The entire flow direction is from left to right)

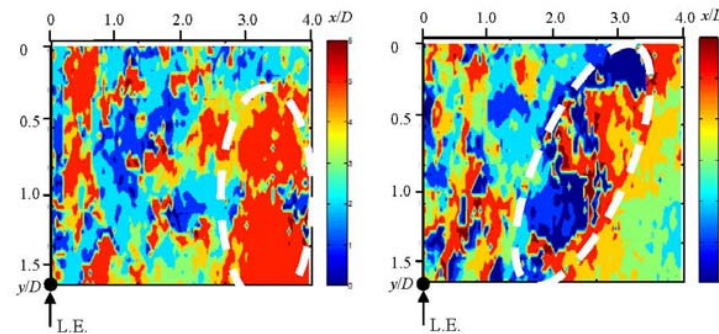


Figure 10: Phase lag from the reference point (indicated by black circle) (v -component, left: 4th mode, right: 32nd mode)

4. CONCLUDING REMARKS

Some remarks to conclude are listed as follows:

- (1) A domain with skew angle to the main flow was observed in the cross correlation coefficient, where the correlation was relatively higher. This implies the cross momentum transport and contributes to the increase of span-wise correlation.
- (2) POD and DMD were applied to the 2-D velocity field near the side surface. Some mode shapes were not in parallel to the leading edge but skewed. This may supports the above observation in the pressure field.

ACKNOWLEDGMENT

Special thanks to Mr. Yutaro Kawata (Obayashi Corp. (former graduate student)) for his pioneering research on DMD.

REFERENCES

- 1) A. G. Davenport, "A statistical approach to the treatment of wind loading on tall masts and suspension bridges", Ph.D. Dissertation, Univ. of Bristol, 1961
- 2) G. L. Larose, "The span-wise coherence of wind forces on streamlined bridge decks", Proc. of the 3rd International Colloquium on Bluff Body Aerodynamics and its Applications, 1996.
- 3) J. B. Jakobsen, "Span-wise structure of lift and overturning moment on a motionless bridge girder", Journal of Wind Engineering and Industrial Aerodynamics, 69-71, 795-805, 1997.
- 4) K. Kimura, Y. Fujino, S. Nakato, H. Tamura, "Characteristics off buffeting forces on Flat Cylinders", Journal of Wind Engineering and Industrial Aerodynamics , 69-71, 365-374, 1997
- 5) M. Matsumoto, H. Shirato, K. Araki, T. Haramura, T. Hashimoto, "Spanwise coherence characteristics of surface pressure field on 2-D bluff bodies", Journal of Wind Engineering and Industrial Aerodynamics, vol.91(1-2), 155-163, 2003.
- 6) M. Matsumoto, H. Shirato, T. Haramura, Y. Odawara. "Spanwise coherent structure of surface pressure on a 2-D bluff body in turbulent flow", Proceedings of the 11th International Conference on Wind Engineering, Lubbock, Texas, 681-688, 2003.
- 7) H. Shirato and M. Matsumoto, "Temporal and Spatial Correlated Properties of Surface pressure and gust forces on a rectangular section in vertical fluctuating winds", Journal of Structural Engineering A, JSCE, 162(3), 669-680, 2006 (in Japanese).
- 8) Y. Ito, H. Shirato, M. Matsumoto, "Span-wise correlations of fluctuating lift forces on 2D rectangular cylinders", Journal of Wind and Engineering, vol.11, No.2, pp.1-10, 2014.
- 9) J. C. R. Hunt, "Turbulent Velocities near and Fluctuating Surface Pressures on Structures in Turbulent Winds", Proceedings of the 4th International Conference on Wind Engineering, pp.309-320, 1975.
- 10) H. Shirato, Y. Sato, O. Sasaki, A. Mahindra and R. Mitsugi, "Surface pressure correlation and buffeting force evaluation", Proceedings of the 13th International Conference on Wind Engineering, Amsterdam, 2011.
- 11) Y. Tamura, H. Ueda, H. Kikuchi, K. Hibi and B. Bienkiewics, "Proper orthogonal decomposition study of approach wind – building pressure correlation", Proceedings of the 9th International Conference on Wind Engineering, Retrospect and Prospect, vol.IV, pp.2115-2126, 1995.
- 12) L. Carassale, G. Solari and F. Tubino, "Proper orthogonal decomposition in wind engineering, Part 2: Theoretical aspects and some applications", Wind & Structures, 10(2), pp.177-208, 2007.
- 13) K. Taira, "Proper Orthogonal Decomposition in Fluid Flow Analysis: 1. Introduction", Nagare, 30, pp.115-123, 2011 (in Japanese).
- 14) M. Sakai, Y. Sunada, T. Imamura and K. Rinoie, "Experimental and Numerical Flow Analysis around Circular Cylinders Using POD and DMD", AIAA Fluid Dynamic Conference, pp.1-19, 2014.
- 15) P. J. Schmid, "Dynamic mode decomposition of numerical and experimental data", Journal of Fluid Mechanics, vol.656, pp.5-28, 2010.

EXPERIMENTAL STUDY ON THE EFFECTS OF FREQUENCY RATIO ON IN-LINE OSCILLATION OF TWO SQUARE CYLINDERS IN TANDEM ARRANGEMENT

Kazutoshi Matsuda⁺¹, Kusuo Kato⁺¹, Itsuki Aratsu⁺¹ and Yoko Tashiro⁺¹
⁺¹ Kyushu Institute of Technology, Kitakyushu, Japan

In a past research concerning the in-line oscillation of two square cylinders with an aspect ratio of $B/D=1$ arranged in tandem along the flow, a spring supported test was conducted by changing the distance between the two cylinders by elastically supporting a cylinder and fixating another one. However, in real structures, both cylinders are considered to be elastically supported in most cases. Therefore, in this research, a spring supported test was conducted under the condition that both of cylinders with an aspect ratio of $B/D=1$ arranged in tandem were elastically supported, and the effect of the difference of model support condition on the in-line oscillation response was experimentally investigated. Furthermore, the effect of the natural frequency ratio of the two square cylinders on the in-line oscillation response was also discussed. Flow visualization test by smoke at the time when the two square cylinders were shaking by the forced oscillating method was conducted based on the phase difference and amplitude ratio obtained from the spring supported test. The result of the spring supported test was discussed using the results from the flow visualization tests by smoke. Furthermore, the hysteresis in flow depending upon the distance between the two square cylinders was reported in a previous report. This also was discussed from the result of flow visualization tests.

Keyword: in-line oscillation, wind tunnel test, two square cylinders, frequency ratio, hysteresis in flow

1. INTRODUCTION

When multiple structures, such as the main towers for a bridge, heat exchangers and offshore structures, are placed adjacently in fluid, structures placed in the downstream side are exposed to complicated flow regions, because the separated shear layer reattaches to the downstream structures or interferes with the flow. For this reason, the distance between structures greatly influences changes in flow patterns around the downstream cylinder structures, so that the response characteristics of structures can be altered correspondingly. Okajima et al.¹⁾ conducted an in-line oscillation²⁾ research of two square cylinders in a tandem arrangement. Spring-supported tests were carried out using two square cylinders with one suspended elastically and the other fixed. Chia-Hung Liu and Jerry M. Chen³⁾ measured drag coefficients of the tandem square cylinders and experimentally observed the existence of the hysteresis region in a flow around the square cylinders. The hysteresis region depends on the Reynolds number as well as the distance between the cylinders.

The purpose of this study is to identify the basic in-line oscillation characteristics of two square cylinders in a tandem arrangement. Based on the supposition of actual structures, spring-supported tests, with both square cylinders elastically suspended, were conducted in the hysteresis region. Not only the distance between the two cylinders but also the ratio of the natural frequency of the upstream cylinder to that of the downstream one, was chosen as the parameters. Furthermore, flow visualization tests were performed for consideration from the results of the spring-supported test; one was done when the tandem square cylinders remained stationary, and the other was done when they were forced-oscillating.

⁺¹isfa0001@jaxa.jp, ⁺²isfa0002@company.com, ⁺³isfa0003@univ.ac-u.jp

2. EXPERIMENTAL SETUPS

The models used for the spring-supported test in the wind tunnel had a two-dimensional rigid body; the structural specifications of the model are shown in Table 1. Keeping the Scruton number steady, the natural frequency of the oscillation was altered by changing the weight of the model. Ratio K of two cylinders is defined as ratio of the natural frequency of the cylinder placed upstream to the natural frequency of the downstream cylinder. The definition of the distance between the two square cylinders is described in Figure 1. The two square cylinder models for spring-supported test mounted in the wind tunnel are shown in Figure 2. The test was conducted, using the wind tunnel at Kyushu Institute of Technology. The models used for the flow field visualization test were square prisms whose base was a square 20 mm on a side. The flow visualization test system is shown in Figure 3. The flow visualization test conditions are shown in Tables 2 and 3.

Table 1: Spring-supported test conditions

Angle of attack, α	0 deg.
S/D	1.0, 1.5, 2.0, 2.5, 3.0
Mass per unit length, m	5.00 kg/m
Natural frequency ratio K (= natural frequency of upstream cylinder) / (natural frequency of downstream cylinder)	0.98, 1.0, 1.005, 1.02
Structural damping (in logarithmic decrement), δ	0.0032
Scruton number, $Sc=2m\delta/\rho D^2$	0.80

S: distance between the two square cylinders, ρ : air density=1.23kg/m³, D: model height =0.180m,
L: Model length=0.80m

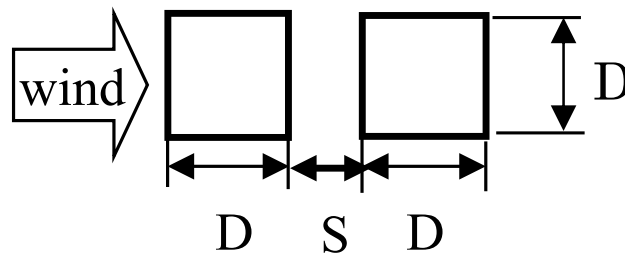


Figure 1: Two square cylinders in the tandem arrangement



Figure 2: Two square cylinder models for spring-supported test mounted in Kyushu Institute of Technology wind tunnel

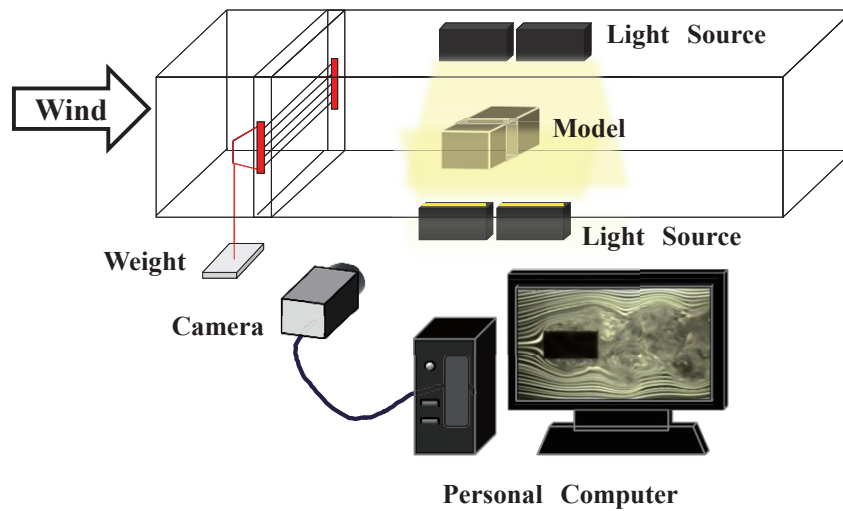


Figure 3: Flow visualization test system

Table 2: Flow visualization test conditions (fixed models)

	S/D=2.0	S/D=3.5	S/D=4.5
Wind speed	0.8 m/s		
Reynolds number (Re_D)	1100		
Spacing	Progressively increasing to reach S/D=2.0	Progressively increasing to reach S/D=3.5	Progressively increasing to reach S/D=4.5
	Progressively decreasing to reach S/D=2.0	Progressively decreasing to reach S/D=3.5	Progressively decreasing to reach S/D=4.5

Model height; $D=0.020m$

Table 3: Flow visualization test conditions (forced-oscillating models)

S/D=2.0			S/D=3.5		
Reduced wind speed; $V_r=V/fD$	Phase angle (deg.)	Forced-oscillating frequency; $f(Hz)$	Reduced wind speed; $V_r=V/fD$	Phase angle (deg.)	Forced-oscillating frequency; $f(Hz)$
3.7	-99	10.8	3.1	-91	12.7
4.2	-43	9.6	3.8	-3	10.5
4.5	-68	8.9	4.1	+8	9.9
4.7	-127	8.5	4.5	-30	8.8

Model height; $D=0.020m$, Wind speed; $V=0.8m/s$, Reynolds number; $(Re)_D=1100$

Amplitude; upstream model $A=0.8mm$, $A/D=0.04$, downstream model $A=1.6mm$, $A/D=0.08$

Phase difference; ϕ is shown with a plus sign when the phase of the downstream model progresses against that of the upstream cylinder, and when the phase of the downstream model falls behind that of the upstream square cylinders, it is shown with a minus sign.

3. EXPERIMENTAL RESULTS AND DISCUSSION

(1) Spring-supported test

The responses of the upstream and downstream cylinders are shown in Table 4. The black solid lines in Table 4 show the response of the single cylinder.

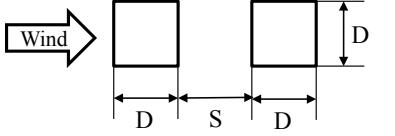
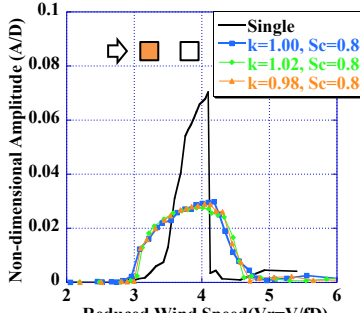
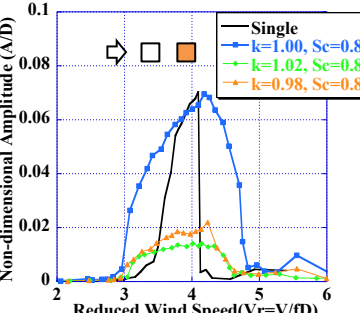
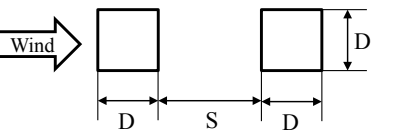
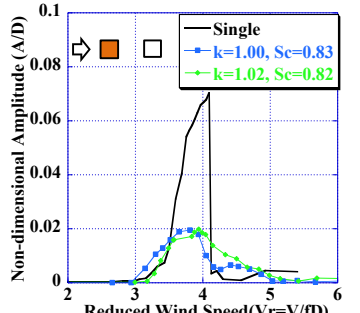
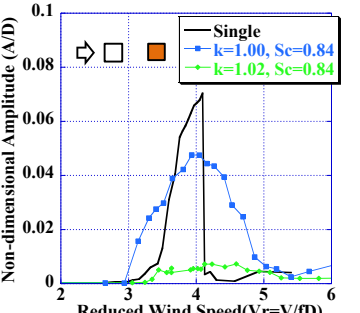
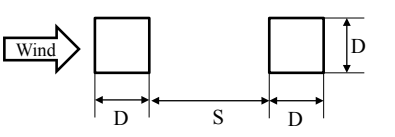
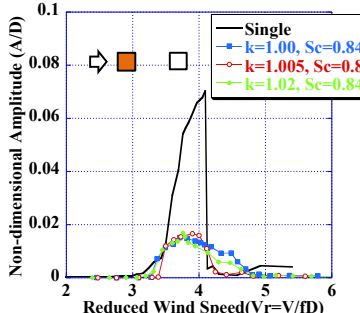
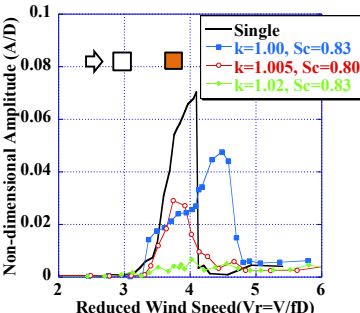
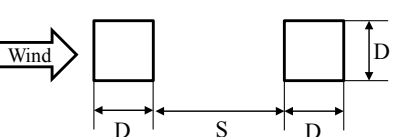
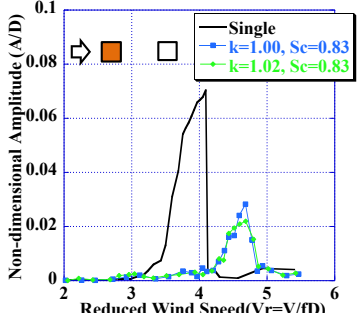
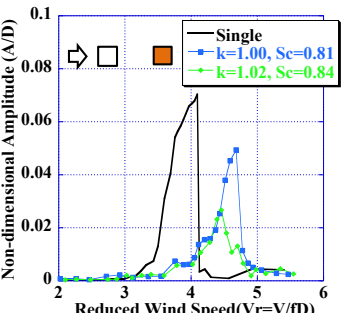
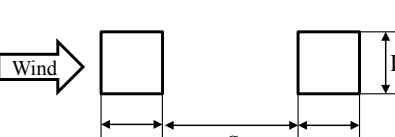
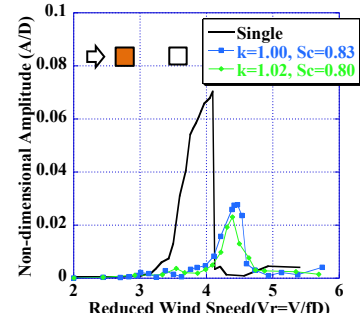
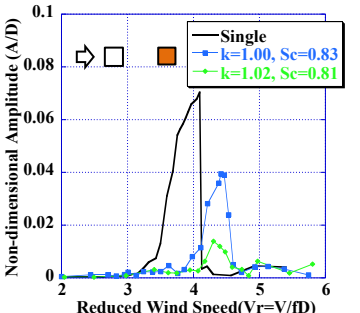
The response of the downstream square cylinders is 1.6-3 times that of the upstream square cylinder. The same response characteristics were reported as a result of a wind tunnel test of cable-stayed bridges with flat box girders in tandem arrangement⁴⁾. This is considered to be because the vibration of the downstream cylinders was excited by the vortex separated from the upstream square cylinders. In the cases for which $S/D=1.0-2.0$, a vibration occurs which peaks between the reduced wind speeds $V_r=3-5$. In the cases for which $S/D=2.5$ and 3.0 , a vibration occurs which peaks between the reduced wind speeds $V_r=4-5$. The reduced wind speed $V_r=4$ corresponds to $1/2$ of the reduced resonant wind speed of the Kármán vortex excitation of a single square cylinder. Therefore, the vibration at the reduced wind speed $V_r=4-5$ in the cases of $S/D=2.5$ and 3.0 is considered to be an in-line oscillation caused by an alternate Kármán vortex. On the other hand, the vibration in the excitation region of the reduced wind speed $V_r=3-4$ is considered to be a self-excited vibration resulting from movement-induced excitation⁵⁾ caused by a symmetric vortex. The reduced wind-speed range where symmetric vortex and alternate vortex generate was confirmed by the flow visualization test.

When S/D (S : distance between two cylinders, D : width of cylinder) became longer, the critical wind speed of in-line oscillation, for both the upstream and the downstream cylinders, was likely to move to the high-wind-speed side. Takeuchi and Kitahara⁶⁾ showed that two different Strouhal numbers existed in the range of $S/D=1.5-2.5$; the definition of S/D was based on this research. Adding further explanation, when the separated shear layer from the upstream cylinder reattached to the top and bottom of the downstream cylinder (zone A), the Strouhal number was high. When the separated shear layer from the upstream cylinder rolled up forming vortices in front of the downstream cylinder (zone B), the Strouhal number was low. The results of this study showed that as the distance between the two cylinders, S/D , became longer, the critical wind speed of the in-line oscillation shifts to the high-wind-speed side, because the flow pattern around the cylinders gradually shifted from zone A to zone B.

The difference between the natural frequency of the upstream cylinder and that of the downstream one is likely to affect the response of the downstream cylinder, while barely affecting that of the upstream cylinder. When the ratio K of two cylinders was 1.02 , the maximum amplitude of the downstream cylinder became less than half in comparison to $K=1.00$. Keeping the ratio of the natural frequency of the cylinders over 1.02 can be one of the countermeasures for actual structures which have tandem square cylinders with small Scruton number.

The phase differences φ between the two square cylinders in the cases for which $S/D=1.0$ and 2.0 are shown in Figures 4 and 5, respectively. The phase difference φ is shown with a plus sign when the phase of the downstream model progresses against that of the upstream square cylinders, which is shown with a minus sign when the phase of the downstream model falls behind that of the upstream square cylinder. In both cases, with the increase of reduced wind speed, the phase difference also changes. Under the wind speed less than that giving the maximum response, when the wind speed increases, the phase difference gradually becomes larger, and under the wind speed larger than that giving the maximum response, when the wind speed increases, the phase difference gradually becomes smaller on the contrary. This trend was also the same in the cases of $S/D=1.5$, 2.0 , and 2.5 .

Table 4: Spring-supported test results

S/D	Upstream Cylinder	Downstream Cylinder
 <p style="text-align: center;">$S/D=1.0$</p>		
 <p style="text-align: center;">$S/D=1.5$</p>		
 <p style="text-align: center;">$S/D=2.0$</p>		
 <p style="text-align: center;">$S/D=2.5$</p>		
 <p style="text-align: center;">$S/D=3.0$</p>		

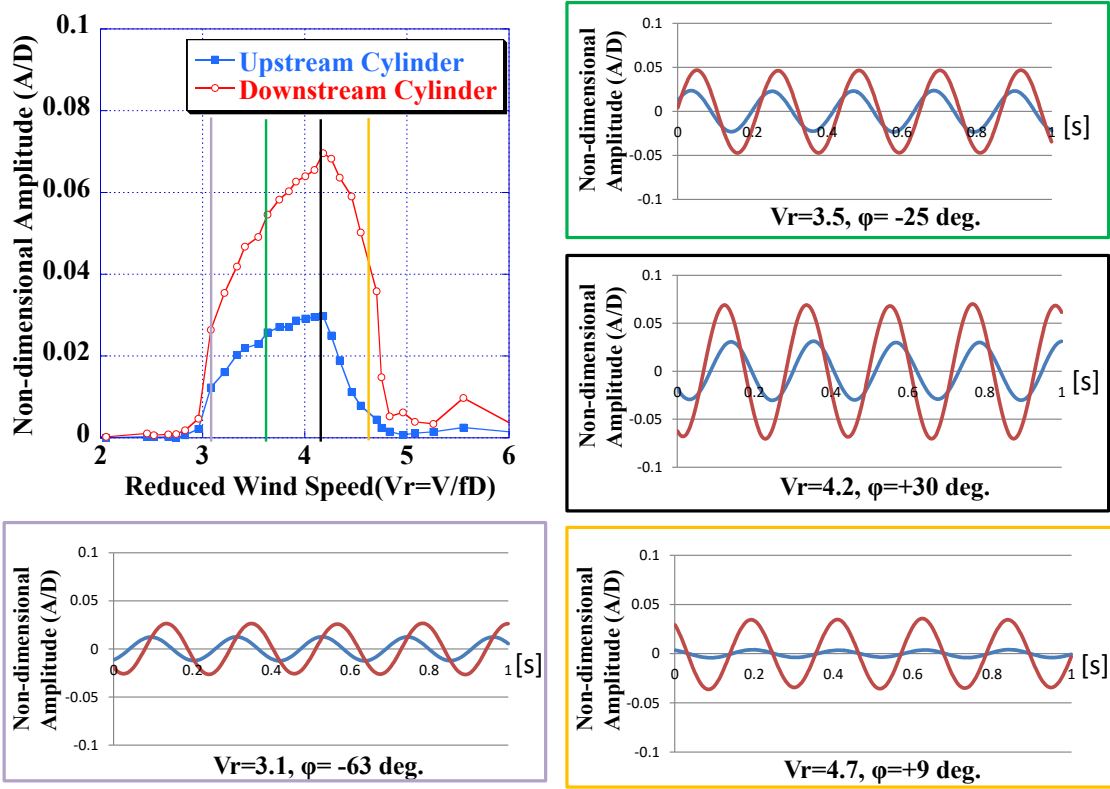


Figure 4: Phase difference ϕ between two square cylinder models ($S/D=1.0$, $K=1.0$)

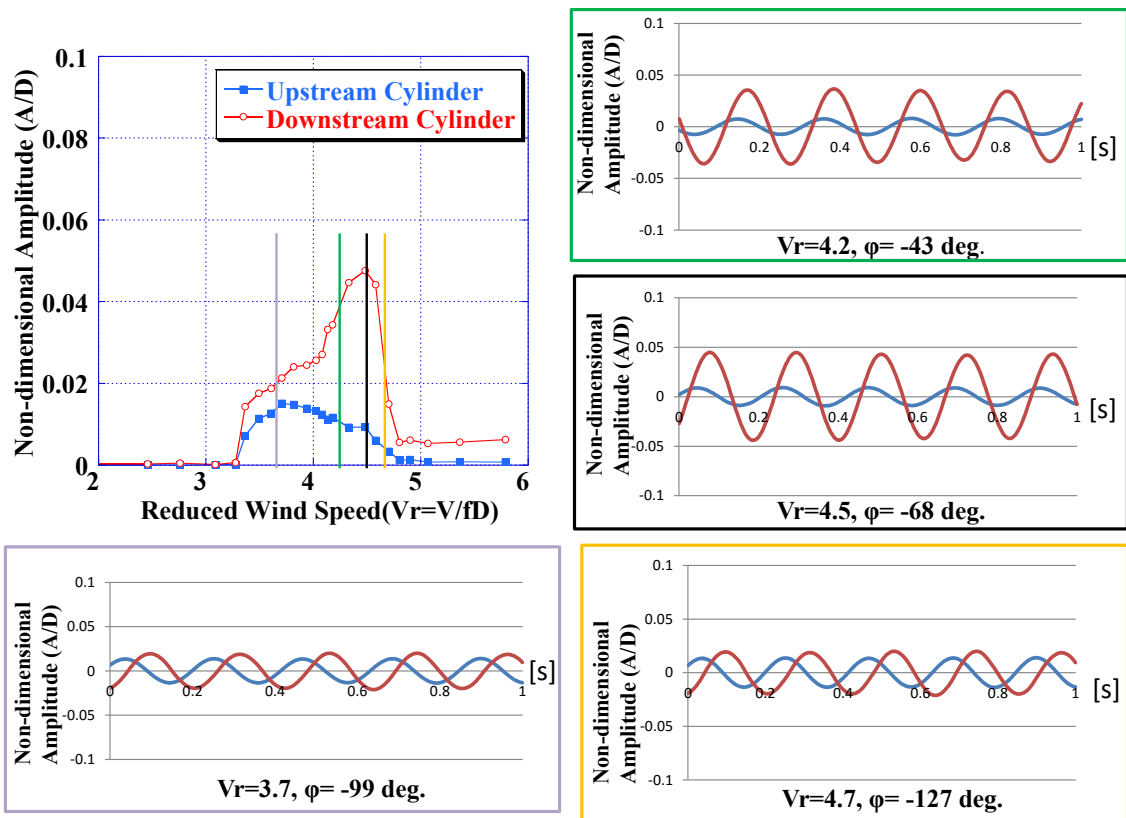


Figure 5: Phase difference ϕ between two square cylinder models ($S/D=2.0$, $K=1.0$)

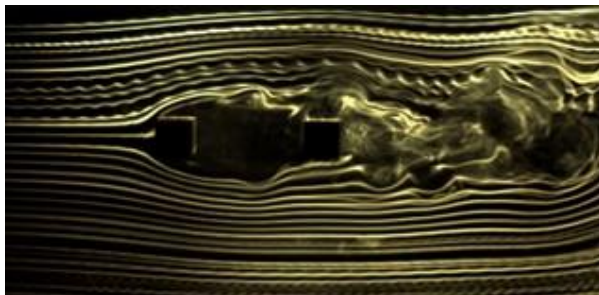
(2) Flow visualization

Figure 6 shows the results of the flow visualization test in the condition where models had a fixed distance between cylinders, $S/D = 3.5$. Both in (a) and (b), the distance between the two cylinders was set at $S/D = 3.5$. Figure 6 (a) shows the case where the distance between the two cylinders had been broadened gradually to reach $S/D = 3.5$. On the other hand, (b) was the case where the distance was gradually narrowed to reach $S/D = 3.5$. While (a) shows that the separated shear layer from the upstream cylinder reattaches to the top and bottom of the downstream cylinder, (b) shows the separated shear layer from the upstream cylinder rolls up forming vortices in front of the downstream cylinder. The test results verified the hysteresis in flow to be the same as the research from the past³⁾. These results are considered to verify the flow visualization test implemented in this research.

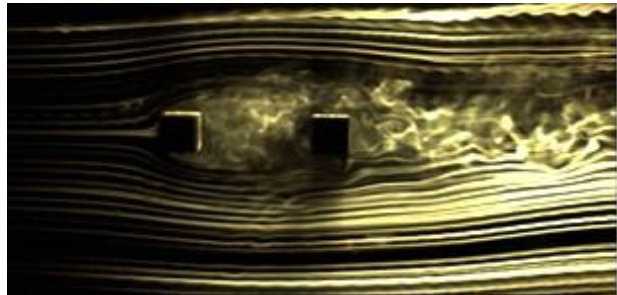
The results of the flow visualization tests at the time when the model was fixed in the cases of $S/D = 2.0$ and 4.5 are shown in Figures 7 and 8, respectively. Even if the distance between the two square cylinders was gradually closed and S/D was set to 2.0 or 4.5 , or the distance between the two square cylinders was gradually widened and S/D was set to 2.0 or 4.5 , the flow pattern was that the separated shear layer from upstream square cylinder reattached to the upper and lower surfaces of the square cylinder of the downstream and a hysteresis in flow was not observed. This is considered to be because $S/D = 2.0$ and 4.5 deviate from the hysteresis region of the flow according to the past research³⁾ when the definition of S/D was based on this research.

Figures 9 and 10 show the results of the flow visualization tests by the forced oscillation method in the cases of $S/D = 2.0$ and 3.5 , respectively. The amplitudes of forced oscillation of the two square cylinders were set, as shown in Table 3, based upon the spring supported test results. In both cases of $S/D = 2.0$ and 3.5 , symmetric vortex shedding occurred in the reduced wind speed V_r smaller than around $V_r = 4$, which is half of the reduced resonant wind speed of the Kármán vortex excitation of the single-square cylinder, and an alternate Kármán vortex occurred in V_r larger than $V_r = 4$.

Flow patterns around the models $S/D = 3.5$ by the forced oscillation method in the hysteresis region as shown in Figure 10 are quite different from those around the fixed models in Figure 6. Therefore, there can be little effect of the hysteresis in flow on the in-line oscillation characteristics of two square cylinders in a tandem arrangement.

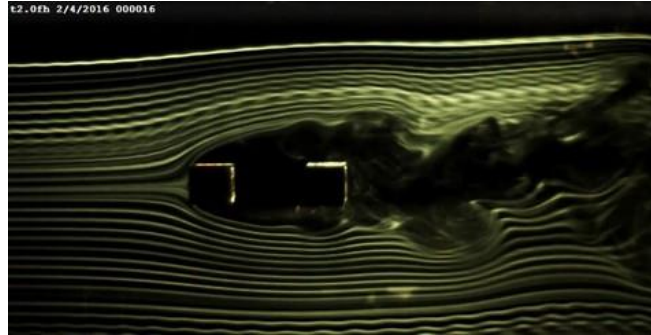


(a) The spacing is progressively increased to reach $S/D = 3.5$.

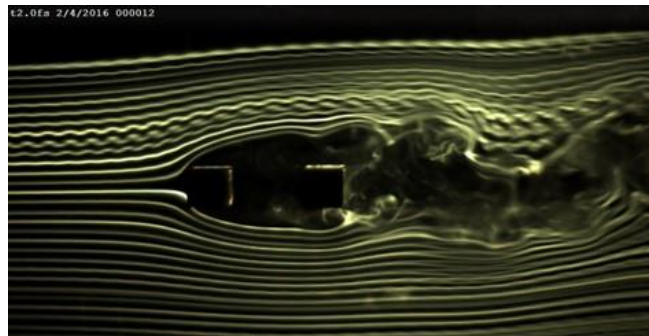


(b) The spacing is progressively decreased to reach $S/D = 3.5$.

Figure 6: Flow visualization test results for fixed models, $S/D = 3.5$

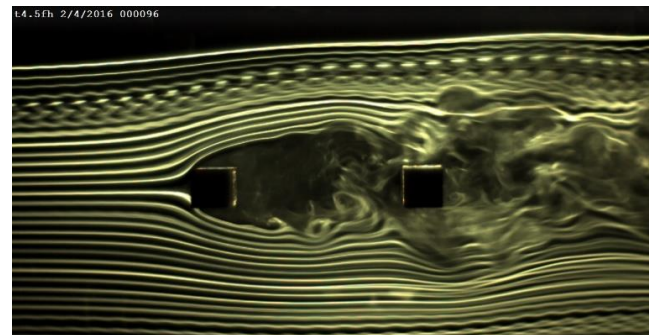


(a)The spacing is progressively increased to reach $S/D=2.0$.

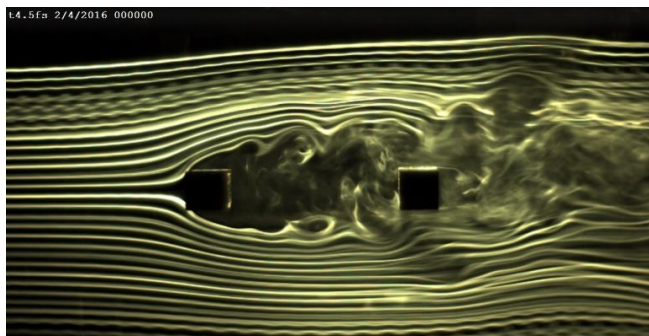


(b)The spacing is progressively decreased to reach $S/D=2.0$.

Figure 7: Flow visualization test results for fixed models, $S/D=2.0$

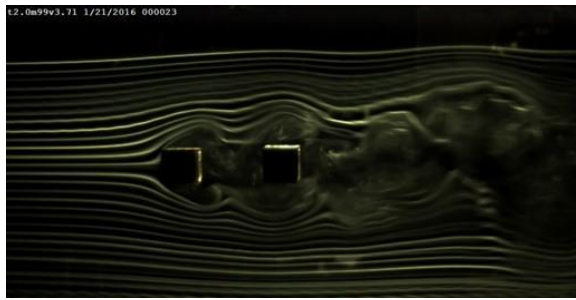


(a)The spacing is progressively increased to reach $S/D=4.5$.

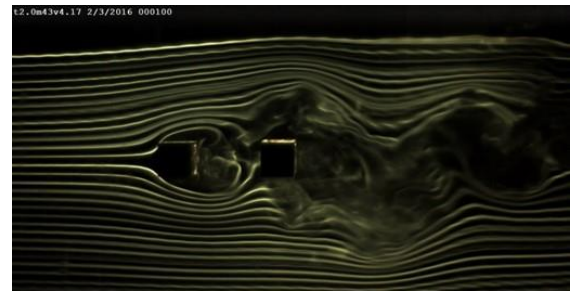


(b)The spacing is progressively decreased to reach $S/D=4.5$.

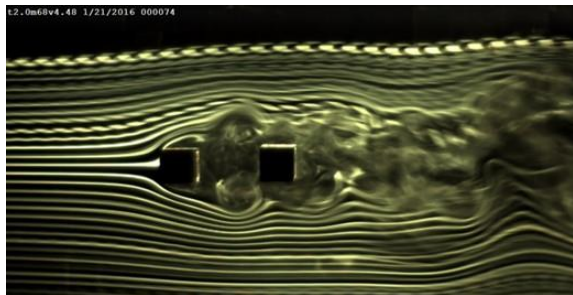
Figure 8: Flow visualization test results for fixed models, $S/D=4.5$



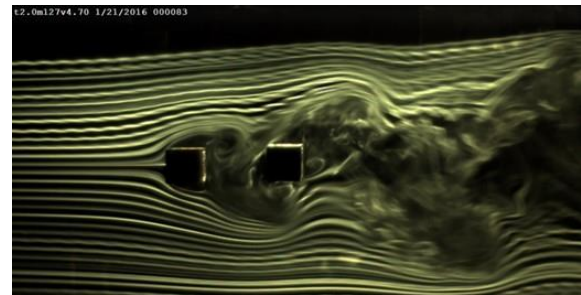
$V_r=3.7, \phi=-99$ deg.



$V_r=4.2, \phi=-43$ deg.

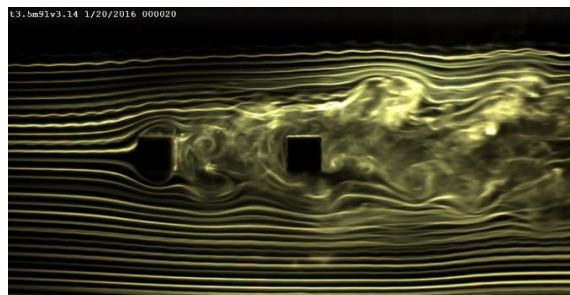


$V_r=4.5, \phi=-68$ deg.

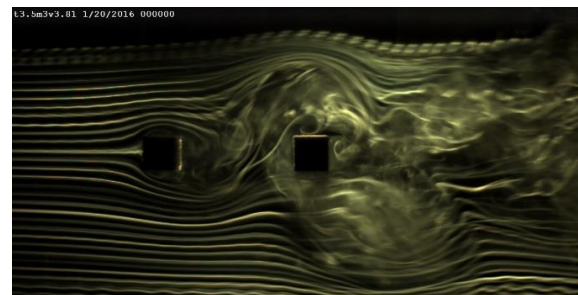


$V_r=4.7, \phi=-127$ deg.

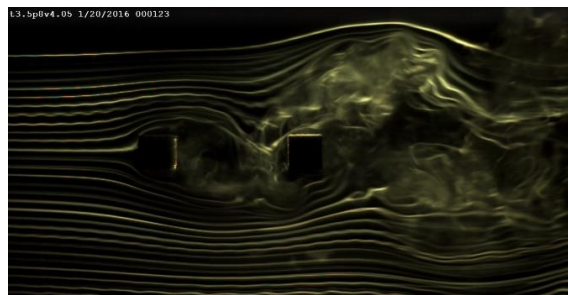
Figure 9: Flow visualization test results for forced oscillating models, $S/D=2.0$



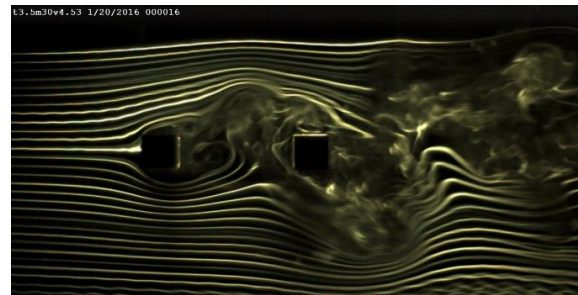
$V_r=3.1, \phi=-91$ deg.



$V_r=3.8, \phi=-3$ deg.



$V_r=4.1, \phi=+8$ deg.



$V_r=4.5, \phi=-30$ deg.

Figure 10: Flow visualization test results for forced oscillating models, $S/D=3.5$

4. CONCLUSIONS

The purpose of this study is to identify the basic in-line oscillation characteristics of two square cylinders in a tandem arrangement. Based on the supposition of actual structures, spring-supported tests, with both square cylinders elastically suspended, were conducted in the hysteresis region. This study verified the followings:

- (1) The difference between the natural frequency of the upstream cylinder and that of the downstream one is likely to affect the response of the downstream cylinder, while barely affecting that of the upstream cylinder. When the ratio K of two cylinders was 1.02, the maximum amplitude of the downstream cylinder became less than half in comparison to $K=1.00$. Keeping the ratio of the natural frequency of the cylinders over 1.02 can be one of the countermeasures for actual structures which have tandem square cylinders with small Scruton number.
- (2) When S/D (distance between two cylinders) became longer, the critical wind speed of in-line oscillation, for both the upstream and the downstream cylinders, was likely to shift to the high-wind-speed side. This was because the flow pattern was gradually changed as S/D became longer; the shift from the state where the separated shear layer from the upstream cylinder reattaches to the downstream cylinder, to the state where the separated shear layer from the upstream cylinder rolls up forming vortices in front of the downstream cylinder.
- (3) Flow patterns around the models $S/D=3.5$ by the forced oscillation method in the hysteresis region are quite different from those around the fixed models. Therefore, there can be little effect of the hysteresis in flow on the in-line oscillation characteristics of two square cylinders in a tandem arrangement.

REFERENCES

- 1) Okajima, A., Yasui, S., Mori, Y., Kimura, S. and Kiwata T. : Flow-Induced In-Line Oscillation of Two Square Cylinders in Tandem Arrangement, Journal of the Japan Society of Mechanical Engineers, Vol.73, No.725, pp.76-84, 2007. (in Japanese)
- 2) The Japan Society of Mechanical Engineers: Guideline for Evaluation of Flow-Induced Vibration of a Cylindrical Structure in a Pipe, Standard JSME S012-1998, 1998.(in Japanese)
- 3) Liu, C.-H. and Chen, J. M.: Observations of hysteresis in flow around two square cylinders in a tandem arrangement, Journal of Wind Engineering and Industrial Aerodynamics, Vol.90, pp.1019-1050, 2002.
- 4) Nagai, T., Sakuma, A., Maekawa, T., Ueda, T., Tanaka, H., Shimodoi, H. and Hatanaka A. :Aerodynamic responses of cable-stayed bridges with flat box girders in tandem arrangement, Proceedings of 14th National Symposium on Wind Engineering, pp.581-586, 1996.(in Japanese)
- 5) Naudasher, E. and Wang, Y.: Flow-induced vibrations of prismatic bodies and grids of prisms, Journal of Fluids & Structures., Vol. 7, pp. 341-373, 1993.
- 6) Takeuchi, T. and Kitahara, T. : Effects of Geometrical and Shape of Tandem Prisms on Vortex-Induced Oscillations, Proceedings of the 10th National Symposium on Wind Engineering, pp.325-330,1988. (in Japanese)

EFFECTS OF VERTICAL PLATES ON THE UNSTEADY PRESSURE CHARACTERISTICS OF RECTANGULAR CYLINDERS

Cristiano Augusto Trein⁺¹, Hiromichi Shirato⁺², Masaru Matsumoto⁺³

^{1,2,3}Department of Civil and Earth Resources Engineering, Kyoto University, Kyoto, Japan
ctrein@cristianotrein.com, shirato@brdgeng.gee.kyoto-u.ac.jp, matsu@brdgeng.gee.kyoto-u.ac.jp

This study investigates the effects of vertical plates on the unsteady pressure characteristics of rectangular cylinders. Effects on phase difference distributions appear as a negative jump at plate's location, followed by a recovering tendency. As for amplitude distributions, two peaks are observed; one at plate's location, another in its downstream. The magnitudes of peaks and jumps are related to size of plate and its distance from leading edge. A peculiar behavior is identified in configurations with two vertical plates. The unsteady pressure characteristics of such arrangements result from a superposition of the effects obtained separately from the corresponding single plates configurations.

Keyword: flutter, unsteady pressure characteristics, fairing, vertical plate, rectangular cylinder, wind tunnel experiment.

1. INTRODUCTION

Aerodynamic instabilities have been of major concern in the design of modern long-span bridges. As spans get longer, decks get slender and fluid-structure interactions get more important. In this scenario, flutter instability has drawn the attention of the scientific and engineering communities. The present investigation is inserted in this context. Motivated by flutter stabilization efforts, experimental studies on rectangular cylinders equipped with vertical plates at different locations are developed. The objective is to clarify relationships between flutter and deck geometry towards the development of methods for flutter stabilization in long-span bridges.

Because aerodynamic interactions are very complex, every new arrangement of cross-section has to be investigated from scratch, resulting in repetitive costs and time consumption. In practical terms, investigations have focused on finding relationships between geometry and flutter stabilization, through the control of aerodynamic derivatives. The goal has been to lead aerodynamic derivatives to stable configurations. In this sense, relationships between geometry and aerodynamic derivatives have been proposed. However, such relationships are very complex and no universal rule has been achieved so far.

Based on such investigations, some guidelines for flutter stabilization have been accepted as common sense among bridge designers. The most important of them refers to the stabilizing role played by negative values of A_2^* derivative^{1;2;3}. Also, A_1^* has been regarded as of relevance in terms of onset velocity. Considering the interdependence between aerodynamic derivatives⁴, variations in A_3^* derivative can relate to flutter instabilization as well. Nevertheless, derivatives interdependence holds well only in streamlined cross-sections⁵, which means that relying only on them may lead to uncertainties, when it comes to more complex geometries of cross-sections.

Because aerodynamic derivatives can derive from the unsteady pressure characteristics developed along the bridge deck, it must be also possible to face the problem of stability of bridges by considering directly the relationships between geometry and unsteady pressure characteristics. Previous investigations demonstrated that flutter can be stabilized by moving peaks in amplitude distributions to downstream while keeping phase difference distributions within the limits of a stability range⁶. The drawback is that relationships between geometry and unsteady pressure characteristics can be achieved only through time consuming techniques. Because of that, they are scarce in the literature. That is a motivation to propose studies in this sense.

By understanding the effects of every *geometric singularity* (geometric modification such as vertical plates, slots, etc) on the unsteady pressure characteristics, it would be possible to compose unsteady pressure characteristics conveniently for flutter stabilization in a preliminary design stage. By doing so, experimental

⁺¹ctrein@cristianotrein.com, ⁺²shirato@brdgeng.gee.kyoto-u.ac.jp, ⁺³matsu@brdgeng.gee.kyoto-u.ac.jp

procedures would be reserved to more advanced stages in the design process. In this sense, investigations with two-box girders have demonstrated that unsteady pressure characteristics of downstream boxes are defined mainly by the characteristics of the slot and the geometry of its cross-section itself⁷, regardless the upstream box geometric configuration. Moreover, slots were found to cancel effects of vertical plates on the upstream box. Despite non-linearities in terms of aerodynamic derivatives, there were simple patterns in terms of relationships between geometry and unsteady pressure characteristics.

Results to be reported herein expand such investigations. Based on studies previously conducted by the authors^{7;8;9;10}, influences of vertical plates on the unsteady pressure characteristics of rectangular cylinders were investigated. As a result, proportionality relationships between size and location of vertical plates with both amplitude and phase difference distributions are identified. Plates of different sizes at different locations along the body were considered.

2. EXPERIMENTAL SET-UP

Investigations were based on wind tunnel tests of harmonically oscillating models in Kyoto University Bridge Engineering Laboratory. Models consisted of rectangular cylinders with vertical plates of two different sizes disposed on its upper surface at different locations. Pressure distributions were measured and analyzed. Discussions on results focused on the role played by location and size of vertical plates in the formation of unsteady pressure characteristics along the upper surface of the models.

The wind tunnel used in the experiments was a room-circuit Eiffel-type tunnel, with a working section 1.8m in height and 1.0m in width. The base model was a $B/D=20$ rectangular cylinder (where B is the width and D is the thickness) made of wood. Fig.1(a) illustrates the experimental set-up.

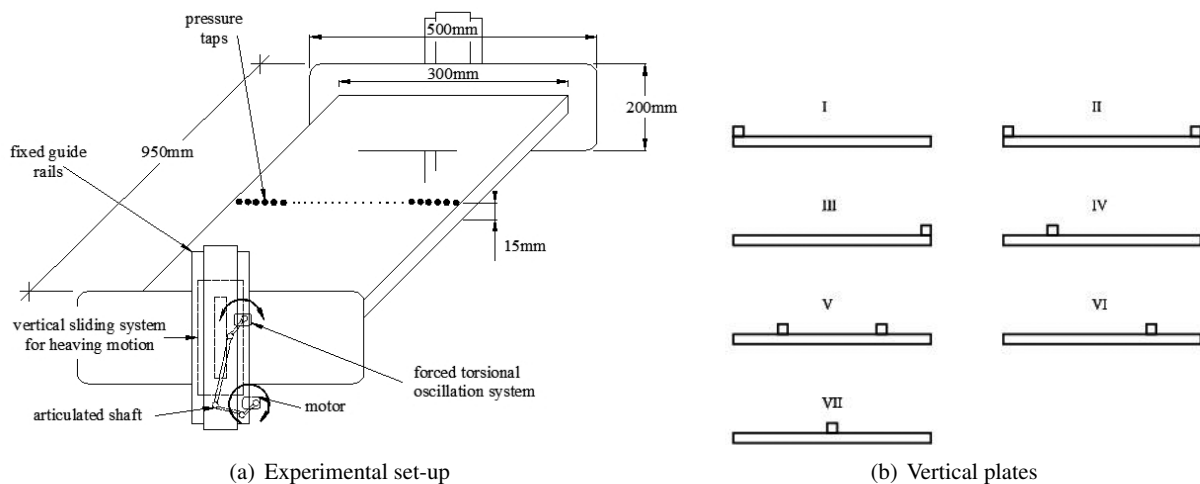


Figure 1: Models

Vertical plates were made of naval wood with a thickness of 3mm and heights equivalent to $D/2$ and D . They were affixed to the upper surface of the models, according to configurations of Fig.1(b). Models were instrumented with 30 equidistant pressure taps, placed on their upper surface, along the chordwise direction at the center of their spans. Pressure measurements were performed in a smooth flow, with turbulence less than 0.5%, via the forced heaving/torsional 1-DOF (degree of freedom) oscillation method. For both motions, frequency of forced oscillation was set to $f=2\text{Hz}$. Amplitude of oscillation in torsional system was $2\phi_0=4^\circ$; in heaving system, amplitude was $2\eta_0=20\text{mm}$. Reduced wind velocities, defined by $U/f.B$ (where U is the wind velocity), ranged from $U/f.B = 5$ to $U/f.B = 25$, in steps of 5.

In the analysis of pressure distributions in harmonically oscillating bodies, information is discretized according to the non-dimensionalized (normalized by the half width b) x widthwise coordinate. This parameter is defined as x^* and ranges from -1 to $+1$, where 0 is the center of the cross-section. For every normalized location x^* , pressure signals are divided into mean and fluctuating pressure components. In this study, discussions are restricted to fluctuating pressure components, which correspond to the so-called *unsteady pressure characteristics*.

The equation below describes the fluctuation pressure components.

$$\tilde{C}_p(x^*, t) = -\tilde{C}_p(x^*) \cdot \cos(2 \cdot \pi \cdot f \cdot t - \psi(x^*)) \tag{1}$$

where $\tilde{C}_p(x^*, t)$ is the fluctuating pressure coefficient at x^* at time t ; $\tilde{C}_p(x^*)$ is the full amplitude (negative to positive peaks) of the unsteady pressures, normalized by the dynamic pressure of the flow $1/2 \cdot \rho \cdot U^2$; ρ is the air density; f is the forced oscillation frequency; t is the time; $\psi(x^*)$ is the phase difference between the maximum relative angle of attack of the model and the negative pressure peak on its upper surface at every location x^* .

Models are identified by a composition of the code of the regular $B/D=20$ rectangular cylinder (NF), the set-up code (Fig.1(b)) and the size code of the vertical plates, which is A for height= $D/2$ and B for height= D .

3. EXPERIMENTAL RESULTS

Rectangular cylinders have been widely used as fundamental geometries in investigations on bridge decks. Because of that, a large amount of data regarding such a cross-section is available in literature. In order to profit from such a database, a rectangular cylinder was chosen for this investigation. The decision for a large side ratio ($B/D=20$) was based on the current tendency modern bridges have experienced towards slender decks.

In rectangular cylinders, remarkable similarities between unsteady pressure characteristics obtained from heaving and torsional forced oscillations have been identified⁴. However, in bridge decks, this phenomenon has shown dependence on the shape of the cross-section. Studies have demonstrated that the similarity between torsional and heaving systems in bridge decks decreases with the increase of the complexity of the deck geometry^{11;12;13}. Such an effect has a great impact on the aerodynamic derivatives, especially on the interdependence mentioned in the Introduction. Consequently, flutter stability itself is also affected. The understanding of how modifications in geometry can exert influence on such a break of similarity is a factor to be understood to control flutter stabilization from the unsteady pressure characteristics point of view.

Results of investigations are organized according to set-ups and sizes of vertical plates. They are accompanied by considerations on the relationships of size and location of the vertical plates with the resulting impacts on phase difference $\psi(x^*)$ and amplitude $\tilde{C}_p(x^*)$ distributions. The results may be also considered as an assessment of the effects of separation points and blockages along the chord direction in the upper surface of rectangular cylinders. Fig.2 presents the unsteady pressure characteristics for the $B/D=20$ rectangular cylinders (model NF). The following sections present other results.

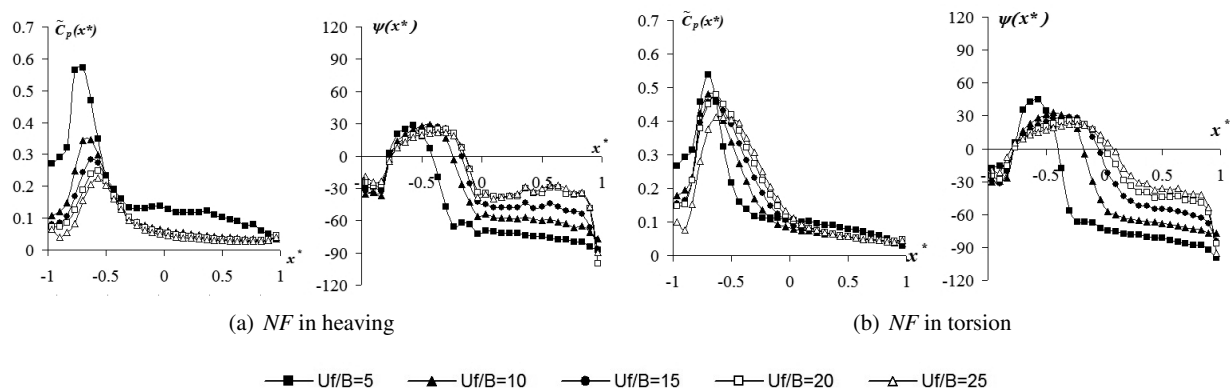


Figure 2: Unsteady pressure characteristics of $B/D=20$ rectangular cylinder

(1) Vertical plate at the leading edge

Fig.3 reports the experimental data obtained by installing vertical plates of two different sizes at the leading edge. For both plates, amplitude $\tilde{C}_p(x^*)$ distributions resemble those obtained for a regular $B/D = 20$ rectangular cylinder (Fig.2). However, a shift downstream of the peak is observed with the increase of the size of the plate. Techniques of flow visualization combined with pressure measurements have pointed out that the location of the peak of the fluctuating pressures in stationary rectangular cross sections is related to the reattachment of the separated flow, revealing the dimension of the separation bubble¹⁴. This location was found

to be in a distance $x_0^* = 4.4D/b$ from the leading edge. Even though this relationship refers to stationary cylinders, peaks in the distributions of Fig.2 at the highest reduced wind velocity ($U/f.B=25$) were situated within that limit.

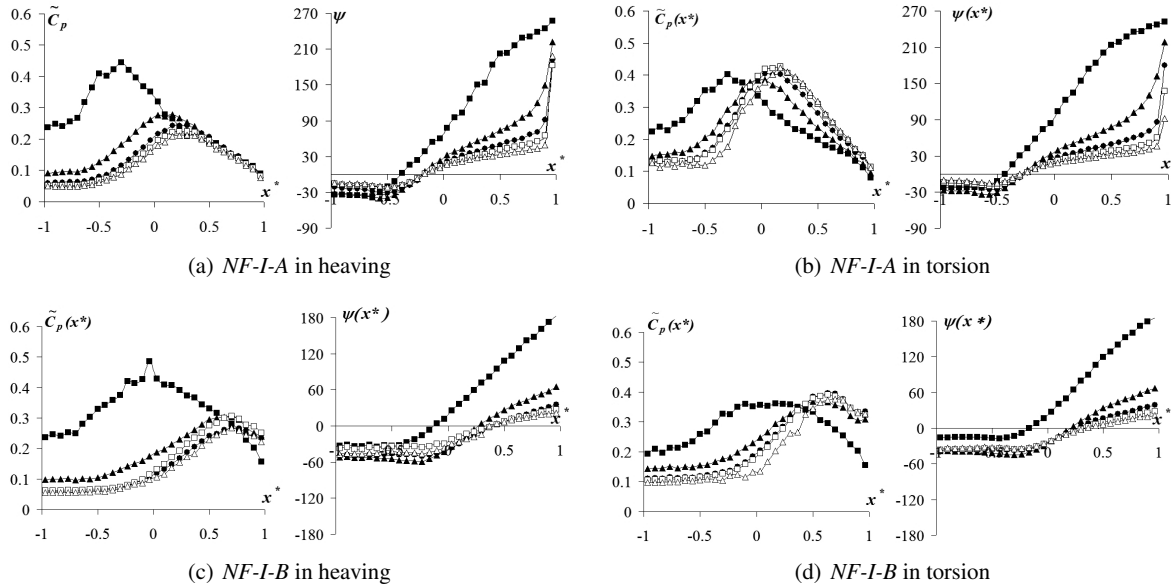


Figure 3: Unsteady pressure characteristics of B/D=20 rectangular cylinders with vertical plates A and B at the leading edge

It was so attempted to check whether the relationship above could be applied to the results of Fig.3. Even though the original relationship was obtained with stationary models and results presented herein related to models in harmonic motion, such comparison may provide an insight for the definition of semi-empirical relationships to be used in investigations with rectangular cylinders.

The distances x_0^* between the leading edge and the peaks of all $\tilde{C}_p(x^*)$ distributions of Fig.3 were used in the calculation of an *equivalent thickness* D_{eq} that would satisfy the equality $x_0^* = 4.4.D_{eq}/b$. From this *equivalent thickness* D_{eq} , an *equivalent side ratio* BD_{eq} was calculated. In this context, another convenient parameter is the *apparent side ratio* $(B/D)_{ap}$. This index is defined as a ratio between width B of the original rectangular cross-section and the resulting cross-flow dimension, which is composed of the actual thickness D of the cylinder and the height of the vertical plate. Results are reported in Table 1.

Table 1: Equivalent side ratio, equivalent thickness and apparent side ratio for NF-I-A and NF-I-B, calculated through $x_0^* = 4.4D_{eq}$

U/f.B	5		10		15		20		25		$(B/D)_{ap}$
	D_{eq}	BD_{eq}									
NF-I-A in torsion	0.16	12.57	0.23	8.52	0.23	8.52	0.27	7.54	0.27	7.54	13.3
NF-I-A in heaving	0.16	12.57	0.27	7.54	0.30	6.77	0.30	6.77	0.30	6.77	13.3
NF-I-B in torsion	0.27	7.54	0.34	5.87	0.37	5.39	0.37	5.39	0.39	5.18	10.0
NF-I-B in heaving	0.22	9.10	0.37	5.39	0.39	5.18	0.39	5.18	0.39	5.18	10.0

With the increase of the reduced wind velocity, *equivalent side ratios* BD_{eq} tend to values nearly the

half of the *apparent side ratios* $(B/D)_{ap}$. Comparing the amplitude distributions $\tilde{C}_p(x^*)$ of these cases with previous experimental data⁴, it is observed that distributions of Fig.3 assume, indeed, configurations similar to the ones related to their *equivalent side ratios* BD_{eq} . Amplitude distribution of *NF-I-A* is in an intermediate state between rectangular cylinders with side ratios $B/D=5$ and $B/D=7.5$. Although magnitude of peaks do not show a full concordance, their positions do. Such a comparison can be seen in Fig.4, for *NF-I-A* in torsion. Similar comparison is provided for *NF-I-B* in torsion in Fig.5.

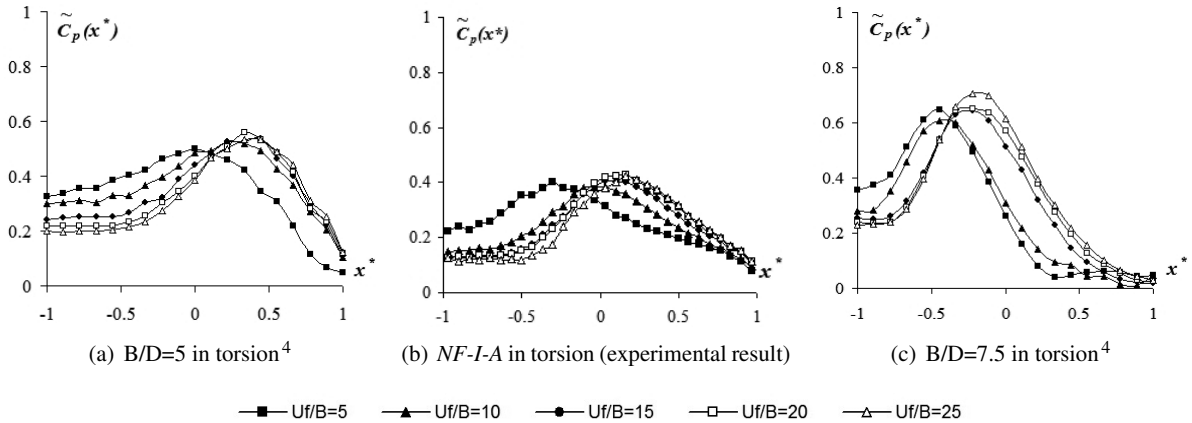


Figure 4: Comparison between amplitude $\tilde{C}_p(x^*)$ distributions of rectangular cylinders with side ratios $B/D=5$, $B/D=7.5$ and *NF-I-A*, in torsion

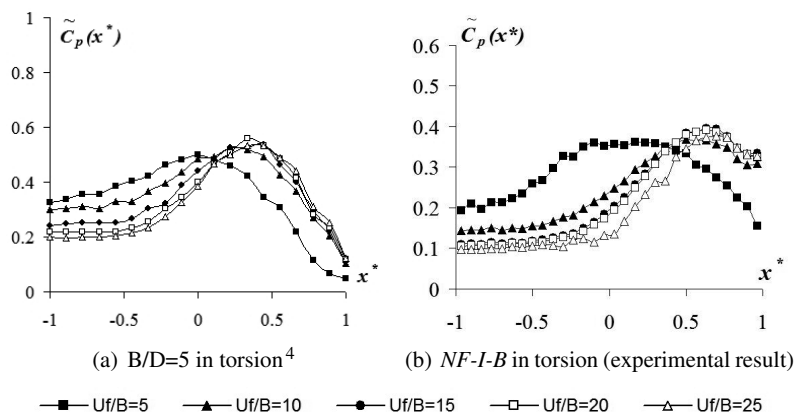


Figure 5: Comparison between amplitude $\tilde{C}_p(x^*)$ distributions of rectangular cylinders with side ratios $B/D=5$ and *NF-I-B*, in torsion

A vertical plate at the leading edge induces amplitude distributions $\tilde{C}_p(x^*)$ to behave as if it derived from a regular rectangular cylinder with an *equivalent side ratio* 50% smaller than the *apparent side ratio*. Based on that, a comparison link between modified rectangular cylinders (with a vertical plate at the leading edge) and the basic $B/D=20$ configuration can be proposed. Relationships in terms of unsteady pressure characteristics might be established from this perspective.

When it comes to phase difference distributions $\psi(x^*)$, a comparison between distributions $\psi(x^*)$ of Fig.3 and Fig.2 shows that a vertical plate at the leading edge promotes a kind of *scale amplification* on the distributions, as if the region near the leading edge is zoomed in. Curves become elongated, which implies in transferring the first crossing point of the x axis to downstream. For a sake o brevity, in Fig.6, a comparison similar to the one of Fig.4 is provided for the phase difference distributions $\psi(x^*)$ of *NF-I-A*. It is shown that the phase difference distributions of *NF-I-A* are comparable to the ones of a rectangular cylinder with side ratio B/D between 5 and 7.5, which is a conclusion similar to the one obtained for the $\tilde{C}_p(x^*)$ distributions.

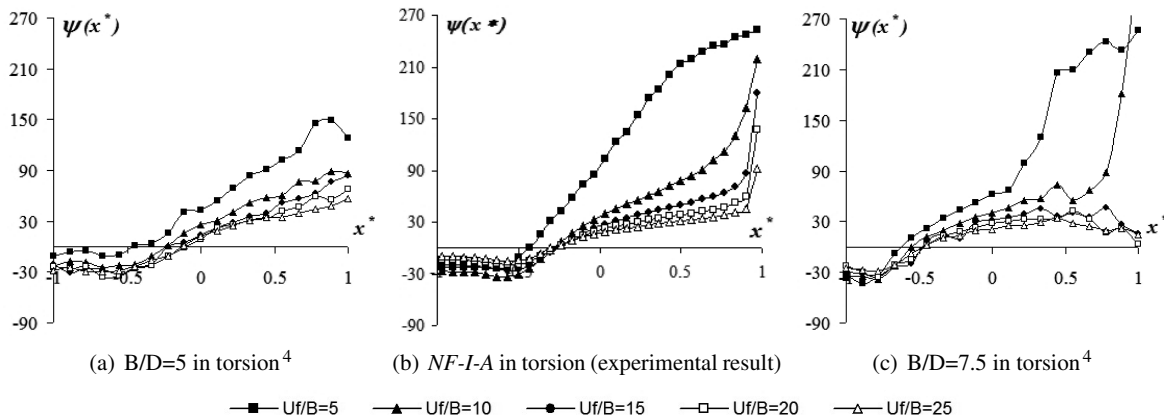


Figure 6: Comparison between phase difference $\psi(x^*)$ distributions of rectangular cylinders with side ratios $B/D=5$, $B/D=7.5$ and $NF-I-A$, in torsion

In the phase difference distributions $\psi(x^*)$ of NF in Fig.2 ($B/D = 20$), all curves cross x axis almost at the same point x_1^* , which is in a distance $\Delta x^* \simeq 0.22$ from leading edge in torsional system and $\Delta x^* \simeq 0.25$ from leading edge in heaving system. For $NF-I-A$, apart from the lowest reduced wind velocity ($Uf/B=5$), all curves also cross x axis almost at the same point x_1^* : $\Delta x^* \simeq 0.70$ in torsional system and $\Delta x^* \simeq 0.80$ in heaving system. These values keep nearly the same 1/3 proportionality existent between equivalent side ratio BD_{eq} and actual side ratios for $B/D=20$ model.

Checking the same assumptions for $NF-I-B$, the conclusions are similar. Even though apparent side ratio is $(B/D)_{ap} = 10$, equivalent side ratio BD_{eq} is induced to present half of this value, Fig.7.

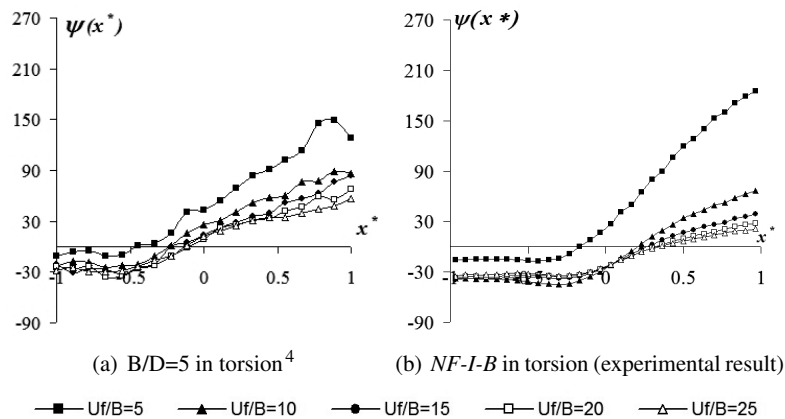


Figure 7: Comparison between phase difference $\psi(x^*)$ distributions of rectangular cylinders with side ratios $B/D=5$ and $NF-I-B$, in torsion

(2) Single vertical plates of size A and B along the chord direction

In Fig.8, unsteady pressure characteristics of models with plate of size A and B installed at three different locations – set-ups IV, VI and VII – are compared with distributions from the configuration without vertical plate (NF). For a sake of brevity, only $Uf/B=25$ is reported.

Effects of vertical plates are perceived in both upstream and downstream of their locations, in both amplitude and phase difference distributions. Upstream of the vertical plate, flow is blocked. The recirculation created by this blockage increases the level of the fluctuating components of the pressure signal and delays the development of the flow. This is translated into a broadening of the amplitude distributions $\tilde{C}_p(x^*)$ in that region and into the imposition of a positive bias on the phase difference distributions $\psi(x^*)$. Positive values of phase difference $\psi(x^*)$ represent a delay in the flow. These effects are perceived throughout all wind velocities range

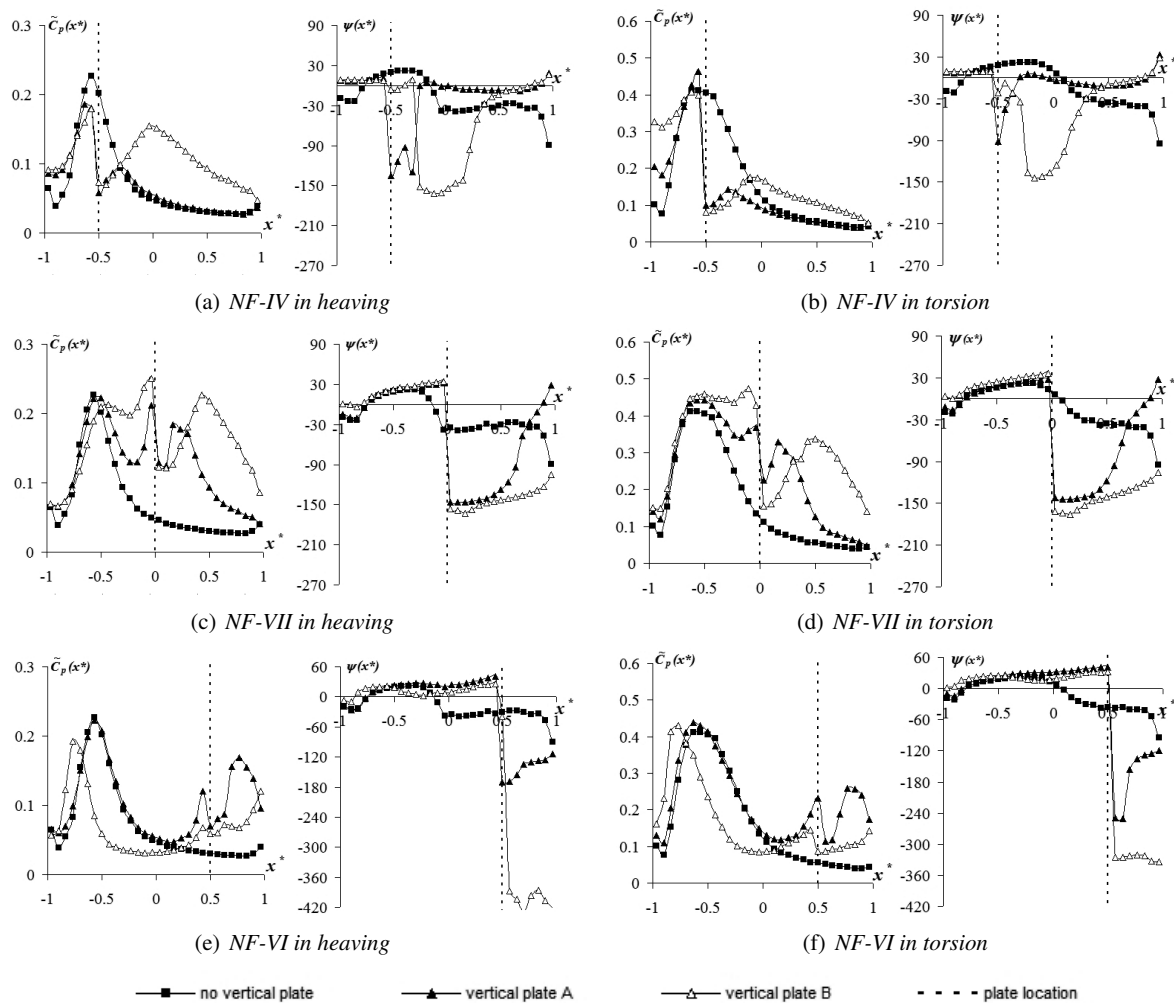


Figure 8: Set-ups *IV*, *VII* and *VI*, with plates of size *A* and *B*, superimposed for leading edges *NF* at $U/f.B=25$

and are emphasized with the increase of the velocity.

In amplitude $\tilde{C}_p(x^*)$ distributions, effects are summarized by the presence of two peaks: one at the vertical plate's location and another in its downstream. When the plate is inside the limits of the peak promoted by the leading edge (set-up *IV*), both peaks get superimposed. As vertical plate moves towards trailing edge (set-ups *VII* and *VI*), peaks become separated. The peak due to the leading edge reappears and its corresponding curve develops itself until reaching some point before the vertical plate, where the curve inverts its decaying tendency and goes up towards the peak related to the vertical plate.

At the vertical plate, flow is separated again. A valley is induced, followed by an ascendant tendency towards the second peak. This last peak must be associated to the reattachment of the flow separated by the vertical plate. The values reached by both peaks depend on the location of the plate. In set-up *IV*, the second peak is weaker and located at a shorter distance from the vertical plate, compared to set-ups *VI* and *VII*. This is a consequence of the high vorticity of that region, in a scale larger than the size of the vertical plate. So, the influences of the plate get proportionally reduced.

In set-ups *VI* and *VII*, amplitude distributions $\tilde{C}_p(x^*)$ start the inversion of the decaying tendency (upstream of the vertical plate) at a location nearly symmetric to the location of the peak induced downstream of the plate. Both distances vary with vertical plate's location and size. In heaving system, they tend to be longer than in torsional system. In average, they reach values around $\Delta x^* = 0.3$ in non-dimensional units for set-up *VII* – *A* and $\Delta x^* = 0.4$ for set-up *VI* – *B*. These values double for plate *B*. Also, with the increase of size, a slight increase in the values of the peaks is noticed. In set-up *VI* – *B*, the larger size of plate results in a compression of the

distribution, displacing the first peak to upstream.

As for phase difference distributions $\psi(x^*)$, influences of plates behave differently. In the upstream side, the distance from the plate where the effects start to be "felt" (inflection point) does not change with the plate's location. This is the same for both heaving and torsional motions. From the inflection point on, distributions get softened. When the plate is reached, a separation point is provided, the flow is accelerated and the tendency gets broken. Downstream of the vertical plate, this acceleration is translated into a "jump" to the negative side of the phase difference distribution $\psi(x^*)$. The magnitude of this jump varies with the configurations, which means that it is influenced by location of vertical plate. Downstream of the negative peak promoted by the jump, phase difference $\psi(x^*)$ distributions tend to gradually recover positive values.

The increase of the size of the plate enhances the effects on the unsteady pressure characteristics. Although some dependence on the location of the plate can be identified, results show same general tendencies for both sizes. As plate moves to downstream and its size increases, amplitude and phase difference distributions follow opposite tendencies. The influences of the vertical plate on amplitude distributions $\tilde{C}_p(x^*)$ decrease with the increase of its distance from leading edge. This is the opposite of what is observed in phase difference distributions $\psi(x^*)$. Increasing of size of plate enhances this disparity.

A larger size of plate enhances the effects on phase difference distributions $\psi(x^*)$. The "jump" reaches higher values and there is an increase in the distance where the influence of the vertical plate starts to be felt upstream. Downstream of the vertical plate, the recovering tendency is softened and the negative values induced by the vertical plate are kept for longer distances.

(3) Two vertical plates along the chord direction

Further comparisons can be established by checking the effects of two vertical plates of same size installed along chord direction. Vertical plates of sizes *A* and *B* were arranged according set-up *V*. The unsteady pressure characteristics of the resulting configurations, *NF-V-A* and *NF-V-B*, are superimposed in Fig.9 for $U/f.B=25$, along with data from model *NF*. The effects obtained are similar for both sizes and follow similar tendencies as described in the previous section.

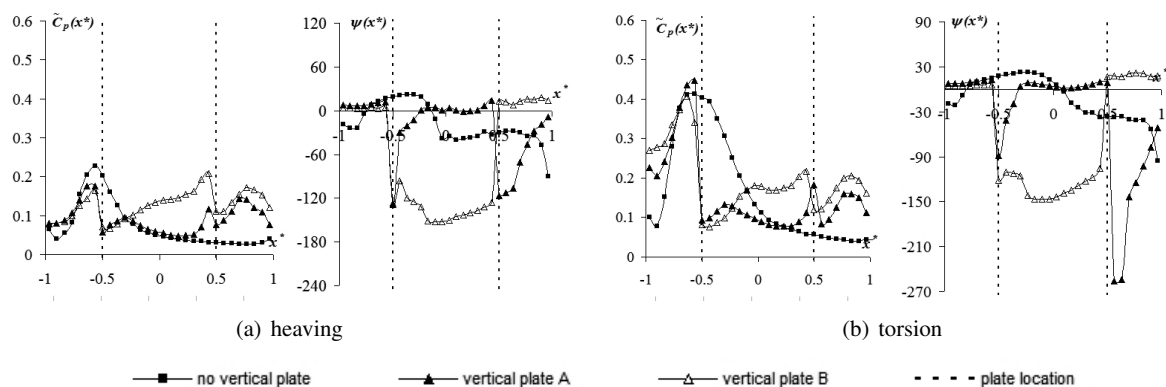


Figure 9: Unsteady pressure characteristics of *NF-V-A* and *NF-V-B* at $U/f.B=25$

Upstream of the plate corresponding to set-up *VI*, both amplitude $\tilde{C}_p(x^*)$ and phase difference $\psi(x^*)$ distributions of set-up *V* behave essentially as they do for case *NF-IV* (Fig.8). Effects of the plate of size *A* corresponding to set-up *VI* on its upstream are practically imperceptible. In the case of plate of size *B*, effects upstream are slightly noticeable. The blockage effect causes an increase in the values of the amplitude $\tilde{C}_p(x^*)$ and the maintenance of the positive values of $\psi(x^*)$. Downstream of the plate corresponding to set-up *VI*, the unsteady pressure characteristics of set-up *V* are similar to those of set-up *VI* itself (Fig.8). As a result, the unsteady pressure characteristics of set-ups *NF-V* become a composition of effects of set-ups *NF-IV* and *NF-VI*, as if both configurations are obtained separately. They can be described as a non cumulative superposition of effects of cases *NF-IV* and *NF-VI*. Such a feature is confirmed from Fig.10.

This is an important characteristic of the compositions of vertical plates studied herein. There seems not to exist a strong interaction between the individual effects of each plate. The unsteady pressure character-

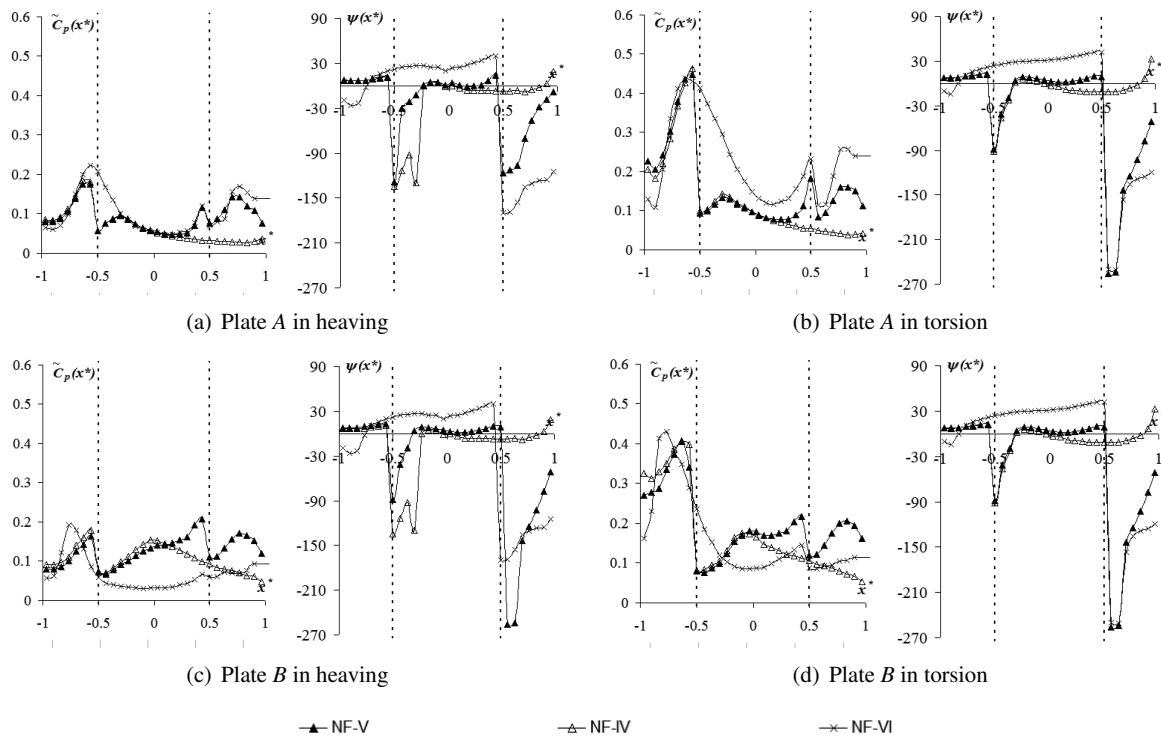


Figure 10: Superimposition of the unsteady pressure characteristics for plates A and B at $U/f.B=25$

istics downstream of a plate are determined, basically, by only that plate itself, which has little influence on its upstream. Similar effects were observed in two-box configurations⁷, which point out a way towards the manipulation of unsteady pressure characteristics.

4. CONCLUDING REMARKS

Effects of vertical plates on the unsteady pressure characteristics of $B/D=20$ rectangular cylinders were investigated. Vertical plates were found to exert influences not only downstream of their locations, but also upstream, due to the recirculation of the flow caused by a blockage effect. By changing the location of plates was possible to provide plates with different oncoming flow conditions. The resulting effects on the unsteady pressure characteristics varied with such modifications. As a conclusion, influences of plates may be dependent on the characteristics of the flow upstream of their locations. The increase of reduced wind velocity reduced such influences.

Vertical plates were found to induce two peaks in amplitude $\tilde{C}_p(x^*)$ distributions. The first peak occurs at the plate's location and is caused by the blockage of the flow, which is forced to recirculate. The same way that occurs at the leading edge, there is a valley right after the flow separation at the vertical plate. Downstream of the valley, a second peak is promoted, which must be related to flow reattachment. A relationship between size of plate and location of the second peak in amplitude distributions $\tilde{C}_p(x^*)$ could be identified.

As for phase difference $\psi(x^*)$ distributions, a "jump" is promoted at plate's location, aligned with the first peak in amplitude distribution. Peaks in amplitude distributions $\tilde{C}_p(x^*)$ got reduced with the increase of the distance from leading edge, contrarily to what was observed in phase difference distributions $\psi(x^*)$. The increase of the size of plate enhanced this opposition. When the plate was close enough to the leading edge, effects of both leading edge and plate got superimposed.

In compositions with two vertical plates, there seems to exist a superposition of effects of the both plates. Between the plates, the unsteady pressure characteristics are a composition of the effects obtained separately. Upstream the first plate, unsteady pressure characteristics are similar to those obtained with just that plate. Downstream of the second plate, distributions are influenced, basically, by only that vertical plate itself, regardless the configuration in its upstream.

The combination of all these effects lead to non-linear relationships between size and location of vertical plates and aerodynamic derivatives. Such relationships can be rationalized only by considering the impacts of plates on amplitude and phase difference distributions separately. By doing so, flutter stabilization can be pursued through the proposition of schemes to *manipulate* unsteady pressure characteristics along bridge deck. In this context, the idea of *geometric singularities* was proposed. The concept refers to the insertion of "geometric accidents" along the deck, in proper locations, with the objective of leading phase difference and amplitude distributions to assume configurations suitable for flutter stabilization, according to optimal conditions as discussed in literature⁶. The use of vertical plates in this sense was assessed and attested to be a useful resource.

ACKNOWLEDGEMENTS

The authors thank Mr. Shinya Fujiwara and Mr. Do Van Bao, graduate students of Kyoto University Bridge Engineering Laboratory at the time of the experiments, for their contributions in the wind tunnel test.

REFERENCES

- 1) M. Matsumoto, K. Okubo, Y. Ito, H. Matsumiya, and G. Kim. The complex branch characteristics of coupled flutter. *Journal of Wind Engineering and Industrial Aerodynamics*, 96:1843–1855, 2008.
- 2) M. Matsumoto, H. Shirato, K. Mizuno, R. Shijo, and T. Hikida. Flutter characteristics of h-shaped cylinders with various side-ratios and comparisons with characteristics of rectangular cylinders. *Journal of Wind Engineering and Industrial Aerodynamics*, 96:963–970, 2008.
- 3) X. Chen. Improved understanding of bimodal coupled bridge flutter based on closed-form solutions. *Journal of Structural Engineering*, 60:22–31, 2007.
- 4) M. Matsumoto. Aerodynamic damping of prisms. *Journal of Wind Engineering and Industrial Aerodynamics*, 59:159–175, 1996.
- 5) R.H. Scanlan, N.P. Jones, and L. Singh. Inter-relations among flutter derivatives. *Journal of Wind Engineering and Industrial Aerodynamics*, 69-71:829–837, 1997.
- 6) C. A. Trein and H. Shirato. Coupled flutter stability from the unsteady pressure characteristics point of view. *Journal of Wind Engineering and Industrial Aerodynamics*, 99:114–122, 2011.
- 7) C. A. Trein, H. Shirato, and M. Matsumoto. On the effects of the gap on the unsteady pressure characteristics of two-box bridge girders. *Engineering Structures*, 82:121–133, 2015.
- 8) C. A. Trein, H. Shirato, and M. Matsumoto. On the unsteady pressure characteristics of modified rectangular cylinders. *Proceedings of VII Asian Pacific Conference on Wind Engineering - APCWE-VII*, 2009.
- 9) C. A. Trein, H. Shirato, and M. Matsumoto. Semi-empirical evaluation of the unsteady pressure characteristics of bluff bodies. *Journal of Wind and Engineering*, 7-2:28–38, 2010.
- 10) C. A. Trein, H. Shirato, and M. Matsumoto. On the effects of the leading edge on the unsteady pressure characteristics of rectangular cylinders. *14th International Conference on Wind Engineering - ICWE14*, 2015.
- 11) M. Matsumoto, Y. Kobayashi, and H. Shirato. The influence of aerodynamic derivatives on flutter. *Journal of Wind Engineering and Industrial Aerodynamics*, 60:227–239, 1996.
- 12) M. Matsumoto, F. Yoshizumi, T. Yabutani, K. Abe, and N. Nakajima. Flutter stabilization and heaving-branch flutter. *Journal of Wind Engineering and Industrial Aerodynamics*, 83:289–299, 1999.
- 13) M. Matsumoto, T. Hikida, and K. Mizuno. On improvement of flutter stability for long-span bridge girders - the case of separated box girders. *Flow Induced Vibration*, 2004.
- 14) P. J. Saathoff and W. H. Melbourne. The generation of peak pressures in separated/reattaching flows. *Journal of Wind Engineering and Industrial Aerodynamics*, 32:121–134, 1989.

CORRELATION OF FLUCTUATING VELOCITY IN THE WAKE OF AN OSCILLATING SQUARE CYLINDER WITH OPENINGS OR APPENDAGES

Seiji NAKATO⁺¹

⁺¹Associate Professor, Kanto-gakuin University, Yokohama, Japan

Correlation of wind velocity in the wake of stationary and oscillating square cylinders was studied in wind tunnel experiment. Models of square cylinders with openings or appendages for preventing vortex shedding were employed and oscillated with approximate triangle wave of two different periods. For normal square cylinder, component of vortex shedding frequency was dominant and oscillation did not affect spectra, correlation coefficient and coherence of fluctuating velocity. For square cylinder with openings, correlation increased with oscillation. On the contrary, both stationary and oscillated cylinders with appendages show low correlation. In general, vortex shedding was not strengthened or stabilized by forced oscillation without case that vortex shedding frequency is close to frequency of oscillation.

Keyword: square cylinder, fluctuating velocity, correlation coefficient, coherence.

1. INTRODUCTION

Wind-induced vibration tends to take place for cylinder-like structure, e.g. bridge, cable, chimney, member of structure. When its width to depth ratio (B/D) is small like square, vortex-induced vibration as well as galloping tends to occur. Important parameters to capture wind-induced vibration phenomena of cylinder like structure are fluctuating lift coefficient, the vortex shedding frequency and the correlation length. The correlation length represents three-dimensionality in the shedding flow. The measurement data of the correlation length is not enough compared to other parameters, and major focus of extensive research for investigating correlation length is circular cylinder. C. Norberg¹⁾ reviewed coefficients of spanwise correlation based on near-cylinder velocity fluctuations as well as fluctuating lift on a circular cylinder. A spanwise correlation length of about 30 cylinder diameters is indicated at the beginning of the subcritical regime ($Re \approx 0.3 \times 10^3$).

Vortex shedding from circular cylinder is relevant to many engineering application. For example, for application of marine riser with sheared flow, correlation length related to typical flexible circular cylinder was studied using a water flume²⁾. When circular cylinder oscillates at or very near the shedding frequency, the correlation coefficient remains higher for larger separation. In contrast, when the cylinder oscillation frequency differs from the shedding frequency, correlation length drops off quickly toward the values for stationary cylinders.

Fluctuating lift and drag on a square cylinder in a smooth and in a turbulent stream was experimentally studied by B. J. Vickery³⁾. This shows that fluctuating lift is greater than that for circular cylinder and spanwise correlation much stronger. P.W. Bearman and E.D. Obasaju⁴⁾ describe measurements of pressure fluctuations on a stationary and oscillating square cylinder. Amplitudes of oscillation is up to 25% of the length of a side. Because of intermittent reattachment at side face, at lock-in the fluctuating lift and drag coefficient is reduced. Correlation of fluctuating velocity has also been discussed in buffeting response. Matsumoto et al⁵⁾ evaluate spanwise coherence of rectangular cylinder of width-to-depth ratio B/D=5, focusing on the higher coherence of surface pressure than that of approaching flow in buffeting response.

Aerodynamic instability of cylinder-like structure is often described two-dimensional sections. But it has uncorrelated section along axis, which could stabilize instability. One method to suppress vortex-induced vibration is add-on devices helical strake, axial slats, splitter plate, spoiler plates and so on⁶⁾. The author

⁺¹nakato@kanto-gakuin.ac.jp

investigated reduction of fluctuating lift force for square cylinder with changing cross section along axis with openings or appendages⁷⁾. Experimental results of correlation of spanwise fluctuating velocity in the wake indicated that simultaneous vortex shedding was disturbed. However, if these cylinders are oscillated, vortex shedding may become well-organized again.

Therefore in this study, correlation of wind velocity in the wake of oscillating cylinders is studied in wind tunnel experiment. The models in the previous study were fixed⁷⁾, so in this study the model is forced to oscillate transversely. For three models are employed; a prototype square cylinder, a square cylinder with openings, and a square cylinder with appendages. The objective of present study is evaluation of correlation due to the modification of cross section along axis. Motion of oscillation is triangle wave controlled by stepper motor.

2. EXPERIMENTAL SETUP

The experimental tests are carried out in the Eiffel-type wind tunnel with nozzle section $400 \text{ mm} \times 400 \text{ mm}$. The model was placed 200mm downward from the wind tunnel nozzle and 200 mm above the floor in open type test section.

In present study, three models are employed; one is a square cylinder (prism) with $15 \text{ mm} \times 15 \text{ mm}$ ($=D$) square and 400 mm length ($26.7D$), another is a cylinder with openings, and the other is a cylinder with appendages (Fig. 1). Openings of the second model are 5 mm height by 10 mm width with space of 20 mm at center of square cylinder height. Appendages of the third model are 15 mm height, 20 mm width, and 5 mm length with space of 10 mm on the windward surface of square cylinder.

Aspect ratio of 26.7 is enough to neglect end disturbances. Since the blockage ratio is 3.75% for square cylinder, no blockage correction was adopted.

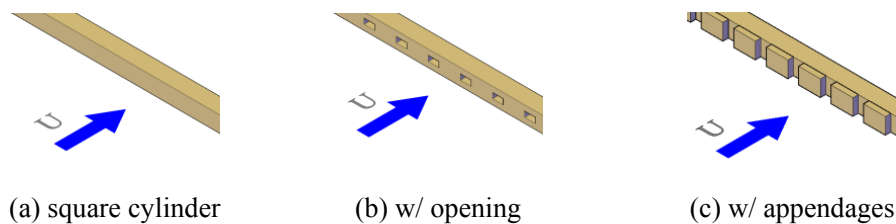


Figure 1 Experimental Models

Two hot wires with horizontal spacing $s=35 \text{ mm}$ ($2.33D$) were placed at 37.5 mm ($2.5D$) leeward direction and 10 mm ($0.67D$) below from center of the model (Figure 2). Two hot wires were at the same relative position within a cross-sectional plane. End plates are mounted at both ends of models to keep a two-dimensional air flow (Figure 3). Each experimental run was 20 second long with the sampling rate of 1000 Hz.

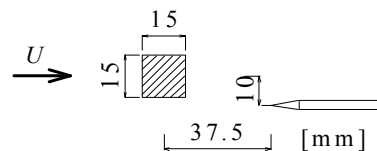


Figure 2 Arrangement of model and hot wire



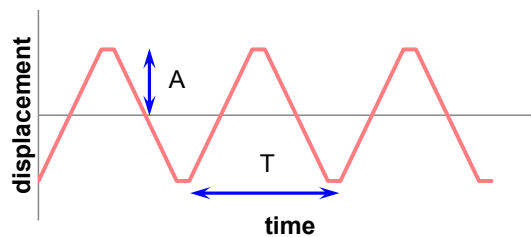
Figure 3 Model with openings and hot wires

The model was supported at one end like cantilever beam and forced to oscillate vertically by linear actuator with a stepper motor. Oscillating system was composed of stepping motor driver (Oriental Motor Co.: ARD-A), actuator (Oriental Motor Co.: EASM4RXE065ARAC) and linear slide. Two oscillation patterns, osc. (A) and osc. (B), were shown in Figure 4. Stepper motor was controlled by digital IO from AD board (National Instruments Co.: PCI-6259). Oscillation like triangular wave was employed due to the limitation imposed by the oscillation system. Harmonic oscillation by stepper motor has to be slow because of maximum speed limitation. Amplitude and frequency of vibration were maximized under the condition preventing a step-out of stepper motor. Although maximum speed is 220mm/s in specifications, approximately 400 mm/s is obtained. Oscillation time period was obtained from peak frequency of power spectrum of acceleration data.

Forced oscillating by stepper motor used in this experiment has advantage for non-sinusoidal motion, such as large amplitude motion of a cable with non-sinusoidal motion, long span bridge motion with some restriction of displacement and so on.

Figure 5 shows arrangement when the model was forced to oscillated. It is noted that hot wires were inside of separated shear layers in a certain arrangement.

The wind is uniform smooth flow and up to $U=5.9\text{m/s}$ ($Re=5.6 \times 10^3$). Wind speed is controlled by inverter frequency given by analog signal applied from AD/DA board on a computer.



	A (mm)	T (sec)	f (Hz)
osc. (A)	25mm (1.67D)	0.256	3.9
osc. (B)	10mm (0.67D)	0.105	9.5

Figure 4 Oscillation pattern

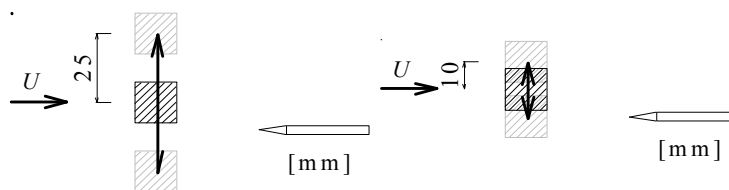


Figure 5 Arrangement of model in oscillation, left: osc. (A), right: osc. (B)

3. EXPERIMENTAL RESULTS AND DISCUSSION

(1) Power spectral density and time series of fluctuating wind velocity

Power spectral density of fluctuating wind velocity is shown in Figure 6. Spectrum was averaged using 5000 points data with overlapped by 2500 points. Frequency resolution is 0.2Hz.

Top row is graph for square cylinder, center row for openings and bottom row for appendages; left column for fixed, center column for osc. (A), and right column for osc. (B). In graph, the horizontal axis shows frequency. The vertical axis is logarithmic scale, with power spectral density of wind velocity and its increments are $10^2 \text{ (m/s)}^2/\text{Hz}$ of the values between each grid line. Each power spectral density at wind speed, 0.48, 1.07, 1.68, 2.28, 3.02, 3.67, 4.23, 4.75, 5.33, 5.88 m/s is plotted from bottom to top.

For stationary square cylinder, a spectral peak is observed and its frequency is proportional to wind speed. So this peak is related to vortex shedding. When square cylinder is oscillated, spectra are almost same

behavior as that of stationary cylinder. Peak at oscillation frequency is weak for osc. (A) and not clear for osc. (B). This results reflect the fact that motion-correlated separating flow from the leading edge declines in dominant Karman vortex shedding.

For model with openings, a weak spectral peak of vortex shedding is indicated. When model is forced to oscillate, there is a peak at oscillation frequency, 3.9 Hz and 9.5 Hz respectively in contrast to square cylinder. For model with appendages, a peak of vortex shedding is weak than model with openings as well as a peak of oscillation frequency. It is indicated that motion-correlated vortex shedding is not organized because motion-directional projection shape is irregular.

From the viewpoint of amplitude of fluctuation velocity in the wake, appendage is effective for reduction of each periodic fluctuation.

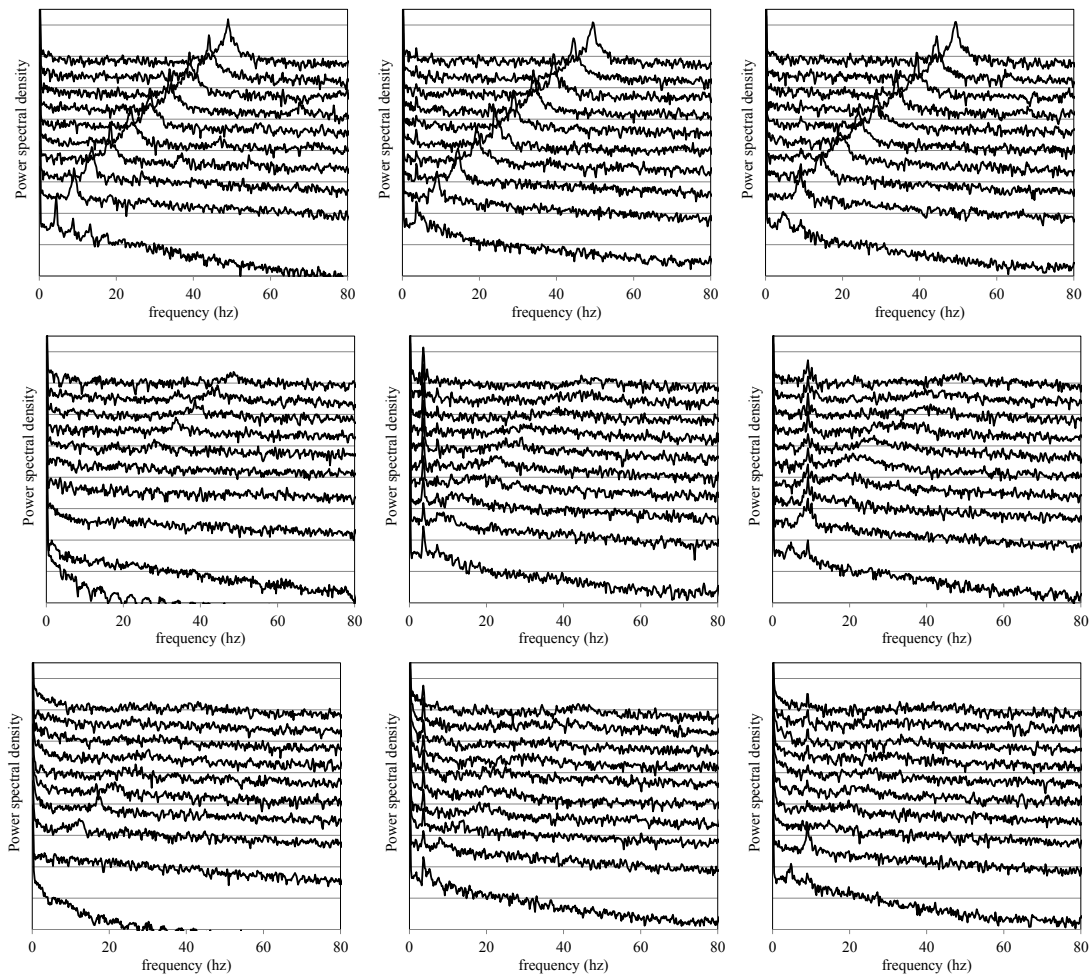


Figure 6 Power spectral density of fluctuating wind velocity.

top: square cylinder, center: openings, bottom: appendages, left: fixed, center: osc. (A), right: osc.(B)

Please note the 20 dB shift between successive cases.

Figure 7 shows example of fluctuating velocity time series, from 5 to 5.4 second, at $U=3.0\text{m/s}$ corresponding to 5th graph from bottom in each graph of Figure 6. For stationary square cylinder, periodic wave is observed which looks like triangle wave rather than sinusoidal wave. For oscillating square cylinder, spiky noise overlap periodic wave. The time series for cylinder with openings or appendages are dominated by random fluctuations of the velocity. For stationary model, velocity is lower than others because position of hot wire is in the wake affected by openings or appendages.

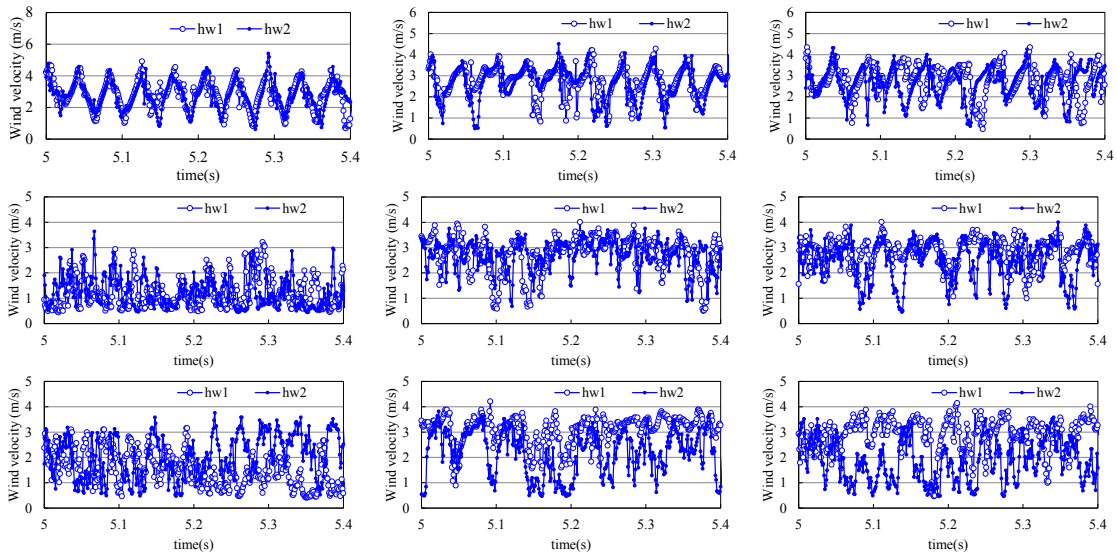


Figure 7 time series of fluctuating velocity, $U=3.0$ m/s
 top: square cylinder, center: openings, bottom: appendages
 left: fixed, center: osc. (A), right: osc.(B)

Peak frequencies of vortex shedding is the Strouhal number (St) is defined as

$$St = \frac{f_s B}{U} \tag{1}$$

where f_s is the vortex shedding peak frequency, B is characteristic length (here is $d=15$ mm), and U is wind speed.

The Strouhal number of square cylinder is shown in Figure 8. The Strouhal number of stationary square cylinder is slightly depends on wind speed and less than the past reported data $St=0.13$. These results are probably due to open type test section of the wind tunnel. The Strouhal number of oscillation square cylinder is greater than that of stationary cylinder at $U=1.7, 2.3$ m/s, implying that separation flow reattaches intermittently at side face. For $U > 3.7$ m/s, flow around cylinder is supposed to become fully separated flow again.

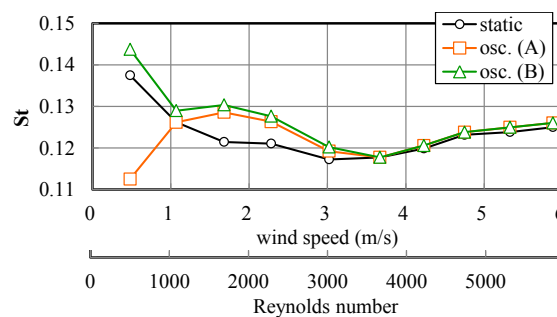


Figure 8 Strouhal number

There is a spectral peak at 17Hz for fixed cylinder with appendages at $U=2.28$ m/s in left and bottom graph in Figure 6, from which Strouhal number is 0.11 corresponding to increase of side ratio, $B/D=1.33$, at section with appendages.

(2) Coherence and Correlation coefficient of fluctuating wind velocities

Spanwise correlation is depends on the three-dimensionality in the vortex shedding. At small separation coherence is almost 1, while at large separations coherence is expected to close to 0.

The root-coherence function of two wake velocity is defined as follows:

$$\text{coh}(f, r) = \frac{|P(j, j+s, f)|}{\sqrt{P(j, f) \cdot P(j+s, f)}} \quad (3)$$

where $P(j, j+s, f)$ is the cross-spectral density function, $P(j, f)$ and $P(j+S, f)$ are power spectra, and s is the spanwise separation. If two signals of hot-wire correspond to each other with a constant phase difference at a given frequency, the magnitude of coherence is 1. Even if ensemble average times is increased, peak of coherence does not become clear, since the coherence does not have power.

Figure 9 shows coherence for each wind speed. Coherence (square of eq. (3)) in spite of root coherence (eq. (3)) is shown in these figures because of making peak clear. Each coherence at wind speed is plotted from bottom to top like Figure 6. The vertical axis is from 0 to 1 between each grid line.

For stationary square cylinders, there is peak coherence at vortex shedding frequency. While peak at vortex shedding frequency is also observed for oscillating cylinder, peak at oscillation frequency is not clear. For model with openings, a weak and broad coherence peak of vortex shedding is indicated. When model is forced to oscillate, there is a peak at oscillation frequency, 3.9 Hz and 9.5 Hz respectively. For fixed model with appendages, no distinct peak was observed in the coherence. A weaker peak at vortex shedding frequency is indicated than model with openings.

In this measurement, hot-wire probes were fixed in position, and therefore wake due to cylinder motion could reduce coherence. However, higher coherence level at vortex shedding frequency is obtained for oscillating square cylinder, and also higher coherence level at oscillation frequency is obtained for cylinder with openings, which implying that evaluation of both spanwise correlation of vortex shedding and separating flow with force oscillation can be detected with position of hot wire in this experiment.

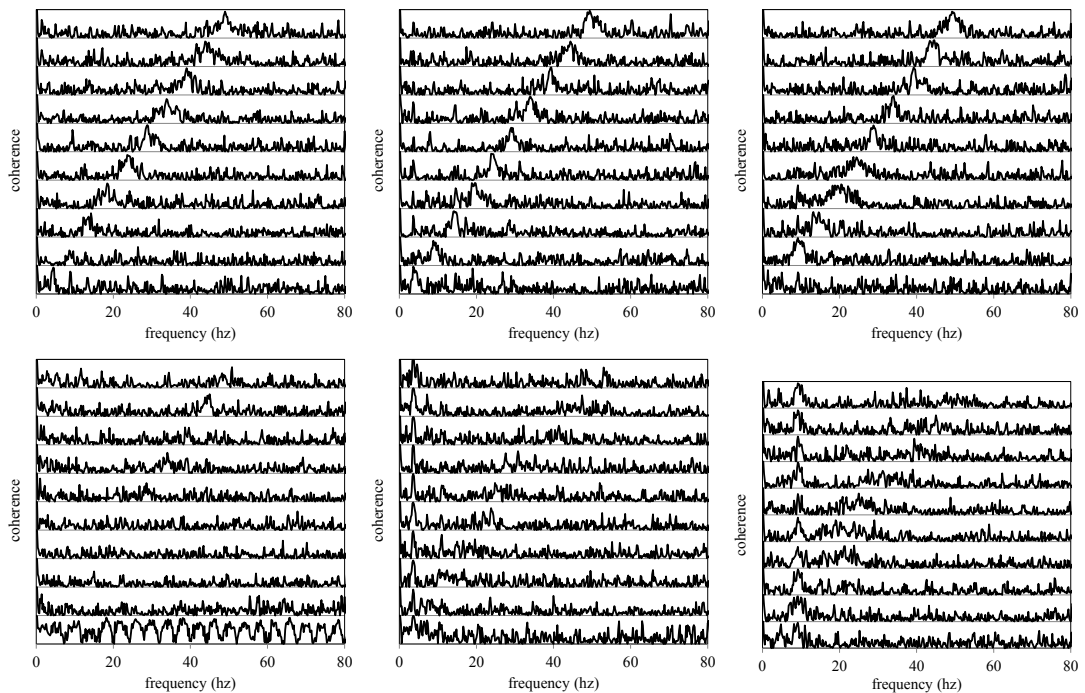


Figure 9 Coherence of fluctuating wind velocity
top: square cylinder, center: openings, bottom: appendages
left: fixed, center: osc. (A), right: osc.(B)

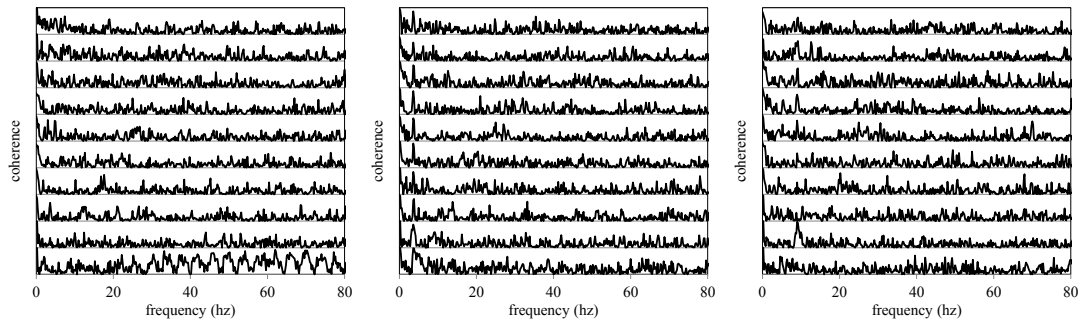


Figure 9 Coherence of fluctuating wind velocity (*Continued*)

Figure 10 shows correlation coefficients R and coherence level of each experimental case.

For the square cylinder, R is approximately at 0.5 in all range of wind speed, and forced oscillation did not affect correlation. In most cases, R had peak at 0.43m/s and 1.1m/s for osc. (A) and (B) respectively where oscillation frequency was almost same as vortex shedding frequency. Coherence level at oscillation frequency 3.9 Hz of osc. (A) is greater than stationary model. However, coherence level at oscillation frequency 9.4 Hz of osc. (B) is slightly greater than stationary model. This implies that oscillation of osc. (B) with small amplitude and high frequency produces smaller-scale vortex shedding. In this study, value of coherence at 3.8 Hz and 9.4 Hz are used since frequency resolution is 0.2 Hz in spectral analysis.

For fixed model with openings, R is almost zero which means fluctuating velocities were not correlated in the wake. For both oscillating cases, R increased but was still less than that of square cylinder, while coherence level at oscillation frequency is same as or a little greater than it.

For fixed model with appendages, small or negative correlation was observed. Coherence level at vortex shedding frequency shows similar behavior to cylinder with openings except at oscillation frequency coincides with Strouhal frequency. Coherence level at oscillation frequency 3.8Hz of osc. (A) is high. However, coherence level at 3.6Hz is higher than it. This tendency is clear for osc. (B), so that coherence level at 9.0 Hz is higher than oscillation frequency 9.4 Hz in all wind speed. Reason for this need further study.

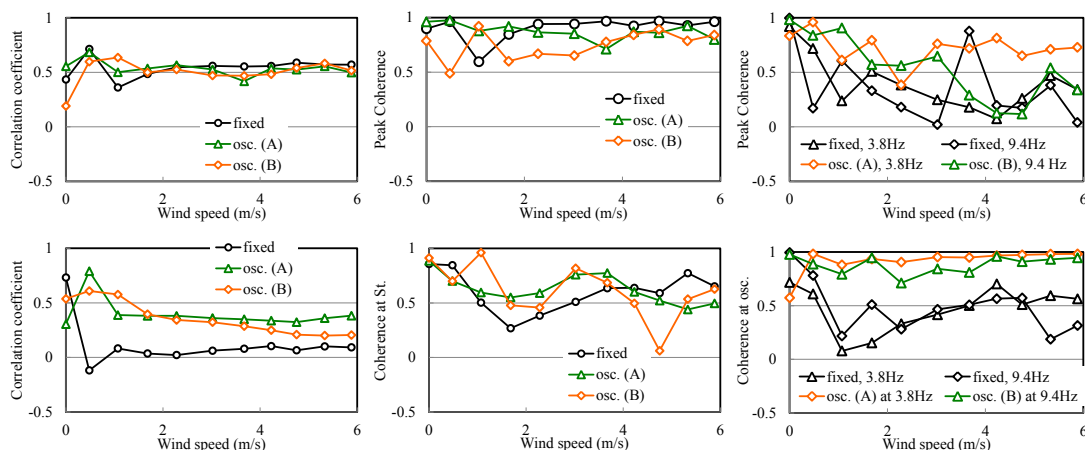


Figure 10 Correlation coefficient and coherence

top: square cylinder, center: openings, bottom: appendages

left: correlation coefficient, center: coherence at frequency of Strouhal component, right: coherence at oscillation frequency

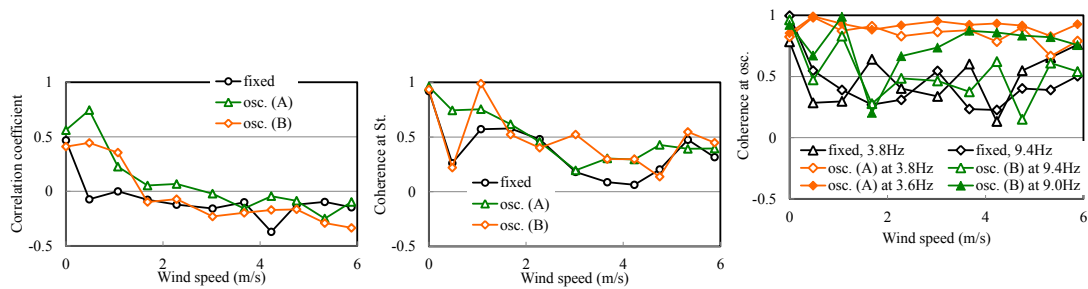


Figure 10 Correlation coefficient and coherence (*Continued*)

Here, it is worthwhile to roughly apply the results of present study to bridge application. Supposing that cylinder discussed here is bridge-handrail beam with $50\text{mm} \times 50\text{mm}$ square section attached to long span bridge. When the cylinder is forced to oscillate with 0.2 Hz of heaving natural frequency of the bridge, vortex shedding frequency coincides with 0.2 Hz at wind speed $U=0.08\text{m/s}$. In the range of wind speed where aerodynamic instability could be problem, frequency of vortex shedding from cylinder is larger than that of bridge natural frequency. In this condition, it can be indicated from the present result that periodic flow in the wake of cylinder (handrail beam) was not affected by motion of the bridge. In addition, countermeasure on the cylinder such as openings or appendages to suppress vortex shedding is also effective even in forced oscillation.

4. CONCLUSIONS

Correlation of wind velocity in the near wake of stationary and forced oscillating cylinder was studied through the wind-tunnel experiments.

It has been found that for the square cylinder, oscillation did not affect correlation and component of vortex shedding frequency was dominant. For square cylinder with openings, correlation increased with oscillation. On the contrary, both stationary and oscillated cylinders with appendages show low correlation. In general, vortex shedding was not strengthened or stabilized by forced oscillation without case that vortex shedding frequency is close to frequency of oscillation.

The next procedure is to change the hot-wire space parametrically and to evaluate correlation length.

REFERENCES

- 1) C. Norberg: Fluctuating lift on a circular cylinder: review and new measurements, *Journal of Fluids and Structures*, Vol. 17, pp. 57- 96, 2003.
- 2) Michael S. Pantazopoulos: Vortex-Induced Vibration Parameters: Critical Review, *ASME Offshore Technology*, Vol. 1, pp. 199-255, 1994.
- 3) B. J. Vickery: Fluctuating lift and drag on a long cylinder of square cross-section in a smooth and in a turbulent stream, *Journal of Fluid Mechanics*, Vol. 25, Part 3, 1966, pp. 481- 494.
- 4) Bearman, P.W. and Obasaju, E.D.: An Experimental Study of Pressure Fluctuations on Fixed and Oscillating Square-section Cylinders, *J. Fluid Mech.*, vol.119, pp.297-321, 1982
- 5) M. Matsumoto, H. Shirato, K. Aaraki, T. Haramura, T. Hashimoto: Spanwise coherence characteristics of surface pressure field on 2D bluff bodies. *Journal of Wind Engineering and Industrial Aerodynamics*, 91, 155–163, 2003.
- 6) R.D. Blevins: *Flow Induced Vibrations*, Krieger Publishing Co., 1990
- 7) S. Nakato: Experimental Study of Fluctuating Lift Force and Correlation Length for Rectangular Cylinder, SS-26, IABSE Conference Nara, 2015.

STUDY ON IDENTIFICATION OF BRIDGE DECK FLUTTER DERIVATIVES BY GUST RESPONSE

Hoang Trong Lam⁺¹, Hiroshi Katsuchi⁺² and Hitoshi Yamada⁺³
^{+1, +2, +3} Dept. of Civil Engineering, Yokohama National University, Yokohama 240-8501, Japan

This study presents the method to approach flutter derivatives (FDs) of bridge section from simulation method. The more challenging is the application the system identification method to extract FDs from the stochastic vibration technique via simulated buffeting responses for section model. The flow analysis includes the investigation on: the fluctuated wind velocities were simulated from target power spectrum, the buffeting responses of a bridge section model obtained from numerical dynamic solution at different mean wind speeds. Next, the gust responses data has been analysis by the system identification technique in extracting FDs and investigate the difficulties involved in this method are discussed. The time domain analysis of gust response, stochastic system identification is proposed to estimate two degree of freedom systems. Finally, some adverse effects of gust response data on the accuracy of these methods to obtain FDs was discussed and concluded. The result of the study can clarify the effects of turbulence on FDs and further apply to estimate FDs from response of full-scale under buffeting load.

Keyword: Flutter¹, Flutter derivative², System identification³, Gust response⁴, Turbulence⁵

1. INTRODUCTION

For the slender and flexible structures, such as long-span cable supported bridges are very sensitive to wind excitation. Base on aerodynamic the flutter and buffeting is vital important problem of great concern. The predictions of flutter instability and buffeting response related to flutter derivatives (FDs). The wind-tunnel test is the best choice to identify FDs. There are two type techniques for identification FDs of bridge section model, such as force vibration technique, free vibration technique [1]. Force vibration approach is a reliable one but it requires sophisticated driving equipment, somewhat expensive and time consuming. Free vibration approach seems to be more tractable and widely adopted technique but the free vibration response need to use the system identification techniques to extract modal parameters. Various system identifications to extract FDs from wind-tunnel experiment were developed by many authors [2-5], and in these systems the buffeting force and their response consider as external noise so this cause more difficulties at high wind velocity and particularly appears turbulence.

The regarding the turbulent effect on FDs was investigated by some authors. G. Bartoli and M. Righi [5] used CSIM is based on Sarkar MITD [3] to extract simultaneously all FDs from 2DOF (degree of freedom) section model. The conclusion is that identification of flutter derivatives in turbulent flow resulted satisfactory in spite of the difficulties encountered due to the process caused by the locally induced noise owing to signature of turbulence. The main reason is that, the CSIM is the deterministic system identification and the effects of turbulence are regarded as a more noisy-input signal to the system makes more problems in the identification process. N. Nikitas, J.H.G. Macdonal and J.B. Jakobsen [7] are employed to extract FDs from ambient vibration data from full-scale monitoring has been using more elaborate stochastic identification technique (CBHM) [6] and the study also illustrated the viability of system identification techniques for extracting valuable result from full-scale data. V. Boonyapinyo and T. Janesupasaeree [1] applied data-driven stochastic subspace identification technique (SSI-DATA in short) to extract the flutter derivatives of bridge deck from wind tunnel test under smooth and turbulent flow. The conclusion of this paper saying that the SSI-DATA can be used to estimate FDs from buffeting responses with reliable results and an advantage of stochastic system is that its considers the buffeting force and response like input instead of noise. So, the ratio

⁺¹hoanglam289@gmail.com, ⁺²katsuchi@cvg.ynu.ac.jp, ⁺³yamada@cvg.ynu.ac.jp

of signal to noise is not effect by wind speed and the flutter derivatives at high wind speeds are readily available. From these consideration it was bring to the idea for applying the stochastic system identification (SSI in short) to estimate the FDs from simulated gust responses of bridge deck.

This study concentrates on the buffeting responses to obtain from the numerical method of bridge deck under fluctuated wind excitation. The turbulent wind speed was simulated from target given power spectrum. Afterward, the output only system identification SSI [8] has been applied to extract flutter derivatives.

2. THEORITICAL BACKGROUND

(1) Wind load on a line-like structure

Wind flow consist of a mean time-invariant component in the along wind direction and a fluctuating (turbulence) component in each of the flow direction. The components of flow are defined as: along-wind involve mean time-invariant and horizontal fluctuation $U(t)=U+u(t)$, and vertical fluctuating $w(t)$. Diana (1986) [10] extended the quasi-steady theory by using the relative wind velocity (V_{rel} in short) in the calculation of the forces. The aerodynamic forces acting on the structure including three parts: drag, lift and aerodynamic moment, see fig. 1.

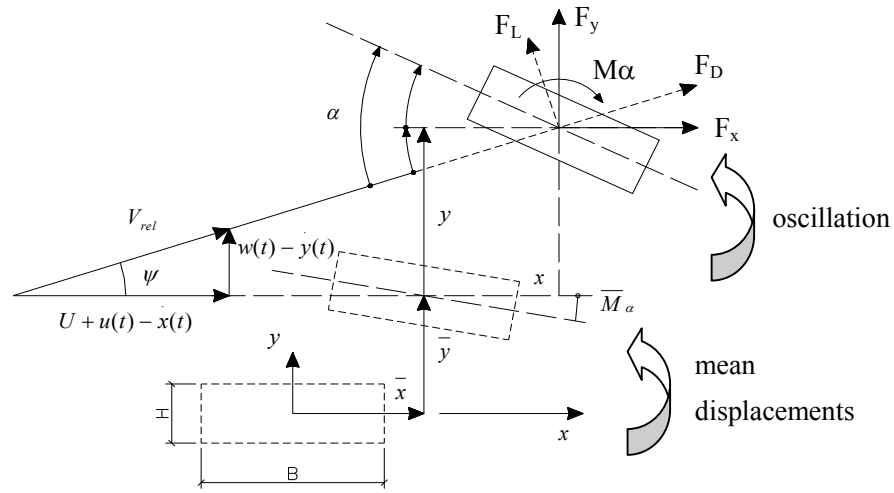


Figure 1: Instantaneous velocity and deck motion

From the quasi-steady theory and considering on the deck motion, the aerodynamic force per unit length can be express in the structural axis system as:

$$F_x = \frac{1}{2} \rho V_{rel}^2 H C_D(\alpha) \cos \psi - \frac{1}{2} \rho V_{rel}^2 B C_L(\alpha) \sin \psi \quad (1)$$

$$F_y = \frac{1}{2} \rho V_{rel}^2 H C_D(\alpha) \sin \psi + \frac{1}{2} \rho V_{rel}^2 B C_L(\alpha) \cos \psi \quad (2)$$

$$M_\alpha = \frac{1}{2} \rho V_{rel}^2 B^2 C_M(\alpha) \quad (3)$$

$$V_{rel}^2 = (U + u(t) - \dot{x}(t))^2 + (w(t) - \dot{y}(t))^2 \quad (4)$$

Where: α is the angle of attack, H is the deck height, B is the deck width, x is the horizontal displacement, y is the vertical displacement, $C_D(\alpha)$, $C_L(\alpha)$, $C_M(\alpha)$ is the draft, lift and moment force coefficient respectively.

Assume the fluctuating wind components and velocities of structure are small compared to mean velocity U , so the higher order terms will neglect. The resulting force contains a part of structural motion $x(t)$

dot and $\dot{y}(t)$ which is component of damping. These force due to self-excited force which is attributed to the aerodynamic damping.

The equation of motion of bridge deck with 2 DOF: bending mode h and torsion mode α can be written as follow:

$$m[\ddot{h} + 2\xi_h \omega_h \dot{h} + \omega_h^2 h] = L_h \tag{5}$$

$$I[\ddot{\alpha} + 2\xi_\alpha \omega_\alpha \dot{\alpha} + \omega_\alpha^2 \alpha] = M_\alpha \tag{6}$$

where m and I is mass and mass moment of inertial per unit length; $\omega_h = 2\pi f_h$ and $\omega_\alpha = 2\pi f_\alpha$ is circular frequencies of heaving and pitching mode (in still air); ξ_h and ξ_α is critical damping ratio; L_h (or F_y) and M_α is the lift force and pitching moment per unit length; and the dot denotes derivative with time.

The lift and moment can be split into three parts: mean, buffeting and self-excited forces. By substituting the above equation Eq.2, Eq.3, Eq.4 into the Eq.5 and Eq.6, by moving the aerodynamic damping and stiffness terms to the left hand side Eq.5 and Eq.6 can be rewritten as follow:

$$[M]\ddot{q}(t) + [C^e]\dot{q}(t) + [K^e]q(t) = \{f(t)\} = B_2 u(t) \tag{7}$$

where $\{q(t)\} = \{h(t) \ \alpha(t)\}^T$ = generalized buffeting response; $\{f(t)\}$ = generalized static and buffeting force; $\{f(t)\}$ is factorized into matrix B_2 and input vector $u(t)$; $[M]$ = mass matrix; $[C^e]$ = gross damping matrix including the physical damping of structure and aerodynamic damping; $[K^e]$ = gross stiffness matrix.

Solution the Eq.7 by the constant acceleration method (Newmark- β) of numerical integration will obtain the buffeting response of bridge deck.

(2) Stochastic state-space models

The previous second-order of differential equation, Eq.7 is generalized n_2 -DOF can be transformed into a first-order the state equation Eq.8.

$$\dot{x}(t) = \begin{Bmatrix} \dot{q}(t) \\ \ddot{q}(t) \end{Bmatrix} = \begin{bmatrix} 0_{n_2 \times n_2} & I_{n_2 \times n_2} \\ -[M]^{-1}[K^e] & -[M]^{-1}[C^e] \end{bmatrix}_{n \times n} \begin{Bmatrix} q(t) \\ \dot{q}(t) \end{Bmatrix} + \begin{bmatrix} 0_{n_2 \times m} \\ [M]^{-1} B_2 \end{bmatrix} u(t) \tag{8}$$

$$\dot{x}(t) = A_c x(t) + B u(t)$$

The combination of the state equation and the observation equation fully describes the input and output behavior of the structural system and is as such named state-space system.

$$\begin{aligned} \dot{x}(t) &= A_c x(t) + B u(t) \\ y(t) &= C_c x(t) + D(u(t)) \end{aligned} \tag{9}$$

where A_c designated the state matrix is a n -by- n ($n=2n_2$); $x(t)$ is the state vector; B is the input matrix; C_c is the output and D is the direct transmission matrix at continuous time.

In the modal analysis, sometime the input is unknown and measurements are mostly sampled at discrete-time. On the other hand, it is impossible to measure all DOFs and the last one, when measurements always have disturbance effects [8]. For all these reasons, the continuous deterministic system will be converted to suitable form: discrete-time stochastic state-space model as follow:

$$\begin{aligned} x_{k+1} &= A x_k + w_k \\ y_k &= C x_k + v_k \end{aligned} \tag{10}$$

where $x_k = x(k\Delta t) = \{q_k \ \dot{q}_k\}^T$ is the discrete-time state vector containing the discrete sample displacement q_k and velocity \dot{q}_k ; w_k is the process noise due to disturbances and modelling

inaccuracies; v_k is the measurement noise due to sensor inaccuracy. Following assumption w_k and v_k is zero mean and with covariance matrix:

$$E \begin{bmatrix} \begin{pmatrix} w_p \\ v_p \end{pmatrix} \begin{pmatrix} w_q^T & v_q^T \end{pmatrix} \end{bmatrix} = \begin{pmatrix} Q & S \\ S^T & R \end{pmatrix} \delta_{pq} \quad (11)$$

where the index p and q are time-instants; E is the expected value; δ_{pq} is the Kronecker delta. As the correlation $E(w_p w_q^T)$ and $E(v_p v_q^T)$ are equal zero if different time-instant.

Further the stochastic model is assumed that $\{x_k\}$, $\{w_k\}$ and $\{v_k\}$ are mutual dependent: $E(x_k w_k^T)=0$ and $E(x_k v_k^T)=0$. According to B. Peeters and G.D. Roeck [8] proven that the output covariance $R=E[y_{k+i} y_k^T]$ for any arbitrary time-lags $i\Delta t$ can be considered as impulse response (Eq.12) of the deterministic linear time-invariance system A, C, G ; where $G=E[x_{k+1} y_k^T]$ is the next state-output covariance matrix.

$$R_i = CA^{i-1}G \quad (12)$$

Therefore, the theoretical application of stochastic system can go back to eigen-system realization algorithm (ERA) method in [9]. The classification of stochastic system identification based on the key step of these methods, by following [8] they are covariance-driven stochastic subspace identification (COV-SSI) and data-driven stochastic subspace identification (DATA-SSI).

a) COV-SSI

The heart of COV-SSI method is the ERA developed by Juang and Pappa [8]. It is the famous technique for modal parameter from free vibration response or impulse response. The key step in the COV-SSI system is the computation output covariance can be expressed assuming ergodicity process as:

$$R_i = E[y_{k+i} y_k^T] = \lim_{N \rightarrow \infty} \frac{1}{N} \sum_{k=0}^{N-1} y_{k+i} y_k^T \approx \frac{1}{N} \sum_{k=0}^{N-1} y_{k+i} y_k^T \quad (13)$$

where i time lag; N finite number of data

All output covariance R_i in Eq.12 is stored in block Toeplitz matrix as:

$$T_{1\bar{i}} = \begin{bmatrix} R_i & R_{i-1} & \cdots & R_1 \\ R_{i+1} & R_i & \cdots & R_2 \\ \cdots & \cdots & \cdots & \cdots \\ R_{2i-1} & R_{2i-2} & \cdots & R_i \end{bmatrix}_{ixi} \quad (14)$$

Combination Eq.12, and Eq.14, then block Toeplitz matrix can be decomposed as following:

$$T_{1\bar{i}} = \begin{bmatrix} C \\ CA \\ \cdots \\ CA^{i-1} \end{bmatrix} \begin{bmatrix} A^{i-1}G & A^{i-2}G & \cdots & AG & G \end{bmatrix} = O_i C_i \quad (15)$$

On the other hand, the observability matrix O_i and controllability matrix C_i can be obtained from singular value decomposition (SVD) of the Toeplitz matrix:

$$T_{1\bar{i}} = [U_1 \quad U_2] \begin{bmatrix} S_1 & 0 \\ 0 & 0 \end{bmatrix} \begin{bmatrix} V_1^T \\ V_2^T \end{bmatrix} = U_1 S_1 V_1^T \quad (16)$$

S is a diagonal matrix containing singular value. The numbers of non-zero give the rank of the decomposed matrix and coincide with the size $n=2n_2$ of the state-space matrix A . Comparison the Eq.15 and Eq.16, we can

rewrite that:

$$\begin{aligned} O_i &= U_1 S_1^{1/2} \\ C_i &= S_1^{1/2} V_1^T \end{aligned} \quad (17)$$

Now the realization of all system matrixes A and C are achieved. The state matrix A can be obtained by decomposing a shift block Toeplitz matrix:

$$T_{2l+1} = O_i A C_i \quad (18)$$

Combining Eq.17 and Eq.18 gives

$$A = O_i^+ T_{2l+1} C_i = S_i^{-1/2} U_1^T T_{2l+1} V_1 S_1^{-1/2} \quad (19)$$

where $(.)^+$ is the pseudo-inverse of a matrix. The output matrix C equals the first l rows of O_i , where l number of outputs (in this study l=2).

b) Identification of flutter derivatives

The modal parameters of system can be obtained by solving the eigenvalue problem state matrix A:

$$A = \Psi \Lambda \Psi^{-1}; \quad \Phi = C \Psi \quad (20)$$

where Ψ the complex eigenvector; Λ the complex eigenvalue is the diagonal matrix; Φ the mode shape matrix. When the complex modal parameters known, the gross damping C^e and gross stiffness K^e in Eq.8 is determined by following:

$$[K^e \ C^e] = -M \left[\Phi \Lambda^2 \quad \Phi^* (\Lambda^*)^2 \right] \left[\begin{array}{cc} \Phi & \Phi^* \\ \Phi \Lambda & \Phi^* \Lambda^* \end{array} \right]^{-1} \quad (21)$$

$$\text{Let } \begin{aligned} \bar{C}^e &= M^{-1} C^e; & \bar{K}^e &= M^{-1} K^e \\ \bar{C} &= M^{-1} C^0; & \bar{K} &= M^{-1} K^0 \end{aligned}$$

where C^0 and K^0 the mechanical damping and stiffness matrix of system under no-wind condition.

Following E. Simiu and R.H. Scanlan [13], the aerodynamic self-excited force and moment given by:

$$\begin{aligned} L_{se} &= \frac{1}{2} \rho U^2 B \left[K_h H_1^*(K_h) \frac{\dot{h}}{U} + K_\alpha H_2^*(K_\alpha) \frac{B \dot{\alpha}}{U} + K_\alpha^2 H_3^*(K_\alpha) \alpha + K_h^2 H_4^*(K_h) \frac{h}{B} \right] \\ M_{se} &= \frac{1}{2} \rho U^2 B^2 \left[K_h A_1^*(K_h) \frac{\dot{h}}{U} + K_\alpha A_2^*(K_\alpha) \frac{B \dot{\alpha}}{U} + K_\alpha^2 A_3^*(K_\alpha) \alpha + K_h^2 A_4^*(K_h) \frac{h}{B} \right] \end{aligned} \quad (22)$$

where $K_i = \omega_i B / U$ the reduce frequency ($i=h, \alpha$); H_i^* and A_i^* ($i=1,2,3,4$) are the flutter derivatives.

Substituting Eq.22 into Eq.7 and combining Eq.21, the flutter derivatives of two DOF can be defined as:

$$\begin{aligned} H_1^*(k_h) &= -\frac{2m}{\rho B^2 \omega_h} (\bar{C}_{11}^e - \bar{C}_{11}), & A_1^*(k_h) &= -\frac{2I}{\rho B^3 \omega_h} (\bar{C}_{21}^e - \bar{C}_{21}) \\ H_2^*(k_\alpha) &= -\frac{2m}{\rho B^3 \omega_\alpha} (\bar{C}_{12}^e - \bar{C}_{12}), & A_2^*(k_\alpha) &= -\frac{2I}{\rho B^4 \omega_\alpha} (\bar{C}_{22}^e - \bar{C}_{22}) \\ H_3^*(k_\alpha) &= -\frac{2m}{\rho B^3 \omega_\alpha^2} (\bar{K}_{12}^e - \bar{K}_{12}), & A_3^*(k_h) &= -\frac{2I}{\rho B^4 \omega_\alpha} (\bar{K}_{22}^e - \bar{K}_{22}) \end{aligned} \quad (23)$$

$$H_4^*(k_h) = -\frac{2m}{\rho B^3 \omega_h^2} (\bar{K}_{11}^e - \bar{K}_{11}), \quad A_4^*(k_h) = -\frac{2I}{\rho B^4 \omega_h^2} (\bar{K}_{21}^e - \bar{K}_{21}) \quad (23)$$

3. TURBULENT WIND FIELD SIMULATION

Investigation on the aerodynamic bridge response in the time domain, turbulent wind field is obtained by simulation method first. The time histories of fluctuating wind velocity was generated from the target Kaimal's power spectral density (PSD) of horizontal and vertical fluctuating wind Eq.24

$$\frac{nS_u(n)}{\sigma_u^2} = \frac{105f}{(1+33f)^{5/3}} \quad (24)$$

$$\frac{nS_w(n)}{\sigma_w^2} = \frac{2f}{1+5.3f^{5/3}}$$

where $S_{u,w}(n)$ is the PSD of longitudinal and vertical velocity fluctuations u and w ; n the frequency; σ_u the standard deviation of u ; and $f=nz/U$: reduced frequency, and z : the reference height.

The generated wind velocity fluctuations are illustrated in Fig.2, fluctuated time series data and Fig.3, generated power spectrums and target spectrums.

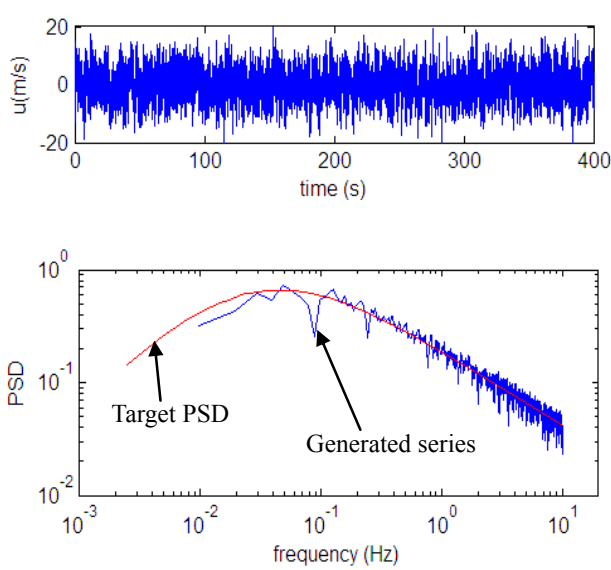


Figure 2: Longitudinal wind

Generated fluctuation wind velocity (upper)
Spectra of generated series and target (lower)

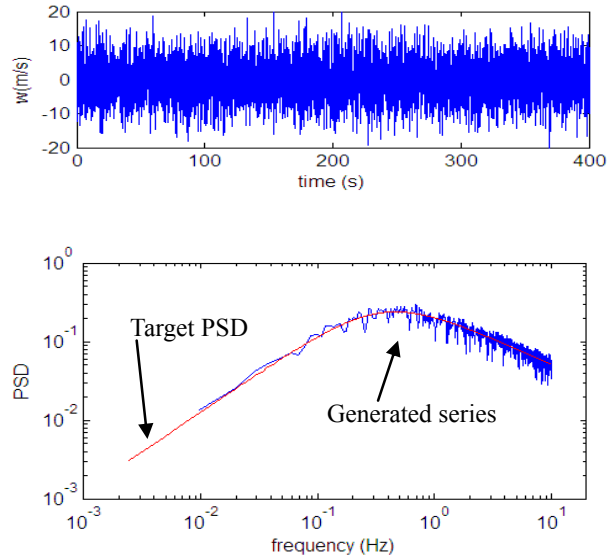


Figure 3: Vertical wind

Generated fluctuation wind velocity (upper)
Spectra of generated series and target (lower)

4. NUMERICAL SIMULATION RESULTS

(1) White noise excitation

To verify the proposed method for identifying FDs, the response time-series of section model excited by lift and moment white-noise was computed by numerical integration method. The section model properties assumed following (Jakobsen and Hjorth-Hansen, 1995) [6]: $f_h=1.947$ Hz; $f_a=5.76$ Hz; logarithm decrements $\delta_h=0.035$ and $\delta_a=0.033$. The mean wind speed $U=10.26$ m/s, air density 1.181 kg/m³. The effective stiffness and damping were pre-set at:

$$M_0 = \begin{bmatrix} 2.6526 & 0 \\ 0 & 0.0189 \end{bmatrix}; \quad C^e = \begin{bmatrix} 8.9308 & -0.0799 \\ 0.4345 & 0.0386 \end{bmatrix}; \quad K^e = \begin{bmatrix} 420.1002 & -59.1805 \\ 1.7552 & 19.6592 \end{bmatrix}$$

The SSI method applied to these response data and obtained the effective structural matrix and the deviation of identified matrices from the pre-set ones:

$$C_r^e = \begin{bmatrix} 8.9875 & -0.059 \\ 0.4468 & 0.0378 \end{bmatrix}; K_r^e = \begin{bmatrix} 420.99 & -58.2082 \\ 2.0345 & 19.6516 \end{bmatrix}; \Delta C\% = \begin{bmatrix} 0.63 & -26.15 \\ 2.83 & -2.07 \end{bmatrix}; \Delta K\% = \begin{bmatrix} 0.21 & -1.64 \\ 15.91 & 0.07 \end{bmatrix}$$

The results are plausible to compare with the pre-set values. The maximum differences in the off-diagonal term C_{12} around 26%, this parameter related to H_2^* , but the magnitude value quite small so the effect is trivial.

(2) Buffeting excitation

The buffeting response obtained by following the procedure in section 2.1 with different mean wind speed. Assuming the section prototype parameters per unit length of prototype bridge are following: mass is 4300 kg/m; mass moment of inertia $4.11 \times 10^4 \text{ kg.m}^2/\text{m}$; the width of deck B is 30m; the height of deck is 3.2m; vertical mode frequency $f_h=0.15\text{Hz}$; torsional mode frequency $f_\alpha=0.35\text{Hz}$; vertical damping ratio $\xi_h=0.15$; torsional damping ratio $\xi_\alpha=0.25$.

The vertical and torsional responses were obtained at mean wind speeds varying from 10m/s to 90m/s and added turbulent of along and vertical wind. The buffeting responses were simulated at a sampling frequency of 20Hz. Fig.4 shows the simulated buffeting responses of two DOFs by numerical integration with constant acceleration method at mean wind speed $U=10\text{m/s}$.

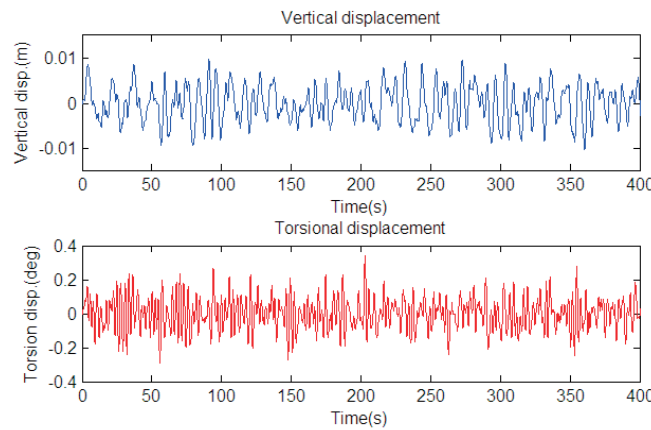


Figure 4: Buffeting response vertical displacement (upper), torsional displacement (lower))

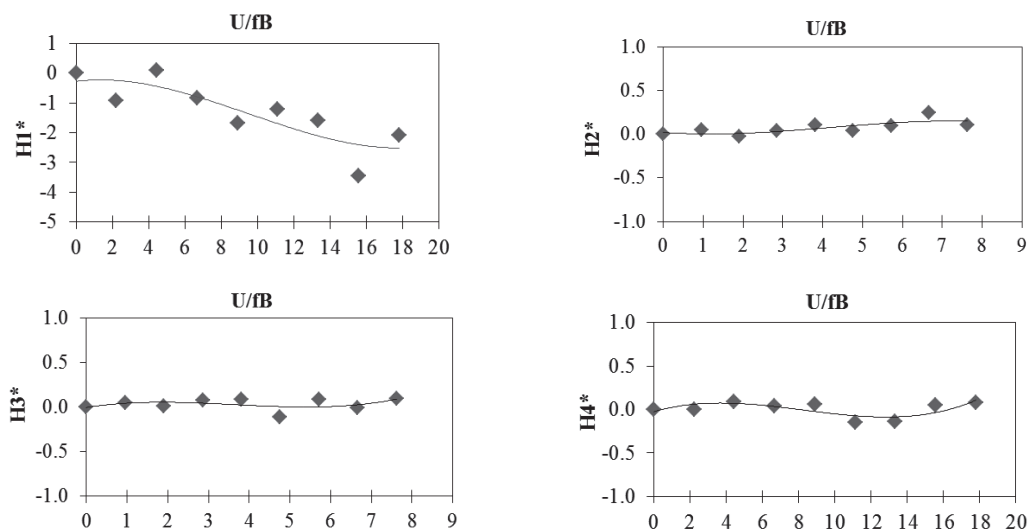


Figure 5: Vertical flutter derivatives and three order fitted polynomial, indicated by solid line

In this study, the actual model order is known and is equal to the order of state matrix A ($=4$) and also number of out-puts equal two (h and α). In order to extract the FDs, the SSI technique a computer program developed in Matlab's program following the procedure mention in section 2. From the eigenvalue and mode shapes, the effective damping and stiffness were determined from Eq.21 and physical matrices, the values of all FDs at a particular wind speed were obtained following Eq.23. Fig.5 and Fig.6 shows the FDs values at discretely located of each parameter respect to reduce wind speed and also the three order polynomials are depicted as continuous curves.

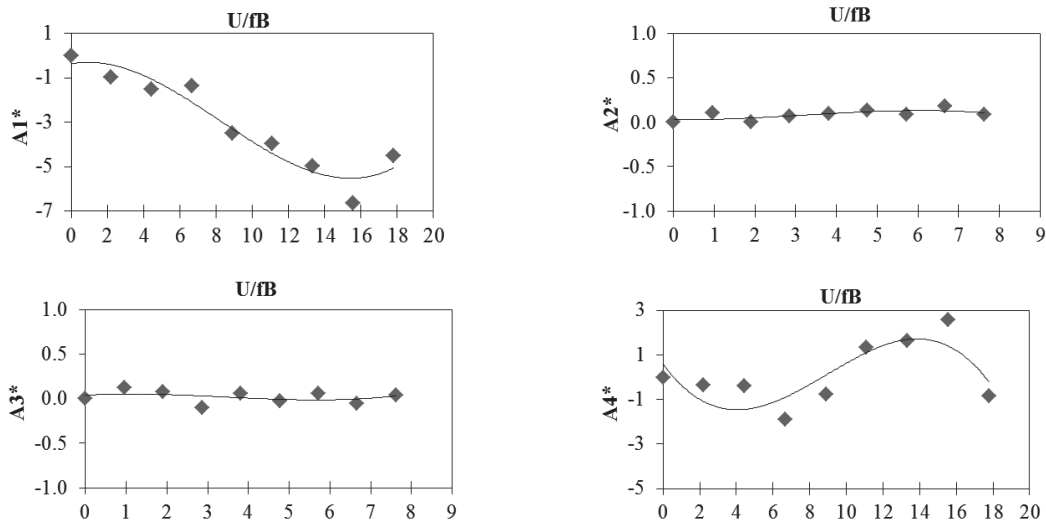


Figure 6: Torsional flutter derivatives and three order fitted polynomial, indicated by solid line

Identifying flutter derivatives of prototype section under turbulent wind has been hard work; the results $H1^*$ and $A1^*$ is plausible. As can be seen from the chart, the $H1^*$ derivative trend intended to larger negative with increase reduce wind speed, this indicated aerodynamic damping in vertical bending vibration is positive. $A4^*$ shows small scatter and changes trend at high reduce wind speed. The $H2^*$, $H3^*$ derivatives, which control the coupling from torsional to vertical have very small value. The $A2^*$, $A3^*$ derivatives, which related to aerodynamic torsional stiffness and torsional damping is also small.

5. CONCLUSIONS

These research attempts to apply the stochastic system identification method have been determined flutter derivatives of two DOFs system. The method uses only out-put from buffeting responses data. The flutter derivatives $H1^*$ and $A1^*$ are plausible, but the coupling term between the torsional and vertical mode $H2^*$, $H3^*$ derivatives are quite small. The aerodynamic effected on torsional mode $A2^*$ and $A3^*$ derivatives are also small. Extraction the FDs from buffeting of the prototype bridge is more challenging and the errors in the values may be attributed to the stochastic method itself. The authors will effort to minimize the errors by adopting better signal processing technique. The results show the potential to extract FDs from ambient vibration data on full-scale bridge.

ACKNOWLEDGMENT

The authors gratefully acknowledge the supported of Department of Civil Engineering, Yokohama National University.

REFERENCES

- 1) V. Boonyapinyo, T. Janesupasaeree: Data-driven stochastic subspace identification of flutter derivatives of bridge decks, *J. Wind Eng. Ind. Aerodyn*, 98, pp. 784-799, 2010.

- 2) H. Yamada, T. Miyata and H. Ichikawa: Measurement of aerodynamic coefficients by system identification method, *J. Wind Eng. Ind. Aerodyn*, 42, pp. 1255-1263, 1992.
- 3) P.P. Sarkar, N.P Jones, R.H Scanlan: System identification for estimation of flutter derivatives, *J. Wind Eng. Ind. Aerodyn*, 42, pp. 1243-1254, 1992v.
- 4) G. Bartoli, S. Contri, C. Mannini, and M. Righi: Toward an improvement in the identification of bridge deck flutter derivatives, *Journal of Engineering Mechanical (ASCE)*, Vol.135, pp.771-785, 2009.
- 5) G. Bartoli, M. Righi: Flutter mechanism for rectangular prism in smooth and turbulent flow, *J. Wind Eng. Ind. Aerodyn*, 94, pp. 275-291, 2006.
- 6) J.B Jakobsen, E. Hjorth-Hansen: Determination of the aerodynamic derivatives by a system identification method, *J. Wind Eng. Ind. Aerodyn*, 57, pp. 295-305, 1995.
- 7) N. Nikitas, John H.G. Macdonal and Jasna B. Jakobsen: Identification of flutter derivatives from full-scale ambient vibration measurements of the Clifton suspension bridge, *J. Wind and Structures*, Vol.14, pp. 221-238, 2011.
- 8) Bart Peeters and Guido De Roeck: Reference-based stochastic subspace identification for output-only modal analysis, *Mechanical Systems and Signal Processing*, 13(6), pp. 855-878, 1999.
- 9) J.N. Juang and R.S. Pappa: An eigensystem realization algorithm (ERA) for modal parameter identification and model reduction, *J. Guid. Contr. Dyn.*, pp. 299-318, 1985
- 10) Diana, G. et al. Wind effects on the dynamic behaviour of suspension bridge, Politecnico di Malano, Dipartimento di Meccanica. 1986.
- 11) P.H. Kirkegaard and P. Andersen: State space identification of civil engineering structures from output measurement, *Proceedings of the 15th International Modal Analysis Conference, Orlando, Florida, USA*, 1997
- 12) P.V. Ovrsee, B.D Moor: *Subspace Identification for Linear Systems*, Kluwer academic publisher, 1996
- 13) Emil Simiu and Robert H. Scanlan: *Wind Effects on Structures*, Third Edition, John Wiley & Sons, New York, 1996.
- 14) Claes Dyrbye and Svend O. Hansen, *Wind Loads on Structures*, John Wiley & Sons, New York, 1997.

THE ROLE OF HORIZONTAL AERODYNAMIC DERIVATIVES IN BRIDGE FLUTTER ANALYSIS

Allan Larsen⁺¹

⁺¹ COWI Consulting Engineers, Lyngby, Denmark

Inclusion of a horizontal degree of freedom along with the vertical and twisting degrees of freedom has been an active area of research in bridge flutter predictions for the past three decades. While much work has been published on theoretical aspects, limited experience as to the importance of the horizontal degree of freedom is available in the literature. Three cases of actual long span bridge designs are examined with respect to the critical wind speed for onset of classical flutter. For the three cases examined inclusion of the horizontal modes of motion had almost negligible influence on the flutter wind speed.

Keyword: Long span bridges; Horizontal aerodynamic derivatives; Mode shapes; Multimode flutter analysis.

1. INTRODUCTION

Flutter of bridge decks and aircraft wings is a fluid structure instability combining the elastic and aerodynamic properties of the structural member in question. In 1971 Scanlan [1] re-launched Theodorsen's [2] 1935 theory for application in bridge aerodynamics now with the flat plate theoretical coefficients replaced by experimental aerodynamic derivatives obtained from wind tunnel tests with elastically suspended section models free to oscillate in the vertical and the torsion degree of freedom (H^* and A^* aerodynamic derivatives). During the 1980's Scanlan and co-workers expanded the theory to include the horizontal (along wind) degree of freedom expressed in terms of the P^* derivatives, Jones et al. [3]. While the inclusion of the third degree of freedom was meant to make flutter predictions more accurate, it complicates wind tunnel testing considerably by increasing the number of required derivatives from 8 to 18. Despite the theoretical advantage of including the horizontal aerodynamic effects in flutter predictions for bridges the adequacy has only been published for a single practical design application Miyata [6]. Still it is often required in design verifications.

The author's company is carrying out aerodynamic analyses of long span cable-stay and suspension bridges on a regular basis. The effect of the horizontal aerodynamic derivatives has been investigated in three cases involving a cable-stayed bridge of 1088 m main span and two suspension bridges of 1550 m and 3300 m main span, the latter being a tri-girder deck structure with large wind screens generating considerable along-wind drag loading.

2. ELEMENTS OF FLUTTER THEORY

The key assumption in flutter analyses is that the aerodynamic lift L_{ae} , and drag D_{ae} forces and moment M_{ae} caused by the oscillatory motion of a section of the bridge deck can be expressed as (the nomenclature utilized is supplied at the end):

$$\begin{aligned}
 L_{ae} &= \rho \omega^2 B^3 \left[(H_4^* + iH_1^*) \frac{h}{B} + (H_3^* + iH_2^*) \alpha + (H_6^* + iH_5^*) \frac{p}{B} \right] \\
 D_{ae} &= \rho \omega^2 B^3 \left[(P_6^* + iP_5^*) \frac{h}{B} + (P_3^* + iP_2^*) \alpha + (P_4^* + iP_1^*) \frac{p}{B} \right] \\
 M_{ae} &= \rho \omega^2 B^4 \left[(A_4^* + iA_1^*) \frac{h}{B} + (A_3^* + iA_2^*) \alpha + (A_6^* + iA_5^*) \frac{p}{B} \right]
 \end{aligned} \tag{1}$$

⁺¹aln@cowi.dk

The underlying assumption for Eq. 1 is that the flutter motion is pure harmonic with a common frequency ω for vertical, horizontal and twisting modes of motion. The 18 coefficients in Eq. 1 $H_{1..6}^*$, $P_{1..6}^*$, $A_{1..6}^*$ known as the aerodynamic or flutter derivatives or flutter coefficients are functions of the reduced wind speed U/fB and links the aerodynamic forces to the motion of bridge section given by the vertical, horizontal and angular displacements and velocities of the centroid of the bridge deck section. The cross coupling between the vertical and twisting degrees of freedom, i.e. aerodynamic moment caused by vertical movement or aerodynamic vertical lift caused by twisting motion, is the primary mechanism responsible for flutter identified by Theodorsen and defines the flutter wind speed of a given bridge. The cross coupling between the horizontal and the vertical and twisting degrees of freedom postulated in Eq. 1 may affect the flutter dynamic in two ways:

- 1) Twisting motion of a vertically or horizontally curved bridge girder (i.e. due to mean wind loading) will have a horizontal component. The structurally coupled horizontal motion will create drag forces which in turn will influence the flutter dynamics.
- 2) Aerodynamic coupling between vertical and twisting motions will cause horizontal modes to be excited which in turn will influence the flutter dynamics.

While the influence of the horizontal degrees of freedom has been a research topic in bridge aeroelasticity for about three decades, only limited practical experience has been reported in the literature, Miyata [6]. The present paper seeks to remedy this situation.

(1) Measurement of flutter derivatives

Flutter derivatives are traditionally measured in a wind tunnel using a spring mounted section model of the bridge deck under investigation. This free oscillation technique originates from Scanlan's 1971 landmark paper on bridge deck flutter [1]. In the free oscillation method decay traces of the deck section model are measured following either an impulsive displacement or random excitation by turbulence. The aerodynamic derivatives are then inferred from either the damping or the frequency shifts measured relative to a situation with no air flow in the wind tunnel. While the free oscillation technique is experimentally simple it becomes increasingly inaccurate as the test conditions approaches the flutter point mainly because only a few oscillation cycles are available for making the required analysis. This point becomes particularly critical for extraction of the horizontal derivatives as responses in this degree of freedom are observed to be small compared to the vertical and torsional degrees of freedom. The inherent accuracy of the free oscillation technique is often sought compensated for by repeating the individual sub-tests a large number of times.

A much more accurate experimental method is the forced oscillation technique by which the aerodynamic derivatives are obtained directly as transfer functions between imposed oscillatory motions and resulting measured aerodynamic forces. The drawback is that the experimental apparatus is much more complicated than what is called for when using the free oscillation technique. The wind tunnel set-up must be capable of moving the deck section model in accurate horizontal, vertical and twisting motions while the resulting aerodynamic forces are measured simultaneously. FORCE Technology, Copenhagen owns and operates a 2.2 m x 1.7 m wind tunnel with a forced oscillation apparatus, Fig. 1, Larsen et. al. [4]. This set-up was applied for obtaining the three sets of aerodynamic derivatives shown in the appendix at the end of the paper and applied in the analyses discussed in the following. It is noted that the important aerodynamic derivatives H_1^* , H_3^* , A_2^* , A_3^* , are almost identical for the two mono box deck sections but markedly different for the tri-box deck of the Messina Bridge.

(2) Multimode flutter analysis

Multimode flutter analysis based on structural modal analysis has been a reoccurring topic at wind engineering conferences for the past three decades. A good state-of-the-art review is presented in [3]. A more recent paper [5] discusses multimode flutter analysis applied to a long single span suspension bridge built recently in Norway.

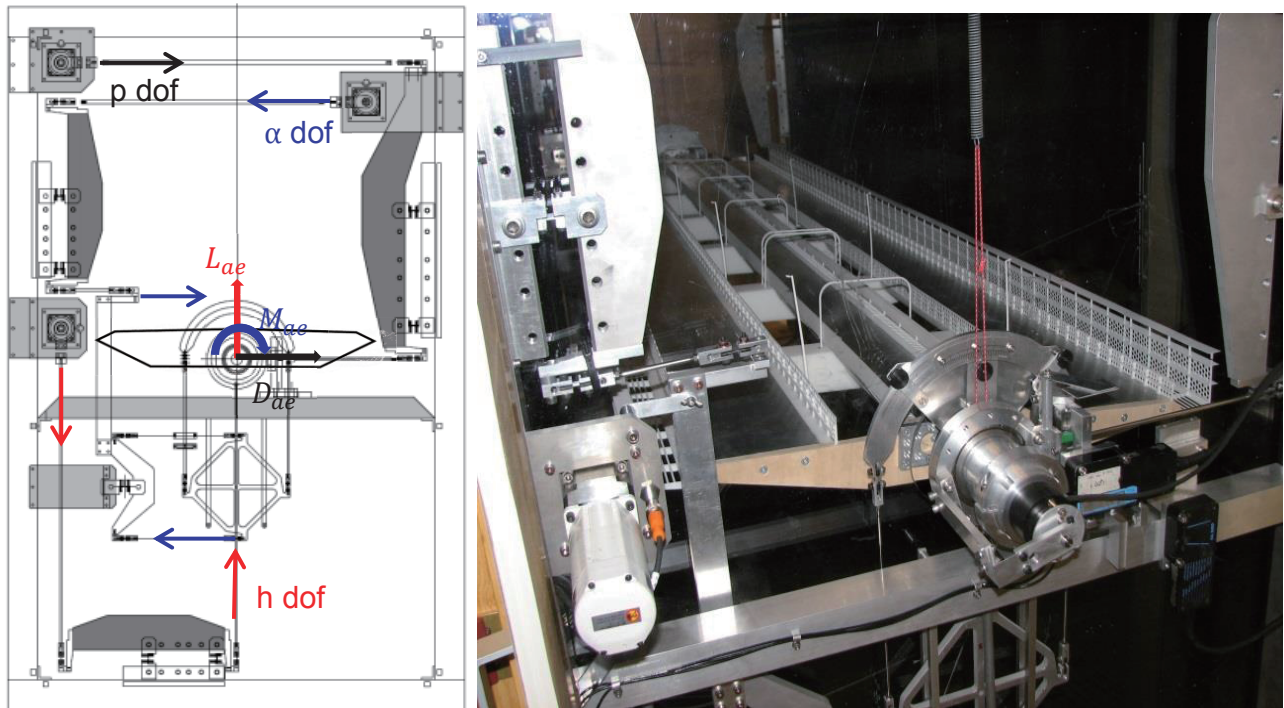


Figure 1. Forced oscillation apparatus (left). The Messina Bridge deck section in the Force Technology wind tunnel (right).

One of the conclusions of [5] is that the flutter wind speed is reasonably well predicted if the flutter analysis is based on three structural modes only being the lowest torsion mode which happens to be the first symmetric torsion and the lowest two symmetrical vertical bending modes. Including a third bending mode only changes the flutter wind speed by only 0.3%. Based on this result and for the sake of simplicity, the following discussion will involve four modes: The first symmetry or asymmetric torsion mode depending on which mode has the lowest eigenfrequency, the corresponding two lowest vertical modes (symmetric or antisymmetric to match the torsion mode) and the lowest horizontal mode to match the torsion or alternatively horizontal component of the lowest torsion mode. Analysis of the flutter stability problem and determination of the critical wind speed for onset of flutter can be pursued in different ways. A common method first proposed by Theodorsen is outlined in [1] and calls for solving two algebraic equations representing the real and imaginary parts of a complex valued determinant. The Theodorsen method allows different viscous damping levels to be assigned to the various eigenmodes involved in the flutter motion. A variation of the Theodorsen method sometimes referred to as the AMC method transforms the problem into an eigenvalue problem which is easily tackled by standard computing routines. In the AMC method the viscous damping ζ which is proportional to vibration velocity is replaced the structural damping g which is proportional to the vibration displacement but leading it by a 90 deg. phase shift. For harmonic motion it can be demonstrated that the structural damping level is equal to twice the viscous damping level $g = 2\zeta$.

The formulation of the flutter determinant starts out by equating the equation of motion for each elastic mode expressed as a one-degree-of-freedom oscillator to the self-excited wind forces given in Eq. 1. It can be demonstrated that solution of this system of equations corresponds to finding the eigenvalues λ_j of the determinant Eq. 2. The A_{ab}, H_{ab}, P_{ab} terms in Eq. 2 is shorthand notation for quantities set in the format:

$$A_{\alpha\alpha} = \frac{\rho B^4}{I^*} C_{\alpha\alpha} (A_3^* + iA_2^*) \quad A_{\alpha h1} = \frac{\rho B^4}{I^*} C_{\alpha h1} (A_4^* + iA_1^*) \quad A_{\alpha p} = \frac{\rho B^4}{I^*} C_{\alpha p} (A_6^* + iA_5^*)$$

$$C_{\alpha\alpha} = \frac{1}{L} \int_0^L \alpha(s)^2 ds \quad C_{\alpha h1} = \frac{1}{L} \int_0^L \alpha(s) h1(s) ds \quad C_{\alpha p} = \frac{1}{L} \int_0^L \alpha(s) p(s) ds \quad I^* = \frac{1}{L} \int_0^L I(s) \alpha(s)^2 ds$$

$$\begin{vmatrix} 1 + A_{\alpha\alpha} - \lambda_1 & A_{\alpha h1} & A_{\alpha h2} & A_{\alpha p} \\ H_{h1\alpha} \left(\frac{\omega_\alpha}{\omega_{h1}}\right)^2 & (1 + H_{h1h1}) \left(\frac{\omega_\alpha}{\omega_{h1}}\right)^2 - \lambda_2 & H_{h1h2} \left(\frac{\omega_\alpha}{\omega_{h1}}\right)^2 & H_{h1p} \left(\frac{\omega_\alpha}{\omega_{h1}}\right)^2 \\ H_{h2\alpha} \left(\frac{\omega_\alpha}{\omega_{h2}}\right)^2 & H_{h2h1} \left(\frac{\omega_\alpha}{\omega_{h2}}\right)^2 & (1 + H_{h2h2}) \left(\frac{\omega_\alpha}{\omega_{h2}}\right)^2 - \lambda_3 & H_{h2p} \left(\frac{\omega_\alpha}{\omega_{h2}}\right)^2 \\ P_{p\alpha} \left(\frac{\omega_\alpha}{\omega_p}\right)^2 & P_{ph1} \left(\frac{\omega_\alpha}{\omega_p}\right)^2 & P_{ph2} \left(\frac{\omega_\alpha}{\omega_p}\right)^2 & (1 + P_{pp}) \left(\frac{\omega_\alpha}{\omega_p}\right)^2 - \lambda_4 \end{vmatrix} = 0 \quad (2)$$

The unknown to be solved for is the flutter frequency ω which is embedded in the eigenvalues through the identity:

$$Re(\lambda_j) + i Im(\lambda_j) = (1 + ig) \left(\frac{\omega_\alpha}{\omega}\right)^2 \quad (3)$$

Once the complex eigenvalues are determined for each of the non-dimensional wind speeds $(U/fB) = U^*$ for which the aerodynamic derivatives are available the structural damping and the corresponding wind speed are obtained as:

$$g = \frac{Im(\lambda_j)}{Re(\lambda_j)}, U = U^* \frac{f_\alpha B}{\sqrt{Re(\lambda_j)}} \quad (4)$$

By plotting the structural damping g as function of the wind speed following Eq. 4 the critical wind speed U_c is identified as the wind speed at which the structural damping matches the negative value of the damping expected for the bridge structure. This procedure will be demonstrated in the subsequent examples.

3. BRIDGE STRUCTURES INVESTIGATED

Three different long span bridge structures has been chosen for the present analysis because they display distinctly different dynamic properties as is apparent from the mode shapes derived from Finite Element Models of the structures. The lowest torsion mode is particularly important as this is the mode that drives the flutter instability.

(1) The SuTong cable-stayed bridge

The SuTong Bridge is a cable-stayed bridge with a main span of 1088 m crossing the Yangtze River in China. The bridge carries a 6 lane highway on a 41.0 m wide and 4.0 m deep steel box girder of trapezoidal cross section. The bridge girder is supported by edge anchored stay cables arranged in 8 fans, 4 radiating from each pylon. Mode shapes and eigenfrequencies were determined from FE modelling of the bridge structure.

Three degree of freedom flutter derivatives were never measured for the design work of the SuTong Bridge, hence the present analysis uses aerodynamic derivatives for a similar bridge deck cross section designated H9.1, Tab. 1 right. The flutter derivatives were measured for the H9.1 section as part of the design and verification of the wind tunnel set-up discussed in the previous section. With an over-all width of 31.0 m and a depth of 4.4 m the H9.1 section is slightly more bluff than the SuTong deck section. However, with the steady state lift, drag and moment slopes being almost identical, it is expected that the flutter derivatives of the H9.1 section will be representative of the SuTong Bridge. The flutter modes (h1, h2, $\alpha 16$, p16) considered in the present analysis, Fig. 3, shows that the lowest torsion mode ($\alpha 16$) is symmetric about mid-span but it may also be recognized that the torsion mode has a pronounced horizontal component ($\alpha 16$) brought about by structural coupling. Dynamic properties such as inertia and eigenfrequencies of relevance to the SuTong flutter analysis are given in Tab. 1.

From Fig. 2 it is noted that the critical wind speed corresponding to $g = 0.01$ is $U_c = 111$ m/s irrespective of the horizontal aerodynamic derivatives ($P_{1..6}^*$) are included or not. Thus the structural coupling between the torsion and vertical mode has no appreciable influence on the flutter dynamics.

Table 1. SuTong Bridge dynamic properties and deck cross section shape

Mode	Eigenfrequency	Inertia	Deck cross section shape
1. Torsion ($\alpha 16$)	$f_{\alpha} = 0.506$ Hz	$I = 2.98 \cdot 10^6$ kgm ² /m	
1. Vertical (h1)	$f_{h1} = 0.177$ Hz	$m = 21.7 \cdot 10^3$ kg/m	
2. Vertical (h2)	$f_{h2} = 0.307$ Hz	$m = 21.7 \cdot 10^3$ kg/m	
1. Horizontal (p16)	$f_p = 0.506$ Hz	$m = 21.7 \cdot 10^3$ kg/m	

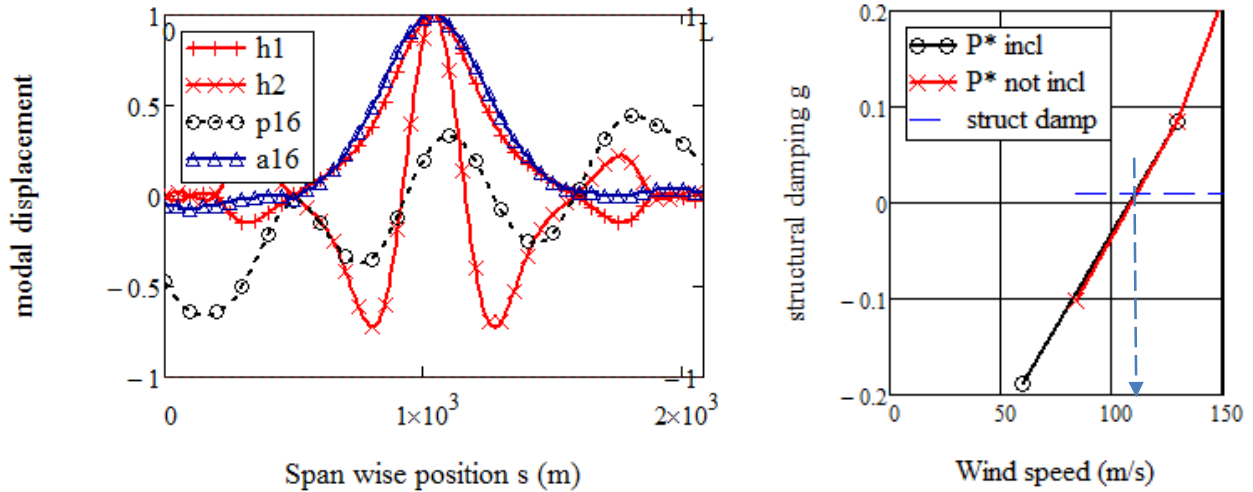
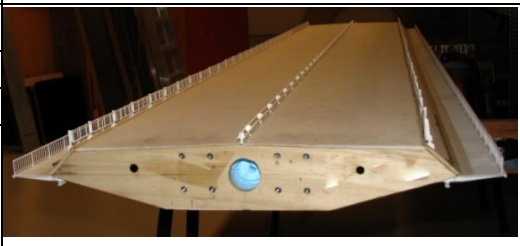


Figure 2. Mode shapes (left) and plot of structural damping as function of wind speed (left) for the SuTong Bridge.

(2) The Izmit suspension bridge

The first suspension bridge considered is the 1550 m main span Izmit Bridge currently under construction in Turkey. The bridge carries a 6 lane highway on a trapezoidal box girder. Two walkways are cantilevered at the apex points of the 35.8 m wide and 4.75 m deep section, Tab. 2 (right). The bridge girder is supported by two classical wire suspension cables arranged over the attachment points of the cantilevered walkways. Mode shapes obtained from FE analysis of the bridge structure are shown in Fig. 3 (left). It is noted that the modes are symmetric about mid-span and it may also be recognized that the torsion mode ($\alpha 8$) has small horizontal mode ($p 8$) due to structural coupling. The FE model is loaded by a horizontal static load corresponding to a mean wind speed of 40 m/s at bridge girder level yielding a horizontal mean deck deflection of approximately 2.5 m at mid span. Dynamic properties such as inertia and eigenfrequencies of relevance to the flutter analysis and the deck section shape is presented in Tab. 2.

Table 2. Izmit Bridge dynamic properties

Mode	Eigenfrequency	Inertia	Deck cross section shape
1. Torsion ($\alpha 21$)	$f_{\alpha} = 0.258$ Hz	$I = 2.51 \cdot 10^6$ kgm ² /m	
1. Vertical (h1)	$f_{h1} = 0.091$ Hz	$m = 21.09 \cdot 10^3$ kg/m	
2. Vertical (h2)	$f_{h2} = 0.136$ Hz	$m = 21.09 \cdot 10^3$ kg/m	
1. Horizontal (p21)	$f_p = 0.258$ Hz	$m = 21.09 \cdot 10^3$ kg/m	

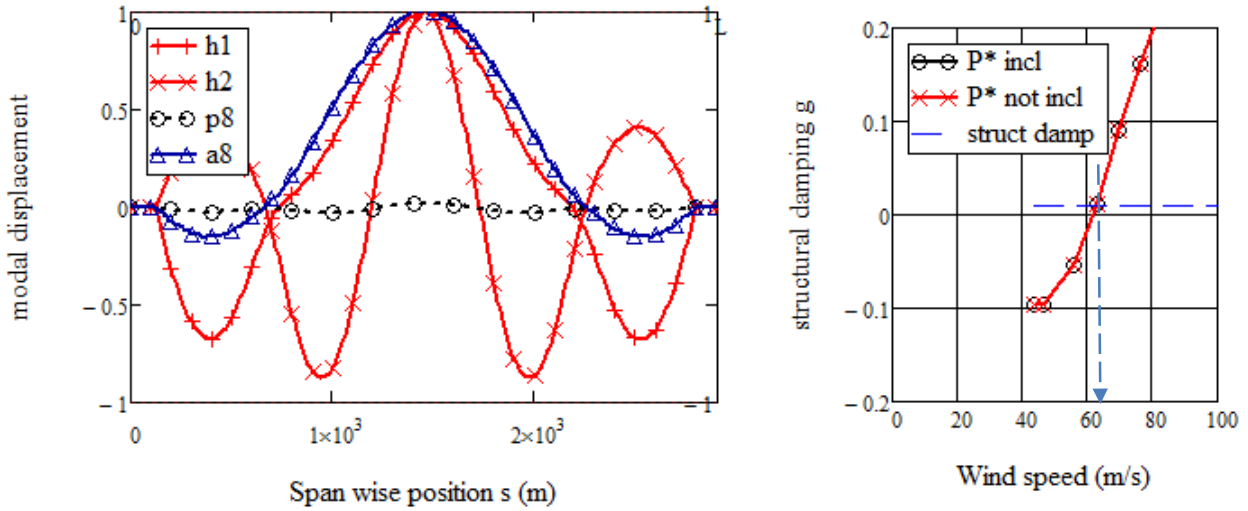


Figure 3. Mode shapes (left) and plot of structural damping as function of wind speed (right) for the Izmit Bridge. Horizontal deflection of the main span due to mean wind loading included.

The result of the flutter analysis is shown in Fig. 3 (right). It is noted that the critical wind speed corresponding to $g = 0.01$ is $U_c = 63$ m/s irrespective of the horizontal aerodynamic derivatives ($P_{1.6}^*$) are included or not. This is not surprising in view of the very small horizontal deflection brought about by the structural coupling to the torsion mode. Full aeroelastic tests of a 1:220 scale model of this bridge carried out at the University of Milan yielded a critical wind speed $U_c = 66$ m/s in good agreement with the flutter predictions above.

Experience gained from the flutter analysis and full aeroelastic model wind tunnel tests of the Akashi-Kaikyo Bridge [6] indicates that the torsion/horizontal coupling due to large mean wind deflections may yield a significant decrease of the flutter wind speed relative to the undeflected bridge. In order to investigate this scenario the mean wind deflection of the finite element model was increased to 36 m corresponding roughly to one deck width. The resulting mode shapes and flutter diagram is shown in Fig. 4 below.

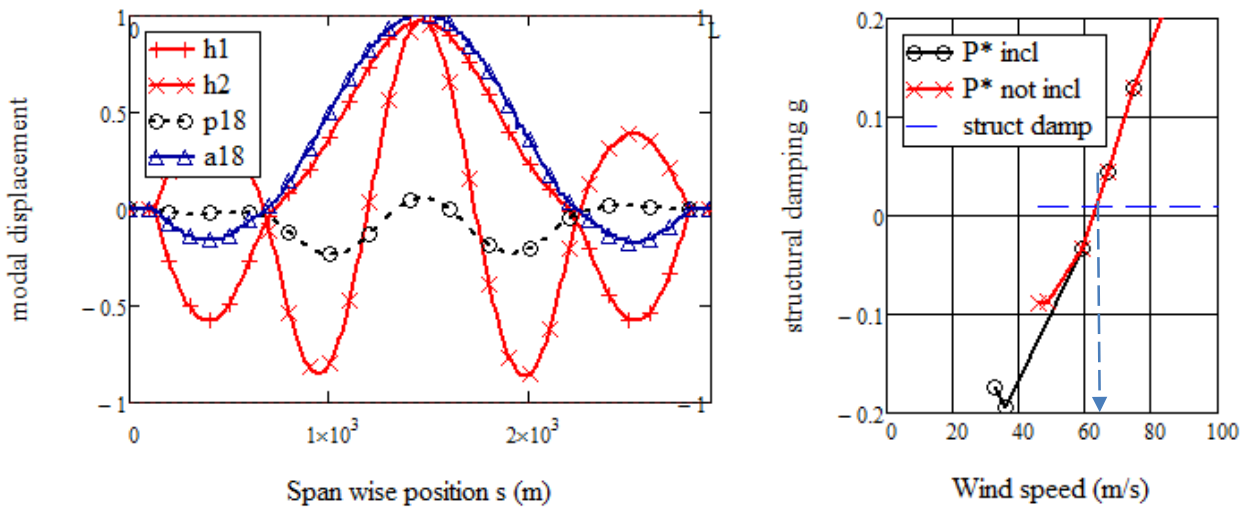


Figure 4. Mode shapes (left) and plot of structural damping as function of wind speed (right) for the Izmit Bridge. Horizontal deflection of the main span corresponding to one deck width at central node.

Comparison of the mode shapes in Fig. 3 and 4 demonstrates that the increased horizontal deflection gives rise to an increased modal amplitude of the horizontal mode shape. Also the torsion/horizontal eigenfrequency increases slightly from $f_{\alpha} = 0.258$ Hz to $f_{\alpha} = 0.271$ Hz. However, the critical wind speed is not significantly affected yielding a critical wind speed $U_c = 64$ m/s.

(3) The Messina suspension bridge

The second suspension bridge considered is the 3300 m main span Messina Bridge designed for crossing the Messina Strait, linking Sicily to the Italian main land. The bridge carries 6 lanes of highway traffic and two railway tracks as well as maintenance paths. The bridge deck is unique in that it is split in three separate box girder structures separated by air gaps but held structurally together by heavy cross beams at the hanger locations. A design developed for enhancement of the aerodynamic stability. The bridge girder is supported by two twinned classical wire suspension cables arranged over the attachment points of the cantilevered maintenance paths. The deck cross section is a total of 60.0 m wide and the individual girders have a depth of 2.5 m, Tab. 3 (right). The lowest eignemodes relevant to the flutter analysis is shown in Fig. 5 (left). It is noted that the torsion mode ($\alpha 8$) now is asymmetric about mid-span and as in the case of the Izmit Bridge little horizontal girder movement ($p 8$) due to structural coupling is noted. Dynamic properties such as inertia and eigenfrequencies of relevance to the analysis are given in Tab. 3.

Table 3. Messina Bridge dynamic properties

Mode	Eigenfrequency	Inertia	Deck cross section shape
1. Torsion ($\alpha 8$)	$f_{\alpha} = 0.081$ Hz	$I = 28.93 \cdot 10^6$ kgm ² /m	
1. Vertical ($h 1$)	$f_{h1} = 0.065$ Hz	$m = 58.1 \cdot 10^3$ kg/m	
2. Vertical ($h 2$)	$f_{h2} = 0.125$ Hz	$m = 58.1 \cdot 10^3$ kg/m	
1. Horizontal ($p 1$)	$f_{p1} = 0.055$ Hz	$m = 58.1 \cdot 10^3$ kg/m	
2. Horizontal ($p 8$)	$f_{p2} = 0.081$ Hz	$m = 58.1 \cdot 10^3$ kg/m	

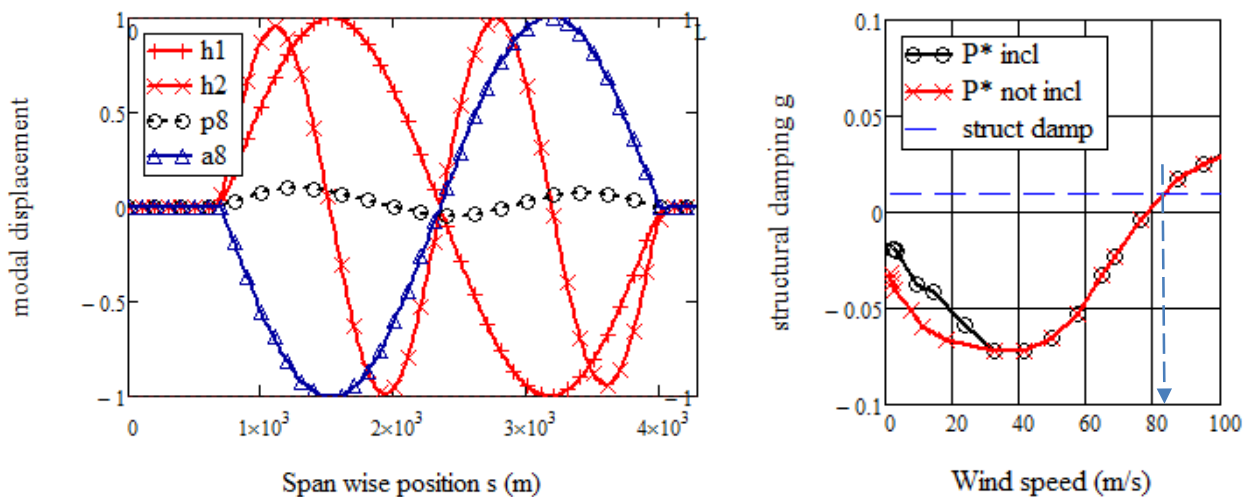


Figure 5. Mode shapes resulting from torsion / horizontal structural coupling (left) and plot of structural damping as function of wind speed (right) for the Messina Bridge.

The Messina Bridge is equipped with large wind screens with airfoil dampers at the outer edges of the cantilevered maintenance service lanes and solid noise barriers running along the central railway girder. This

configuration yields a relatively high drag coefficient which in turn results in a horizontal mean wind displacement of approximately 11 m at the design wind speed of 54 m/s.

As in the case of the Izmit Bridge the horizontal mean wind deflection leads to a horizontal component of the governing asymmetric torsion mode ($p8$). From Fig. 6 it is noted that the horizontal component of the torsion mode has virtually no influence on the critical wind speed which is read of Fig. 6 (right) as $U_c = 84$ m/s.

From Table 3 it is noted that the basic horizontal mode is much closer in frequency to the fundamental torsion mode (a frequency ratio f_{p1}/f_α of 0.68) than is common in suspension bridges having torsional stiff closed box girders. For the Izmit Bridge f_{p1}/f_α is 0.2 as an example. The large wind screens which creates substantial drag combined with the small frequency difference between the basic horizontal and the torsion mode lead to some concern that the basic horizontal mode would influence the flutter wind speed of the bridge through aerodynamic coupling.

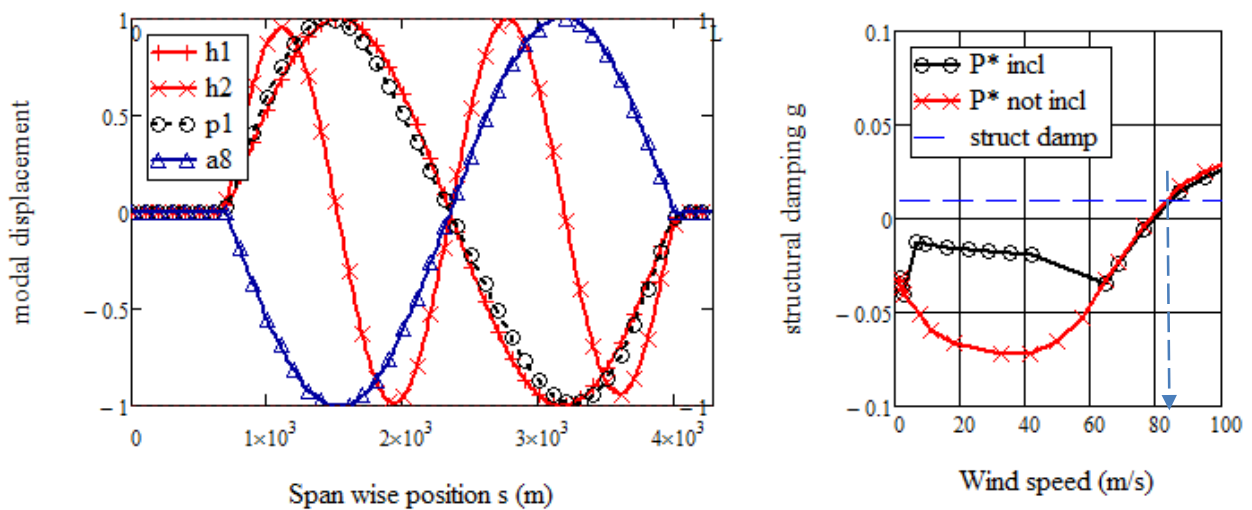


Figure 6. Mode shapes (left) and plot of structural damping as function of wind speed (right) for the Messina Bridge

From Fig. 6 it is noted that the influence of the horizontal aerodynamic derivatives are notable at wind speeds below 40 m/s resulting in a significantly lower apparent damping level when the horizontal aerodynamic derivatives are taken into account. However, the critical wind speed is not significantly affected by the horizontal aerodynamics yielding a critical wind speed $U_c = 85$ m/s, i.e. slightly higher than when the horizontal aerodynamic derivatives are not included in the analysis.

4 CONCLUSION

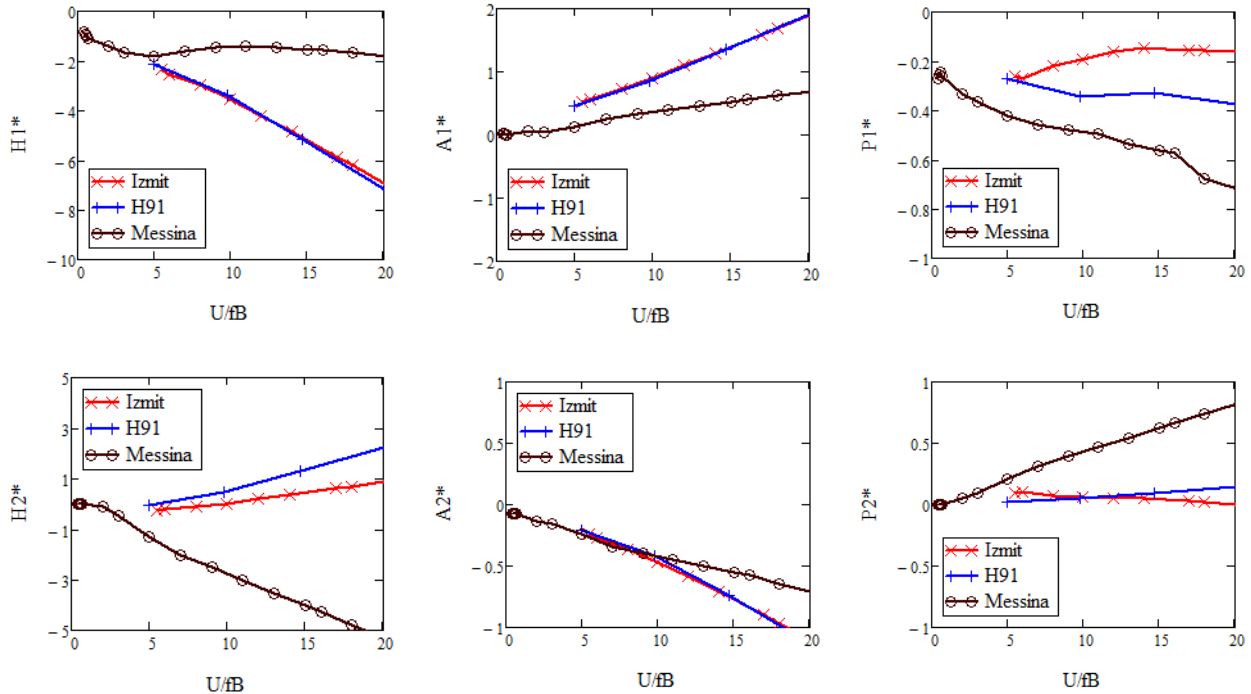
The present analysis has considered the influence of the horizontal aerodynamics on the flutter speed of three major cable supported bridges. It is concluded that the critical wind speed for onset of flutter is not significantly affected by the horizontal aerodynamics. A result markedly in contrast to Miyata [6]. In closing it is noted that the cable supported bridge considered in the present analysis are bridges having very long span and thus are characterized by relatively small structural coupling between the individual modes. The above conclusion may not hold for some smaller contemporary cable supported foot bridges which sometimes are built with pronounced curvature in the horizontal plane of the deck.

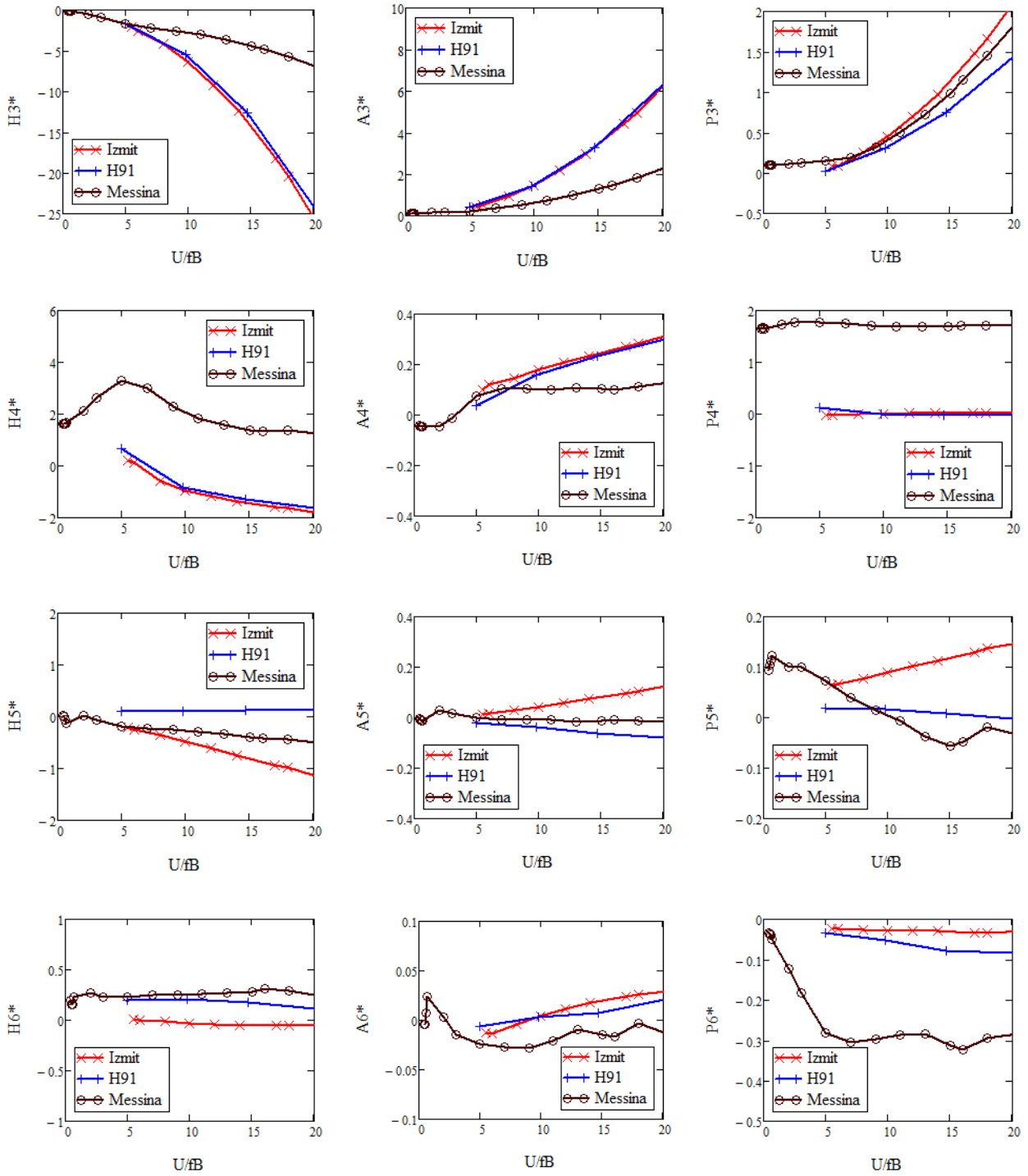
REFERENCES

- 1) Scanlan, R.H. and Tomko, J.J., 1971. Airfoil and Bridge Deck Flutter Derivatives. *J. Eng. Mech.*, ASCE (97) EM6, 1717-1737.
- 2) Theodorsen, T., 1935. General Theory of Aerodynamic Instability and the Mechanism of Flutter. NACA TR 496, in *Classical Aerodynamic Theory*. Jones R.T. (ed) NASA Reference Publication 1050, 1979.
- 3) Jones, N.P., Scanlan, R.H., Aurang, J. and Katuchi, H., 1998. Advances (and challenges) in the prediction of long span bridge response to wind. In *Bridge Aerodynamics*, Larsen and Esdahl (ed.) Balkema, Rotterdam.
- 4) Larsen, S.V., Sinding, P., Smitt, L.W., 2002. Extraction of aerodynamic flutter derivatives in newly developed forced motion rig with 3 degrees-of-freedom. *Proceedings, 13th International Conference on Wind Engineering*.
- 5) Jakobsen, J.B. Hjort-Hansen, E. Arne Selberg's formula for flutter speed in light of multimodal flutter analysis. *Proceedings of the 12th International Conference on Wind Engineering*, Cairns, Australia, vol. 1, pp. 143-150. 2007.
- 6) Miyata, T. Historical review of long-span bridge aerodynamics. *Journal of Wind Engineering and Industrial Aerodynamics*. 91 (1393 – 1410). 2003.

APPENDIX: AERODYNAMIC DERIVATIVES FROM SECTION MODEL TESTS

This appendix presents aerodynamic derivatives measured by forced motion section model tests. It is to be noted that the flutter coefficients presented below are normalized in accordance with Scanlan's original definition using ρU^2 as reference dynamic head. A more recent definition uses the full deck width B , with the implication that the numerical value of the flutter coefficients are smaller by a factor 2.





NONLINEAR PHENOMENA OF COUPLED FLUTTER RESPONSES AND SELF-EXCITED FORCES OF A FLAT CLOSED-BOX BRIDGE DECK

Ledong Zhu⁺¹, Guangzhong Gao⁺² and Hao Wu⁺³

⁺¹State Key Laboratory of Disaster Reduction in Civil Engineering / Key Laboratory for Wind Resistance Technology of Bridges of Ministry of Transport / Department of Bridge Engineering, Tongji University, Shanghai 200092, China

⁺² Department of Bridge Engineering, Tongji University, Shanghai 200092, China

⁺³China Resources Land (Shanghai) Co.Ltd, Shanghai 200122, China

The nonlinear behaviors of post-flutter and corresponding self-excited forces of a flat closed-box bridge deck were investigated through spring-suspended sectional model (SSSM) tests. The sectional model was found to undergo nonlinear post-critical flutters, often called soft flutters, beyond the different linear flutter boundaries at common attack angles, i.e., 5° , $\pm 3^\circ$ and 0° , which exhibited self-limiting vibration behaviors in time domain and limit cycle oscillations (LCOs) in the final stable states of oscillation. The post-flutter LCOs occurred in a coupled mode which was dominated by the vibration in torsional degree of freedom (DOF) and coupled with obvious vibration in heaving DOF. The coupling effect of torsional-heaving vibrations increased with the rising wind speed in the post-critical region. The nonlinear self-excited lift force and torsional moment were measured by using four elaborate high-accuracy miniature three-component dynamic force balances installed inside the sectional model to reduce the inertia forces, and were validated by comparing the calculated and measured post-critical displacement responses. Both the measured self-excited lift force and torsional moment were found to contain significant higher-order multiple-frequency components, which indicate strong aeroelastic nonlinearity.

Keyword: flat closed-box deck, soft coupled flutter, self-limiting vibration, limit cycle oscillation, nonlinear self-excited forces

1. INTRODUCTION

Suppressing flutter instability is of great concern for long-span bridges. With continuous increase of span length and application of low-damping material, modern long-span bridges are becoming more susceptible to wind actions, which pose new challenges for engineers in guaranteeing aeroelastic stability. Up to now, widely-accepted approaches for flutter analyses of long-span bridges are commonly based on the linear unsteady self-excited force model proposed by Scanlan¹⁾ in 1970s. Because the nonlinear aeroelastic effect is neglected in Scanlan's linear model, it is only suitable for the cases of vibration with amplitudes small enough, in which the change of transient aerodynamic shape due to the vibration can be negligible. In this connection, the classical linear approaches for flutter analyses can only be used to predict the linear boundary, i.e., the lowest critical point or wind speed of divergent-type flutter instability with rapidly-increasing amplitude to infinite. They are incompetent for predicting the post-critical responses of soft flutter, which is strongly nonlinear in both aeroelastic and structural behaviors and shows a vibration manner of limit cycle oscillation (LCO). However, for most long-span bridges with bluff decks the flutter responses or at least the post flutter responses are actually soft, namely, exhibit self-limiting vibration behaviors in time domain and LCOs in the final stable states of oscillation because of the nonlinearity of aerodynamic forces pertaining to the vibration responses. For instance, the flutter of Tacoma Narrows Bridge really happened in 1940 was not a strict divergent-type vibration, but was a LCO-type vibration with the largest torsional amplitude of about 35° and lasting for about 70 minutes before final collapse²⁾. Considering the LOC behavior

⁺¹ledong@tongji.edu.cn, ⁺²guangzhonggao88@gmail.com, ⁺³wh.seu@163.com

of the soft flutter, flutter with small amplitude in short period should perhaps be allowed in the wind resistant design of long-span flexible bridges, just like that already done for the vortex-induced vibration. It is thus very necessary to investigate the nonlinear behavior of post flutter and to modeling mathematically the nonlinear aeroelastic self-excited forces of typical bluff bridge decks under states of large-amplitude oscillation for the purposes of reasonable prediction on post flutter responses of long span bridges.

The source of aeroelastic nonlinearity of flutter can be qualitatively attributed to the change of transient relative attack angle of wind due to the bridge deck motion, which is equivalent to the change of transient aerodynamic shape of the bridge deck relative to the direction of the transient equivalent resultant wind. Therefore, the nonlinearity of self-excited force will become more and more significant with the increasing vibration amplitude. The investigations of nonlinear aeroelastic effects and self-excited force modeling have been carried out extensively in the field of aeronautics³⁾, wind turbine⁴⁾ and energy harvesting⁵⁾. In recent years, the related topics have attracted wide attentions in structural engineering. Noda⁶⁾ found the amplitude-dependence effect of linear flutter derivatives via forced vibration tests on two rectangular plates with aspect ratio $B/D=13$ and $B/D=150$. Diana et al.⁷⁾ studied the nonlinear hysteresis effect of a typical closed-box section and later proposed a numerical approach to model the various aerodynamic nonlinearities using a rheological mechanical model. Later, Liao et al.⁸⁾ measured aerodynamic forces of thin airfoil and closed-box bridge girder through large-amplitude forced vibration tests, and investigated the nonlinear hysteresis effect and post-flutter behaviors based on the measured results. Amandolese⁹⁾ studied the post-flutter behavior of a flat plate and found that it would exhibit LCO characterized by significant heaving-torsional coupling effect in post-critical state. Naprstek et al.¹⁰⁾ studied the nonlinear post-critical LCO of a rectangular 1:4 section and proposed a nonlinear self-excited forced model of Rayleigh or Van der Pol with Duffing types. Wu and Kareem¹¹⁾ established a nonlinear convolution scheme using Volterra series to model nonlinear self-excited force. Liu and Ge¹²⁾ proposed a set of nonlinear differential equations with internal states to model nonlinear and unsteady characteristics of bridge aerodynamics.

Considering that flat closed-box decks are often used on long-span bridges for its high performance of flutter stability, such as the decks of Great Belt Bridge with a main span of 1624m, Xiangshan Harbor Bridge with a main span of 688m, the nonlinear phenomena of the coupled flutter and the aeroelastic self-excited lift force and torsional moment of a typical flat closed-box deck under post flutter states were investigated in this study through SSSM tests in wind tunnel, and are to be discussed in this paper.

2. WIND TUNNEL TESTS OF POST-FLUTTER

(1) Brief information of wind tunnel and sectional model

The post-flutter tests of a flat closed-box deck were performed in TJ-2 wind tunnel. The wind tunnel is a boundary layer tunnel of horizontal closed-circuit type with a testing section of 3m wide, 2.5m high and 15m long. Wind speed can be continuously adjusted from 0.5 to 68.0 m/s. Fig.1 and Fig.2 display the sectional model and its cross section. The general experimental setup is illustrated in Fig.3. The sectional model was elastically supported by 8 helical springs through 2 arms. The horizontal long steel wires were used to constrain the horizontal degree of freedom of the model. To avoid disturbing the two-dimensional flow around the sectional model, the elastic supporting system (the helical springs, the suspending arms and the supporting frame) and 3 displacement sensors were hidden inside the two fairing walls parallel to the longitudinal axis of the wind tunnel. The fairing walls were 0.12m thick, 2.4m high and 4.0m long. Its windward ends were of arc shape to improve the flow quality between the two fairing walls.

The total length of sectional model is 1.920m. The total effective mass and mass moment of inertia are 23.221kg and $2.594\text{kg}\cdot\text{m}^2$, respectively, including the 1/3 mass of helical springs. The vertical and torsional frequencies (f_{h0} and $f_{\omega 0}$) in still air were 1.245Hz and 2.075Hz, respectively. The structural damping ratios in vertical and torsional modes (ζ_h and ζ_t) in still air were nonlinear and vary, respectively, from 0.6% to 1.13%, and from 0.08% to 0.37%, which will be further discussed infra.

All tests were carried out in smooth flow field and the Reynolds number Re varied within the range of $1.0\times 10^5\sim 6.0\times 10^5$. The maximal allowed ranges of the torsional and heaving vibration were $\pm 6.6^\circ$ and $\pm 0.05\text{m}$,

respectively by considering the limitation of the linear range of pre-tensioned springs and the linear measurement ranges of laser displacement sensors.



Figure 1: Spring-suspended sectional model between two fairing walls in TJ-2 wind tunnel

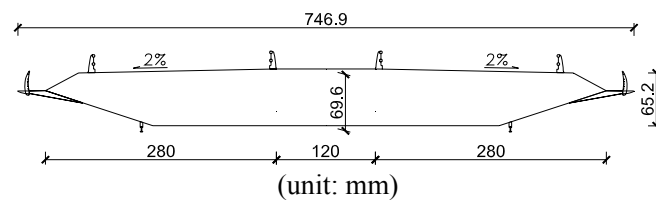


Figure 2: Cross section of sectional model

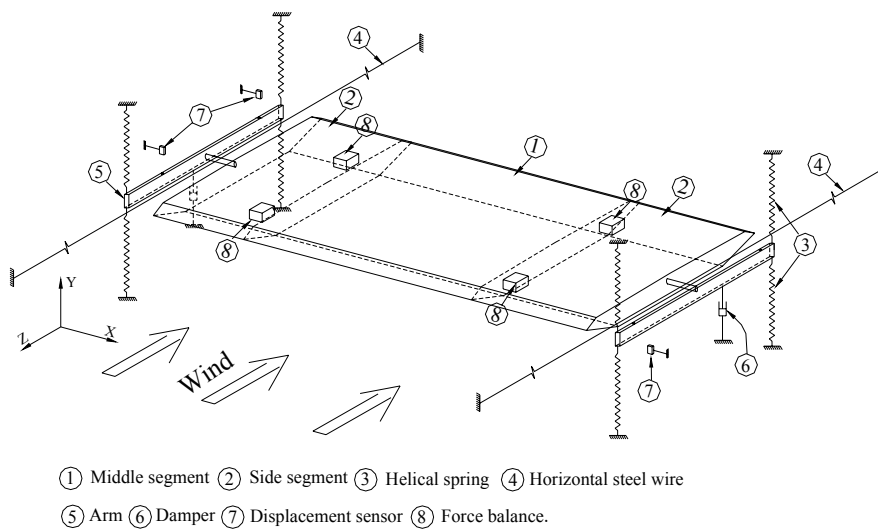


Figure 3: Schematic diagram of general experimental setup

(2) Test results of post-flutter behaviors

The post-flutter responses of the closed-box deck were investigated for four cases of wind attack angles of 5° , $\pm 3^\circ$ and 0° . For each case of attack angle, the sectional model vibration was random around its static equilibrium position when the wind speed was lower than a critical value (U_{cr}). Beyond this critical wind speed, the vibration became unstable and shows a divergent tendency with outward-concaved envelopes of oscillation crest and trough in the initial stage after a small excitation. But, with the increase of amplitude, the increase rate of the vibration amplitude became lower and lower until to zero when the vibration finally reached to a stable LCO state. The divergent tendency in the initial stage must be caused by the negative aerodynamic damping provided by the linear or even nonlinear components of self-excited forces whilst the self-limiting phenomenon must be resulted in by the positive aerodynamic damping provided by the high-order nonlinear components of self-excited forces. This kind of nonlinear flutter phenomenon is totally different from the divergent-type linear flutter, also called as “hard” flutter, as predicted by classical flutter

theory, and is often called as ‘soft flutter’.

Fig.4 displays the root mean square (RMS) values of heaving and torsional displacements in different attack angles, where the upper arrows denote that the stable amplitudes were larger than the values of the relevant data symbols. One can then find from Fig.4 that the post-flutter of the flat closed-box deck was featured by obvious heave-torsion coupling effect. The stable amplitude of heaving and torsional LCO both increased unrestrictedly with wind speed. The critical wind speed U_{cr} was smaller and the LCO amplitude increased much slowly at a larger attack angle than at a smaller attack angle. These are mainly due to the fact that the larger the attack angle is, the bluffer the aerodynamic shape of the deck is, and the much significant the aeroelastic nonlinearity is.

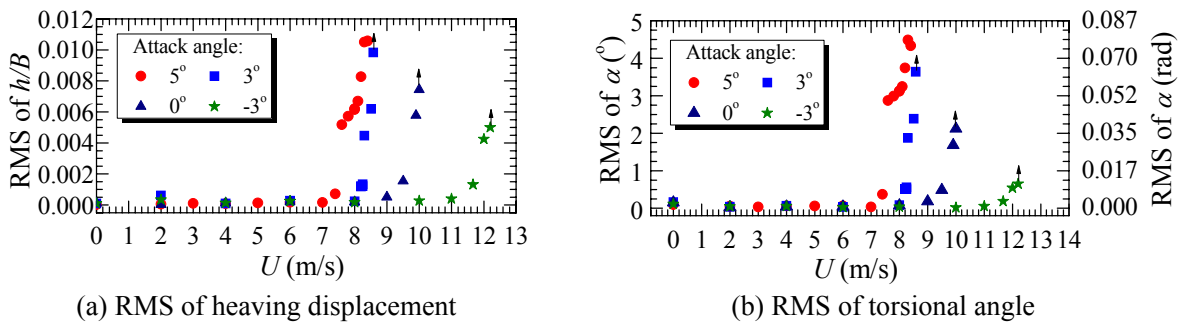


Figure 4: RMS values of stable responses of post-flutter

Fig.5 shows the post-critical LCOs in heaving and torsional degree of freedom at the attack angle of 5° and the wind speed of 7.8m/s . It can be found that both the heaving and torsional signals are not strictly harmonic and with slight higher-order components because of aereelastic nonlinearity, but dominated by the second mode corresponding to the torsional mode at zero wind speed, indicating that the observed post-critical instability occurred in the torsional mode. Fig.6 further displays the evolution of vibration frequency in the heaving and torsional modes with wind speed. One can find that the vibration responses beyond critical wind speed U_{cr} were only in torsional branch.

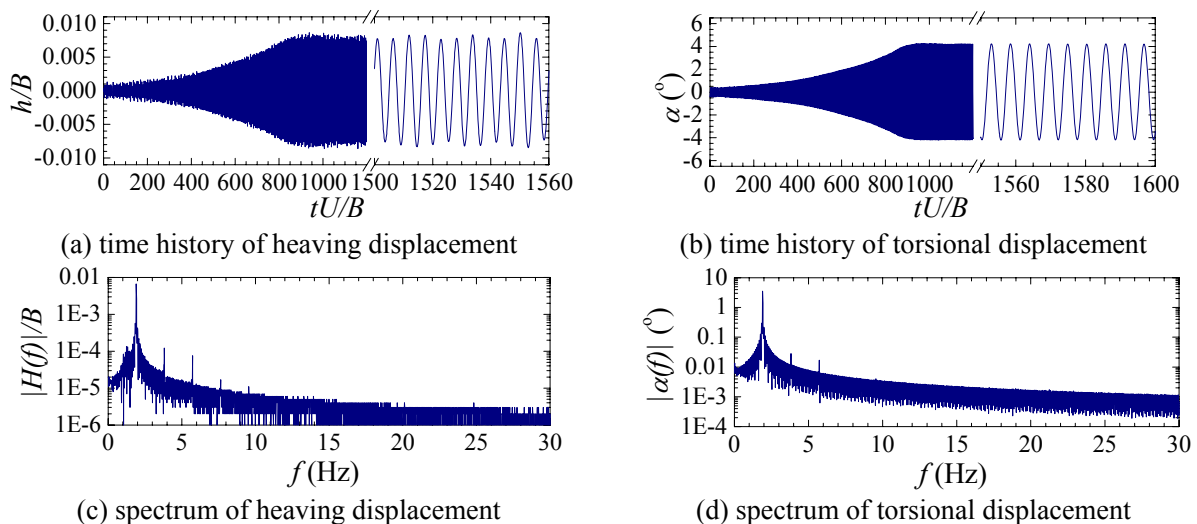


Figure 5: Post-critical responses at $U=7.8\text{m/s}$ ($U^*=U/tB=5.466$, attack angle 5°)

The coupling ratio of heaving and torsional responses γ can be defined as $\text{RMS}(h) / (\text{RMS}(\alpha b))$, where $\text{RMS}()$ represents the RMS value of the relevant variable in parentheses; $b=B/2$ is the half width of bridge deck. Fig.7 shows the variations of γ with wind speed in the post-critical state for the attack angle of 5° and 3° . It can be found that the coupling ratio increases with the wind speed in the post-critical region and the

variation laws are approximately same for different attack angles.

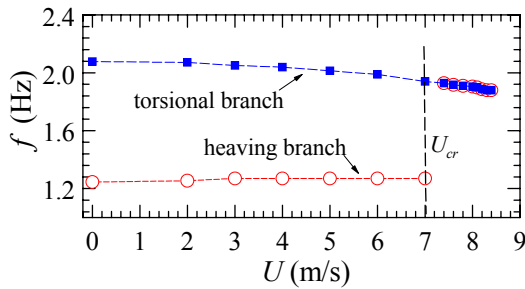


Figure 6: Evolution of vibration frequency with wind speed (attack angle 5°)

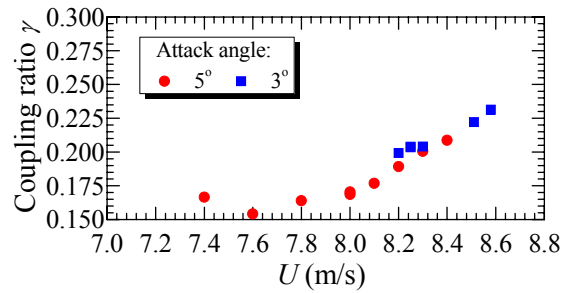


Figure 7: The coupling ratio of heaving and torsional degree of freedom in post-critical state

3. MEASUREMENT OF NONLINEAR SELF-EXCITED FORCES

(1) Improved force measurement technique

An improved technique, including the development of four elaborate high-accuracy miniature three-component dynamic force balances (see Fig.8) and the installation of the force balance inside the sectional model (see Fig.3 and Fig.9) to reduce the inertia forces, was adopted in this study to measure the nonlinear self-excited forces on a vibrating SSSM during the post-critical LCOs. The force balance was piezoelectric type with high sensitivity and small size of 0.035×0.05×0.05m. The weight of each balance is about 0.128kg. The linear range of vertical shear force is 12N and torque 0.9N·m with measurement error less than 4.57%F.S.

To further improve the measurement accuracy of self-excited force, the exterior ‘coat’ of the sectional model was separated into two 0.420m-long side segments and one 1.08m-long middle measurement segment. There were 1~2mm gaps between the middle and side ‘coat’ to avoid any interference. The middle ‘coat’ was mounted on the internal rigid frame of the model through the 4 force balances while the side ‘coats’ were directly fixed on the rigid frame. Hence, only the dynamic forces on the middle ‘coat’ were measured. The ‘coats’ were made of light wooden plates stiffened by thin-walled duralumin to reduce the mass and thus the inertial force acting on the force balances as possible. The mass and mass moment of inertia of the middle ‘coat’ were 3.228kg/m and 0.0991kg·m²/m, respectively, which were only about 1/3.75 and 1/13.6 of the total ones of the SSSM system (12.094 kg/m and 1.351kg·m²/m), respectively.



Figure 8: Three-component force balance

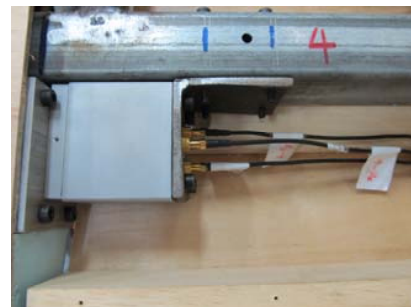


Figure 9: Force balance installed inside the sectional model

The loading state of the middle exterior ‘coat’ during post-critical LCO was shown in Fig.10. From the dynamic equilibrium conditions of exterior ‘coat’, the self-excited lift and moment per unit length can be expressed as follows:

$$M_{se}(t) = M_{ms}(t) - M_{se}^0(t) - M_I(t) \tag{1}$$

$$L_{se}(t) = L_{ms}(t) - L_{se}^0(t) - L_I(t) \tag{2}$$

where $M_I(t) = -J_s \cdot \ddot{\alpha}(t)$ and $L_I(t) = -m_s \cdot \ddot{h}(t)$ are inertial moment and force acting on the exterior ‘coat’ per unit length. $M_{ms}(t)$ and $L_{ms}(t)$ are the total dynamic moment and force measured by the 4 balances, which can be expressed as:

$$M_{ms}(t) = \left[(M_{m1} + M_{m2} - M_{m3} - M_{m4}) + (F_{my1} - F_{my2} + F_{my3} - F_{my4}) \times b_m / 2 \right] / l_m \quad (3)$$

$$L_{ms}(t) = -(F_{my1} + F_{my2} + F_{my3} + F_{my4}) \times \cos \alpha_0 + (-F_{mx1} - F_{mx2} + F_{mx3} + F_{mx4}) \times \sin \alpha_0 \quad (4)$$

Where, $M_{mi}, F_{myi}, F_{mxi} (i=1,2,3,4)$ represent the force signals measured by each force balance. l_m is the length of middle ‘coat’, b_m is the transverse distance between force balance, as shown in Fig.10. α_0 represents the static angle of attack.

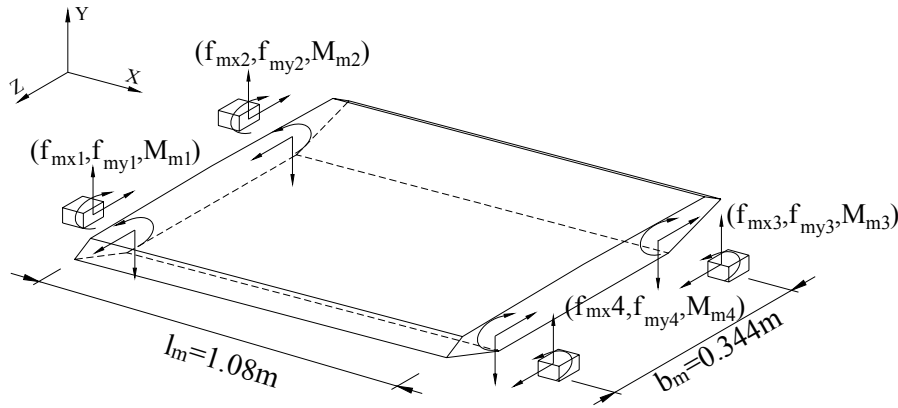


Figure 10: Loading state of the middle exterior ‘coat’

$M_{se}^0(t)$ in Eq.(1) represents the non-wind-induced aerodynamic moment, which is caused by the interaction of sectional model and its surrounding air. Non-wind-induced effect exists in both still air and flowing air conditions. $M_{se}^0(t)$ can be represented by additional moment of inertia and additional damping coefficient as follows, where, the nonlinearity of additional damping coefficient should be considered in large amplitude cases:¹⁴⁾

$$M_{se}^0(t) = -J_0 \cdot \ddot{\alpha}(t) - c_{\alpha 0}(\rho_\alpha) \cdot \dot{\alpha}(t) \quad (5)$$

where J_0 is the non-wind-induced additional moment of inertia, $c_{\alpha 0}$ is the non-wind-induced additional damping coefficient which is a nonlinear function of instantaneous torsional amplitude ρ_α .

Similarly, $L_{se}^0(t)$ in Eq.(2) represents the non-wind-induced aerodynamic force and can be expressed as:

$$L_{se}^0(t) = -m_0 \cdot \ddot{h}(t) - c_{h0}(\rho_h) \cdot \dot{h}(t) \quad (6)$$

where m_0 is the non-wind-induced additional mass, c_{h0} is the non-wind-induced additional damping coefficient which is a nonlinear function of instantaneous heaving amplitude ρ_h .

(2) Structural and non-wind-induced aerodynamic nonlinearities

It is known from Eq.(1)~Eq.(2) and Eq.(5)~Eq.(6) that non-wind-induced aerodynamic parameters, i.e., $J_0, m_0, c_{\alpha 0}(\rho_\alpha)$ and $c_{h0}(\rho_h)$, are necessary in extracting self-excited force $M_{se}(t)$ and $L_{se}(t)$. The nonlinear structural parameters, i.e., mechanical damping ratio $\xi_\alpha(\rho_\alpha)$, $\xi_h(\rho_h)$ and mechanical frequency $f_\alpha(\rho_\alpha)$, $f_h(\rho_h)$, are also needed later when verifying the extracted self-excited force $M_{se}(t)$ and $L_{se}(t)$. The above non-wind-induced aerodynamic parameters can be identified from the measured force and displacement signals during free decay process in still air¹⁴⁾. The nonlinear structural parameters can be identified from the

free-decay displacement in still air¹⁵).

The identified additional mass parameters, i.e., m_0 and J_0 , are 3.425 kg/m and 0.0300 kg-m²/m, respectively, when the attack angle is 5°. Fig.11 illustrates the identified nonlinear structural and non-wind-induced additional damping ratios for both the heaving and torsional modes at different vibration amplitudes, where the additional damping ratios of heaving and torsional modes are represented by $\xi_{\alpha 0}(\rho_\alpha) = c_{\alpha 0}(\rho_\alpha) / [2\omega_{\alpha 0}(I + J_0)]$ and $\xi_{h 0}(\rho_h) = c_{h 0}(\rho_h) / [2\omega_{h 0}(m + m_0)]$, respectively. Fig.12 shows variation patterns of the heaving and torsional model frequencies with vibration amplitudes. As can be seen, the mechanical damping ratios, $\xi_\alpha(\rho_\alpha)$ and $\xi_h(\rho_h)$, and the non-wind-induced additional damping ratios, $\xi_{\alpha 0}(\rho_\alpha)$ and $\xi_{h 0}(\rho_h)$ increases all with the instantaneous amplitude, ρ_α or ρ_h , roughly in a linear manner. The mechanical frequency of the torsional mode $f_\alpha(\rho_\alpha)$ decreases with the instantaneous torsional amplitude ρ_α also in a linear way, whereas, that of the heaving mode $f_h(\rho_h)$ decreases with the heaving amplitude ρ_h in a nonlinear way, indicating the softening effect of the SSSM system at large-amplitude states. Note that two different symbols were used in Fig. 11 and Fig.12, respectively, for the results obtained in the two repeated tests of free decay vibration, which agree well to each other, indicating the good repeatability of identified results.

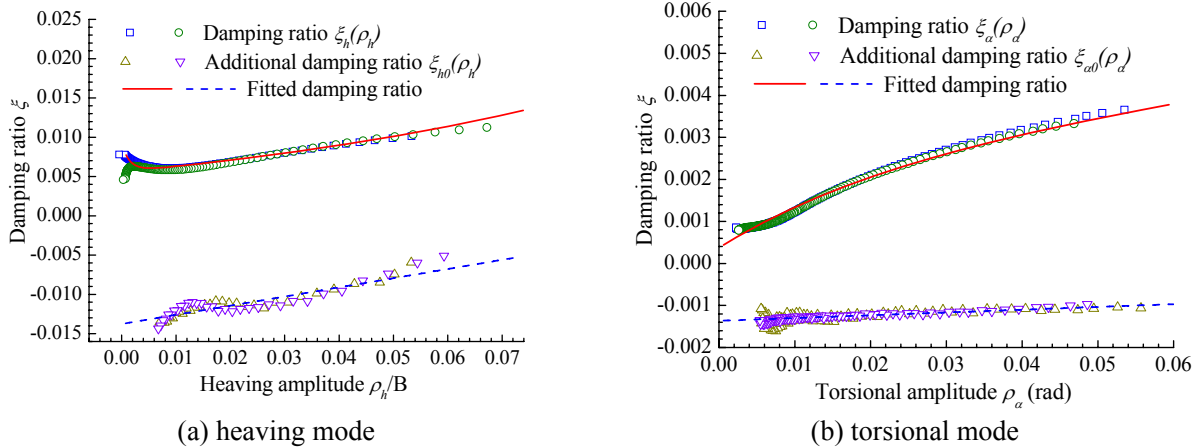


Figure 11: Variations of identified structural and non-wind-induced additional damping ratios in still air with vibration amplitude

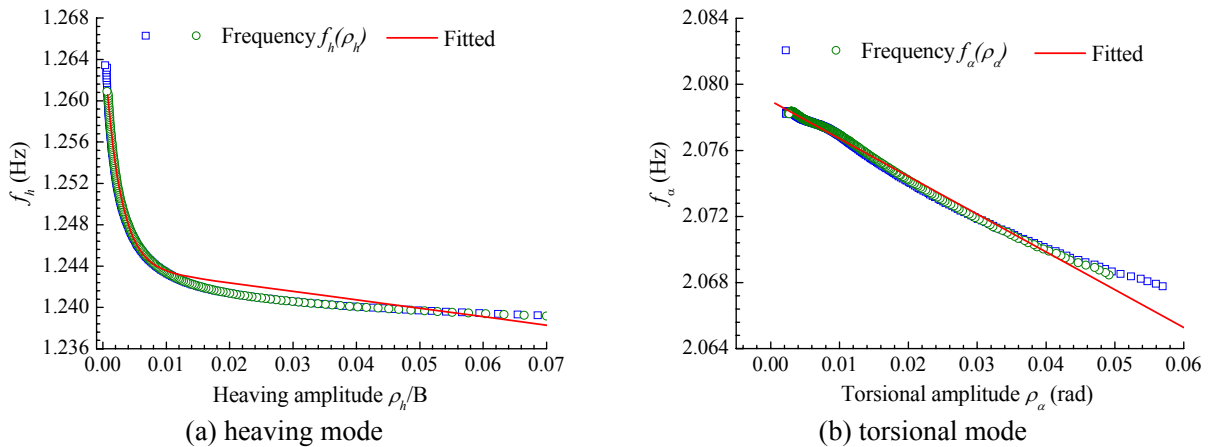


Figure 12: Variations of identified modal frequencies of SSSM system in still air with vibration amplitude

It should be pointed out that the nonlinear parameters identified in still air cannot be directly used in the flowing air conditions, because the above parameters are also functions of vibration frequency, and according to Fig.6 it one be known that the vibration frequencies change with wind speed and the heaving

frequency can even switch between two modes. Therefore, the fitted nonlinear functions in Fig.11 and Fig.12 should be revised when used by considering the frequency change or switch. Taking $\xi_h(\rho_h)$ as an example, the fitted $\xi_h(\rho_h)$ in Fig.11a corresponds to the heaving frequency f_{h0} , and when used in the case of heaving frequency f_{hi} , $\xi_h(\rho_h)$ should be revised to $\tilde{\xi}_h(\rho_h \cdot f_{hi} / f_{h0})$.

(3) Measured nonlinear self-excited lift force and torsional moment

After identifying the non-wind-induced aerodynamic parameters, the self-excited lift force $L_{se}(t)$ and torsional moment $M_{se}(t)$ can then be extracted from dynamic forces by subtracting the inertial forces and the non-wind-induced aerodynamic forces by Eq.(1)~Eq.(6). Fig.13 shows the time history of obtained self-excited lift force $L_{se}(t)$ and torsional moment $M_{se}(t)$ during post-critical LCO at $U=7.8\text{m/s}$. As can be seen, the curve shapes of $L_{se}(t)$ and $M_{se}(t)$ are distorted from simple sinusoid. Fig.14 demonstrates the amplitude spectra of $L_{se}(t)$ and $M_{se}(t)$ at stable amplitude stage of post-critical LCO. Significant higher-order multiple-frequency peaks can be found. Both of the above phenomena indicate that the extracted $L_{se}(t)$ and $M_{se}(t)$ have strong aerodynamic nonlinearity.

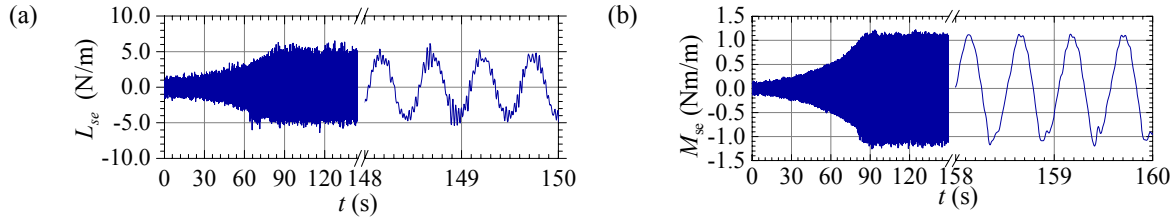


Figure 13: Time histories of Measured $L_{se}(t)$ and $M_{se}(t)$ at $U=7.8\text{m/s}$ ($U^*=U/f_i B=5.466$, attack angle 5°)

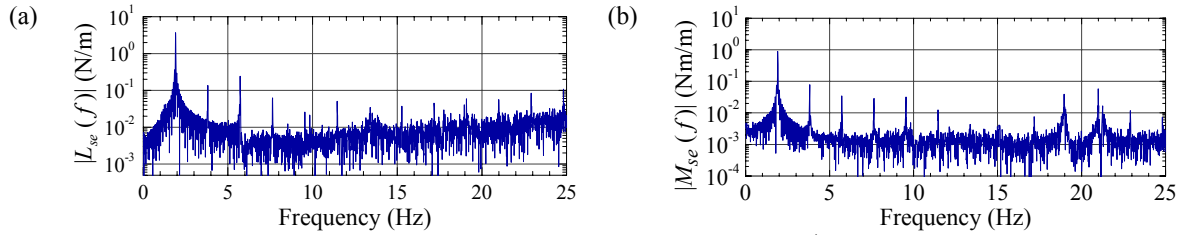


Figure 14: Spectra of measured $L_{se}(t)$ and $M_{se}(t)$ at $U=7.8\text{m/s}$ ($U^*=U/f_i B=5.466$, attack angle 5°)

4. VALIDATION OF MEASURED SELF-EXCITED FORCE

To verify the accuracy and reliability of the measured self-excited forces, the extracted time histories of $L_{se}(t)$ and $M_{se}(t)$ were directly applied to the governing equations of SSSM system, that is

$$(I + J_0)\ddot{\alpha} + \tilde{c}_\alpha(\rho_\alpha)\dot{\alpha} + \tilde{k}_\alpha(\rho_\alpha)\alpha = M_{se}(t) \quad (7)$$

$$(m + m_0)\ddot{h} + \tilde{c}_h(\rho_h)\dot{h} + \tilde{k}_h(\rho_h)h = L_{se}(t) \quad (8)$$

Where, $\tilde{c}_\alpha(\rho_\alpha) = 2(I + J_0)\omega_{\alpha 0}\tilde{\xi}_\alpha(\rho_\alpha)$ and $\tilde{c}_h(\rho_h) = 2(m + m_0)\omega_{h 0}\tilde{\xi}_h(\rho_h)$ are the nonlinear structural damping coefficients. $\tilde{k}_\alpha(\rho_\alpha) = (I + J_0)\tilde{\omega}_\alpha^2(\rho_\alpha)$ and $\tilde{k}_h(\rho_h) = (m + m_0)\tilde{\omega}_h^2(\rho_h)$ are the nonlinear structural stiffness coefficients. The superscript ‘ \sim ’ means the revision of the parameter values by considering frequency change of switch in the light of the corresponding fitted cured based on the tested data in still air. The instantaneous amplitude ρ_α and ρ_h are expressed as

$$\rho_\alpha = \sqrt{\alpha^2 + (\dot{\alpha} / \omega_{\alpha i})^2} \quad (9)$$

$$\rho_h = \sqrt{h^2 + (\dot{h} / \omega_{h i})^2} \quad (10)$$

The post-critical responses of the SSSM system were then calculated numerically by Newmark- β

method according to Eq.(7) ~ Eq.(10), and were compared with the relevant measured results. Fig.15 shows the time history comparisons between the calculated and measured results of the heaving and torsional displacement responses at $U=7.8\text{m/s}$ ($U^*=5.466$), while the RMS response comparisons between the calculated and tested results for different wind speeds in the tested post-critical region are plotted in Fig.16. Quite good agreements can then be found between the two sets of post-flutter responses with the discrepancies of RMS no more than 11%. Hence, the measurement accuracy and reliability of self-excited forces using the improved technique of interiorly-placed force balances are acceptable. The measured self-excited forces $L_{se}(t)$ and $M_{se}(t)$ can be further used to propose a feasible nonlinear self-excited force model, which suitable for large amplitudes of oscillation.

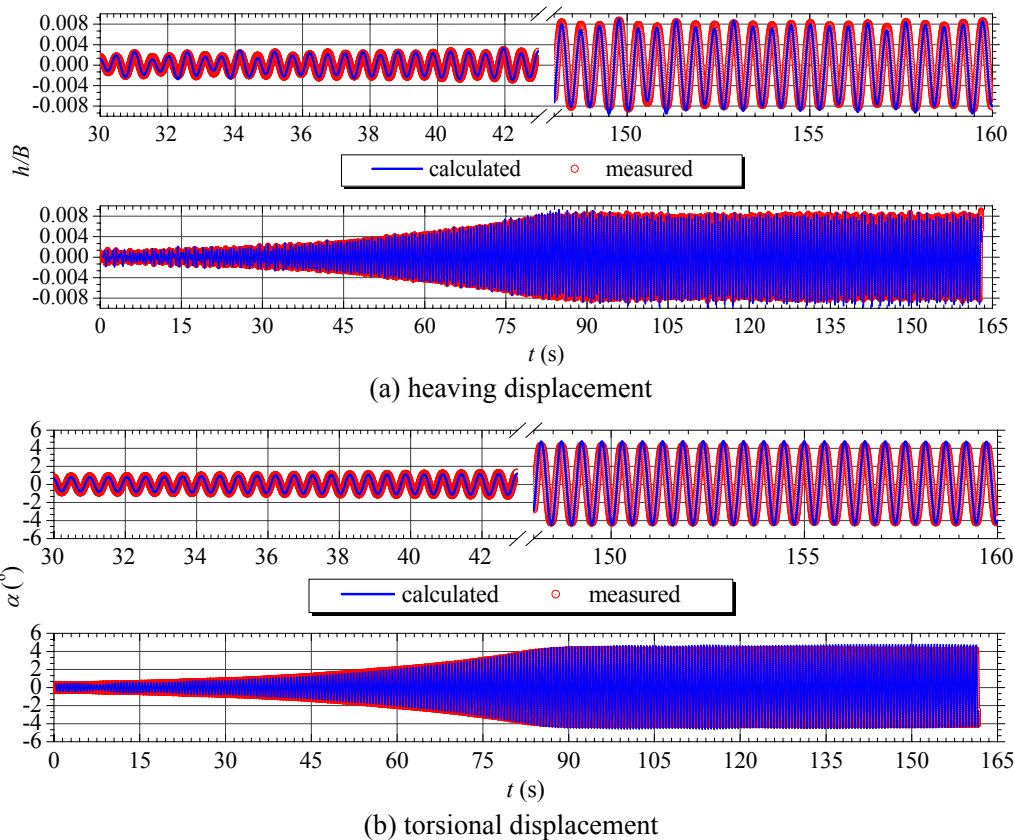


Figure 15: Comparison between calculated and measured time histories of post-critical LCO at $U=7.8\text{m/s}$ ($U^*=U/f_iB=5.466$)

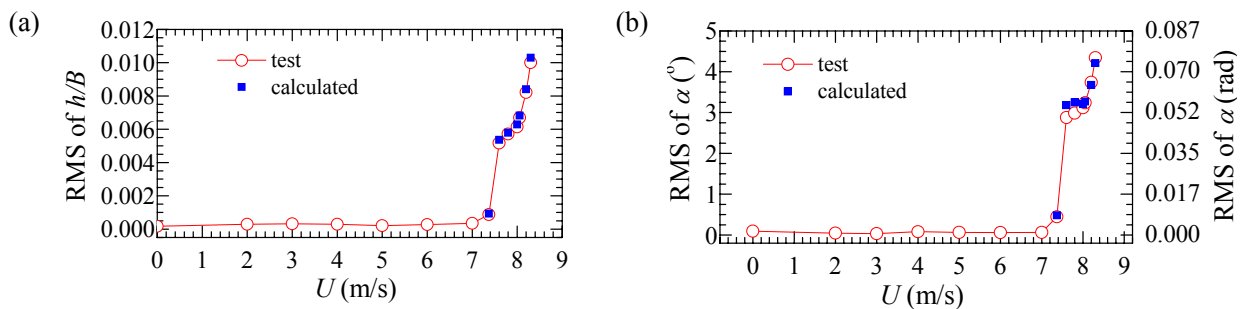


Figure 16: Comparison between calculated and measured RMS of post-flutter responses

5. CONCLUSIONS

The nonlinear behaviors of the post-critical soft flutter and aerelastic self-excited forces of a flat

closed-box deck were investigated through sectional model tests. An improved testing technique of internally-placed force balances was developed to measure the self-excited forces during post-flutter and was verified to have a good accuracy. The test results showed that the flat closed-box deck would undergo coupled-flutter LCOs in post-critical region, which were in the second mode corresponding to the torsional mode in the zero wind case and featured by significant heaving-torsion coupling effect. Both the measured self-excited lift force and torsional moment during post-critical LCO contain strong nonlinear components. The mathematical models of the nonlinear self-excited lift force and torsional moment need to be further investigated in the next step.

ACKNOWLEDGMENT

The work described in this paper was supported by the National Natural Science Foundation of China (Grant 51478360, 91215302 and 51323013). Any opinions and concluding remarks presented in this paper are entirely those of the writers.

REFERENCES

- 1) Scanlan, R.H. and Tomko, J.J. : Airfoil and bridge deck flutter derivatives, *Journal of Engineering Mechanics, ASCE*, Vol. 97, Pt. 6, pp. 1717-1737, 1971.
- 2) Xiang, H.F., Ge, Y.J., Zhu, L.D., Chen, A.R., Lin, Z.X., Gu, M., et al. : Modern theory and practice on bridge wind resistance, *Beijing: China Communication Press*, pp. 1-6, 2005.
- 3) Tobak, M. and Chapman, G.T. : Nonlinear problems in flight dynamics involving aerodynamic bifurcations, *Technical report*, NASA TM 86707, 1985.
- 4) Leishman, J.G. : Challenge in modeling the unsteady aerodynamics of wind turbines, *Wind Energ.*, Vol. 5, pp. 85-132, 2002.
- 5) Pigolotti, L., Mannini, C., Bartoli, G. and Thiele, K. : Wind tunnel tests on elongated rectangular plates under flutter motion: limit-cycle oscillations and preliminary energy harvesting considerations, *The 14th International Conference on Wind Engineering (ICWE14)*, Portal Alegre, 2015.
- 6) Noda, M., Utsunomiya, H., Nagao, F., Kanda, M. and Shiraishi, N. : Effects of oscillation amplitude on aerodynamic derivatives, *J. Wind Eng. Ind. Aerodyn.*, Vol. 91, pp.101-111, 2003.
- 7) Diana, G., Resta, F. and Rocchi, D. : A new numerical approach to reproduce bridge aerodynamic non-linearities in time domain, *J. Wind Eng. Ind. Aerodyn.*, Vol. 96, pp. 1871-1884, 2008.
- 8) Liao, H.L., Wang, Q., Li, M.S. and Ma, C.M. : Aerodynamic hysteresis effects of thin airfoil and streamline box girder under large amplitude oscillation, *Proceedings of the 13th International Conference on Wind Engineering*, Amsterdam, The Netherlands, July 10-15, 2011.
- 9) Amandolese, X., Michelin, S. and Choquel, M. : Low speed flutter and limit cycle oscillations of a two-degree-of-freedom flat plate in a wind tunnel, *J. Fluid Stru.*, Vol. 31, pp. 244-255, 2013.
- 10) Náprstek, J., Pospíšil, S. and Hračov, S.: Analytical and experimental modeling of non-linear aeroelastic effects on prismatic bodies. *J. Wind Eng. Ind. Aerodyn.*, Vol. 95, pp. 1315-1328, 2007.
- 11) Wu, T. and Kareem, A. : A nonlinear convolution scheme to simulate bridge aerodynamics, *Computers and Structures*, Vol. 128, pp. 259-271, 2013.
- 12) Liu, S.Y. and Ge, Y. J. : Fitting method of nonlinear differential equations for aerodynamic forces of bridge decks, *Proceedings of the 12th Americas Conference on Wind Engineering*, Seattle, 2013.
- 13) Zhu, L.D., Meng, X.L. and Guo, Z.S. : Nonlinear mathematical model of vortex-induced vertical force on a flat closed-box bridge deck, *J. Wind Eng. Ind. Aerodyn.*, Vol. 122, pp. 69-82, 2013.
- 14) Gao, G.Z., Zhu, L.D. and Ding, Q.S. : Identification of nonlinear damping and stiffness of spring-suspended sectional model, *Proceedings of the Eighth Asia-Pacific Conference on Wind Engineering*, Chennai, India, pp. 127-130, 2013.
- 15) Gao, G. Z. and Zhu, L.D. : Nonlinearity of mechanical damping and stiffness of a spring-suspended sectional model system for wind tunnel tests. *Journal of Sound and Vibration*, Vol. 355, pp. 369-391, 2015.

MULTI-SCALE EXPERIMENTAL COMPARISONS OF AERODYNAMIC VIBRATIONS OF A SUSPENSION BRIDGE

Haotian DONG⁺¹, Yaojun GE⁺² and Yongxin YANG⁺³
SLDRCE, Tongji University, Shanghai 200092, China

Multi-scale wind tunnel model tests are based on a suspension bridge crossing a sea strait in China. Currently, the scale effect of aerodynamic vibrations like flutter and vortex-induced vibration (VIV) in model test of long span bridges is generally regarded as a combination of Reynolds number effect and manufacturing accuracy. In this paper, the scale effect of flutter and VIV are carefully studied by comparisons of two sectional model tests with different scale ratios and a full-bridge aeroelastic model test. The results of flutter tests shows that, a) the difference of critical flutter wind speed between Test B and Test C is below 5%; b) the vibration mode of Test C is the first-order torsional vibration of middle span girder, which is the same as Test B predicts; c) the difference between frequencies of flutter vibration of Test B and Test C is within 5%. In general, scale effect in flutter tests is not remarkable and sectional model test has enough accuracy in the prediction of flutter. On the other hand, different VIV characteristics are witnessed in three tests. In Test A and test B, first-order torsional VIV are witnessed. Comparing Test A with Test B, Reynold number effect in VIV presents as the advancing and shortening of “lock-in” wind speed domain and decreasing of VIV amplitude with scale ratio and Reynolds number. In test C, however, coupling VIV is observed at higher lock-in wind speed.

Keyword: Flutter; VIV; Sectional Model Testing; Aeroelastic Model Testing; Suspension Bridge.

1. INTRODUCTION

Sectional model wind tunnel test and full-bridge aeroelastic model test are two important methods to study torsional flutter, vortex-induced vibration (VIV), aerostatic instability and buffeting of long span bridges. In sectional model experiments, models with relatively large scale ratios are probable, which can provide better details of section shape and reduce Reynolds number effect due to scaling. In aeroelastic model tests, however, more vibration modes, especially higher-order modes of girder and coupling modes introducing cables and towers in, are simulated.

Scale effect exist not only between sectional models of various scale ratio, but also between sectional model tests and aeroelastic tests. Reynolds number and difference between simulated vibration modes are two main subjects of scale effect. Xian¹⁾ compared VIV tests of 1:50 and 1:20 sectional models for flat box girder. Scale effect between sectional model testing and aeroelastic model testing, however, has not been greatly studied, especially for VIV, since VIV is difficult to reproduce in full-bridge testing. In this study, scale effect in flutter and VIV of suspension bridge is carefully studied by comparison of three groups of wind tunnel model tests with different scale factors.

2. WIND TUNNEL MODEL TESTS

Multi-scale wind tunnel model tests are based on a suspension bridge crossing a sea strait in southeast

⁺¹90donghaotian@tongji.edu.cn, ⁺²yaojunge@tongji.edu.cn

China, whose mid-span length was 926 meters (Fig 1). The bridge has a flat closed steel box girder with 30m in width and 3m in depth (Fig.2). Since the height from the sea level to bridge deck at mid-span is 66.7m, the designing wind speed reaches as high as $U_d = 55.9m/s$.

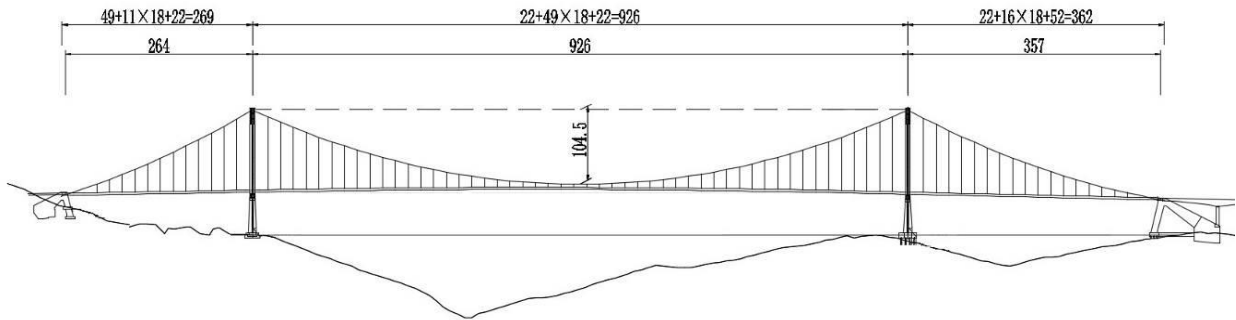


Figure 1: Span arrangement of the suspension bridge (m).

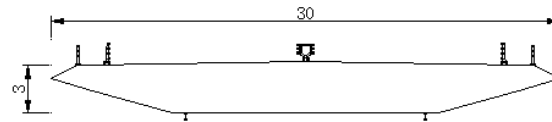


Figure 2: Cross section of closed steel box girder (m).

Three groups of wind tunnel model tests of different scale ratios are conducted in wind tunnels of State Key Laboratory of Disaster Reduction in Civil Engineering, Tongji University. All tests are performed with blockage ratio $h/H < 5\%$ and turbulent density $I < 1\%$ at deck level.

(1) Test A: VIV test of a sectional model with scale ratio $\lambda=1:20$.



Figure 3: Sectional model for Test A.

Sectional model for Test A is illustrated as Fig.3. The VIV test was conducted in TJ-3 atmosphere boundary layer wind tunnel. The tunnel has a height of 2m, a width of 15m and a length of 14m. The adjustable wind speed in wind tunnel is from 1.0m/s to 17.6m/s. Length of sectional model is 3.6m, 2.4 times of model width. Vertical and torsional displacements are measured by laser sensors, corresponding to first order vertical bending and torsional vibration modes of the suspension bridge.

(2) Test B: flutter and VIV tests of a sectional model where $\lambda=1:60$

Fig.3 shows the 1:60 sectional model used in Test B. Tests for flutter and VIV test were performed in

TJ-2 atmosphere boundary layer wind tunnel. The tunnel has a height of 2.5m, a width of 3m and a length of 15m. The adjustable wind speed in wind tunnel is from 1.0m/s to 68m/s. Length of sectional model is 1.74m, 3.48 times of model width. Vertical and torsional displacements are measured by laser sensors, too, with different frequency scale ratio.



Figure 4: Sectional model for Test B.

(3) Test C: flutter and VIV tests of a full-bridge aeroelastic model where $\lambda=1:122.4$

The aeroelastic model is illustrated as Fig. 5. To be mentioned, attack angles are simulated by a slope on the ground (Fig. 5.b, 5.c). Three dimensional wind speed near the upwind edge of girder is carefully measured, making sure that attack angle is +3 or -3 degree. The tests were conducted in TJ-3 atmosphere boundary layer wind tunnel. The aeroelastic model is 12.7m in length (distance between cable anchors) and 1.42m in height (towers). Vertical, torsional and lateral displacements are measured by laser sensors at $\frac{1}{2}$, $\frac{1}{4}$ and $\frac{3}{4}$ of middle span girder, $\frac{1}{2}$ of side span girders and top of towers. Alongwind displacement is measured by laser sensors at $\frac{1}{2}$ and $\frac{1}{4}$ of middle span cables.



a) Attack angle: 0 degree.



b) Attack angle: +3 degree.



c) Attack angle: -3 degree.

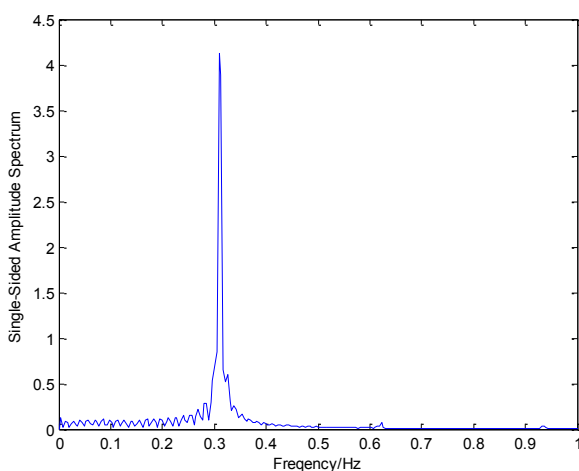
Figure 5: Aeroelastic model for Test C.

3. FLUTTER

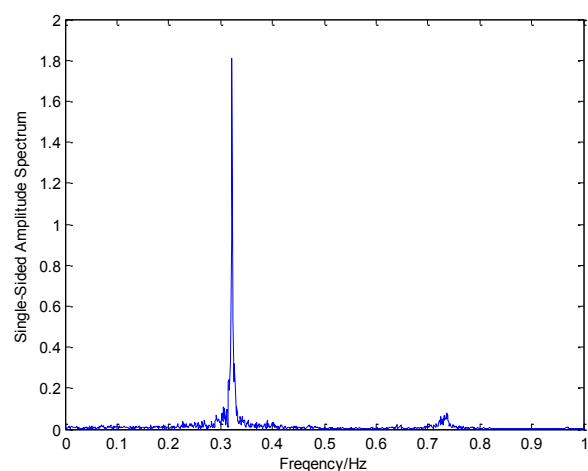
In Test B, bending and torsional damping ratios are measured to identify the occurrence of flutter. By adding an external excitation, we identify damping ratios from historical displacement curve of free vibration. To be mentioned, since the sectional model testing system only simulates first order bending frequency and first order torsional frequency of main girder, higher order modes are neglected. First order torsional flutter is witnessed in Test B. Critical flutter wind speed was found as $U_{cr} = 90\text{m/s}$ at $\alpha = +3^\circ$, $U_{cr} = 95\text{m/s}$ at $\alpha = 0^\circ$ and $U_{cr} = 100\text{m/s}$ at $\alpha = -3^\circ$. Reynolds number is about $Re = 64,000$ in flutter test of 1:60 sectional model.

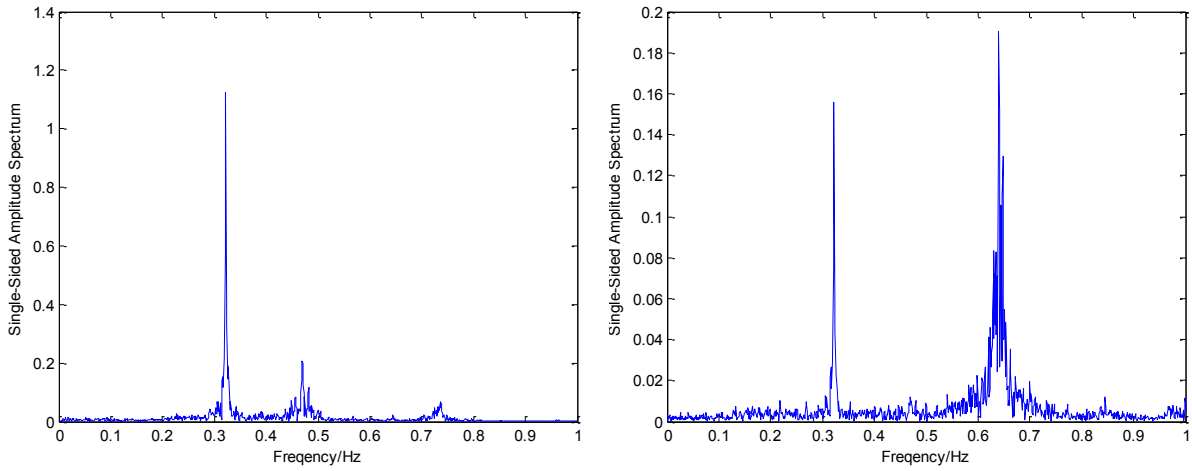
In Test C, however, no external excitation is applied and flutter phenomenon is observed by critical change in displacement historical curve. First order torsional flutter of girder is observed in Test C. Critical flutter wind speed was found as $U_{cr} = 92\text{m/s}$ at $\alpha = +3^\circ$, $U_{cr} = 91\text{m/s}$ at $\alpha = 0^\circ$ and $U_{cr} = 96\text{m/s}$ at $\alpha = -3^\circ$. Reynolds number is about $Re = 14,000$ in flutter test of aeroelastic model.

Fig. 6 illustrates single-sided amplitude spectrum curves of Test B and $\frac{1}{2}$ midspan, $\frac{1}{4}$ midspan and $\frac{1}{2}$ side span of Test C. Obviously, in sectional model test, the flutter has a single frequency (Fig. 6.a). In aeroelastic model test, midspan torsional displacement reproduces the two-degree-of-freedom sectional model test well, with only very little energy of higher mode vibration around 0.67Hz (Fig. 6.b1). However, higher vibration modes become noticeable at $\frac{1}{4}$ of midspan (Fig. 6.b2) and is dominate at side span (Fig. 6.b3). In general, the flutter phenomenon of suspension bridge has multi-modes feature. Sectional model test can only simulate flutter action at middle of midspan.



a) Test B.

b1) Test C at $\frac{1}{2}$ of midspan.



b2) Test C at 1/4 of midspan.

b3) Test C at 1/2 of side span.

Figure 6: Single-side amplitude spectrum of torsional displacement of Test B and Test C.

Comparing flutter test results of Test B and Test C, we can see the difference of U_{cr} between Test B and Test C is below 5%. The vibration mode of Test C is the first-order torsional vibration of middle span girder, which is the same as Test B predicts, and the difference between frequencies of flutter vibration of Test B and Test C is within 5%. Reynolds number is about $Re = 64,000$ in Test B, $Re = 14,000$ in Test C and $Re = 2 \times 10^7$ in real bridge, with Re defined by girder height and U_{cr} . We may conclude that Reynolds number effect and manufacturing error effect on flutter is small between models with different λ and between sectional and aeroelastic models, and error due to missing of vibration mode is not significant since higher order frequency component in flutter is small, especially for torsional displacement at middle of midspan. In general, scale effect in flutter tests is not remarkable and sectional model test has enough accuracy in the prediction of flutter.

4. VIV

Comparison of basic parameters of VIV tests is listed in Tab. 1. To be mentioned, since model test with larger scale ratio could have better details of cross section shape and reduce natural damp ratios, for example, damp ratios in Test A is smaller than in Test B and Test C, usually VIV is easier to reproduce in sectional model tests with large scale ratio.

Table 1: Comparison of basic parameters of VIV tests.

Model	Test A	Test B	Test C
Scale factor λ	1:20	1:60	1:122.4
Wind speed scale ratio λ_v	1:1.5	1:3	1:11.06
Natural bending damp ratio ζ_b	0.2-0.29%	0.3%	0.5%
Natural torsional damp ratio ζ_t	0.1-0.2%	0.3%	0.5%
Attack angles	$-3^\circ, 0^\circ, +3^\circ$	$-3^\circ, 0^\circ, +3^\circ$	$-3^\circ, 0^\circ, +3^\circ$
Wind speed zone (real)	1.9m/s ~ 18.2m/s	3m/s ~ 57m/s	10m/s ~ 60m/s

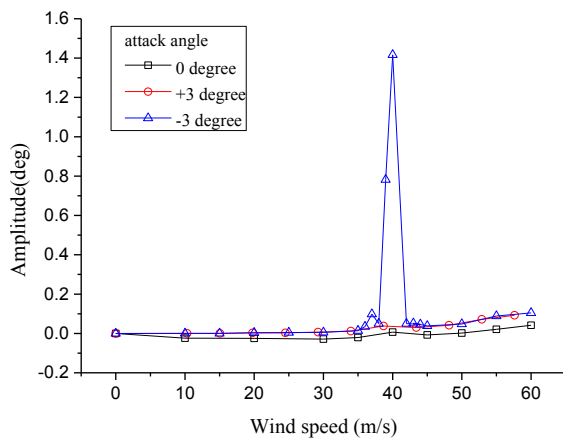
Comparison of VIV test results are listed in Tab. 2. Different VIV characteristics are witnessed with respect to different lock-in wind speed, vibration amplitude and vibration modes. To be mentioned, for sectional model tests, Eq. (1) is applied to transfer model amplitude to real amplitude²⁾³⁾.

$$y_{full} = \frac{4}{\pi} \frac{y_{sectional}}{\lambda_L}; \quad \alpha_{full} = \frac{4}{\pi} \alpha_{sectional} \tag{1}$$

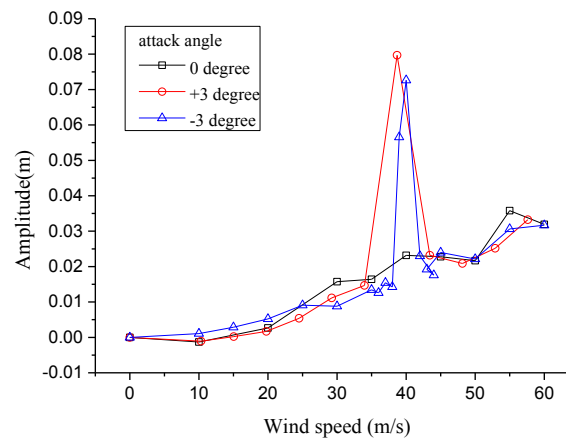
Where $y_{sectional}$ and $\alpha_{sectional}$ are model vertical and torsional amplitude in sectional model tests, y_{full} and α_{full} correspond to amplitude in real bridge. In test A, first-order vertical bending VIV occurs at wind speed $U = 2.2$ to 2.5 m/s, $\alpha = -3^\circ$ and $Re = 16,000$; first-order torsional VIV happens at $U = 9.0$ to 10.5 m/s, $\alpha = -3^\circ$ and $Re = 65,000$. In test B, first-order torsional VIV happens at $U = 9.9$ to 12.3 m/s, $\alpha = -3^\circ$ and $U = 10.5$ to 11.1 m/s, $\alpha = +3^\circ$, with $Re = 12,000$. In Test C, however, VIV with higher-order coupling mode is found at higher wind speed, namely $U = 39$ to 41 m/s, $\alpha = -3^\circ$ and $Re = 6,000$.

Table 2: Comparison of VIV test results.

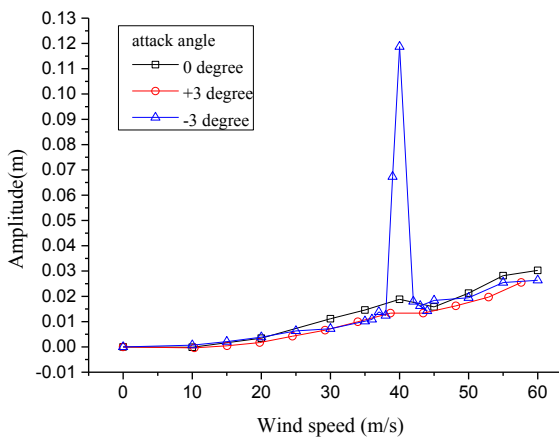
Vibration mode	Test	Attack angle	Lock-in wind speed (m/s)	Amplitude	Re_c
Torsional	B	-3°	9.9 ~ 12.3	0.352°	12,000
		$+3^\circ$	10.5 ~ 11.1	0.136°	12,000
	A	-3°	8.95 ~ 10.46	0.179°	65,000
	C	-3°	39 ~ 41	1.417°	6,000
Vertical bending	A	-3°	2.17 ~ 2.54	0.057m	16,000



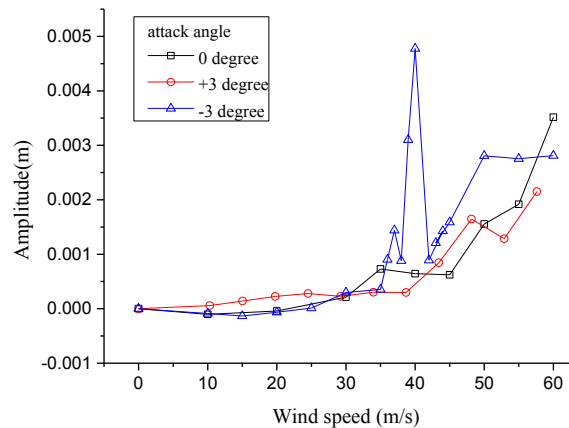
a) Torsional vibration of 1/2 midspan girder.



b) Alongwind vibration of cable at 1/2 midspan.



c) Alongwind vibration at top of tower.



d) Crosswind vibration at top of tower.

Figure 7: Variation of vibration amplitude with wind speed of Test C.

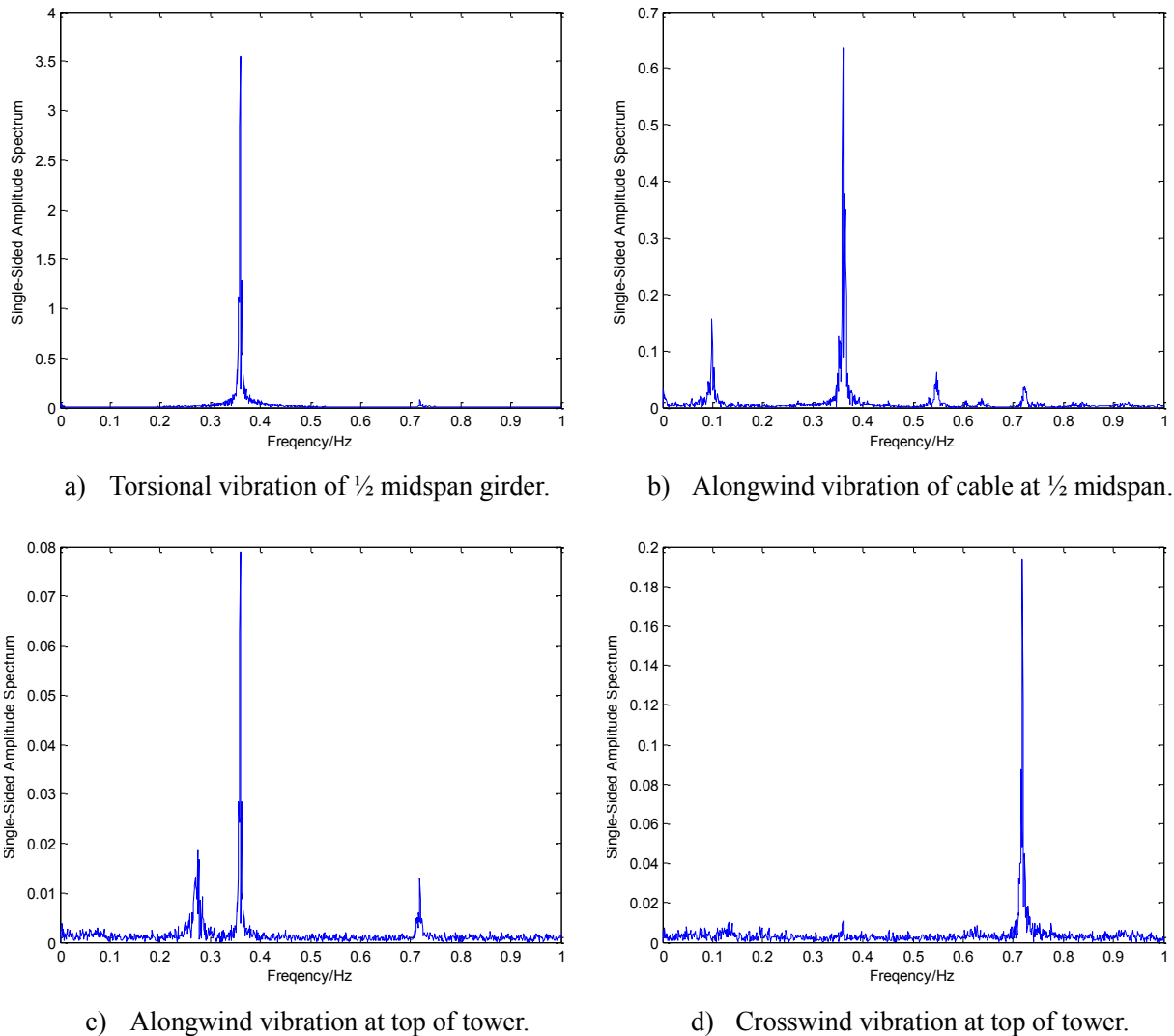


Figure 8: Single-side amplitude spectrum of VIV displacement of Test C at $U = 40\text{m/s}$ and $\alpha = -3^\circ$.

Fig. 7 and Fig. 8 present the variation of vibration amplitude with wind speed of Test C and single-side amplitude spectrum of VIV displacement of Test C at $U = 40\text{m/s}$ and $\alpha = -3^\circ$. The coupling VIV in Test C combines four components: 1) torsional vibration of girder; 2) alongwind (direction of incoming wind) second order bending vibration of towers; 3) stream wise vibration of the two cables in direction of incoming wind; 4) crosswind (direction along axis of girder) first-order bending vibration of towers. The coupling VIV can be regarded as a resonance phenomenon due to closed torsional vibration frequency of girder (which would reduce as wind speed grows), natural frequency of cables and half of natural alongwind bending frequency of tower. The mechanism of coupling VIV can be explained as follows. Firstly, VIV mode of alongwind second order bending of towers happens at $U=35$ to 45m/s , as is proved by full-bridge test with all girders dismantled. Then, since the natural frequency of alongwind bending of towers happens to be two times that of windwise vibration of cables, resonance of towers and cables happens, which is also witnessed in the test without girders. Finally, as wind speed arise from zero, the natural frequency of first order torsional vibration of girder would

decrease because of arising aerodynamic stiffness. The original natural torsional frequency of girders was about 107.5% that of cables and as wind speed reaches around $U=39$ to 40m/s , this difference vanishes. As a result, full-bridge resonance happens.

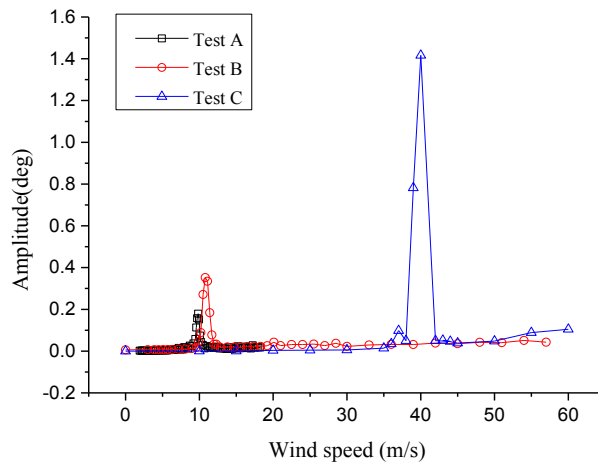


Figure 9: Comparison of torsional VIV amplitude changing with wind speed at $\alpha = -3^\circ$.

Fig. 9 illustrates the comparison of torsional VIV amplitude changing with wind speed at attack angle $\alpha = -3^\circ$. From Tab. 2 and Fig. 9 we can see that, compared with Test A and Test B, in aeroelastic model test coupling VIV happens at a different lock-in wind speed zone with significantly larger amplitude. On the other hand, compared Test A with Test B, we may find that sectional model test with larger scale ratio will have small amplitude and earlier and shorter lock-in zone. Also, vertical bending mode is witnessed in Test A, which is difficult to reproduce in Test B because of smaller wind speed ratio. In general, scale effect in VIV consists of Reynolds number effect and missing of higher vibration modes. Firstly, as λ and Re increase, Reynolds number effect in VIV presents as the advancing and shortening of “lock-in” wind speed zone and decreasing of vibration amplitude, which agree with Xian’s¹⁾ study. Secondly, missing of higher vibration modes indicate us that traditional two-degree-of-freedom sectional model tests may not be sufficient enough for VIV study. Sectional model tests which simulate more natural frequencies or a aeroelastic model test is recommended in VIV study of long-span suspension bridge.

5. CONCLUSION

This paper compares the flutter and VIV characteristics of sectional model testing of a suspension bridge with different scale ratios and between sectional model testing and aeroelastic model testing. In comparison of flutter testing, scale effect is not remarkable. Higher modes plays small role in flutter at middle of main span, but is noticeable at other components of the bridge, for example, side span. On the other hand, scale effect in VIV testing can not be ignored since differences in lock-in wind speed, vibration amplitude and vibration mode are witnessed between the tests. In general, this paper suggest that for flutter prediction, sectional model testing is accurate enough, but in study of VIV, traditional two-degree-of-freedom sectional model tests may not be sufficient enough.

ACKNOWLEDGMENT

This research was funded by the National Nature Science Foundation of China with the grant of 91215302 and Ministry of Science and Technology with the 973 Program of 2013CB036300.

REFERENCES

- 1) XIAN R, LIAO H. Wind Tunnel Test for Vortex-Induced Vibration of Different Geometry Scale Sectional Models of Flat Box Girder [J][J]. Bridge Construction, 2010, 2: 004.
- 2) Zhengqing Z Z C. Similarity of amplitude of sectional model to that of full bridge in the case of vortex-induced resonance [J][J]. China Civil Engineering Journal, 2011, 7: 013.
- 3) Le-Dong Z. MASS SIMULATION AND AMPLITUDE CONVERSION OF BRIDGE SECTIONAL MODEL TEST FOR VORTEX-EXCITED RESONANCE [J][J]. Engineering Mechanics, 2005, 5: 036.

Experimental Flutter Suppression of a Long-Span Suspension Bridge Section

Kevin Gouder⁺¹, Xiaowei Zhao⁺², David Limebeer⁺³ and J. Michael R. Graham⁺⁴
^{+1, +4} Imperial College, London, United Kingdom
⁺² University of Warwick, Warwick, United Kingdom
⁺³ University of Oxford, Oxford, United Kingdom

The suppression or delay of flutter in long-span suspension bridges is investigated experimentally. Since the torsional stiffness of a bridge deck decreases with increasing length, an active flap flutter suppression system could potentially enable the construction of longer spans without costly increases in deck width and depth. An active flap flutter suppression system could be deployed as a temporary measure during construction when the deck, not yet tied down at one or both ends, is particularly vulnerable to flutter instability. In the current experiment, a rigid sectional model of a long-span suspension bridge is mounted on a suspension system in a wind tunnel. Moving flaps attached to the bridge section's leading and trailing edges are controlled in real-time in response to the bridge section's heave and pitch motions. Other modes of bridge section motion, such as sway, were suppressed through the use of drag wires. Experimental assessment of the deck's aerodynamic derivatives and their similarity to those of a flat plate justified the aerodynamic force modeling using a theoretical model based on Theodorsen's theory; the flap control system is designed through an \mathcal{H}_∞ optimisation. The control system design was constrained to low-order passive controllers that could be effectively replaced by reliable, passive (no external energy input) mechanical networks that drive the flaps through the bridge deck motion. The flutter-suppression effectiveness of various controllers with one or both actuated flaps, and different feedback quantities including one, or a combination of the bridge section's pitch angle and heave positions or velocities, was tested. Flutter velocity increases in excess of 20% were attained with very good robustness margins.

Keyword: flutter, wind-tunnel, long-span suspension bridge, robust control, flaps.

1. INTRODUCTION

Low structural damping¹⁾ and structural flexibility²⁾ of cable-supported bridges makes them sensitive to wind-induced influences, where oscillatory or even divergent unstable modes may exist. Torsional flutter oscillation³⁾ caused by a sign reversal in the aerodynamic derivative A_2^* related to torsional damping caused the Tacoma Narrows Bridge collapse when oscillations in the first asymmetric torsion mode grew over a period of about 45 minutes. Since this collapse, advances in deck design have prevented similar incidents but the flutter problem is still a formidable challenge owing to the need to construct longer spans with a resulting lower critical, flutter wind velocity. Deck stiffening, particularly in torsion, with the inevitable increases in cost and weight, is the traditional flutter delay effort. Adding a solid or porous spanwise beam along the deck centre-line, creating a gap between the carriageways, leading and trailing edges cross section modifications⁴⁾, the addition of fairings and turning vanes around the leading and trailing deck edges⁵⁾ have been proven beneficial in flutter delay. Such efforts have a limited capability in raising the flutter velocity and therefore research into active flow control has also been carried out. One active control method is based on controllable moving surfaces that respond to bridge deck motion. Flap control for aeroelastic load alleviation – flutter and buffet suppression – has already been successfully used in the aeronautics industry, where flap motions respond to suppress main wing motions^{6)–11)}. In a long-span bridge deck setting, the concept has also been investigated for the suppression of flutter and buffet loads. A number of patents have been granted for systems

⁺¹kevin.gouder04@imperial.ac.uk, ⁺²xiaowei.zhao@warwick.ac.uk, ⁺³david.limebeer@eng.ox.ac.uk, ⁺⁴m.graham@imperial.ac.uk

that delay deck flutter using active flaps^{12), 13)}. The scheme has also been the subject of research reported in the literature^{14 – 22, 26, 27)}. The problem was theoretically investigated for cable-suspended bridges with flaps on both sides of the deck^{16)–20)}.

Using unsteady thin aerofoil derivations by Theodorsen²³⁾, where the deck is treated as a 2D thin section on an elastic suspension, classical 2-DOF (heave and pitch) flutter is reasonably well modelled and good predictions of the flutter velocity can be obtained. When this analysis is applied to more realistic, thicker, bluffer cross-sections, the method could be supplemented with *measured* section aerodynamic derivatives within the reduced frequency range of interest. Strip theory is often utilised to extend the 2D section results to 3D deck modal response²⁴⁾. The analysis of a wing-aileron-tab system²⁵⁾ was transformed and utilised for the aeroelastic control of a bridge deck with leading and trailing edge flaps, using an approximation for the leading edge flap¹⁶⁾, and exactly²⁶⁾, where an increase in flutter velocity was shown to be feasible. A number of experimental implementations have also been reported. One variation of twin control surface implementation was tested¹⁴⁾ where aerofoil flaps were suspended below a model deck, with the rather poor assumption²⁶⁾ that the deck and control surfaces in practical close proximity are aerodynamically independent of each other. An adoption of the same assumption, where a deck-mounted pendulum was the prime mover of the flap control system, led to good agreements with theoretical results, although only for small flap angles²⁷⁾. Coupled deck-flap aerodynamics, albeit with an approximation for the leading-edge flap, were utilised in another experiment¹⁶⁾, where measured control flap-induced aerodynamic damping performance was reported and compared to Theodorsen theory predictions.

This paper is an extension of an earlier study²¹⁾ where flutter delay of a section of a long-span suspension bridge is experimentally and numerically investigated utilising Theodorsen theory (aerofoil with flap and tab transformed to represent a deck with leading and trailing edge flaps) and \mathcal{H}_∞ optimisation. A 1:50 scale model of a representative bridge deck had controllable leading and trailing full-span flaps installed and was mounted on a suspension system with heave and pitch degrees of freedom. Although the flaps used in these experiments were along the whole span of the sectional model, it is envisaged that in a practical full-scale application, a number of part-span flaps would be installed straddling the bending and torsion flutter modes' antinodes. Wind tunnel tests were carried out in low-turbulence levels although the control system robustness was further assessed when grid-generated turbulence provided supplementary random perturbations²¹⁾. The tested flap controllers were limited to low order passive networks where passivity implies that springs, dampers and inerters could in principle be utilised to construct the control system. In [21], a number of controllers based on deck position feedback (heave, pitch, or a combination of the two to the leading edge, trailing edge or both flaps) were reported. The objective of this paper is to report about the performance of a number of other controller configurations, including one based on position feedback of the trailing edge flap hinge point and others based on the deck heave and/or pitch velocity, and compare their performance with the theoretical predictions.

Active control surface flutter delay could be one technology enabling the construction of longer deck spans. It also has the potential to be deployed as a temporary measure during bridge construction when both ends of the deck are still unconnected and the flutter velocity of either end is well below the design value for the completed superstructure. The rest of this paper is organised as follows. In Section 2 a summary of the theoretical model is presented, followed by a description and design of the control systems. A summary of the experimental setup is presented in Section 3 and results from a number of controller configurations presented in Section 4 and discussed shortly in Section 5.

2. THEORETICAL MODEL AND CONTROL SYSTEM DESIGN

In this section, the theoretical structural and aerodynamic models used in the analysis and design of the control systems are briefly described. Figure 1 shows the kinematic model of the bridge deck with flaps.

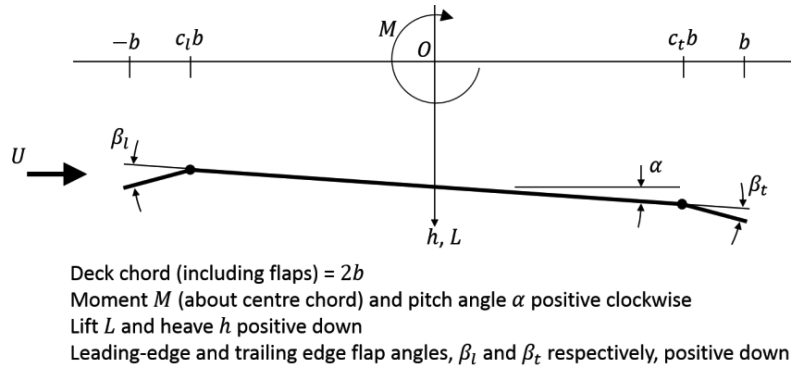


Figure 1: The kinematic model of the bridge deck with leading and trailing edge flaps.

Referring to Figure 1, the equations of motion for the two degrees of freedom, heave and pitch, of the deck model are:

$$M_h(\ddot{h} + 2\zeta_h\omega_h\dot{h} + \omega_h^2h) = L \quad \text{and} \quad J_\alpha(\ddot{\alpha} + 2\zeta_\alpha\omega_\alpha\dot{\alpha} + \omega_\alpha^2\alpha) = M \quad (1)$$

where M_h is the deck mass and J_α is the deck moment of inertia about the mid-chord axis, both quantities defined per unit span of deck
 L is Lift force and M is Moment about the mid-chord axis
 ω_h, ζ_h and $\omega_\alpha, \zeta_\alpha$ are the undamped natural frequency and damping ratio, respectively for heave (h) and pitch (α).

The aerodynamic model derived and used in this work was based on the wing-flap-tab system reported in (25). The Lift L and Moment M in equation (1) are a function of wind speed, heave, pitch and flap angles and their derivatives,

$$L = \rho b^3 \omega^2 \left(L_h \frac{h}{b} + L_\alpha \alpha + L_{\beta_t} \beta_t + L_{\beta_l} \beta_l \right) \quad \text{and} \quad M = \rho b^4 \omega^2 \left(M_h \frac{h}{b} + M_\alpha \alpha + M_{\beta_t} \beta_t + M_{\beta_l} \beta_l \right). \quad (2)$$

The quantities L and M with subscripts within the brackets in equation (2) are aerodynamic derivatives, all a function of the Theodorsen function $C(k)$. Further details on the wing-flap-tab transformation into a deck with leading and trailing edge flaps can be found in reference [26].

Table 1: Details about controllers tested indicating which flaps were used, the corresponding feedback and the controller transfer function. The abbreviations LE and TE refer to the leading- and trailing-edge flaps; $\alpha, \dot{\alpha}, h, \dot{h}$ refer to pitch position, pitch velocity, heave position and heave velocity feedbacks respectively.

Type	#	Flap (s) : Feedback	Transfer function
Position Feedback	1	TE : $h + 0.407\alpha$	$\frac{-59.9059s}{s^2 + 14.8262s + 147.9288}$
Mechanical Controller (velocity feedbacks)	2	LE : $\dot{h} - 0.407\dot{\alpha}$	$\frac{305.4957s}{107.9075s^2 + 1072.55s + 24629.33}$
	3	TE : $\dot{h} + 0.407\dot{\alpha}$	$\frac{150.286s}{65.475s^2 + 1238.746s + 29060.9333}$
	4	LE : $\dot{h} - 0.407\dot{\alpha}$ TE : $\dot{h} + 0.407\dot{\alpha}$	$\frac{392.455s}{66.7287s^2 + 2137.2609s + 42636.1042}$ to both flaps.

Based on the root locus analysis, it was established that the theoretical critical flutter speed was 20 m/s (see Figure 6 of reference [21]). The control aim was to improve the critical flutter speed to 24 m/s, therefore to a wind speed lower than the predicted divergence speed. \mathcal{H}_∞ theory was used to design the flutter controller; see Figure 5 of reference [21] for the control system configuration. The details about the control design can be found in reference [21]. The designed controllers are summarised in Table 1 including which flap is active, what feedback its controller receives and the controller's transfer function. Controller 1 receives deck position feedback while controllers 2 to 4 receive velocity feedback. The constant 0.407 in the feedback expressions refers to the position, in metres, of the hinge point relative to the centre-chord origin. All controllers are low order passive networks as described earlier, although controllers 2 to 4 are explicitly designed using passive mechanical components. The root locus of the closed-loop systems with these controllers are shown in Figure 2, showing that the heave, pitch, and torsional divergence modes are all well damped up to 24 m/s, i.e. 20% improvement in theory. It was expected that similar flutter alleviation improvements were possible in the wind tunnel experiments using these controllers.

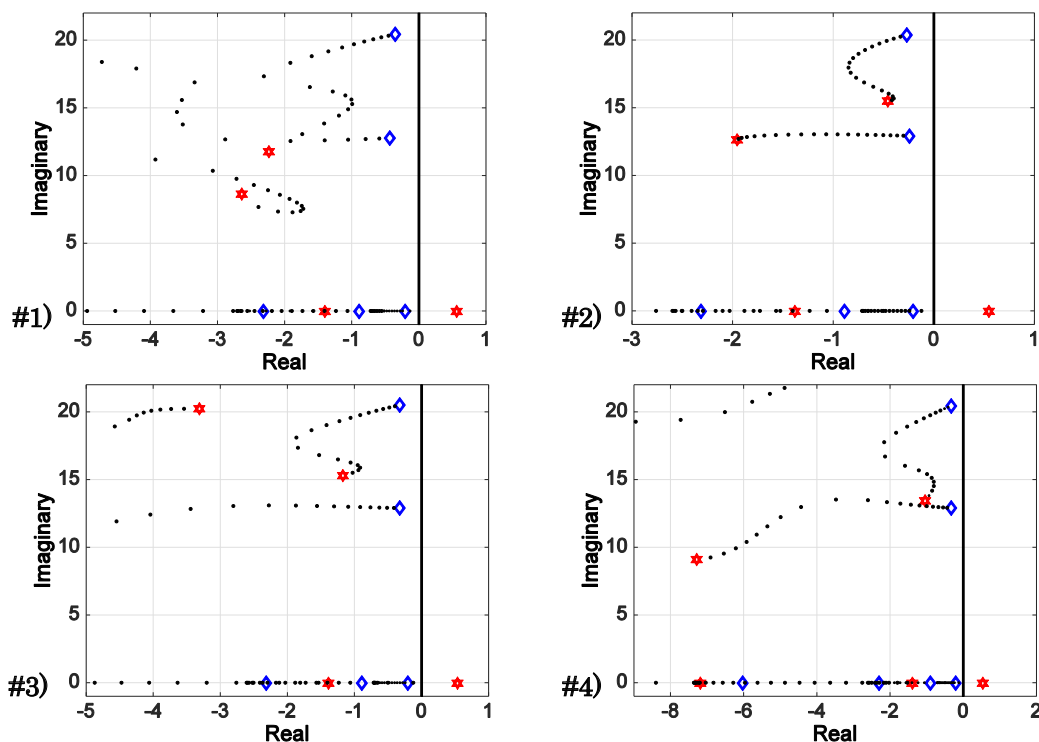


Figure 2: Root loci of the controllers shown in Table 1. The wind speed is swept from 5 to 25 m/s, with the low-speed end of the root loci marked with blue diamonds and the high-speed ends marked with red hexagons.

3. EXPERIMENTAL SETUP

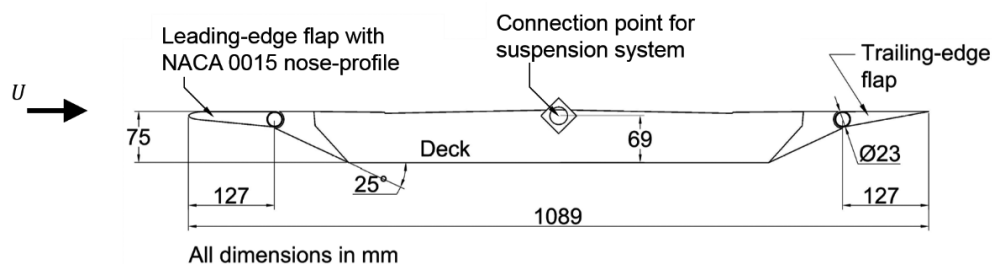


Figure 3: A schematic of the cross-section of the bridge deck model. The model is a 1:50 scale reconstruction of a prototype previously tested at BMT Fluid Mechanics.

The bridge deck utilised in these experiments is a rigid structure made from carbon-fibre-reinforced composite material with chord 0.82 m, span of 2.74 m and a depth of 0.075 m. The original deck's leading- and trailing-edges were faired using low-density styrofoam so that the cross-section was made identical to a proposed long-span crossing design previously tested at BMT Fluid Mechanics. Flap-type control surfaces were installed along the whole span at the deck leading- and trailing-edges. Each flap had a chord of 12% of the total deck chord, which, including fairings and both flaps, had a total chord of 1.09 m. The flaps initially had a triangular cross section and although flow separation observed occurring at the sharp leading edge of the upstream flap was potentially causing additional buffet loading, this did not appear to be reducing control performance. However, for all experiments reported here, the leading-edge of the upstream flap was slightly rounded following a NACA0015 profile, (3 mm nose curvature), in order to inhibit separation there and improve the accuracy of linear theory (where the deck and control surfaces are treated as aerodynamically thin) in predicting deck response. The trailing edge flap was however not modified since a rounded trailing edge reduces control surface effectiveness. But where extreme winds normal to the deck are possible from either side, rounding of both flaps could be required and further work is needed. The natural frequency of the two flap control surfaces around their hinge-lines, $\omega_{\beta l}$ and $\omega_{\beta t}$, were substantially high so that at any velocity tested here, the flaps did not experience any form of excitation that could have caused early deck flutter through a deck-flap interaction. Two Nanotec ST8918S4508 NEMA34 3 Nm stepper motors were utilised, each driving one flap control surface through a 1:5 reduction gearbox located at one end of an aluminium shaft running along the span. A Nanotec SMC147-S stepper motor positioning controller controlled each motor in analogue positioning mode where an analogue voltage input was proportional to motor shaft position. A Nanotec WEDS5541-B shaft encoder (4000 counts per revolution) was utilised for shaft positional feedback. An internal, hardware, PID controller monitored shaft demand and actual positions, governed corrections and ensured shaft positional fidelity.

An H-assembly of springs (each of stiffness 1160 N/m) suspension system, either side of the tunnel test section allowed deck pitch and heave degrees of freedom. The heave frequency depended on the deck mass and the combined stiffness of the two spring H-assemblies (8 springs in total); the pitch frequency, on the other hand, could be adjusted by varying the horizontal separation between two arms of the springs H-assembly²¹⁾. The deck's roll degree of freedom was unconstrained but this mode was never excited, owing to the aerodynamic forces being predominantly 2-dimensional given that the deck spanned the tunnel width. The bottom of each arm of the H-assembly was connected to a load-cell and so through the known spring stiffnesses, the heave and pitch positions of the deck were inferred. Further details about the setup can be found in reference [21]. The deck was balanced such that it had no static moment making the term a equal to zero in equations XVIII-XX²³⁾. The deck still attained a small mean incidence in tests, mainly due to the position of the aerodynamic centre close to the deck's quarter chord position and also due to the deck's cambered cross-section. Spanwise and streamwise sway modes were constrained through drag wires connected to the deck through small leaf-springs in order to avoid the introduction of damping. The measured structural heave and pitch damping ratios were $\zeta_h = 0.0057$ and $\zeta_\alpha = 0.0033$ respectively, or $\delta_h = 0.036$ and $\delta_\alpha = 0.021$ in log-dec representation.

BMT Fluid Mechanics provided full-scale prototype properties, specifically a deck bending frequency $f_B \approx 0.29$ Hz and a torsional frequency $f_T \approx 0.45$ Hz giving a frequency ratio $f_T/f_B = 1.51$. The full-scale mass ratio $M_h/\rho A_x \approx 190$, where M_h is the deck mass per unit length and A_x is an area defined as the deck chord $2b \times$ deck depth. Both the frequency ratio and the mass ratio of the model were matched to those of the full-scale prototype. Since the model utilised here is a stiff section model where the mode frequencies are defined by the springs in the external suspension system, the Froude number was not matched to that of the full-scale prototype. This dimensionless group only becomes important when part of the structural stiffness is provided by gravitational forces, for example when full 3D model testing of a suspension bridge is performed²⁸⁾. The Reynolds number based on deck chord was just above 1×10^6 .

Table 2: Parameters of the model bridge deck used in these experiments.

Parameter	Value	Parameter	Value
b (half-chord incl. flap)	0.545 m	M_h	18.9 kg
ρ	1.23 kg/m ³	J_α	1.8 kg m ²
		ω_h	13.45 rad/s
		ω_α	20.74 rad/s

Using data from Table 2, the flutter velocity was predicted at 19.4 m/s (Selberg’s formula) and at 20.1m/s using codes based on Theodorsen thin-aerofoil theory and a vortex-panel method. The theoretical values were corrected using a correction factor²⁾ for predicted thin-aerofoil theory flutter velocity applied to non-thin bodies, to between 16 and 18 m/s. Experimentally, the flutter velocity was obtained through a number of experiments where the rate of decay or growth of oscillations was noted and the velocity at $\zeta = 0$ evaluated. A value of 17.5 m/s was obtained and will be adopted henceforth as the critical, flutter velocity. The divergence speed was estimated to be around 28.5 m/s, around 62% higher than the measured flutter speed and therefore beyond the percentage increases in flutter speed attained through the current flap control system. Experiments were run at the tunnel no. 5 at BMT Fluid Mechanics with a test-section width 2.75 m and height of 2.7 m, and in the Honda tunnel at Imperial College with a test section of 3 m by 1.5 metres; the deck exactly spanned the tunnel in the former case, while false walls were utilised in the Honda tunnel.

4. RESULTS

Results from the four tested controllers of Table 1 are presented in this section. The left-hand subfigure in each of Figures 4 to 7 shows typical tests where at a velocity 15% above the flutter velocity, the control was repeatedly toggled open (indicated by the red dashed vertical line) allowing oscillations to grow naturally. The control was subsequently toggled closed (indicated by the green dashed vertical line) allowing the control surfaces to impart the necessary control to dampen the oscillations. The damping performance was evaluated by computing the damping ratio of the deck’s assumed second order response as described in reference [21]. Each right-hand figure shows the evolution of the damping ratio, for both the heave and pitch modes, with freestream velocity for various gains. The reason behind the repeat of experiments for various gains is explained in the next section.

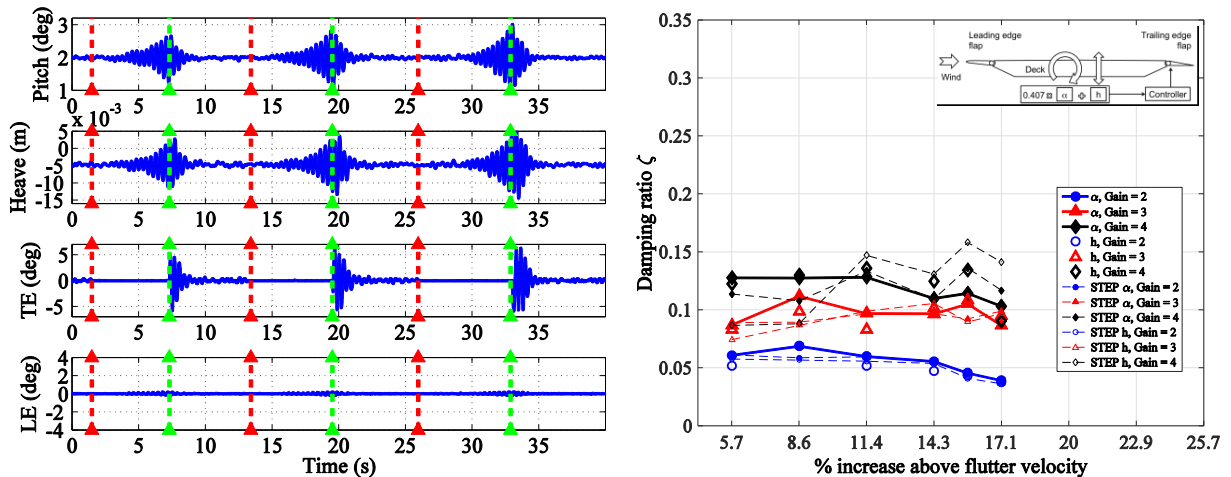


Figure 4: Controller #1: *Left*: Time-traces of the pitch and heave positions of the deck, and the corresponding trailing- and leading-edge flaps angles. The leading edge flap is held rigid while the trailing edge flap has a combination of deck heave and pitch position feedback, as shown in the inset sub-figure on the Right. The gain of the trailing-edge flap actuator is 3, and the wind velocity is 15% higher than flutter. *Right*: The evolution of the closed-loop damping ratio ζ as a function of %velocity increase above the flutter velocity.

The gain (multiplier of theoretical flap angle demand) is varied from 2 to 3 to 4 at each velocity.

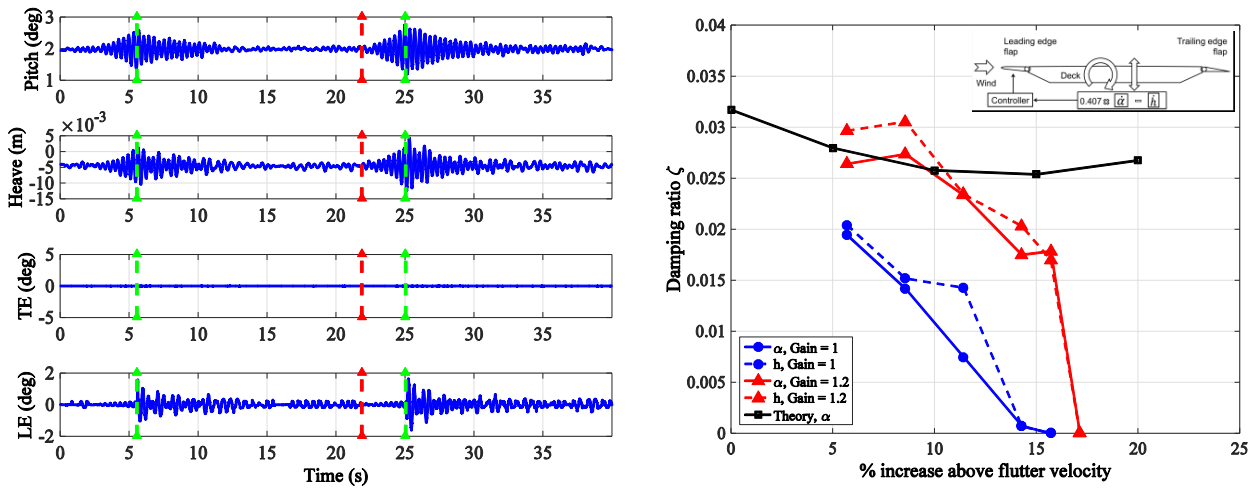


Figure 5: Controller #2: *Left*: Time-traces of the pitch and heave positions of the deck, and the corresponding trailing- and leading-edge flaps angles. The trailing edge flap is held rigid while the leading edge flap has a combination of deck heave and pitch **velocity** feedback. The gain of the leading-edge flap actuator is 1.2, and the wind velocity is 15% higher than flutter. *Right*: The evolution of the closed-loop damping ratio ζ as a function of %velocity increase above the flutter velocity. The gain is varied to 1 and 1.2 at each velocity.

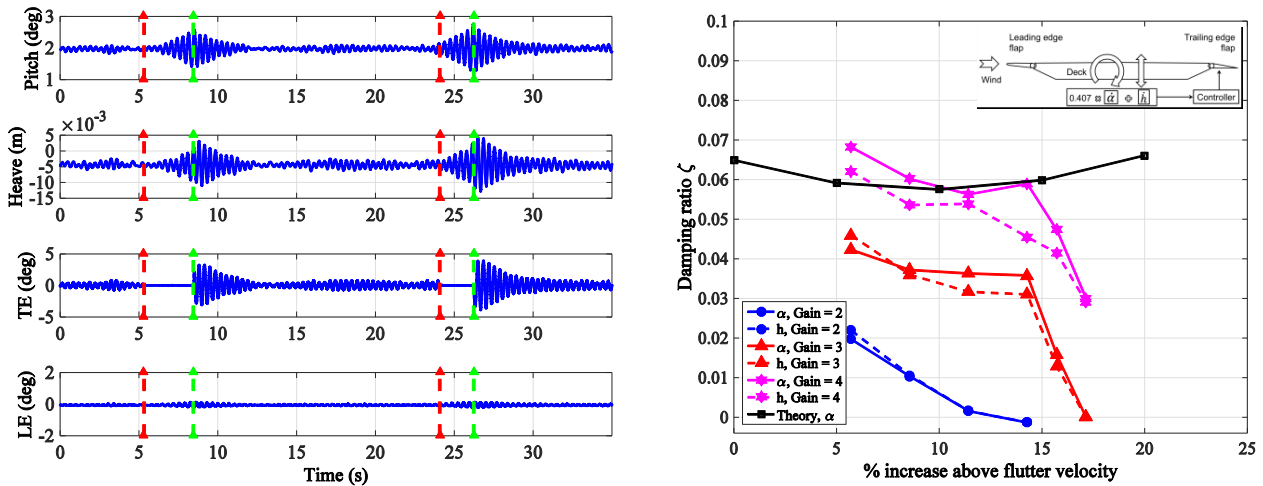


Figure 6: Controller #3: *Left*: Time-traces of the pitch and heave positions of the deck, and the corresponding trailing- and leading-edge flaps angles. The leading edge flap is held rigid while the trailing edge flap has a combination of deck heave and pitch **velocity** feedback. The gain of the trailing-edge flap actuator is 3, and the wind velocity is 15% higher than flutter. *Right*: The evolution of the closed-loop damping ratio ζ as a function of %velocity increase above the flutter velocity. The gain is varied to 2, 3 and 4 at each velocity.

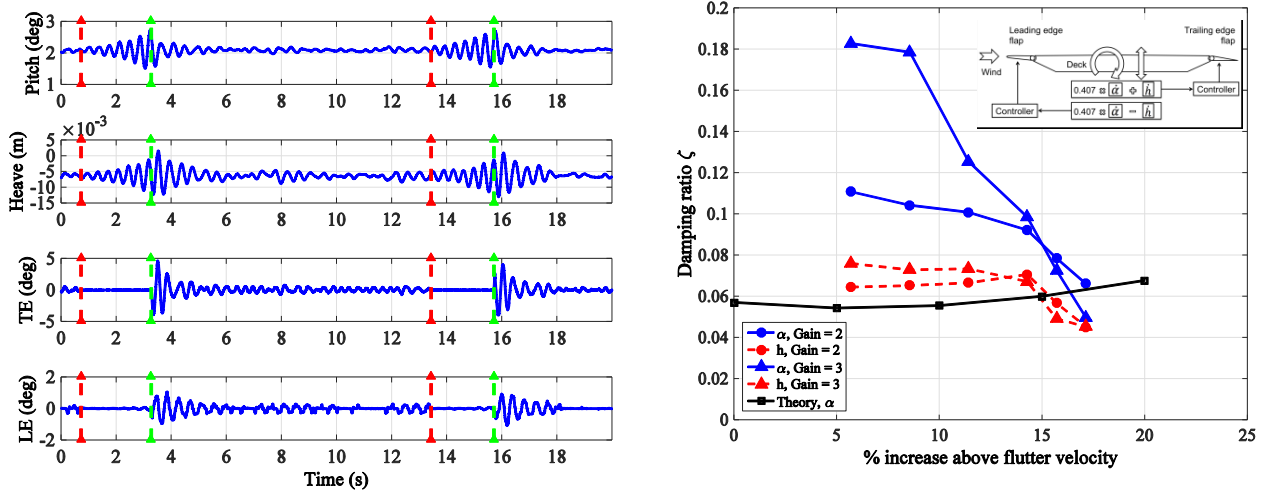


Figure 7: Controller #4: *Left*: Time-traces of the pitch and heave positions of the deck, and the corresponding trailing- and leading-edge flaps angles. The leading edge flap and trailing edge flaps have a combination of deck heave and pitch **velocity** feedback. The gain of the trailing-edge flap actuator is 3, and the wind velocity is 15% higher than flutter. *Right*: The evolution of the closed-loop damping ratio ζ as a function of %velocity increase above the flutter velocity. The gain of the leading edge flap was equal to 1 and that of the trailing edge flap is varied between 2 and 3 at each velocity.

5. DISCUSSION

The gain of the leading edge flap controller was in most cases set to 1 while that for the trailing edge flap controller was varied between 2 and 4. This increase in gain above the theoretical value of 1 was followed to compensate for the effects of the trailing edge flap operating in the separated wake of the deck. This is observed in Figure 8 showing a pressure distribution around the deck as well as from flow visualisation. The reduced effectiveness of the trailing edge flap was also observed through measurements of $dC_L/d\beta_t$ and $dC_M/d\beta_t$ as reported in Figures 22 and 23 of reference [21].

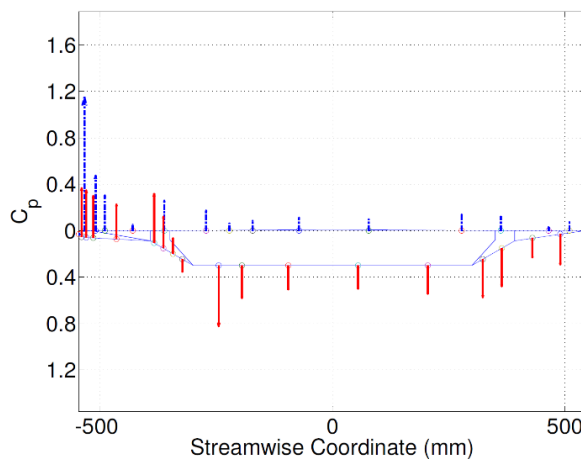


Figure 8: Pressure distribution around the deck at a velocity just below the onset of flutter (flow is from left to right). It was confirmed the trailing edge flap is operating in the deck wake and at reduced effectiveness.

Fair agreement was obtained between the theoretical damping ratios (extracted from the Root-Locus figures) and the values obtained experimentally. Good agreement was attained for Controllers 2 and 3, albeit at experimentally raised gain. For controller 4, for both tested gains, the experimental results indicate a better

performance than that predicted. Differences (though not very significant) in aerodynamic derivatives between the theoretical and measured ones were deemed responsible for the discrepancy between the theoretical and experimental values of the flutter velocity and controller performances²¹⁾. In this work, the controllers were designed using the theoretical aerodynamic derivatives and no attempt was made to introduce any corrections for the discrepancies indicated by measured aerodynamic derivatives. This was done in order to justify using the theoretical model for decks which are quasi-streamline like some trapezoidal section modern decks.

6. CONCLUSIONS

In this work, an extension of the work reported in reference [21], the performance in delay of the onset of flutter was reported for a number of leading-edge and trailing-edge flap controllers and feedbacks. Pitch and heave position and velocity feedbacks were investigated in conjunction with the use of the leading-edge, trailing-edge or both flaps. The controllers were based around thin aerofoil theory even though aerodynamic derivative measurements showed some discrepancies with their theoretical, utilised, counterparts. This approach was to justify and demonstrate the retention of controller effectiveness at least for decks which are streamlined or quasi-streamlined. The controllers reported here were found to delay the flutter velocity by an estimated (extrapolated) 20% (closely matching the theoretical predictions) and were based around the use of passive mechanical elements, increasing the chances of survivability of the system in extreme conditions.

ACKNOWLEDGMENTS

The authors would like to thank the Engineering and Physical Sciences Research Council (UK) grant number EP/H029982/1 and by BMT Fluid Mechanics Ltd who supported this work. The additional wind tunnel time granted by BMT and the support and advice given by their staff S. Cammelli and A. Elliot is gratefully acknowledged. They would also like to thank Prof. T. Wyatt for his many insights and invaluable advice.

REFERENCES

- 1) Schlaich, M., Brownlie, K., Conzett, J., Sobrino, J., Strasky, J. and Takenouchi, K., Guidelines for the design of footbridges: Guide to good practice, Int. Fed. Struct. Concrete, Lausanne, Switzerland, Tech. Rep., 2005.
- 2) Dyrbye, C. and Hansen, S. O., Wind Loads on Structures, 1st ed. Chichester, U.K.: Wiley, 1999.
- 3) Billah, K. Y. and Scanlan, R. H., Resonance, Tacoma Narrows bridge failure, and undergraduate physics textbooks, Amer. J. Phys., vol. 59, no. 2, pp. 118–124, 1991.
- 4) Larsen, A., Savage, M., Lafrenière, A., Hui, M. C. H., and Larsen, S. V., Investigation of vortex response of a twin box bridge section at high and low Reynolds numbers, J. Wind Eng. Ind. Aerodyn., vol. 96, nos. 6–7, pp. 934–944, 2008.
- 5) Larsen, A., Esdahl, S., Andersen, J. E., and Vejrum, T., Storebælt suspension bridge—Vortex shedding excitation and mitigation by guide vanes, J. Wind Eng. Ind. Aerodyn., vol. 88, nos. 2–3, pp. 283–296, 2000.
- 6) Triplett, W. E., 1972. A feasibility study of active wing/store flutter control. J. Aircraft 9 (6), 438–444.
- 7) Triplett, W. E., Kappus, H. P. F., Landy, R. J., 1973. Active flutter control - an adaptable application to wing/store flutter. J. Aircraft 10 (11), 669–678.
- 8) Roger, K. L., Hodges, G. E., Felt, L., 1975. Active flutter suppression – a flight test demonstration. J. Aircraft 12 (6), 551–556.
- 9) Karpel, M., 1982. Design for active flutter suppression and gust alleviation using state-space aeroelastic modeling. Journal of Aircraft 19 (3), 221–227.
- 10) Borglund, D., Kuttenukeuler, J., 2002. Active wing flutter suppression using a trailing edge flap. Journal of Fluids and Structures 16 (3), 271 – 294.
- 11) Burnett, E., Atkinson, C., Sibbitt, B., Holm-Hansen, B., Nicolai, L., 2010. N dof simulation model for flight control development with flight test correlation. In: AIAA Modeling and Simulation Technologies

- Conference, Toronto, Canada, AIAA paper 2010-7780.
- 12) Ostenfeld, K. H., A system and a method of counteracting wind induced oscillations in a bridge girder, European Patent 0 627 031 B1, Jun. 12, 1996.
 - 13) Corney, J. M., Bridge stabilization, WO Patent 1997 045 593, Dec. 4, 1997. [Online]. Available: <http://www.google.com.ar/patents/WO1997045593A1?cl=en>
 - 14) Kobayashi, H. and Nagaoka, H., Active control of flutter of a suspension bridge, *J. Wind Eng. Ind. Aerodyn.*, vol. 41, nos. 1–3, pp. 143–151, 1992.
 - 15) Ostenfeld, K. H. and Larsen, A., Bridge engineering and aerodynamics, in *Proc. 1st Int. Symp. Aerodyn. Large Bridges*, 1992, pp. 3–22.
 - 16) Hansen, H. I. and Thoft-Christensen, P., Active flap control of long suspension bridges, *J. Struct. Control*, vol. 8, no. 1, pp. 33–82, 2001.
 - 17) Wilde, K. and Fujino, Y., Aerodynamic control of bridge deck flutter by active surfaces, *J. Eng. Mech.*, vol. 124, no. 7, pp. 718–727, 1998.
 - 18) Omenzetter, P., Wilde, K., and Fujino, Y., Suppression of wind-induced instabilities of a long span bridge by a passive deck-flaps control system: Part I: Formulation, *J. Wind Eng. Ind. Aerodyn.*, vol. 87, no. 1, pp. 61–79, 2000.
 - 19) Omenzetter, P., Wilde, K., and Fujino, Y., Suppression of wind-induced instabilities of a long span bridge by a passive deck-flaps control system: Part II: Numerical simulations, *J. Wind Eng. Ind. Aerodyn.*, vol. 87, no. 1, pp. 81–91, 2000.
 - 20) Nissen, H. D., Sørensen, P. H. and Jannerup, O., Active aerodynamic stabilisation of long suspension bridges, *J. Wind Eng. Ind. Aerodyn.*, vol. 92, no. 10, pp. 829–847, 2004.
 - 21) Gouder, K., Zhao, X., Limebeer, D., Graham, J., 2015. Experimental aerodynamic control of a section of long-span suspension bridge using leading and trailing-edge control surfaces. *IEEE Trans Control System Technology*. In press. DOI:10.1109/TCST.2015.2501346
 - 22) Zhao, X., Gouder, K., Graham, J., Limebeer, D., 2015. Buffet Loading, Dynamic Response and Aerodynamic Control of a Suspension Bridge in a Turbulent Wind, *Journal of Fluids and Structures*. In press.
 - 23) Theodorsen, T., General theory of aerodynamic instability and the mechanism of flutter, NASA Langley Res. Center, Hampton, VA, USA, Tech. Rep. NACA-TR-496, 1934.
 - 24) Massaro, M. and Graham, J. M. R., The effect of three-dimensionality on the aerodynamic admittance of thin sections in free stream turbulence, *J. Fluids Struct.*, vol. 57, pp. 81–90, Aug. 2015.
 - 25) Theodorsen, T. and Garrick, I. E., Nonstationary flow about a wing-aileron-tab combination including aerodynamic balance, NASA Langley Res. Center, Hampton, VA, USA, Tech. Rep. NACA-TR-736, 1942.
 - 26) Graham, J. M. R., Limebeer, D. J. N. and Zhao, X., Aeroelastic control of long-span suspension bridges, *ASME J. Appl. Mech.*, vol. 78, no. 4, pp. 041018-1–041018-12, 2011.
 - 27) Wilde, K. Fujino, Y. and Kawakami, T., Analytical and experimental study on passive aerodynamic control of flutter of a bridge deck, *J. Wind Eng. Ind. Aerodyn.*, vol. 80, nos. 1–2, pp. 105–119, 1999.
 - 28) Holmes, J. D., *Wind Loading of Structures*. Boca Raton, FL, USA: CRC Press, 2015.

ENERGY CONVERSION MECHANISM OF AERODYNAMIC FLUTTER OF A BOX GIRDER

Yaojun GE⁺¹, Zujun LIU⁺² and Yongxin YANG⁺³

^{+1,3} State Key Laboratory of Disaster Reduction in Civil Engineering, Tongji University, Shanghai 200092, China

⁺² School of Civil Engineering and Communication, North China University of Water Resources and Electric Power, Zhengzhou 450011, Henan Province, China

Based on the flutter control equations with two degrees of freedom, including heaving and pitching vibration, the energy control equations of flutter oscillation were firstly derived. In order to solve the coupled energy equations of heaving degree and pitching degree, the step-by-step method was adopted to find out two decoupled solutions. Then, the calculation formulas of aerodynamic energy in these two degrees were achieved, and the criterion of flutter instability was derived due to system energy change rate. Through the wind tunnel testing with the sectional model of a box girder, the energy conversion rule of the heaving and pitching vibration was studied, and the transmission and feedback mechanism of airflow energy distributed on these two degrees was analyzed. The mechanism of coupled flutter of a box girder was finally described by energy input and output through the heaving and pitching degrees of freedom with the phase difference. It can be concluded that aerodynamic flutter is controlled by the energy conversion in the pitching degree of freedom, including three components, aerodynamic force, aerodynamic damping and aerodynamic stiffness. With the increase of oscillation time or cycles, the energy input from aerodynamic force will increase, and the energy output through aerodynamic damping will also increase, while the energy output through aerodynamic stiffness will change slightly and periodically.

Keyword: flutter, energy conversion, heaving vibration, pitching vibration, box girder

1. INTRODUCTION

Though aerodynamic flutter of long span bridges has been widely studied with two-dimensional or three-dimensional models since the collapse of the original Tacoma Narrows Bridge in 1940, the mechanism of driven flutter, divergent oscillation and energy input and output has attracted a little attention. In order to reveal energy conversion mechanism of aerodynamic flutter of a long-span bridge, a two-dimensional model with two degrees of freedom is usually used based on the traditional coupled flutter analysis model and method proposed by Scanlan¹. He firstly established the coupled flutter analysis model, with two degrees of freedom (2DOF), including heaving and pitching vibration, described by eight flutter derivatives (H_i^* and A_i^* , $i = 1\sim 4$), and also found the frequency domain method to solve these two coupled flutter equations based on the assumption that the structure is performing a simple harmonic motion both in heaving and pitching simultaneously with the same frequency and infinitesimally small amplitudes¹. He pointed out that the energy inputting to the structure is not only related to heaving and pitching displacement amplitudes but also has an influence from the phase difference between heaving vibration and pitching vibration¹. Unfortunately, he only gave a theoretical framework of energy conversion analysis but not a concrete method.

Following the pioneering work contributed by Scanlan, many researchers have made great contributions to bridge flutter analysis, including theoretical model, analytical approach and driven mechanism, as well as energy conversation. Matsumoto put forward the flutter classification of bridge girders² and the flutter stabilization of long span bridges³ based on a step-by-step analysis method, by which the coupled flutter motion equations can be decoupled and solved for critical flutter speeds. Flutter instability

⁺¹yaojunge@tongji.edu.cn, ⁺²liuzujunhs@126.com, ⁺³yang_y_x@tongji.edu.cn

mechanism has been investigated through aerodynamic damping and aerodynamic derivatives of various cross sections including rectangles with different height-to-width ratios, diamond, oval and triangle⁴. Based on the discrete vortex method of computational fluid dynamics, Larsen took the Tacoma Narrows Bridge deck as an example to provide a simplified analysis model and study in the flutter mechanism from doing work capability of moving vortices to vibrating structure in a cycle, but the application of the method has many limitations⁵. Yang developed a two-dimensional three degrees method for coupled flutter analysis based on the step-by-step method, and investigated the flutter mechanism of 13 popular bridge decks⁶. He concluded that classical coupled heaving-pitching flutter of an ideal thin plate occurs with such an incentive - feedback route: the coupled heaving vibration was inspired by the aerodynamic lift force produced by the displacement of pitching main movement, and then the coupled pitching moment by the speed of heaving vibration feedback to pitching vibration⁷, and can be improved by making a central slot⁸. In addition, Ding also used the step-by-step method to study in coupled flutter mechanism of bridge decks⁹, and Liu developed a full-bridge multi-mode flutter energy analysis method to deal with the energy balance of a structure-airflow system¹⁰.

The present paper tries to reveal energy conversion mechanism of aerodynamic flutter with a two-dimensional and 2DOF model of a typical box girder section. Based on two-degree coupled flutter equations, including heaving and pitching vibration, the energy control equations of flutter oscillation were firstly derived. The step-by-step method was adopted to deal with the coupled energy equations of heaving degree and pitching degree. After the calculation formulas of aerodynamic energy in these two degrees were achieved, the criterion of flutter instability was derived due to system energy change rate. Through the wind tunnel testing with the sectional model of a box girder, the energy conversion rule of the heaving and pitching vibration was studied, and the transmission and feedback mechanism of airflow energy distributed on these two degrees was analyzed. The mechanism of coupled flutter of a box girder was finally described by energy input and output through the heaving and pitching degrees of freedom with the phase difference.

2. 2DOF CONTROL EQUATIONS AND SOLUTIONS

Based on the 2DOF bridge girder model in Fig. 1, the 2DOF coupled flutter equations of heaving h and pitching α displacements can be represented by eight flutter derivatives (H_i^* and A_i^* , $i = 1\sim 4$) as follows:

$$\ddot{h} + 2\xi_{h0}\omega_{h0}\dot{h} + \omega_{h0}^2 h = \frac{\rho B^2}{m_h} \omega H_1^* \dot{h} + \frac{\rho B^2}{m_h} \omega^2 H_4^* h + \frac{\rho B^3}{m_h} \omega^2 H_3^* a + \frac{\rho B^3}{m_h} \omega H_2^* \dot{a} \quad (1a)$$

$$\ddot{\alpha} + 2\xi_{\alpha 0}\omega_{\alpha 0}\dot{\alpha} + \omega_{\alpha 0}^2 \alpha = \frac{\rho B^3}{I} \omega A_1^* \dot{h} + \frac{\rho B^3}{I} \omega^2 A_4^* h + \frac{\rho B^4}{I} \omega^2 A_3^* a + \frac{\rho B^4}{I} \omega A_2^* \dot{a} \quad (1b)$$

where m_h and I are the generalized mass and mass moment of inertia respectively, ξ_{h0} and $\xi_{\alpha 0}$ are the structural damping ratios of heaving and pitching vibration, ω_{h0} and $\omega_{\alpha 0}$ are the natural frequencies of heaving and pitching vibration, ω is the vibration frequency of structure-fluid system, ρ is the air density, and B is the girder width.

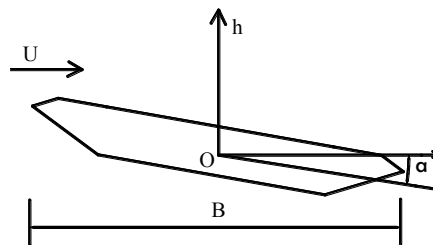


Figure 1: 2DOF bridge girder model

In order to derive 2DOF energy control equations, the 2DOF coupled flutter equations, Eqs. 1a and 1b, can be integrated with respect to time t as:

$$\int_0^t \ddot{h} \cdot \dot{h} dt + \int_0^t 2\xi_{h0} \omega_{h0} \dot{h} \cdot \dot{h} dt + \int_0^t \omega_{h0}^2 h \cdot \dot{h} dt = \int_0^t \frac{\rho B^2}{m_h} \omega_h H_1^* \dot{h} \cdot \dot{h} dt + \int_0^t \frac{\rho B^2}{m_h} \omega_h^2 H_4^* h \cdot \dot{h} dt \quad (2a)$$

$$+ \int_0^t \frac{\rho B^3}{m_h} \omega_a^2 H_3^* a \cdot \dot{h} dt + \int_0^t \frac{\rho B^3}{m_h} \omega_a H_2^* \dot{a} \cdot \dot{h} dt$$

$$\int_0^t \ddot{\alpha} \cdot \dot{\alpha} dt + \int_0^t 2\xi_{\alpha 0} \omega_{\alpha 0} \dot{\alpha} \cdot \dot{\alpha} dt + \int_0^t \omega_{\alpha 0}^2 \alpha \cdot \dot{\alpha} dt = \int_0^t \frac{\rho B^3}{I} \omega_h A_1^* \dot{h} \cdot \dot{\alpha} dt + \int_0^t \frac{\rho B^3}{I} \omega_h^2 A_4^* h \cdot \dot{\alpha} dt \quad (2b)$$

$$+ \int_0^t \frac{\rho B^4}{I} \omega_a^2 A_3^* a \cdot \dot{\alpha} dt + \int_0^t \frac{\rho B^4}{I} \omega_a A_2^* \dot{a} \cdot \dot{\alpha} dt$$

Assuming pitching vibration containing heaving vibration frequency component ω_h and heaving vibration containing pitching vibration frequency component ω_α , the heaving and pitching displacements, $h(t)$ and $\alpha(t)$, can be divided into two components as follows:

$$h(t) = h_0(t) + h_1(t) \quad (3a)$$

$$\alpha(t) = \alpha_0(t) + \alpha_1(t) \quad (3b)$$

where $h_0(t)$ and $\alpha_0(t)$ are the main heaving and pitching vibration with the vibration frequency ω_h and ω_α , respectively, and $h_1(t)$ and $\alpha_1(t)$ are the heaving and pitching vibration induced by pitching vibration and heaving vibration, respectively.

In the above Eq. 1 or 2, the left-hand sides are established with respect to time and yet the aerodynamic force terms are actually given in the frequency domain. It means that the equations are applicable only when the structure is performing the following coupled motion of $h_0(t)$ and $\alpha_0(t)$ as:

$$h_0(t) = h_0 e^{-\xi_h \omega_h t} \sin(\omega_h t + \theta) \quad (4a)$$

$$\alpha_0(t) = \alpha_0 e^{-\xi_\alpha \omega_\alpha t} \sin \omega_\alpha t \quad (4b)$$

By substituting Eqs. 3 and 4 into Eq. 1, $h_1(t)$ and $\alpha_1(t)$ can be obtained with two parts as follows:

$$h_1(t) = h_{11}(t) + h_{12}(t) = \frac{\rho B^3}{m_h \Omega_h} \omega_a^2 \alpha_0 e^{-\xi_\alpha \omega_\alpha t} H_3^* \sin(\omega_\alpha t + \phi_1) + \frac{\rho B^3}{m_h \Omega_h} \omega_a^2 \sqrt{1 + \xi_\alpha^2} \alpha_0 e^{-\xi_\alpha \omega_\alpha t} H_2^* \sin(\omega_\alpha t + \phi_1 + \beta) \quad (5a)$$

$$\alpha_1(t) = \alpha_{11}(t) + \alpha_{12}(t) = \frac{\rho B^3}{I \Omega_\alpha} \omega_h^2 h_0 \sqrt{1 + \xi_h^2} e^{-\xi_h \omega_h t} A_1^* \sin(\omega_h t + \phi_2 + \theta + \gamma) + \frac{\rho B^3}{I \Omega_\alpha} \omega_h^2 h_0 e^{-\xi_h \omega_h t} A_4^* \sin(\omega_h t + \phi_2 + \theta) \quad (5b)$$

where all parameters in Eq. 5 are given as:

$$\Omega_\alpha = \sqrt{(a_\alpha^2 + \omega_{D\alpha}^2 - \omega_h^2)^2 + 4a_\alpha^2 \omega_\alpha^2} \quad (6a)$$

$$\Omega_h = \sqrt{(a_h^2 + \omega_{Dh}^2 - \omega_\alpha^2)^2 + 4a_h^2 \omega_\alpha^2} \quad (6b)$$

$$\omega_{D\alpha} = \omega_\alpha \sqrt{1 - \xi_\alpha^2}, \quad \omega_{Dh} = \omega_h \sqrt{1 - \xi_h^2} \quad (6c)$$

$$a_h = \xi_{h0} \omega_{h0} - \xi_\alpha \omega_\alpha, \quad a_\alpha = \xi_{\alpha 0} \omega_{\alpha 0} - \xi_h \omega_h \quad (6d)$$

$$\phi_1 = \arctg \frac{-2a_h \omega_\alpha}{a_h^2 + \omega_{Dh}^2 - \omega_\alpha^2}, \quad \phi_2 = \arctg \frac{-2a_\alpha \omega_h}{a_\alpha^2 + \omega_{D\alpha}^2 - \omega_h^2} \quad (6e)$$

$$\beta = \arctg \frac{-1}{\xi_\alpha}, \quad \gamma = \arctg \frac{-1}{\xi_h} \quad (6f)$$

Based on the assumptions of Eqs. 3 and 4, the maximum and minimum amplitudes of heaving vibration, h_{max} and h_{min} , and pitching vibration, α_{max} and α_{min} , happen at different moments, and the phase difference between two degrees, heaving and pitching, can be generally describe by Fig. 2.

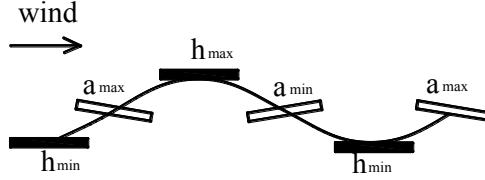


Figure 2: Phase difference between two degrees

3. PITCHING AND HEAVING VIBRATION ENERGY

(1) Pitching vibration energy

According to the law of conservation of energy, the total energy gained by a structure-fluid system must be equal to the total energy consumed by the system. The total gained energy of pitching vibration in a system can be represented by the total input energy, E_{input} , which can be easily obtained as the right hand side of Eq. 2b as:

$$E_{input} = \int_0^t \frac{\rho B^3}{I} \omega_h A_1^* \dot{h} \cdot \dot{\alpha} dt + \int_0^t \frac{\rho B^3}{I} \omega_h^2 A_4^* h \cdot \dot{\alpha} dt + \int_0^t \frac{\rho B^4}{I} \omega_a^2 A_3^* a \cdot \dot{\alpha} dt + \int_0^t \frac{\rho B^4}{I} \omega_a A_2^* \dot{a} \cdot \dot{\alpha} dt \quad (7)$$

where the first and second terms of the right hand side are the energy feedback from coupled aerodynamic pitching moment $(\rho B^3/I)\omega_h A_1^* \dot{h}$ and $(\rho B^3/I)\omega_h^2 A_4^* h$ indirectly reproduced by heaving vibration, and the last two terms are the direct energy from pitching vibration.

The total consumed energy includes the sum of kinetic energy and potential energy, E_{ck} , and the output energy, E_{out} , which can be given as the left hand side of Eq. 2b as:

$$E_{ck} = \frac{1}{2} I [\dot{\alpha}(t)]^2 + \frac{1}{2} I \omega_{\alpha 0}^2 [\alpha(t)]^2 \quad (8)$$

$$E_{out} = \int_0^t 2\xi_{\alpha 0} \omega_{\alpha 0} \dot{\alpha} \cdot \dot{\alpha} dt \quad (9)$$

(2) Heaving vibration energy

Similar to the pitching vibration system, the total input energy E_{input} , the sum of kinetic energy and potential energy, E_{ck} , and the output energy, E_{out} , of the heaving vibration system can be given based on Eq. 2a as:

$$E_{input} = \int_0^t \frac{\rho B^2}{m_h} \omega_h H_1^* \dot{h} \cdot \dot{h} dt + \int_0^t \frac{\rho B^2}{m_h} \omega_h^2 H_4^* h \cdot \dot{h} dt + \int_0^t \frac{\rho B^3}{m_h} \omega_a^2 H_3^* a \cdot \dot{h} dt + \int_0^t \frac{\rho B^3}{m_h} \omega_a H_2^* \dot{a} \cdot \dot{h} dt \quad (10)$$

$$E_{ck} = \frac{1}{2} m_h [\dot{h}(t)]^2 + \frac{1}{2} m_h \omega_{h 0}^2 [h(t)]^2 \quad (11)$$

$$E_{out} = \int_0^t 2\xi_{h 0} \omega_{h 0} \dot{h} \cdot \dot{h} dt \quad (12)$$

In Eq. 10, the first and second terms of the right hand side are the energy feedback from coupled

aerodynamic lift force $(\rho B^3/m_h)\omega^2 H_3^* a$ and $(\rho B^3/m_h)\omega H_2^* \dot{a}$ indirectly reproduced by pitching vibration, and the last two terms are the direct energy from heaving vibration.

(3) Criterion of flutter instability

Combined with Eq. 8 and Eq. 11, the total sum of kinetic and potential energy in both heaving and pitching vibrations of a system, V , can be derived as:

$$V = E_{ck} + E_{hk} \quad (13)$$

And the change rate of this total sum of kinetic and potential energy can be defined as:

$$\dot{V} = \frac{dV}{dt} = \frac{d(E_{ck} + E_{hk})}{dt} \quad (14)$$

The flutter instability of a system can be judged by the change rate of the total sum of kinetic and potential energy in both heaving and pitching vibrations. When the value of the energy change rate is equal to zero ($\dot{V} = 0$), the total input energy to the system is just equal to the output energy or consumed by structural damping and the system oscillation is at the critical state with fixed certain amplitude. When the energy change rate is greater ($\dot{V} > 0$) or smaller ($\dot{V} < 0$) than zero, the total input energy is greater or smaller than the output energy and the system oscillation is not stable or stable. Therefore, the energy change rate being zero, $\dot{V} = 0$, corresponds to critical flutter state of the system and can be used as a criterion of flutter instability.

Under the critical flutter condition, the heaving vibration and the pitching vibration can be approximately expressed as:

$$h_0(t) = h_0 \sin \omega t \quad (15a)$$

$$\alpha_0(t) = \alpha_0 \sin \omega t \quad (15b)$$

By substituting Eq. 15 into Eq. 14 and setting $\dot{V} = 0$, the vibration frequency of the system in critical flutter state is obtained as follows:

$$\omega_0 = \sqrt{\omega_{\alpha 0}^2 - \frac{m_h \cdot (\omega_{h 0}^2 - \omega_{\alpha 0}^2)}{I \left(\frac{\alpha_0}{h_0} \right)^2 - m_h}} \quad (16)$$

where α_0/h_0 is the amplitude ratio of heaving and pitching vibration. The vibration conditions of a system can be summarized due to the criterion of flutter instability in three states, that is, not stable with $\omega < \omega_0$ when $\dot{V} > 0$, critical with $\omega = \omega_0$ when $\dot{V} = 0$, and stable with $\omega > \omega_0$ when $\dot{V} < 0$.

4. INPUT ENERGY OF A CLOSED BOX DURING PITCHING VIBRATION

The closed box model is 3.3m in depth and 25.8m in total width, shown in Fig. 3. The main parameters of the closed box are listed as: $m_h = 5.26$ kg/m, $I = 0.128$ kg·m²/m, $f_h = 1.83$ Hz and $f_\alpha = 3.45$ rad/s. Through a wind tunnel with the sectional model, the flutter derivatives related to heaving and pitching degrees were identified and shown in Fig. 4, and the critical flutter wind speed was determined to be 13.5 m/s.

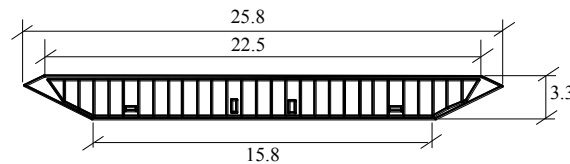


Figure 3: Closed box model

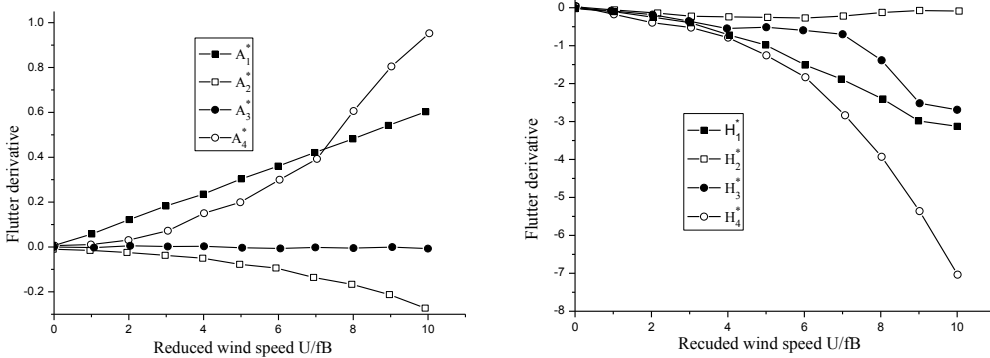


Figure 4: Flutter derivatives of the closed box model

(1) Input energy from $(\rho B^3/I)\omega_h A_1^* \dot{h}$

Based on the step-by-step analysis, if the energy from the air is firstly to excite pitching main motion with the frequency ω_α , the heaving displacement of this motion will bring about, in the heaving vibration system, the coupled aerodynamic lift force $(\rho B^3/m_h)\omega_a^2 H_3^* \alpha_0(t)$, and accordingly this coupled lift force will cause heaving implicated motion $h_{11}(t)$ in the heaving vibration system. The heaving implicated motion results in coupled pitching moment $(\rho B^3/I)\omega_h A_1^* \dot{h}_{11}(t)$, which is reacted on the pitching main motion $\alpha_0(t)$ to feedback or input energy to the pitching vibration system. This input energy can be calculated as follows:

$$w_1 = \frac{\rho^2 B^6}{4\Omega_h I \times m_h} \alpha_0^2 \omega_h \omega_a^3 (1 + \xi_\alpha^2) A_1^* H_3^* \times \left[\frac{\cos \phi_1 (1 - e^{-2\xi_\alpha \omega_a t})}{\xi_\alpha} - \frac{1}{\sqrt{1 + \xi_\alpha^2}} \left[e^{-2\xi_\alpha \omega_a t} \cdot \cos(2\omega_a t + \phi_1 + \beta) - \cos(\phi_1 + \beta) \right] \right] \quad (17)$$

It can be seen from Eq. 17 that the input energy w_1 is related to the multiplication of the coupled flutter derivatives $A_1^* H_3^*$.

Under the critical flutter wind speed, $U=13.5\text{m/s}$, the relationship between the coupled pitching moment $(\rho B^3/I)\omega_h A_1^* \dot{h}$ and the vibration velocity is shown as Fig. 5a. Because the curve slope is always positive, this pitching moment can continuously promote the pitching vibration with a phase difference between them due to non-zero intercept of this curve. As the product of force and velocity, the power in any period is always greater than zero, and the same amount of positive energy is input to the pitching vibration system in each cycle as shown in Fig. 5b. With the increase of time or oscillation cycles, the system energy is accumulated and must destroy the system vibration stability if the accumulated energy cannot be consumed by structural damping.

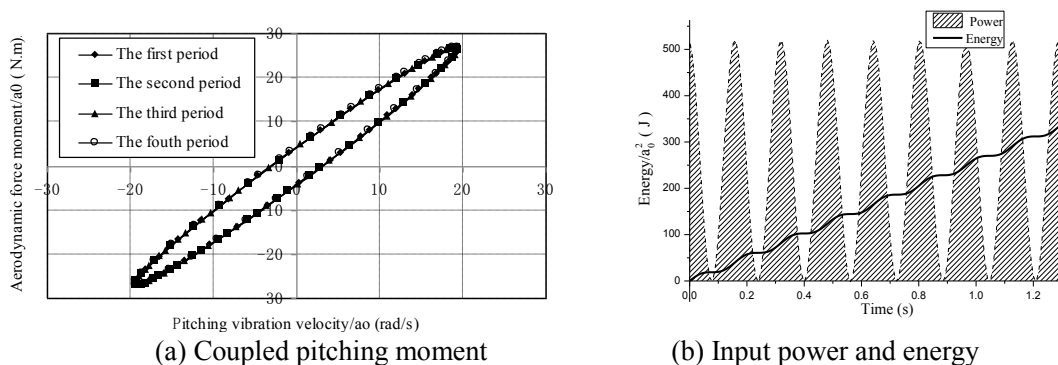


Figure 5: Moment and energy related to $(\rho B^3/I)\omega_h A_1^* \dot{h}$

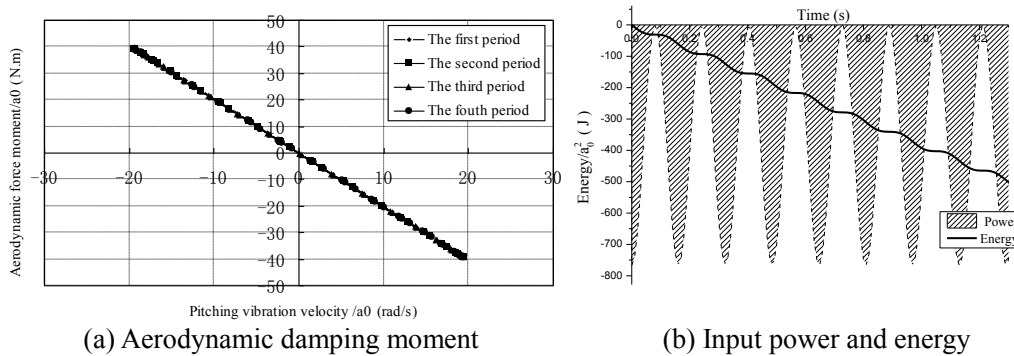
(2) Input energy from $(\rho B^4/I)\omega_a A_2^* \dot{\alpha}$

The input energy from the aerodynamic damping moment of $(\rho B^4/I)\omega_a A_2^* \dot{\alpha}$ to the pitching vibration system can be determined as:

$$w_2 = \frac{\rho B^4}{4I} A_2^* \alpha_{01}^2 \left[\frac{(1 - e^{-2\xi_\alpha \omega_\alpha t})}{\xi_\alpha} - \frac{1}{\sqrt{1 + \xi_\alpha^2}} \times [e^{-2\xi_\alpha \omega_\alpha t} \cdot \cos(2\omega_\alpha t + \beta) - \cos \beta] \right] \quad (18)$$

where α_{01} is the coefficient without including any flutter derivative, thus the input energy w_2 is only determined by the single uncoupled flutter derivative A_2^* .

The relationship between the aerodynamic damping moment $(\rho B^4 / I) \omega_\alpha A_2^* \dot{\alpha}_0(t)$ and the pitching vibration velocity $\dot{\alpha}_0(t)$ is shown in Fig. 6a under $U=13.5\text{m/s}$. because the curve has negative slope and zero intercept, the aerodynamic damping moment and the pitching velocity have completely opposite phase each other. During each vibration period, the aerodynamic damping moment consumes the same amount system energy as its input shown in Fig. 6b, which plays an important role for the system stability.



(a) Aerodynamic damping moment (b) Input power and energy
Figure 6: Moment and energy related to $(\rho B^4 / I) \omega_\alpha A_2^* \dot{\alpha}$

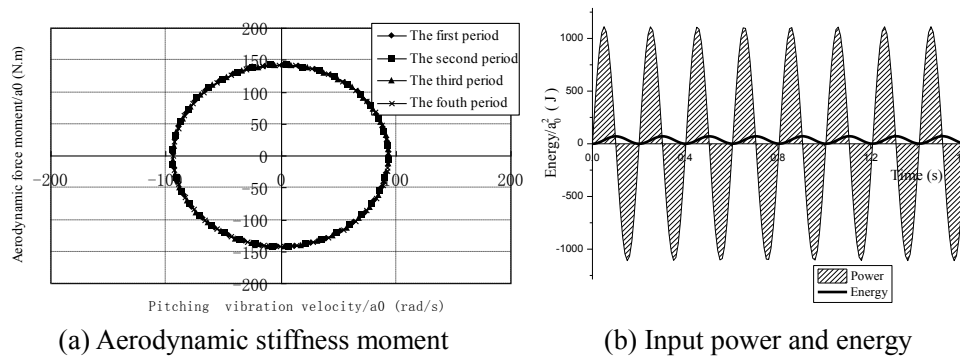
(3) Input energy from $(\rho B^4 / I) \omega_\alpha^2 A_3^* a_0(t)$

The input energy from the aerodynamic stiffness moment of $(\rho B^4 / I) \omega_\alpha^2 A_3^* a_0(t)$ can be written as:

$$w_3 = \frac{\rho B^4}{4I} \omega_\alpha A_3^* \alpha_{01} \times \left[\frac{\cos \beta \cdot (1 - e^{-2\xi_\alpha \omega_\alpha t})}{\xi_\alpha} - \frac{1}{\sqrt{1 + \xi_\alpha^2}} [e^{-2\xi_\alpha \omega_\alpha t} \cos(2\omega_\alpha t) - 1] \right] \quad (19)$$

where α_0 and α_{01} are the coefficients without including any flutter derivative, thus the input energy w_3 is only determined by the single uncoupled flutter derivative A_3^* .

The aerodynamic stiffness moment and the input energy from the moment with time are shown in Figs. 7a and 7b. In the first half cycle in Fig. 7a, the aerodynamic stiffness moment and the vibration velocity are in phase, so the power is positive and the aerodynamic stiffness moment does positive work for the system in Fig.7b, while in the next half cycle in Fig. 7a, the phase between them becomes opposite, so the power becomes negative and the system energy is accordingly consumed in Fig. 7b. As a result of the summation of one period vibration, the input energy and the consumed energy are counteracted each other, and have no influence on the system vibration stability.



(a) Aerodynamic stiffness moment (b) Input power and energy
Figure 7: Moment and energy related to $(\rho B^4 / I) \omega_\alpha^2 A_3^* a_0(t)$

(4) Input energy from $(\rho B^3 / I) \omega_a^2 A_4^* h_0(t)$

The coupled aerodynamic pitching moment $(\rho B^3 / I) \omega_a^2 A_4^* h_0(t)$ has small value and the input energy from the moment to the pitching vibration system gradually reduces with time shown in Figs. 8a and 8b. Therefore, this input energy can be neglected.

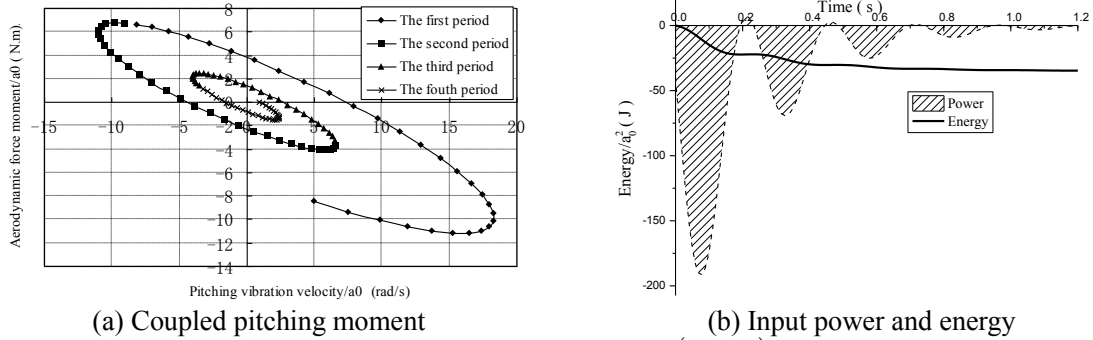


Figure 8: Moment and energy related to $(\rho B^3 / I) \omega_a^2 A_4^* h_0(t)$

5. INPUT ENERGY OF A CLOSED BOX DURING HEAVING VIBRATION

During heaving vibration, the heaving damping increases with the increase of wind speed, and the amplitude of heaving vibration with the frequency ω_h decreases accordingly. The coupled lift force induced by pitching vibration, however, generates the forced heaving motion with the frequency ω_α , by which the heaving vibration energy is feedback to pitching vibration system.

(1) Input energy from $(\rho B^2 / m_h) \omega_h H_1^* \dot{h}$

The aerodynamic damping force $(\rho B^2 / m_h) \omega_h H_1^* \dot{h}$ in heaving vibration system acts on the heaving implicated motion induced by the coupled aerodynamic force $(\rho B^3 / m_h) \omega_a^2 H_3^* \alpha$, which affects heaving vibration energy.

Under the critical flutter wind speed, $U=13.5\text{m/s}$, the relationship between the aerodynamic damping force $(\rho B^2 / m_h) \omega_h H_1^* \dot{h}$ and the vibration velocity is shown as Fig. 9a. In the first two periods, the aerodynamic damping force and the heaving velocity is out phase, so the heaving vibration energy is consumed, while in the following several periods, both of them have the same phase, so the heaving vibration gets positive energy. Due to the larger consumed energy, however, the total energy form the aerodynamic damping force $(\rho B^2 / m_h) \omega_h H_1^* \dot{h}$ is negative shown in Fig. 9b.

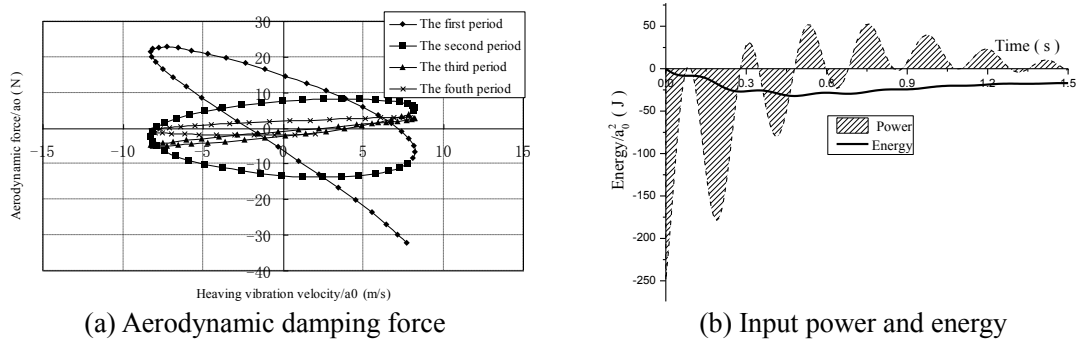


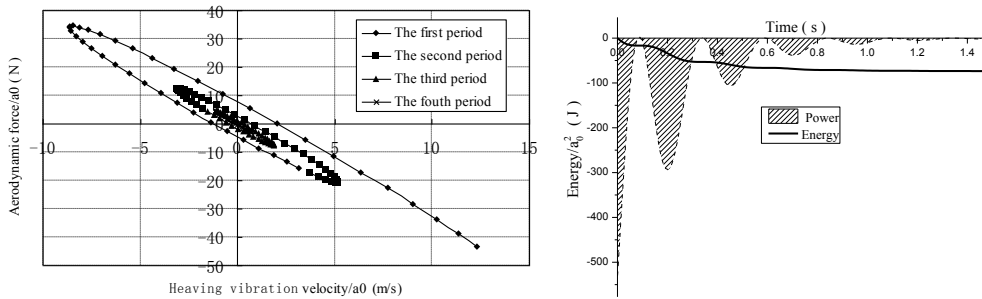
Figure 9: Force and energy related to $(\rho B^2 / m_h) \omega_h H_1^* \dot{h}$

(2) Input energy from $(\rho B^3 / m_h) \omega_a H_2^* \dot{\alpha}$ and $(\rho B^3 / m_h) \omega_a^2 H_3^* \alpha$

When the coupled aerodynamic lift forces, $(\rho B^3 / m_h) \omega_a H_2^* \dot{\alpha}$ and $(\rho B^3 / m_h) \omega_a^2 H_3^* \alpha$, induced by the

pitching main motion, act on heaving vibration, these two forces transfer some energy in pitching vibration to heaving vibration, and then feed more energy back to pitching vibration due to the feedback of heaving vibration. With this feedback action, pitching vibration energy is getting more and more, but heaving vibration reduces gradually. The coupled aerodynamic force of $(\rho B^3/m_h)\omega_a^2 H_3^* \alpha$ feeds more energy back to pitching vibration than the force of $(\rho B^3/m_h)\omega_a H_2^* \dot{\alpha}$ does.

The relationship between the coupled aerodynamic lift force related to $(\rho B^3/m_h)\omega_a^2 H_3^* \alpha$ and $(\rho B^3/m_h)\omega_a H_2^* \dot{\alpha}$ and the heaving vibration velocity is shown in Fig. 10a. Because the phase between them is opposite, the coupled aerodynamic lift force consumed the heaving vibration energy. Since the curve intercept is not equal but close to zero in each cycle, the consumed energy is closely related to the phase difference, and its variation with time is shown in Fig. 10b.



(a) Coupled aerodynamic lift force (b) Input power and energy
 Figure 10: Force and energy related to $(\rho B^3/m_h)\omega_a H_2^* \dot{\alpha}$ and $(\rho B^3/m_h)\omega_a^2 H_3^* \alpha$

(3) Input energy from $(\rho B^2/m_h)\omega_h^2 H_4^* h$

The aerodynamic stiffness force $(\rho B^2/m_h)\omega_h^2 H_4^* h$ has small value, and the input energy from the force to the heaving vibration system gradually reduces and can be neglected.

6. ENERGY CONVERSION MECHANISM OF AERODYNAMIC FLUTTER

The energy conversion mechanism of aerodynamic flutter of the closed box can be illustrated by the total pitching vibration energy and the total heaving vibration energy contributed by all kinds of aerodynamic moments and forces.

The total input energy in the pitching vibration system is contributed by the coupled pitching moment of $(\rho B^3/I)\omega_h A_1^* h_{11}(t)$, the aerodynamic damping moment of $(\rho B^4/I)\omega_a A_2^* \dot{\alpha}$ and the aerodynamic stiffness moment of $(\rho B^4/I)\omega_a^2 A_3^* a_0(t)$, and can be calculated by the summation of the right hand sides of Eqs. 17, 18 and 19. The total input energy and the dissipation energy, the damping consumed energy, of the pitching vibration system vary with wind speeds as shown in Fig. 11. Although both kinds of energy decrease and increase with the increase of the wind speed during $2\text{m/s} < V < 7\text{m/s}$ and $7\text{m/s} < V < 13.5\text{m/s}$, respectively, the total input energy is always smaller than the dissipation energy, and there is no vibration or stable vibration occurred. When the wind speed exceeds 13.5m/s, the total input energy is obviously greater than the dissipation energy, and accordingly the pitching vibration becomes unstable or flutter divergence. The critical wind speed, $U = 13.5\text{m/s}$, is regarded as critical flutter speed of the system.

The total input energy in the heaving vibration system is contributed by the aerodynamic damping force of $(\rho B^2/m_h)\omega_h H_1^* \dot{h}$ and the coupled aerodynamic lift force of $(\rho B^3/m_h)\omega_a H_2^* \dot{\alpha}$. Fig. 12 describes the variation of the total input energy and the dissipation energy of the heaving vibration system with wind speeds. When the wind speed is less than 10m/s, the total input energy is always smaller than the dissipation energy, and there is no vibration or stable vibration occurred. With the increase of wind speed beyond 10m/s, the heaving vibration with the frequency of ω_h is damped out, and the heaving vibration energy is feedback to pitching vibration system through the forced heaving motion with the frequency of ω_a since the total input energy is greater than the dissipation energy.

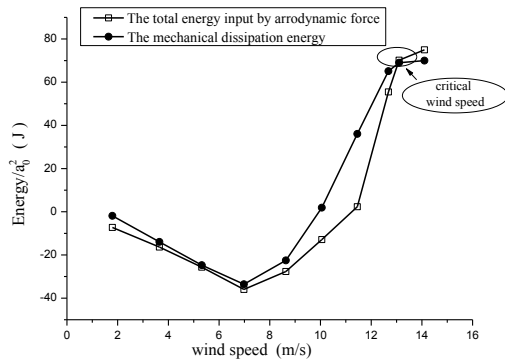


Figure 11: Pitching vibration energy

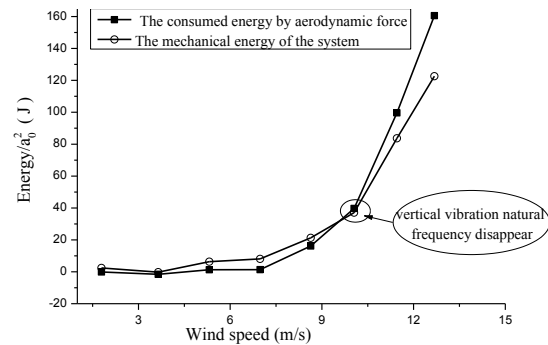


Figure 12: Heaving vibration energy

7. CONCLUSIONS

The energy conversion mechanism of coupled aerodynamic flutter has been revealed by a two-dimensional and 2DOF model for a typical box girder section. The coupled aerodynamic flutter is controlled by energy input and output through the heaving and pitching degrees of freedom with the phase difference. The input energy in the pitching degree of freedom is composed of coupled aerodynamic moment, aerodynamic damping moment and aerodynamic stiffness moment, and the output energy is only the dissipation energy through structural damping during pitching vibration. The input energy in the heaving degree of freedom consists of coupled aerodynamic lift force and aerodynamic damping force, and the output energy includes not only the dissipation energy, which damps out the heaving vibration with the frequency of ω_h , but also the feedback energy to pitching vibration system through the forced heaving motion with the frequency of ω_α . It can be concluded that the pitching vibration energy during the box girder coupled flutter constantly increases, but the heaving vibration energy gradually decreases due to its feedback to the pitching vibration system, which result in coupled aerodynamic flutter dominated by the pitching vibration when the total input pitching vibration energy is greater than the dissipation energy through structural damping.

ACKNOWLEDGEMENT

The authors gratefully acknowledge the support of Ministry of Science and Technology under the grants of 973 Program with 2013CB036300 and SLDRCE Program with SLDRCE09-A-01, and National Natural Science Foundation of China under the grants of 51323013 and 51208197.

REFERENCES

- 1) Scanlan, R H.: The action of flexible bridges under wind, I: flutter theory, *J. Sound and Vib.*, Vol. 60, No.2, pp. 187-199, 1978.
- 2) Matsumoto, M.: Flutter classification of bridge girders, *Proceedings of the 1st International Symposium on Wind and Structures for the 21st Century*, pp. 39-79, 2000.
- 3) Matsumoto, M., Shirato, H., Shijo, R.: Flutter stabilization of long span bridges, *Proceedings of the 2nd International Symposium on Advances in Wind and Structures*, pp. 257-264, 2002.
- 4) Matsumoto, M., Mizuno, K., Okubo, K., Ito, Y., Kim, G.: Flutter instability mechanism – coupled flutter and torsional flutter, *Proceedings of the 6th Asia-Pacific Conference on Wind Engineering*, 2005.
- 5) Larsen A.: Aerodynamics of the Tacoma Narrow Bridge - 60 years later, *J. Journal of Structural Engineering International*, Vol. 10, No. 4, pp. 243-248, 2000.
- 6) Yang, Y.X., Ge, Y.J., Xiang, H.F.: Coupling effects of degrees of freedom in flutter instability of long span bridges, *Proceedings of the 2nd International Symposium on Advances in Wind and Structures*, pp. 625-632, 2002.
- 7) Yang, Y.X., Ge, Y.J., Xiang, H.F.: Research on the coupled bending-torsional flutter mechanism for thin

- plate sections, *J. Engineering Mechanics*, Vol. 23, No. 12, pp. 2-8, 2006.
- 8) Yang, Y.X., Ge, Y.J., Xiang, H.F.: Flutter control effect and mechanism of central-slotting for long-span bridges, *J. China Civil Engineering (in Chinese)*, Vol. 39, No. 7, pp. 74-80, 2006.
 - 9) Ding, Q.S., Zhu, L.D.: Aerodynamically coupling flutter analysis and flutter mechanism for bridge deck section1, *J. China Civil Engineering (in Chinese)*, Vol. 40, No. 3, pp. 69-73, 2007.
 - 10) Liu, G.: Flutter analysis of long-span suspension bridges by energy method, *J. China Highway and Transport*, Vol. 12, No. 3, pp. 20-24, 2000.

On the historical mistakes of classic fluid dynamics theory

Baku M. NAGAI⁺¹

⁺¹ Okinawa Peace Club, Okinawa, Japan

Since the Year 2002, the author has pointed out the historical mistakes of classic fluid dynamics theory and of vortex flow theory. A typical mistaken theory says that every vortex pair shall move at the fixed velocity ($\Gamma/2\pi a$) relatively to the fluid filled static space and any vortex ring shall have their fixed self moving speed. Owing to author's presentations over 13 years in international and domestic conferences, today, his discovery has been recognized almost all over the world especially among the specialists and authorities in this academic field. However, in spite of the crucial importance of the problem, his discovery has not yet been officially accepted nor recognized as a true. This paper may be the final presentation about the mistaken theory, because the mistakes are very simple as easy as to be understood by even high-school students when it is cleared. We must not hesitate to correct mistakes when we aware the facts.

Keyword: Fluid Dynamics Theory, Vortex Flow, and Historical Mistakes.

1. TRUTH OF THE VORTEX MOTION

With the ideal fluid dynamics theory, flow field around a vortex pair is presented as in Figure 1¹⁾. The vortex pair is of course stationary relative to the fluid filled space. As there is no outer force on the system of flow, the vortex pair does not necessarily move at any special speed. It may have arbitral moving speed including zero speed relative to the space. Obviously Figure 1 shows the zero speed case.

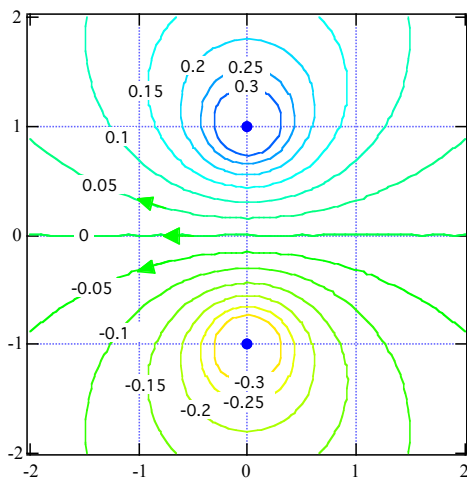


Figure 1. Flow field around a stationary vortex pair

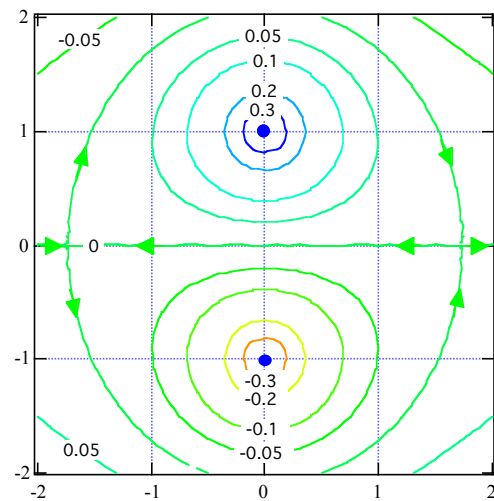


Figure 2. Superposition of a uniform flow on the flow field around the static vortex pair

Figure 2 shows another case of flow field when the vortex pair has a slowly moving speed. The flow is obtained by the superposition of a uniform flow on the flow around the stationary vortex pair. This flow is a special case, because the superimposed uniform flow speed is just $\Gamma/2\pi a$ at which the vortex pair has been believed to have to move for long time. Where, Γ is circulation of the vortex and a is length between two vortices.

⁺¹megumi-wind@woody.ocn.ne.jp

The difference of the flow fields between Figures 1 and 2 is very clear, one is the static vortex pair and other is the moving pair. So, why the mistaken theory “Every vortex pair shall move at the fixed speed $\Gamma / 2\pi a$ ” has been survived so long time? Fortunately, the author has noticed the reason at early time on the textbook of Professor Ludwig Prandtl²⁾, Founder of the Boundary Layer Theory.

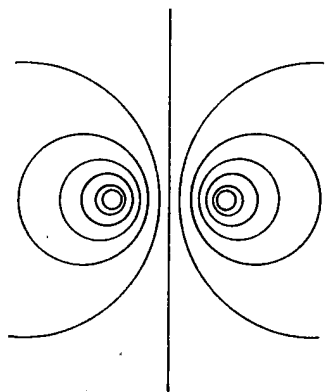


Bild 2/47. Stromlinien eines Wirbelpaares; ruhendes Bezugssystem

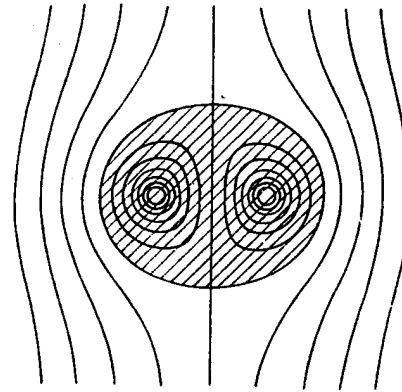


Bild 2/48. Stromlinien eines Wirbelpaares; Bezugssystem mit den Wirbelkernen mitbewegt

Figure 3. From Prandtl’s Textbook

Figure 3 represents streamlines around a stationary vortex pair and a moving vortex pair from the textbook. However in the textbook, Prandtl says Fig. 2/47 (LHS) shows stream lines around a moving vortex pair observed by Static System of Coordinates and Fig. 2/48 (RHS) shows same flow field observed by Moving System of Coordinates so that two flow fields are the same of an actually moving vortex pair in fluid filled static space. Is it right? Observers coordinates systems are different?

Obviously it was a very simple mistake of Professor Prandtl about the relativity of motions and about the observation coordinates. However his saying had a crucial effect on his colleagues and successors, and contributed the settling of the fundamental misunderstandings over about a century.

In the next, the author looked for any examples of the static vortex pair in nature. One has been found in his own book “Thinking fluid dynamics with dolphins”, printed in year 2002 the same year of the discovery of mistaken theory. Figure 4 represented from the book.

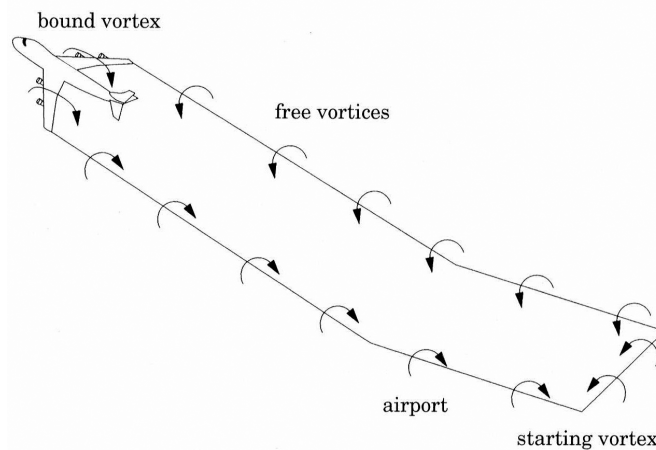


Figure 4. Vortices generated by an airplane³⁾



Figure 5 An example of stationary vortex pair (Photo. Nov. 10th, 2002 by Mr. Saizo Uchida)

In sunny days, we often see airplane clouds spreading from the airplane wingtips in the blue sky as in Figure 5. As well known, the cloud is the visualization of the free vortices generated by airplane lifting wings. Figure 4 is the illustration of an airplane generating vortices⁽⁵⁾. Starting vortex that is left at airport, bound vortex that is the airplane wing and the spreading free vortices all together make a huge vortex ring as in the figure. The author happened to know that the elongated two straight lines of free vortices be a vortex pair. An example of stationary vortex pair does exist only above our heads in daily life. Theoretically, we can treat stationary vortex pair and moving vortex pair with arbitral constant speed.

As in the cases of vortex pair, we can say that there may exist space fixed vortex ring and moving vortex ring of arbitrary moving speed. Vortex rings do not necessarily move at the fixed velocity as believed in fluid dynamics theory for long time.

2. New development of vortex flow theory

After finding the historical mistakes of vortex flow theory, the author examined some other flow fields, which are connecting with vortices. One case of the very simple flow fields is the flow around a rotating circular cylinder. In two-dimensional steady flow problem, classical theory taught us that the circumferential velocity distribution becomes hyperbola. How about in the unsteady case problem? The modern viscous fluid dynamic theory explains as follows. At the first instance of rotation, fluid particles neighbor to the circular cylinder wall start to move by the effect of fluid viscosity, then the outer particles start to move one by one. Finally viscosity spread out to infinity, then the velocity distribution becomes coincident to that of non-viscous fluid theory.

At the first instance fluid particle begin to move by the influence of fluid viscosity, but finally there is no effect of viscosity. So, it seems strange enough and very paradoxical. Actually in the physical experiment, circumferential velocity could not reach the theoretical value. Differences between theory and experiment are very large. To solute this new paradox, the author has recently introduced a hypothesis that there remains the finite vortex layer neighbour to rotating circular cylinder surface⁴⁾.

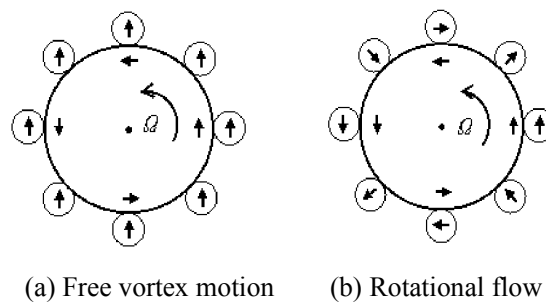


Figure 6. Concepts of free vortex motion and rotational motion of the outer flow

Figure 6 shows the concept of the hypothesis. In the figure, (a) represents so far theoretical free vortex motion and (b) is the rotational flow case of the hypothesis. Every inner fluid particle rotates anticlockwise once at a cylinder rotation in both case. Outer fluid particle does not rotate in conventional free vortex motion case. While in rotational flow case, particle adjacent to the outer wall rotate clockwise once at a cylinder rotation. When fluid particles are resembled like as wheels of finite radius, the wheels should not slip over the wall surface but rotate on.

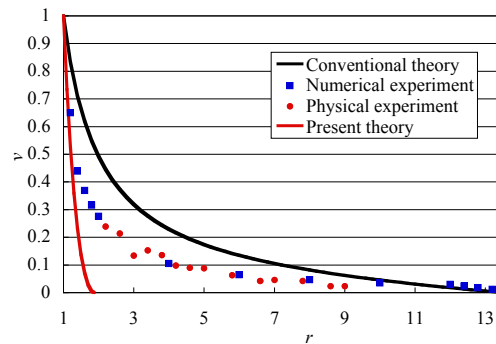


Figure 7. Velocity distributions comparing the conventional theory with numerical, physical experiments and the author's new theory

Figure 7 represents the comparison of the conventional theory and the author's new hypothesis theory with numerical and physical experiments. The figure suggests us that the hypothesis might show a route to solve the problem. While, it is very interesting that the numerical and physical experiments show almost same behavior of velocity distributions. How is it understood? One of possible reasons may be in digital characteristics of CFD, divergence or molecular character as like as actual fluid particles. Digital data distribution is not smooth, nor continuous. On the other hand, an analytical differential equation forms on the assumption of continuous fluid. It may be said that the digital character of CFD has happened to represent the behaviour as like as actual fluid particle.

ACKNOWLEDGMENT

The author acknowledges every member who discussed in deep about the problem in the term of preparation of this first international symposium on flutter. The author also sincerely hopes early rewriting of all fluid dynamic textbooks about the mistaken vortex theory and early co researching on the fine fluid flow mechanics at the boundary between fluid and solid surface.

REFERENCES

- 1) Nagai, M., and Ameku, K., "On the Motion of a Vortex Ring and a Vortex Pair", *Proceedings of the 5th JSME-KSME Fluids Engineering Conference held in Nagoya, Japan, 2002-11*, 5p.
- 2) Prandtl, L., *Führer durch die Strömungslehre*, Friedr. Vieweg & Sohn, 1949, 72.
- 3) Nagai, M., *Thinking Fluid Dynamics with Dolphins*, Ohm sha, 2002-2, 33.
- 4) Nagai, B.M. and Ameku, K. *The 4th International Symposium on Aero Aqua Bio-Mechanisms*, Shanghai, China, 2009-8.

LES OF AERODYNAMIC INSTABILITY OF A THREE-DIMENSIONAL SQUARE CYLINDER IN TURBULENT BOUNDARY LAYER

Yoshiyuki ONO⁺¹, Tetsuro Tamura⁺²

⁺¹ Technical Research Institute, Obayashi Corporation 4-640 Simokiyoto, Kiyose, Tokyo, Japan

⁺² Department of Environmental Science and Technology, Tokyo Institute of Technology
4259 Nagatsuta, Midori-ku, Yokohama, Japan

LES method is applied to the flow around a freely oscillating three-dimensional square cylinder in turbulent boundary-layer. The computed results are validated through comparison with the previous experiments and the unstable response characteristics of a three-dimensional square cylinder are investigated.

Keyword: Aerodynamic instability, LES, three-dimensional cylinder, rocking oscillation mode

1. INTRODUCTION

Recent advancements in computer performances have made it possible to carry out simulations of wind flows around buildings more easily than before. Descriptions concerning CFD-based wind load prediction methods appeared for the first time in the “Recommendations for Loads on Buildings (2015, Architectural Institute of Japan)”. Therefore the validations of the LES model under the adequate numerical model and an appropriate computational condition are required. Especially, the estimation of aerodynamic instability is associated with the safety of the structure. The applicability of the LES models should be carefully examined.

Until now, many computational investigations regarding as aerodynamic instability have been reported. However, almost all of the computations are simulate the flow around a two-dimensional bluff body in smooth flow. Few simulations have so far been made as to the flows around a freely-oscillating three-dimensional structure in turbulent boundary-layer. Furthermore, number of the reduced velocities is not enough to discuss the applicability of CFD model due to the lack of computational resources.

In the previous researches, the various characteristics of a two-dimensional square cylinder in the smooth flow are reported. Scruton¹⁾ showed the response characteristics depending on damping ratio. The onset occurs near the resonant velocity of the vortex shedding and then nearly linearly increases as the velocity increases in the case of low damping ratio. In the high damping cases, the separation of the onset region is recognized. The vortex-induced oscillation occurs near the resonant velocity of the vortex shedding and the galloping oscillation is recognized in the high velocity region. On the other hand, according to the previous research by Kawai²⁾ in the case of the three-dimensional square cylinder in the boundary-layer turbulence, the response characteristics are not greatly affected by damping ratio²⁾. Even in the case of high damping ratio, the oscillations were recognized in the high velocity region. Also, according to the previous research by Novak³⁾, the response in the case of the three-dimensional square cylinder gradually increases in comparison with those of the two-dimensional cylinder.

In this paper, LES method⁵⁾ is applied to the flow around a freely-oscillating square cylinder in the boundary-layer turbulence in order to clarify the applicability of CFD model to the estimation of the aerodynamic instability.

On the other hand, the development of the recent computer ability is remarkable, and the super parallel computer brings enormous computed results at a time. Concerning the computation of aerodynamic instability,

⁺¹ono.yoshiyuki@obayashi.co.jp, ⁺²tamura.t.ab@m.titech.ac.jp

the response amplitudes in many cases which are set various reduced velocities can be computed at a time. The same initial condition is used such as the computed flow around the rest cylinder. It is well known that the bifurcation of the response of a square cylinder is recognized⁴⁾, when the oscillations are started from the rest.

First, in order to investigate the above bifurcation of the response when oscillation starts from rest, the LES method is applied to the flow around a free oscillating two-dimensional square cylinder in smooth flow. The response characteristics of the two-dimensional square cylinder are discussed. Next, the response characteristics of the three-dimensional square cylinder in the boundary-layer turbulence are validated compared with the previous experiments and the response characteristics are investigated.

2. PROBLEM FORMULATION

2.1 Methods of LES Analysis

The governing equations are given by the incompressible Navier-Stokes and the continuity equations as follows;

$$\frac{\partial u_i}{\partial t} = -\frac{\partial}{\partial_j} u_i u_j + \frac{1}{Re} \frac{\partial^2 u_i}{\partial x_j \partial x_j} - \frac{\partial p}{\partial x_i}, \quad (i=1,2,3) \quad (1)$$

$$\frac{\partial u_i}{\partial x_i} = 0 \quad (2)$$

where u_i ($i=1,2,3$), p , t denote the velocity, pressure and time. $Re (= U_0 B/\nu)$ is the Reynolds number, B : breadth of the square cylinder ($U_0 = U_\infty$: free stream incoming velocity, $U_0 = U_H$: incoming velocity at the height of the cylinder top in the case of a three dimensional cylinder in boundary-layer turbulence), ν is the kinematic viscosity.

To advance the solutions of velocities and pressure in time, a fractional step method is employed. The time integral of the momentum equation is hybrid, that is to say, the Crank-Nicolson scheme is applied to the viscous terms and the explicit third-order Runge-Kutta method is used for convective terms.

In this simulation, the original governing equations (t, x_1, x_2, x_3) are transformed to curvilinear coordinate system ($\tau, \xi^1, \xi^2, \xi^3$) and then are filtered. The present scheme can be written as

$$\frac{(J\bar{u}_i^*)^k - (J\bar{u}_i)^{k-1}}{\Delta \tau} = -\gamma_k N(\bar{u}_i, u_{gi})^{k-1} - \delta_k N(\bar{u}_i, u_{gi})^{k-2} + \alpha_k (L(\bar{u}_i^*)^k + L(\bar{u}_i)^{k-1}) \quad (3)$$

$$\frac{(J\bar{u}_i)^k - (J\bar{u}_i^*)^k}{\Delta t} = -\left(\frac{\partial}{\partial \xi^m} \frac{\partial \xi^m}{\partial x_i} \bar{\phi} \right)^k, \quad (k=1,2,3) \quad (4)$$

$$\left(\frac{1}{J} \left(\frac{\partial (J\bar{U}^m)}{\partial \xi^m} \right) \right)^k = 0, \quad \bar{U}^m = \frac{\partial \xi^m}{\partial x_j} \bar{u}_j \quad (5),(6)$$

where $k=1,2,3$ denotes the sub-step number for the Runge-Kutta method, and \bar{u}_i^0 and \bar{u}_i^3 are equivalent to the velocities at time step n and $n+1$. J denotes Jacobian of the transformation. $L(\bar{u}_i)$, $N(\bar{u}_i, u_{gi})$ represent finite difference approximations to the viscous and convective terms:

$$L(\bar{u}_i) = \frac{\partial}{\partial \xi^m} \left(\left(\frac{1}{Re} + \nu_{SGS} \right) J \frac{\partial \xi^m}{\partial x_j} \bar{S}_{ij} \right) \quad (7)$$

$$N(\bar{u}_i, u_{gi}) = \frac{\partial}{\partial \xi^m} (J(\bar{U}^m - U_g^m) \bar{u}_i) \quad (8)$$

$$U_g^m = \frac{\partial \xi^m}{\partial x_j} u_{gj} \quad (9)$$

where $\bar{\phi}$ is the scalar potential function. $\bar{\phi}$ and the pressure \bar{p} are related by

$$\frac{\partial \bar{\phi}^k}{\partial x_i} = 2\alpha_k \frac{\partial \bar{p}^k}{\partial x_i} - \alpha_k L(\bar{u}_i^k - \bar{u}_i^{*k}) \quad (10)$$

The pressure at time step n+1 is computed by

$$\bar{p}^{n+1} = 3 \left(\bar{\phi}^3 + \frac{\Delta t}{2} \left(\frac{1}{\text{Re}} + \nu_{SGS} \right) \nabla^2 \bar{\phi}^3 \right). \quad (11)$$

The parameters in Eq. (3) are given by

$$\begin{aligned} \alpha_1 &= \frac{4}{15}, \quad \alpha_2 = \frac{1}{15}, \quad \alpha_3 = \frac{1}{6}, \\ \gamma_1 &= \frac{8}{15}, \quad \gamma_2 = \frac{5}{12}, \quad \gamma_3 = \frac{3}{4}, \\ \delta_1 &= 0, \quad \delta_2 = -\frac{17}{60}, \quad \delta_3 = -\frac{5}{12} \end{aligned} \quad (12)$$

\bar{S}_{ij}, ν_{SGS} in equation (6) are given by

$$\bar{S}_{ij} = \frac{1}{2} \left(\frac{\partial \bar{u}_i}{\partial \xi^m} \frac{\partial \xi^m}{\partial x_j} + \frac{\partial \bar{u}_j}{\partial \xi^n} \frac{\partial \xi^n}{\partial x_i} \right) \quad (13)$$

$$\nu_{SGS} = 2C J^{2/3} |\bar{S}|, \quad |\bar{S}| = \sqrt{2\bar{S}_{ij}\bar{S}_{ij}} \quad (14),(15)$$

u_{gj} ($i=1,2,3$) in equation (9) represent the velocities of the grid point on the moving mesh. The velocities at sub-step k is calculated by

$$u_{gi}^k = u_{gi}^n + (u_{gi}^{n+1} - u_{gi}^n) \left(\sum_{l=1}^k 2\alpha(l) \right) \quad (16)$$

To obtain the solutions that satisfy the conservation laws, a finite volume method is employed in a collocated grid system. Spatial derivatives of variables are treated as second-order central difference. Convective terms are approximated using the higher-order interpolation method (Kajishima, 1993).

It is not easy to carry out stable computation, when dealing with high Reynolds number flow. To avoid the numerical instability near a circular cylinder, the very slight numerical dissipation is added to convective terms. Namely, the convective terms are approximated as follows;

$$\left[\frac{\partial}{\partial \xi} J(U - U_g)u \right]_{(i)} \cong \left[\delta_\xi (J(U - U_g) \bar{u}^\xi) \right]_{(i)} \quad (17)$$

$$+ \varepsilon \left[J|U \right]_{(i)} \frac{u_{i-2} - 4u_{i-1} + 6u_i - 4u_{i+1} + u_{i+2}}{12}$$

$$\left[\bar{u}^\xi \right]_{(i)} = \frac{-u_{i-3/2} + 9u_{i-1/2} + 9u_{i+1/2} - u_{i+3/2}}{16}$$

$$\left[\delta_\xi f \right]_{(i)} = \frac{f_{i-3/2} - 27f_{i-1/2} + 27f_{i+1/2} - f_{i+3/2}}{24} \quad (18)$$

ε is numerical dissipation parameter for controlling the effects on the solutions. In the present computation, computational mesh is regenerated at the every sub-step k as follows;

$$x_{gi}^k = x_{gi}^n + (x_{gi}^{n+1} - x_{gi}^n) \left(\sum_{l=1}^k 2\alpha(l) \right) \quad (19)$$

It is well known that conservation laws for discretized fluid dynamics equation may be violated, when computational grids moves and transformed. This problems lead to unphysical fluctuation of the flow around a cylinder. In the present computation, according to the Geometric Conservation Law (Thomas, 1979), the following terms $G(u_i, u_{gi})$ is add to equation (3).

$$G(\bar{u}_i, u_{gi}) = -\gamma_k N_g(\bar{u}_i, u_{gi})^{k-1} - \delta_k N_g(\bar{u}_i, u_{gi})^{k-2} + \bar{u}_i^{k-1} \frac{J^k - J^{k-1}}{\Delta \tau} \quad (20)$$

$$\text{where } N_g(\bar{u}_i, u_{gi}) = \bar{u}_i \frac{\partial J U_g^m}{\partial \xi^m} \quad (21)$$

Concerning SGS model, the dynamic Smagorinsky model (Lilly, 1992) is chosen.

An equation of motion of a three-dimensional circular cylinder with rocking oscillating mode is written by

$$I \frac{d^2 \varphi(t)}{dt^2} + c \frac{d\varphi(t)}{dt} + k\varphi(t) = \frac{1}{2} \rho U_0^2 D H^2 C_{MX} \quad (22)$$

Where φ is the response angle around x-axis (as shown in Figure 1 (b)) ; I is moment of inertia; C_{MX} is moment coefficient around x-axis, H is the height of the cylinder.

In the case of three-dimensional circular cylinder, the Scruton number and mass-ratio are defined as follows:

$$Sc = \frac{2m^*}{\rho D^2} 2\pi h \quad \gamma = \frac{m^*}{3\rho D^2} \quad (23),(24)$$

Where $m^* = m/H$.

By using $\tau = tU_0 / D$, $Vr = 2\pi U_0 / (D\sqrt{I/k})$, Sc and γ , the equation (22) becomes

$$\frac{d^2 \varphi(\tau)}{d\tau^2} + \frac{Sc}{2\pi\gamma} \left(\frac{2\pi}{Vr} \right) \frac{d\varphi(\tau)}{d\tau} + \left(\frac{2\pi}{Vr} \right)^2 \varphi(\tau) = \frac{D}{H} \frac{C_{MX}}{2\gamma} \quad (25)$$

where $c = 2h\omega I$. The equation (25) are calculated by the linear acceleration method.

3. NUMERICAL MODEL

As a computational model, we deal with a square cylinder. In the case of a two-dimensional cylinder, the length of the span-wise direction of the cylinder is set to $4B$. The three kinds of Scruton number ($Sc=10, 20, 30$) are used and the mass ratio is set to 120.

On the other hand, in the case of three-dimensional cylinder, the aspect ratio (H/B) is 10 according to the experiments by Kawai²⁾. In the experiments, Sc numbers are 9.5,73 and mass ratio γ is 31. The experiments are performed in some kinds of boundary-layer turbulence, we choose the urban type where power index of the mean velocity profile is 0.3.

Inflow turbulence is generated using the Lund's methods (1998) on the smooth boundary, and then developed over the upwind fetch with the surface roughness. Fig.1 shows the comparison of computed results for profiles of time-averaged velocity and turbulent intensity with the experimental data. The present computations show good agreement with the experimental results.

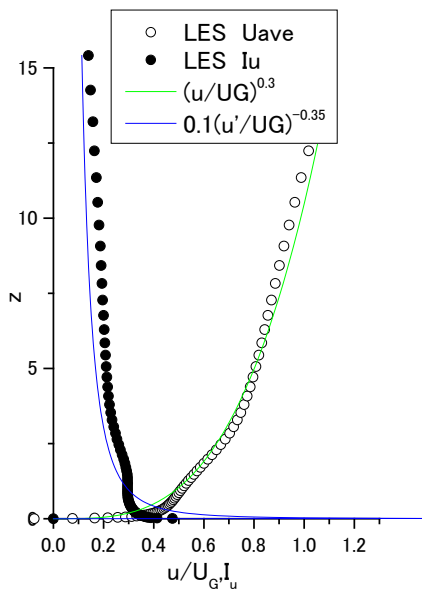


Fig.1 Profile of the computed inflow turbulence

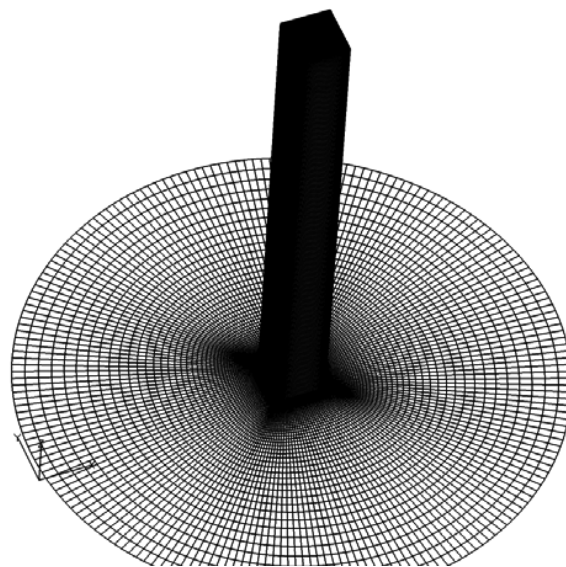


Fig.2 Computational mesh

4. NUMERICAL CONDITION

Fig.2 shows the computational mesh in the present computations. We set 200×90 grid points to a partly O -type region on the X - Y cross section. The grid point in the vertical direction is 220. Smallest grid size near the cylinder surface is $0.1 / (Re)^{0.5}$ ($Re = U_H B / \nu$; U_H is oncoming velocity at the height of the cylinder, ν is the kinematic viscosity). The computational mesh for a two-dimensional cylinder is the same of the bottom surface of the three-dimensional case.

In the case of uniform flow in $2D$ and $3D$ cases, $U_0 = U_\infty$ is imposed at upstream boundary, while the generated inflow turbulence is given in the case of turbulent flow. The convective condition is used at the downstream boundary. No-slip condition is used at the cylinder surface. The initial condition is given by the

flow around a stationary circular cylinder. In the case of a two-dimensional circular cylinder, the periodic condition is used in the span-wise direction. On the other hand, the free-slip condition and no-slip condition are imposed at the upper and the bottom boundary in the case of a three-dimensional circular cylinder. The Reynolds number ($= U_0 D/\nu$, $U_0 = U_\infty$, $U_0 = U_H$ in 3D cases in boundary-layer turbulence) is equal to 20,000. The dimensionless time interval $\Delta t U_0/D$ is 0.004.

5. COMPUTATIONAL RESULTS

5.1 Two-dimensional square cylinder

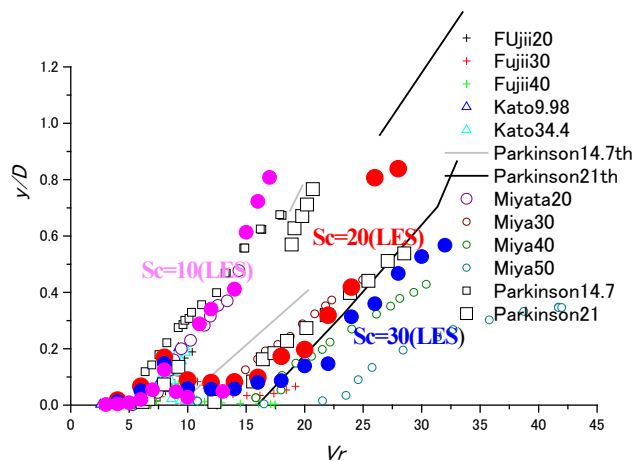


Fig. 3 Comparison of the computed response amplitude with the experiments^(6,7)

In 5., the response characteristics for a two-dimensional square cylinder in smooth flow computed results are compared with the previous experiments. Fig.3 shows comparison of the computed results with the experimental results, including the theoretical galloping curve by Parkinson⁴⁾.

In the case of $Sc=10$, the response increases from near $Vr=6$ and nearly linearly develops as the velocity increases. On the other hand, in the case of $Sc=20, 30$, the vortex-induced oscillation are recognized near $Vr=8$, and then the response decreases near $Vr=10$. Furthermore the response amplitude also shows the onset near $Vr=15$. Namely, it is confirmed that the present computations can simulate the separation of the vortex-induced oscillation from galloping-type oscillation. Scruton shows that separation of vortex-induced oscillation from the galloping-type oscillation occurs under the lower Scruton number than around 16 conditions. The present computations show good agreement with the experiments¹⁾ by Scruton. Concerning the response values at $Sc=20, 30$, the present computations are in good agreement with the experimental results by Parkinson⁴⁾. Also, the response amplitudes approach the upper branch of the theoretical galloping curve in the higher velocity region. Looking at the Fig. 3 in details, the unstable amplitudes are recognized in the reduced velocity region from $Vr=10$ to $Vr=13$. Fig. 4 shows the time history of the response amplitude in the unstable region from $Vr=10$ to $Vr=14$. In the cases of $Vr=10$ and 12, the response amplitudes are small and randomly oscillating. On the other hand, in the cases of $Vr=13$ and 14, after small amplitudes are randomly repeated, the response amplitudes gradually increase and converge to the constant value. Namely, only if the amplitude instantaneously reaches a constant value, the response amplitude develops to the galloping-type oscillation. If the response doesn't reach to a constant value, the small amplitudes are maintained. Therefore it is recognized the present computation can simulate the tendency as shown the previous experiments. It is noted that the response amplitude tends to converge fast in the velocity region that is higher than an unstable region as shown Fig. 5.

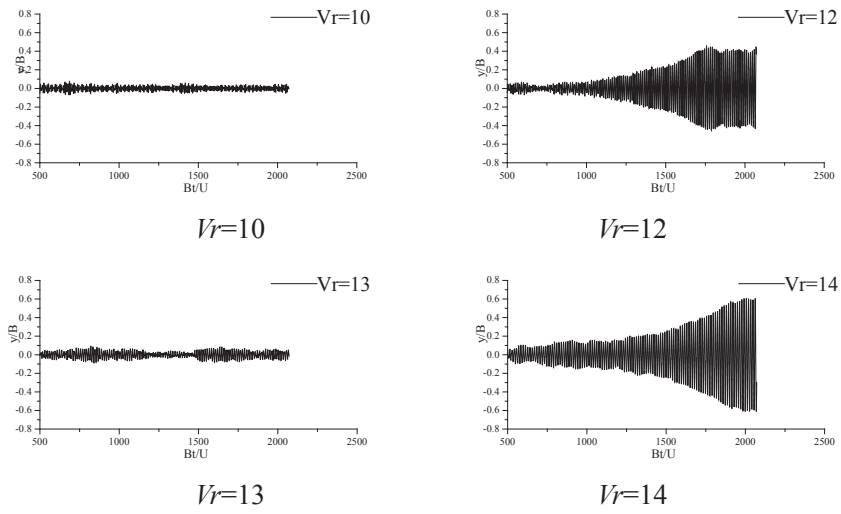


Fig. 4 The time history in the unstable region (two-dimensional square, $Sc=10$)

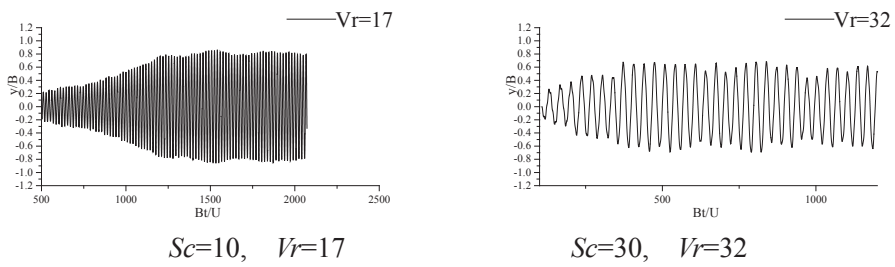


Fig. 5 The time history in the higher velocity region (two-dimensional square, $Sc=10$)

5.2 Three-dimensional square cylinder

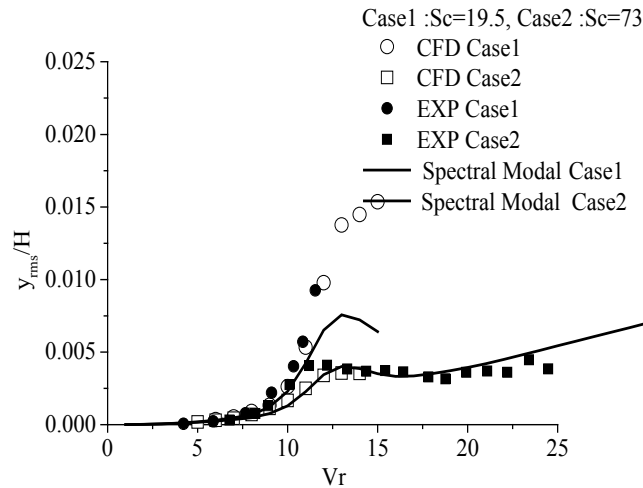


Fig. 6 The comparison of the response.

The response characteristics of the three-dimensional square cylinder in boundary-layer turbulence are investigated through comparison with those of the experiments. Fig.6 shows the comparison of the computed results of the response amplitude in the transverse direction to the stream-wise direction with those of the experimental results by Kawai ²⁾. Fig. 6 includes the predicted curves which are calculated by the spectral modal analysis method using fluctuating moment coefficients and power spectra of the stationary square cylinder.

In the case of high damping ratio ($Sc=73$), the response amplitudes gradually increases, as the velocity increases. The both results of the computations and the experiments tend to be roughly fit to the curve predicted by spectral modal analysis. Namely, the oscillations are not affected by motion-induced flow. The oscillation is forced by the turbulent flow around a square cylinder in boundary-layer turbulence. Namely, the response amplitudes in the higher velocity region which are recognized in the experiments by Kawai are the buffeting.

On the other hand, in the case of low damping ratio ($Sc=19.5$), the response amplitudes rapidly increase, and exceed the curve predicted by the spectral model analysis in the velocity region larger than $Vr=8$. The present computation can accurately simulate the response amplitudes in the experimental results, as the reduce velocity changes. The computed response amplitudes gradually increase in the velocity region larger than $Vr=12$, though the experimental data doesn't exist. This tendency is similar to the experimental results by Novak³⁾. It may be the response characteristics of a three-dimensional square cylinder in the boundary-layer turbulence.

In the case of the two-dimensional square cylinder in smooth flow, the bifurcations of the response in the unstable region are recognized as the oscillations are started from the rest. On the other hand, the bifurcation of the response is not recognized in the cases of the three-dimensional square cylinder in boundary-layer turbulence. Some response amplitude is forced by the turbulence even if the oscillation is started from the rest. Fig.7 shows the time history of the response in the cases of $Vr=8\sim 15$. In the case of $Vr=8$ where the response amplitude is corresponds to the predicted value by spectral moment method, the small amplitude randomly repeated affected by the turbulence. On the other hand, the unstable oscillations in the time history are recognized in the case $Vr=12\sim 15$ where the response amplitudes are exceed the predicted value by the spectral moment method. The large and the small amplitudes occur repeatedly. The large amplitude becomes dominant as the velocity increase.

In the case of the two-dimensional square cylinder in smooth flow, the bifurcation of the response occurred whether the amplitude reached a constant value or not. On the other hand, in the three dimensional cases, the amplitudes change in the vertical direction due to the oscillation mode. If the amplitude of the cylinder top exceeds a constant value, the amplitude in the lower region cannot reach to a constant value. The different response amplitude in the vertical direction causes the unsteady aerodynamic force to be disturbed, and results in the unstable response characteristics. As the velocity increases, the large amplitudes become dominant because the region more than a constant value expands.

6. CONCLUSION

The LES method was applied to the flow around a freely oscillating square cylinder in boundary-layer turbulence, the applicability of CFD approach to the estimation of the aerodynamic instability of the high-rise building was investigated. First, the LES method was applied to the flow around a free oscillating two-dimensional square cylinder in smooth flow and investigated the bifurcation of the response when oscillation starts from rest. Next, the response characteristics of the three-dimensional square cylinder in the boundary-layer turbulence were validated compared with the previous experiments and the response characteristics were discussed.

The following results are obtained.

1. First, the response characteristics for a two-dimensional square cylinder in smooth flow investigated. In the case of low damping ratio, the computed results showed that the response increased from near the resonant velocity and nearly linearly developed as the velocity increased. On the other hand, in the case of high damping ratio, the separation of vortex-induced oscillation from galloping-type oscillation was simulated. Therefore, it was confirmed the present computations showed good agreement with the experiments in the case of the two-dimensional square cylinder in smooth flow.
2. The bifurcation of the response of a two-dimensional square cylinder in smooth flow was investigated when the oscillation started from the rest. The computed response amplitude developed to the galloping-type oscillation, when the amplitude instantaneously reached a constant value. The small amplitudes were maintained if the response didn't reach a constant value.
3. Next, the response characteristics of the three-dimensional square cylinder in boundary-layer turbulence were investigated. The computed results were compared with those of the experiments for a three-dimensional square cylinder in boundary-layer turbulence. In the case of high damping ratio, the response amplitudes tended to be roughly fit to the curve predicted by spectral modal analysis. Namely, the response amplitudes in the higher velocity region which had been recognized in the experiments by Kawai were buffeting.
4. The response amplitudes rapidly increased at low damping ratio when the reduce velocity increased as observed in the experiments. The response amplitudes larger than $V_r=12$ show gradually increased. This tendency was similar to the experimental results in the case of a three-dimensional square cylinder.
5. The bifurcation of the response was not recognized in the cases of the three-dimensional square cylinder in boundary-layer turbulence. Some amplitude was caused by the turbulence even if the oscillation was started from the rest.
6. The unstable oscillations in the time history were recognized in the cases of the three-dimensional square cylinder in boundary-layer turbulence. The large and the small amplitudes were recognized repeatedly. The different response amplitude in the vertical direction by the oscillation mode caused the unsteady aerodynamic force to be disturbed, and resulted in the unstable response characteristics.

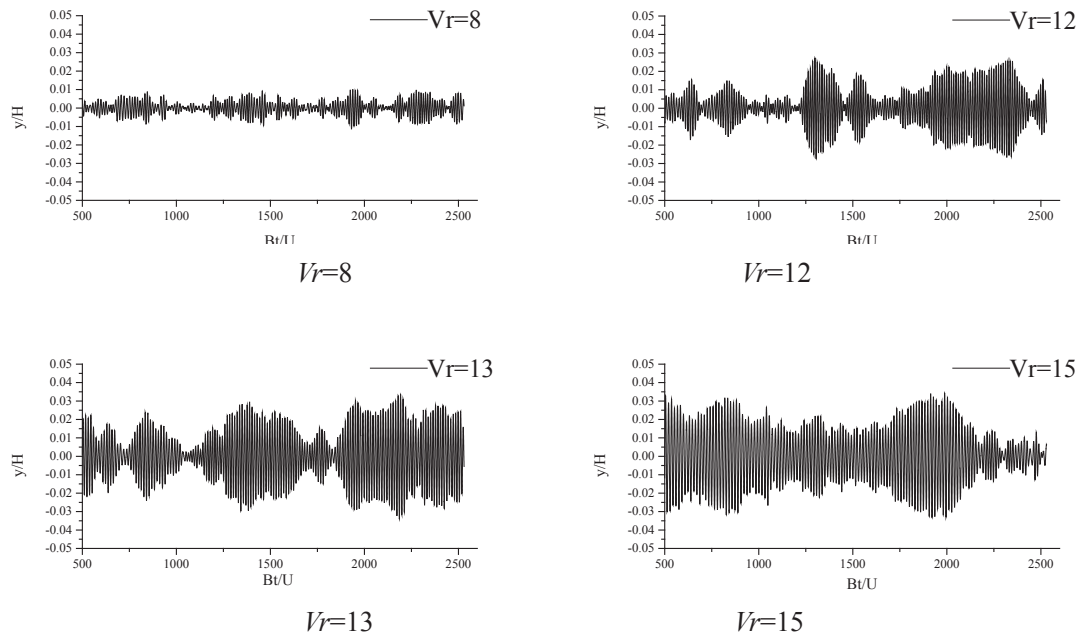


Fig.7 the time history of the response (three-dimensional square)

REFERENCES

- 1) C., Scruton: On the wind excited oscillations of stacks, towers and masts, Proc. Int. Conf. Wind Effects on Build and Struct. , 298, 1963.
- 2) H. Kawai: Vortex Induced Vibration of Tall Buildings, Journal of Wind Engineering and Industrial Aerodynamics, Vol.41, pp.117-128, 1992.
- 3) M. Novak, A. Davenport: Aero-elastic instability of prism in turbulent flow, J. of Engineering mechanics division, Proceeding of American Society of Civil Engineers, 17,1970.
- 4) G., V., Parkinson: Some considerations of combined effects of galloping and vortex resonance, Journal of Wind Eng., Ind., Aerodynamics, 8, 135, 1981.
- 5) Y., Ono, T., Tamura: Large eddy simulation using a curvilinear coordinate system for the flow around a square cylinder, Wind & Structure, Vol5, No2, 369-378, 2002.
- 6) M., Miyazaki and T. Miyata: Effect of turbulence scale on aerodynamic response of rectangular cylinders, Proc. 5th Int. Conf. Wind Effects on Structures, Tokyo, 191, 1978.
- 7) T. Miyata, M. Miyazaki and H. Yamada: Pressure Distribution measurements for wind induced vibrations of box girder bridges, J. of Wind Eng. Ind. Aero., 14, 223, 1983.

Parametric Model Reduction for Unsteady Flow about Airfoil based on Compressible CFD Solver

Zhao Xiang⁺¹, Taehyoun Kim⁺²

^{+1,+2}National University of Singapore, Singapore, Singapore

In this work, a new Parametric Reduced-Order Model (PROM) with use of the Modally Equivalent Perturbed System (MEPS) and the Proper Orthogonal Decomposition (POD) is applied to unsteady flow about Airfoil with parameter variations in Mach. By applying the method, the original parameter-varied fluid system can be reduced from a very large dimension to a small dimension (e.g. for 2D case from 10,000 states to 100 states). While traditional Reduced-Order Model (ROM) cannot account for parameter variations, the present PROM is efficient to treat parameter changes adaptively. This means the POD modes obtained are valid for a wide range of parameter values. Towards this end, we have developed a frequency-domain CFD solver in which the fluid model is statically nonlinear, dynamically linearized (SNL DL) allowing unsteady simulations with small oscillations in subsonic, transonic, and supersonic flows in state-space format. With the state-space model, one can predict system responses (e.g. unsteady aerodynamic responses due to small amplitude oscillations of the lifting surface), conduct eigen-analysis, and build the PROMs. The ability of the new method to save substantial amount of computation for the varying parameter will be demonstrated using a 2D airfoil configuration.

Keyword: Unsteady CFD, Parametric Reduced Ordered Model, POD

1. Introduction

In this paper, we are to build a new Parametric Reduced-Order Model (PROM) for Computational Fluid Dynamics Model of unsteady flow about airfoil with parameter variations in Mach. Since traditional Reduced-Order Model (ROM) is only valid for a specific set of parameters, such ROM has to be built repeatedly every time when parameters vary^{1,2,3}. The PROM method proposed herein results in a global basis that can cover a wide range of the parameter variations⁴. This can save substantial amount of time when investigating a system with many varying parameters

To handle parameter variations efficiently, the system matrices are divided into a nominal and a perturbed system. A Modally Equivalent Perturbed System (MEPS)⁸ is constructed to represent the same parameter space as the original perturbed system, where the perturbed matrices are isolated into the forcing term and no longer appear in the homogeneous part of the equation. Thus, it becomes possible to interpret and analyze the effects and impact of the parameter variations in the context of conventional forced response problems in which the system matrix is that of the nominal system and driven by the perturbed matrices. To handle multi-inputs in the forcing term, the single-composite-input (SCI) method^{9,10} is invoked with a number of preselected perturbed matrices acting as simultaneous inputs. For demonstration, the new procedure is applied to a CFD model of unsteady flow about airfoil with parameter variations in Mach and is shown to produce extremely accurate PROM for both subsonic and transonic flow regime. The new approach can efficiently identify the parameter space with only two set of modes, one for the nominal system, the other for the perturbed system.

2. Governing Equations

(1) Small-Disturbance Unsteady Flow¹¹)

In this paper, we consider small-disturbance unsteady two-dimensional inviscid flows with Mach

⁺¹xiang_zhao@u.nus.edu, ⁺²mpekimt@nus.edu.sg

variation. To build a parametric reduced order unsteady flow model which is valid within certain Mach range, especially transonic regime, we should first build a small-disturbance unsteady flow model¹¹⁾. The time-dependent, two-dimensional Euler equations are given here as,

$$\frac{\partial \mathbf{u}}{\partial t} + \frac{\partial F(\mathbf{u})}{\partial x} + \frac{\partial G(\mathbf{u})}{\partial y} = 0 \quad (1)$$

where x and y are the Cartesian coordinates, t is time, ρ , u , v , and e are density, x- and y-components of velocity, and total specific energy, respectively. Conservation variables \mathbf{u} , flux vectors F and G are given by

$$\mathbf{u} = \begin{bmatrix} \rho \\ \rho u \\ \rho v \\ \rho e \end{bmatrix}, F(\mathbf{u}) = \begin{bmatrix} \rho u \\ \rho u^2 + p \\ \rho uv \\ \rho uh \end{bmatrix}, G(\mathbf{u}) = \begin{bmatrix} \rho v \\ \rho uv \\ \rho v^2 \\ \rho vh \end{bmatrix} \quad (2)$$

and calorically perfect gas is assumed here

In the present investigation, we are interested in small disturbance varying unsteady flows about some nonlinear mean operating condition. Here we assume the conservative variables as the combination of nonlinear steady flow and small disturbance.

$$\mathbf{u} = \mathbf{U} + \hat{\mathbf{u}} \quad (3)$$

where \mathbf{U} represents nonlinear steady flow for a given problem, which is also a solution to Eq. 1. Also, $\hat{\mathbf{u}}$ is the small-disturbance unsteady flow that arises from an external excitation. The steady Euler equation is given by,

$$\frac{\partial F(\mathbf{U})}{\partial x} + \frac{\partial G(\mathbf{U})}{\partial y} = 0 \quad (4)$$

Substituting Eq. 3 into the nonlinear Euler equations, Eq. 1, we can obtain the small-disturbance unsteady Flow, and is given by

$$\frac{\partial \hat{\mathbf{u}}}{\partial t} + \frac{\partial}{\partial x} \left(\frac{\partial F}{\partial \mathbf{U}} \hat{\mathbf{u}} \right) + \frac{\partial}{\partial x} \left(\frac{\partial G}{\partial \mathbf{U}} \hat{\mathbf{u}} \right) = 0 \quad (5)$$

Eq. 4 and Eq. 5 are solved sequentially, with boundary conditions that depend on the particular physical problem to be solved.

(2) Semi-discretized Equation

To discretize the steady Euler equations, Godunov¹²⁾ method using Roe's¹³⁾ approximate Riemann solver is applied. To achieve second-order accuracy, piecewise linear reconstruction¹⁴⁾ technique, limiter¹⁵⁾ is used to preserve monotonicity. The steady Euler equation Eq. 4 is solved in the first place to obtain the steady background flow \mathbf{U} . Then, the Time-linearized small-disturbance Euler equation is discretized on spatial term in the same way as before. And the overall continuous linear system can be written in a compact form as,

$$\frac{\partial \hat{\mathbf{u}}}{\partial t} = \mathbf{A}(\mathbf{U}) \hat{\mathbf{u}} + \mathbf{B}(\mathbf{U}) \mathbf{u}_{boundary} \quad (6)$$

\mathbf{A} is a large sparse matrix and \mathbf{B} is a vector arising from imposition of the unsteady inhomogeneous boundary conditions. For unsteady flows about isolated airfoils, the matrices \mathbf{A} are purely real and asymmetric. $\mathbf{u}_{boundary}$ is the external excitation such as pitching and plunging of the airfoil.

3. Parametric Reduced Order Model (PROM) for Aerodynamic System

To treat variations in the system parameters, we will build the Parametric Reduced-Order Model (PROM) for the original large-scale system. The methodology is based on the idea proposed by Kim⁸⁾. The following description is valid for variations in any system parameter. In this study, we will focus mainly on Mach number, because the Mach variation represents the most severe case that affects the entirely flow field.

(1) Linear System with Parameter Variations

Let us consider a linear dynamic system whose properties are functions of a set of parameters.

Linear dynamic system with parameter:

$$\begin{aligned} \frac{dx(\boldsymbol{\mu}, t)}{dt} &= \mathbf{A}(\boldsymbol{\mu})x(\boldsymbol{\mu}, t) + \mathbf{B}(\boldsymbol{\mu})u(t), & \mathbf{A}(\boldsymbol{\mu}) \in \mathbb{R}^{N \times N}, \mathbf{B}(\boldsymbol{\mu}) \in \mathbb{R}^{N \times I} \\ \mathbf{y}(\boldsymbol{\mu}, t) &= \mathbf{C}(\boldsymbol{\mu})x(\boldsymbol{\mu}, t), & \mathbf{C}(\boldsymbol{\mu}) \in \mathbb{R}^{L \times N} \end{aligned} \quad (7)$$

where $\mathbf{A}(\boldsymbol{\mu})$ is usually a very large N by N matrix, $\boldsymbol{\mu}$ is the parameter of system matrices, with lower and upper bounds of the parameters

$$\mu_{i,1} \leq \mu_i \leq \mu_{i,2}, \quad \text{nominal}(\mu_i) = \mu_{i,0}, \quad (i = 1, 2, \dots, H) \quad (8)$$

As stated above, Mach number M is one of the components in $\boldsymbol{\mu}$. The objective of our innovative PROM is to find a single set of basis vectors, $\boldsymbol{\Phi} \equiv [\boldsymbol{\Phi}^1, \boldsymbol{\Phi}^2 \dots \boldsymbol{\Phi}^R]$ that will span the broad solution space spanned by the parameter variations. We call them ‘‘Global Basis Vectors’’. Once the modes are found, the PROM is constructed via Galerkin’s projection²³⁾:

$$\begin{aligned} \frac{dx(\boldsymbol{\mu}, t)}{dt} &= \mathbf{A}_R(\boldsymbol{\mu})x(\boldsymbol{\mu}, t) + \mathbf{B}_R(\boldsymbol{\mu})u(t), & \mathbf{A}_R(\boldsymbol{\mu}) &\equiv \boldsymbol{\Phi}^T \mathbf{A}(\boldsymbol{\mu}) \boldsymbol{\Phi} \quad (R \times R) \\ \mathbf{y}(\boldsymbol{\mu}, t) &= \mathbf{C}_R(\boldsymbol{\mu})x(\boldsymbol{\mu}, t) & \mathbf{B}_R(\boldsymbol{\mu}) &\equiv \boldsymbol{\Phi}^T \mathbf{B}(\boldsymbol{\mu}) \quad (R \times I) \\ & & \mathbf{C}_R(\boldsymbol{\mu}) &\equiv \mathbf{C}(\boldsymbol{\mu}) \boldsymbol{\Phi} \quad (L \times R) \end{aligned}, \text{ where} \quad (11)$$

The resulted PROM represented by \mathbf{A}_R , \mathbf{B}_R , \mathbf{C}_R has much smaller size than the Full Order Model (FOM) represented by \mathbf{A} , \mathbf{B} , \mathbf{C} , since $R < N$. The PROM can accurately reproduce results of the FOM for any combination of the parameters in the range given by Eq. 8. Typically, to find the modes, we sort to POD (Karhunen–Loeve) procedure well discussed in^{5,6,7)}.

(2) Expansion of Matrices

We split the system equation into the nominal and perturbed parts.

$$\begin{aligned} \boldsymbol{\mu} &= \boldsymbol{\mu}_{\text{nominal}} + \Delta \boldsymbol{\mu} \\ \mathbf{x}(\boldsymbol{\mu}, t) &= \mathbf{x}_{\text{nominal}}(\boldsymbol{\mu}, t) + \Delta \mathbf{x}(\boldsymbol{\mu}, t) \\ \mathbf{A}(\boldsymbol{\mu}) &= \mathbf{A}_{\text{nominal}} + \Delta \mathbf{A} \\ \mathbf{B}(\boldsymbol{\mu}) &= \mathbf{B}_{\text{nominal}} + \Delta \mathbf{B} \\ \mathbf{C}(\boldsymbol{\mu}) &= \mathbf{C}_{\text{nominal}} + \Delta \mathbf{C} \end{aligned} \quad (12)$$

where $(\)_{\text{nominal}}$ refers to the nominal part, and Δ , the perturbed part.

Nominal System:

$$\begin{aligned} \frac{d\mathbf{x}_{\text{nominal}}}{dt} &= \mathbf{A}_{\text{nominal}} \mathbf{x}_{\text{nominal}} + \mathbf{B}_{\text{nominal}} \mathbf{u} \\ \mathbf{y}_{\text{nominal}} &= \mathbf{C}_{\text{nominal}} \mathbf{x}_{\text{nominal}} \end{aligned} \quad (13)$$

We name the system above nominal system. Theoretically, it can be set as anything as long as the system matrix is non-singular and well-behaved. The POD basis vectors obtained from the responses of this nominal system are named as ‘‘Nominal Modes’’ in this paper.

The perturbed system matrices are bounded as in Eq.

$$\|\Delta \mathbf{A}\| \leq \delta_A, \|\Delta \mathbf{B}\| \leq \delta_B, \|\Delta \mathbf{C}\| \leq \delta_C \quad (14)$$

Subtracting Eq. 13 (nominal part), we have

Perturbed System:

$$\frac{d\Delta\mathbf{x}(\boldsymbol{\mu}, t)}{dt} = \left(\mathbf{A}_{\text{nominal}} + \Delta\mathbf{A} \right) \Delta\mathbf{x}(\boldsymbol{\mu}, t) + \Delta\mathbf{A}\mathbf{x}_{\text{nominal}}(\boldsymbol{\mu}, t) + \Delta\mathbf{B}\mathbf{u}(t) \quad (15)$$

The objective of constructing this perturbed system is to calculate additional POD basis vectors which can compensate for parameter variations. We call these additional vectors ‘‘Perturbed Modes’’. However, the perturbed system has $\Delta\mathbf{A}$ in its homogeneous term which will cause much computation when calculating system responses for different $\Delta\mathbf{A}_i$ ’s. This leads us to the so called Modally Equivalent Perturbed System, a system that maintains the feature of the original additional basis vectors but at cheaper cost.

(3) Modally Equivalent Perturbed System (MEPS)⁸⁾

If one is to use (15), since $\Delta\mathbf{A}$ is in the homogenous term it will be necessary to solve a different equation for a different $\Delta\mathbf{A}_i$. The modally equivalent perturbed system, as its name suggests, shares the same solution space as the original perturbed system although its solution may not be the same. MEPS is very computationally beneficial in that $\Delta\mathbf{A}$ doesn’t appear in homogenous solution anymore.

In frequency domain, the original perturbed system Eq. 15 can be written as

$$\Delta\mathbf{X}(\omega) = \left(j\omega\mathbf{I} - \mathbf{A}_{\text{nominal}} + \Delta\mathbf{A} \right)^{-1} \left[\Delta\mathbf{A}\mathbf{X}_{\text{nominal}}(\omega) + \Delta\mathbf{B}\mathbf{U}(\omega) \right] \quad (16)$$

It is possible to find a pseudo inverse of such that $\Delta\mathbf{B} = \Delta\mathbf{A}\Delta\mathbf{A}^{-p}\Delta\mathbf{B}$, then Eq. 16 can be written as

$$\Delta\mathbf{X}(\omega) = \left(j\omega\mathbf{I} - \mathbf{A}_{\text{nominal}} + \Delta\mathbf{A} \right)^{-1} \Delta\mathbf{A} \left[\mathbf{X}_{\text{nominal}}(\omega) + \Delta\mathbf{A}^{-p}\Delta\mathbf{B}\mathbf{U}(\omega) \right] \quad (17)$$

Let’s decompose the transfer function through eigen-decomposition

$$\left(j\omega\mathbf{I} - \mathbf{A}_{\text{nominal}} + \Delta\mathbf{A} \right)^{-1} \Delta\mathbf{A} \equiv \mathbf{V}_v(\omega)\boldsymbol{\Lambda}_v(\omega)\mathbf{W}_v^T(\omega) \quad (18)$$

and apply the Caley-Hamilton Theorem¹⁶⁾ to Eq. 18, given a function:

$$g(\lambda) \equiv (1 + \lambda)^{-1} \lambda \quad (19)$$

Denoting,

$$\mathbf{K}(\omega) \equiv \left(j\omega\mathbf{I} - \mathbf{A}_{\text{nominal}} + \Delta\mathbf{A} \right)^{-1} \quad (20)$$

we have:

$$\begin{aligned} g(\mathbf{K}(\omega)\Delta\mathbf{A}) &= \mathbf{V}_v(\omega)g(\boldsymbol{\Lambda}_v(\omega))\mathbf{W}_v^T(\omega) \\ (\mathbf{I} - \mathbf{K}(\omega)\Delta\mathbf{A})^{-1} \mathbf{K}(\omega)\Delta\mathbf{A} &= \mathbf{V}_v(\omega) \left[\mathbf{I} + \boldsymbol{\Lambda}_v(\omega) \right]^{-1} \boldsymbol{\Lambda}_v(\omega) \mathbf{W}_v^T(\omega) \\ (j\omega\mathbf{I} - \mathbf{A}_{\text{nominal}})^{-1} \Delta\mathbf{A} &= \mathbf{V}_v(\omega)\boldsymbol{\Lambda}_v'(\omega)\mathbf{W}_v^T(\omega) \end{aligned} \quad (21)$$

where

$$\boldsymbol{\Lambda}_v' \equiv \left[\mathbf{I} + \boldsymbol{\Lambda}_v(\omega) \right]^{-1} \boldsymbol{\Lambda}_v(\omega) \quad (22)$$

The original perturbed system is

$$\begin{aligned} \Delta\mathbf{X}(\omega) &= \left(j\omega\mathbf{I} - \mathbf{A}_{\text{nominal}} + \Delta\mathbf{A} \right)^{-1} \Delta\mathbf{A} \left[\mathbf{X}_{\text{nominal}}(\omega) + \Delta\mathbf{A}^{-p}\Delta\mathbf{B}\mathbf{U}(\omega) \right] \\ &= \mathbf{V}_v(\omega)\boldsymbol{\Lambda}_v(\omega)\mathbf{W}_v^T(\omega)\Delta\mathbf{A} \left[\mathbf{X}_{\text{nominal}}(\omega) + \Delta\mathbf{A}^{-p}\Delta\mathbf{B}\mathbf{U}(\omega) \right] \\ &\equiv \mathbf{V}_v(\omega)\mathbf{z}_v(\omega) \end{aligned} \quad (23)$$

And we define a new perturbed system, which we call as **Modally Equivalent Perturbed System (MEPS)** as

$$\begin{aligned}
 \Delta \mathbf{X}'(\omega) &= (j\omega \mathbf{I} - \mathbf{A}_{\text{nominal}})^{-1} \Delta \mathbf{A} [\mathbf{X}_{\text{nominal}}(\omega) + \Delta \mathbf{A}^{-p} \Delta \mathbf{B} \mathbf{U}(\omega)] \\
 &= \mathbf{V}_v(\omega) \Lambda'_v(\omega) \mathbf{W}_v^T(\omega) \Delta \mathbf{A} [\mathbf{X}_{\text{nominal}}(\omega) + \Delta \mathbf{A}^{-p} \Delta \mathbf{B} \mathbf{U}(\omega)] \\
 &\equiv \mathbf{V}_v(\omega) \mathbf{z}'_v(\omega)
 \end{aligned} \tag{24}$$

Let's compare the solution of original perturbed system and MEPS. It can be seen that they span the same solution space, since they are the linear combination of the same eigenvectors. The two systems are modally equivalent. This means we can use MEPS to calculate perturbed modes instead of using original perturbed system. Fig. 1 illustrates the solution space of the original perturbed system and MEPS.

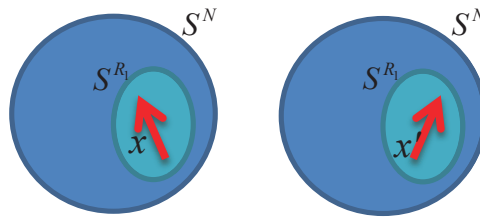


Figure 1: Solution space.

Then we can write the new perturbed system in time domain as

$$\frac{d\Delta \mathbf{x}(\boldsymbol{\mu}, t)}{dt} = \mathbf{A}_{\text{nominal}} \Delta \mathbf{x}(\boldsymbol{\mu}, t) + \Delta \mathbf{A} \mathbf{x}_{\text{nominal}}(\boldsymbol{\mu}, t) + \Delta \mathbf{B} \mathbf{u}(t) \tag{25}$$

As before, the perturbed modes set will be calculated using POD method. However, now we use MEPS as in Eq. 24, Eq. 25, Eq. in lieu of the original perturbed system for modes calculation for PROM.

a) Treatment to the forcing terms: Single Composite Input (SCI)

In practice, however, it may be intuitive to look into the effects of the changes by taking a few predetermined but representative $\Delta \mathbf{A}_i$, $\Delta \mathbf{B}_i$. The challenge is to know how they would behave to simulate the effects of the continuous variation. Towards this end, we resort to the SCI method^{9,10}. The SCI can be implemented either in frequency domain^{9,10} or in time-domain^{17,18,19}. To be concise, details of this method is saved in this paper. By applying the SCI scheme, the response of MEPS can be calculated by

$$\begin{aligned}
 \Delta \mathbf{X}(\omega) &= (j\omega \mathbf{I} - \mathbf{A}_{\text{nominal}})^{-1} \left[\sum_{i=1}^K \Delta \mathbf{A}_i \Phi_0 \mathcal{r}_i(\omega) + \sum_{i=1}^K \Delta \mathbf{B}_i \mathbf{u}_i(\omega) \right] \\
 \mathcal{r}_i &\equiv (R_0 \times 1) \text{ random uncorrelated signal vector} \\
 \mathbf{u}_i &\equiv (I \times 1) \text{ random uncorrelated signal vector}
 \end{aligned} \tag{26}$$

b) The Algorithm for Parametric Model Reduction

Step 1: Calculate nominal modes Φ_0 from the snapshot of the nominal system using POD technique

$$\mathbf{X}_{\text{nominal}}(\omega) = (j\omega \mathbf{I} - \mathbf{A}_{\text{nominal}})^{-1} \mathbf{B}_{\text{nominal}} \mathbf{U}(\omega) \tag{27}$$

Step 2: Calculate perturbed modes Φ_1 from the snapshot of MEPS with static correction using POD technique

$$\Delta \mathbf{X}(\omega) = (j\omega \mathbf{I} - \mathbf{A}_{\text{nominal}})^{-1} \left[\sum_{j=1}^J \Delta \mathbf{A}_j \Phi_0 \mathcal{r}_j(\omega) + \sum_{j=1}^J \Delta \mathbf{B}_j \mathbf{u}_j(\omega) \right] \tag{28}$$

Step 3: Combine nominal and perturbed mode sets to form the global modes, and finally undergo Galerkin's projection. The combined mode set is $\Phi = [\Phi_0, \Phi_1]$

$$\begin{aligned} \frac{d\mathbf{x}(\boldsymbol{\mu}, t)}{dt} &= \mathbf{A}_R(\boldsymbol{\mu})\mathbf{x}(\boldsymbol{\mu}, t) + \mathbf{B}_R(\boldsymbol{\mu})\mathbf{u}(t), \text{ where } & \mathbf{A}_R(\boldsymbol{\mu}) &\equiv \boldsymbol{\Phi}^T \mathbf{A}(\boldsymbol{\mu}) \boldsymbol{\Phi} & (R \times R) \\ \mathbf{y}(\boldsymbol{\mu}, t) &= \mathbf{C}_R(\boldsymbol{\mu})\mathbf{x}(\boldsymbol{\mu}, t) & \mathbf{B}_R(\boldsymbol{\mu}) &\equiv \boldsymbol{\Phi}^T \mathbf{B}(\boldsymbol{\mu}) & (R \times I) \\ & & \mathbf{C}_R(\boldsymbol{\mu}) &\equiv \mathbf{C}(\boldsymbol{\mu}) \boldsymbol{\Phi} & (L \times R) \end{aligned} \quad (29)$$

The above algorithm gives us a set of global POD basis vectors that are valid over a range of parameter variations.

Step 4: A further reduced order model can be built on top step 3. Since the global modes are used for model with parameter variations, it is not optimal for a specific combination of the parameters. In the later case, the smallest possible reduced order model may be desirable. When $\boldsymbol{\mu} = \boldsymbol{\mu}_s$, a second set of basis vectors can be found by performing the POD technique based on the snapshots of the first PROM.

$$\begin{aligned} \frac{d\mathbf{x}(\boldsymbol{\mu}_s, t)}{dt} &= \mathbf{A}_S(\boldsymbol{\mu}_s)\mathbf{x}(\boldsymbol{\mu}_s, t) + \mathbf{B}_S(\boldsymbol{\mu}_s)\mathbf{u}(t), \text{ where } & \mathbf{A}_S(\boldsymbol{\mu}_s) &\equiv \boldsymbol{\Psi}^T \mathbf{A}_R(\boldsymbol{\mu}_s) \boldsymbol{\Psi} & (S \times S) \\ \mathbf{y}(\boldsymbol{\mu}_s, t) &= \mathbf{C}_S(\boldsymbol{\mu}_s)\mathbf{x}(\boldsymbol{\mu}_s, t) & \mathbf{B}_S(\boldsymbol{\mu}_s) &\equiv \boldsymbol{\Psi}^T \mathbf{B}_R(\boldsymbol{\mu}_s) & (S \times I) \\ & & \mathbf{C}_S(\boldsymbol{\mu}_s) &\equiv \mathbf{C}_R(\boldsymbol{\mu}_s) \boldsymbol{\Psi} & (L \times S) \end{aligned} \quad (30)$$

The size of this second reduced order model is further reduced compared to the first PROM. Let's take \mathbf{A} matrix for example. The original is \mathbf{A} N by N matrix, \mathbf{A}_R is R by R , and \mathbf{A}_S is S by S , where $S < R < N$.

4. Numeric Results

In this section, we present some typical two-dimensional steady and unsteady small-disturbance flow solutions for a simple model problem. We will examine the lift response due to pitch and plunging motion of the airfoil NACA0012. The CFD model is built on a 76x20 meshes with 7220 degree of freedoms (DoFs).

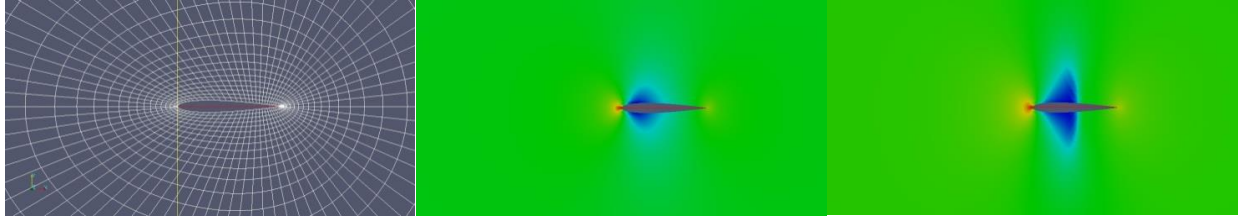


Figure 2: 76x20 meshes. Figure 3: Pressure contour M=0.7. Figure 4: Pressure contour at M=0.8.

$$\text{rank}(\mathbf{A}_{0.9} - \mathbf{A}_{0.8}) = \text{full}, \quad \text{rank}(\mathbf{A}_{0.9} - \mathbf{A}_{0.8}) = \text{full} \quad (31)$$

(31) shows that the change of Mach number affects the entirely flow field. It has to be noted that, in ROM, POD basis obtained for condition cannot be used for another parameter condition, especially when the system matrix undergoes dramatic change due to varying parameter. In unsteady flow, this is quite evident in transonic flow regime. The flow fields at Mach 0.7, 0.8 in Fig. 3,4 are quite different as can be seen in the pressure plots above.

(1) Perform Step 1 for Nominal Basis Vectors

By looking at the singular values^{20,21)} of snapshot matrix in Fig. 5, we can decide how many basis vectors are necessary to achieve a satisfactory accuracy. Ignoring those small singular values in Fig. 5, we can take the first 50~100 modes as the basis vectors for nominal system. Fig 6 shows the comparison of Eigenvalues of ROM and FOM for nominal system with Mach=0.8. Fig.7 shows frequency responses of lift by the FOM and ROM for the nominal system which match extremely well. However, when the nominal modes are used for another parameter condition, Mach = 0.9 (Fig. 8), the ROM does not match with FOM at all as can be expected. This is why we prefer to build PROM.

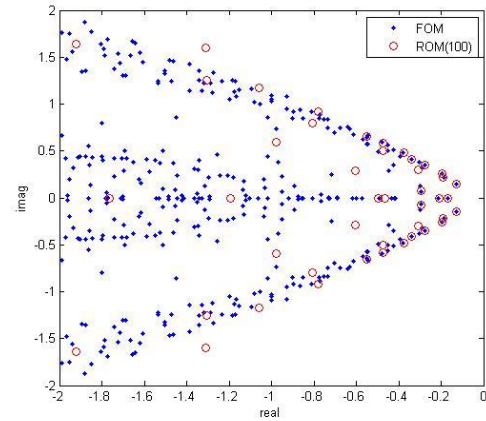
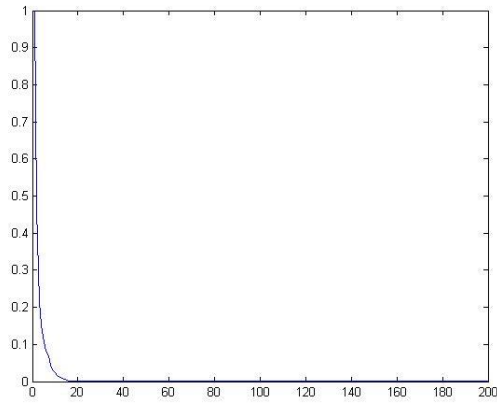


Figure 5: Singular values of nominal snapshots matrix. Figure 6: Eigenvalues of ROM and FOM at M=0.8

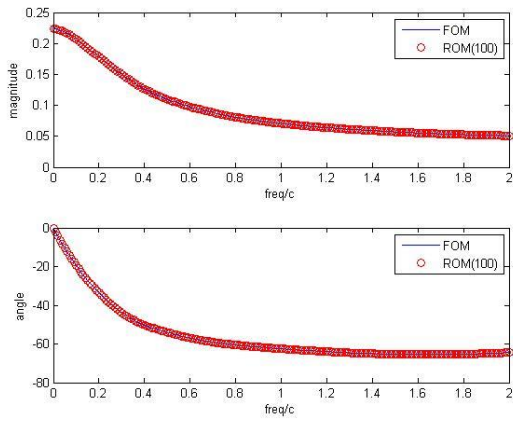


Figure 7: Freq response of lift of ROM and FOM due to pitching motion at M=0.8.

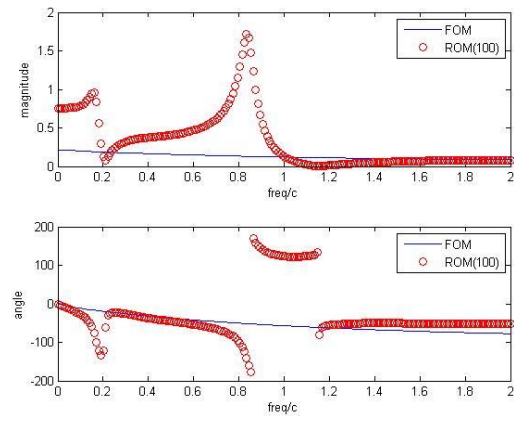


Figure 8: Freq response of lift of ROM and FOM due to pitching motion at M=0.9

(2) Check the Convergence of Driving Term

In Fig 9, the singular values of $[\Delta\mathbf{A}_1\Phi_0, \Delta\mathbf{A}_2\Phi_0, \dots, \Delta\mathbf{A}_K\Phi_0]$ with different numbers of $\Delta\mathbf{A}_i$ are compared. The parameter considered here is the Mach number. Nominal Mach number is 0.8. The variation of Mach is between 0.7~0.9 in transonic regime. $\Delta\mathbf{A}_i$ is defined as

$$\begin{aligned} \Delta\mathbf{A}_{0.7} &= \mathbf{A}_{0.7} - \mathbf{A}_{0.8}, & \Delta\mathbf{A}_{0.75} &= \mathbf{A}_{0.75} - \mathbf{A}_{0.8} \\ \Delta\mathbf{A}_{0.85} &= \mathbf{A}_{0.85} - \mathbf{A}_{0.8}, & \Delta\mathbf{A}_{0.9} &= \mathbf{A}_{0.9} - \mathbf{A}_{0.8} \end{aligned} \quad (32)$$

D_i is defined as below to represent the driving term with different number of $\Delta\mathbf{A}_i$

$$\begin{aligned} D_1 &= [\Delta\mathbf{A}_{0.7}\Phi_0] \\ D_2 &= [\Delta\mathbf{A}_{0.7}\Phi_0, \Delta\mathbf{A}_{0.9}\Phi_0] \\ D_3 &= [\Delta\mathbf{A}_{0.7}\Phi_0, \Delta\mathbf{A}_{0.9}\Phi_0, \Delta\mathbf{A}_{0.75}\Phi_0] \\ D_4 &= [\Delta\mathbf{A}_{0.7}\Phi_0, \Delta\mathbf{A}_{0.9}\Phi_0, \Delta\mathbf{A}_{0.75}\Phi_0, \Delta\mathbf{A}_{0.85}\Phi_0] \\ D_5 &= [\Delta\mathbf{A}_{0.7}\Phi_0, \Delta\mathbf{A}_{0.9}\Phi_0, \Delta\mathbf{A}_{0.75}\Phi_0, \Delta\mathbf{A}_{0.85}\Phi_0, \Delta\mathbf{A}_{0.775}\Phi_0, \Delta\mathbf{A}_{0.825}\Phi_0] \\ D_6 &= [\Delta\mathbf{A}_{0.7}\Phi_0, \Delta\mathbf{A}_{0.9}\Phi_0, \Delta\mathbf{A}_{0.75}\Phi_0, \Delta\mathbf{A}_{0.85}\Phi_0, \Delta\mathbf{A}_{0.775}\Phi_0, \Delta\mathbf{A}_{0.825}\Phi_0, \Delta\mathbf{A}_{0.725}\Phi_0, \Delta\mathbf{A}_{0.875}\Phi_0] \end{aligned} \quad (33)$$

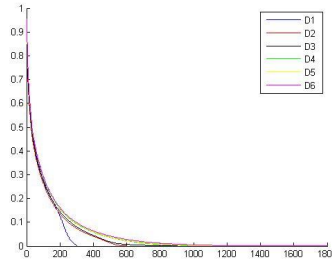


Figure 9: Convergence of the driving term.

After applying SVD on each D_i , their normalized singular values are compared in Fig 9. By comparing the singular values of each D_i , we notice that the curves of singular values are very steep. They all go down to zero very quickly, which means many of the columns in the driving term contributes very little in the sense of exciting the system. Those columns can be neglected, although they are counted as independent columns when calculating rank of D_i . When $i = 4$, the curves converge pretty much. This means enough ΔA_i have been included in the driving term already. In practice, we may set a tolerance, for example tolerance = 10^{-4} , in order to tell how many “useful” columns are there in the driving term. And we may say the driving term has rich enough columns when the number of those “useful” columns converges.

(3) Perform Step 2 and 3 for Perturbed Basis Vectors

PROM is developed to obtain a global POD basis vectors that are valid for a range of parameter variations. After we execute the PROM step 2 and 3 in the algorithm, we have the perturbed modes. The singular values of perturbed snapshot matrix is shown in Fig 10. To have a good PROM, we may take about 2000 perturbed modes. The resulting global POD basis has 2200 modes (nominal and perturbed) and can be used for any Mach number within 0.7~0.9. The comparison of frequency responses of the PROM and FOM at different Mach numbers are shown below in Fig. 11-13.

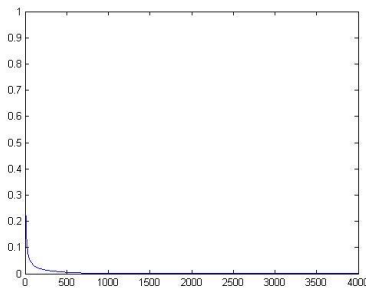


Figure 10: Singular values of perturbed snapshots matrix

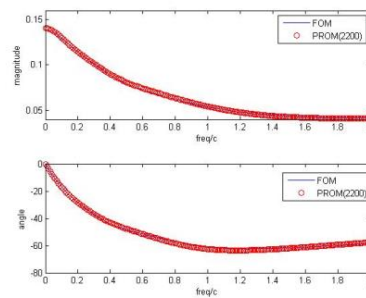


Figure 11: Freq response of lift of ROM and PROM due to pitching motion at M=0.7.

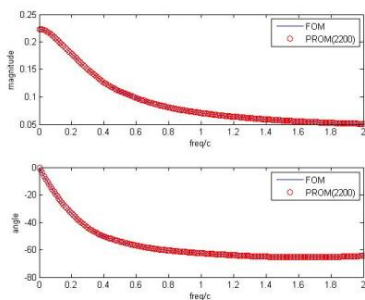


Figure 12: Freq response of lift of ROM and PROM due to pitching motion at Mach =0.8

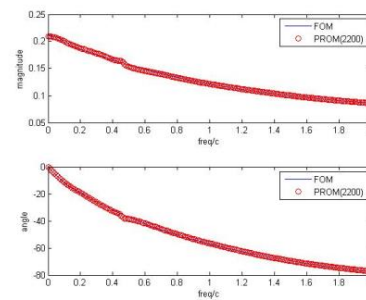


Figure 13: Freq response of lift of ROM and PROM due to pitching motion at Mach =0.9.

(4) Time History Comparison

Now let's compare the lift time history of FOM and PROM due to a sinusoidal pitching motion in Fig.14.

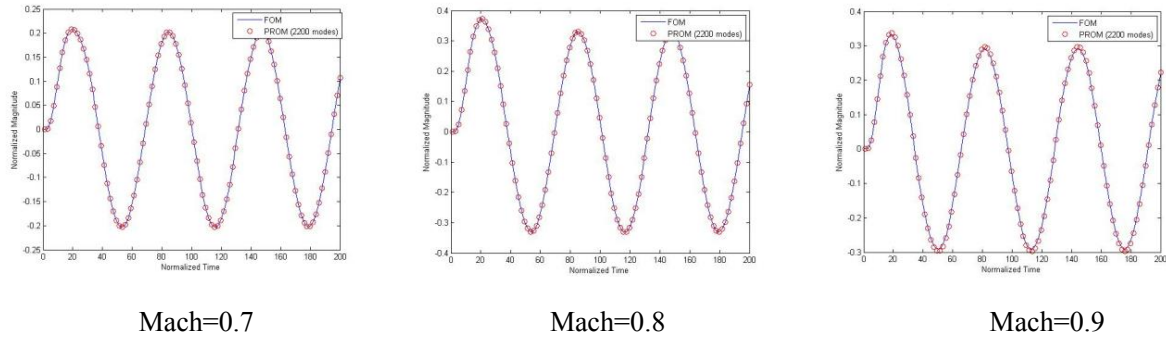


Figure 14: Life history due to sinusoidal pitching motion

4. Discussion

A general observation we can make is the number of basis vectors for the nominal system is about 50~100. Based on the snapshots at M=0.7, 0.75, 0.8, 0.85, 0.9, the new PROM algorithm results in a global basis vectors with 2200 columns. A natural question readers may ask is why is this global basis vectors has this many columns? Assuming for each Mach number in M=0.7, 0.75, 0.8, 0.85, 0.9 the number of basis vectors is about 50~100, then we would have less than 500 columns by collecting all of the basis vectors together. On the other hand, the global basis vectors set based on this PROM has more columns than 500. The rationale behind this is, the global basis vectors from our new PROM algorithm cover any Mach number in the interval M=0.7~0.9, spanning a larger space than the basis vectors of the 5 Mach numbers collected together. Therefore, our global basis vectors have more columns. We can illustrate this point by the Fig. 15 below. Finally, in order to reduce the size of PROM further we can do a second model reduction on the PROM obtained. The second model reduction will produce a ROM of 100~200 DoFs for a specific Mach number, the demonstration is not included in this paper in due to the page limit.

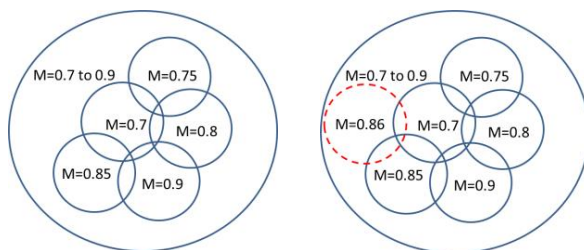


Figure 15: illustration of PROM

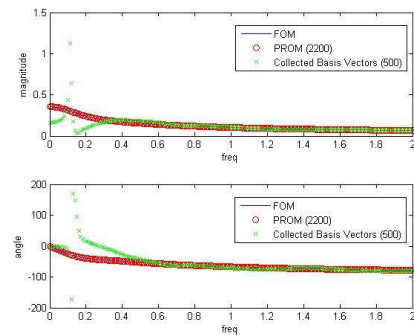


Figure 16: Freq Response of lift of ROM and PROM due to pitching motion at Mach =0.86.

To validate this point, let's compare the response at M=0.86 by using Φ_{PROM} and $\Phi_{collected} = [\Phi_{0.7}, \Phi_{0.75}, \Phi_{0.8}, \Phi_{0.85}, \Phi_{0.9}]$. In Fig. 16, we can see that $\Phi_{collected}$ doesn't have a good match at M=0.86, while our PROM with basis vector Φ_{PROM} gives identical frequency responses as FOM.

REFERENCES

1) Hall, K. C. : Eigenanalysis of Unsteady Flows About Airfoils, Cascades, and Wings, *AIAA Journal.*, Vol.

- 32, No. 12, 1994, pp. 2426-2432.
- 2) Hall, K. C., Florea, R., and Lanzkon, P. J : A Reduced Order Model of Unsteady Flows in Turbomachinery, *Journal of Turbomachinery*, Vol. 117, No. 3, 1995, pp. 375-383.
 - 3) Florea, R., Hall, K. C.,: Eigenmode Analysis of Unsteady Flows about Airfoils, *Journal of Computational Physics*, Vol. 147, Dec. 1998, pp. 568-593.
 - 4) Paul-Dubois-Taine A, Amsallem D. , An adaptive and efficient greedy procedure for the optimal training of parametric reduced-order models. *Int. J Numeric Methods Eng*, 2014, 0:1–32
 - 5) Kim, T., "Frequency-domain Karhunen-Loeve method and its application to linear dynamic systems." *AIAA journal* 36.11 (1998): 2117-2123.
 - 6) Kim, T., Kanivenahalli S. Nagaraja, and Kumar G. Bhatia. "Order reduction of state-space aeroelastic models using optimal modal analysis." *Journal of aircraft* 41.6 (2004): 1440-1448.
 - 7) Sirovich, L., M. Kirby, and M. Winter. "An eigenfunction approach to large scale transitional structures in jet flow." *Physics of Fluids A: Fluid Dynamics* (1989-1993) 2.2 (1990): 127-136.
 - 8) Kim, T, Surrogate model reduction for linear dynamic systems based on a frequency domain modal analysis, *Computational Mechanics*, 2015, Vol 56, Issue 4, pp 709-723.
 - 9) Kim T, Bussoletti JE An optimal reduced-order aeroelastic modeling based on a response-based modal analysis of unsteady CFD models. In: *42nd AIAA/ASME/ASCE/AHS/ASC structures, structural dynamics, and materials conference*, Seattle, WA, AIAA, 2001
 - 10) Kim, T., "Component mode synthesis method based on optimal modal analysis." *AIAA J* (2002): 2202-1226.
 - 11) Kenneth C. Hall, Jeffrey P. Thomas, and Earl H. Dowell. "Proper Orthogonal Decomposition Technique for Transonic Unsteady Aerodynamic Flows", *AIAA Journal*, Vol. 38, No. 10 (2000), pp. 1853-1862.
 - 12) Godunov, S. K., A Finite Difference Method of the Numerical Computation of Discontinuous Solutions of the Equations of Fluid Dynamics, *Matematicheskii Sbornik*, Vol. 47, 1959, pp. 357-393.
 - 13) Roe, P. L., Approximate Riemann Solvers, Parameter Vectors, and Difference Schemes, *Journal of Computational Physics*, Vol. 43, 1981, pp. 357-372..
 - 14) Barth, Timothy J., and Dennis C. Jespersen. "The design and application of upwind schemes on unstructured meshes." (1989).
 - 15) Venkatakrishnan, V. "On the Accuracy of Limiters and Convergence to Steady State Solutions," *AIAA Paper* 93-0880, Jan. 1993."
 - 16) Chen CT, Linear system theory and design. Oxford University Press, New York, 2012
 - 17) Kim T, "Efficient reduced-order system identification for linear systems with multiple inputs." *AIAA J.*, 43(7):1455–1464, 2005
 - 18) Kim, T. "Aeroelastic model reduction for affordable computational fluid dynamics-based flutter analysis." *AIAA Journal* 43.12 (2005): 2487-2495.
 - 19) Silva, Walter A. "Simultaneous excitation of multiple-input/multiple-output CFD-based unsteady aerodynamic systems." *Journal of Aircraft* 45.4 (2008): 1267-1274.
 - 20) Klema, Virginia C., and Alan J. Laub. "The singular value decomposition: Its computation and some applications." *Automatic Control*, IEEE Transactions on 25.2 (1980): 164-176.
 - 21) Wall, Michael E., Andreas Rechtsteiner, and Luis M. Rocha. "Singular value decomposition and principal component analysis." A practical approach to microarray data analysis. Springer US, 2003. 91-109.
 - 22) Hoffmann, Walter. "Iterative algorithms for Gram-Schmidt orthogonalization." *Computing* 41.4 (1989): 335-348.
 - 23) Antoulas, Athanasios C. Approximation of large-scale dynamical systems. Vol. 6. SIAM, 2005.

STRUCTURAL DESIGN OF AEROELASTIC FLAPPING WING

Hiroto Nagai⁺¹, Shunsuke Nakamura⁺², Masahiko Murozono⁺¹, Kosei Ono⁺¹ and Nobuhide Uda⁺¹
⁺¹Kyushu University, Fukuoka, Japan
⁺²Toyota Motor Corporation, Toyota, Japan

We have conducted aeroelastic analysis for the resonant type elastic flapping wing and investigated the effect of planform and thickness of the plate on the vibrational and aerodynamic characteristics. The resonant type elastic flapping wing consists of a CFRP rod and EPP plate. When a small oscillation is input to the wing base, bending and torsional wing deformation are produced passively due to aeroelastic phenomenon. To search an optimal design parameters of the wing to maximize thrust coefficient, parametric studies have been conducted with respect to the plate thickness, span location with the maximum chord, chord length at wing base, and chord length at wing tip. From these calculation, an optimal structure of the elastic wing have been obtained, which generates larger thrust coefficient than the initial value. When the resonant type elastic flapping wing have an optimal wing structure, both first and second mode have coupling mode shape of spanwise bending and torsion, and the first and second natural frequencies are close to each other. Such an optimal wing can produce an appropriate wing kinematics with the phase difference of near 90 deg by coupling the two vibrational modes. These results indicate that it is possible to conduct approximative optimal design only by using vibrational analysis without any aeroelastic analysis, which can save the calculation cost of numerical optimization.

Keyword: Flapping Wing, Aeroelasticity, Numerical Analysis, MAV, Structural Design

1. INTRODUCTION

Multicopter UAV (unmanned aerial vehicle), known as a drone, have been put into practical use for various applications, and the market size of commercial drones is expanded rapidly. The success of the drone encourages development of a much smaller UAV than the existing drones, called micro aerial vehicles (MAVs). Insect flight mechanisms have fascinated many researchers as a good candidate for a MAV. Despite of their small sizes, insects have good flight maneuverability and stability indoors or not. Their advantage is mainly gained from their flapping wings. The flapping wing kinematics of insects consists of flapping and feathering motions. The flapping motion is a rotational oscillation around a body axis (up- and downstroke), and the feathering motion is a rotational oscillation around a span axis of the wing (supination and pronation). Insects control their wing kinematics appropriately to generate larger lift with high efficiency. When a MAV mechanically realizes such an appropriate flapping kinematics like insects, it needs a complex mechanical system with gears, cum, and linkages at the wing base in order to achieve both flapping and feathering motions of wings, which causes excessive body weight and mechanical power loss. Therefore, a simple mechanical system for flapping wings are expected for a MAV. Recently, many flapping MAVs have been developed, some of which have attained success of free flight^{1, 2)}. The light weight technology by micro mechanical engineering has contributed to the success of the flapping type MAVs. However, more powerful flapping MAVs which can carry more payloads are required for future practical missions by autonomous flight.

To solve the problem, an aeroelastic flapping wing using resonance phenomenon has been proposed^{3, 4)}, which realizes complicated wing kinematics like insects by using passive aeroelastic wing deformation with a simple driving system. In this system, bending and torsional wing deformation are produced passively due to aeroelastic phenomenon with a simple input oscillation only in the flapping direction (see Fig. 1). When a small flapping oscillation is applied to the wing base at an input frequency near the natural frequency of the elastic wing, both bending and twisting oscillations of the wing appear with high amplitude due to resonance phenomenon. If the stiffness and mass distribution of the wing are designed appropriately, the preferable wing kinematics are attained, which has the phase difference of 90 deg between the flapping and feathering oscillations⁵⁾. The advantage of the resonance type elastic flapping wing is a simple actuating mechanism to drive a flapping wing.

⁺¹nagai@aero.kyushu-u.ac.jp

A flapping wing is generally subjected to aeroelastic deformation during a flapping cycle because of the demand of lightweight wings. The aerodynamic performance of such an elastic flapping wing is dominated by many design parameters: planform, distributions of stiffness and mass, input oscillation, and so on. These parameters influence the deformation of the elastic flapping wing and, as a result, the aerodynamic force. Despite of the complexity of the phenomenon, the structural design method for the elastic flapping wing is still not established: therefore, it is still unknown what structural design is optimal for the elastic flapping wing. For investigation of the wing characteristics and optimization of the structural design of the wing, numerical simulation for the elastic flapping wing are required. Recently, the characteristics of flexible flapping wings made of membrane have been investigated by many researchers⁷⁻¹⁰. However, the structural and aerodynamic characteristics for the elastic flapping wing using a resonant phenomenon have not been investigated.

The resonance type elastic flapping wings have also been developed by the trial and error method. The developed flapping wing is composed of a single CFRP (Carbon Fiber Reinforced Plastic) rod and a thin EPP (Expanded Polypropylene) foam plate with the semi-span length of 110 mm. Isogai et al.^{3, 4}) have conducted numerical simulation for the resonant flapping wing and compared with the experimental results. Based on the numerical results, Nagai et al.⁶) have developed a prototype of flapping type MAV mounting four resonant type flapping wings with the size of the 224 mm and succeeded in lifting of the body of 125 g with four DC motor and controller, a receiver, and a Li-Po battery (see Fig. 2). However, the design of the resonant type flapping wing is not still optimized.

In this study, we conduct a parametric study for the structural design of an aeroelastic flapping wing by using numerical simulation and investigate an optimal structural design for an aeroelastic flapping wing with larger lift and higher efficiency. The plate thickness, planform shape, and aspect ratio of the wing are considered as design parameters. In the numerical simulation, we conduct vibrational mode analysis using FEM (finite element method) and aeroelastic analysis using 3D Navier-Stokes code coupled with the structural equation of motion based on the mode method.

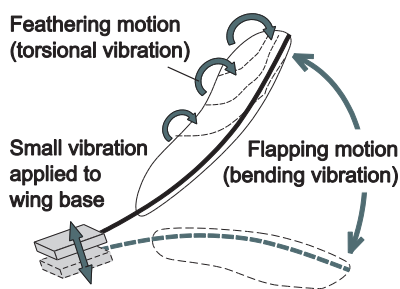


Figure 1: Aeroelastic flapping wing system.

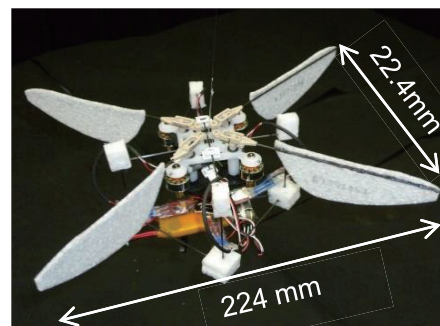


Figure 2: Prototype of Flapping type MAV.

2. MATERIALS AND METHODS

(1) Flapping wing model

The resonant type elastic flapping wing consisted of a single CFRP rod and a thin EPP foam plate with the expansion ratio of 30 times, as shown in Fig. 3. The CFRP rod with the diameter of 1.2mm adhered to the EPP plate at 2 mm apart from the leading-edge. The CFRP rod was fixed at the flapping arm at 10 mm apart from the wing base of the EPP plate. Based on our development of the wings, the planform of the EPP plate was simplified as shown in Fig. 3: a straight line at the leading-edge, and two parabolic curves at the trailing-edge. The vertices of the two parabola were connected each other at the span location with the maximum chord length. When the area of the planform keeps the same value even with a different planform, the planform can be represented as three parameters: 1) span location with the maximum chord length x_C , 2) the chord length at the wing base y_B , and 3) the chord length at the wing tip y_T . Note that y is in the chordwise direction from the rod to the trailing-edge. In this study, the three planform parameters are non-dimensionalized as follows,

$$\lambda_C = x_C/l, \quad \lambda_B = y_B/y_C, \quad \lambda_T = y_T/y_C \quad (1)$$

when l is the semi-span length of the EPP plate. In this study, the three parameters were varied from 0 to 1 to investigate the effect of planform and find an optimal shape. The thickness of the plate was also varied as a design parameter. Two kinds of wing area were employed: $S = 3.50 \times 10^{-3}$ and $4.53 \times 10^{-3} \text{ m}^2$. The former is called “Model 1” with the aspect ratio AR of 3.46, based on our developed wing in the previous works⁶⁾. The latter is called “Model 2” with $AR = 2.67$.

The flapping arm was oscillated in the out-of-plane direction with the amplitude of ± 10 deg about the flapping axis. The input frequency was changed in the range from 30 to 70 Hz with increment of 2.5 or 5 Hz. The forced-oscillation causes aeroelastic deformation of the wing with bending and torsion, which generates thrust in the negative y -direction. In this study, the time-averaged thrust was used to evaluate the aerodynamic performance of the flapping wing. The thrust generated by the flapping wing is generally proportional to the input frequency squared. In order to cancel the contribution of the input frequency, we introduce the thrust coefficient given by,

$$C_T = Thrust / (0.5 \rho V_{ref}^2 S) \quad (2)$$

where S is the wing area, ρ is the density of the air, V_{ref} is the reference velocity. In this study, V_{ref} is defined as the maximum flapping velocity at the 75% semi-span location when the wing is assumed to be rigid with no deformation as follows,

$$V_{ref} = 2\pi f \phi_0 \cdot (0.75l) \quad (3)$$

where ϕ_0 is the amplitude of the input flapping motion ($\phi_0 = 10$ deg). In this study, the wing structure was designed so that the thrust coefficient was maximized. Such an optimal wing can generate larger thrust at a lower input frequency, which means the wing can be driven by a small-sized actuator.

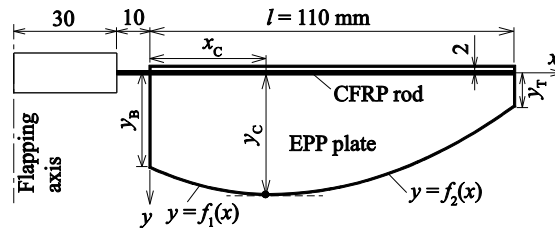


Figure 3: Definition of planform of the wing and wing-fixed coordinate system.

(2) Numerical Methods

Vibration modal analysis for the resonant type elastic flapping wing was conducted using self-developed FEM. Beam elements and shell elements were used to model the CFRP rod and EPP plate, respectively. The material properties were used based on our measurement⁶⁾, as follows; Young’s modulus is 108.5 GPa for CFRP and 1.113 MPa for EPP; the density is 1508.7 kg/m³ for CFRP and 31.66 kg/m³ for EPP; Poisson’s ratio is 0.3. The mass of adhesive of 0.074 g was considered as added mass of the beam. All degrees of freedom were fixed at one end of the rod with the length of 120 mm. Displacement was considered only in the out-of-plane direction. From the modal analysis, we obtained the natural frequency, mode shape, and generalized mass for each mode.

On the basis of the vibrational modal analysis, we conducted aeroelastic analysis using a self-developed 3D Navier-stokes coupled with the structural equation of motion^{3, 4)}. The displacement w of the wing normal to the wing surface is expressed as

$$w(x, y, t) = w_r(x, y, t) + \sum_{i=1}^N \Phi_i(x, y) q_i(t) \quad (4)$$

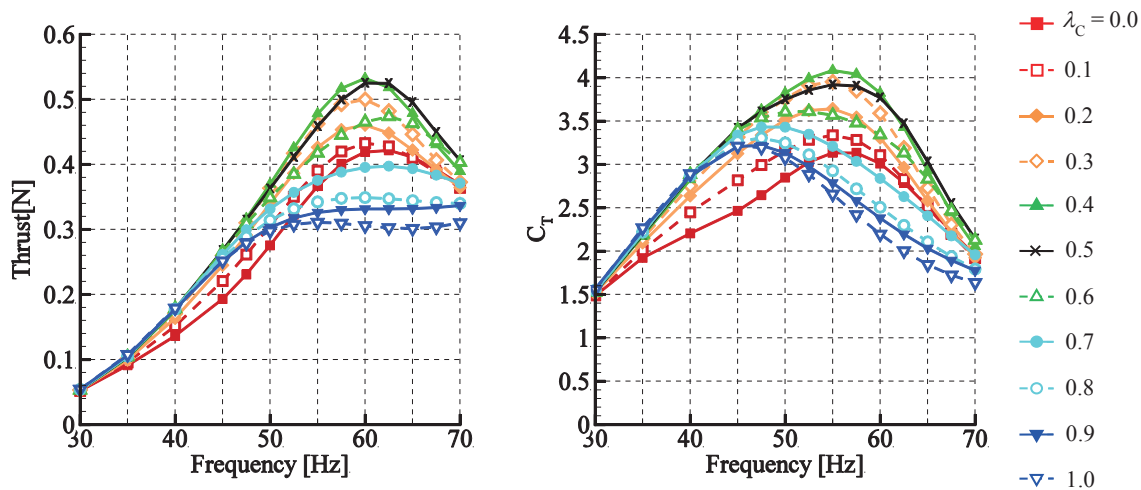
where t is time, x is the spanwise coordinate, y is the chordwise coordinate, as shown in Fig. 3, q_i is the generalized coordinate, and Φ_i is the natural vibrational mode shape of the i -th mode. w_r is the displacement of the forced oscillation as defined by

$$w_r(x, y, t) = (R_r + \phi_0 x) \sin(\omega t) \quad (5)$$

where R_r is the displacement of the wing at root section and ϕ_0 is the input flapping amplitude. Using Lagrange's equations of motion, we obtain the ordinary differential equations of motion with respect to q_i as follows,

$$M_i \left(\ddot{q}_i + \frac{\omega_i^2}{\omega} g_i \dot{q}_i + \omega_i^2 q_i \right) = - \iint_S \Phi_i m \dot{w} dx dy + \iint_S \Phi_i \Delta P dx dy \quad (i = 1, N) \quad (6)$$

where M_i is the generalized mass, ω_i is the natural angular frequency, ω is the input frequency, g_i is the damping coefficient, m is the mass per unit area of the wing surface, and ΔP is the pressure difference computed using the 3D Navier-Stokes code. Equations coupled with the 3D Navier-Stokes equation are solved at each time step to obtain the aeroelastic responses of the wing. The detail of the 3D Navier-Stokes code written in Ref. 6) and 10). A body-fitted H-H type structural grid were used around the wing with the node points of $161 \times 61 \times 35$. A no-turbulence model was used because of a low Reynolds number regime. For validation of the aeroelastic analysis code, comparison between the numerical and experimental results have been conducted for some resonant type elastic flapping wings and showed a good agreement each other^{4, 6)}.



(a) Time-averaged thrust vs input Frequency (b) Thrust coefficient vs input frequency

Figure 4: Thrust characteristics with respect to input frequency for each λ_c of Model 1.

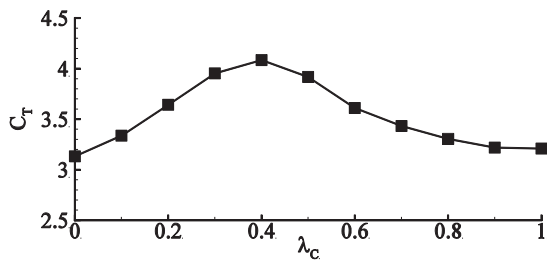
3. RESULTS AND DISCUSSION

1) Structural design for Model 1 ($AR = 3.46$)

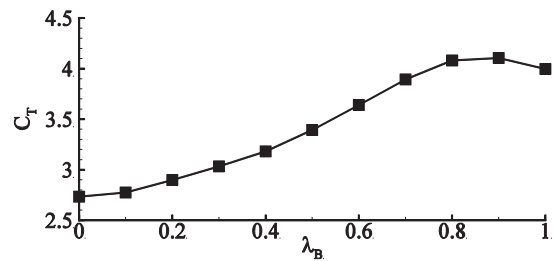
In order to design the wing structure for the Model 1 with $AR = 3.46$, we changed the design parameters one by one. First, we employed the design parameters designed by trial and error shown in Fig. 3 as initial values. Those parameters were as follows: $y_c = 36$ mm ($\lambda_c = 0.33$), $y_B = 28.5$ mm ($\lambda_B = 0.78$), $y_T = 10$ mm ($\lambda_T = 0.27$), thickness $h = 2.1$ mm. In this initial condition, the maximum thrust is 0.505 N at 60 Hz and the maximum thrust coefficient is 4.01 at 55 Hz. Second, the span location with the maximum chord length λ_c was changed from 0 to 1 when the other parameters, y_B , y_T , and h , were kept with the initial values. Third, the chord length at the wing base λ_B was changed from 0 to 1 when the λ_c is set to the optimal value obtained by the previous calculation, and y_T and h were kept with the initial values. Forth, the chord length at the wing tip λ_T was changed from 0 to 1 when λ_c and λ_B are the optimal values but h was the initial value. Finally, the thickness of the plate h was changed when λ_c , λ_B and λ_T were the optimal values.

First, we investigated the effect of the span location with the maximum chord length λ_c when the other parameters were kept with the initial values. Figures 4a shows the time-averaged thrust with respect to the input frequency from 30 to 70 Hz for each λ_c . As shown in Fig. 4a, thrust increases with an increase of the input frequency and has a peak value for each λ_c ; for example, maximum thrust is 0.532 N at 60 Hz for $\lambda_c = 0.4$.

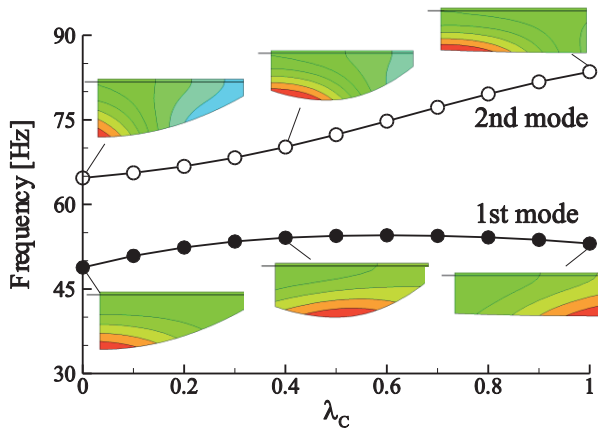
Using the results of Fig. 4a, the thrust coefficient are calculated with respect to the input frequency as shown in Fig. 4b. There is also a peak value of thrust coefficient for each λ_C ; for example, maximum C_T is 4.09 at 55 Hz for $\lambda_C = 0.4$. The maximum C_T for each λ_C are plotted with respect to λ_C in Fig. 5a. As can be seen in Fig. 5a, the maximum C_T is 4.09 among all λ_C when $\lambda_C = 0.4$. Figure 5b shows the relation of the first and second natural frequencies with respect to λ_C in addition to the typical mode shapes. With an increase of λ_C , the first natural frequency increases from 0.0 to 0.6 and decrease from 0.6 to 1.0. The second natural frequency increases monotonically, but the increment is different between low and high λ_C . These facts indicate that the mode shapes changes between low and high λ_C . When $\lambda_C = 0.0$, the first mode is first chordwise bending (or first torsion) without any spanwise bending, and the second mode is second torsion with spanwise bending. When $\lambda_C = 1.0$, the first mode has spanwise bending with slight torsion only around the wing tip, and the second mode is torsion only around the wing base. When $\lambda_C = 0.4$, or the optimal value in this case, the first mode includes both spanwise bending and torsion, and the second mode has second torsion with slight spanwise bending. Therefore, in the optimal case of $\lambda_C = 0.4$, both first and second mode shapes have coupling modes of spanwise bending and torsion. Moreover, the first and second natural frequencies is close to each other around $\lambda_C = 0.4$.



(a) Maximum C_T for each λ_C

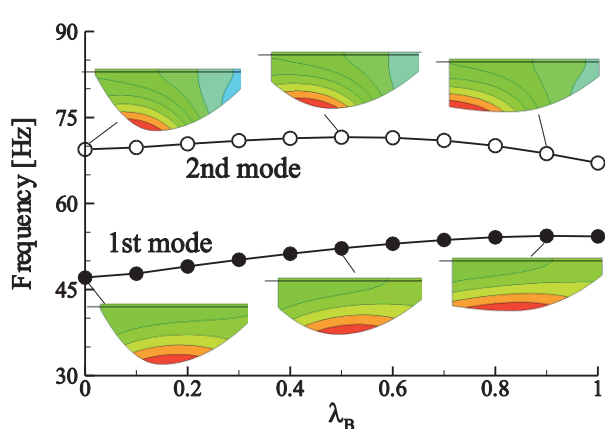


(a) Maximum C_T for each λ_B



(b) Natural frequencies and modal shapes for 1st and 2nd mode for each λ_C

Figure 5: Relation of maximum C_T to vibrational characteristics with respect to λ_C of Model 1.



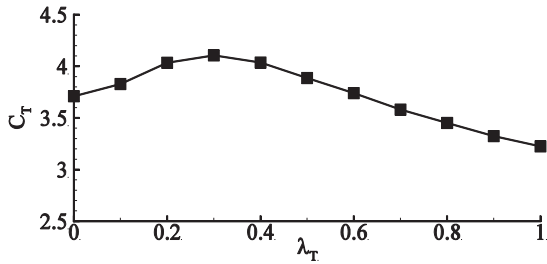
(b) Natural frequencies and modal shapes for 1st and 2nd mode for each λ_B

Figure 6: Relation of maximum C_T to vibrational characteristics with respect to λ_B of Model 1.

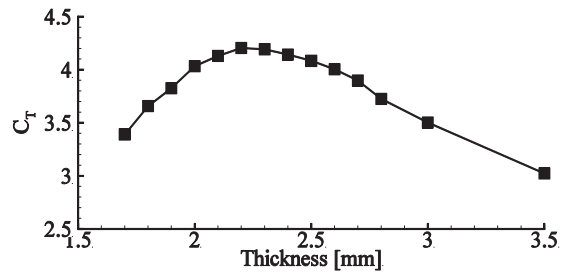
Next, we investigated the effect of the chord length at the wing base λ_B when λ_C was set to 0.4 from the previous result and the other parameters, y_T and h , were kept with the initial values. Figure 6a shows the relation of the maximum C_T with respect to λ_B . From this figure, the maximum C_T is 4.10 at $\lambda_B = 0.9$. Figure 6b shows the relation of the first and second natural frequencies with respect to λ_B in addition to the typical mode shapes. As shown in Fig. 5b, the first natural frequency increases monotonically with an increase of λ_B , and the first mode shape is first torsion all through λ_B although slight spanwise bending also appears at $\lambda_C = 0.9$. The second natural frequency is almost not changed all through λ_B although it has a slight peak at $\lambda_B = 0.5$. The second

mode shape includes spanwise bending and second torsion. As with the case of λ_C , in the optimal case of $\lambda_B = 0.9$, both first and second mode shape have coupling modes of bending and torsion. Moreover, the first and second frequencies are close to each other around $\lambda_B = 0.9$.

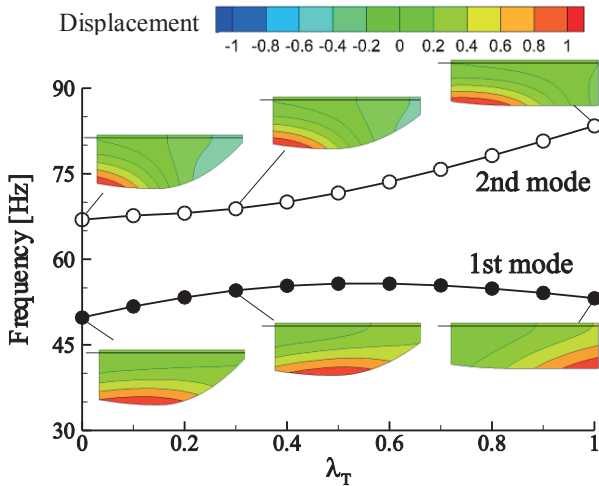
Third, we investigated the effect of the chord length at the wing tip λ_T when $\lambda_C = 0.4$, and $\lambda_B = 0.9$, $h = 2.1$ mm. Figure 7a shows the relation of maximum C_T with respect to λ_T . From this figure, the maximum C_T is 4.11 at $\lambda_T = 0.3$. Figure 7b shows the relation of the first and second natural frequencies with respect to λ_T in addition to the typical mode shapes. As with the case for λ_C and λ_B , in the optimal value of $\lambda_T = 0.3$, both first and second mode shapes have coupling modes of spanwise bending and torsion, and the first and second natural frequencies are close to each other around the optimal λ_T .



(a) Maximum C_T for each λ_T

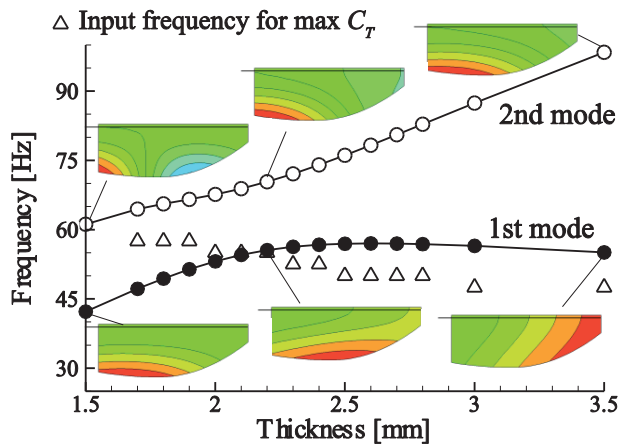


(a) Maximum C_T for each thickness of plate



(b) Natural frequencies and modal shapes for 1st and 2nd mode for each λ_T

Figure 7: Relation of maximum C_T to vibrational characteristics with respect to λ_T of Model 1.



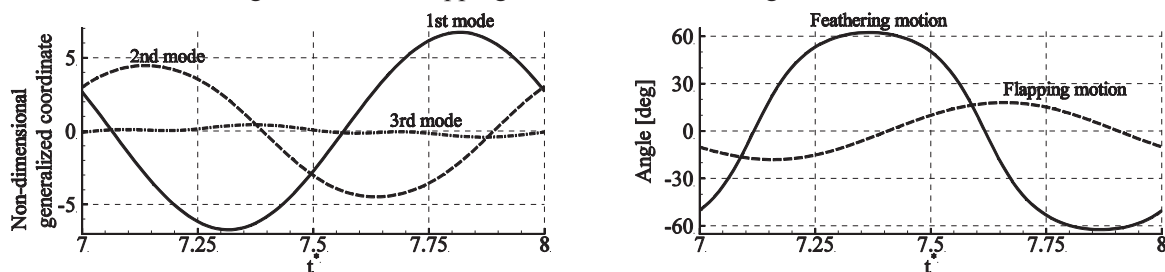
(b) Natural frequencies and modal shapes for 1st and 2nd mode for each thickness

Figure 8: Relation of maximum C_T to vibrational characteristics with respect to thickness of Model 1.

Finally, we investigated the effect of the plate thickness when $\lambda_C = 0.4$, $\lambda_B = 0.9$, and $\lambda_T = 0.3$ obtained from the previous calculation. Figure 8a shows the relation of the maximum C_T with respect to thickness. From this figure, the maximum C_T is 4.21 at $h = 2.2$ mm. Figure 8b shows the relation of the first and second natural frequencies with respect to thickness in addition to the typical mode shapes. As with the previous cases, the optimal case of $h = 2.2$ has coupling modes of spanwise bending and torsion in both first and second mode shape, and the first and second natural frequencies are close to each other around the optimal thickness. In addition, the input frequency when the maximum C_T appears is also plotted in Fig. 8b. As shown in Fig. 8b, the maximum C_T appears at the input frequency a little smaller than the natural frequency with banding mode, which means that spanwise bending mode shape is required for the maximum C_T .

From these parametric studies, we summarize as follows. When the resonant type elastic flapping wing has an optimal structural design, both first and second modes have coupling mode shapes of spanwise bending

and torsion. When the wing has such coupling mode shapes in both first and second modes, the first and second natural frequencies are close to each other. For the resonant type elastic flapping wing, the bending mode is related to the flapping motion, and the torsional mode is related to the feathering motion. Therefore, it is important that the wing has both spanwise bending and torsional modes. However, if such a coupling mode appears only in a single mode, the wing cannot achieve effective thrust generation because the bending oscillation occurs in-phase with the torsional oscillation. As is well known from the previous works⁵⁾, the efficient flapping wing kinematics has a phase difference of approximately 90 deg between the flapping and feathering motions. In order to achieve such an efficient wing kinematics with the phase difference of 90 deg, two different vibrational modes are required to be excited. For that purpose, when the first and second natural frequencies are close to each other, the two vibrational modes are likely to be coupled each other, which causes the elastic response with the phase difference of approximately 90 deg. Figures 9a and 9b shows the time histories of flapping and feathering angles, and the non-dimensional generalized coordinates from first to third modes, respectively. As shown in Fig. 9a, the dominant mode is first and second modes, and there is a phase difference of 117.1 deg between the two modes. As a result, the feathering motion is oscillated with the phase difference of 104.1 deg ahead of the flapping motion as shown in Fig. 9b.



(a) Non-dimensional generalized coordinates

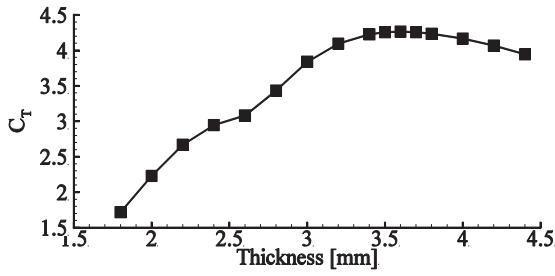
(b) Wing kinematics for flapping and feathering angles

Figure 9: Time histories of generalized coordinates and wing motion during a flapping cycle for the optimal case of Model 1 when the wing has a maximum C_T at input frequency of 55 Hz.

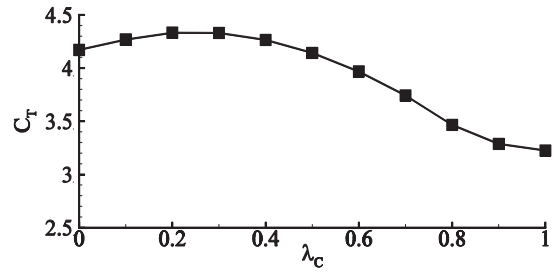
2) Structural design for Model 2 ($AR = 2.67$)

In this chapter, we investigated the optimal planform and thickness of plate for the Model 2 with the aspect ratio of 2.67, comparing the optimal wing structure of $AR = 3.46$. We changed the design parameters one by one as well as the previous chapter. First, the thickness of the plate was changed when the other parameters were set to the optimal values for the Model 1; $\lambda_C = 0.4$, $\lambda_B = 0.9$, $\lambda_T = 0.3$. Second, the span location with the maximum chord length λ_C was changed from 0 to 1 when the thickness is set to the optimal value and the other parameters, y_B , and y_T were kept with the initial values. Third, the chord length at the wing base λ_B was changed from 0 to 1 when the h and λ_C is set to the optimal value obtained by the previous calculation, and λ_T was kept with the initial values. Finally, the chord length at the wing tip λ_T was changed from 0 to 1 when h , λ_C and λ_B were set to the optimal values.

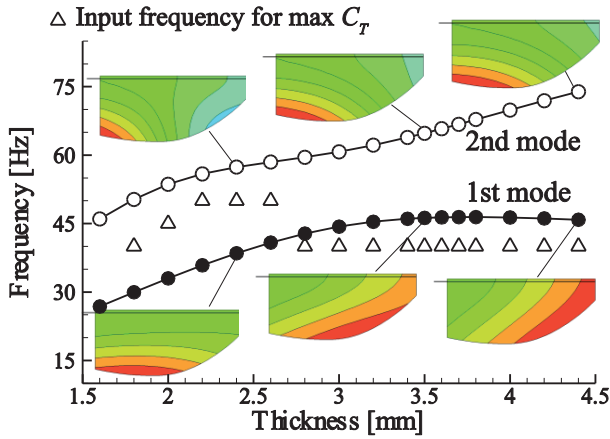
First, we investigated the effect of the plate thickness when λ_C , λ_B , and λ_T were set to the initial value. Figure 10a shows the relation of the maximum C_T with respect to thickness. From this figure, the maximum C_T is 4.26 at $h = 3.6$ mm. Figure 10b shows the relation of the first and second natural frequencies with respect to thickness in addition to the typical mode shapes. When the $h = 2.4$ mm, the first mode has first torsion, and the second mode has second torsion with slight spanwise bending. When $h = 4.4$ mm, the first mode has spanwise bending with slight torsion, and the second mode has the first torsion with slight spanwise bending. When the optimal value of $h = 3.6$ mm, the first and second modes have coupling of spanwise bending and torsion, and the first and second natural frequencies are close to each other around $h = 3.6$ mm. Moreover, the input frequency when the maximum C_T appears is also plotted in Fig. 10b. As shown in Fig. 10b, the input frequency with the maximum C_T increases with a decrease of thickness because it is related to the natural frequency with spanwise bending mode.



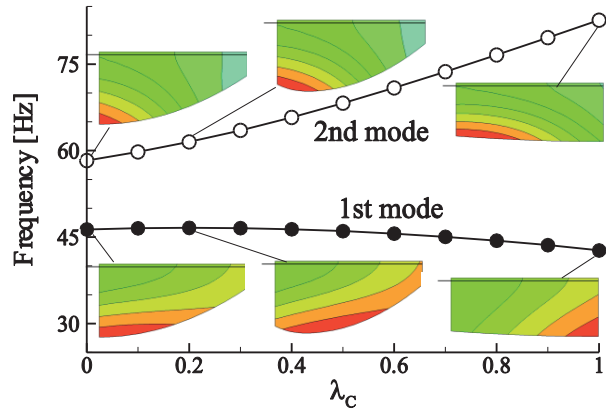
(a) Maximum C_T for each thickness of plate



(a) Maximum C_T for each λ_c



(b) Natural frequencies and modal shapes for 1st and 2nd mode for each thickness of plate



(b) Natural frequencies and modal shapes for 1st and 2nd mode for each λ_c

Figure 10: Relation of maximum C_T to vibrational characteristics with respect to thickness of Model 2.

Figure 11: Relation of maximum C_T to vibrational characteristics with respect to λ_c of Model 2.

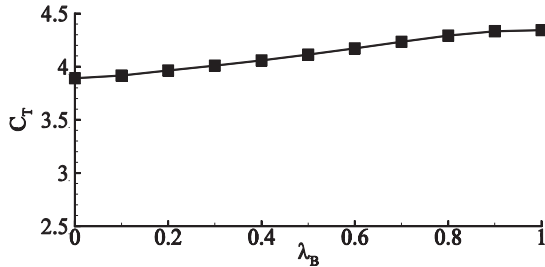
Second, we investigated the effect of λ_c when $h = 3.6$ as an optimal value and λ_B and λ_T were set to the initial value. Figure 11 shows the relation of the maximum C_T and vibrational characteristics with respect to λ_c . From Fig. 11a, the maximum C_T is 4.33 when $\lambda_c = 0.2$. From Fig. 11b, the first and second modes has coupling modes of spanwise bending and torsion, and the first and second natural frequencies are close to each other around $\lambda_c = 0.2$.

Third, we investigated the effect of λ_B when $h = 3.6$ and $\lambda_c = 0.2$ as optimal values, and λ_T was kept with the initial value. Figure 12 shows the relation of the maximum C_T and vibrational characteristics with respect to λ_B . From Fig. 12a, the maximum C_T is 4.32 for $\lambda_B = 1.0$. As can be seen in Fig. 12b, the first and second mode shapes are almost the same among all λ_B , but the first and second frequencies are closest at $\lambda_B = 1.0$.

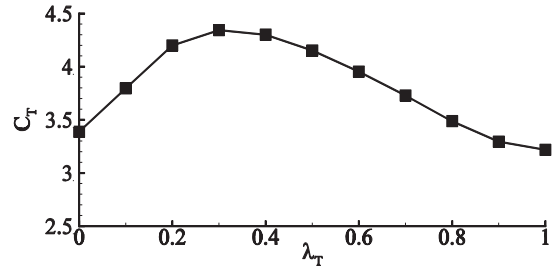
Finally, we investigated the effect of λ_T when $h = 3.6$, $\lambda_c = 0.2$, and $\lambda_B = 1.0$ as optimal values. Figure 13 shows the relation of the maximum C_T and vibrational characteristics with respect to λ_T . From Fig. 13a, the maximum C_T is 4.34 for $\lambda_T = 0.3$. From Fig. 13b, both first and second modes have coupling mode of spanwise bending and torsion, and the first and second natural frequencies are close to each other around $\lambda_T = 0.3$. Figures 14a and 14b shows the time histories of flapping and feathering angles, and the non-dimensional generalized coordinates from first to third modes, respectively. As shown in Fig. 14a, the dominant mode is first and second modes, and there is a phase difference of 105.5 deg between the two modes. As a result, the feathering motion is oscillated with the phase difference of 118.9 deg ahead of the flapping motion as shown in Fig. 14b. Compared to the maximum C_T of 4.21 for Model 1 with $AR = 3.46$, Model 2 with the optimal structure has larger maximum C_T of 4.34

These discussion are quite similar to those for Model 1. As with the case of the Model 1, when the

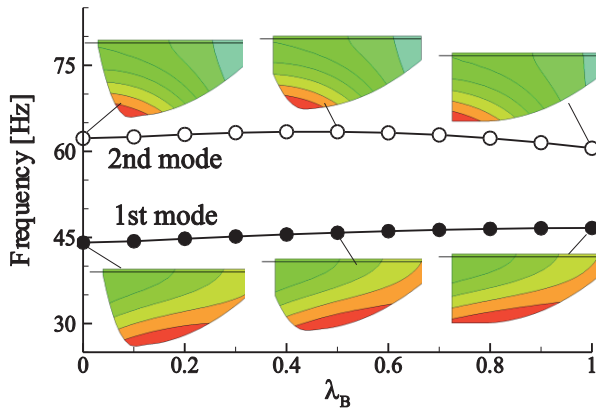
wing has an optimal structure, both first and second modes have coupling mode shape of spanwise bending and torsion, and the first and second frequencies are close to each other. This fact indicates that it is possible to conduct approximative optimal design by using only the results of vibrational characteristics without any aeroelastic analysis, which can save the calculation cost of numerical optimization.



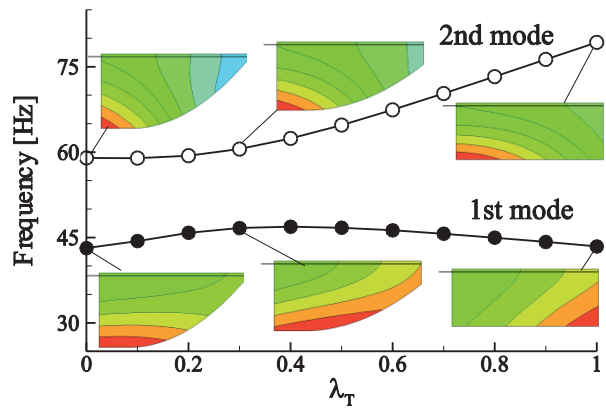
(a) Maximum C_T for each λ_B



(a) Maximum C_T for each λ_T



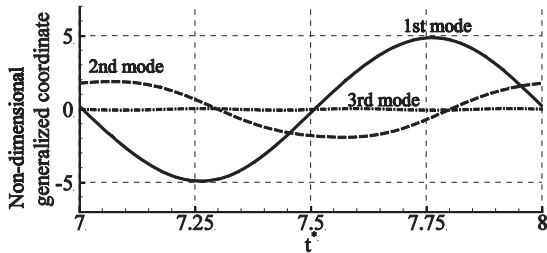
(b) Natural frequencies and modal shapes for 1st and 2nd mode for each λ_B



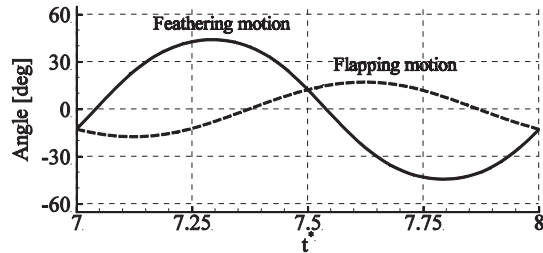
(b) Natural frequencies and modal shapes for 1st and 2nd mode for each λ_T

Figure 12: Relation of maximum C_T to vibrational characteristics with respect to λ_B of Model 2.

Figure 13: Relation of maximum C_T to vibrational characteristics with respect to λ_T of Model 2.



(a) Non-dimensional generalized coordinates



(b) Wing kinematics for flapping and feathering angles

Figure 14: Time histories of generalized coordinates and wing motion during a flapping cycle for the optimal case of Model 2 when the wing has a maximum C_T at input frequency of 40 Hz.

4. CONCLUSIONS

We have conducted aeroelastic analysis for the resonant type elastic flapping wing and investigated the effect of planform and thickness of the plate on the vibrational and aerodynamic characteristics. To search an optimal design parameters to maximize thrust coefficient, parametric studies have been conducted with respect

to the plate thickness, span location with the maximum chord, chord length at wing base, and chord length at wing tip. From these calculation, we obtained an optimal structure of the elastic wing, which generated larger thrust coefficient than the initial value. When the resonant type elastic flapping wing have an optimal wing structure, both first and second mode have coupling mode shape of spanwise bending and torsion, and the first and second natural frequencies are close to each other. Such an optimal wing can produce an appropriate wing kinematics with the phase difference of near 90 deg by coupling the two vibrational modes. These results indicate that it is possible to conduct approximative optimal design only by using vibrational analysis without any aeroelastic analysis, which can save the calculation cost of numerical optimization. Although we have not conducted numerical optimization but parametric study, the optimal structural design shown in this paper is never the global optimum solution. In the future work, we will conduct numerical optimization to obtain a global optimum solution. For practical design, we have to include not only thrust coefficient but also power and torque performance in an objective function.

ACKNOWLEDGMENT

Part of this study was supported by Japan Society for the Promotion of Science (JSPS) KAKENHI Grant-in-Aid for Young Scientists (B).

REFERENCES

- 1) Lentink, D., Jongerius, S. R., and Bradshaw, N. L. : The Scalable Design of Flapping Micro-Air Vehicles Inspired by Insect Flight. Control, *Springer-Verlag*, Berlin, Chapter 14, pp 185-205, 2009.
- 2) Keennon, M., Klingebiel, K., Won, H., and Andriukov, A. : Development of the Nano Hummingbird: A Tailless Flapping Wing Micro Air Vehicle, *Proc 50th AIAA Aerospace Science Meeting including the New Horizons Forum and Aerospace Exposition*, Nashville, Tennessee, AIAA 2012-0588, 2012.
- 3) Isogai, K., Kamisawa, Y and Sato, S. : Resonance Type Flapping Wing for Micro Air Vehicle, *Trans. of the Japan Soc. for Aeronautical and Space Science*, Vol. 52, No. 178, pp 199-205, 2010.
- 4) Isogai, K. and Kawabe, H. : Transition Flight Simulation of Flapping-Wing Micro-Aerial Vehicle Using Aerodynamic Database, *Trans. of the Japan Soc. for Aeronautical and Space Science*, Vol. 53, No. 180, pp 138-146, 2010.
- 5) Nagai, H. and Isogai, K. : Effects of Flapping Wing Kinematics on Hovering and Forward Flight Aerodynamics, *AIAA Journal*, Vol. 49, No. 8, pp 1750-1762, 2011.
- 6) Nagai, H., Isogai, K., Murozono, M. and Fujishiro, T. : Investigation on Structural and Aerodynamic characteristics of Resonant Type Elastic Flapping Wing, *28th Congress of International Council of Aeronautical Sciences*, ICAS2012-9.5.3, 2012
- 7) Gopalakrishnan, P. and Tafti, D. K. : Effect of Wing Flexibility on Lift and Thrust Production in Flapping Flight, *AIAA Journal*, Vol. 8, No. 5, pp 865-877, 2010.
- 8) Bansmer, S., Radespiel, R., Unger, R., Haupt, M., Horst, P. : Experimental and Numerical Fluid-Structure Analysis of Rigid and Flexible Flapping Airfoils, *AIAA Journal*, Vol. 48, No. 9, pp 1959-1974, 2010.
- 9) Wu, P., Ifju, P., and Stanford, B. : Flapping Wing Structural Deformation and Thrust Correlation Study with Flexible Membrane Wings, *AIAA Journal*, Vol. 48, No. 9, pp 2111-2122, 2010.
- 10) Yang, T., Wei, M., and Zhao, H. : Numerical Study of Flexible Flapping Wing Propulsion. *AIAA Journal*, Vol. 48, No. 12, pp 2909-2915, 2010.
- 11) Nagai, H., Isogai, K., Fujimoto, T. and Hayase T. : Experimental and Numerical Study of Forward Flight Aerodynamics of Insect Flapping Wing, *AIAA Journal*, Vol.47, No.3, pp.730-742, 2009.

ANALYSIS OF KINEMATICS OF FLAPPING WING MAV USING OPTITRACK SYSTEMS

Matthew NG Rongfa⁺¹, Teppatat PANTUPHAG⁺², Sutthiphong SRIGRAROM⁺³ and Chinnapat THIPYOPAS⁺⁴

^{+1, +3} University of Glasgow Singapore, Singapore

^{+2, +4} Kasertsart University, Bangkok, Thailand

This paper presents the kinematics of the wing of the ornithopter-like MAV by means of motion-capturing technique (Optitrack). The positions of the marker(s) of one complete oscillation are presented with respect to time in a two-dimensional plane and understand the wing dynamic behaviour of an ornithopter through these graphs. Specifically the wing geometry and kinematics with time in three dimensional space is analysed on the kinematic data of the wing tip path, leading edge bending and trailing edge flap. With the wing geometry obtained, fluid-structure interaction of this flapping wing MAV, by means of CFD. The commercial software ANSYS Fluent is used.

Keyword: Motion-capturing¹, Optitrack², Kinematics³, Fluid-Structure Interaction⁴, Ornithopter MAV⁵.

1. INTRODUCTION

Flapping wing flight is one of the most successful and widely used forms of locomotion in the natural world. Approximately ten thousand scientifically described species of birds and nearly a million known insects rely on powered flight as a form of aerial locomotion¹. Unlike conventional aerial vehicles which rely on a rigid wing and propeller to generate lift and thrust respectively, or a rotary wing in the case of a rotorcraft to generate lift and thrust, birds generate lift and thrust by moving their wings relative to their body in an oscillatory (flapping) motion.

Aerial vehicles that imitate this oscillatory motion for the purpose of flight are known as ornithopters. Ornithopters offer several potential advantageous performance benefits which includes an increase of propulsive efficiency and manoeuvrability compared to a fixed-wing aircraft. Recent theoretical work concerning minimum induced loss suggests that ornithopters may be able to reach a propulsive efficiency of 85% for micro air vehicles (MAV)² and for large ornithopters with wingspans up to 3m, the wing's propulsive efficiency may reach 77%³.

Based on observations of birds, researchers claim that ornithopters are capable of operating with better manoeuvrability compared to fixed-wing vehicles and can be made to hover more easily than conventional aircraft. In theory, this signifies a promising alternative to conventional aerial vehicles. While it is unlikely that humans can engineer ornithopters that perform as well as nature's flyers in the near term, the propulsive efficiency of flapping flight has been shown to meet and possibly even exceed that of more traditional means of propulsion. The goal of this study is to provide an insight to ornithopter flight by analyzing the flapping wing kinematics and flexible wing membrane shapes of a 1.3m wingspan ornithopter by means of motion capture.

⁺¹Matthew.Ng_2014@SIT.SingaporeTech.edu.sg, ⁺²teppatat06@gmail.com, ⁺³spot.srigarom@glasgow.ac.uk, ⁺⁴fengcpt@ku.ac.th

2. WING TRACKING EXPERIMENTS

The aim of the experiments is to isolate the wing geometry and kinematics with time in three dimensional space and perform analysis on the kinematic data of the wing tip path, leading edge bending and trailing edge flap.

(1) Description of the ornithopter platform

The ornithopter studied in this experiment, see Figure 1, is a commercially available 1.3 metre wingspan, rib-stop fabric remote controlled ornithopter kit. Figure 1 illustrates the axes orientation, with respect to the ornithopter, which will be used when describing the kinematic results in the subsequent subsections. The origin for the axes of the graphs will be set at the pivot joint of the wing.

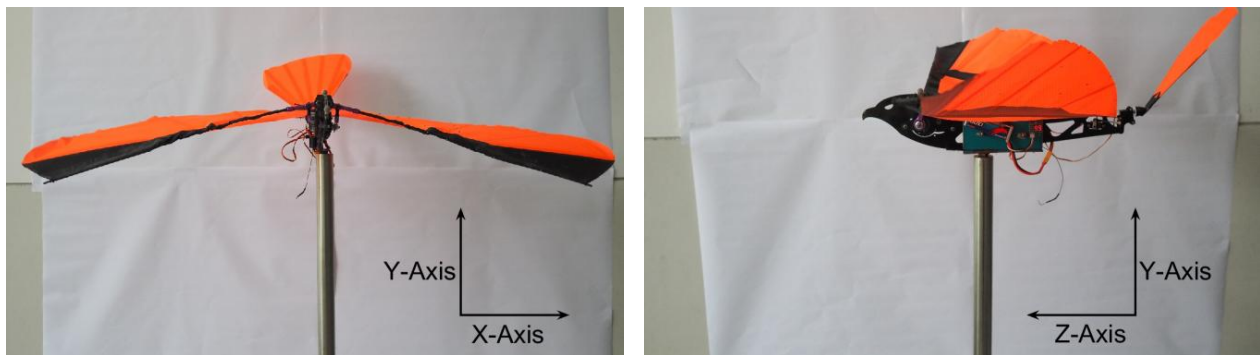


Figure 1: Axes orientation with respect to ornithopter

(2) Experiment setup and procedure

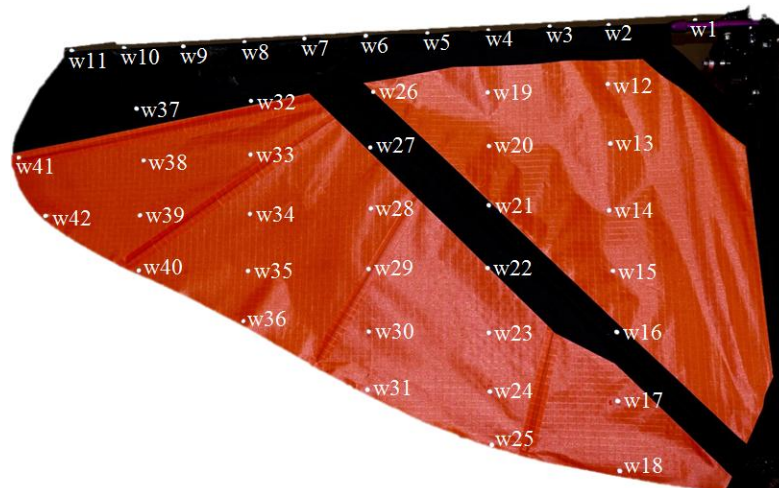


Figure 2: Reflective marker layout on the ornithopter

To prepare for the experiments, forty-two 3mm retroreflective hemispherical markers were fitted onto the left wing of the ornithopter. The wing was split up into six sections: the leading edge and five 'blade elements' along the wing membrane. Markers were placed at a 5cm interval along both the leading edge spar and each 'blade elements'. Each 'blade elements' were spaced at 10cm intervals. Lastly two markers were

placed at the wing tip along the membrane. The markers were labelled from w1 to w42 as shown in Figure 2. Blade elements are defined as follows: blade element 1 is made up of markers w12 to w18, blade element 2 is made up of markers w19 to w25, blade element 3 is made up of markers w26 to w31, blade element 4 is made up of markers w32 to w36 and blade element 5 is made up of markers w37 to w40.

(3) Kinematic Results

a) Wing Tip Path

The left wing leading edge support rod is made from carbon fibre. Due to the possibility of the wing spar flexing, the wing tip path (the tip of the rod furthest from the wing root) was expected to travel in an elliptical or figure-of-eight motion along the z-y axis with minimal flex in the z-direction, similar to the wingtip strokes of larger birds. While the plot of the wing tip path on the x-y axis would follow a predictable crescent movement due to the wing flexing in the y-direction.

Figure 3 shows the trajectories of the wingtip and its deflection from the zero point of the Y-axis (when the wing is horizontal) as captured by Optitrack motion tracking system. For this motion capture take, the wing oscillated at an approximate 3.93Hz when throttle is at 50%. The upward and downward stroke path had been identified by analysing the translational position of the wing tip marker from the data exported from motive.

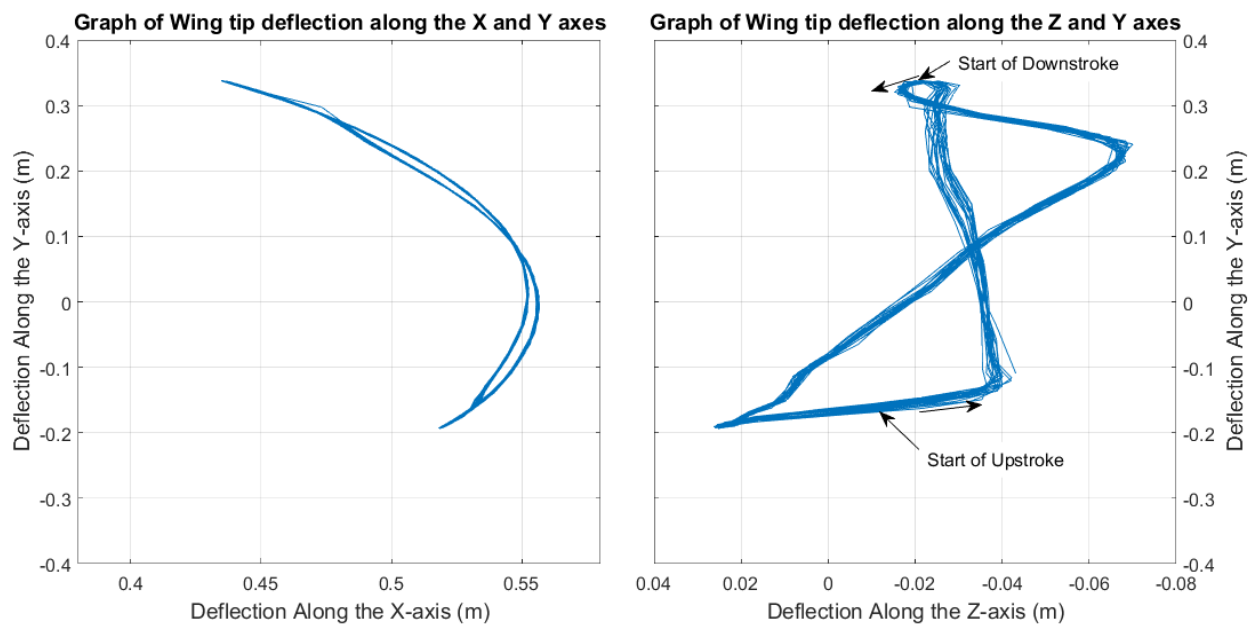


Figure 3: Graph of trajectories of wingtip for X-Y and Z-Y views

The experiment confirmed predictions of the wing bending along the y-axis during one complete cycle of an upward and downward stroke. A single stroke phase can be subdivided into three sub-phases: (1) initial acceleration, (2) mid swing and (3) final deceleration. For deflections along the z-axis, while the wing tip took a figure-of-eight path, there is additional flexing between 0.2m to 0.3m of the y-axis as the wing decelerated at the end of an upstroke to transit into a downstroke. This additional bending by observation of a

frame-by-frame video of the wing flapping at 50% throttle, can be attributed to the elastic energy stored in the wing spar as it travels up and down a stroke, this energy is released when the pivoting arm stops at the end of an upstroke and downstroke causing the wing tip to travel a few additional centimeters. It was also noted that some elastic energy could have been transferred from the stand to the wing when the stand flexed as it resisted the forward thrust of the ornithopter, adding to the z-axis motion.

b) Leading edge bending

The motivation for analysing the kinematic results of the leading edge bending is due in part to the observation of a large difference in leading edge flex when comparing a single upstroke to a single downstroke (see Figure 4).



Figure 4: Side-by-side views of a single downstroke (left) and upstroke (right) of an ornithopter

The trajectories of markers w1 to w11 which represented the leading edge of the wing were plotted for the purpose of this experiment. Figure 5 shows the X-Y axis (front view) of the ornithopter at flapping frequency 3.93Hz.

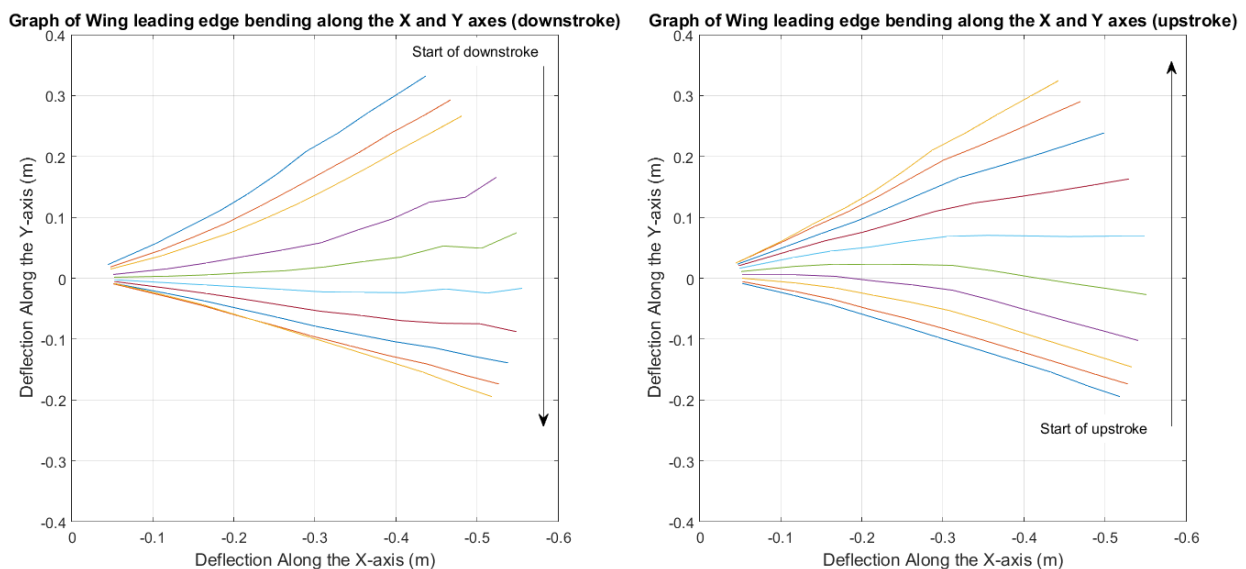


Figure 5: Graph of trajectories of leading edge plot for a downstroke (left) and an upstroke (right)

In subsection 3a, the wingtip path showed up to 7cm rearward deflection and 2cm forward deflection along the z-axis due to passive leading edge bending in the downstroke phase. The downstroke phase theoretically being the “power” phase is the period which most of lift and thrust is generated. In addition to the body force acting on the leading edge due to its acceleration through the air, there is a combined vectored force of lift and thrust also acting on the leading edge. As a result the leading edge experiences high inertial loads causing it to flex. This flex is greatest at mid swing when the acceleration reaches its peak, see Figure 5. A response to high inertial loading which is especially strong near the wing tip increases the local stroke angle. A lag then forms between the wing root and wing tip stroke angle.

c) Wing membrane shape

Unlike conventional aerial vehicles where the wing profile is generally constant throughout flight, the wing profile of an ornithopter in a single wing-beat cycle is in constant change as it reacts to the changes in airflow and forces acting on the wing. This subsection examines the nominal wing profile by examining blade element 3 which is located at the centre of the wing, at various frames for a single downstroke and upstroke cycle mid-flight.

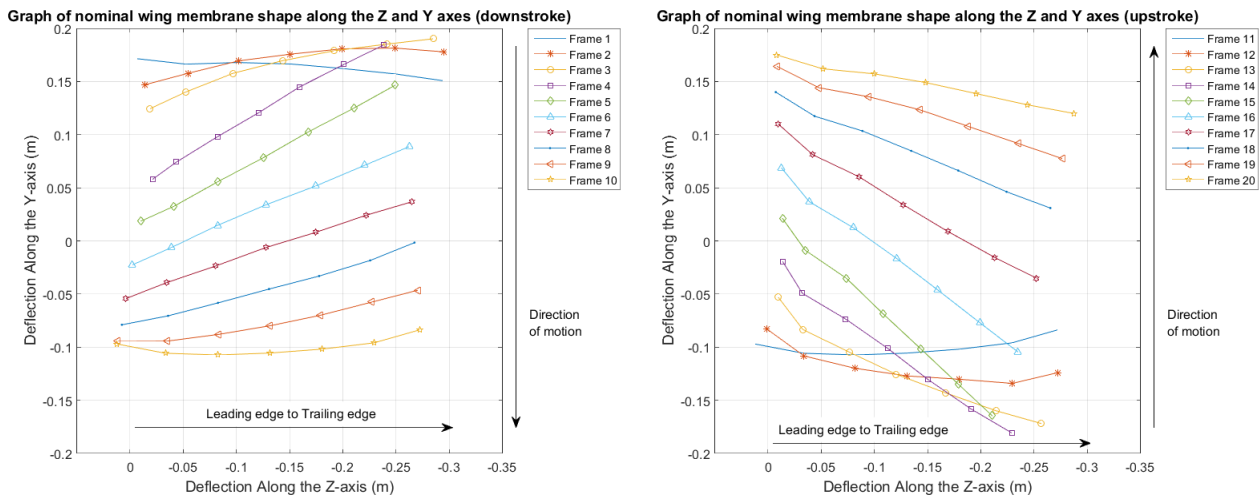


Figure 6: Graph of nominal wing membrane shape along the Z and Y axes of a downstroke (left) and an upstroke (right)

Frame 1 to 3 as seen in Figure 6 shows the transition from an upstroke of the previous wing-beat cycle to the start of a downstroke of the current wing-beat cycle. Similarly Frame 11 to 13 shows the transition from the downstroke to an upstroke. These transition phases demonstrate the lead-lag behaviour of the wing between the leading edge and the trailing edge. This lead-lag behaviour contributes to the twisting motion component of the wing.

The Movie of the entire experiments can be viewed at this Youtube link: <https://www.youtube.com/watch?v=83RvX7pw0ew&feature=youtu.be>

3. AERODYNAMICS OF FLAPPING WINGS

With the geometry information obtained in previous section, we do create the 3D CAD model of this flapping wing model and analyze the flow and aerodynamics around this wing models, corresponds to each of the flapping mode. The geometry is created by SolidWorks, and analyse using commercial finite element analysis software ANSYS Fluent Release 13.

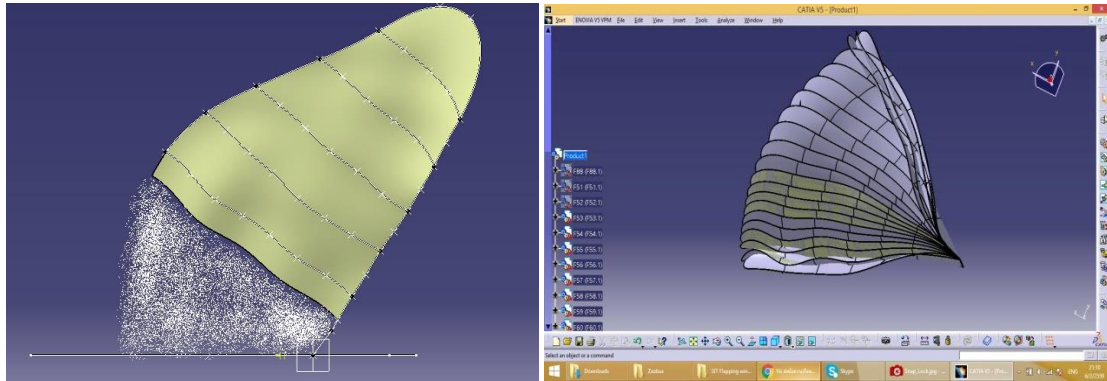
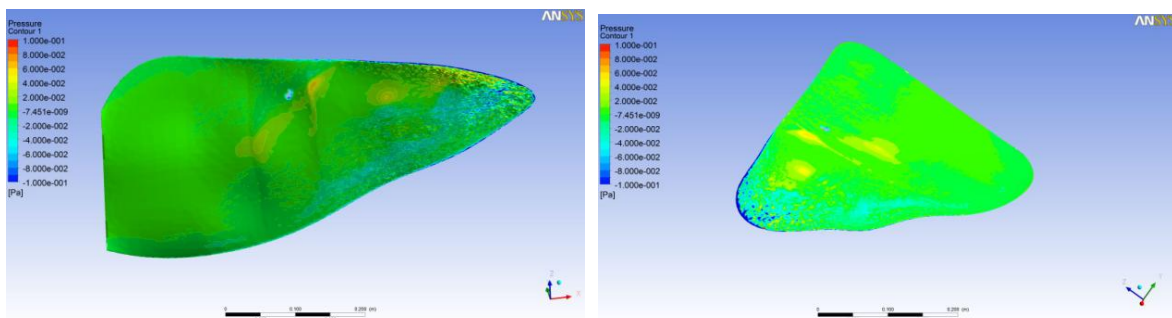


Figure 7 (left): Ornithopter wing reconstructed from Optitrack systems,
Figure 8 (right): Ornithopter wing positions during downwards (powered) flaps, rebuilt in SolidWorks.

We truncate the body of the flapping wing model and consider only the flexible wing. The undulating texture of the wing is due to the flexibility of the wing, obtained from tracing point in previous section. We focus attention to the middle of the upward (recovery) stroke and the middle of the downward (power) stroke. Figures 9 and 10 show the pressure contours on the flapping wing, while the wing was in the middle of the upward (recovery) stroke. On the lower surface (figure 9), there is mostly suction (negative) pressure. On the upper surface (figure 10), there pressure is positive, as anticipated. We notice that most force applied mostly in the inboard part of the wing (toward straight edge -which are the truncated body). Figure 12 show the streamline plot, where the trailing edge is obvious, following the motion of the wing.



Figures 9 (left) and 10 (right): Pressure contours on the lower (suction) side (figure 9), and the upper (pressure) side (figure 10) of flapping wing, while the wing is in the middle of recovery stroke.

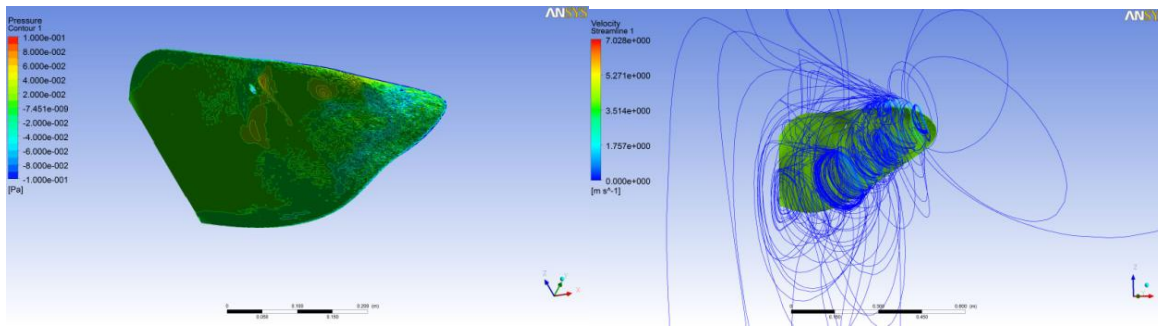
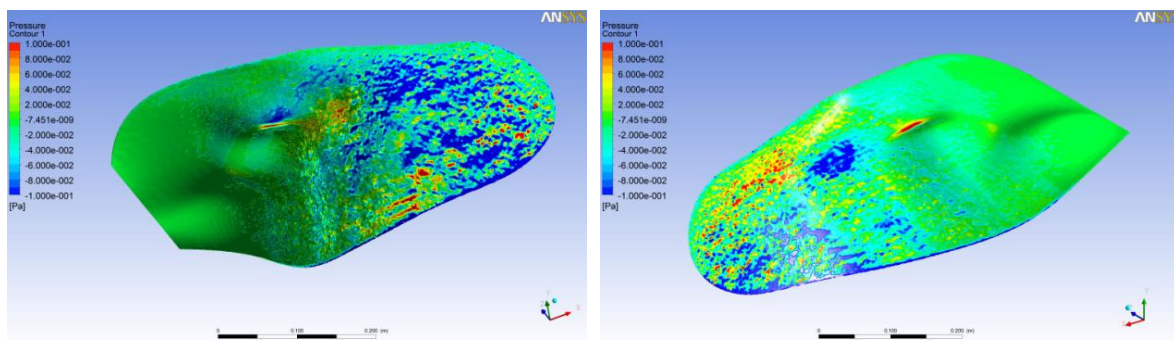


Figure 11 (left): Pressure contours on the lower (suction) side while the wing is in recovery stroke.

Figure 12 (right): Streamline around the wing, indicating the strong trailing edge vortex.

Figures 13 and 14 show the pressure contours on the flapping wing, while the wing was in the middle of the downward (power) stroke. Likewise, the undulating texture of the wing is due to the flexibility of the wing, obtained from tracing point in previous section. On the lower surface (figure 13), there is mostly positive pressure, indicating the lift force is generated. Also, figure 13 show that the lift is mostly from the inboard part of the wing, where the pressure is more smooth. The outboard part (to the right of the figure), there is more separated and highly unsteady. This shows that the outboard part of the wing is mostly for direction control. Also, it is flexed upwards following the downwards motion of the wing. On the upper surface (figure 14), there pressure is negative (suction), as anticipated. Again, the contour shows that most force applied mostly in the inboard part of the wing, whereas the outboard part of the wing (to the left of the figure), the flow is simply separated with small scales eddies. Figure 15 shows the 3D view of the wing. The wing is under highly twisted position in this power stroke. Figure 16 shows the streamline plot. The extent of the wake behind the wing (area around the upper right part) is obvious.



Figures 13 (left) and 14 (right): Pressure contours on the lower (suction) side (figure 9), and the upper (pressure) side (figure 10) of flapping wing, while the wing is in the middle of power stroke.

From these figures 9 to 16, we find that the flexibility of wing allows the wing appear to produce more pressure (lift and thrust forces subsequently) at the inboard section of the wing. Whereas in the area at the outboard part of the wing, the wing is more deflected following the flapping motion, and that, the flow is mostly separated and highly unsteady with lesser pressure force applied.

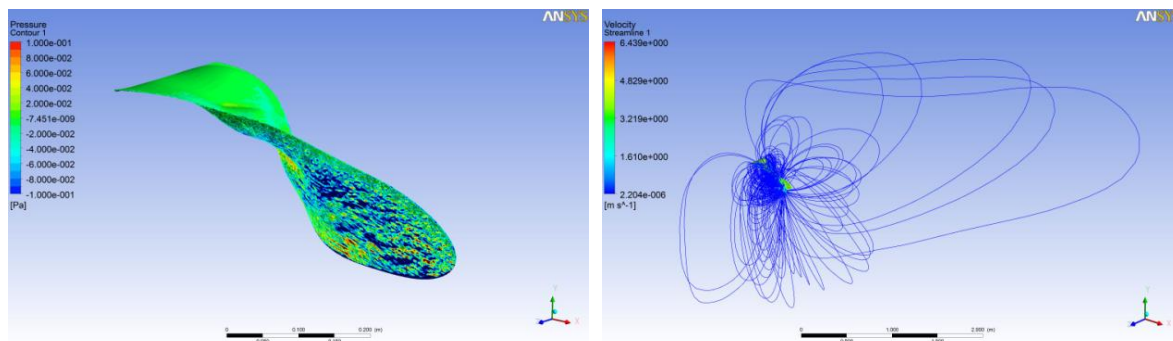


Figure 15 (left): 3D view of this highly twisted flapping wing, while the wing is in recovery stroke.

Figure 16 (right): Streamline around the wing, showing the extend of the wake.

4. CONCLUSIONS

This the kinematics of the wing of the ornithopter-like MAV by means of motion-capturing technique (Optitrack). We could capture the full motion of the flapping ornithopter at various position and obtain the geometry (texture) of the deformed wing. This gives us opportunity to analyse the fluid-structure interaction behaviour of this flapping wing. The passive deformation of the wing surface follows the motion of the wing and gives more lift and propulsive force. We analyse the flow around this deformed wing, using information of the geometry obtained. The flexibility of wing allows the wing appear to produce more force at the inboard section of the wing.

REFERENCES

- 1) Alexander, D.D.E. and S.L. Taliaferro, *On the Wing: Insects, Pterosaurs, Birds, Bats and the Evolution of Animal Flight*. 2015: Oxford University Press Incorporated.
- 2) Hall, K.C. and S.R. Hall, *Minimum induced power requirements for flapping flight*. *Journal of Fluid Mechanics*, 1996. **323**: p. 285-315.
- 3) DeLaurier, J.D., *An ornithopter wing design*. *Canadian aeronautics and space journal*, 1994. **40**(1): p. 10-18.

ORNITHOPTER TYPE FLAPPING WINGS FOR AUTONOMOUS MICRO AERIAL VEHICLES

Sutthiphong Srigrarom ⁺¹ and Woei-Leong Chan ⁺²

⁺¹ University of Glasgow Singapore, Singapore

⁺² Temasek Laboratories, National University of Singapore, Singapore

In this paper, an ornithopter prototype that mimics the flapping motion of bird flight is developed, and the lift and thrust generation characteristics of different wing designs are evaluated. Various wings of insects and birds were evaluated to understand how these natural flyers with flapping wings are able to produce sufficient lift to fly. Experiments on different wing designs and materials were conducted and a paramount wing was built for a test flight. The first prototype has a length of 46.5cm, wing span of 88cm, and weighs 161g. A mechanism which produced flapping motion was fabricated and designed to create flapping flight. The flapping flight was produced by using a single motor and a flexible and light wing structure. A force balance made of load cell was then designed to measure the thrust and lift force of the ornithopter. Three sets of wings varying flexibility were fabricated, therefore lift and thrust measurements were acquired from each different sets of wings. The lift was measured in ten cycles computing the average lift and frequency in three different speeds or frequencies (slow, medium and fast). The thrust measurement was measure likewise but in two cycles only. Several observations were made regarding the behaviour of flexible flapping wings that should aid in the design of future flexible flapping wing vehicles. The wings angle or phase characteristic were analyzed and studied.

Keyword: Ornithopter-like Flapping Wing, PET, Orcon, cambered wing, flat wing, MAV

1. INTRODUCTION

At University of Glasgow Singapore (UGS), we are developing the resonance type flapping wing models, as shown in figures 1 and 2 . The proposed resonance type flapping wing will utilize the resonance phenomenon of a two-degree of freedom elastic system, that is, the wing is supported by the springs for flapping and feathering motions, being oscillated, at the resonance frequency of the system. The movie of our flapping wing can be seen at these Youtube links: <http://www.youtube.com/user/HarpagornisUniSIM> and <https://www.youtube.com/watch?v=E5U4Cwm0qMw> .



Figure 1 (left) and 2 (right): UGS 1st and current Ornithopter-like flapping wing MAVs

2. LIFT AND THRUST FORCE MEASUREMENTS

The experimental apparatus utilised by the authors include a force measuring load cell, a test assembly, and video recording is also taken of the mechanism with the various wing designs flapped. The force

⁺¹spot.srigrarom@glasgow.ac.uk, ⁺²tslclw@nus.edu.sg

measurement system used was the transducer. It should be noted that the expected measured thrust and lift are very small, i.e. around 0.1-1.0 N. The force measuring load cell utilised in this project is an Omega Engineering, LCMFD-20N load cell. This LCMFD-20N load cell is small in size and capable of providing highly accurate readings of a 2041 gram capacity. In addition, this model is selected because of its high frequency resonant characteristics, minimal contamination from off-axis loads, and robust overloading tolerances. The load cell measures the forces when the prototype ornithopter flaps its wing on a force balance by converting these forces into electric signals, which will be displayed on the Omega DP41 digital panel.

The objective of this project is to characterise the different lift and thrust generation performance from three different wing designs, namely PET cambered thin wing, Orcon cambered thick wing and Orcon flat wing, different thrust measurement techniques will be investigated. Here we present the method for testing the lift and thrust generation of the prototype ornithopter. Kevlar thread is used extensively in this project as this innovative thread is light and its strength to weight ratio makes it five times as strong as steel. Kevlar thread does not break instantly but progressively, providing a non-catastrophic failure mode allowing safety margin.

In our thrust and lift measurement setup, the mounting orientation of the load cell is shown in Figure 3. The load cell is fixed onto the test assembly in a stationary position. The front portion of the flapping mechanism is attached to the load cell while the top and bottom segments of the flapping mechanism are tied vertically to the test assembly with the use of kevlar thread. Thus, after mounting the pair of wings onto the flapping mechanism and turn on the motor, the flapping mechanism is constrained by the kevlar thread so that it is only capable of motion in the X—direction for thrust or Y- direction for lift only

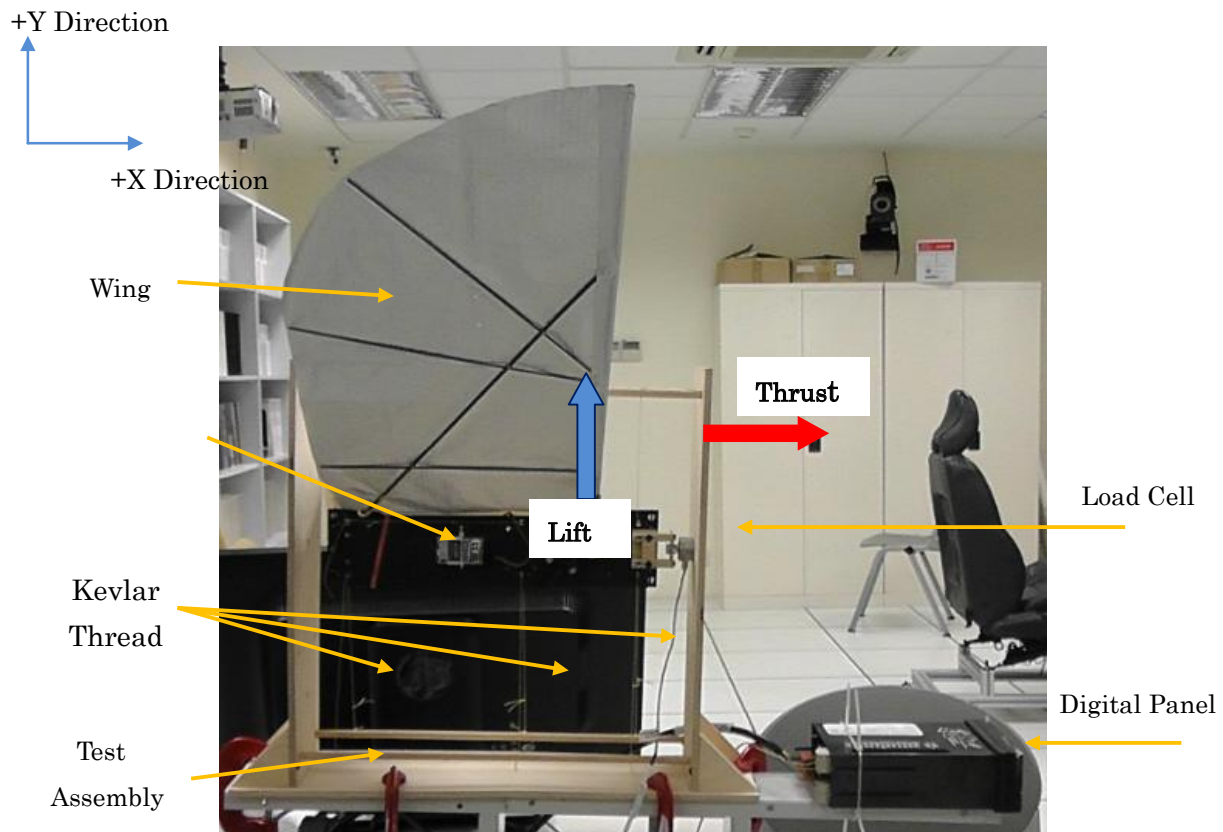


Figure 3: Load Cell Thrust and Lift Measurement Setup.

As the flapping mechanism is moving, the load cell is under both compression and tension, which resulting in negative and positive values respectively displayed on the digital panel. This is due to that a flapping wing is an aerodynamic machine with two strokes, the upstroke and the downstroke. In this experiment, the lift produced for the three different wing designs at three different flapping frequency will be

measured and recorded in an Excel spreadsheet. Before recording the lift values during the flapping period, the weight of the flapping mechanism with the wings attached is measured at static condition. By subtracting the weight measured at static condition from all the values obtained during the flapping phase, the true lift force produced by the prototype is then recorded for analysis.

The measurement of the flapping frequency of the prototype is achieved through the use of a digital camera. The digital camera is placed in front of the test assembly which allows the author to analyse how the wings are flapped in up- and downstroke manner. The videos are then loaded into the Ulead software to process the captured video into frames. There are 25 frames for each second of the video recorded. Hence, by calculating the number of frames taken for the prototype to produce a full cycle consisting of upstroke and downstroke, the period (T) can be obtained using the following equation:

$$T = (1 / 25) \times \text{Number of frames per Full cycle.} \quad (1)$$

Once the period is obtained, the flapping frequency (f) is calculated using $f = 1/T$. Hence, the flapping frequency can then be determined. The figure below shows the motion of the flapping wings in one full cycle.

3. MATERIAL SELECTION AND RESULTS

The material that we used for our prototype was the transparency that we used for OHP. This material has good strength but is heavy. The second material that we used is the orco film AN-57W. It is very light, strong and is made with metallized polyvinyl fluoride film reinforced with nylon yarns.. We felt we could reduce the weight of the wing further and after much investigation, we felt we could remove a layer of carbon fibre wing used for the structure.

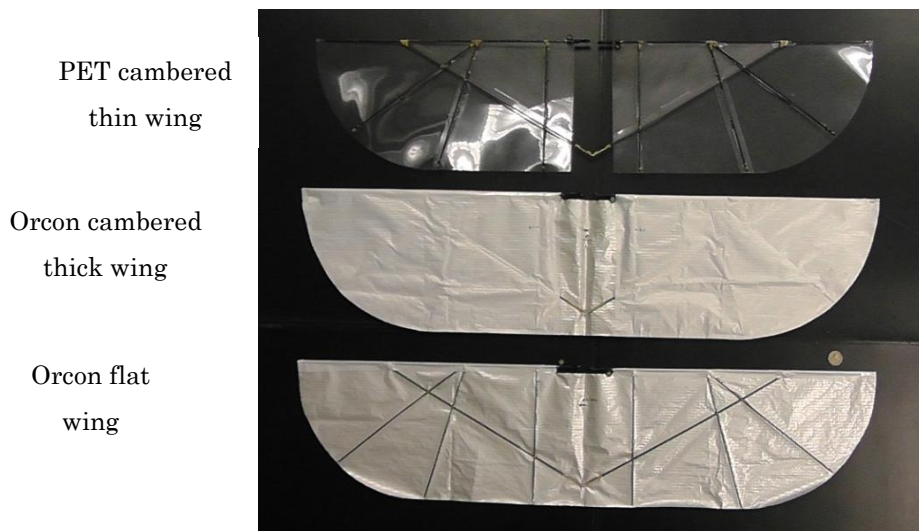


Figure 4: Three Different Wing Designs (Bottom View)

Next, we presents the findings of various experiments that the author has conducted. The main element is the results and analysis of evaluation of different wing designs. The average thrust and lift output are measured and compared to different wing designs to understand what styles of wings are more effective. The time-varying force profile can be examined to gain understanding into why particular wing designs prove more effective than others.

It is observed from Figure 5 that the thrust tends to produce four peaks. This is due to the motion of

flapping wings. For each test, thrust performance is recorded in terms of 2 flapping cycle that consist of upstroke, downstroke, upstroke and downstroke motion, which explains the 4 peaks that are captured in the graph.

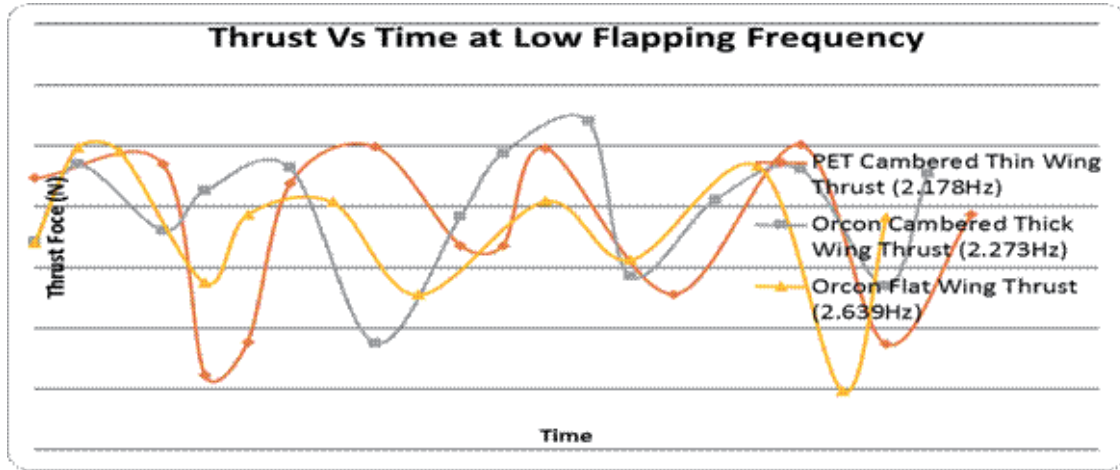


Figure 5: Thrust against Low Flapping Frequency (2 Full cycle)

As mentioned in earlier, negative values are obtained when the load cell is under compression. Since the load cell is experiencing compression throughout the flapping period, it means that thrust is always being generated throughout the flapping cycle. More thrust is generated on the downstroke as compared to upstroke.

Apart from that, the slight periodic nature of the thrust is due to the inertial effects of the flapping mechanism. In the graphs above, the inertial effects have not been removed. When flapping with the test set up as described earlier, some inertial effects were present in the thrust direction. This is because the clearances between the flapping mechanism and the test assembly did not purely constrain the flapping in the vertical direction.

(1) Thrust Comparison between Wings of Various Design

It can be observed from the results as shown in the figure below that Orcon Flat wing has a better thrust generation performance as compared to the rest of the wing designs. It is interesting to note that the thrust for the Orcon flat wing resulted in a linear relationship when compared against the flapping frequency.

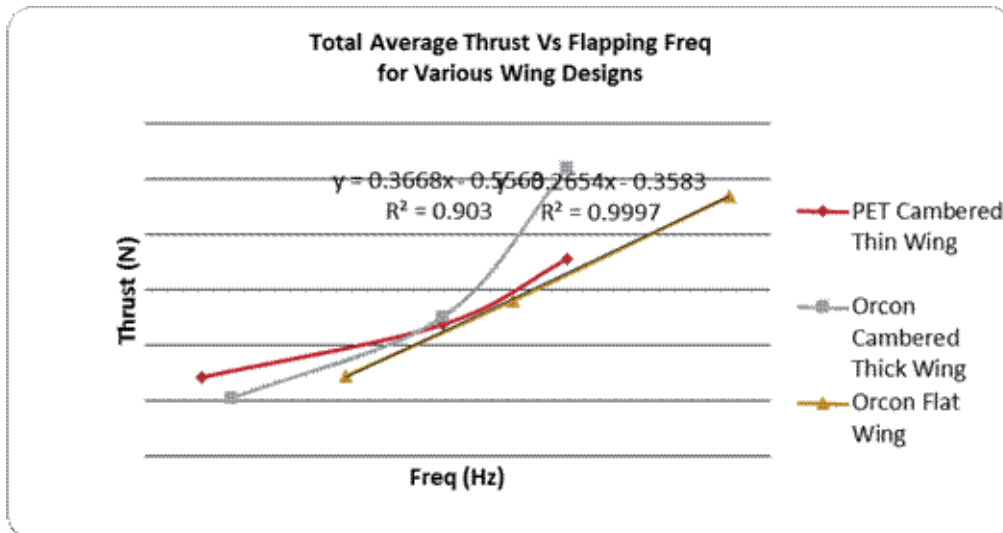


Figure 6: Total Average Thrust against Flapping Frequency for Various Wings

The flapping wing mechanism constantly appears to produce thrust. The reason for this is that the wing is constantly changing its shape and angle of attack dynamically. On the downstroke the wing is pitched down, forcing air in the $-Y$ direction, while in the upstroke the wing sweeps forward and up, minimizing the movement of air in the direction causing negative thrust. For both cases the thrust is relatively constant throughout the cycle. The magnitude of the thrust appears to slightly increase for the higher frequency.

Orcon Flat wing is much flexible than the other wing designs. Flexible wings can attain efficiency as more elastic the wing is, the more thrust produced and Orcon material is used to achieve a minimum weight. It is observed that PET cambered thin wing has a slightly slower flapping rate. It is because the weight of the flapping mechanism with that pair of wings on is 1.6N, which weights the highest and tends to have more inertia. Hence, the motor will require more torque to drive the wings. With the same torque, heavier wing will have slightly slower flapping rate which results in a lesser thrust as compared to the Orcon Flat wing.

(2) Lift Comparison between Wings of Various Design

Lift generation tests are done using the load cell setup method as mentioned earlier on three different wing designs. Three sets of wings are tested at three different flapping frequency starting from low, then medium and lastly to high, and the lift force is compared at each speed. As the flapping mechanism is moving in the $\pm Y$ direction, the load cell is under both compression and tension, which resulting in negative and positive values respectively displayed on the digital panel. This is due to the matter of fact that a flapping wing is an aerodynamic machine with two strokes, the upstroke and the downstroke. During the upstroke, the flapping mechanism will be 'pushing' at the load cell, which results a compression at the load cell and negative lift values will be displayed. During the downstroke, lift is generated and the flapping mechanism will be 'pulling' the load cell, which results a tension at the load cell and positive lift values will be shown.

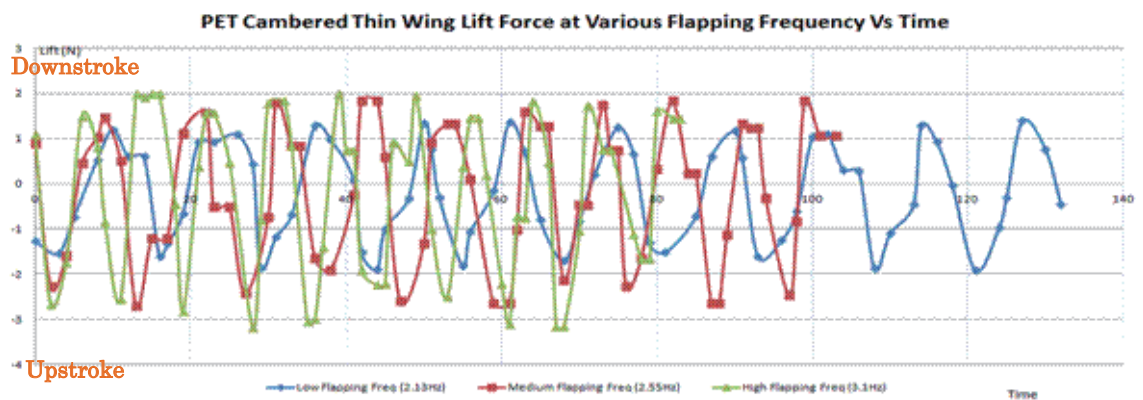


Figure 7: PET Cambered Thin Wing Lift against Time (10 Full cycle)

The first wing design to test is the PET cambered thin wing and the plots in Figure 7 shows the lift against a period of time of 10 full flapping cycle for three different flapping frequency. It is observed that as the flapping frequency goes higher, the lift is slightly increased. The average lift force generated during the low, medium and high flapping cycle are -0.196N , -0.14N and -0.218N respectively. From the figure above, the results are consistent with the research made as discussed in earlier section that lift is generated at the down stroke, which reaches the maximum lift of 1.38N at about 0° to -10° angle. However, the minimum lift of -1.92N is reached when the flapping wing is on its upstroke. Note that the peak negative lift is greater than the peak positive lift, thus indicating that no net lift is generated.

The second wing design to test is the Orcon cambered thick wing and the plots in Figure 8 shows the lift against a period of time of 10 full flapping cycle for three different flapping frequency. It is observed from the figure above that faster the flapping frequency, the higher the lift is generated. The average lift force generated during the low, medium and high flapping cycle are -0.23N , -0.26N and -0.3N respectively.

Therefore, it is also observed that faster the flapping frequency will result a higher negative lift force value.

From the figure 8, the result is similar to the PET cambered thin wing that lift is generated at the down stroke, which reaches the maximum lift of 1.46N at about 0° to -10° angle. However, the minimum lift of -2.04N is reached when the flapping wing is on its upstroke. Note that the peak negative lift is greater than the peak positive lift, thus indicating that no net lift is generated.

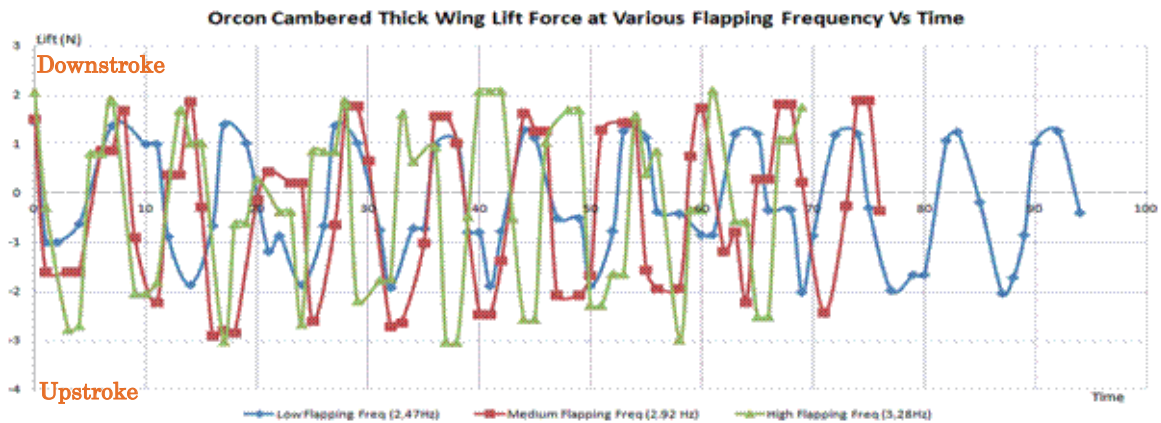


Figure 8: Orcon Cambered Thick Wing Lift against Time (10 Full cycle)

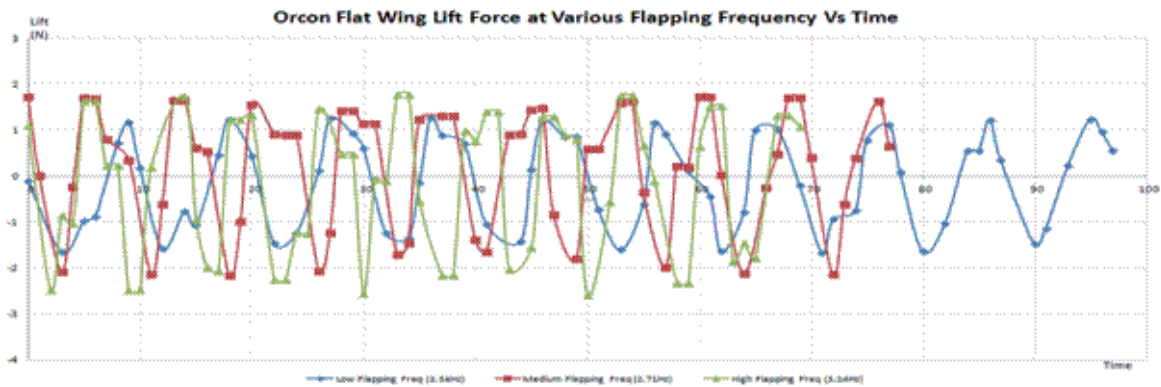


Figure 9: Orcon Flat Wing Lift against Time (10 Full cycle)

The third wing design to test is the Orcon flat wing and the plots in Figure 9 shows the lift against a period of time of 10 full flapping cycle for three different flapping frequency. From Figure 39, it is observed that faster the flapping frequency, the higher the lift is generated. The average lift force generated during the low, medium and high flapping cycle are -0.07N, 0.26N and -0.14N respectively. It is interesting to find that a small amount of lift is generated at medium flapping frequency.

From these figures, the result is similar to the previous 2 tests that lift is generated at the down stroke, which reaches the maximum lift of 1.25N at about 0° to -10° angle. However, the minimum lift of -1.66N is reached when the flapping wing is on its upstroke. Note that the peak negative lift is greater than the peak positive lift, thus indicating that no net lift is generated.

4. INVESTIGATION OF PHASE ANGLES

Figures 10,11 and 12 show the investigation of phase angles against the lift generation for the 3 different wing designs at various flapping frequency. The first wing design to be discussed is the PET

cambered thin wing, followed by the Orcon cambered thick wing and lastly the Orcon flat wing.

It is observed from the previous figures that as the flapping frequency increases, there is a transition from a "smooth circular" graph to a "figure-of-eight" graph. An example of the lift generation from the Orcon flat wing flapping at the medium frequency graph as shown below, during the initial downstroke, there is a sudden rise in lift until it reaches its peak. When the lift reaches its peak somewhere around 30° , it is noticed that constant lift is produced until it reaches at an angle of 0° . This could be the leading edge vortex (LEV) that causes it. It appears that LEV can enhance lift by attaching the bounded vortex core to the leading edge during wing translation. The vortex, formed roughly parallel to the leading edge of the wing, is trapped by the airflow and remains fixed to the upper surface of the wing. As air flows around the leading edge, it flows over the trapped vortex and is pulled in and down to generate the lift.

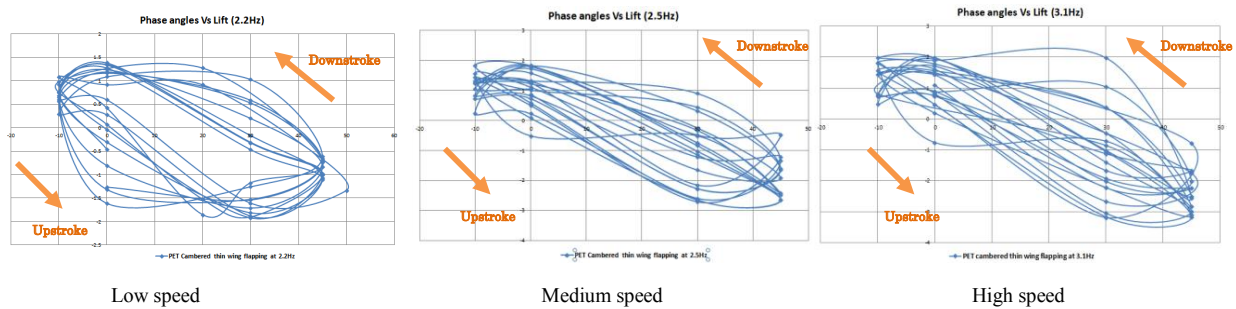


Figure 10: Phase Angle Vs Lift for PET Cambered Thin Wing

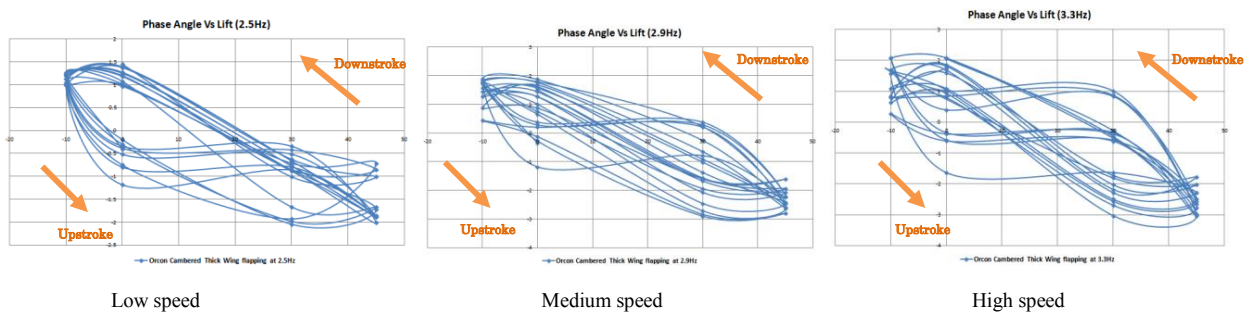


Figure 11: Phase Angle Vs Lift for Orcon Cambered Thick Wing

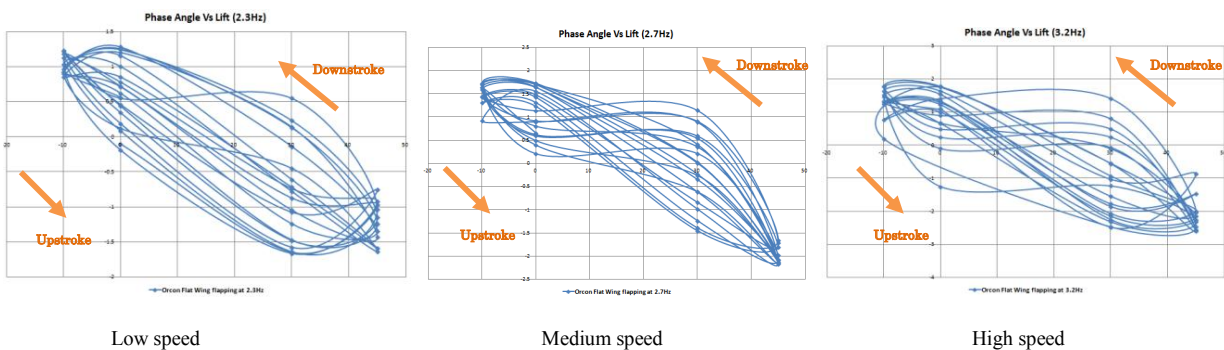


Figure 12: Phase Angle Vs Lift for Orcon Flat Wing

There are two routes that can be seen from the graphs, the first route which is the positive angle transit to negative angle (Downstroke) and the second route is the reverse of the first route (Upstroke). From Figure 46, the net lift can be easily seen by looking at the difference between the 2 routes.

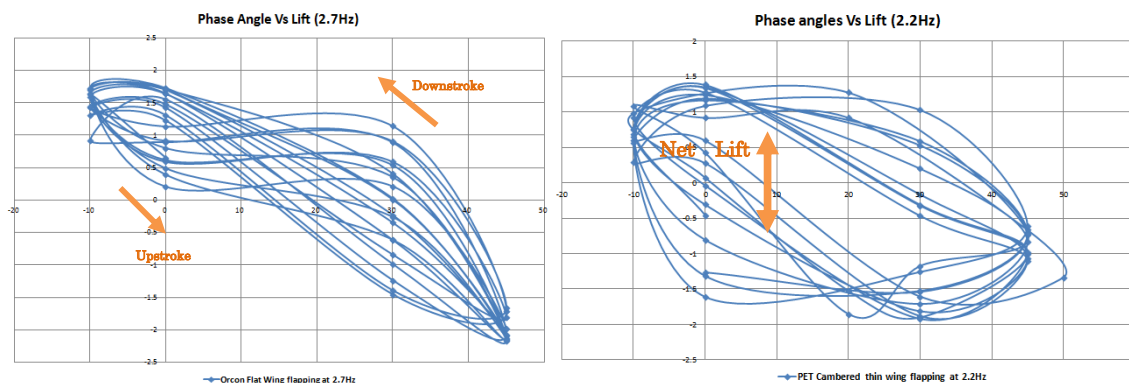


Figure 13 (left): Phase Angle Vs Lift for Orcon Flat Wing Flapping at 2.7Hz

Figure 14 (right): Net Lift Generation

5. CONCLUSION

This paper reports the research and development of our in-house near-resonance type albatross-like flapping wing models for MAV. When measuring the aerodynamic forces produced in the experiments, it was found that thrust was constantly generated, while lift was periodic in nature following a sinusoidal trend. It was found that lift is predominantly generated on the downstroke, with negative lift being generated on the upstroke. It was found out that the thin wing has both lift and thrust produced on than the PET film and thick cambered wing. Flexible wing generated higher velocities, frequency, lift and thrust. In observing the wing angle motion, it was found out that the lift occurs most when the wing is at 0° and -10° , while negative lift at 30° and 45° . With remote control, our prototype was able to take off, climb, cruise and land in flapping mode successfully.

REFERENCES

1. W. Shyy, Y. Lian, J. Tang, D. Vileru, and H. Liu, *Aerodynamics of Low Reynolds Number Flyers*, 1 ed. New York: Cambridge University Press, (2008)
2. M.A. Groen, PIV and force measurements on the flapping-wing MAV DelFly II, Delft University of Technology M.Sc. thesis, (2010)
3. C.P. Ellington., C. Van den Berg, A.P. Willmott, A.L.R. Thomas, Leading-Edge Vortices in Insect Flight, *Nature*, Vol. 384, pp. 626-630, (1996)
4. K. D. Jones and M. F. Platzer, Design and development considerations for biologically inspired flapping-wing micro air vehicles, *Experiments in Fluids*, vol. 46, pp. 799-810, (2009)
5. F. V. Breugel, W. Regan, and H. Lipson, From Insects to Machines. *IEEE Robotics & Automation Magazine*, pp. 68-74 (2008)
6. C.P., Ellington, The aerodynamics of hovering insect flight III Kinematics, *Phil. Trans. R. Soc. Lond. B*, vol. 305 (1984)
7. M. H. Dickinson, The effects of wing rotation on unsteady aerodynamic performance at low reynolds numbers, *The Journal of Experimental Biology* 192, 179-206, (1994)
8. M. H., Dickinson, F. -O. Lehmann, and S. P. ,Sane, Wing rotation and the aerodynamic basis of insect flight, *Science* 284: 1954-1960 (1999)
9. P. S. Sane, The aerodynamics of insect flight, *The Journal of Experimental Biology*, vol. 206, pp. 4191 - 4208, (2003)

10. R. Sayaman S. N. Fry and M. H. Dickinson, Unsteady mechanisms of force generation in aquatic and aerial locomotion., *Amer. Zool.*, 36, 537-554, (1996)
11. A. Azuma, "The Biokinetics of Flying and Swimming," Springer, Tokyo, (1992)
12. R. F. Chapman, *The Insects: Structures and Function*, 4 ed. New York: Combridge University Press (1998)
13. D. E. Alexander, *Nature's Flyers: Birds, Insects and the Biomechanics of Flight*: The Johns Hopkins University Press, (2004)
14. C. Ellington, "The Novel Aerodynamics of Insect Flight: Applications to Micro Air Vechicles," *The Journal of Experimental Biology*, pp. 3439-3448, 15/09/1999 (1999)
15. F-O. Lehmann; S. Pick, The aerodynamic benefit of wing - wing interaction depends on stroke trajectory in flapping insect wings, *The Journal of Experimental Biology* 210, 1362-1377, (2007)
16. A. Roland Ennos, The kinematics and aerodynamics of the free flight of some diptera, *The Journal of Experimental Biology* 142, 49-85, (1989)
17. C. Van Den Berg, C.P. Ellington, The three-dimensional leading-edge vortex of a hovering model hawkmoth, *Philosophical Transactions: Biological Sciences* 352, 329-340, (1997)
18. D. R. Warrick; B.W. Tobalske; D.R. Powers., Aerodynamics of the hovering hummingbird, *Nature* 435 1094-1097, (2005)
19. K. P. Dial, B. W. Tobalske, W. L. Peacock, Kinematics of flap-bounding flight in the zebra finch over a wide range of speeds, *The Journal of Experimental Biology* 202, 1725-1739, (1999).
20. Y.S. Hong, A. Altman, An Experimental Study on Lift Force Generation Resulting from Spanwise Flow in Flapping Wings, 44th AIAA Aerospace Sciences Meeting and Exhibit, Reno, Nevada, (2006)
21. C.H. Blake, More data on the wing flapping rates of birds, *The Condor*, Vol. 50, No. 4, p. 148 (1948)
22. N.L. Bradshaw, , D. Lentink, Aerodynamic and structural dynamic identification of a flapping wing micro air vehicle, AIAA conference, Hawaii (2008)
23. S.N. Fry, R. Sayaman, M.H. Dickinson, The aerodynamics of free-flight maneuvers in *Drosophila*, *Science* 300, 495-498 (2003)
24. S.R. Jongerius, D. Lentink, Structural analysis of a dragonfly wing, *Journal of Experimental Mechanics*, special issue on Locomotion (2009)
25. Y. Kawamura, S. Soudal, S. Nishimoto, C.P. Ellington, Clapping-wing Micro Air Vehicle of Insect Size. In: N. Kato, S. Kamimura (eds.) *Bio-mechanisms of Swimming and Flying*. Springer Verlag. (2008)
26. A.B. Kesel, Aerodynamic characteristics of dragonfly wing sections compared with technical aerofoils, *The Journal of Experimental Biology* 203, 3125-3135 (2000)
27. T.N. Pornsin-Sirirak, Y.C. Tai, C.H. Ho, M. Keennon, *Microbat-A Palm-Sized Electrically Powered Ornithopter*, NASA/JPL Workshop on Biomorphic Robotics. Pasadena (2001)
28. J.R. Usherwood, C.P. Ellington, The aerodynamics of revolving wings I-II, *The Journal of Experimental Biology* 205, 1547-1576(2002)

DYNAMIC STABILITY OF PIPES SUBJECTED TO INTERNAL FLOW AND EXTERNAL ANNULAR AXIAL FLOW SIMULTANEOUSLY

Katsuhisa Fujita⁺¹ and Akinori Moriasa⁺²

^{+1,+2}Mechanical and Physical Engineering, Graduate School of Engineering, Osaka City University,
3-3-138 Sugimoto-cho, Sumiyoshi-ku, Osaka, 558-8585, Japan

When slender pipes are subjected to internal flow, the pipes lose stability by flutter and divergence in increasing the fluid velocity. In addition, they also lose stability when they are subjected to external annular axial flow. In the development of a piping system in the field of ocean mining, and in the field of fluid energy utilization, and so forth, the double walled pipe structure system subjected to an internal flow and an external flow simultaneously is thought to be one of the important pipe structures. In this paper, the pipe structures are assumed to be composed of the cantilevered beam structures. For the analysis of the internal flow, the conventional inviscid stability analysis method is applied. For the analysis of the external annular axial flow, two kinds of solutions are applied. The one is the viscous solution using the Navier-Stokes equation of motion and it is called as NS solution hereafter. The other is the ideal fluid solution which the viscous influence is added to later and it is called as R&P solution hereafter. Changing the flow direction and the fluid velocity of the internal flow and the external flow, and the specifications of modeling, the stability of the double walled pipes is investigated and discussed.

Keyword: flutter, flow induced vibration, coupled vibration, axial flow, double wall pipe

1. INTRODUCTION

When slender pipes are subjected to internal flow, the pipes lose stability by flutter and divergence in increasing the fluid velocity. In addition, they also lose stability when they are subjected to external annular axial flow. In this paper, the dynamic stability of flexible pipe is investigated when a flexible pipe is subjected to an internal flow and an external flow simultaneously. Concerning the double walled pipe system subjected to an internal flow and an external flow, the piping system for transporting sea bottom resources such as methane hydrate, and the cooling and heating piping system for gas energy utilization so on are enumerated.

When the flexible pipe subjected to an internal flow and an external annular axial flow simultaneously, it is considered that the direction of flow has much effect on the dynamic stability in the case of the cantilevered pipe. Especially, the case that the direction of an internal flow is the opposite of an external flow is predicted to have stronger interaction than the same direction. Therefore, in this paper, the case that the direction of an internal flow is the opposite direction of an external flow is investigated.

The dynamic stability analyses of a flexible pipe subjected to an internal flow have been already reported by Paidoussis and Luu¹⁾, Paidoussis²⁾. In these studies, it has been reported that the stability analysis of an aspirating pipe can be performed by replacing the minus velocity in stead of the plus velocity in the analysis of a discharged pipe. However, the jet from the free end of the discharged pipe can not become the inverse jet at the time of aspirating fluid. The reverse is found to be not truth. Giacobbi et al.³⁾ has reported the more accurate analytical method on the dynamics of a cantilevered pipe aspirating fluid. The stability analysis of an internal flow is based on these references in this paper. On the other hand, the dynamic stability analyses of an external annular axial flow have been reported by Fujita and Shintani⁴⁾, Fujita and Ohkuma^{5, 6)}. Combining the two kind of the dynamic stability analysis method, the dynamic stability of the flexible cantilevered pipe subjected to an internal and an external annular axial flow simultaneously is investigated. Besides, in the case of an external annular flow, the viscous solution is derived by using the Navier-Stokes

⁺¹fujita@mech.eng.osaka-cu.ac.jp

equation under the assumption that the gap at the annulus is small. The drop of accuracy is predicted when the gap becomes wider. On the other hand, Rinaldi and Paidoussis⁷⁾ have reported the dynamic stability analysis method of the flexible cantilevered pipe subjected to an external annular axial flow by adding the viscous effect on the theory of ideal fluid. Therefore, applying this method, the effect of the gap so forth on the accuracy of the dynamic stability of the flexible pipe subjected to an internal flow and an external annular flow simultaneously is also investigated.

2. MODELING

(1) Flexible pipe subjected to internal flow and external flow simultaneously

As one of the piping structure subjected to an internal flow and an external flow, Fig. 1 shows the modeling of a double walled pipe structure in which an inner flexible pipe is subjected to an internal flow and an external flow. The outer pipe is assumed to be rigid and the inner pipe is assumed to be flexible, for the simplicity of calculations. The fluid flows through the inside of the inner pipe as an internal flow, and the fluid flows through the annular gap between the rigid outer pipe and the flexible inner pipe as an external flow.

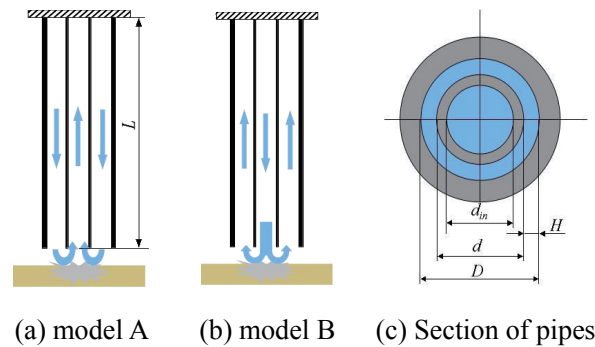


Figure 1: Structure of double walled pipe.

In the case of model A, the external flow outside of the flexible pipe flows from the clamped edge to the free edge as a discharged flow, and the internal flow of the flexible pipe flows from the free edge to the clamped edge as an aspirated flow. On the other hand, model B is totally reverse to model A. In model B, the external flow flows from the free edge to the clamped edge as an aspirated flow, and the internal flow flows from the clamped edge to the free edge as a discharged flow. Even if we change the specifications of model, the external flow rate is assumed to be always equal with the internal flow rate for each flow velocity. Besides, the specifications of the section of a double walled pipe structure are shown in Fig. 1(c). Where, d is the outer diameter of an inner flexible pipe, d_{in} is the inner diameter of the inner flexible pipe, L is the length of the inner flexible pipe, D is the inner diameter of an outer rigid pipe, and H is the gap between the inner pipe and the outer pipe, which means the width of flow passage.

(2) Stability of flexible pipe subjected to only internal flow

a) Equation of motion of flexible pipe subjected to only internal flow

The equation of motion of the cantilevered flexible pipe which discharges fluid from the free end as an internal flow is expressed based on the ideal fluid theory by Paidoussis²⁾ as shown in Eq. (1). And, also the nondimensional equation of motion is also shown in the following as Eqs. (2) and (3).

$$EI \frac{\partial^4 w}{\partial x^4} + \rho_f A_m V^2 \frac{\partial^2 w}{\partial x^2} + 2\rho_f A_m V \frac{\partial^2 w}{\partial x \partial t} + (\rho_s A_s + \rho_f A_m) \frac{\partial^2 w}{\partial t^2} = 0, \quad (1)$$

$$\xi = \frac{x}{L}, \quad \eta = \frac{w}{L}, \quad \tau = \left(\frac{EI}{\rho_f A_s} \right)^{1/2} \frac{t}{L^2}, \quad v = \left(\frac{\rho_f A_s}{EI} \right)^{1/2} LV, \quad m = \frac{\rho_s}{\rho_f}, \quad \sigma = \frac{d}{d_m}, \quad (2)$$

$$\frac{\partial^4 \eta}{\partial \xi^4} + \frac{1}{\sigma^2 - 1} \left(\frac{\partial}{\partial \tau} + v \frac{\partial}{\partial \xi} \right)^2 \eta + m \frac{\partial^2 \eta}{\partial \tau^2} = 0. \quad (3)$$

The equation of motion of the flexible cantilevered pipe which aspirates fluid from the free end as an internal flow is expressed using Giacobbi et al.³⁾ as follows because it is thought to be improved from the equations reported by Paidoussis and Luu¹⁾.

$$EI \frac{\partial^4 w}{\partial x^4} + \left[1 - (1 + \bar{\gamma}) \left(\frac{3}{2} - \alpha \right) \right] \rho_f A_m V^2 \frac{\partial^2 w}{\partial x^2} - 2 \rho_f A_m V \frac{\partial^2 w}{\partial t \partial x} + (\rho_s A_s + \rho_f A_m) \frac{\partial^2 w}{\partial t^2} + \left[\rho_f A_m V \frac{\partial w}{\partial t} - \alpha \rho_f A_m V^2 (1 - \psi) \frac{\partial w}{\partial x} \right] \delta(x - L) = 0. \quad (4)$$

And, nondimensional equation of motion is also shown in the following.

$$\frac{\partial^4 \eta}{\partial \xi^4} + \left[\left\{ 1 - (1 + \bar{\gamma}) \left(\frac{3}{2} - \alpha \right) \right\} \frac{1}{\sigma^2 - 1} v^2 \right] \frac{\partial^2 \eta}{\partial \xi^2} - 2 \frac{1}{\sigma^2 - 1} v \frac{\partial^2 \eta}{\partial \tau \partial \xi} + \left(m + \frac{1}{\sigma^2 - 1} \right) \frac{\partial^2 \eta}{\partial \tau^2} + \left[\frac{1}{\sigma^2 - 1} v \frac{\partial \eta}{\partial \tau} - \frac{1}{\sigma^2 - 1} \alpha v^2 (1 - \psi) \frac{\partial \eta}{\partial \xi} \right] \delta(\xi - 1) = 0, \quad (5)$$

where, EI is the bending rigidity of inner flexible pipe, ρ_f is the density of fluid, A_m is the sectional area of the passage, A_s is the sectional area of the flexible pipe, V is fluid velocity, ρ_s is the density of flexible pipe, w is the deflection of flexible pipe, and x is the axial coordinate of flexible pipe. And, ξ is the nondimensional axial coordinate, η is the nondimensional deflection of flexible pipe, σ is the ratio of outer diameter and inner diameter of flexible pipe, v is the nondimensional fluid velocity, $\delta(\cdot)$ is the delta function, and m is the ratio of the density of flexible pipe for the density of fluid. The numerical parameters in aspirating fluid are $\alpha = 0.86$, $\bar{\gamma} = 0.35$, $\psi = 0.94$.

b) Comparison of dynamic stability of cantilevered pipe subjected to only internal flow between aspirating and discharging flow

Figure 2 shows the root loci, these are Argand diagrams, of cantilevered flexible pipe subjected to an internal flow in both cases of aspirating and discharging flow at the free edge.

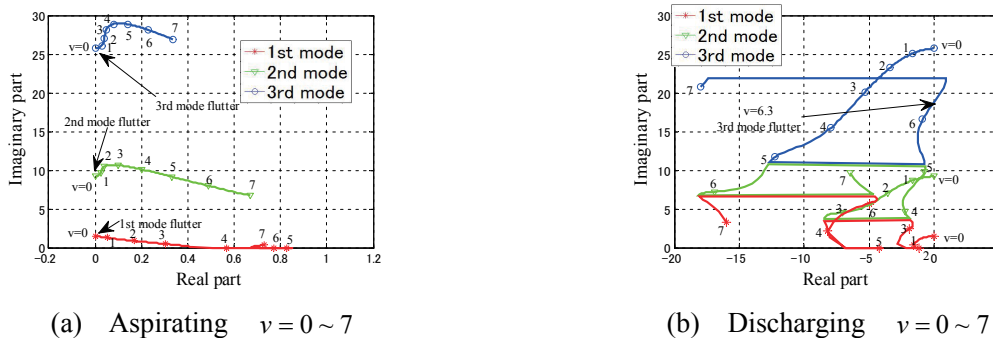


Figure 2: Root loci of cantilevered flexible pipe subjected to internal flow. ($\sigma = 1.1$)

This figure shows from the first mode to the higher modes. The first lowest frequency in complex eigenvalue analysis for each flow velocity is defined as the first mode, and the second lowest frequency is also

defined as the second mode, so forth. The stability analysis about the fluid discharged at the free edge of the cantilevered pipe is based on the solution by Paidoussis²⁾, and that about the fluid aspirated at the free edge is based on the solution by Giacobbi et al.³⁾. The ratio of the density of structure for the density of fluid m is 1, which means that the effect of fluid density is large.

From Fig. 2(a), it is found that the stability is lost from the first mode to the third mode when the fluid is aspirated from the free edge of the cantilevered flexible pipe as an internal flow. However, the real part which means the growth rate of vibration is smaller than that of the solution by Paidoussis and Luu¹⁾. The stability by Giacobbi³⁾ becomes better than that by Paidoussis and Luu¹⁾. On the other hand, in the case of the fluid discharged from the free edge of the cantilevered pipe, it is found that the third mode becomes flutter first at $\nu = 6.3$.

(3) Stability of flexible pipe subjected to only external annular axial flow

a) Equation of motion of cantilevered flexible pipe subjected to only external annular axial flow

The fluid structure coupled equations is derived by using the Euler-Bernoulli equation and the Navier-Stokes equation. These equations have been already reported by Fujita and Shintani⁴⁾, Fujita and Ohkuma^{5, 6)}. Besides, this solution is called as NS solution hereafter. X and Y are defined in the orthogonal coordinate system when the gap between the outer pipe and the inner pipe is changed from the cylindrical coordinate system to the orthogonal coordinate system. X denotes the circumferential direction, and Y the axial direction. When Q_X and Q_Y mean the circumferential and axial flow rate, respectively, P is the fluid pressure, ν is the kinematic viscosity, and H is the gap width as shown in Fig. 1(c), the equation of fluid is obtained as follows.

$$\frac{\partial Q_X}{\partial X} + \frac{\partial Q_Y}{\partial Y} + \frac{\partial H}{\partial t} = 0, \quad (6)$$

$$\frac{1}{\rho_f} \frac{\partial P}{\partial X} = -\frac{1}{H} \left\{ \frac{\partial Q_X}{\partial t} + \frac{\partial}{\partial X} \left(\frac{Q_X^2}{H} \right) + \frac{\partial}{\partial Y} \left(\frac{Q_X Q_Y}{H} \right) + \frac{12\nu Q_X}{H^2} \right\}, \quad (7)$$

$$\frac{1}{\rho_f} \frac{\partial P}{\partial Y} = -\frac{1}{H} \left\{ \frac{\partial Q_Y}{\partial t} + \frac{\partial}{\partial X} \left(\frac{Q_X Q_Y}{H} \right) + \frac{\partial}{\partial Y} \left(\frac{Q_Y^2}{H} \right) + \frac{12\nu Q_Y}{H^2} \right\}, \quad (8)$$

$$\begin{aligned} P(X, Y, t) &= \bar{P}(Y) + \Delta P(X, Y, t), \quad H(X, Y, t) = \bar{H} + \Delta H(X, Y, t), \\ Q_X(X, Y, t) &= \Delta Q_X(X, Y, t), \quad Q_Y(X, Y, t) = \bar{Q}_Y + \Delta Q_Y(X, Y, t), \end{aligned} \quad (9)$$

where, $\bar{(\quad)}$ denotes the steady component, and $\Delta(\quad)$ denotes the unsteady component. The fluid force acting on a flexible pipe can be obtained by Eqs. (6), (7) and (8), using the relationship of Eq. (9).

For the flexible pipe, the equation of motion based on the Euler-Bernoulli equation is applied as follows.

$$\rho_s A_s \frac{\partial^2 \Delta H}{\partial t^2} + EI \frac{\partial^4 \Delta H}{\partial Y^4} + W(L - Y) \frac{\partial^2 \Delta H}{\partial Y^2} = \Delta F, \quad (10)$$

where, ΔH is the unsteady displacement of a flexible pipe, W is the axial fluid force, and ΔF are the unsteady fluid forces which consist of the normal force, that is pressure, and the circumferential shear force. The fluid forces which are calculated using Eqs. (6), (7), (8) and (9) is coupled with the equation of motion of the flexible pipe by Eq. (10), and then the nondimensional equation of motion can be obtained using the following relationship.

$$\xi = \frac{Y}{L}, \quad \tau = \left(\frac{EI}{\rho_f A_s} \right)^{1/2} \frac{t}{L^2}, \quad u = \left(\frac{\rho_f A_s}{EI} \right)^{1/2} LU, \quad m = \frac{\rho_s}{\rho_f}, \quad \sigma = \frac{d}{d_m}, \quad \varepsilon = \frac{R}{L}, \quad r = \frac{R}{H}, \quad \beta = 12\nu \left(\frac{\rho_f A_s}{EI} \right)^{1/2}. \quad (11)$$

Applying the modal expansions using the Galerkin method, the coupled equation of motion between structure and fluid can be given as follows.

$$([M_s] + [M_a]) \frac{d^2}{d\tau^2} \{W_n(\tau)\} + ([C_s] + [C_a]) \frac{d}{d\tau} \{W_n(\tau)\} + ([K_s] + [K_a]) \{W_n(\tau)\} = \{0\}, \quad (12)$$

where $\{W_n(\tau)\}$ denotes the mode vector, $[M]$, $[C]$ and $[K]$ denote the mass, damping, and stiffness matrices, respectively. The suffix s shows the matrices of the flexible pipe, and the suffix a shows the added matrices by fluid.

b) Comparison of dynamic stability of cantilevered pipe subjected to only external annular flow between aspirating and discharging flow

Figure 3 shows the root loci of the cantilevered flexible pipe subjected to only an external flow in both cases of aspirating and discharging flow at the free edge. The ratio ε of the inner radius for the length of the flexible pipe is 0.02, and the ratio r of the inner radius for the gap between the outer pipe and the inner pipe is 2. And, the ratio m of the density of structure for the density of fluid is 1. The ratio σ of the outer diameter for the inner diameter of flexible pipe is 1.1. The nondimensional viscosity β is 5×10^{-6} .

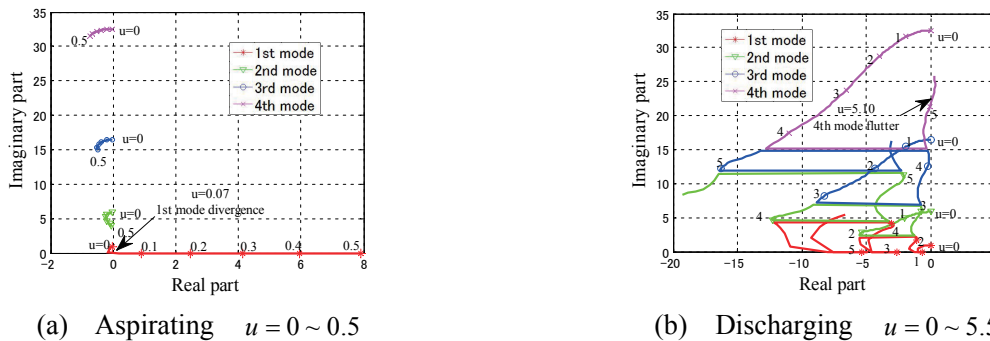


Figure 3: Root loci of cantilevered flexible pipe subjected to external flow by NS solution. ($\varepsilon = 0.02, r = 2$)

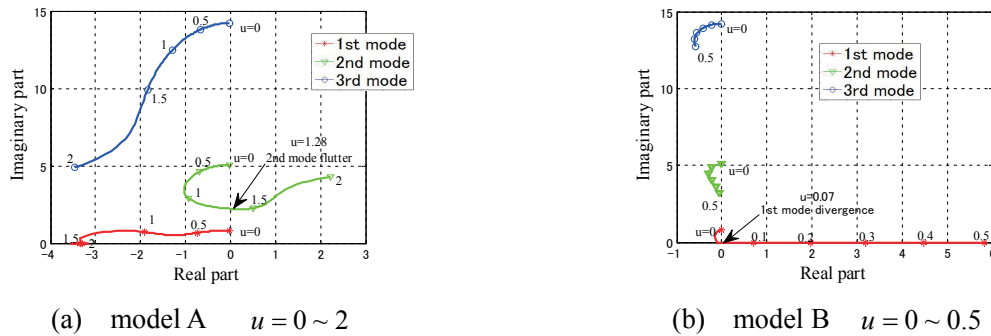
From Fig. 3(a), only the first mode is found to become unstable at very low velocity when the cantilevered flexible pipe is subjected to an external flow as an aspirated flow. Increasing the flow velocity a little, the real part which means the growth rate of vibration is found to become larger than the aspirating internal flow shown in Fig. 2(a). That is, this system is found to be more unstable. When the cantilevered pipe is subjected to an external flow as a discharged flow as shown in Fig. 3(b), each mode in the nondimensional root loci shows the same characteristics as that of the internal flow in Fig. 2(b). The flutter of fourth mode occurs first at $u = 5.10$.

3. NUMEICAL SIMULATIONS OF DOUBLE WALLED PIPE

(1) Comparison of root loci between model A and model B

The dynamic response of a double walled pipe is assumed to be calculated using principle of superposition. Figure 4 shows the comparison of the root loci between model A and model B which have the structure of double walled pipe as shown in Fig. 1. Figure 4 shows the case of $\varepsilon = 0.02, r = 2$ and $m = 1$, as

well as Fig. 3. When it is thought that an internal flow and an external flow circulate each other, the fluid velocity of an internal flow and that of an external flow are changed so that the external flow rate is always equal with the internal flow rate. Let's decide the critical velocity is displayed by the external velocity. Besides, as mentioned before, the parameters σ and β are fixed as $\sigma = 1.1$, $\beta = 5 \times 10^{-6}$.



(a) model A $u = 0 \sim 2$ (b) model B $u = 0 \sim 0.5$
Figure 4: Root loci subjected to external flow by NS solution. ($\varepsilon = 0.02$, $r = 2$)

The root locus of model A in Fig. 4(a) is a combination of the case subjected to the aspirated internal flow shown in Fig. 2(a) and the case subjected to the discharged external flow shown in Fig. 3(b). The second mode is found to be destabilized due to the influence of the aspirated internal flow in Fig. 2(a). On the other hand, the root locus of model B in Fig. 4(b) is a combination of the case subjected to the discharged internal flow shown in Fig. 2(b) and the case subjected to the aspirated external flow shown in Fig. 3(a). The root locus of model B is similar with that of the aspirated external flow of Fig. 3(a), and the first mode is destabilized due to the influence of Fig. 3(a).

(2) Comparison of critical velocity between model A and model B

First, let's investigate the influence of the specifications of structure on the critical velocity in the case of $m = 1$ which means the smaller ratio of the density of structure for the density of fluid. After rearranging the root loci in Fig. 4, the influences on the critical velocities in model A and model B by the ratio ε and the ratio r are shown in Fig. 5. As mentioned above, ε is the ratio of the inner radius for the length and r is the ratio of the inner radius for the annular gap. The horizontal axis shows the nondimensional viscosity β , and the vertical axis shows the nondimensional critical velocity.

From Fig. 5, model A is found to be more stable than model B. The larger r means the narrower gap, and the smaller value of ε means the longer length in Fig. 5. As the flow velocities are calculated under the condition that the internal flow rate is always equal to the external flow rate, the external flow velocity becomes larger when the gap becomes narrower, that is, the influence of external flow becomes large. Therefore, the influence of the discharged external flow shown in Fig. 3(b) increases in model A when the gap becomes narrower. As a result, when the value of ratio r increases, it is found that the higher modes become critical in model A. In model B, when the gap becomes narrower, the influence of the aspirated external flow shown in Fig. 3(a) increases. Therefore, the first mode is always unstable even if the specifications are changed.

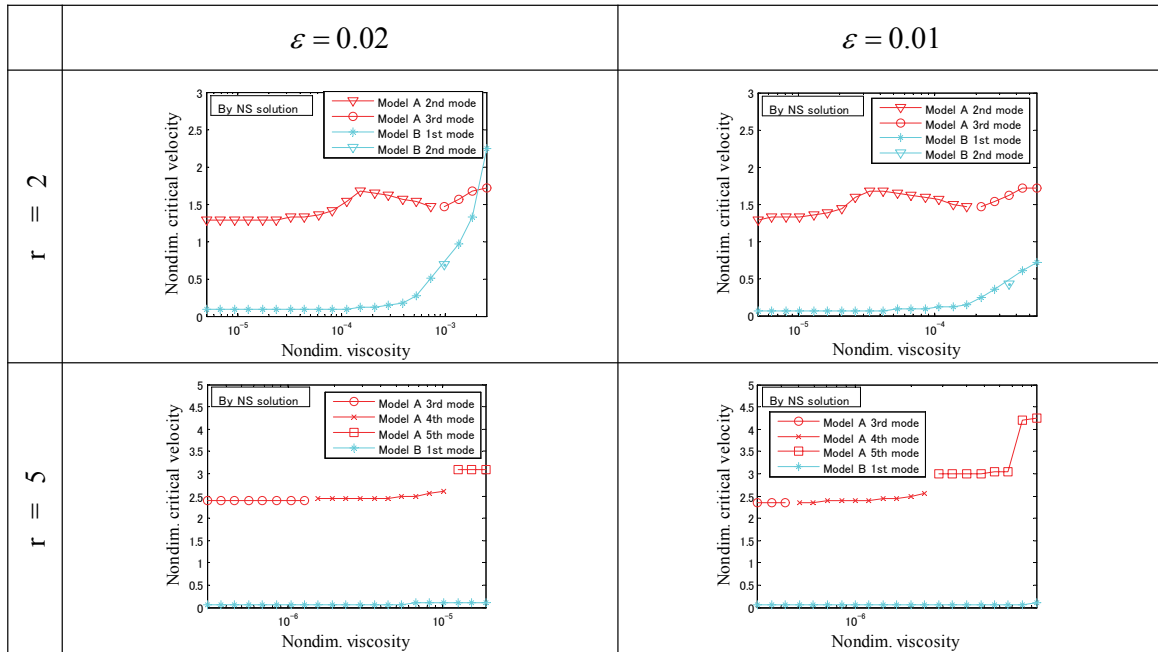


Figure 5: Comparison of critical velocity between model A and model B by using NS solution for the external flow. ($m = 1$)

Next, Fig. 6 shows the similar comparison as well as Fig. 5 in the case of $m = 1000$ which corresponds to the higher ratio of the density of structure for the density of fluid. From Fig. 6, model A is found to be more stable than model B in the case of $m = 1000$, as well as $m = 1$. When the nondimensional viscosity which is shown in Eq. (11)₈ increases, the critical velocity of model A approaches to that of model B.

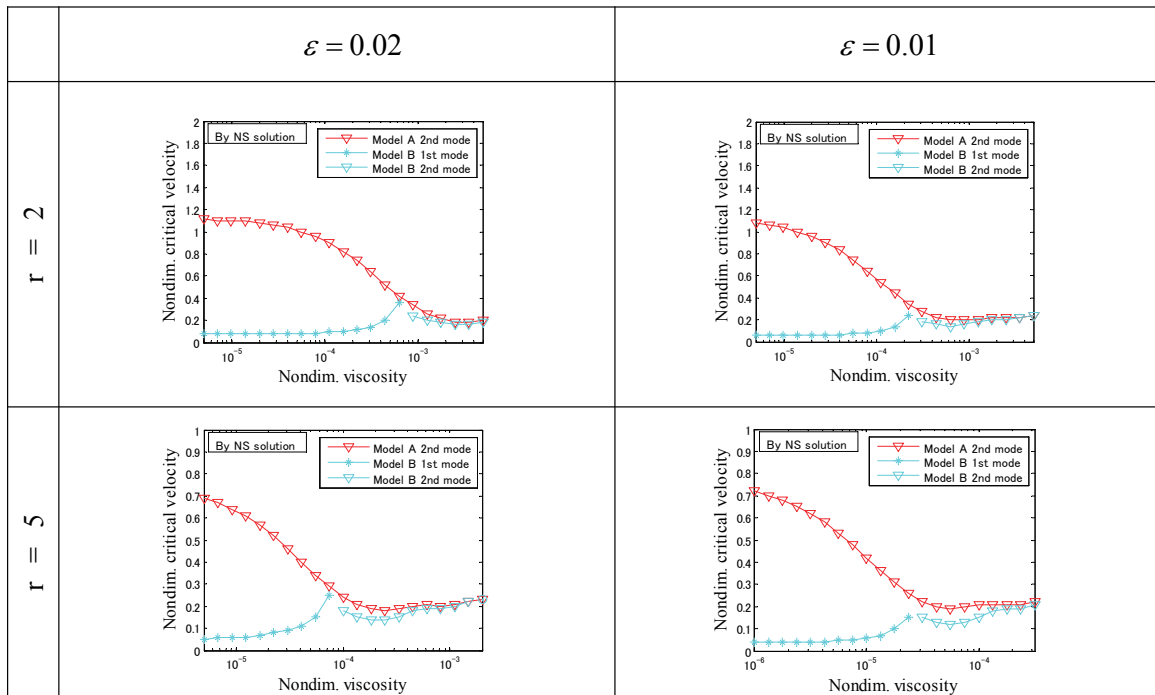


Figure 6: Comparison of critical velocity between model A and model B by using NS solution for the external flow. ($m = 1000$)

It is understood that the critical flow velocity of model A decreases when the nondimensional viscosity increases. In other words, the destabilization effect of the fluid viscosity is recognized. Especially, the effect becomes intense in the region of the large value of the ratio r which means the narrow gap between the inner pipe and the outer pipe decreases.

4. CONSIDRATIONS

(1) R&P solution on dynamic stability of cantilevered pipe subjected to only external flow

Rinaldi and Paidoussis⁷⁾ derived the dynamic stability analysis method of the flexible cantilevered pipe subjected to an external annular axial flow by adding the viscous effect on the ideal fluid acting on the pipe for a turbulent flow. In this paper, applying this solution to a laminar flow, the results are compared with NS solution which has already been reported in the above section. Besides, the solution which is obtained by applying the theory by Rinaldi and Paidoussis⁷⁾ to a laminar flow is called as R&P solution hereafter.

First, let's investigate the stability of a cantilevered flexible pipe subjected to only an external annular axial flow.

(2) Equation of motion of cantilevered pipe subjected to only external annular flow by using R&P solution

The following equation of motion can be obtained by applying the theory of Rinaldi and Paidoussis⁷⁾ on the cantilevered flexible pipe subjected to an external annular axial flow when the flow is laminar.

$$EI \frac{\partial^4 w}{\partial x^4} + \chi \rho_f A U^2 \frac{\partial^2 w}{\partial x^2} + 2 \chi \rho_f A U \frac{\partial^2 w}{\partial t \partial x} + (\chi \rho_f A + \rho_s A) \frac{\partial^2 w}{\partial t^2} + \left[\frac{12 \pi \mu d}{D-d} U \left(1 + \frac{d}{D-d} \right) \right] \frac{\partial w}{\partial x} - \left(\left[\frac{12 \pi \mu d}{D-d} U \left(1 + \frac{d}{D-d} \right) \right] (L-x) \right) \frac{\partial^2 w}{\partial x^2} + \frac{12 \pi \mu d}{D-d} \frac{\partial w}{\partial t} = 0, \quad (13)$$

where, $A = A_s + A_{in}$. μ is the viscosity. χ is the confinement parameter. The nondimensional parameters and the nondimensional equation of motion are as follows.

$$\xi = \frac{x}{L}, \quad \eta = \frac{w}{L}, \quad \tau = \left(\frac{EI}{\rho_f A_s} \right)^{1/2} \frac{t}{L^2}, \quad u = \left(\frac{\rho_f A_s}{EI} \right)^{1/2} LU, \quad m = \frac{\rho_s}{\rho_f}, \quad \varepsilon = \frac{R}{L}, \quad \chi = \frac{1+2r+2r^2}{1+2r}, \quad (14)$$

$$r = \frac{R}{H}, \quad \beta = 12 \nu \left(\frac{\rho_f A_s}{EI} \right)^{1/2}, \quad \sigma = \frac{d}{d_m}, \quad \gamma = \frac{1}{\sigma^2 - 1},$$

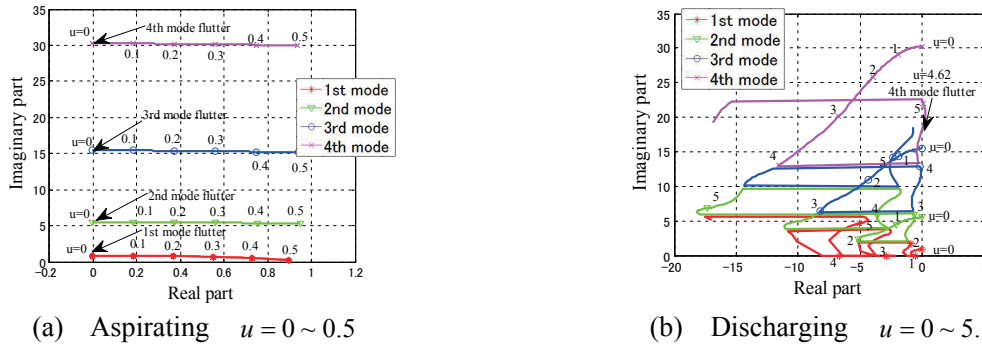
$$\frac{\partial^4 \eta}{\partial \xi^4} + \chi(1+\gamma)u^2 \frac{\partial^2 \eta}{\partial \xi^2} + 2\chi(1+\gamma)u \frac{\partial^2 \eta}{\partial \tau \partial \xi} + [\chi(1+\gamma)+m] \frac{\partial^2 \eta}{\partial \tau^2} + \left[\beta(1+\gamma) \frac{ru}{\varepsilon^2} (1+r) \right] \frac{\partial \eta}{\partial \xi} - \left(\left[\beta(1+\gamma) \frac{ru}{\varepsilon^2} (1+r) \right] (1-\xi) \right) \frac{\partial^2 \eta}{\partial \xi^2} + \beta(1+\gamma) \frac{r}{\varepsilon^2} \frac{\partial \eta}{\partial \tau} = 0. \quad (15)$$

(3) Root loci of cantilevered pipe subjected to only external annular flow by using R&P solution

Figure 7 shows the root loci of the cantilevered pipe subjected to the aspirated and the discharged external flow by R&P solution. This figure shows the case of $\varepsilon = 0.02$, $r = 2$ as well as Fig. 3 and 4. Besides in this case, $m = 1$, $\sigma = 1.1$ and $\beta = 5 \times 10^{-6}$. As the root loci by NS solution have been shown in Fig. 3, the comparison between NS solution and R&P solution can be clarified when Fig. 7 is compared with Fig. 3.

In aspirating fluid, the first mode becomes unstable in NS solution, and all modes of the first to third modes become unstable in R&P solution. NS solution is found to be stable a little than R&P solution. However, as the real part shows the high growth rate of vibration in NS solution, NS solution cannot be necessarily thought to be stable. In discharging fluid, Fig. 3(b) by NS solution is similar to Fig. 7(b) by R&P

solution. The fourth mode of NS solution in Fig. 3(b) becomes flutter at $u = 5.10$. On the other hand, the fourth mode of R&P solution in Fig. 7(b) becomes flutter at $u = 4.62$.

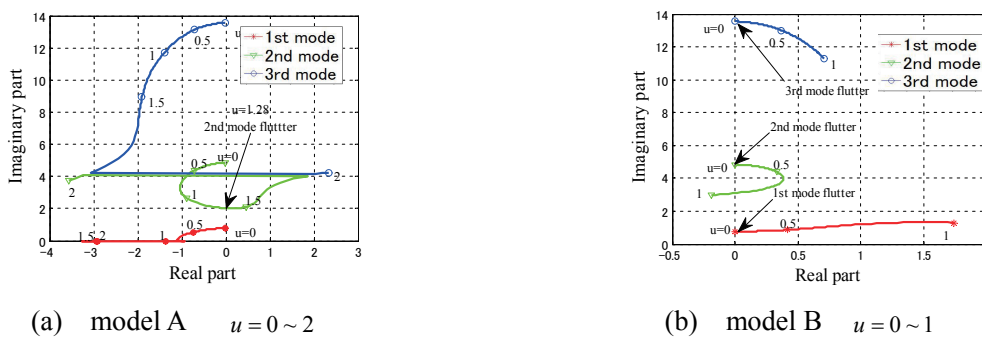


(a) Aspirating $u = 0 \sim 0.5$ (b) Discharging $u = 0 \sim 5.5$
 Figure 7: Root loci of cantilevered pipe subjected to only external flow by using R&P solution. ($\varepsilon = 0.02, r = 2$)

(4) Root loci of model A and model B subjected to internal and external annular flows by using R&P solution

Figure 8 shows the root loci of model A and model B in which the internal flow is based on the ideal fluid theory by Eq. (1)~(5), and the external flow is based on R&P solution in stead of NS solution. This figure shows the case of $\varepsilon = 0.02, r = 2$ as well as Fig. 3 and 4.

When NS solution in Fig. 4 is compared with R&P solution in Fig. 8, it is found that both root loci show the similar results in both model A and model B macroscopically. Concerning model A, the second mode becomes flutter at $u = 1.28$ in both solutions. In the case of model B, the first mode of NS solution becomes divergence at the low flow velocity, although all modes of the first to third mode of R&P solution become flutter at the low flow velocity.



(a) model A $u = 0 \sim 2$ (b) model B $u = 0 \sim 1$
 Figure 8: Root loci of double walled pipe subjected to internal flow, and to external flow by using R&P solution. ($\varepsilon = 0.02, r = 2$)

5. CONCLUSIONS

When the double walled pipe is subjected to the aspirated flow and the discharged flow simultaneously, the dynamic stability of pipe becomes complex. Therefore, when such a piping system is adopted in actual plant, it is necessary to pay enough consideration about the dynamic stability.

The piping system of the double walled pipe structure subjected to the discharged external flow and the aspirated internal flow simultaneously can be said to be one of the dynamically stable piping systems in the field of ocean mining and in the field of fluid energy utilization, and so forth. In other words, if the combination of the internal flow and the external flow is devised, it is found that the more dynamically stable system of the double walled pipe structure may be provided.

When the cantilevered flexible pipe discharges a fluid through the gap between the inner pipe and the outer pipe, NS solution and R&P solution are thought to show considerably a good agreement. However, when the cantilevered pipe aspirates a fluid, the both solutions show a little difference. Therefore, it can be understood that there are a little differences in the critical flow velocities of model A and model B, which are a double walled pipe structure, between NS solution and R&P solution.

ACKNOWLEDGMENT

On performing this study, we thank Professor Tadao Kawai of Osaka City University for his much support.

REFERENCES

- 1) Paidoussis, M. P. and Luu T. P. : Dynamics of a pipe aspirating fluid such as might be used in ocean mining, *Transactions of the ASME, Journal of Energy Resources Technology*, Vol. 107, pp. 250-255, 1985.
- 2) Paidoussis, M. P. : Fluid-structure interactions slender structures and axial flow, Vol. 1, Elsevier Academic Press, 1998.
- 3) Giacobbi, D. B., Rinaldi, S., Semler, C. and Paidoussis, M., P. : The dynamics of cantilevered pipe aspirating fluid studied by experimental, numerical and analytical methods, *Journal of Fluids and Structures*, Vol. 30, pp. 73-96, 2012.
- 4) Fujita, K. and Shintani, A. : Axial leakage flow-induced vibration of the elastic rod as the axisymmetric continuous flexible beam, *Transactions of the ASME, Journal of Pressure Vessel Technology*, Vol. 123, No.4, pp. 421-428, 2001.
- 5) Fujita, K. and Ohkuma, A. : Effect of structural dimensions on dynamic stability of elastic beam subjected to axial flow in confined narrow passage, *Transactions of the JSME, Journal of System Design and Dynamics*, Vol.4, No.6, pp. 809-821, 2012.
- 6) Fujita, K. and Ohkuma, A. : Influence of fluid viscosity and structural specifications on stability in the vicinity of critical velocity of an elastic beam subjected to confined axial flow, *Transactions of the JSME, Journal of System Design and Dynamics*, Vol.5, No.8, pp. 1593-1604, 2011.
- 7) Rinaldi, S. and Paidoussis, M., P. : Theory and experiments on the dynamics of a free-clamped cylinder in confined axial air-flow, *Journal of Fluids and Structures*, Vol. 28, pp. 167-179, 2012.

FLUTTER IN COLLAPSIBLE TUBES AT TURBULENT AND LAMINAR FLOW REGIMES

Julia Zayko⁺¹, Vladimir Yushutin⁺², and Vasily Vedeneev⁺³
^{+1,2,3}Lomonosov Moscow State University, Moscow, Russia

Stability and self-exciting oscillations of elastic tubes conveying fluid are investigated at laminar and turbulent flow regimes. We experimentally analyze the effect of the flow regime (laminar vs turbulent) on the limit cycle properties and the flow rate limitation. The influence of the fluid viscosity on these characteristics at turbulent regimes is also explored. Maps of regimes (pressure drop/flow rate relations) are obtained. It is shown that the stability boundary does not significantly depend on the fluid viscosity at turbulent regime. The stability boundary at the same flow rates corresponds to less pressure drops for laminar regimes than for turbulent regimes. The frequency for different regimes of oscillations does not change much when changing the pressure drop in turbulent case, and essentially depends on the pressure drop in laminar case. Measurements also reveal that the amplitude of observed oscillations is essentially higher for the turbulent flow through the collapsible tube than for the laminar flow.

Keyword: self-excited oscillations, instability, flutter.

1. INTRODUCTION

Study self-exciting oscillations of elastic tubes conveying fluid have been studied during last 50 years in the context of biological applications (for example, cardiovascular system, including blood vessel vibrations; respiratory system) [1 – 11]. An extensive review of advances in experimental, analytical and computational investigations of such flows is given in [1]. In numerous experiments such phenomena as pressure drop/flow rate relations, wave propagation and generation of instabilities were observed. These phenomena are of interest for many researches because of their various applications. Different mathematical models are proposed to define the behavior of the elastic tube conveying fluid, for example [2 – 4]; [3] outlines several models that have been developed to describe standard experiments in Starling resistor. There are a lot of numerical simulations of these experiments [2, 3, 6, 7].

Detailed description of the behavior of thick-walled silicone rubber tubes conveying aqueous fluid was given in the paper [8]. The instability was caused by changing of the external pressure. Three types of the behavior were found: stability at high downstream flow resistance, self-excited oscillations at low downstream flow resistance and exponential instability at the intermediate downstream flow resistance. Pressure drop/flow rate curves for steady flow and equilibrium characteristics of the collapsed tube were obtained, various types of oscillations of the collapsible tube were exemplified, and little detail of the wave-forms of pressure, flow rate and area were revealed. Analogous experiments for thick-walled tubes of different lengths were described in [9]. It was shown, that the frequency of self-excited oscillations is not strongly dependent on the tube length, and the effect of the tube length is to predispose the system to a particular mode of oscillation. The form of thick-walled tubes oscillations is qualitatively similar to oscillations, which occur in the larynx or sphygmomanometer cuff. The investigations of the flow through thin-wall axisymmetric tubes are presented in the paper [2]. Cross-sectional area from transmural pressure and pressure drop/flow rate relations, obtained in experiments, were used to verify the proposed lumped parameter system model. The validity of the model was confirmed by the comparison of experimental and simulation results. In the paper [10] the formulation was proposed to predict the critical flow at which the instability can develop. The wave phase velocity and the mean flow velocity were measured and it was shown that the oscillations are related to the event of the fluid velocity exceeding the phase velocity in a contracted section of the tube.

⁺¹juliazaiko@yandex.ru, ⁺²vladimir.yushutin@gmail.com, ⁺³vasily@vedeneev.ru

Although biofluid flows are generally laminar [7], most experimental studies span a wide range of the Reynolds numbers (from hundred to several thousand) and mostly deal with turbulent flows. In [11] it was shown that for thick-walled tubes oscillations are not possible at laminar regimes. In [5] the laminar flows of various viscosities through thin-walled tubes were investigated to facilitate numerical simulations of the flow in “Starling resistor”. Results of the experiments showed that the flow rate and Reynolds number at the oscillation onset do not strongly depend on downstream rigid pipe length, the oscillation frequency depends on this parameter significantly; the oscillation amplitude decreased as fluid viscosity increased.

In this paper we find the stability boundaries for laminar and turbulent regimes, analyze the effect of the flow regime (laminar vs turbulent) on the limit cycle properties, the flow rate limitation and the influence of the fluid viscosity on these characteristics at turbulent regimes.

2. EXPERIMENTAL APPARATUS

The apparatus for the recirculation of liquid through the collapsible tube is shown in Fig. 1. The flow circulates in a closed loop. A working fluid is carried to the base tank by the pump and enters to the elastic tube from there. The working fluid is water or glycerin mixture, so it is isolated from the ambient air to protect the mixture from aeration. Latex Penrose tubes of 0.01 m in diameter is attached at each end to the rigid tubes of the same diameters. Elastic tubes with a length-to-diameter ratio from 50:1 to 35:1 were used. (The results presented here are similar for the elastic tubes with the length-to-diameter ratio in this range.)

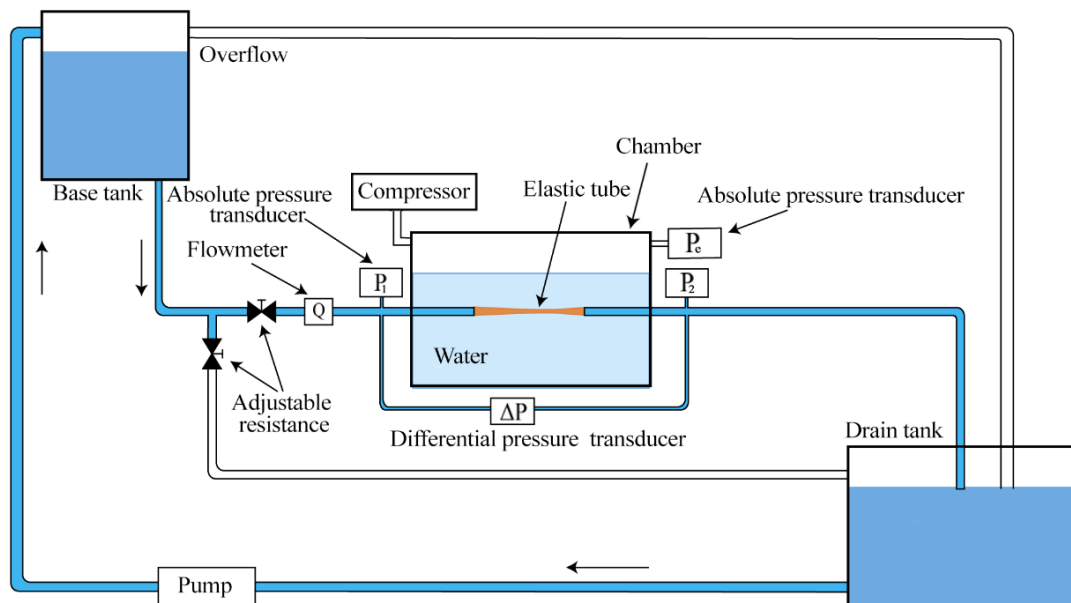


Figure 1: Apparatus for investigations of self-exciting oscillations of elastic tubes conveying fluid.

The external pressure p_e in the chamber is constant. The flow through the elastic tube occurs under the pressure drop $\Delta p = p_1 - p_2$, where p_1 and p_2 are the upstream and downstream pressures. The pressure drop is changed by the flow rate Q or downstream pressure p_2 . The flow rate Q may be controlled by the adjustable resistance and is measured by flowmeter, p_2 may be controlled by the position of draining hose.

Absolute pressure transducer, differential pressure transducer and microphone are used to record the frequency and the amplitude of the elastic tube oscillations. Location of these devices is shown in Fig. 1.

The elastic tube is fastened to the rigid tubes through connecting pipes. The differential pressure transducer measures the pressure drop in rigid tubes, connecting pipes and the elastic tube. We subtract the pressure drop Δp_0 in rigid tubes and connecting pipes from the measured $\Delta p = p_1 - p_2$ to obtain actual pressure drop in the elastic tube Δp_{el} . To do that the values of the pressure drop Δp_0 in rigid tubes and

connecting pipes are measured for the set of the flow rate values (Fig. 2), and the relation obtained is approximated by the formula (1) (dashed line in the Fig. 2)

$$\Delta p_0 = 200.18Q^2 + 214.32Q \quad (1)$$

The pressure drop in the elastic tube Δp_{el} is calculated as the residual $\Delta p - \Delta p_0$, where Δp is the measured pressure drop in rigid tubes, connecting pipes and the elastic tube, Δp_0 is calculated according to the formula (1). Hereunder we omit the index *el*, and use the notation Δp for the actual pressure drop in the elastic tube.

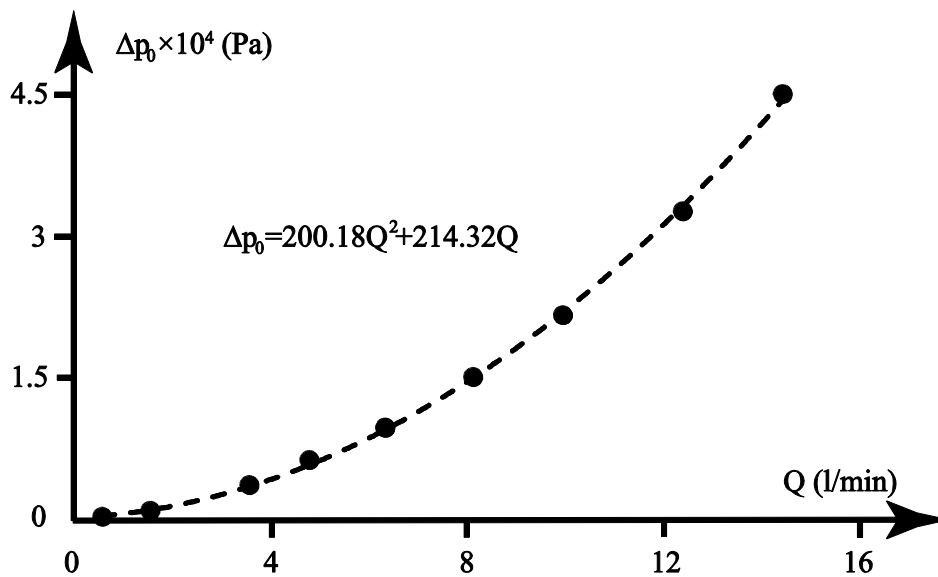


Figure 2: Pressure drop Δp_0 in rigid tubes and connecting pipes. Experimental data (points) and approximation (dashed line).

3. RESULTS OF EXPERIMENTS

The first series of experiments was conducted for fluids with various viscosities corresponding to turbulent regimes. Reynolds number based on the Penrose tube diameter was varied in the range $2300 < Re < 26000$. The experiments reveals that the stability boundary and the character of limit cycle oscillations do not significantly depend on the fluid viscosity. This is explained by the fact that the molecular viscosity is negligible compared to the turbulent viscosity. When the stability was lost while keeping $p_1 - p_e$ constant and increasing $\Delta p = p_1 - p_2$, the tube first oscillates in the following manner (Fig. 3, Fig. 4, a): two collapses followed by a delay in the stable state (Fig. 3, a), then again two collapses, etc. For higher Δp , the tube collapsed three times followed by a delay (Fig. 3, b); then four, five, and up to nine times; for higher Δp single-frequency oscillations were finally established and locked the tube (Fig. 3, i). After establishing of single-frequency oscillations neither frequency nor flow rate are changed when Δp is increased more.

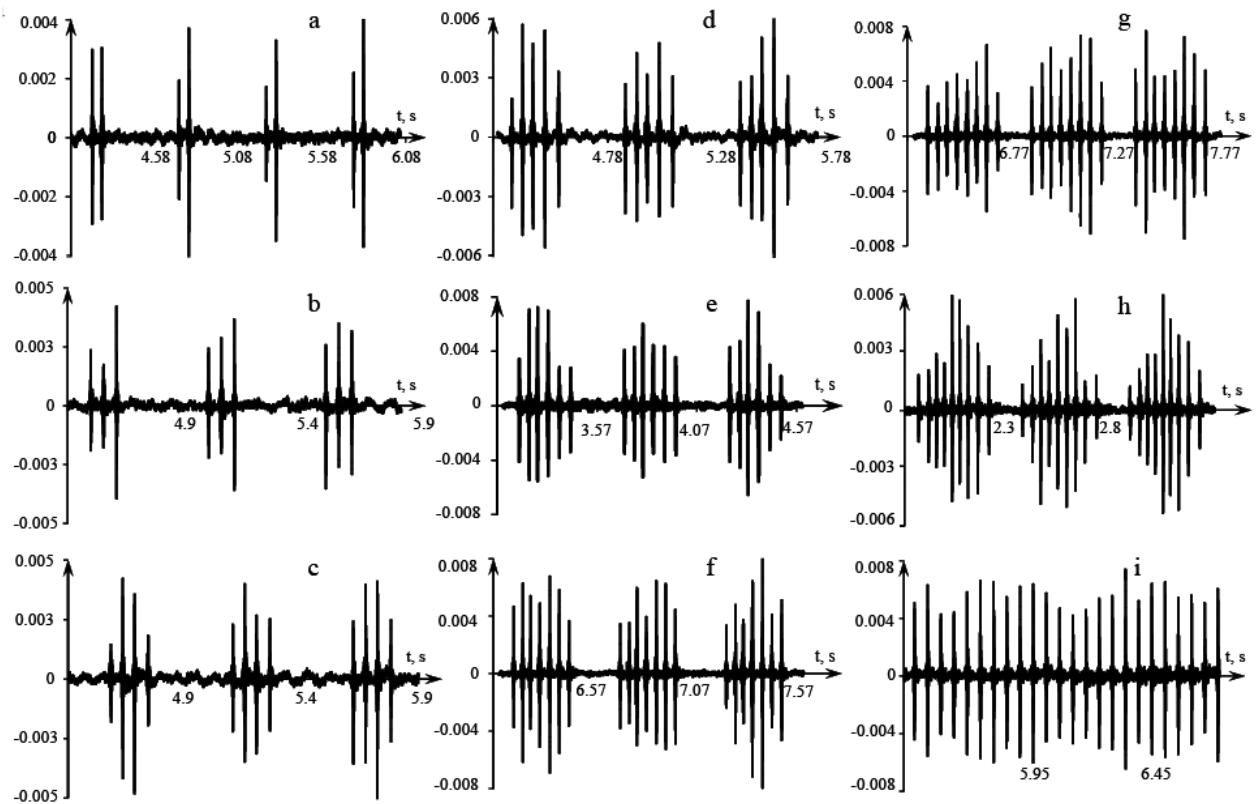


Figure 3: Various types of oscillations (corresponding to various numbers of consecutive tube collapses followed by a delay). Turbulent regime.

At the second series of tests a more viscous glycerine solution was used, which provides laminar flow at the unstable regimes with $100 < Re < 2000$ with similar pressure drop along the Penrose tube. Unstable behaviour at laminar regimes is quite different from the behavior in the turbulent case. For most flow rates, single-frequency oscillations developed immediately after the loss of stability (Fig. 4, b) in contrast to the turbulent case (Fig. 4, a). The measurements also demonstrate (Fig. 5) that the oscillation amplitude at the turbulent regimes is higher than at the laminar regimes for similar flow rates and identical types of oscillations (with equal number of consecutive tube collapses followed by a delay).

The map of regimes (Fig. 4) shows the stability boundaries (dashed curves) and the boundaries between various types of oscillations (corresponding to various numbers of consecutive tube collapses flowed by a delay) for different flow rates and pressure drops at turbulent (a) and laminar (b) regimes. As can be seen, the instability thresholds at the same flow rates corresponds to less pressure drops at laminar regimes than at turbulent regimes.

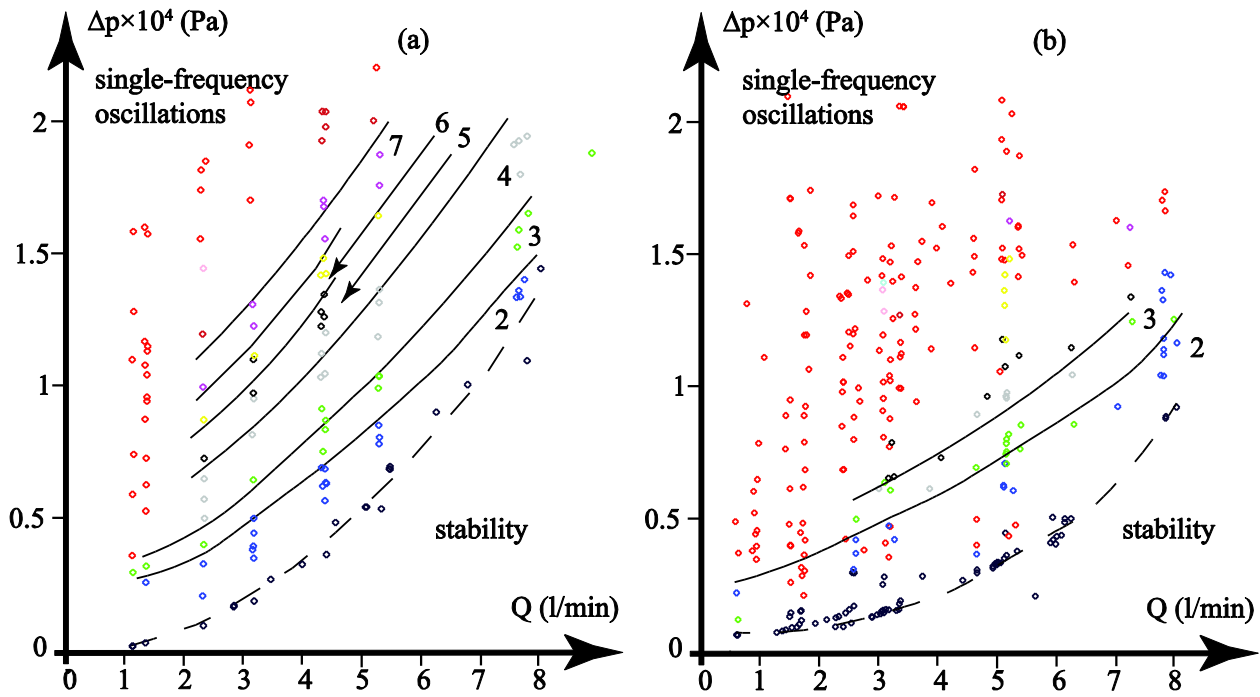


Figure 4: Map of the limit cycle oscillations for turbulent (a) and laminar (b) flow regimes. Number of consecutive tube collapses followed by a delay for each limit cycle type is marked by number and color.

There are operating points (where an operating point is a pair of the flow rate and the pressure drop), for which the dimensionless resistance coefficients λ at turbulent and laminar regimes are close. The resistance coefficient for the steady flows is calculated from the measured pressure drop Δp /flow rate Q relationships by the formula

$$\lambda = \frac{\Delta p}{l} \cdot \frac{2d}{\rho v^2}, \tag{2}$$

where l is the elastic tube length, d is the elastic tube diameter, ρ is the fluid density, $v = 4Q/(\pi d^2)$ is the fluid velocity in the elastic tube. The values calculated by the formula (2) are in agreement with the analytical formula (3) for the resistance coefficient for the laminar flow through round tubes:

$$\lambda = \frac{64}{Re} \tag{3}$$

The resistance coefficients for the stability at the turbulent regime are calculated by the empirical formula

$$\lambda = \frac{64/Re}{1 - (1 - \frac{576}{576 + Re})^4} \tag{4}$$

Fig. 6 demonstrates that resistance coefficients for turbulent and laminar regimes at similar operating points are close.

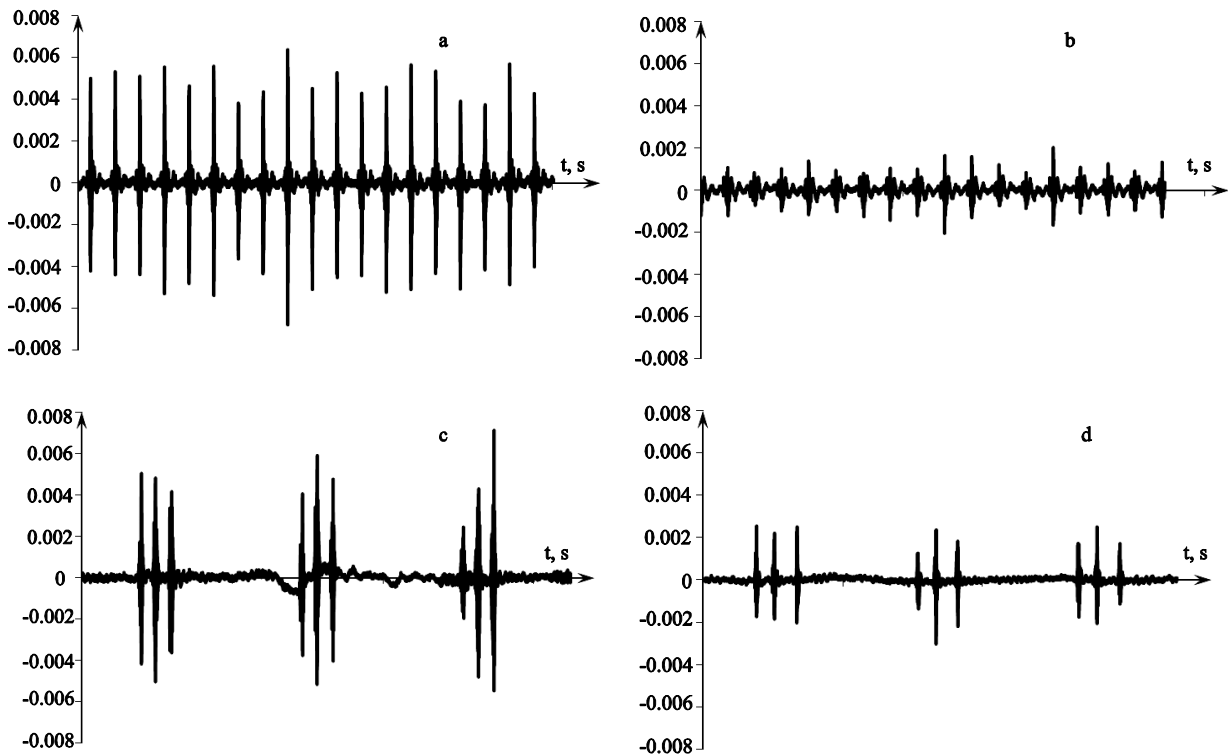


Figure 5: Oscillation amplitudes at turbulent (a, c) and laminar (b, d) regimes; a, b — single-frequency oscillations; c, d — three collapses followed by a delay in the stable state.

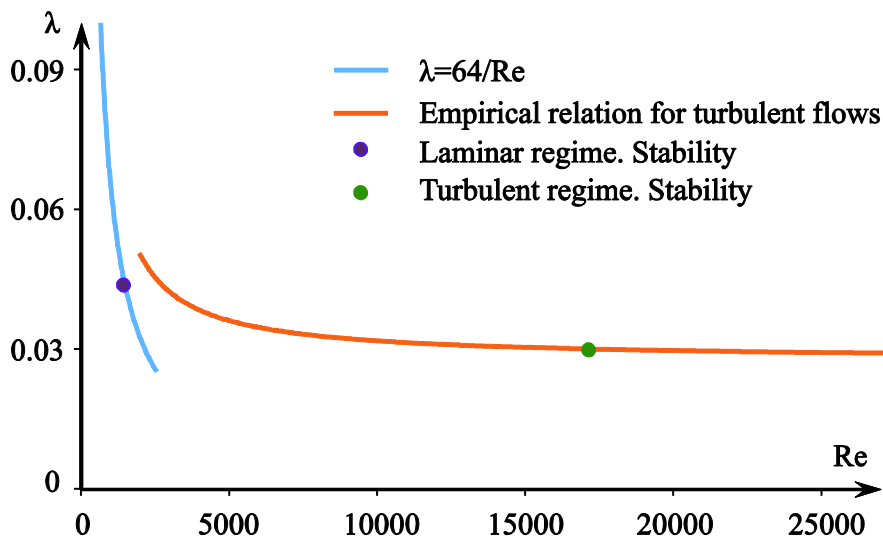


Figure 6: Resistance coefficients for turbulent and laminar regimes at similar operating points ($Q, \Delta p$). Tube stability. Operating point for laminar regime: $Q = 4.42 l/min, \Delta p = 2677.62 Pa \cdot s$. Operating point for turbulent regime: $Q = 4.39 l/min, \Delta p = 3665.45 Pa \cdot s$.

The experimental relations $f(Q, \Delta p)$ for laminar and turbulent regimes are approximated and contour charts on the $(Q, \Delta p)$ plane are drawn (Fig. 7). The oscillation frequency f representing consecutive collapses depends on pressure drop Δp for fixed flow rate Q more essentially at laminar regimes than at turbulent regimes.

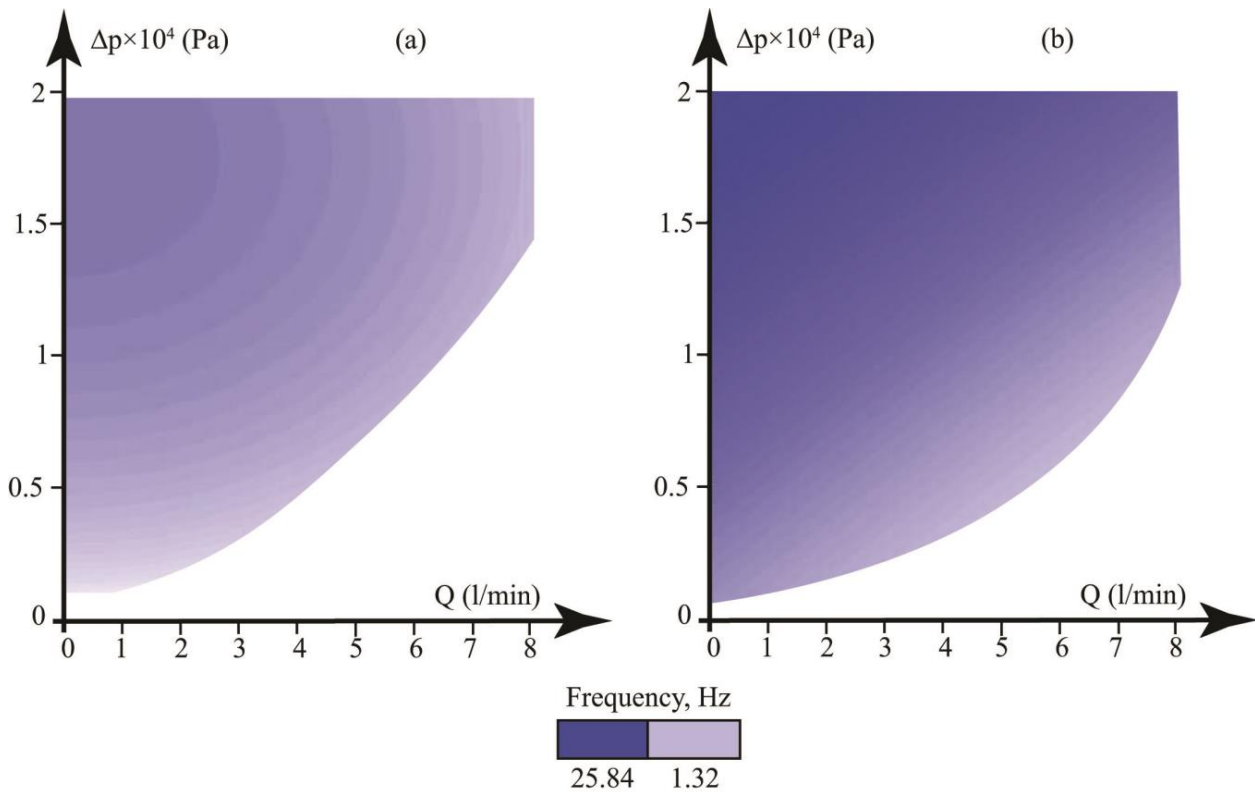


Figure 7: The oscillation frequency vs the flow rate and pressure drop relations for turbulent (a) and laminar (b) regimes.

ACKNOWLEDGMENT

The work is supported by grant MD-4544.2015.1.

REFERENCES

- 1) James B. Grotbrg, Oliver E. Jensen : Biofluid Mechanics in Flexible Tubes, *Annu. Rev. Fluid Mech.*, Vol. 36, pp. 121-47, 2004.
- 2) Adolf I. Katz, Yu Chen, Augusto H. Moreno : Flow through a collapsible tube. Experimental analysis and mathematical model, *Biophysical Journal*, Vol. 9, pp. 1261-1279, 1969.
- 3) Pedley, T.J., Luo, X.Y. : Modelling flow and oscillations in collapsible tubes, *Theoret. Comput. Fluid Dynamics*. Vol. 10, pp. 277-294, 1998.
- 4) Jensen, O. E. : Instabilities of flow in a collapsed tube, *J. Fluid Mech.*, Vol. 220, pp. 623-659, 1990.
- 5) Bertram, C. D., Tscherry, J. : The onset of flow-rate limitation and flow-induced oscillations in collapsible tubes, *J. of Fluids and Structures*, No. 22, pp. 1029-1045, 2006.
- 6) Heil, M. & Hazel, A.L. : Fluid-Structure Interaction in Internal Physiological Flows, *Ann. Rev. Fluid Mech.* 43, 141-162, 2011.
- 7) Hazel, A. L., Heil, M. : Steady finite-Reynolds-number flows in three-dimensional collapsible tubes, *J. Fluid Mech.*, Vol. 486, pp. 79-103, 2003.
- 8) Bertram, C. D. : Unstable equilibrium behaviour in collapsible tubes, *J. Biomechanics*, Vol. 19, No. 1, pp.

- 61-69, 1986.
- 9) Bertram, C. D., Raymond, C. J., Pedley, T.J.: Mapping of instabilities for flow through collapsed tubes of different length, *J. of Fluids and Structures*, No. 4, pp. 125-153, 1990.
 - 10) Brower, R. W., Scholten C. S. : Experimental evidence on the mechanism for the instability of flow in collapsible vessels, *Medical and Biological Engineering*, 1975.
 - 11) Bertram, C. D., Elliot, N. S. J. : Aqueous flow limitation in uniform collapsible tubes: multiple flow-rates at the same pressure drop and upstream transmural pressure, *Proceedings of the ASME Summer Bioengineering Conference 27 June – 1 July, Snowbird, Utah*. BED Vol. 50, pp. 383-384, 2001.

HIGH-SPEED COMPUTATION AND EXPERIMENT ON ADDED-MASS AND VISCOUS-DAMPING FORCES ACTING ON VARIOUS OSCILLATING 3D OBJECTS

Ryuta Tanaka⁺¹, Hajime Onishi⁺¹, Hideki Shimohara⁺²,
Hirochika Tanigawa⁺³ and Katsuya Hirata⁺¹

⁺¹ Department of Mechanical Engineering Doshisha University, Kyoto, Japan

⁺² Doshisha International High School, Kyoto, Japan

⁺³ Department of Mechanical Engineering, NIT, Maizuru College, Kyoto, Japan

In many fluid-structure-interaction problems, the added mass is one of important interests. In the present study, we propose a simple and efficient method to specify fluid-force coefficients of a three-dimensional oscillating object in viscous fluid. The solving method is based on a discrete singularity method DSM. Then, we apply the DSM to some three-dimensional basic objects such as square-cross-section cylinders with various aspect ratios. Furthermore, we conduct experiments, and reveal the fluid-force coefficients of them comparing between computations and experiments, which show good agreement.

Keyword: Fluid Force, Numerical Analysis, Added Mass, Virtual Mass,
Discrete Singularity Method

1. INTRODUCTION

In many fluid-structure interaction problems, we often needed to consider the fluid forces caused by arbitral accelerated motions of fluid and/or solid objects. Such forces have been understood using the concept of “the added mas,” “the virtual mass,” “the carried mass” or “included mass.” Then, the added mass is one of important and essential interests in various engineering aspects such as marine vehicles and structures. In general, we need to consider the added mass of the fluid in arbitral accelerated motion. One of the simplest and the most fundamental accelerated motion is a periodical-forcing case, that is, (1) a sinusoidally-oscillating solid object in stationary fluid and (2) a stationary solid object in sinusoidally-moving fluid. Both the cases (1) and (2) are identical under the assumption of infinitesimal amplitudes, as one can be approximately converted into the other by considering the Floude-Krylov force.^{1) & 2)} So, we now consider the case (1). Due to the importance of the added mass, there have been many past studies in concern, which are mainly related with two-dimensional flow.^{3) - 13)} However, there have been a few researches concerning the three-dimensional flow around a three-dimensional object,^{16) - 21)} despite its importance in various industrial aspects.

In the present study, we propose a simple method where the solving method is based on a discrete singularity method (hereinafter, referred to as DSM) in order to specify the added mass of a three-dimensional object, as well as our previous studies^{14) & 15)} for a two-dimensional object. In this method, we consider an incompressible viscous fluid under the assumption of an infinitesimal oscillation amplitude of an object, and properly modify the three-dimensional full Navier-Stokes equations, namely, into linear equations the Brinkman equations. In two-dimensional-flow problems, we can introduce complex-variable functions supposing the Gauss-Argand planes. Instead, in the present three-dimensional-flow problems, we employ a fundamental solution of the Brinkman equations proposed by Tsai²²⁾ as a singularity of the DSM. Furthermore, we conduct experiments, and attempt to reveal the fluid-force coefficients of them comparing between computations and experiments.

⁺¹khirata@mail4.doshisha.ac.jp, ⁺³tanigawa@maizuru-ct.ac.jp

2. MODEL, GOVERNING PARAMETERS AND FLUID FORCE

(1) Model

Figure 1 shows the concept of model. A three-dimensional object sinusoidally oscillates in stationary and infinite fluid with incompressibility and viscosity. The object's displacement is given by $x = A\sin(\omega t)$, $y = 0$ and $z = 0$, where t denotes time.

(2) Governing parameters

Dimensionless governing parameters are kinetic Reynolds number S ($\equiv \omega L^2/\nu$) and Keulegan-Carpenter number KC ($\equiv 2\pi A/L$), where L and ν denote a characteristic length scale and the viscosity of fluid, respectively. In the present study, we discuss various square-cross-section cylinders with low aspect ratios as the oscillating object. Figure 2 is those models. The cylinders with an aspect ratio b/a oscillates in the x direction, where a and b denote a side length and a height of the cylinder, respectively. V is the volume of the cylinder, and L is an equivalent diameter d_e ($\equiv (6V/\pi)^{1/3} = (6a^2b/\pi)^{1/3}$). We consider both the cylinder in transverse oscillation like figure(a) and the cylinder in axial oscillation like figure(b). Tables 1 and 2 summarise the range of the governing parameters in computation and experiment, respectively.

(3) Fluid force

We solely consider the three-dimensional object whose cross section is symmetric on an arbitrary plane parallel to the x -axis. Then, the flow can be symmetric to the x -axis on every planes parallel to the x -axis, as well. In such a case, as the y - and z -components F_y and F_z of the fluid force \mathbf{F} acting on the object is cancelled out into zero, the x -component F_x is exclusively meaningful. Following to Chen,⁶⁾ we normalise F_x as a non-dimensional fluid force H_x . The real part $\text{Re}(H_x)$ and the imaginary part $\text{Im}(H_x)$ of H_x denote an added-mass coefficient and a negative damping coefficient, respectively. Then, we refer to $-\text{Im}(H_x)$ as a damping coefficient. —In some cases, we conventionally use the drag and inertia coefficients C_D and C_M as alternates to $\text{Re}(H_x)$ and $-\text{Im}(H_x)$. The definitions of C_D and C_M are given by the Morison's equation.²⁸⁾—

3. NUMERICAL PROCEDURE

(1) Linear approximation

The governing equations for incompressible and viscous flow are the three-dimensional Navier-Stokes equations and the continuity equation. We linearly approximate them under the assumption of an infinitesimal amplitude, and get the Brinkman equations and continuity equation as the present governing equations.^{14) & 15)}

(2) DSM

Now, we consider a DSM^{5), 14), 15), 24) - 27)} to solve the linearly-approximated governing equations, numerically. A fundamental solution of the governing equations; namely, a three-dimensional Brinkmanlet is given by Tsai (2008).²²⁾ Figure 3 shows an analytical model of the DSM for a square cross-section cylinder, where singularities and control points are arranged inside and on the cylinder, respectively.

4. EXPERIMENTAL PROCEDURE

(1) Theory

We consider the Newton's second law of motion of a pendulum in fluid. In the small angle approximation,²⁹⁾ we get the coordinate s measured along the arc of the pendulum in damping free oscillation as follows.

$$s(t) = Ae^{-\zeta\omega_n t} \sin(\omega_n t) \quad \text{with} \quad \omega_n = \sqrt{\frac{m_g}{m_i}} \omega_a \quad \text{and} \quad \zeta = \frac{C}{2\omega_a \sqrt{m_g m_i}}, \quad (1)$$

where C denotes the damping factor. The mass corresponding to the gravitational force is m_g , and the mass

reacting to acceleration is m_i for the pendulum. ω_n denotes the natural frequency (angular frequency at $C = 0$), and ζ denotes the damping ratio. $\omega_a (\equiv \sqrt{g/l})$ is the natural frequency in a, which is taken to be equivalent to that in vacuum. We should note that $\sqrt{1 - \zeta^2} = 0.999 - 1.000 \approx 1$ as for the present experiments. Then, $\text{Re}(H_x)$ and $-\text{Im}(H_x)$ are given by the following equations.

$$\text{Re}(H_x) (= C_M) = \left(\frac{\omega_a}{\omega_n}\right)^2 \left(\frac{\rho_o}{\rho} - 1\right) - \frac{\rho_o}{\rho} \quad \text{and} \quad -\text{Im}(H_x) = \frac{2\zeta\omega_n}{\omega_n} \left(\frac{\rho_o}{\rho} + C_M\right), \quad (2)$$

where ρ and ρ_o are the densities of fluid and the object, respectively. Both ω_n and $\zeta\omega_n$ are obtained from the time history of the object's motion in damping free oscillation.

(2) Experimental apparatus

Figure 4 shows the schematic diagram of the present experimental apparatus. Figure(a) represents an overall view. We fill a tank made from acrylics with water. And, a pendulum in water is hung above the tank by a knife edge. A high-speed video camera is perpendicularly installed to the oscillating plane of the pendulum. The recorded motion of the pendulum is analysed using a picture-correlation method. And, we can observe the time history of the object's motion in damping free oscillation. Figure(b) shows the dimensions of the pendulum and the tank. Figure(c) shows the details of the pendulum.

5. RESULTS AND DISCUSSION

(1) Linear theory

Figure 5 summarises the computational results for the cylinders with $b/a = 0.5-5.0$ in transverse oscillation, in a range of $S = 10-10,000$. That is to say, this figure shows $\text{Re}(H_x)$ and $-\text{Im}(H_x)$ as functions of S in figures(a) and (b), respectively. An arrow in figure(a) is the experiment for the cylinder at $S \gg 1$ with $b/a = 1.0$ (cube).¹¹⁾ A dashed line in each figure is the analytical solution for a sphere.¹⁷⁾

We can see that $\text{Re}(H_x)$ and $-\text{Im}(H_x)$ have remarkable tendencies being independent of b/a . Namely, $\text{Re}(H_x)$ monotonically decreases and asymptotes to a certain value (potential theory), with increasing S . $-\text{Im}(H_x)$ monotonically decreases with increasing S , as well as $\text{Re}(H_x)$. In contrast with $\text{Re}(H_x)$, $-\text{Im}(H_x)$ asymptotes to zero at $S = \infty$. Of course, these tendencies of $\text{Re}(H_x)$ and $-\text{Im}(H_x)$ are the same as those for a sphere as shown in figure. The tendencies are appropriate, as the viscosity of fluid relatively decreases with increasing S .

Besides, we can discuss the effects of b/a upon $\text{Re}(H_x)$ and $-\text{Im}(H_x)$. Namely, both $\text{Re}(H_x)$ and $-\text{Im}(H_x)$ monotonically increase with increasing b/a . Both these b/a effects becomes less remarkable, when S increases. Thus, $-\text{Im}(H_x)$ becomes close to zero at $S > 10^3$ being independent of b/a . —From a quantitative point of view, both $\text{Re}(H_x)$ and $-\text{Im}(H_x)$ for a square cylinder with $b/a = 0.5$ are almost identical to those for a sphere at any S . — Both the b/a effects seem acceptable, because we regard the equivalent diameter as the present characteristic length scale. As for the b/a effect upon $\text{Re}(H_x)$, the projected area of a cylinder on the plane perpendicular to the direction of forced oscillation increases with increasing b/a . As for the b/a effect upon $-\text{Im}(H_x)$, the total surface area of a cylinder increases, when b/a increases from about unity.

As well as the cylinders in transverse oscillation, we get the computational results for the cylinders with $b/a = 0.5-5.0$ in axial oscillation. Again, we can see that $\text{Re}(H_x)$ and $-\text{Im}(H_x)$ have remarkable tendencies being independent of b/a . These tendencies are the same as those in transverse oscillation. In contrast, the effects of b/a upon $\text{Re}(H_x)$ and $-\text{Im}(H_x)$ are different from those in transverse oscillation. Namely, $\text{Re}(H_x)$ monotonically decreases with increasing S . This b/a effect upon $\text{Re}(H_x)$ does not become less remarkable, when S increases. $-\text{Im}(H_x)$ almost coincides with one another, then $-\text{Im}(H_x)$ is approximately determined by only S being independent of b/a . The b/a effect upon $\text{Re}(H_x)$ seems acceptable. Because the projected area of a cylinder on the plane perpendicular to the direction of forced oscillation decreases with increasing b/a . As for the b/a effect upon $-\text{Im}(H_x)$, we need further study over wider ranges of parameters than the present study.

(2) Experiments

a) Non-linearity

In this sub-section, we consider the experiment for a square-cross-section cylinder at $S=4,900$ with $b/a = 1.0$ (cube) in transverse oscillation as an example, comparing with the linear theory at $KC = 0$ (computational solution).

Figures 6(a) and (b) show the experimental $\text{Re}(H_x)$ and $-\text{Im}(H_x)$ as functions of KC , respectively. In each figure, a dashed line denotes the linear theory for comparison. In the present study, we conduct the all experiments in condition of $\sin\theta \approx \theta$. —In a preliminary experiment, we have demonstrated that we can suppose translation motion, if the angle θ of a pendulum is less than 5° .—

At first, we see figure(a) ($\text{Re}(H_x)$). When KC decreases from 13 to zero, $\text{Re}(H_x)$ tends to monotonically decrease and to approaches to a constant value. More specifically, this approaching manner seems complicated. Thus, we divide the range of KC into two: namely, a small-amplitude range at $KC \lesssim 2$ and a large-amplitude range at $KC \gtrsim 2$. In the small-amplitude range, the approaching manner can be exponential. So, we approximate the experimental results by an empirical formula such as $\text{Re}(H_x) = 0.76(1 + 0.07KC^{3.9})$ using the least squares method, whose curve is drawn by a solid line in the figure. According to this empirical formula, we see that the approaching constant value at $KC = 0$ is 0.76, which almost coincides with the linear theory (0.73).

Second, we see figure(b) ($-\text{Im}(H_x)$). When KC decreases from 13 to zero, $-\text{Im}(H_x)$ as well as $\text{Re}(H_x)$ tends to monotonically decrease and to approaches to a constant value. More specifically, this approaching manner seems complicated. Thus, we divide the range of KC into two: namely, a small-amplitude range at $KC \lesssim 2$ and a large-amplitude range at $KC \gtrsim 2$. —We should note that these two ranges are the same as those of $\text{Re}(H_x)$. This fact suggests that the non-linearities in the two ranges are not qualitatively the same each other.— In the small-amplitude range, the approaching manner can be exponential, as well as $\text{Re}(H_x)$. So, we approximate the experimental results by an empirical formula such as $-\text{Im}(H_x) = 0.15(1 + 0.59KC^{1.6})$ using the least squares method, whose curve is drawn by a solid line in the figure. According to this empirical formula, we see that the approaching constant value at $KC = 0$ is 0.15, which almost coincides with the linear theory (0.13).

b) Comparison between linear theory and experiment

Figure 7 summarises the experiment for a square-cross-section cylinder in transverse oscillation at $KC = 0$, which are predicted on the basis of such empirical formula as Figure 6. Figure 7(a) and (b) show $\text{Re}(H_x)$ and $-\text{Im}(H_x)$ as functions of S , respectively. In each figure, solid lines denote the linear theory, and a dashed line denotes the linear theory for a sphere. We can confirm that $\text{Re}(H_x)$ by the experiment agree well with that by the linear theory at any S and b/a . As for the experiment in axial oscillation as well as that in transverse oscillation in Figure 7, we can again confirm that both $\text{Re}(H_x)$ and $-\text{Im}(H_x)$ by the experiment agree well with those by the linear theory at any S and b/a .

6. CONCLUSION

In order to specify the added mass of basic three-dimensional objects such as square-cross-section cylinders with various aspect ratios, we have solved linearly-modified three-dimensional Navier-Stokes equations considering an incompressible viscous fluid under the assumption of an infinitesimal oscillation amplitude of an object. Furthermore, we have conducted experiments, and revealed the fluid-force coefficients of the cylinders comparing between computations and experiments, which show good agreement.

7. ACKNOWLEDGEMENT

We profoundly appreciate academic support by Professor Masashi Kashiwagi (Osaka University).

REFERENCES

- 1) Meneghini and Bearman: *Journal of Fluids and Structures*, Vol. 9, pp. 435–455, 1995.
- 2) Chakrabarti: *Handbook of Offshore Engineering*, Vol. 1, Elsevier, Amsterdam, pp. 158–160, 2005.
- 3) Patton: *ASME Paper*, No. 65-WA/UNT-2, pp. 1–7, 1965.
- 4) Dalton and Helfinstine: *Transactions of ASME*, Ser. D, Vol. 934, pp. 636–642, 1971.
- 5) Yano and Ooe: *Transactions of JSME, Ser. B*, Vol. 58, No. 554, pp. 3094–3099, 1992. (in Japanese)
- 6) Chen: *Flow-Induced vibration of circular cylindrical structures*, Hemisphere, New York, pp. 30–35, 1987.
- 7) Scolan and Faltnsen: *Journal of Fluids and Structures*, Vol. 8, pp. 201–230, 1994.
- 8) Zheng and Dalton: *Journal of Fluids and Structures*, Vol. 13, pp. 225–249, 1999.
- 9) Keulegan and Carpenter: *Journal of Research of National Bureau of Standards*, Vol. 60, No. 5, pp. 423–440, 1958.
- 10) Morison, et al.: *Petroleum Transactions of American Institute of Mining, Metallurgical, and Petroleum Engineers*, Vol. 189, pp. 149–157, 1950.
- 11) Sarpkaya: *Transactions of ASME, Ser. E*, Vol. 42, pp. 32–37, 1975.
- 12) Minamizawa and Endoh: *Kagaku Kogaku Ronbun-shu*, Vol. 9, No. 4, pp. 353–358, 1983. (in Japanese)
- 13) Bearman, et al.: *Applied Ocean Research*, Vol. 6, pp. 83–89, 1984.
- 14) Shimohara and Hirata: *Transactions of JSME, Ser. B*, Vol. 66, No. 644, pp. 1061–1066, 2000. (in Japanese)
- 15) Shimohara, et al.: *Transactions of JSME, Ser. B*, Vol. 77, No. 782, pp. 1904–1919, 2011. (in Japanese)
- 16) Lamb, H.: *Hydrodynamics, 6th Ed.*, Dover Publications, New York, pp. 738, 1932.
- 17) Stokes: *Cambridge Philosophical Transactions*, Vol. IX, pt. 2, pp. 8–106, 1851.
- 18) Landau and Lifshitz: *2nd Ed.*, Pergamon Press, Oxford, pp. 89, 1987.
- 19) Isobe: *Applied Physics*, Vol. 17, No. 1–2 (a), pp. 250–253, 1948.
- 20) Isobe: *Applied Physics*, Vol. 17, No. 3–4 (b), pp. 55–59, 1948.
- 21) Inoue and Sato: *Bulletin of Japanese Society of Scientific Fisheries*, Vol. 51, No. 12, pp. 1997–2006, 1985. (in Japanese)
- 22) Tsai: *International Journal for Numerical Methods in Fluids*, Vol. 56, pp. 927–940, 2008.
- 23) Sarpkaya: *Journal of Fluids and Structures*, Vol. 21, pp. 435–440, 2005.
- 24) Yano, et al.: *Transactions of ASME, Journal of Applied Mechanics*, Vol. 63, pp. 990–996, 1996.
- 25) Tanigawa, et al.: *Transactions of JSME, Ser. B*, Vol. 66, No. 645, pp. 1300–1310, 2000. (in Japanese)
- 26) Tanigawa, et al.: *Transactions of JSME, Ser. B*, Vol. 69, No. 684, pp. 1854–1861, 2003. (in Japanese)
- 27) Hirata, et al.: *Transactions of JSME, Ser. B*, Vol. 74, No. 748, pp. 2485–2493, 2008. (in Japanese)
- 28) Morison, et al.: *Petroleum Transactions of American Institute of Mining, Metallurgical, and Petroleum Engineers*, Vol. 189, pp. 149–157, 1950.
- 29) Neill, et al.: *American Journal of Physics*, Vol. 75, pp. 226–229, 2007.

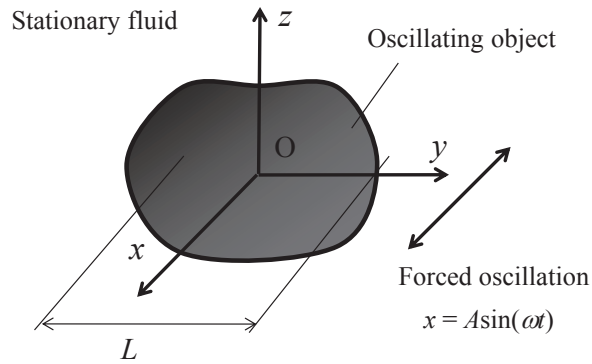
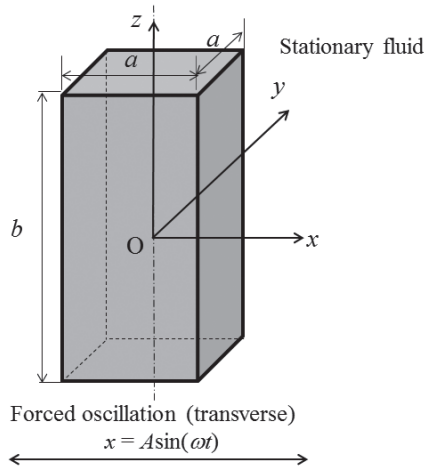
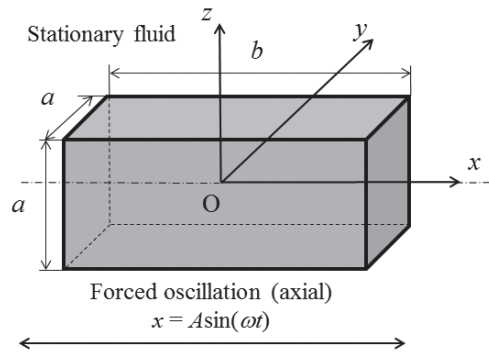


Figure 1: Model: an oscillating 3D object in stationary fluid.



(a) A cylinder oscillating perpendicularly to the cylinder's axis and perpendicularly to a pair of opposing cylinder's lateral faces.



(b) A cylinder oscillating parallel to the cylinder's axis.

Figure 2: Model: an oscillating square-cross-section cylinder (right square prism) with an aspect ratio b/a in stationary fluid.

Table 1: Parameters in linear analyses.

	b/a	S	KC
In transverse oscillation	0.5–5.0	10–10,000	0
In axial oscillation	0.5–5.0	10–10,000	0

Table 2: Parameters in experiments.

	b/a	S	KC
In transverse oscillation	1.0, 2.0, 3.0 and 4.0	1,600–7,300	0.065–13
In axial oscillation	1.0, 2.0 and 3.0	1,600–7,800	0.065–13

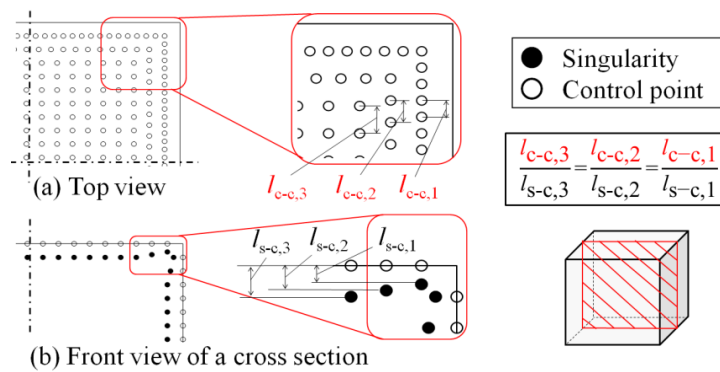


Figure 3: An analytical model of DSM for a corner of a square-cross-section cylinder.

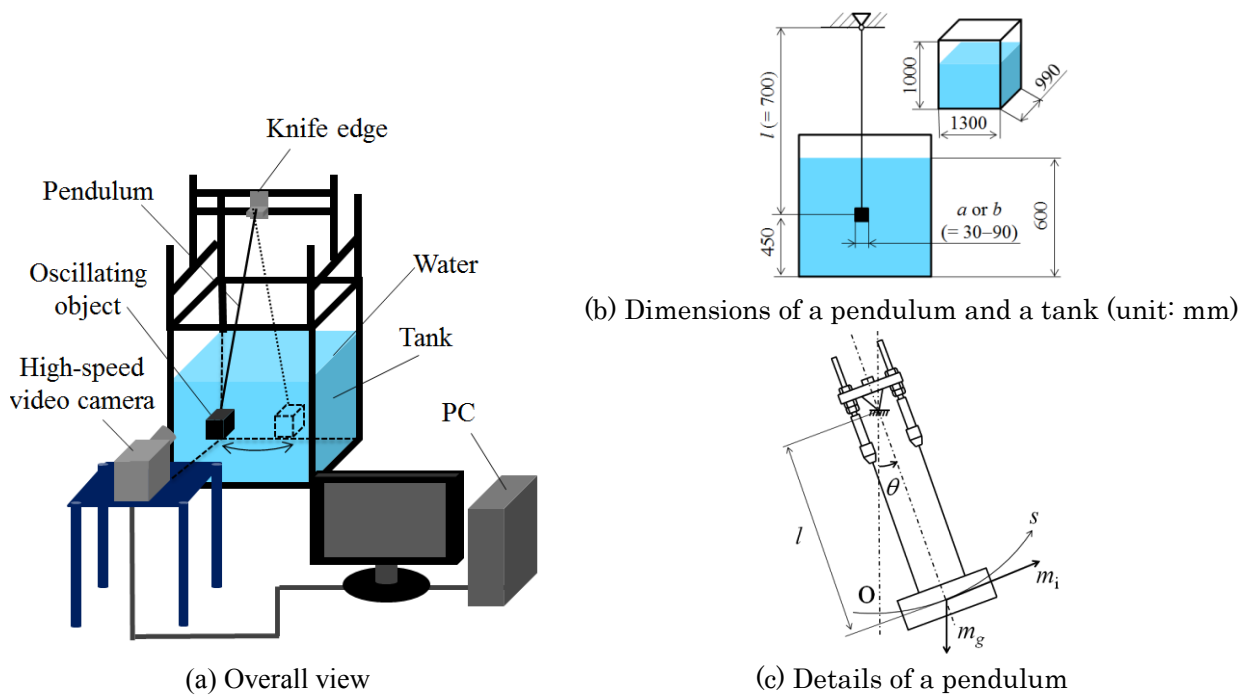
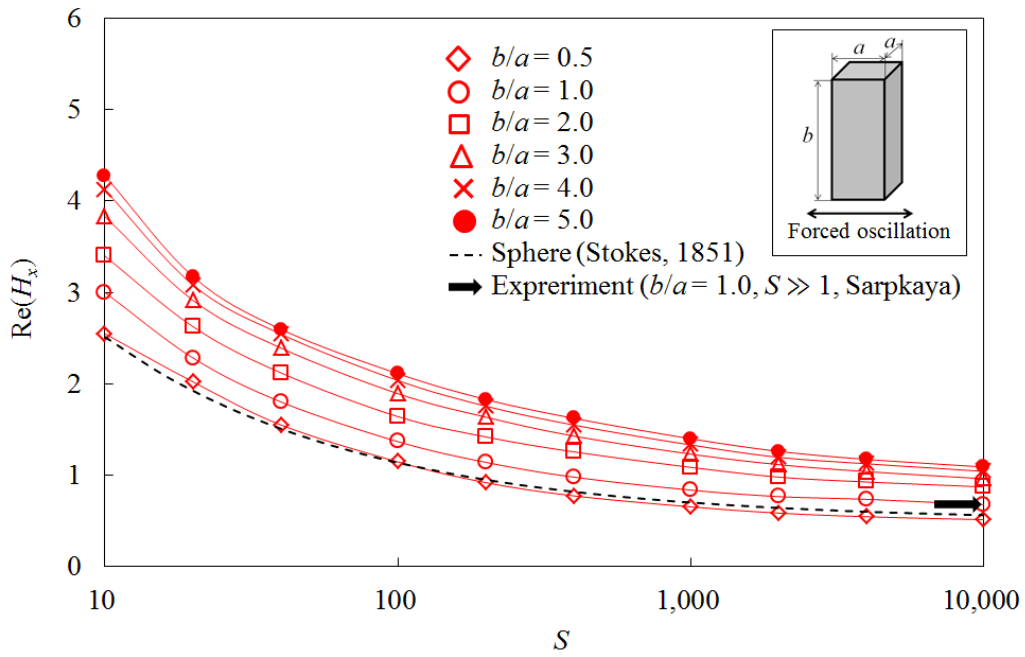
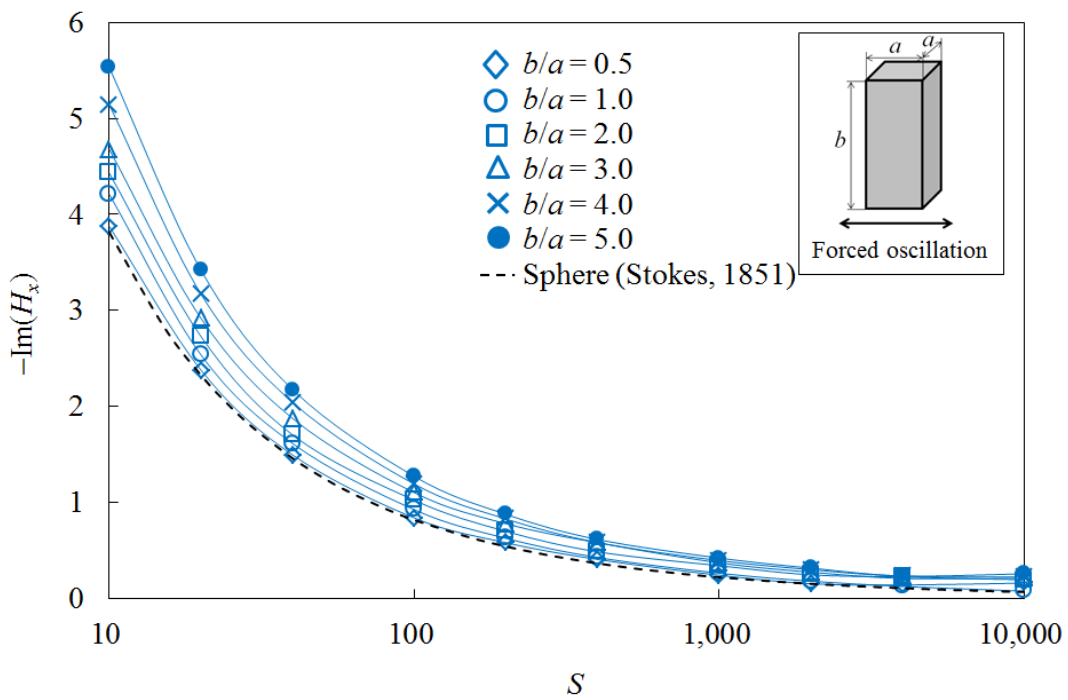


Figure 4: Schematic diagram of experimental apparatus.

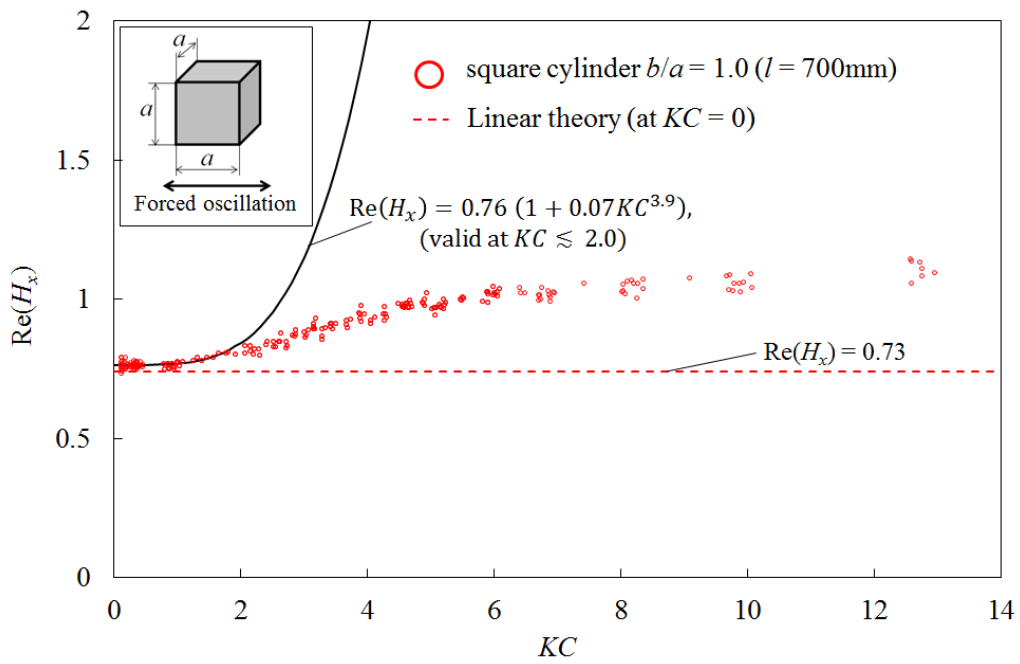


(a) $\text{Re}(H_x)$

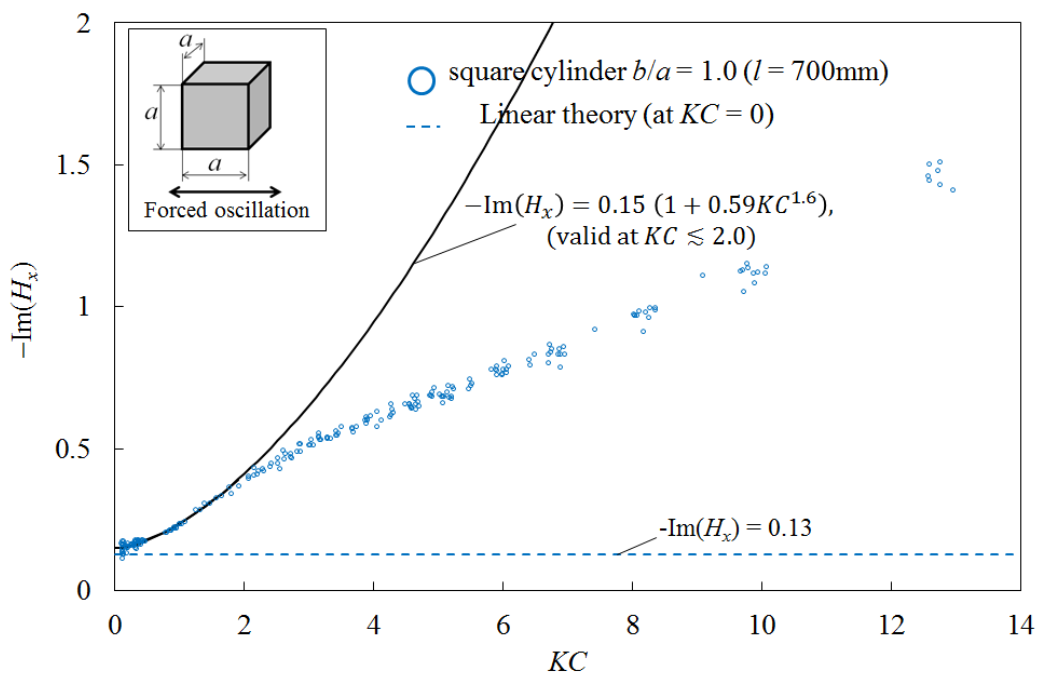


(b) $-\text{Im}(H_x)$

Figure 5: Analytical results of H_x as a function of S for square-cross-section cylinders with $b/a = 0.5-5.0$ in transverse oscillation.

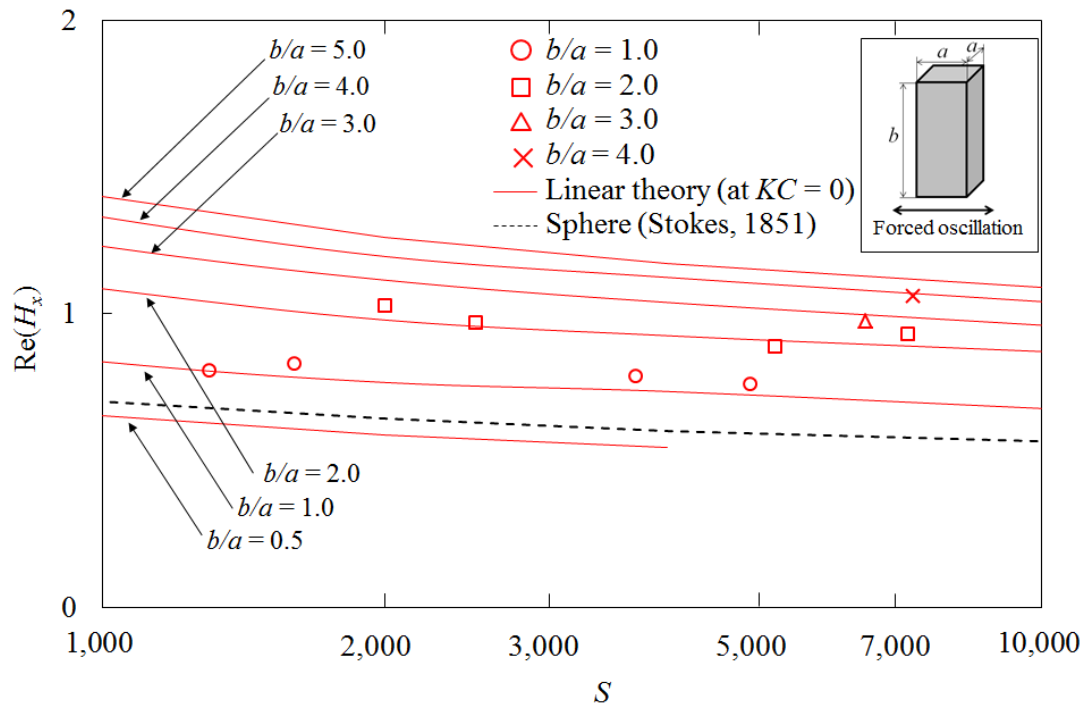


(a) $Re(H_x)$

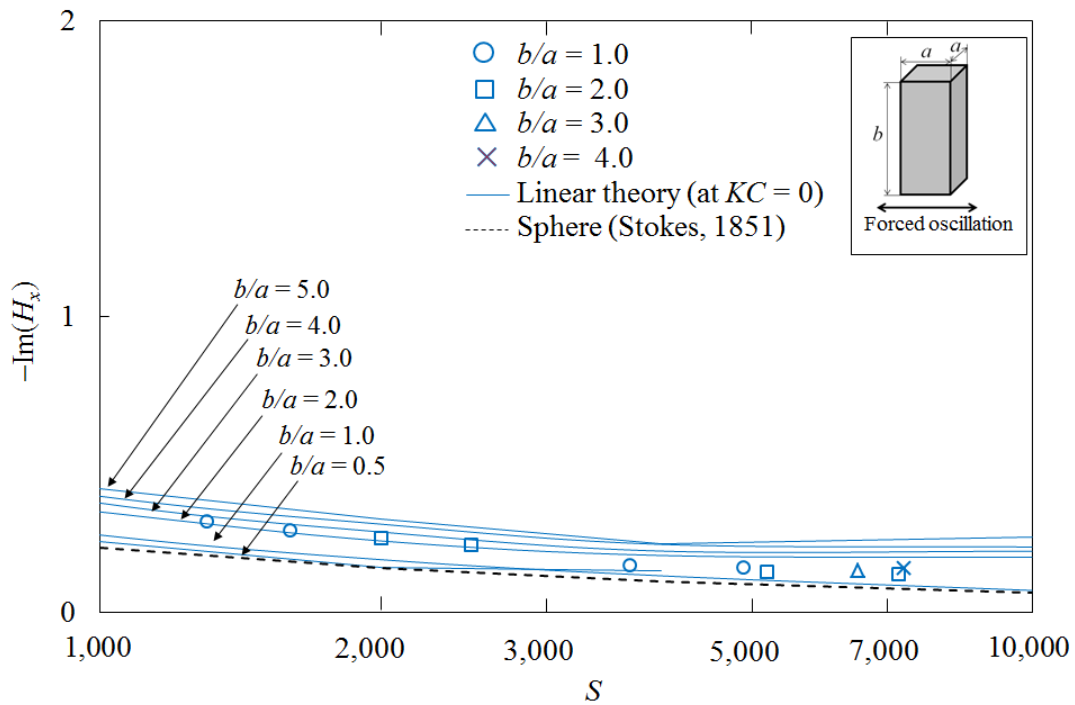


(b) $-Im(H_x)$

Figure 6: Experimental results of H_x at $S = 4,900$ against KC for a square-cross-section cylinder with $b/a = 1.0$ (a cube) in transverse oscillation.



(a) $Re(H_x)$



(b) $-Im(H_x)$

Figure 7: Experimental results of H_x at $KC \cong 0$ as a function of S for square-cross-section cylinders with $b/a = 1.0-4.0$ in transverse oscillation.

PROPERTIES OF WAKE EXCITATION OF CIRCULAR CYLINDER

Fumiaki Nagao⁺¹, Minoru Noda⁺², Masahiro Inoue⁺³, Shota Matsukawa⁺⁴, and Akihiro Shitamori⁺⁵
^{+1,+2} Institute of Technology and Science, Tokushima University, Tokushima, Japan
⁺³ Chuden Plant Co., Ltd., Hiroshima, Japan
⁺⁴ Anan Technical High School, Anan, Japan
⁺⁵ Graduate School of Tokushima University, Tokushima, Japan

The wake excitation of close-spaced tandem or staggered circular cylinders is known to develop from the interaction between the leeward circular cylinder and wake flow of the windward circular cylinder. However, this phenomenon is strongly influenced by the Reynolds number, which controls the flow around the cylinders, and by the arrangement of the circular cylinders. Experiments were performed to investigate the wake-induced vibrations of circular cylinders arranged in tandem with a central distance of three diameters and having several kinds of surface roughness. For smooth circular cylinders, two types of stable limit cycles for the transverse response were measured. The larger response, which had a double amplitude of about three diameters ($2Y/D \approx 3$), was much more sensitive to the Scruton number and surface roughness of the cylinders. The smaller response ($2Y/D = 1-1.25$) was closely related to the separated flow from the windward cylinder. The Reynolds number was found to have a relatively large effect on wake galloping. The surface roughness of the leeward circular cylinder played a more important role in wake galloping than that of the windward circular cylinder. However, installing helical wires on both cylinders produced a synergistic stabilizing effect. The effect of the Reynolds number on the wake excitation was investigated over the critical Re range.

Keyword: Wake excitation, Surface roughness of circular cylinder, Critical Reynolds number

1. INTRODUCTION

Many studies have focused on the aerodynamic instabilities of tandem or staggered circular cylinders such as sub-conductors, chimneys, towers, antennas, and the twin cables of cable-stayed bridges^{1,2}). The wake-induced vibrations of the leeward cylinder in tandem or staggered circular cylinders are known to develop from the interaction between the leeward circular cylinder and the wake flow of the windward circular cylinder. The present authors previously investigated the instability of closely spaced triple circular cylinders³) and found that the Reynolds number Re affects the onset velocity of wake galloping. In order to reduce the effects of Re , the wake excitation properties of a circular cylinder in the wake of several kinds of rectangular cylinders were tested with interesting results^{4), 5)}. The properties of unsteady pressures on the leeward circular cylinder in the wake of a square cylinder with free vibrations were experimentally measured to understand the excitation mechanism of the leeward circular cylinder⁵⁾. Using the ensemble-averaged fluctuating pressures during one period, it was clarified that the timing of the leeward circular cylinder across the shear flow of the windward square cylinder played an important role in the formation of the wake excitation force.

This paper presents an experimental investigation on the effects of the surface roughness on the wake galloping of tandem circular cylinders; some of the results have already been reported elsewhere⁶⁾⁻⁸⁾. Moreover, the responses of wake galloping were also examined beyond the critical Re range.

2. EXPERIMENTAL PROCEDURE

Two kinds of wind tunnels were used here. One was used to investigate the effects of the surface roughness of the circular cylinder on wake galloping. The other was used to examine the response of the wake galloping over the critical Re range. The tandem circular cylinders were set at a central interval of three

⁺¹fumi@ce.tokushima-u.ac.jp, ⁺²noda@ce.tokushima-u.ac.jp

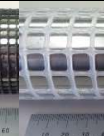
diameters for both wind tunnel tests.

One semi-closed circuit wind tunnel had a working section of 1 m wide, 1.5 m high, and 4 m long and was used to investigate the effects of the surface roughness of the circular cylinder on the wake galloping of the tandem circular cylinders. The circular cylinders were made of stainless steel and had a diameter of $D = 42$ mm and length of 900 mm. The windward cylinder was fixed to the sidewalls. The responses of the leeward circular cylinder were measured for two degrees of freedom (2DOF), longitudinal and transverse. The Scruton number $Sc = 2m\delta/\rho D^2$, where m is the mass, δ is the logarithmic damping, and ρ is the air density, was changed from 6.8 to 35.1. The natural frequencies for the longitudinal direction f_x and transverse direction f_y of the leeward cylinder were almost the same and changed from 1.7 to 2.7 Hz. However, only the results obtained under the conditions of $Sc = 16.4$ and $f = 2.2$ Hz are explained in this paper. Table 1 summarizes the experimental conditions examined here. The surface roughness of the cylinders was changed by rough plastic meshes and helical wires with a pitch of 229 mm ($\pi/6$ inclination from the cylinder axis) and intervals of $2\pi/3$ (three wires were installed), $\pi/3$ (six wires), or $\pi/6$ (12 wires), respectively. For 12 wires, the inclination from the cylinder axis θ was changed from 0° to 30° at 10° intervals. Table 2 summarizes the roughness lengths for the surface roughness of the materials; these were measured with an I-type hot wire anemometer.

Table 1: Experimental conditions for investigating the surface roughness.

Working section (m)	1 (width) \times 1.5 (height) \times 4 (length)
Diameter and length of model, D (m), L (m)	0.042, 0.9
Reynolds number, Re	2800–30,700
Mass, m (kg/m)	2.58
Scruton numbers, $Sc = 2m\delta/\rho D^2$	6.8, 16.4, 35.1
Degrees of freedom	Two (longitudinal and transverse directions)
Natural frequency, f (Hz)	1.7, 2.2, 2.7
Surface roughness of cylinders	Plain (smooth), rough plastic meshes (Mesh A: width $b = 1$ mm, thickness $t = 1$ mm, central distance $B = 4$ mm; Mesh B: $b = 2$ mm, $t = 1.85$ mm, $B = 10$ mm), parallel wires (diameter $d = 2$ mm, interval of wires = $\pi/6$), and helical wires (inclination from cylinder axis $\theta = \pi/18, \pi/9, \pi/6$; $d = 2$ mm; interval of wires = $2\pi/3, \pi/3$, and $\pi/6$)

Table 2: Roughness length and appearance of surface materials.

Surface material	Plain	Mesh A (M-A)	Mesh B (M-B)	12 parallel wires	12 helical wires $\theta = \pi/18$	12 helical wires $\theta = \pi/9$	12 helical wires $\theta = \pi/6$	6 helical wires $\theta = \pi/6$	3 helical wires $\theta = \pi/6$
Roughness length (mm)	0.0025	0.20	0.52	0.51	0.43	0.40	0.25	0.19	0.06
Solidity ratio (%)	-	43.8	36	18.1	185.5	19.3	20.9	9.2	4.6
Appearance									

The other semi-closed circuit wind tunnel had a maximum wind speed of 50 m/s and was used to investigate the effects of extremely high Re exceeding the critical Re on the wake galloping of tandem circular cylinders. The working section was 0.5 m wide, 2 m high, and 4.5 m long, respectively. Polyvinyl chloride

circular cylinders with a diameter of $D = 216$ mm and length of 400 mm were used. The windward cylinder was fixed to the sidewalls. The responses of the leeward circular cylinder were also measured for 2DOF with a very small Scruton number of $Sc = 6$. The natural frequencies (longitudinal direction: $f_x = 1.47$ Hz, transverse direction: $f_y = 1.45$ Hz) of the leeward cylinder were almost the same. Table 3 summarizes the experimental conditions examined here.

In order to confirm the critical Re for the circular cylinder, the drag acting on the cylinder and fluctuating wind speed in the wake of the cylinder were measured with a load cell and I-type hot wire anemometer, respectively. Fig. 1 shows the drag coefficient of the circular cylinder for $D = 100$ mm. The drag coefficient for $D = 216$ mm decreased suddenly around $Re = 3.4 \times 10^5$. However, no drag crisis was observed for the circular cylinder with $D = 100$ mm. Beyond the critical Re , an almost constant value of C_d was measured for the circular cylinder with $D = 216$ mm. As shown in the figure, Schewe⁹) obtained almost the same tendency. Figure 2 shows the power spectral densities of fluctuating wind velocities around the critical Re in the wake of the circular cylinder with $D = 216$. At $Re = 3.31 \times 10^5$, the apparent peak fluctuating frequency was present, and the frequency coincided with the Strouhal number of the circular cylinder $St = 0.2$ in the region of subcritical Re . On the other hand, a clear fluctuation peak was not detected at $Re = 3.46 \times 10^5$. As shown in these figures, the circular cylinder with $D = 216$ mm reached the critical and supercritical Re regions.

Table 3: Experimental conditions for investigating higher Re .

Maximum wind speed (m/s)	50
Working section (m)	0.5 (width) \times 2.0 (height) \times 4.5 (length)
Diameter D (m) and length L (m) of model	0.216, 0.4
Reynolds number, Re	14,400–72,000
Mass, m (kg/m)	50
Scruton number, $Sc = 2m\delta/\rho D^2$	6
Degrees of freedom	Two (longitudinal and transverse directions)
Natural frequency, f (Hz)	1.47 (longitudinal), 1.45 (transverse)

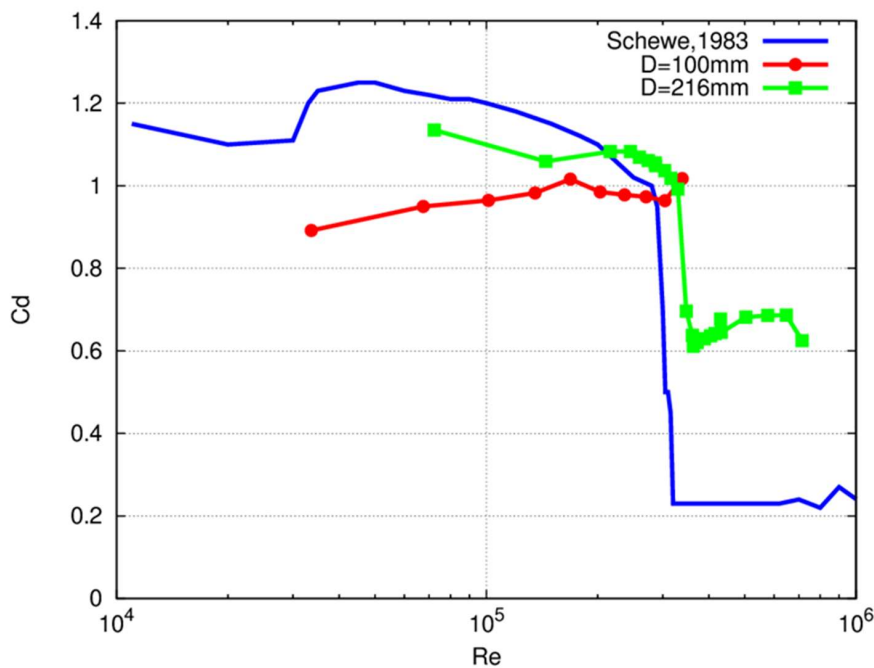


Figure 1: Effects of Re on the drag coefficient of the circular cylinder C_d .

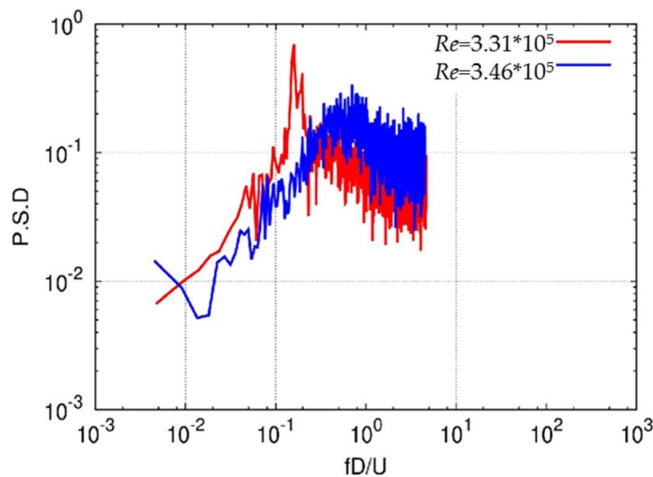
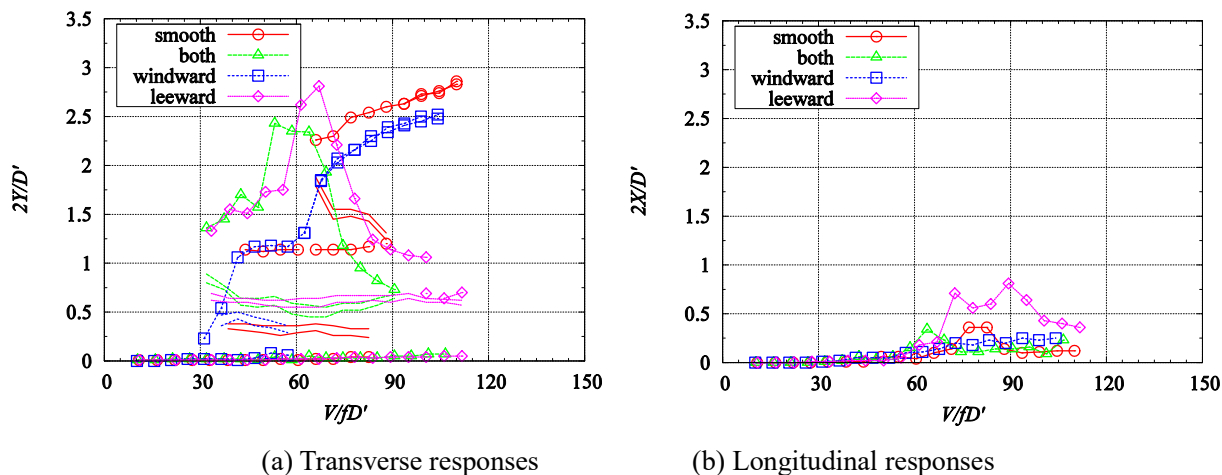


Figure 2: Power spectral densities of the fluctuating wind in the wake of the circular cylinder.

3. EFFECTS OF THE SURFACE ROUGHNESS OF THE CIRCULAR CYLINDER ON THE WAKE EXCITATION

(1) Effects of the rough plastic Mesh A (M-A)

Figure 3 shows the effects on the wake excitation of installing Mesh A (M-A) on the circular cylinders. The amplitudes and wind speeds were normalized by the relative diameter of the circular cylinders accounting for the thickness t of the meshes: $D' = D + 2t$. Figure 3(a) summarizes the effects of M-A on the transverse responses, and Figure 3(b) shows the longitudinal responses. The responses of the circular cylinder with the smooth surface are given in the figure for comparison. As shown in Figure 3(a), two different transverse responses were measured. The first stable limit cycle (1-SLC) had an almost constant amplitude of $2Y/D \approx 1.2$, which was closely related to the formation of a wake for the windward circular cylinder. In contrast, the second cycle (2-SLC) vibrated beyond the separated shear flow of the windward cylinder and developed from $2Y/D = 2.25$ to $2Y/D = 3.0$ with increasing wind speed. With installation of M-A on the windward cylinder, the transverse responses developed at lower wind speeds, and smaller amplitudes of 2-SLC were measured at higher wind speeds in comparison with those of the smooth surface circular cylinder. On the contrary, when M-A was installed on the leeward cylinder, larger transverse responses were measured at lower wind speeds. However, the responses decreased suddenly at higher wind speeds of more than 70. When M-A was installed on both cylinders, the responses converged to those of installation on the leeward cylinder.



(a) Transverse responses

(b) Longitudinal responses

Figure 3: Effect of installing Mesh A on the wake excitation.

These changes in responses were led by the relative increase in Re due to the increase in surface roughness of the circular cylinders by the installation of M-A. For the longitudinal direction shown in Figure 3(b), comparatively large amplitudes were only measured when M-A was installed on the leeward cylinder.

(2) Effects of the rough plastic Mesh B (M-B)

Figures 4 (a) and (b) show the transverse and longitudinal responses of the leeward cylinder with and without Mesh B (M-B). M-B was installed on the windward cylinder, the leeward cylinder, or both cylinders, respectively. As shown in Figure 4 (a), when M-B was installed on the windward cylinder, the large transverse responses of 2-SLC developed at lower wind speeds relative to those of the smooth surface circular cylinder and when M-A was installed on the windward cylinder as given in Figure 3 (a). In contrast, when M-B was installed on the leeward cylinder, the larger transverse responses of 2-SLC were only measured at lower wind speeds of less than 70, and the amplitudes of 1-SLC decreased. When M-B was installed on both cylinders, the responses also converged to those of installation on the leeward cylinder, similar to M-A. For the longitudinal direction, which is shown in Figure 4 (b), comparatively large amplitudes were measured in the high wind speed region for all cases of M-B installation when the transverse responses were held down by the unstable limit cycles.

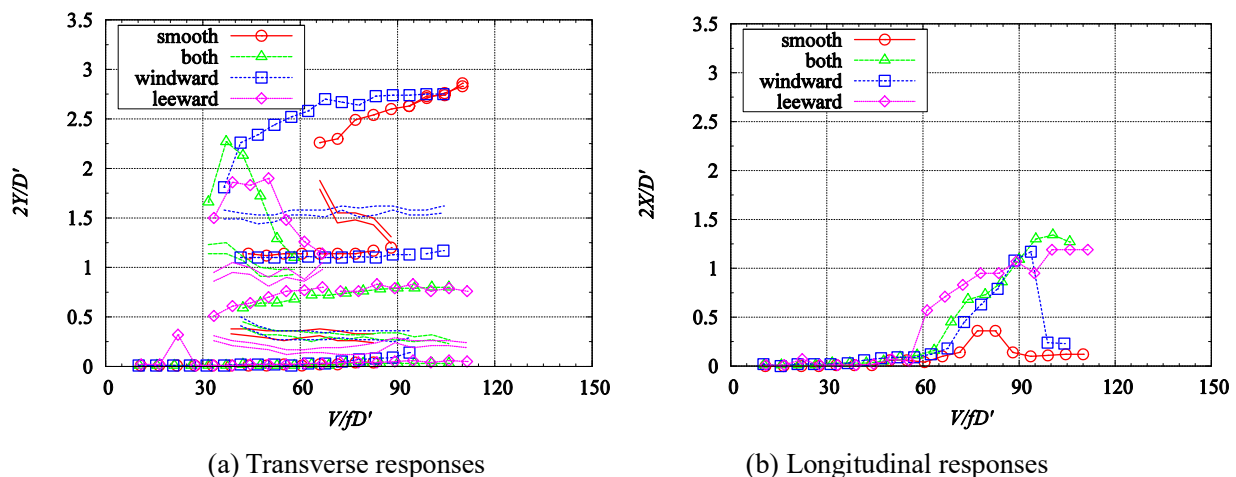


Figure 4: Effect of installing Mesh B on the wake excitations.

(3) Effects of helical wires

Figures 5 (a) and (b) show the transverse and longitudinal responses, respectively, of the leeward cylinder with zero, three, six, and twelve helical wires under the conditions of $Sc = 16.4$, $f = 2.2$ Hz, and 2DOF. The helical wires were installed on both cylinders, and the amplitudes and wind speeds were normalized by the relative diameter with helical wires $D' = D + 2d$. As shown in Figure 5 (a), when three helical wires were installed, the large amplitudes of 2-SLC completely disappeared. When six helical wires were installed, 1-SLC moved toward higher wind speeds, and 1-USLC was also larger in comparison with the results of installing three helical wires. When twelve helical wires were installed, the wake excitation completely disappeared. Therefore, even though the roughness length of the twelve helical wires was shorter than that of the rough plastic M-B, increasing the number of helical wires on the cylinders efficiently improved the wake excitation. For the longitudinal direction as shown in Figure 5 (b), no vibrations were observed for all helical wire installation cases, even when the transverse responses were held down.

Figures 6 (a) and (b) show the transverse and longitudinal responses, respectively, with and without twelve straight wires under the conditions of $Sc = 16.4$, $f = 2.2$ Hz, and 2DOF. The straight wires were installed on both cylinders. When the straight wires, as shown in Figure 6 (a) were installed, the large amplitudes of 2-SLC were suppressed. However, 1-SLC and large amplitudes at lower wind speeds were observed, similar to

the results for M-A and M-B. Therefore, when helical wires are installed, the reduced uniformity of the flow properties in the axial direction should play an important role in suppressing wake galloping. From Figure 6 (b), small amplitudes were measured in the longitudinal mode.

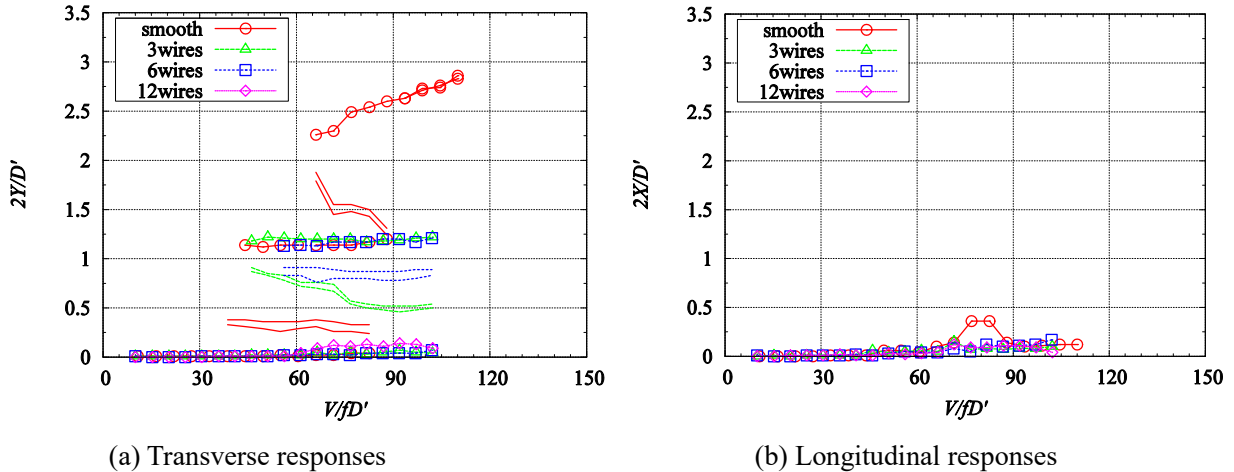


Figure 5: Responses of the leeward circular cylinder with and without the helical wires: $Sc = 16.4, f = 2.2$ Hz.

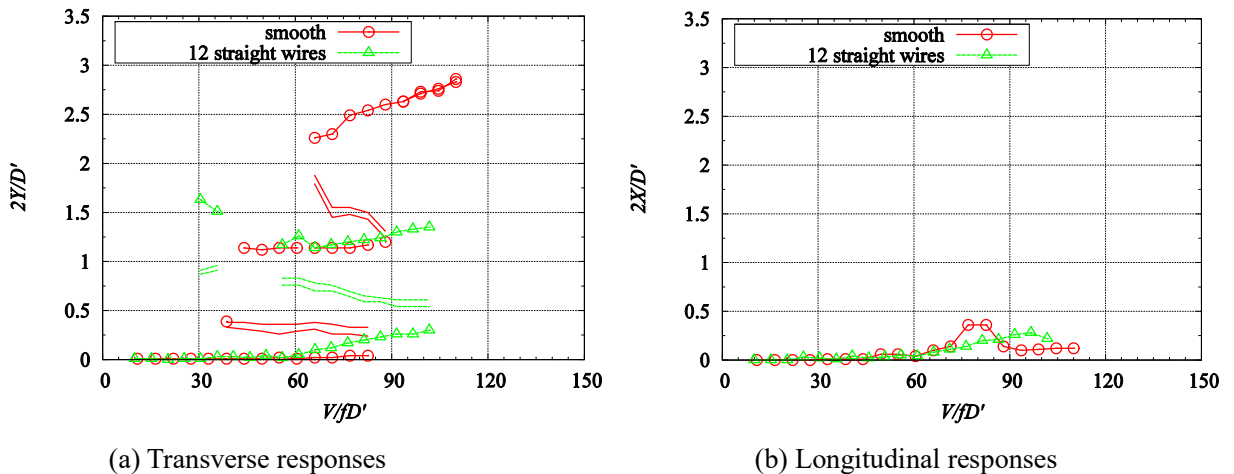


Figure 6: Responses of the leeward circular cylinder with and without 12 straight wires: $Sc = 16.4, f = 2.2$ Hz.

Figure 7 (a) and (b) represent the transverse responses and static displacements, respectively, with twelve helical wires attached to the windward cylinder, the leeward cylinder, or both cylinders under the conditions of $Sc = 16.4, f = 2.2$ Hz, and 2DOF. As shown in Figure 7 (a), when wires were installed on only the leeward cylinder, the amplitudes of 1-SLC decreased. However, 1-SLC occurred at lower wind speeds and developed from the rest condition without 1-USLC. On the other hand, the amplitudes of 1-USLC increased when wires were installed on only the windward cylinder. Furthermore, the amplitudes of 1-USLC when wires were installed on the windward cylinder were almost the same as that of 1-SLC when the wires were installed on only the leeward cylinder. When wires were installed on both cylinders, the stabilizing effects of the windward and leeward cylinders acted together. No longitudinal response was observed at all. As shown in Figure 7 (b), the static displacements when helical wires were installed on the windward or leeward cylinder increased at higher wind speeds.

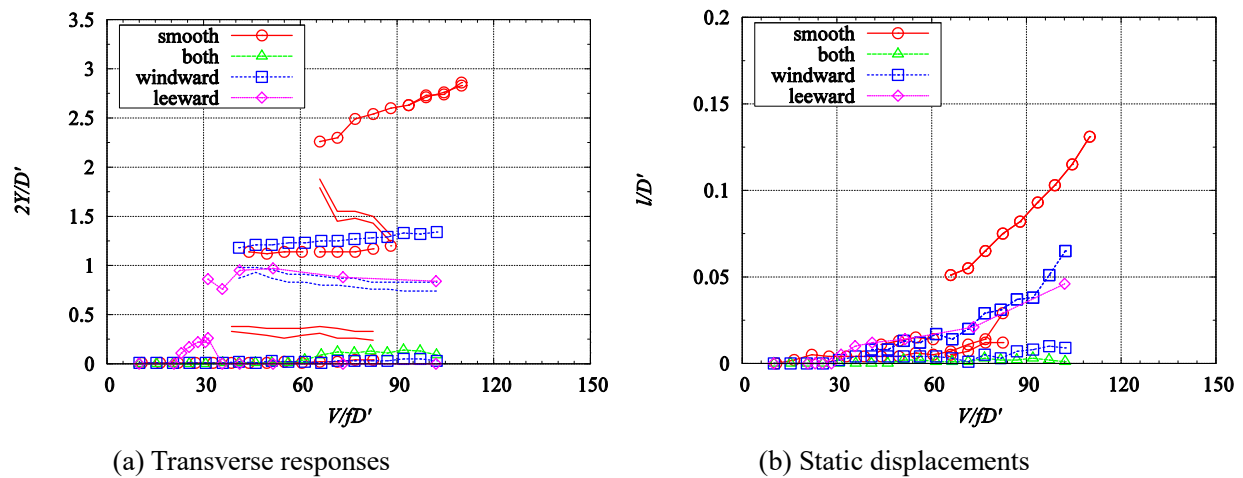


Figure 7: Responses of the leeward circular cylinder with and without the 12 helical wires, $Sc=16.4$, $f=2.2$ Hz.

4. EFFECTS OF THE REYNOLDS NUMBER ON WAKE EXCITATION

Figure 8 (a) and (b) show the transverse and longitudinal responses with the larger diameter model ($D = 0.216$ m), including the high Re numbers. As shown in Figure 8 (a), large transverse responses occurred when the wind velocity V/fD was reduced to about 29, which is consistent with the onset velocity of the small Sc circular cylinder model $Sc = 6$. However, when compared with the responses of the smooth surface shown in the previous figures, the first stable limit cycle (1-SLC) having an almost constant amplitude of $2Y/D \approx 1.2$, which is closely related to the formation of the wake of the windward circular cylinder, disappeared. The second stable limit cycle (2-SLC) vibrated beyond the separated shear flow of windward cylinder with increasing amplitudes from $2Y/D = 2.25$ to $2Y/D = 3.0$ and was the only one measured. The unstable limit cycle also appeared at the same subcritical Re . As shown in Figure 8 (b), the longitudinal responses were also measured with large transverse responses. However, the longitudinal amplitude demonstrated quite large fluctuations. Beyond the critical Re of around $Re = 3.5 \times 10^5$, the large transverse responses decreased with increasing Re . Finally, at supercritical Re of greater than $Re = 4.2 \times 10^5$, the wake galloping vanished.

In order to suppress the wake galloping of tandem circular cylinders in the subcritical Re region, countermeasures such as relative increases of Re of the circular cylinder may be efficient approaches.

5. CONCLUSIONS

Two wind tunnels were used to investigate the wake excitation of tandem circular cylinders having a central distance of three diameters:

Installing surface roughness on the leeward circular cylinder has a more important effect on wake galloping than installing it on the windward circular cylinder. However, installing helical wires on both cylinders achieved a synergistic stabilizing effect.

The Reynolds number has a relatively large effect on wake galloping. Above the critical Re , wake galloping disappears. Countermeasures such as relative increases of Re for the circular cylinder may efficiently suppress wake galloping.

ACKNOWLEDGMENT

This work was supported by JSPS KAKENHI, Grant Number 26420460.

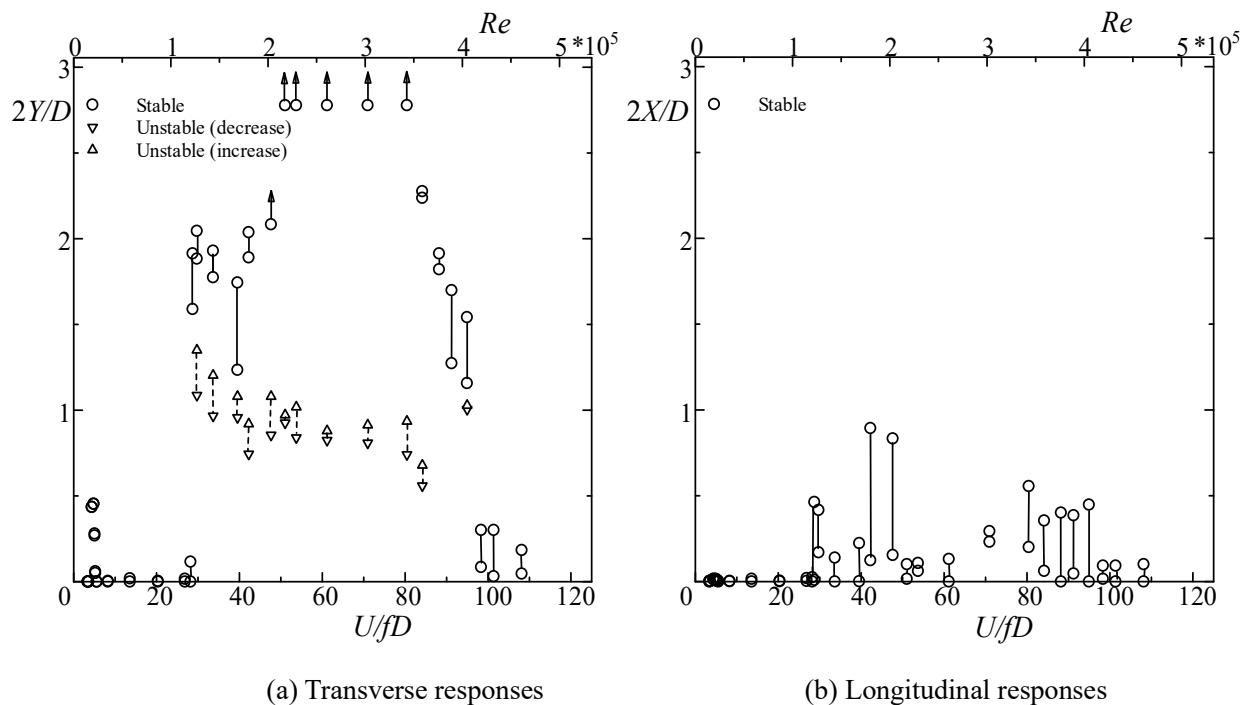


Figure 8: Responses of the leeward circular cylinder with the large-diameter model: $D = 0.216$ m, $Sc = 6$, $f = 1.45$ Hz.

REFERENCES

- 1) Cooper, K.R. and Wardlaw, R.L. : Aeroelastic instabilities in wakes, Proceedings of 3rd International Conference on Wind Effects on Buildings and Structures, Tokyo, Japan, pp. 647-655, 1971.
- 2) Simpson, A. : On the flutter of a smooth circular cylinder in a wake, Aeronautical Quarterly, Vol. 22, pp. 25-41, 1971.
- 3) Nagao, F., Utsunomiya, H., Noda, M., Imoto, M., and Sato, R. : Aerodynamic properties for closely spaced triple circular cylinders, Journal of Wind Engineering and Industrial Aerodynamics, Vol. 91, pp. 75-82, 2003.
- 4) Nagao, F., Utsunomiya, H., Noda, M., and Katayama, M. : Properties of aerodynamic vibrations of a circular cylinder in the wake of several kinds of rectangular cylinders, Proceedings of 11th International Conference on Wind Engineering, Vol. 2, pp. 2469-2476, 2003.
- 5) Nagao, F., Noda, M., Koori, T., Wada, K., and Utsunomiya, H. : Wake-excitation mechanism for a circular cylinder in the wake of a square cylinder, Proceedings of 12th International Conference on Wind Engineering, Vol.2, pp. 1711-1718, 2007.
- 6) Nagao, F., Noda, M., and Inoue, M. : Effects of surface roughness of circular cylinders on wake galloping, Proceedings of 13th International Conference on Wind Engineering, 2011.
- 7) Nagao, F., Noda, M., and Inoue, M. : Basic study on wake excitation of tandem circular cylinders under central distance of three diameters, Proceedings of 9th International Symposium on Cable Dynamics, 2011.
- 8) Nagao, F., Noda, M., Inoue, M., and Matsukawa, S. : Properties of wake excitation in tandem circular cylinders with several kinds of surface roughness, Proceedings of 7th International Colloquium on Bluff Body Aerodynamics and Applications, 2012.
- 9) Schewe, G. : On the force fluctuations acting on a circular cylinder in crossflow from subcritical up to transcritical Reynolds numbers, *J. Fluid Mech.*, Vol. 133, 1983.

STUDY ON SPATIAL CORRELATION STRUCTURE OF FLUCTUATING PRESSURE ACTING ON A CIRCULAR CYLINDER

Minoru Noda⁺¹, Shinya Onishi⁺² and Fumiaki Nagao⁺³

⁺¹Tokushima University, Tokushima, Japan

⁺²Graduate school of Tokushima University, Tokushima, Japan

⁺³Tokushima University, Tokushima, Japan

In this study, the spatial correlation structure of fluctuating surface pressure acting on a fixed circular cylinder was investigated by wind tunnel tests and the computational fluid dynamics (CFD). Our study involved an examination of the following two effects: 1.) the aspect ratio of the model and 2.) the boundary conditions of the sidewalls for CFD on the fluctuating surface pressure acting on a fixed circular. This study produced the finding that the special correlation of the fluctuating pressure on a fixed circular cylinder was affected by the aspect ratio of the model. A proper orthogonal decomposition (POD) analysis indicated that the fluctuating surface pressure acting on a circular cylinder had symmetric and asymmetric mode shapes along the axis of the cylinder, and these modes affected the spatial correlation of the fluctuating aerodynamic forces acting on the cylinder.

Keyword: Coherence, Aspect ratio, Boundary condition, Proper orthogonal decomposition (POD) analysis

1. INTRODUCTION

A circular cylinder is a fundamental element of structures such as the cables of cable-stayed bridges, and transmission lines. However, since the stiffness and damping of these members are low, they often show aerodynamic instability in wind. One of the causes of aerodynamic instabilities is the periodic pressure fluctuation acting on the surface of these members caused by Karman's vortex. If the member is short, the fluctuating surface pressure due to Karman's vortex has complete correlation along the axis of the cylinder. However, in the case of long members, the fluctuating surface pressure acting on the cylinder shows complex behavior, and the spatial correlation along the cylinder axis is reduced. Therefore, it is necessary to understand the spatial correlation characteristics of fluctuating pressure when the member is long in order to accurately estimate the aerodynamic response of those members, and many researchers have investigated this phenomenon for rectangular cylinders. Vickery investigated the spatial correlation of fluctuating lift and drag acting on a square prism in smooth and turbulent flows¹⁾. On the other hand, the spatial correlation of fluctuating velocity near a circular cylinder was investigated by El Baroudi²⁾. In this study, the correlation coefficient of fluctuating velocity between two points near a circular cylinder was measured and it was found that the correlation length became about three to six times the diameter of the circular cylinder. Moreover, the correlation coefficient of fluctuating forces on a circular cylinder was measured by Keefe³⁾. This investigation indicated that the correlation length of fluctuating forces was about five times the diameter of the circular cylinder. However, the correlation structure of fluctuating surface pressure on a circular cylinder has not yet been clarified in detail.

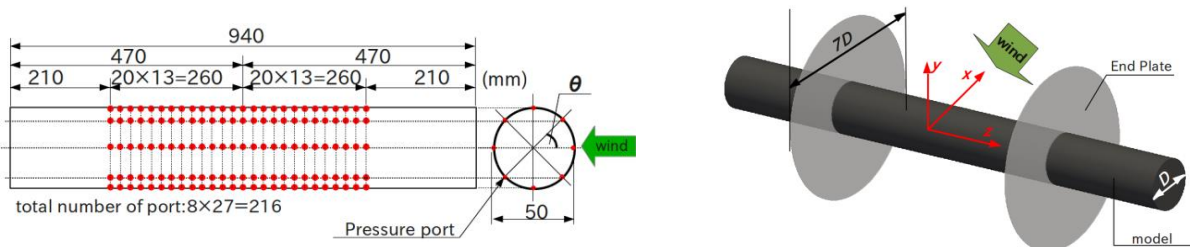
In addition, it is important to maintain reproducibility in terms of the fluctuation of aerodynamic forces on cylindrical models in wind tunnel tests. However, it is not clear at which level the aspect ratio of cylindrical models should be maintained in order to reproduce the fluctuation aerodynamic forces on slender models. Therefore, the effects of the aspect ratio of the circular cylinder for wind tunnel tests on fluctuating aerodynamic forces acting on a circular cylinder have not been investigated yet. Furthermore, the effects of the boundary condition of sidewalls on the numerical field for computational fluid dynamics (CFD) should also be clarified.

⁺¹noda@ce.tokushima-u.ac.jp, ⁺²c501431027@tokushima-u.ac.jp, ⁺³fumi@ce.tokushima-u.ac.jp

In this study, the spatial correlation structure of fluctuating surface pressure acting on a fixed circular cylinder was investigated by proper orthogonal decomposition (POD) analysis for wind tunnel tests and computational fluid dynamics (CFD) with large eddy simulation (LES).

2. CONFIGURATION OF WIND TUNNEL TEST

Fig. 1 shows the configuration of the wind tunnel tests. The circular cylinder model shown in Fig. 1 (a) was used. The diameter of the circular cylinder, D , was 50 mm, and the length of the model, L , was 940 mm. Therefore, the maximum aspect ratio, L/D , was 18.8. This model had 27 cross sections with 8 pressure holes arranged at equal intervals in the circumferential direction as shown in Fig. 1 (a). This model was placed at the center of the test section whose width, height, and length were 1,000, 1,500, and 4,000 mm, respectively. The aspect ratio was changed in the range from 3.6 to 10.8 by installing end plates whose diameter and thickness were 350 ($7D$) and 1.5 mm, respectively, as shown in Fig. 1 (b). In this study, the wind speed, U , was changed in the range from 4 to 10 m/s. This wind speed range corresponds to the range of Reynolds numbers from 13,000 to 33,000. The pressure at all the pressure holes was simultaneously measured at a 1 kHz sampling rate for a period of 40 s.



(a) Arrangement of pressure ports on the model (b) End plates on the model to change the aspect ratio

Figure 1. Experimental configuration.

3. CONFIGURATION OF CFD

Fig. 2 shows the numerical grid for LES. In this study, an LES of which the sub-grid scale model was a standard Smagorinsky model, was carried out by OpenFOAM⁴⁾ based on the finite volume method (FVM). The width of the numerical region was changed in the range from $2.7D$ to $10D$ to investigate the effects of aspect ratio on the aerodynamic forces. The number of grids was specified as shown in Tab. 1. The boundary conditions of the sidewalls were cyclic and slip. In this calculation, the Reynolds number, Re , was set to 20,000. The pressures at the points on the surface in the 40 s during which the flow became a stationary state were recorded at a 100 Hz sampling rate.

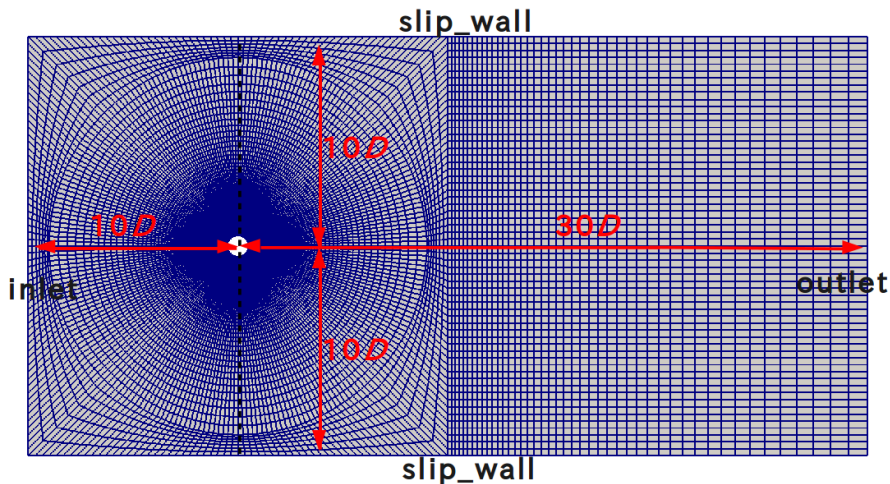


Figure 2: Numerical grid for LES.

Table 1: Number of grids along circumferential and axial directions.

Case	Circumferential direction	Axial direction (Δz)
2.7D-cyclic, slip	240	90 (0.03D)
5D-cyclic, slip	240	60 (0.083D)
10D-cyclic, slip	240	120 (0.083D)

4. RESULTS AND DISCUSSIONS

(1) Aerodynamic force coefficients

The obtained aerodynamic force coefficients acting on the whole circular cylinder are listed in Tab. 2. The CFD results for the different cases almost had the same value for the mean drag coefficient, C_D . The fluctuating drag and lift coefficients, $C_{D'}$ and $C_{L'}$, for the cyclic condition were higher than those for the slip condition. $C_{D'}$ and $C_{L'}$ for the cyclic condition decreased in proportion with the aspect ratio, L/D . Considering that strong fluctuating forces are produced by two-dimensional (2D) flows, it is found that the cyclic condition strengthens and the aspect ratio weakens the 2D structure of the flow. On the other hand, the C_D that was measured experimentally was higher than that obtained for CFD, and $C_{D'}$ and $C_{L'}$ were located between the slip and cyclic conditions. The reason for this is not clear.

Fig. 3 shows the power spectrum density (PSD) of the fluctuating lift for all cases. It is found that the Strouhal number stabilizes at 0.2 for all cases.

Table 2: Aerodynamic force coefficients.

Case	C_D	$C_{D'}$	$C_{L'}$
2.7D-cyclic	1.161	0.115	0.303
2.7D-slip	1.046	0.040	0.101
5D-cyclic	1.167	0.084	0.270
5D-slip	1.220	0.055	0.182
10D-cyclic	1.174	0.053	0.256
10D-slip	1.119	0.059	0.167
Exp. ($Re=33,000$)	1.321	0.079	0.217

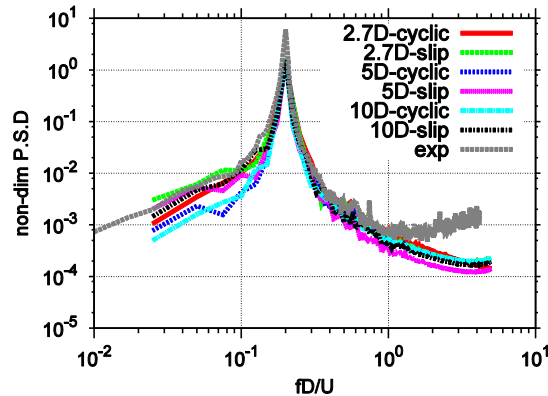


Figure 3: Power spectrum density of lift force.

(2) Spatial correlation of lift force

The root coherence of the fluctuating lift calculated between the middle of the span and each z/D is shown in Fig. 4. The curve in this figure is the Gaussian function defined by Eq. 1.

$$Rcoh = \exp\left\{-\frac{\pi}{4}\left(\frac{z}{L_c}\right)^2\right\} \quad (1)$$

where L_c is the correlation length based on the root coherence. Fitting formula (1) to the distribution of the root coherence for each case shown in Fig. 5 (a), the relation between the L_c and the L/D was obtained as shown in Fig. 5 (b). This figure shows that the correlation length for the cyclic condition is higher than that for the slip condition. Moreover, L_c decreases in proportion to L/D . This result reflects the results obtained for CFD in the previous section. On the other hand, L_c for CFD is higher than that measured experimentally at

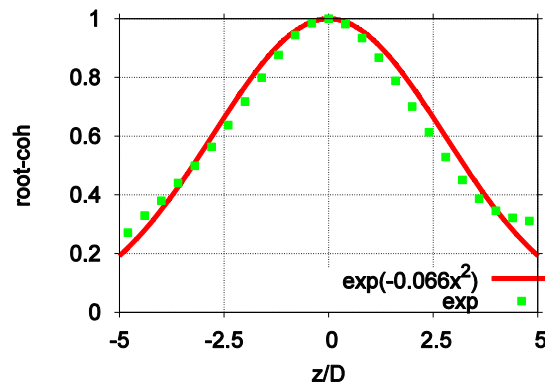
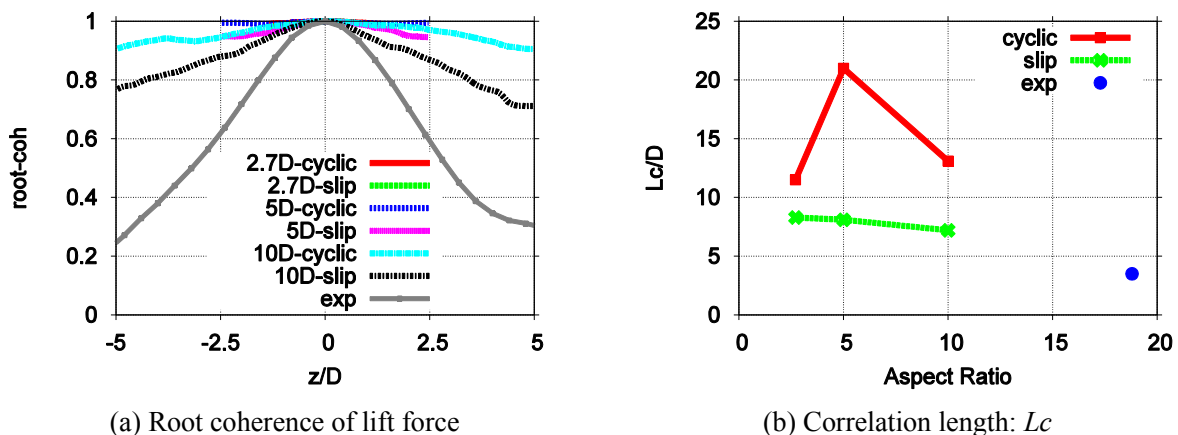


Figure 4: Root coherence distribution of lift force and fitting curve



(a) Root coherence of lift force

(b) Correlation length: L_c

$L/D=18.8$. Thus, it can be assumed that the L/D for this experiment was larger than for CFD.

(3) Structure of fluctuating surface pressure

The mechanism of the effects of the aspect ratio and the boundary condition of sidewalls on the special correlation of fluctuating aerodynamic forces on the circular cylinder was investigated by carrying out a proper orthogonal decomposition (POD) analysis⁵⁾ for the fluctuating surface pressure on the circular cylinder. Figs. 6 and 7 show the results of the POD analysis for the cases of the 2.7D-cyclic and the 10D-slip. In these figures, the longitudinal and transverse axes are defined as the angle of circumferential direction and the coordinate along the axial direction of the circular cylinder, respectively, as shown in Fig. 1. The pressure fluctuations from the 1st to the 5th mode are indicated as (a) – (e) in Figs. 6 and 7, and the power spectrum densities of the normal coordinate for each mode are shown as (f).

Figs. 6 and 7 indicate that the shapes of the 1st and 2nd modes were the same in both cases, and both modes were uniform along the axis of the cylinder. The power spectrum densities for the 1st and 2nd modes indicate that these two modes produce the fluctuating lift and fluctuating drag respectively, because the peak frequencies of these two modes were found to be equal to the Strouhal number and twice the Strouhal number, respectively. However, it is clear that the shapes of the mode were different between the cyclic condition and the slip condition in the case of the 3rd mode. The power spectrum densities of the 3rd, 4th, and 5th modes in the case of the 2.7D-cyclic indicate that these modes are independent of the fluctuations caused by the Karman vortex in Fig. 6. On the other hand, Fig. 7 shows that the 3rd and 5th modes, whose peak frequencies of the normal coordinates were equal to the Strouhal number, produced the fluctuating lift, whereas the 4th mode, whose peak frequency was determined to be twice the Strouhal number, produced the fluctuating drag.

The results for the modes beyond the 3rd mode for the other conditions are shown in Fig. 8. Figs. 6, 7, and 8 indicate that the modes representing the cyclic condition never showed an asymmetric pressure distribution responsible for producing the lift force. On the other hand, it is found that the modes for the slip

condition showed an asymmetric pressure distribution which could produce the lift force. Therefore, it can be said that the boundary condition of the sidewalls for CFD controls the mode shapes of higher degrees.

The modes and the power spectrum densities of each mode measured by using the wind tunnel test are presented in Fig. 9. This figure shows that the shapes of the modes for the result of the wind tunnel measurement were similar to the results obtained for the slip condition for CFD. In addition, it was found that the number of nodes along the axis of the cylinder increased in proportion with the mode degree as the common characteristics for the cases of the slip condition and the experiment.

The results of the POD analysis of the fluctuating surface pressure clarified that the cyclic condition of the sidewalls for CFD produced unnatural surface pressure fluctuation, and the slip condition of the sidewalls for CFD produced a similar pressure fluctuation in comparison with the experimental result. As the cause of this result, it can be mentioned that the flow fields near the sidewalls were forced to be the same by

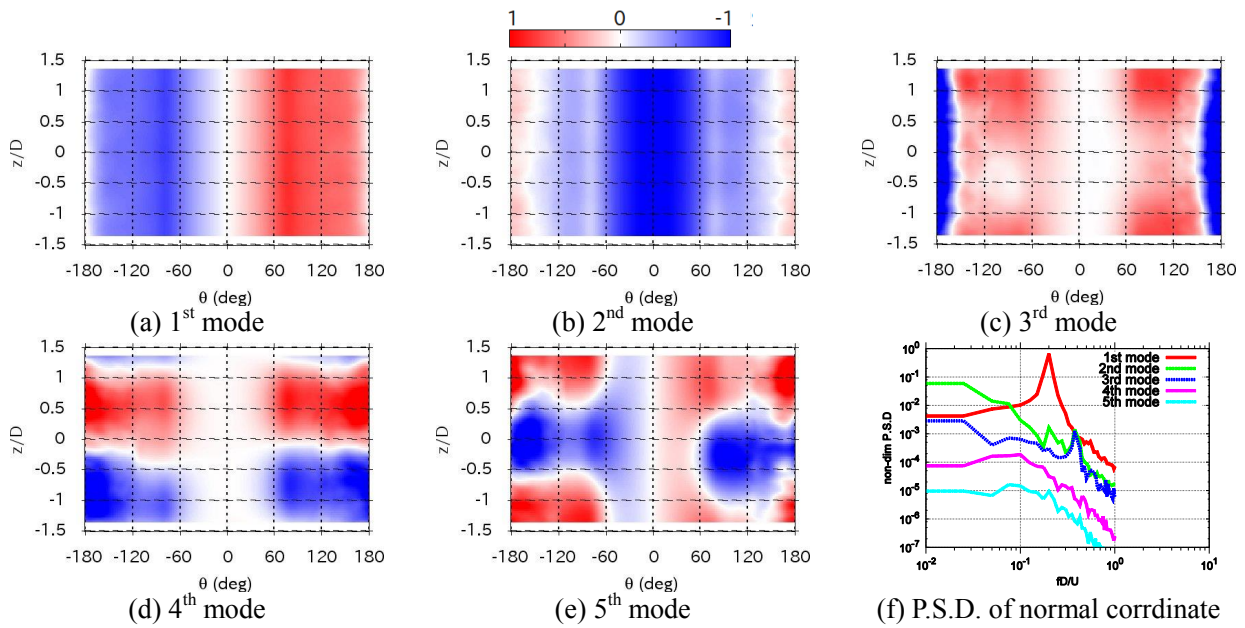


Figure 6: Result of POD analysis for CFD (2.7D-cyclic)

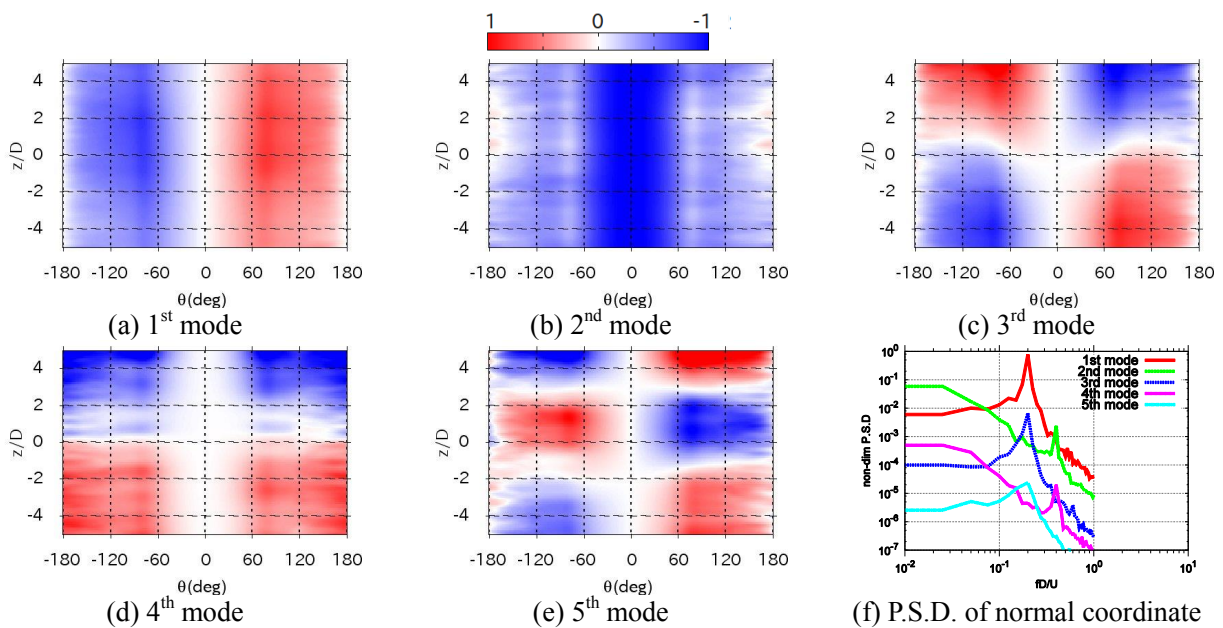


Figure 7: Result of POD analysis for CFD (10D-slip)

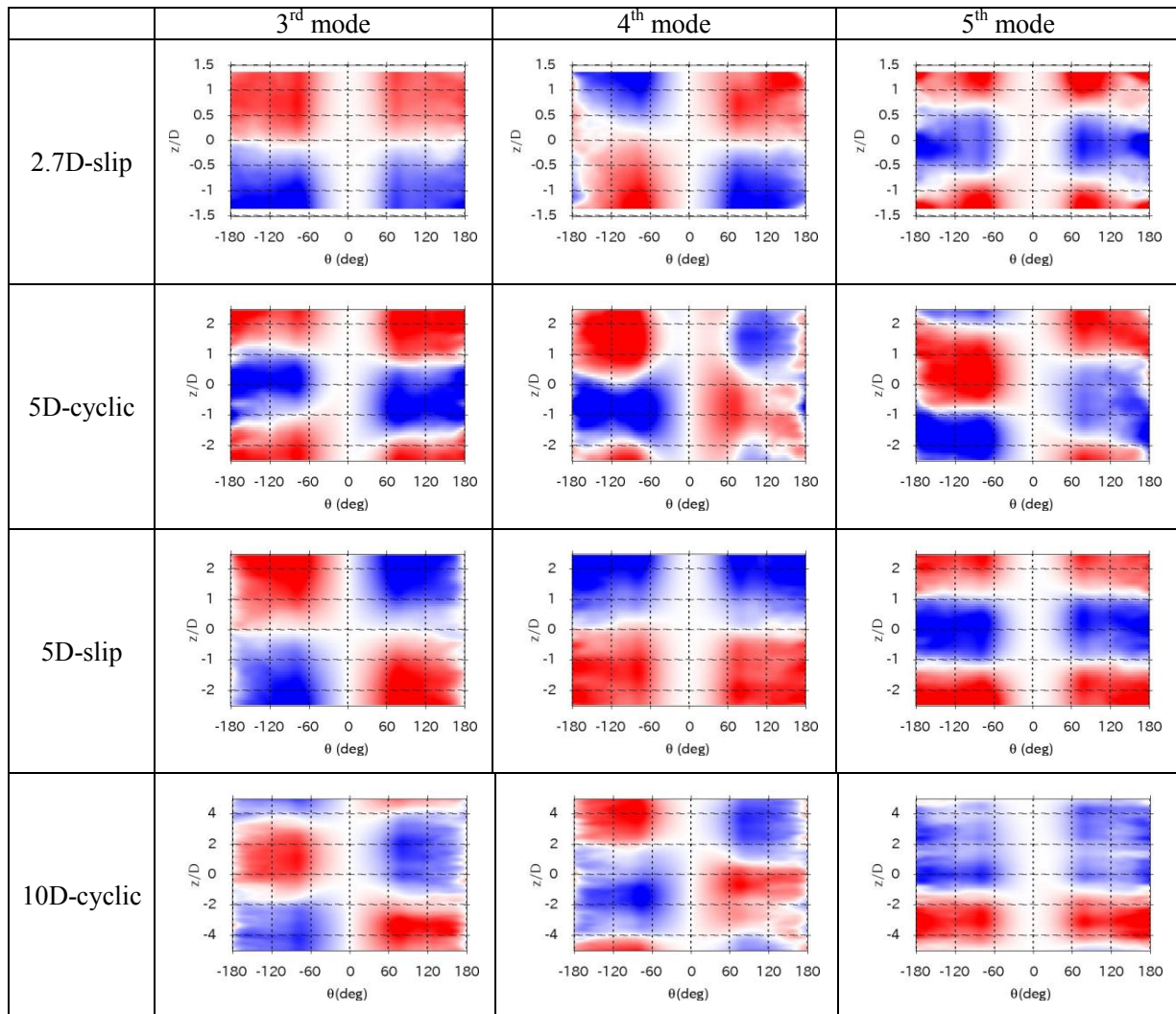


Figure 8: Results of POD analysis for each case

the cyclic condition. Therefore, the cyclic condition of sidewalls should not be used for the investigation of the correlation along the direction of the axis of the cylinder.

Fig. 10 indicates the contribution ratio for the results of the POD analyses. Fig. 10 (a) and (b) show the cumulative contribution ratio for all cases and the contribution ratio of the lift force component for the 2.7D-cyclic and experiment, respectively. Fig. 10 (a) shows that the cumulative contribution ratio up to the 2nd mode for the cyclic condition became large in comparison with the other cases. This result indicates that the 2D nature of the flow was strengthened because the cyclic condition of the 1st and 2nd modes, whose shapes were uniform along the cylinder axis, was strongly two-dimensional in nature. On the other hand, Fig. 10 (b) indicates that the fluctuating lift force depended on the 1st and 2nd mode shapes. Therefore, the spatial correlation along the axis of the cylinder is strengthened by the 1st and 2nd mode and weakened by modes larger than the 3rd degree.

5. CONCLUSION

In this study, the fluctuating forces acting on a fixed circular cylinder were investigated by conducting a POD analysis of the fluctuating surface pressure. At the same time, the effects of the boundary condition of the sidewalls for CFD and the aspect ratio on the fluctuating forces were tested. The following conclusions are based on the results of this study.

The aspect ratio and the boundary condition of sidewalls control the correlation of the fluctuating lift along the axis of the cylinder. Therefore, the cyclic condition should not be used to investigate the correlation

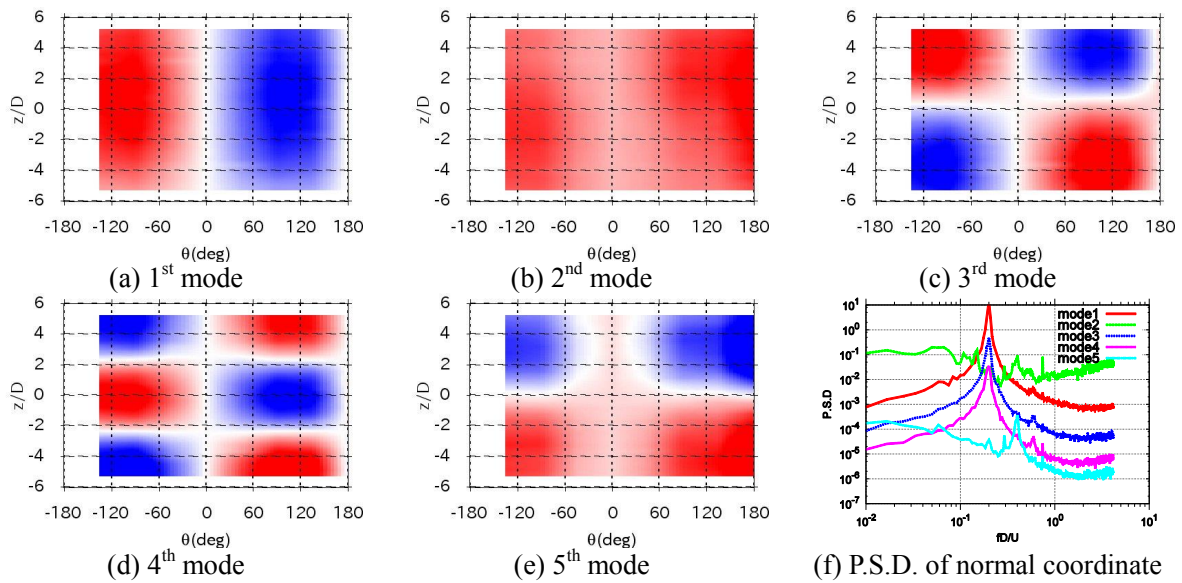


Figure 9: Result of POD analysis for experiment

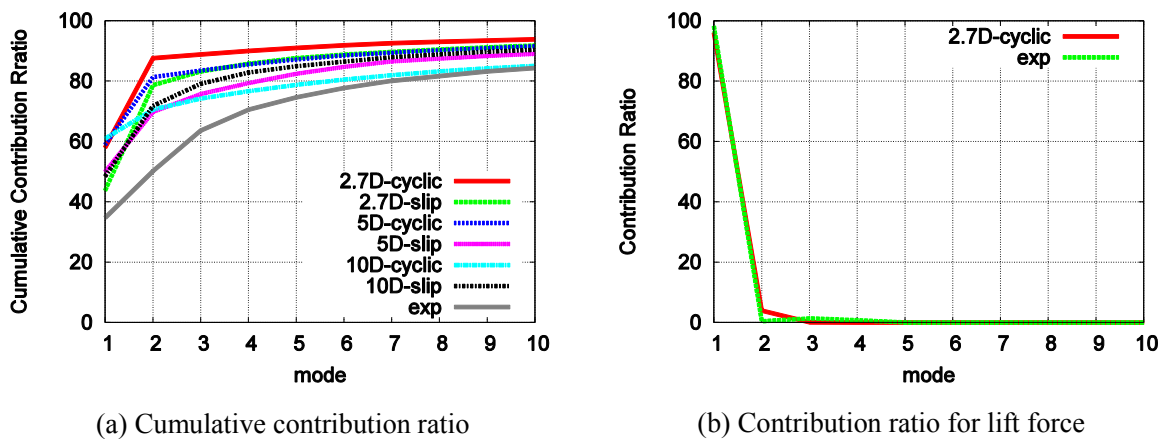


Figure 10: Contribution ratio for results of POD analysis

of the flow along this axis, and it is necessary to ensure an aspect ratio that is as large as possible on CFD in order to reproduce a result close to the natural phenomenon.

The spatial correlation along the cylinder axis of fluctuating forces acting on the cylinder is strengthened by the 1st and 2nd POD modes and weakened by POD modes higher than the 3rd. Moreover, it was found that POD modes beyond the 3rd are controlled by the boundary condition of sidewalls for CFD. Therefore, the cyclic condition should not be used in CFD to investigate the correlation characteristics along the cylinder axis of the flow.

ACKNOWLEDGMENT

This work was supported by JSPS KAKENHI, Grant Number 26420460.

REFERENCES

- 1) Vickery, B. J. : Fluctuating lift and drag on a long cylinder of square cross-section in a smooth and in a turbulent stream, *J. Fluid Mech.*, Vol. 25, Pt. 3, pp. 481-494, 1965.
- 2) El Baroudi, M. Y. : Measurement of two-point correlations of velocity near a circular cylinder shedding a Karman vortex street, UTIA Technical Note, No.31, AFOSR TN-60-835, 1960.
- 3) Keefe, R. T. : An investigation of the fluctuating forces acting on a stationary circular cylinder in a

subsonic stream, and of the associated sound field, Report No.76, Institute of Aerophysics, University of Toronto, 1961.

- 4) OpenFOAM Ltd. : OpenFOAM. <http://www.openfoam.org>, 2011.
- 5) Bienkiewicz, B., Tamura, Y., Ham, H. J., Ueda, H., Hibi, K. : Proper orthogonal decomposition and construction of multi-channel roof pressure, *J. Wind Eng. Ind. Aerodyn.*, Vol. 54-55, pp. 369-381, 1995.

AERODYNAMIC FORCES ON A SQUARE PRISM IN CONTROLLED MOTION: A PHENOMENOLOGICAL DISCUSSION

Luigi Carassale⁺¹, Lorenzo Banfi⁺², Andrea Freda⁺³

⁺¹Dept. of Civil, Chemical and Environmental Engineering, University of Genova, Italy

The generation of aerodynamic forces of oscillating bodies is the result of several physical phenomena interacting each other. The classification of Vortex-Induced Excitation (VIE) and Motion-Induced Excitation (MIE), together with their modeling, is only partially satisfactory mostly due to the mentioned interactions. In this paper, we describe the apparently simple case of a square prism oscillating within a smooth flow demonstrating the occurrence of VIE-MIE interactions and multiple lock-in conditions. The discussion is largely based on the distinction between synchronous and asynchronous force components and their separated analysis.

Keywords: Vortex Induced Excitation, Motion Induced Excitation, lock-in, Square Prism

1. INTRODUCTION

The aerodynamic forces acting on an oscillating bluff body are produced by a combination of different phenomena interacting with each other. Conventionally, it is common to distinguish between Vortex-Induced Excitation (VIE) and Motion-Induced Excitation (MIE), but this separation is largely artificial and is mostly invoked for modelling simplicity. A possible way to investigate this problem involves wind-tunnel experiments on bodies oscillating in controlled motion and the processing of the measured forces by means of deterministic or stochastic tools. Most of the contributions on this subject are related to the case of circular cylinders in water and focus on relatively low Reynolds number and high reduced frequency¹⁻³).

In this work we consider a square prism oscillating in cross-flow direction with a harmonic controlled motion. The Reynolds number is relatively high, while the RF ranges from a very-low value up to a value close to the Strouhal number. The data processing starts with a spectral analysis of the lift force used to recognize several non-standard lock-in conditions^{4, 5}). Then, the synchronous components of the lift force are estimated and represented according to a Hammerstein model⁶) and compared to the classical aeroelastic derivatives⁷) and the quasi-steady formulation⁸). Finally, we discuss, from a qualitative point of view, the spectral structure of the aerodynamic forces in different lock-in conditions, including the case of non-integer lock-in, which, to our knowledge, was never documented before.

2. EXPERIMENTAL SETUP

The experimental setup is constituted by a rigid prism with square cross section and sharp edges constrained to oscillate in cross-flow direction (vertical). The motion is harmonic with frequency and amplitude variable in a relatively large range. The forced motion is produced by a crankshaft system connected to an electric motor driven through a closed-loop controller. A heavy flywheel is used to reduce possible high-frequency fluctuations of the angular velocity. The prism is mounted on linear-motion bearings and connected to the flywheel by two long rods. The non-linearity of the crank-shaft mechanism generates a small second-order harmonics of the motion, whose amplitude is below 0.2% of the first-harmonics amplitude for the range of the parameters considered.

(1) Definitions and scaling

Let $y(t)$ be the vertical position of the prism, which can be conveniently expressed through the complex notation:

⁺¹luigi.carassale@unige.it, ⁺²lorenzo.banfi@dicca.unige.it, ⁺³andrea.freda@unige.it

$$y(t) = Y e^{i\bar{\omega}t} \quad (1)$$

where Y and $\bar{\omega}$ are, respectively, the amplitude and the rotational frequency of the imposed motion and t is the time. The lift force (per unit span length) acting on the prism is calculated from the pressure field as:

$$L(t) = \int_C n_y(s) p(s,t) ds \quad (2)$$

where $p(s,t)$ is the pressure in the point with curvilinear abscissa s of the prism cross section, considered as positive if directed outwards (suction) and n_y is the projection along the motion direction of the unit vector normal to the cross-section border. The pressure field is measured through an instrumented ring of 20 pressure taps located at the mid-span of the model and connected to a pressure scanner mounted on board. Accordingly, the integral in Eq. (2) is calculated for each time sample using the rectangle method.

The physical quantities involved in the experiment are scaled in traditional fashion, i.e.:

$$y(t) = b\tilde{y}(\tilde{t}) = b\tilde{Y} e^{i\tilde{\omega}\tilde{t}}; \quad L(t) = qb\tilde{L}(\tilde{t}) \quad (3)$$

where b is the cross-section size, \tilde{t} the non-dimensional time, \tilde{Y} the non-dimensional motion amplitude, $\tilde{\omega}$ the non-dimensional motion frequency, referred to as motion Reduced Frequency (RF), q is the kinetic pressure:

$$\tilde{t} = t \frac{U}{b}; \quad \tilde{Y} = \frac{Y}{b}; \quad \tilde{\omega} = \frac{\bar{\omega}b}{U}; \quad q = \frac{1}{2}\rho U^2 \quad (4)$$

in which U is the free-stream velocity.

(2) Experimental parameters

The experimental results that are discussed herein refers to a prism with size $b = 50$ mm and length $l = 500$ mm, oriented at the angles of incidence $\alpha = 0^\circ, 6^\circ, 9^\circ, 12^\circ$ (positive angles are nose up), oscillating with non-dimensional amplitude $\tilde{Y} = 10\%, 20\%, 30\%$. The motion frequency range in the interval $\bar{\omega}/2\pi = 1.25 \div 14.4$ Hz. The wind velocity is $U = 5.5$ m/s, corresponding to the Reynolds number $Re = 1.8 \times 10^4$; the freestream turbulence intensity is about 1%. The motion RF is in the interval $\tilde{\omega}/2\pi = 0.011 \div 0.13$, corresponding to the reduced velocity range $7.7 \div 88.6$.

The pressure signals are sampled at 500 Hz and synchronized with the instantaneous position of the prism through a tachometric signal obtained by a laser probe.

During the measurements, the motion frequency is changed according to a stepped sweep. The length of the constant-frequency steps is 30 s.

3. SPECTRAL STRUCTURE OF THE LIFT FORCE

Considering an experimental condition in which the motion frequency $\tilde{\omega}$ and amplitude \tilde{Y} are constant, the lift force may be idealized as a sum of three contributions: the static component $L^{(0)}$, the synchronous component $L^{(s)}$ and the asynchronous component $L^{(a)}$

$$L(t) = L^{(0)} + L^{(s)}(t) + L^{(a)}(t) \quad (5)$$

The synchronous component is periodic with the same period of the motion and is assumed to be deterministically related to it by a possibly non-linear transformation, while, the asynchronous component may be idealized as a zero-mean stationary or cycle-stationary random process whose characteristics are determined by the motion frequency and amplitude. From a different point of view, it can be observed that the synchronous component has a discrete spectrum comprising harmonics whose frequency is an integer multiple of the motion frequency, while, the asynchronous component usually has a continuous spectrum with the possible presence of pure tones whose frequency is not an integer multiple of the motion frequency.

This section describes, from a qualitative point of view, the spectral structure of the lift force identifying synchronous and asynchronous force components for the case of $\tilde{Y} = 30\%$ and $\alpha = 0^\circ, 6^\circ, 9^\circ, 12^\circ$. The discussion is based on the Power Spectral Density function (PSD) estimated for each value of the motion frequency $\tilde{\omega}$ and

represented as color maps in Figure 1. The frequency reported in the vertical axes is scaled in the same fashion of the motion frequency, i.e. $\kappa = \omega b/U$, while the color scale represents the logarithm of the PSD amplitude. The maps show several spectral details of the lift force that have been preliminary described in⁹⁾. In particular, the most evident features are: 1) the frequency band of the Karman Vortex Shedding (KVS), 2) the synchronous components determined by the motion frequency and its super-harmonics (straight lines directed upwards), 3) asynchronous components at the sum or difference of the KVS frequency and motion frequency.

For $\alpha = 0^\circ$, in the very low RF range, the Strouhal number St of the oscillating prism decreases from its static value St^* until $\bar{\kappa}/2\pi \approx 0.04$; then St increases progressively as $\bar{\kappa}$ increases, and its trace becomes parallel to the motion frequency before disappearing at lock-in. The trace of KVS disappears at $\bar{\kappa}/2\pi \approx 0.09$, while the 1st-order synchronous force component increases its intensity from $\bar{\kappa}/2\pi \approx 0.07$.

For $\alpha = 6^\circ$, the trace of the KVS is interrupted at $\bar{\kappa}/2\pi \approx 0.065$ and $\bar{\kappa}/2\pi \approx 0.045$ where the secondary and tertiary lock-in (i.e. synchronization of the wake with the second and third harmonics of the motion) take place. In the low RF range, before the tertiary lock-in, St increases linearly with $\bar{\kappa}$. Between the tertiary and secondary lock-in St is constant and the intensity of the VIE is lower than in the low RF range. The passage through the secondary lock-in produces a reduction of St and a further reduction of VIE intensity. Beside the trace of KVS, the line with non-dimensional frequency $St - \bar{\kappa}$ is clearly visible.

For $\alpha = 9^\circ$, most of the spectral features are common to the case $\alpha = 6^\circ$, but two relevant differences can be noted. First, KVS is present, even if weak, up to $\bar{\kappa}/2\pi \approx 0.11$ and deviates upwards just before disappearing (likewise for $\alpha = 0^\circ$). Second, it is clearly visible a lock-in phase at $\bar{\kappa}/2\pi \approx 0.09$, corresponding to $St = 1.5\bar{\kappa}$. At the same RF, it is also visible the harmonics with frequency $0.5\bar{\kappa}$. In this case, it is not possible to speak about vortex-motion synchronization, since St and $\bar{\kappa}$ are not integer multiples. We refer to this condition as non-integer lock-in.

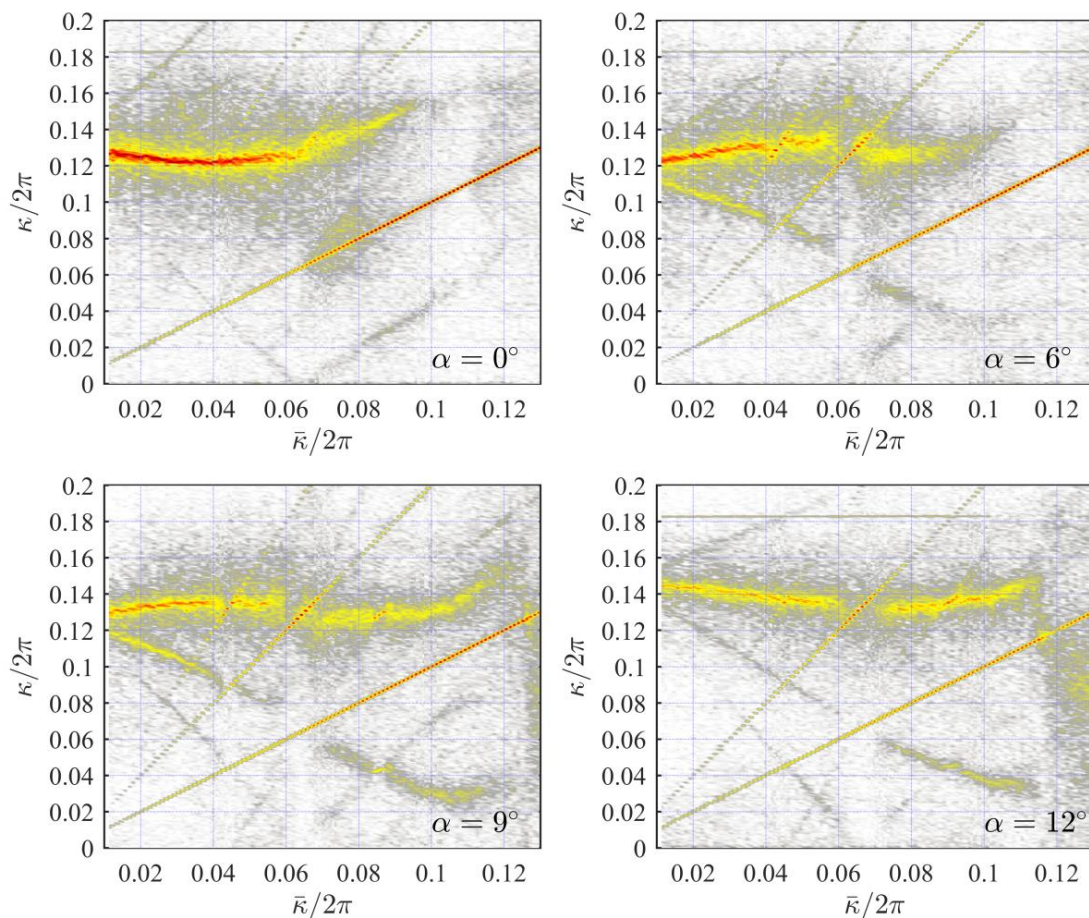


Figure 1. PSD of the lift force for $Y/b = 30\%$. Colors are in logarithmic scale.

For $\alpha = 12^\circ$, in the low RF range St decreases until the secondary lock-in, than it increases becoming roughly parallel to the motion line before disappearing at $\bar{\kappa}/2\pi \simeq 0.11$. The tertiary lock-in is very weak, while the lock-in with $1.5\bar{\kappa}$ is well visible like for $\alpha = 9^\circ$. Besides, it can be observed that just below $\bar{\kappa}/2\pi = 0.12$, i.e. where KVS disappears, the 1st-order synchronous component loses most of its intensity within a quite small RF range.

4. SYNCHRONOUS COMPONENTS OF THE LIFT FORCES

The spectral analysis of the lift force showed the simultaneous presence of both synchronous and asynchronous components. In this section we focus on the synchronous force components addressing their estimation and modeling.

(1) Estimation

The synchronous component of the lift force is periodic by definition, thus it can be expanded into the Fourier series:

$$L^{(s)}(t) = \sum_{r=1}^{\infty} L_r e^{ir\bar{\omega}t} \quad (6)$$

where L_r are the Fourier coefficients depending on the motion frequency and amplitude. In principle, the Fourier coefficients can be calculated from the time history of $L^{(s)}$ by the orthogonal projection:

$$L_r = \frac{1}{T} \int_0^T L^{(s)}(t) e^{-ir\bar{\omega}t} dt \quad (7)$$

where $T = 2\pi/\bar{\omega}$. In practice, Eq. (7) cannot be directly used for the estimation of L_r , as $L^{(s)}$ is not accessible, being additively combined with $L^{(a)}$. On the other hand, since $L^{(a)}$ is random and zero-mean, Eq. (7) can be rewritten in the form:

$$L_r = E \left[\frac{1}{T} \int_0^T L(t) e^{-ir\bar{\omega}t} dt \right] \quad (8)$$

where $E[\cdot]$ represents the expectation operator, through which $L^{(a)}$ is cancelled due to the zero-mean assumption. Practically, the expectation is estimated, invoking ergodicity, by averaging the projection of the lift force on the harmonics of the motion for all the motion periods available in the data, i.e.:

$$L_r \simeq \frac{1}{n_T T} \sum_{k=1}^{N_T} \int_{(k-1)T}^{kT} L(t) e^{-ir\bar{\omega}t} dt \quad (9)$$

where n_T is the number of complete motion periods.

(2) Modeling

The synchronous lift force is related to the body motion by a non-linear transformation depending on the motion amplitude and frequency. The dependency on the frequency, in particular, reflects the presence of memory in the transformation, which is the basic feature of unsteady forces. A relatively wide class of non-linear systems with memory can be represented by a Hammerstein model, which is the parallel combination of a set of linear systems with memory preceded by non-linear memoryless systems. Accordingly, we assume that the synchronous non-dimensional lift force $\tilde{L}^{(s)} = L^{(s)}/qb$ is related to the non-dimensional displacement \tilde{y} by the model:

$$\tilde{L}^{(s)}(t) = \sum_{r=1}^{\infty} \int_{-\infty}^{\infty} g_r(t-\tau) \tilde{y}^r(\tau) d\tau \quad (10)$$

where g_r are kernel functions to be identified. Substituting Eq. (3) into Eq. (10) yields:

$$\begin{aligned}
\tilde{L}^{(s)}(\tilde{t}) &= \sum_{r=1}^{\infty} \int_{-\infty}^{\infty} g_r(\tilde{t} - \tau) \tilde{Y}^r e^{ir\bar{\kappa}\tau} d\tau \\
&= \sum_{r=1}^{\infty} \tilde{Y}^r e^{ir\bar{\kappa}\tilde{t}} \int_{-\infty}^{\infty} g_r(\theta) e^{-ir\bar{\kappa}\theta} d\theta \\
&= \sum_{r=1}^{\infty} \tilde{Y}^r G_r(r\bar{\kappa}) e^{ir\bar{\kappa}\tilde{t}}
\end{aligned} \tag{11}$$

in which G_r are the Fourier transforms of the kernels g_r and are, therefore, the Frequency Response Functions (FRF) of the dynamical systems mapping the integer powers of the motion into the force. The comparison between the last of Eqs. (11) and Eq. (6) provides the FRFs of the Hammerstein model as:

$$G_r(r\bar{\kappa}) = \frac{1}{qb\tilde{Y}^r} L_r(\bar{\kappa}, \tilde{Y}) \tag{12}$$

in which the Fourier coefficients depend on the motion frequency and amplitude and are estimated through Eq. (9) for the range of parameters explored during the test.

(3) Identity with flutter derivative notation

In bridge aerodynamics, self-excited forces are traditionally represented through the flutter derivatives. Accordingly, for a pure-plunge motion, the lift force is given as:

$$L(t) = qb \left[\frac{H_1^*}{U^*} \dot{y} + \frac{H_4^*}{U^{*2}} \frac{y}{b} \right] \tag{13}$$

where $U^* = 1/\bar{\kappa}$ is the reduced velocity, while H_1^* and H_4^* are the flutter derivatives, which are estimated experimentally and depends on the RF $\bar{\kappa}$. Substituting Eq. (1) into Eq. (13) and taking into account the scaling (4), the lift force remains expressed as:

$$L(t) = qY\bar{\kappa}^2 [iH_1^* + H_4^*] e^{i\bar{\omega}t} \tag{14}$$

The comparison with Eqs. (6) and (12) suggests that the 1st-order ($r = 1$) Hammerstein FRF is related to the flutter derivatives H_1^* and H_4^* as:

$$G_1(\bar{\kappa}) = \bar{\kappa}^2 [iH_1^*(\bar{\kappa}) + H_4^*(\bar{\kappa})] \tag{15}$$

(4) Identity with quasi-steady modeling

When the motion frequency is very low compared to the characteristic frequency of the wake, i.e. if $\bar{\kappa} \ll St$, the motion-excited forces may be modeled invoking the quasi-steady assumption. Accordingly, the lift force is given by the expression:

$$L^{(QS)}(t) = -qb(C_D + C_L') \frac{\dot{y}}{U} \tag{16}$$

where C_D and C_L' are, respectively, the static drag coefficient and the slope of the static lift coefficient estimated for the steady angle of incidence of the body.

Besides, the effect of the added mass may be modelled as proportional to the force necessary to accelerate a volume of fluid equal to the body volume, i.e.:

$$L^{(AM)}(t) = -\rho b^2 A \ddot{y} \tag{17}$$

where A is the added-mass coefficient. Substituting Eq. (1) into Eqs. (16)-(17) and taking into account the scaling (4), the lift force becomes:

$$L(t) = qY [-i\bar{\kappa}(C_D + C_L') + 2\bar{\kappa}^2 A] e^{i\bar{\omega}t} \tag{18}$$

The comparison with Eqs. (6) and (18) suggests that, in the quasi-steady limit, the 1st-order Hammerstein FRF is related to the static aerodynamic coefficients and to the added-mass coefficient as:

$$G_1(\bar{\kappa}) = -i\bar{\kappa}(C_D + C_L') + 2\bar{\kappa}^2 A \quad (19)$$

(5) Stability analysis

The 1st-order synchronous forces have a fundamental role in stability analysis of aeroelastic systems. When the body is supported by visco-elastic devices, indeed, the imaginary part of G_1 can be interpreted as a frequency-variant aerodynamic damping, while its real part may be considered as an aerodynamic stiffness. For pure-plunge motion, the effect of the aerodynamic stiffness is usually negligible¹⁰⁾, while a negative value of the aerodynamic damping can easily lead to galloping instability. In this case, the stability analysis is carried out by studying the sign of the galloping coefficient $a_g = -(C_D + C_L')$ or of the flutter derivative H_1^* .

Figure 2 shows the imaginary and real part of the 1st-order Hammerstein FRF G_1 . As proposed by¹¹⁾ the imaginary part is divided by $\bar{\kappa}$, while the real part is divided by $\bar{\kappa}^2$, so that the former can be interpreted as a frequency-variant galloping coefficient and the latter as a frequency-variant added mass coefficient. In the plots of the imaginary part, the galloping coefficient is reported by a black dashed line.

For the case $\alpha=0^\circ$, $\text{Im}(G_1)/\bar{\kappa}$ is almost constant up to the primary lock-in with a value that is up to 70% greater (more unstable) than the quasi-steady prediction. Also $\text{Re}(G_1)/\bar{\kappa}^2$ is rather constant until the primary lock-in, with the exception of the very-low frequency range for which the estimation may be inaccurate due to the very low acceleration level.

The case $\alpha=6^\circ$ is characterized by a galloping coefficient that is very close to zero due to the equal opposite contribution of C_D and C_L' . The function $\text{Im}(G_1)/\bar{\kappa}$ attains this value for very low RF, while it becomes positive (unstable) with values similar to the case $\alpha=0^\circ$, even for relatively low RF. Crossing the secondary lock-in, $\text{Im}(G_1)/\bar{\kappa}$ has a jump downwards, becoming negative for $\tilde{Y}=30\%$. $\text{Re}(G_1)/\bar{\kappa}^2$ is similar to the case $\alpha=0^\circ$, with the exception of the low-RF range (which may be not significant), a discontinuity at the secondary lock-in and a smoother variation at the primary lock-in.

The case $\alpha=9^\circ$ is qualitatively similar to $\alpha=6^\circ$. The function $\text{Im}(G_1)/\bar{\kappa}$ seems to tend to a_g for $\bar{\kappa} \rightarrow 0$, however, the quasi-steady limit has not been reached in the investigated conditions.

The case $\alpha=12^\circ$ is very close to the critical angle of incidence for which the flow reattaches on the lateral face exposed to the flow¹²⁾. The flow reattachment produces the change of sign of C_L' , making the galloping coefficient to pass from positive (unstable) to negative (stable). In the figure, both the values of a_g estimated before and after the critical angle of incidence are reported. The function $\text{Im}(G_1)/\bar{\kappa}$ tends to the post-critical quasi-steady limit for $\bar{\kappa} \rightarrow 0$, even if for the steady prism at $\alpha=12^\circ$ the flow is still fully separated. Besides, it remains negative up to the primary lock-in. The added mass coefficient is smaller than for the other angles considered.

5. AERODYNAMIC FORCES AT LOCK-IN

In this section we describe the aerodynamic behavior of the prism at lock-in. The discussion is based on the time histories of the forces acting on the lateral faces defined as:

$$F_t(t) = \frac{1}{qb} \int_{\text{top face}} p(s,t) ds; \quad F_b(t) = -\frac{1}{qb} \int_{\text{bottom face}} p(s,t) ds \quad (20)$$

F_t and F_b being, respectively, the forces per unit span acting on the top and bottom faces of the prism. For $\alpha=0^\circ$, the sum of F_t and F_b provides the (non-dimensional) lift force; for the other considered angles of incidence it is not rigorously true, but for small α the contribution of the windward and leeward faces is negligible. The advantage of considering the two lateral faces separately is twofold. First, for $\alpha=0^\circ$, this gives the chance to see the effects of harmonic components that in the lift force are cancelled due to symmetry. Second, at incidence, the pressure field acting on the two lateral faces has different characteristics that should be investigated separately.

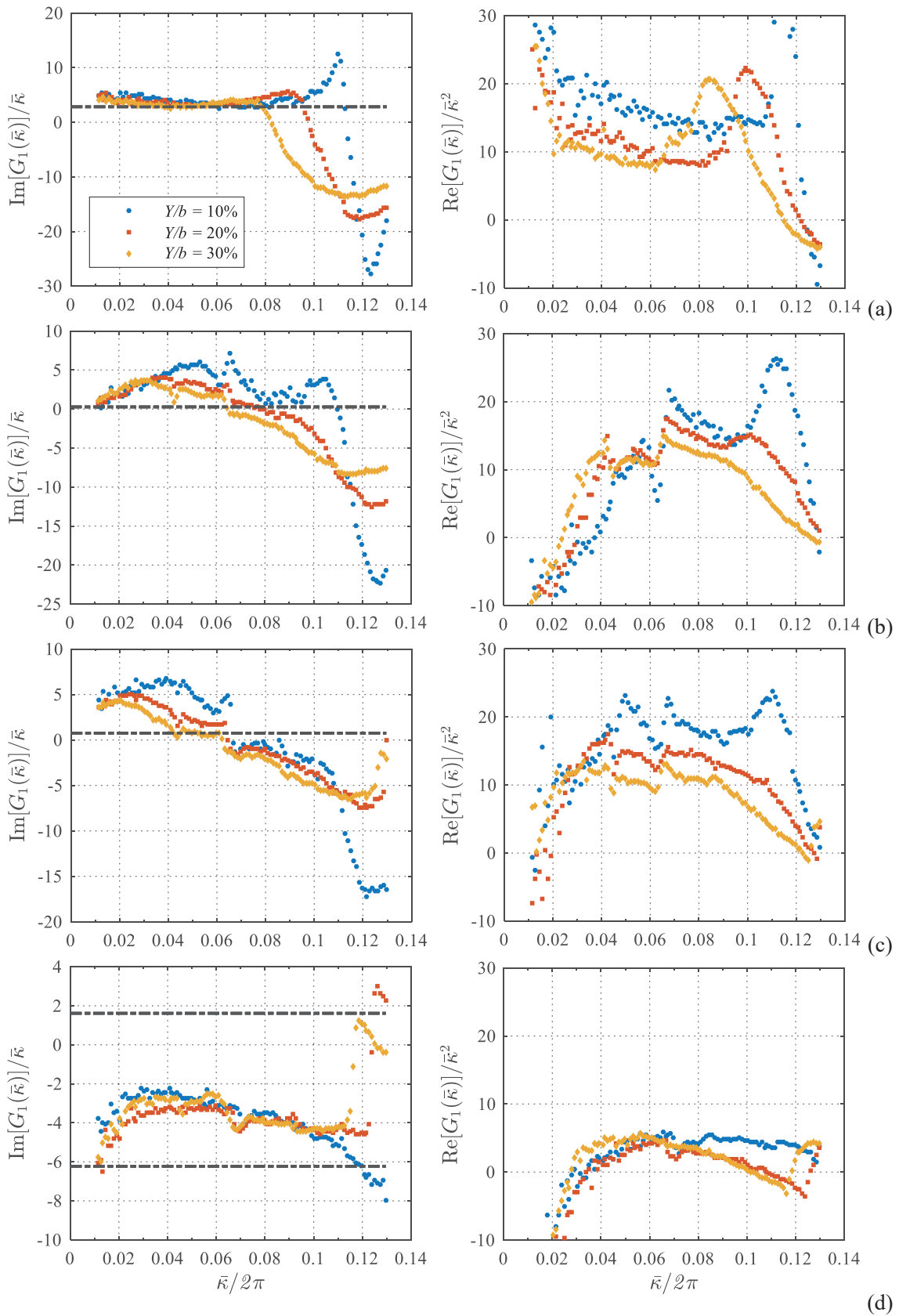


Figure 2. Imaginary and real part of the 1st-order Hammerstein FRF for $\alpha = 0^\circ$ (a), 6° (b), 9° (c), 12° (d). The black lines represent the galloping coefficient $a_g = -(C_D + C_L')$

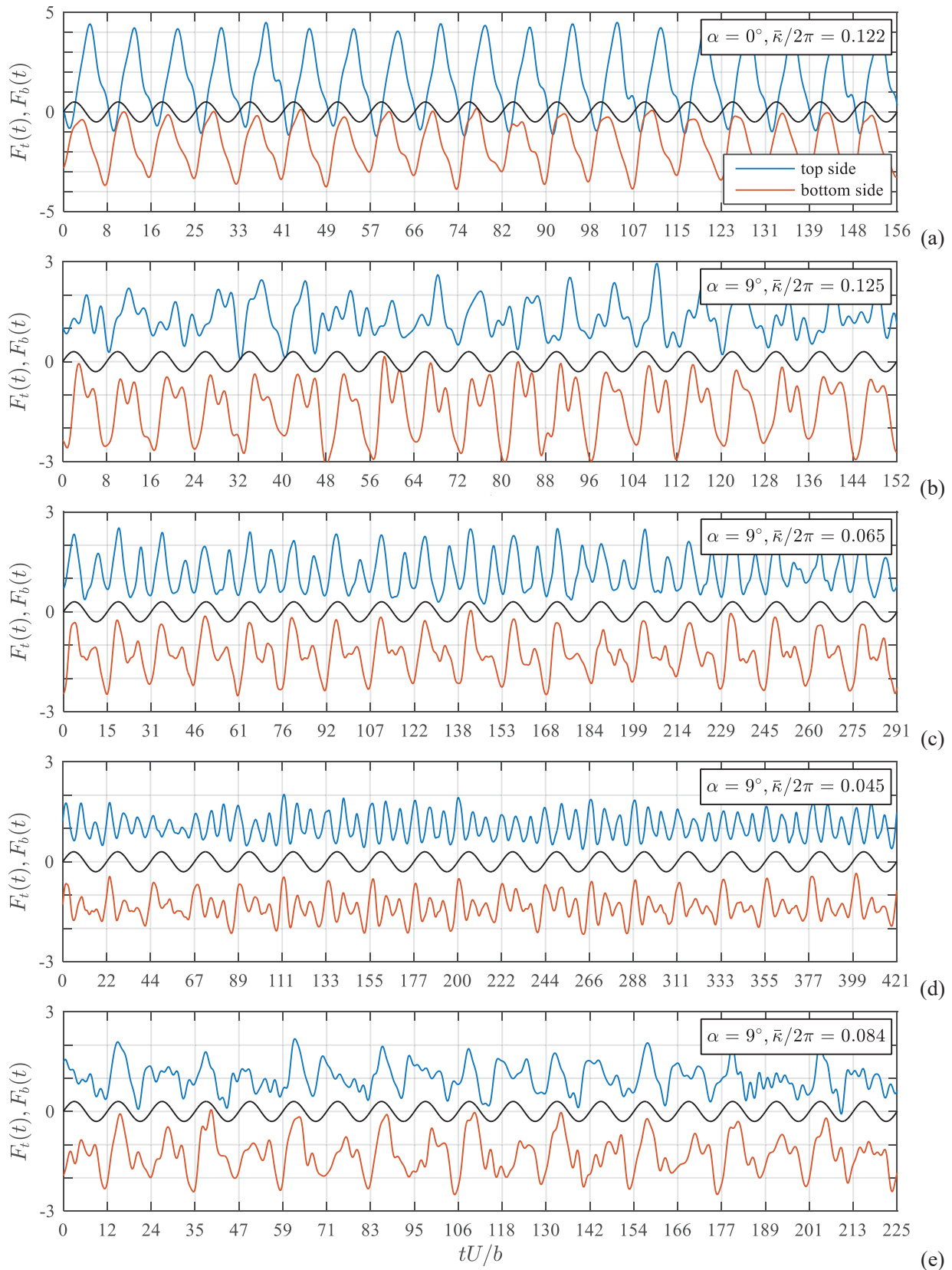


Figure 3. Time histories of the forces on the side faces of the prism at lock-in: $\alpha = 0^\circ$, primary lock-in (a); $\alpha = 9^\circ$, primary (b), secondary (c) and tertiary (d) lock-in; $\alpha = 9^\circ$, lock-in at $2\pi St\bar{k} = 1.5$ (e).

Figure 3 shows the time histories of F_t and F_b along with the trajectory of the motion $y(t)$. The vertical lines of the grid represent the time instants corresponding to the zero-level up-crossing of the displacement. To simplify the interpretation, the time histories of the forces are low-pass filtered at the RF $\kappa/2\pi = 0.5$. All the plots refers to the motion amplitude $\tilde{Y} = 30\%$.

The primary lock-in for $\alpha=0^\circ$ (Fig. 3a) is reported mostly as a reference case. The forces on the lateral faces are almost harmonic with a phase delay about $\pi/2$ with respect to the motion. Beside these expected characteristics, a number of relevant features can be observed. First, the forces acting on the top and bottom side of the prism are rather different in terms of amplitude of fluctuation, while are practically equal as far as their mean value is concerned. It should be emphasized that the experimental setup is nominally symmetric and that the static lift coefficient is practically zero. Second, the fluctuation of F_b is not symmetric, having the suction peaks (downwards) generally sharper than the overpressure peaks. This behavior is mostly determined by the second harmonics of the motion. On the other hand, the fluctuation of F_t is symmetric, but with peaks that are sharper than for a harmonic wave. This feature is mostly related to the presence of the 3rd harmonics of the motion.

In the case $\alpha=9^\circ$ at primary lock-in (Fig. 3b) the forces F_t and F_b are significantly different both in terms of amplitude and waveform. On the bottom face, which is the one exposed to the wind, a series of intense suction peaks appear at the motion frequency with a phase delay about $\pi/2$ (like for $\alpha = 0^\circ$). These peaks are followed by shorter peaks appearing during the downward motion of the prism (when for $\alpha = 0^\circ$ we see the overpressure peak). These secondary peaks are probably produced by the interference between the separated shear layers and the lateral face of the prism. From a spectral point of view, they reflects the presence of an intense 2nd-harmonics of the motion. On the top side, the force is quite irregular. The main suction peaks generally appear with the same timing as for $\alpha=0^\circ$, but the 3rd harmonics of the motion is very evident and often is dominant.

For $\alpha = 9^\circ$ at the secondary lock-in (Fig. 3c), both the forces F_t and F_b have two suction peaks per motion period suggesting the shedding of vortexes at the frequency $St = 2\pi S_t = 2\bar{\kappa}$. Those vortexes come in pairs so that two strong vortexes appearing about phase zero are followed by two weaker vortexes delayed about half of the motion period. The different amplitude of those pairs of vortexes is due to an additive harmonic component at the motion frequency. This is quite evident on the bottom face where the separated shear layers stay closer to the body and, therefore, are more influenced by the body motion.

For $\alpha = 9^\circ$ at the tertiary lock-in (Fig. 3d), the behavior is similar to the secondary lock-in, with the obvious difference that the forces are dominated by the harmonics at the frequency $2\pi S_t = 3\bar{\kappa}$. A pair of intense vortexes are shed near phase zero, then two pairs of weaker vortexes follow. In addition, the variation of the peak amplitude is more evident on the bottom face where the separated shear layers are more influenced by the motion.

Figure 3e shows the non-integer lock-in observed for $2\pi S_t = 1.5\bar{\kappa}$. The forces are quite irregular, however it can be noted that the main suction peaks on the bottom face appear once per motion cycle. On the top face the peaks appear more erratically, however it happens relatively often that three suction peaks occur evenly distributed along two consecutive motion cycles (e.g. between the non-dimensional times 106 and 130 or between 154 and 177).

6. CLOSING REMARKS

The discussion of the experimental results concerning a square prism in controlled motion suggests some observations whose relevance goes beyond the treated case study.

The distinction between synchronous and asynchronous forces seems to be more rational than the traditional classification of vortex-induced and motion-induced actions, as it includes force components generated by the non-linear interaction between VIE and MIE.

Synchronous forces can be represented by a Hammerstein model, which, at the first order, reproduces the classical concept of flutter derivative and can be interpreted, in the limit for $\bar{\kappa} \rightarrow 0$, consistently with the quasi-steady formulation. The interpretation of higher-order Hammerstein FRFs, which have not been reports

herein due to space limitations, is still to be investigated, and may be related to higher-order terms of the quasi-steady expansion or to other weakly non-linear models for the motion-excited forces¹³⁻¹⁵).

The study of the synchronous forces revealed the existence of numerous lock-in regions. Beside the well-known primary lock-in (for $2\pi S_t = \bar{\kappa}$), a secondary and tertiary lock-in conditions are documented for the prism with incidence. In these conditions, the forces acting on the lateral faces of the prism are weaker than at the primary lock-in (30 to 50% less), but may be relevant in practical applications.

It has been discovered a non-integer lock-in condition related to the intermittent occurrence of three vortices in two consecutive motion cycles. This phenomenon may be regarded as a quantization effect produced by the motion on the vortex shedding. Accordingly, the number of vortices that are released during an integer number (typically one) of consecutive motion cycles must be an integer.

The analysis of the symmetric configuration ($\alpha=0^\circ$) showed the existence of some RF ranges in which the unavoidable lack of symmetry of the experimental setup produces a substantial asymmetric pressure field. The reason of this behavior is not clear yet and should be carefully investigated.

REFERENCES

- 1) Gopalkrishnan, R.: Vortex-induced forces on oscillating bluff cylinders, Sc.D. thesis, Massachusetts Institute of Technology, 1993
- 2) Krishnamoorthy, S., Price, S. and Païdoussis, M.: Cross-flow past an oscillating circular cylinder: synchronization phenomena in the near wake, *Journal of Fluids and Structures*, Vol. 15, pp. 955-980, 2001
- 3) Carberry, J., Sheridan, J. and Rockwell, D.: Controlled oscillations of a cylinder: forces and wake modes, *Journal of Fluid Mechanics*, Vol. 538, pp. 31-69, 2005
- 4) Ongoren, A. and Rockwell, D.: Flow structure from an oscillating cylinder. Part 1: Mechanisms of phase shift and recovery in the near wake, *Journal of Fluid Mechanics*, Vol. 191, pp. 197-223, 1988
- 5) Yi, D. and Okajima, A.: Aerodynamic forces acting on an oscillating rectangular cylinder and the aeroelastic instabilities at moderate Reynolds numbers. Experiments, *JSME International Journal Series B*, Vol. 39, pp. 343-353, 1996
- 6) Bai, E.-W.: Frequency domain identification of Hammerstein models, *IEEE Transactions on Automatic Control*, Vol. 48, pp. 530-542, 2003
- 7) Scanlan, R. H. and Tomko, J.: Airfoil and bridge deck flutter derivatives, *Journal of Engineering Mechanics Division, ASCE*, Vol. 97, pp. 1717-1737, 1971
- 8) Païdoussis, M. P., Price, S. J. and De Langre, E.: Fluid-structure interactions: cross-flow-induced instabilities, Cambridge University Press, 2010
- 9) Carassale, L., Freda, A. and Banfi, L.: Motion-excited forces acting on a square prism: a qualitative analysis, Proceedings of 14th International Conference on Wind Engineering, Porto Alegre, Brazil, 2015
- 10) Banfi, L. and Carassale, L.: Uncertainty in the motion-excited forces on a square prism and probabilistic assessment of galloping instability, Proceedings of 1st International Conference on Uncertainty Quantification in Computational Sciences and Engineering, Crete, Greece, 2015
- 11) Zasso, A.: Flutter derivatives: advantages of a new representation convention, *Journal of wind engineering and industrial aerodynamics*, Vol. 60, pp. 35-47, 1996
- 12) Carassale, L., Freda, A. and Marrè-Brunenghi, M.: Experimental investigation on the aerodynamic behavior of square cylinders with rounded corners, *Journal of Fluids and Structures*, Vol. 44, pp. 195-204, 2014
- 13) Diana, G., Falco, M., Bruni, S., Cigada, A., Larose, G. L., Damsgaard, A. and Collina, A.: Comparisons between wind tunnel tests on a full aeroelastic model of the proposed bridge over Stretto di Messina and numerical results, *Journal of Wind Engineering and Industrial Aerodynamics*, Vol. 54-55, pp. 101-113, 1995
- 14) Chen, X. and Kareem, A.: Aeroelastic analysis of bridges: Effects of turbulence and aerodynamic nonlinearities, *Journal of Engineering Mechanics, ASCE*, Vol. 129, pp. 233-264, 2003
- 15) Carassale, L., Wu, T. and Kareem, A.: Nonlinear aerodynamic and aeroelastic analysis of bridges: a frequency domain approach, *Journal of Engineering Mechanics, ASCE*, Vol. 140(8), 04014051, 2014

VIBRATION OF MULTIPLE CIRCULAR CYLINDERS IN TANDEM ALIGNMENT

Takashi Nomura⁺¹, Nariaki Saegusa⁺² and Hiroshi Hasebe⁺³

⁺¹ Nihon University, Tokyo, Japan

⁺² Ohmoto Gumi, Co. Ltd., Okayama, Japan

⁺³ Nihon University, Tokyo, Japan

There have been various attempts and investigations to capture wind energy through wind-induced vibration of some kind of structural elements. The wake galloping is one of the candidates due to its divergent nature, and the wake galloping of a single circular cylinder has been investigated in a couple of studies. However, if multiple cylinders can vibrate simultaneously, it would be favorable to capture more wind energy through the vibration. Based on this idea, a basic wind tunnel experiment has been conducted in the present study. In the present experiment, in the wake of a fixed circular cylinder, multiple circular cylinders of the same diameter as the fixed one are supported by coil springs and deployed in tandem alignment. The numbers of spring-supported cylinders are changed from 1 to 3, and the distance between their centers is another experimental parameter. As the results, two cylinders or even three cylinders vibrate together. It is worth to note that, in case that the distance between their centers is double of the cylinder diameter, the two or three cylinders vibrate in bigger amplitude than other wider distance cases though the single cylinder does not reveal wake galloping in such narrow spacing.

Keyword: Wake galloping, Multiple circular cylinders, Wind energy

1. INTRODUCTION

Machine devices to capture energy from wind mostly consist of a rotor with some number of blades. Large wind turbines usually have three blades to the horizontal axis rotor. Some small or middle size wind turbines have vertical axis rotor. As well known, wind turbines of these types can lead to quite rapid rotational motion if their cutout mechanism does not work. This is due to the self-excited process in which lift force to the blades accelerate the blade rotation.

As ordinary wind turbines utilize vigorous wind-induced motion, other types of devices which are equipped with some sort of self-excited wind-induced motion can capture wind energy. Various attempts have been made to develop new devices base on the knowledge of wind engineering. Matsumoto, et al. investigated the devices utilizing flutter of plate¹⁾. Pimentel, et al.²⁾ reported a device in which flutter of textile belts generates electricity. Meanwhile, Hiejima, et al.³⁾ is working on wake galloping of a circular cylinder. They investigate a method to magnify the cylinder amplitude by oscillating the upstream cylinder. Jung, et al.⁴⁾ also conducted a series of experiment to generate electricity from wake galloping of circular cylinder.

In the preceding works to utilize wake galloping^{5,6)}, the number of vibrating cylinder is one. If we can increase the number of vibrating cylinder, we may capture more wind energy. Based on this idea, we place multiple spring-supported circular cylinders in the wake of a fixed cylinder. The numbers of vibrating cylinder in the present study are one, two and three.

Wake galloping of circular cylindrical object is observed in transmission lines or stay cables of cable-stayed bridges. This phenomenon has been investigated in wind engineering, but in most cases number of circular cylinders are two and only one of the two vibrates. Although Nagao, et al.⁷⁾ or Kubo, et al.⁸⁾ investigated three parallel cables of cable stayed bridge, only one of the three cables is allowed to vibrate in either study.

⁺¹nomura@civil.cst.nihon-u.ac.jp, ⁺³hasebe@civil.cst.nihon-u.ac.jp

2. WIND TUNNEL EXPERIMENT

(1) The experimental setup

Fig. 1 shows the schematic view of the experiment conducted in the present study. A circular cylinder of diameter d is fixed at the blowing outlet of the wind tunnel. In the wake of the fixed circular cylinder, circular cylinders of the same diameter d are suspended by coil springs. These circular cylinder are straightly aligned in the direction of the wind flow with an identical distance nd between the centers of cylinder, where n is an integer. Fig. 2(a) and 2(b) are the photographs of the present experiment. The wind tunnel of Fig. 2(a) has a square section of 22.5 cm by 22.5 cm. The fixed circular cylinder is made of wood and its diameter d is 2cm. The spring-supported circular cylinders are made of acrylic, of which length is 30 cm and mass is 113 g. As shown in Fig. 2(b), four coil springs are used to suspend each acrylic cylinder. These springs are outside of the air stream. No end plates are used.

The cylinder-spring system has two modes of vertical vibration as shown in Fig. 3(a) and 3(b), that is, the translational mode of Fig. 3(a) and the rotational mode of Fig. 3(b) both in the vertical plane perpendicular to the air stream. In addition, since there is no restriction against the horizontal motions of the cylinder, the horizontal translational motion and the horizontal rotational motion are possible. Table 1 summarizes the natural frequencies of these four modes. The damping coefficients of the two cases shown in Fig.3 are: 0.3% for the vertical translational mode of Fig. 3(a), and 0.4% for the vertical rotational mode of Fig. 3(b), respectively.

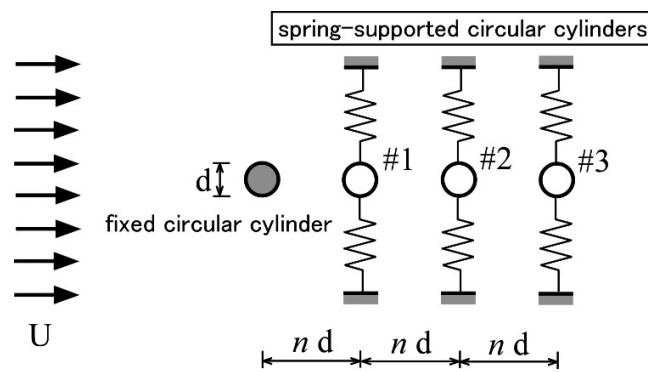


Figure 1: Schematic view of the experimental setup.



Figure 2: (a) Overall view of the present experiment; (b) the cylinders.

(2) The experimental conditions and procedures

As summarized in Table 2, number of the vibrating circular cylinders and the spacing between the cylinders are changed. Consequently, the combination of these two parameters results in 9 cases. For each case, the wind speed U is increased from 1 m/s to 13 m/s by the increment 1 m/s. At each wind speed, the vibration amplitude and the frequency are measured from the video images. The referential wind speeds are measured by removing all cylinders including the fixed one. The location of the measurement is that the fixed cylinder will be located.

Table 1: Captions should be centered above tables.

Vibration modes	Natural frequency (Hz)
Vertical translation	$f_{VT} = 2.3$
Vertical rotation	$f_{VR} = 3.3$
Horizontal translation	$f_{HT} = 2.0$
Horizontal rotation	$f_{HR} = 3.0$

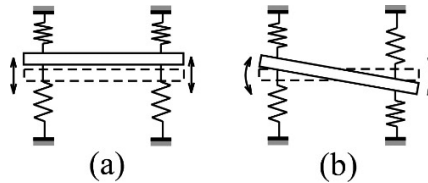


Figure 3: Vibration modes of the spring-cylinder system: (a) the vertical translational mode; (b) the vertical rotational mode.

Table 2: Experimental cases.

Number of spring-supported cylinders	1, 2, 3
Distance between the center of the circular cylinders	2d, 3d, 4d

As noted above, horizontal motions of the cylinders are allowed in the present experiment. Therefore, horizontal motion like swaying occurs in some experimental cases, in some experimental cases. In such cases, in order to restrict cylinder vibration to vertical ones, those cylinders are displaced vertically by human hands and then released to let them vibrate vertically.

3. EXPERIMENTAL RESULTS

(1) Preliminary remarks

Figures 4, 6 and 8 below show the experimental results of cylinder vibration and frequency against wind speed for different numbers of vibrating cylinders.

- [1] In case of vertical rotational vibration, the amount of the amplitudes plotted by a symbol mark is the amplitude of the end of the cylinder. Based on a rough and simple calculation, the kinematic energy of the rotational motion is about 80% of that of the translational motion if the end displacements of both modes are same.
- [2] The amplitude of the vertical translational vibration is plotted by black solid marks while the amplitude of the vertical rotational vibration is plotted by white marks.
- [3] In these figures of amplitude, if the cylinder motion is small and ambiguous or not clear, no symbol mark is plotted.
- [4] Static horizontal displacement occurs to each circular cylinder. The amounts are about $d/5$ at wind speed 7 m/s, $d/4$ at 9 m/s and $d/3 \sim d/2$ at 11 m/s.
- [5] When the cylinder vibrates vertically at considerably large amplitude, horizontal vibration is quite small.
- [6] At wind speed 12 m/s or 13 m/s, it occurs large motion which is a combination of vertical vibration and horizontal one. In such cases a symbol \times is plotted in the amplitude figures.

(2) The cases of single vibrating circular cylinder

Fig. 4 shows the amplitude and the frequency against the wind speed in the cases of single

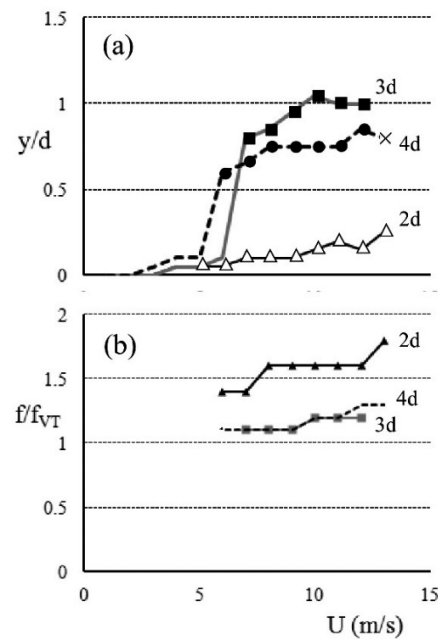


Fig. 4 Experimental results of single vibration circular cylinder in the wake of the fixed cylinder (2d, 3d and 4d denote the center distance between cylinders): (a) non-dimensional amplitude (white symbols are vertical rotational vibration, black symbols are vertical translational vibration, \times indicates combination of vertical and horizontal motion) ; (b) non-dimensional frequency (the ratio to the natural frequency of the vertical translational vibration mode f_{VT})

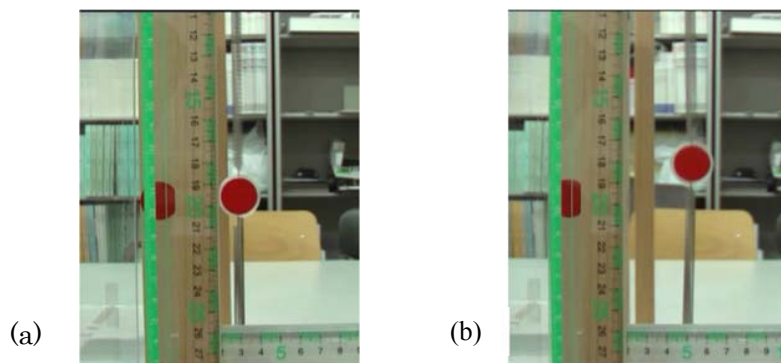


Fig. 5 Snapshots of the cylinder vibration of the cases of single spring-supported cylinder: (a) the center distance 2d at wind speed 8 m/s; (b) the center distance 3d at wind speed 8 m/s.

spring-supported circular cylinder for three cases of the cylinder distance from the fixed cylinder. As shown in Fig. 4(a), at the distance 2d, the cylinder vibrates rotationally but the amplitude is small. See also the snapshot of experiment Fig. 5(a). On the contrary, at the distance 3d and 4d, the amplitude of vertical translational vibration increases at wind speed 5 m/s. The case of the distance 3d reached the largest amplitude. See also the snapshot of Fig. 5(b). Shiraishi, et al.⁶⁾ indicated that the wake galloping of circular cylinder occurs when the distance is 3d. Jung, et al.⁴⁾ showed in their experiments that wake galloping occurs from 3d to 6d though they did not conduct the case of 2d. Our results shown in Fig. 4 consist with these observations.

As noted above, the vibration at the distance 2d is vertical rotational vibration. As shown in Fig. 4(b),

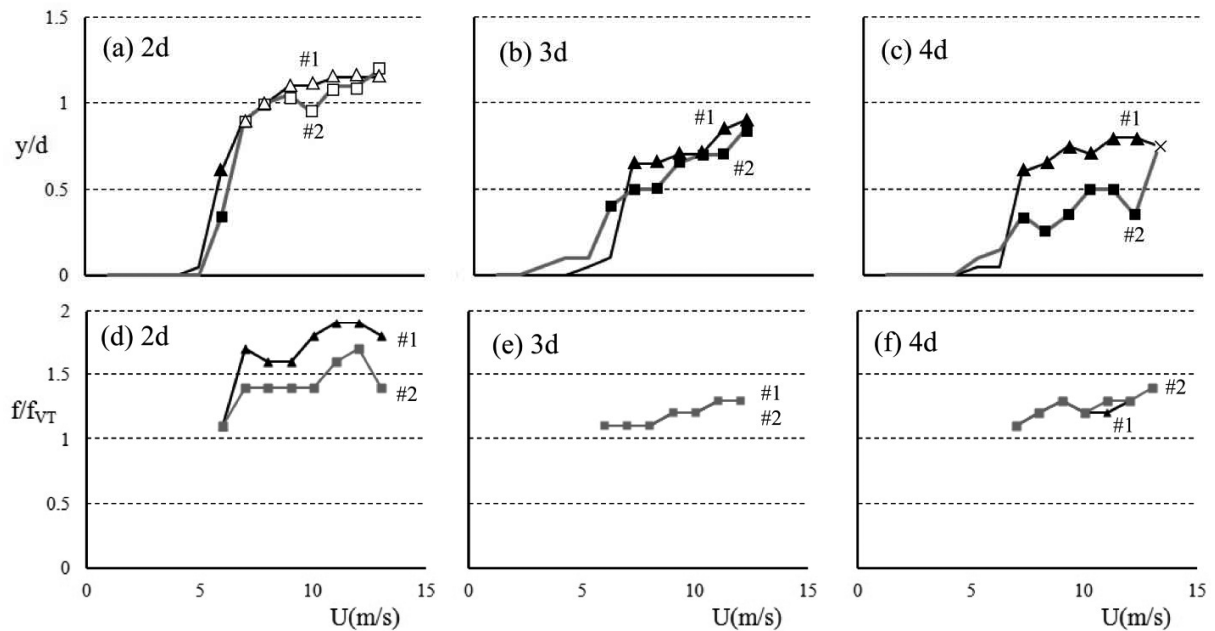


Fig. 6 Experimental results of two vibration circular cylinders in the wake of the fixed cylinder (#1 and #2 are the cylinder number from counted from the fixed cylinder) : (a) non-dimensional amplitude of the cylinder distance $2d$; (b) non-dimensional amplitude of the cylinder distance $3d$; (c) non-dimensional amplitude of the cylinder distance $3d$; (d) non-dimensional frequency of the cylinder distance $2d$; (e) non-dimensional frequency of the cylinder distance $3d$; (f) non-dimensional frequency of the cylinder distance $4d$ (colors of the symbols in Fig. 6(a)~(c) have the same meaning as in Fig. 4).

the observed frequencies of $2d$ are larger than those of $3d$ and $4d$ and the ratio to the natural frequency of vertical translational vibration f_{VT} is 1.5 to 1.6. This is corresponding to the natural frequency of vertical rotational vibration f_{VR} .

(3) The cases of two vibrating circular cylinders

Fig. 6 shows the amplitude and the frequency against the wind speed in the cases of two spring-supported circular cylinders for three cases of the cylinder distances. As shown in Fig. 6(a), at the distance $2d$, both of the cylinders vibrate at fairly large amplitude of vertical rotational vibration after vertical translational vibration at first. These two cylinders rotate at almost opposite phases as shown in a snapshot of Fig. 7(a). Since the second cylinder (the downward cylinder) revealed an intermittent fluctuation, the vibration frequencies of these two cylinders are a little different.

The cylinders at the distances $3d$ and $4d$ revealed vertical translational vibration as shown in a snapshot of Fig. 7(b). The case of $4d$, the amplitude of the second cylinder is relatively small. Consequently, in the cases of the distance $2d$, the largest amplitudes are observed. Although the vibration mode of $2d$ is different from $3d$ or $4d$, the kinematic energy of the vibration of $2d$ is the largest based on the energy evaluation described in the item [1] of 3.1(1).

It may be curious that the vibration is more excited in the case of $2d$ than the cases of $3d$ or $4d$ because this is different from the case of single vibrating cylinder of Fig. 4. It can be said that the vibration of the downward cylinder may affects the vibration of the upward cylinder in some way and these two cylinders synchronize to each other together with surrounding air stream. This should be clarified by flow visualization or simulation in future.

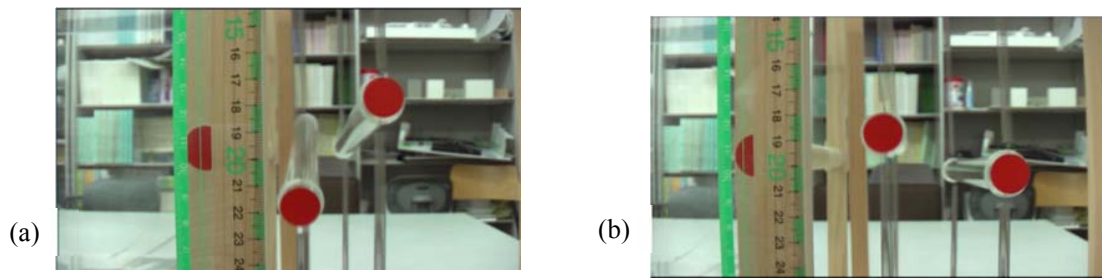


Fig. 7 Snapshots of the cylinder vibration of the cases of two spring-supported cylinders: (a) the center distance $2d$ at wind speed 9 m/s (vertical rotational vibration); (b) the center distance $3d$ at wind speed 9 m/s (vertical translational vibration).

(4) The cases of three vibrating circular cylinders

Fig. 8 shows the amplitude and the frequency against the wind speed in the cases of three spring-supported circular cylinders for three cases of the cylinder distances. As shown in Fig. 8, the vibration amplitude of the case of distance $2d$ is larger than the cases of $3d$ or $4d$. The vibration mode up to 10 m/s is generally vertical translational vibration and the phase of cylinders are opposite for each pair of succeeding two cylinders as shown in the snapshots of Fig. 9(a) and 9(b). At higher wind speeds, the cylinder motions are complicated with intermittent motion or horizontal motion.

By comparing Fig. 8(b) and Fig. 8(b), in the case of distance $4d$, the vibration initiates at higher wind speed and the amplitudes are smaller than the case of $3d$. Even in case of two vibration cylinders, as shown in

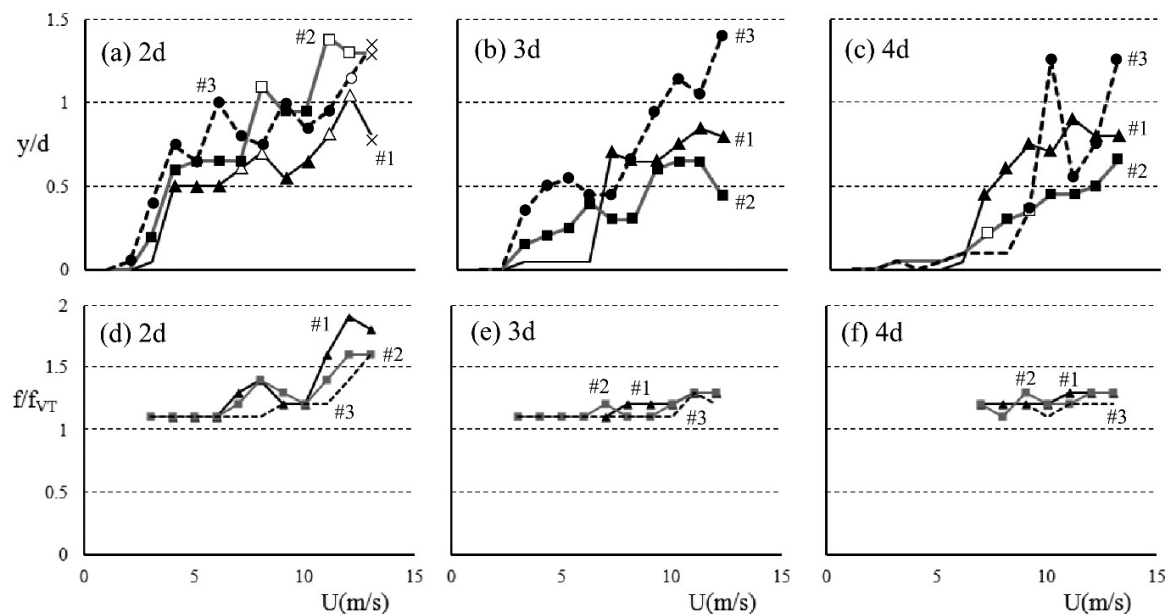


Fig. 8 Experimental results of three vibration circular cylinders in the wake of the fixed cylinder (#1, #2 and #3 are the cylinder number from counted from the fixed cylinder) : (a) non-dimensional amplitude of the cylinder distance $2d$; (b) non-dimensional amplitude of the cylinder distance $3d$; (c) non-dimensional amplitude of the cylinder distance $3d$; (d) non-dimensional frequency of the cylinder distance $2d$; (e) non-dimensional frequency of the cylinder distance $3d$; (f) non-dimensional frequency of the cylinder distance $4d$ (colors of the symbols in Fig. 8(a)~(c) have the same meaning as in Fig. 4).

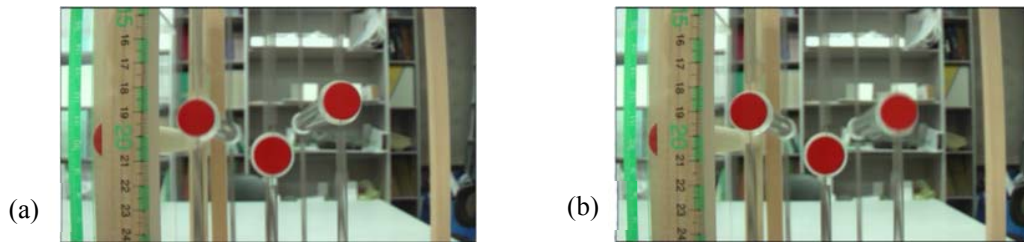


Fig. 9 Snapshots of the cylinder vibration of the cases of three spring-supported cylinders: (a) the center distance $2d$ at wind speed 4 m/s (vertical translational vibration); (b) the center distance $3d$ at wind speed 4 m/s (vertical translational vibration).

Fig. 6(c), at the distance $4d$ the vibration amplitude of the second cylinder is relatively small. Based on these results, we may lead to an understanding that, at longer distance between cylinders, the fluctuating streams from the fixed cylinder lost their energy by shaking the upstream cylinders. However, as shown in Fig. 8(c), the third cylinder vibrates at larger amplitude than the other two at wind speed 10 m/s . We should make further effort to investigate the mechanism of these phenomena.

As shown in Fig. 8(a), at the distance $2d$, the vertical translational vibration occurs over the wind range of wind speed, and at fairly high wind speed the vertical rotational vibration begins to occur. This is different from the case of two cylinders at distance $2d$ of Fig. 6(a) where the vertical rotational vibration dominates for most of wind speeds. In addition, the wind speed to initiate vibration is smaller for the distance $3d$ than $2d$. These differences between the different number of vibrating cylinder are uncertain. In the present study, both translational and rotational vibrations are allowed. We should conduct further experiment by restricting vibration mode.

4. CONCLUDING REMARKS

In this study, a series of wind tunnel experiments are conducted in which one or more spring-supported circular cylinders are aligned straightly in the wake of a fixed circular cylinder of the same diameter. The purpose of the present experiments is to acquire fundamental idea that in what situation these cylinders vibrate and how they vibrate. The number of the vibrating cylinders in the present experiment is one, two and three. The following results are obtained.

- [1] In case of the single vibrating cylinder, the wake galloping occurred in the cases that the distance between the center of the fixed cylinder and the vibrating cylinder is $3d$ or $4d$. In the case that the center distance is $2d$, the vibration amplitude is relatively small. These results of wake galloping are consistent with the observation in literature.
- [2] In the cases of two or three vibrating cylinders, all the spring-supported cylinders vibrate. Basically, they vibrate in the vertical translational mode at the phase opposite to the next cylinder.
- [3] In the cases of two or three vibrating cylinders, on the contrary to the case of single vibrating cylinder, vibration occurred even at the center distance $2d$ as well as the amplitude are larger than the distance $3d$ and $4d$. It should be future work to clarify the mechanism of these phenomena, but it may be inferred that the closer the vibrating cylinders the more intensified the interaction between the cylinder motion and the surrounding streams.

Further investigation should be conducted on the cases that more numbers of vibrating cylinders or other cylinder distances. Especially, the vibration mode should be restricted. In addition, investigation from the view point of fluid-structure interaction mechanism is essentially important.

REFERENCES

- 1) Matsumoto, M., Mizuno, K. Okubo, K. and Itoh, Y.: Fundamental study on the efficiency of power generation system by use of the flutter instability, Proc. of ASME 2006 Pressure Vessels and Piping/ICPV-11 Conference, pp.277-286, 2006
- 2) Pimentel, D, Musilek, P. , Knight, A. and Heckenbergerova, J.: Characterization of a wind flutter generator, 9th International Conference on Environment and Electrical Engineering, pp.81-84, 2010
- 3) Hiejima, S. and Hiyoshi, Y. : Vibrational amplification technique for power generation using wind-induced vibration, Wind Energy, vol.34, No.4, pp.135-141, 2010 (in Japanese)
- 4) Jung, H.-J. and Lee, S.-W.: The experimental validation of a new energy harvesting system based on the wake galloping phenomenon, Smart Materials and Structures, vol.20, pp.1-10, 2011
- 5) Utsunomiya, H. and Kamakura, Y.: The aerodynamic behavior of tandem-type circular cylinders, J. of JSCE, No.336, pp.1-8, 1983
- 6) Shiraishi, N., Matsumoto, M. and Shirato, H.: On aerodynamic instabilities of tandem structures, Journal of Wind Engineering and Industrial Aerodynamics, Vol. 23, pp.437-447, 1986.
- 7) Nagao, F., Utsunomiya, H., Noda, M., Imoto, M. and Sato, R.: Aerodynamic properties of closely space triple circular cylinders, J. Wind Eng. Ind. Aerodyn., vol.91, pp.75-82, 2003
- 8) Kubo, Y., Yuki, Y. Ishii, H., Hatanaka, S. and Kawai, C.: A feature of wake galloping of a bridge in full sized parallel cable model, J. of Structural Engineering, vol.58A, pp.518-527, 2012 (in Japanese)

TOIPCS ON VARIATIONAL PRINCIPLES IN ENGINEERING

Jiro Nakamichi^{†1}

Japan Aerospace Exploration Agency, Tokyo, Japan

More or less, the objectives of the engineering are to find optimal solution for the design of the products. Classically the variational methods have been used to find the optimal design in the engineering fields. So many numerical solutions are based upon the variational methods or its similar approaches even if the variational principle does not exist. Variational principles in the fluid dynamics has not been established yet, while those in elasticity and plasticity and optimal control theory have been highly confirmed and applied to actual problems.

In this presentation, the methods of calculus variations are reviewed in the fields of structure and elasticity, optimal control theory and fluid dynamics. Firstly the fields of elasticity and optimal control theory are briefly reviewed. The details of them are not discussed here. Focusing on the fluid dynamics, a process of deriving the Hamilton's principle is shown toward the applications for fluid-structure interaction problems like flutter or other interdisciplinary problems in engineering. The principle of virtual work is applied to the governing equations with boundary conditions. The conservation laws of mass and energy as well as the geometrical boundary conditions are treated as subsidiary conditions. In the present approach, a new concept of substantial variations of the state variables is introduced in order to describe the transportation terms and subsidiary conditions in a simple manner.

It is a classical approach but might be useful for the development of computer aided design tools for aeroelasticity system and its optimal design.

Keyword: fluid dynamics, variational principle, fluid- structure interactions

1. INTRODUCTION^{1,2,3,5,8,9)}

Calculus of variations takes an important roles in a variety of engineering fields. This is due to the fact that a physical system often behaves in a manner such that some functional (function of functions) depending on its behavior assumes a stationary value. It is actually employed to find the optimal solutions of dynamic problems as well as static ones, and mechanical systems or physical phenomena, through the procedure of making properly defined functional stationary by calculus of variations.

The variational formulation has advantages; i) it is helpful in carrying out a common mathematical procedure. ii) it provides transformation of a given problem into an equivalent one that can be solved more easily than original, and iii) when a problem can not be solved exactly, it often provides an approximate formulation for the problem which yields a solution compatible with assumed degree of approximation. If it is applied a discretized model or a distributed parametered system, the problems are reduced finally to solve a set of algebraic equations which are directly obtained by making the discretized functional minimum or maximum, instead of solving a set of differential or integral equations with the boundary or initial conditions analytically. Moreover, in many cases, the functional consists of quantities which have definite physical meanings such as kinetic energy, potential energy and so on. This fact helps us to observe the physical phenomena from the viewpoint of the basic physical principles.

The variational principles for elasticity are highly and phylogenically ordered as a system in which several variational principles are clearly derived based upon the principle of virtual work and they can be mutually converted from one to another through systematic procedures. The reduced principles are applied to analyses of beams, plates, membranes and their combined structures. The Rayleigh-Ritz Method

^{†1}nakamichi.jiro@jaxa.jp

and the Finite Element Method (FEM) are the typical examples of its applications.

In the optimal control theory, calculus of variations is inevitable to obtain the governing equations and boundary conditions for the solutions of minimum/maximum problems. In the optimization problem, whichever it is a static or a dynamical problem, an artificial functional is defined depending on the purpose of the analyses, which is so called objective function or performance index. If the functional is accompanied by constraints, it will be augmented by introducing those constraints with the Lagrange multipliers. A set of necessary equations including a part of boundary conditions (or initial and terminal conditions) can be obtained by making the objective function or performance index stationary. It should be noted that there is a big difference between the variational principles in the theory of elasticity and those in the optimal control theory because those in elasticity are conservative while not in the optimal control theory. The Lagrange multipliers will take important roles to easily manipulate the imposed constraints in the non-conservative system as is found later.

As long as the author knows, the calculus of variations was initially applied to fluid dynamics by D'Alembert (1717~83). A contribution of Clebsch in 1800's should be noted, but in 1900's a remarkable progress was made by Hargreaves, Herivel and Lin. Hargreaves suggested that in the inviscid and irrotational fluid dynamics, the governing equations would be obtained as stationary conditions of a functional which is defined by an integral of static pressure in the whole flow field. After the Hargreaves achievements, Bateman also insisted that the functional is written by use of velocity potential if the flow is inviscid and irrotational. Bateman's principle is used frequently for the solution of potential flow even today. Herivel and Lin showed that the Hamilton's principle in kinetics is valid for inviscid and compressible flow and that the stationary conditions of a functional expressed by kinetic energy minus internal energy are equivalent to the governing equations and the boundary conditions of the flow fields.

It is reasonably considered that there are no differences between elasticity and fluid dynamics from the view point that both are continuums. However, a small particle in elasticity is assumed to be steady while in fluid dynamics a particle is moving even if the phenomena is steady. Therefore, we encounter difficulties in deriving the variational principles for the fluid dynamics. In order to avoid this difficulties, it is valid to adopt a procedure similar to that used in the kinetics for the fluid dynamics as well. In the present studies, we use the Lagrangian description of the fluid flow. We will apply the principle of virtual work to the equations of motion of the fluid, with the conservation laws of mass and energy as subsidiary conditions. Finally, we will reach a functional of which stationary conditions are identical to the governing equations and the boundary conditions for the flow field.

The considerations is limited within the inviscid and irrotational flows throughout present paper.

2.CALCULUS OF VARIATIONS IN IN ELASTICITY ¹⁾

There are numerous texts and literatures on the Calculus of variations in elasticity and plasticity. The principle of virtual work, the principle of minimum potential energy, the principle of complementary energy and their mutual theoretical relations are detailed, for example, in Ref.[1]. Those variational principles can be converted from one to another (Fig.1) by rigorous manipulations with the help of Lagrange multipliers.

It is well known that the associate theories are actually applied to the formulation for Finite Element Method (FEM), a computer software such as NASTRAN. The FEM was originally invented in the middle of 1950's in the fields of aeronautics for the structural analyses of a swept-back wing which could not be done by beam theory. However, in a short time, it became to be widely utilized not only for the aircraft structural analyses but also for the structural analyses in various engineering fields. In Fig.1, the inter-relationships among various variational principles in elasticity and plasticity are shown. When we must consider the problems with subsidiary conditions, the functional is augmented by introducing those subsidiary conditions with Lagrange multipliers. The augmented functional will take a very important roles in converting a variational principle to another in a common mathematical procedure. The details of their relationships are so beautifully and clearly summarized in Ref.[1]. We are not going further into the details here.

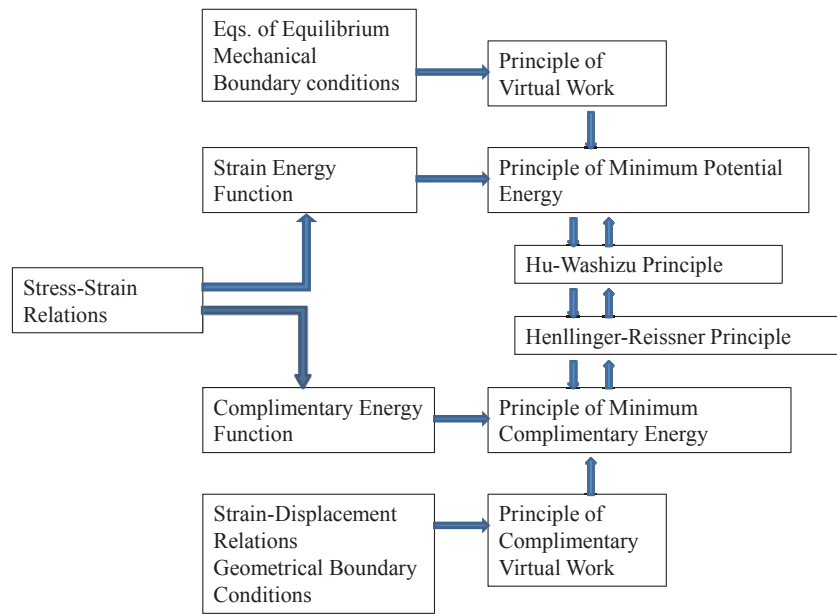


Figure 1: Relationships among variational principles in elasticity and plasticity

from one to another (Fig.1) by rigorous manipulations with the help of Lagrange multipliers.

It is well known that the associate theories are actually applied to the formulation for Finite Element Method (FEM) , a computer software such as NASTRAN.

The FEM was originally invented in the middle of 1950’s in the fields of aeronautics for the structural analyses of a swept-back wing which could not be done by beam theory. However, in a short time, it became to be widely utilized not only for the aircraft structural analyses but also for the structural analyses in various engineering fields. In Fig.1, the inter-relationships among various variational principles in elasticity and plasticity are shown. When we must consider the problems with subsidiary conditions, the functional is augmented by introducing those subsidiary conditions with Lagrange multipliers. The augmented functional will take a very important roles in converting a variational principle to another in a common mathematical procedure. The details of their relationships are so beautifully and clearly summarized in Ref.[1]. We are not going further into the details here.

3.CALCULUS OF VARIATIONS IN OPTIMAL CONTROL THEORY ^{2,5)}

The Euler equations in the optimal control theory are briefed bellow. As an example to show the outline of the optimal control theory, a problem with the terminal time t_f relaxed is considered. The necessary conditions to obtain the optimal solution are generally derived as follows.

The equations of motion and the initial condition can be expressed as

$$\dot{\mathbf{x}} = \mathbf{f}(\mathbf{x}, \mathbf{u}, t) \quad , \quad (3.1)$$

$$\mathbf{x}(t_0) = \mathbf{x}_0 \quad . \quad (3.2)$$

Where \mathbf{x} is the state variable vector; \mathbf{u} is the control variable vector. The terminal condition may be imposed by functions of state variables at $t = t_f$ as

$$\boldsymbol{\psi}[\mathbf{x}(t_f), t_f] = 0 \quad . \quad (3.3)$$

If the objective function which should be minimized (or maximizes) is defined by

$$J = \phi[\mathbf{x}(t_f)] + \int_{t_0}^{t_f} L[\mathbf{x}, \mathbf{u}, t]dt \quad , \quad (3.4)$$

the problem is to obtain the optimal control \mathbf{u} which minimizes(or maximizes) the quantity defined by Eq.3.4 under the subsidiary conditions Eqs.3.1~3.3.

By use of calculus of variations, the necessary conditions for J to be stationary are obtained by making the following augmented functional stationary.

$$J = [\phi + \mathbf{v}\psi]_{t=t_f} + \int_{t_0}^{t_f} \{L[\mathbf{x}, \mathbf{u}, t] + \boldsymbol{\lambda}[f(\mathbf{x}, \mathbf{u}, t) - \dot{\mathbf{x}}]\} dt \quad (3.5)$$

where, $\boldsymbol{\lambda}$, \mathbf{v} are the Lagrange multipliers to introduce the Eq.3.1 and 3.3 .

and where the independent variables subject to variation in Eq. 3.5 are \mathbf{x} , \mathbf{u} , t_f and Lagrange multipliers $\boldsymbol{\lambda}$ and \mathbf{v} . The initial conditions Eq.3.2 still remains as subsidiary conditions.

By taking the first variation and setting it to be zero,

$$\delta J = 0 \quad (3.6)$$

the adjoint system and its initial and terminal conditions are obtained as

$$\delta \mathbf{x}: \quad \dot{\boldsymbol{\lambda}} = -\frac{\partial L}{\partial \mathbf{x}} - \boldsymbol{\lambda} \frac{\partial f}{\partial \mathbf{x}} \quad \text{or} \quad \dot{\boldsymbol{\lambda}} = -\frac{\partial H}{\partial \mathbf{x}} \quad , \quad (3.7)$$

$$\delta^* \mathbf{x}_f: \quad \boldsymbol{\lambda}(t_f) = \left(\frac{\partial \phi}{\partial \mathbf{x}} + \mathbf{v} \frac{\partial \psi}{\partial \mathbf{x}} \right)_{t_f} \quad , \quad (3.8)$$

$$\delta \mathbf{x}_0 = 0: \quad \boldsymbol{\lambda}(t_0) = \text{free} \quad (3.9)$$

And the optimality condition is led as

$$\delta \mathbf{u}: \quad \frac{\partial H}{\partial \mathbf{u}} = \frac{\partial L}{\partial \mathbf{u}} + \boldsymbol{\lambda} \frac{\partial f}{\partial \mathbf{u}} = 0 \quad . \quad (3.10)$$

$$\delta t_f: \quad \left(\frac{d\phi}{dt} + L + \boldsymbol{\lambda} \dot{\mathbf{x}} \right)_{t_f} = 0 \quad . \quad (3.11)$$

Where H is called Hamiltonian in the optimal control theory and defined by

$$H = L[\mathbf{x}, \mathbf{u}, t] + \boldsymbol{\lambda} f(\mathbf{x}, \mathbf{u}, t) \quad (3.12)$$

If the terminal time t_f is free (not specified priori), then the Eq.3.11 is led with the help of transversality condition with respect to terminal time t_f , which is very important necessary condition to solve such problems that the boundaries are not priori specified.

Among the admissible trajectories, the exact solution makes the function J stationary. Then we find that the original problem is reduced to the one to solve the set of differential equations defined Eq.3.1 and Eqs.3.7 with the initial conditions and the terminal conditions defined by Eqs.3.2~3.3, Eq.3.8~3.9 and Eq.3.11 . The optimal control law, that is , the control variable \mathbf{u} is obtained as a solution from Eq.3.10. It is of interest that the optimal solution will keep the Hamiltonian H constant on the optimal trajectory. Actually the fact is derived from the stationary conditions Eqs.3.7 and Eq.3.10.

Usually the equations of motion and the adjoint equations are iteratively integrated by use of the Runge-Kutta algorithm and a shooting method so that the initial and terminal conditions are satisfied. For another choice, direct solution method based upon the variational technique can be found in Ref.[2,3].

4. CALCULUS OF VARIATIONS IN FLUID DYNAMICS ^{5~9)}

(1)Governing equations for inviscid and irrotational fluid dynamics

We consider a fluid particle moving with the flow. Supposing that a particle which is initially at $\mathbf{X} = (X_1, X_2, X_3)$ moves to $\mathbf{x} = (x_1, x_2, x_3)$ at $t=t$ (Fig.2), then the vector \mathbf{x} is defined as a function of the initial location coordinates vector \mathbf{X} and time t as,

$$\mathbf{x} = \boldsymbol{\theta}(\mathbf{X}, t) \quad . \quad (4.1)$$

We postulate a cluster which consists of given fluid particles at $t=0$ will be still together with each other at $t=t$ even if its shape, volume and location are changed. Then the inversion relation of Eq.4.1 can be hold in a form as

$$\mathbf{X} = \boldsymbol{\Theta}(\mathbf{x}, t) \quad . \quad (4.2)$$

Then an arbitrary state variable is expressed by

$$F = F(\mathbf{x}, t) \tag{4.3}$$

or by use of Eq.4.1,

$$\begin{aligned} F &= F[\boldsymbol{\theta}(\mathbf{x}, t), t] \\ &= F(\mathbf{X}, t) \end{aligned} \tag{4.4}$$

The state variables expressed by Eq.4.3 and 4.4 are called space state variable and material state variable, respectively. It is well known that if we describe the fluid motion by use of \mathbf{x} and t , it is called Eulerian description of fluid motion. Otherwise Lagrangian description by use of vector \mathbf{X} and t .

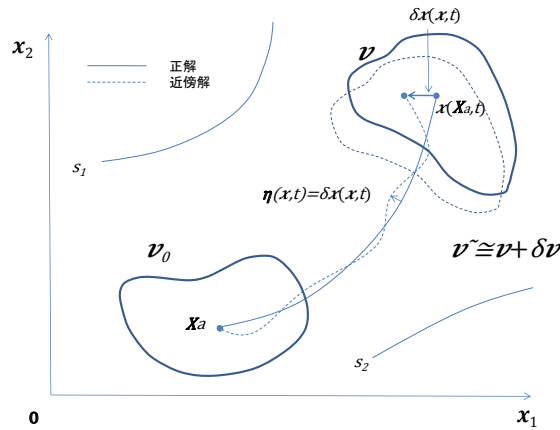


Figure 2: Lagrangian expression of fluid motion

The conservation law of mass is written as

$$\int_v \rho d v = \text{const.} \tag{4.5}$$

where v is a given volume occupied by the same particles moving with the flow, ρ is the density of fluid.

If the flow is assumed to be isentropic, the conservation law of energy is expressed by entropy per unit volume S as

$$S = \text{const.} \quad \text{along streamline} \tag{4.6}$$

The equation of motion becomes

$$\rho \mathbf{a} = \rho \bar{\mathbf{f}} - \text{grad } p \tag{4.7}$$

Here the vector \mathbf{a} is acceleration and defined with the velocity vector \mathbf{q}

$$\mathbf{a} = \frac{d\mathbf{q}}{dt} = \frac{\partial \mathbf{q}}{\partial t} + \mathbf{q} \text{grad} \mathbf{q} \tag{4.8}$$

and where p is pressure, $\bar{\mathbf{f}}$, a body force vector per unit mass, respectively.

The boundary conditions are treated in the same manner to the case of elasticity theory,

$$\mathbf{t} = \bar{\mathbf{t}} \quad \text{on } s_1 \tag{4.9}$$

$$\mathbf{x} = \bar{\mathbf{x}} \quad \text{on } s_2 \tag{4.10}$$

Where, the vector \mathbf{t} is a kind of stress vector defined by $\mathbf{t} = -p\mathbf{n}$ on the boundary s_1 . $\bar{(\)}$ denotes that the value of the state variable parenthesized is specified.

Eq.4.9 is mechanical boundary condition which means the stress on the surface s_1 is specified and Eq.4.10 is geometrical boundary condition which denotes that the motion of the fluid is geometrically constrained on the boundary s_2 .

(2) Principle of virtual work in Lagrangian descriptions

The principle of the virtual work is applied to the equations of motion Eqs.4.7 and the boundary conditions 4.9. In the Lagrangian description, a flow particle identified by the initial condition \mathbf{X} , is moving on a track expressed by $\mathbf{x} = \boldsymbol{\theta}(\mathbf{X}, t)$. If the state variables, $p(\mathbf{x}, t)$, $\mathbf{q}(\mathbf{x}, t)$ and $S(\mathbf{x}, t)$ satisfy all

governing equations and boundary conditions, the corresponding \mathbf{x} are obviously the solutions of the problem which is defined in the previous section.

Now, we give a set of arbitrary infinitesimal virtual displacements $\boldsymbol{\eta}(\mathbf{x}, t) = \delta\mathbf{x}$ to the nominal solution \mathbf{x} . Then,

$$-\int_v(\rho\bar{\mathbf{f}} - \text{grad } p - \rho\mathbf{a})\delta\mathbf{x}dv + \int_{s_1}(\mathbf{t} - \bar{\mathbf{t}})\delta\mathbf{x}ds = 0 \quad , \quad (4.11)$$

is obtained. The subsidiary conditions are the geometric boundary conditions,

$$\mathbf{n}\delta\mathbf{x} = 0 \quad \text{on } s_2 \quad (4.12)$$

and the conservation laws of mass, 4.5 and energy, 4.6.

Eq.4.11 can be easily rewritten with the help of Gaussian integral theorem as

$$\int_v\rho\mathbf{a}\delta\mathbf{x}dv - \int_v p\text{div}(\delta\mathbf{x})dv - \int_v\rho\bar{\mathbf{f}}\delta\mathbf{x}dv - \int_{s_1}(\mathbf{t} - \bar{\mathbf{t}})\delta\mathbf{x}ds = 0 \quad (4.13)$$

As Eq.4.11 or Eq.4.13 is definitely held to be zero at $t = t$, the following equation which is integrated Eq.4.13 with respect to time in the interval of $t_1 \leq t \leq t_2$,

$$\iint_{t_1}^{t_2} \int_v\rho\mathbf{a}\delta\mathbf{x}dvdt - \iint_{t_1}^{t_2} \int_v p\text{div}(\delta\mathbf{x})dvdt - \iint_{t_1}^{t_2} \int_v\rho\bar{\mathbf{f}}\delta\mathbf{x}dvdt - \iint_{t_1}^{t_2} \int_{s_1}\bar{\mathbf{t}}\delta\mathbf{x}dsdt = 0 \quad . \quad (4.14)$$

is confirmed.

The expression of 4.13 is so called the Principle of Virtual Work, which is similar to that in the fields of elasticity or mechanical dynamics.

Except for simple case like steady incompressible flow, it is extremely difficult to argue the variational principles and to explore the physical meaning, as long as we use Eulerian descriptions of the fluid.

On the other hand, by use of Lagrangian description, the functional to be stationary can be easily led with proper subsidiary conditions, in a similar manner in elasticity and dynamical problems. The procedures will be shown in the following sections.

(3)Introduction of substantial variation

In calculus of variations in elasticity and plasticity, the independent variables subject to variation are defined as functions of space coordinates which are not subject to variation. In the present formulation, however, all of the state variables are the functions expressed by use of the coordinates of fluid particles, \mathbf{x} . When we consider the variation of a given state variable $F(\mathbf{x}, t)$, attention should be paid to the variation of $F(\mathbf{x}, t)$.

In Fig.3, it is shown that if variations, $\delta\mathbf{x}$ are given to \mathbf{x} . $F(\mathbf{x}, t)$ will change from nominal solution $F(\mathbf{x}, t)$ to neighboring solution $\tilde{F}(\mathbf{x}, t)$, then the substantial variation of F , becomes,

$$\begin{aligned} \delta^*F(\mathbf{x}, t) &= \tilde{F}(\mathbf{x} + \delta\mathbf{x}, t) - F(\mathbf{x}, t) \\ &\cong \tilde{F}(\mathbf{x}, t) - F(\mathbf{x}, t) + \delta\mathbf{x} \text{ grad}F \\ &= \delta F(\mathbf{x}, t) + \delta\mathbf{x} \text{ grad}F \end{aligned} \quad (4.15)$$

Where,

$$\delta F(\mathbf{x}, t) = \tilde{F}(\mathbf{x} + \delta\mathbf{x}, t) - F(\mathbf{x}, t). \quad (4.16)$$

and δF is the variation of F at $\mathbf{x} = \mathbf{x}$.

The similar concept configured by Eq.(4.15) is frequently encountered in the cases, for example, minimum time optimization problem, fluid dynamics with free surfaces and so on, where the boundaries are not defined priori the problem is solved.

As far as the present case concerns, the definition 4.15 well corresponds to the substantial derivative which is used in the fluid dynamics, if perfunctorily replace δ^* , δ and $\delta\mathbf{x}$ by d/dt , $\partial/\partial t$ and \mathbf{q} , respectively.

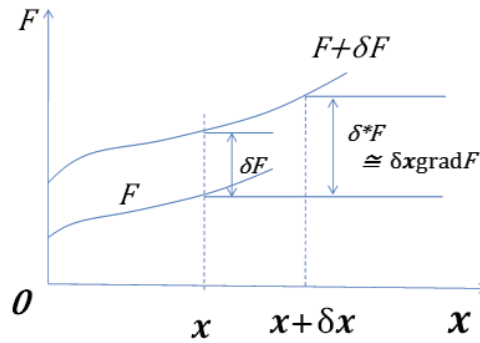


Figure 3: Concept of substantial variation

Then, we distinguish the quantity defined by 4.15 from usual variation defined by the expression 4.16 and call it “substantial variation” in this text.

The substantial variations of velocity \mathbf{q} , density ρ and entropy S are expressed as

$$\delta^* \mathbf{q} = \delta \mathbf{q} + \delta \mathbf{x} \text{ grad} \mathbf{q} \quad , \quad (4.17)$$

$$\delta^* \rho = \delta \rho + \delta \mathbf{x} \text{ grad} \rho \quad (4.18)$$

and
$$\delta^* S = \delta S + \delta \mathbf{x} \text{ grad} S \quad , \quad (4.19)$$

respectively. In case the vector \mathbf{x} is not subject to variation, that is, $\delta \mathbf{x} = 0$, they are identical with the usual variations and obviously there is a relation between $\delta^* \mathbf{q}$ and $\delta \mathbf{x}$ written as

$$\delta^* \mathbf{q} = \frac{d}{dt} \delta \mathbf{x} \quad . \quad (4.20)$$

(4)Variational expression of mass conservation

In the present case, if the variation vector $\delta \mathbf{x}$ are given to the particle coordinates \mathbf{x} , the density of fluid must be relaxed because $\delta \mathbf{x}$ and $\delta \rho$ can not change independently due to the constraint of conservation law of mass. The constraints between $\delta \mathbf{x}$ and $\delta \rho$ are explicitly derived as follows.

Consider a given small volume v closed by a surface moving with the flow as is shown in Fig.2. Supposing that the variation vector $\delta \mathbf{x}$ is given to the volume v at $t = t$ and that the volume will move and also be

deformed, the mass in the volume is still conserved. Therefore,

$$\int_{\tilde{v}} (\rho + \delta \rho) dv = \int_v \rho dv \quad (4.21)$$

is satisfied. Assuming that the variation vector $\delta \mathbf{x}$ is small enough and that the second powers of $\delta \mathbf{x}$ can be neglected, then Eq.4.21 leads to

$$\int_v \delta \rho dv + \int_s \rho \delta \mathbf{x} \mathbf{n} ds = 0 \quad , \quad (4.22)$$

And applying the Gaussian integral theorem, it can be rewritten as

$$\int_v [\delta \rho + \text{div}(\rho \delta \mathbf{x})] dv = 0 \quad . \quad (4.23)$$

Here v is arbitrary, then,

$$\delta \rho + \text{div}(\rho \delta \mathbf{x}) = 0 \quad , \quad (4.24)$$

or using Eq.4.18, we obtain

$$\delta^* \rho = -\rho \text{div}(\delta \mathbf{x}) \quad . \quad (4.25)$$

Eq.4.24 is the explicit form of the constraints between $\delta \rho$ and $\delta \mathbf{x}$.

Next, when the variation vector $\delta \mathbf{x}$ and δv are given, the first variation of quantity $\int_v \rho F dv$ is expressed as

$$\delta^* \left[\int_v \rho F dv \right] = \int_v (\rho + \delta\rho)(F + \delta F) dv - \int_v \rho F dv \quad , \quad (4.26)$$

which deduces a form using the relationship 4.25,

$$\delta^* \left[\int_v \rho F dv \right] = \int_v \rho \delta^* F dv \quad . \quad (4.27)$$

It is correctly concluded that when the first variation of $\int_v \rho F dv$ is evaluated, the density ρ can be treated as if it were not subject to variation, as long as the constraint 4.24 is maintained as subsidiary condition.

(5) Variational expression of equations of energy conservation

The entropy S of the fluid is one of the thermodynamic state variables and a function of absolute temperature T which has a relationship with the internal energy per unit mass e and ρ as,

$$TdS = de + pd\left(\frac{1}{\rho}\right) \quad . \quad (4.28)$$

If we choose S and ρ as independent variables in Eq.4.28, the internal energy e is expressed as

$$e = e(S, \rho) \quad . \quad (4.29)$$

Eq.4.28 is the first law of thermodynamics and can be applied to a given small volume v of fluid which always consists of same particles. Therefore, δ^*S , δ^*e and $\delta^*\rho$ are governed by the first law of thermodynamics in a form of

$$T\delta^*S = \delta^*e + p\delta^*\left(\frac{1}{\rho}\right) \quad . \quad (4.30)$$

For the adiabatic flow, the conservation law of energy is expressed as Eq.4.6 using entropy S .

Maintaining the entropy to be constant, the variation vector $\delta\mathbf{x}$ are given to a small volume moving with flow. This constraint will be expressed as

$$\delta^*S = 0 \quad , \quad (4.31)$$

or in another form by use of Eq.4.30,

$$\delta^*e + p\delta^*\left(\frac{1}{\rho}\right) = 0 \quad . \quad (4.32)$$

Furthermore, Eq.(4.32) is reformed with the help of Eq.4.25 as

$$\rho\delta^*e + p\text{div}(\delta\mathbf{x}) = 0 \quad , \quad (4.33)$$

which is the relationship between δ^*e and $\delta\mathbf{x}$ and can be applied to a small volume v in an integral form;

$$\int_v [\rho\delta^*e + p\text{div}(\delta\mathbf{x})] dv = 0 \quad . \quad (4.44)$$

Eq.4.44 will be led by use of relation 4.27 and Gaussian Integral theorem to

$$\delta^* \left[\int_v \rho e dv \right] = \int_v (\text{grad}p)\delta\mathbf{x} dv - \int_{s_1} \mathbf{t} \delta\mathbf{x} ds \quad . \quad (4.45)$$

Eq.4.45 means that the substantial variation of internal energy in v due to $\delta\mathbf{x}$, which equals the sum of the work done by pressure p and the work done by the adjacent fluid volume having common boundary s_1 . By integration Eq.4.33 or Eq.4.44 with respect to t ,

$$\delta^* \iint_{t_1 v}^{t_2} \rho e dv dt = - \iint_{t_1 v}^{t_2} p \text{div}(\delta\mathbf{x}) dv dt \quad (4.46)$$

is obtained.

The second term in the right-hand side of Eq.4.45 will take a very important role when we consider fluid and structure interference problems in future because there are mutual transfers of the kinetic energy and the potential energy through the boundaries between the fluid and the structure.

(6) Variational expression of energy conservation

In this section, the substantial variation of the kinematic energy is considered, which are due to the

variation vector $\delta \mathbf{x}$ given to the nominal solutions of the fluid particle path vector \mathbf{x} . The similar procedures used in the classical kinetics can be properly applied. The virtual work done due to inertia force $\rho \mathbf{a}$ is calculated as

$$\begin{aligned} \rho \mathbf{a} \delta \mathbf{x} &= \rho \frac{d}{dt} (\mathbf{q} \delta \mathbf{x}) - \rho \mathbf{q} \frac{d \delta \mathbf{x}}{dt} \\ &= \rho \frac{d}{dt} (\mathbf{q} \delta \mathbf{x}) - \rho \delta^* \left(\frac{1}{2} q^2 \right) \end{aligned} \quad (4.47)$$

By applying Eq.4.47 to a small volume v , and integrating it with respect to time in the interval of $t_0 \leq t \leq t_1$, then we obtain

$$\iint_{t_0}^{t_1} \rho \mathbf{a} \delta \mathbf{x} dv dt = \iint_{t_0}^{t_1} \rho \frac{d}{dt} (\mathbf{q} \delta \mathbf{x}) dv dt - \iint_{t_0}^{t_1} \rho \delta^* \left(\frac{1}{2} q^2 \right) dv dt \quad (4.48)$$

By use of the relation of Eq.4.27

$$\frac{d}{dt} \int_v \rho F dv = \int_v \rho \frac{d}{dt} F dv \quad (4.49)$$

Eq.4.48 can be rewritten and the substantial variation of kinetic energy is expressed as

$$\delta^* \iint_{t_0}^{t_1} \frac{1}{2} \rho q^2 dv dt = - \iint_{t_0}^{t_1} \rho \mathbf{a} \delta \mathbf{x} dv dt + \int_v \rho \mathbf{q} \delta \mathbf{x} dv \Big|_{t_0}^{t_1} \quad (4.50)$$

Here we employ the convention

$$\delta \mathbf{x}(\mathbf{x}, t_0) = 0 \quad , \quad (4.51)$$

$$\delta \mathbf{x}(\mathbf{x}, t_1) = 0 \quad . \quad (4.52)$$

Finally, Eq.4.47 leads

$$\delta^* \iint_{t_0}^{t_1} \frac{1}{2} \rho q^2 dv dt = - \iint_{t_0}^{t_1} \rho \mathbf{a} \delta \mathbf{x} dv dt \quad (4.52)$$

(7) Derivation of functional to be stationary

Based upon the arguments from section (2) to (6), we can easily reach a functional to be stationary in the present fluid dynamic problem.

For the sake of simplicity, the body forces and the forces applied at the boundaries are assumed to be conservative forces that can be introduced from the potential $\bar{\Omega}$ and $\bar{\Phi}$ in the forms as

$$- \int_v \rho \bar{f} \delta \mathbf{x} dv = \delta^* \int_v \rho \bar{\Omega} dv \quad , \quad (4.53)$$

$$- \int_{s_1} \mathbf{t} \delta \mathbf{x} ds = \delta^* \int_{s_1} \bar{\Phi} ds \quad . \quad (4.54)$$

In the previous sections, the considered integral area v is small and arbitrary, then we can apply the same concepts to the total area of interest $\Gamma = \sum v$ and we have the expressions of

$$- \iint_{t_0}^{t_1} p \operatorname{div}(\delta \mathbf{x}) dv dt = \delta^* \iint_{t_0}^{t_1} \rho e dv dt \quad , \quad (4.56)$$

$$- \iint_{t_0}^{t_1} \rho \mathbf{a} \delta \mathbf{x} dv dt = \delta^* \iint_{t_0}^{t_1} \frac{1}{2} \rho q^2 dv dt \quad . \quad (4.57)$$

The principle of virtual work 4.11 can be written with the help of Eq.4.53~4.57 as

$$\delta^* \left[\iint_{t_0}^{t_1} L dv dt - \iint_{t_0}^{t_1} \bar{\Phi} ds dt \right] = 0 \quad , \quad (4.58)$$

where,

$$L = \frac{1}{2}\rho q^2 - \rho(e + \bar{\Omega}) \quad . \quad (4.59)$$

In Eq.4.58, the independent variables subject to variation are the coordinate vector \mathbf{x} of the fluid particles. The subsidiary conditions are geometric boundary conditions 4.10, conservation equations of mass 4.5 and energy 4.6.

They are summarized in variational forms as

$$\mathbf{n}\delta\mathbf{x} = 0 \quad \text{on } s_2 \quad , \quad (4.12)$$

$$\delta^*\rho = -\rho \operatorname{div}(\delta\mathbf{x}) \quad \text{in } v \quad , \quad (4.24)$$

$$\delta^*e = -\frac{p}{\rho} \operatorname{div}(\delta\mathbf{x}) \quad \text{in } v \quad . \quad (4.32)$$

In the integrand L of Eq.4.59, the first term is kinetic energy; the second is internal energy; the third is potential energy; respectively, that is,

$$L = (\text{kinetic energy}) - (\text{internal energy} + \text{potential energy})$$

It is found that the functional 4.59 is similar to the Hamiltonian which appears in the Hamilton's Principle in the kinetics.

If we define a functional Π by

$$\Pi = \iint_{t_0}^{t_1} L \, dv \, dt - \iint_{t_0}^{t_1} \bar{\Phi} \, ds \, dt \quad , \quad (4.60)$$

then for the inviscid and isentropic flow we may state a variational principle as follows; *Of all admissible functions \mathbf{x} which satisfy Eq.4.12, Eq.4.24 and Eq.4.32, the actual solution makes the functional Π stationary.*

5. FINAL REMARKS

The topics are a little bit classical but it is noted that modern analytical tools in engineering which perform a huge amount of jobs on supercomputers are more or less based on the variational methods. Therefore in order for engineers to understand a part of schemes of numerical methods used today, it has a meaning that the basic disciplines concerning the variational principles in engineering have been summarized in this paper.

By introducing the concept of substantial variation, it was shown that the Hamilton's principle is exactly derived from the principle of the virtual work in fluid dynamics. The orderly processes of conversion from the principle of virtual work to the Hamilton's principle provides a logical thread that links various variational principles in the fluid dynamics.

REFERENCES

- 1) Washizu, K.: Variational method in elasticity and plasticity, 3rd ed., Pergamon Press, Oxford, 1982.
- 2) Bryson, A. and Ho, Y.: Applied optimal control, Taylor & Francis Group, 1975.
- 3) Hestenes, M.R.: Calculus of variations and optimal control theory, John Wiley & Sons, Inc., New York, 1966.
- 4) Nakamichi, J.: A direct approach using the finite element method for the solution of institute the linear optimal control problem with a quadratic criterion, The Franklin Institute Vol.304, No.4, 1978
- 5) Selinger, R.L., Whitham, G.B.: Variational principle in continuum mechanics, Proc.Roy.Society, A 305, 1-25, 1968.
- 6) Serrin, J.: Mathematical principles of classical fluid mechanics, Handbuch der Physik, Band VIII/1, Stromungsmechanik. Springer-Verlag, Berlin, 1959.
- 7) Bateman, H.: Partial differential equations of mathematical physics, Dover, New York, 1994
- 8) Selinger, R.L., Whitham, G.B.: Variational principle in continuum mechanics, Proc.Roy.Society, A 305, 1-25, 1968.
- 9) Wang, C.: Variational method in the theory of compressible fluid, J. Aeronaut, Sci., Vol. 15, No.11, pp.675-685, 1948.

Development of a surgical instrument using an elastic vibration wing mechanism

Ren Ota⁺¹, Ikuo Yamamoto⁺¹, Murray Lawn⁺²

Takeshi Nagayasu⁺³, Naoya Yamasaki⁺³, Keitaro Matsumoto⁺³

⁺¹*Dept. of Mechanical Science, Nagasaki Univ. Graduate School, Nagasaki, Japan*

⁺²*Medical-Engineering Hybrid Professional Development Program, Nagasaki Univ. Graduate School of Biomedical Sciences, Nagasaki, Japan*

⁺³*Dept. of Surgery, Nagasaki Univ. Graduate School of Biomedical Sciences, Nagasaki, Japan*

Abstract. In the field of surgery the ability to handle organs and their associated systems in a stable yet delicate manner is of paramount importance for both the patient and the surgeon to ensure operation efficacy. This paper focuses on the development of flexible tipped surgical forceps. The mechanism is based on a previously developed “elastic vibration wing” which is biomimicry of the propulsion mechanism of a typical fish. The flexible forceps distributes pressure through a network of articulated linkages in order to softly envelop the object to be held. This mechanism was specifically designed for use in endoscopic surgery, however it could also be used in robotics where gentle grasp of an object is required at the end of a robotic arm. The mechanism was designed in 3D-CAD and conceptually prototyped using a 3D printer.

Keyword: Elastic Vibration wing¹, Surgical forceps², 3D-printer³, CAD simulation⁴, Pressure relief⁵

1. INTRODUCTION

Recently, there has been an increasing need for surgical instruments that can hold organs delicately yet stably. Such an instrument increases the efficacy of surgical operations by decreasing the physical and mental strain on both surgeons and patients. New bio-mechanism based surgical instruments based in part on the anatomical structure of a fish provide soft handling forceps. The maneuvering mechanism of robotic fish technology in particular has been applied to medical mechatronics. Aquatic animals like fish can swim very fast using minimal power. In regard to prototyping the mechanism the authors have used a seamless design and prototyping process. This process has been used to prototype biologically based mechanisms using 3D-CAD and a 3D-printer. Specifically, this fish based mechanism which produces an elastic oscillating fin combined with the use of a shark skin like surface which effectively reduces hydrodynamic resistance have been found to be effective in creating superior surgical instruments. Classical surgical instruments which exert a large amount of force on a limited number of points on organs are stressful for both surgeons and patients. Furthermore classical instrument’s ergonomics often do not consider the surgeon and are often awkward and thus stressful to use.

The purpose of this research is to develop user-friendly surgical instruments that enable more efficient surgery. This process is effectively facilitated by using a more seamless design through to the prototyping process using 3D-CAD and a 3D-printer. The Fig.1 shows the 3D printer used. The basic steps of the system design and prototyping are shown in Fig.2.



Fig.1 3D-Printer

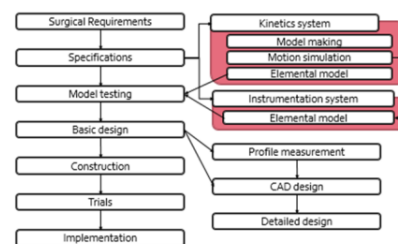


Fig.2 Basic steps of design

⁺¹hare.mabuta25@gmail.com

2. Elastic vibration wing forceps

(1) Problems with conventional forceps

Firstly, we outline some of the problems with conventional endoscopic forceps, based on conversations with a number of surgeons. There are three main problems. The first point is about contact, because pressure is focused at two contact points. The second point is about slip, because organs are coated in body fluids. The third point is about the angle of usage, because awkward wrist adjustments need to be made. These problems make operations difficult for doctors and negatively impact patients. So, we have improved the design as follows.

a) Contact points

Firstly regarding the contact points, with a standard set of forceps the points of contact are focused at two points resulting in a high contact pressure. As mentioned earlier by applying the elastic vibration wing of the fish robot mechanism (Fig.3) the pressure is reduced because the contact area is better distributed (Fig.4).



Fig.3 Robotic fish

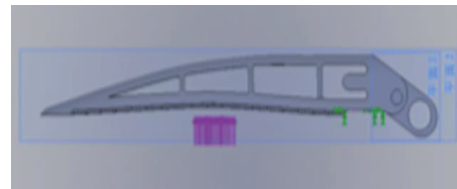


Fig.4 Forceps elasticity shape

b) Contact surface slip

Next, regarding contact surface slip. Particularly in the case of endoscopic surgery, as body organs are often coated in body fluids they are very slippery to handle. To deal with this, we have applied a design that is biomimicry of shark skin. Shark skin reduces fluid resistance in one direction but increases it in the opposite direction because of its inherent structure shown in Fig.5. This mechanism has been proven to be effective in reducing slip on the forceps tips. The use of this mechanism has become increasingly used in the medical industry.

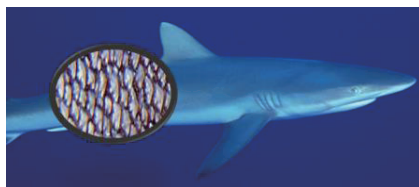


Fig.5 Shark skin

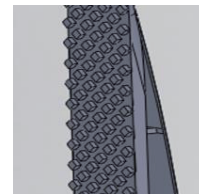


Fig.6 Shark skin surface based flexible forceps

c) Angle of usage

Finally, regarding the angle of usage. In any kind of surgery the angle of operation of the forceps needs to be adapted as required, the required angle is often awkward therefore we designed the forceps to make transformation of the operating angle possible. Rotation of the forceps angle can easily be carried out with one hand including lock and release of the angle. The forceps are opened and closed by pulling the trigger shown in Fig. 7. The rotation and rotation lock and release are thumb operated.



Fig.7 Rotation function

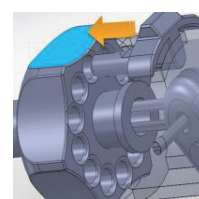


Fig.8 Rotation lock function

3. Modeling by 3D-Printer

After checking the operational functionality, a concept prototype was made using a 3D printer. These are the parts that make up the forceps (Fig.9, Fig.10). Table 1 shows the specifications, the values within the blue frames were specified by the medical staff.



Fig.9 Parts of the Elastic vibration wing forceps

Fig.10 Elastic vibration wing forceps (3D-Printed)

Table 1 Specification of forceps

Description	Size
Total length	360mm
Hand grasp section length	150mm
Tip length	45mm
Tip thickness	7mm
Overall thickness closed	12mm
Opening angle (max)	90°

4. Pressure analysis of forceps

Finally, we conducted an experiment in order to confirm whether the elastic vibration wing forceps reduces the contact pressure. This section explains the method and equipment used to carry out the test.

The experiment was carried out as follows: Firstly, 5 newtons of pressure was applied to the trigger, a plastic hose was used to simulate an organ. This resulted in deformation of the hose. A pressure measuring sheet (PMS) was inserted between the forceps jaw and the hose to obtain a reading of the pressure (Fig.11). This was repeated at 5mm intervals from the tip (Fig.12). The PMS data was then input with a scanner and analyzed by special software (FPD-8010J). The pressure measurement sheet provides a proportional display of pressure exerted.

Fig.13 shows the pressure distribution using regular (solid) forceps and Fig.14 shows the resulting improved pressure distribution using the flexible forceps. The regular forceps were made from the same resin material for comparison. Comparing them, the pressure contact area of the elastic vibration wing forceps is clearly better distributed. So, it was shown that the elastic vibration wing mechanism is effective.

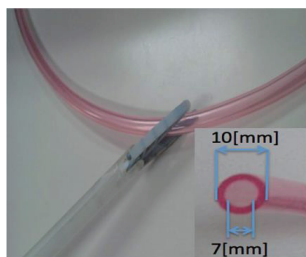


Fig.11 Experimental situation

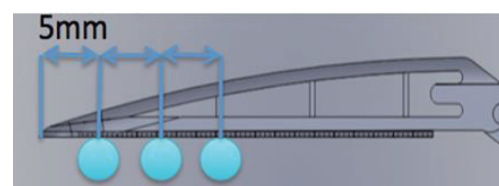


Fig.12 Analysis points

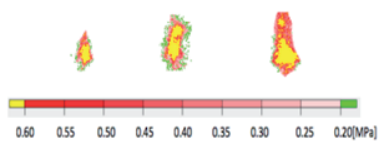


Fig.13 Regular forceps grip

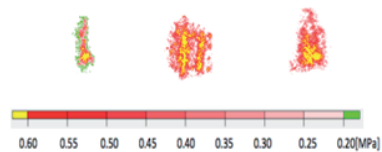


Fig.14 Flexible forceps grip

5. Conclusion

Although these forceps are still under development, the elastic vibration wing forceps concept has potential in a wide variety of situations. We are in the process of designing an actual scale working prototype of the forceps in metal in preparation for the next stage which will be animal testing.

We succeeded in developing a prototype of an endoscopic surgical instrument based on the operating requirements using 3D-CAD and a 3D printer. The motion was simulation in 3D-CAD and a prototype created using a 3D printer confirmed the functionality. This rapid prototype process allows medical personnel to provide feedback regarding user friendliness at an early stage. It is possible to obtain operational evaluation by medical professionals at the design stage, thus it is possible to improve development efficiency of the surgical instrument.

ACKNOWLEDGMENTS

A part of this study was supported by the Medical Engineering Hybrid professional development program staff. The authors would like to express their sincere gratitude to Mr. Naoto Matsuo, Mr. Nobuo Kakinoki, Nagasaki University and related personnel in this research and development.

REFERENCES

- 1) Z. Gu, I. Yamamoto, N. Inagawa. Development of Forceps robot for surgical operation by bio mechanism application, 4th International Conference on BMEI 2011
- 2) Z. Gu, I. Yamamoto, N. Inagawa, T. Nakamura, K. Yamaguchi, K. Shibao. Modeling and Analysis of Flexible Forceps Robot for Surgical operation. International Conference on Engineering and Business Management, 2011
- 3) Z. Gu, I. Yamamoto, N. Inagawa. Research and Development of Biomechanical Robot for Medical operation. Advanced Materials Research. Vols. 452-453, 2012
- 4) I. Yamamoto. Marine Control Systems, international Journal of Robust and Nonlinear Control, IFAC. Vol. 11, No. 13, Wiley, 2001
- 5) I. Yamamoto, Y. Terada, T. Nagamatsu, Y. Imaizumi. Development research of oscillating in propulsion system Proceedings SICE94, 1994
- 6) I. Yamamoto. Propulsion System with Flexible / Rigid Oscillating Fin, IEEE Journal of Oceanic Engineering. Vol. 20, No. 1, 1995
- 7) Madeen, E., Doctor Robopet, ANA Wingspan, No. 416, pp. 24-29, 2004
- 8) T. Ichikizaki and I. Yamamoto, Development of High Performance Robotic Fish, Proceedings Techno-Ocean 2006 / 19th JASNAOE Ocean Engineering Symposium Kobe, JAPAN, October 18-20, Paper No. 207, 2006
- 9) Oppenheimer MJ, Mann FC, Intestinal capillary circulation during distention. Surgery 13, pp. 548--554, 1974

FLUTTER INHIBITION IN ANIMAL WINGS

Yoshinobu Inada⁺¹ and Ryoya Saito

Department of Aeronautics and Astronautics, School of Engineering, Tokai University,
Hiratsuka, Kanagawa, Japan

Animal wings are usually made of elastic materials and thus have different characteristics from conventional airplane wing made of hard stuff. The elasticity of wing provides merits such as a large straight-line stability but causes a serious problem of flutter. This study investigates how animals withstand this problem focusing on the bird wing. The wing of birds is composed of many feathers, the representative of which is a primary feather. Interestingly, flutters are hardly observed in the primary feathers. The reflection in the primary feather was supposed to be the key factor of flutter inhibition. The wind tunnel tests with feather models with and without reflection were conducted and it was confirmed that the feather with reflection more effectively inhibited the flutter generation than the feather without reflection.

Keyword: flutter inhibition, bird wing, primary feather, reflection

1. INTRODUCTION

Wing of flying animals such as birds or insects is made of elastic materials. Feather of bird wing is made of “keratin” which is a kind of protein known as a main component of human hair. Wing of insect is made of “chitin” which is a kind of saccharide. Both materials have moderate elasticity and thus it raises a question that why birds or insects use elastic materials instead of hard one such as calcium for wings. It may involve both aerodynamic and structural contexts. For the structural one, a wing made of hard material may be easy to crash or hurt subjects and heavy. In contrast, the aerodynamic one was not fully clarified so far.

Investigations to solve this problem were conducted previously focusing on a bird wing. Bird wing is composed of several kinds of feathers. Primary feathers are generally longer than other feathers and located at the wing tip. About 10 pieces of primary feather align anteroposteriorly and generally bend up while flying which is typically observed in the gliding hawk or condor wings¹⁾. In the previous researches, the aerodynamic effects of primary feathers were investigated and several benefits were pointed out such as a reduction of induced drag or an increase of lift slope²⁻⁵⁾. However, those studies were based on hard wing models made of aluminum or stainless steel and thus the elasticity was not considered.

The study to clarify the function of elasticity in a bird wing was conducted previously in our laboratory⁶⁾ and some benefits were pointed out such as a large resistance force to prevent a side slip or a large restoring moment of rolling both of which were larger than that of the hard wing models, and thus were

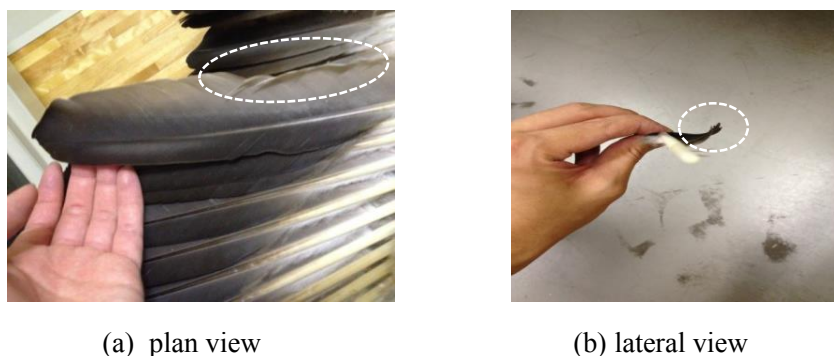


Figure 1: Primary feather of a bird wing. The part in the dashed circle shows the reflection

⁺¹inada@tokai-u.jp

effective for enhancing a straight-line stability. However, the elasticity in the wing model caused a problem of flutter. The flutter is generally caused by a coupling of the aerodynamic force and the elastic force of the subject⁷⁾. So, the soft and flexible subject is easy to generate flutter. The feather model used in the previous study was made of elastic plate such as vinyl chloride, so the flutter was unavoidable.

In contrast, flutters are hardly observed in the bird wing even though the feather of the wing is flexible. We supposed that the reflection in the primary feather as shown in Fig. 1 was a key factor for this flutter inhibition. The reflection of the wing has the characteristics of pitching stability which stabilize the pitching angle of the wing and inhibit its divergence¹⁾. The flutter generally starts with the torsion of the wing, so, the pitching stability may inhibit the torsion and thus have the effective role of flutter inhibition. The wind tunnel test was conducted to confirm this role and the results are reported in the following sections.

2. METHOD

The reflection wing model for the wind tunnel test is fabricated using a thin aluminum plate. The plate size is 45[mm]x180[mm]x0.3[mm] and is bent convexly in front and concavely in rear to reproduce the reflection shape as shown in Fig. 2. The height h_1 and the depth h_2 are varied to make several types of the reflection. For instance, the normal reflection type has $h_1=2$ [mm] and $h_2=2$ [mm]. The length of the convex c_1 and the concave c_2 are also varied. For the normal type, $c_1=(2/3)c$ and $c_2=(1/3)c$, where c is the wing chord length. The other values are shown in Table 1. The large type has the double size of h_1 and h_2 to the normal type; the even type has the same size of the convex and the concave parts, i.e. the border of the convex and the concave part is the center line of the wing; the camber type has only a convex part; the oblique type has the border which runs obliquely from the root to the tip of the model. Figures 3(a)-(d) show the typical types of the wing model.

The reflection or the camber type is hard to bend or twist because the structural stiffness becomes larger than the flat plate. This means the wing model is hard to flutter itself. So the plastic plate is attached to the wing root as shown in Fig. 4 and the opposite side of this plate is fixed to a sting in the wind tunnel. The wing model, then, becomes easy to twist or bend and thus can generate the flutter under 4[m/s] air currency.

The wind tunnel is equipped with a closed type test section which is surrounded by walls. The wind tunnel can make the wind speed up to 20[m/s], but we use 4[m/s] because the wind faster than 4[m/s] generates large flutters which makes the wing touch the surrounding walls and thus prevents the correct measurement.

The flutter is recorded by a high speed video camera (NAC MEMRECAM fx-k4). The torsion θ [deg] and the bending d [mm] of the wing are measured by the motion tracking software (DITECT Dipp-MotionPRO). The definition of them are shown in Fig. 5, where a , b , p are the leading edge, the trailing edge, and the central point of the wing section, respectively.

Table 1: Reflection parameter

Type	h_1 [mm]	h_2 [mm]	c_1	c_2
Flat plate	0	0	n/a	n/a
Normal	2	2	$(2/3)c$	$(1/3)c$
Large	4	4	$(2/3)c$	$(1/3)c$
Even	2	2	$(1/2)c$	$(1/2)c$
Camber	2	0	c	0
Oblique	2	5*	root: c tip: $(2/3)c$	root: 0 tip: $(1/3)c$

*maximum value at the wing tip

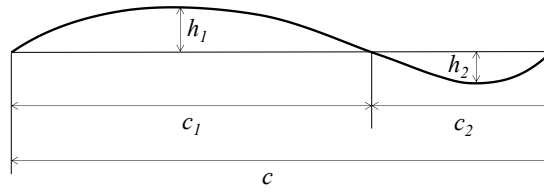


Figure 2: Parameters of reflection wing



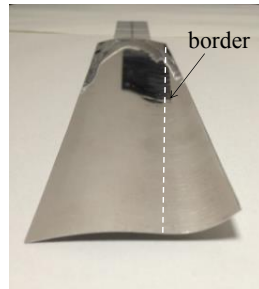
(a) Normal



(b) Even



(c) Camber

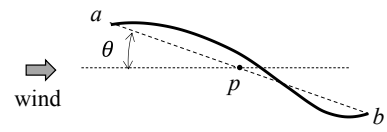


(d) Oblique

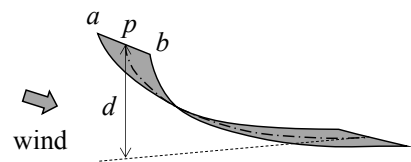
Figure 3: Typical wing models



Figure 4: Plastic plate at the root of the wing



(a) Torsion



(b) Bending

Figure 5: Definition of torsion and bending

3. RESULTS AND DISCUSSION

The temporal change of torsion of wing models is shown in Figs. 6(a)-(d) for various angles of attack α . Distinct flutter was not observed when α was small ($\alpha < 14^\circ$). So the results are shown for $\alpha \geq 14^\circ$. The torsion and the bending of wing became oscillatory when $\alpha \geq 14^\circ$ and both the amplitude and the frequency were different for different wing models. When $\alpha = 14^\circ$, the amplitude of torsion oscillation was large for the flat plate and the normal type as shown in Fig. 6(a). The camber type was next large. The amplitudes of even and large types were small and the oblique type had the smallest amplitude. When $\alpha = 16^\circ$, the normal and the flat plate types had a large amplitude and the camber type followed it as shown in Fig. 6(b). This tendency was same for $\alpha = 18^\circ$ and $\alpha = 20^\circ$ as shown in Figs. 6(c) and 6(d) and the amplitude did not show the obvious dependency on the angle of attack. Namely, the amplitude was about $\pm 30^\circ$ for the flat plate and the normal types for all angles of attack, and it was about $\pm 10^\circ$ or less for other types of the wing.

The temporal change of bending of wing models is shown in Figs. 7(a)-(d) for various angles of attack α . Period of oscillation for bending tended to differ among wing models and the oscillation was recorded for one or several cycles. So, the lines of oscillation with small periods ended earlier than that of the longer one in the graphs. As shown in Fig. 7(a), the amplitude of bending oscillation was large for the flat plate when $\alpha = 14^\circ$. The amplitude for other types was significantly smaller than that of the flat plate. When $\alpha = 16^\circ$, the bending oscillation of flat plate showed a conspicuously large amplitude and slow oscillation as shown in Fig. 7(b). This means the quality of bending oscillation changed from a local one at the wing tip to the global one which made the whole wing oscillate up and down largely. When $\alpha = 18^\circ$, the camber type also showed a large and slow oscillation as shown in Fig. 7(c), and when $\alpha = 20^\circ$, the normal type also showed a large and slow oscillation as shown in Fig. 7(d). Meanwhile, the oblique, the large, and the even types showed conspicuously small oscillations. In particular, the oblique type hardly oscillated when $\alpha = 20^\circ$.

In summary, the wings with reflection showed flutter inhibition characteristics except the normal type. They showed a small oscillation of torsion and bending for all values of angle of attack. Meanwhile, the flat plate, the normal, and the camber types showed a large oscillation for all angles of attack and did not show the flutter inhibition. The reason for this difference might be the pitching stability of the reflection wing. From the thin wing theory [1, 8], the reflection wing has the stability of pitching rotation. When the angle of attack increases or decreases from the equilibrium angle, the center of pressure tends to move backward or forward, respectively, to generate a restoring moment and the wing recovers its original angle. This pitching stability inhibits the torsion of the wing and thus inhibits the rapid increase or decrease of the angle of attack of the wing. The lift of the wing may then relatively stay stable and thus the bending oscillation may also be inhibited.

The flat plate and the camber types did not have this characteristics, thus the significant flutter was generated both in torsion and bending. The normal type showed a large flutter although it had the reflection. This means small size reflection is not enough to inhibit the flutter. The values of h_1 and h_2 of the normal type were both 2[mm] which was 4.4% of the chord length, whereas h_1 and h_2 of the large type were both 4[mm] which was 8.9% of the chord length. This result indicates that the necessary values of height and depth of reflection exist for the flutter inhibition. The even type showed the flutter inhibition although h_1 and h_2 were both 2[mm]. The even type had larger space of concave than the normal type. Therefore, the effect of reflection may be augmented both/either by making the height (h_1) and the depth (h_2) larger and/or the space of concave larger.

The primary feather of bird wing generally has a large and oblique reflection. The oblique type in this study mimicked it and showed a conspicuous flutter inhibition effect. This may be because the continuous change of wing section shape from the root to the tip of the wing realizes the flutter inhibition over the wide range of angle of attack. The conspicuous flutter inhibition of oblique type reflection in a bird wing may realize the stable lift generation and stability in the flight, thus significantly advantageous for the long duration and long range flight.

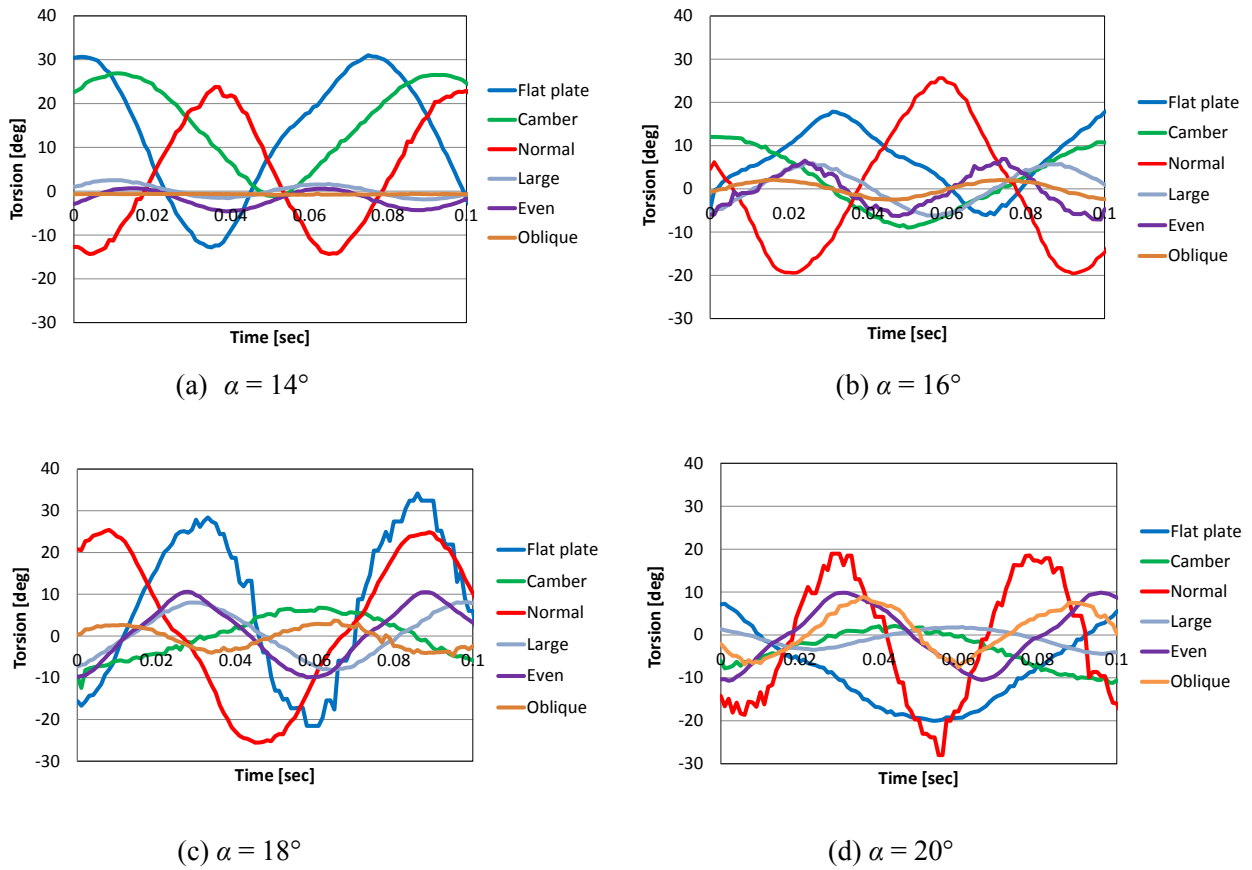


Figure 6: Torsion for various angles of attack

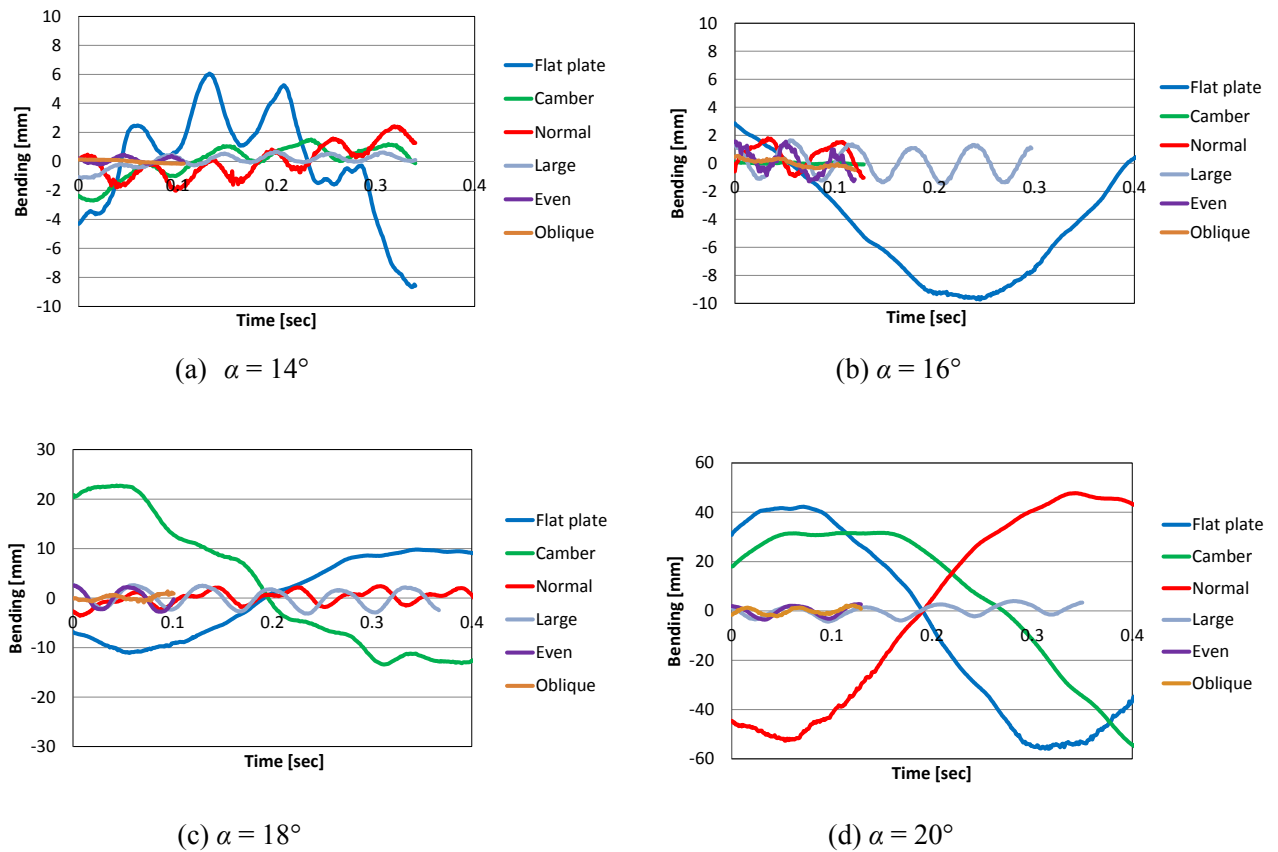


Figure 7: Bending for various angles of attack

REFERENCES

- 1) A. Azuma, The Biokinetics of Flying and Swimming, Second Edition, AIAA Education Series, AIAA, Virginia, USA, 2006.
- 2) V. A. Tucker, Gliding Birds: Reduction of Induced Drag by Wing Tip Slots between the Primary Feathers, *J. exp. Biol.*, vol 180, pp. 285-310, 1993 .
- 3) V. A. Tucker, Drag Reduction by Wing Tip Slots in a Gliding Harris' Hawk, *Parabuteo Unicinctus*, *J. exp. Biol.*, vol 198, pp. 775-781, 1995.
- 4) D. S. Miklosovic, Analytic and Experimental Investigation of Dihedral Configuration s of Three-Winglet Planforms, *J. Fluid. Eng.*, vol. 130, pp.07113-1-07113-10 , 2008.
- 5) J. E. Guerrero, D. Maestro, A. Bottaro, Biomimetic Spiroid Winglets for Lift and Drag Control, *C. R. Mecanique*, vol 340, pp. 67-80, 2012
- 6) M. Motomatsu, Y. Inada, Effect of Elasticity in the Bird-like Primary Feather Wing on the Flight Stability, Proceeding of the 29th Congress of the International Council of the Aeronautical Sciences (ICAS 2014), 2014.
- 7) R. L. Bisplinghoff, H. Ashley, R. L. Halfman, Aeroelasticity, Dover Publications, Inc. Minesota, New York, 1996.
- 8) J. J. Bertin, Aerodynamics for Engineers, Fourth Edition, Prentice-Hall, New York, 2002.

Development of Flutter Analysis Tool using Next-Generation CFD (Computational Fluid Dynamics) Algorithms

1st Takaaki Yumitori+1, 2nd Katsutoshi Ishikawa+1,
3rd Keizo Takenaka+1 and 4rd Toshihiko Azuma+2
+1Mitsubishi Heavy Industries, Ltd., 10, Oye-cho, Minato-ku, Nagoya 455-8515, Japan
+2Japan Aircraft Development Corporation/ Churyo Engineering Co.,Ltd.,
Hibiya Kokusai Bldg. 7F, 2-2-3, Uchisawai-cho, Chiyoda-ku, Tokyo, 100-001, Japan

Both high accuracy and high efficiency are strongly required for flutter analysis. To achieve these requirements, MHI developed a flutter analysis tool based on the BCM (Building-Cube Method), which is a next-generation CFD (Computational Fluid Dynamics) algorithm using an advanced Cartesian mesh method.

The BCM has several advantages such as rapid mesh generation, simple data structure for handling complex geometry, adaptive space-time resolution, and easy parallelization with ideal load balance.

The developed tool is validated with the NASA ARROW WING model. Computational time is greatly reduced to less than one-third by applying adaptive inner time iteration technique. Predicted flutter boundary agrees well with experimental data.

Keyword: flutter, CFD, cartesian mesh

1. INTRODUCTION

Flutter must be avoided for safe operation of aircraft, not to cause the structure destruction. Recently, the structure weight saving is necessary for performance improvement, operational and manufacturing cost reduction in aircraft design. This weight saving reduces the structural margin of safety and increases the risk of flutter. It is necessary to carry out the trade-off between structure weight saving and flutter prevention design with high accuracy. Also, since the flutter prevention design is linked with both aircraft aerodynamic shape design and structural design closely, high efficiency is required in design development cycles.

Flutter analysis is a coupled analysis between aerodynamics and structural vibration. The current primary analysis tool is NASTRAN¹⁾ which is widely applied in the field of aircraft design, and is accepted by the U.S. Federal Aviation Administration (FAA) in type certification. NASTRAN is high efficiency because it uses a linear analysis for aerodynamics, and required computer resource is personal PC level. On the other hand, they cannot evaluate nonlinear aerodynamics such as shockwave and flow separation in transonic regime including cruise condition. Flutter velocity drop caused by nonlinear aerodynamics is widely known as transonic dip, and linear aerodynamic analysis of NASTRAN cannot estimate accurately. Consideration of the transonic dip in actual aircraft design is achieved with an empirical safety margin to the analytical outputs based on experience. Application of the safety margin leads to the weight penalty of the aircraft.

The influence of nonlinear aerodynamics is now evaluated by the flutter wind tunnel test using small scale model. There are so many difficulties in the flutter wind tunnel test. It takes a lot of time and cost for model design, manufacturing and tunnel operation. The small scale model is required to simulate aerodynamic shape, mass and stiffness of the aircraft simultaneously, based on the similarity law, which is not easy task. The required number of the model is large, since the model is going to be broken by flutter during the test.

In recent years, CFD has become matured reasonable to evaluate nonlinear aerodynamics. Steady state analysis to deal with time-averaged flow has become a primary aerodynamic shape design tool. However, unsteady, time-dependent analysis even with a shape deformation, such as flutter, has still huge computational

⁺¹takaaki_yumitori@mhi.co.jp

cost, then, there is a problem in the design application in terms of analysis efficiency. Although the computational time can be decreased by using a large-scale parallel computer, pre-processing (Mesh generation, mesh deformation, etc.) and post-processing (visualization, data extraction, etc.) is expected to become a bottleneck.

To solve the problem, the authors developed a flutter analysis tool based on the BCM (Building-Cube Method)²⁾, which is a next-generation CFD (Computational Fluid Dynamics) algorithm using an advanced Cartesian mesh method.

In this paper, the developed flutter analysis tool and its validation results are explained.

2. OVERVIEW OF ANALYSIS TOOL

BCM based on block-structured Cartesian mesh method is applied to flutter analysis.

BCM has several advantages by its essential strategies. These strategies employed building-up of sub-domains, called ‘Cube’, which has various sizes and equal number of cells. Fig. 1 shows schematic of BCM mesh.

Various sizes cubes enable to adapt to the geometry and flow features. Equal number of cells enables rapid mesh generation, simple data structure for handling complex geometry, and easy parallelization with ideal load balance.

BCM solves three-dimensional Euler and Reynolds averaged Navier–Stokes equations using a cell-centered finite volume method. The HLLW (Harten-Lax-van Lee-Wada)³⁾ is used for the numerical flux computations. The third spatial accuracy is realized by Venkatakrisnan’s limiter⁴⁾ and MUSCL (Monotone Upstream-Centered Schemes for Conservation Laws) scheme. For time integration, the second-order accurate LU-SGS (Lower/Upper Symmetric Gauss-Seidel) implicit method⁵⁾ with dual-time stepping using the three-point Euler backward difference is applied. The flow equations, coupled with a second-order linear dynamic solver, are solved using the fully implicit second-order accuracy scheme⁶⁾ developed by Melville.

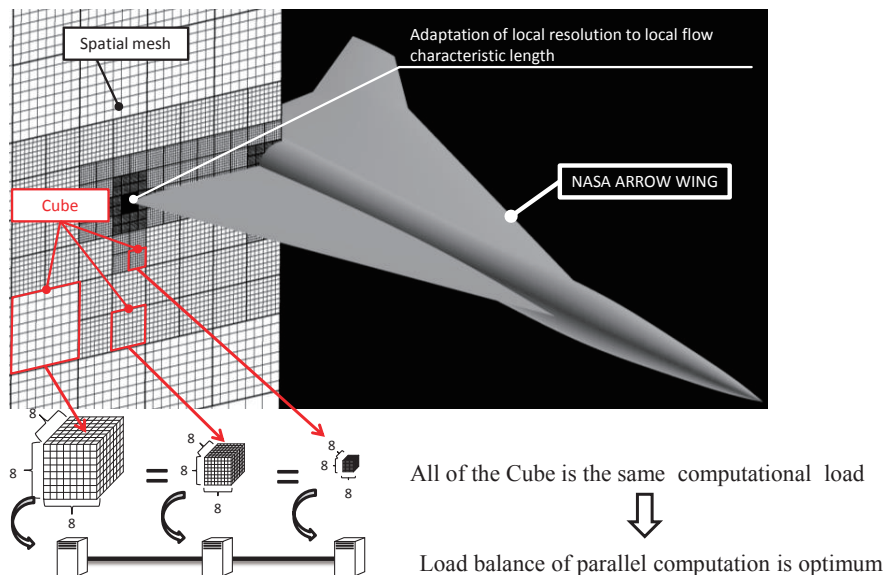


Figure 1: BCM mesh

(1) Treatment of wall boundary condition for BCM

a) Wall boundary condition

Immersed boundary method⁷⁾ using Ghost Cell (GC) and Image Point (IP) on the wall boundary is applied. Fig.2 shows the schematic of interpolation to GC from IP. GC is defined as cells in the solid that have at least one neighbor in the fluid, and IP is defined from the wall in the normal direction to 1.75 times of the length of the smallest cell size (larger than cell diagonal length). IP is interpolated using geometric weighting function⁸⁾ from 3 x 3 x 3 fluid cells around IP. Interpolation from IP to GC used formulation eq. 1 and eq. 2. Slip velocity and zero wall normal pressure gradient is applied.

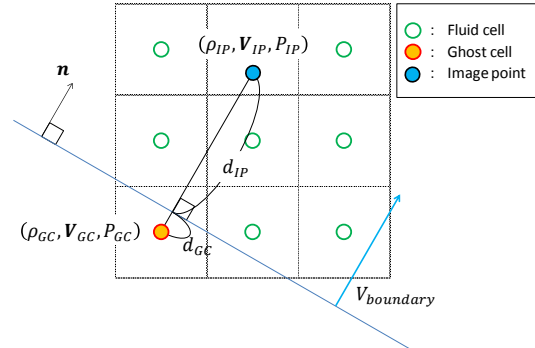


Figure 2: Schematic of interpolation to GC from IP

$$\mathbf{V}_{GC} = \mathbf{V}_{IP} - \left\{ 1 + \left(\frac{d_{IP}}{d_{GC}} \right) \right\} (\mathbf{V}_{IP} \cdot \mathbf{n}) \mathbf{n} \quad (1)$$

$$\left. \frac{\partial P}{\partial \mathbf{n}} \right|_{WALL} = 0 \quad (2)$$

Where \mathbf{V}_{GC} is Velocity of Ghost cell, \mathbf{V}_{IP} is Velocity of Image point, d_{IP} is distance between wall boundary and Image point, d_{GC} is distance between wall boundary and Ghost cell, and \mathbf{n} is normal vector of wall boundary.

b) Moving wall boundary condition

Deforming mesh at each CFD time-step for unsteady simulation like moving wall can cause inefficiency and troubles such as mesh cross-over or over-skewed meshes. In order to avoid the problem, transpiration boundary method is applied for moving wall boundary. It was reported to predicted flutter boundary successfully^{9),10),11)}.

Transpiration boundary method is a simple technique to update boundary velocity, acceleration and normal vector for a thin wing small moving or deformation. The boundary condition can be written as follows.

$$\mathbf{V}_{GC} = (\mathbf{V}_{IP} - \mathbf{V}_{boundary}) - \left\{ 1 + \left(\frac{d_{IP}}{d_{GC}} \right) \right\} \{ (\mathbf{V}_{IP} - \mathbf{V}_{boundary}) \cdot \mathbf{n} \} \mathbf{n} \quad (3)$$

$$\left. \frac{\partial P}{\partial \mathbf{n}} \right|_{WALL} = -\rho_{IP} (\mathbf{a}_{boundary} \cdot \mathbf{n}) \quad (4)$$

$$\rho_{GC} = \rho_{IP} \left(\frac{P_{GC}}{P_{IP}} \right)^{\frac{1}{\gamma}} \quad (5)$$

Where ρ_{IP} is density of Image Point, $\mathbf{a}_{boundary}$ is acceleration of Wall boundary, ρ_{GC} is density of Ghost cell, P_{IP} is pressure of Image Point, P_{GC} is pressure of Ghost cell, and γ is ratio of specific heat.

(2) Adaptive iteration techniques

Aerodynamic and structural equations are coupled as fully implicit second-order scheme. Fig. 3 shows aerodynamic and structural equations coupling method

Aerodynamics and structure are solved independently in a decoupled way. By using inner time iteration, the phase difference between aerodynamics and structure can be eliminated. The approach allows for the use of independent solvers for the aerodynamics and structural equations, but accuracy and efficiency of the solution is affected by the inner time iteration.

In this study, two adaptive inner iteration techniques are developed and applied to improve efficiency of the analysis.

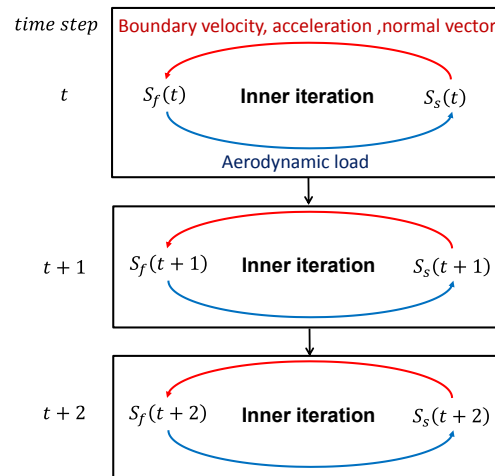


Figure 3: Aerodynamic and structural equations coupling method.

a) Reducing number of inner time iteration

Fig. 4(a) shows schematic of adaptive inner iteration.

We tried to improve the efficiency of calculation by adaptive inner time iteration using the convergence criteria based on the residual of generalized aerodynamics force is applied. Generalized aerodynamics force is shown as follows.

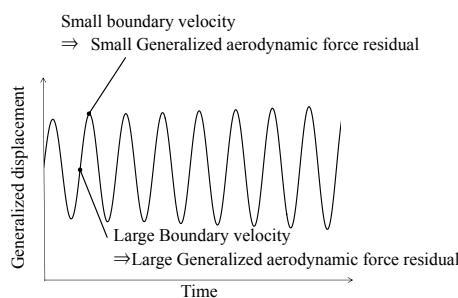
$$Q = \Phi^T F(\omega, \Phi) \tag{6}$$

Where Q is generalized aerodynamics force, F is aerodynamics force, ω is frequency vector, Φ is modal matrix, and Φ^T is transpose of modal matrix.

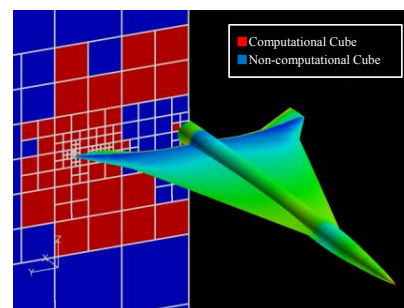
When generalized aerodynamic force residual is sufficiently small during inner iteration, BCM generates correct approximate solution, and inner iteration is stopped. Generalized aerodynamic force residual has a characteristic that when boundary velocity is small, generalized aerodynamics force becomes small. So, we introduced stopping tolerance to improve efficiency but also maintain accuracy by taking advantage of this characteristic.

b) Reducing number of computational cubes

Each cube of BCM has different convergence characteristics by its own flow field. Far field cubes have little flow change and converges rapidly. Therefore, BCM cubes are automatically divided into computational cubes and non-computational cubes during inner time iteration, based on residual values of flow variables. Fig. 4(b) shows schematic of computational cube groups and non-computational cube groups.



(a) Reducing number of inner time iteration



(b) Reducing number of computational cubes

Figure 4: Adaptive iteration techniques

3. VALIDATION RESULT (2D PITCHING AIRFOIL)

BCM was utilized to simulate a transonic NACA 0012 pitching airfoil¹²⁾. Fig.5 shows BCM mesh around the NACA 0012 airfoil.

As the airfoil oscillates, the shock transitions occur between the upper and lower surfaces of the airfoil. This hysteresis loop is evident in the C_l history plotted in Fig. 6(a). After an initial transient of approximately 1/2 cycle, the solution becomes periodic. At a given angle of attack, the C_l is multi-valued, depending on whether the airfoil is pitching up or down. Fig. 6(b) shows pitching down C_p distribution as an example.

The computed C_l hysteresis loop and C_p distribution are in good agreement with the experimental data.

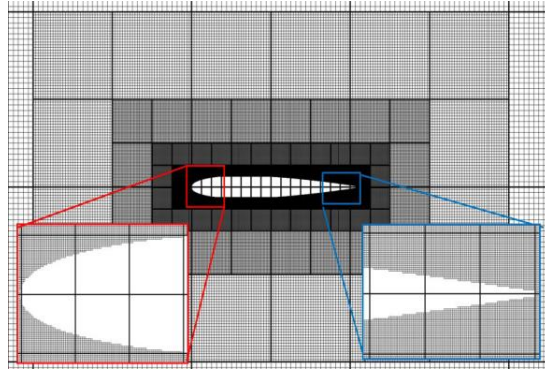
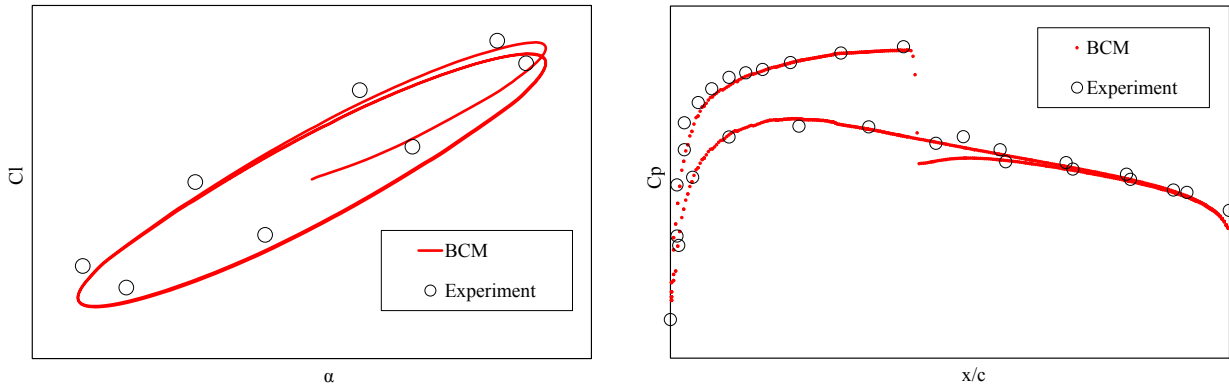


Figure 5: BCM mesh around the NACA 0012 airfoil



(a) C_l hysteresis loop

(b) pitching down C_p distribution

Figure 6: Example of validation analysis on a pitching airfoil

4. VALIDATION RESULT (3D FULLTER ANALYSIS)

Validation example with NASA ARROW WING¹³⁾ is shown in this section.

Fig. 7 shows the first four modal shapes, and Fig. 8 shows BCM cubes around NASA ARROW WING.

Fig. 9 shows the time history of generalized displacement. BCM fixed inner time iteration (fine) was sufficiently converged. On the other hand, BCM fixed inner time iteration (coarse) was not sufficiently converged. BCM adaptive iteration showed good agreement with BCM fixed inner time iteration (fine) by improving efficiency treatments.

Fig.10 shows the flutter boundary. BCM fixed inner time iteration (fine) and BCM adaptive iteration showed good agreement with the experimental flutter boundary. BCM fixed inner time iteration (coarse) was lower than the experimental flutter boundary around 1.0Mach.

Fig.11 shows calculation time. BCM adaptive iteration reduces to less than one-third of the total calculation times.

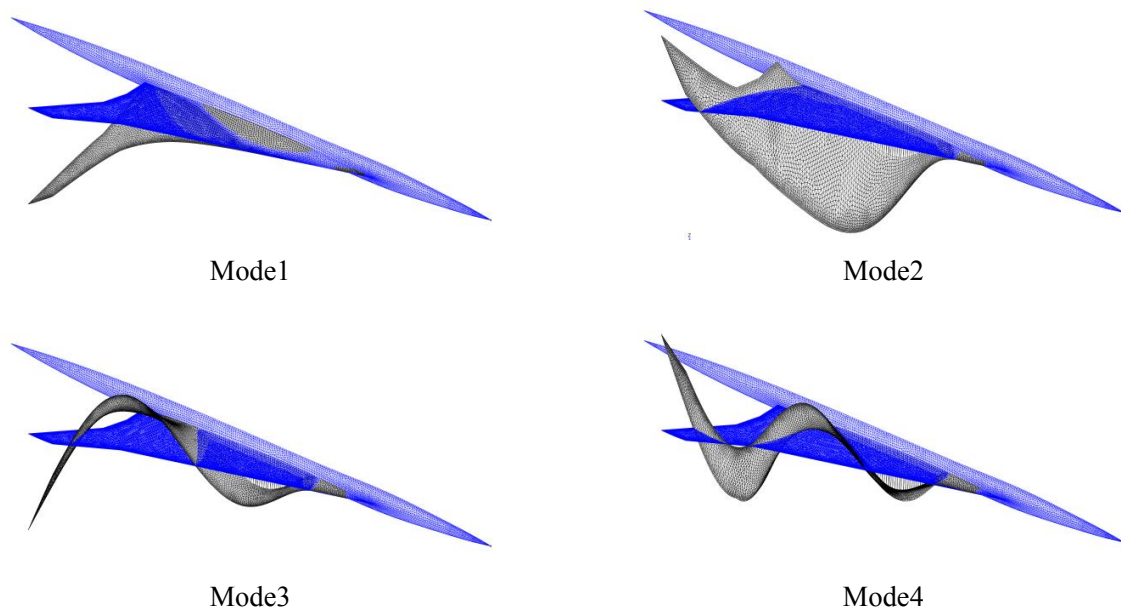


Figure 7: Mode shapes of NASA ARROW WING

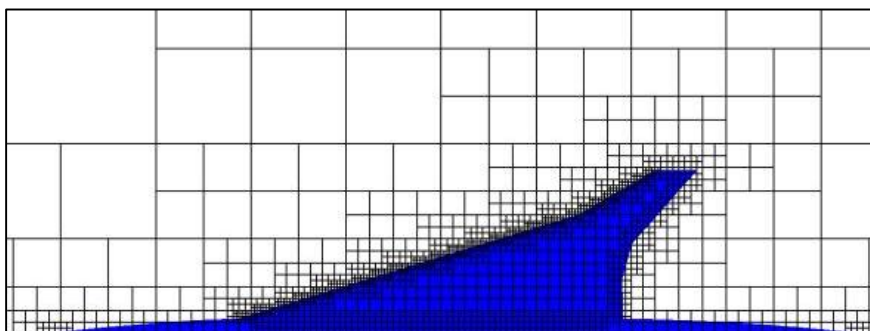


Figure 8: BCM cubes around NASA ARROW WING

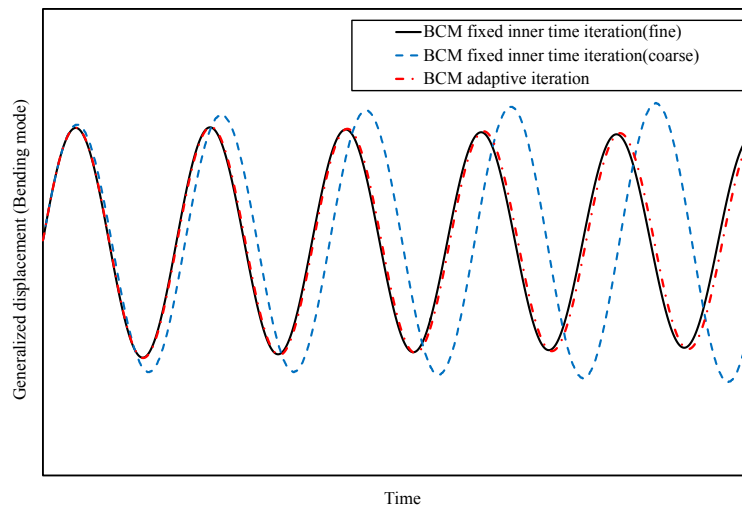


Figure 9: Generalized displacement time history

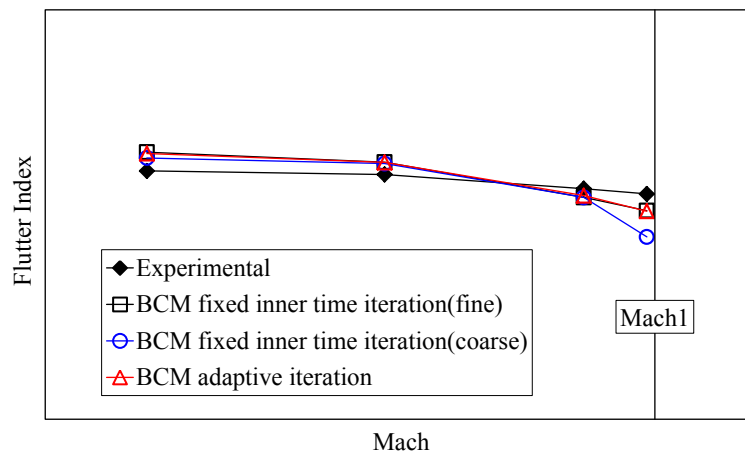


Figure 10: Flutter boundary

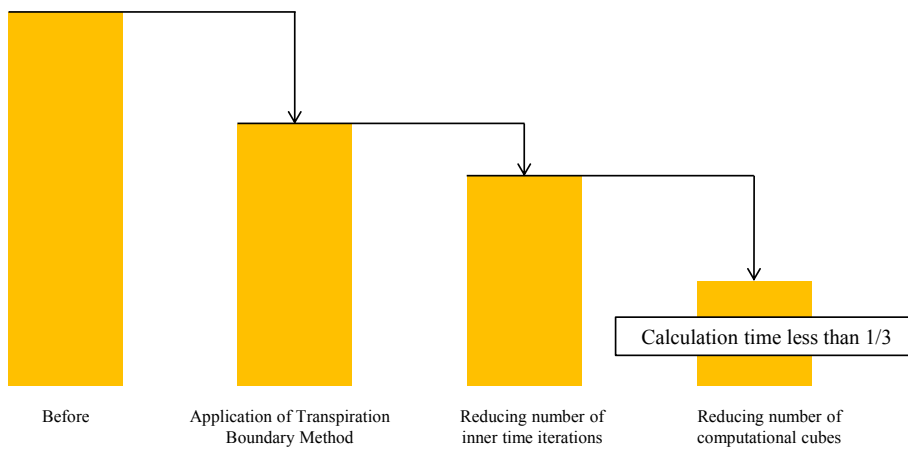


Figure 11: Improving efficiency flutter boundary analysis

5. CONCLUSIONS

The developed tool is validated with the NASA ARROW WING model. Computational time is greatly reduced to less than one-third by applying adaptive inner time iteration technique and reducing number of computational cubes. Predicted flutter boundary agrees well with experimental data.

ACKNOWLEDGMENT

This research has been conducted under auspice of JADC(Japan Aircraft Development Corporation) within HSTP (High Speed TransPort) Program.

REFERENCES

- 1) MSC/NASTRAN Aeroelastic Analysis USER'S GUIDE.
- 2) Nakahashi, K. and Kim, L. S. : Building-Cube Method for Large-Scale, High Resolution Flow Computations, AIAA Paper 2004-0423, 2004.
- 3) Obayashi, S. and Guruswamy, G. P. : Convergence acceleration of a navier-stokes solver for efficient static aeroelastic computations, *AIAA Journal*, 35(6):1134–1141, 1995.
- 4) Venkatakrisnan, V. : Preconditioned Conjugate Gradient Methods for the Compressible Navier - stokes Equations, *AIAA Journal*, Vol. 29, No.7, pp 1092-1099, 1991.
- 5) Yoon, S. and Jameson, A. : Lower-Upper Symmetric-Gauss Seidel Method for the Euler and Navier-Stokes Equations, *AIAA Journal*, Vol. 26 No. 9, pp. 1025-1026, .
- 6) Melville, R. B., Morton, S. A., and Rizzetta, D. P. : Implementation of a Fully-Implicit, Aeroelastic Navier-Stokes Solver, AIAA Paper 97-2039,1997.
- 7) Mittal, R., Dong, H., Bozkurttas, M., Najjar, F. M., and von Loebbecke, A. : A versatile sharp interface immersed boundary method for incompressible flows with complex boundaries, *Journal of Computational. Physics*. 227(10), 4825-4852, 2008.
- 8) Franke, R. : Scattered data interpolation tests of some methods, *Math. Compt.* 38 181-200, 1982.
- 9) Stephens, C. H., Aerna, A. S. Jr, and Gupta, K. K. : Application of the Transpiration Method for Aeroservoelastic Prediction Using CFD, AIAA Paper 98-2071, 1998.
- 10) Yang, S., Zhang, Z., Liu, F., Luo, S., Tsai, H. -M., and Schuster, D. M. : Time-Domain Aeroelastic Simulation by a Coupled Euler and Integral Boundary-Layer Method, AIAA Paper 2004-5377, 2004.
- 11) Chen, P. C., Zhang, Z., Sengupta, A., and Liu, D. D. : Overset Euler/Boundary-Layer Solver with Panel-Based Aerodynamic Modeling for Aeroelastic Applications, *Journal of Aircraft*, Vol. 46, No. 6 , pp. 2054-2068,2009
- 12) Landon, R. H. : Compendium of Unsteady Aerodynamic Measurements, AGARD Report No. 702, 1982.
- 13) Keller, D. F., and Bullock, E. P. : Span Reduction Effects on Flutter Characteristics of Arrow-Wing Supersonic Transport Configurations, NASA Technical Paper 3077,1991.

NUMERICAL SIMULATION TECHNIQUE FOR AEROELASTIC RESPONSE USING INVERSE FOURIER TRANSFORM

Tetsuhiko UEDA⁺¹ and Kenichi SAITOH⁺²

⁺¹Visiting Scholar JAXA, Professor emeritus Nagoya University, Japan

⁺²Institute of Aeronautical Technology JAXA, Tokyo, Japan

This paper reports a new simulation technique for aeroelastic systems which respond to external forces due to spatially distributed atmospheric turbulence. If the system equation includes the effects of unsteady aerodynamics which is analytically derived in the frequency domain, then the Inverse Discrete Fourier Transform (IDFT) can be utilized for simulating the response in the time domain. The response against the vertical gust is first calculated through a transfer function given in the frequency domain and then converted whole to in the time domain. The objective of the present study is to provide the system transfer function including the effects of unsteady aerodynamic characteristics and to simulate the response to external forces come from the random or spatially frozen gust. The technique may be utilized to establish the control law of active control device coping with discrete and/or random turbulence. The method can also be utilized to calculate mathematical time history data for evaluating the control performance against the realistic gust.

Keywords: Aeroelasticity, Random gust, Numerical simulation, Fourier transform, Flutter prediction, IDFT

1. INTRODUCTION

Wing flutter is one of the most critical problems to be solved before the final stage of aircraft design. After completing the design procedure, it must be demonstrated by flight tests that the airplane is completely free from fluttering. During the design procedure, flutter tests are also conducted with scaled models to confirm the flutter boundaries in the wind tunnel. In the following actual flight tests, it will be of importance to estimate the flutter boundary from the subcritical response data in the flight envelope¹⁾. Even during the wind tunnel test, it could happen that a precious wing model would be lost by abrupt occurrence of fluttering. Therefore, in both cases, the reliable prediction of the critical speed before flutter onset is highly required. Although quite a few methods have been proposed, it is still difficult to predict flutter. Difficulties are also for evaluating various prediction methods because the data acquisition by experiments and/or by the analysis is not an easy task. The aeroelastic analysis includes the complicate calculation of unsteady aerodynamic forces for the response of the system. As long as to find the flutter point, the method is thought to be matured with the aid of the linear theory of unsteady lifting surfaces. There is no efficient method, however, to simulate the subcritical response since the unsteady aerodynamics is mostly provided in the frequency domain except for the costly CFD. The other reason of the lack of reliable method for prediction is that it is quite difficult to obtain subcritical response data together with actual flutter occurrence experimentally. Hence, the numerical simulation with random external loads and/or with random internal noise from instruments is eagerly desired.

The phenomena of flutter involve the unsteady forces which are induced by the wing motion itself. In order to analyse them, theoretical aerodynamic forces are calculated with the functions of the so-called reduced frequency which is non-dimensionalized by a flow speed and a representative length. In the practical process, these forces are computed with at most about twenty reduced frequencies for several wing-deflection modes. Values between frequencies are interpolated to reduce cumbersome calculations of the generalized forces which are obtained by solving the singular integral equation.

Nowadays, however, the performance of an electric computer progressed tremendously and has made it easy to compute the unsteady aerodynamic forces even with a small workstation. Therefore it has become feasible to give them with respect to literally thousands of frequencies. This leads us to an idea that the time response of an aeroelastic system can be simulated by using thousands of discrete digital data in the frequency domain through the Inverse Discrete Fourier Transform (IDFT). Furthermore, if we choose the number of data as, say 1024 or 2048 for example, we can utilize the technique of FFT²⁾ directly even for the inverse transform without any approximation of interpolation between frequencies. This enables us to obtain the time series of response data with a constant flow speed below the

⁺¹ueda@nagoya-u.jp, ⁺²ksaitoh@chofu.jaxa.jp

flutter by converting the analysis in the frequency domain.

This paper reports the data handling in details of the conversion to simulate the aeroelastic response. It assumes the aeroelastic response is caused by the random turbulence or by spatially frozen gust.

The results can be applied to evaluate the reliability of various flutter prediction methods and to find the proper location of sensors which depends on the flutter characteristics. The simulation technique is also expected to contribute for examining the active control effects to attenuate the gust load.

2. DISCRETE FOURIER TRANSFORM (DFT)

The discrete Fourier transform and its inverse³⁾ are defined by the following pair of equations

$$G(m) = \frac{1}{N} \sum_{n=0}^{N-1} g(n) e^{-i \frac{2\pi m n}{N}} \quad (1)$$

$$g(n) = \sum_{m=0}^{N-1} G(m) e^{i \frac{2\pi m n}{N}} \quad (2)$$

where $g(n)$ denotes a series of digital signal with equally sampled in the time domain and $G(m)$ its DFT. Equation (2) is called as the inverse discrete Fourier transform which is abbreviated as IDFT. The variables m and n are integers and N is selected as multiple powers of 2 so as to utilize the efficient Fast Fourier Transform technique developed by Cooley and Tukey. Mathematically, DFT has the assumption that the time signal should be periodic. In practical cases, however, this restriction does not cause any problem because the duration of the actual signal is always finite and it can be treated as if it were one period.

3. IMPULSIVE RESPONSE AND TRANSFER FUNCTION

Generally, time history of the response can be obtained with a convolution integral of an impulsive response function and the external loads. An impulsive response function is equivalent to the inverse of the Laplace transform of the transfer function itself⁴⁾. Therefore it can be calculated with the inverse Fourier transform when the frequency response function of the system is given.

For the continuous signal, the impulsive response function of a system is directly related to the inverse Laplace transform of a transfer function $H(s)$.

$$g(t) = \mathcal{L}^{-1}[H(s)] \quad (3)$$

In the Laplace transformation domain, the impulse as an external force can be given by a unit function. Then the response becomes

$$G(s) = H(s) \cdot 1 \quad (4)$$

In case of the steady state response by harmonic excitation, Eq.(4) yields, by putting $s = i\omega$,

$$G(i\omega) = H(i\omega) \cdot 1 \quad (5)$$

This relationship describes the response with the uniformly distributed exciting force in the frequency domain. On the other hand, the definition of the Laplace transform is given by

$$G(s) = \int_0^{\infty} g(t) e^{-st} dt \quad (6)$$

Putting $s = i\omega$ in Eq.(6) leads us to an expression for the steady state response by the harmonic excitation.

$$G(i\omega) = \int_0^{\infty} g(t) e^{-i\omega t} dt \quad (7)$$

Here, in order to clarify the relationship between the Laplace transform and the Fourier transform, we extend the impulsive response function to the negative region of time as

$$g(-t) = g(t), (t > 0) \quad (8)$$

Then, the corresponding part of the function in the frequency domain becomes

$$G(-i\omega) = \overline{G(i\omega)} = \int_0^{\infty} g(t)e^{i\omega t} dt = \int_{-\infty}^0 g(-t)e^{-i\omega t} dt = \int_{-\infty}^0 g(t)e^{-i\omega t} dt. \quad (9)$$

Thus, we can obtain the Fourier transform as

$$G(i\omega) + \overline{G(i\omega)} = \int_{-\infty}^{\infty} g(t)e^{-i\omega t} dt = \hat{g}(\omega) \quad (10)$$

If we assume the transfer function $G(s)$ for an aeroelastic system including the effects of unsteady aerodynamic forces, then the spectrum of frequency response function becomes

$$G(i\omega) = \hat{g}(\omega) \quad (11)$$

This enables us to write the impulsive response $g(t)$ as an inverse Fourier transform.

$$g(t) = \mathcal{F}^{-1}[G(i\omega)], (t > 0) \quad (12)$$

Equation (12) implies that the discrete data of the time history can be converted from the discrete frequency data and vice versa through the pair of relations, Eqs.(1) and (2).

It should be noted that the amplitudes of the response calculated from the transfer function in the frequency domain by using the digital data with finite values are different from those obtained with a unit impulse in the continuous time domain. We have to adjust the level of each input whenever comparing those results.

Once the impulsive response function of a system has been obtained, then the time history for arbitrary external forces can be generated by the convolution integral⁵⁾. There is an alternative method, however, to obtain the response in the time domain, i.e. the application of inverse Fourier transform after the multiplication of the transfer function and the Fourier transform of the external forces. The present paper explains the latter technique since it is much efficient to simulate the response.

4. PROCESSING OF DIGITAL SIGNALS

(1) Implementation

The Theodorsen function for a two dimensional airfoil, or the unsteady lifting surface theory⁶⁾ for a finite wing, provides the unsteady aerodynamic force due to the system motion as functions of the reduced frequency, i.e. given in the frequency domain. Therefore, they cannot be expressed directly with the Laplace operator s which is corresponding to the differentiation with respect to time. This means that the transfer function of an aerodynamic system is written in the matrix of complex numbers while its responses of Eq.(2) are real numbers. In the application of IDFT to obtain time history data, we have to take this consideration correctly into account. The procedure is described as follows.

- (i) Assume $G(m)$ as an the aeroelastic response function in the frequency domain and calculate $(N/2+1)$ number of complex values for each frequency with an interval $\Delta\omega$ from $\omega=0$ up to $\omega=(N/2)\Delta\omega$.
- (ii) The corresponding duration time (a theoretical periodic interval in the time domain) and the sampling period of digital signal become, respectively,

$$T = 2\pi / \Delta\omega \quad \text{and} \quad \Delta t = T / N \quad (13)$$

- (iii) In order to hold the causality valid, the following complex conjugates are allotted to $G(m)$ for $m = (N/2+1), \dots, (N-1)$.

$$G(m) = \text{conj}[G(N-m)] \quad (14)$$

- (iv) Particularly at a center of the data series, we enforce to put

$$\text{Im}[G(N/2)] = 0 \quad (15)$$

(v) Since the present simulation is aimed for the aeroelastic subcritical analysis, there is no need to include the static displacement. Hence

$$G(0) = 0 \quad (16)$$

(vi) Applying IDFT to $G(0), \dots, G(N-1)$ thus formed yields a time history consisting of N number of digital data.

(2) Mathematical background

The discrete time signal can be written with the frequency response function $G(m)$ in the discrete frequency domain as

$$\begin{aligned} g(n) &= \sum_{m=0}^{N-1} G(m) e^{+i \frac{2\pi m n}{N}} \\ &= G(0) + \sum_{m=1}^{\frac{N}{2}-1} G(m) e^{+i \frac{2\pi m n}{N}} + G(\frac{N}{2}) e^{in\pi} + \sum_{m=\frac{N}{2}+1}^{N-1} G(m) e^{+i \frac{2\pi m n}{N}} \\ &= G(0) + \sum_{m=1}^{\frac{N}{2}-1} G(m) e^{+i \frac{2\pi m n}{N}} + G(\frac{N}{2}) e^{in\pi} + \sum_{m=1}^{\frac{N}{2}-1} G(N-m) e^{-i \frac{2\pi m n}{N}} \end{aligned} \quad (17)$$

The necessary and sufficient condition that the left hand side of Eq.(17) becomes a real number for any complex response data in the frequency domain can be given by

$$G(N-m) = \overline{G(m)}, \quad \text{for } m = 1, \dots, \frac{N}{2}-1, \quad \text{and } \text{Im}[G(\frac{N}{2})] = 0. \quad (18)$$

5. GOVERNING EQUATION OF AEROELASTIC SYSTEM

Assuming $D(i\omega)$ as the impedance matrix of a mechanical system and $A(\omega)$ as the unsteady aerodynamic matrix, we can write the governing equation for an aeroelastic system with the generalized coordinates \mathbf{q} as

$$[D(s) + A(\omega)] \mathbf{q} = \mathbf{f} \quad (19)$$

where the \mathbf{f} in the right hand side of the equation denotes the generalized external forces, which may also be random aerodynamic noise. If we re-define the transfer function of the system $H(i\omega)$ in the frequency domain as $H(\omega)$, then it can be obtained from Eq.(17) as

$$H(\omega) = [D(i\omega) + A(\omega)]^{-1} \quad (20)$$

Then the impulsive response of the system including the effects of the unsteady aerodynamic force is written for each component as

$$h_{ij}(t) = \mathcal{F}^{-1}[H_{ij}(\omega)], \quad (t > 0) \quad (21)$$

6. TYPICAL SECTION AIRFOIL

As an example problem, we shall use a typical section of the two-dimensional airfoil shown in Fig.1. Each parameter

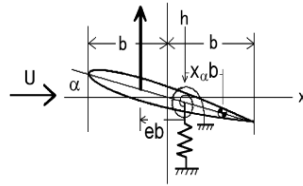


Figure 1: Typical Section Airfoil

is defined in the non-dimensionalized form. Different from the flutter analysis, the frequency Ω is normalized with respect to a pitching frequency ω_α instead of the so-called reduced frequency k . Defining the generalized coordinate vector as $\{h, \alpha\}^T$, we obtain a part of the transfer function except for the aerodynamic force as

$$D(s) = s^2 \begin{bmatrix} 1 & x_\alpha \\ x_\alpha & r_\alpha^2 \end{bmatrix} + \begin{bmatrix} R^2 & 0 \\ 0 & r_\alpha^2 \end{bmatrix}, \tag{22}$$

where R is a frequency ratio and r_α^2 is moment of inertia of the section which has been non-dimensionalized by the representative length and mass.

A textbook⁷⁾ provides the two-dimensional incompressible unsteady aerodynamic matrix for Eq.(19) with Theodorsen function having the argument of the reduced frequency. We denote the mass ratio as μ and the non-dimensional speed $U^* = U/(b\omega_\alpha)$. Additionally, the non-dimensional dynamic pressure and time are introduced by $Q = 2U^{*2} / \mu$ and $t^* = \omega_\alpha t$, respectively. As the flow is fixed to a certain speed in the present problem, the Theodorsen function $C(k) = C(\Omega/U^*)$ is written as $C(\Omega)$. Then the aerodynamic matrix can be given by

$$\begin{aligned} \mu A(\Omega) &= -\Omega^2 \begin{bmatrix} 1 & -e + \frac{1}{2} \\ -e + \frac{1}{2} & e^2 - e + \frac{3}{8} \end{bmatrix} + \\ i\Omega U^* &\begin{bmatrix} 2C(\Omega) & 1 + 2(1-e)C(\Omega) \\ -2eC(\Omega) & (1-e) - 2e(1-e)C(\Omega) \end{bmatrix} + U^{*2} C(\Omega) \begin{bmatrix} 0 & 2 \\ 0 & -2e \end{bmatrix}. \end{aligned} \tag{23}$$

In the following numerical examples, the parameters of the system are set as the same as the case(n) on the P538 of the reference. Those are $\mu = 10$, $e = 0.2$, $x_\alpha = 0.1$, $r_\alpha^2 = 0.25$, and $R = 0.3$. This combination of parameters results in the flutter critical dynamic pressure $Q_F = 0.80$ with the flutter frequency $\Omega_F = 0.62$.

7. FINITE STATE MODEL

In order to compare the results obtained by the present IDFT procedure, a time domain method using the finite state model is introduced. The aerodynamic effect is embedded in the system of differential equations approximately with the augmented state variables. For unsteady aerodynamic terms, the following form of the finite state⁸⁾ is used,

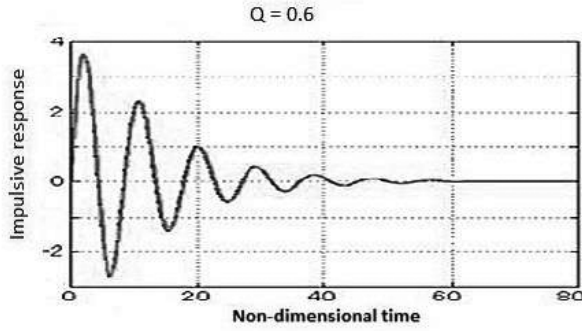
$$F_a(s, \mathbf{q}) = \left(A_2 s^2 + A_1 s + A_0 + \sum_{i=1}^3 \frac{A_{L_i}}{s + \lambda_i} \right) \mathbf{q}, \tag{24}$$

where the symbol \mathbf{q} denotes the generalized coordinate vector. The coefficients in Eq.(24), A_2 , A_1 , A_0 , and A_{L_i} are determined with the aid of the least square method after the calculation by DPM⁹⁾ for the frequencies from 0.01 to 2.0. The interval of the frequency is selected as 0.01 and the three arbitrary parameters λ_i 's are selected as 0.1, 0.5, and 1.5.

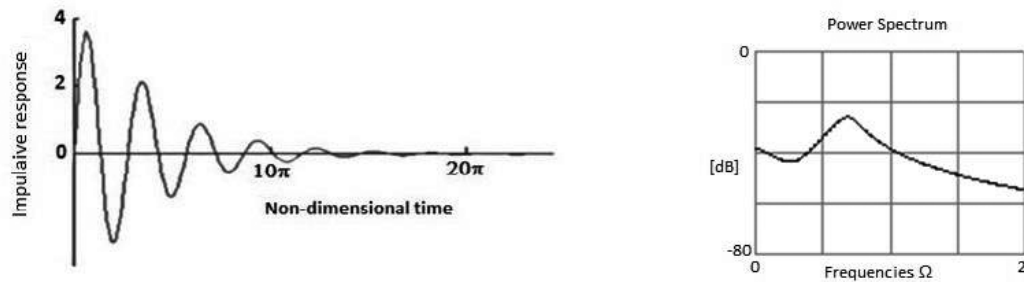
8. NUMERICAL EXAMPLES

(1) Impulsive response

For a certain dynamic pressure below the flutter critical speed, the impulsive response is calculated by applying IDFT to the transfer function which is given by Eq.(20). The discrete values of the function are computed for $N/2=1024$ frequencies with a frequency increment $\Delta\Omega=0.01$. This yields 2048 data in the time domain with the sampling rate $\Delta t^*=0.3068$. In the practical calculation, this distribution may be appropriately cut for higher frequencies above $\Omega=5$ since the two natural frequencies of the system in this case are well below as $\Omega=0.3$ and 1. Figure 2 illustrates the response of $h(t^*) = h_{\alpha h} + h_{\alpha\alpha}$ due to the α impulse.



(a) Impulsive response by the finite state model



(b) Impulsive response by the inverse Fourier transform

Figure 2: Comparisons of two Methods

It should be noted that a unit impulse, which is Dirac’s delta function mathematically in the continuous domain, corresponds to a single finite value of $1/\Delta t$ at the starting point of the discrete data series and that the constant amplitude in the frequency domain must be $1/(N\Delta t)$ to make the powers of both signals equal to each other. It can be seen from the figures that the results obtained by IDFT agree well with those by the finite state model in the time domain.

(2) Discrete gust response

As mentioned before, once the impulsive response becomes known, it enables us to calculate a system response against general shapes of the external input by using the convolution integral. If we put the input and the impulsive response of the system as $f(t)$ and $h(t)$, respectively, then the response $x(t)$ is given by so-called Duhamel’s integral.

$$x(t) = \int_0^t h(t - \tau) f(\tau) d\tau \tag{25}$$

In the frequency domain, this relationship becomes

$$\hat{x}(\omega) = \mathfrak{F}[h * f(t)] = \hat{h}(\omega) \hat{f}(\omega) . \tag{26}$$

Therefore, the response in the time domain for the discrete data can be calculated as

$$x(n) = \text{IDFT}[\hat{x}(m)] = \text{IDFT}[\hat{h}(m) \hat{f}(m)] . \tag{27}$$

An example result of this procedure is shown in Fig. 3.

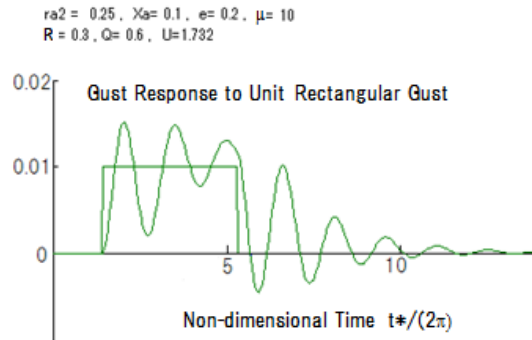


Figure 3: Transient response of the aeroelastic system

(3) Random noise

The random noise can be generated by the present method as follows. First, assume the transfer function of Eq.(20) as a unit matrix. Then, the components of random external forces in Eq.(19) are calculated in the frequency domain as

$$F(m) = \Phi(m)e^{i\phi_m}, \tag{28}$$

where the phase ϕ_m can be provided with the uniformly distributed random number between 0 and 2π . In case of the white Gaussian noise, the spectrum $\Phi(m)$ must be the Gaussian distribution. The IDFT conversion after these calculations gives a series of the random signal. The similar noise can be also generated in the time domain by superimposing the cosine function for the entire interval¹⁰⁾. Results by both methods are compared in Fig.4 for a series of random signal having the unit average amplitude and the standard deviation of 0.3.

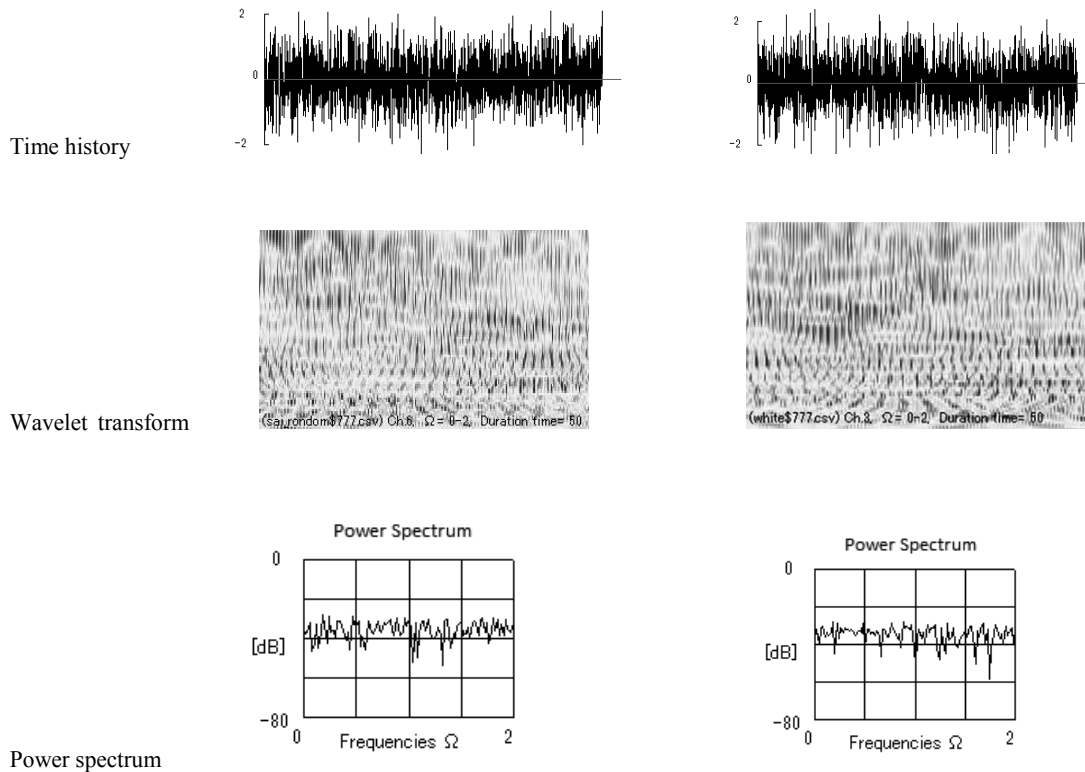


Figure 4: (a) Time Domain Method (b) Present IDFT Method

The result looks being agreed well to each other because the both procedures are theoretically equivalent. It should be noted that the present method is much more efficient in view of the computation time due to the FFT algorithm.

(4) Simulation of random response of a typical section airfoil

For the same dynamic pressure as that in the example of 8.1, an aeroelastic response due to the random noise has been calculated. The result is depicted in Fig. 5(a) with its power spectrum 5(b). The smooth curve in the figure indicates the power spectrum of the impulsive response, i.e. the response without noise. It can be seen that the random noise is properly included in the response.

Furthermore, the dependency of the cross spectrum between the h and α of the response on the dynamic pressure is illustrated in Fig.5(c). The figure reveals the coupling of two modes which is going into flutter at the dynamic pressure of $Q=0.8$.

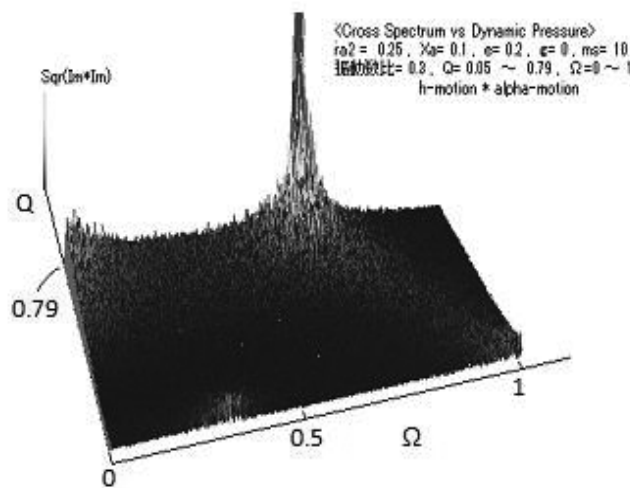
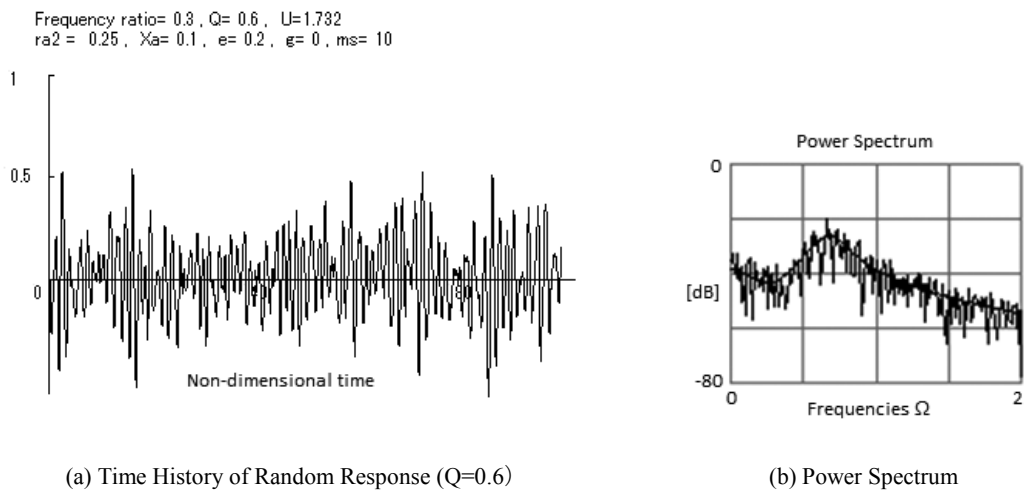


Figure 5: Simulation results

9. APPLICATION OF IDFT SIMULATION METHOD FOR RANDOM GUSTS

An example application of the present technique has been carried out on the flutter prediction using the wavelet transform¹¹⁾. The definition of the wavelet is given by

$$f_{\psi}^w(b,a) = \frac{1}{\sqrt{|a|}} \int_{-\infty}^{\infty} f(t) \overline{\psi\left(\frac{t-b}{a}\right)} dt \tag{29}$$

$$\psi(t) = \frac{1}{\sqrt{2\pi\sigma^2}} \exp\left(-\frac{t^2}{2\sigma^2}\right) \exp(i\omega_0 t) \tag{30}$$

Here we use Gabor’s mother wavelet as described in Eq.(30).

In Fig.6, the simulated signals of the α motion are displayed for eight different dynamic pressures.

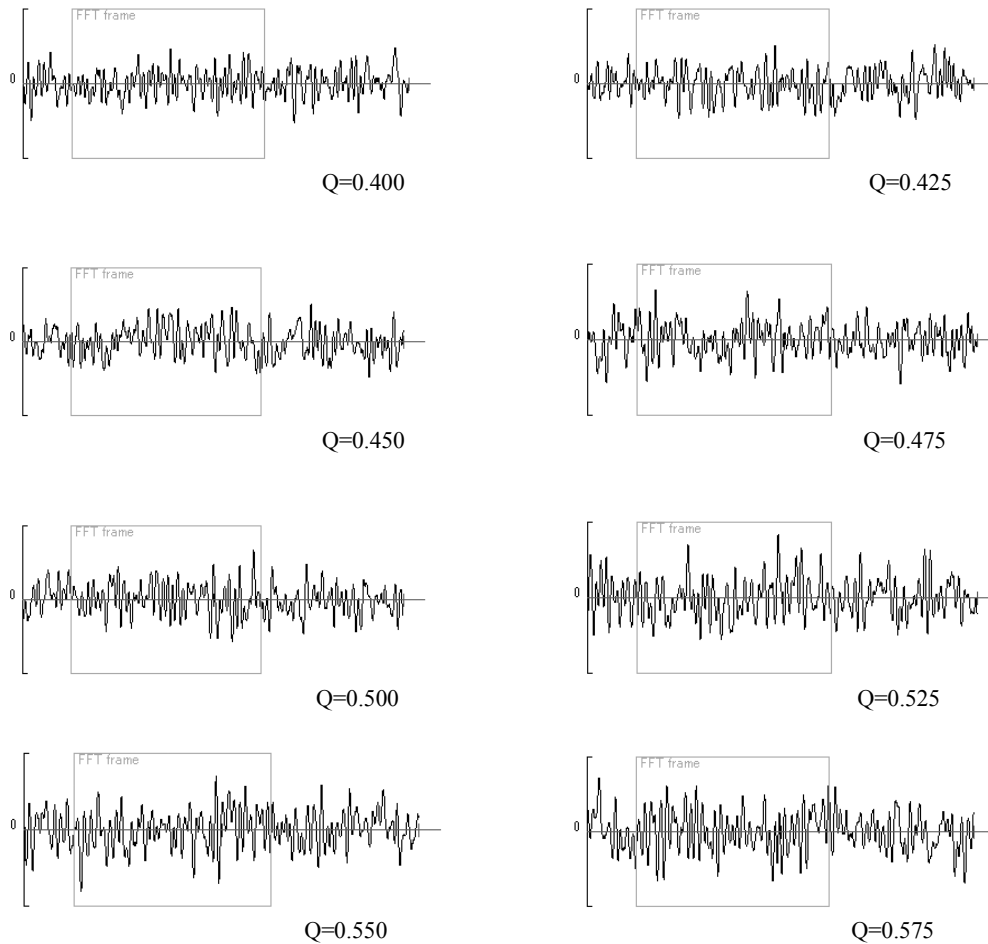


Figure 6: Simulated Response Signals for each Dynaic Pressure

These may be regarded as the output of ‘virtual experiments’ for the purpose of examining flutter prediction methods. The data in the frameworks above have been applied to the wavelet prediction method. The result is shown in Fig.7.

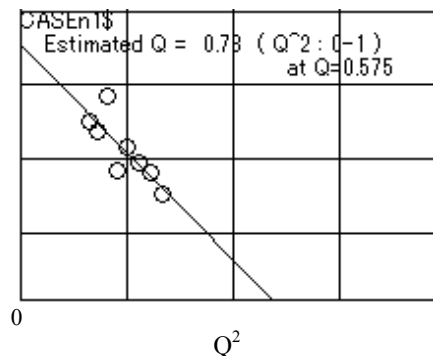


Figure 7: Wavelet Flutter Prediction from the Simulated Signals

It can be seen from the figure that the present simulation technique provides realistic output of the virtual experiment.

10. CONCLUDING REMARKS

The method using the inverse discrete Fourier transform to simulate the aeroelastic response to the random and/or discrete gust has been proposed and demonstrated. It is expected to be utilized for evaluating various methods to predict flutter and the performance of the active control technique to attenuate the response against the atmospheric turbulence.

REFERENCES

- 1) Zimmerman, N. H., Weissenburger, J. T. :Prediction of Flutter Onset Speed Based on Flight Testing at Subcritical Speeds, *Journal of Aircraft*, Vol.1, No.4, pp.190–202, 1964.
- 2) Cooley, J. W., Tukey, J. W. :An Algorithm for the Machine Calculation of Complex Fourier Series, *Mathematics of Computation*, Vol.19, pp.297-301, 1965.
- 3) e.g. Randall, T. B. :Application of B & K Equipment to Frequency Analysis, Denmark, Naerum Offset Tryk, p.187, 1977.
- 4) Thomson, W. T. :Laplace Transformation, Englewood Cliffs, Prentice-Hall, Inc., p.37, 1960.
- 5) Nishijima, H., Ueda, T., Ikeda, T. :A Study on Reliability of Flutter Prediction Method, *JSASS 51st Conference on Aircraft Structures*, 2A12 (in Japanese), 2009.
- 6) Küssner, H. G. : General Airfoil Theory, *Luftfahrtforschung* Vo.17, No.11/12, pp.370-378, 1940.
- 7) Bisplinghoff, R. L., Ashley, H., Halfman, R. L. :Aeroelasticity, Cambridge, Addison-Wesley Pub. Co. Inc., p.272, 1955.
- 8) Baldelli, D. H., Ohta, H., Matsushita, H., Hashidate, M., Saitoh, K. :Flutter Margin Augmentation Synthesis Using Normalized Coprime Factors Approach, *Journal of Guidance, Control, and Dynamics* Vol.18, No.4, pp.802–811, 1995.
- 9) Ueda, T. :Unsteady Aerodynamic Calculation for General Configuration by the Doublet-Point Method, *Technical Report of National Aerospace Laboratory (NAL) TR-1101T*, Tokyo, 1991.
- 10) Shinozuka, M., Jan, C.-M. :Digital Simulation of Random Processes and its Applications, *Journal of Sound and Vibration*, Vol.25, No.1, pp.111–128, 1972.
- 11) Ueda, T., Iio, M, Ikeda, T. :Flutter Prediction Using Continuous Wavelet Transform, *Transaction of the Japan Society for Aeronautical and Space Sciences* No.174, pp.275–281, 2009.

FLUTTER PREDICTION IN MODERN AIRCRAFT ENGINES AND GAS TURBINES

Mikhail Kolotnikov⁺¹, Pavel Makarov⁺², Farrukh Abdukhakimov⁺³, and Vasily Vedeneev⁺⁴
^{+1,3,4}Lomonosov Moscow State University, Moscow, Russia
⁺²Gas Turbine Engineering Research and Production Center “Salut”, Moscow, Russia

Blade flutter of modern jet engines and gas turbines is one of the main issues that engine designers have to face. The most used numerical method that is employed for flutter prediction is the energy method. Although a lot of papers are devoted to the analysis of different blade wheels, this method was rarely validated by experiments. Typical mesh size, time step, and various modeling approaches that guarantee reliable flutter prediction are not commonly known, whereas some examples show that predictions obtained through nonvalidated codes can be inaccurate. In this paper, we describe the implementation of the energy method that is employed in the design of jet engines and gas turbines in Gas Turbine Engineering Research and Production Center “Salut”. Flutter onset predictions are obtained for two wheel models representing two stages of the same compressor. For the model of a blade wheel, blade oscillations in a natural mode are specified and unsteady aerodynamic analysis is conducted. Then the work done by unsteady pressure over the oscillation cycle is calculated, and based on its sign the flutter prediction is made. Numerical results are verified by compressor and full engine flutter test data. Tests were conducted in two operating regimes: stable and flutter. It is shown that the prediction of flutter onset is rather reliable so that the modeling approaches presented in this paper can be used by other researchers for the flutter analysis of industrial compressor and turbine blades.

Keyword: blade flutter, jet engines, gas turbines

1. INTRODUCTION

AIRCRAFT gas-turbine engine designers were faced with compressor blade flutter in the middle of the 1950s while developing the second generation of jet engines. At the present day, a huge theoretical and practical experience has been accumulated. Typically, regions of the various flutter types are plotted on the compressor operating map. They were developed by different researchers and are very similar [1-5]. The scheme in Fig. 1 proposed in [2] can be considered as atypical example. This map clearly shows that possible flutter regions are mainly located near the surge line or significantly lower than the compressor operating line. When operating in these regions, the airflow in the blade passages is unsteady, including unsteady recirculation zones and possibly shocks. The only exceptions are the regions bounded by lines 3, 4, and 6. They lead to the blade flutter near the operating line for unstalled flow. Recently, it was demonstrated [6] that the region bounded by line 2 can also be located near the operating line, and the flow can be continuous.

The problem of numerical flutter prediction for the compressor or fan blade wheels is associated with the coupled aeroelastic problem, which first needs a solution for a steady-state flow in blade passages. Modern computational codes, such as Ansys CFX, Star-CCM, Fluent, FlowVision, etc., provide reliable airflow parameters in blade passages near the operating line, where the flow is unstalled.

For surge line (region 1) and for stalled flow (regions 2, 5, and 7), it is very difficult (and usually impossible) to determine reliable airflow parameters numerically, which is why the numerical prediction of blade flutter boundaries for these regions usually cannot give any valid results.

⁺¹mekolotnikov@mail.ru, ⁺²makarovpv@yandex.ru, ⁺³farruh.abduhakimov7@gmail.com, ⁺⁴vasily@vedeneev.ru

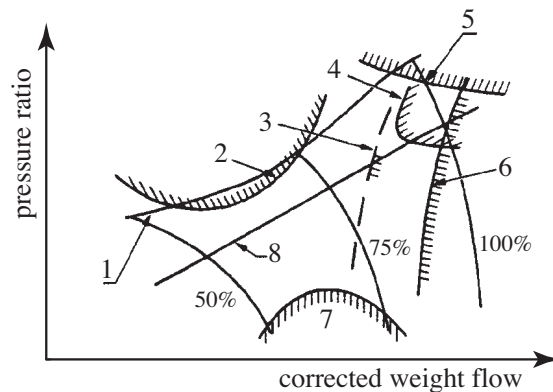


Fig. 1 Compressor map [2]: 1) surge line, 2) subsonic stalled flutter, 3) bending-torsional flutter, 4) supersonic unstalled flutter induced by shocks, 5) supersonic stalled flutter, 6) supersonic unstalled flutter, 7) choking flutter, and 8) operating line.

However, for the design phase of modern gas-turbine engine compressors and fans, the most important is to suppress flutter around the operating line with required safety margins because this provides the ability for test validation of the main characteristics of the new compressors. The dynamic stress state of compressor or fan blades operating near the surge line and in regions of stalled flow is typically determined experimentally during the refinement of the engine.

In this paper, we implement the energy method in 3-D formulation for blade flutter analysis, which uses unsteady aerodynamics from the industry-recognized code Ansys CFX. We investigate the influence of modeling different features: number of blades simulated, modeling of the blade shroud, and effects of manufacturing tolerances, expressed in the distortion of the blade mode shapes, tension in the blade shroud, and the inlet angle of attack. Results are validated by test results obtained for two blade wheels. Each wheel is tested and numerically analyzed at two regimes, one of which is stable and the other is the flutter regime. Numerical parameters used in calculations and the influence of various modeling features validated in this paper can be used by other investigators for reliable predictions of the flutter onset.

The structure of the paper is as follows. First, in Sec. 2, we describe in detail the energy method and formulate a step-by-step algorithm. In Sec. 3, we numerically analyze two blade wheels. Finally, in Sec. 4, we present results of an experimental study of the wheels analyzed, which validate the method developed.

2. METHOD OF FLUTTER PREDICTION

We assume that the influence of the flow on natural blade modes and frequencies is negligible. This assumption is valid for the case of sufficiently stiff blades, when flow disturbances excited by small blade vibration have no significant action on blade eigenmodes. Therefore, the airflow can result only in small additional damping (for stability case) or additional energy inflow (for flutter case) without change of natural modes and frequencies. The energy equation for a blade in a coordinate system rotating with the wheel is

$$\frac{dE(t)}{dt} = A(t) \quad (1)$$

where $E(t)$ is the total energy, and $A(t)$ is the power of internal and external forces. Neglecting structural damping and viscous forces of the flow, we assume that the only force is the air pressure distributed along the blade surface. Then the change of the total energy over the cycle of oscillation is

$$\Delta E = W = \int_{t_0}^{t_0+T} \int_S p(x, y, z, t) \mathbf{n}(x, y, z, t) \mathbf{v}(x, y, z, t) ds dt \quad (2)$$

where $T = 1/f$ is the blade oscillation period (f is the natural frequency), S is the blade surface, p is the flow flow pressure, \mathbf{n} is the blade surface normal, and \mathbf{v} is the velocity of the blade points.

Since the flow influence on the blade oscillations is small, the work W done over actual (growing or

damped) oscillation is also small. The work over harmonic (i.e., constant amplitude) oscillation is different from the actual work by a second-order infinitesimal term, which is neglected. Harmonic oscillation shape is assumed to be obtained from the modal analysis of the blade in vacuum using standard engineering software.

Thus, we calculate the work done by pressure over specified oscillations of the blade during one oscillation period. The following inequality is a criterion of flutter:

$$W > 0 \quad (3)$$

The finite-volume model of the flow consists of three or five consecutive blade passages of one stage (Figs. 2a and 2b). For unsteady fluid flow analysis, initial and boundary conditions are extracted from steady-state flow calculated for the full compressor (where all stages are modeled), verified by full-scale compressor tests. Namely, we specify the distribution of the total pressure, total temperature, velocity, and turbulence parameters at the inlet (Fig. 2c) and distribution of static pressure at the outlet. A no-slip condition

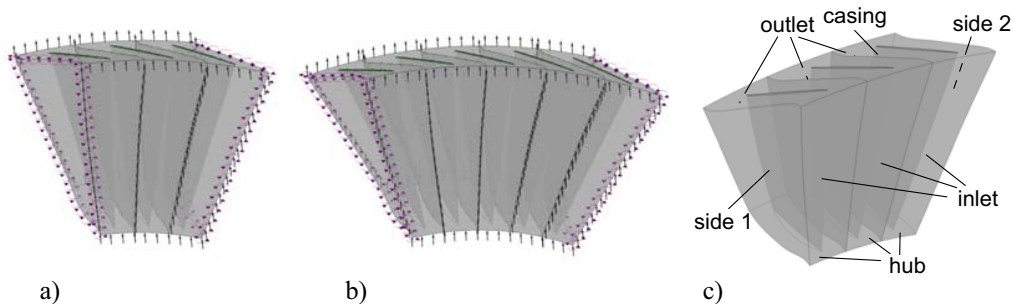


Figure 2 Models of consecutive blade passages: a) three, b) five; and c) boundary conditions.

is assigned at solid body surfaces: hub, blades, and casing; for the latter surface, the no-slip condition is applied in the counterrotating coordinate system. The condition of rotational periodicity connects flow parameters at sides 1 and 2 (Fig. 2c). Note that latter boundary condition (the only available in the aerodynamic code used) distorts the traveling wave in the flow, so that it is necessary to model several consecutive blade passages and calculate the work done over the middle blade, which is the most remote from sides 1 and 2. For codes where the phase lag between sides 1 and 2 can be taken into account, one passage is enough for the modeling the traveling wave.

Mesh displacement in the form of the wheel natural mode with a specified number of nodal diameters is applied to each blade surface: $\mathbf{u}(x, y, z, t) = A \sin \omega t \times L_n(x, z)$, where A and $\omega = 2\pi f$ are the blade oscillation amplitude and circular frequency, and $L_n(x, z)$ is a function representing the mode shape. We use the 10th-order Lagrange interpolation polynomial for interpolating finite-element mode shape results and transferring them to the computational-fluid-dynamics code.

For modeling a forward (or backward) traveling wave, which is typical for compressor blade flutter [7], phase lag $\sin(\omega t - \varphi)$ and lead $\sin(\omega t + \varphi)$ with respect to the middle blade are specified for neighboring blades, where the phase shift $\varphi = 2\pi m/N$ corresponds to the number of nodal diameters m . In the case of the five-blade model, the phase shift for the side blades is $\pm 2\varphi$.

In accordance with the procedure described, flutter analysis consists of four stages: 1) modal analysis of elastic blades, interpolation of mode shapes by Lagrange polynomials; 2) steady-state flow analysis in compressor; 3) unsteady flow analysis of a certain compressor stage with blades oscillating (i.e., fluid mesh moving) in a specified mode obtained in step 1; and 4) the calculation of work Eq. (2) done by pressure for the middle blade and check of criterion (3).

Steps 3 and 4 are executed for each natural mode potentially sensitive to flutter. Work is calculated for the last of several simulated cycles of oscillations, such that the flow response to the blade oscillations is pure harmonic. Calculations show that three periods are typically enough to have a harmonic response.

A structural modal analysis is performed using the Ansys Mechanical finite-element software. For fluid flow analysis, we use Ansys CFX, version 12.1. Reynolds-averaged Navier-Stokes (RANS) equations with $k - \epsilon$ turbulence model are solved. For polynomial interpolation and calculation of work done by unsteady pressure,

special in-house codes have been developed.

Table 1 Parameters of the wheels and regimes considered

Parameter	Wheel 1	Wheel 2
Number of blades (N)	45	37
Rotor speed n , Hz	136.0	159.5/170.0
Inner to outer diameter ratio d/D	0.570	0.435
Relative blade spacing $t_{0.5}/b_{0.5}$	0.800	0.766
Blade aspect ratio $h/b_{0.5}$	3.120	3.554
Midspan shroud location h_s/h	0.710/ (n/a)	0.772

Flutter onset predictions and test data presented in this paper are obtained for two wheel models representing two stages of the same compressor (Table 1, index “0.5” means the middle of the blade span). Each wheel is analyzed in two configurations:

1) Wheel 1 with shrouded and with cantilever blades. The cantilever blade wheel is a special test wheel with blade shrouds cut to be out of contact with other blade shrouds. This wheel represents wear of material in contact pairs of the shroud. A fixed rotation speed specific for the throttle regime (compressor operating near region 3 in Fig. 1) is studied. Airflow parameters correspond to zero altitude and zero Mach number at the engine inlet. The flow at the stage inlet is transonic, with average Mach number $M \approx 0.9$ and 0.95 at 50 and 90% of the blade span, respectively. The flow at the blade passage has a certain supersonic region.

2) Wheel 2 with shrouded blades. Rotor speeds $n = 159.5$ and 170 Hz are analyzed. In the first case, the average Mach number at the stage inlet is subsonic, $M \approx 0.7$ and 0.9 at 50 and 90% of the blade span, respectively; in the second case, the flow is supersonic: $M \approx 1.2$ and 1.4 . The flow in the interblade passage is fully subsonic in the first case and has a significant supersonic portion in the second case. Because of the closeness of the physical rotation speeds, we assume that the blade natural modes and frequencies are the same and consider only the difference in the aerodynamics.

Previously we have studied numerical convergence, implementation features (number of blades in the model, oscillation amplitude, etc) and structural effects: assembling force between contact surfaces of midspan shroud, deviation of the blade mode shape due to manufacturing tolerances, and inlet flow incidence angle [8].

To make sure that the steady aerodynamics, which is the basis for flutter analysis, is correctly obtained, let us consider the operating map of the compressor (Fig. 3), where the results of the numerical analysis and experimental points are shown. It is seen that the agreement between steady flow calculations and experiments is rather good. Thus, we consider the steady flow as correctly representing real airflow and can use it for unsteady flow analysis due to blade oscillations.

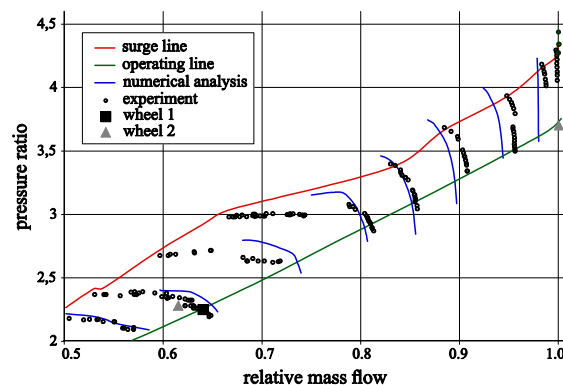


Figure 3 Operating map of the compressor. Flow regimes corresponding to the analysis of wheels 1 and 2 are shown by black squares and gray triangles, respectively.

3. RESULTS OF NUMERICAL FLUTTER PREDICTION IN BLADE WHEELS

(1) Wheel 1

The calculation of work done by pressure was conducted for the first four natural modes. Each mode was analyzed in a full range of possible numbers of nodal diameters. Oscillations are specified in the form of forward (along the wheel rotation) or backward traveling wave. Amplitude was normalized such that the maximum blade stress was 5×10^7 Pa. As explained previously, we investigated two configurations of this wheel. The first, “shrouded”, is a production wheel; in particular, shroud contact pairs are in a perfect contact. The other, “cantilever” wheel, has blade shrouds slightly cut to be out of contact with shrouds of the neighboring blades. This wheel represents wear of material in shroud contact pairs after long operation time. The first four frequencies and mode shapes are shown in Fig. 4 for both wheel configurations; it is implied that the disk does not influence the blade eigenmodes, hence the mode shapes do not depend on the nodal diameter m . It is seen, first, that the natural frequencies of the cantilever wheel are lower than those of the shrouded one due to the less overall stiffness of the structure. Second, and most important, in the range $n = 70 \dots 80\%$, there is a mode shape exchange between the second and the third modes of cantilever blades; bending mode becomes torsional, and vice versa, which signifies a possible flutter occurrence. That is why flutter analysis has been conducted for $n = 80\%$, where the frequencies of the first four modes are 232, 576, 664, and 1328 Hz for cantilever blades and 683, 1069, 1501, and 2299 Hz for shrouded blades (note that the lowest mode in Fig. 4a cannot appear on a real wheel because the shroud has essentially nonzero displacement; this mode is excluded from consideration).

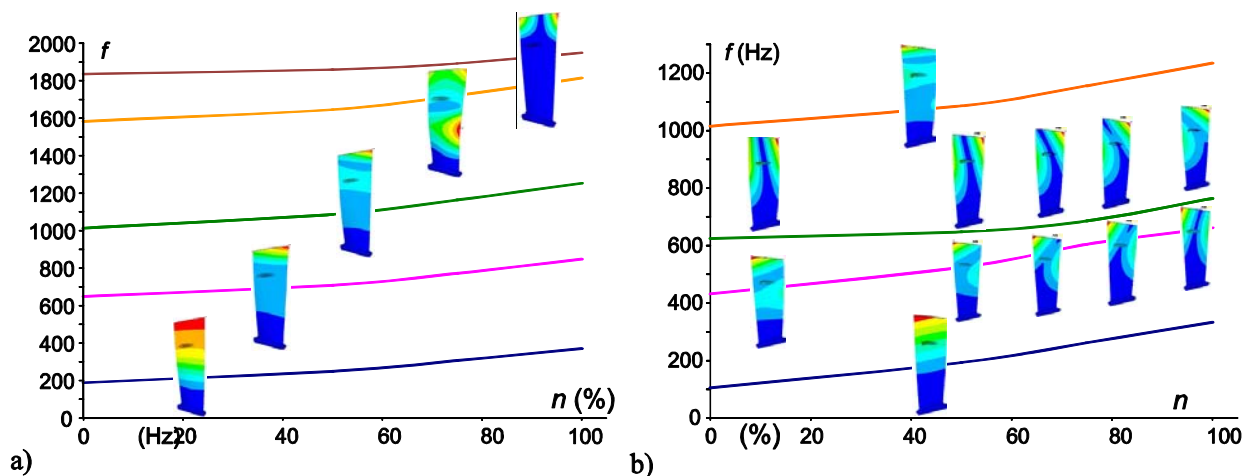


Figure 4 Campbell diagram of wheel 1: a) shrouded, and b) cantilever. Blade contours represent relative displacement amplitude.

We assume that the cut of the blade shroud does not affect aerodynamics and use the same steady flow for both configurations. Work done over modes of cantilever blades is shown in Fig. 5a. Work for the first and fourth modes is negative, whereas for the second and third modes it is positive for $m = 5 \dots 11$ and $5 \dots 16$, respectively. Therefore, for this wheel, we predict blade flutter in the second and third modes.

Work calculated for the same wheel with shrouded blades is shown in Fig. 5b. For the first four natural modes, the work is negative. We therefore predict the stability of this blade wheel. The difference in flutter predictions for blades that are in and out of contact with each other through the midspan shroud leads us to a conclusion that a wheel that was initially designed to be flutter-free can actually flutter after some time of operation due to wear of material in the shroud and following change of the blade mode shapes and frequencies. To avoid this, the designer should determine safe operation period by taking into account change of modes and frequencies due to wear.

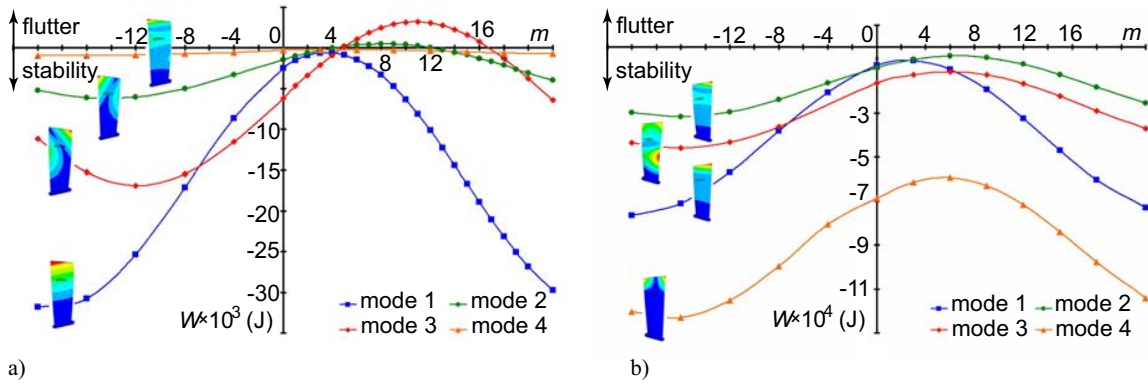


Figure 5 Work done by unsteady pressure vs the number of nodal diameters for wheel 1: a) with cantilever blades, b) with shrouded blades.

(2) Wheel 2

Flutter analysis for the shrouded wheel 2 has been conducted for two operating regimes, corresponding to very close rotation speeds, $n = 94$ and 100% , which is why we used the same mode shapes and frequencies; the difference is only in aerodynamics. Blade eigenmode calculation was conducted with the disk elasticity taken into account; blades are in perfect contact through the shroud contact pairs. The resulting eigenmodes turned to be very sensitive to nodal diameters; the interference diagram is shown in Fig. 6. For the work calculation, we specified oscillation amplitude such that the maximum blade stress was 10^7 Pa. Work-per-cycle calculated for these modes is shown in Fig. 7c as “no tension” line. In contrast to wheel 1, it is not sinelike because each nodal diameter was modeled not only by a different phase shift but also by a different mode shape. It is seen that, for $m = 8 \dots 10$, the work, though negative, comes close to zero, which means that the flutter boundary is somewhere close, and a slight change in the problem formulation can replace stability by flutter.

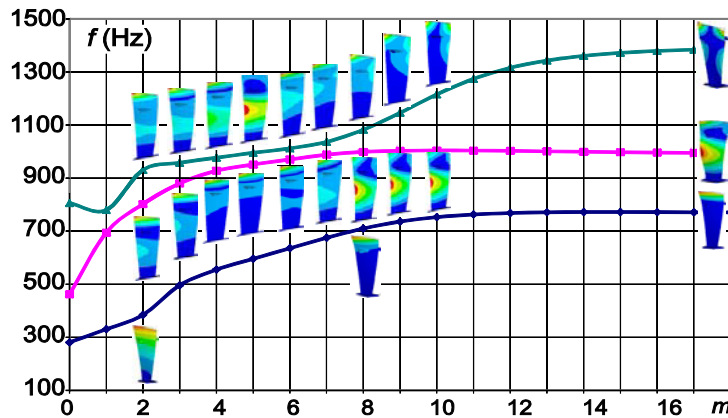


Figure 6 Interference diagram of the wheel 2 at $n = 100\%$ (first three modes are shown).

Such an important feature ignored so far is a shroud force. Indeed, when assembling the wheel, one should apply some force to a blade to make its shroud contacting with the neighboring blade shroud. As a result, in the assembled wheel, each blade is pretensioned by a force, which makes blades contacting each other through the shroud. Such a tension can affect the mode shapes and change flutter prediction. Calculated mode shapes with shroud tension taken into account show that the first family of modes (bending modes, Fig. 8a) is close to those with no tension; however, the second and the third mode families (bending-torsional modes) are mixed, and one cannot clearly distinguish nodal diameters (Fig. 8b). In this situation, we took a blade mode that is closest to the one of untensioned wheel modes (namely, $m = 3$ for bending modes and $m = 9$ for bending-torsional modes) and changed nodal diameters without changing the mode shape and frequency.

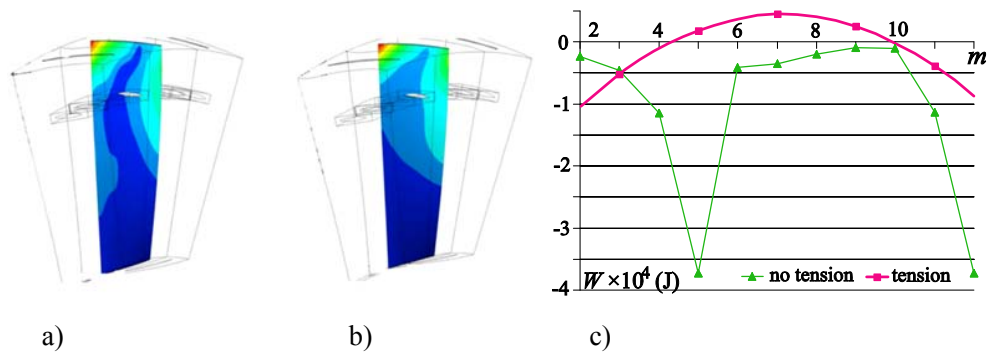


Figure 7 Effect of shroud tension of the wheel 2 on the second mode at $n=159.5$ Hz: a) tensioned blades ($m=9$), b) untensioned blades, and c) work vs m .

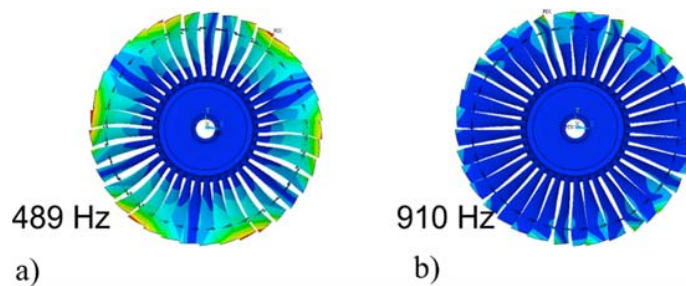


Figure 8 Examples of natural modes calculated with shroud force taken into account: a) bending family, nodal diameters are clearly distinguished, and b) bending-torsional mode, no clear nodal diameters are seen.

This simplified approach does not exactly represent the physics but gives a qualitative effect of the shroud tension. The tension turned out to be extremely important due to change of the mode shapes (Figs. 7a, 7b). Shown in Fig. 7c, by “tension” curve is the work calculated for a tensioned wheel in the manner described. It is seen that the prediction is changed from stability to flutter, which means that the shroud tension can significantly affect the result, at least near the flutter boundary.

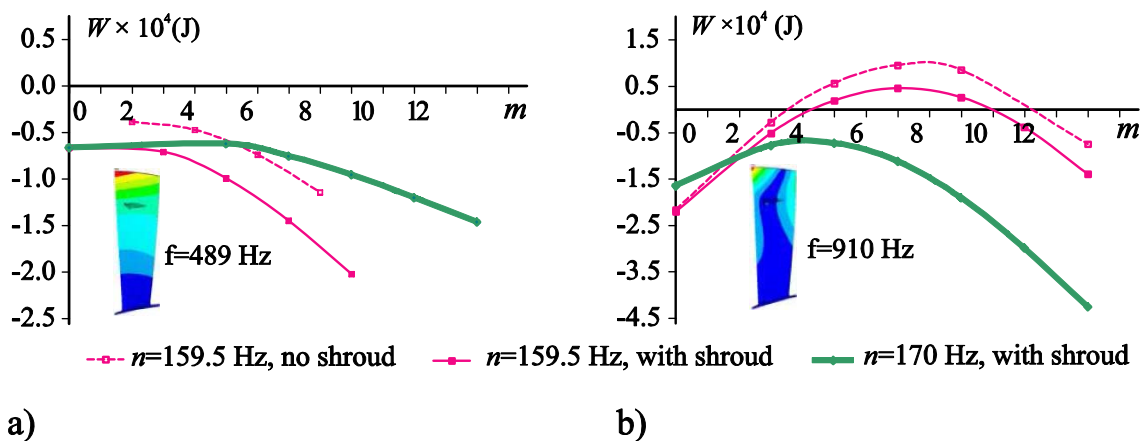


Figure 9 Work done by unsteady pressure vs nodal diameter for wheel 2; effect of shroud modeling in aerodynamic analysis: a) first (bending) mode, and b) second (bending-torsional) mode.

Work done by unsteady pressure over the first two natural modes of tensioned wheel is shown in Fig. 9 by continuous curves. It is seen that both modes are damped at $n=170$ Hz; hence, we predict stability, whereas at $n=159.5$ Hz, the second mode ($f=910$ Hz) with 5 ... 9 nodal diameters is in flutter zone.

4. EXPERIMENTAL VALIDATION OF NUMERICAL RESULTS

The validation of numerical flutter prediction for wheels 1 and 2 was conducted at special full-scale tests of the gas-turbine engine.

(1) Test Facility, Strain Gauge Locations, and Test Procedure

An experimental detection of compressor blade flutter was conducted using a special test facility (Fig. 10) with a simulation of altitude, speed, and environmental air conditions, including required flow irregularity, flow pressure, and temperature at the engine inlet.

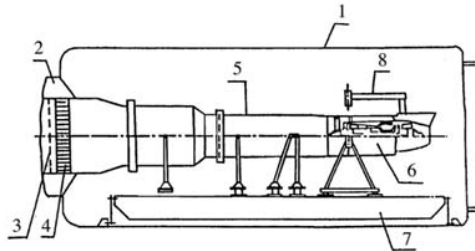


Figure 10 Sketch of the test facility for blade flutter detection during engine test: 1) altitude chamber, 2) receiver, 3) honeycomb, 4) mesh, 5) piping, 6) engine, 7) force meter platform, and 8) engine mounting.

Airflow at the inlet of the fan has average values of the total pressure and stagnation temperature equal to the averaged values of the parameters of the fan operating at flight conditions on an aircraft with required margins of safety. From a compressor station, the air flows through refrigerating units or air heaters providing required pressure and temperature values.

The blades of wheels 1 and 2 were prepared with strain gauges located in the regions of maximum stress for the first four natural modes, which are usually most unstable (Fig. 11a,b). The maximum stress zones for these modes were obtained by a numerical study and during laboratory tests on a vibration-testing machine. To perform a phase shift analysis for the detection of a number of nodal diameters in coupled blade-disc-flow vibrations, several consecutive blades were prepared with strain gauges.

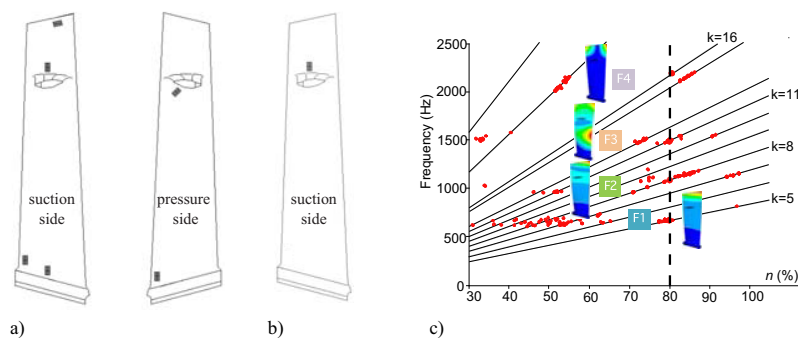


Figure 11 Strain gauge locations on tested blades: a) wheel 1, and b) wheel 2. c) Strains measured for shrouded blade wheel 1 (Campbell diagram). Dots represent spectral peaks with amplitudes exceeding noise level.

A multichannel high-efficiency recording apparatus was used to record and control data from the strain gauges. It provides the required discretization frequency of signal processing with a spectral resolution of 1 Hz and an amplitude accuracy of 2%. The connection between strain gauges and processing apparatus is established through a multichannel remote converter.

The processing of data from strain gauges consisted of the analysis of spectral structure and the

correlation analysis of data from consecutive blades using narrowband spectral analysis.

(2) Test Results

As well as in numerical analysis, two modifications of wheel 1 were tested: blades with midspan shroud and cantilever blades. Based on the analysis of strain gauge data from the shrouded wheel, no flutter was detected in the whole range of the fan speed. At two speed ranges, the vibration amplitudes were at increased but still acceptable levels. First, at $n = 40\% \dots 60\%$ (i.e., at relatively low rotation speeds, where the flow is unstable), random forced vibrations with low amplitudes were detected. Second, at $n = 80\%$, resonant vibrations occurred in the first four modes with an acceptable level of stress amplitudes (Fig. 11c).

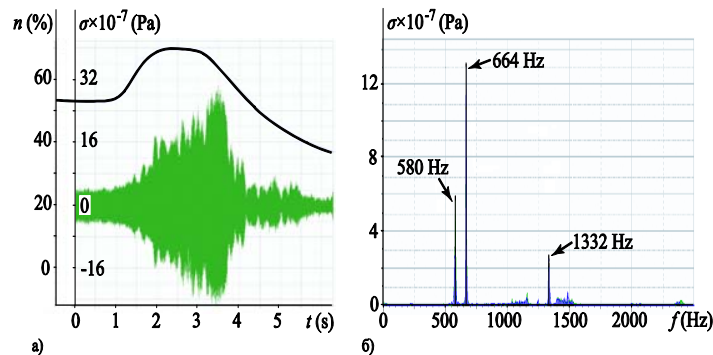


Figure 12 Test results of the cantilever blade wheel 1: a) rotation speed and blade stress, and b) spectrum of the blade stress during flutter

However, signal processing from the strain gauges of wheel 1 with cantilever blades shows that starting from rotor speed $n = 55\%$, nonresonant vibrations occur in modes 2, 3, and 4 with a high total level of vibration stress (Fig. 12a). Spectral and correlation analysis from both neighboring and remote blades shows flutter onset in second ($m = 6 \dots 7$) and third ($m = 5 \dots 14$) natural modes (Fig. 12b). Based on correlation analysis, oscillations in the fourth mode were classified as random forced vibrations.

Thus, test results of wheel 1 are in full agreement with the numerical predictions (Sec. 3. (1)). Indeed, the predicted stability and flutter regimes coincide with the test stability and flutter regimes; moreover, flutter was observed in the same modes and nodal diameters as predicted to be unstable (compare Figs. 5a, 12b).

The test results for wheel 2 were obtained for the full range of rotation speeds; inlet airflow parameters included regimes with heating and compressing the flow. During the test, flutter was detected at the regime $n = 159.5$ Hz with a dominating frequency of 906 Hz (Fig. 13). Signal processing showed that vibrations occurred in the second mode with forward traveling wave and a number of nodal diameters $m = 6 \dots 8$. Pressure gauges installed on the casing over the wheel detected forward traveling rotating pressure wave with $m = 8$. At other operating regimes, including $n = 170$ Hz, no flutter was detected. These results demonstrate excellent agreement between test data and the numerical prediction of flutter onset (Fig. 9b) for the wheel considered.

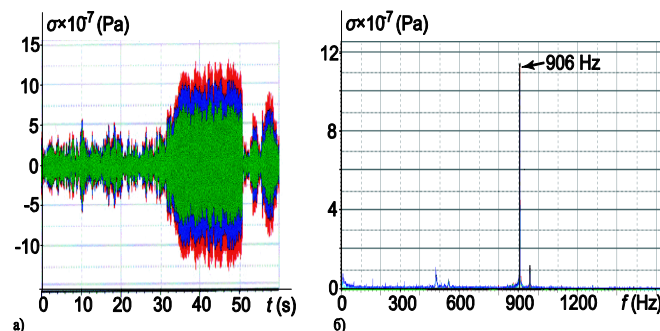


Fig. 13 Test results of the wheel 2 at $n = 159.5$ Hz: a) blade stress (data from different blades with the same strain gauge location), and b) spectrum of the blade stress during flutter.

Good correlation between numerical and test data for both wheels considered validates the procedure and the workflow developed, which will be used in the design of new compressor blades.

5. CONCLUSIONS

A flutter prediction procedure based on the energy method has been developed. It is valid for the unstalled flow conditions, which are typical for operating regimes. Two examples of application of this procedure to real blade wheels are given. Both are verified by full-scale tests in two operating regimes: stable and flutter.

The influence of numerical parameters, as well as blade design parameters and assembling conditions on flutter onset, is studied. It is shown that there is no significant influence of increased numerical accuracy and flow angle of attack variation within manufacturing tolerance. Tension in the midspan shroud has a considerable effect on the predicted flutter onset, although the inclusion of the midspan shroud in the unsteady aerodynamic model does not have significant effect. It is shown that, for a reliable flutter prediction, it is enough to use the three-blade one-stage aerodynamic model and to calculate work done by unsteady pressure for the middle blade during the third oscillation period.

The parameters of the modeling experimentally verified in this paper can be used in the design of new compressors that have a nontypical blade or disc shape for the prediction of flutter onset. They are also suitable for blade wheel design or redesign for flutter suppression near compressor operating regimes with unstalled airflow.

ACKNOWLEDGMENTS

The work is supported by grant MD-4544.2015.1.

REFERENCES

- 1) Bolcs, A., and Suter, P., *Transsonische Turbomaschinen*, G. Braun Verlag, Karlsruhe, 1986.
- 2) Bendiksen, O., "Recent Developments in Flutter Suppression Techniques for Turbomachinery Rotors," *Journal of Propulsion and Power*, Vol. 4, No. 2, 1988, pp. 164-171. doi:10.2514/3.51283
- 3) Marshall, J. G., and Imregun, M., "A Review of Aeroelasticity Methods with Emphasis on Turbomachinery Applications," *Journal of Fluids and Structures*, Vol.10, No.3, 1996, pp. 237-267. doi:10.1006/jfls.1996.0015
- 4) Shrinivasan, A. V., "Flutter and Resonant Vibration Characteristics of Engine Blades," *Journal of Engineering for Gas Turbines and Power*, Vol. 119, No. 4, 1997, pp. 742-775. doi:10.1115/1.2817053
- 5) Petrie-Repar, P., McGhee, A., Jacobs, P., and Gollan, R., "Analytical Maps of Aerodynamic Damping as a Function of Operating Condition for a Compressor Profile," *Proceedings of the ASME Turbo Expo 2006*, American Soc. of Mechanical Engineers, New York, May 2006.
- 6) Khorikov, A. A., and Danilkin, S. Y., "Research of the Fan Blades Flutter on the Stalling Airflow Mode," *Herald of Samara State Aerospace University*, Vol. 2, No. 3, 2011, pp. 57-63 (in Russian).
- 7) Kolotnikov, M. E., Makarov, P. V., and Sachin, V. M., "Study of Wide-Chord Blade Dynamic Strength During Tests," *Aviation and Space Techniques and Technology*, Vol. 56, No. 9, 2008, pp. 58-64 (in Russian).
- 8) Vasily V. Vedeneev, Mikhail Kolotnikov, Pavel Makarov. Experimental validation of numerical blade flutter prediction. *Journal of Propulsion and Power*, 2015, Vol. 31, No. 5, pp. 1281-1291.

FLUTTER ANALYSIS AND EXPERIMENTS OF A RECTANGULAR SHEET NEAR SIDE WALLS

Keiichi Hiroaki⁺¹, Chihiro Kumakura⁺¹ and Masahiro Watanabe⁺¹

⁺¹Department of Mechanical Engineering, Aoyama Gakuin University, Kanagawa, Japan

This paper deals with the flutter analysis of a rectangular flexible sheet under the influences of side walls, in which the sheet is subjected to axial fluid flow. The unsteady fluid force acting on the sheet surface is calculated by using Doublet-point method, which is based on unsteady lifting surface theory. The effect of the side walls is considered by using a mirror-image method. The equation of motion of the sheet coupled with fluid flow is derived by employing the finite element method. Flutter velocity and the effect of the gap width between the sheet and walls are examined analytically. Then, we measure flutter velocity and compared with the analytical results.

Keyword: Flutter analysis, Side wall, Flexible sheet, Doublet-point method, Experiment

1. INTRODUCTION

In manufacturing process of flexible sheets, these sheets are carried near walls. It is reported that flutter occurs due to the interaction between motion of the sheet and axial fluid flow, when the flow velocity becomes higher. Then, the resulting flutter causes scratch damage on the sheet due to collision to the inner wall of machine. Therefore, it is important to clarify the flutter characteristics of the sheet near the walls to avoid quality defects. In this paper, we focus on the sheet near side walls in axial fluid flow.

Up to the present time, several studies have been conducted on the flutter of flexible sheets near parallel and side walls in axial fluid flow[1]~[4]. However, there are little study conducted experiments to verify the validation of the analytical results.

In this paper, we present a flutter analysis of a rectangular sheet near side walls in axial flow by using DPM (Doublet-point method) [5]. The effect of the side walls is considered by using the mirror-image method. The flutter velocities, frequencies and flutter modes are examined analytically. Then, experiments are conducted and compared with the analytical results.

2. FLUTTER ANALYSIS

(1) EQUATION OF MOTION OF THE SHEET

By employing the finite element method (FEM), we obtain the equation of motion of the sheet. Using the virtual work principle, we can obtain the local equation of motion of the sheet

$$\mathbf{m}_s \ddot{\mathbf{e}}_s(t) + \mathbf{k}_s \mathbf{e}_s(t) = \mathbf{f} \quad (2)$$

where \mathbf{m}_s , \mathbf{k}_s and \mathbf{f} are mass matrix, stiffness matrix and nodal external force matrix of sheet, respectively.

Finally, applying the superposition principle to the Eq. (2) we obtain the equation of motion of the sheet, which is related to the nodal displacement vector $\mathbf{X}(t)$ in the global coordinate system,

$$\mathbf{M}\ddot{\mathbf{X}} + \mathbf{C}\dot{\mathbf{X}} + \mathbf{K}\mathbf{X} = \mathbf{Q} \quad (5)$$

where \mathbf{C} is the damping matrix added for considering structural damping, and \mathbf{Q} is unsteady fluid force given by the following unsteady lifting surface theory transformed to the Laplace domain [6].

⁺¹watanabe@me.aoyama.ac.jp

(2) UNSTEADY FLUID FORCE ACTING ON THE SHEET SURFACE

The unsteady fluid force \mathbf{Q} acting on the sheet surface is derived by unsteady lifting theory. In this study, the unsteady fluid force is calculated by using DPM. Multiplying coordinate transform matrix and using the superposition principle, we obtain the nodal external force, which is the fluid force vector coupled with elastic deformation of the sheet in the global coordinate system,

$$\mathbf{Q} = \frac{1}{2} \rho_f U^2 b (\mathbf{A}_{e11} \mathbf{X}_1 + \mathbf{A}_{e12} \mathbf{X}_2 + \mathbf{A}_{e13} \mathbf{X}_3) \quad (15)$$

where \mathbf{A}_{e11} , \mathbf{A}_{e12} , \mathbf{A}_{e13} are a dimensionless fluid-elastic complex matrix. Then the effects of side walls are added the utilizing mirror-image method. We assume a series of mirror image which oscillate in the same phase for the sheet to realize the side walls. That is, the displacement vectors of the mirror images describe Eq.(16)

$$\mathbf{X}_3 = \mathbf{X}_2 = \mathbf{X}_1 \quad (16)$$

Generally, infinite mirror images are used to realize walls in mirror-image method. In this paper, mirror images are used one to each wall. Substituting Eq. (16) into Eq. (15), gives the fluid force vector

$$\mathbf{Q} = \frac{1}{2} \rho_f U^2 b \mathbf{A}_e \mathbf{X}_1 \quad (17)$$

$$\mathbf{A}_e = \mathbf{A}_{e11} + \mathbf{A}_{e12} + \mathbf{A}_{e13}$$

where fluid-elastic complex matrix \mathbf{A}_e includes the effects of side walls. The following, we describe $\mathbf{X}_1 = \mathbf{X}$.

(3) EQUATION OF MOTION OF THE SYSTEM

Substituting Eq. (17) into Eq. (5), gives the following equation of motion in the global coordinate system.

$$\mathbf{M} \ddot{\mathbf{X}} + \mathbf{C} \dot{\mathbf{X}} + (\mathbf{K} + \mathbf{K}_g) \mathbf{X} = \frac{1}{2} \rho U^2 b (\mathbf{A}_e - \mathbf{K}_f) \mathbf{X} \quad (19)$$

where \mathbf{K}_g and \mathbf{K}_f are geometric stiffness matrices caused by gravity and fluid friction, respectively. The right-hand side of the Eq. (19) is equation of motion of the structural system, and the left-hand side of the equation is fluid force coupled with the structural system. Moreover, by applying the modal approximation to Eq. (19), the order of the equation is lowered to reduce the computational load. Nodal displacement matrix \mathbf{X} can be expressed as $\mathbf{X} = \mathbf{\Phi} \mathbf{q}(t)$ using the modal coordinate $\mathbf{q}(t)$ and modal matrix $\mathbf{\Phi}$. By using this equation, we can obtain the equation of motion Eq.(20) related to the modal coordinates.

$$\ddot{\mathbf{q}}(t) + \mathbf{\Gamma} \dot{\mathbf{q}}(t) + \mathbf{\Omega} \mathbf{q}(t) - \frac{1}{2} \rho_f U^2 b \{ \tilde{\mathbf{A}}_e - \tilde{\mathbf{K}}_f \} \mathbf{q}(t) = \mathbf{0} \quad (20)$$

where $\tilde{\mathbf{A}}_e$ and $\tilde{\mathbf{K}}_f$ are given by

$$\tilde{\mathbf{A}}_e = \mathbf{\Phi}^T \mathbf{A}_e \mathbf{\Phi}, \quad \tilde{\mathbf{K}}_f = \mathbf{\Phi}^T \mathbf{K}_f \mathbf{\Phi} \quad (21)$$

$\mathbf{\Omega}$ and $\mathbf{\Gamma}$ are given by following equations using the i -th order modal angular frequency ω_i and damping ratio ζ_i . The structural damping ratio is experimentally determined from the free vibration of the sheet. The measured structural damping ratio ζ of the lowest mode is indicated in Table 1. To simplify the calculation, we assume that the modal damping ratio ζ_i for each mode is equal to the structural damping ratio ζ .

$$\mathbf{\Omega} = \text{diag} [\omega_1^2 \quad \cdots \quad \omega_i^2 \quad \cdots \quad \omega_m^2] \quad (22)$$

$$\mathbf{\Gamma} = \text{diag} [2\omega_1 \zeta_1 \quad \cdots \quad 2\omega_i \zeta_i \quad \cdots \quad 2\omega_m \zeta_m] \quad (23)$$

Therefore, flutter determinant, which is the characteristic equation related to the modal coordinate $\mathbf{q}(t)$, is given by

$$\det \left[s^2 \mathbf{I} + s \mathbf{\Gamma} + \mathbf{\Omega} - \frac{1}{2} \rho_f U^2 b (\tilde{\mathbf{A}}_e(\bar{s}) - \tilde{\mathbf{K}}_f) \right] = 0 \quad (24)$$

The stability of the system is clarified by determining Laplace variable \bar{s} , which is a characteristic root satisfying Eq. (24), with changing velocity U . The system becomes unstable if there is even one root of which real part is plus ($\text{Re}[\bar{s}] > 0$) out of the characteristic root \bar{s} obtained from flutter determinant. Moreover, the flutter occurs in the case of $\text{Im}[\bar{s}] \neq 0$. The flow velocity and frequency at which the system loses stability are defined as a flutter velocity and a flutter frequency, respectively. Similarly, flutter mode at the velocity in which the system becomes unstable is determined. Here, the flutter mode is given by a complex mode.

(4) Dimensionless parameters

The major dimensionless parameters governing the flutter phenomenon of the sheet near side walls are gap ratio H^* , aspect ratio Λ , mass ratio μ , dimensionless velocity U^* , and dimensionless frequency f^* . These dimensionless parameters are defined as follows. Similarly, dimensionless flutter velocity U_f^* and dimensionless flutter frequency f_f^* are defined as follows. Analytical and experimental results are compared by using these dimensionless parameters.

$$H^* = H/L, \quad \Lambda = b/L, \quad \mu = \rho_f L / \rho_s h \quad (27)$$

The major parameters used in analysis are shown in Table 1. The structural damping ratio was determined by the free vibration of the lowest order mode. The impact test is conducted in a vacuum to remove the influence of fluid. Then, the structural damping ratio of the other modes were adopted the same value as well. In the calculation, the axial division number n_x was set in 13 and the across-the-span division number of the sheet n_y was set in 11. Here, the division number n_x and n_y were determined by increasing its number until calculation results converge to a substantially constant value. The lowest nine natural modes determined by FEM analysis were used for the modal approximation in the flutter analysis.

Table 1: Parameters used in calculation

Chord L	100 mm
Span b	50 mm
Thickness h	0.2 mm
Young's modulus of sheet E_s	3.2 GPa
Poisson's ratio of sheet ν_s	0.4
Sheet density ρ_s	1380 kg/m ³
Fluid density ρ_f	1.2 kg/m ³
Fluid friction coefficient C_f	0.01
Damping ratio ζ	0.002
Gravity acceleration g	9.81 m ² /s

2. EXPERIMENT

(1) Experimental setup and measurement system

A test sheet is set in a wind tunnel. In the wind tunnel, the sheet is cantilevered at the leading edge and set near the side walls. The vibration displacement of the sheet was measured by using a laser displacement sensor installed at the test section. In the experiment, the vibration displacement of the sheet was measured while gradually increasing the flow velocity of air. The flow velocity at which the flutter occurs was determined as the flutter velocity. Experiments were conducted with changing the gap width between the sheet and side walls. In this study, the analytical results are compared with experimental results. The major

parameters of the sheet are shown in Table 1.

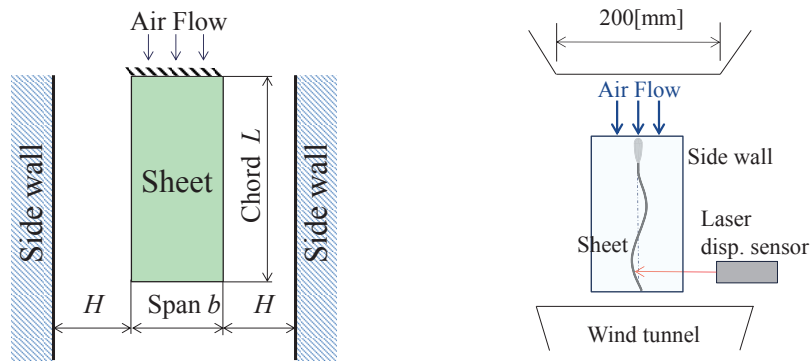


Figure 1: The experimental apparatus.

5. ANALYTICAL AND EXPERIMENTAL RESULTS

(1) Flutter characteristics (Influence of side walls)

Figure 2 and 3 show characteristic root with changing flow velocity U in the case of gap ratio $H^*=0.01$ and ∞ (without walls), respectively. From these figures, it is seen that flutter velocity decrease in the case of with side walls compared to that of without walls. This means that the side walls have strong influence on the flutter velocity. Moreover, the analytical results are in good agreement with the experimental results.

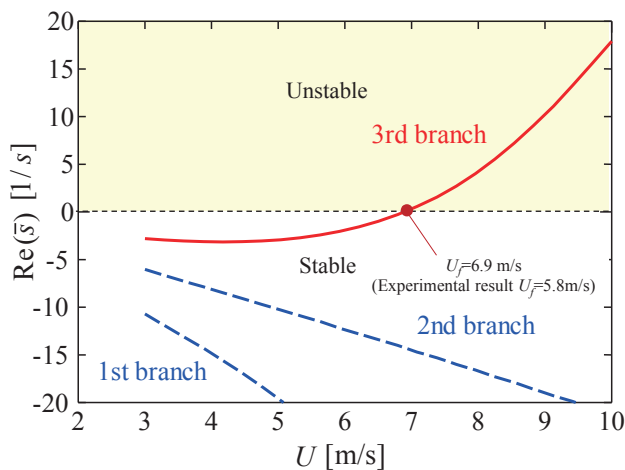


Figure 2: Real part of root with changing flow velocity U in the case of $H^*=0.01$.

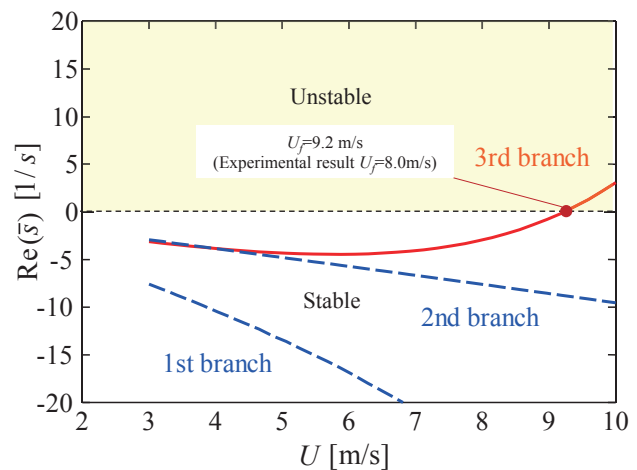


Figure 3: Real part of root with changing flow velocity U in the case of $H^*=\infty$.

6. CONCLUSIONS

In the present paper, we presented a flutter analysis of a cantilevered sheet in axial fluid flow bounded by two side walls. The analytical results were in good agreements with the experimental results for the flutter velocities. The effect of side walls on flutter characteristics is clarified. The results obtained are summarized as follows:

Flutter velocity decrease in the case of with side walls compared to that of without walls

REFERENCES

- 1) Guo, C. Q., and Paidoussis, M. P. : Stability of Rectangular Plates with Free Side-Edges in Two-Dimensional Inviscid Channel Flow, *ASME Journal of Applied Mechanics*, **67**, pp.171-176, 2000.
- 2) Nagakura, H., and Kaneko, S. : The Stability of a Cantilever Beam Subjected to One-Dimensional Leakage Flow, Transactions of the JSME. Series C, **58**, pp.352-350, 1992 (in Japanese).
- 3) Wu, X., and Kaneko, S. : Linear and Nonlinear Analyses of sheet flutter induced by leakage flow, *Journal of Fluids and Structures*, **20**, pp.927-948, 2005.
- 4) Doare, O., Sauzade, M, Eloy, C. : Flutter of an elastic plate in a channel flow: Confinement and finite-size effects, *Journal of Fluids and Structures*, **27**, pp.76-88, 2011.
- 5) Ueda, T. and Dowell, E.H. : A New Solution Method for Lifting Surface in Subsonic Flow, *AIAA Journal*, **20**, pp.348-355, 1982.
- 6) Küssner, H.G. : General Airfoil Theory, NACA TM 979, 1941.

LOW SPEED FLUTTER AND POST-CRITICAL BEHAVIOUR OF FLAT PLATE AND NACA0018 SECTION MODELS IN A WIND TUNNEL

X. Amandolese^{+1,2}

⁺¹ LadHyX, Ecole Polytechnique-CNRS, Palaiseau, France

⁺² CNAM (Conservatoire National des Arts et Métiers), Paris, France

This paper explores the post-critical behaviour of two-degree-of-freedom flat plate and NACA0018 section model undergoing coupled-mode flutter in a wind tunnel. Tests are performed at moderate Reynolds number $Re \sim 1 - 8 \times 10^4$ using an aeroelastic set-up that enables high amplitude pitch-plunge motion without nonlinear structural limitations. For both models, two aeroelastic configurations have been studied: for a centre of rotation at the first quarter chord and for a centre of rotation at the mid-chord. Each configuration exhibits self-limited oscillations due to nonlinear aerodynamics saturation beyond the critical velocity. However, limit cycle oscillations (LCOs) evolution versus the reduced velocity highlight strong different behaviours between the flat plate and the NACA0018 model, along with a significant impact of the position of the elastic center. For the flat plate model two LCOs branches have been found in the post-critical regime. The first one is reached increasing the velocity beyond the coupled-mode flutter critical velocity and the second one occurs when the LCOs amplitude in pitch enter the stall region. This second LCO branch is then associated to a symmetric stall flutter regime. For the flat plate model the switch to symmetric stall flutter has only been observed for the configuration with the elastic axis at the mid-chord. For the NACA0018 model two LCOs branches have also been observed but the dynamical responses are also significantly impacted by a pure pitch instability that can be attributed to the motion-induced dynamics of a laminar separation bubble at moderate Reynolds number.

Keyword: low speed flutter, limit cycle oscillation, nonlinear aeroelasticity, stall flutter, wind tunnel

1. INTRODUCTION

Observed since the early days of flight the coupled-mode flutter of airplane wing is a dynamic instability for which self-sustained oscillations of great violence occurs above a critical speed. Often called “classical” flutter this instability involves at least two modes of the system and, unlike the stall flutter, its onset does not rely on any flow separation. It can hence be observed on wing with no angle of attack if not properly designed. Theory of flutter based upon linear unsteady aerodynamic formulations has been successfully developed to predict the critical conditions for the generic case of a two degrees of freedom “pitch-plunge” oscillating wing (Theodorsen¹; Sears²). Since those early works the physical explanation of bending-torsion flutter has also been highlighted (see for example Fung³, Bisplinghoff and Ashley⁴ or Dowell⁵). It is now well understood that the classical flutter relies on fluid-elastic coupling between the structural modes. Indeed combined plunging and pitching motions can produce, above a critical flow velocity, interactions and phase shifts in a way that energy is transferred from the flow to the structure.

Unlike classical flutter, stall flutter is a dynamic instability that does not depend on coupling (Naudascher and Rockwell⁶). This phenomenon is of particular importance for wing or blade operating at high angle of attack as for helicopter aerodynamics⁷ and wind turbine blades⁸. In such cases torsion is the mode of vibration most commonly involved. The mechanism for energy transfer then relies on a dynamic stall process for which the flow separates partially or completely during each cycle of oscillation⁶. Due to the nonlinear nature of the aerodynamic load involved, stall flutter is limited in amplitude (McCroskey⁹), Li and

⁺¹xavier.amandolese@ladhyx.polytechnique.fr

Dimitriadis¹⁰). Many studies have been devoted to the dynamic stall process experienced by a wing oscillating around the static stall angle of attack (McCroskey and Philippe¹¹; Carr et al¹²).

Regarding coupled-mode or stall flutter of airfoils numerous investigations on the post-critical behaviour can be found. Most of this studies focus on the impact of nonlinearities encountered in aeronautics (see Dowell et al¹³ and Lee et al¹⁴ for a review), such as the impact of concentrated structural nonlinearities¹⁵, control surface freeplay¹⁶, shock wave motion in transonic flow¹⁷ or stall flutter of airfoil^{18,19,20}. Recent experimental studies performed by Dimitriadis & Li²¹ and Razak et al²² using a pitch-plunge section model setup are also to be mentioned. In the former study experiments conducted on a NACA0012 section model focussed on the bifurcation behaviour to stall flutter after large perturbation are imposed to the system. In the later study the authors mainly focused on the effect of the mean static angle of a NACA0018 section model to the dynamical response of the system. Price and Fragiskatos²³ also performed a numerical aeroelastic study on a two-degree-of-freedom pitch-plunge airfoil using a dynamic stall model for the prediction of the high amplitude nonlinear unsteady aerodynamics. They identified limit cycle oscillations (LCO) beyond the critical velocity and a gradual increase of LCO amplitude with the velocity, which was recently confirmed experimentally by Amandolese et al²⁴.

In the new and challenging field of energy harvesting through fluid-structure instabilities, the coupled-mode flutter mechanism has been recently scrutinized^{25,26}. A greater focus on post-critical behaviour is however necessary in order to improve the characterization, physical understanding and modeling of the large amplitude self-sustained vibrations resulting from these instabilities. The aim of this paper is to provide experimental results in that context.

The paper is organized as follows: the experimental set-up along with the relevant non-dimensional parameters of the four tested configurations are presented in section 2. Post-critical flutter results are then reported and discussed in Section 3, highlighting LCOs amplitudes and frequencies evolutions with the reduced velocity.

2. EXPERIMENTAL SET-UP

The experiments were performed on two section models: a rigid flat rectangular steel plate of span $E=0.225\text{m}$, chord length $c=0.035\text{m}$ and thickness $t_c=0.0015\text{m}$, corresponding to a thickness-to-chord ratio of 4.3% and a NACA0018 section model of span $E=0.225\text{m}$ and chord length $c=0.04\text{m}$, made of aluminum. For the NACA0018 model, sand grains were glued near the leading edge in order to trigger the boundary layer laminar-turbulent transition.

Each model was flexibly mounted in plunge and pitch in a small Eiffel wind tunnel (Fig. 1), with a closed rectangular test-section of 0.26 m width and 0.24 m height. A particular attention was paid to the design of a set-up that can allow high amplitude linear response in pitch and plunge. Small chord dimension have been chosen for both models in order to limit blockage effects for high amplitude oscillations. End plates were also mounted at each extremity in order to limit end effects. The set-up is shown in Fig. 1.

The vertical stiffness of the system was set by two long steel laminated springs and two sets of additional linear springs. The axis of rotation was linked to the laminated springs by two bearings mounted at both end and the rotational stiffness was set by two spiral torsion springs. For each section model two position of the centre of rotation have been tested: at the first quarter chord and at the mid-chord. Results will then be presented for four aeroelastic configurations named: “FP14”, “FP12” for the flat-plate with axis of rotation at the first quarter chord and mid-chord respectively and “N14”, “N12” for the NACA18 model with axis of rotation at the first quarter and mid chord respectively.

Tests were performed for a mean velocity in the test-section varying from 4 to 30m/s, with a turbulence level less than 0.4% over this velocity range. In the present study the mean angle of attack of the model is set to zero.

The two degrees of freedom $h(t)$ and $\alpha(t)$ (see Fig. 1) were measured using two laser displacement sensors connected to a 24 bits resolution acquisition system. The first one directly measured the vertical plunging motion at the elastic axis, while the second one measured the combined movement in plunge and

pitch. Recovery of the physical quantities $h(t)$ and $\alpha(t)$ was performed by numerical post-processing with an accuracy less than 2%. The sampling frequency was chosen as 1024Hz and spectral analysis was performed on time block over 8 seconds which gives a frequency resolution lower than 0.125 Hz.

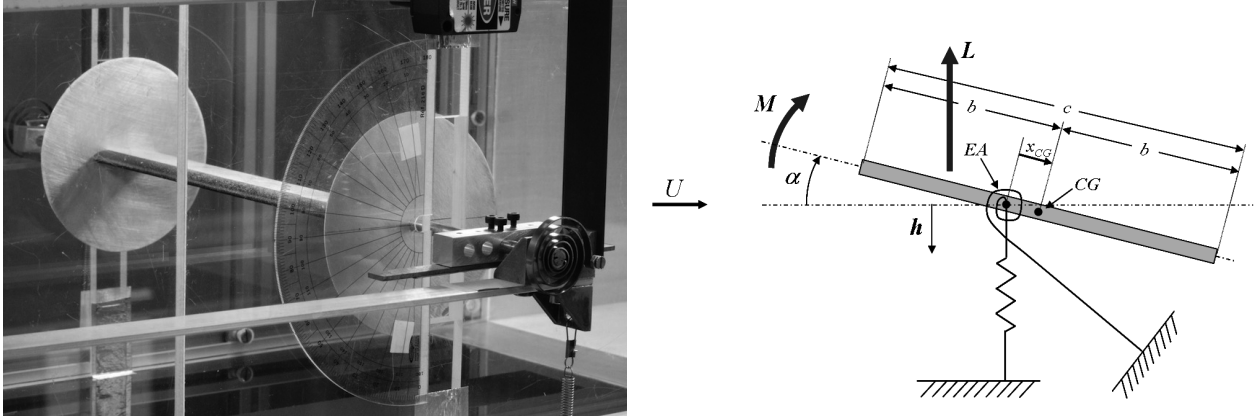


Figure 1: Side view of the setup with the NACA0018 section model (left); definitions and notations of the aeroelastic setup (right).

(2.1) Structural parameters

Under zero wind condition, the linearized equations of motion can be expressed as in Eq. 1 :

$$\begin{aligned} m\ddot{h} + D_h\dot{h} + K_h h + S_\alpha \ddot{\alpha} &= 0, \\ I_\alpha \ddot{\alpha} + D_\alpha \dot{\alpha} + K_\alpha \alpha + S_\alpha \ddot{h} &= 0, \end{aligned} \quad (1)$$

where the parameters $m, I_\alpha, D_h, D_\alpha, K_h, K_\alpha$, are the system's mass, moment of inertia about the elastic axis, structural damping and stiffness in plunge and pitch, respectively. $S_\alpha = mx_{CG}$ is the static moment about the elastic axis, positive if the distance x_{CG} from the elastic axis to the centre of gravity is positive. A static weight calibration technique was used to measure both the stiffness in plunge and pitch. Free decay tests were performed for each degree of freedom taken independently (the other one being locked) to identify the natural frequencies, $\omega_h = \sqrt{K_h/m}$ and $\omega_\alpha = \sqrt{K_\alpha/I_\alpha}$ by spectral analysis, and the damping ratios, $\eta_h = D_h/2\sqrt{K_h m}$ and $\eta_\alpha = D_\alpha/2\sqrt{K_\alpha I_\alpha}$ using a standard decrement technique. The total mass m and inertia I_α of the system were then calculated using the measured stiffness and natural frequencies.

The static unbalance of the section model about the elastic axis S_α was identified using the following expression (see Bisplinghoff and Ashley⁴):

$$S_\alpha = \sqrt{mI_\alpha \left(1 - \frac{\omega_h^2 + \omega_\alpha^2}{\omega_1^2 + \omega_2^2}\right)}, \quad (2)$$

where ω_1 and ω_2 are the natural frequencies of the coupled system.

A particular attention was devoted to design a setup that allows a structural linear behaviour in stiffness and damping. Static calibration that has been performed showed that the bending stiffness behaves linearly in the range $-0.6 \leq h/b \leq 0.6$ and that the stiffness in rotation is linear up to 90° of amplitude. Regarding the damping, results of free decay tests performed for various amplitude showed that the structural damping behaves linearly in plunge but significantly increases in pitch for low angle of attack ($|\alpha| < 2$ deg), because of the solid friction induced by the bearings. As a consequence, the system can be affected by nonlinear behaviour of the setup at small amplitude in pitch. This will be discussed later.

Four different configurations have been studied (two section model and two position of the centre of rotation). The non-dimensional parameters of each configuration are reported in Tab. 1 with ω_h/ω_α the ratio of plunge to pitch natural frequencies, $r_G = \sqrt{I_\alpha/m b^2}$ the non-dimensional radius of gyration of the system about its elastic centre, $\mu = m/(\pi \rho b^2 E)$ the solid/fluid mass ratio (introducing E , the span of the model) and $x_\alpha = x_{CG}/b$ the non-dimensional distance from the elastic centre to the centre of gravity (counted positively

toward the trailing edge). Note that for each position of the centre of rotation mass and inertia have been adjusted to maintain the same value of x_α for both the flat-plate and NACA0018 configurations.

For each configuration the coupled-mode flutter critical reduced velocity $U_c^* = U_c/b \omega_\alpha$ has been calculated solving the eigenvalue problem of the aeroelastic system using the full linear Theodorsen's formulations¹⁾ for the motion induced lift and moment (see Bisplinghoff and Ashley⁴⁾ and Amandolese et al²⁴⁾ for more details on the procedure). Results are reported on Table 1 along with the critical reduced velocity U_{TD}^* associated to torsional divergence static stability. According to those results each configuration should start to flutter for $U_c^* < 16$ and their post-critical behaviour can be studied up to 2.5 times the flutter critical velocity.

Table 1: Non-dimensional parameters of the four aeroelastic configurations

	ω_h/ω_α	r_G	μ	η_h	η_α	x_α	U_c^*	U_{TD}^*
FP1/4	0.805	0.695	2887	0.0008	0.01	0.12	15.2	/
FP1/2	0.792	0.684	2896	0.0008	0.01	0.06	13.8	36.8
N1/4	0.808	0.610	1996	0.0008	0.01	0.12	11.9	/
N1/2	0.785	0.593	2247	0.0008	0.01	0.06	11	28.1

3. LOW SPEED FLUTTER RESULTS

Experiments were performed in the velocity range of the wind tunnel ranging from 4 up to 30m/s (i.e. $Re \sim 1 - 8 \times 10^4$). For each configuration (a section model for a specific position of the axis of rotation), the bifurcation diagrams were identified as following: for a fixed wind tunnel speed the stability of the system is checked to small initial perturbations. If the system is stable the procedure is repeated for a higher velocity until the critical reduced velocity, U_c^* , is found. The dynamical response is then measured increasing the velocity up to a limit value and decreasing the velocity down to a lower critical velocity, U_c^{**} , for which the system is damped.

For each velocity beyond U_c^{**} the system reaches LCO regime for which frequency and amplitude in pitch and plunge have been measured. In some case the amplitude of the LCO are modulated with time. An « error bar » is then associated to each point reported on Figs 2-8 in order to appreciate the maximum value (top of the bar) and minimum value (bottom of the bar) of the LCOs amplitude.

(3.1) Flat-plate and NACA0018 section models for the elastic axis at the first quarter chord

The bifurcation diagrams, i.e. LCO amplitude in pitch and plunge versus the reduced velocity, are reported in Figs. 2 for the “FP14” configuration and Fig 3 for the “N14” configuration. For both configurations the elastic axis is set to the first quarter chord and apart from the mass ratio the non-dimensional aeroelastic parameters are close. Nevertheless one can clearly notice that the post-critical behaviours are strongly different.

For the flat-plate model with velocity increasing the system undergoes a first bifurcation for a critical velocity $U_c^* \approx 18$ which is 20% higher than the value predicted by the linear stability analysis. Following an initial small perturbation the system reaches a stable limit cycle oscillation regime of small amplitude in pitch, $\alpha_{LCO} \approx 5^\circ$ and moderate amplitude in plunge $h_{LCO}/b \approx 0.13$ that increase almost linearly to reach values up to $\alpha_{LCO} \approx 10^\circ$ in pitch and $h_{LCO}/b \approx 0.25$ in plunge at $U^* \approx 30$. Decreasing the reduced velocity the system remains in the same LCO branch down to a smaller critical velocity $U_c^{**} \approx 13$ for which the system is damped. This hysteretic behavior, suggesting a subcritical instability is certainly due to the structural nonlinearity induced by the bearings at low amplitude of rotation.

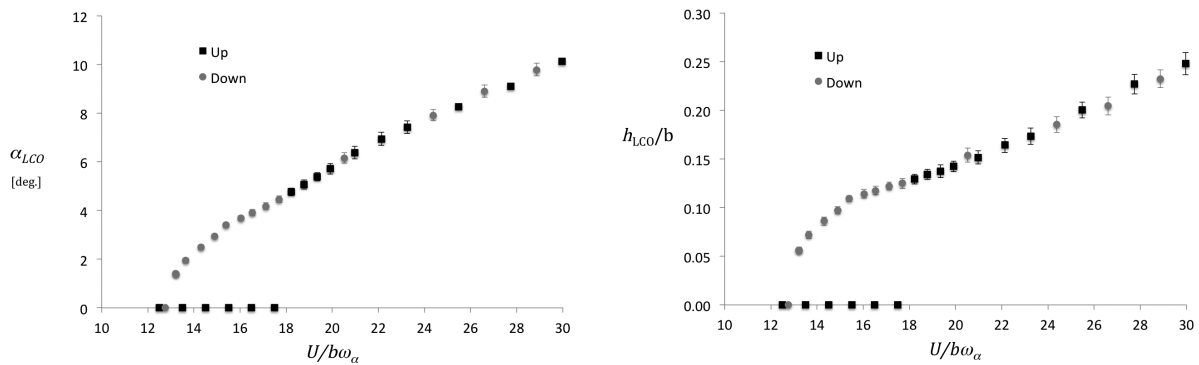


Figure 2: LCO amplitude in pitch (left) and plunge (right) versus the reduced velocity for the « FP14 » configuration: flat-plate section model with the elastic axis at the first quarter chord;

For the NACA0018 model the dynamic of the system is strongly different. The system undergoes a first bifurcation for a critical velocity $U_c^* \approx 11$ which is 7.5% lower than the one predicted by the linear stability analysis. The system then follow a first LCO branch characterized by small amplitude of oscillation in pitch $3^\circ < \alpha_{LCO} < 8^\circ$ and moderate amplitude in plunge $0.09 < h_{LCO}/b < 0.12$. For a reduced velocity $U^* \approx 16$ the system undergoes a second bifurcation and switches to a LCO branch characterized by higher amplitude in pitch $30^\circ < \alpha_{LCO} < 35^\circ$ and amplitude in plunge that gradually increases with the reduced velocity up to $h_{LCO}/b \approx 0.19$ at $U^* \approx 25$. Decreasing the reduced velocity the system remains in the second LCO branch down to a critical velocity $U_c^{**} \approx 11.3$ for which it goes back to the first LCO branch.

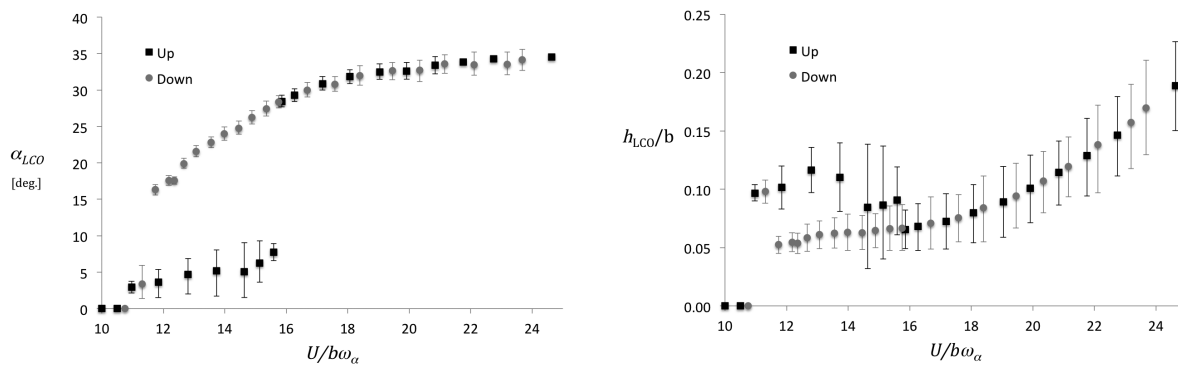


Figure 3: LCO amplitude in pitch (left) and plunge (right) versus the reduced velocity for the « N14 » configuration: NACA0018 model with the elastic axis at the first quarter chord.

LCOs frequencies evolution with the reduced velocity are reported in Fig. 4 for both the « FP14 » and « N14 » configurations. It is interesting to notice that for the flat-plate model the couple mode flutter frequency start close to the plunge natural frequency and gradually increases with the reduced velocity. Those results are in accordance with the linear stability analysis that predicts a destabilization of the plunging branch of the system. On the other hand if the frequency evolution behaves the same way in the first LCO branch for the NACA0018 model, the switch to the second LCO branch is associated to a sudden increase of the frequency of oscillations that is now slightly over the natural frequency in pitch. Those results suggest that the second LCO branch is dominated by a symmetric stall flutter regime.

To further investigate the observed discrepancy between the flat plate and NACA0018 model the aeroelastic response of the NACA0018 profile have been tested in a one degree of freedom “pure pitch” configuration. The LCO amplitude evolution versus the reduced velocity is reported in Fig. 5. It clearly shows that the model experiences self-sustained oscillations of small amplitude in the reduced velocity range $9.5 < U^* < 16$. That kind of velocity bounded instability in pure pitch was first reported by Poirel^(27,28) on a

NACA0012 section model at moderate Reynolds number $Re \sim 4.5 - 13 \times 10^4$. According to Poirel it can be attributed to the motion-induced dynamics of a laminar separation bubble. In the light of these results it is then possible that the “N14” pitch-plunge configuration was significantly affected by a laminar separation flutter²⁸⁾ process that can trig the first onset of flutter and plays a role in the quick entrance in the symmetric stall flutter regime.

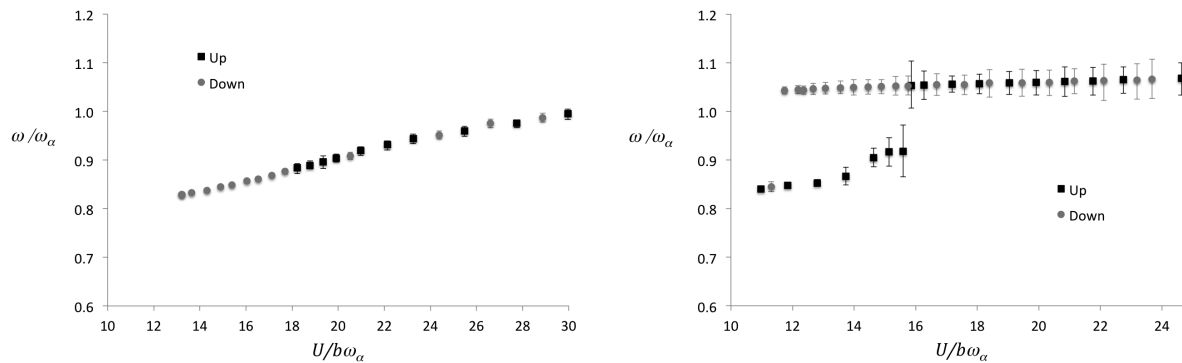


Figure 4: LCO frequency evolution versus the reduced velocity for the « F14 » configuration (left) and « N14 » configuration (right).

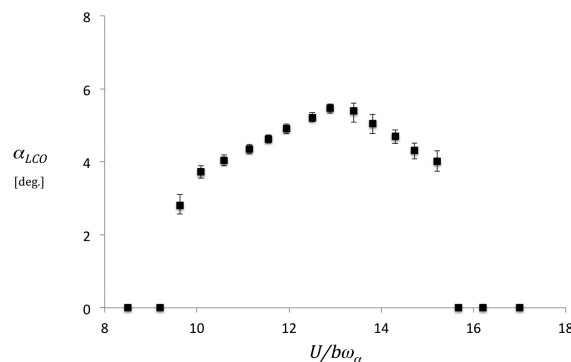


Figure 5: LCO amplitude versus the reduced velocity for the NACA0018 section model in pure pitch with the elastic axis at the first quarter chord.

(3.2) Flat-plate and NACA0018 section models for the elastic axis at the mid-chord

The bifurcation diagrams in pitch and plunge are reported in Figs. 6 for the “FP12” configuration and Fig 7 for the “N12” configuration. The elastic axis is set here at the mid-chord and as for the previous configurations, mass and inertia have been adjusted in order to set the main non-dimensional aeroelastic parameters as close as possible. Here again the flat-plate and NACA0018 models exhibit strongly different behaviours.

With the flat-plate model the system undergoes a first bifurcation for a critical velocity $U_c^* \approx 11.9$ which is 14% lower than the value predicted by the linear stability analysis. Increasing the wind velocity the system then follows a first stable LCO branch characterized by small and gradually increasing amplitude in pitch $2^\circ < \alpha_{LCO} < 7^\circ$ for $12 < U^* < 16$, and moderate amplitude in plunge that first increases to reach a top value $h_{LCO}/b \approx 0.22$ at $U^* \approx 14$. Beyond that reduced velocity the amplitude of oscillation in plunge decreases and is strongly modulated. The amplitude of modulation grows until $U^* \approx 16$ where the system switches to a second LCO branch characterized by high oscillations in pitch with amplitude that increases linearly up to $\alpha_{LCO} \approx 60^\circ$ at $U^* \approx 20$. In the same time the amplitude of oscillation in plunge also increases with the reduced velocity but remain significantly modulated. Decreasing the reduced velocity from $U^* \approx 20$ the system remains in the second LCO branch down to almost the same critical velocity $U_c^{**} \approx 12$ for which the system is damped.

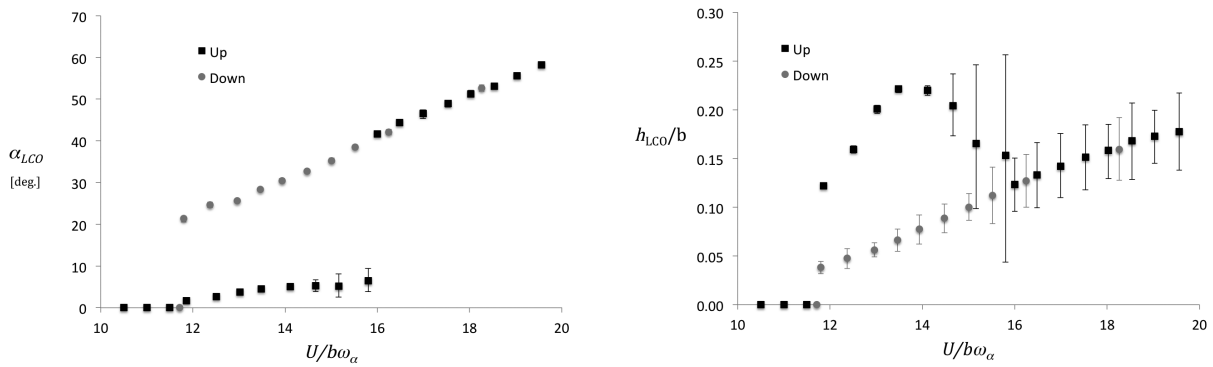


Figure 6: LCO amplitude in pitch (left) and plunge (right) versus the reduced velocity for the « FP12 » configuration: flat-plate section model with the elastic axis at the mid-chord.

For the NACA0018 model the dynamics of the system is strongly different. The system undergoes a first bifurcation for a critical velocity $U_c^* \approx 8$ which is 25% lower than the value predicted by the linear stability analysis. Beyond that critical point the system gradually follow a stable LCO branch characterized by moderate amplitude of oscillation in plunge but large amplitude of oscillation in pitch. At $U^* \approx 15$ the system reaches $\alpha_{LCO} \approx 65^\circ$. The self-sustained response of the system in pure pitch configuration is also reported in Figure 7 (left). It clearly shows that the dynamic of the system is dominated by a pure pitch instability. The onset of this instability is certainly due to a laminar separation bubble fluttering process that trigs the system to a very energetic symmetric stall flutter regime.

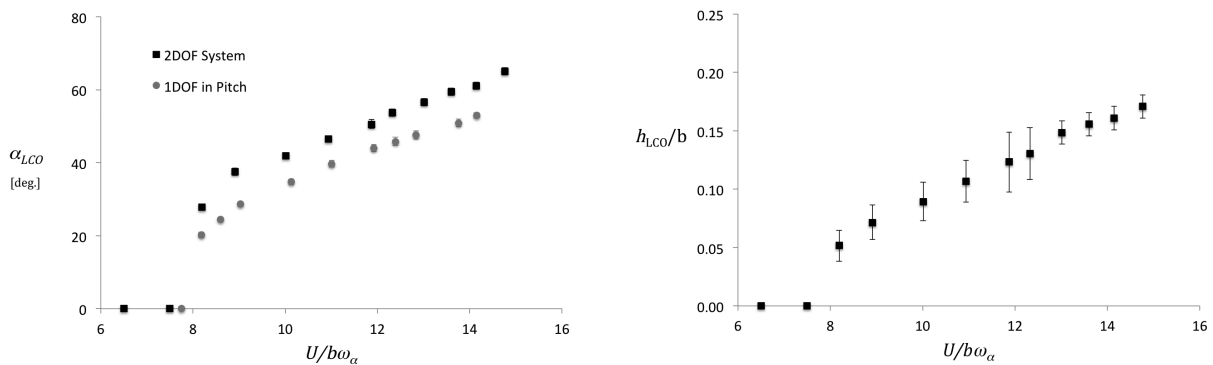


Figure 7: LCO amplitude in pitch (left) and plunge (right) versus the reduced velocity for the « N12 » configuration : NACA0018 section model with the elastic axis at the mid-chord.

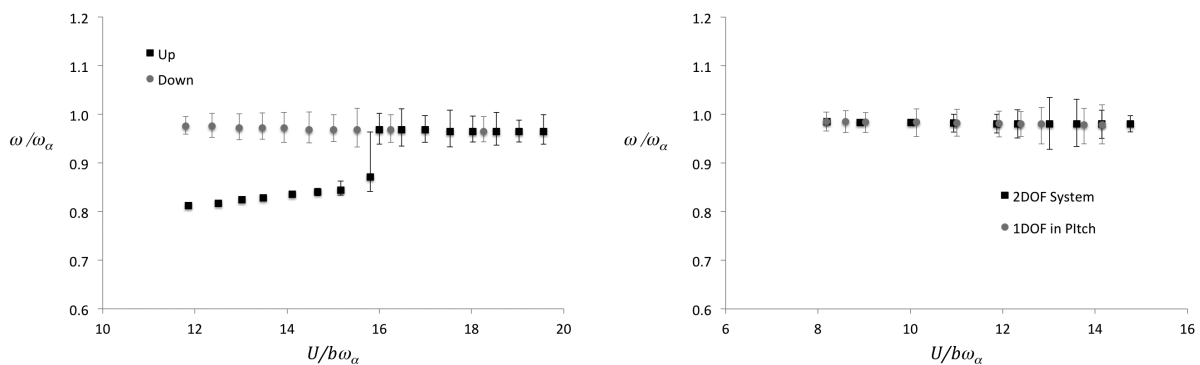


Figure 8: LCO frequency evolution versus the reduced velocity for the « F12 » configuration (left) and « N12 » configuration (right).

LCOs frequencies evolution with the reduced velocity are reported in Fig. 8 for both the « FP12 » and « N12 » configurations. For the flat-plate two frequency regimes are clearly highlighted: the first one is associated to the first coupled-mode flutter branch and the second one shows that the system is dominated by the natural frequency in pitch and thus a stall flutter regime. For the NACA0018 configuration the system is fully dominated by a pure pitch instability and the LCO frequencies remains close to the natural frequency in pitch.

4. CONCLUSIONS

The post-critical behaviour of two degree-of-freedom airfoils undergoing low speed flutter have been studied in wind tunnel for moderate Reynolds number $Re \sim 1 - 8 \times 10^4$. Tests have been performed on both flat-plate and NACA0018 section models, using an aeroelastic set-up that enables high amplitude pitch-plunge motion. For each section model two aeroelastic configurations have been studied : first for a centre of rotation at the first quarter chord and a non-dimensional distance from the elastic centre to the centre of gravity $x_\alpha \approx 0.12$ and second, for a centre of rotation at the mid-chord and $x_\alpha \approx 0.06$. Each configuration was designed to observe the onset of coupled-mode flutter at moderate reduced velocity $U_c^* < 16$ away from an eventual static divergence instability so that their post-critical behaviour can be studied over a large velocity range. Results have been reported in terms of bifurcation diagrams, i.e. LCOs amplitude and frequency evolution in both pitch and plunge versus the reduced velocity, increasing the velocity up to a limit value and then decreasing the reduced velocity down to stable position.

Results have highlighted strong discrepancies between the flat-plate and the NACA0018 section model. For both the elastic axis position, the flat-plate model first undergoes a coupled mode flutter in accordance with the prediction of linear stability analysis, i.e. a destabilisation of the heaving branch. For the elastic centre at the first quarter chord the system remains in a unique LCOs branch characterized by a low increasing amplitude in pitch and moderate amplitude in plunge up to a reduced velocity 2.5 times higher than the critical flutter velocity. For the elastic centre at the mid-chord the system switches to a symmetric stall flutter regime for $U^* \approx 1.4 \times U_c^*$ which is characterized by high amplitude in pitch and moderate amplitude in plunge that increase linearly with the reduced velocity.

For the NACA0018 model two LCOs branches have also been observed but here only for the configuration with the elastic axis at the first quarter chord. Indeed the dynamics of the system seems to be significantly enhanced by a laminar separation bubble fluttering process. For the configuration with the elastic axis at the mid-chord the post-critical flutter behaviour is then fully dominated by a pure pitch instability. The onset of this instability is certainly due to a laminar separation flutter that triggers the system to a strong symmetric stall flutter regime characterized by very high and stable limit cycle oscillations in pitch and moderate amplitude of oscillations in plunge.

ACKNOWLEDGMENT

The author gratefully acknowledges the DGA for its financial support through the DYSACCI project.

REFERENCES

- 1) Theodorsen, T. : General Theory of aerodynamic instability and the mechanism of flutter, *NACA Technical Report 496*, 1935.
- 2) Sears, W. R. : Some aspects of non-stationary airfoil theory and its practical application, *Journal of the Aeronautical Sciences*, Vol. 8, pp. 104-108, 1941.
- 3) Fung, Y.C. : An introduction to the theory of aeroelasticity, John Wiley and Sons, Inc., New-York, N.Y., 1955. Also available in Dover Edition.
- 4) Bisplinghoff, R. L., Ashley, H. : Principles of aeroelasticity, John Wiley and Sons, Inc., New-York, N.Y., 1962. Also available in Dover Edition.
- 5) Dowell, E.H., Clark, R., Cox, D., Curtiss, H.C., Edwards, J.W., Peters, D.A., Scanlan, R., Simiu, E., Sisto, F., Hall, K.C. and others : A modern course in aeroelasticity. Ed. Kluwer, U.S.A., 2004.

- 6) Naudascher, E. Rockwell, D. : Flow-induced vibrations: An engineering guide, Ed. Balkema, Netherlands, 1994.
- 7) Leishman, J. G. : Principles of Helicopter Aerodynamics, Cambridge university press, 2006.
- 8) Hansen, M.O.L., Sørensen, J.N., Voutsinas, S., Sørensen, N., Madsen, H.Aa. : State of the art in wind turbine aerodynamics and aeroelasticity, *Progress in Aerospace Sciences*, Vol. 42, Pt. 4, pp. 285-330, 2006.
- 9) McCroskey, W. J. : Unsteady airfoils. *Annual Review of Fluid Mechanics*, Vol. 14, pp. 285–311, 1982.
- 10) Li, J., Dimitriadis, G. : Experimental Study of Stall Induced LCOS of Free-Vibrating Wings, in *Proceedings of the CEAS International Forum on Aeroelasticity and Structural Dynamics*, Paper IF-026, Stockholm, 2007.
- 11) McCroskey, W.J., Philippe, J.J. : Unsteady viscous flow on oscillating airfoils, *AIAA Journal*, Vol. 13, Pt. 1, pp. 71–79, 1975.
- 12) Carr, L.W., McAlister, K.W., McCroskey, W.J. : Analysis of the development of dynamic stall based on oscillating airfoil experiments. *NASA-TN-D-8382*, 1977.
- 13) Dowell, E., Edwards, J., Strganac, T.W. : Nonlinear Aeroelasticity, *AIAA Journal of Aircraft*, Vol. 40, Pt. 5, pp. 857-874, 2003
- 14) Lee, B.H.K., Price, S.J., Wong, Y.S. : Nonlinear aeroelastic analysis of airfoils: bifurcations and chaos, *Progress in Aerospace Sciences*, Vol. 35, pp. 205-334, 1999.
- 15) Lee B.H.K., LeBlanc P. : Flutter analysis of a two-dimensional airfoil with cubic nonlinear restoring force. Aeronautical Note NAE-AN-36, NRC No. 25438, National Research Council of Canada, 1986.
- 16) Conner, M.D., Tang, D.M., Dowell, E.H., Virgin, L.N. : Nonlinear behavior of a typical airfoil section with control surface freeplay, *Journal of Fluids and Structures*, Vol. 11, Pt. 1, pp. 89-109, 1997
- 17) Schewe, G., Mai, H., Dietz, G. : Nonlinear effects in transonic flutter with emphasis on manifestations of limit cycle oscillations, *Journal of Fluids and Structures*, Vol. 18, pp. 3–22, 2003.
- 18) Ericsson, L.E., Reding, J.P. : Unsteady Airfoil Stall and Stall Flutter, NASA, CR 111906, 1971.
- 19) Dunn, P., Dugundji, J. : Nonlinear stall flutter and divergence analysis of cantilevered graphite/epoxy wings. *AIAA journal*, Vol. 30, Pt. 1, pp. 153-162, 1992.
- 20) Sarkar, S., Bijl, H. : Nonlinear aeroelastic behavior of an oscillating airfoil during stall induced vibration, *Journal of Fluids and Structures*, Vol. 24, pp. 757-777, 2008.
- 21) Dimitriadis, G., & Li, J. : Bifurcation behavior of airfoil undergoing stall flutter oscillations in low-speed wind tunnel, *AIAA journal*, Vol. 47, Pt. 11, pp. 2577-2596, 2009.
- 22) Razak, N. A., Andrienne, T., & Dimitriadis, G. : Flutter and stall flutter of a rectangular wing in a wind tunnel, *AIAA journal*, Vol. 49, Pt. 10, pp. 2258-2271, 2011.
- 23) Price, S.J., Fragiskatos, G. : Nonlinear aeroelastic response of a two-degree-of-freedom airfoil oscillating in dynamic stall, in: Ziada, S., Staubli, T. (Eds.), *Proceedings of the Seventh International Conference on Flow Induced Vibration*, Rotterdam, The Netherlands, pp. 437–444, 2000.
- 24) Amandolese, X., Michelin, S., & Choquel, M. : Low speed flutter and limit cycle oscillations of a two-degree-of-freedom flat plate in a wind tunnel, *J. Fluids and Structures*, Vol. 43, pp. 244-255, 2013.
- 25) Peng, Z., Zhu, Q. : Energy harvesting through flow-induced oscillations of a foil, *Physics of Fluids*, Vol. 21, 123602, 2009.
- 26) Bryant, M., & Garcia, E. : Modeling and testing of a novel aeroelastic flutter energy harvester, *Journal of vibration and acoustics*, Vol. 133, Pt. 1, 011010, 2011.
- 27) Poirel, D., Harris, Y., & Benaissa, A. : Self-sustained aeroelastic oscillations of a NACA0012 airfoil at low-to-moderate Reynolds numbers, *Journal of Fluids and Structures*, Vol. 24, Pt. 5, pp. 700-719, 2008.
- 28) Poirel, D., & Yuan, W. : Aerodynamics of laminar separation flutter at a transitional Reynolds number, *Journal of Fluids and Structures*, Vol. 26, Pt. 7, pp. 1174-1194, 2010.

NUMERICAL STUDY ON ADAPTIVE WING STRUCTURE USING LEADING AND TRAILING EDGE FLAPS FOR REDUCTION OF BENDING MOMENT

Kanata FUJII⁺¹, Tomohiro YOKOZEKI⁺², Hitoshi ARIZONO⁺³ and Masato TAMAYAMA⁺⁴
^{+1, +2}The University of Tokyo, Tokyo, Japan
^{+3, +4}Japan Aerospace Exploration Agency, Tokyo, Japan

Recent commercial aircraft have high aspect ratio wings to improve the fuel efficiency. However, it is concerned that the margin of wing strength gets smaller, especially at the wing root. In order to deal with the problem, adaptive wing structure, which can change the lift-to-drag ratio in flight, is considered. By using the adaptive wing structure, the lift distribution can be modified so that the bending moment decreases. The purpose of this paper is to investigate the effectiveness of adaptive wing structure for reducing the bending moment and the stress. For this purpose, static aeroelastic analysis is conducted with a semispan wing model using MSC/NASTRAN. The model is composed of spars, ribs and skins, and has 4 flaps at each of its leading and trailing edges. The set of flap deflection angles is optimized to minimize the wing root bending moment in a 2.5 pull-up maneuver with Response Surface Methodology (RSM) using MATLAB. As a result, the wing root bending moment is successfully reduced by 10~35% in comparison to that of the original configuration whose flaps have 0° deflection angles.

Keyword: Adaptive wing, Aeroelasticity, Optimization, Response surface methodology

1. INTRODUCTION

With recent emphasis on the environmental feasibility, the demand for fuel efficient aircraft is increasing. These aircraft have some features to reduce the fuel consumption and to improve the fuel efficiency. One of the remarkable features of these aircraft is to introduce lightweight materials, such as carbon fiber reinforced plastics, to reduce the total weight. Another remarkable feature is to introduce a high aspect ratio wing to reduce the induced drag. Many of today's commercial aircraft have high aspect ratio wing on the order of 10, and the future aircraft concept proposed by Boeing and NASA has that of about 20¹⁾. The wing aspect ratio is expected to increase. However, such a high aspect ratio wing usually shows the decrease of its stiffness and the increase of wing root bending moment, and causes the deterioration of wing strength performance. Especially, the wing root bending moment is the most serious when the aircraft is in high g maneuver or in the condition encountering gust. One of the solutions to improve wing strength is to add some structural members, such as strut. These members support a part of the wing load and reduce the load applied on the wing. However, these members make the drag and the weight larger, and this results in the decrease of fuel efficiency. In order to deal with this problem without the increase of drag or weight, an adaptive wing structure is considered.

Adaptive wing structure is the structure whose wing can change the camber and the lift-to-drag ratio in flight. The typical constitution of this wing has variable camber surfaces at its leading and trailing edges. Here, the variable camber surfaces refer to control surfaces such as flaps, ailerons and other discontinuous surfaces although Powers et al. permit only smooth surfaces²⁾. By introducing adaptive wing structure, the wing can change its spanwise distribution of camber, and also, the spanwise distribution of lift can be controlled. This controllability of lift distribution is the best merit of adaptive wing structure. Generally, aircraft's wings are designed to be either optimal for a single cruise flight condition or near-optimal for multiple flight conditions, that is, the wings are less optimal for any other flight conditions³⁾. Adaptive wing can modify the spanwise lift distribution in flight to be more suitable for wider condition in flight profile. Several previous studies have been conducted to investigate the potential performance of adaptive wing structure for drag reduction²⁻⁷⁾ or load

⁺¹fujii@aastr.t.u-tokyo.ac.jp, ⁺²yokozeki@aastr.t.u-tokyo.ac.jp, ⁺³arizono.hitoshi@jaxa.jp, ⁺⁴masato@chofu.jaxa.jp

alleviation^{8,10}. Rodriguez et al. conducted aeroelastic analysis of a wing of Generic Transport Model (GTM) aircraft with the adaptive wing which is known as the Variable Camber Continuous Trailing Edge Flap (VCCTEF), and showed the wave drag reduction³. Lebofsky et al. showed the large reduction of the bending moment of the Truss-Braced Wing (TBW) by deflecting the VCCTEF⁸. Tamayama et al. also applied adaptive wing to High Altitude Long Endurance Aerial Vehicle (HALE) whose wing aspect ratio is about 20, and large amount of wing root bending moment was reduced¹⁰. By using this adaptive wing, it is possible to concentrate the lift on the inboard wing so that the bending moment decreases.

The purpose of this paper is to investigate the effectiveness of the adaptive wing structure for reducing bending moment and stress by controlling the spanwise lift distribution. For this purpose, static aeroelastic analysis is conducted using the semispan wing model based on the 120-passenger commercial transport aircraft¹¹) with SOL144 solver in MSC NASTRAN. The wing model has 4 flaps which can be deflected independently at each of its leading and trailing edges. To improve the fidelity, the wing model is composed of spars, ribs and skins in this study; many of previous researches treated the wing as bars or plates. The particular flight condition under the consideration is a 2.5g pull-up maneuver. The set of flap deflection angles is optimized to minimize the bending moment at the wing root with Response Surface Methodology (RSM) using MATLAB.

2. ANALYSIS

In this paper, aeroelastic analysis is conducted to consider the change of aerodynamic force generated by the wing deformation. To perform aeroelastic analysis, two analysis models are needed: one is structural model and another is aerodynamic model. These two analysis models and the analysis conditions are explained in this section.

(1) Analysis model

The semispan wing model is based on the 120-passenger commercial transport aircraft JAXA Technology Reference Aircraft (TRA) 2012A¹¹). The specification of the JAXA TRA2012A is shown in Tab. 1. By using the values in Tab.1, the semispan wing model is generated and its two-view drawing is shown in Fig. 1. Here, the swept-back angle at 25% chord line and the dihedral angle are assumed to be both 0°, and taper ratio is set to be 0.3. The root and tip chord lengths are 5.13 m and 1.66 m, respectively. The semispan length is 15.2 m. The wing thickness at root and tip are 0.718 m and 0.234 m, respectively. The chord length and the wing thickness vary linearly along the spanwise direction. There are 4 flaps whose spanwise length are equally 3.8 m at each of the wing leading and trailing edges as devices to modify the spanwise lift distribution. The leading- and trailing-edge flaps are tagged as “LEF *i*” and “TEF *i*” respectively: here *i*=1~4 and “*i*” is the flap number counting from the most inboard one. Finite Element Analysis (FEA) model is shown in Fig. 2. The wing model is composed of spars, ribs and skins in order to investigate the stress of each member, though many of previous researches treated the wing as bars or plates in their structural model. In Fig. 2 the skins at Flap 3 and 4 are removed so that it is easy to see the inner structure. A geometrical gap exists between each of LEFs and TEFs and wing box in structural model; there are no gaps in aerodynamic model. The wing section has the super critical airfoil NASA/Langley SC (2)-0714¹²). The front and rear spars are placed at 15% and 60% chord line from leading edge, and each flap section has 7 ribs. The FEA nodes are generated by dividing the wing into 25 elements in chordwise direction and 96 elements in spanwise direction. The elements used in the FEA model

Table 1: Specification of JAXA TRA2012A.

Cruise Mach Number	0.78
Wing Area	122.4 m ²
Aspect Ratio, <i>AR</i>	9.5
Fuselage Diameter	3.7 m
Coefficient of Lift at Cruise, <i>C_L</i>	0.5194

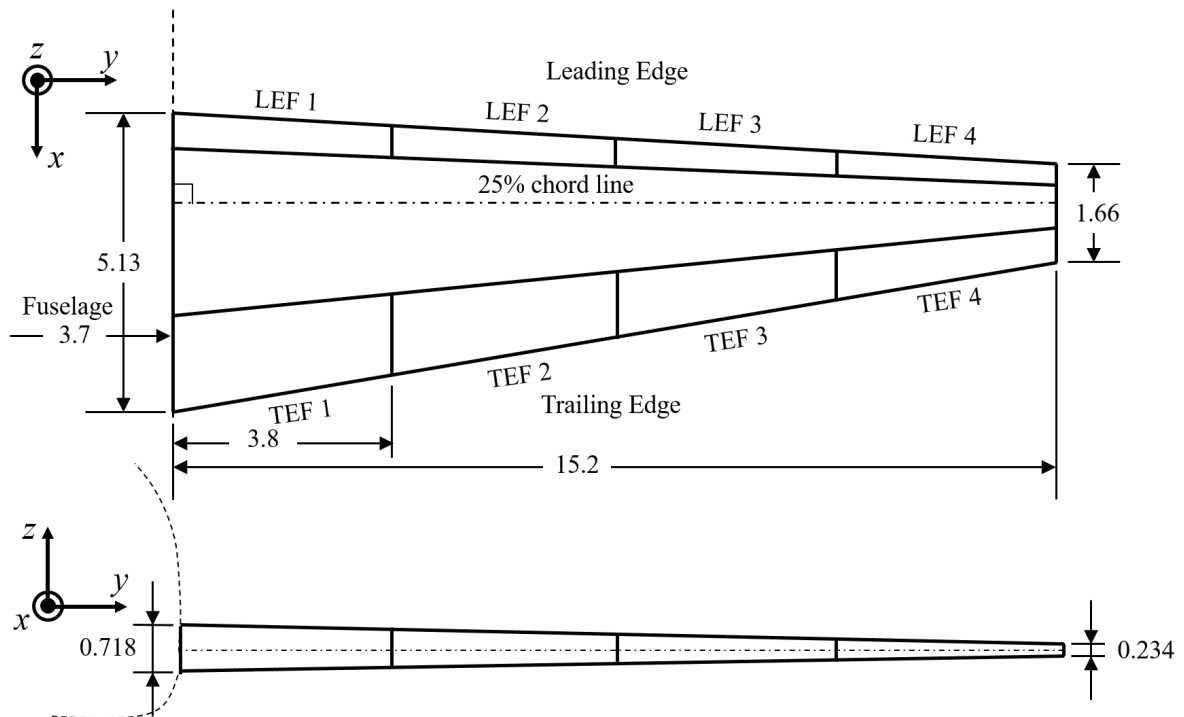


Figure 1: Two-view drawing of wing model (unit: m).

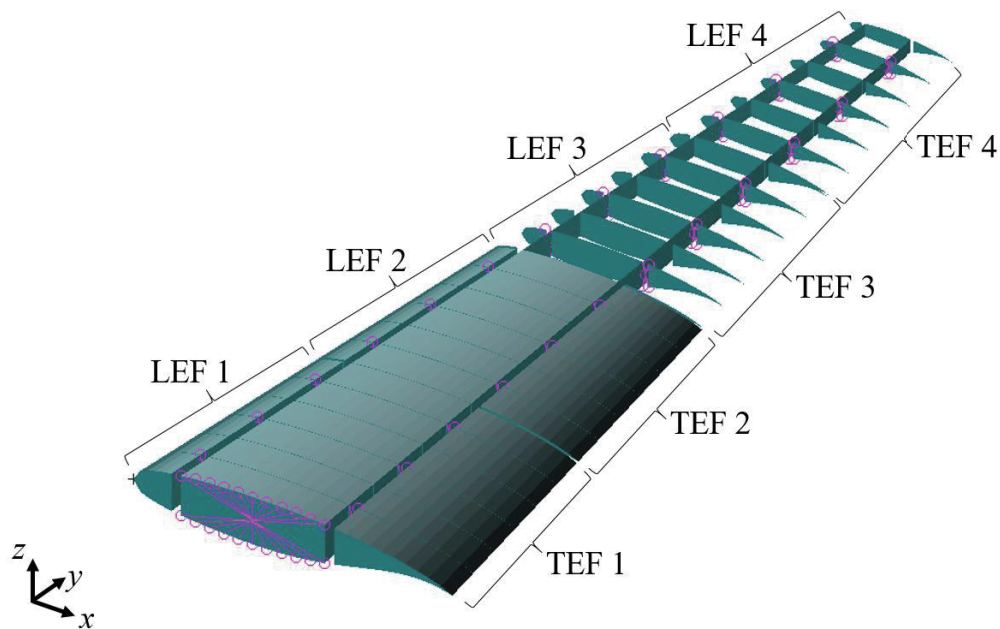


Figure 2: Finite element analysis model.

are shell elements (CTRIA3 or CQUAD4 in MSC Nastran) with 3 or 4 nodes. The material of the structure is assumed ultra-duralumin. The thicknesses of each member at root and tip are shown in Tab. 2, and those vary linearly along the wing span. The flaps are attached to the wing box with rigid bar elements placed at the 2nd, 4th and 6th ribs of each flap counting from inboard. The wing model is constrained rigidly at the wing root with

the node placed at the center of the wing root which are connected to all of the nodes of wing box at root with the constraint having 6 degrees of freedom.

The aerodynamic model is shown in Fig. 3. The wing is divided into 10 panels in chordwise direction and 40 panels in spanwise direction. In SOL144 solver of MSC NASTRAN, all lifting surfaces are assumed to be the panels lying nearly parallel to the flow, and camber is included as a downwash of each panel.

(2) Analysis conditions

The particular flight condition considered in this study is a 2.5g pull-up maneuver. The cruise mach number is 0.78 from Tab. 1 and the cruise altitude is assumed to be 35,000 ft; and then the cruise speed, V_c , is 231.2 m/s. The load factor n is assumed to be 2.5. The Angle Of Attack (AOA) is set to be 7.6° so that the wing generates 2.5 times as large lift as that of cruise condition at the speed V_c without any flap deflections. This case is taken as the baseline in this study and is called as “base condition”. The gross lift, wing root bending moment and maximum von-Mises stress of spars, ribs and skins of the base condition are presented in Tab.3.

Table 2: Thicknesses of spars, ribs and skins [mm].

		Root	Tip
Spar		5.0	3.0
Rib		4.0	2.0
Skin	Wing Box	12.0	4.0
	Flap	4.0	2.0

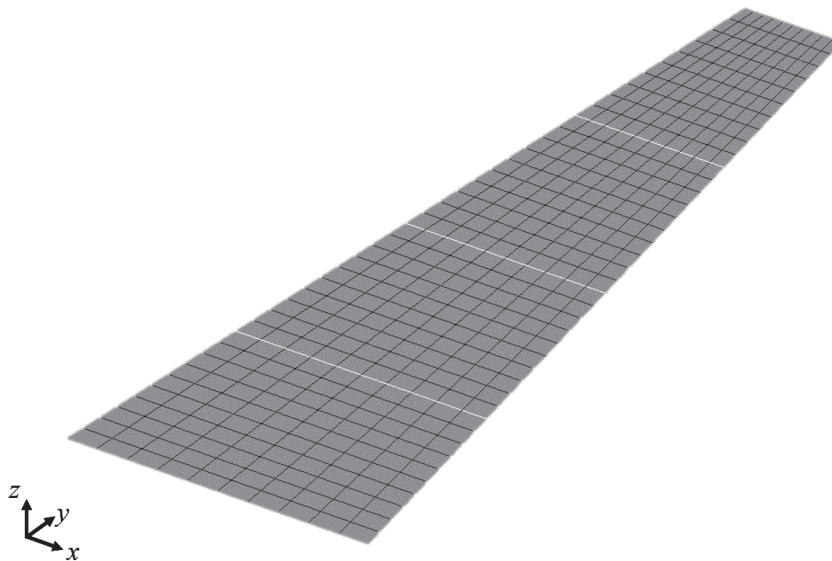


Figure 3. Aerodynamic model.

Table 3: Gross lift, wing root bending moment and maximum von-Mises stress of the base condition.

Gross Lift, L_0 [N]		8.086×10^5
Wing Root Bending Moment [Nm]		5.087×10^6
Maximum von-Mises Stress [N/m ²]	Spars	1.740×10^8
	Ribs	5.884×10^7
	Skins	3.006×10^8

3. OPTIMIZATION OF A SET OF FLAP DEFLECTION ANGLES

(1) Response Surface Methodology ¹³⁾

In this paper, many design parameters are used to minimize the wing root bending moment. To get more precise result, all sets of flap deflection angles should be analyzed; however, it is not realistic because it takes much calculation cost. Therefore, Response Surface Methodology (RSM) is used to approximate the relationship between design parameters and a response of interest, and to reduce the calculation cost. In general, response y can be expressed as a function of design parameters, x_1, x_2, \dots, x_k , by a low-degree polynomial model as follows.

$$y = \beta_0 + \sum_{i=1}^k \beta_i x_i + \sum_{i < j} \beta_{ij} x_i x_j + \sum_{i=1}^k \beta_{ii} x_i^2 + \varepsilon \tag{1}$$

Here, the second-degree model is chosen. β s ($\beta_i, \beta_{ij}, \beta_{ii}$) are unknown constant coefficients and ε is a error. In order to determine the coefficients β s, a series of experiments should be carried out, and the number of experiments is determined by central composite design: the design of experiments which is usually used for second-degree model. In this study, the lift and the wing root bending moment are approximated as functions of flap deflection angles.

(2) Design parameters

The design parameters for the optimization problem are flap deflection angles.

$$\boldsymbol{\delta} = \{\delta_{LEF1}, \delta_{LEF2}, \delta_{LEF3}, \delta_{LEF4}, \delta_{TEF1}, \delta_{TEF2}, \delta_{TEF3}, \delta_{TEF4}\} \tag{2}$$

δ_{LEFi} and δ_{TEFi} are flap deflection angles of LEF i and TEF i , respectively. Fig. 4 shows the definition of flap angle sign. Nose-up is positive for the LEFs and nose-down is positive for TEFs.

(3) Objective function

For the cantilever wing in a 2.5g pull-up maneuver, the maximum spanwise bending moment occurs at the wing root. Reducing the maximum bending moment also causes the reduction of bending moment at other parts. Therefore, the objective function is the wing root bending moment ($M_{root}(\boldsymbol{\delta})$, a function of $\boldsymbol{\delta}$), and the optimization analysis is conducted to find $\boldsymbol{\delta}$ to attain minimum $M_{root}(\boldsymbol{\delta})$. Here, the wing root bending moment $M_{root}(\boldsymbol{\delta})$ is positive when the wing deformation curve shows its center of curvature beyond the wing upper surface.

(4) Constraints

If there were no constraints in this optimization problem, the result would be unrealistic, such as a result whose gross lift is 0. Therefore, the minimization problem is subjected to several constraints. First of all, the upper and lower limit, δ_{max} , should be applied to δ s ($\delta_{LEF}, \delta_{TEF}$), that is $-\delta_{max} \leq \delta \leq \delta_{max}$. This limitation is required to avoid reaching the results which include extremely large angle values. Four cases of δ_{max} , 5°, 10°, 15° and 20°, are considered. Next, in order to maintain the flight condition, the gross lift $L(\boldsymbol{\delta})$ is made to be



Figure 4: Definition of flap angle sign ($i=1\sim 4$).

equal to and not to be less than the base condition value of $L_0=8.086 \times 10^5$ N, that is $0 \leq (L(\boldsymbol{\delta})-L_0)/L_0 \leq 0.01$. The summary of the objective function and constraints is as follows.

$$\min_{\boldsymbol{\delta}} M_{\text{root}}(\boldsymbol{\delta}) \text{ such that } \begin{cases} -\delta_{\text{max}} \leq \delta_s \leq \delta_{\text{max}} (\delta_{\text{max}} = 5^\circ, 10^\circ, 15^\circ, 20^\circ) \\ 0 \leq \frac{L(\boldsymbol{\delta}) - L_0}{L_0} \leq 0.01 \end{cases} \quad (3)$$

The bending moment $M_{\text{root}}(\boldsymbol{\delta})$ and gross lift $L(\boldsymbol{\delta})$ are approximated by Response Surface Methodology (RSM).

4. RESULTS & DISCUSSIONS

The optimization under the conditions presented by Eq. (3) was conducted. The optimized sets of flap deflection angles are shown in Fig. 5 and Tab. 4. Regardless of the value of δ_{max} , flaps are similarly deflected as the inboard lift to increase and the outboard lift to decrease.

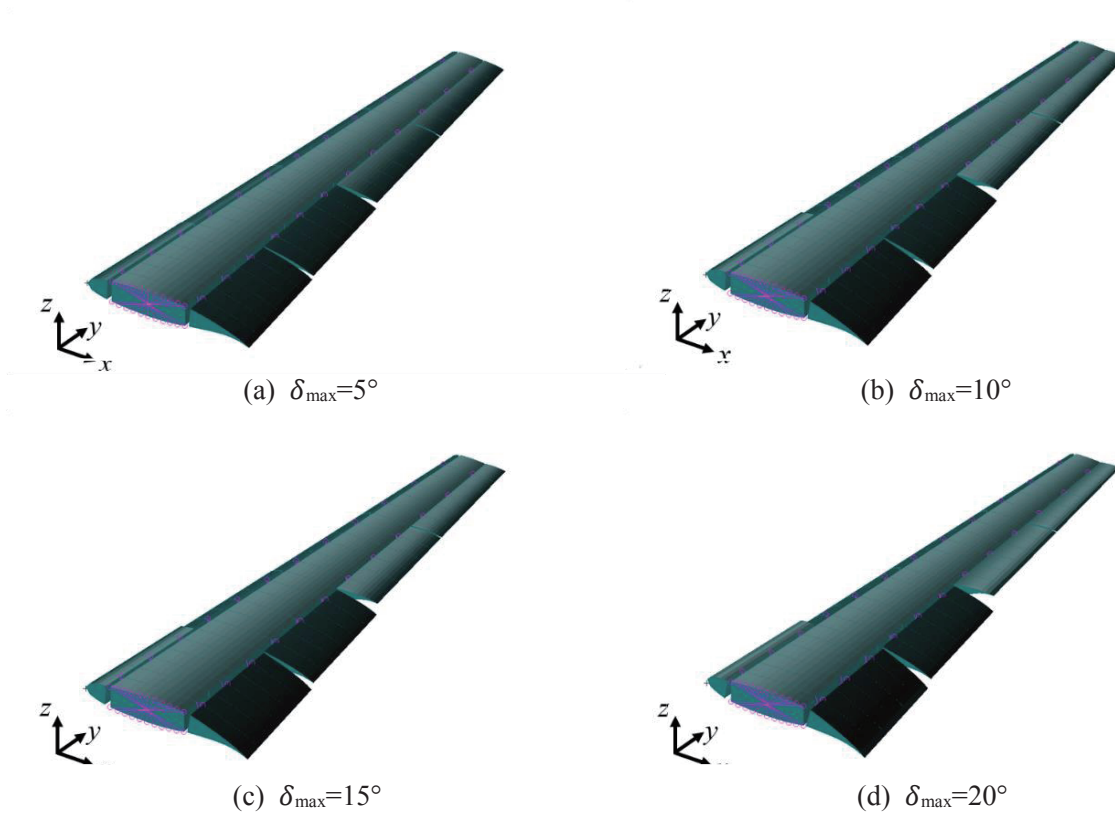


Figure 5: Optimized flap deflections.

Table 4: Optimized set of flap deflection angles [°].

δ_{max}	δ_{LEF1}	δ_{LEF2}	δ_{LEF3}	δ_{LEF4}	δ_{TEF1}	δ_{TEF2}	δ_{TEF3}	δ_{TEF4}
5	1.0	-1.9	-5.0	-5.0	5.0	1.8	-5.0	-5.0
10	4.2	-7.0	-10.0	-10.0	10.0	3.5	-10.0	-10.0
15	10.7	-15.0	-15.0	-15.0	15.0	4.8	-15.0	-15.0
20	20.0	-20.0	-20.0	-20.0	20.0	4.6	-20.0	-20.0

Static aeroelastic analysis was conducted with the optimized sets of flap deflection angles using MSC NASTRAN. The spanwise lift and bending moment distributions are shown in Fig. 6 and Fig. 7 respectively. In Fig. 6, the lift generated on the inboard wing increases and that generated on the outboard wing decreases in comparison to that of the base condition. The larger δ_{max} is, the larger the lift deviation from that of the base condition is. Therefore, the bending moment decreases not only at the wing root but also along the wing span as δ_{max} increases as shown in Fig.7. The wing root bending moments M_{root} obtained from RSM and MSC NASTRAN are shown in Tab. 5, the M_{root} reducing rates of base condition for the NASTRAN result are also presented in Tab. 5. The M_{root} are well approximated by RSM. As a result, the M_{root} is reduced by 10~35%.

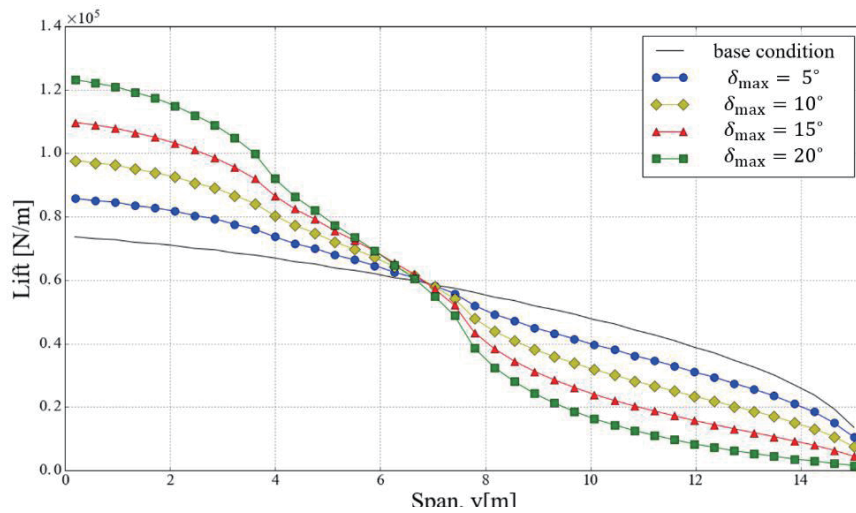


Figure 6: Optimized lift distribution.

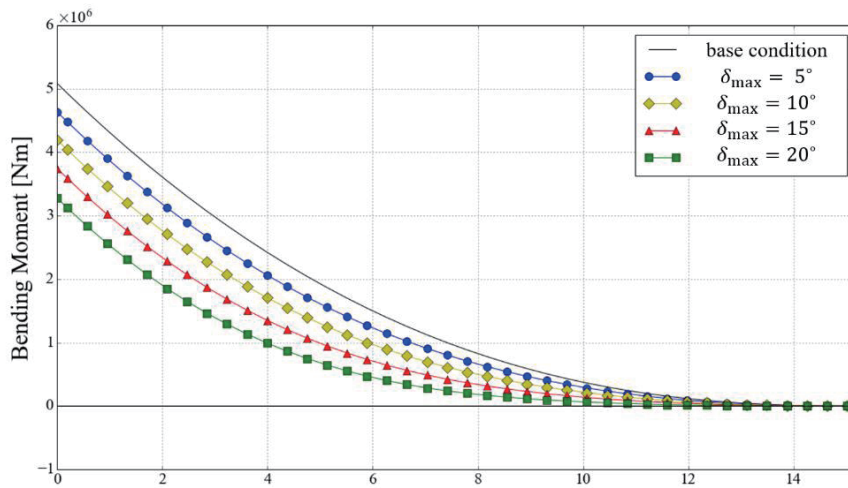


Figure 7: Optimized bending moment distribution.

Table 5: Wing root bending moment obtained from RSM and NASTRAN, and reducing rate.

δ_{max} [°]	RSM [$\times 10^6$ Nm]	MSC NASTRAN [$\times 10^6$ Nm]	Reducing Rate (Nastran) [%]
5	4.635	4.637	-8.8
10	4.187	4.196	-17.5
15	3.746	3.746	-26.4
20	3.291	3.279	-35.5

The von-Mises stress distribution of each case is shown in Fig. 8. The high stress area, which locates in the wing box for the base condition, moves to the vicinity of wing root as δ_{max} increases. This is caused by the bending moment decrease owing to the flap deflection. The maximum von-Mises stress in each of spars, ribs and skins is plotted in Fig. 9. The maximum stress in skins decreases while that in each of spars and ribs increases as δ_{max} increases. This is caused by the increase of torsional moment. However, overall maximum stress decrease from that of base condition.

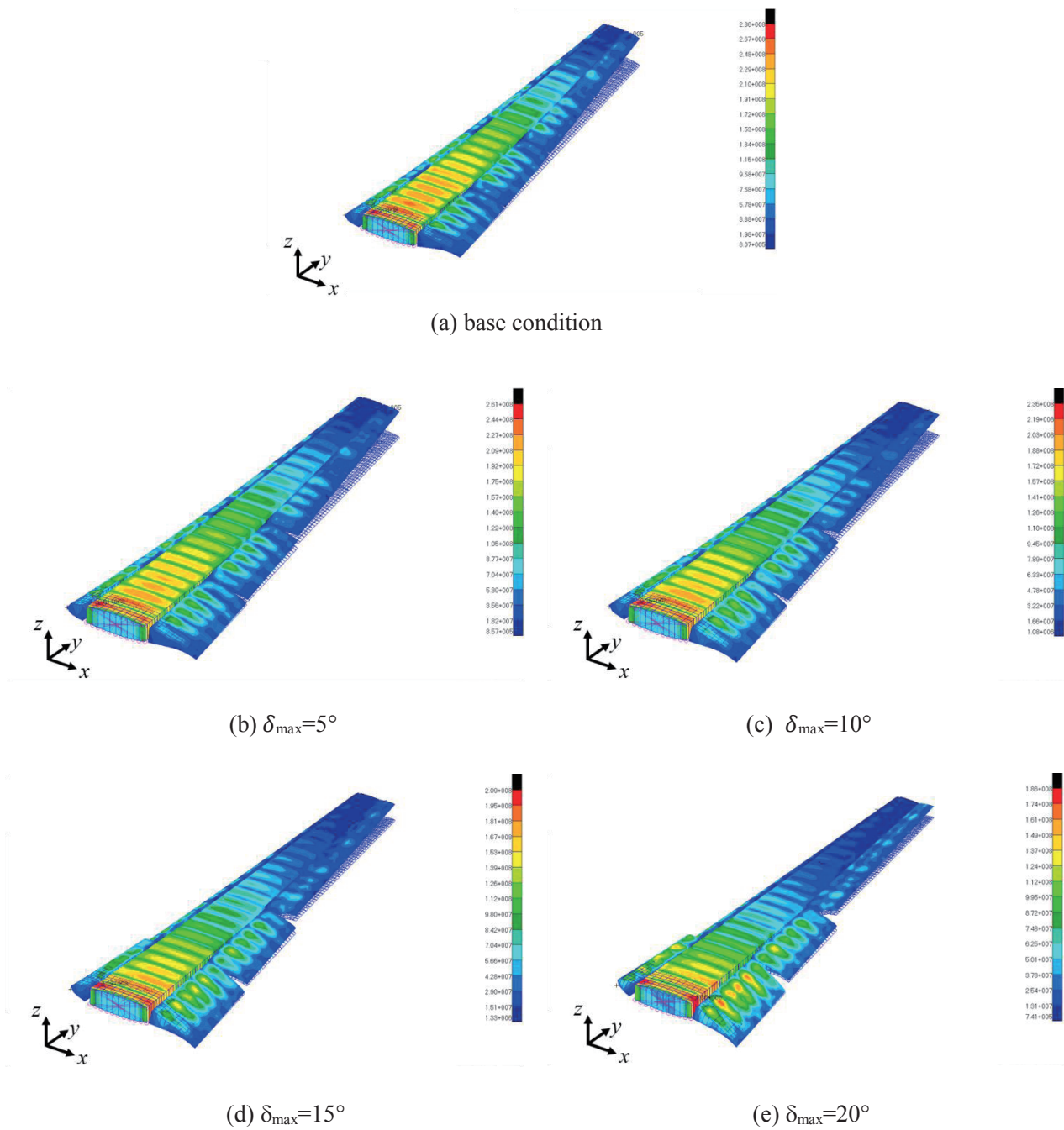


Figure 8: von-Mises stress distributions.

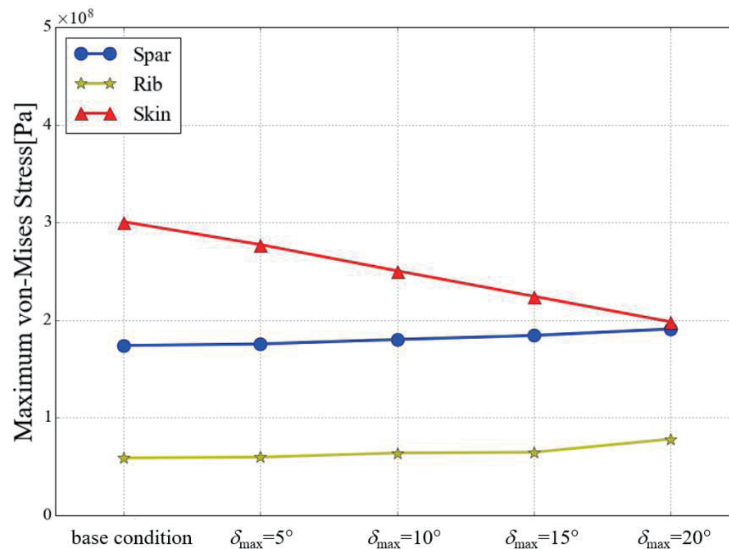


Figure 9: Maximum von-Mises stress of spars, ribs and skins of each case.

5. CONCLUSION

In order to reduce the wing bending moment of commercial transport aircraft, the adaptive wing structure which had 4 flaps at its leading and trailing edges was considered. Static aeroelastic analysis was conducted using semispan wing model composed of spars, ribs and skins with MSC NASTRAN, and a set of flap deflection angles was optimized to minimize the wing root bending moment by using the response surface methodology. As a result, the wing root bending moment was successfully reduced by 10~35% in comparison to that of the base condition. The maximum stress was also reduced from that of the base condition, and therefore the potential effectiveness has been shown as the adaptive wing structure can make the margin of wing strength larger. As the future works, it is needed to consider drag, weight and stall to evaluate the practical importance of adaptive wing structure.

REFERENCES

- 1) Bradley, M. K., Dronney, C. K. and Allen, T. J. : Subsonic Ultra Green Aircraft Research: Phase II –Volume I– Truss Braced Wing Design Exploration, NASA/CR-2015-218704, 2015.
- 2) Powers, S. G., Webb, L. D., Friend, E. L. and Lokos, W. A. : Flight Test Results From a Supercritical Mission Adaptive Wing With Smooth Variable Camber, NASA Technical Memorandum 4415, 1992.
- 3) Rodriguez, D. L., Aftosmis, M. J., Nemec, M. and Anderson, G. R. : Optimized Off-Design Performance of Flexible Wings with Continuous Trailing-Edge Flaps, AIAA-2015-1409, 2015.
- 4) Zink, P. S., Love, M. H. and Youngren, H. : Drag Minimization Through the Use of Mission Adaptive Trailing Edge Flaps and Fuel State Control, AIAA-2004-4365, 2004.
- 5) Nguyen, N., Precup, N., Urnes, J. Sr., Nelson, C., Lebofsky, S., Ting, E. and Livne, E. : Experimental Investigation of a Flexible Wing with a Variable Camber Continuous Trailing Edge Flap Design, AIAA-2014-2441, 2014.
- 6) Precup, N., Mor, M. and Livne, E. : Design, Construction, and Tests of an Aeroelastic Wind Tunnel Model of a Variable Camber Continuous Trailing Edge Flap (VCCTEF) Concept Wing, AIAA-2014-2442, 2014.
- 7) Nguyen, N. and Tal, E. : A Multi-Objective Flight Control Approach for Performance Adaptive Aeroelastic Wing, AIAA-2015-1843, 2015.
- 8) Lebofsky, S., Ting, E., Nguyen, N. and Trinh, K. : Optimization for Load Alleviation of Truss-Braced Wing Aircraft With Variable Camber Continuous Trailing Edge Flap, AIAA-2015-2723, 2015.
- 9) Xu, J. and Kroo, I. : Aircraft Design with Maneuver and Gust Load Alleviation, AIAA-2011-3180, 2011.

- 10) Tamayama, M., Fujii, K., Arizono, H. and Yokozeki, T. : Bending Moment Reduction of a High Aspect Ratio Wing, ICAST2015#32, 26th International Conference on Adaptive Structures and Technologies, 2015.
- 11) Kwak, D., Tamayama, M., Nomura, T. and Arizono, H. : Preliminary Studies on the Lift Distribution and Aspect ratio of Subsonic Aircraft Wing for Fuel Consumption Reduction, 3A12, 53rd Aircraft Symposium, 2015.
- 12) UIUC Airfoil Coordinate Database, http://m-selig.ae.illinois.edu/ads/coord_database.html.
- 13) Khuri, A., I. and Mukhopadhyay, S. : Response surface methodology, *WIREs Computational Statistics*, Vol. 2, pp. 128-149, 2010.

FLAT-PLATE HIGH-FREQUENCY SMALL THRUSTER ON FREE SURFACE

Yutaka Terao
Tokai University, Shizuoka, Japan

The experiments using small propulsion system that uses surface tension rather than gravitational waves to generate thrust is discussed. It consists of a flat-plate fin thruster that rests on a free surface and is driven at over 110 Hz by a small vibration motor and 8-cm-long model achieved speeds is of up to $F_n = 0.212$ based on the model length Froude number.

Keywords: High-frequency propulsion, Surface tension wave, Wave momentum flux

1. INTRODUCTION

Waves are not commonly used to create thrust. However, wave-making¹⁾ and wave-devouring²⁾ propulsion systems generate thrust by employing the radiation force of waves and the relative wave orbital velocity acting on the hydrofoil. Both systems use gravitational waves and it's theories. If the floating body size decreases by less than 10 cm, gravitational waves are no longer dominant, and the waves generated by the small model become surface tension waves. Fig.1 shows the phase velocity of the waves and indicates that if the wavelength is less than 1.7 cm, the surface tension wave phase velocity exceeds the gravitational waves. In ocean engineering or naval structures, this higher-frequency wave zone is not commonly employed in practical applications. This paper discusses experiments on a small propulsion system model ($L_{oa} = 80$ mm, $B = 40$ mm, 20 mm slit in the bottom centerline) equipped with a 7000 rpm vibration motor on the deck to know the surface wave making propulsion is possible or not.

In these experiments, as in the gravitational wave-making propulsion system, a high propulsion speed was achieved in the high-frequency tension wave zone. To achieve a much higher speed, an elastic horizontal fin was installed on the aft of the model. A strong flow was observed behind the fin, and the model achieved a high speed. These results indicate the usefulness of the proposed propulsion system.

2. MODEL TEST

2.1 MODEL

A simple model configuration was adopted because it's easy construction. The hull was constructed from styrene foam with a density ρ of 0.02, and cut using a heat wire in a shape similar to a soap box with a trench under the bottom plane. The cut-out surfaces were waterproofed with paint. Because the model material is styrene, the cutting was easy, but ensuring the precision of the finished dimensions of the model was difficult, necessitating careful cutting. A trench was cut square in the bottom of the model, and the hull was shaped like a catamaran to ensure course stability during the self-propulsion test.

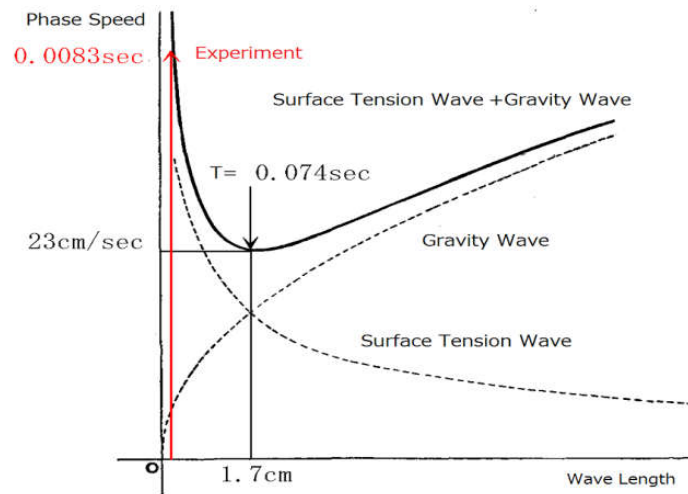


Figure 1. Phase speed as a function of wavelength.

2.2 SMALL VIBRATOR

The small vibrator shown in Photo.1 was used in this study. It is a light-weight direct current (DC) vibrator motor that is commonly used in cellular phones. The vibrator has one unbalanced weight installed along the rotating axis, and the high-frequency revolution of the motor produces a centrifugal force that causes vibration. A photo-interrupter type rotation meter was built and used to determine the motor voltage to rotating characteristics rpm/V. In this measurement, a newly developed system based on the PIC16F873A microcontroller was used, and the measurement results are shown in Fig.2. This figure shows that a 1.5 V battery drives the motor at 110 rps and produces a 110 Hz vibration.

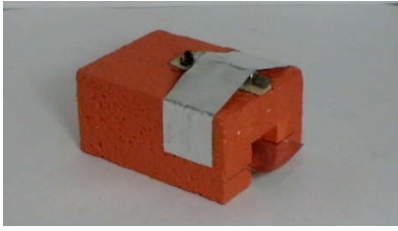
Photo.2 shows the micro vibration motor integrated into a circuit consisting of a micro-switch and 1.5 V button-type cell battery to drive the vibrator assembled on a universal base measuring 10 mm × 40 mm. The gross weight of the model is 12 grf (1.22 dyne). Photo.3 shows how the micro forced oscillator was attached to the model during testing.



Photograph 1. Micro vibration motor.



Photograph 2. Circuit of micro forced oscillator, including micro vibration motor, battery, and switch.



Photograph 3. Model setup during testing.

A flexible horizontal fin was attached to the aft of the model, and the micro forced oscillator was mounted on the model deck.

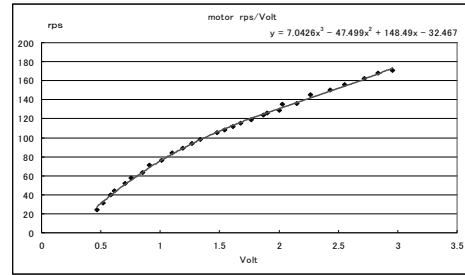


Figure 2. Rotational speed of micro motor vs. input voltage.

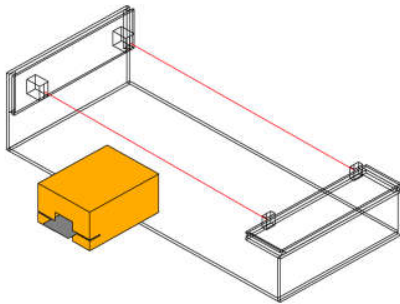
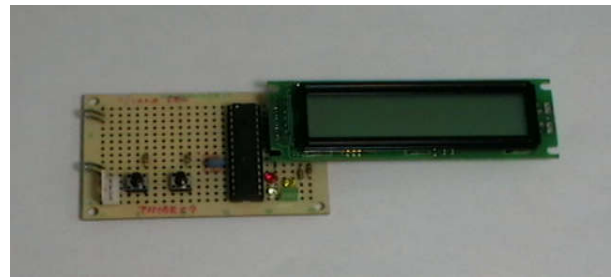


Figure 3. Schematic of test setup. Infrared (IR) photogates were constructed to measure the model speed.



Photograph 4. Newly designed 1/000 s precision count up stopwatch based on PIC16F873A microcontroller.



Photograph 5. Model measurement setup. The shallow water tank was constructed from acrylic plates. Paper was attached to the tank side plates to intercept extra light. The water depth was 27 mm, and the length and breadth of the tank were 1770 and 540 mm, respectively.

2.3 MEASUREMENT SYSTEM

Fig.3 shows the noncontact photogate that was built to measure the forward speed of the model. The measurement system was constructed using two infrared (IR) light-emitting diodes (LEDs) with 40 kHz pulse emissions to set the start and end signals. Two sets of photogates were used to receive the start and end signals and count up the elapsed time between them, representing the time required for the model to pass between the two photogates. To eliminate the effects of wind, a shallow water tank made of acrylic fiber was used, as shown in Photo.5. The depth of the water in the tank was set to 27 mm. To measure the time required for the model to pass between the photogates, a 1/1000 s precision stop watch system was developed using a PIC16F873A controller and a 20 MHz clock, and the forward speed of the model was recorded.

2.4 EXPERIMENTAL RESULTS

At a battery voltage of 1.5 V, the model vibration is 110 Hz, as shown in Fig.2, and the forward speed depends on the fin width. A fin made of steel use stainless (SUS) with a thickness of 0.02 mm was installed on the stern of the model at the same height as the surface elevation. A parallel cut was made 10 mm from the bottom surface. The fin was inserted in and glued to the hull. Fig.4 shows the model forward speed plotted against the fin width; the optimal conditions occur when the forward speed reaches a maximum. The maximum forward speed of 0.18 m/s obtained in this test was relatively high in comparison with the model length (0.08 m).

To observe the flow field behind the fin, a bollard pull test was conducted. A video of this test was recorded, and a still from this video is shown in Photo.6. In this case, the vibration motor was installed on the upper part of the fin. A strong flow formed from the trailing edge of the fin, and a big wave front formed behind the fin. Photo.7, which was taken using a strobe light, shows the wave pattern around the square hull. When this photograph was taken, a surface tension wave had also formed around the hull, but at the aft of the hull and behind the fin, more complex and higher waves were observed.

The jet flow caused by the beating motion of the fin near the free surface significantly contributed to the thrust force generated on the high-frequency vibration fin. As shown in the appendix, the surface tension wave propulsion effect was rather low. In the many experiments conducted on the same small vibrator without a fin, the forward speed is very slow and did not match that achieved with the fin. Moreover, observations revealed that a strong jet flow formed when the high-frequency vibration fin was switched on, even if the vibration frequency was changed. To investigate the frequency dependence of the jet flow formation, power was supplied from outside of the model with an umbilical cable. The voltage was varied from 1 to 3 V, corresponding to a forced frequency of 90–190 Hz, and a strong jet flow was observed at each voltage.

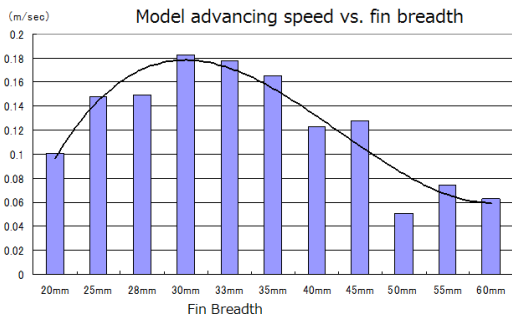
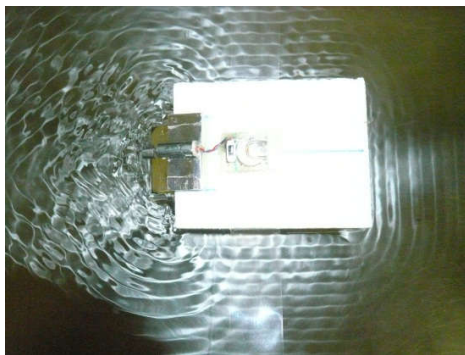


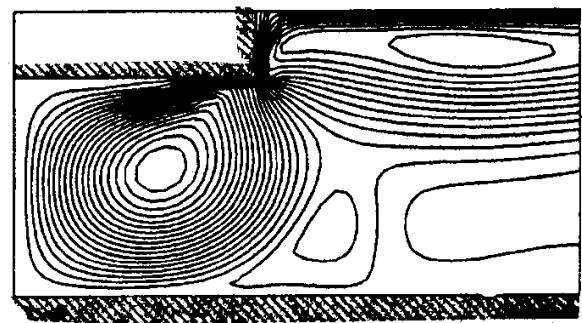
Figure 4. Model forward speed plotted against fin width with fin length of 20 mm.



Photograph 7. Surface tension wave pattern generated by high-frequency vibration system. Model was moored by transparent tape.



Photograph 6. Flow field during bollard pull test. Steady surface elevation and strong jet flow were observed at the aft of the fin. Large air bubbles were thrown with strong flow.



Streaming flow $R_s = 1000.0$

Figure 5. Calculated sample of acoustic streaming³⁾.

3. CONCLUSION

In naval architecture, gravitational waves are very common, and their high-frequency surface tension wave region is not currently an area of interest. Therefore, when we began this study, we found no reports or investigations concerning such phenomenon. However, after the experiments in this study were conducted, we discovered that similar phenomena have been reported in studies on acoustic flow³⁾.

Acoustic flow is flow caused by the acoustic pressure that occurs on a vertical vibrating surface when an ultrasonic device is submerged in a fluid. Additionally, a strong flow is generated in the direction tangential to the acting face. The ultrasonic frequency is near 40 kHz, but the frequency of the vibration of the fin in this case is less than 0.1 kHz. Furthermore, the direction of the fin vibration is the same as that in the ultrasonic vibration device discussed in this paper.

The figure is the numerical analysis of this acoustic problem and discusses a phenomenon that accompanies ultrasonic vibration. An example of a calculated acoustic flow field is shown in Fig.5. This figure shows that the flow caused by the ultrasonic vibration includes a strong circular flow started from the rear edge part. This phenomenon is regarded to be the same as that investigated in the present study, but it must be considered in more detail in future works.

REFERENCES

- 1) Longuet-Higgins, M. S. : The mean force extracted by waves on floating or submerged bodies with application to sand bars and wave power machines, Proc. R. Soc. London. A. 352, 1977,p463
- 2) Yutaka Terao; The floating object which drift against the wave- Possibility of the wave propulsion system-,1982,KSNAJ No.184, pp51-54
- 3) Charles Thompson, et.al: Acoustic streaming generated by an oscillating surface, Frontiers of nonlinear Acoustics; Proc. 12th ISNA,1990, pp365-370

APPENDIX

A1. THRUST GENERATION BY RADIATING SURFACE WAVE

Surface tension waves can be described by the equation

$$p_{z=\eta} - p_0 = -\frac{\alpha \partial^2 \eta}{\partial x^2}, \quad (1)$$

where α is the surface tension and η is the wave height. The kinematic equation is then

$$\varphi_t + \frac{1}{2} u^2 + \frac{p}{\rho} + g\eta = \frac{\alpha}{p_0} \frac{\partial^2 \eta}{\partial x^2}. \quad (2)$$

Equations (1) and (2) can be linearized as

$$\eta_t = \varphi_z \quad (3)$$

$$\varphi_t = -g\eta + \frac{\alpha}{p_0} \frac{\partial^2 \eta}{\partial x^2}. \quad (4)$$

The following solutions satisfy equations (3) and (4):

$$\eta = \sum_k A_k e^{i\omega t} \sinh k(h+z) \quad (5)$$

$$\varphi = \sum_k B_k e^{i\omega t} \sinh k(h+z). \quad (6)$$

Then

$$\frac{\partial^2 A_k}{\partial t^2} = -(gk + \frac{\alpha}{\rho} k^3) \tanh kh A_k \quad (7)$$

$$\omega = \sqrt{(gk + \frac{\alpha}{\rho} k^3) \tanh kh}. \quad (8)$$

In this case, $h \gg 0$, and

$$\omega = \sqrt{gk + \frac{\alpha}{\rho} k^3}. \quad (9)$$

The region in which surface waves are dominant is given by

$$k_m = \sqrt{\frac{g\rho}{\alpha}} \quad (10)$$

$$\lambda_m = 1.7(\text{cm}). \quad (11)$$

The phase speed C is defined as

$$C = \sqrt{\frac{\omega}{k}} = \sqrt{\frac{g}{k}} \sqrt{1 + \frac{k^2}{k_m^2}} \quad (12)$$

$$c_m = \sqrt{\frac{2g}{k_m}} = 23(\text{cm/sec}) \quad \text{at } k = k_m. \quad (13)$$

Following the momentum theory by Longuet-Higgins¹⁾, the thrust force can be derived from the radiating surface tension wave. The energy E_s of the surface tension wave is

$$E_s = \frac{A}{2} \frac{\alpha}{2} k^2 \eta^2, \quad (14)$$

and the surface tension wave group velocity C_g is

$$kh \gg 1, \text{ and } \tanh kh = 1 \quad (15)$$

$$C_g = \frac{3}{2} C. \quad (16)$$

Therefore, the phase speed C is

$$C = \left(\frac{2\pi\alpha}{\rho\lambda} \right)^{1/2} = \left(\frac{\alpha k}{\rho} \right)^{1/2}. \quad (17)$$

The thrust produced by the radiating surface tension wave of the height A is then given as

$$\begin{aligned} F &= E_s / C_g \\ &= \frac{1}{2} A \frac{1}{2} \alpha k^2 \eta^2 \\ &= \frac{3}{2} \left(\frac{\alpha k}{\rho} \right)^{1/2} \\ &= \frac{A}{6} (\alpha k^3 \rho)^{1/2} \eta^2 \end{aligned} \quad (18)$$

A2. PURE SURFACE TENSION WAVE MAKING PROPULSION SYSTEM

Some experiments were conducted without a fin in the floating body. The bow down trim was 30 mm, as shown in Photo.8. The vibration motor was used as well as in the present study. In this case, a forced vibration made directly the hull vibration and surface tension waves were generated as shown in Photo.9. In this case, the hull moved to the right in Photo.9. The surface tension wave height was a few millimeters, and it was difficult to distinguish whether the bow or the stern wave had a greater height. This small difference of the surface tension wave height, bow and stern wave, caused poor propulsion efficiency and also showed slow advanced speed performance.

If the direction of the diverging surface tension wave and height can be controlled freely, a thrust force

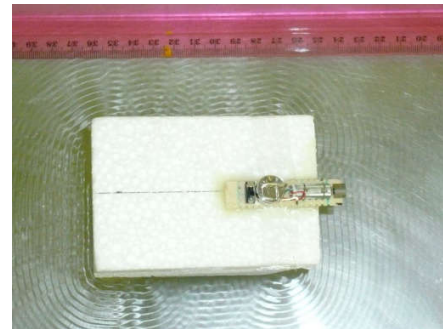
will be larger than that as shown in Photo.9. Our forced oscillator is composed one unbalanced DC motor vibrating system and quite simple but at the same time, vibrate the hull with 6-degree of the hull motion. And undesired hull motion causes plane-diverging waves. This is reason why the low forward speed achieved by the surface tension wave-making propulsion system.

However, with a horizontal fin, the height of the stern surface tension wave may surpass that of the bow surface tension wave, as shown in Photo.7. The combined effect of this and the effect of the fin jet flow allow the high speed performance of the floating body.

For the simple model shown in Photo.8 and Photo.9, the forward speed is only several centimeters per second, and the course stability is quite poor. Therefore, while there is hydrodynamic interest in this model, its application as a small hull thruster would be ineffective.



Photograph 8. Surface tension wave making propulsor. Model advancing direction is right of the photo.



Photograph 9. Generated surface tension waves with model running condition. The model moving direction is right.

AN EXAMPLE OF LANDING GEAR SHIMMY EXPERIENCE ON SMALL JET AIRCRAFT

Kohei Inoue ⁺¹

⁺¹Sumitomo Precision Products Co., LTD., Amagasaki, Japan

Wheel shimmy of an aircraft landing gear is one of self-induced vibration. Wheels and tires equipped at the bottom of a landing gear will have yaw oscillation about the vertical axis when shimmy occurs. Such shimmy was observed at the nose landing gear on a small jet aircraft. Investigation succeeded to replicate the shimmy at the laboratory component test, which determined some specific conditions where shimmy would occur. The shimmy problem was finally resolved by the following improvement - The steering collar was modified to have a viscous resistance feature for more damping and a more stable friction feature.

Keyword: Shimmy, Aircraft, Landing gear

1. INTRODUCTION

Wheel shimmy of an aircraft landing gear is one of self-induced vibration. An aircraft landing gear basically consists of vertical column structure, and its wheel with tires equipped at the bottom will have yaw oscillation about the landing gear axis as shown in Figure 1 when shimmy occurs. Sometimes this vibration will affect aircraft controllability at the ground operation when it has great amplitude, or even cause damage on the aircraft structure or equipment. Detailed in this article is one example of the shimmy vibration problem which occurred on a small jet aircraft and the countermeasure applied to stop the problem recurring.

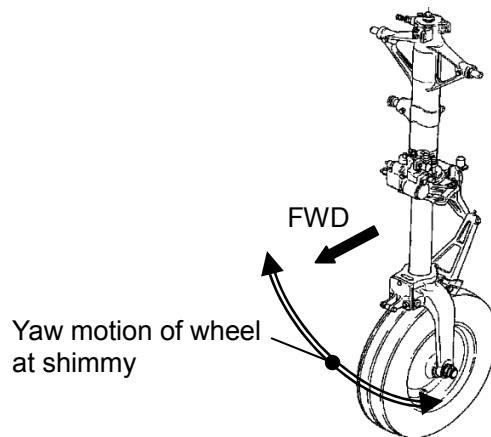


Figure 1: Basic motion of landing gear shimmy

(1) About landing gear

Landing gear is a structural component which supports aircraft on the ground. Typically three landing gears are fitted on an aircraft, these are one nose landing gear located just under the cockpit and two main landing gears located under each of the main wings. Each landing gear provides functions to handle the aircraft on the ground such as steering by nose landing gear, braking by main landing gear as well as shock absorbing at the aircraft landing and taxiing by both nose and main.

There are several types of landing gear, one of which is articulated type with rotatable jointed links, and another is non-articulated type which is also called cantilevered type. The wheel is directly mounted at the bottom end of the shock absorber for the cantilevered type and shimmy is typically prevalent on this type of

⁺¹isfa0001@jaxa.jp, ⁺²isfa0002@company.com, ⁺³isfa0003@univ.ac-u.jp

landing gear. Typical examples are shown in Figure 2 for both types of landing gear.

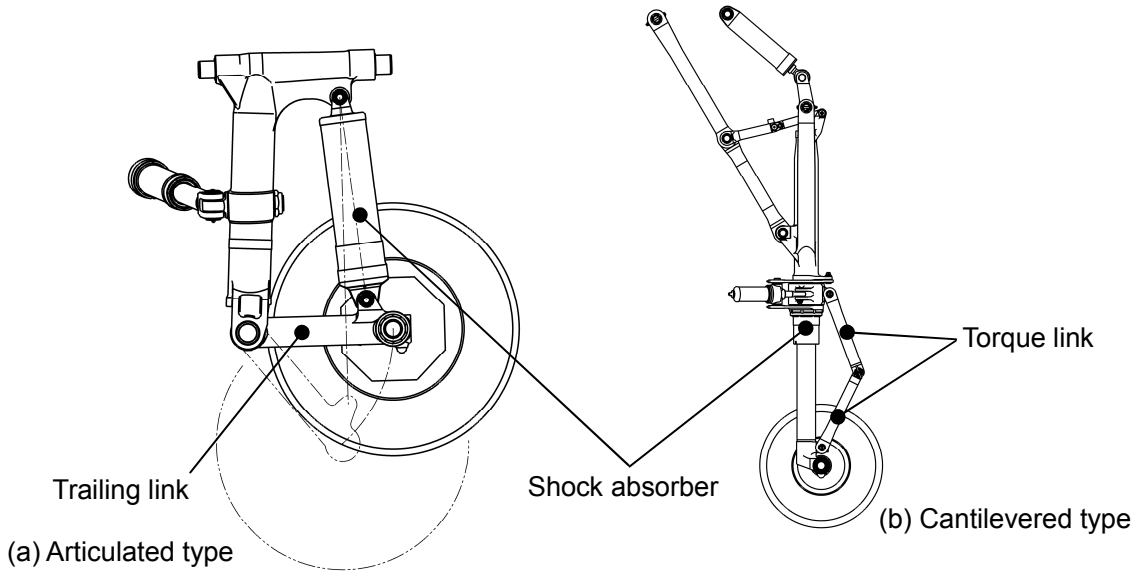


Figure 2: Types of landing gear

Shock absorbing function is usually achieved by gas and oil type shock absorber which is composed of two telescopically connected cylinders for the containment of the nitrogen gas for gas spring effect and hydraulic fluid for oil damping effect. Typical composition is shown in Figure 3. For the cantilevered landing gear, the outer cylinder and piston (inner cylinder) can be rotated about their co-axis which provides the degree of freedom for the yaw motion on the wheel at the shimmy. This is the reason this type is most typically related to the shimmy. For mitigation, torque links are connected to these cylinders so that their relative rotation is restrained while axial compression can be freely obtained.

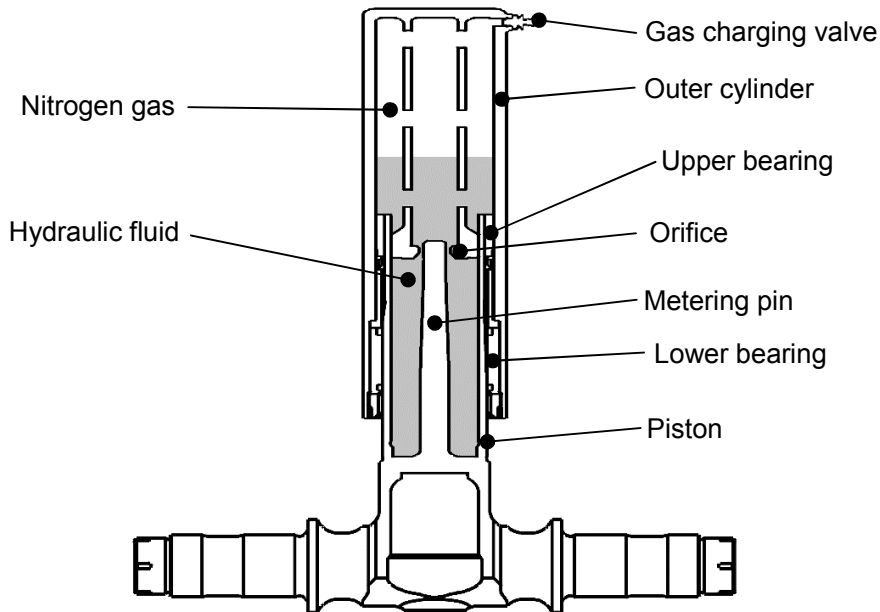


Figure 3: Gas and oil type shock absorber composition

Nose landing gears are usually equipped with a steering mechanism which swivels the wheel about the landing gear axis. An example of a steering mechanism is shown in Figure 4. Hydraulic or electrical actuators rotate the steering collar and connected torque links, which finally changes tire orientation. Obviously this

mechanism also provides the degree of freedom of yaw motion on the wheel. In many cases the steering control system is activated while the aircraft is on the ground and deactivated while the aircraft is in air or at landing.

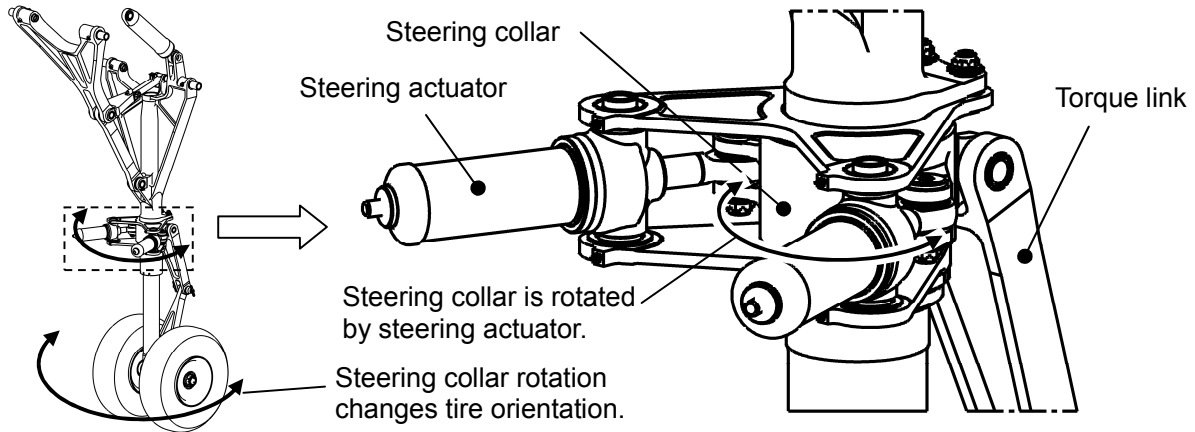


Figure 4: Steering mechanism

(2) Factor for shimmy

Input load on the tire will cause excitation resulting in shimmy vibration. In some cases dynamic or static unbalance of the tire will make periodical input to the tire which causes shimmy. In some cases an uneven ground surface will cause random loads on the tire which can also cause shimmy.

When the wheel has displacement by the input load from the tire, elasticity of the tire or of the landing gear structure will provide the restoring force to the wheel back to the original position. In some case the landing gear has some geometrical trail or caster angle, as illustrated in Figure 5, which provides additional restoring force when the aircraft moves forward.

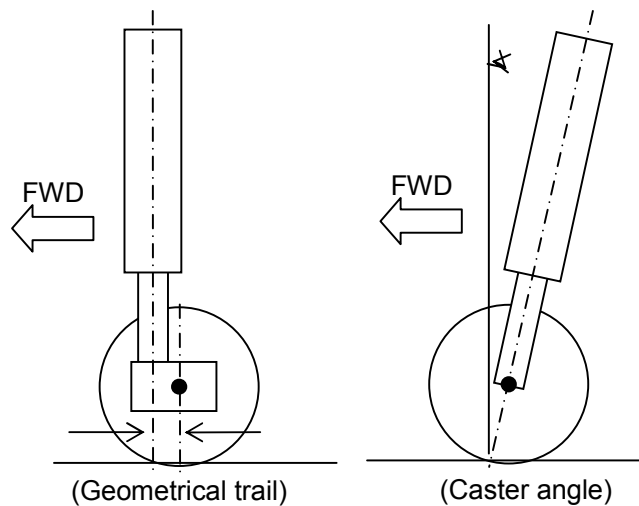


Figure 5: Wheel trail and caster

Friction at each movable joint provides damping effect against the shimmy vibration. Bearing friction or seal friction inside the shock absorber, or joint friction of the linkage system provides this effect. Sometimes greater friction is intentionally added for more damping. For the nose landing gear with hydraulic steering system, damping element is often added in the hydraulic line. When the steering system is activated, hydraulic source will apply pressure to the actuator to control the wheel orientation. When the system is deactivated, hydraulic pressure will be blocked and internal hydraulic line will make a closed circuit. At this

condition, the steering actuator can move freely by external loading. Damping orifice is placed in such closed line to generate damping force when the actuator is forced to move by external loading such as shimmy vibration.

At the design phase of the landing gear, dynamic simulation will usually be performed to confirm the structural stability against the shimmy vibration. In some cases landing gear component test will be performed to verify the simulation results. Even after these simulations and tests shimmy may occur at the aircraft ground operation. This may be because the simulation model has not completely represented the conditions and also predicted parameters used in the simulation are not always exactly correct. In some case shimmy will be observed some years after the aircraft has been in service. It will often be a great impact to modify mass or stiffness properties as a countermeasure against the observed shimmy, so the approach tends to be to modify the damping property.

2. OBSERVED SHIMMY

Wheel shimmy was observed on the nose landing gear of the small jet aircraft. The nose landing gear is a cantilevered type equipped with hydraulic steering. Similarly to many other aircraft the hydraulic steering system of the nose landing gear has a damping element. In addition, the nose landing gear is equipped with additional friction element at the steering collar. The steering collar is rotatable and installed onto the outer cylinder. A disk spring below the collar applies compression load which results in additional friction to the collar rotation. Composition of the steering collar is shown in Figure 6.

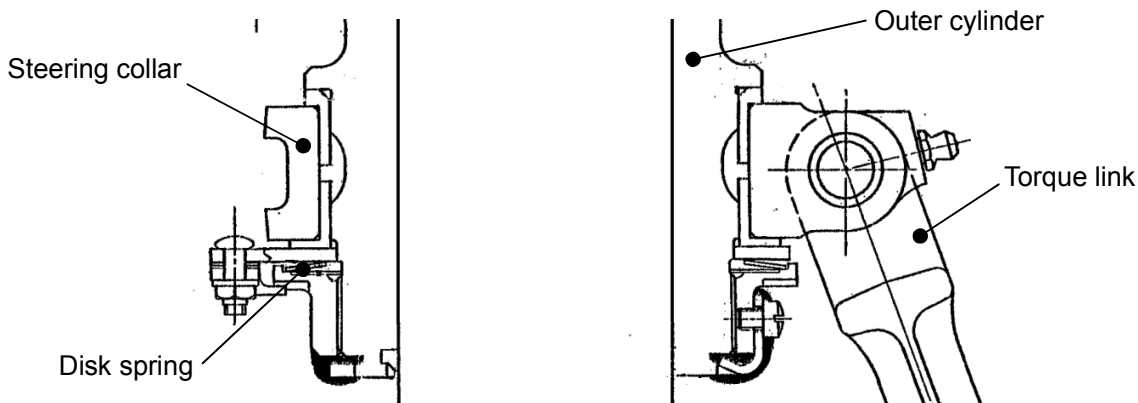


Figure 6: Steering collar composition

Shimmy was observed several times as shown in Table 1. In some cases, shimmy vibration was so severe that it became an obstacle to the safe ground operation of the aircraft. As shown in Table 1, it was considered that observed shimmy did not have any relation with specific aircraft or airport.

Table 1: Aircraft conditions when shimmy occurred

	#1	#2	#3	#4	#5	#6	#7	#8	#9
Aircraft	A	B	C	D	C	C	E	F	G
Airport	a	b	c	d	c	c	d	b	d
Aircraft speed [knot>(*1)	100	90	80	85	90	90	100	78	105
Collar Friction [lbf>(*2)	50	50	70	60	75	75	77	88	104
Tire unbalance [kgf>(*3)	-	-	18.4	19.5	-	-	-	10.3	17
Steering system (*4)	ON	OFF	ON	ON	ON	ON	ON	ON	ON
Brake (*5)	Yes	Yes	Yes	Yes	Yes	Yes	Yes	Yes	Yes

Note:

(*1) 100knot = approx. 185km/h.

- (*2) 100lbf = approx. 445N. Tangential force to rotate collar applied at the location 72mm from center of rotation.
- (*3) 10kgf = approx. 98.1N. Centrifugal force generated at 70knot tire rotation.
- (*4) ON: Steering system activated/ OFF Steering system inactivated.
- (*5) Yes: Aircraft was under braking condition when shimmy occurred.

3. INVESTIGATION

This section describes the investigation performed for observed shimmy. From the conditions where shimmy was observed, followings were assumed to be related to the shimmy occurrence.

- Aircraft speed
- Steering system condition (Activated/Deactivated)
- Braking operation

(1) Investigation on nose landing gear

Investigation was started on the nose landing gear to find any trouble factor causing shimmy vibration. As a result, however, no significant evidence was observed. No excessive wear was observed on the parts which would cause larger free play. Stiffness of the landing gear structure was similar to previous measurement. Tire unbalance was also similar to previous measurement which was within expected.

(2) Shimmy replication test

Comprehensive shimmy test was performed with the nose landing gear at the dynamic test facility to obtain the condition where shimmy would occur. Nose landing gear was installed on the test equipment, vertically loaded onto the large wheel drum which was rotating to simulate the ground speed, and its behavior was observed if shimmy occurred or not. Detail of test setup is described below.

Nose landing gear is installed with the attachment fixture onto the bottom of the weight carriage which can vertically slide along the guide rails. The weight carriage is supported by lifting actuators and is operated to move up and down by adjusting pressure for the lifting actuators. The test equipment also has the large wheel drum under the weight carriage which is electrically operated to rotate. When the pressure is reduced from the lifting actuators the weight carriage with attached nose landing gear is lowered, and when it contacts with the peripheral surface of the rotating wheel drum the tire will be forced to rotate by the rotating drum. Thus intended vertical loading condition will be achieved by adjusting lifting actuator pressure and forward speed will be achieved by adjusting the drum rotation. When the vertical load and tire rotation becomes steady condition without severe vibration, impulse load is laterally applied by the loading actuator at the lower part of the nose landing gear to intentionally add a disturbance. If severe vibration occurs beyond the predetermined acceleration level, or if it does not recover steady condition soon within 0.3second after the impulse loading, then it is considered as shimmy occurrence.

In addition, the attachment fixture is designed to simulate the stiffness and weight distribution of the aircraft structure. In many cases the structure of this kind of test equipment is much more rigid than it actually is on the aircraft. It can be easily understood that the aircraft structure is designed to minimize its weight which will result in lower stiffness than test equipment. This stiffness gap often makes it difficult to replicate the behavior on the aircraft at the laboratory component test. Some device is added to minimize this gap, and its effect was validated by simplified modal testing. Lateral acceleration was measured at some points of nose landing gear and of the fixture when the hammering test was performed. Natural frequency and phase difference of those measurement points were confirmed similar to those obtained at the measurement on the aircraft¹⁾.

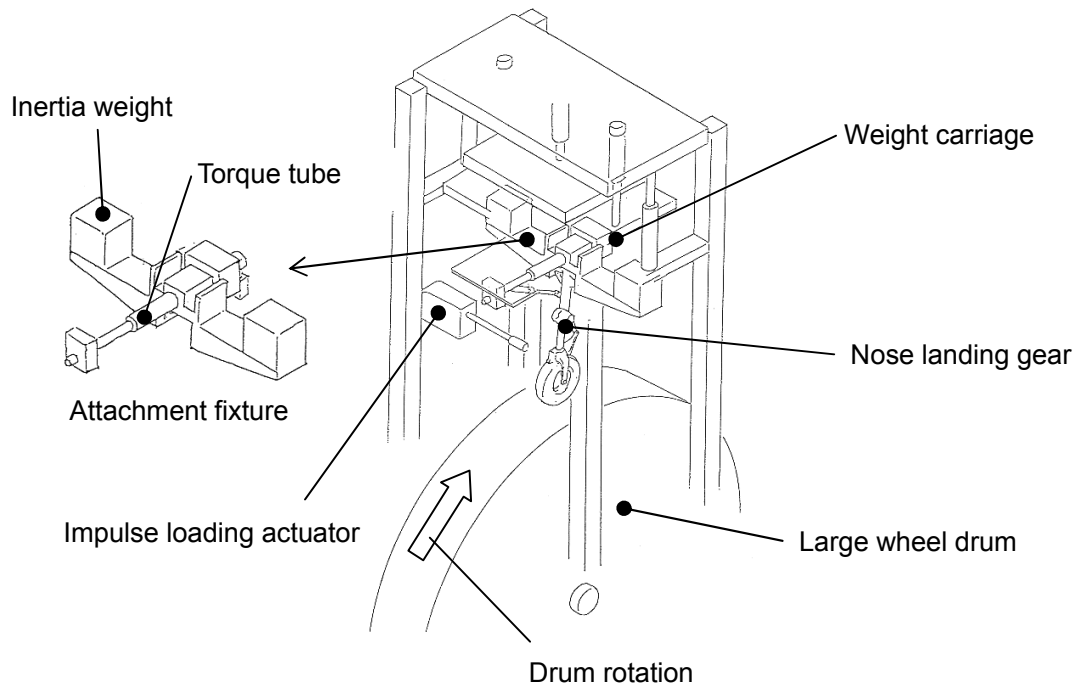


Figure 7: Shimmy test setup

To find the condition where shimmy occurs, some parameters were varied as test conditions. Following table summarizes the test conditions.

Table 2: Test conditions

	#1	#2	#3	#4	#5	#6	#7	#8
Tire unbalance [kgf>(*1)	44	44	44	44	25	25	25	17.5
Collar Friction [lbf>(*2)	92	92	92	92	92	70	44	44
Vertical load [tonf>(*3)	1.3	1.3	0.7	0.7	1.3	1.3	1.3	1.3
Steering system (*4)	ON	OFF	ON	OFF	ON	ON	ON	ON
Ground speed [knot>(*5)	60-90	60-120	50-120	50-120	80-120	80-95	80-85	85-95
	#9	#10	#11	#12	#13	#14	#15	
Tire unbalance [kgf>(*1)	17.5	17.5	17.5	17.5	11	11	11	
Collar Friction [lbf>(*2)	39	39	39	39	40	40	40	
Vertical load [tonf>(*3)	1.3	1.2	0.9-1.1	1.0-1.3	0.7	0.3	0.3	
Steering system (*4)	ON	ON	ON	ON	ON	ON	OFF	
Ground speed [knot>(*5)	80-120	80-95	83-87	85-90	70-100	50-120	50-120	

Note:

- (*1) 10kgf = approx. 98.1N. Centrifugal force generated at 70knot tire rotation.
- (*2) 100lbf = approx. 445N. Tangential force to rotate collar applied at the location 72mm from center of rotation.
- (*3) 1tonf = approx. 9.81kN. 1.3tonf corresponds to load at max takeoff weight + braked roll load.
- (*4) ON: Steering system activated/ OFF Steering system inactivated.
- (*5) 100knot = approx. 185km/h.

(3) Shimmy test result

More than 100 cases were tested to cover the conditions shown in Table 2, and shimmy was observed at the following cases out of them. Record of the acceleration measurement is shown in Figure 8.

Table 3: Shimmy observed conditions

	#1a	#1b	#7	#9a	#9b			
Tire unbalance [kgf>(*1)	44	44	25	17.5	17.5			
Collar Friction [lbf>(*2)	92	92	44	39	39			
Vertical load [tonf>(*3)	1.3	1.3	1.3	1.3	1.3			
Steering system (*4)	ON	ON	ON	ON	ON			
Ground speed [knot>(*5)	90	89	85	85	85			
Note: See Table 2 for definition of (*1) ~ (*5).								

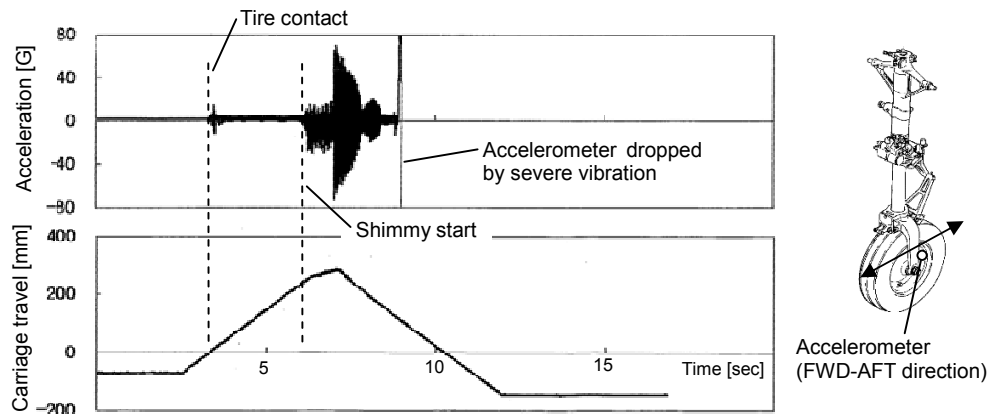


Figure 8: Acceleration record at shimmy observed case (Case #1b)

Severe vibration was observed while the nose landing gear was being compressed without lateral pulse loading at each case. Test conditions of ground speed, vertical load and steering mode coincided with those on the aircraft when shimmy occurred, and therefore it was concluded that shimmy observed on the aircraft was successfully replicated at these laboratory tests. As assumed from observations on the aircraft, it has been confirmed by the tests that shimmy occurs when following conditions, at least, are obtained;

- Steering system is activated
- Nose landing gear is being compressed by certain amount of loading
- Ground speed is at 80-100 knot.

(4) Consideration for shimmy occurring condition

a) Steering system condition

Similar to other aircraft, a damping orifice is placed in the hydraulic line for the steering system, which will, however, effectively generate damping force only when the steering system is deactivated. From the fact that shimmy always occurs when the steering system is activated, it is considered damping is insufficient against the shimmy vibration.

b) Loading condition

When shimmy occurs on the aircraft, it is always under the braking operation. This can generate two effects inducing shimmy. When the braking force is applied on the tire, the aircraft will have rolling motion to rotate about the lateral axis which will result in more load and more compression on the nose landing gear. When the cantilevered nose landing gear is compressed, its natural frequency goes higher, and when it reaches certain condition to meet the aircraft mass and stiffness properties, shimmy can start with the excitation by the tire rotation at certain speed.

In addition, compressive motion of the nose landing gear might reduce its friction damping against the shimmy. When the nose landing gear is compressed, the inner cylinder slides on the bearing parts into the outer cylinder. If it is assumed that normal force on the sliding surface, friction coefficient, and resultant

friction force are same as before sliding, rotational friction component will be reduced as axial friction component increases. This reduction of friction can result in less damping and have some effect for the shimmy.

c) Ground speed

Ground speed will make tire rotation, which will result in the periodical centrifugal force by the tire unbalance. When frequency of this periodic input meets certain condition at 80-100 knot, shimmy can occur. It was confirmed by the laboratory test that not only the frequency but also the extent of tire unbalance will decide the shimmy occurrence as less unbalance case does not generate shimmy when the friction damping is sufficient. For example, when tire unbalance was reduced from 44 kgf (case #1-#4) to 25 kgf (case #5-#7), shimmy did not occur until collar friction was reduced from 92 lbf to 44 lbf.

4. COUNTERMEASURE

It was concluded from the test result that damping was insufficient against shimmy vibration when tire unbalance was large. Since it was considered that adding more friction at the steering collar might adversely affect steering function, new damping feature has been introduced to the steering collar.

(1) New steering collar

Narrow gap between the rotating part (rotor) and fixed part (stator) is filled with high viscosity fluid to generate damping force. Composition is shown in Figure 9. When the rotor relatively rotates to the stator, it is expected that viscous resistance will generate shear force by the fluid. Damping property can be modified by changing viscosity or gap. Thus new steering collar has been designed to have viscous damping feature.

In addition, friction feature has also been modified at the new steering collar. When the friction at the original steering collar was measured on the aircraft after shimmy was observed, it appeared to take wide range exceeding tolerance range at the initial set value. Sliding surface of the collar was lubricated with liquid grease and this lubrication tended to cause unstable friction property, often reduced the friction. Periodical friction check and adjustment had been necessary for maintenance. In order to improve it, solid lubrication is introduced as friction feature for the new steering collar²⁾.

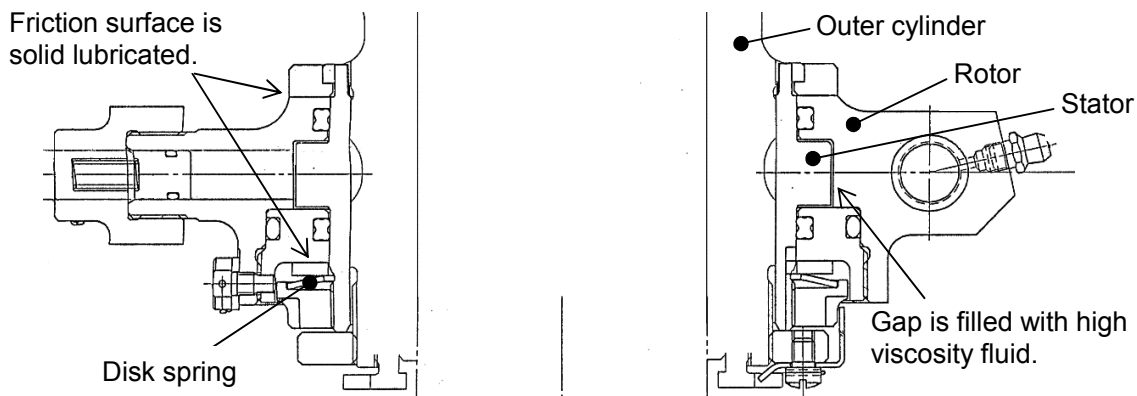


Figure 9: New steering collar composition²⁾

(2) Shimmy test with new collar

Comprehensive shimmy test was performed on the nose landing gear with the new steering collar. Tested conditions are shown in Table 4. As a result, no shimmy was observed at each test case including those where shimmy had been observed on the nose landing gear with the original steering collar. Lateral impulse load was applied at each test, but it did not induce shimmy, either. Figure 10 shows sample record of the acceleration measurement at the test with the new steering collar.

Table 4: Test conditions with new steering collar

	#1	#2	#3	#4	#5	#6	#7	#8
Tire unbalance [kgf>(*1)	60	60	60	60	60	60	60	60
Collar Friction [lbf>(*2)	80	80	80	80	80	80	40	40
Vertical load [tonf>(*3)	1.3	1.3	0.7	0.7	0.3	0.3	1.3	1.3
Steering system (*4)	ON	OFF	ON	OFF	ON	OFF	ON	OFF
Ground speed [knot>(*5)	50-120							
Fluid viscosity (*6)	High							
	#9	#10	#11	#12	#13	#14	#15	#16
Tire unbalance [kgf>(*1)	60	60	60	60	60	60	60	60
Collar Friction [lbf>(*2)	80	80	40	40	40	40	40	40
Vertical load [tonf>(*3)	1.3	1.3	1.3	1.3	0.7	0.7	0.3	0.3
Steering system (*4)	ON	OFF	ON	OFF	ON	OFF	ON	OFF
Ground speed [knot>(*5)	50-120							
Fluid viscosity (*6)	Low							

Note: See Table 2 for note (*1) ~ (*5).
 (*6) High: High viscosity fluid/ Low: Low viscosity fluid

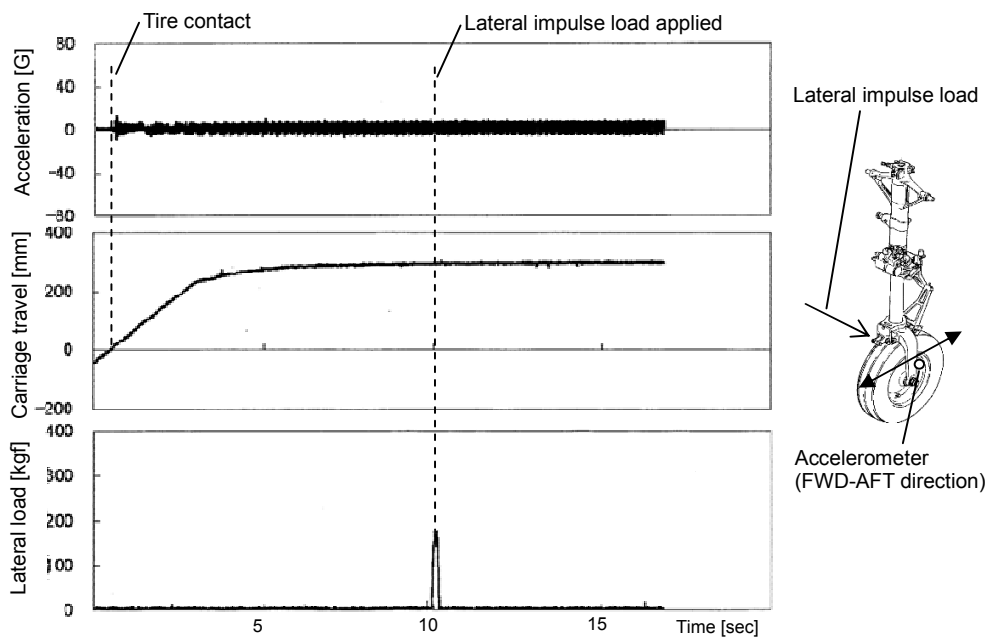


Figure 10: Acceleration record with new steering collar (Case #9 at 90knot ground speed)

With the original steering collar, friction setting needed to be higher to prevent shimmy when tire unbalance became greater. With new steering collar, even lower friction could prevent shimmy against greater tire unbalance. This should be considered as the effect of viscous damping by the included fluid. There was no problem observed with the friction damping feature with solid lubrication, such as excessive wear or others.

With these successful test results, it was decided that the nose landing gear should be modified to have viscous damping feature and solid lubrication feature at the steering collar. Design change has been already completed and neither shimmy nor other problem caused by the change has been observed for more than 10years.

5. CONCLUSION

Because shimmy had been observed on the nose landing gear, comprehensive shimmy test was

performed as laboratory component test. By simulating the stiffness and mass property of the aircraft, shimmy was successfully replicated at the similar conditions observed on the aircraft. Viscous damping feature and solid lubrication feature was tested as the countermeasure for the shimmy and it was concluded those were effective to prevent the shimmy.

ACKNOWLEDGMENT

The author gratefully acknowledges the contribution of Kawasaki Heavy Industry at the development activity and also the advice to complete this paper.

REFERENCES

- 1) Japanese patent #2886158 (Patent assignee: Kawasaki Heavy Industry).
- 2) Japanese patent #3102777 (Patent assignee: Kawasaki Heavy Industry).

BETZ ANALYSIS OF A SINGLE FLAPPING FOIL POWER GENERATOR

John Young⁺¹, Fang-Bao Tian and Joseph C.S. Lai
University of New South Wales, Canberra, Australia

The Betz limit for extraction of power from a flowing fluid is based upon an assumption of steady flow, and effects from viscosity and non-uniform pressures are ignored. Flapping foils used for power generation involve inherently highly unsteady flows, and operate most effectively when there is significant vortex shedding from the foil leading edge. This work conducts an analysis of the theoretical limits of efficiency for such an unsteady system, for the first time. Analysis of the magnitude and impact of the unsteady effects shows that the action of shed vortices as they convect downstream entrains a significant amount of momentum and kinetic energy into the wake of the foil. This entrainment is likely insufficient to render the Betz limit invalid for a single foil, however it is promising for a tandem foil system where the downstream foil benefits from this re-energisation of the upstream foil wake, and suggests a mechanism by which the Betz limit for such a system (64%) might theoretically be exceeded.

Keywords: Flapping foil, Power generation, Betz analysis.

1. BACKGROUND

Conventional rotary turbines are generally accepted to be governed by the Betz limit in the maximum power that they can extract from a flow. This is based on an analysis of the streamtube enclosing the flow passing through the swept area of the turbine, which is treated as an idealised actuator disk¹⁾, and makes no particular assumptions about the nature of the turbine. The flow is assumed to be inviscid and steady, rotation of the flow in the wake is ignored, and ambient pressure at the far upstream and downstream ends of the streamtube as well along its outer boundary is assumed²⁾. The analysis states that the maximum power that can be extracted from a given flow is in the ratio 16/27, or 0.5926, of that which flows through the turbine swept area.

Various models incorporating the wake rotation differ in their predictions about efficiency versus turbine blade tip speed ratio. Sorensen et al.^{3,4)} discuss some recent controversy suggesting that at low tip speed ratios, rotary turbines may in fact substantially exceed the Betz limit.^{5,6)} However when the effect of lateral pressure and friction forces are included in the axial momentum equation, the Betz limit is again respected at all tip speed ratios.^{3,4)}

Vennell⁷⁾ notes that the 16/27 limit can be exceeded significantly when tidal flow in a channel is considered, due to the constraints imposed by the channel walls (whereas wind turbines are usually considered operating in an infinite, unconstrained space). Incidentally this is also the source of many claims of systems exceeding the Betz limit, by using a flow constriction (e.g. a shroud) ahead of and around the turbine to speed the flow, but using the original flow speed for non-dimensionalisation.

In a similar vein, Vennell⁷⁾ makes a distinction between high power, and high power coefficient non-dimensionalised by the local mean flow velocity that the turbine is exposed to, which may be much lower than the free stream velocity at the front of a turbine "farm". He thus proposes a stricter definition of the Betz limit, which poses the question of whether a turbine within a farm in a channel can generate more power than a single turbine operating at the Betz limit in the same channel.

The Betz limit for two turbines in tandem, i.e. one behind the other so that the downstream turbine is in the wake of the upstream one, is 0.64⁸⁾ and asymptotes to 0.66 for many turbines in tandem⁹⁾. There have been some statements that flapping foils are not subject to the Betz limit⁹⁾, at least for two in tandem, due to the vortical nature of the wake of the leading foil entraining additional momentum from the free stream to re-energise the wake somewhat before it encounters the trailing foil. This is supported by simulations⁹⁾ of two foils in tandem achieving an efficiency of $\eta = 0.64$, right against the Betz limit for this configuration, which

⁺¹j.young@adfa.edu.au

seems unlikely without such a mechanism. Dabiri¹⁰⁾ also states that the Betz limit does not apply to flapping foil systems because of the unsteadiness, and that vortex dynamics could be used to exceed the Betz limit.

Flapping foil turbines are under consideration as alternatives to rotary turbines in river and tidal flow applications^{11,12)}, due to their potential for higher relative performance at lower Reynolds numbers (i.e. low flow speeds and small scales). However there is as yet no rigorous assessment of the theoretical maximum power extraction capability of flapping foils as there is for rotary systems¹¹⁾. This paper performs that analysis for the first time to determine whether claims of the effects of unsteady momentum and energy transport on the limits of performance have a basis in fact.

2. TIME AVERAGED FLOW OF A FLAPPING WING TURBINE

The Betz limit is derived with the assumption of steady flow²⁾, and in the simplest form also ignores viscous effects. The efficiency of power extraction from the flow depends on the so-called 'axial induction factor' defined as the fractional decrease in flow velocity between the free stream and the plane of the turbine. This in turn determines the extent to which the streamtube passing through the maximum extent of the turbine frontal area, spreads between the free stream far upstream and the wake far downstream. How may we then perform a similar analysis of the highly unsteady flow through a flapping wing turbine? A starting point is to time-average the flow field over one cycle of flapping motion (with the provision that the flow is periodic with period T equal to that of the flapping cycle), and to obtain the streamtube passing through the maximum extent of the swept area of the flapping wing, based on the time-averaged velocities.

The unsteady flow satisfies the incompressible Navier Stokes equation (in tensor notation):

$$\frac{\partial u_i}{\partial t} + u_j \frac{\partial u_i}{\partial x_j} = -\frac{1}{\rho} \frac{\partial p}{\partial x_i} + \nu \frac{\partial^2 u_i}{\partial x_j^2} \quad (1)$$

The flow variables may be split into average and fluctuating terms:

$$u_i = U_i + u'_i, \quad p = P + p' \quad (2)$$

where u_i and p are defined as flow variables time-averaged over one flapping cycle (using the usual overbar as shorthand for the averaging process):

$$U_i = \overline{u_i} = \frac{1}{T} \int_t^{t+T} u_i(t) dt, \quad P = \overline{p} = \frac{1}{T} \int_t^{t+T} p(t) dt \quad (3)$$

and thus are independent of time. This is notationally precisely equivalent to the Reynolds Averaged Navier Stokes (RANS) process more generally employed in modeling the effects of turbulence, although noting that there is no assumption here of turbulence in the flow, and the averaging process is *explicitly defined as a time-average with period equal to one flapping cycle*. The time-averaged flow then satisfies the steady RANS equation:

$$U_j \frac{\partial U_i}{\partial x_j} = -\frac{1}{\rho} \frac{\partial P}{\partial x_i} + \nu \frac{\partial^2 U_i}{\partial x_j^2} - \frac{\partial}{\partial x_j} \left(\overline{u'_i u'_j} \right) \quad (4)$$

The effect of unsteadiness in the flow is thus encompassed entirely within the Reynolds stress term $R_{ij} = \overline{u'_i u'_j}$, which manifests as a diffusive effect.

There is no convection of any flow property across a streamline locally tangent to the time-averaged velocity components U_i , and diffusion of momentum across streamlines via molecular viscosity is usually ignored in the Betz analysis as being small. However the Reynolds stress term now provides an additional mechanism for diffusion of momentum across the sides of the time-average streamtube, and in principle this diffusion may be large enough that it must be considered in the Betz analysis. Additional transport of kinetic energy across the streamtube sides is similarly apparent from time-averaging the conservation of energy equation.

The integral forms of conservation equations for mass, momentum and mechanical energy (i.e. ignoring changes in internal and potential energy, and no heat transfer) in a control volume constituting the streamtube enclosing the maximum extent of the turbine frontal area are used to perform the analysis in detail (Eq. 5 to 7).

Here that streamtube is defined by streamlines locally tangent to the time-averaged velocity field, as shown in Fig. 1.

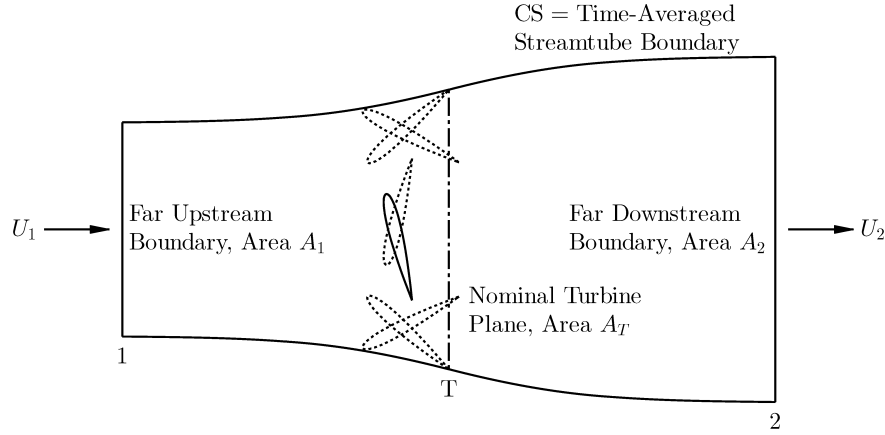


Figure 1: Time-averaged streamtube as the control surface (CS) for analysis of the flapping foil turbine.

$$\frac{\partial}{\partial t} \int_{CV} \rho dV + \int_{CS} \rho u_i n_i dA = 0 \quad (5)$$

$$-F_{T,i} - \int_{CS} p n_i dA + \int_{CS} \mu \left(\frac{\partial u_i}{\partial x_j} + \frac{\partial u_j}{\partial x_i} \right) n_j dA = \frac{\partial}{\partial t} \int_{CV} \rho u_i dV + \int_{CS} \rho u_i u_j n_j dA \quad (6)$$

$$-\dot{W} = \frac{\partial}{\partial t} \int_{CV} \frac{1}{2} \rho u_i u_i dV + \int_{CS} \left(p + \frac{1}{2} \rho u_i u_i \right) u_j n_j dA \quad (7)$$

where $F_{T,i}$ represents the fluid forces on the turbine and \dot{W} represents the power produced by the turbine. Splitting flow variables into mean and fluctuating components and time-averaging results in:

$$\int_{CS} U_i n_i dA = 0 \quad (8)$$

$$-\bar{F}_{T,i} = \int_{CS} P n_i dA - \int_{CS} \mu \left(\frac{\partial U_i}{\partial x_j} + \frac{\partial U_j}{\partial x_i} \right) n_j dA + \int_{CS} \rho U_i U_j n_j dA + \int_{CS} \rho \overline{u'_i u'_j} n_j dA \quad (9)$$

$$-\bar{W} = \int_{CS} \left(P U_j + \frac{1}{2} \rho U_i U_i U_j + \overline{p' u'_j} + \frac{1}{2} \rho \left(\overline{u'_i u'_i} U_j + 2 U_i \overline{u'_i u'_j} + \overline{u'_i u'_i u'_j} \right) \right) n_j dA \quad (10)$$

For clarity and as an aid to later calculation, the triple-correlation tensor terms in Eq. 10 are here written as vectors in two dimensions in Tab. 1:

Table 1: Triple-correlation tensor terms as two-dimensional vectors.

$U_i U_i U_j = \begin{bmatrix} (U^2 + V^2)U \\ (U^2 + V^2)V \end{bmatrix}$	$\overline{u'_i u'_i} U_j = \begin{bmatrix} (\overline{u'^2} + \overline{v'^2})U \\ (\overline{u'^2} + \overline{v'^2})V \end{bmatrix}$
$2U_i \overline{u'_i u'_j} = \begin{bmatrix} 2U \overline{u'^2} + 2V \overline{u'v'} \\ 2U \overline{u'v'} + 2V \overline{v'^2} \end{bmatrix}$	$\overline{u'_i u'_i u'_j} = \begin{bmatrix} (\overline{u'^2} + \overline{v'^2})u' \\ (\overline{u'^2} + \overline{v'^2})v' \end{bmatrix}$

Continuity is unaffected by this process, so that from Eq. 8, $U_1 A_1 = U_2 A_2 = U_T A_T = \dot{m}/\rho$ in Fig. 1. The momentum and energy equations now have a number of additional correlation terms that are not apparent in

steady flow, which may be directly calculated and their effect quantified.

In turbulence modeling the Reynolds stress term cannot be determined exactly and is the subject of a closure problem. Here however we may directly compute the unsteady correlation terms, R_{ij} for example, by solving the unsteady flow u_i, u_j then time-averaging to obtain:

$$R_{ij} = \overline{u'_i u'_j} = \overline{u_i u_j} - U_i U_j \quad (11)$$

3. IMPLICATIONS FOR THE BETZ ANALYSIS OF A SINGLE FOIL SYSTEM

The horizontal components of Eq. 9 and 10 are rewritten as:

$$\overline{F}_{T,x} = C_\alpha \frac{1}{2} \dot{m} U_1 - \int_{CS} \rho U U_j n_j dA = \frac{1}{2} \dot{m} U_1 (C_{FM} + C_\alpha) \quad (12)$$

$$\overline{W} = C_\beta \frac{1}{2} \dot{m} U_1^2 - \int_{CS} \rho U_i U_j n_j dA = \frac{1}{2} \dot{m} U_1^2 (C_{WKE} + C_\beta) \quad (13)$$

$$C_\alpha = \frac{1}{\frac{1}{2} \dot{m} U_1} (F_P + F_V + F_R) = C_{FP} + C_{FV} + C_{FR} \quad (14)$$

$$C_\beta = \frac{1}{\frac{1}{2} \dot{m} U_1^2} (\dot{W}_{PA} + \dot{W}_{PF} + \dot{W}_A + \dot{W}_B + \dot{W}_C) = C_{WPA} + C_{WPF} + C_{WA} + C_{WB} + C_{WC} \quad (15)$$

where the coefficients C_α and C_β encompass all the effects due to Reynolds averaging of the unsteady terms, as well as the pressure and viscous terms, leaving just the momentum and power terms due to average velocities remaining in Eq. 12 and 13 (these being the only ones normally accounted in the Betz analysis). The Reynolds average, pressure and viscous pressure-based force and power contributions to the coefficients C_α and C_β are described in Tab. 2.

Table 2: Reynolds average, pressure and viscous force and power contributions.

$C_{FP} = -\frac{1}{\frac{1}{2} \dot{m} U_1} \int_{CS} P n_x dA$	$C_{FV} = \frac{1}{\frac{1}{2} \dot{m} U_1} \int_{CS} \mu \left(\frac{\partial U}{\partial x_j} + \frac{\partial U_j}{\partial x} \right) n_j dA$	$C_{FR} = -\frac{1}{\frac{1}{2} \dot{m} U_1} \int_{CS} \rho \overline{u'_i u'_j} n_j dA$
$C_{WPA} = -\frac{1}{\frac{1}{2} \dot{m} U_1^2} \int_{CS} P U_j n_j dA$		$C_{WPF} = -\frac{1}{\frac{1}{2} \dot{m} U_1^2} \int_{CS} \overline{p' u'_j} n_j dA$
$C_{WA} = -\frac{1}{\frac{1}{2} \dot{m} U_1^2} \int_{CS} \frac{1}{2} \rho \overline{u'_i u'_i} U_j n_j dA$	$C_{WB} = -\frac{1}{\frac{1}{2} \dot{m} U_1^2} \int_{CS} \rho U_i \overline{u'_i u'_j} n_j dA$	$C_{WC} = -\frac{1}{\frac{1}{2} \dot{m} U_1^2} \int_{CS} \frac{1}{2} \rho \overline{u'_i u'_i u'_j} n_j dA$

We take the usual step of equating the power extracted by the turbine, with the force on the turbine multiplied by the average horizontal velocity through the turbine plane U_T , and then solving for this velocity:

$$\overline{W} = \overline{F}_{T,x} U_T \quad (16)$$

$$U_T = \frac{C_\beta \frac{1}{2} \dot{m} U_1^2 + \frac{1}{2} \rho U_1^2 U_{1A_1} - \frac{1}{2} \rho U_2^2 U_{2A_2}}{C_\alpha \frac{1}{2} \dot{m} U_1 + \rho (U_1^2 A_1 - U_2^2 A_2)} = \frac{C_\beta U_1^2 + U_1^2 - U_2^2}{C_\alpha U_1 + 2(U_1 - U_2)} \quad (17)$$

where it is noted that the only places on the control surface where the time-averaged velocity is not orthogonal to the local outward normal are the inlet and exit. The horizontal time-averaged velocity components at the CS inlet and exit, U_1 and U_2 are taken to be uniform across those boundaries, and the vertical components V_1 and V_2 are ignored as small relative to the horizontal components. These assumptions are examined for two example cases in Sec. 4. As a check, if $C_\alpha = C_\beta = 0$ (indicating no unsteadiness and no mean pressure flow work, i.e. $\dot{W}_{PA} = 0$) then we recover the usual $U_T = (U_1 + U_2)/2$.

The efficiency of power extraction is:

$$\eta = \frac{\overline{W}}{\frac{1}{2} \rho U_1^3 A_T} = \frac{C_\beta \frac{1}{2} \dot{m} U_1^2 + \frac{1}{2} \rho U_1^2 U_{1A_1} - \frac{1}{2} \rho U_2^2 U_{2A_2}}{\frac{1}{2} \rho U_1^3 A_T} = \frac{U_T}{U_1} \left(\frac{C_\beta U_1^2 + U_1^2 - U_2^2}{U_1^2} \right) \quad (18)$$

Substituting Eq. 17 and defining $a = U_2/U_1$ gives:

$$\eta = \frac{(C_\beta + 1 - a^2)^2}{C_\alpha + 2(1-a)} \quad (19)$$

Differentiating with respect to a and setting the result to zero to find the a value for maximum efficiency gives:

$$a_{opt} = \frac{1}{3} \left(2 + C_\alpha - \sqrt{1 + C_\alpha^2 + 4C_\alpha - 3C_\beta} \right) \quad (20)$$

$$\eta_{max} = \frac{\left(9 + 9C_\beta - \left(2 + C_\alpha - \sqrt{1 + C_\alpha^2 + 4C_\alpha - 3C_\beta} \right)^2 \right)^2}{27 \left(2 + C_\alpha + 2 \sqrt{1 + C_\alpha^2 + 4C_\alpha - 3C_\beta} \right)} \quad (21)$$

where again as a check we note that when $C_\alpha = C_\beta = 0$ we recover the well-known $a_{opt} = 1/3$, $U_T/U_1 = 2/3$ and $\eta_{max} = 16/27$.

Operating under the constraint $1 + C_\alpha^2 + 4C_\alpha - 3C_\beta \geq 0$ we can determine that there exist numerical combinations of C_α and C_β that result in $\eta_{max} > 16/27$ (0.5926). Combining this with the further constraints that $0 < a_{opt} < 1$ (i.e. the downstream flow velocity remains both positive and less than the upstream velocity) and $\eta_{max} < 1$ (the turbine cannot extract more energy than exists in the flow) results in the region shown in Fig. 2, suggesting that in principle the Betz limit may be exceeded. The question then becomes *whether these numerical values are physically realistic or indeed possible* for the flapping foil turbine.

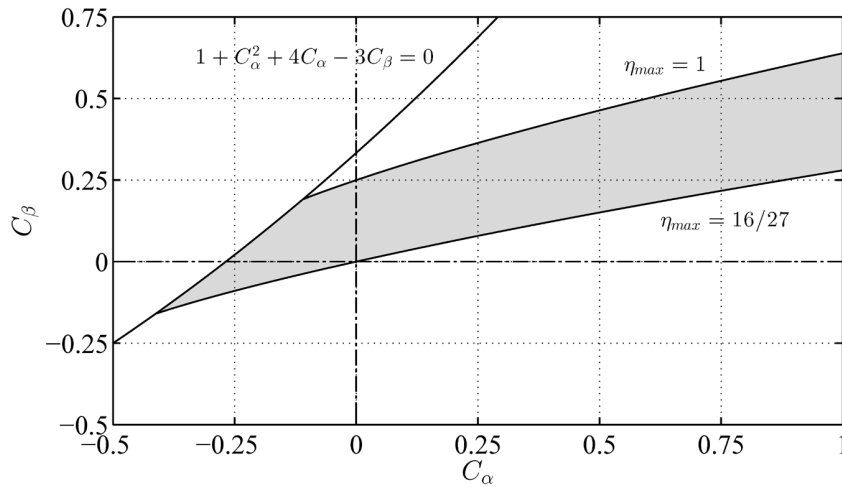


Figure 2: Region of C_α and C_β space (shaded) for which $16/27 < \eta_{max} < 1$ and $0 < a_{opt} < 1$, from Eq. 20 and 21.

For example, leaving $C_\beta = 0$, positive values of C_α reduce η_{max} , but $-0.26795 < C_\alpha < 0$ results in $0.7698 > \eta_{max} > 0.5926$. This would require either the net force due to non-uniform pressure on the control surface to be negative (pressure at the downstream CS outlet higher than at the inlet, which is not physically realistic), or the viscous force on the sides of the CS to be negative (again not physically realistic given that the flow on the CS sides is in the downstream direction), or that there is a net transport of momentum out of the CS sides due to unsteady effects. Whether the latter is realistic is not immediately apparent, but is evaluated in Sec. 4. Alternatively, leaving $C_\alpha = 0$, $\eta_{max} > 16/27$ for $0 < C_\beta < 0.25$. The \dot{W}_{PA} component due to non-uniform pressure would be zero along the CS sides (no time average flow across the boundary) but would be expected to be small and positive from contributions at the CS inlet and outlet since again $P_1 < P_2$ is not physically realistic. Similarly the \dot{W}_A component (transport of turbulent kinetic energy by the mean flow) along the CS sides is zero, and should be small overall due to unsteady kinetic energy differences at the CS inlet and

exit far from the turbine. The expected sign and magnitude of the other terms comprising C_β are again harder to estimate without direct evaluation as in Sec. 4.

4. EVALUATION OF PRESSURE AND VELOCITY CORRELATION TERMS

The two-dimensional unsteady viscous incompressible flow around a flapping foil was simulated with an in-house sharp-interface immersed-boundary method Navier-Stokes solver.^{13,14)} Two flapping parameter combinations were chosen to examine the relative size and impact of each of the terms comprising C_α and C_β in Sec. 3. The two cases were taken from Kinsey and Dumas¹⁵⁾, representing the most efficient case from that study, and a low efficiency case for comparison.

(1) Single Foil High Efficiency Case

In Case 1 a NACA0015 aerofoil section oscillates in heave $y(t) = hc \sin(\omega t)$ and pitch $\theta(t) = \theta_0 \sin(\omega t + \phi)$, pitching about the 1/3 chord point with heave amplitude $h = 1.0$ chords, pitch amplitude $\theta_0 = 76.3^\circ$, pitch leading heave with phase $\phi = 90^\circ$, non-dimensional frequency $f^* = \omega c / 2\pi U_1 = 0.14$, at Reynolds number $Re = 1100$. This case serves also as a validation of the solver and mesh, conducted and reported in Tian et. al.¹⁴⁾ and repeated in Tab. 3 showing the time-averaged power coefficient based on the foil chord c and (unit) span b , and the efficiency based on foil swept area A_T . The computational domain is a $25c \times 20c$ rectangular box discretised by 461×413 Cartesian nodes. The domain boundaries are thus $5c$ upstream, $20c$ downstream, and $10c$ cross-stream from the foil pivot point. The Cartesian grid is uniform in both x and y directions within a $4c \times 4c$ inner box enclosing the flapping foil, with grid spacing of $\Delta x = \Delta y = 0.0133c$. The grid is stretched in the remainder of the domain. In one flapping cycle, 2000 time steps were applied. To validate the mesh size convergence, simulations of finer mesh ($\Delta x = \Delta y = 0.008c$) and coarser mesh ($\Delta x = \Delta y = 0.02c$) were conducted. The medium mesh was chosen for the remainder of the present work based on agreement within 2% with both the fine mesh and Kinsey and Dumas¹⁵⁾ results.

Table 3: Mesh refinement validation against previous published work.

Source	Power Coefficient $\overline{C_P} = \overline{W} / \frac{1}{2} \rho U_1^3 bc$	Efficiency $\eta = \overline{W} / \frac{1}{2} \rho U_1^3 A_T$ (%)
Coarse, $\Delta x = \Delta y = 0.02c$	0.828	32.3
Medium, $\Delta x = \Delta y = 0.0133c$	0.878	34.2
Fine, $\Delta x = \Delta y = 0.008c$	0.861	33.6
Kinsey and Dumas ¹⁵⁾	0.860	33.7

Fig. 3 shows the time-averaged values of the non-dimensional velocity field magnitude, pressure coefficient, and non-dimensional vorticity, with the control surface CS defined as the streamlines based on the time-averaged velocities U and V passing through the maximum extent of the swept area of the flapping wing. This may be compared to the schematic of the situation shown in Fig. 1. In the velocity field we see some unexpected features, such as the lowest velocity point in the wake not immediately behind the turbine plane but some 4 to 5 chord lengths downstream, as well as a non-monotonic variation of velocity magnitude along the streamtube boundaries. Similarly in the pressure field there is an x-shaped structure of low pressure that extends significantly downstream of the turbine and again leads to a non-monotonic variation of pressure along the streamtube boundaries. The low pressure regions are seen to correspond closely to the regions of high vorticity magnitude, indicating the paths of vortices shed from the leading edge of the foil during the flapping cycle and convecting downstream. This suggests that unsteady effects will make a significant contribution to the time-average behaviour of the system.

Each of the terms in Eq. 12 to 15 are now integrated on the control surface shown in Fig. 3, to determine

their respective contributions to the time-average force and power output from the flapping foil turbine. The upstream and downstream boundaries (inlet and exit of the streamtube) are placed at $x/c = -4.5$ and $x/c = 19.5$ respectively, just inside the boundaries of the computational domain.

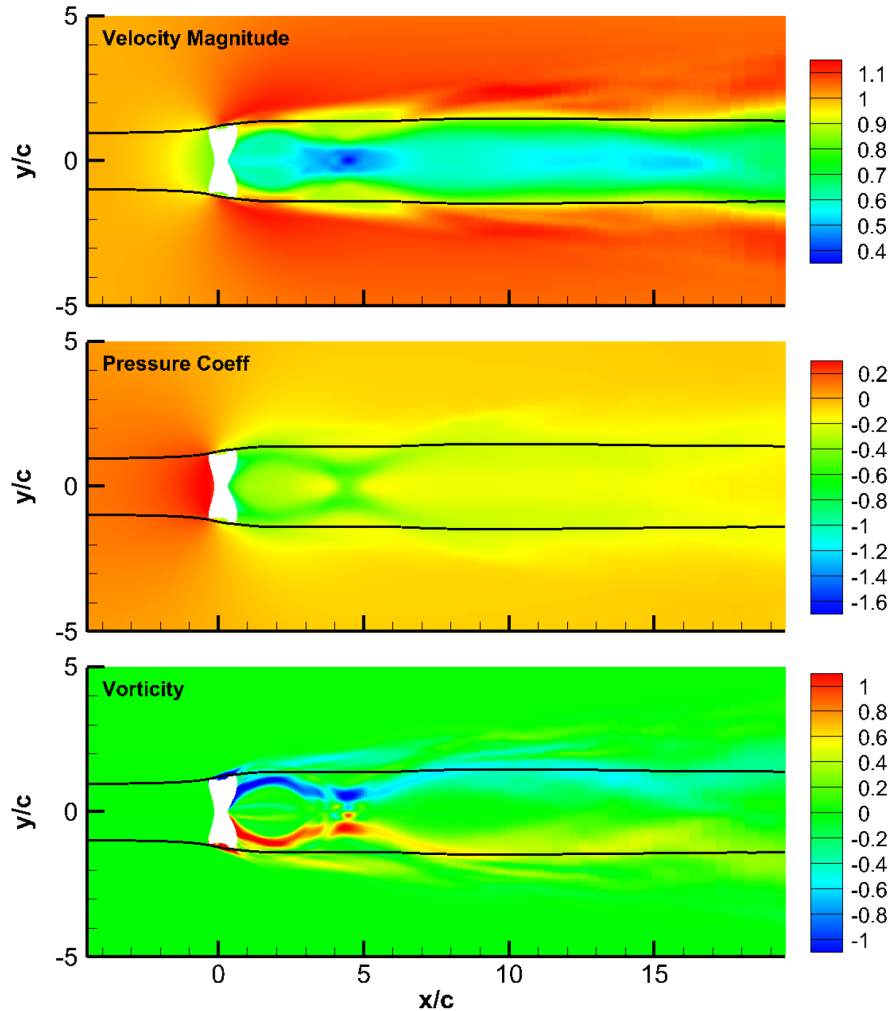


Figure 3: Time averaged values of non-dimensional $U_{mag} = \sqrt{U^2 + V^2}/U_1$ (top), pressure coefficient C_P (middle) and non-dimensional vorticity $\Omega c/U_1$ (anticlockwise positive, bottom) for Case 1. White region in each plot indicates the area swept by the foil, black lines show the control volume.

Fig. 4 shows the contribution of each of the terms in Tab. 2, as functions of distance along the streamtube sides. Here the upstream control volume boundary is kept fixed at $x/c = -4.5$, and the contributions integrated from that point to a variable point represented by the x/c coordinate. We see weak force contributions from viscous effects and pressure along the streamtube sides, but a strong diffusion of unsteady momentum from the Reynolds stress (represented by the C_{FR} term) into the streamtube between 0 and 5 chords downstream of the foil pivot. Momentum is removed between 5 and 7.5 chords, then increases again further downstream. Examining the power contributions, C_{WPA} and C_{WA} are exactly zero as expected due to the time-averaged flow field being aligned to the streamtube sides. There is a relatively weak negative contribution in C_{WPF} (power reduced by correlation of fluctuating pressure and velocity), and a stronger negative contribution in C_{WC} (transport of turbulent kinetic energy by fluctuating velocities) from 7.5 chords onwards. These are more than balanced by a strong contribution in C_{WB} (flow work done by the Reynolds stresses) with the same spatial distribution as C_{FR} . The regions of strong inwards diffusion of unsteady momentum and kinetic energy correspond to the regions of high vorticity in Fig. 3, where the shed vortex paths come close to the streamtube

sides and would appear to be instrumental in drawing in momentum and kinetic energy into the wake of the foil, as proposed by Kinsey and Dumas⁹).

The contributions are further tabulated in Tab. 4, separately for the inlet, exit, and complete sides of the streamtube, and as a combined total. Thus the values for the sides here correspond to the $x/c = 19.5$ values plotted in Fig. 4.

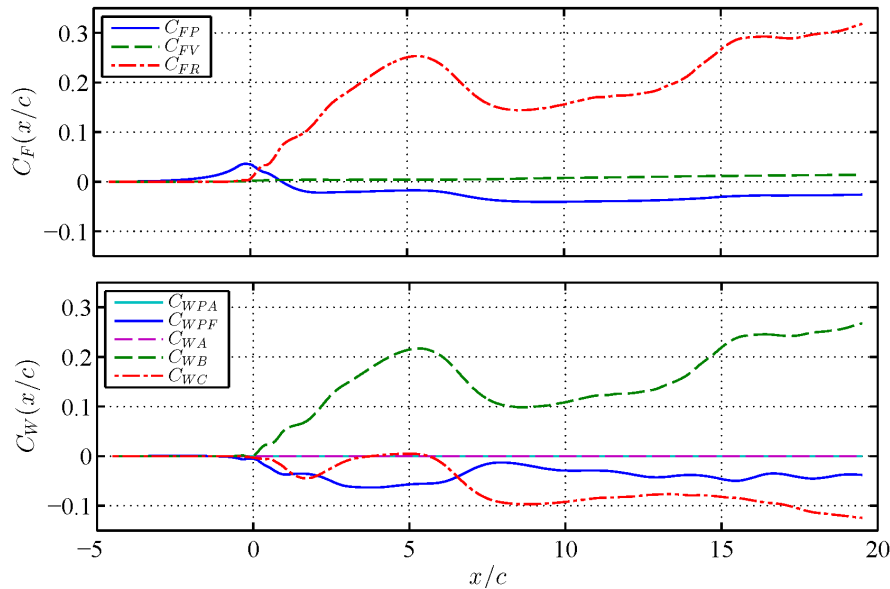


Figure 4: Force and power coefficient contributions as functions of distance along the streamtube sides, Case 1.

Table 4. Force and power contributions integrated on the control surface, Case 1 (high efficiency). *Total values in parentheses are excluding the inlet and exit values of C_{FP} and C_{WPA} , as discussed in the text.

	Inlet	Exit	Sides	Total
C_{FM}	1.9985	-1.3990	0.0	0.5995
C_{FP}	0.1166	0.1969	-0.0261	0.2873
C_{FV}	0.0	0.0	0.0141	0.0141
C_{FR}	0.0	-0.0118	0.3184	0.3066
C_{α}	0.1166	0.1851	0.3064	0.6080 (0.2945)*
C_{WKE}	1.9972	-0.9834	0.0	1.0138
C_{WPA}	0.1165	0.1380	0.0	0.2545
C_{WPF}	0.0	-0.0039	-0.0379	-0.0418
C_{WA}	0.0	-0.0555	0.0	-0.0555
C_{WB}	0.0	-0.0083	0.2677	0.2594
C_{WC}	0.0	0.0001	-0.1244	-0.1243
C_{β}	0.1165	0.0704	0.1054	0.2922 (0.0378)*

Examining the values of C_{α} and C_{β} we see that they fall well within the shaded region of Fig. 2, however the pressure field plotted in Fig. 3 shows that the pressure at the upstream and downstream boundaries of the streamtube is still significantly different from the free-stream value. The original Betz analysis ignores any such pressure contributions at the inlet and exit, assuming that the pressure here are equal to the free stream,

and also ignores any contributions from pressure variation along the streamtube sides. It is clear from Fig. 3 that the upstream and downstream boundaries are insufficiently far from the foil to bring the pressure to near free-stream. It is also worth noting that even 20 chords downstream, the contributions in Fig. 4 have not yet asymptoted to fixed values. Future work will extend the simulations to larger domains, but for this work the C_α and C_β totals are also given with the simple expedient of neglecting the inlet and exit contributions from C_{FP} and C_{WPA} . This modification places the coefficients close to but outside the shaded region in Fig. 2. Nevertheless, this analysis shows that for this set of flapping kinematics parameters, there are effects ignored in the standard Betz analysis that make a strong contribution to the force and power output. This is particularly true of the force due to diffusion of unsteady momentum across the streamtube sides which is approximately half that due to momentum in and out of the streamtube through the inlet and exit.

(2) Single Foil Low Efficiency Case

In Case 2 the pitch amplitude is $\theta_0 = 40.0^\circ$, non-dimensional frequency $f^* = 0.10$, and all other parameters remain unchanged. Kinsey and Dumas¹⁵⁾ estimated the efficiency of this parameter combination as 5%, with our estimate as 4% in good agreement. For this kinematics there is little evidence of leading edge vortex shedding in contrast to Case 1, since the angle of attack on the foil remains small throughout the flapping cycle and the vorticity is shed symmetrically from the trailing edge. This can be seen in Fig. 5, as can the low efficiency as shown by the minimal spreading of the streamtube. Fig. 6 shows the unsteady force contributions, which are an order of magnitude smaller than for Case 1. Using the same procedure as for Case 1 we find values of $C_\alpha = 0.0772$ and $C_\beta = 0.0576$, or with the inlet and exit values of C_{FP} and C_{WPA} discounted we have $C_\alpha = 0.0490$ and $C_\beta = 0.0300$, showing only very small unsteady effects in this case.

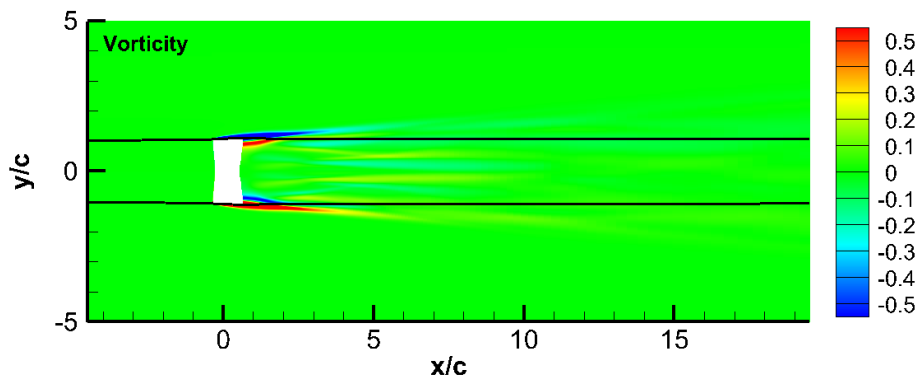


Figure 5: Time averaged non-dimensional vorticity $\Omega c/U_1$ (anticlockwise positive) for Case 2.

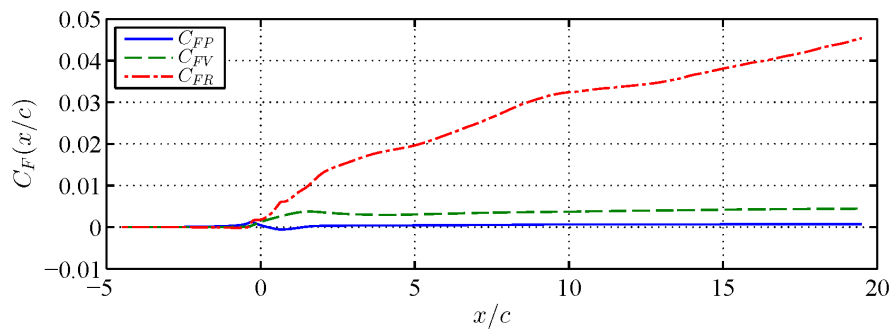


Figure 6: Force coefficient contributions as functions of distance along the streamtube sides, Case 2.

5. CONCLUSIONS

Both the high efficiency case and the low efficiency case considered here yielded values of C_α and C_β

that fell outside the shaded region of Fig. 2, indicating that the effects of diffusion of unsteady momentum and kinetic energy across the time-average streamtube boundary were insufficient to allow violation of the Betz limit. However in the high efficiency case, these effects were significant and promising - the action of the vortices shed from the leading edge of the foil during the flapping cycle is to draw momentum and energy into the wake, in a manner not accounted by the standard Betz analysis. This suggests that a second foil in tandem, at the correct downstream location, may benefit from these effects and might indeed account for the high efficiencies for tandem foils reported in the literature⁹⁾, right up against the tandem-foil Betz limit. A similar analysis as the present work, for such a tandem arrangement, will accordingly be the focus of future work.

ACKNOWLEDGMENTS

This work was supported under the Australian Research Council's Discovery Projects funding scheme (project number DP130103850), and conducted with the assistance of resources from the Australian National Computational Infrastructure (NCI).

REFERENCES

- 1) Betz, A. Das Maximum der theoretisch möglichen Ausnützung des Windes durch Windmotoren, *Z. Gesamte Turbinenwesen*, Vol. 26, .pp. 307–9, 1920.
- 2) Manwell, J.F., McGowan, J.G. and Rogers, A.L. *Wind Energy Explained*, John Wiley & Sons, Ltd, 2009.
- 3) Sørensen, J.N. Aerodynamic aspects of wind energy conversion, *Annual Review of Fluid Mechanics*, Vol. 43, pp. 427-448, 2011.
- 4) Sørensen, J.N. and van Kuik, G.A.M. General momentum theory for wind turbines at low tip speed ratios, *Wind Energy*, Vol. 14, pp. 821-839, 2011.
- 5) Sharpe, D.J. A general momentum theory applied to an energy-extracting actuator disc, *Wind Energy*, Vol. 7, pp. 177–188, 2004.
- 6) Lam, G.C.K. Wind Energy Conversion Efficiency Limit, *Wind Engineering*, Vol. 30, pp. 431-437, 2006.
- 7) Vennell, R. Exceeding the Betz limit with tidal turbines, *Renewable Energy*, Vol. 55, pp. 277-285, 2013.
- 8) Newman, B. Multiple actuator-disc theory for wind turbines, *Journal of Wind Engineering and Industrial Aerodynamics*, Vol. 24, pp. 215-225, 1986.
- 9) Kinsey, T. and Dumas, G. Optimal tandem configuration for oscillating-foils hydrokinetic turbine, *Journal of Fluids Engineering*, Vol. 134, pp. 031103-1 to 11, 2012.
- 10) Dabiri, J.O. Renewable fluid dynamic energy derived from aquatic animal locomotion, *Bioinspiration and Biomimetics*, Vol. 2, No. 3, p. L1, 2007.
- 11) Young, J., Lai, J.C.S and Platzer, M.F. A Review of Progress and Challenges in Flapping Foil Power Generation, *Progress in Aerospace Sciences*, Vol. 67, pp. 2-28, 2014.
- 12) Xiao, Q. and Zhu, Q. A review on flow energy harvesters based on flapping foils, *Journal of Fluids and Structures*, Vol. 46, pp. 174-191, 2014.
- 13) Tian, F.-B., Dai, H., Luo, H., Doyle, J.F. and Rousseau, B. Fluid-structure interaction involving large deformations: 3D simulations and applications to biological systems, *Journal of Computational Physics*, Vol 258, pp. 451-469, 2014.
- 14) Tian, F.-B., Young, J. and Lai, J.C.S. Improving power-extraction efficiency of a flapping plate: From passive deformation to active control, *Journal of Fluids and Structures*, Vol. 51, pp. 384-392, 2014.
- 15) Kinsey, T. and Dumas, G. Parametric Study of an Oscillating Airfoil in a Power-Extraction Regime, *AIAA Journal*, Vol. 46, pp. 1318-1330, 2008.

Effect of Angle of Attack on Vibration Characteristics of a Cantilevered Prism for Energy Harvest

Takahiro Kiwata⁺¹, Aguri Nakajima⁺², Shunichi Mizukami⁺³, Toshiyuki Ueno⁺⁴ and Takaaki Kono⁺⁵

⁺¹ Research Center for Sustainable Energy and Technology, Kanazawa University, Kakuma-machi, Kanazawa-shi, Ishikawa, 920-1192, Japan

⁺² Graduate School of Natural Science and Technology, Kanazawa University

⁺³ Graduate School of Natural Science and Technology, Kanazawa University

⁺⁴ School of Electrical and Computer Engineering, Kanazawa University

⁺⁵ Research Center for Sustainable Energy and Technology, Kanazawa University

To develop the power generation system using iron-gallium alloy, we focus on the transverse galloping vibration for a rectangular prism with a critical depth section of less than the side ratio $D/H \approx 0.6$, and for a D-section prism which vibrates at a reduced velocity $V_r (=U/f_c H)$ lower than the resonant velocity. The free vibration test using a plate spring was carried out in the water tunnel to investigate effects of the angle of attack and the vibration direction on the vibration characteristics. The vibration direction I of the prism is the same as the longitudinal direction of the prism. The vibration direction II of the prism is the same as the transverse direction to flow. We also carried out a power generation experiment using the iron-gallium alloy to investigate effects of angle of attack on energy harvesting. The D-section prism with the side ratio of 0.23 for the vibration direction I vibrates at a wide range of angle of attack in comparison with the other prisms. The maximum electric power P using a D-section prism with $D/H=0.23$ is 26 mW at $V_r = 4.15$.

Keyword: Flow-Induced Vibration, Low-Speed Galloping, Rectangular Prism, Angle of Attack, Energy Harvesting

1. INTRODUCTION

The carbon dioxide emissions that lead to global warming are increased by the fossil fuel consumption in the world. To present of global warming, countries are proceeding the development of technologies for utilizing renewable power sources, i.e. solar, wind, biomass and hydraulic powers, in recent years. Although the utilization of vibrations for power generation is not new technology, a number of researches have recently investigated the harvesting of power from various vibrations¹⁾. Therefore, a large variety types of power generators that use flow-induced vibration has been invented, e.g., power generation of the vortex-induced vibration using tandem circular cylinders having electrical coils with steel cores and a ferrite magnet²⁾, hydroelectric power generation using an inverted pendulum formed by a cylindrical body³⁾, wave energy power generation using a piezoelectric element⁴⁾, power generation by mechanical vibration due to the fluid-structure interaction between a flexible belt and the airflow⁵⁾, wind energy harvester of a T-shaped piezoelectric bimorph cantilever⁶⁾, electromagnetic generator using the galloping vibration of a lightweight box having a square, triangular, or semicircular cross-section⁷⁾, and piezoelectric energy harvester using flapping-foils flutter vibration occur⁸⁾. However, these devices have not seem to be able to provide sufficient electric energy. Practical applications require a mechanism that will generate vibration in the presence of a low-velocity flow. In order to harvest energy from flowing water, we need to develop a simple and efficient power generator using a structure that flow-induced vibration occurs.

The relationship between galloping vibration and geometry of a structure has investigated by a number of researchers⁹⁾⁻²²⁾ for more than half a century. Galloping vibration is characterized by large amplitude

⁺¹kiwata@se.kanazawa-u.ac.jp, ⁺²anakajima@ryuko.ms.t.kanazawa-u.ac.jp, ⁺³mizukami@ryuko.ms.t.kanazawa-u.ac.jp,

⁺⁴ueno@ec.t.kanazawa-u.ac.jp, ⁺⁵t-kono@se.kanazawa-u.ac.jp

vibrations normal to the direction of flow, which causes damage to the structures in some cases. Although most of the effort in galloping vibration research has been concentrated in bodies with square or rectangular cross-sections⁹⁾⁻¹³⁾, the galloping-induced vibrations primarily occur in flexible and lightly damped structures with special and non-axisymmetric cross-sections such as D-shaped, L-shaped, cross-shaped, triangular and trapezium prisms¹⁶⁾⁻²²⁾.

To develop the power generation system using iron-gallium alloy²³⁾, we focus on transverse galloping for a rectangular prism with a critical depth section of less than $D/H \approx 0.6$ (where D : depth of a prism in the flow direction, H : height of a prism normal to the flow direction), and a D-section (semi-circle) prism, which vibrate at a flow velocity lower than the resonant velocity¹²⁾⁻¹⁵⁾. For the low-speed galloping, the transverse vibration depends on lateral force coefficient C_{FY} which varies as angle of attacks varies so that many researcher investigate influence of angle of attack on aerodynamics forces, i.e., drag and lift coefficients for various shape of cross-sections^{11),17),18),29)-32)}. However, there are a little study about the effect of angle of attack on vibration characteristics^{32),33)}. The purpose of the present study is to investigate the effect of angle of attack on the transverse galloping vibration of cantilevered rectangular and D-section prisms, and the performance of a power generator using an iron-gallium alloy as a magnetostrictive material and cantilevered prisms in a water tunnel.

2. EXPERIMENTAL APPARATUS AND METHOD

(1) Water tunnel

A schematic diagram of the experimental apparatus is shown in Figure 2. The experiments were performed in a water tunnel with a rectangular working section having a height of 400 mm, a width of 167 mm, and a length of 780 mm. A variable-frequency induction motor and an inverter (YASUKAWA ELECTRIC, VRISPEED-686SS5) were used to drive a double suction centrifugal pump (DMW, DF-SC). In the experiment, the water velocity U was changed from 1.0 m/s to 2.7 m/s by controlling the pump rotational speed. The Reynolds number $Re (=UH/\nu; \nu$, kinematic viscosity of water) was in the range of 2×10^4 to 5×10^4 . The non-uniform level and the turbulence intensity in the working section at a water speed of $U = 1.5$ m/s were less than $\pm 1.5\%$ and about 2.0%, respectively.

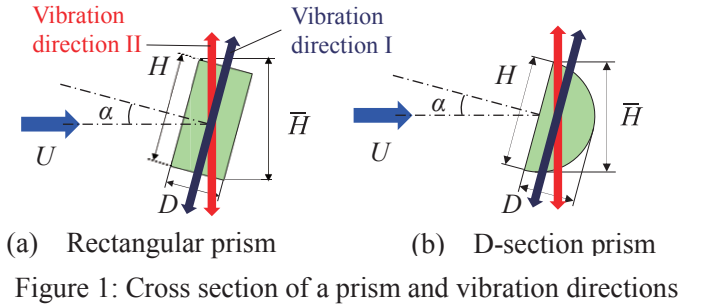
(2) Test models and experimental method for free vibration

The experiment used rectangular and D-section prisms constructed of stainless steel with a smooth surface and sharp edges, as shown in Figure 3. Table 1(a) shows the specifications of the test prisms. Table 2(a) also shows the natural frequency of the test prisms. All prisms had a cross-section height H of 20 mm. The side ratio D/H of the rectangular prism was varied 0.2 and 0.5. The side ratio D/H of the D-section prism was varied 0.23 and 0.5. The span length of prisms L was 200 mm, and the aspect ratio was 10. The prism was mounted elastically to a plate spring attached to the ceiling wall of the test section with a jig as shown in Figure 2(a). The jig can change an angle of attack α of the prism between 5° and 60° . Furthermore, we investigated the effect of the vibration direction of the prism, namely, the vibration direction I of the prism is the same as the longitudinal direction of the prism, and the vibration direction II of the prism is the same as the transverse direction to flow. The characteristic frequency f_c of the prism was adjusted to a constant value between 22 and 46 Hz by using different plate springs. The tip displacement of the prism y and the characteristic frequency of the tested model f_c were measured using an acceleration sensor (Showa measuring instruments, 2302CW) implanted inside the tip of the prism using an integrator and an FFT analyzer (Ono sokki, CF-5201). The output signals of the integrator were converted using a 12-bit A/D converter with a sampling frequency of 2 kHz, and 10^4 data points were stored. The root-mean-square value of the fluctuation of displacement of a prism tip y_{rms} , reduced velocity $V_r (=U/f_c H)$ or $\bar{V}_r (=Uf_c/\bar{H})$ and non-dimensional amplitudes $\eta_{rms} (=y_{rms}/H)$ or $\bar{\eta}_{rms} (=y_{rms}/\bar{H})$ was calculated using a personal computer.

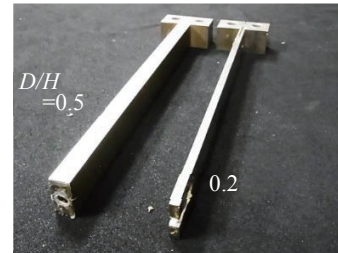
(3) Test models and experimental method for vibration-power generation

Figure 2(b) shows the experimental setup in the water tunnel in order to investigate the performance of the vibration-power generation device. Tables 1(b) and 2(b) show the specifications and natural frequency of the test models. The rectangular prisms had a cross-section height H of 20 mm and a span length L of 350 mm. We use the two test models that have different cross-section rectangular prism with $D/H = 0.2$ and D-section

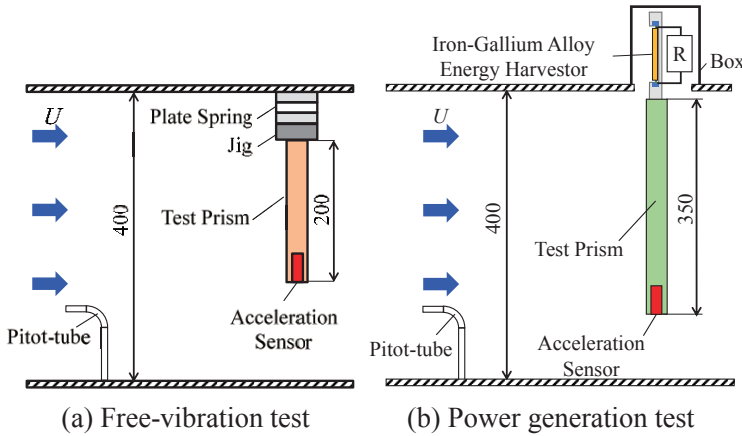
prism with $D/H = 0.23$. The power-generation device was placed in an airtight acrylic resin box in order to prevent water intrusion. The Galfenol beam acted as a plate spring. The Galfenol had a tensile strength of 200 MPa. The dimensions of Galfenol beams were $5 \text{ mm} \times 3 \text{ mm} \times 100 \text{ mm}$, and the winding coils were 1,190 turns of 0.05-mm-diameter wire (internal resistance of 6.5Ω). The time variations of the internal magnetic flux density caused by periodic bending deformation generate a voltage on the coils according to Faraday's law of induction. The harvester was connected in series to the resistance, $R = 10 \Omega$. The generated voltage V was measured by an A/D converter with a sampling frequency of 2 kHz, and 10^4 data point were stored. The power



(a) Rectangular prism (b) D-section prism
Figure 1: Cross section of a prism and vibration directions



(a) Rectangular prisms



(a) Free-vibration test (b) Power generation test



(b) D-section prisms

Figure 3: Test prisms

Figure 2: Schematic diagram of the test section in water tunnel

Table 1: Specification of the test prisms

(a) Free-vibration test				(b) Power generation test			
Retangular prism ($\alpha=0^\circ$)				Retangular prism			
D/H	δ	m [kg/m]	C_n	D/H	δ	m [kg/m]	C_n
0.5	0.026	1.58	0.42	0.2	0.15	0.67	2.4
0.2	0.036	0.65	0.59	D-section prism			
D-section prism ($\alpha=0^\circ$)				D/H	δ	m [kg/m]	C_n
D/H	δ	m [kg/m]	C_n	0.23	0.12	0.52	2.0
0.5	0.018	1.35	0.31				
0.23	0.023	0.51	0.36				

Table 2: Natural frequency f_c of test prisms

(a) Free-vibration test					(b) Power generation test		
Cross section	Rectangular		D-section		Cross section	Rectangular	D-section
D/H	0.5	0.2	0.5	0.23	D/H	0.2	0.23
Direction I [Hz]	27.0	43.4	25.2	28.9	Direction II [Hz]	35.9	35.8
Direction II [Hz]	22.9	35.6	$(\alpha \leq 25) \quad (\alpha \geq 35)$				
			22.8	39.5			

generation $P (= V_{rms}^2/R)$ was calculated by a personal computer, where V_{rms} is the effective value of the generated voltage. The tip displacement of the prism y was also measured using an acceleration sensor simultaneously implanted inside the tip of the prism.

3. EXPERIMENTAL RESULT AND DISCUSSION

3.1 FREE-VIBRATION

(1) Vibration direction I

We investigated the response amplitude for the vibration direction I of the rectangular and D-section prisms. The vibration direction I is the same as the longitudinal direction of the prism (Figure 1).

a) Prism with side ratio $D/H \approx 0.2$

Figure 4 shows the effect of angle of attack α on variation of the root-mean-square value of the amplitudes $\eta_{rms} (= y_{rms}/H)$ in vibration direction I for a rectangular prism with a side ratio of $D/H = 0.2$, and a D-section prism with a side ratio of $D/H = 0.23$ with the reduced velocity $V_r (= Uf_c/H)$. In the case of a rectangular prism with $D/H = 0.2$ vibration begins to occur near reduced velocity $V_r \approx 1.5$ lower than the resonant velocity and the amplitudes of a prism increase linearly with an increase in the reduced velocity V_r at angle of attack $\alpha = 0^\circ$. The rectangular prism until $\alpha = 25^\circ$ vibrates the same as one with $\alpha = 0^\circ$. For $\alpha \geq 30^\circ$, the reduced velocity of the vibration onset for a rectangular prism increases at $V_r = 2.1$, and a rectangular prism of $\alpha = 35^\circ$ do not occur the vibration. In the case of a D-section prism with $D/H = 0.23$ at $\alpha = 0^\circ$, the vibration also begins to occur near reduced velocity $V_r \approx 1.5$ and the amplitudes of a prism increase linearly with an increase in the reduced velocity V_r as with the rectangular prism with $D/H = 0.2$. In the range of angle of attack between 10° and 45° , a D-section prism vibrates the same as one with $\alpha = 0^\circ$. The reduced velocity of the vibration onset for a D-section prism of $\alpha = 55^\circ$ increases at $V_r = 2.1$, and a D-section prism of $\alpha = 60^\circ$ do not occur the vibration. Thus, a D-section prism with $D/H = 0.23$ can vibrate at the larger angle of attack than a rectangular prism with $D/H = 0.2$.

Figure 5 shows the response amplitude $\eta_{rms} (= y_{rms}/H)$ for a rectangular prism and D-section prism with the reduced velocity $\bar{V}_r (= Uf_c/\bar{H})$, which is non-dimensionalized by a characteristics length normal to the incident flow \bar{H} , for various angles of attack α . For a rectangular prism with $D/H = 0.2$, there are a little difference between Figures 4(a) and 5(a). For the D-section prism with $D/H = 0.23$, as shown in Figure 5(b), the reduced velocity \bar{V}_r of onset of vibration increases as angle of attack α increase. Because \bar{H} decreases as the angle of attack α increase.

b) Prism with side ratio $D/H = 0.5$

Figure 6 shows the effect of angle of attack α on the response amplitudes η_{rms} for a rectangular prism and a D-section prism with side ratio $D/H = 0.5$ with respect to the reduced velocity V_r in the vibration direction I. In the case of a rectangular prism with $D/H = 0.5$, a prism at $\alpha = 0^\circ$ begin to vibrate near $V_r \approx 3.0$. The reduced velocity of the vibration onset for a rectangular prism of $\alpha = 15^\circ$ increases at $V_r \approx 3.5$, and the vibration is suppressed gradually at $\alpha \geq 10^\circ$. Especially, the rectangular prism at only $\alpha = 20^\circ$ for $V_r = 3.0 - 4.2$ vibrates with a half of natural frequency $f_c/2$, i.e. 14 - 17 Hz. This phenomenon has a concern in the change of flow separation point from the leading to trailing edge on the rectangular prism with $D/H = 0.5$ at $\alpha \approx 23^\circ$ ³⁰⁾. In the case of a D-section prism with $D/H = 0.5$ at $\alpha = 0^\circ$, a prism begins to vibrate smaller the reduced velocity at $V_r \approx 2.5$ than a rectangular prism with side ratio $D/H = 0.5$, and the response amplitude of a D-section prism vibrates until $\alpha = 25^\circ$ the same as $\alpha = 0^\circ$. The vibration is suppressed at $\alpha = 35^\circ$ and the response amplitudes do not increases more than $\eta_{rms} = 0.02$. Thus, a D-section prism with side ratio $D/H = 0.5$ can vibrate at larger angle of attack than a rectangular prism with side ratio $D/H = 0.5$.

c) 5 % non-dimensional and increment rate of response amplitude

Figures 7 shows the reduced velocity at the 5 % non-dimensional response amplitude of the prism $V_{r0.05}$ with respect to the angle of attack α . The reduced velocity $V_{r0.05}$ of a rectangular prism with $D/H = 0.2$ and a D-section prism with $D/H = 0.23$ is smaller than prisms with $D/H = 0.5$. The vibration of a D-section prism with $D/H = 0.23$ is kept until $\alpha = 45^\circ$. Figures 7 shows the increment rate of the response amplitude for a prism

$d\eta_{rms}/dV_r$, which is the average rate of measured points, with respect to the angle of attack α . The increment rate of the response amplitude $d\eta_{rms}/dV_r$ of a D-section prism with $D/H=0.23$ are larger than that of a rectangular prism with $D/H = 0.2$ and a D-section with $D/H=0.5$. In particular, the increment rate of a D-section prism with $D/H=0.23$ indicates large value in a wide range of angle of attack until $\alpha = 45^\circ$.

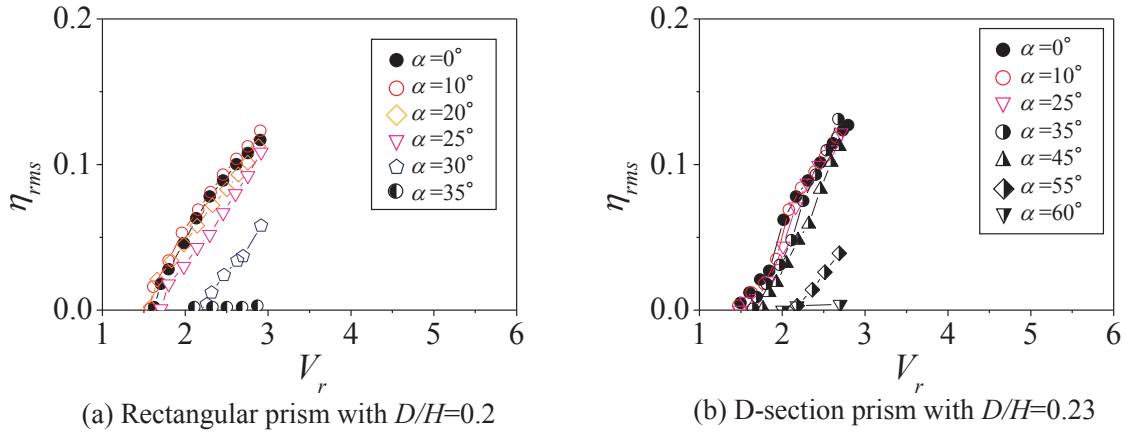


Figure 4: Response amplitude η_{rms} of prism for vibration direction I with respect to the reduced velocity V_r .

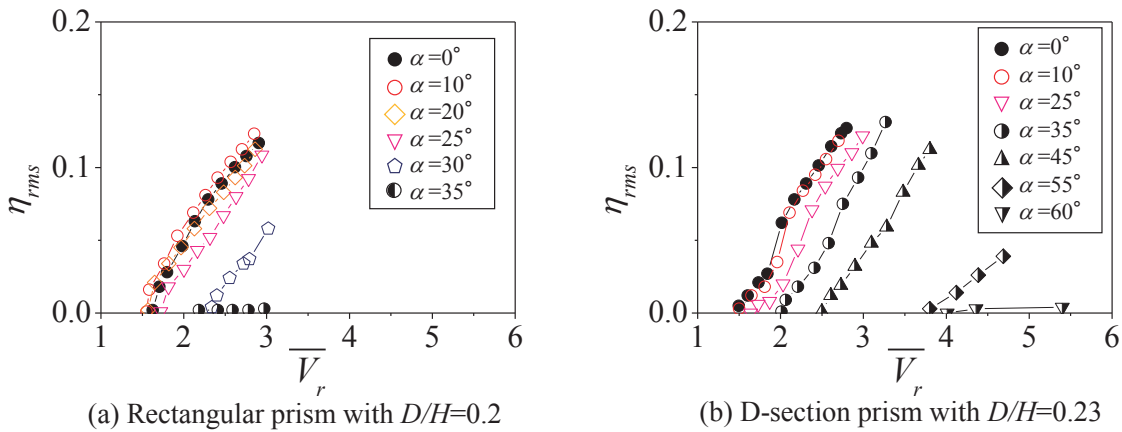


Figure 5: Response amplitude η_{rms} of prism for vibration direction I with respect to the reduced velocity V_r .

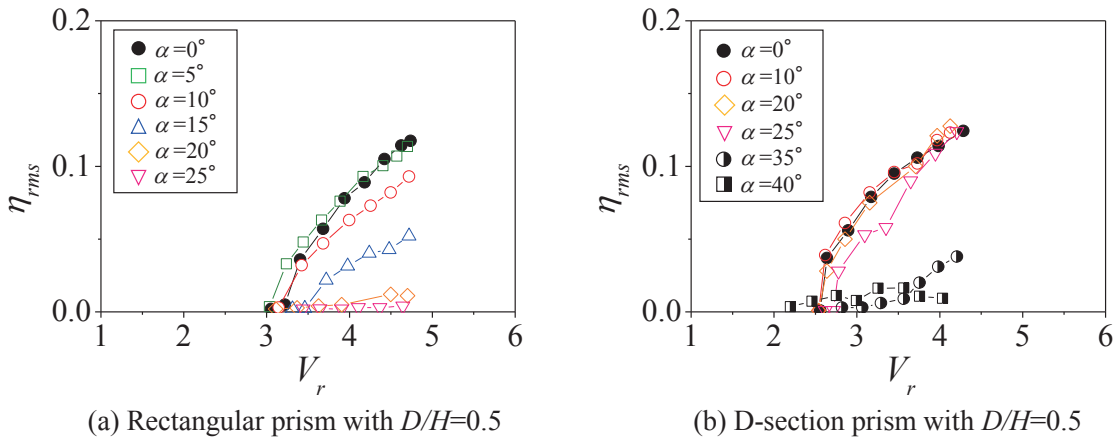


Figure 6: Response amplitude of the prism η_{rms} respect to the reduced velocity V_r with $D/H=0.5$

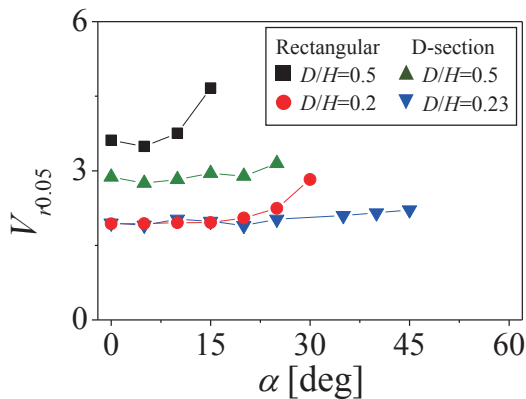


Figure 7: Reduced velocity at the 5% non-dimensional response amplitude $V_{r0.05}$ for direction I

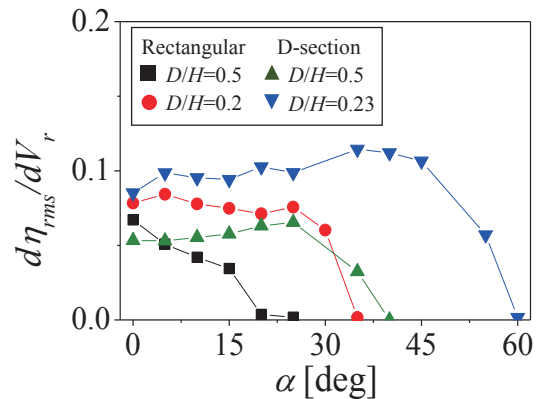


Figure 8: Increment rate of the response amplitude $d\eta_{rms}/dV_r$ for direction I

Knisely presented the Strouhal number for rectangular prisms with side ratios ranging from 0.04 to 1 and with angles of attack from 0° to 90° ³⁰⁾. For the side ratio of $D/H = 0.2$, the reattachment of the separated shear layer occurs near 35° . For the side ratio of $D/H = 0.5$, the reattachment occurs near 20° . Takizawa et al. shows that the lift force of a D-section prism with $D/H = 0.5$ changes at $\alpha \approx 40^\circ$ ³⁴⁾. These angles of attack coincide with a change in the response amplitude of prisms. Therefore, the rectangular prism with a small afterbody and D-section prism can vibrate until larger angle of attack.

(2) Vibration direction II

Next, we investigated the response amplitude of the prisms for the vibration direction II, which is the same as the normal direction to flow (Figure 1).

a) Prism with side ratio $D/H \approx 0.2$

Figure 9 shows the response amplitudes $\bar{\eta}_{rms}$ ($=y_{rms}/\bar{H}$) of a rectangular prism with side ratio $D/H = 0.2$ and a D-section prism with side ratio $D/H = 0.23$ for vibration direction II with respect to the reduced velocity V_r ($=Uf_c/H$). The response amplitudes of a rectangular prism with $D/H = 0.2$ increase linearly with an increase in the reduced velocity V_r at angle of attack $\alpha \leq 15^\circ$. The rectangular prism at $\alpha \geq 20^\circ$ vibrates very little. Thus, the range of angle of attack ($0^\circ \leq \alpha < 20^\circ$) in which a rectangular prism with $D/H = 0.2$ can vibrate for the direction II is narrower than that ($0^\circ \leq \alpha < 35^\circ$) for the direction I. Although a D-section prism with $D/H=0.23$ for the direction I vibrates at large angle of attack, i.e. $\alpha = 45^\circ$, the D-section prism for the direction II at $\alpha = 15^\circ$ vibrates very little.

b) Prism with side ratio $D/H = 0.5$

Figure 10 shows the response amplitudes $\bar{\eta}_{rms}$ ($=y_{rms}/\bar{H}$) of the rectangular and D-section prisms with side ratio $D/H=0.5$ for the vibration direction II with respect to the reduced velocity V_r ($=Uf_c/H$). The response amplitudes of a rectangular prism with $D/H = 0.5$ increase linearly with an increase in the reduced velocity V_r at angle of attack $\alpha \leq 15^\circ$. The rectangular prism at $\alpha = 20^\circ$ and 25° vibrates slightly. Especially, the rectangular prism at only $\alpha = 25^\circ$ for $V_r = 2.5 - 5.2$ vibrates with a half of natural frequency $f_c/2$, i.e. 10 - 17 Hz. This phenomenon has a concern in the unsteady flow separation point similar to the rectangular prism with $D/H = 0.5$ for the vibration direction I. In the case of D-section prism with $D/H=0.5$, the reduced velocity of the vibration onset increase gradually from $V_r = 2.8$ of $\alpha = 10^\circ$ to $V_r = 3.0$ of $\alpha = 25^\circ$, and the vibration is suppressed at $\alpha \approx 35^\circ$ the same as the vibration direction I.

c) 5 % non-dimensional and increment rate of response amplitude

Figures 11 shows the reduced velocity at the 5 % non-dimensional response amplitude of the prism $V_{r0.05}$ with respect to the angle of attack α . The reduced velocity $V_{r0.05}$ of a rectangular prism with $D/H = 0.2$ and a D-section prism with $D/H=0.23$ is smaller than prisms with $D/H=0.5$. The vibration of a D-section prism with $D/H=0.5$ is kept until $\alpha = 25^\circ$. Figures 7 shows the increment rate of the response amplitude for a prism $d\bar{\eta}_{rms}$

$/dV_r$ with respect to the angle of attack α . Although the increment rate of the response amplitude $d\overline{\eta}_{rms}/dV_r$ of a D-section prism with $D/H=0.23$ are larger, the range of vibratile angle of attack is narrower than the other prism. In particular, the increment rate of the response amplitude $d\overline{\eta}_{rms}/dV_r$ of a D-section prism with $D/H=0.5$ indicates large value in a wide range of angle of attack until $\alpha = 30^\circ$.

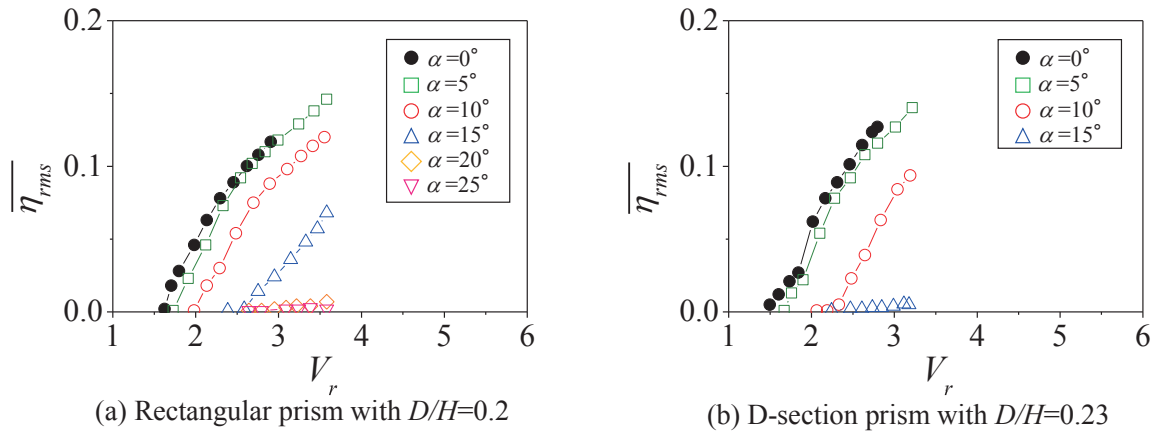


Figure 9: Response amplitude of the prism $\overline{\eta}_{rms}$ respect to the reduced velocity V_r with $D/H \approx 0.2$

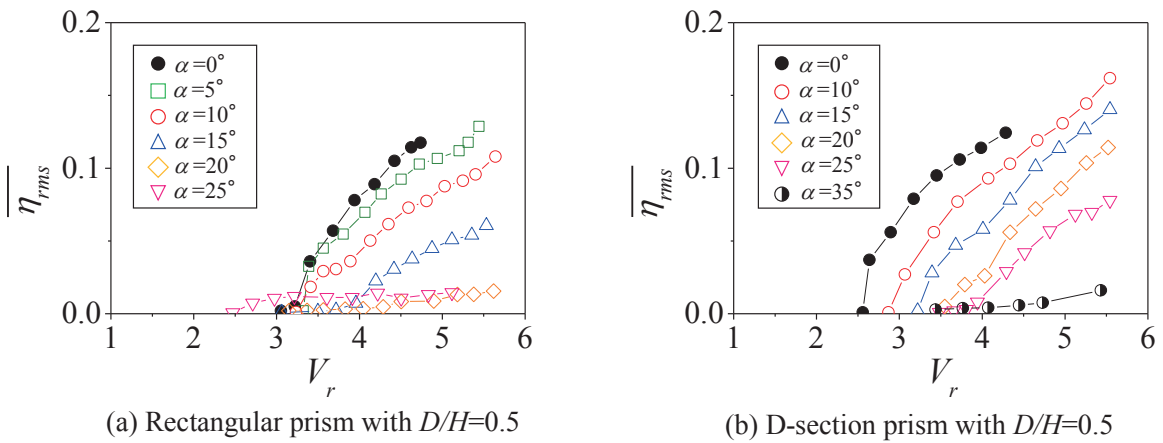


Figure 10: Response amplitude of the prism $\overline{\eta}_{rms}$ respect to the reduced velocity V_r with $D/H=0.5$

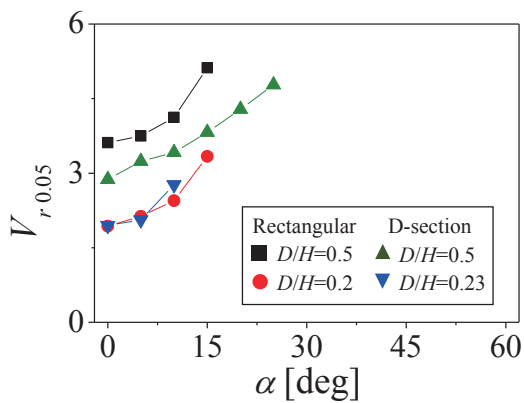


Figure 11: Reduced velocity at the 5% non-dimensional response amplitude $V_{r,0.05}$ for direction II

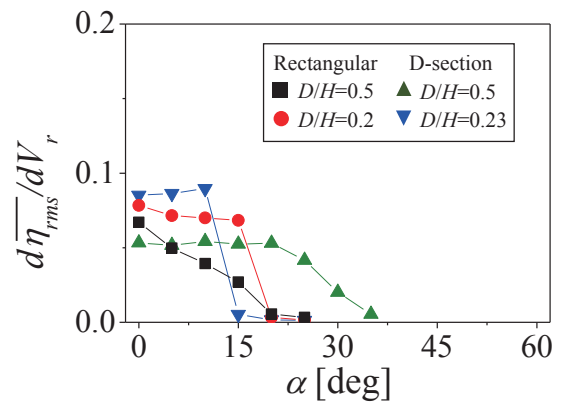


Figure 12: Increment rate of the response amplitude $d\overline{\eta}_{rms}/dV_r$ for direction II

3.2 VIBRATION-POWER GENERATION

From the result of free-vibration experiment, the prisms with small side ratio for the vibration direction I are suitable for the power generation of flow-induced vibration. So, the power generation experiment is conducted by using a rectangular prisms with side ratio $D/H = 0.2$ and a D-section prisms with side ratio $D/H = 0.23$. Figures 13 and 14 show time histories of the response amplitudes and the generated voltage at $\alpha = 0^\circ$ and 25° . Although there is a phase difference between waveforms of amplitude and voltage, each waveform of the amplitudes and voltages is almost stable against times. Figure 15 shows the response amplitudes η_{rms} ($= y_{rms}/H$) and the generated power P of a rectangular prisms with side ratio $D/H = 0.2$ and a D-section prisms with side ratio $D/H = 0.23$ at angles of attack $\alpha = 0^\circ$ and 25° . The response amplitudes and the generated power increase with increase of the reduced velocity. There are no marked difference between $\alpha = 0^\circ$ and $\alpha = 25^\circ$ on the response amplitudes and generated power. The generated power at $V_r = 4.15$ for a D-section prism is about 26 mW. Figure 16 shows the coefficient of power generation of the prisms with respect to the reduced velocity.

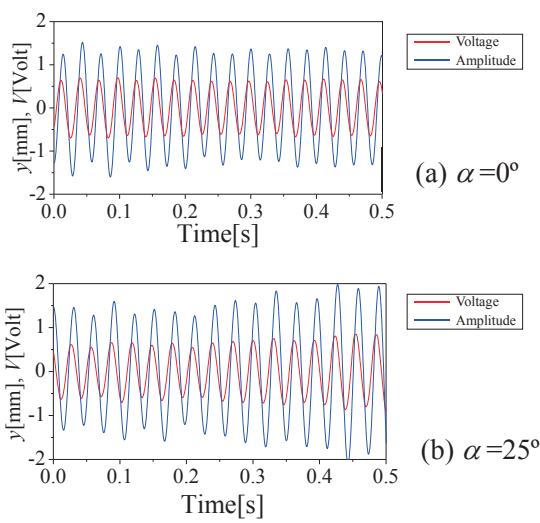


Figure 13: Time history of the response amplitudes of rectangular prism and generated voltage at $V_r=3.6$

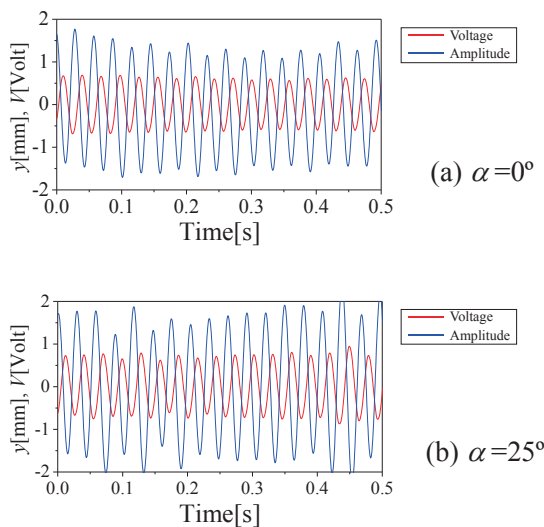
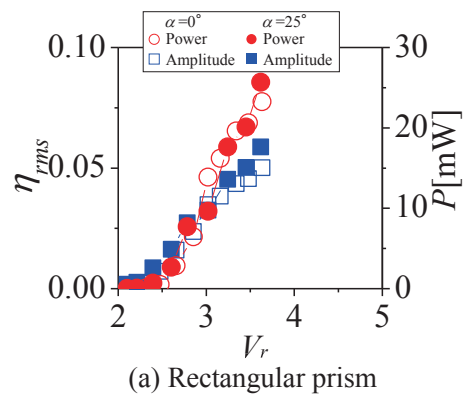
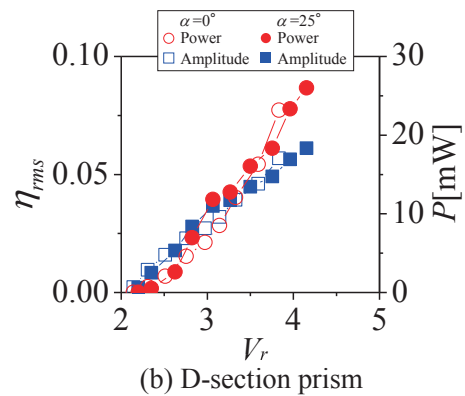


Figure 14: Time history of the response amplitudes of D-section prism and generated voltage at $V_r=3.8$



(a) Rectangular prism



(b) D-section prism

Figure 15: Response amplitudes of a prism and generated power

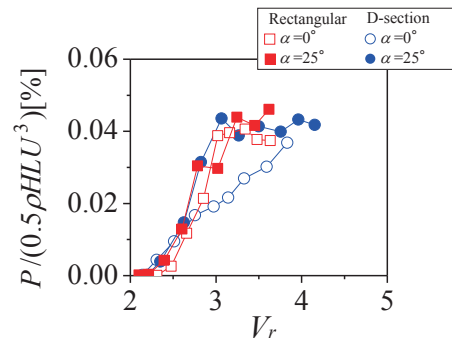


Figure 16: Coefficient of power generation

For $V_r > 3$, the coefficient of power generation becomes saturated. Maximum coefficient of power generation of the prism is about 0.045%.

4. CONCLUSIONS

Free-vibration and power generation tests using rectangular and D-section prisms with side ratio $D/H \approx 0.2$ and 0.5 were performed in a water tunnel. The main conclusions of the present study are as follows:

- (1) For the vibration direction I which is the same as the longitudinal direction of the prism, the D-section prism with side ratio $D/H = 0.23$ has the highest increment rate of the response amplitude, and vibrates in the wide range of angle of attack than the other prisms.
- (2) For the vibration direction II which is the normal direction to flow, the D-section prism with side ratio $D/H = 0.23$ has the highest increment rate of the response amplitude. The range of vibratile angle of attack is narrower than that for the vibration direction I.
- (3) The generated power and the maximum coefficient of the prism for the vibration direction I are 26 mW and 0.045 %, respectively.

ACKNOWLEDGMENT

The authors are thankful to Dr. Okajima for productive discussions and to technician Mr. Kuratani for his help with the experiment.

REFERENCES

- 1) Sodano, H.A., Inman, D.J. and Park, G., "A Review of Power Harvesting from Vibration using Piezoelectric Materials," *Smart Materials and Structures*, Vol.16, No.3, pp.1-9, 2007.
- 2) Uno, M. and Kawashima, R., "Proposal of Oscillating Type Hydraulic Power Generation," *Proceedings of Renewable Energy 2010*, Yokohama, Japan, Paper No.P-Sh-7, pp.1-4, 2010.
- 3) Hiejima, S., Oka, K., Hayashi, K. and Inoue, H., "Investigation on Energy Harvesting Efficiency for Flow-induced Vibration Based Power Generation Using Inverted Pendulum," *Proceedings of the 22nd National Symposium on Wind Engineering*, Tokyo, Japan, pp.425-430, 2012 (in Japanese).
- 4) Tanaka, Y., Matsumura, K. and Mutsuda, H., "Study on Flexible Power Generation Device Using Piezoelectric Film," *Journal of Energy and Power Engineering*, Vol.6, pp.353-360, 2012.
- 5) Fei, F., Mai, J.D. and Li, W.J., "A Wind-flutter Energy Converter for Powering Wireless Sensors," *Sensors and Actuators A*, Vol.173, pp.163-171, 2012.
- 6) Kwon, S.D., Lee, H. and Lee, S., "Wind Energy Harvesting from Flutter," *Proceedings of the 13th International Conference on Wind Engineering*, Amsterdam, Netherlands, 071_8page, pp.1-5, 2011.
- 7) Ali, M., Arafa, M. and Elaraby, M., "Harvesting Energy from Galloping Oscillations," *Proceedings of the World Congress on Engineering 2013*, London, U.K., Vol. III, pp.1-6, 2013.
- 8) Qiang Zhu, Max Hasse and Chin H. Wu, "Modeling the capacity of a novel flow-energy harvester", *Applied Mathematic Modelling*, Vol.33 No.5, pp.2207-2217, 2009.
- 9) Parkinson, G.V. and Smith, J.D., "The Square Prism as Aeroelastic Non-Linear Oscillator," *The Quarterly Journal of Mechanics and Applied Mathematics*, Vol. 17, pp.225-239, 1964.
- 10) Van Oudheusden, B.W., "On the Quasi-steady Analysis of One-degree-of-freedom Galloping with Combined Translational and Rotational Effects," *Nonlinear Dynamics*, Vol.8, pp.435-451, 1995.
- 11) Luo, C., Chew, Y.T. and Ng, Y.T., "Hysteresis Phenomenon in the Galloping Oscillation of a Square Cylinder," *Journal of Fluids and Structures*, Vol.18, pp.103-118, 2003.
- 12) Tamura, T. and Dias, P.P.N.L., "Unstable Aerodynamic Phenomena Around the Resonant Velocity of a Rectangular Cylinder with Small Side Ratio," *Journal of Wind Engineering and Industrial Aerodynamics*, Vol.91, pp.127-138, 2003.
- 13) Nakamura, Y., Hirata, K. and Urabe, T., "Galloping of rectangular cylinders in the presence of a splitter plate," *Journal of Fluids and Structures*, Vol.5, pp. 521-549, 1991.
- 14) Kiwata, T., Yamaguchi, M., Kono, T. and Ueno, T., "Water tunnel experiments on transverse-galloping of

- cantilevered rectangular and D-section prisms,” *Journal of Fluid Science and Technology*, Vol. 9, No. 3, <http://doi.org/10.1299/jfst.2014jfst0056>, pp.1-11, 2014.
- 15) Kiwata,T., Yamaguchi,M., Nakajima,A., Kono,T. and Ueno,T., “Flow-Induced Transverse Vibration of a Cantilevered Prism for Energy Harvesting”, *Proceedings of the ASME 2014 Pressure Vessels & Piping Division Conference*, California, USA, PVP2014-28939, pp.1-10, 2014.
 - 16) Bokaian,A.R. and Geoola,F., “On the Cross Flow Response of Cylindrical Structures”, *Proceedings Institution Civil Engineers*, London, Vol.75, Paper8654, pp.397-418, 1983.
 - 17) Alonso,G. and Meseguer,J., “A Parametric Study of the Galloping Stability of Two-dimensional Triangular Cross-section Bodies,” *Journal of Wind Engineering and Industrial Aerodynamics*, Vol. 94, pp.241–253, 2006.
 - 18) Luo,S.C., Yazdani,M.G., Chew,Y.T. and Lee,T.S., "Effects of Incidence and Afterbody Shape on Flow Past Bluff Cylinders," *Journal of Wind Engineering and Industrial Aerodynamics*, Vol.53, pp.375–399, 1993.
 - 19) Luo,S.C., Chew,Y.T. and Yazdani,M.G., "Stability to Translational Galloping Vibration of Cylinders at Different Mean Angles of Attack", *Journal of Sound and Vibration*, Vol.215, pp.1183–1194, 1998.
 - 20) Barrero-Gil,A., "Energy Harvesting from Transverse Galloping," *Journal of Sound and Vibration*, Vol.329, pp.2873–2883, , 2010.
 - 21) Kluger, J.M., Moon, F.C. and Rand,R.H., “Shape Optimization of a Blunt Body Vibro-wind Galloping Oscillator,” *Journal of Fluids and Structures*, Vol. 40, pp.185-200, 2013.
 - 22) Naudascher,E. and Rockwell,D., “Flow-induced Vibrations: An Engineering Guide,” Dover Publications, Inc., 2005.
 - 23) Ueno,T. and Yamada,S., “Performance of Energy harvester using Iron-Gallium Alloy in Free Vibration,” *IEEE Transactions on Magnetics*, Vol.47, pp. 2407–2409, 2010.
 - 24) Japan Society of Mechanical Engineers, “Guideline for Evaluation of Flow-induced Vibration of a Cylindrical Structure in a Pipe,” JSME S 012-1998, pp.B6-B14, Maruzen Co. Ltd., 1998 (in Japanese).
 - 25) Nakaguchi,H., Hashimoto,K. and Muto,S., “An Experimental Study on Aerodynamic Drag of Rectangular Cylinders,” *Journal of Japan Society for Aeronautical and Space Sciences*, Vol. 16, No. 168, pp.1-5 , 1968 (in Japanese).
 - 26) Okajima,A., Kimura,S., Katayama,T., Ohtsuyama,S. and Ojima,A., “Fluid-dynamic Characteristics of a Rectangular Cylinder with Various Width-to-ratios in Wide Range of Reynolds Number,” *Journal of Structural Engineering*, Vol.44A, pp.971-977, 1998 (in Japanese).
 - 27) Ohya,Y., “Note on a Discontinuous Change in Wake Pattern for a Rectangular Cylinder”, *Journal of Fluids and Structures*, Vol.8, pp.325-330, 1994.
 - 28) Feng,C.C., 1968, “The Measurement of Vortex Induced Effects in Flow Past Stationary Circular and D-section Cylinder,” *Thesis of M.A.Sc., The University of British Columbia*.
 - 29) Tamura,T. and Miyagi,T., “The effect of turbulence on aerodynamics force on a square cylinder with various corner shapes”, *Journal of Wind Engineering*, Vol.83, pp.135-145, 1999.
 - 30) Knisely,C.W., “Strouhal numbers of rectangular cylinders at incidence: A review and new data”, *Journal of Fluids and Structures*, Vol.4, No.4, pp.371-393, 1990
 - 31) Alonso,G., Valero,E. and Meseguer,J., “An analysis on the dependence on cross section geometry of galloping stability of two-dimensional bodies having either biconvex or rhomboidal cross sections”, *European Journal of Mechanics B/Fluids*, Vol.28, No.2, pp.328-334, 2009
 - 32) Matsumoto,M., Ishizaki,H., Matsuoka,C., Daito,Y., Ishikawa,Y. and Shimahara,A., “Aerodynamic effects of the angle of attack on a rectangular prism”, *Journal of Wind Engineering and Industrial Aerodynamics*, Vol.77-78, pp.531-542, 1998
 - 33) Naudascher,E. and Wang,Y., “Flow-Induced Vibrations of Prismatic Bodies and Grids of Prisms”, *Journal of Fluids and Structures*, Vol.7, No.4, pp.341-343, 1993.
 - 34) Takizawa,N., Okada,N., Iwasaki,A., “Wind-tunnel Investigation of Pressure Distribution and Deduced Characteristics of Semi-Circular Cylinder in the Vicinity of Critical Reynolds Number,” Technical Report of National Aerospace Laboratory, TR-871, pp.1-42, 1985 (in Japanese).

AEROELASTIC AND PERFORMANCE BASELINE ANALYSIS OF PIEZO-AEROELASTIC WING SECTION FOR ENERGY HARVESTER

Harijono Djojodihardjo¹

Key issues: Aeroelasticity and Flapping Mechanism, Bio-Inspired, Flapping Piezoelectric Energy Harvester, Flow Energy Harvesting, Oscillatory Foil.

ABSTRACT.

Piezo-aeroelastic energy harvesters convert airflow induced vibrations into electrical energy, while the availability and affordability of piezoelectric transducers offer a class of flapping foil energy harvesters mostly in micro- to milliwatts scale which need to be tuned to match the characteristic frequencies. The present work presents a brief review of aeroelastic instability of a generic typical wing section due to the free stream flow field which is utilized as an oscillating foil energy converter. For propaedeutic analysis a generic piezo-aeroelastic cantilevered beam is defined and treated as a typical section. The basic governing equation of this generic structure is treated as a three degrees of freedom electro-dynamic system, with the first two-degree-of-freedom comprising the standard binary aeroelastic system with additional relevant terms to represent the influence of a piezoelectric embedded element on the cantilevered wing. Following the philosophical approach of binary aeroelastic system, the problem is mathematically formulated and solved for the range of solutions that can be obtained depending on the prevailing physical properties of the system, focusing on the stability characteristics of the generic system. The characteristic of the unsteady aerodynamics of the oscillating system associated with favorable energy harvesting capabilities are assessed.

I. INTRODUCTION AND BRIEF REVIEW

The progress of energy harvesting technology and self-powered systems that has been prompted by the development of low power electronics offers autonomous systems that require minimum maintenance that are essential for their deployment in previously inaccessible locations (Zhu, 2011). Energy Harvesting can be defined as the process of capturing energy, which are relatively minute, from the naturally occurring (“Green”) energy sources, and then accumulating them and storing them for later use. Autonomous system and smart material technology that are now widely utilized take advantage of the thermal energy that can be converted to electrical energy by the Seebeck-Peltier effect, or mechanical energy extraction in piezoelectric system (first discovered by Jacques and Pierre Curie). These make extracting energy from mechanical energy an attractive approach for powering electronic systems, as in piezoelectric system.

The piezoelectric effect was discovered by the bothers Pierre Curie and Jacques Curie in 1880, while the converse effect was later discovered by Gabriel Lippmann in 1881 through the mathematical aspect of the theory. These behaviors were labelled the piezoelectric effect and the inverse piezoelectric effect, respectively (Ledoux, 2011). New approaches have been developed using first-principles computations, based on fundamental physics. First-principles theory laid the framework for a basic understanding of the origins of piezoelectric behavior and properties.

The principle of the composite energy harvesting system relies on the fact that the material, such as Polyvinylidene fluoride (PVDF) has natural piezoelectric properties. The conversion of mechanical

¹The Institute for the Advancement of Aerospace Science and Technology, Jakarta, Indonesia 15419; email: harijono.djojodihardjo@yahoo.com; harijono.djojodihardjo@gmail.com

energy electricity by the piezoelectric PVDF is characterized by the coupling coefficient k , which can be as high as 15%.

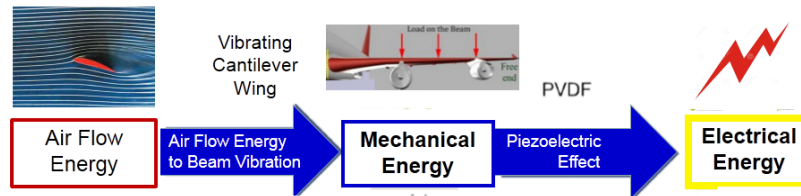


Figure 1: Schematic estimation of flow energy-to-electrical energy conversion using vibrating wing section and piezoelectric effects

A generic model for energy-to-electrical energy conversion using vibrating wing section and piezoelectric effects for energy harvesters is illustrated in Fig. 1. The conversion of flow energy to aeroelastic vibrational energy consists of two parts, in conformity to the concept of aeroelasticity, as illustrated in Fig 2, consisting of the mechanical vibration part (a) and the aerodynamic part (b).

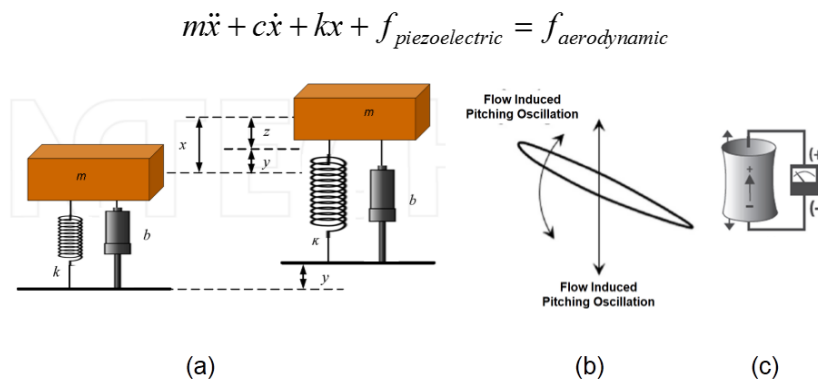


Figure 2: Generic model of piezo-aeroelastic vibration energy harvester comprising the mechanical-structural (a), aerodynamic (b) and piezoelectric (c) parts.

The damping consists of two parts, the mechanical structural damping incorporated in part (a) and the aerodynamic damping incorporated in the aerodynamic forcing of part (b), as shown in Fig.2. The piezoelectric element then establishes the piezo-aeroelastic vibration energy harvester, which harvests the flow energy to be delivered to the electrical loads (Zhu, 2011)

II. MECHANICS OF PIEZOELECTRIC PATCHED CANTILEVERED BEAM AS ENERGY HARVESTER

For purposes of propaedeutic analysis a generic piezo-aeroelastic cantilevered beam is defined and treated as a binary aeroelastic cantilevered wing section as the base line, with piezoelectric element embedded at the wing root, as further simplified implementation of the generic piezo-aeroelastic vibration energy harvester. The schematic of the piezoaeroelastic energy harvesting system from airflow excitation is depicted in Fig. 3 as the baseline of the present analysis. Aeroelastic vibrations of the cantilever wing bending (plunge or heaving motion, represented by bending angular deflection) strain the piezoelectric patches dynamically and produces the electrical output. Therefore, if piezoelectric coupling is added to the plunge DOF of the typical section as schematically depicted in Figs.2 and 3, the resultant force on the piezoelectric element will result in a resultant voltage.

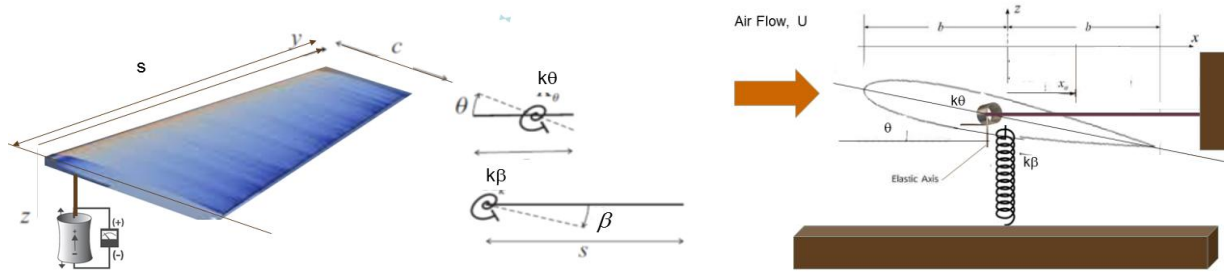


Figure 3: Generic model of linear piezoaeroelastic energy harvester

The governing linear aeroelastic equations to be utilized in the piezo-aeroelastic energy harvesting system can be derived from the binary aeroelastic system as given in the classical literature (for example, Bisplinghoff, Ashley and Halfman, 1955; Wright and Cooper, 2011; Djodjodhardjo and Yee, 2009; Djodjodhardjo, 2015):

$$(m + m_e)\ddot{h} + mbx_\alpha\ddot{\alpha} + d_h\dot{h} + K_h h = -L \quad (1)$$

$$mbx_\alpha\ddot{h} + I_\alpha\ddot{\alpha} + d_h\dot{\alpha} + K_\alpha\alpha = M \quad (2)$$

where m is the airfoil mass per length (in the span direction), m_e is the fixture mass (connecting the airfoil to the plunge springs) per length, M is the aerodynamic moment, L is the aerodynamic lift, and the over-dot represents differentiation with respect to time (t).

Incorporating piezoelectric element in the model, the following set of piezo-aeroelastic model is obtained (similar to that obtained by Marqui and Erturk, 2011):

$$(m + m_e)\ddot{h} + mbx_\alpha\ddot{\alpha} + d_h\dot{h} + K_h h - \frac{\Theta}{l}V = -L \quad (3)$$

$$mbx_\alpha\ddot{h} + I_\alpha\ddot{\alpha} + d_h\dot{\alpha} + K_\alpha\alpha = M \quad (4)$$

$$C_{piezo}\dot{V} + \frac{V}{R_l} + \Theta\dot{h} = 0 \quad (5)$$

Here the fixture mass (m_e) is defined for the case when the system slightly deviates from the ideal typical section depicted in Figure 5 due to the masses of the shaft, spring mass, and other attachments in real experiments (Sousa et al., 2011), while it is zero in the ideal representation of Fig. 3, which is assumed here for the baseline solution.

After incorporating all these factors, further simplification, modification, and redefinition of the relevant and prevailing piezo-aeroelastic parameters, equations (3-5) can be reduced to:

$$I_\beta\ddot{\beta} + k_\beta\beta + I_{\beta\theta}\ddot{\theta} + qSC_{L\alpha}\theta - \frac{k_\beta}{s}DV = 0 \quad (6)$$

$$I_{\beta\theta}s\ddot{\beta} + I_\theta\ddot{\theta} + k_\theta\theta - 2qSebC_{L\alpha}\theta = 0 \quad (7)$$

$$+ k_\beta D\dot{\beta} + C_{piezo}\dot{V} + \frac{1}{R_l}V = 0 \quad (8)$$

which will be utilized as the baseline for the solution procedure developed subsequently. All the symbols are given in the Nomenclature. It should also be noted that for the present case the structural and aerodynamic damping have been ignored; further analysis which incorporate these ignored terms will follow after the baseline case is established.

III. SYNTHESIS OF BASELINE SOLUTION PROCEDURE

The problem posed by the set of equations (6) to (8) will be formulated in the following sequence of problems, which is considered to follow an appropriate rationale

1. Formulate the equation as stability equation, which may be met by certain behavior of piezoelectric terms.
2. Establish the relationships between the piezo-electric output in terms of the aeroelastic parameters setting and flow parameters, and determine the related setting of the piezo-electric system to meet certain objectives.

Based on the insight gained in the solution of the problem, preliminary design specifications for a piezo-aeroelastic system can be defined.

Following the technique introduced by Wright and Cooper (2011), the general form of the baseline aeroelastic equations (1) and (2) are in the classical second-order form for N degrees of freedom system:

$$\mathbf{A}\ddot{\mathbf{q}} + (\rho_0\mathbf{UB} + \mathbf{D})\dot{\mathbf{q}} + (\rho U^2\mathbf{C} + \mathbf{E})\mathbf{q} = 0 \quad (9)$$

where $\mathbf{A}, \mathbf{B}, \mathbf{C}, \mathbf{D}, \mathbf{E}$ are the structural inertia, aerodynamic damping, aerodynamic stiffness, structural damping and structural stiffness matrices respectively, and \mathbf{q} are the generalized coordinates (typically modal coordinates). It is important to note that the \mathbf{B}, \mathbf{C} matrices only apply for the reduced frequency for which they are defined.

Equation (16) can be transformed to Eigenvalue formulation of flutter equations by adding an identity equation of the form

$$\mathbf{I}\dot{\mathbf{q}} - \mathbf{I}\dot{\mathbf{q}} = 0 \quad (10)$$

Upon combining equation (9) with equation (10), the following equation (11) is obtained

$$\begin{bmatrix} \mathbf{I} & 0 \\ 0 & \mathbf{A} \end{bmatrix} \begin{Bmatrix} \dot{\mathbf{q}} \\ \ddot{\mathbf{q}} \end{Bmatrix} - \begin{bmatrix} 0 & \mathbf{I} \\ -(\rho U^2\mathbf{C} + \mathbf{E}) & -(\rho\mathbf{UB} + \mathbf{D}) \end{bmatrix} \begin{Bmatrix} \mathbf{q} \\ \dot{\mathbf{q}} \end{Bmatrix} = \begin{Bmatrix} 0 \\ 0 \end{Bmatrix} \quad (11)$$

Equation (11) can further be reduced to as

$$\begin{Bmatrix} \dot{\mathbf{q}} \\ \ddot{\mathbf{q}} \end{Bmatrix} - \begin{bmatrix} 0 & \mathbf{I} \\ -\mathbf{A}^{-1}(\rho U^2\mathbf{C} + \mathbf{E}) & -\mathbf{A}^{-1}(\rho\mathbf{UB} + \mathbf{D}) \end{bmatrix} \begin{Bmatrix} \mathbf{q} \\ \dot{\mathbf{q}} \end{Bmatrix} = \begin{Bmatrix} 0 \\ 0 \end{Bmatrix} \quad \text{or} \quad \dot{\mathbf{x}} - \mathbf{Q}\mathbf{x} = 0 \quad (12)$$

Equations (12) are now in first-order form although the Q matrix has the size of $2N \times 2N$, twice the size of the matrices in the aeroelastic Equations (6) to (8) and (9).

For convenience, following the practice in aeroelasticity, the analysis of flutter stability can be obtained by assuming oscillatory solution of the form:

$$\{\mathbf{x}\} = \{\mathbf{x}_0\} e^{\lambda t}; \quad \lambda = \sigma + i\omega \quad (13)$$

where σ is the real (damping) part and ω is the imaginary (oscillatory) part.

Hence by assuming $\mathbf{x} = \mathbf{x}_0 e^{\lambda t}$ equation (12) can be reduced to the form

$$(\mathbf{I}\lambda - \mathbf{Q})\mathbf{x}_0 = 0 \quad \text{or} \quad (\mathbf{Q} - \mathbf{I}\lambda)\mathbf{x}_0 = 0 \quad (14)$$

Two approaches can be taken to solve equations (12) and/ or (14), namely the frequency domain method and time-integration method in the time domain.

a. Frequency Domain Method:

The Frequency Domain Method is used to solve the eigenvalue problem as defined by equations (12) or (14). The eigenvalue solutions are computed for a range of reasonable flow velocity range, calculated for any airspeed. The appearance of positive real part of the eigenvalues indicates the occurrence of instability or flutter.

b. The time-integration method

The time-integration method is used to integrate equations (12) or (14) numerically and calculate the time response for a specific air flow velocity using a conveniently chosen numerical integration method, such as the Runge-Kutta method.

IV. FUNDAMENTAL SOLUTION PROCEDURE – DECOUPLED LINEAR APPROACH

The baseline aeroelastic equation (14) can be decoupled into two sets of equations, in order that each set has similar solution vector.

Hence one can write:

$$\begin{bmatrix} I_\beta & I_{\beta\theta} \\ I_{\beta\theta} & I_\theta \end{bmatrix} \begin{Bmatrix} \ddot{\beta} \\ \ddot{\theta} \end{Bmatrix} + \begin{bmatrix} 0 & 0 & 0 \\ 0 & 0 & 0 \\ k_\beta D & 0 & C_{piezo} \end{bmatrix} \begin{Bmatrix} \dot{\beta} \\ \dot{\theta} \\ \dot{V} \end{Bmatrix} + \begin{bmatrix} k_\beta & 0 & -\frac{k_\beta}{s} D \\ 0 & k_\alpha & 0 \\ 0 & 0 & \frac{1}{R_l} \end{bmatrix} \begin{Bmatrix} \beta \\ \theta \\ V \end{Bmatrix} = \begin{bmatrix} 0 & -qSC_{L\alpha} \\ 0 & qSebC_{L\alpha} \end{bmatrix} \begin{Bmatrix} \beta \\ \theta \end{Bmatrix} \quad (15)$$

After substituting equation (13) into the equation (15), one obtains

$$\lambda^2 \begin{Bmatrix} \beta \\ \theta \end{Bmatrix} - \begin{bmatrix} I_\beta & I_{\beta\theta} \\ I_{\beta\theta} & I_\theta \end{bmatrix}^{-1} \begin{bmatrix} 0 & -qSC_{L\alpha} \\ 0 & qSebC_{L\alpha} \end{bmatrix} \begin{Bmatrix} \beta \\ \theta \end{Bmatrix} = -\lambda \begin{bmatrix} I_\beta & I_{\beta\theta} \\ I_{\beta\theta} & I_\theta \end{bmatrix}^{-1} \begin{bmatrix} 0 & 0 & 0 \\ 0 & 0 & 0 \\ k_\beta D & 0 & C_{piezo} \end{bmatrix} \begin{Bmatrix} \beta \\ \theta \\ V \end{Bmatrix} - \begin{bmatrix} I_\beta & I_{\beta\theta} \\ I_{\beta\theta} & I_\theta \end{bmatrix}^{-1} \begin{bmatrix} k_\beta & 0 & -\frac{k_\beta}{s} D \\ 0 & k_\alpha & 0 \\ 0 & 0 & \frac{1}{R_l} \end{bmatrix} \begin{Bmatrix} \beta \\ \theta \\ V \end{Bmatrix} \quad (16)$$

In the simplified analysis, equation (16) is split into two sets of equations. These are

$$\lambda^2 \{Q\} + \lambda [M_d] \{Q\} + [M_k] \{Q\} - [M_A] \{Q\} = 0 \quad (17)$$

and

$$\lambda [M_d] \{V\} + [M_k] \{V\} = 0 \quad (18)$$

The latter equation can be reduced to

$$V \left(\lambda C_{piezo} + \frac{1}{R_l} \right) = \lambda k_\beta D \beta \rightarrow V = \frac{\lambda k_\beta D \beta}{\lambda C_{piezo} + \frac{1}{R_l}} \quad (20)$$

A significant loss of information is noted here, since the simplified piezo-aeroelastic instability formulation failed to include any piezoelectric variable. D disappear from the eigenvalue problem, since the second row of the “simplified” piezo-aeroelastic problem does not contain a term incorporating β . Nevertheless, for the interest of developing the solution further, the piezo-aeroelastic eigenvalue problem will be treated. The piezo electric variables, however, is determined by the eigenvalues and the flow

$$\text{dynamic pressure } q = \rho U^2 / 2 \text{ in } V = \frac{\lambda k_\beta D \beta}{\lambda C_{piezo} + \frac{1}{R_l}}$$

The solution procedure then can be formulated as follows:

1. Find the four eigenvalues $\lambda = p = \sigma + i\omega$ of

$$\lambda^4 (I_\beta I_\theta - I_{\beta\theta}^2) + \left(k_\beta k_\theta - \rho U^2 \frac{cS^2 C_{L\alpha}}{4} k_\beta \right) = 0 \quad (21)$$

2. For each set of eigen-value, find the harvested voltage

$$V = \frac{\lambda k_\beta D \beta}{\lambda C_{piezo} + \frac{1}{R_l}} \quad (22)$$

which consists of

$$\mathbf{V} = \mathbf{V}_{\text{real}}(\lambda) + i\mathbf{V}_{\text{imag}}(\lambda) \quad (21)$$

The sustained fluctuating values of voltage V will be considered as plausible solutions, dictated by the prevailing aeroelastic properties to be further analysed.

V. PRINCIPAL PIEZO-AEROELASTIC STABILITY EQUATION

Following the approach similar to the transformation of Equation (10) to Eigenvalue (flutter equations) formulation Equation (20) by adding an identity equation,

$$\mathbf{I}\dot{\mathbf{Q}} - \mathbf{I}\dot{\mathbf{Q}} = 0 \quad (22)$$

$$\text{where } \mathbf{Q} \equiv \begin{Bmatrix} \beta \\ \theta \\ V \end{Bmatrix} \quad (23)$$

to the equations (5) to (6) which have been written in a form similar to equation(9), then one gets

$$\begin{bmatrix} 1 & 0 & 0 & 0 & 0 & 0 \\ 0 & 1 & 0 & 0 & 0 & 0 \\ 0 & 0 & 1 & 0 & 0 & 0 \\ 0 & 0 & 0 & I_\beta & I_{\beta\theta} & 0 \\ 0 & 0 & 0 & I_{\beta\theta} & I_\theta & 0 \\ 0 & 0 & 0 & 0 & 0 & 0 \end{bmatrix} \begin{Bmatrix} \dot{\beta} \\ \dot{\theta} \\ \dot{V} \\ \ddot{\beta} \\ \ddot{\theta} \\ \ddot{V} \end{Bmatrix} - \begin{bmatrix} 0 & 0 & 0 & 1 & 0 & 0 \\ 0 & 0 & 0 & 0 & 1 & 0 \\ 0 & 0 & 0 & 0 & 0 & 1 \\ k_\beta & qSC_{L\alpha} & -\frac{k_\beta}{s}D & 0 & 0 & 0 \\ 0 & k_\theta - 2qSebC_{L\alpha} & 0 & 0 & 0 & 0 \\ 0 & 0 & \frac{1}{R_l} & k_\beta D & 0 & C_{piezo} \end{bmatrix} \begin{Bmatrix} \beta \\ \theta \\ V \\ \dot{\beta} \\ \dot{\theta} \\ \dot{V} \end{Bmatrix} = \begin{Bmatrix} 0 \\ 0 \\ 0 \end{Bmatrix} \quad (24)$$

$$\text{or } \begin{bmatrix} \mathbf{I} & 0 \\ 0 & \mathbf{A}' \end{bmatrix} \begin{Bmatrix} \dot{\mathbf{Q}} \\ \ddot{\mathbf{Q}} \end{Bmatrix} - \begin{bmatrix} 0 & \mathbf{I} \\ \mathbf{C}' & \mathbf{B} \end{bmatrix} \begin{Bmatrix} \mathbf{Q} \\ \dot{\mathbf{Q}} \end{Bmatrix} = \begin{Bmatrix} 0 \\ 0 \end{Bmatrix} \quad (25)$$

$$\text{where } [\mathbf{A}'] \equiv \begin{bmatrix} I_\beta & I_{\beta\theta} & 0 \\ I_{\beta\theta} & I_\theta & 0 \\ 0 & 0 & 0 \end{bmatrix} \quad [\mathbf{B}] \equiv \begin{bmatrix} 0 & 0 & 0 \\ 0 & 0 & 0 \\ k_\beta D & 0 & C_{piezo} \end{bmatrix} \quad [\mathbf{C}'] \equiv \begin{bmatrix} k_\beta & qSC_{L\alpha} & -\frac{k_\beta}{s}D \\ 0 & k_\theta - 2qSebC_{L\alpha} & 0 \\ 0 & 0 & \frac{1}{R_l} \end{bmatrix}$$

$$\text{and } [\mathbf{I}] \equiv \begin{bmatrix} 1 & 0 & 0 \\ 0 & 1 & 0 \\ 0 & 0 & 1 \end{bmatrix} \quad (26a,b,c,d)$$

Equation (24) or (25) can be written as

a. Eigen value problem in frequency domain:

$$\begin{Bmatrix} \dot{\mathbf{Q}} \\ \ddot{\mathbf{Q}} \end{Bmatrix} - \begin{bmatrix} \mathbf{I} & 0 \\ 0 & \mathbf{A}' \end{bmatrix}^{-1} \begin{bmatrix} 0 & \mathbf{I} \\ \mathbf{C}' & \mathbf{B} \end{bmatrix} \begin{Bmatrix} \mathbf{Q} \\ \dot{\mathbf{Q}} \end{Bmatrix} = \begin{Bmatrix} 0 \\ 0 \end{Bmatrix} \quad (27)$$

or

$$\{\dot{\mathbf{G}}\} - [\mathbf{A}''][\mathbf{B}'']\{\mathbf{G}\} = \{\mathbf{0}\} \quad \text{or} \quad \{\dot{\mathbf{G}}\} - [\mathbf{M}_G]\{\mathbf{G}\} = \{\mathbf{0}\} \quad (28)$$

where

$$\{\mathbf{G}\} = \begin{Bmatrix} \mathbf{Q} \\ \dot{\mathbf{Q}} \end{Bmatrix} = \begin{Bmatrix} \beta \\ \theta \\ V \\ \dot{\beta} \\ \dot{\theta} \\ \dot{V} \end{Bmatrix} \quad (29) \quad [\mathbf{A}'''] \equiv \begin{bmatrix} \mathbf{I} & 0 \\ 0 & \mathbf{A}' \end{bmatrix}^{-1}; [\mathbf{B}'''] \equiv \begin{bmatrix} 0 & \mathbf{I} \\ \mathbf{C}' & \mathbf{B} \end{bmatrix} \quad (30) \quad [\mathbf{M}_G] \equiv [\mathbf{A}'''] [\mathbf{B}'''] \quad (31)$$

For further elaboration, different from the simplified split equations approach, one should again look at the oscillating solution assumption to obtain the solution of the extended matrix solution of Equation (28): Assuming periodic solution of $\{\mathbf{G}\}$ in the form:

$$\{\mathbf{G}\} = \{\mathbf{G}_0\} e^{\lambda t} = \{\mathbf{G}_0\} e^{(\sigma+i\omega)t} \quad (32)$$

where $\lambda = (\sigma + i\omega)t$

then Equation (28) can be converted to

$$\lambda \{\mathbf{G}\} = [\mathbf{M}_G] \{\mathbf{G}\} \rightarrow \{\mathbf{G}\} = \frac{1}{\lambda} [\mathbf{M}_G] \{\mathbf{G}\} \quad \text{or} \quad [\lambda - [\mathbf{M}_G]] = 0 \quad (33)$$

which leads to finding the roots λ that satisfy

$$\{\lambda - [\mathbf{M}_G]\} = 0 \quad (34)$$

or

$$\begin{bmatrix} \lambda & 0 & 0 & 0 & 0 & 0 \\ 0 & \lambda & 0 & 0 & 0 & 0 \\ 0 & 0 & \lambda & 0 & 0 & 0 \\ 0 & 0 & 0 & \lambda & 0 & 0 \\ 0 & 0 & 0 & 0 & \lambda & 0 \\ 0 & 0 & 0 & 0 & 0 & \lambda \end{bmatrix} - \begin{bmatrix} 1 & 0 & 0 & 0 & 0 & 0 \\ 0 & 1 & 0 & 0 & 0 & 0 \\ 0 & 0 & 1 & 0 & 0 & 0 \\ 0 & 0 & 0 & I_\beta & I_{\beta\theta} & 0 \\ 0 & 0 & 0 & I_{\beta\theta} & I_\theta & 0 \\ 0 & 0 & 0 & 0 & 0 & 0 \end{bmatrix}^{-1} \begin{bmatrix} 0 & 0 & 0 & 1 & 0 & 0 \\ 0 & 0 & 0 & 0 & 1 & 0 \\ 0 & 0 & 0 & 0 & 0 & 1 \\ k_\beta & qSC_{L\alpha} & -\frac{k_\beta}{s}D & 0 & 0 & 0 \\ 0 & k_\theta - 2qSebC_{L\alpha} & 0 & 0 & 0 & 0 \\ 0 & 0 & \frac{1}{R_l} & k_\beta D & 0 & C_{piezo} \end{bmatrix} = 0 \quad (35)$$

Then, for each set of piezo-aeroelastic parameters and wind velocity, represented by q, there are 6 roots of λ and consequently 6 each of the corresponding σ and ω values. The voltage V of the piezoelectric elements will be the solution vector. The latter notion will be the subject of further investigation.

b. Time-Integration Problem in the time domain/ state space

$$\begin{bmatrix} \mathbf{I} & 0 \\ 0 & \mathbf{A}' \end{bmatrix} \begin{Bmatrix} \dot{\mathbf{Q}} \\ \ddot{\mathbf{Q}} \end{Bmatrix} = \begin{bmatrix} 0 & \mathbf{I} \\ \mathbf{C}' & \mathbf{B} \end{bmatrix} \begin{Bmatrix} \mathbf{Q} \\ \dot{\mathbf{Q}} \end{Bmatrix} \rightarrow \begin{Bmatrix} \dot{\mathbf{Q}} \\ \ddot{\mathbf{Q}} \end{Bmatrix} = \begin{bmatrix} \mathbf{I} & 0 \\ 0 & \mathbf{A}' \end{bmatrix}^{-1} \begin{bmatrix} 0 & \mathbf{I} \\ \mathbf{C}' & \mathbf{B} \end{bmatrix} \begin{Bmatrix} \mathbf{Q} \\ \dot{\mathbf{Q}} \end{Bmatrix} \quad (36a)$$

or $\{\dot{\mathbf{G}}\} = [\mathbf{A}'''] [\mathbf{B}'''] \{\mathbf{G}\} \quad (36a) \quad \text{or} \quad \{\dot{\mathbf{G}}\} = [\mathbf{M}_G] \{\mathbf{G}\} \quad (36b)$

VI. RESULTS

6.1. Baseline Aeroelastic Stability Results

For the purpose of comparison and assessment, the baseline flutter stability results for a typical section as a binary aeroelastic system representing a cantilever Isogai Wing with low frequency aerodynamics following Done-Zwaan aeroelastic stability analysis

are exhibited in Figure 4. The favourable agreement validate the aeroelastic stability analysis algorithm used in developing the extended piezo-aeroelastic stability analysis.

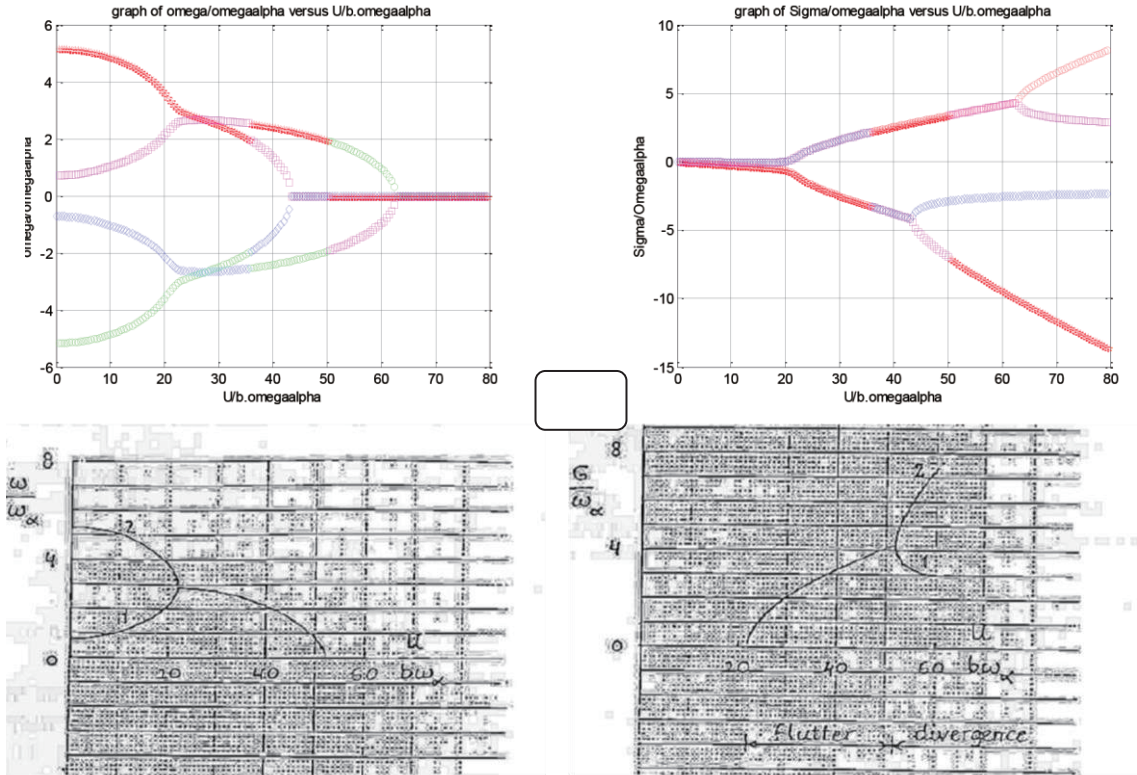
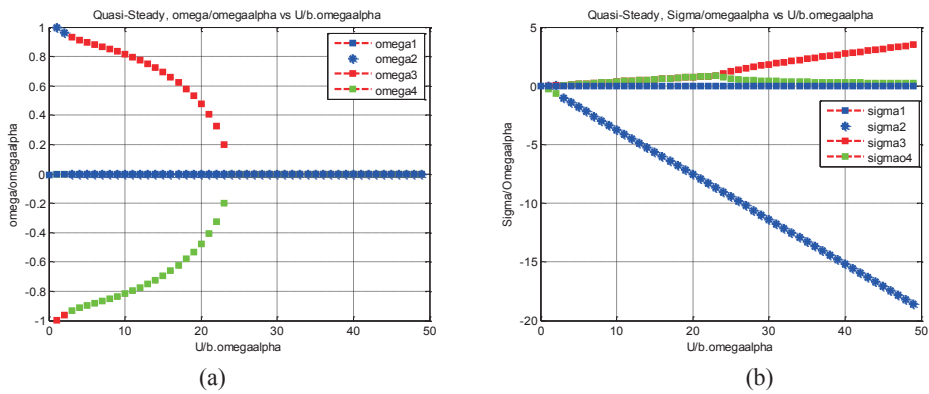


Figure 4: Upper-left: Frequency-Reduced Velocity Diagram for Low Frequency Aerodynamic Model. Upper-right: Damping-Reduced Velocity Diagram for Low Frequency Aerodynamic Model . Lower images: corresponding diagram reproduced from Zwaan (1990) for similar analysis.

The baseline flutter stability results for a typical section as a binary aeroelastic system representing a cantilever wing section utilizing quasi-steady aerodynamics following the aeroelastic stability algorithm. for a typical section as a binary aeroelastic system representing a cantilever wing section utilizing Theodorsen unsteady aerodynamics are reproduced in Fig.5. The data utilized in the present study is presented in Table 1.



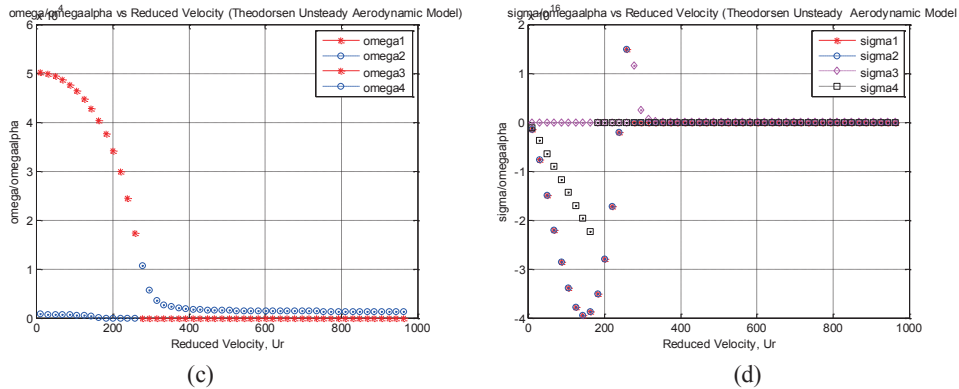


Figure 5: (a). Frequency-Reduced Velocity Diagram Low Frequency Aerodynamic Model; (b). Damping-Reduced Velocity Diagram Low Frequency Aerodynamic Model;; (c). Frequency-Reduced Velocity Diagram Theodorsen Unsteady Aerodynamic Model; (d) Damping-Reduced Velocity Diagram Theodorsen Unsteady Aerodynamic Model

Table 1: Cantilever Wing Section Parameters

Cantilever Wing Section Parameters		
Parameter	Magnitude	Information
s	7.5	m, semi-span
c	2.0	m
x_r	0.48c	$x=0$ at the leading edge
e	$(x_r-c/4)-1.0$	
a	$2x_r/c-1.0$	
b	c/2	m, Half-chord
th	0.12c	m, wing section thickness
I_θ	$(10 \times 2\pi)^2$	Nm/rad
x_α	b/2	m
Area	$\pi \times c \times th$	m ² , Wing Section cross-sectional area, approximated by an ellipse

Table 2: Piezoelectric Element and Cantilever Wing Section and Baseline Parameters

Piezoelectric Element and Cantilever Wing Section and Baseline Parameters			
Item	Magnitude	Unit	
D_{piezo}	1.0.	m/Volt	Reference values and will be followed by parametric study
R_{piezo}	1.0	Ohm	
C_{piezo}	1.0	Coulomb/Volt	
Beta	1.0	radian	the angular bending deflection of the cantilever beam for initialization, if required

Fig. 6 exhibits the Flutter stability diagram for the pure wing section treated as a binary system, solved using quartic root approach to solve the eigenvalues of equation (15) using steady aerodynamic approximation. The computation of the corresponding solutions using Theodorsen unsteady aerodynamics is in progress.

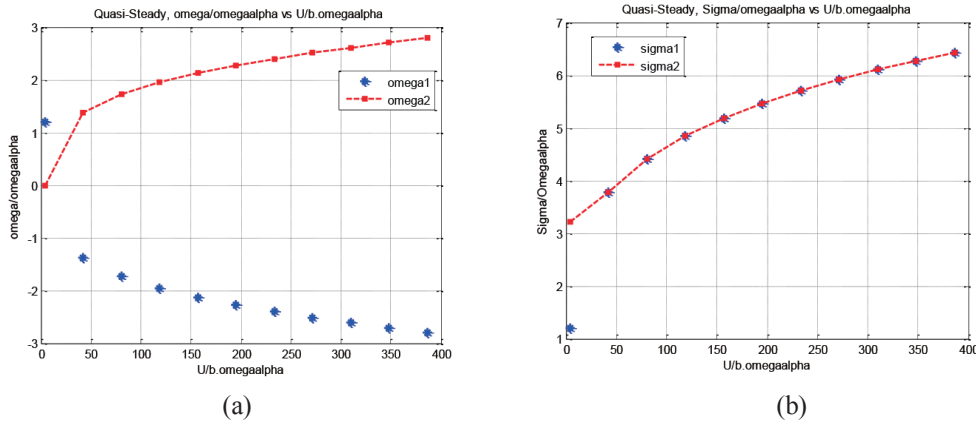


Figure 6: Aeroelastic Stability of the reference wing using Quartic Root approach; (a) Normalized frequency ω/ω_α versus normalized velocity; (b) Normalized damping σ/ω_α versus normalized velocity

6.2. Decoupled Linear Equations Approach for the Binary Aeroelasticity Based Piezo-Aeroelastic System for solving the System Output Voltage

The parameters utilized for the cantilevered wing section are those tabulated in Table 1. Table 2 tabulates the reference value of bending angle β of the cantilever wing section and various reference parameters for the piezoelectric element utilized in the piezo-aeroelastic system.

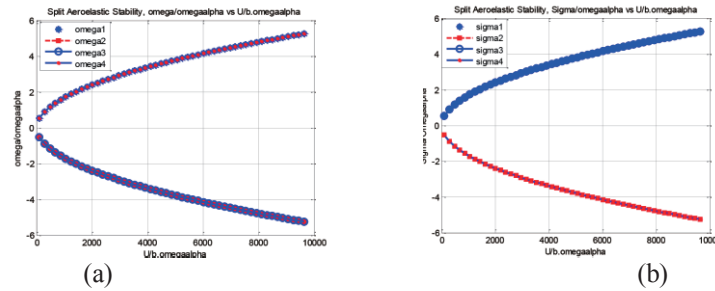


Figure 7: The resulting frequency and damping of the wing section represented as typical section as a function of the airflow velocity (represented by its normalized values $\omega U/b$); (a) Variation of the normalized frequency ω/ω_α versus normalized airflow velocity $\omega U/b$; (b) Variation of the normalized damping σ/ω_α versus normalized airflow velocity $\omega U/b$. Results are obtained for $\beta = 0.1$.

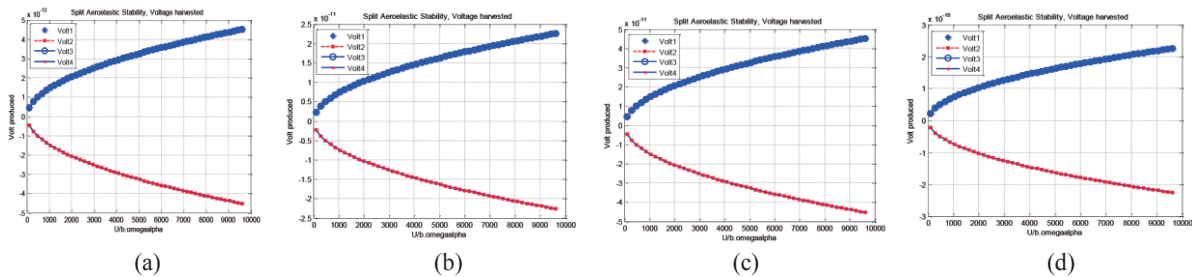


Figure 8: The output voltage produced by the piezoelectric element of the piezo-aeroelastic wing sectionsystem represented as typical section as a function of the airflow velocity (represented by its normalized values $\omega U/b$ and various values of β). (a) For $\beta = 0.1$. (b) For $\beta = 0.5$; (c) For $\beta = 1.0$; (d) For $\beta = 5.0$.

The resulting frequency and damping of the wing section represented as typical section as a function of the airflow velocity (represented by its normalized values $\omega U/b$) are shown in Fig. 7 (a) and (b). The corresponding voltage generated by the piezoelectric element for various values of the cantilever wing section bending angle β as functions of the airflow velocity are shown in the Fig. 8 (a) to (d).

VII. DISCUSSIONS AND CONCLUDING REMARKS

Following the simplified aeroelastic binary system based piezo-aerolastic energy harvester depicted in Fig. 3, the aeroelastic stability problem associated with the system using a baseline data has been formulated, elaborated and solved using various approaches. In addition, the baseline solutions obtained and presented in the figures are based on quasi-steady aerodynamics. The formulation and computation of the solution using more elaborate Theodorsen aerodynamics are in progress. The formulation of two fundamental solution approaches for the piezo-aerolastic energy harvester system have also been formulated, which incorporate systematic solution procedures using frequency domain binary aeroelastic based stability approach and time integration in the time domain using a conveniently chosen numerical integration method. Based on the simplest approach presented, the output voltage produced by the piezoelectric element for a defined piezo-aeroelastic system parameters can be predicted and have been obtained as presented in Figs. 7 and 8. These results can be used as the basis for assessment and further refinement of the method. Judging from the results, a more or less stable and consistent relationship between output voltage produced and airflow energy provided by the airflow on the piezo-aeroelastic binary based system has been indicated, using linearized approach and quasi-steady aerodynamics. However, based on the comparison of Figs.4 and 5, instability regions could be predicted using more refined unsteady aerodynamics. Further development is in progress.

References:

- [1]. Dubin Zhu, *Vibration Energy Harvesting: Machinery Vibration, Human Movement and Flow Induced Vibration*, U Southampton, Intechopen, 2011, <http://citeseerx.ist.psu.edu/>, accessed 20 February 2016.
- [2]. Antoine Ledoux, *Theory of Piezoelectric Materials and Their Applications in Civil Engineering*, 2011, Master of Engineering Thesis, MIT.
- [3]. Qing Xiao a, Qiang Zhu, A review on flow energy harvesters based on flapping foils, *Journal of Fluids and Structures* 46 (2014) 174–191
- [4]. Djojodihardjo, H., 2015, Analysis and Parametric Study of Aircraft Wings for Aeroelastic Stability and Flutter Characteristics, submitted for publication
- [5]. Djojodihardjo, H. and Yee, HH., Parametric Study of the Aeroelastic Stability and Flutter Characteristics Of Generic Aircraft Wings, *Proceedings, Aerotech II*, 2007, Kuala Lumpur
- [6]. Jan R. Wright and Jonathan E. Cooper, *Introduction to Aircraft Aeroelasticity and Loads*, John Wiley & Sons, 2007
- [7]. V C Sousa, M de M Anicezio, C De Marqui Jr and A Erturk, Enhanced aeroelastic energy harvesting by exploiting combined nonlinearities: theory and experiment , *Smart Mater. Struct.* **20** (2011) 094007 (8pp)
- [8]. Bisplinghoff, R.L., Ashley, H. and Halfman, R.L., 1955, *Aeroelasticity*, Addison & Wesley, 1955.
- [9]. Carlos De Marqui Jr and Alper Erturk, 2012, Electroaeroelastic analysis of airfoil based wind energy harvesting using piezoelectric transduction and electromagnetic induction, *Journal of Intelligent Material Systems and Structures*, 24(7) 846–854, © The Author(s) 2012.
- [10]. Bae, J.S., and Inman, D.J., “Aeroelastic Characteristics of Linear and Nonlinear Piezo-aeroelastic Energy Harvester,” *Journal of Intelligent Material System and Structures*, Vol. 25, Vol. 4, 2014, (4), pp. 401-416.

PIEZOELECTRIC ENERGY HARVESTING FROM AEROELASTIC VIBRATION WITH COMPOSITE PLATE WINGS

Masaki KAMEYAMA⁺¹ and Kanjuro MAKIHARA⁺²

⁺¹Department of Mechanical Systems Engineering, Shinshu University, Nagano, JAPAN

⁺²Department of Aerospace Engineering, Tohoku University, Sendai, JAPAN

The present paper treats the piezoelectric energy harvesting from aeroelastic vibration with cantilevered laminated plates. The aeroelastic flutter energy harvester is composed of a piezoelectric patch attached to the structures and a conventional harvesting circuit. A diode bridge of four diodes is connected to the piezoelectric patch and it provides a mechanism of current rectification. Aeroelastic analysis of composite plate wings with a piezoelectric patch is based on the finite element method and the subsonic unsteady lifting surface theory. The effect on location of piezoelectric patch on converged voltage in the harvesting system is examined through the numerical examples.

Keyword: Energy Harvesting, Subsonic Flutter, Piezoelectrics, Composite Materials

1. INTRODUCTION

Aeroelastic characteristics have played the significant role in structural design. Flutter is one of the representative dynamic phenomena of aeroelastic instability, which results in catastrophic destruction of structures. Although flutter is recognized as a harmful phenomenon from the viewpoint of structural integrity, it can be conversely utilized as profitable energy source for vibration-based energy harvesting. So far, a lot of research on energy harvesting from aeroelastic vibration has been carried out¹⁻¹⁰⁾.

The present paper treats the piezoelectric energy harvesting from aeroelastic vibration with cantilevered laminated plates. Aeroelastic analysis of composite plate wings with a piezoelectric patch is based on the finite element method and the subsonic unsteady lifting surface theory. The effect on location of piezoelectric patch on converged voltage in the harvesting system is examined through the numerical examples.

2. FUNDAMENTAL EQUATIONS¹¹⁾

The aeroelastic flutter energy harvester is composed of a piezoelectric patch attached to the structures and a harvesting circuit as shown in Fig. 1(a) and 1(b), respectively. A diode bridge of four diodes is connected to the piezoelectric patch and it provides a mechanism of current rectification. The finite element equations for aeroelastic response of cantilevered laminated plates with a piezoelectric patch can be described as follows¹²⁾:

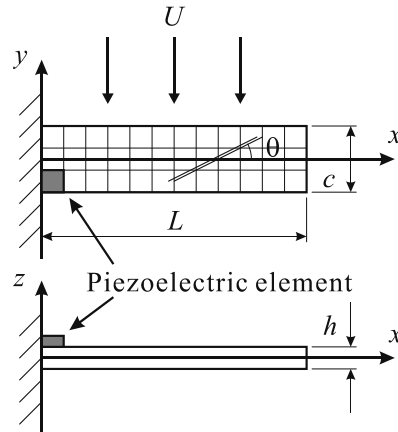
$$[M]\{\ddot{w}(t)\} + [C]\{\dot{w}(t)\} + [K]\{w(t)\} + \{\Theta\}V_p(t) = q[Q]\{w(t)\}, \quad (1)$$

$$-\{\Theta\}^T \{\dot{w}(t)\} + C_p \dot{V}_p(t) = -i(t), \quad (2)$$

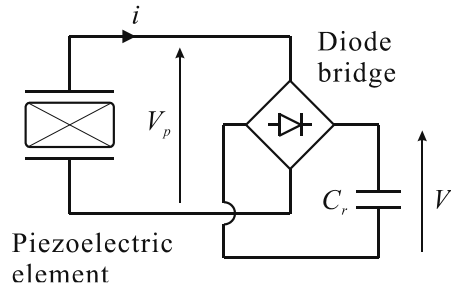
where the mass, damping and stiffness matrices are denoted by M , C and K , respectively, the nodal displacement vector is denoted by $w(t)$ and the dynamic pressure is denoted by q . The aerodynamic influence matrix is denoted by Q , which can be expressed by using the Mach number and the reduced frequency defined as

$$k = \frac{b\omega}{U}, \quad (3)$$

⁺¹kameyama@shinshu-u.ac.jp, ⁺²makihara@ssl.mech.tohoku.ac.jp



(a) Cantilevered laminated plates ($L = 360$ mm, $c = 2b = 90$ mm, $h = 1$ mm).



(b) Conventional harvesting circuit.

Figure 1: Schematic of aeroelastic flutter energy harvester.

where the semi-chord length at the wing root, angular frequency and free stream velocity are denoted by b ($= c/2$), ω and U , respectively. In this research, the aerodynamic influence matrix Q , which represents the unsteady aerodynamic forces acting on the vibratory wing surface in subsonic flow, is evaluated based on the doublet point method¹³⁾.

Amplitudes of pressure distributions on oscillatory lifting surfaces, and of their upwash velocity are related by integral equation as follows:

$$\bar{w}(x_u, y_u) = \frac{1}{8\pi} \iint_S \Delta p(\xi_d, \eta_d) Ke(x_u - \xi_d, y_u - \eta_d) d\xi_d d\eta_d, \quad (4)$$

where the non-dimensional amplitudes of upwash velocity and pressure differential is denoted by \bar{w} and Δp , respectively. The kernel function is denoted by Ke . A doublet point, where the acceleration potential is placed, is located at (ξ_d, η_d) . An upwash point, where the normal velocity of the upwash is placed, is located at (x_u, y_u) . The lifting surface is assumed to lie in the plane $z = 0$. The symbol S denotes the region of the wing area. The wing planform is divided into panel segments called element surfaces and each element surface is constructed such that the two side edges are parallel to the free stream. A doublet point and an upwash point are located on each element surface. Then the above integral equation is discretized into linear algebraic equations and the aerodynamic influence matrix Q can be evaluated.

As the doublet points of aerodynamic elements are different from the structural nodal points, it is necessary to convert the aerodynamic loading acting on the doublet points of aerodynamic element to the nodal forces of finite element. This interpolation was performed by the surface spline method¹⁴⁾.

Besides, the effective piezoelectric coefficient vector and capacitance are denoted by Θ and C_p , the voltage across the piezoelectric patch is denoted by $V_p(t)$ and the current flowing into a harvesting circuit is denoted by $i(t)$, which is related to the rectified voltage $V_c(t)$ by

$$i(t) = \begin{cases} C_r \dot{V}_c & \text{if } V_p = V_c \\ -C_r \dot{V}_c & \text{if } V_p = -V_c \\ 0 & \text{if } |V_p| < V_c \end{cases}, \quad (5)$$

where the storage capacitance is denoted by C_r .

When a modal approach is introduced, the following equation can be obtained by the modal transformation ($w = \Phi w_m$) for Eqs. 1 and 2:

$$[I]\{\ddot{w}_m(t)\} + [C_m]\{\dot{w}_m(t)\} + [\Omega]\{w_m(t)\} + [\Phi]^T \{\Theta\} V_p(t) = q [Q_m]\{w_m(t)\}, \quad (6)$$

$$-\{\Theta\}^T [\Phi]\{\dot{w}_m(t)\} + C_p \dot{V}_p(t) = -i(t), \quad (7)$$

$$[Q_m] = [\Phi]^T [Q] [\Phi], \quad (8)$$

where the matrix with free-vibration eigenvalues on the diagonal and the corresponding modal matrix are denoted by Ω and Φ , respectively, and modal damping matrix is denoted by C_m . The identity matrix is denoted by I .

It is necessary to transform the equations of motion into the linear time-invariant (abbreviated to LTI) state-space form for the piezoaeroelastic analysis, and the unsteady aerodynamic forces should be approximated in terms of rational functions of Laplace variable. In this research, the minimum state method¹⁵⁾ combined with optimization technique is adopted for the rational function approximation. The minimum state method approximates the aerodynamic influence matrix by

$$[\bar{Q}_m(\bar{s})] = [Q_0] + [Q_1]\bar{s} + [Q_2]\bar{s}^2 + [D](\bar{s}[I] - [R])^{-1}[E]\bar{s}, \quad (9)$$

where the non-dimensional Laplace variable ($= sb/U$) is denoted by \bar{s} , semi-chord length at the wing root, free stream velocity and the Laplace variable are denoted by b , U and s , respectively. Physically, Q_0 , Q_1 and Q_2 capture the dependence of the unsteady aerodynamics on displacement, velocity and acceleration, respectively. The last term in the right hand side of Eq. 9 captures the lag in the construction of aerodynamic forces associated with the circulatory effects. Here the coefficient matrices Q_0 , Q_1 , Q_2 , D , R and E are unknown. The components of diagonal matrix R are negative constants that are selected arbitrarily. For a given R matrix, the other unknown coefficient matrices are determined by using iterative, nonlinear least-square method. Then the minimization problem of the overall least-square errors for the rational function approximation of the aerodynamic influence matrix can be stated as follows:

$$[\text{objective}] \quad \min \sum_{i,j} \sqrt{\sum_{l=1}^{nk} \left\{ \frac{|Q_{m,ij}(ik_l) - \bar{Q}_{m,ij}(ik_l)|}{\max(\max_l(|Q_{m,ij}(ik_l)|), 1)} \right\}^2}, \quad (10a)$$

$$[\text{constraints}] \quad r_{ir} < 0 \quad (ir = 1, \dots, nr), \quad (10b)$$

$$[\text{design variables}] \quad r_{ir} \quad (ir = 1, \dots, nr), \quad (10c)$$

where a tabulated reduced frequency is denoted by k_l ($l = 1, \dots, nk$), tabular and approximate values of the aerodynamic influence coefficient at a specified value of reduced frequency are denoted by $Q_{m,ij}$ and $\bar{Q}_{m,ij}$,

respectively, and a diagonal component of the matrix R is denoted by r_{ir} . As an optimizer, the DFP (Davidon-Fletcher-Powell) variable metric method is adopted with the golden section method in the ADS (Automated Design Synthesis) program¹⁶.

The substitution of Eq. 9 into Eq. 6 yields

$$\begin{aligned} & ([I]s^2 + [C_m]s + [\Omega])\{w_m(t)\} + [\Phi]^T \{\Theta\}V_p(t) = q([Q_0] + (b/U)[Q_1]s + (b/U)^2[Q_2]s^2 \\ & + [D](\bar{s}[I] - (U/b)[R])^{-1}[E]s)\{w_m(t)\} \end{aligned} \quad (11)$$

Then the following state-space equations can be obtained from Eqs. 11 and 7:

$$\{\dot{x}\} = [A_s]\{x\}, \quad (12)$$

$$\{x\} = \left\{ \{w_m\}^T, \{\dot{w}_m\}^T, \{p\}^T, \{V_p\}^T \right\}^T, \quad (13)$$

$$[A_s] = \begin{bmatrix} 0 & [I] & 0 & 0 \\ -[\bar{M}]^{-1}[\bar{K}] & -[\bar{M}]^{-1}[\bar{C}] & q[\bar{M}]^{-1}[D] & -[\bar{M}]^{-1}[\Phi]^T\{\Theta\} \\ 0 & [E] & (U/b)[R] & 0 \\ 0 & (1/C')\{\Theta\}^T[\Phi] & 0 & 0 \end{bmatrix}, \quad (14)$$

$$[\bar{M}] = [I] - q(b/U)^2[Q_2], \quad (15)$$

$$[\bar{C}] = [C_m] - q(b/U)[Q_1], \quad (16)$$

$$[\bar{K}] = [\Omega] - q[Q_0], \quad (17)$$

$$C' = \begin{cases} C_p + C_r & \text{if } V_p = V_c \\ C_p - C_r & \text{if } V_p = -V_c \\ C_p & \text{if } |V_p| < V_c \end{cases}, \quad (18)$$

where the system matrix is denoted by A_s . The state vector is denoted by x , which consists of the modal displacements w_m , modal velocities \dot{w}_m , the augmented aerodynamic states p and voltage across the piezoelectric patch is denoted by V_p .

3. NUMERICAL RESULTS AND DISCUSSION

(1) Numerical model

In this research, aeroelastic flutter energy harvesting with a $[0_3/90]_s$ cantilevered laminated plate is examined. Cantilevered laminated plates with a piezoelectric element shown in Fig. 1 are employed, where a ply fiber angle is denoted by θ . Lead zirconate titanate (PZT) element is placed on the top surface of the plate. The material properties of lamina of carbon/epoxy composite and PZT element are shown in Tabs. 1 and 2. Here the in-plane stiffness and piezoelectric characteristics of piezoelectric material is assumed to be isotropic in this research. The four-node rectangular plate-bending element is employed in the present structural analysis based on the classical laminated plate theory, and 12×3 elements are used for the structural analysis. The sizes of PZT element are the same as that of a finite element in the structural analysis. On the other side, 8×6 elements are used for the aerodynamic analysis. The aerodynamic influence matrices are tabulated at 10 values of reduced frequency of 0.1, 0.111, 0.125, 0.143, 0.167, 0.2, 0.25, 0.333, 0.5 and 1, and the number of poles of transfer function r_{ir} is set to be 10. After the vibration analysis, a modal reduction is performed using

the lowest 10 modes to solve Eqs. 6 and 7, and then the Runge-Kutta method of the fourth order is adopted to integrate the state-space equations described as Eq. 12. Here the damping of the structure is neglected and the storage capacitor has a capacitance of 1.0 μF in this research.

(2) Results and discussion

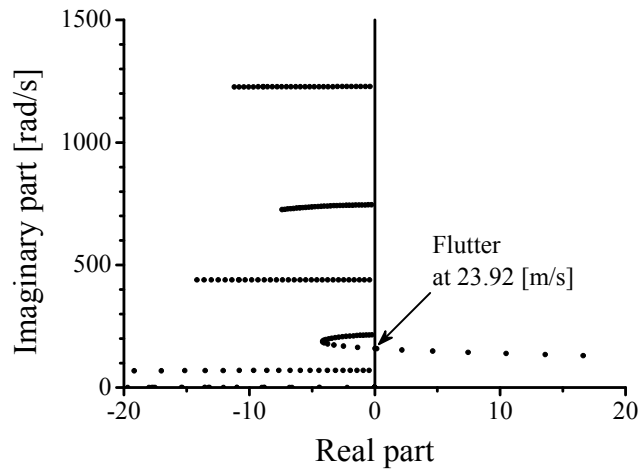
Fig. 2 shows the aeroelastic characteristics of $[0_3/90]_s$ cantilevered laminated plates without piezoelectric patches. Figs. 2(a) and 2(b) correspond to the root loci with increasing free stream velocity and the flutter mode shape, respectively. It is found that the bending-torsional flutter due to coupling between the second and the first modes, which correspond to the first torsional and the first bending vibration modes, occurs at the speed $U = 23.92$ m/s.

Table 1: Material properties of CFRP.

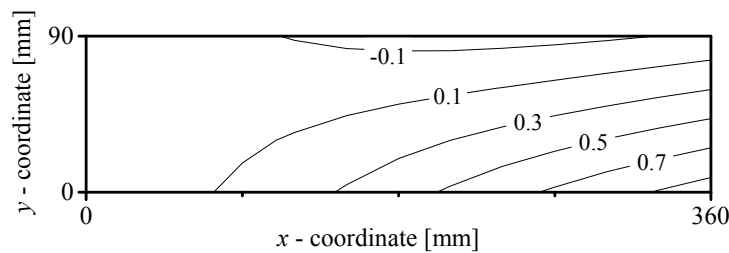
E_{11} [GPa]	E_{22} [GPa]	G_{12} [GPa]	ν_{12}	ρ [kg/m ³]	Thickness [mm]
127.0	11.0	4.90	0.30	1541	0.125

Table 2: Material properties of PZT.

d_{31} [pm/V]	C_p [nF]	E [GPa]	ν	ρ [kg/m ³]	Thickness [mm]
-240	74.3	63.0	0.30	7800	0.25

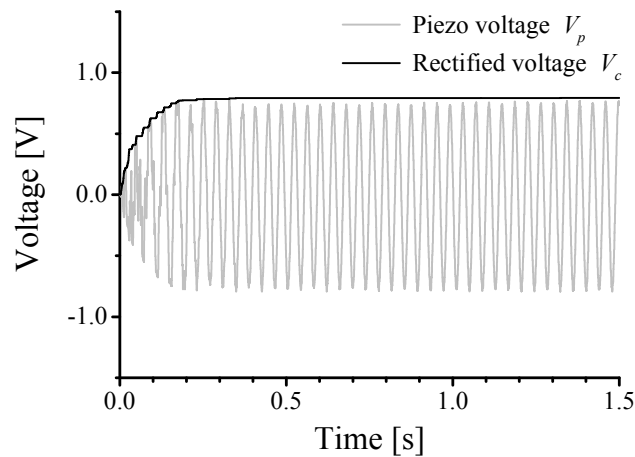


(a) Root loci with increasing free stream velocity.

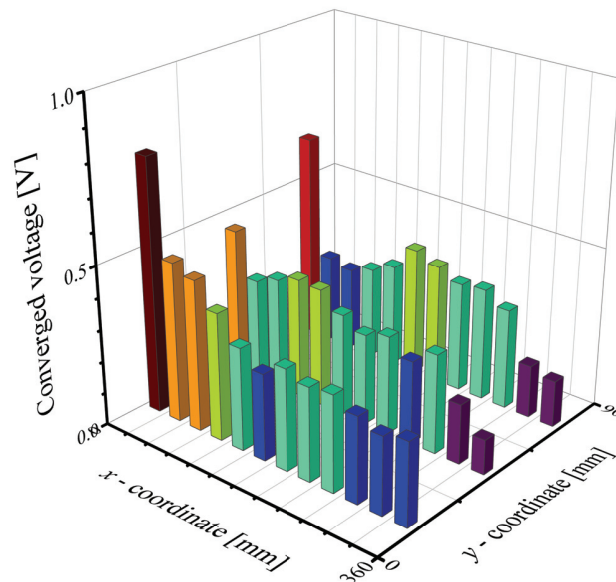


(b) Flutter mode shape.

Figure 2: Flutter characteristics.



(a) Time histories of piezoelectric voltage and rectified voltage ($U = U_F = 24.56$ m/s).



(b) Effect of location of piezoelectric patch on converged voltage in harvesting system.

Figure 3: Results of energy harvesting at flutter speed.

Fig. 3 shows the results of energy harvesting at the flutter speed $U = U_F$. Here the vibration of the plate is induced by sudden release of 1 mm initial deflection of the leading edge of the wing tip. Time histories of piezoelectric voltage and rectified voltage are shown in Fig. 3(a). As the aeroelastic vibration continued, the piezoelectric voltage and rectified voltage increased. Then the energy harvesting system reached a steady state and rectified voltage converged. Fig. 3(b) shows the effect of location of piezoelectric patch on converged voltage in the harvesting system, which corresponds to the flutter curvature mode shape. Fig. 4 shows the absolute values of a sum of plate bending curvature at the center of each finite element, which is obtained from Fig. 2(b). It is indicated that the optimal location of piezoelectric patch for energy harvesting can be determined based on the flutter curvature mode shape, by comparing with Fig. 3(b).

The effect of change of the operating condition on the result of energy harvesting is examined. Fig. 5 shows the effect of location of piezoelectric patch on converged voltage in the harvesting system at the speed $U = 0.9U_F$. It is found by comparing with Fig. 3(b) that the effect of location of piezoelectric patch on converged voltage is qualitatively same, although it becomes lower than that at the flutter speed $U = U_F$.

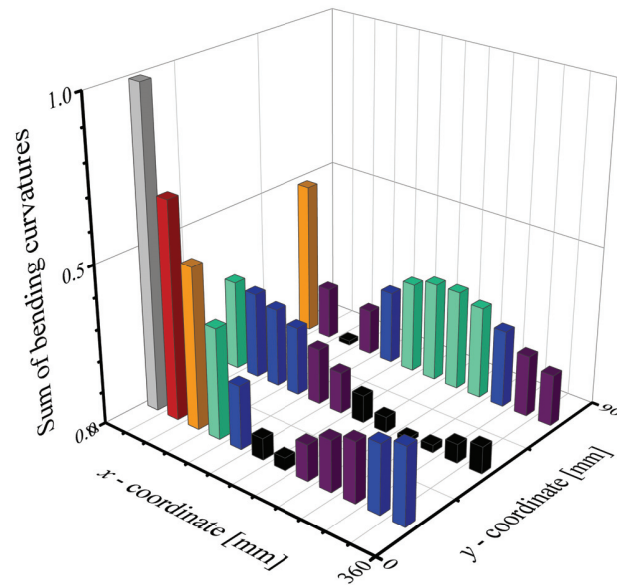


Figure 4: Absolute values of sum of plate bending curvatures.

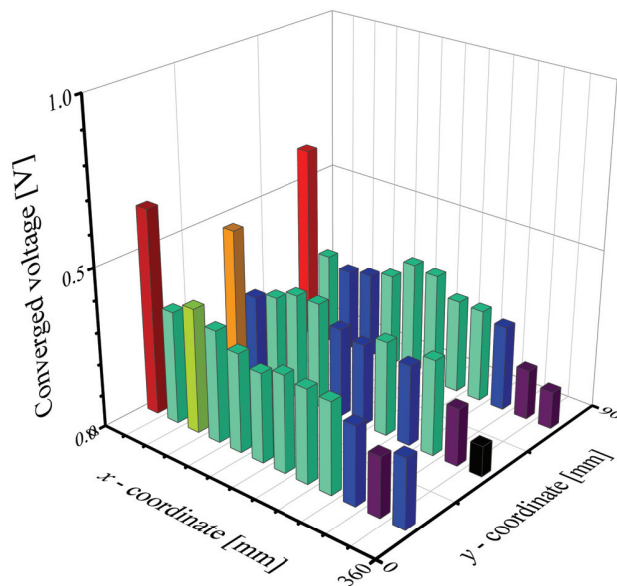


Figure 5: Effect of location of piezoelectric patch on converged voltage in harvesting system ($U = 0.9 U_F$).

4. CONCLUSIONS

The present paper treats the piezoelectric energy harvesting from aeroelastic vibration with cantilevered laminated plates. It is indicated through the numerical examples that the optimal location of piezoelectric patch for energy harvesting can be determined based on the flutter curvature mode shape of the plate.

ACKNOWLEDGMENT

The author would like to thank Mr. I. Nakagawa and Mr. N. Kasahara, Department of Mechanical Systems Engineering, Shinshu University, for his support in the numerical simulation.

REFERENCES

- 1) De Marqui, C., Jr, Erturk, A. and Inman, D. J. : Piezoaeroelastic modeling and analysis of a generator wing with continuous and segmented electrodes, *J. Intell. Mater. Syst. Struct.*, Vol. 21, No. 10, pp. 983-993, 2010.
- 2) De Marqui, C., Jr, Vieira, W. G. R., Erturk, A. and Inman, D. J. : Modeling and analysis piezoelectric energy harvesting from aeroelastic vibrations using the doublet-lattice method, *J. Vib. Acoust.*, Vol. 133, No. 1, pp. 011003-1 - 011003-9, 2011.
- 3) Bryant, M. and Garcia, E. : Modeling and testing of a novel aeroelastic flutter energy harvester, *J. Vib. Acoust.*, Vol. 133, No. 1, pp. 011010-1 - 011010-11, 2011.
- 4) Dunnmon, J. A., Stanton, S. C., Mann, B. P. and Dowell, E. H. : Power extraction from aeroelastic limit cycle oscillations, *J. Fluids Struct.*, Vol. 27, No. 8, pp. 1182-1198, 2011.
- 5) Abdelkefi, A., Nayfeh, A. H. and Hajj, M. R. : Modeling and analysis of piezoelectric energy harvesters, *Nonlinear Dyn.*, Vol. 67, No. 2, pp. 925-939, 2012.
- 6) Hosking, N. S. and Sotoudeh, Z. : Energy harvesting from aeroelastic instabilities, AIAA-2016-0210, pp. 1-16, 2016.
- 7) Makihara, K. and Shimose, S. : Supersonic flutter utilization for effective energy-harvesting based on piezoelectric switching control, *Smart Mater. Res.*, Vol. 2012, pp. 181645-1 - 181645-10, 2012.
- 8) Isogai, K., Yamasaki, M. and Asaoka, T. : Application of CFD to design study of flutter-power-generation, NAL SP-57, pp. 106-111, 2003 (in Japanese).
- 9) Abiru, H. and Yoshitake, A. : Study on a flapping wing hydroelectric power generation system, *Trans. Jpn. Soc. Mech. Eng. (Ser. B)*, Vol. 75, No. 758, pp. 2036-2041, 2009 (in Japanese).
- 10) Yan, Z. and Abdelkefi, A. : Nonlinear characterization of concurrent energy harvesting from galloping and base excitations, *Nonlinear Dyn.*, Vol. 77, No. 4, pp. 1171-1189, 2014.
- 11) Kameyama, M. : An efficient design approach for aeroelastic tailoring and control of composite plate wings, Ph. D. Thesis, 2006.
- 12) Shu, Y. C. and Lien, I. C. : Analysis of power output for piezoelectric energy harvesting systems, *Smart Mater. Struct.*, Vol. 15, No. 6, pp. 1499-1512, 2006.
- 13) Ueda, T. and Dowell, E. H. : A new solution method for lifting surfaces in subsonic flow, *AIAA J.*, Vol. 20, No. 3, pp. 348-355, 1982.
- 14) Harder, R. H. and Desmarais, R. N. : Interpolation using surface spline, *J. Aircr.*, Vol. 9, No. 2, pp. 189-191, 1972.
- 15) Karpel, M. : Time-domain aeroservoelastic modeling using weighted unsteady aerodynamic forces, *J. Guid. Control Dyn.*, Vol. 13, No. 1, pp. 30-37, 1990.
- 16) Vanderplaats, G. N. and Sugimoto, H. : A general-purpose optimization program for engineering design, *Comput. Struct.*, Vol. 24, No. 1, pp. 13-21, 1986.

PENDULUM WITH HOOP-TYPE FLOW ENERGY CONVERTER SYSTEM

Yutaka Terao
Tokai University, Shizuoka, Japan

A new hoop-type energy conversion system installed in a pendulum-type device is proposed and tested. The rolling cylinder is used VIM phenomena and rotating hoop comprise the double pendulum system and these systems exhibit chaos in some cases. An equation of pendulum–hoop motion was developed to provide numerical solutions when the onset of chaos occurs.

Keywords: Hoop generator, Vortex-induced motion (VIM), Chaos, Flow energy harvesting

1. INTRODUCTION

Energy harvesting is an important and necessary process for determining how to utilize natural energy resources. This paper discusses a new energy absorption system that takes advantage of flow energy. [The speed of the flow is relatively low but has not yet been fully utilized. The relatively slow flow energy absorption means that the extraction and conversion of energy from thin density energy distribution is difficult. One advanced and elegant energy harvesting device is the VIVACE converter proposed by the University of Michigan in the USA. Using the vortex-induced motion (VIM) of a cylinder, the VIVACE converter has high performance even in a fluid flow, and most importantly, the mechanism of this system is simple. The cylinder in the VIVACE converter produces a large parallel motion and is connected to a generator, and electric power is then generated from the oscillating motion of the cylinder. In contrast, Japanese researchers proposed another device utilizing vortex-induced vibration (VIV), hereafter referred to as the pendulum-type generator. This device consists of a floater cylinder pendulum connected to a pin joint, as shown in Figure 1, and the cylinder moves with a swinging roll motion in the fluid flow. The pendulum-type generator showed higher performance than the VIVACE converter.

This paper discusses a newly developed hoop-type generator system installed on a swinging cylinder, similar to that shown in Fig 2. The purpose of this system is to improve the generating performance of the pendulum-type generator. Our system comprises a double pendulum; one pendulum is an oscillating cylinder, and the other is a hoop with unbalanced mass. In this case, it is expected that the rotational motion of the hoop will be chaotic. Because the large amplitudes of the motions of the hoop angle and pendulum easily cause nonlinear oscillation and a nonlinear restoring force, the gravitational force component may lead to the onset of chaos, which makes describing the system much more complex.

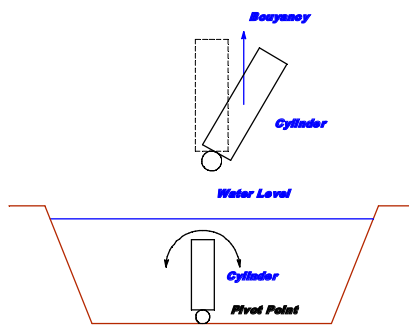


Figure 1. Schematic of pendulum-type generator¹⁾.

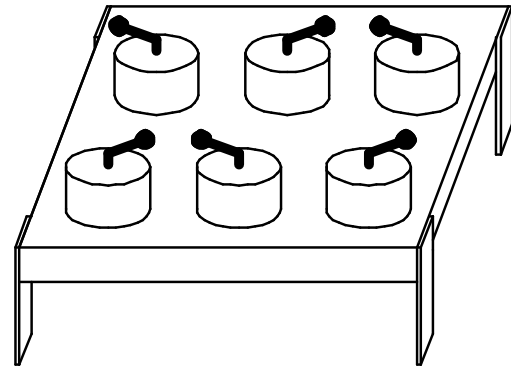


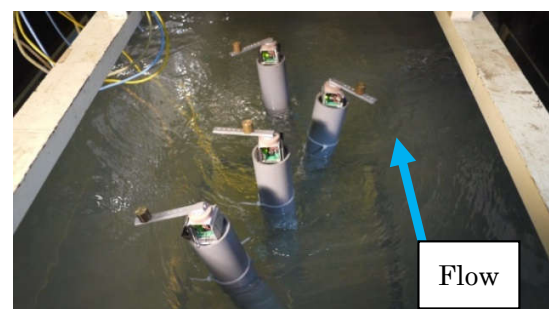
Figure 2. Hula-hoop energy absorber³⁾.

2. WATER TANK TEST

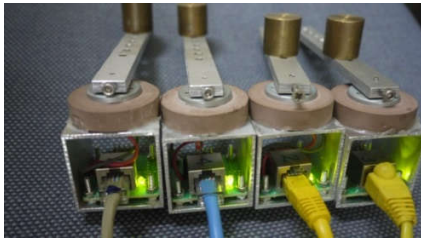
A circular water tank test was conducted with polyvinyl chloride cylinders of a small diameter to confirm the VIM phenomenon. The test setup is shown in Photographs 1 and 2. The cylinder pivot point is set 500 mm under the free surface. The hoop system was set on the top of the cylinder. Four sets of hoop generators and measurement equipment were prepared as shown in Photograph 3. The electric power generated by the hoop generator and the roll angle sensor of the cylinder were included in the devices. Data were obtained via a local area network (LAN) cable. The measured 8-channel (8CH) signal was amplified by operation amplifiers, and the offset was simultaneously adjusted. Photograph 4 shows the newly developed data logger system, which uses the single-chip microcontroller PIC18F2553. A 12-bit analog-to-digital (A/D) converter output an 8CH signal every 20-Hz sampling period, and these output signals were downloaded to a PC through RS-232C communication and a USB converter.



Photograph 1. Cylinder model test setup.



Photograph 2. Test setup with model in circular water channel.



Photograph 3. Hoop generator and sensor. The amplified generator and gravitational acceleration outputs were transmitted via a LAN cable.



Photograph 4. Newly developed PIC18F2523-based data logger system. This system can achieve 8CH 12-bit A/D conversion at a sampling rate of 20 Hz. Measured data are transmitted to a PC via RS232C communication.

Table 1. Test conditions

Weight length [mm]	Velocity [m/s]	Flow angle [deg.]	Cylinder gap [mm]
100	0.25	0°	100
80	0.3	30°	
60	0.35		
40			
without			

Table 2. Generated power

Flow angle 0°		Flow angle 30°	
Vel.[m/s]	Mean[mw]	Vel.[m/s]	Mean[mw]
0.25	0.92	0.25	0.93
0.3	1.16	0.3	1.69
0.35	1.76	0.35	2.02

(Diameter 76mmcylinder)

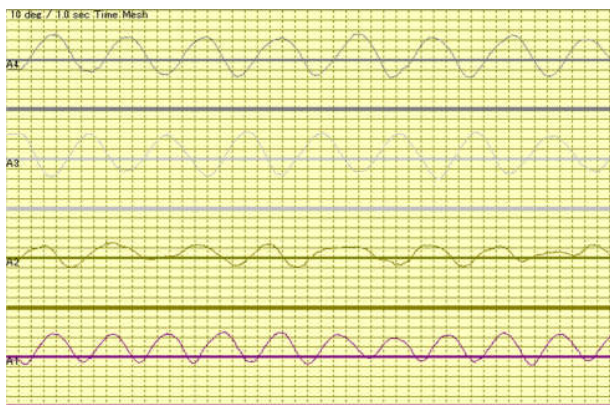


Figure 3. Sample of rolling motion records (horizontal mesh spacing: 10°).



Figure 4. Sample of measured generated power records (horizontal mesh spacing: 0.01 W).

Table 1 lists the experimental conditions of the water tank test, in which two flow attack angles, 0° and 30°, were tested. Figs. 3 and 4 show the rolling motion and measured generated power of each cylinder, respectively, with a flow attack angle of 30°, a tank flow speed of 0.3 m/s, and no weight.

In this system, steady hoop motion and a high energy gain were expected, but the motion of the hoop in the experiment was oscillatory. Table 2 gives the measured generated power, which was rather low because of the oscillatory motion of the hoop. Fig.4 shows that the frequency of the generated energy was higher than that of the hoop motion. This is because the hoop motion is not cyclic but oscillatory.

In this system, the hoop motion should be steady and cyclic, and the generated energy should be higher. To know the hoop motion under many different conditions, an equation of the hoop motion was constructed, as discussed in Section 3. Numerical analysis was then performed, as described in Section 4, allowing the optimal hoop control method and conditions to be found.

3. EQUATION OF HOOP MOTION

The variables describing the hoop weight motion and the coordinate axes used in this study are shown in Fig. 5 and 6.

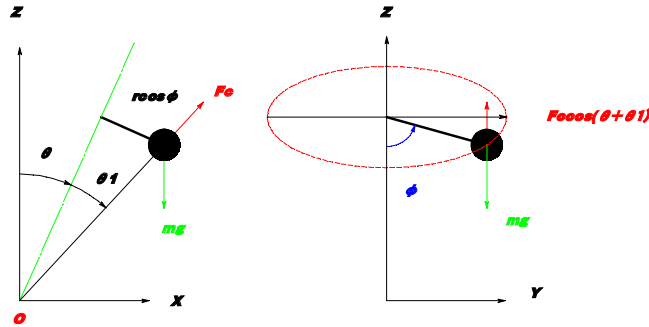


Figure 5. Definition of axes and forces acting on weight. Figure 6. Circular motion of weight.

The y-axis is the roll axis.

The equation of motion for the weight shown in Fig.5 and 6 is given as

$$mr\ddot{\varphi} + cr\dot{\varphi} + \sin\varphi(mg\sin\theta + F_c\sin\theta) = 0 \quad (1)$$

The apparent centrifugal force F_c is defined as

$$F_c = \frac{mv^2}{R_1} = \frac{m(R_1\dot{\varphi})^2}{R_1} = mR_1\dot{\varphi}^2 \quad (2)$$

The geometrical constraint on the angles is

$$\sin\theta_1 = \frac{r_1}{R_1} = \frac{rcos\varphi}{R_1} \quad (3)$$

By substituting equations (2) and (3) into equation (1), the equation of motion can be transformed into

$$mr\ddot{\varphi} + cr\dot{\varphi} + m\sin\varphi(g\sin\theta + r\dot{\theta}^2\cos\varphi) = 0 \quad (4)$$

In this way, R_1 has been eliminated from all terms. Equation (4) can be simplified by making the angular acceleration coefficient equal 1, as

$$\ddot{\varphi} + \frac{c}{m}\dot{\varphi} + \sin\varphi\left(\frac{g}{r}\sin\theta + \dot{\theta}^2\cos\varphi\right) = 0 \quad (5)$$

The solution to equation (5) describes the motion of the system. However, the more common form of the equation of motion includes the term describing the excitation force on the right-hand side of the equation, as

$$\ddot{\varphi} + \frac{c}{m} \dot{\varphi} + \sin\varphi \frac{g}{r} \sin\theta = -\dot{\theta}^2 \cos\varphi \sin\varphi \quad (6)$$

Defining $C = c/m$, $K = (g/r)\sin\theta$, and $F_\theta = -\dot{\theta}^2 \cos\varphi \sin\varphi$ yields

$$\ddot{\varphi} + c\dot{\varphi} + K\sin\varphi = F_\theta \quad (7)$$

The obtained equation of motion for the hoop describes nonlinear large-amplitude pendulum motion, and the difficulty of solving it mainly arises from the strong nonlinear external force. Based on this equation of motion, it is possible that the hoop motion will be chaotic. This equation was solved using the numerical Newmark-beta method under the steady constant-amplitude rolling motion of the cylinder. An analysis program was developed in Visual Basic 2010, including a graphical user interface (GUI) to allow the visualization of the hoop motion and generated power.

4 .NUMERICAL ANALYSIS

The numerical analysis conducted in this study considered a simple oscillating sinusoidal form for the external force, which yielded various types of oscillatory hoop motions, as shown in Figs. 7–10. The phase plane diagrams of the hoop motion in Figs. 7–10 are shown in Figs. 11–14, respectively. The motion shown in Fig.7 demonstrated steady and continuous hoop rotation, which is divergent hoop motion. This case had the highest energy generation. This phase of the hoop motion has the divergent tendency, as shown in Fig.11, and represents the chaotic motion. The hoop motion shown in Fig.7 appears to be a steady rotating motion. If the damping force is increased while maintaining steady rotation, the energy absorption from the system increases.

Figs 11–14 show the phase plane diagrams of the hoop motion shown in Figs 7–10, respectively. Fig. 11 shows the chaos divergent condition and corresponds to Fig.7. In Fig.12, which corresponds to Fig.8, a stable trajectory was not found. Conversely, Figs 13 and 14, which correspond to Figs 9 and 10, respectively, show hoop motions that appear to have achieved steady oscillation. In this motion, the phase trajectory stabilized after some oscillation; this type of stability is called Lyapunov stability.

In Table 3, the numerical results of the phase analysis are classified based on the calculation conditions and shows the chaos zone. If the forced oscillation period increases, double-period hoop motion first appears. Further increasing the forced oscillation period causes the chaos divergence zone to appear. Increasing the period beyond this zone destabilizes the hoop motion and causes constant stable oscillation to appear.



Figure 7. Sample of a diverging motion appeared in the hoop weight roll angle. The roll angle is shown from $-\pi$ to π .



Figure 8. Sample of unstable hoop motion. Calculation result is shown in the log period.



Figure 9. Sample of stable motion.



Figure 10. Sample of stable double period motion.



Figure 11. Phase plane diagram for motion shown in Figure 7.

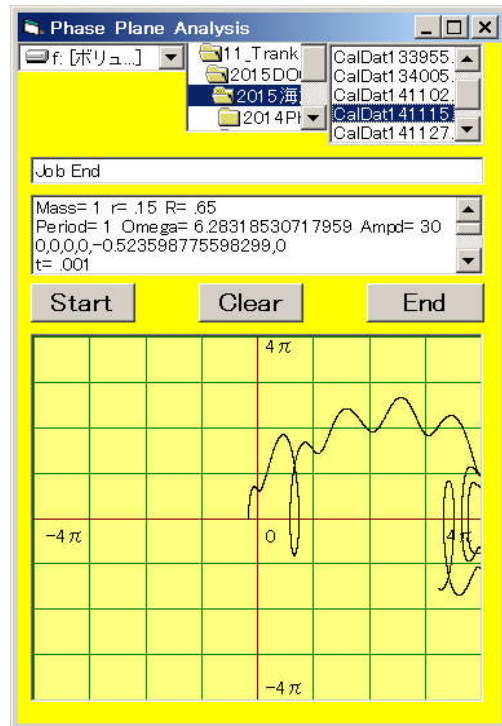


Figure 12. Phase plane diagram for motion shown in Figure 8.

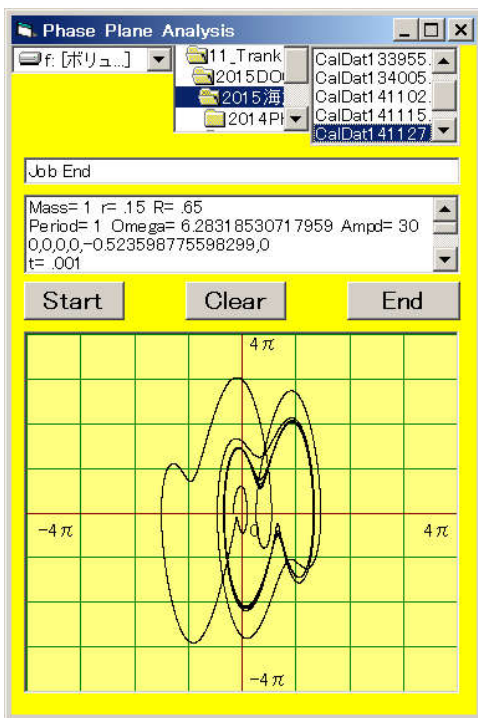


Figure 13. Phase plane diagram for motion shown in Figure 9.

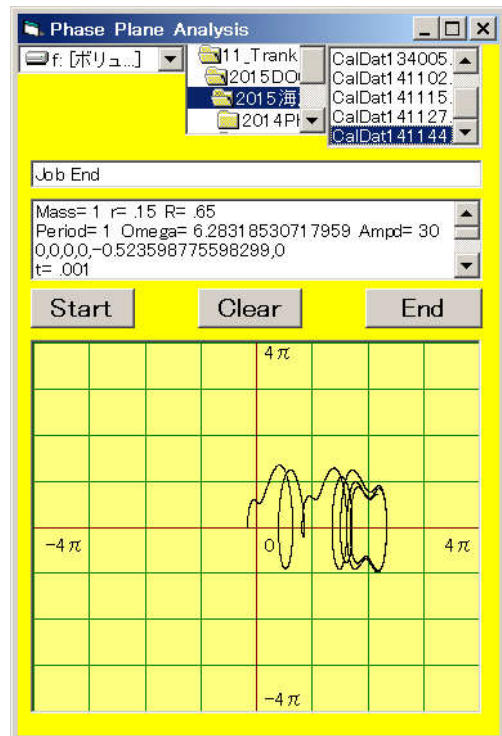


Figure 14. Phase plane diagram for motion shown in Figure 10.

Table 3. Categories of calculated double pendulum hoop motion.

Applitude		10 dg.									
Period(sec)		1		1.5	1.6	1.7		3	4	5	
Motion		Without motion	Stable double period	Unstable	Stable diverging			Unstable	Stable		

Applitude		20 deg.									
Period(sec)		0.9	1	1.05	1.5	1.7	2	2.6	3	4	
Motion		Without motion	Stable double period	Unstable	Stable diverging		Unstable		Stable		

Applitude		30 deg.									
Period(sec)		0.7	0.8	0.9	1	1.05	1.5	1.7	2	2.6	3
Motion		Without motion	Unstable		Stable diverging		Unstable			Stable	

5.EFFICIENCY OF GENERATED POWER

The following two patterns, θ_1 $\theta_{2,2}$ are considered:

$$\theta_1 = \theta_a \sin \omega t \tag{8}$$

$$\theta_2 = \theta_b \sin \omega t + n \omega t \tag{9}$$

where θ is the hoop angle and the subscripts 1 and 2 indicate sinusoidal and hoop-type pendulum motion, respectively. Equation (9) describes simple chaotic hoop-type motion. The angular velocities are given by

$$\dot{\theta}_1 = \theta_a \omega \cos \omega t \tag{10}$$

$$\dot{\theta}_2 = \theta_b \omega \cos \omega t + n t \tag{11}$$

The generated voltage is proportional to these angular velocities, as

$$V_1 = C \theta_a \omega \cos \omega t \tag{12}$$

$$V_2 = C (\theta_b \omega \cos \omega t + n t) \tag{13}$$

and the electric power W is defined as

$$W = \frac{V^2}{R} \tag{14}$$

The power averaged over one period is

$$E = \frac{1}{T} \int_0^T W dt \tag{15}$$

If we assume that the amplitudes of the angular velocities are the same, i.e.,

$$\theta_a = \theta_b \tag{16}$$

then the energies generated by the pendulum-type and chaotic motions are given respectively by

$$E_1 = \frac{1}{2} (C \theta_a \omega)^2 \tag{17}$$

$$E_2 = \frac{1}{2} (C \theta_a \omega)^2 + (C n \omega)^2 \tag{18}$$

Equations (17) and (18) can be used to find the absorption energy difference ΔE caused by the difference between the two types of motion, as

$$\Delta E \equiv E_2 - E_1 \quad (19)$$

$$= (Cn\omega)^2 > 0 \quad (20)$$

where C is the damping coefficient, n is the rotation number, and ω is the steady rotation frequency at the divergence point. Equation (20) demonstrates how energy absorption can be increased. Increasing the damping coefficient increases the absorption energy until the motion is no longer chaotic, and constant rotations also increase the absorption energy. This is called the rotation bias effect.

6. CONCLUSION

1. A new type of VIM pendulum with a hoop generator was proposed in this paper. A circular tank test was conducted on a small model of the system to determine its performance. A newly designed data logger was used to obtain the cylinder VIM motion in a flow and the hoop generating power. However, the system performance proved low because the hoop did not achieve a steady turning motion.

2. To theoretically determine the system performance, a new equation of motion for the hoop was developed, and the motion of the hoop was numerically simulated. In the simulated results of the hoop motion, chaotic motion occurred under various conditions because of the large oscillation of the double pendulum. If this chaos phenomenon will be controlled, steady rotation of the generator motor can be easily achieved and leading to higher power generating performance. However, the chaos phenomenon cannot be confirmed by conducting water tank tests. This problem will be addressed in future work.

REFERENCES

- 1) Shinji Hiejima, Keito Oka, Kenichi Hayashi and Hiroo Inoue : Fundamental experiment for tidal current power generation using flow-induced vibration; The First Flutter Control and it's application, Sept.,(2011), 4-1.pdf, pp88-93
- 2) J. H. Lee, M. M. Rernitsas: High-damping, high-Reynolds VIV tests for energy harnessing using the VIVACE converter, Ocean Engineering 38, (2011) 1697-1712
- 3) Yutaka Yoshitake, Katsuya yamakami, Akizumi Fukushima: Various Motions of Hula-Hoop and Utilization as Vibration Quenching, JSME, No.98-8, 1998.8.17~20, Sapporo, Japan

A Study on Numerical Simulation of Wave Energy Converter Considering Nonlinear Wave Interaction Using BEM

Takeshi KAMIO⁺¹, Makoto IIDA⁺² and Chuichi ARAKAWA⁺³

⁺¹Researcher, The University of Tokyo, School of Engineering, Department of Mechanical Engineering, 7-3-1 Hongo, Bunkyo-ku, Tokyo, 113-8656, Japan

⁺²Associate Professor, The University of Tokyo, Research Center for Advanced Science and Technology (RCAST), 4-6-1 Komaba, Meguro-ku, Tokyo, 153-8904, Japan

⁺³Professor, The University of Tokyo, School of Engineering, Department of Mechanical Engineering, 7-3-1 Hongo, Bunkyo-ku, Tokyo, 113-8656, Japan

Marine renewable energy is an important future energy source. For wave energy, a point absorber with an oscillating body is a well-known type of wave energy converter and its features are relatively simpler system and lower cost than other types of wave energy converters. Reactive control concept is important to achieve larger energy income, but large motion of the float by reactive control is matter. The understanding of the device's behavior is important for the design but the large motion of the float is difficult to predict by the numerical simulation. The numerical simulation of the point absorber's behavior is often based on the so-called "linear theory". Linear problems are easy to analyze with BEM software like WAMIT, but nonlinear problems with the large motion of the float are difficult to analyze. CFD or FEM techniques will predict the nonlinear problems, but those techniques need the huge computer resources. In this study, the authors tried to simulate the large motion of the float using BEM and a fluid parameter table look-up technique is used. In the fluid parameter table look-up technique, several cases of the float's position are considered and fluid parameters for each case are calculated by BEM software. The calculated fluid parameters are kept in a memory and the time domain simulation program uses the parameters correspond to the position of the float. Using that technique, the numerical simulations of wave energy converters with cylinder shape float and tapered shape floats are demonstrated.

Keyword: Wave energy converter, Wave interaction, Reactive control, Time domain simulation

1. INTRODUCTION

Marine renewable energy is an important future energy source. There has been many research projects and commercialization challenge but there are still many problems to be solved. For wave energy, a point absorber with an oscillating body is a well-known type of wave energy converter and it is considered that the system will be simpler than other types of wave energy converters and the cost will be lower¹⁾. This type devices may be most studied and tested by researchers and many types of control strategies from resistive control to model predictive control are suggested^{2,3,4)}, and the important basic understanding may be that the large motion is need to achieve the large energy income.

Reactive control is a basic concept to achieve larger energy income by enlarging the motion of the float based on the resonant phenomena, but large motion of the float by reactive control causes many problems. The difficulty of the numerical simulation is focused in this study. The understanding of the device's behavior is important for the design but the large motion of the float is difficult to predict by the numerical simulation, of course, the analytical analysis is much more difficult. The numerical simulation of the point absorber's behavior is often based on the so-called "linear theory". Linear theory is based on the small motion assumption and it is widely used for the ocean engineering with the reliability. Linear problems are easy to analyze with BEM software like WAMIT. The nonlinear problems with the large motion of the

⁺¹kamio@cfdl.t.u-tokyo.ac.jp, ⁺²iida@ilab.eco.rcast.u-tokyo.ac.jp, ⁺³arakawa@cfdl.t.u-tokyo.ac.jp

float, which are outside of the linear theory, are difficult to analyze and CFD or FEM techniques will be suitable to analyze the nonlinear problems, but those techniques need the huge computer resources. In this study, the authors tried to simulate the large motion of the float with BEM and some small techniques. To prepare the simulation, several cases of the float's position are considered and fluids parameters for each case are calculated by BEM software. The calculated fluids parameters are kept in a memory table and the time domain simulation program uses the parameters correspond to the position of the float.

If considering only the heave motion, the motion of the float (one body) is described by Eq.1 based on the linear theory. In Eq.1, M is the float's mass, m_ω is the added mass, N_ω is the wave damping coefficient, C_ω is the restoring coefficient, X_ω is the wave excitation force coefficient, H_w is the wave elevation, F_{PTO} is the control force (load by the generator and thrust by the motor) from the power take off (PTO) system, z is the vertical position of the float and the dot means that it is the time differential value. ω means the parameters are depends on the wave frequency ω [rad/s] ($=2\pi / T$, T : wave period [s]). Although there are some techniques those convert the parameters and equations to the frequency independent forms, those techniques were not used in this study because it makes the parameter preparation complex. The control force of reactive control is described by Eq.2. In Eq.2, D_{PTO} and C_{PTO} are the control parameters those should be tuned for the resonance.

$$(M + m_\omega)\ddot{z}_{float}(t) + N_\omega\dot{z}_{float}(t) + C_\omega z_{float}(t) = X_\omega H_w(t) + F_{PTO}(t) \quad (1)$$

$$F_{PTO}(t) = -D_{PTO}\dot{z}_{float}(t) - C_{PTO}z_{float}(t) \quad (2)$$

To simulate the nonlinear behavior, the fluid parameters were prepared considering the position of the float and the simulation program runs referring the parameter table. Similar concepts may have been tried by many researchers, and this study presents just only our trials.



Figure 1: Example of the wave energy converter by Ocean Power Technologies⁶⁾.

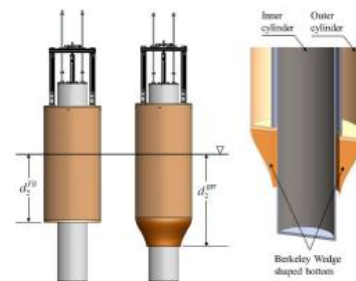


Figure 2: Example of the cylinder shape float by NREL⁷⁾.

2. FLOAT SHAPES AND PARAMETERS

(1) Float shapes

The disc shape floats had been used widely for the wave energy converter (Fig. 1), but recently the cylinder shape floats are increasing for the purpose of using reactive control. Employing the cylinder type floats will be possible to avoid (or reduce) the effects of the position changing and it enables the larger movement and the larger energy achievement. The most unwelcome case is that the float fries out, and it must cause the reduction of the energy income and it matters rather than the difficulty of the simulation. Fig. 2 shows an example of the cylinder shaper float by NREL⁷⁾. They also discussed the effect of the floater bottom shape, but the effect was ignored in this study because the effect was not computed by WAMIT.

In this study, three types of floats were tested based on those cylinder float concepts (Fig. 3). One is the just cylinder shape float, and the other two floats are tapered cylinder shaped (Up-tapered float and down-tapered float). Since approximately 7m-sized floats had been seen much in the many projects, the sizes

of the floats in this study were set based on 7m-length. To simplify the float, the through hole for the spar part was ignored. From the comparison of these floats' behaviors, we want to find the nonlinear effects and its influence on the energy income.

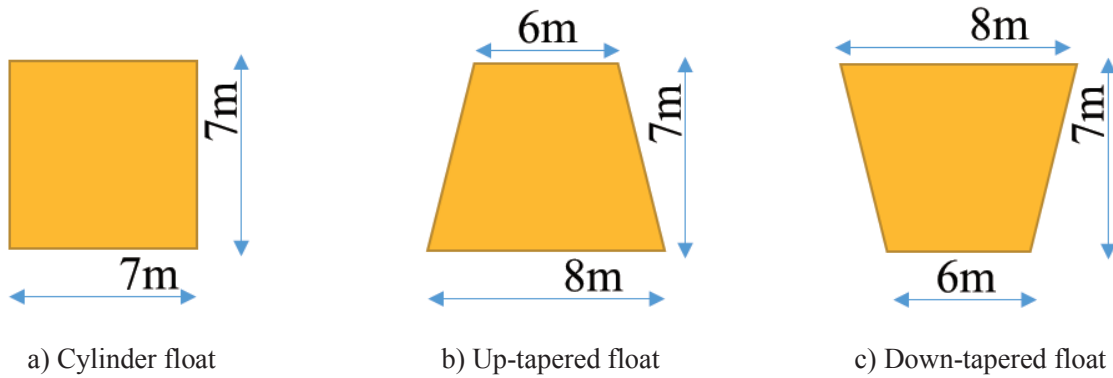


Figure 3: Side-view of the cylinder shape float and two tapered shape floats those were studied in this paper.

(2) Fluid parameters

Fluid parameters were computed by the Boundary Element Methods (BEM) code WAMIT. When using WAMIT, the position of the float and water level is important and often it is same as the equilibrium position. We assumed that the equilibrium position is the vertical center of the float and calculated the fluids parameters at the equilibrium position and several different positions.

The fluid parameters were computed as a following procedure. The seven positions were considered to compute the parameters. Here, the “position” equals the “water level”. The seven positions were the equilibrium position (E: $z = 0\text{m}$), three upper position (U1: $z = 1\text{m}$, U2: $z = 2\text{m}$, U3: $z = 3\text{m}$) and three lower position (L1: $z = -1\text{m}$, L2: $z = -2\text{m}$, L3: $z = -3\text{m}$). In Fig.4, those positions for the cylinder shape float are illustrated. The computed coefficients were shown in Fig. 5, 6, 7 and 8, and those parameters were computed for wave periods, but the restoring coefficient is constant for wave periods. By the same procedure, the fluid parameters of the up-tapered shape float and down-tapered shape float were computed and those were shown in Fig. 10, 11, 12, 13, 15, 16, 17 and 18. The figures show the variations of the parameters because of the shapes.

To simplify the parameters, one regular wave condition with wave period $T=7\text{s}$ was studied in this study. For $T=7\text{s}$, the parameters were picked up and these are shown in the figures. The parameters, especially damping coefficient, were varied by the position, and there were larger changes in the parameters of the tapered shape floats than those of the cylinder shape float (See Fig. 9, 14 and 19).

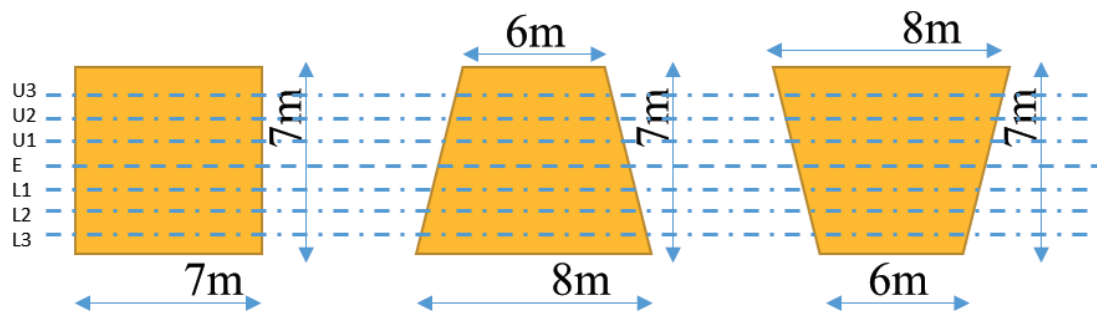


Figure 4: Image view of the seven vertical position for the cylinder shape float.

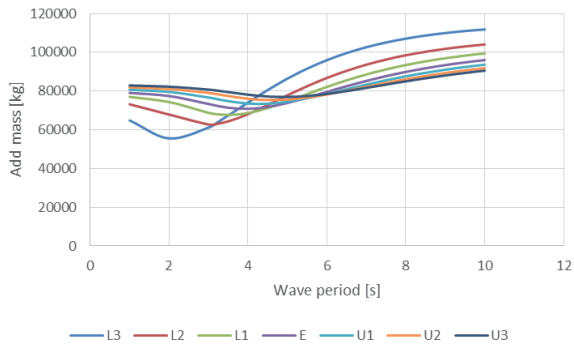


Figure 5: Computed add mass of the cylinder shape float with the seven positions.

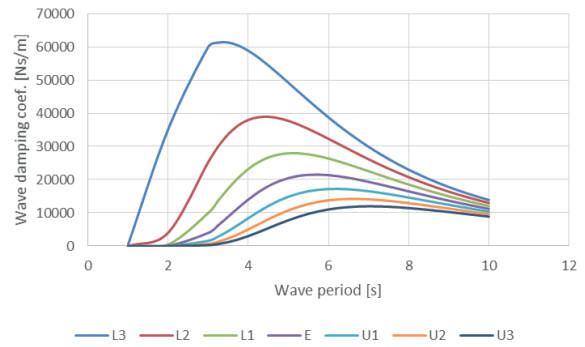


Figure 6: Computed wave damping coefficient of the cylinder shape float with the seven positions.

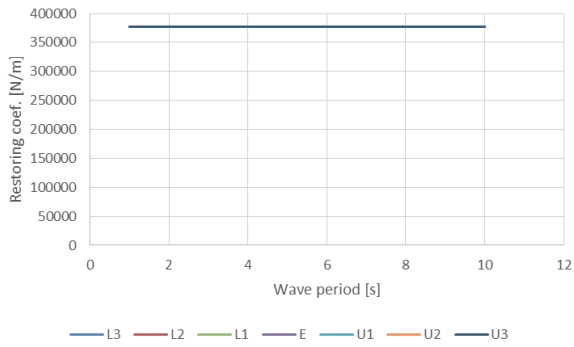


Figure 7: Computed wave restoring coefficient of the cylinder shape float with the seven positions.

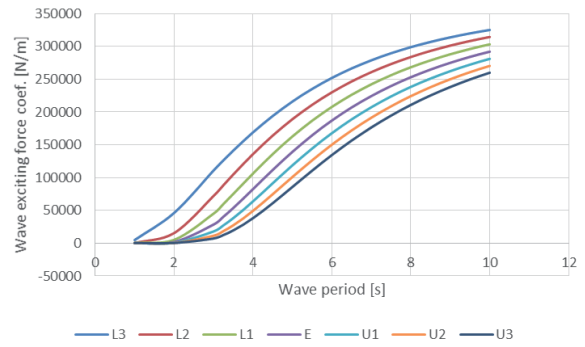


Figure 8: Computed wave exciting force coefficient of the cylinder shape float with the seven positions.

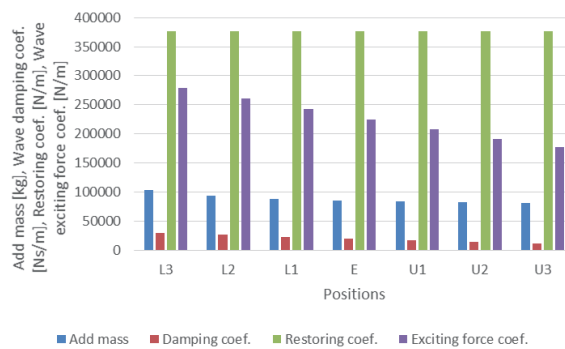


Figure 9: Values at wave period $T=7s$ of the computed coefficients of the cylinder shape float with the seven positions

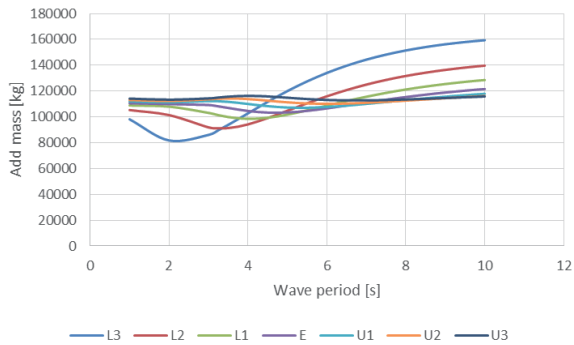


Figure 10: Computed add mass of the up-tapered shape float with the seven positions.

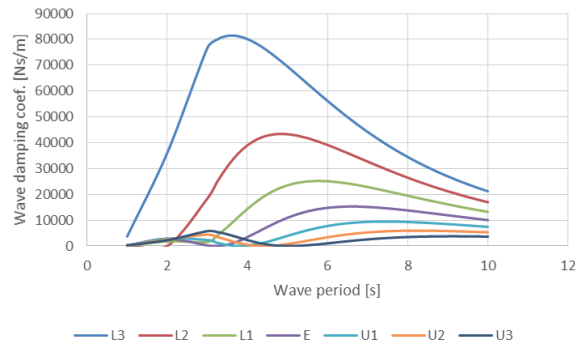


Figure 11: Computed wave damping coefficient of the up-tapered shape float with the seven positions.

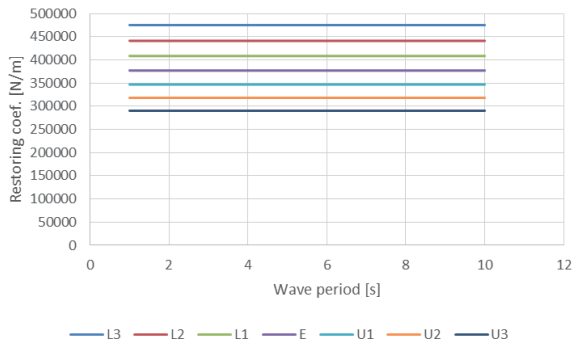


Figure 12: Computed wave restoring coefficient of the up-tapered shape float with the seven positions.

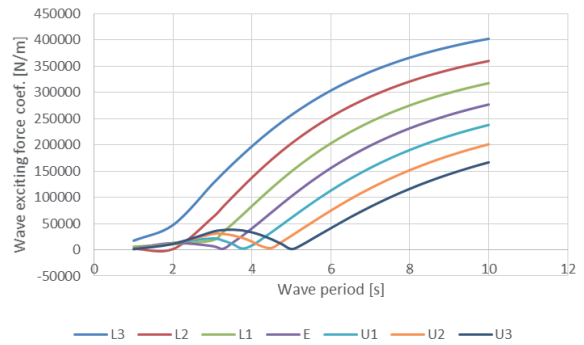


Figure 13: Computed wave exciting force coefficient of the up-tapered shape float with the seven positions.

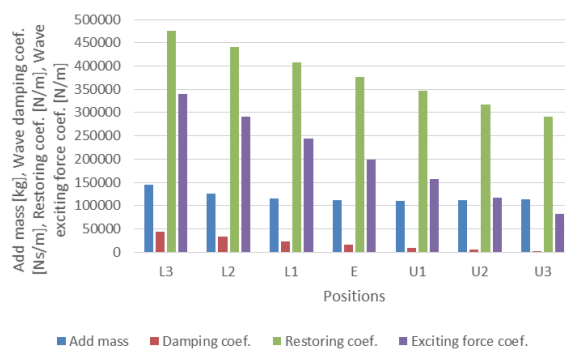


Figure 14: Values at wave period $T=7s$ of the computed coefficients of the up-tapered shape float with the seven positions

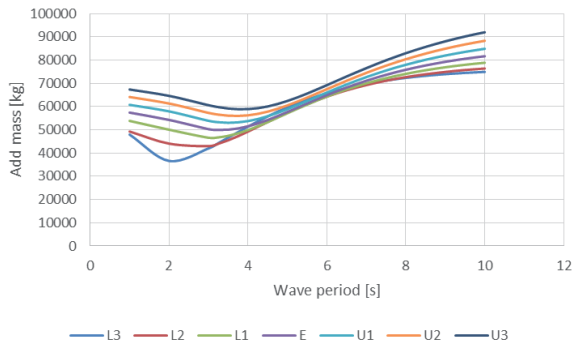


Figure 15: Computed add mass of the down-tapered shape float with the seven positions.

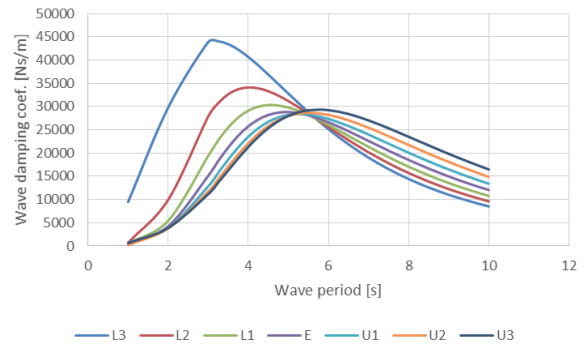


Figure 16: Computed wave damping coefficient of the down-tapered shape float with the seven positions.

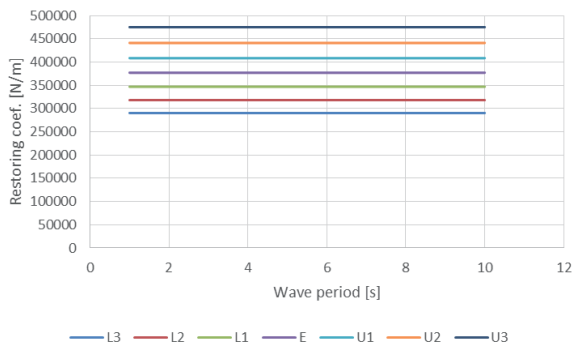


Figure 17: Computed wave restoring coefficient of the down-tapered shape float with the seven positions.

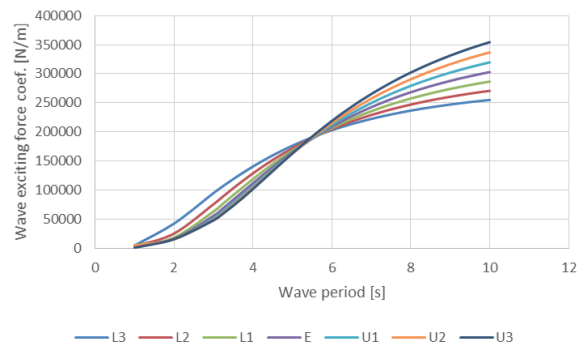


Figure 18: Computed wave exciting force coefficient of the down-tapered shape float with the seven positions.

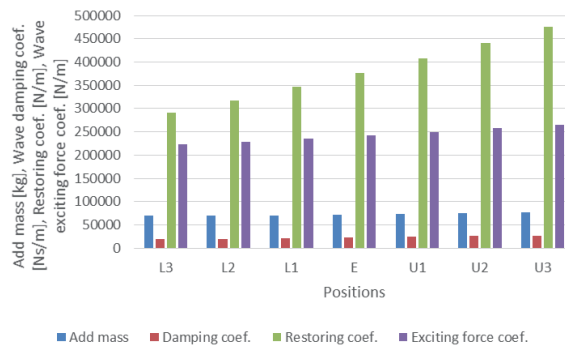


Figure 19: Values at wave period $T=7s$ of the computed coefficients of the down-tapered shape float with the seven positions

(3) Control parameters

The control parameters in Eq.2 for reactive control were prepared based on the conditions of the cylinder shape float. The additional conditions are: (a) Based on linear theory (equilibrium position), (b) The wave is the regular wave (sine wave) with wave period $T=7s$ and wave height $H=1m$, (c) The displacement must be smaller than 3m.

The tested parameters were found by the frequency analysis. When $D_{PTO} = 22kNs/m$, $C_{PTO} = -200kN/m$, the float's displacement will be less than 3m, and then the average output power is guessed to be 81kW. Those values will be change by the nonlinear behaviors.

3. NUMERICAL SIMULATIONS

(1) Fluid parameter table look-up

As mentioned above, the time domain simulation in this study uses the fluid parameters referring the obtained seven position data table with the linear interpolation. Initially, the relative position between the water elevation and float elevation is calculated. Then, the modified fluid parameters in the equation are given. These are described as follows.

$$r(t) = z_{float}(t) - H_w(t) \quad (3)$$

$$(M + m_\omega(r(t)))\ddot{z}_{float}(t) + N_\omega(r(t))\dot{z}_{float}(t) + C_\omega(r(t))z_{float}(t) = X_\omega(r(t))H_w(t) + F_{PTO}(t) \quad (4)$$

(2) Time domain simulation

We performed the time-domain simulations by using the Newmark- β method, which is an implicit method, so that we could use a relatively large time step in the calculations. But the time step of the time-domain simulations in this study was 0.01s, which may be sufficiently small. The time-domain simulation was programmed as MATLAB scripts.

By the Newmark- β method, the velocity and displacement at time step $t + \Delta t$ are described by the values at time step t as:

$$\dot{z}(t + \Delta t) = \dot{z}(t) + \Delta t \cdot [\gamma \cdot \bar{\ddot{z}} + (1 - \gamma) \cdot \ddot{z}(t)] \quad (5)$$

$$z(t + \Delta t) = z(t) + \Delta t \cdot \dot{z}(t) + \Delta t^2 \{ (0.5 - \beta) \cdot \ddot{z}(t) + \beta \cdot \ddot{z}(t + \Delta t) \} \quad (6)$$

where $\bar{\ddot{z}}$ is an assumed acceleration at $t + \Delta t$. β and γ are coefficients, and the values of $\beta = 1/4$ and $\gamma = 1/2$ were used. When those values are used, it is also called the average acceleration method and the solutions are stable against any value of Δt . First, we give the assumed acceleration of the float, which is initially given as the same value of the acceleration at the former time step t , and then calculate the velocity and displacement at $t + \Delta t$ by Eq. 5 and Eq. 6, and also the acceleration at $t + \Delta t$ based by the motion equation. Until satisfying the following condition, the modification of the assumed acceleration and re-calculation of the velocity and displacement are repeated.

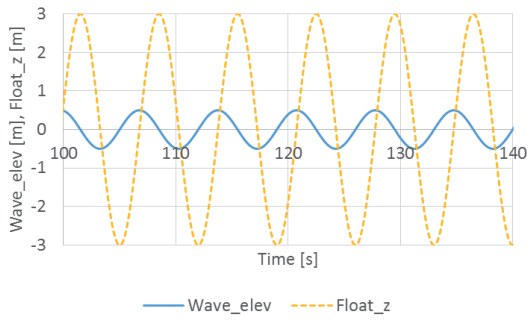
$$|\bar{\ddot{z}} - \ddot{z}(t + \Delta t)| \leq \varepsilon \quad (7)$$

where ε is a constant for the convergence test.

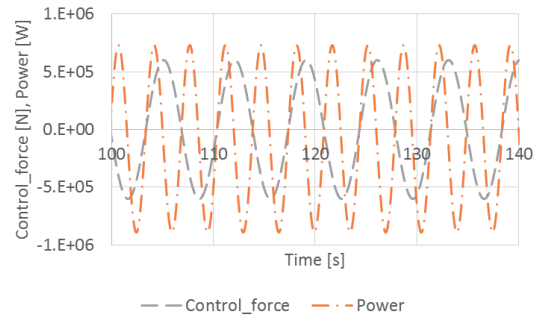
4. SIMULATION RESULTS

(1) Results of the four cases

First, we show the results of the four cases: (1) Linear simulation of the cylinder shape float (General "linear theory" based simulation), (2) Nonlinear simulation of the cylinder shape float, (3) Nonlinear simulation of the up-tapered shape float and (4) Nonlinear simulation of the down-tapered shape float.

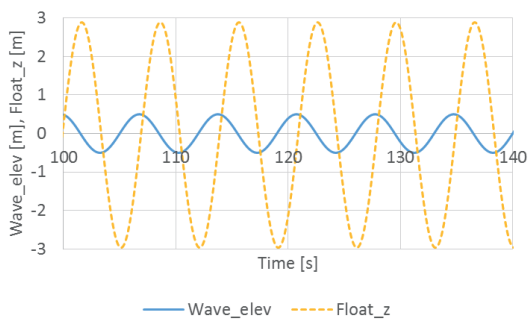


(a) Float's movement

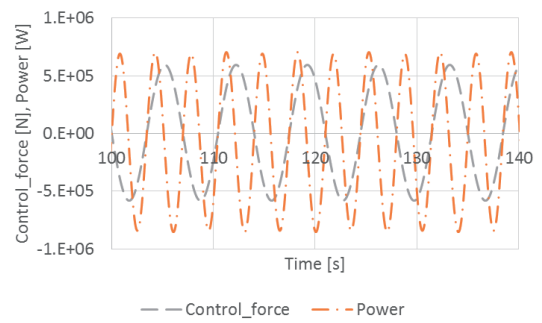


(b) Control force and power

Figure 20: Linear simulation of the cylinder shape float.

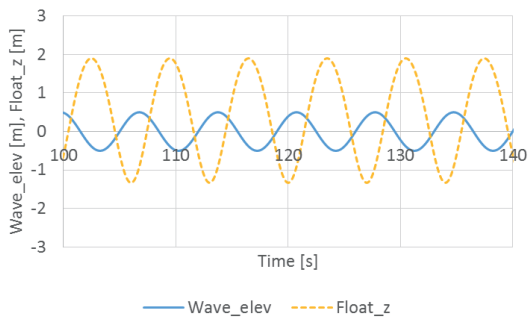


(a) Float's movement

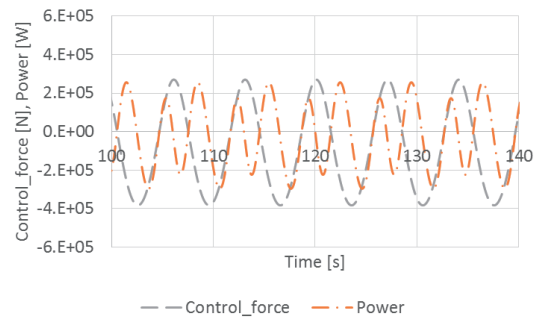


(b) Control force and power

Figure 21: Nonlinear simulation of the cylinder shape float.

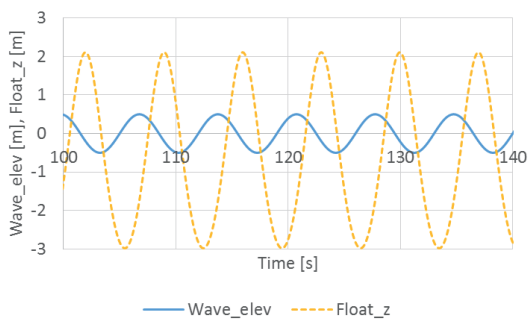


(a) Float's movement

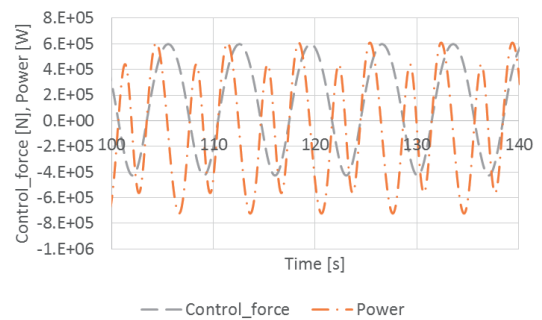


(b) Control force and power

Figure 22: Nonlinear simulation of the up-tapered shape float.



(a) Float's movement



(b) Control force and power

Figure 23: Nonlinear simulation of the down-tapered shape float.

Table 1: Z_{max} , r_{max} , r_{min} and P_{ave} .

Cases	Z_{max} [m]	r_{max} [m]	r_{min} [m]	P_{ave} [kW]
(1)	3.00	3.04	-3.04	80.63
(2)	2.89	2.99	-3.06	76.75
(3)	1.91	2.32	-1.75	23.81
(4)	2.10	2.33	-3.24	58.48

Fig. 20, 21, 22 and 23 show the movements of the floats, control forces and power. Table 1 shows the maximum float's displacement Z_{max} , the maximum relative position between the water elevation and float elevation r_{max} , the minimum of it r_{min} , and the averaged first-conversion power P_{ave} . The values of Z_{max} , r_{max} and r_{min} indicate that the movements of the floats were within the expected movements and within the float's vertical size, and the computed results will be reasonable (It does not mean that the results are real, and it must be confirmed by comparing with the experiments).

(2) Discussions

Firstly, looking the result of the linear simulation of the cylinder shape float, the maximum displacement was 3m and the averaged power was approximate 81kW. Those were agreed with the expected values by the frequency analysis and those results may be some confirmations of the simulation program in this study.

Secondary, comparing the linear simulation and nonlinear simulation of the cylinder shape float, the differences of the movement and the averaged power were very small. This results may support the concept of the cylinder shape for avoiding the nonlinear effects. At the same time, it may be confirmed that the general linear simulation method is available within the float's vertical size.

Thirdly, the movement of the up-tapered shape float was smaller than other cases and the averaged power was much smaller than other cases. Those might be caused by the change of the wave exciting force coefficient for the position. Especially, the decrease of the coefficient from the lower position to the upper position was notable, because the wave exciting force is proportional to the vertical projected area of the float, and the cancellation of the force of the upper part and lower part is caused.

Fourthly, the movement and the averaged power of the down-tapered shape float was smaller than those of the cylinder shape float. For the down-tapered shape float, the change of the wave exciting force coefficient by the positions were small. But the change of the wave damping coefficient was notable and the increase of the coefficient from the lower position to the upper position might cause the slow-down of the float's movement.

The comparison of the three floats indicates that the change of the float's shape will be hard to lead the achieved power. But the control strategy was not optimized for each case in this study, and the result would be changed if the suitable control strategy would be used.

5. CONCLUSION

In this study, the pseudo nonlinear simulations with the table look-up of the fluid parameters for the three different shape floats were demonstrated. The fluid parameters for the floats were prepared by computing with WAMIT for the seven vertical position and those indicated the variations of the parameters. The results of the pseudo nonlinear simulations showed that (1) the linear simulation method does not matter for the cylinder shape float within the float size-order motion and (2) the up-tapered shape float and down-tapered shape float does not lead the increase of the achieved power and the change of the float shape needs more careful thought.

Since there was no comparison nor discussion with the experimental data in this study, the reliability and accuracy of the simulations were unknown. The experimental data will be essential, and the simulation

data by many methods including CFD will be required to discuss the nonlinear simulation as further work.

ACKNOWLEDGMENT

The authors thank for the New Energy and Industrial Technology Development Organization (NEDO) supporting the ocean energy development projects.

REFERENCES

- 1) Falcão, A. F. D. O. : Wave energy utilization: A review of the technologies, *Renew. Sust. Energ. Rev.*, 14, pp.899-918, 2010.
- 2) Falnes, J., “Wave-energy conversion through relative motion between two single-mode oscillating bodies”, *J. Offshore Mech. Arct. Eng.*, 121(1), pp. 32-38, 1999.
- 3) Hals, J., Falnes, J. and Moan, T. : A comparison of selected strategies for adaptive control of wave energy converters, *J. Offshore Mech. Arct. Eng.*, 133(3), pp. 031101, 2011.
- 4) Hals, J., Falnes, J. and Moan, T. : Constrained optimal control of a heaving buoy wave-energy converter, *J. Offshore Mech. Arct. Eng.* 133(1), pp. 011401, 2011.
- 5) WAMIT USER MANUAL Version 7.1, 2015, <http://www.wamit.com/>
- 6) OCEAN POWER TECHNOLOGIES, <http://www.oceanpowertechnologies.com/>
- 7) Son, D., Belissen, V., Yeung, R. W., “OPTIMIZING THE PERFORMANCE OF A DUAL COAXIAL-CYLINDER WAVE-ENERGY EXTRACTOR”, *Proceedings of the ASME 2015 34th International Conference on Ocean, Offshore and Arctic Engineering (OMAE2015)*, 2015.

GALLOPING OSCILLATIONS OF PRISMS AND ENERGY HARVESTING IN WIND TUNNEL

P. Hémon⁺¹, X. Amandolese⁺² and T. Andrianne⁺³

⁺¹LadHyX, Ecole Polytechnique-CNRS, Palaiseau, France

⁺²LadHyX, Ecole Polytechnique-CNRS, Palaiseau, and CNAM, Paris, France

⁺³Aerospace and Mechanical Engineering Department, University of Liège, Belgium

We consider the galloping oscillations of prisms with square and 2/3 rectangular section. Rigid prisms are flexibly mounted in wind tunnel. Energy harvest is performed by a series of magnets mounted on the oscillating prism so that they pass close to the face of a coil-core system externally fixed. The produced power is dissipated through a decade box allowing adjustment of the load resistance. A simple mechanical analysis leads to define several efficiencies for such a galloping setup: the global efficiency is the ratio between electric power and wind power. It is the product of two efficiencies: the ratio of the galloping power referred to wind power, and the one being the electrical power referred to the galloping power. Galloping power is the maximum power that can be extracted from the oscillations of the prism which are governed by the aerodynamic damping and structural damping. It is always found very small compared to wind power. Experimental results notably show that there exists an optimal load resistance for global efficiency while another optimal value is found for the electrical production referred to the galloping power.

Keyword: galloping, energy harvest, wind tunnel

1. INTRODUCTION

We consider the galloping oscillations of prisms with square and 2/3 rectangular section shown Fig. 1. Galloping is a dynamic instability that can affect a slender structure submitted to a cross flow. It is a one degree of freedom instability, in transverse or torsional motion, for which the motion-induced fluid loading creates a negative added damping that trigs the instability beyond a critical velocity.

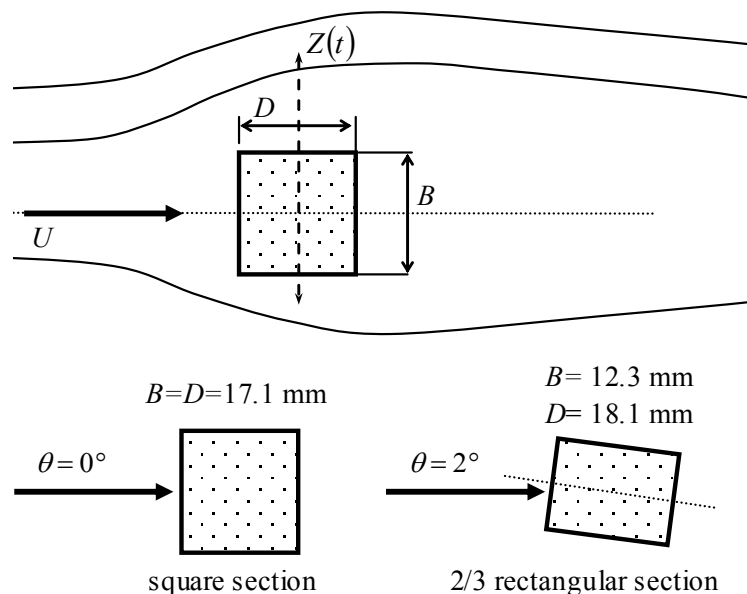


Figure 1: The studied prisms

⁺¹hemon@ladhyx.polytechnique.fr, ⁺²amandolese@ladhyx.polytechnique.fr, ⁺³t.andrianne@ulg.ac.be

Slender structures with non-circular bluff cross section are all susceptible to transverse galloping. The literature on transverse galloping is then important and one can find the most significant references in the book of Blevins ¹⁾, the article of Parkinson ²⁾, and the recent book of Paidoussis *et al.* ³⁾. The basic mechanism of transverse galloping along with a quasi-static criterion for the onset of instability was first proposed by Den Hartog in 1934 ⁴⁾, in the context of transmission line vibration due to sleet.

Once the system is unstable, oscillations growth in amplitude up to limit-cycle regime due to structural or aerodynamic nonlinearities. If one wants to study the post-critical behavior it is then necessary to take into account the nonlinear evolution of the transverse fluid force. This was early done by Parkinson and Brooks ⁵⁾, Parkinson and Smith ⁶⁾ and Novak ⁷⁾ using a nonlinear quasi-steady approach.

Later a number of studies were done on the nonlinear galloping behavior. Effect of turbulence on galloping can also be found in Novak and Tanaka ⁸⁾. The hysteresis behavior in post-critical galloping is also a matter of concern. Following the work of Parkinson and Smith ⁶⁾, Luo *et al.* ⁹⁾ performed a numerical study focusing on the hysteresis oscillation for the case of a square prism. The link between inflexion points and LCOs hysteresis response was also recently scrutinized by Barrero-Gil *et al.* ¹⁰⁾. In another study, Andrianne and Dimitriadis ¹¹⁾ showed that a fifth-order expansion is sufficient to capture the bifurcation behavior of galloping.

In that context, the objective of this paper is to evaluate and discuss the energy harvesting potential of the galloping mechanism. Energy harvesting from transverse galloping has been previously studied analytically by Barrero-Gil *et al.* ¹²⁾ and Vicente-Ludlam *et al.* ¹³⁾. This paper is an experimental contribution that could allow to improve the mathematical models and to assess the performances on an engineering point of view.

2. EXPERIMENTAL SETUP

Tests have been performed in an Eiffel open-loop wind tunnel with a square closed test section of 180 by 180 mm. The air inlet is equipped with honeycomb and thin grid so that the turbulence intensity is less than 1 % in the test section. The mean velocity can be varied from 5 to 25 m/s by means of a centrifugal fan. The reference velocity is measured via a Pitot tube and a Furness pressure transmitter. Air density is corrected by measurement of the air temperature in the wind tunnel with a thermocouple and the atmospheric pressure with a mercury barometer. Global accuracy of the reference velocity measurement is considered better than 1 %. Data acquisition is performed using a PAK system furnished by Muller-BBM. It is based on a 8 channels analyzer with 24 bits of resolution and sampling frequencies up to 52 kHz.

Two prisms have been used in the study. The first one has a square section and the second one has a rectangular section of ratio $B/D = 2/3$ shown Fig. 1. Both are made of aluminum alloy with a span 170 mm. Their shape has been adjusted on a milling machine in order to produce corners with sharp edge. In what follows, the reference length is chosen to be D . For the case of the rectangular section it corresponds to the long dimension. The prism models that almost span the test section are equipped with two end plates to keep the airflow as two-dimensional as possible. They are elastically supported in order to allow a one-degree-of-freedom transverse motion $Z(t)$. Stiffness is provided by combination of linear and laminated springs, suitably mounted in order to produce a very low structural damping. These springs are mounted outside the test section, via two vertical fences (see Fig. 2). Length of laminated springs is large (0.75 m) compared to the expected cylinder vertical displacement so that the system can be considered as linear in the range of use.

The vertical displacement of the cylinder is measured by a laser sensor, i.e. without contact that could corrupt damping of the system. It is connected to the acquisition system providing time histories of the signal and simultaneous spectral analysis. Typically a record is 45 s long and the frequency resolution is 1/8 Hz.

Structural parameters of the system were identified under zero-wind velocity. A static weight calibration technique was used to measure the stiffness of the setup. Free decay tests were then performed to identify the natural frequency, by spectral analysis, and the damping ratio using a standard decrement technique. The total mass of the system was then calculated using the measured stiffness and natural frequency. Results are reported in Table 1.

Table 1. Structural characteristics of the two prisms

	Square	Rectangular
frequency (Hz)	5.875	5.75
mass (kg)	0.340	0.326
reduced damping (%)	0.188 ± 0.007	0.256 ± 0.009
stiffness (N/m)	467.1	425.5
Scruton number S_c	21.5	24.9

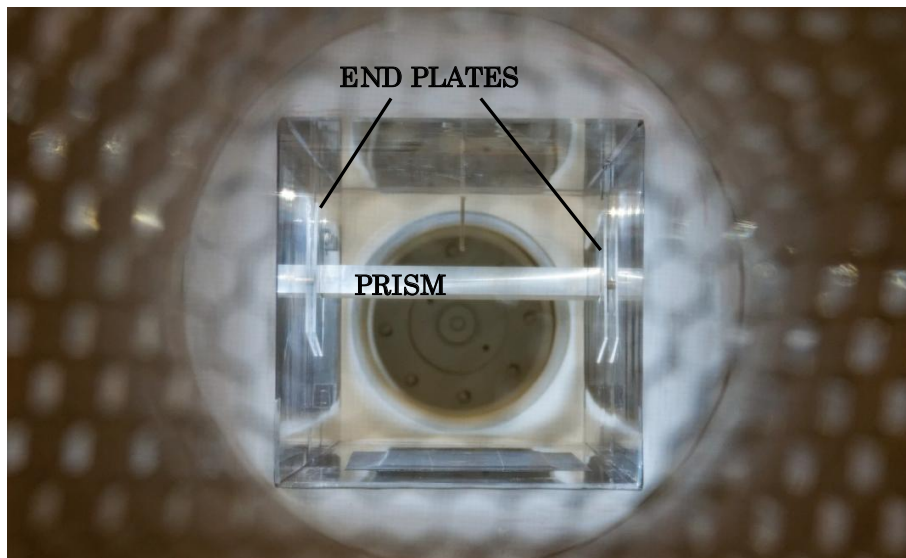
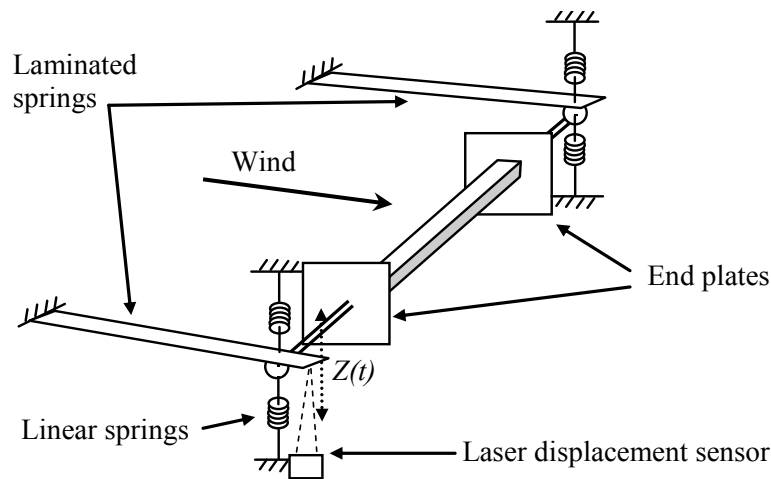


Figure 2. Principle of the experimental setup for galloping and picture taken through the inlet of the wind tunnel

The harvesting device consists in the combination of magnets in motion in the close vicinity of a coil and core static ensemble. The system is depicted in Fig. 3, where the variable electric load is represented. The magnets are located on the suspension beams that ensure the vertical stiffness of the aeroelastic system.

The magnet combination is composed of three Neodymium magnets (NdFeB) of size 10x5x3 mm, with a magnetization type N45. Attraction force of one magnet is 1.5 kg (furnisher data). The total mass of the magnets is equal to 3.33 g. The dimensions of the coil are 22 mm long and 16 mm diameter. Measured inductance is 0.0372 Henry and its electric resistance is 37 Ω. The cylindrical core is 17 mm long and 6 mm

diameter. The distance between magnets and coil is 0.5 mm, which places the core at 5.5 mm from the magnets. The load resistance of the harvesting device is adjustable between 0 Ω (short-circuit) up to 10 M Ω (open-circuit). A decade box from Time Electronics is used in the set-up. The load voltage $V_c(t)$ is measured synchronously with the vertical displacement $Z(t)$ using the PAK system.

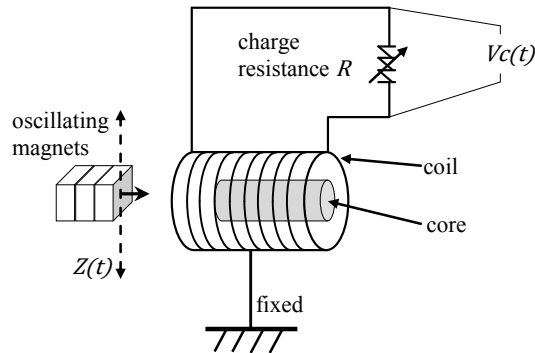


Figure 3. Principle of the electric energy harvesting device

The harvesting device is characterized through shaker tests. A sinusoidal motion of constant amplitude ($Z_{rms} = 7.2\text{mm}$) and frequency (5.75 Hz, see Table 1) is imposed to the magnets in front of the coil. The RMS voltage is measured for different values of the load resistance between 1 Ω and 9 M Ω . Figure 4 shows that the maximum power is reached at 35 Ω . This value is close from the resistance of the coil (37 Ω), in accordance with the Maximum Power Transfer Theorem.

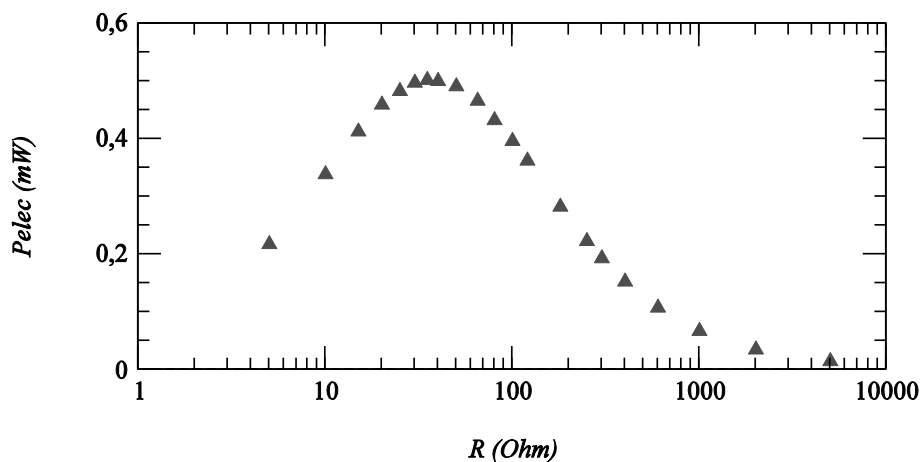


Figure 4. Optimal load resistance of the harvesting device

3. GALLOPING OSCILLATION AMPLITUDE

The aeroelastic response of the square prism is shown Fig. 5 and Fig. 6 for the rectangular prism. The two configurations, i.e. the square prism at $\theta=0^\circ$ and the rectangular prism at $\theta=2^\circ$, have been chosen from the results of a previous study showing their good potential, Hémon et al.¹⁴). In both cases, the response without energy harvest was measured, with and without the core, since it could affect the response amplitude. Results show that with the chosen settings for the harvesting setup, this is not the case.

The square prism presents a quasi linear growth of amplitude with reduced velocity. When harvesting device is active with its optimal setting ($R=90 \Omega$, see section 5) the response amplitude is lower due to the energy harvest.

But the response of the rectangular prism is slightly different. The linear growth of amplitude occurs beyond $Ur=80$ after a rapid increase. This is certainly due to the transverse force evolution which is strongly

nonlinear for this rectangular prism. When harvesting is active the response is lower and smoothed.

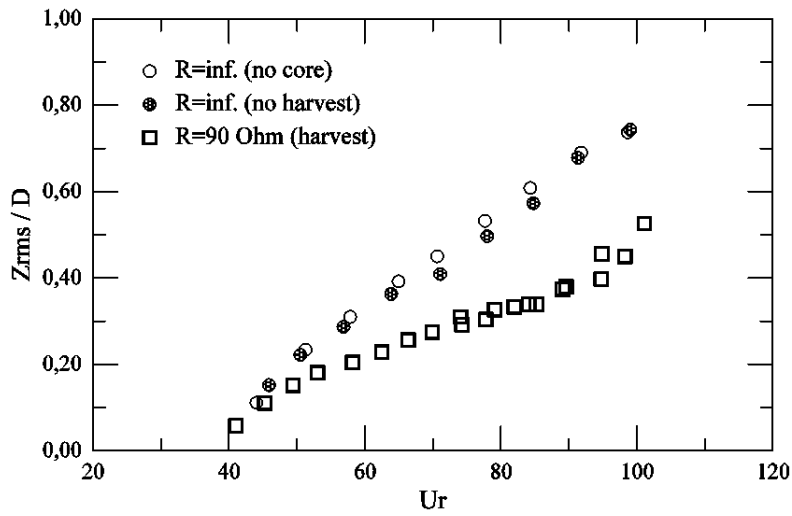


Figure 5: Oscillations amplitude versus reduced velocity for the square prism at $\theta=0^\circ$

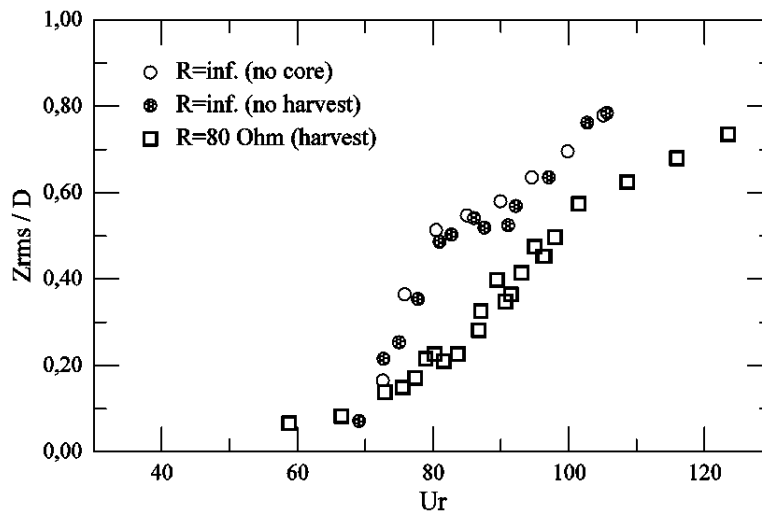


Figure 6: Oscillations amplitude versus reduced velocity for the $2/3$ rectangular prism at $\theta=2^\circ$

4. EFFICIENCIES AS A FUNCTION OF REDUCED VELOCITY

The efficiency of energy harvesting is based on the harvested power, i.e. the electric power P_e and the available power in the wind flow P_w . Electric power is defined as:

$$P_e = Vc^2/R \tag{1}$$

where Vc is the RMS value of $Vc(t)$. The wind power is defined as the kinetic energy flux of air passing through a cross section defined as the area swept by the oscillating prism, which is the product of its span and thickness, increased by the measured amplitude oscillations:

$$P_w = \frac{1}{2} \rho E (D + 2 Z_{rms}) U^3 \tag{2}$$

Another efficiency definition may be of interest for the physical interpretations. Indeed, galloping oscillations are due to the aerodynamic damping and energy harvesting can be performed only from this mechanism. Starting from the linearized equation of motion a characteristic value of the power that can be

harvested is defined as:

$$P_g = \frac{1}{T} \int_0^T \left(-\frac{1}{2} \rho D E U C z' - 2 E m \omega \eta \right) \dot{Z}^2 dt \quad (3)$$

where the transverse lift force derivative Cz' is deduced from the critical velocity measured during the free galloping tests. Assuming a periodic motion such as $Z(t) = \sqrt{2} Z_{RMS} \sin \omega t$ we can compute analytically the previous expression so that:

$$P_g = \left(-\frac{1}{2} \rho D U C z' - 2 m \omega \eta \right) E \omega^2 Z_{RMS}^2 \quad (4)$$

Then the global efficiency can be expressed as the product of two components, an efficiency of the galloping behaviour times the efficiency of the mechanical-electrical process:

$$\frac{P_e}{P_w} = \frac{P_g}{P_w} \frac{P_e}{P_g} \quad (5)$$

The first ratio in (5) is interesting in the sense that it is independent from the electrical production system and should then be the first quantity to analyze in order to choose the best configuration of prism galloping.

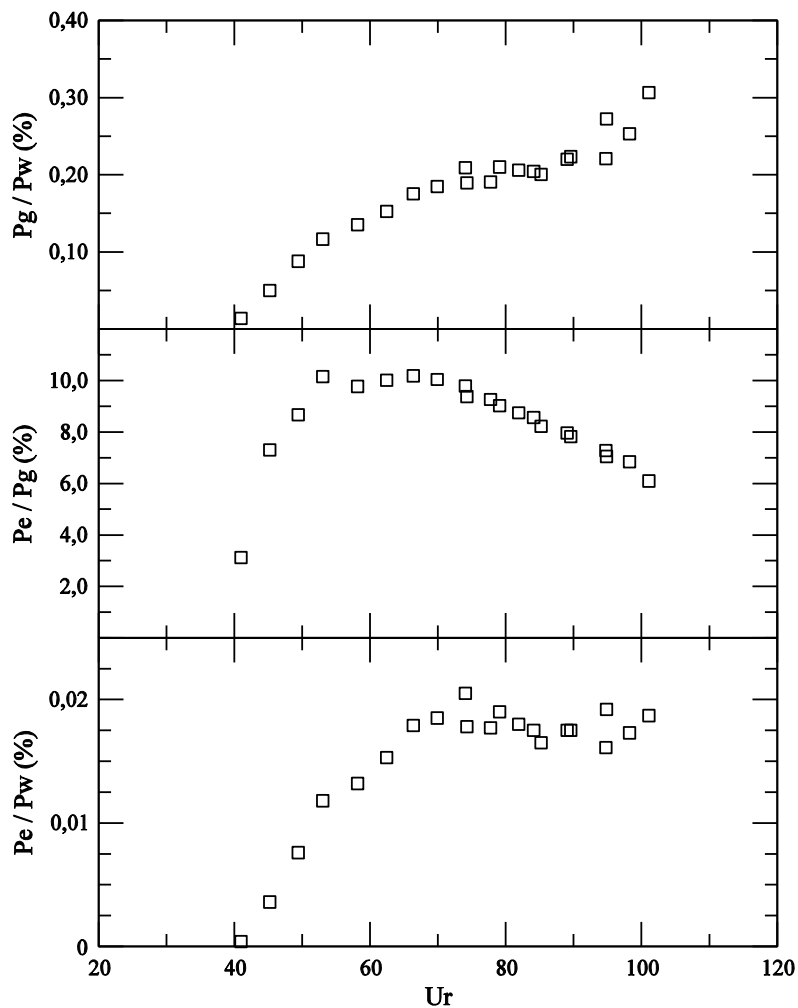


Figure 7: Efficiencies of the energy harvest versus reduced velocity for the square prism at $\theta=0^\circ$ and optimal load resistance $R=90 \Omega$

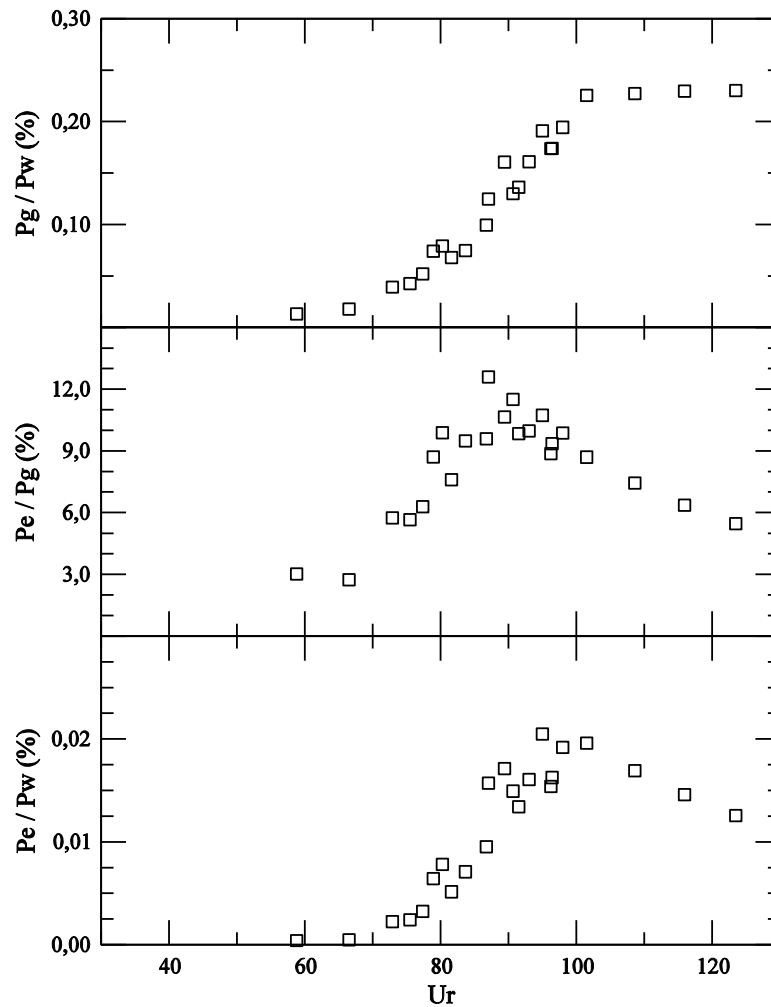


Figure 8: Efficiencies of the energy harvest versus reduced velocity for the 2/3 rectangular prism at $\theta=2^\circ$ and optimal load resistance $R=80 \Omega$

These three efficiencies are given in Fig. 7 for the square prism and Fig. 8 for the rectangular prism. The main observation is the very low value of the galloping power compared to the wind power, around 0.2-0.3%. On the other hand, the energy converter, although its simplicity, reaches efficiencies that rise over 10% in the best conditions.

Finally the global efficiency, which is the product of the two previously mentioned efficiencies, is therefore very small, around 0.02%. However, to the authors knowledge, the experimental investigation of the potential energy harvesting from galloping oscillations was not published before. On an engineering point of view the extreme simplicity and scalability of the vibrating beam under galloping is an important advantage on the classical horizontal axis wind turbine. It is also very noiseless which is certainly an additional advantage in the context of urban area.

5. THE EFFECT OF THE LOAD RESISTANCE

In order to complete the study, the effect of the load resistance is investigated. Experiments are carried out at constant velocity and the resistance is varied through the decade box. Results are reported in Fig. 9 for the square prism and Fig. 10 for the rectangular prism. At high value of resistance, energy harvest is negligible and the oscillations amplitude match those previously measured (Fig. 5 & 6). As far as the resistance decreases, the

oscillations amplitude decreases also and the galloping power decreases more rapidly (proportional to Z_{RMS}^2) than wind power (proportional to Z_{RMS}). Concerning electric power related to galloping power, the resulting efficiency is similar to the energy converter characteristics (Fig. 4) with an optimal resistance close to 40Ω .

Finally, the global efficiency measuring the ratio between electric power and wind power presents an optimal load resistance which differs from the one mentioned above. It is found around 90Ω for the square prism and 80Ω for the rectangular prism, mostly the same value, and independent of the reduced velocity (in the range of tests).

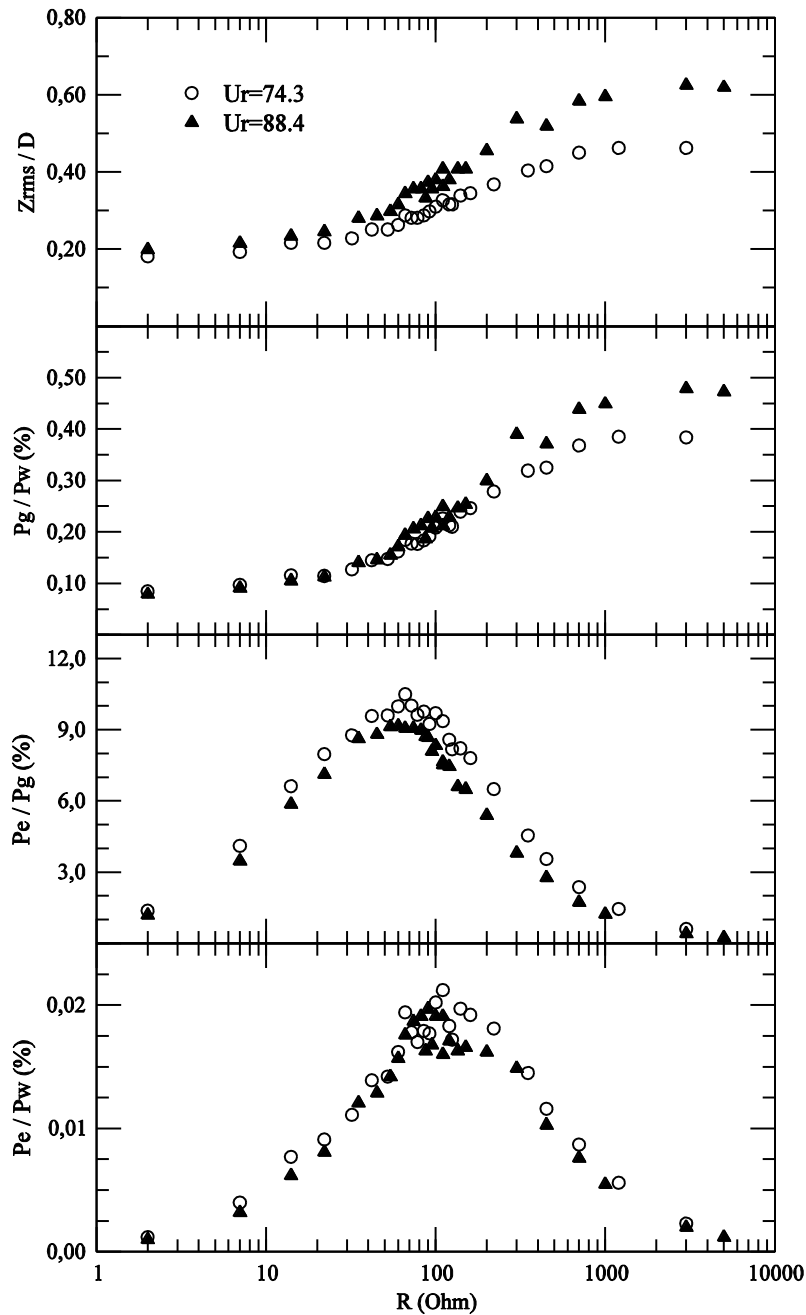


Figure 9: Oscillations amplitude and energy harvest efficiencies versus the electric load resistance for the square prism at $\theta=0^\circ$

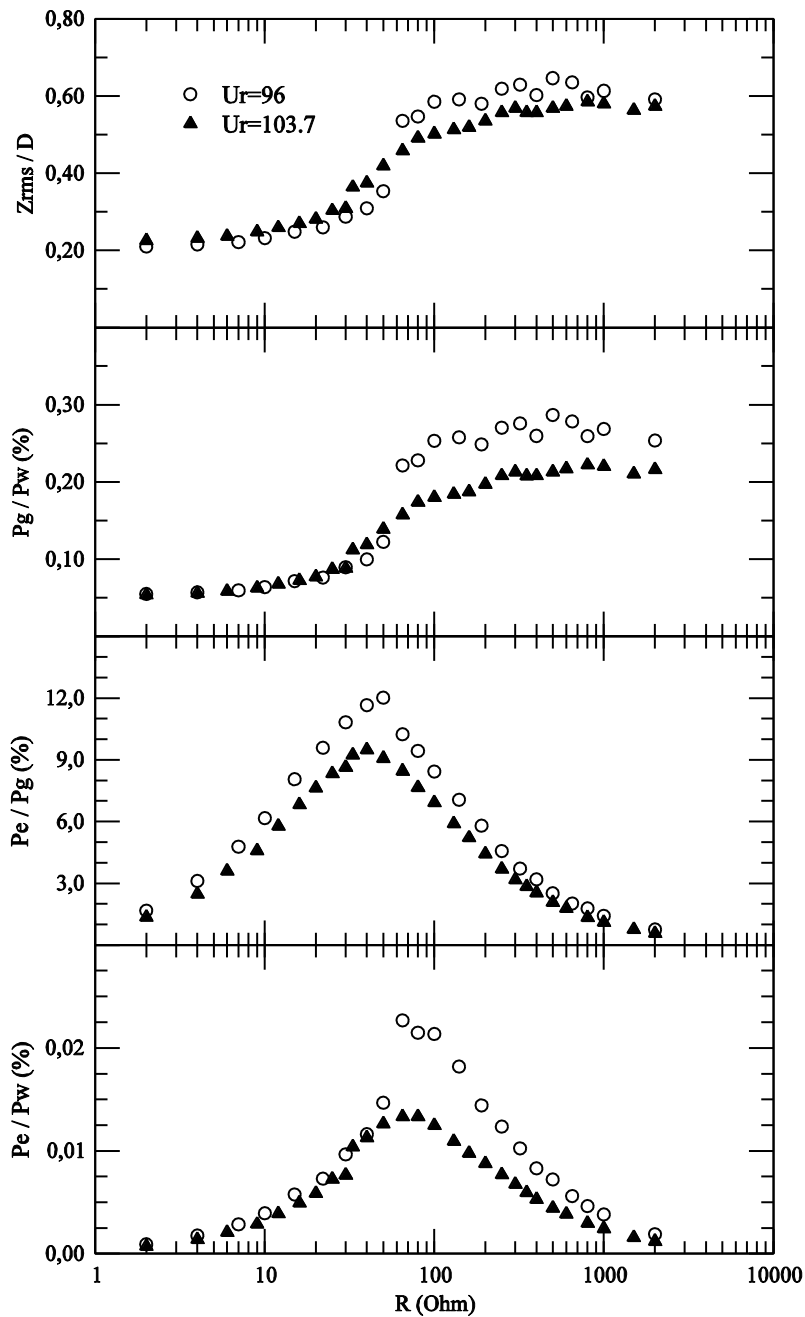


Figure 10: Oscillations amplitude and energy harvest efficiencies versus the electric load resistance for the 2/3 rectangular prism at $\theta=2^\circ$

6. CONCLUSION

Galloping of prisms was investigated experimentally in wind tunnel in order to estimate the potential of this mechanism for producing electric power from the wind. Two configurations were chosen, a square section prism and a 2/3 section prism slightly inclined from the wind direction. A very simple energy harvester system is mounted. It consists in magnets located on the moving prism in front of a coil-core at rest. Efficiency of the system is found very small compared to standard wind turbine due to the galloping mechanism physics. However the electromechanical setup converting translating motion in electric energy is interesting and could certainly improved.

Experiments show also that there exist two optimal load resistances, one linked to the galloping

mechanism and another one linked to the energy converter. Next step of this study could be the design of another setup in which these optimal resistance are joined, which probably could lead to the best efficiency of such a system.

Although efficiency of this "prism wind turbine" is rather weak, it remains interesting to further investigations and optimization because of its extreme simplicity and cost. Moreover such kind of system can be developed at various scales, for water current or wind and, because of the noiseless functioning, it can be placed in a number of situations where standard wind turbines cannot.

REFERENCES

- 1) Blevins, R. D. Flow-Induced Vibrations. Reprint of the 1990 second edition, Krieger Publishing Company, Malabar, Florida. 2001.
- 2) Parkinson, G. V. Phenomena and modelling of flow-induced vibrations of bluff bodies. *Progress in Aerospace Sciences* 26(2), pp. 169-224. 1989.
- 3) Paidoussis, M. P., Price, S. J., De Langre, E. Fluid-structure interactions: cross-flow induced instabilities. Cambridge University Press. 2011.
- 4) Den Hartog, J.P. Mechanical Vibrations. Reprint of the 1934 edition. Dover, New York. 1985.
- 5) Parkinson, G. V., Brooks, N. P. H. On the aeroelastic instability of bluff cylinders. *ASME Journal of Applied Mechanics*, June 1961, pp. 252-258. 1961.
- 6) Parkinson, G. V., Smith, J. D. The Square Prism as an Aeroelastic Non-linear Oscillator. *Quarterly Journal of Mechanics and Applied Mathematics*, XVII, pp. 225-239. 1964.
- 7) Novak, M. Aeroelastic galloping of prismatic bodies. *J. of the Engineering Mechanics Division of the ASCE*, 96, pp. 115-142. 1969.
- 8) Novak, M., Tanaka H. Effect of turbulence on galloping instability. *J. of the Engineering Mechanics Division of the ASCE*, 100, pp. 27-47. 1974.
- 9) Luo, S.C., Chew, Y.T., Ng, Y.T. Hysteresis phenomenon in the galloping oscillation of a square cylinder. *J. Fluids and Structures* 18, pp. 103-118. 2003.
- 10) Barrero-Gil, A., Sanz-Andrés, A. Alonso, G. Hysteresis in transverse galloping: the role of inflection points. *J. Fluids and Structures* 20, pp. 1007-1020. 2009.
- 11) Andrienne , T., Dimitriadis, G. Empirical modelling of the bifurcation behaviour of a bridge deck undergoing across-wind galloping, *J. Wind Engineering and Industrial Aerodynamics* 135, pp. 129–135, 2014.
- 12) Barrero-Gil, A., Alonso, G., Sanz-Andres, A. Energy harvesting from transverse galloping. *J. Sound and Vibration* 329, pp. 2873-2883. 2010.
- 13) Vicente-Ludlam, D., Barrero-Gil, A., Velazquez, A. Optimal electromagnetic energy extraction from transverse galloping. *J. Fluids and Structures* 51, pp. 281-291. 2014.
- 14) Hémon, P., Amandolese, X. & Andrienne, T. Galloping oscillations of prisms and energy harvesting in wind tunnel. Submitted to . *J. Fluids and Structures* 2016.

Energy Recovery Concepts in Actively Controlled LCO Instabilities Caused by Free-Play Induced Aeroelastic Flutter

Atul Kelkar¹, Prachi Deshpande² and Jerald Vogel³

^{1,2} Iowa State University, Ames, Iowa, USA

³VSI Aerospace, Inc., Ames, Iowa, USA

Aeroelastic flutter is characterized as an unstable self-excitation of the aeroelastic structure caused due to an undesirable coupling of structural elasticity and aerodynamics. Flutter is very difficult to predict and it can lead to catastrophic structural failure. Various nonlinear phenomena affecting flutter include nonlinearities in structural stiffness and damping, and free-play in joints. Recent work performed under NAVAIR funded project ¹⁾ provides deeper insights into how free-play affects flutter behavior. This paper extends the work performed by this project to gain further understanding of flutter dynamics from energy viewpoint and to unravel the energy exchange phenomena occurring between fluid and structure domain. While most of the work in the literature has focused on how to avoid potentially catastrophic onset of flutter, the focus of this paper is to investigate how to harness the energy in otherwise undesirable flutter phenomena. The flutter phenomena of interest is the limit cycle oscillations (LCO) which represent marginally stable structural response. The work in²⁾ showed a direct correlation of free-play with LCO. This paper presents a concept for energy harvesting system that uses free-play induced LCO as the energy resource and magnetostrictive device that can harness that energy. The concept is presented using a 2-D aeroelastic system. A complete analytical modeling and simulation results are given and energy transfer phenomena are explained. The harvesting mechanism concept is proposed using advanced magnetostrictive materials like Galfenol¹¹⁾.

Keyword: Aeroelastic flutter, Free-play, Limit cycle oscillations, Energy harvesting

1. INTRODUCTION

Aeroelasticity deals with interaction of fluid and structure dynamics when elastic structure is placed in the fluid flow. An interesting dynamics results when the dynamics of fluid flow couples with the dynamics of structure especially as the parameters of the fluid flow and structure change. Stability of the coupled dynamic system depends on several factors. The key parameters affecting stability of structural sub-system include stiffness, damping, magnitude of free-play, onset velocity, and nature of the incident fluid flow. In particular, the nonlinearities in stiffness, damping, and free-play in joints of aeroelastic structure can lead to nonlinear dynamic response that can exhibit behavior ranging from bounded limit cycle oscillations (LCO) to exponentially divergent response³⁻⁴⁾ It was shown recently in^{1,2)} how free-play in control surfaces of aeroelastic lifting surfaces can lead to Hopf bifurcation phenomena with increasing onset velocity. Both analytical and experimental results were given to validate the Hopf bifurcation phenomena. The undesirable coupling between inertia, elasticity, and external aerodynamic forces gives rise to self-exciting destructive, unstable system behavior called flutter. Because of its highly destructive nature, flutter phenomenon has been

¹⁾akelkar@iastate.edu, ²⁾prachi@iastate.edu, ³⁾jeral.vogel.vsiaero@gmail.com

the topic of interest for researchers for long time and yet new discoveries emerge in understanding of flutter. There are several methods and strategies developed to analyze, understand and control flutter¹⁻⁴⁾. The importance of gaining in-depth understanding of physics behind flutter is evident from numerous examples of destruction of property and human lives that have taken place due to flutter-induced divergent instabilities in aircraft, bridges, buildings, and many other structures. This paper focuses on flutter dynamics in lifting airfoils. In the context of lifting airfoils such as wings, tails, and control surfaces mounted on these wings and tails of aircraft one primary contributor to the LCO and diverging behavior of flutter is the presence of free-play at the mechanical joint^{1,2)}. In spite of stringent manufacturing specifications⁵⁾ there always exists some amount of free-play which over time of use keep increasing. Early study done in 1950's⁵⁾ showed connection of free-play to flutter velocity but not until recently when a more in-depth analysis with experimental validation was performed¹⁾ to uncover the underlying dynamics that can explain the dependence of flutter velocity on size of the free-play. There are several other studies that have provided some insights into flutter in general and those are worth reading⁶⁻⁷⁾. However, one important aspect of the flutter dynamics that has not been properly understood and/or investigated is the dynamics of energy transfer or exchange that takes place between two sub-systems – fluid and structure. It is already known that, in the interaction of two sub-system dynamics two aeroelastic modes get coupled and lead to instabilities. The analytical and simulation studies have shown how eigenvalues of linearized system coalesce as onset of flutter happens or how nonlinear stiffness of the spring leads to bifurcation dynamics. To the best of authors' knowledge there is no study that explores dynamics of energy exchange between two sub-systems and how that can be used to our advantage.

This paper attempts to analyze the aeroelastic flutter in the context of energy and the key motivation is to explore how unstable dynamics of flutter, especially, sustained bounded LCO behavior, can be exploited for the benefit rather than controlling it to avoid failures. There exist studies which also focus on the energy recovery from the aeroelastic response of the structure⁸⁻¹⁰⁾ using piezoelectric materials and electrostatic materials but they do not use the free-play induced instability as the source of flutter. This paper specifically focuses on free-play induced flutter (more importantly LCO) and use of advanced magnetostrictive materials to harvest energy in the flow field by converting it into the electric energy. The paper uses an example 2-D aeroelastic system as used in author's previous work²⁾ to gain deeper understanding of energy dynamics as it pertains to the structural sub-system. After establishing closed-form dynamical equation of 2-D airfoil with free-play nonlinearity the parameters of free-play and onset free-stream velocity are tuned to obtain sustained LCO motion. Once the sustained LCO motion is obtained, the total energy variation of the structural sub-system is computed to understand the energy exchange between flow field and structure in each cycle of the LCO. Several simulation plots are presented to explain various points in the time history when energy exchange changes the direction. After deriving total energy fluctuation in LCO cycles the electrical energy that can be potentially extracted using advanced magnetostrictive materials such as Galfenol produced by Etrema¹¹⁾ is computed using magnetostrictive material properties and associated dynamics. Finally, a concept of energy harvesting system architecture that can be used is presented.

Organization of this paper is as follows. Section 2 gives the details of the 2D aeroelastic system modeled with hyperbolic nonlinearity representing free-play in rotational degree of freedom. Section 3 deals

with simulation results. Section 4 establishes energy transfer analysis followed by details about recovery concept presented in Section 5. Section 6 presents some experimental results followed by the discussion on future scope and conclusion.

2. 2D AIRFOIL SYSTEM DEVELOPMENT

A schematic of 2D airfoil with two degrees of freedom, pitch (θ) and plunge (h), is shown in Fig.1(a). This system configuration is used for development of dynamic model and the analysis of aeroelastic response. This 2D configuration is taken from our earlier work.^{2, 12)} It is assumed that the rotational degree of freedom has free-play nonlinearity.

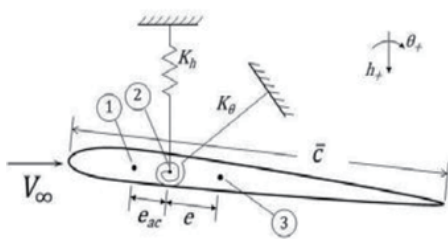


Figure 1(a): Schematic of 2D airfoil system²⁾

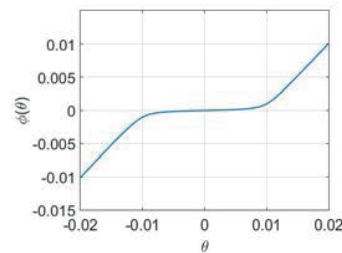


Figure 1(b): Hyperbolic Nonlinearity

The rotational stiffness is modeled by the rotational spring at the elastic axis marked (2) and linear spring is used for plunge motion. The aerodynamic center marked (1) is assumed at quarter chord length where aerodynamic lift and moment are applied. The eccentricity between elastic axis and aerodynamic center is e_{ac} and e shows eccentricity between center of gravity marked (3) and elastic axis. The rotational stiffness with free play is modeled as hyperbolic nonlinearity as shown in fig.1 (b), that asymptotically saturates to a finite linear stiffness. In the earlier work by the authors^{1,2)} various types of free-play nonlinearity models were analyzed including cubic, piecewise linear and hyperbolic functions. This work showed that the hyperbolic function defined below in Eq. 1 gives a better approximation of free-play nonlinearity while providing a unique equilibrium at the origin instead of continuum of equilibria in the case of traditional dead-zone type of representation. The hyperbolic function of the nonlinearity facilitates analytical treatment of stability for linearized dynamics. The hyperbolic function used has the form²⁾:

$$\phi(y) = \text{sgn}(y) \left(\left(\frac{\gamma_1 + \gamma_2}{2} \right) (|y| - \delta) + \left[\frac{(\gamma_2 - \gamma_1)^2 (|y| - \delta)^2 + 4\gamma_1\gamma_2 \delta^2}{4} \right]^{1/2} \right) \quad (1)$$

The nonlinearity representation was first obtained for the first quadrant then completed by joining two antisymmetric hyperbolas in first and third quadrants which are inverted mirror images of each other. The parameters γ_1 , γ_2 , and δ were used to control the shape of the hyperbolic nonlinearity. γ_1 is defined as $\frac{1}{1 + \alpha_\gamma \delta^r}$ Please refer to^{2,12)} for more detailed description of Eq.1 and parameter choices. The dynamics of 2D aeroelastic system under consideration is given by the following set of differential equations:

$$M_s \begin{bmatrix} \ddot{h} \\ \ddot{\theta} \end{bmatrix} + K_s \begin{bmatrix} h \\ \theta \end{bmatrix} = F_{aero} \quad (2)$$

where, M_s , K_s , and F_{aero} represent inertia matrix, stiffness matrix and applied aerodynamic loading vector

on the airfoil. $\begin{bmatrix} \dot{h} \\ \dot{\theta} \end{bmatrix}$ is the vector of translational (plunge) and rotational (pitch) displacement of the airfoil. M_s ,

K_s , and F_{aero} have the form:

$$M_s = \begin{bmatrix} m & -me \\ -me & me^2 + J \end{bmatrix}; \quad K_s = \begin{bmatrix} k_h & 0 \\ 0 & k_\theta \end{bmatrix}; \quad F_{aero} = \begin{bmatrix} -L_a \\ M_a \end{bmatrix}$$

where, m and J are structural mass and inertia, k_h and k_θ are spring stiffness in plunge and pitch motion, and L_a and M_a are total aerodynamic lift and moment acting on the structure. Total lift and moment contributions are determined as:

$$L_a = \bar{q}S(C_{L\alpha}\alpha + C_{L\dot{\alpha}}\dot{\alpha} + C_{Lq}q) \quad (3)$$

$$M_a = \bar{q}S\bar{c}(C_{M\alpha}\alpha + C_{M\dot{\alpha}}\dot{\alpha} + C_{Mq}q) + \bar{q}Se_{ac}(C_{L\alpha}\alpha + C_{L\dot{\alpha}}\dot{\alpha} + C_{Lq}q) \quad (4)$$

Where, \bar{q} is dynamic pressure, S is the plan form area, \bar{c} mean chord length, $C_{L\alpha}$, $C_{L\dot{\alpha}}$, and C_{Lq} are lift coefficients with respect to angle of attack α , angle of attack rate $\dot{\alpha}$, and pitch rate q . Similarly, $C_{M\alpha}$, C_{LM} , and C_{Mq} are corresponding moment coefficients.

Using the definitions,

$$\alpha = \theta + \frac{\dot{h}}{V}; \quad \dot{\alpha} = \dot{\theta} + \frac{\ddot{h}}{V}; \quad q = \dot{\theta}$$

and substituting in the equations (3) and (4), we get

$$L_a = \bar{q}S \left[C_{L\alpha} \left(\theta + \frac{\dot{h}}{V} \right) + C_{L\dot{\alpha}} \left(\dot{\theta} + \frac{\ddot{h}}{V} \right) + C_{Lq} \dot{\theta} \right] \quad (5)$$

$$M_a = \bar{q}S\bar{c} \left[C_{M\alpha} \left(\theta + \frac{\dot{h}}{V} \right) + C_{M\dot{\alpha}} \left(\dot{\theta} + \frac{\ddot{h}}{V} \right) + C_{Mq} \dot{\theta} \right] + \bar{q}Se_{ac} \left[C_{L\alpha} \left(\theta + \frac{\dot{h}}{V} \right) + C_{L\dot{\alpha}} \left(\dot{\theta} + \frac{\ddot{h}}{V} \right) + C_{Lq} \dot{\theta} \right] \quad (6)$$

Rewriting external aerodynamic forces in structural states gives,

$$F_{aero} = M_{app} \begin{bmatrix} \ddot{h} \\ \ddot{\theta} \end{bmatrix} + B_a \begin{bmatrix} \dot{h} \\ \dot{\theta} \end{bmatrix} + K_a \begin{bmatrix} h \\ \theta \end{bmatrix} \quad (7)$$

where,

$$M_{app} = \bar{q}S \begin{bmatrix} \frac{-C_{L\dot{\alpha}}}{V} & 0 \\ \frac{\bar{c}C_{M\dot{\alpha}} + e_{ac}C_{L\dot{\alpha}}}{V} & 0 \end{bmatrix}, \quad K_a = \bar{q}S \begin{bmatrix} 0 & C_{L\alpha} \\ 0 & \bar{c}C_{M\alpha} + e_{ac}C_{L\alpha} \end{bmatrix}$$

$$B_a = \bar{q}S \begin{bmatrix} \frac{-C_{L\alpha}}{V} & -(C_{L\dot{\alpha}} + C_{Lq}) \\ \frac{\bar{c}C_{M\alpha} + e_{ac}C_{L\alpha}}{V} & \bar{c}(C_{M\dot{\alpha}} + C_{Mq}) + e_{ac}(C_{L\dot{\alpha}} + C_{Lq}) \end{bmatrix}$$

Combining equations (2) & (7) yields,

$$(M_s - M_{app}) \begin{bmatrix} \ddot{h} \\ \ddot{\theta} \end{bmatrix} = B_a \begin{bmatrix} \dot{h} \\ \dot{\theta} \end{bmatrix} + (K_a - K_s) \begin{bmatrix} h \\ \theta \end{bmatrix}$$

$$\begin{bmatrix} \ddot{h} \\ \ddot{\theta} \end{bmatrix} = (M_s - M_{app})^{-1} B_a \begin{bmatrix} \dot{h} \\ \dot{\theta} \end{bmatrix} + (M_s - M_{app})^{-1} (K_a - K_s) \begin{bmatrix} h \\ \theta \end{bmatrix} = D \begin{bmatrix} \dot{h} \\ \dot{\theta} \end{bmatrix} + E \begin{bmatrix} h \\ \theta \end{bmatrix} \quad (8)$$

Defining state vector as $x = [h; \theta; \dot{h}; \dot{\theta}]$, the state space representation is obtained as:

$$\dot{x} = \begin{bmatrix} 0 & I \\ E & D \end{bmatrix} x \quad (9)$$

Since nonlinearity is assumed only in the rotational stiffness, the terms involving nonlinearity are separated such as;

$$E_{12NL} = \frac{-V e m}{|(M_s - M_{app})|} K_\theta ; \quad E_{22NL} = \frac{-(V m + C_{L\dot{\alpha}} \bar{q} S)}{|(M_s - M_{app})|} K_\theta \quad (10)$$

The state space representation can be rewritten as:

$$\begin{aligned} \dot{x}_1 &= x_3 \\ \dot{x}_2 &= x_4 \\ \dot{x}_3 &= E_{11}x_1 + (E_{12L}x_2 + E_{12NL}\hat{x}_2) + D_{11}x_3 + D_{12}x_4 \\ \dot{x}_4 &= E_{21}x_1 + (E_{22L}x_2 + E_{22NL}\hat{x}_2) + D_{21}x_3 + D_{22}x_4 \end{aligned}$$

which gives,

$$\dot{x} = \begin{bmatrix} 0 & I \\ E_L & D \end{bmatrix} x + E_{NL}\hat{x}_2$$

where, \hat{x}_2 is now defined in terms of $\phi(\theta)$, a hyperbolic nonlinearity. The state and output equations are:

$$\dot{x} = Ax + B\phi(\theta); \quad y = Cx \quad (11)$$

This analytical model is used for the analysis of the 2D aeroelastic system in the remainder of the paper.

3. SIMULATIONS

The state space equations presented above are solved using Matlab. For simulation results presented in this section the system was excited by using a non-zero initial condition. Table 1 shows the system parameters, nonlinearity parameters, and initial conditions used for simulations.

Table 1: System parameters and initial condition

Parameter	Value	Parameter	Value
Mass, m	4.04 <i>slugs</i>	$C_{L\alpha}$	3.5860
Moment of inertia, J	16 <i>slug.ft</i>	$C_{L\dot{\alpha}}$	0.0230
Chord length, \bar{c}	10 <i>in</i>	C_{Lq}	0.0386
Bending stiffness, K_h	2,500 <i>lb_f/in</i>	$C_{M\alpha}$	2.934
Torsional Stiffness, K_θ	21,000 <i>ft.lb_f/rad</i>	$C_{M\dot{\alpha}}$	-0.0103
Eccentricity, e_{ac}	-0.15 <i>in</i>	C_{Mq}	-0.025
Delta, δ	0.01	γ_2	1
r	100	α_γ	100
Initial Condition ($h, \theta, \dot{h}, \dot{\theta}$)	0.1, 0.05, 0.02, 0.01	Flow velocity	13.3 <i>fps</i>

The plunge and pitch responses are given in Figs. 2(a) and 2(b). As seen in these figures, the system exhibits a response that settles down to a bounded limit cycle for a chosen combination of free stream velocity and free-play. It was shown in earlier work^{1,2)} that the LCO behavior of aeroelastic response lasts over a range of free stream velocities for a given free-play. Fig. 3(a) and 3(b) show the lift and moment time histories for the simulation case.

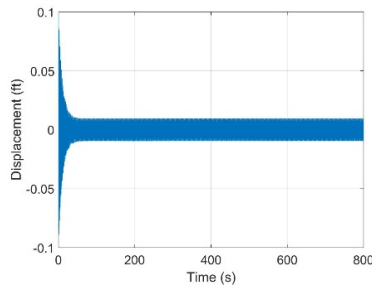


Figure 2(a): Plunge response

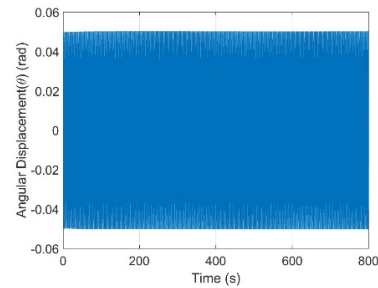


Figure 2(b): Pitch Response

One important point to be noted is that the LCO response will sustain forever as long as the free stream velocity and free-play combination stays the same. That means, from solely structural sub-system's view point there is a continuous cyclic and balanced energy exchange taking place from structural sub-system to fluid sub-system. The idea presented in this paper is to exploit this continuous energy exchange by converting this cyclic energy transfer into useable form of energy such as electrical energy using an efficient transducer mechanism.

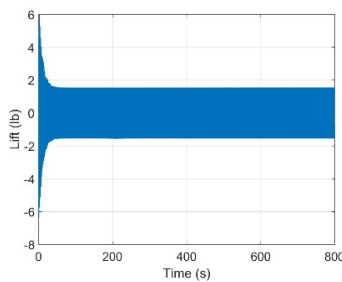


Figure 3(a): Lift

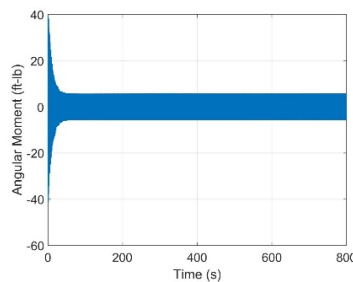


Figure 3(b): Moment

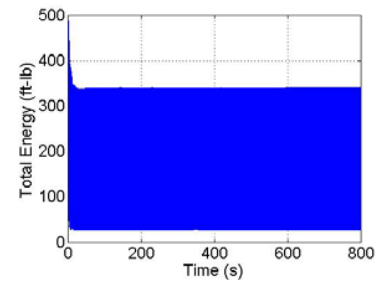


Figure 3(c): Total energy

The next section gives some insights into flutter dynamics from energy viewpoint especially in the case of free-play induced LCO using the 2D example system considered in this paper.

4. ENERGY PERSPECTIVE

In order to assess energy flow into the structure and out of the structure both kinetic and potential energy components of the structural sub-system are computed and depicted in Figs. 4(a) and 4(b). The total energy time history is given in Fig. 3(c). The cyclic variation of energy is evident from the plot. In order to better understand the energy exchange phenomena the time evolution of these energies is plotted for one representative cycle of the response. These plots are given in Figs. 4(a), 4(b), and 4(c), respectively. Figs. 5(a) and 5(b) present plots of lift versus plunge velocity and moment versus pitch rate, respectively. The cyclic nature of these plots is indicative of LCO. The points B, C, D, and E marked on the plots represent points where direction of energy flow is reversed between structural system and flow field. The plot segments AB, CD, and EF indicate parts of the cycle where energy is transferred from structure to the flow field whereas the plot segments BC and DE indicate the parts of the cycle where energy is transferred from flow field to the structure. These energies remain in balance and as a result yield stable but bounded LCO. The system starts with non-zero initial condition given in Tab. 1 and, as a result, it has initial energy state of 39 ft-lb.

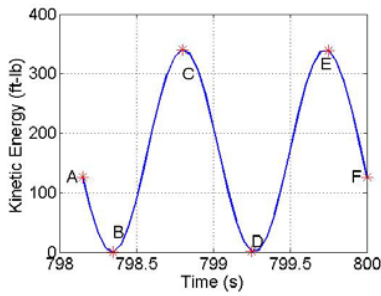


Figure 4(a): Kinetic Energy

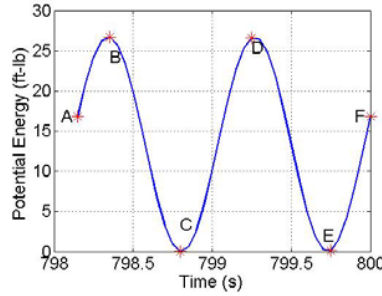


Figure 4(b): Potential Energy

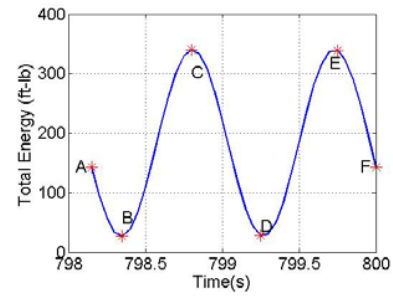


Figure 4(c): Total Energy

As the system is set in motion the energy exchange between two sub-systems evolves. The structural system gains energy from flow-field up to certain point and then the balanced energy exchange sets in about average value of about 156 ft-lb.

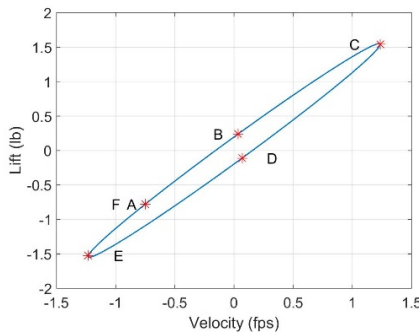


Figure 5(a): Lift versus plunger velocity

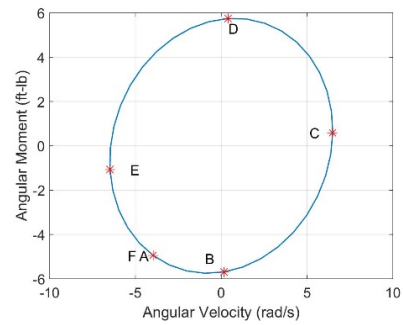


Figure 5(b): Moment versus pitch rate

If the energy flow into the flow field exceeds the flow into the structure the total energy of the structural will dissipate over time due to aerodynamic and structural damping and structure will come to rest. On the other hand if the energy flow into the structure exceeds the energy flow back into the flow field the total energy in the structural will keep increasing leading to divergent response of the structure which will eventually cause failure of the structure.

Experimental Validation:

The above analysis of 2D case extends directly to 3D. The experimental work performed by the authors in their early work¹⁾ showed the pitch-fork bifurcation and LCO phenomena in wind tunnel tests supporting the above analysis. For the sake of completeness some selected results from this earlier testing are presented in Figs 6(a)-6(c). Figure 6a) shows the wind tunnel test article used in¹⁾ which was a close facsimile of the airfoil geometry used in 1950's work⁵⁾.

As seen in the root displacement plot Fig. 6(b) the system settles down to LCO starting from both small and large initial conditions indicating a stable LCO. Fig 6(c) shows the dependence of LCO onset velocity on free-play. For more details on testing please refer to¹⁾. A representative video footage of one of the tests can be seen at <http://youtu.be/Qp2PM6lw5SM> . As seen from the wind tunnel tests there is a wide enough range of free stream velocities and free-play parameter over which one can achieve sustained LCO. The next section presents a concept and proof-of-concept simulations demonstrating how one can exploit the energy absorbed by the structure in cyclic manner from the flow field can be harnessed using magnetostrictive materials.

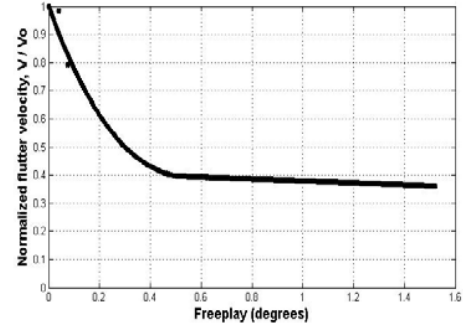
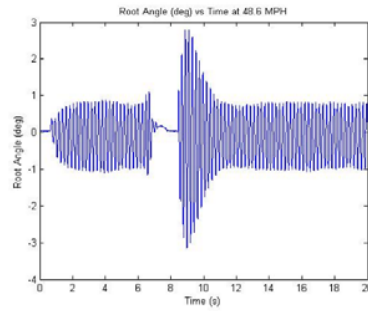


Figure 6(a): Wind tunnel model¹⁾ Figure 6(b): LCO response¹⁾ Figure 6(c): Flutter velocity Vs free-play¹⁾

5. ENERGY HARVESTING FROM SUSTAINED LCOs

This section first presents the model of representative magnetostrictive material and computes the estimates of electrical energy that can be extracted from flow field through structure. While the use of several different types of smart materials, such as, piezoelectric, electrostatic, magnetostrictive, etc. is common, in this paper, we have used an example of a high throughput magnetostrictive material called Galfenol. We will use the published data related to this material for our analysis, more details about both Galfenol and Terfenol-D can be found in ^{11,14}. Magnetostrictive materials responds to the external stresses by changing its magnetic state which can induce voltage in the coil. The study of energy harvesting potential of Terfenol-D and Galfenol is explained in ^{13,14}. Compared to several other magnetostrictive and piezoelectric materials Galfenol provides higher tensile strength and high machinability¹⁰. Depending on the mechanism used for energy harvesting, material with required mechanical properties can be used. Properties of Galfenol used in this work are taken from¹⁰. The governing equation of magnetostrictive material is given as:

$$B = d_{33}^* T + \mu^T H \quad (12)$$

where, B is the magnetic flux density, d_{33}^* is inverse magnetostrictive coefficient, μ^T is magnetic permeability, T is stress and H is the magnetic field. The changing magnetic flux is converted to the useful electrical energy by the following equation governed by Faraday's law of induction for a closely wound coil:

$$V = -NA \frac{dB}{dt} = -Nd_{33}^* A \frac{dT}{dt} \quad (13)$$

This voltage represents an open circuit voltage induced by changing magnetic field. The final output is based on the efficiency of the electric circuit used for further power conversion. For a given system, d_{33}^* is assumed to be equal to d_{33} . Equations 12-13 are simulated in Matlab for the 2D proof-of-concept system under consideration. Figs. 7(a) & 7(b) show the open circuit voltage generated for a given simulation time and in one cycle, respectively, for 100 coils. The alternating nature of the voltage is seen in 7(b).

As stated previously, the LCO onset velocity changes with free-play parameter δ . This property of the system can be used to our advantage by designing a mechanism where we can change the δ and K_θ parameters in real time to maintain LCO motion over a wide range of free-stream velocity. There are several ways in which such mechanism can be designed and built. One such concept is shown in Fig. 8(b) where spar, the primary stress bearing component of the airfoil, is made up of magnetostrictive material like Galfenol or alternately

encased in the outer layer of such material. The airfoil can be built such that the mechanical configuration of the device and hence resulting stiffness and damping properties can be altered in real-time for optimal energy extraction. Fig 7(c) shows that even for reduced flow velocity, LCO can be attained by tuning δ .

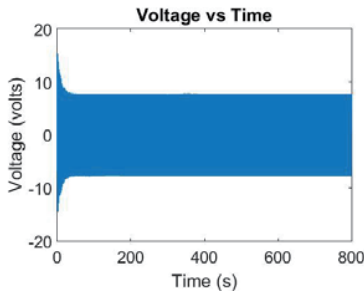


Figure 7(a): Voltage history

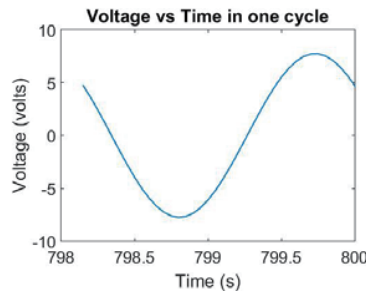


Figure 7(b): Voltage in one cycle

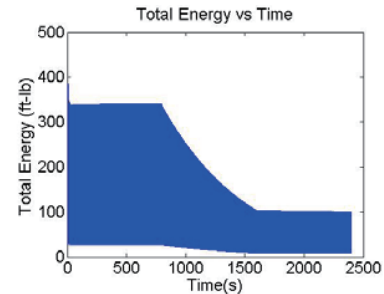


Figure 7(c): LCO behavior

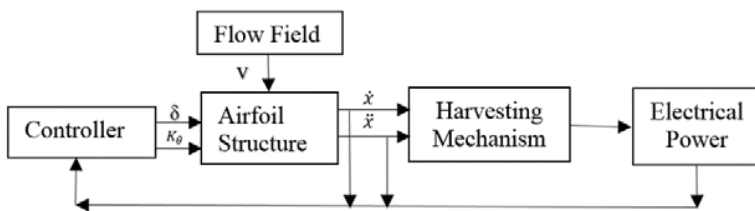


Figure 8(a): Block diagram of the energy harvesting mechanism

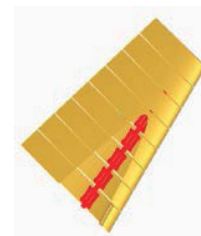


Figure 8(b): Design Concept

The feedback control system block diagram given in Fig. 8(a) represents a possible implementation of energy harvesting control system. Our current work is focused on this very aspect of the research.

7. CONCLUSIONS AND FUTURE WORK

This paper presented an energy-centric perspective on the dynamics of flutter instability phenomena induced by free-play. Flutter has always been considered as an undesirable phenomena in aeroelastic systems and, to a large extent, the research efforts thus far have been in either controlling and/or avoiding the onset of flutter. This paper offers an alternate viewpoint wherein flutter phenomena is considered as a resource for harvesting energy from the flow field. While there is a vast literature on the concept of converting vibrational energy into electricity, obtaining sustained energy generation by capitalizing on a unique free-play induced LCO phenomena taking place in aeroelastic lifting surfaces is innovative and has never been proposed. The authors' future work will address several open issues including designing of most efficient mechanism using appropriate magnetostrictive material, designing robust control system that can achieve sustained bounded LCO performance over wide range of free stream velocities for optimal energy extraction, and extensive experimental testing of this concept.

ACKNOWLEDGMENT

Authors would like to acknowledge VSI Aerospace, Inc., Ames, IA for sharing their wind tunnel testing work and useful discussions. We also acknowledge Etrema for their published data on Galfenol.

REFERENCES

1. C.E. Whitmer, A.G. Kelkar, J. M. Vogel, D. Chaussee, C. Ford and U. Vaidya, “Modelling and characterization of the impact of control surface free play on flutter for an all moving surface”. In proceedings, 2012 American Control Conference, Montreal, QC, pp 5342 – 5347.
2. D. Asjes, A. Diwadkar, U. Vaidya, A. Kelkar, J. M. Vogel, D. Chaussee, “Modeling and Analysis of Rotational Freeplay Nonlinearity of a 2D Airfoil”, 2014 American Control Conference (ACC) June 4-6, 2014. Portland, Oregon, USA, pp. 1162 – 1167.
3. Jeonghwan Ko, Andrew J. Kurdila, and Thomas W. Strganac, “Nonlinear Control of a Prototypical Wing Section with Torsional Nonlinearity”, *Journal of Guidance, Control, and Dynamics* Vol. 20, No. 6, November–December 1997.
4. Jeonghwan Ko and Thomas W. Strganac, “Stability and Control of a Structurally Nonlinear Aeroelastic System”, *Journal of Guidance, Control, and Dynamics* Vol. 21, No. 5, September–October 1998
5. Hoffman, Niles R., and Irvin N. Spielberg. Subsonic Flutter Tests of an Unswept All-Movable Horizontal Tail. No. WADC-TR-54-53. Wright Air Development Center Wright-Patterson AFB OH, 1954.
6. Trickey, Stephen T. Global and local dynamics of an aeroelastic system with a control surface freeplay nonlinearity. Ph.D Thesis, Duke, NC, Publication Number: AAI998918, 2000.
7. Trickey, S. T., L. N. Virgin, and E. H. Dowell. "The stability of limit-cycle oscillations in a nonlinear aeroelastic system." In *Proceedings of the Royal Society of London A: Mathematical, Physical and Engineering Sciences*, vol. 458, no. 2025, pp. 2203-2226. The Royal Society, 2002.
8. Mayuresh J. Patil, “From Fluttering Wings to Flapping Flight: The Energy Connection”, *Journal of Aircraft*, vol 40, No.2 March-April 2003.
9. Mayuresh J. Patil, “Limit Cycle Oscillations of Aircraft due to Flutter-Induced Drag”, 43rd AIAA/ASME/ASCE/AHS/ASC Structures, Structural Dynamics, and Materials Conf. 22-25 April 2002, Denver, CO.
10. Park, Jin-Kyoo, Kyoung-Min Kim, Soon-Dock Kwon, and Kincho H. Law. "An aeroelastic flutter based electromagnetic energy harvester with wind speed augmenting funnel." Online http://eil.stanford.edu/publications/jinkyoo_park/AWAS12.pdf (2012).
11. Source: ETREMA website: <http://www.etrema.com/galfenol/>
12. David C. Asjes, Nonlinear analysis of a two and three degree of freedom aeroelastic system with rotational stiffness free play, Ph.D dissertation, Iowa State University, 2015
13. Olabi, Abdul-Ghani, and Artur Grunwald. "Design and application of magnetostrictive materials." *Materials & Design* 29, no. 2 (2008): 469-483.
14. Staley, Mark E., and Alison B. Flatau. "Characterization of energy harvesting potential of Terfenol-D and Galfenol." In *Smart Structures and Materials*, pp. 630-640. International Society for Optics and Photonics, 2005.

RECENT FINDINGS ON STREAM-WISE FLUIDELASTIC INSTABILITY AND ITS APPLICATION

Tomomichi Nakamura ⁺¹ and Njuki Mureithi ⁺²
⁺¹ Osaka Sangyo University, Daito, Japan
⁺² Polytechnique Montreal, Montreal, Canada

The stream-wise fluidelastic instability of tube arrays has recently been in the limelight due to the practical problem of an event in a steam generator in 2012. Although fluidelastic instability has been studied by many investigators for many years since at least 1968, it has been considered to occur mainly in the transverse direction in steam generators; although the possibility of stream-wise instability may have been anticipated, at least theoretical. Following the confirmation of its existence in the U-bend region of a steam-generator in 2005, some experimental studies have been conducted by a few researchers. This paper summarizes these experimental studies on stream-wise fluidelastic instability of tube arrays with the added aim of providing suggestions for future theoretical and experimental studies on this phenomenon. The work reviewed here may be summarized as follows: (1) Triangular arrays are easily susceptible to stream-wise fluidelastic instability. The same instability is not observed in square arrays, although the transverse fluidelastic instability is observed in both arrays. (2) The number of adjacent flexible cylinders plays an important role; for instance, a single flexible cylinder is found to be stable in the stream-wise direction even in triangular arrays. On the other hand tests show stream-wise instability even in the case of non-adjacent (separated) flexible cylinders. (3) Some experimental tests show the existence of stream-wise instability in two-phase flow, but other tests in water flow show no instability. In air tests stream-wise fluidelastic instability occurs easily. In the last part of this paper, an attempt to generate power by the stream-wise fluidelastic instability is introduced. While it is not considered enough for practical use, the results do confirm the existence of a limit cycle and hence the possibility of energy extraction from the flow.

Keyword: Fluidelastic Instability¹, Stream-wise Instability², Power Generation³

1. INTRODUCTION

Fluidelastic vibration of tube arrays subjected to cross-flow is a kind of flutter phenomenon which has been studied by investigators for many years since 1966¹⁾. It has been considered to occur mainly in the transverse direction of the flow, although the possibility of stream-wise instability may have been anticipated²⁾. The possibility of stream-wise fluidelastic instability can be anticipated from the fact that the motion of tubes, when they are unstable, sometimes shows a figure-of-eight orbit. In addition, the first paper on fluidelastic vibrations describes stream-wise fluidelastic instability³⁾, not transverse direction vibrations. Measured data of the fluidelastic fluid forces had also indicated the possibility of stream-wise fluidelastic instability²⁾. Despite the above information, fluidelastic vibration has been considered to occur mainly in the direction transverse to the flow. This view has been reasonably and generally accepted for the design of many heat exchangers. Steam generators for PWR type nuclear power plants in particular, consist of U-bend tubes which can easily move in the transverse direction. Due to this the tubes are supported with anti-vibration bars.

The stream-wise fluidelastic instability of tube arrays has recently been the focus of interest due to the practical problem related to an event in a steam generator in 2012⁴⁾. However, even after the finding of its existence in the U-bend region in 2005⁵⁾, experimental studies have been conducted only by a few researchers.

⁺¹t-nak@mech.osaka-sandai.ac.jp, ⁺²njuki.mureithi@polymtl.ca

This is because anti-vibration bars in the U-bend region are considered effective in the in-plane direction, which corresponds to the stream-wise direction, due to the friction forces at the anti-vibration bars.

2. EXPERIMENTAL STUDIES

Two groups have conducted and reported experimental work on stream-wise fluidelastic instability in recently published papers. The first one is the Canadian group and the second is the Japanese group. The authors of this paper belong in each group separately. This paper therefore covers all reported information on stream-wise fluidelastic instability.

As mentioned above, cylinder orbits, during instability, sometimes contain motion in both inflow and transverse directions. However, in this case, it is not possible to separate the purely stream-wise direction component. The tests reported below are designed to separate the phenomenon in the two directions.

2.1 Tests in Canada

(1) U-bend two-phase flow test⁵⁾

The AECL group (Janzen et al.) published their U-bend model tests using air-water cross flow in 2005. Fig.1(a) shows the test facility, where the flow traverses part of the U-bend tube bundle (partial admission). Fig.1(b) shows the tube array which has a parallel triangular geometry of $P/D=1.5$. Test results for the stream-wise (in-plane) direction show fluidelastic instability only in the case of liquid flow as shown in Fig.1(c). No instability has been observed for two-phase flow;(perhaps due to the lower maximum velocity tested at AECL compared to the tests by Violette et al. presented below). In the same test apparatus, fluidelastic instability (in the transverse direction) occurs at about half the flow velocity of that in Fig.1(c); but the frequency is 10Hz in the out-of-plane direction and 25Hz in the in-plane direction. It is not easy to directly derive detailed information from this test. However, the test suggests the possibility of stream-wise fluidelastic instability even in the U-bend region of stream generators; the tests that follow are influenced by this result.

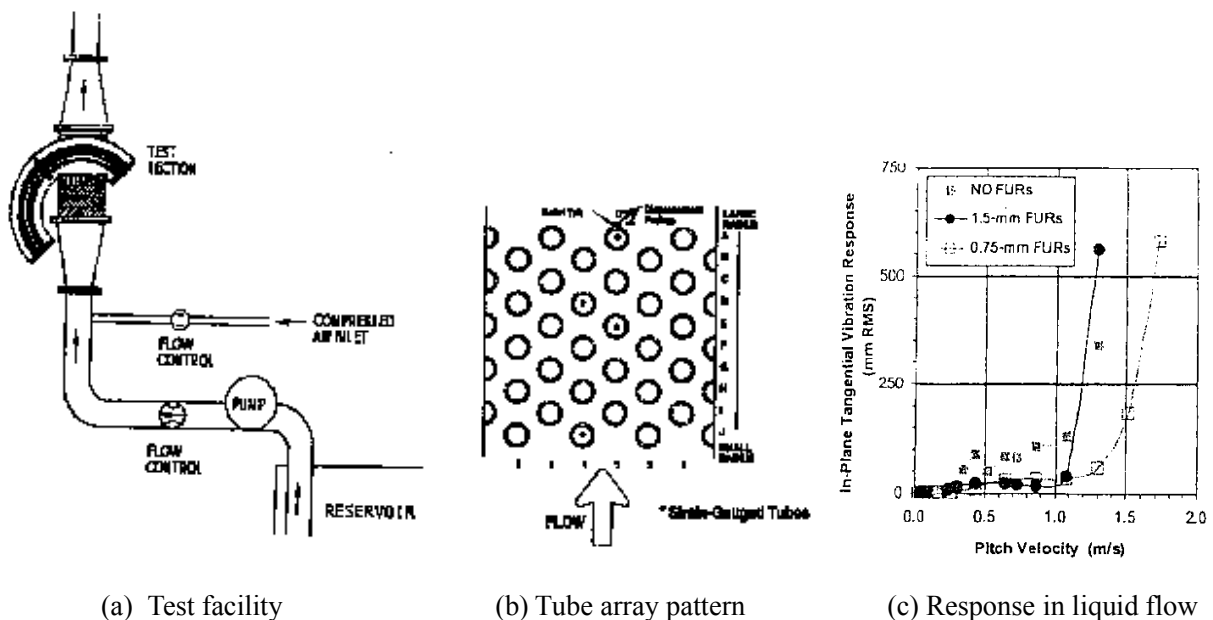


Figure 1 Test equipment and the main results of AECL group⁵⁾

(2) Two-phase flow test by Violette et al.⁶⁾

Violette et al. have done tests on a parallel triangular array of $P/D=1.5$ using air-water two-phase flow in 2006. As shown in Fig.2(a), the array consisted of straight rigid cylinders of 189mm in length supported by rectangular rods in a cantilever configuration. In the tests, the number and the position

of flexible tubes were the parameters; flexible tubes are marked in the four configurations of Fig.2(a). The case of a single flexible tube in tube array, which corresponds to the first pattern “A” in Fig.2(a), shows no instability. On the other hand the two, second “B” and fourth “D”, patterns in Fig.2(a) undergo instability in the stream-wise direction as shown in Fig.2(b) and(c), respectively. However, the case of single flexible column, pattern “C” in Fig.2(a), does not undergo instability similarly to the single flexible cylinder case in Fig.2(a). This is very different from the air tests described later.

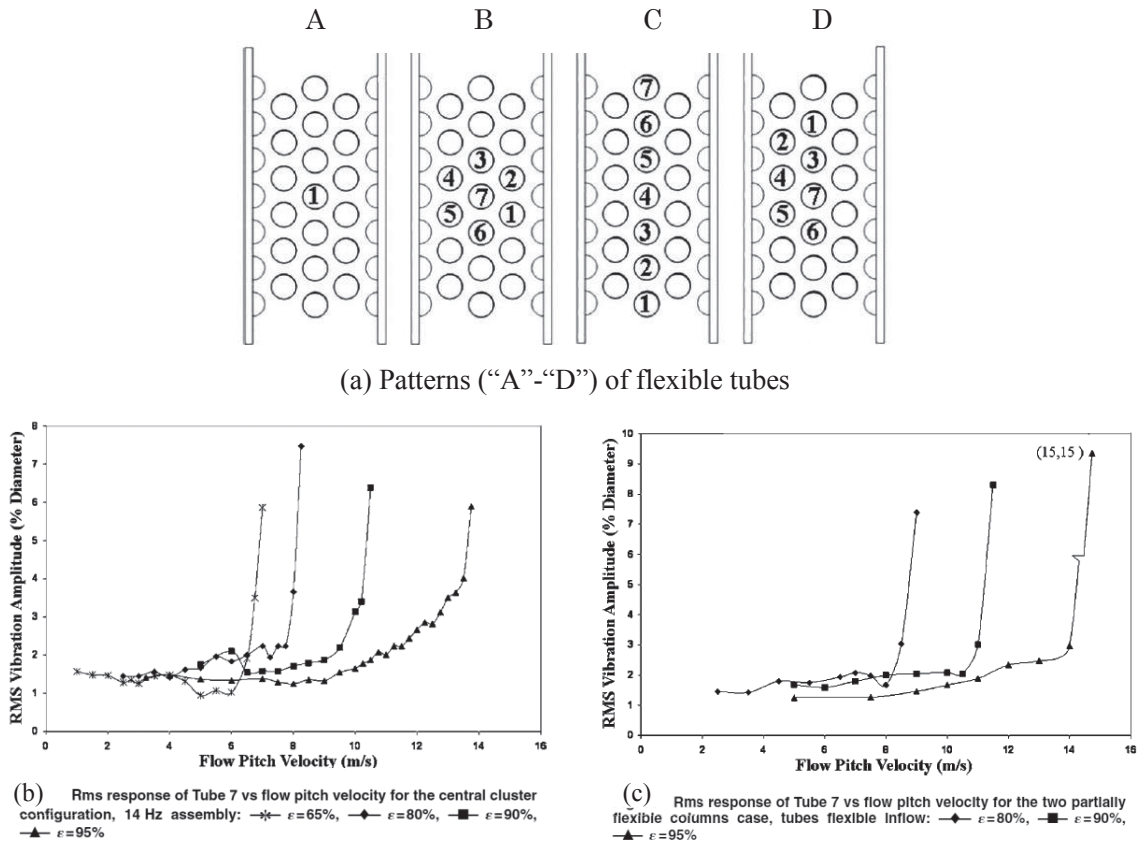


Figure 2 Two-phase flow test of parallel triangular array⁶⁾

(3) Air flow test by Khalvatti et al.⁷⁾

These tests were conducted in a wind-tunnel in 2010. Based on the above results, the positions of the flexible tubes and their number was tested for three cases as shown in Fig.3(a)-(c). However, the pitch to diameter ratio $P/D=1.37$ in this test. The flexibility direction of tubes relative to the flow was varied in four patterns; only two of the patterns are introduced in this paper as shown in Fig.3(d) & (e). Comparison between the transverse direction and the stream-wise direction can therefore be done. Fig.4 shows a comparison of the two different flexibility directions for the fully flexible array pattern (a) in Fig.3. The tubes become unstable in both directions, however, instability in the transverse directions occurs at roughly half the critical velocity for the streamwise instability. The case of three flexible columns (b), in Fig.3, shows a similar trend. The critical flow velocities are 5.1m/s in the transverse direction and 9.2m/s in the stream-wise direction. A similar trend is also observed in the case of the flexible cluster (c), in Fig.3.

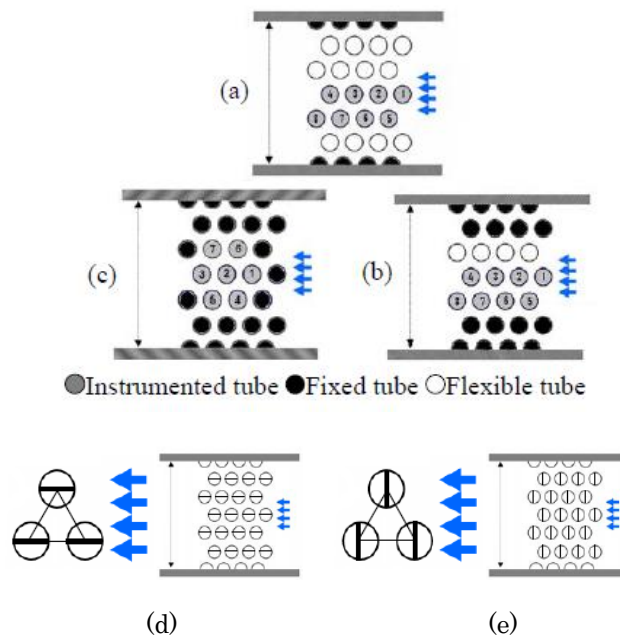
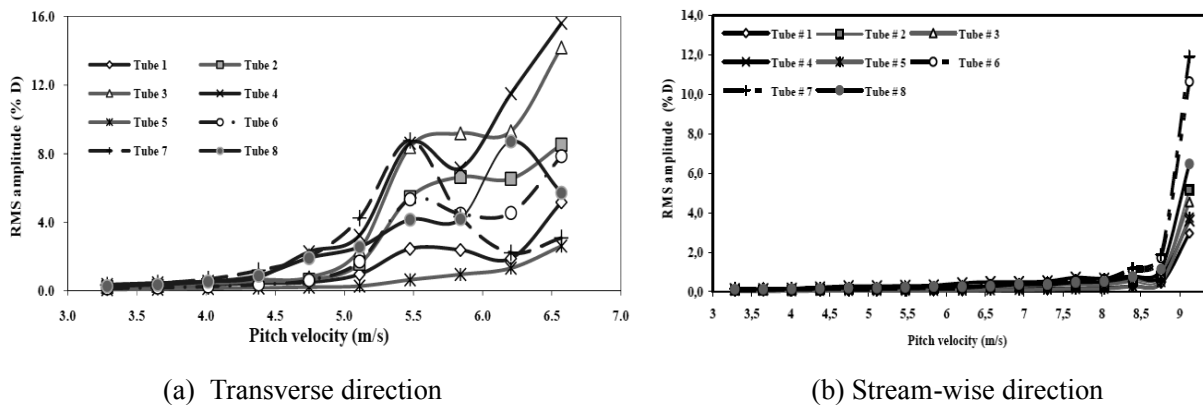


Figure.3 Air flow test configuration and tube flexibility direction ⁷⁾



(a) Transverse direction

(b) Stream-wise direction

Figure 4 Tube responses for the fully flexible array ⁷⁾

2.2 Tests in Japan

(1) Water loop test ⁸⁾

Inspired by the report by Janzen et al. ⁵⁾, a test program using a water-flow loop has started in 2010, supported by a Japanese government fund. Tests were done using the facility shown in Fig.5 ⁸⁾. Different arrays, including the parallel triangular array of P/D=1.2 and the square array, have been tested. However, no unstable vibration has been observed, mainly due to the strong drag forces in water flow. At first, the test cylinders were supported as cantilevers. Later supports were changed to plates fixed at both ends as shown in Fig.5(b). However, again, this configuration showed a different problem: Due to the strong drag force, the natural frequency increased with increasing drag-induced tension force in the thin support plates ⁹⁾.

(2) Air flow tests on a parallel triangular array ¹⁰⁾

As the above water test did not give any instability results, the test working fluid was changed to air flow. Fig.5 shows the air-flow test facility. As shown in the figure, four flexible cylinder patterns were tested: fully flexible, flexible cluster, flexible column and a single flexible cylinder in the array. The

cylinders were 20mm in diameter. Four pitch-to-diameter ratios (P/D) were investigated, $P/D=1.2$, 1.3, 1.4 and 1.5. Fig.6 shows the test results for a typical case. For all patterns, no instability has been observed in the case of a single flexible cylinder in the array in the stream-wise direction, although instability in the transverse direction did occur, except for the case of $P/D=1.2$. Similarly the critical flow velocity in the transverse direction was found to be lower than that in the stream-wise direction except for the $P/D=1.2$ case. The difference in critical velocity was found to depend on the number of flexible cylinders and their position in the array. There is an important difference from the result of the Canadian test for the flexible column. For this case no instability was found in the Canadian tests while instability is observed in Japan. Note, however, that airflow tests in Canada also showed streamwise instability for the single flexible column.

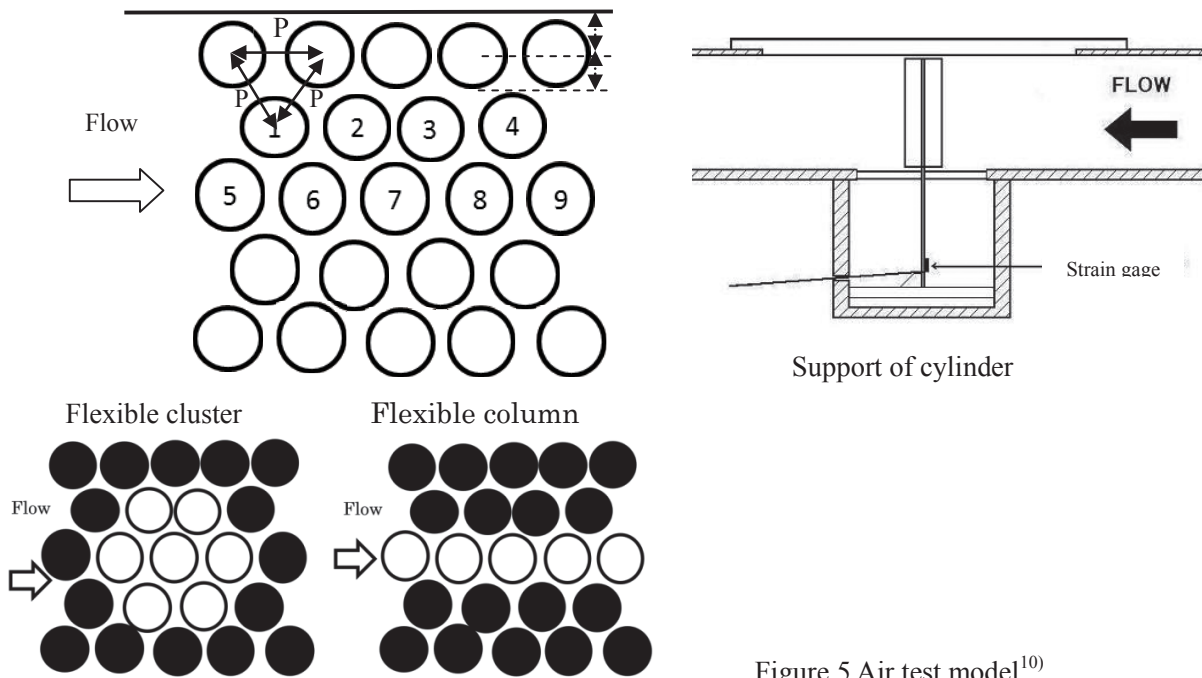


Figure.5 Air test model¹⁰⁾

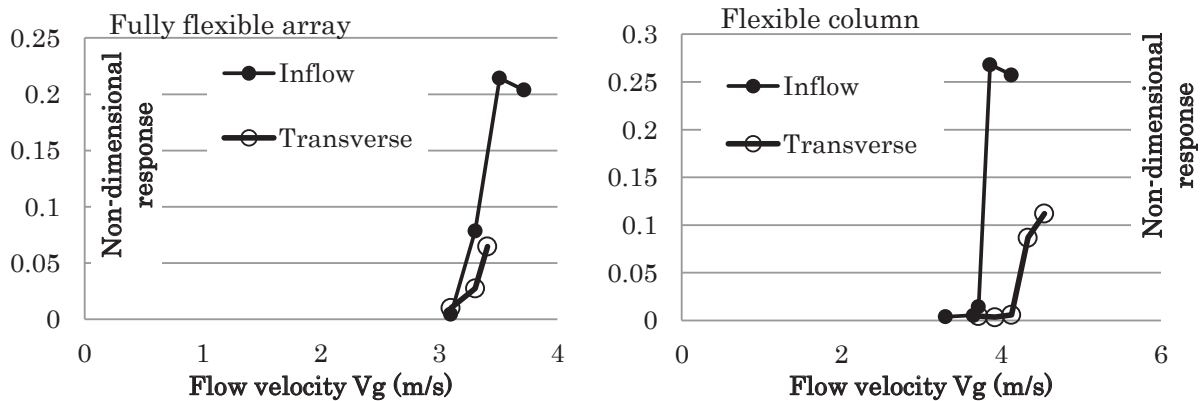


Figure 6 Response for $P/D=1.2$ ¹⁰⁾

(3) Air flow test for the square array¹¹⁾

The square array cylinder bundle was also tested in air flow using the same test facility of Fig.5. The test configurations are shown in Fig.7. Similarly to the above tests on triangular arrays, the pitch-to-diameter ratio was varied in four patterns having, $P/D=1.2, 1.3, 1.4$ and 1.5 . Four possible cases of the number and position of the flexible cylinders were tested for each P/D . However, no clear streamwise instability has been observed in this series of tests. Yet for this square array, cylinders easily become unstable in the transverse direction. Due to the strong instability in this direction, cylinders sometimes show a similar behavior in the stream-wise direction; however this is considered to be due to the effect of the unstable vibration of the upstream cylinders in the transverse direction.

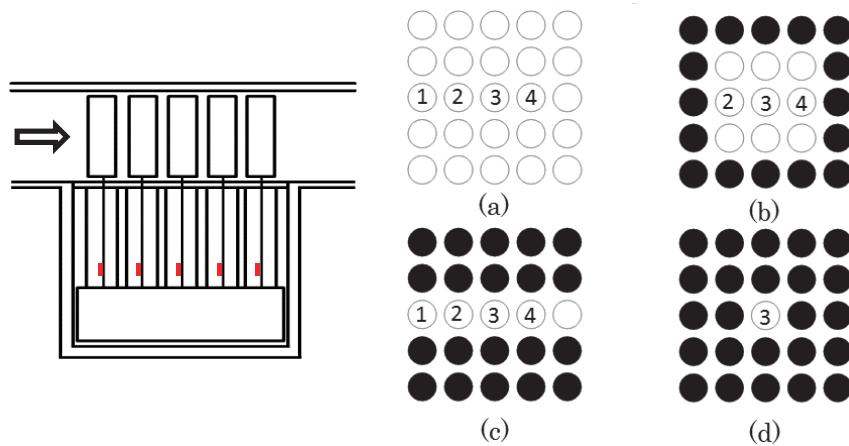


Figure 7 Test model for square array¹¹⁾

(4) Small air flow test for parallel triangular array¹²⁾

Fig.8 shows an additional result from the power generation test described below. Part of this study is included here to convey some important information. The pattern of the flexible cylinders is shown in Fig.8(a). Two flexible cylinders (I & II) with installed magnets are set separated by a rigid cylinder between them as shown in Fig.8(b). Even in this case, fluidelastic instability has been observed.

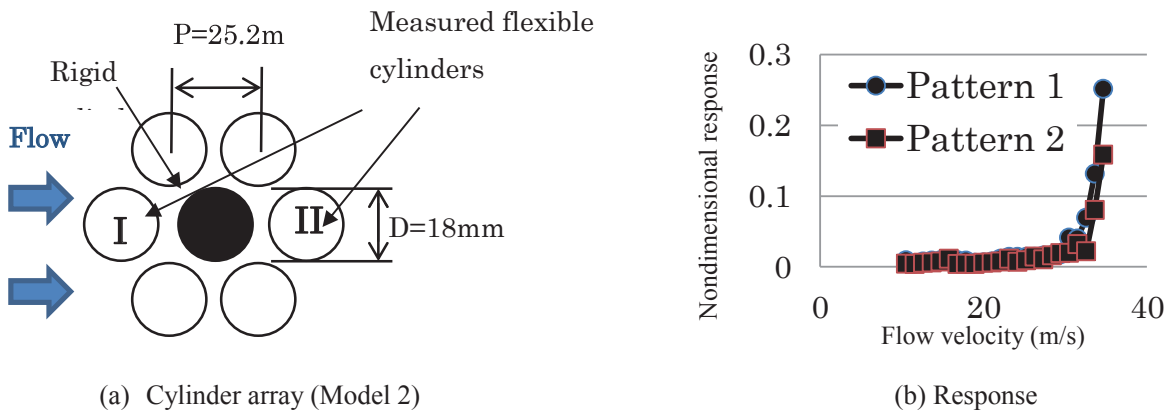


Figure 8 Two power generating cylinders¹²⁾

3. POWER GENERATION ATTEMPT

The stream-wise fluidelastic instability seems like a potentially a good source of power because the

unstable vibrations extract energy from the exciting fluid force, and the stream-wise movement of the cylinder has considerably less effect on the constant fluid flow than the transverse direction motion during instability. The test presented here is based on this idea¹³⁾. Fig.9 shows the test equipment of the power generation setup. A magnet is installed at the top of the moving cylinder and moves inside a coil, where the electric power is produced with this electric-magnetic system. Three positions of the magnet in the coil were considered, but the most interesting result was the case with the magnet set just 0mm from the coil. Fig.10 shows the result for this case. A clear limit cycle trend is observed. However, the obtained electricity is very small, showing that the setup is not enough as a new technology to produce the power.

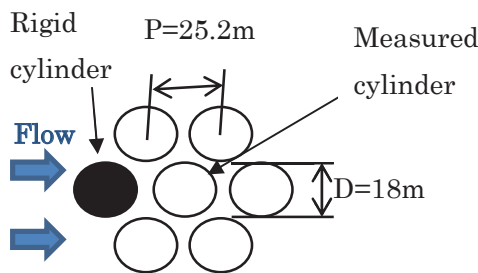
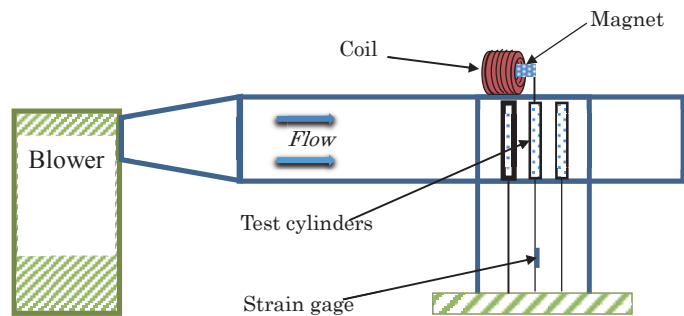
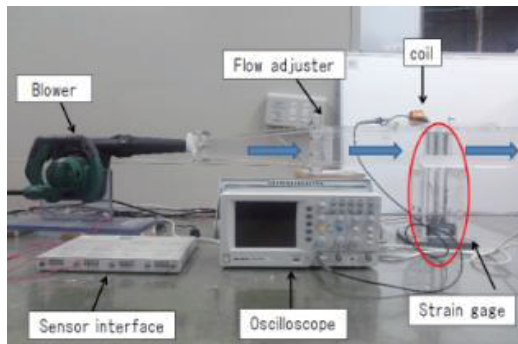
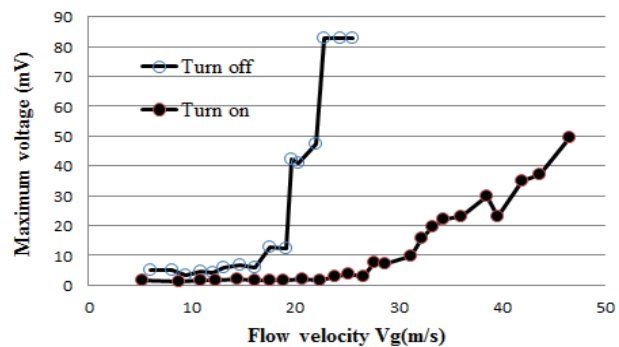
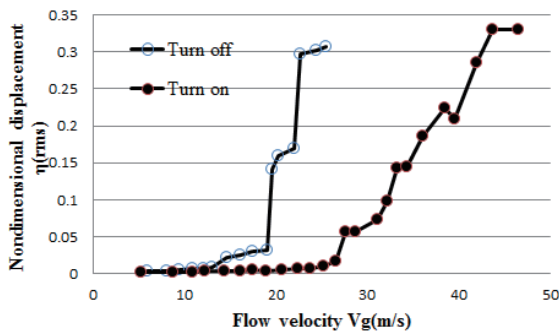


Figure 9 Test facility for power generation¹³⁾
(Model 1)



(a) Response

(b) Voltage

Figure 10 Measured typical results¹³⁾

4. DISCUSSION

It is important, at present, to summarize the results obtained from the above tests to get some insight into the mechanism of stream-wise fluidelastic instability. Table 1 shows a summary of the test results. Despite some discrepancies among the tests, the following can be concluded from these data:

- (1) Triangular arrays are easily susceptible to stream-wise fluidelastic instability, but the same instability is hardly observed in square arrays. The transverse fluidelastic instability is, however, observed in both arrays.

Table 1 Summary of obtained results

Tube Array	P/D	Flexible Tube	Fluid	$K_{\text{Transverse}}$	$K_{\text{Stream-wise}}$
Parallel triangular	1.5	Single tube in array	Two-phase (80% void fraction)	5.9	None (stable)
		Fully flexible		5.2	8.1
		Cluster tubes in center		5.6 (axisymmetric)	8.0
		Single column		5.4 (axisymmetric)	None (stable)
		Two columns		6.1 (axisymmetric)	8.4
Parallel triangular	1.37	Single tube in array	Air	9.6	None
		Fully flexible		3.8	7.1
		Cluster tubes in center		4.7	8.0
		Three columns		4.1	7.4
Several patterns	1.2	Fully flexible	Water	Depend	None
Parallel triangular	1.2	Single tube in array	Air	None	None
		Fully flexible		2.71	2.40
		Cluster tubes in center		3.17	2.65
		Single column		3.29	3.45
	1.3	Single tube in array		3.35	None
		Fully flexible		2.90	3.18
		Cluster tubes in center		3.31	3.47
		Single column		3.32	3.74
	1.4	Single tube in array		4.85	None
		Fully flexible		3.09	3.93
		Cluster tubes in center		3.50	4.82
		Single column		3.52	3.93
	1.5	Single tube in array		5.48	None
		Fully flexible		3.64	4.27
		Cluster tubes in center		4.56	6.96
		Single column		4.29	12.66
Square	1.2-1.5	All the above condition	Air	2.80 – 15.22	None
Parallel triangular	1.4	Two separate cylinders	Air	Not measured	22.4 – 24.8

- (2) The number of adjacent flexible cylinders plays an important role. A single flexible cylinder hardly becomes unstable in the stream-wise direction even in triangular arrays. On the other hand tests show stream-wise instability even in the case of non-adjacent (separated) flexible cylinders.
- (3) Some experimental tests show the existence of stream-wise instability by two-phase flow, but other

tests in water flow show no instability. In air tests stream-wise fluidelastic instability occurs easily.

Some preliminary theoretical work has been done in Canada. In principle, streamwise fluidelastic instability is no different from its transverse direction counterpart hence existing models are applicable with appropriate considerations and inputs. The quasi-static model has been employed by Olala and Mureithi¹⁴⁾ to investigate the streamwise instability. Fig.11 shows a comparison between the predicted critical velocity and the velocity measured by Violette et al.⁶⁾. The results are for a 7-tube flexible cluster in the parallel triangular array of spacing $P/D=1.5$ subjected to two-phase flow. The quasi-static analysis prediction is quite good for a wide range of void fractions. The results suggest that the streamwise fluidelastic instability is a stiffness-controlled instability. This may also explain why a single flexible tube is found to be stable due to lack of cross-coupling.

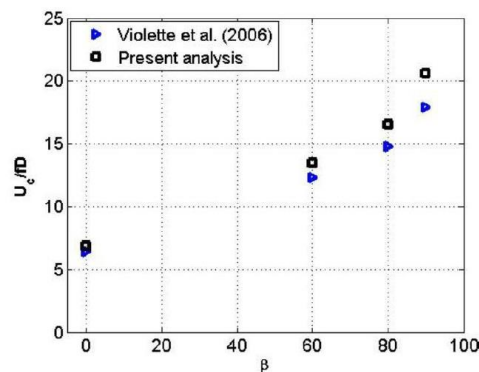


Figure 11 Quasi-static model prediction compared with experiments for two-phase flow¹⁴⁾

The absence of streamwise fluidelastic instability for the inline array suggests that coupling through the cylinder wakes alone is perhaps not sufficiently strong to cause instability. Destabilizing forces would be generated if relative tube displacements led to significant changes in cylinder drag. This seems not to happen for the inline array. For the parallel triangular array, cross-coupling between tubes in neighboring columns is found to be important. The data of Olala and Mureithi¹⁴⁾ confirm this. Such coupling can, however, be expected to be significantly weaker in the inline array thus possibly weakening the stiffness controlled instability mechanism. This is only a hypothesis which needs to be verified.

5. CONCLUSIONS

We've presented some results which give an idea of the limiting conditions for streamwise fluidelastic instability. This phenomenon can be estimated using equations similar to those for the transverse instability. However, currently models are not developed enough to set a new guideline. The existing data confirm the fact that the strong coupling of adjacent cylinders, including the effect from cylinders at the transverse position, is a must for the occurrence streamwise fluidelastic instability. Further studies on this issue are required, and this is ongoing.

Initial results based on the quasi-static model seem to confirm the experimental observation that multiple tubes are needed for streamwise fluidelastic instability. This strongly supports the hypothesis of a stiffness-controlled fluidelastic instability. Much more work however remains to be done.

REFERENCES

- 1) M.P.Paidoussis, S.J.Price, E.de Langre, 2011, "Fluid-Structure Interactions".
- 2) Zhu,S., Cai,Y., Chen,S.S., 1995, "Experimental Fluid-Force Coefficients for Wake-Induced Cylinder Vibration", *Journal of Engineering Mechanics*, 121(9), pp.1003-1015.
- 3) Roberts,B.W., 1966, "Low frequency, aeroelastic vibrations in a cascade of circular cylinders", No.4, *Mechanical Engineering Science Monograph*, pp.1-29.
- 4) Southern California Edison, 2012, "San Onofre Nuclear Generating Station Unit 2 Return to Service Report", Web on NRC, pp.1-54.
- 5) Janzen,V., Hagberg,E.G., Pettigrew,M.J., Taylor,C.E., 2005, "Fluidelastic Instability and Work-Rate Measurements of Steam-Generator U-Tubes in Air-Water Cross-Flow", *ASME's Journal of Pressure Vessel Technology*, 127, pp.84-91.
- 6) Violette,R., Pettigrew,M.J., Mureithi,N.W., 2006, "Fluidelastic Instability of an Array of Tubes Preferentially Flexible in the Flow Direction Subjected to Two-Phase Cross Flow", *ASME's Journal of Pressure Vessel Technology*, 128, pp.148-159.
- 7) Khalvatti,A., Mureithi,N.W., Pettigrew,M.J., 2010, "Effect of Preferential Flexibility Direction on Fluidelastic Instability of a Rotated Triangular Tube Bundle", *ASME's Journal of Pressure Vessel Technology*, 132, pp.041309-1-14.
- 8) Nakamura,T., Nishimura,K., Fujita,Y., Kohara,C., 2011, "Study on in-flow vibration of cylinder arrays caused by cross flow", *Proceedings of the ASME's Pressure Vessels & Piping Conference*, PVP2011-57068, pp.1-8.
- 9) Nakamura,T. Mureithi,N., 2013, "Response of a non-linearly supported cylinder in an array subjected cross-flow", *Proceedings of 15th Asia Pacific Vibration Conference*
- 10) Nakamura,T., Fujita,Y., Sumitani,T. 2014, "Study on In-Flow Fluidelastic Instability of Triangular Tube Arrays Subjected to Air Cross Flow", *ASME's Journal of Pressure Vessel Technology*,
- 11) Nakamura,T. Hagiwara,S. Yamada,J. Usuki,K. 2015, "Investigation of In-Flow Fluidelastic Instability of Square Tube Arrays Subjected to Air Cross Flow", *Proceedings of the ASME's Pressure Vessels & Piping Conference*, PVP2015-45091, pp.1-9.
- 12) Nakamura,T. Sumitani,T., Yamada,J., 2015, "Study on power generation with in-flow fluidelastic instability", *Proceedings of 16th Asia Pacific Vibration Conference*, pp.1-7.
- 13) Sumitani,T., Hagiwara,S., Nakamura,T. 2014, "Study on Power generation using unstable energy by In-flow Fluidelastic Vibration", *Proceedings of the ASME's Pressure Vessels & Piping Conference*, PVP2014-28244, pp.1-7.
- 14) Olala, S., Mureithi, N.W., 2014, "Streamwise fluidelastic instability of tube arrays in two-phase crossflow", *Proceedings of the International Mechanical Engineering Congress (IMECE)*, paper IMECE2014-39234.

DYNAMIC BEHAVIOR OF PARKED WIND TURBINE AT EXTREME WIND SPEED

Yoshitaka TOTSUKA⁺¹, Hiroshi IMAMURA⁺² and Anders YDE⁺³
^{+1,+2}Wind Energy Institute of Tokyo Inc., Tokyo, JAPAN
⁺³Technical University of Denmark, Roskilde, Denmark

In wind turbine design process, a series of load analysis is generally performed to determine ultimate and fatigue loads under various design load cases (DLCs) which is specified in IEC 61400. These design load scenario covers not only normal operating condition but also startup, shutdown, parked and other scenario which is assumed to occur during the expected lifetime of wind turbine. This research focus on vibration problem under 50-year storm conditions while rotor is parked and blades are feathered. In this parked scenario, effect of a wind direction change of up to ± 180 degrees for both cases of standstill and idling is analyzed by time domain simulations using two different coupled aero-hydro-servo-elastic codes. Trend in modern wind turbines is development of bigger, lighter and more flexible rotors where vibration issues may cause aero-elastic instabilities which have a serious impact on the ultimate loads. The DTU 10MW Reference Wind Turbine (RWT) is chosen as wind turbine model in this research.

Keyword: Wind turbine design¹, Aero-elastic simulation², Fluid-structure interaction³

1. BACKGROUND AND INTRODUCTION

Among Renewable energy source, especially offshore wind energy gains prominence because energy potential of offshore wind is abundant in Japan. Toward widespread use of offshore wind energy in Japan, accurate computation of coupled wind turbine structural dynamics, aerodynamics, hydrodynamics, mooring dynamics with control algorithms is highly significant for design optimization and certification process of offshore wind turbine. In the design process, all of design load cases (DLCs) which are prescribed in IEC61400-3¹⁾ have to be analyzed for load estimation in order to design the wind turbine components. In some wind turbine designs, the maximum ultimate load is expected for some components to occur under extreme wind speed condition in DLC6.x, even though wind turbine is parked with the rotor brake or idling to minimize loads. On top of that, effect of a wind direction change of up to $\pm 180^\circ$ is investigated in DLC6.2, since loss of electrical power network at an early stage in a storm is assumed. Figure 1 shows an example yaw misalignment case of 90 degrees to realize the difficulty and challenge in this analysis. Above operating wind speed, wind turbine system is feathering the blades to avoid the unwanted aerodynamic load as it is assuming the rotor confronts wind direction. Besides, in this loss of the electrical power network case, extremely strong wind is coming to the parked rotor from lateral direction and position of each blades try to balance with large vibration due to the strong turbulent inflow and their deflection. As angle of attack is around 90 degrees with large fluctuation due to the turbulent inflow and deflection of blade, the lift and drag coefficient of airfoil data in this angle of attack region are associated with high uncertainties and generally unavailable. Furthermore as the flow is largely separated from whole blade, special care for the wake is also needed. Systematic approach is also required for wind turbine designer to solve this issue.

In this research, authors investigated vibration problem of parked land-based wind turbine by using the DTU 10MW RWT²⁾ under extreme wind speed. Time domain simulation is carried out by coupled structural, hydrodynamic, control and aerodynamic analysis codes HAWC2³⁾ and FAST^{4), 5)}. HAWC2 is developed by the Technical University of Denmark and FAST is developed by National Renewable Energy Laboratory.

⁺¹totsuka@windenergy.co.jp, ⁺²imamura@windenergy.co.jp, ⁺³anyd@dtu.dk

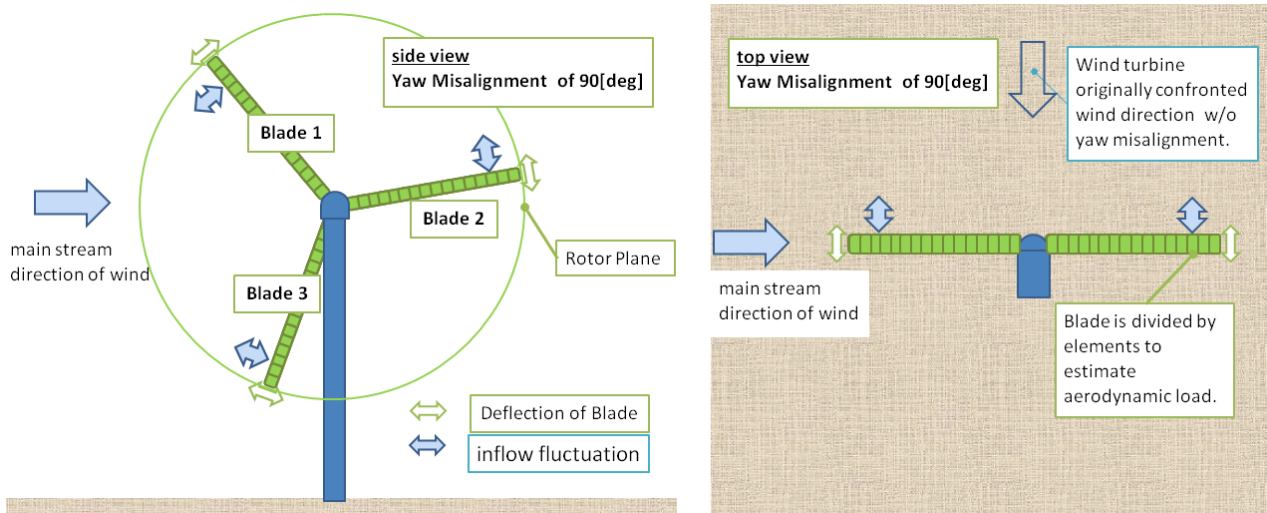


Figure 1: Schematics of a yaw misalignment case of 90 degree

2. DTU 10MW RWT MODEL

In terms of the trend of modern wind turbines, DTU 10MW RWT model (Figure2) is used in this research. Though the biggest size of wind turbine is 8MW for the time being, modern wind turbine is growing its capacity and appearance of 10MW wind turbine is matter of time. DTU 10MW RWT model was designed for offshore site for an IEC class 1A wind climate and was in general a traditional three-bladed, upwind wind turbine by the Technical University of Denmark in the Light Rotor Project. As the focus in the Light Rotor project was the rotor design, the structural definition of DTU 10MW RWT except of the blades was obtained by upscaling the artificial NREL 5MW reference turbine⁶⁾ by applying the classical similarity rules. An overall description of the wind turbine is seen in Table 1. Major change from NREL 5MW is as follows.

- The IEC class changed, because the DTU 10MW RWT is made for an offshore wind climate.
- The hub height is lower, because a shorter tower is possible offshore.
- The drivetrain concept changed from a high speed to a medium speed.
- The DTU 10MW blades have pre-bend to ensure tower clearance.

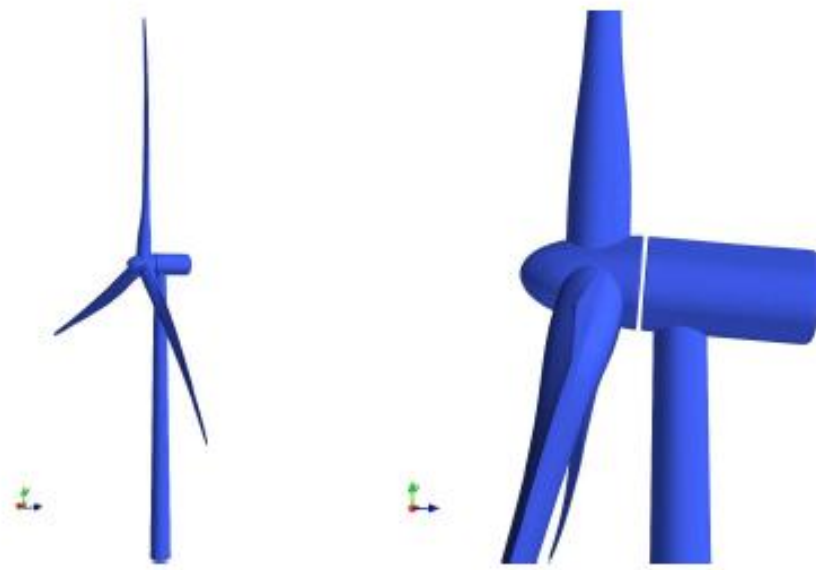


Figure 2: DTU 10 MW RWT MODEL²⁾

Table 1: Specification of DTU 10 MW Reference Wind Turbine²⁾

Description	Value
Rating	10MW
Rotor orientation, configuration	Upwind, 3 blades
Control	Variable speed, collective pitch
Drivetrain	Medium speed, Multiple stage gearbox
Rotor, Hub diameter	178.3m, 5.6m
Hub Height	119m
Cut-in, Rated, Cut-out wind speed	4m/s, 11.4m/s, 25m/s
Cut-in, Rated, Cut-out rotor speed	6RPM, 9.6RPM
Rated tip speed	90m/s
Overhang	7.07m, 5°, 2.5°
Pre bend	3m
Rotor mass	229ton(each blade mass ~41tons)
Nacelle mass	446tons
Tower mass	605tons

3. ANALYSIS CONDITION

To investigate vibration issue while wind turbine is parked with the rotor brake or idling, analysis condition of DLC6.2 was chosen and carried out. In DLC 6.2 extreme wind speed model (EWM) with full range of yaw misalignment shall be considered. Since a loss of the electrical power network at an early stage in a storm containing the extreme wind situation, shall be assumed. Unless power back-up is provided for the control and yaw system with a capacity for yaw alignment for a period of at least 6 h , the effect of a wind direction change of up to $\pm 180^\circ$ shall be analyzed.

To analyze the cases for the full range of yaw misalignment, DLC6.2 by discrete yaw angles in increments of 30° (i.e., -150° , -120° , ..., 180°) is considered in the simulations. Other analysis condition is summarized in Table 2. In this research, a land-based version of the wind turbine used in order to simplify the interpretation of analysis result, though DTU 10MW RWT model is designed for an offshore wind site.

We carried out DLC6.2 analysis by two state of art design analysis codes HAWC2 and FAST. We used the FAST v8.12 model which was provided by Borg.⁷⁾ Regarding the difference between FAST model and HAWC2 model, no pre-bend and no torsional blade DOF in FAST and the turbulence model is different. HAWC2 model is a multi-body formulation based on a finite element implementation of Timoshenko beam theory, while FAST uses a mode shape formulation with limited DOF. However both models are consistent in terms of system identification as shown in Table 3.⁷⁾

Table 2: Summary of analysis condition

Description	Value
Wind Turbine Class (IEC)	Class 1
Wind Model	extreme wind speed model (EWM)
Turbulence Intensity (IEC)	11%
WSP, 50 year recurrence	50 [m/s]
Spectral Model	Kaimal
Yaw Misalignment	-150, -120, 90,,150, 180[deg]
Blade Pitch	Feather to 90 [deg]
Rotor	Idle or Standstill
vertical power-law wind-shear exponent	0.11
Simulation Time	3600[sec]
Random Seed	6 seeds

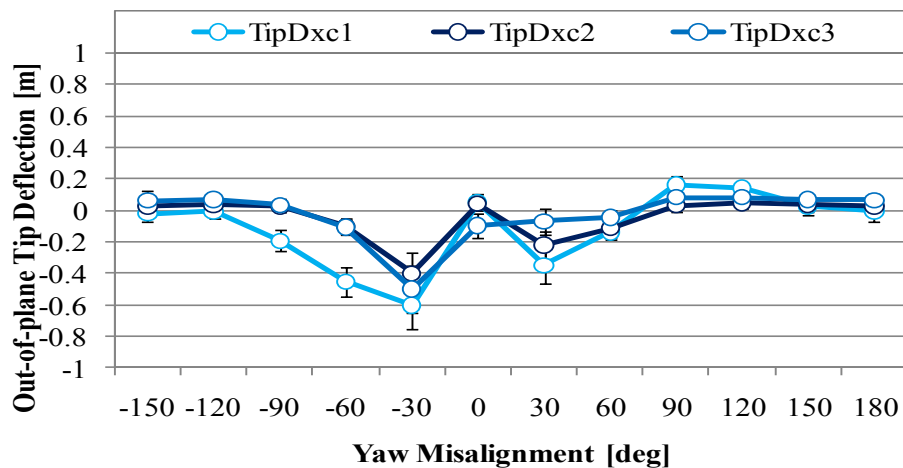
Table 3: Natural frequencies by FAST and HAWC2⁷⁾

Mode description	HAWC2 (Hz)	FAST (Hz)	Difference (%)
1st tower fore-aft and side-side mode	0.251	0.247	1.59
1st collective blade flap mode	0.63	0.636	0.95
1st asymmetric blade edge mode	0.935	0.975	4.28

4. ANALYSIS RESULTS

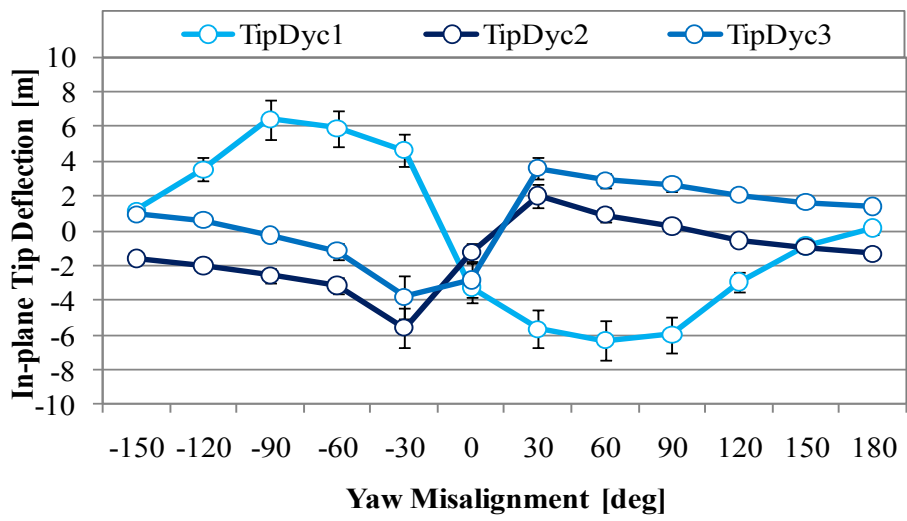
The full range of yaw misalignment results for 'Rotor-brake' and 'Rotor-free' by using the FAST model are summarized in Figure 3 and Figure 4, respectively. Mean value with plus/minus one standard deviation for the computation of 6 seeds about out-of-plane blade tip deflection, in-plane blade tip deflection, out-of-plane bending moment at blade root and in-plane bending moment at blade root are plotted. Apart from idling rotor speed difference, both results have similar magnitude and trend, though 'Rotor-brake' results show slightly larger magnitude of moment and Deflection to compare with 'Rotor-free' results. Fluctuation of blade tip deflection means the magnitude of vibration and has a similar trend with the moment fluctuation at blade root. The strong vibration occurs for cases with yaw misalignment of 30 and 60 degrees. Regarding the in-plane blade tip deflection and in-plane moment at blade root with yaw misalignment case of 30 and 60 degrees, the fluctuation range in 'Rotor-free' is interestingly spread over the value of each blades in 'Rotor-brake'. This is as if blades in 'Rotor-free' alternately changed their roles as one of the blades in 'Rotor-brake'.

The full range of yaw misalignment results for 'Rotor-free' by HAWC2 model are summarized in Figure5. Mean value with plus/minus one standard deviation for the computation of 6 seeds about out-of-plane bending moment at blade root, in-plane bending moment at blade root and Angle of attack at blade tip element are plotted. In HAWC2's 'Rotor-free' result, the large out-of-plane bending moment fluctuation is seen for yaw misalignment case of 30 degree. However this vibration isn't considered as the stall flutter⁸⁾ in terms of the attack angle results in yaw misalignment case of 30 degree and -90degree. Figure 6 indicates the PSDs of bending moment at blade root and blade tip deflection for yaw misalignment of 30degree by HAWC2. Obtained PSDs of both bending moment at blade root and blade tip deflection show the significant peak around 0.8[Hz]. This peak is equivalent to the 9th edgewise blade mode by HAWC2 eigenanalysis result as shown in Table 4 and it could be solved by the redesign of edgewise stiffness distribution. Christian et al.²⁾ also mentioned some combination of pitch sequence can solve the vibration issue. This outstanding peak around 0.8 [Hz] is not clear in other yaw misalignment cases. However FAST doesn't capture HAWC2 trend and it is presumably from that FAST has no prebend, no torsional blade DOF and the limited DOF based on mode shape.

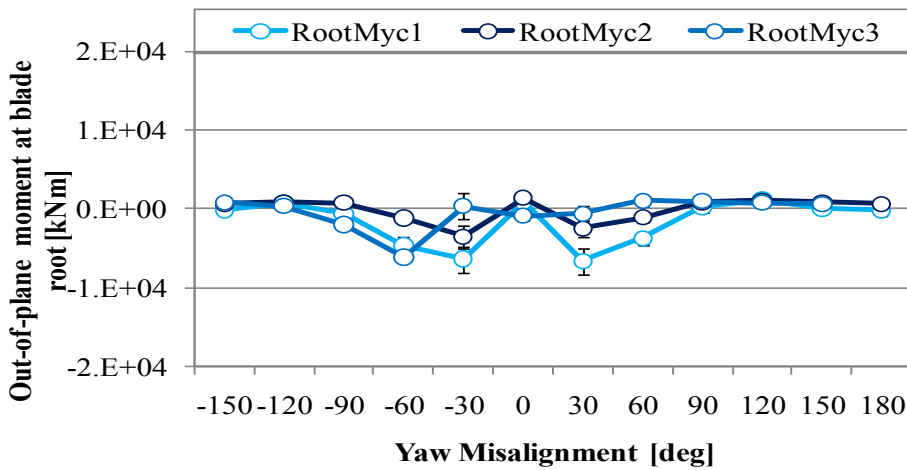


(a) Out-of-plane deflection at blade tip

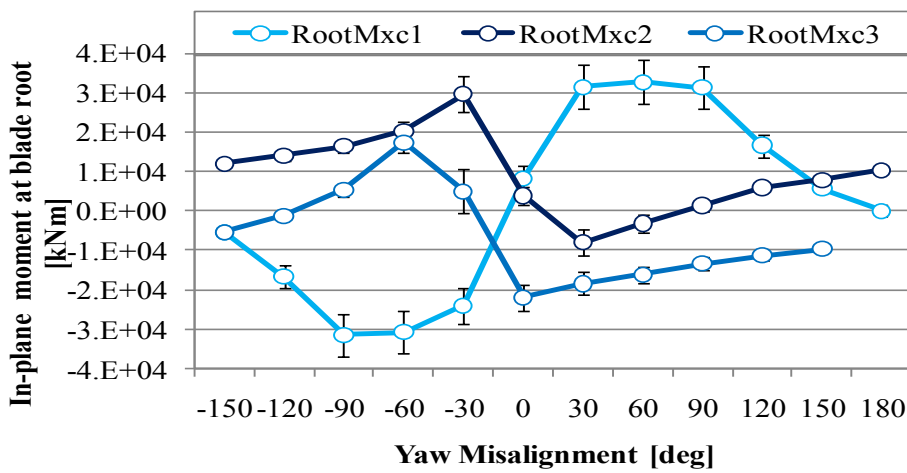
Figure 3:'Rotor-brake' simulation results by FAST



(b) In-plane deflection at blade tip

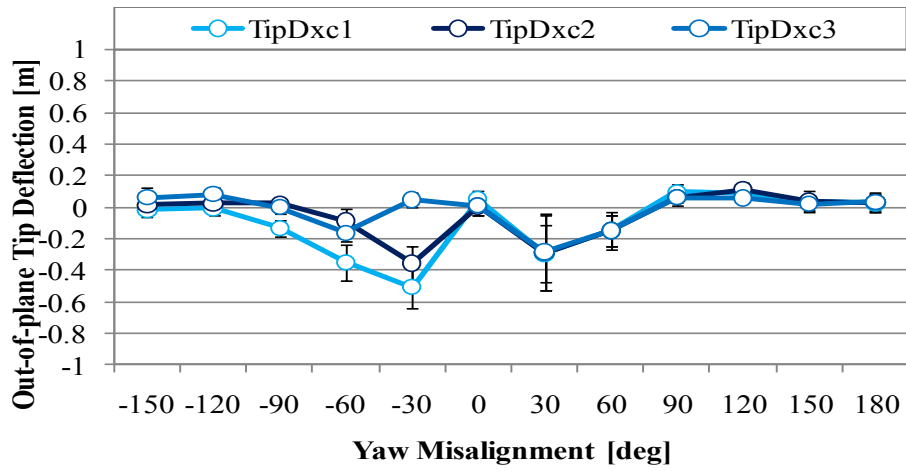


(c) Out-of-plane bending moment at blade root

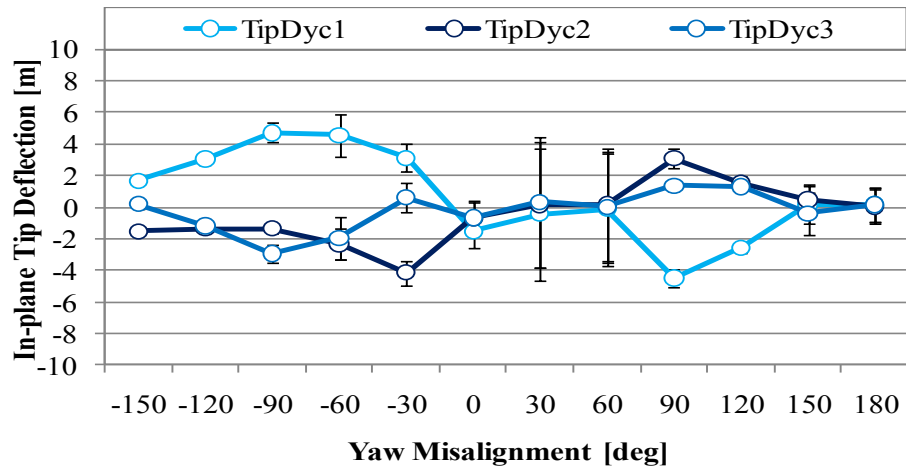


(d) In-plane bending moment at blade root

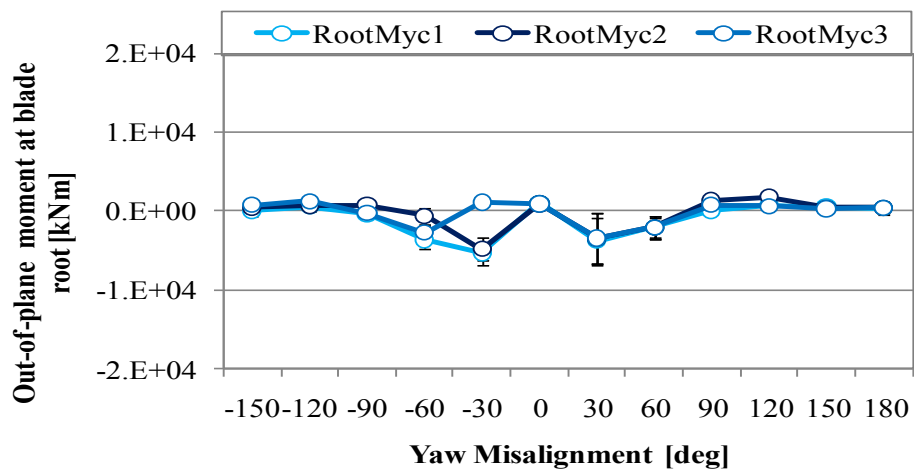
Figure 3: 'Rotor-brake' simulation results by FAST(cont.)



(a) Out-of-plane deflection at blade tip

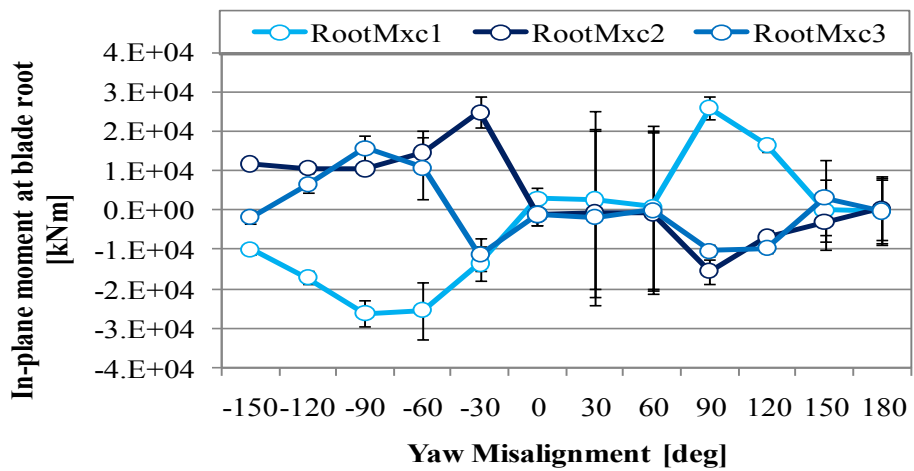


(b) In-plane deflection at blade tip



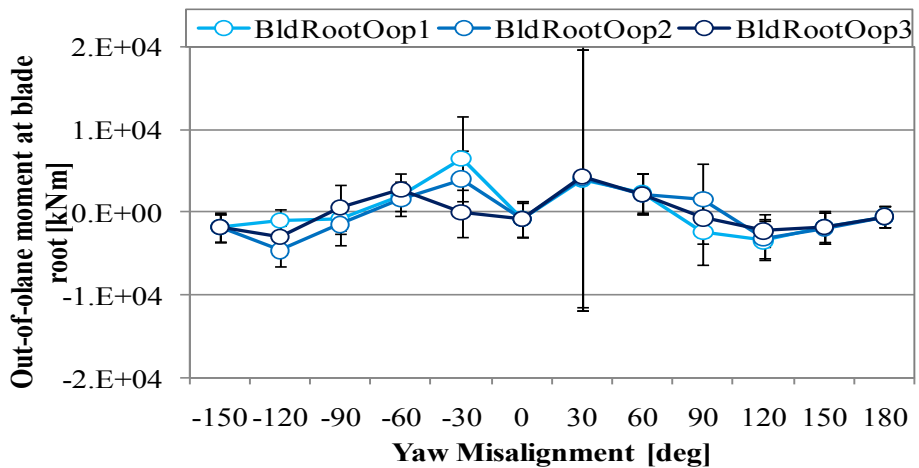
(c) Out-of-plane bending moment at blade root

Figure 4: 'Rotor-free' simulation results by FAST

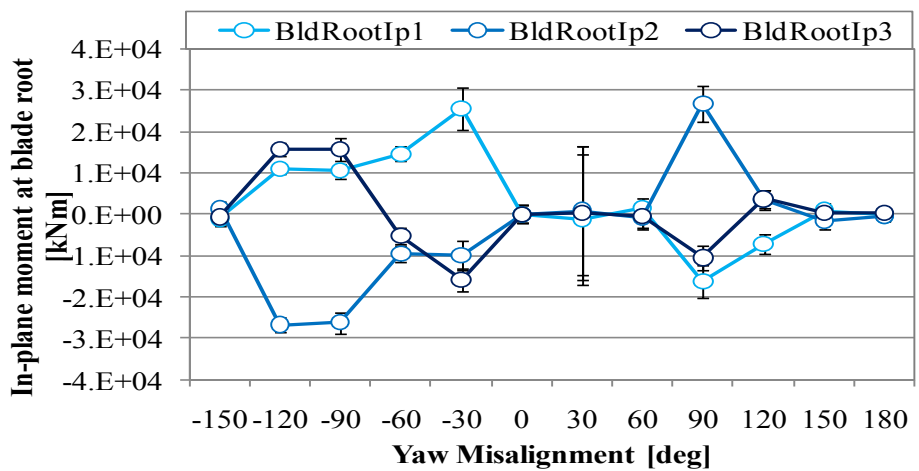


(d) In-plane bending moment at blade root

Figure 4: 'Rotor-free' simulation results by FAST(cont.)

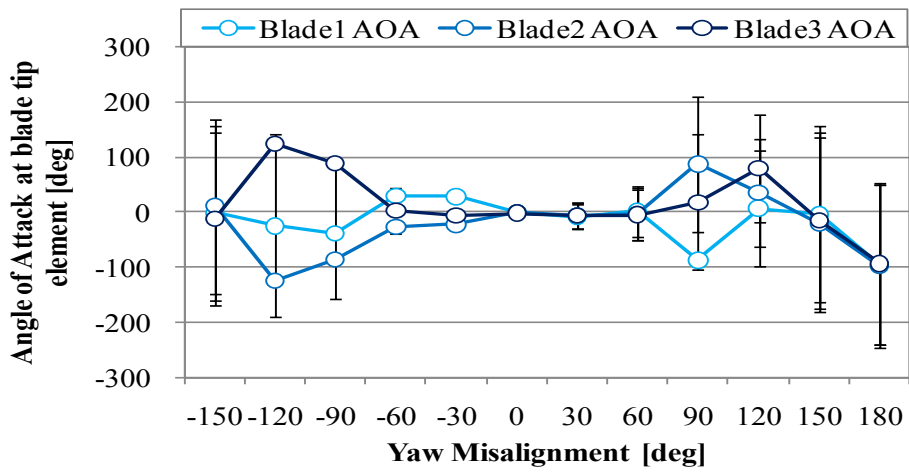


(a) Out-of-plane bending moment at blade root



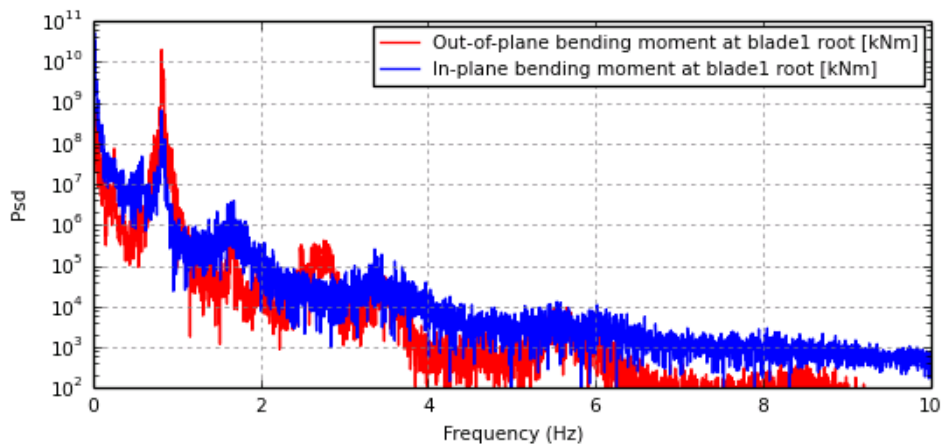
(b) In-plane bending moment at blade root

Figure 5: 'Rotor-free' simulation results by HAWC2

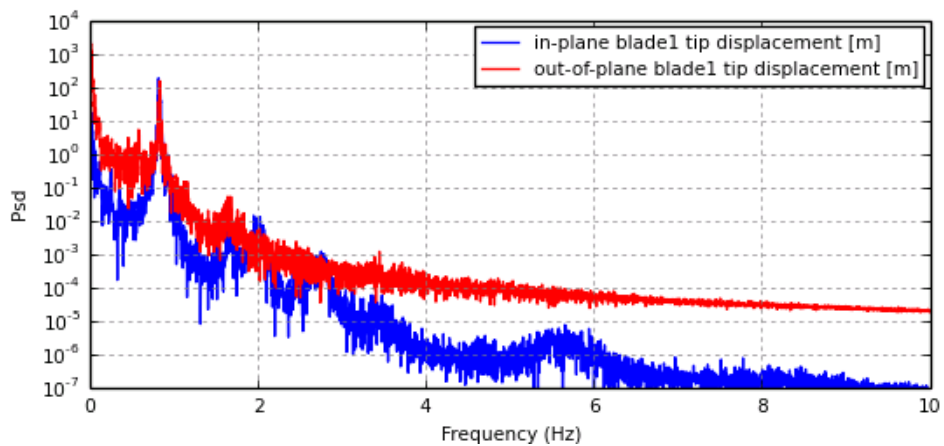


(c) Angle of attack at blade tip element

Figure 5: 'Rotor-free' simulation results by HAWC2(cont.)

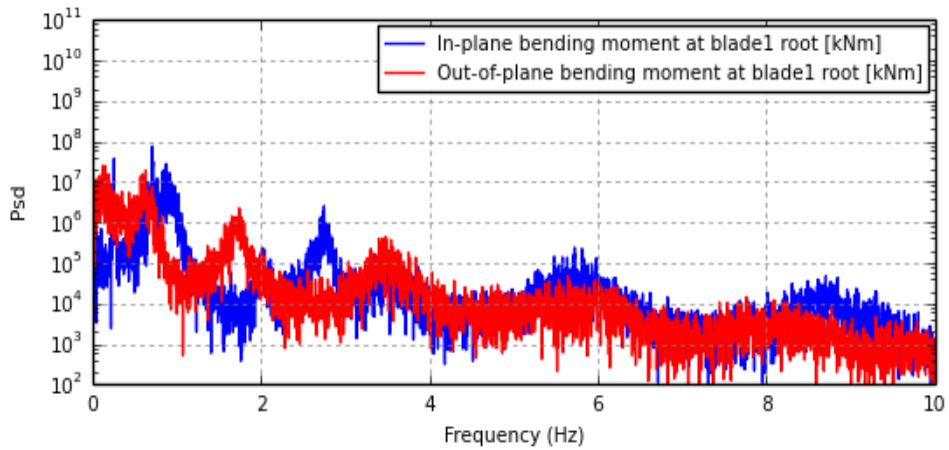


(a) PSD of bending moment at blade root for yaw misalignment of 30[deg]

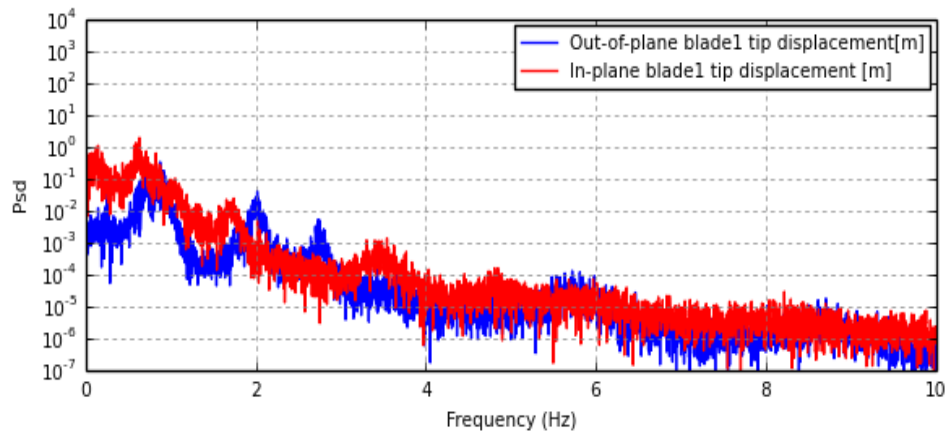


(b) PSD of blade tip Deflection for yaw misalignment of 30[deg]

Figure 6: PSDs of bending moment at blade root and blade tip deflection by HAWC2



(c) PSD of bending moment at blade root for yaw misalignment of -90[deg]



(d) PSD of blade tip Deflection for yaw misalignment of -90[deg]

Figure 6: PSDs of bending moment at blade root and blade tip deflection by HAWC2(cont.)

Table 4: Eigenanalysis results by HAWC2

Mode	Modal Frequency [Hz]	
	Blade pitch angle of 0[deg]	Blade pitch angle of 90[deg]
1	0.251	0.252
2	0.256	0.256
3	0.546	0.606
4	0.590	0.615
5	0.630	0.714
6	0.714	0.714
7	0.714	0.714
8	0.714	0.719
9	0.922	0.841
10	0.936	0.919

5. CONCLUSION

To investigate vibration issue while wind turbine is parked with the rotor brake or idling, analysis condition of DLC6.2 in IEC standard was chosen and carried out by the state of art design analysis codes HAWC2 and FAST. In FAST model results, fluctuation of blade tip deflection has a similar trend with the moment fluctuation at blade root. Obtained HAWC2 results show the serious vibration in bending moment at blade root under the specific yaw misalignment condition of 30degree. Authors assumed this vibration is the 9th edgewise blade mode by eigenanalysis in HAWC2 and it could be solved by the redesign of edgewise stiffness distribution. However FAST doesn't capture HAWC2 trend and it is presumably from that FAST has no prebend, no torsional blade DOF and the limited DOF based on mode shape. Though the several difficulties and challenges exist in this analysis, we have to know if wind turbine endures these extreme loads based on IEC's requirement. The further investigation about design load case of abnormal yaw misalignment is required to verify and support the current engineering tool which is used in the design process of wind turbine.

ACKNOWLEDGMENT

A part of this research was conducted as a NEDO feasibility study on very large wind turbines with rated power of more than 10 MW.

REFERENCES

- 1) IEC 61400-1 wind turbines Part 1: Design Requirements, Edition 3.0, 2005-08.
- 2) Christian Bak, Frederik Zahle, Robert Bitsche, Taeseong Kim, Anders Yde, Lars Christian Henriksen, Anand Natarajan, Morten Hartvig Hansen, Description of the DTU 10 MW Reference Wind Turbine, DTU_Wind_Energy_Report-I-0092, 2013.
- 3) Larsen, Torben J.; Hansen, Anders Melchior, How 2 HAWC2, the user's manual, Technical University of Denmark, 2007.
- 4) J. Jonkman, M. Buhl Jr., FAST User's Guide, NREL/EL-500-29798, NREL, 2005.
- 5) B.J. Jonkman, J.M. Jonkman. Guide to changes in FAST v8: v8.12.00a-bjj. NREL, 2015.
- 6) J. Jonkman, S. Butterfield, W. Musial, and G. Scott. Definition of a 5-MW reference wind turbine for offshore system development. Technical Report NREL/TP-500-38060, NREL, 2009.
- 7) Michael Borg, Mahmood Mirzaei, Henrik Bredmose, LIFES50+ Qualification of innovative floating substructures for 10MW wind turbines and water depths greater than 50m, 2015.
- 8) M. H. Hansen, Aeroelastic stability analysis of wind turbines using an eigenvalue approach, Wind Energy, 7(2), 2004.

FIELD MEASUREMENT OF BLADE TIP RESPONSE OF A MEDIUM SIZE WIND TURBINE IN OPERATION

Kichiro Kimura⁺¹, Hiroshi Torikai⁺¹, Masao Hosomi⁺² and Eijiro Yukoku⁺²
⁺¹Tokyo University of Science, Noda, Japan
⁺²KOMAIHALTEC Inc., Osaka, Japan

The blade tip flap-wise displacements of a medium sized horizontal axis wind turbine during its operation were tried to be measured with relatively simple setup. Motion pictures of the rotor were taken by two high speed cameras and a motion capture software was used to obtain the time histories of the tip locations. Then the coordinates were transformed to obtain the flap-wise component of the blade tips. The calibration was made by pointing the blade tips when the rotor was fixed at four positions respectively and relating them with their known coordinate value. The approximate approaching wind speed was measured with a Doppler lidar at 4Hz sampling rate. The wind turbine used for the measurement is KWT300 of KOMAIHALTEC, with rated power of 300kW, rotor diameter of 33m, and Hub height of 41.5m. The response analysis was conducted with an open source software FAST, which is developed in NREL. The measured wind speed was used as an input, and only vertical wind speed profile was considered, i.e., wind speed was assumed to be fully correlated regardless of the spatial location. Generally, measured tip displacements seem to have taken local minimum values when the blade passed in front of the tower. The three blade tips often took similar response traces when they passed at the same location. On the other hand, the three blade tips sometimes took similar responses at the same time. The cause of these different response characteristics is still not clear. Generally, the amplitude of the measured responses was larger than the analysis, and higher frequency fluctuating components were included in the measurement. These tendencies are probably due to the assumption of full correlation of the wind velocity at different locations in the analysis.

Keyword: wind turbine, motion capture software, blade tip displacement, Doppler lidar, FAST

1. INTRODUCTION

Improving the accuracy of wind turbine response analysis procedure is beneficial, and the response data of actual wind turbine in operation are indispensable to verify the accuracy of the analysis¹⁾. The objectives of this study are to obtain the blade tip flap-wise displacement data of a medium size wind turbine during operation, and to compare the data with analysis.

2. FIELD MEASUREMENT METHOD

The field measurement was conducted with a KWT300 of KOMAIHALTEC Inc. (Fig. 1 and Tab. 1). It is a horizontal axis upwind type turbine with rated power of 300kW, rotor diameter of 33m, and hub height of 41.5m. It is located in Futtsu Factory of the company in Chiba Prefecture, Japan.

Relatively simple measurement method of blade tip displacements was used, where motion pictures taken by two high speed cameras (HAS-D72, DITECT Corp.) and a motion capture software (DIPP Motion V, DITECT Corp.) are used to obtain the time history of the coordinates of the blade tips. The calibration was made by pointing the three blade tips when the rotor was fixed, and the procedure was repeated for the four fixed positions of the rotor. The tips' coordinates were calculated from the position and size of the rotor for the positions and they were used for the calibration as well. The calibration relates the blade tip location on the

⁺¹kichiro@rs.tus.ac.jp

motion pictures with known coordinate value.

The accuracy of the measurement procedure was tried to be clarified by pointing locations that slightly deviated from the blade tips during calibration, and the sensitivity of the measured tip displacements caused by the error in the calibration was checked. Depending on the error during calibration, the diameters of the rotor based on the measurement traces varied as shown in Fig. 2, and they were between 22 and 48 cm larger than the actual value. With those calibration errors, the measured tip displacements differs as shown in Fig. 3. The variation of the tip displacements shown in Fig. 3 can be thought as the possible error in the measurement.

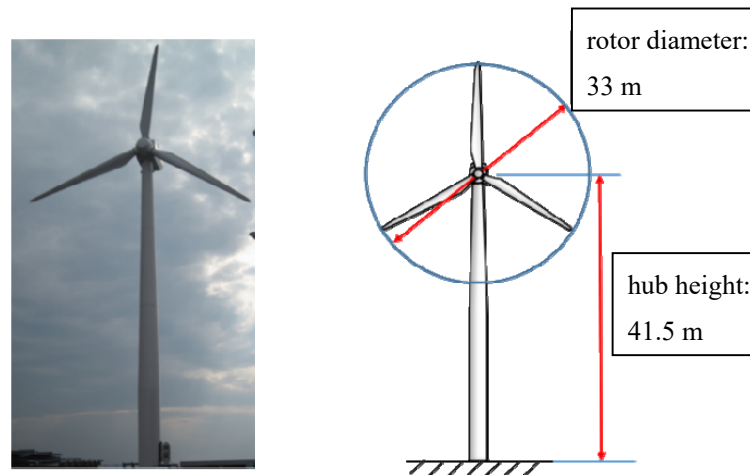


Figure 1: Overview of the wind turbine (KWT300).

Table 1: Specifications of KWT300.

rated power	300 kW
rated rotation rate	40.5 rpm
rated wind speed	11.5 m/s
cut-in wind speed	3.0 m/s
cut-out wind speed	25 m/s
survival wind speed	70 m/s

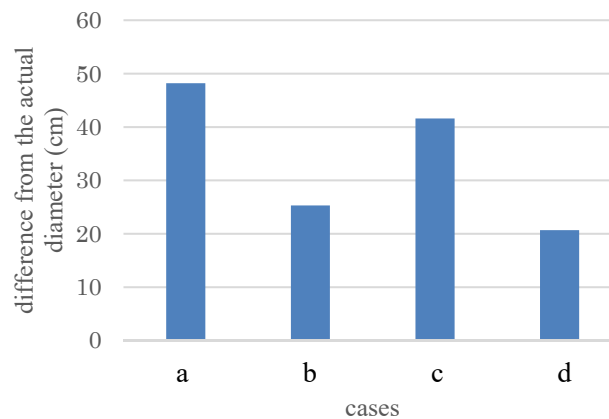


Figure 2: Difference from the correct rotor diameter.

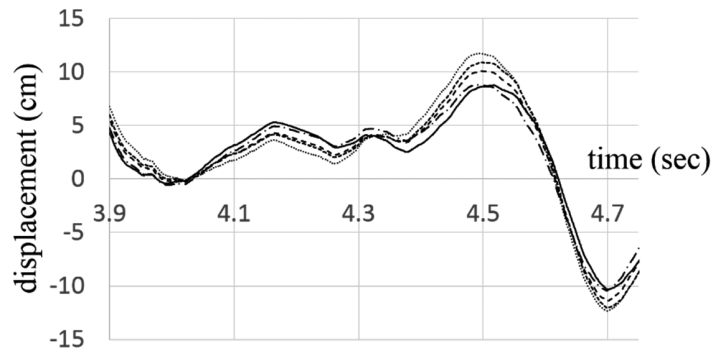


Figure 3: Time histories of blade tip displacements with erroneous calibrations.

The approximate approaching wind speed at the hub height was measured with a Doppler lidar of Mitsubishi Electric Corp. at 4Hz sampling rate. The measured wind speed was at the location about 120 m windward of the turbine. The time history of the wind data was corrected so that it approximates the wind speed at the wind turbine rotor in the following way by assuming that an air volume flows with the same speed as that was measured at the 120 m windward location. The wind speed data was integrated with time, and when the integration reached 120 m, the timing was assumed to be the air mass reached the wind turbine rotor, and the measured wind speed at the beginning was assumed to be observed at the rotor location with that timing. Actually, the measured wind velocity component was inclined by about 20 deg. from horizontal, but it was treated as the horizontal component of the wind speed. These approximations were made to increase the sampling rate as much as possible, with relatively simple setup where the lidar was located at the bottom of the wind turbine tower.

3. WIND-INDUCED RESPONSE ANALYSIS

Analytical results were obtained by using an open source software FAST, which is developed in NREL (National Renewable Energy Laboratory)²⁾. The version of FAST was v8.08.00c-bjj (2014.6). For the modeling of the turbine, structural data for the design stage were used. The natural frequencies of the FAST model and design value were (the latter in parentheses) 1st tower mode: 0.81 (0.81) Hz, 2nd tower mode: 5.74 (5.36) Hz, 1st flap-wise mode: 2.72 (2.64) Hz, 2nd flap-wise mode: 7.58 (7.79) Hz, and 1st edge-wise mode: 4.71 (4.66) Hz. The natural frequencies of the design value and the mode more or less agreed. The measured wind speed was used as an input, and only vertical wind speed profile was considered, i.e., the wind speed was assumed to be fully correlated regardless of the spatial location.

4. MEASURED RESULTS COMPARED WITH ANALYSIS

(1) Example of measured response

The coordinates of the measured tip displacements by the motion capture software were transformed to obtain the component parallel to the rotor axis, which is nearly equal to the mean wind direction. This component is supposed to be dominant in the response and it is presented in the followings. Examples of measured tip responses of the three blades are shown in Fig. 4 and 5 together with the wind speed. Positive tip displacement is defined toward the leeward direction. The gaps between the tip displacement data are due to the timing where the blade tip could not be seen clearly from the camera, and accurate data could not be obtained at those timings. The red dots on the horizontal axis show the timing that the blade passed in front of the tower. Generally, tip displacements seem to take local minimum values when the blade passed in front of the tower. The three blade tips often showed similar response traces when they passed at the same location as in Fig. 4. In this case, the responses of three blades differed with phase lag of 120 degrees. On the other hand, the three blade tips sometimes showed similar responses at the same time (i.e., no time lag) as shown in Fig. 5. The cause of these different response characteristics is still not clear.

(2) Comparison of measured and computed responses

Some of the measured tip displacements are compared with analytical results as shown in Fig. 6. Generally, the amplitude of the measured responses was larger than the analysis, and higher frequency fluctuating components were included in the measurement. These tendencies are probably due to the omission of consideration of spatial wind velocity correlation in the analysis that is actually less than 1 at each location.

5. CONCLUDING REMARKS

More data are planned to be taken in future together with the operation data of the wind turbine such as rate of rotation, pitch angle, acceleration at the tower top. Those data can be used to confirm the agreement of the analysis with the measurements. In addition, the formulation of the aerodynamic forces will be studied and more suitable formulation will be sought. Hopefully, more accurate response predictions such as blade tip displacement and so on will be obtained by the formulation even in different wind condition.

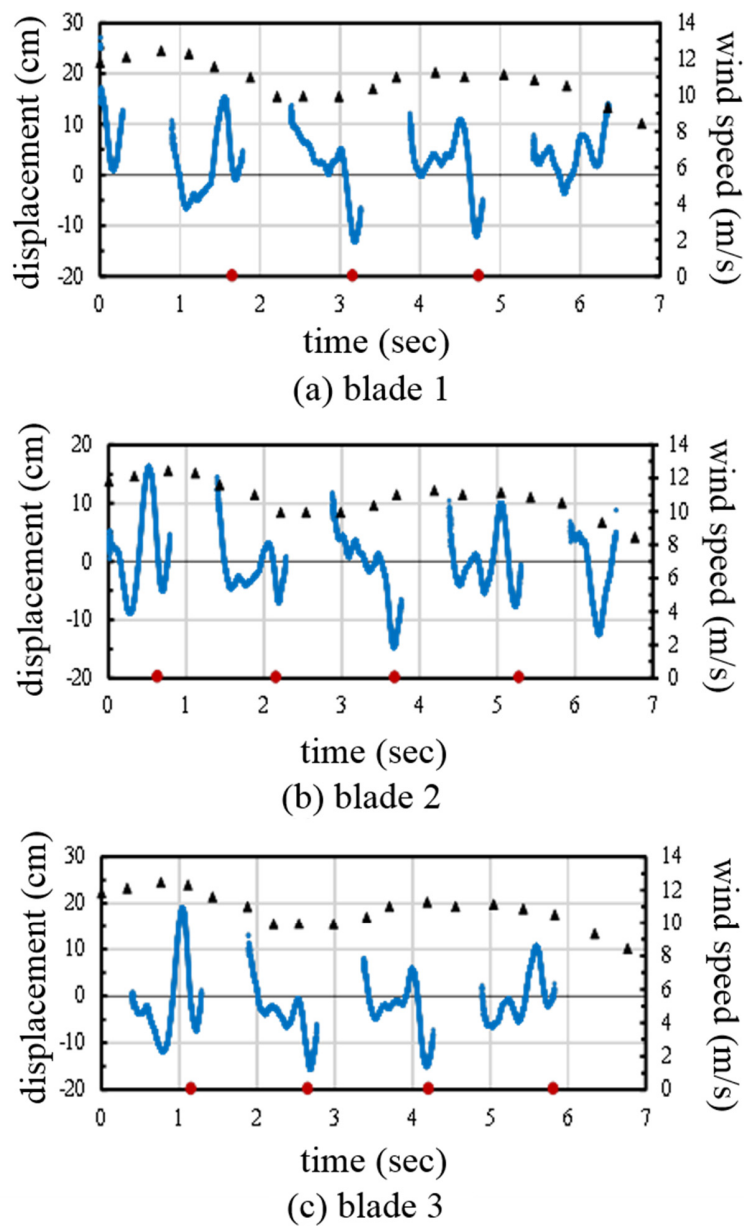


Figure 4: An example of measured blade tip displacements (Nov. 18, 2014).

ACKNOWLEDGMENT

This study has been supported by JSPS Grants-in-Aid for Scientific Research Grant Number 26289146, and it is gratefully appreciated.

REFERENCES

- 1) Ozbek, M., Meng, F. and Rixen D.J. : Challenges in Testing and Monitoring the In-Operation Vibration Characteristics of Wind Turbines, *Mechanical Systems and Signal Processing*, Vol. 41, pp. 649-666, 2013.
- 2) Jonkman, J.N. and Buhl Jr., M.L. : FAST user's guide, NREL/EL-500-38230, 2005.

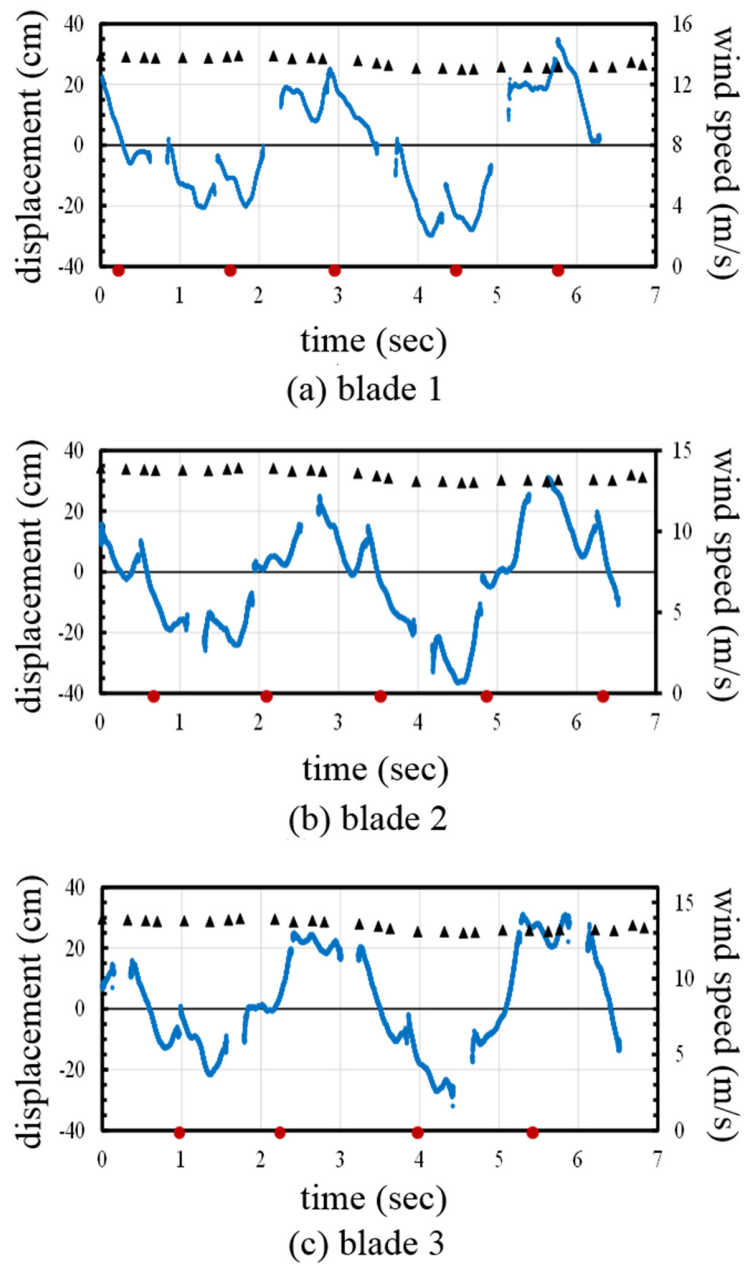


Figure 5: An example of measured blade tip displacements (Dec. 2, 2014).

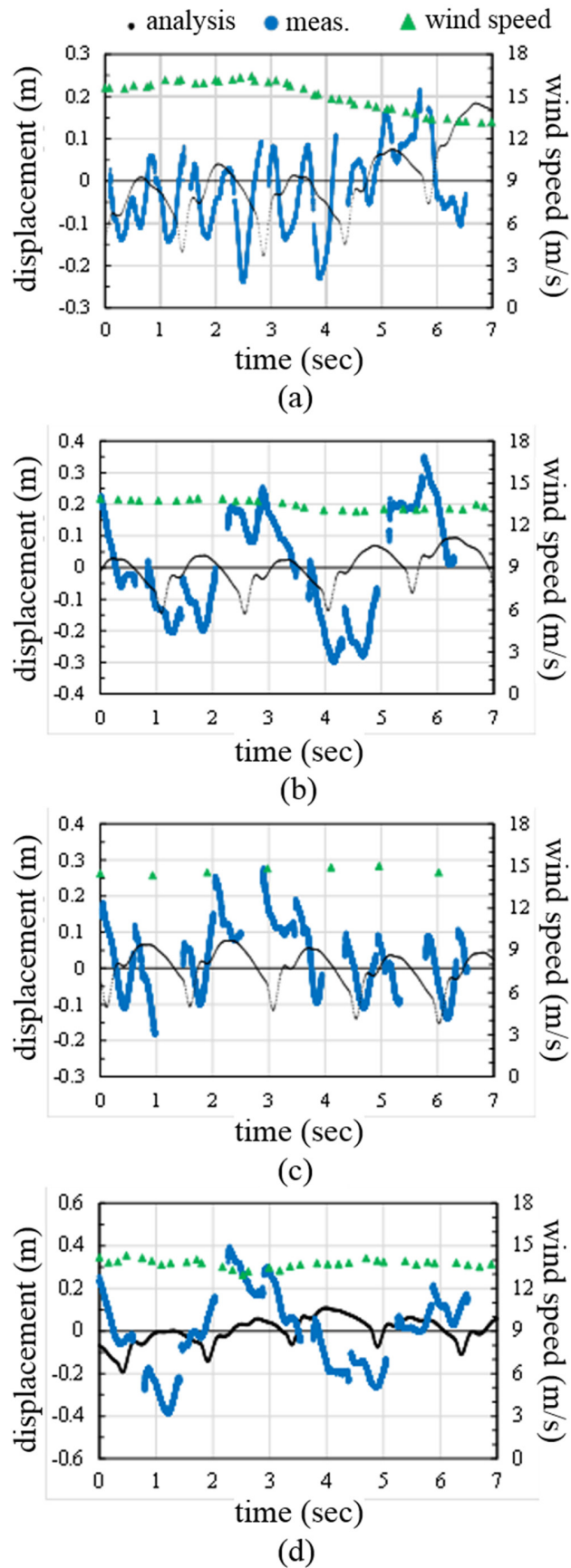


Figure 6: Comparison of measured and analyzed tip displacements.

LOW-SPEED GALLOPING FOR RECTANGULAR CYLINDERS WITH SIDE RATIOS LARGER THAN UNITY

Claudio Mannini⁺¹, Antonino M. Marra⁺², Tommaso Massai⁺³ and Gianni Bartoli⁺⁴

⁺¹ CRIACIV/Department of Civil and Environmental Engineering, University of Florence, Italy

The aeroelastic instability starting at low reduced flow speed due to the interference between vortex-induced vibration (VIV) and transverse galloping, which may be called “low-speed galloping”, was studied in the wind tunnel in the case of an elastically-supported slender rectangular cylinder with a side ratio of 1.5 and the short side face perpendicular to the smooth flow. The tests were carried out in a wide Scruton number range, starting from low values and increasing it in small steps through eddy-current viscous dampers. This study helped understanding the dynamics of the interaction between the excitation mechanisms of VIV and galloping and clearly highlighted the transition through several regimes of interference. It was found that a high value of the mass-damping parameter is required to completely decouple the ranges of excitation due to vortex-induced vibration and galloping and for the quasi-steady theory to correctly predict the galloping critical wind speed. This conclusion is also relevant from the engineering point of view, as it means that structures and structural elements with ordinary mass-damping properties can exhibit sustained vibrations where they are not predicted by classical theories of vortex-induced vibration and galloping. The modeling of this low-speed galloping was attempted by slightly modifying the wake oscillator model proposed in 1987 by Tamura and Shimada to predict the interference of VIV and galloping in the case of a square-section cylinder. It was found that a proper choice of the coupling parameter between the wake and the mechanical oscillators allows reproducing correctly the main features of the cylinder response. Finally, low-speed galloping can be positively exploited for low-power energy-harvesting systems, in view of the low onset flow speed and the weak dependency on the Scruton number up to medium values of it.

Keyword: galloping, vortex-induced vibration, rectangular cylinder, wind tunnel tests, turbulent flow, analytical model

1. INTRODUCTION

The transverse galloping instability of slender prismatic elements is usually approached with the quasi-steady theory¹⁻²⁾. Nevertheless, it is well known that this model can give accurate predictions of the critical threshold and post-critical behavior only for high-reduced flow speed, in particular much higher than the vortex-resonance range. Indeed, when the dissipation capability of the system is small, *i.e.* the so-called Scruton number is relatively low, this requirement cannot be met. Consequently, vortex shedding plays a crucial role in triggering or quenching the instability mechanism, and the behavior of the fluid-structure system can no longer be described by the quasi-steady theory.

A detailed review of transverse galloping of rectangular cylinders with side ratios between 1 and 2 (short side perpendicular to the flow) at low Scruton number is reported in Mannini *et al.*³⁾. Therein, the peculiarities of this aeroelastic instability were highlighted and the phenomenon was addressed as interference (or interaction) between vortex-induced vibration (VIV) and galloping. However, it is also reasonable to consider it as a single-degree-of-freedom instability arising at low reduced flow speed, *i.e.* a “low-speed galloping”. Now, it is worth reminding that Nakamura and co-workers⁴⁻⁵⁾ called low-speed galloping the instability observed for rectangular cylinders with side ratios of 0.2 and 0.4 (long side perpendicular to the flow) at low Scruton number,

⁺¹claudio.mannini@unifi.it, ⁺²antoninomaria.marra@unifi.it, ⁺³tmassai@dicea.unifi.it, ⁺⁴gianni.bartoli@unifi.it

slowly building-up spontaneously from rest for flow speeds significantly lower than the vortex resonance velocity. Its range of excitation was found to merge with the vortex-resonance one, where nevertheless the rate of growth of the oscillation from rest is much higher. The distinction between high-speed and low-speed galloping was also outlined by Matsumoto⁶⁾. However, the phenomenon addressed in the present work is clearly different from the one discussed by Nakamura and co-workers.

In this paper, the interference of vortex-induced vibration and galloping in the case of a rectangular cylinder with a side ratio of 1.5 is investigated through wind tunnel tests in smooth flow. This geometry was found to be very prone to this phenomenon³⁾. The Scruton number was varied in small steps from low to high values by introducing additional damping into the system by means of eddy-current magnetic damper devices. This study allowed putting in evidence the complicated transition between regimes of interference between VIV and galloping.

In literature, there are only few attempts to model the interference of vortex-induced vibration and galloping, all relying on the linear superposition of unsteady and quasi-steady forces⁷⁻⁹⁾. In particular, herein Tamura and Shimada's model⁸⁾ was slightly modified for theoretical reasons and then applied to the considered case study.

2. WIND TUNNEL TESTS

The tests were carried out in the open-circuit boundary-layer CRIACIV wind tunnel in Prato, Italy. The facility presents a test chamber 2.42 m wide, 1.60 m high and 11 m long. The free-stream turbulence intensity is below 0.7%.

A plywood sectional model, 986 mm long (L), 116 mm wide (B) and 77 mm deep (D), was used to perform both static and dynamic tests. To enforce bidimensional flow conditions, symmetric rectangular (450 mm \times 150 mm \times 4 mm) plywood plates were provided at the model ends. The model was placed horizontally in the wind tunnel with the shorter side of the section perpendicular to the flow.

The measurements of the aerodynamic force coefficients at various angles of attack and of the Strouhal number were performed by means of two high-frequency six-components strain-gauges dynamometers placed at the ends of the model.

In the aeroelastic setup, the model was connected through its longitudinal axis-tube to two shear-type steel frames, whose horizontal elements worked as plate-springs (Figure 1(a)). Only the transverse (vertical) displacement was allowed by the two frames due to the very large in-plane bending stiffness of the vertical elements at which the model was connected. The suspension system was sheltered from wind by means of the screens shown in Figure 1(b). The displacements of the model were recorded with two non-contact laser transducers. The viscous damping of the system was increased in small steps through a device based on the electromagnetic induction principle. The dissipation forces produced by the dampers allowed reaching high values of the Scruton number and therefore investigating in details the low-speed galloping instability.



Figure 1: View of the dynamic setup without (left) and with (right) the sheltering system.

3. EXPERIMENTAL RESULTS

The transverse force coefficient as a function of the angle of attack $C_{F_y}(\alpha)$, and in particular its slope in the origin, is of crucial importance for the determination of the galloping behavior of the cylinder with the quasi-steady theory. The convention adopted to express $C_{F_y}(\alpha)$ is shown in Figure 2, while the results of static tests are shown in Figure 3. The force measurements on the fixed cylinder were also used to determine the Strouhal number $St = n_s D/V = 0.106$, where V denotes the undisturbed flow speed and n_s the frequency of vortex shedding, associated with the dominant peak in the lift coefficient spectrum.

During the dynamic tests, the elastically suspended model was let free to vibrate in the transverse degree of freedom and the flow speed was progressively increased, recording the time history of the displacement. In order to highlight hysteresis phenomena and the presence of multiple stable solutions, measurements were also performed either by reducing the flow speed or by stopping the model and letting the vibrations build up from rest. The complete list of dynamic configurations tested is reported in Table 1. Therein, n_0 and ζ_0 denote respectively the still-air natural frequency of oscillation and the damping ratio. Sc is the Scruton number, defined as follows:

$$Sc = \frac{4\pi M \zeta_0}{\rho B D L} \quad (1)$$

$M = 5.5$ kg being the effective mass of the oscillating system. By defining the reduced flow speed as $U = V/n_0 D$, the Kármán-vortex resonance reduced flow speed is denoted as $U_r = 1/St$, while U_g is the galloping critical reduced flow speed predicted by the quasi-steady theory:

$$U_g = \frac{2Sc}{A_1} \cdot \frac{B}{D} \quad (2)$$

where $A_1 = -dC_{F_y}/d\alpha(0)$. Therefore, it results:

$$\frac{U_g}{U_r} = \frac{2Sc \cdot St}{A_1} \cdot \frac{B}{D} \quad (3)$$

A summary of the results for most of the Scruton number values considered is shown in Figure 4 in terms of $\sqrt{2}$ times the standard deviation of the displacement y' normalized with the cross-flow section dimension D . It is clear that the main excitation of the model starts in the vortex resonance region and the oscillation amplitude increases nearly in a linear way with the flow speed. This trend is kept also for high amplitudes of vibration up to a Scruton number of at least 28, corresponding to an estimated value of U_g/U_r of about 1.6 (see Table 1). By contrast, for $Sc = 37$ and 41 ($U_g/U_r = 2.2$ and 2.4), one can observe a decrease of the amplitude of oscillation for reduced velocities between $1.5U_r$ and $2U_r$ followed by a large jump to a higher branch between $2.5U_r$ and $3U_r$. For even higher Scruton numbers ($Sc = 46$ and 52, corresponding to $U_g/U_r = 2.7$ and 3.0), around $U/U_r = 1.5$ the oscillation amplitude decreases down to a low but non-null value, showing quite irregular time histories.

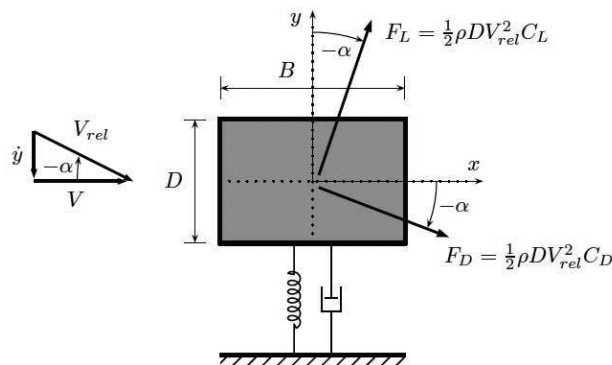


Figure 2: Evaluation of the transverse force on a vibrating rectangular cylinder with the quasi-steady approach. F_D and F_L denote respectively the drag and lift forces per unit length; V_{rel} is the relative flow speed.

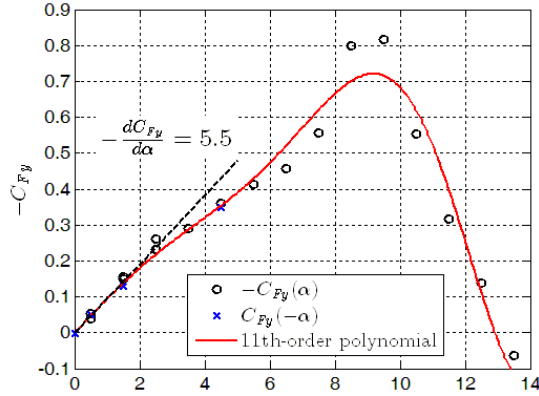


Figure 3: Quasi-steady transverse force coefficient measured in the wind tunnel ($Re = VD/\nu = 146,800$, V being the flow speed and ν the air kinematic viscosity). The coefficient $C_{Fy}(\alpha)$ is referred to the cross-flow section dimension D . The 11th-order polynomial approximation is also shown.

Table 1: Main characteristics of the configurations tested.

#	n_0 [Hz]	ζ_0 [%]	Sc [-]	U_g [-]	U_g/U_r [-]
1	8.97	0.065	4	2.3	0.24
2	8.97	0.087	6	3.1	0.33
3	8.97	0.22	15	8.1	0.85
4	8.95	0.44	28	15.4	1.63
5	8.97	0.57	37	20.3	2.15
6	8.92	0.64	41	22.9	2.42
7	8.89	0.70	46	25.3	2.68
8	8.93	0.79	52	28.5	3.02
9	8.86	0.91	60	32.7	3.46
10	8.87	0.99	65	36.1	3.82
11	8.84	1.31	86	47.8	5.07
12	8.84	1.85	122	66.6	7.06

A progressive boost of the response is then found commencing at a velocity slightly lower than $2.5U_r$. Finally, for the largest values of the mass-damping parameter considered in the figure ($Sc = 60, 65$ and 86 , corresponding to $U_g/U_r = 3.5, 3.8$ and 5.0), the vibration of the model sharply dies out slightly after the vortex-resonance flow speed and an excitation appears again with a jump at much higher wind velocities.

Figure 5(a) shows a close-up view of the response in the Kármán-vortex resonance region. It is apparent that in all the tests the initial trend of the response is the same but, increasing the Scruton number, the flow speed at which the maximum amplitude is reached progressively decreases.

Figure 5(b) focuses on the self-limited excitation exhibited by the system for very low reduced flow speed and low values of the Scruton number. This secondary excitation, whose onset velocity does not depend on Sc , can be ascribed to the resonance with the impinging leading-edge vortex mechanism⁽¹⁰⁻¹¹⁾, which in this particular condition overwhelms the usually dominant Kármán vortex-shedding mechanism.

Figure 6 reports the results for high values of the Scruton number according to the universal plot proposed by Parkinson and Smith⁽²⁾. The picture suggests that for $Sc \geq 60$ the high reduced flow speed instability of the rectangular cylinder is due to quasi-steady galloping, as the normalized onset velocity does not change appreciably with the Scruton number. By contrast, a non-negligible anticipation of the instability is already found for $Sc = 52$. It is also worth noting that the first part of the response beyond the critical flow speed predicted by the quasi-steady theory is significantly different from the experimental results.

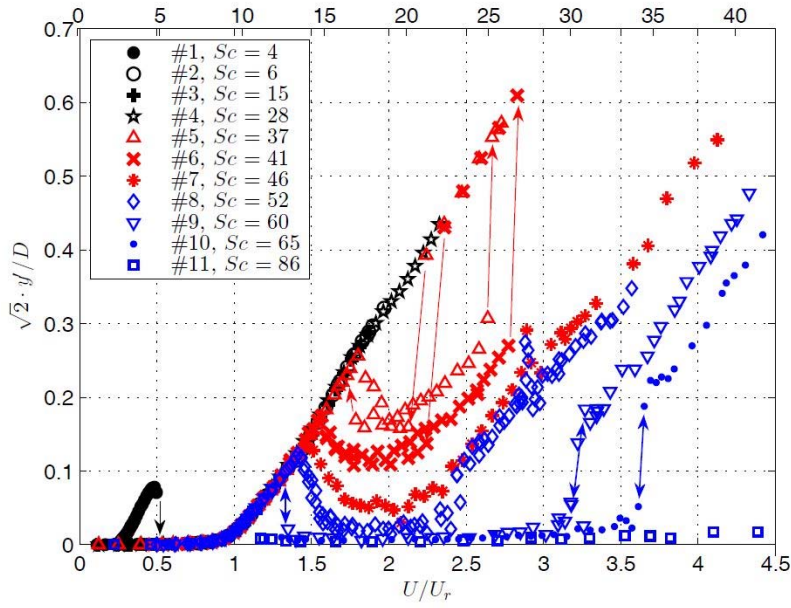


Figure 4: Summary of the amplitude-velocity curves for various Scruton numbers.

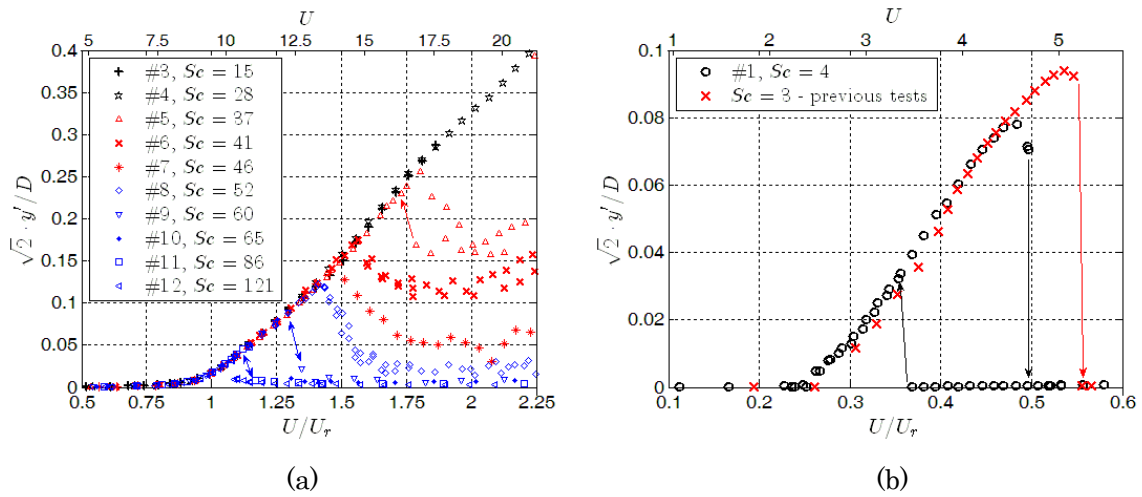


Figure 5: (a) Amplitude-velocity curves for various Scruton numbers in the Kármán-vortex resonance region; (b) close-up of the response in the low-reduced-flow-speed excitation range for two Scruton numbers.

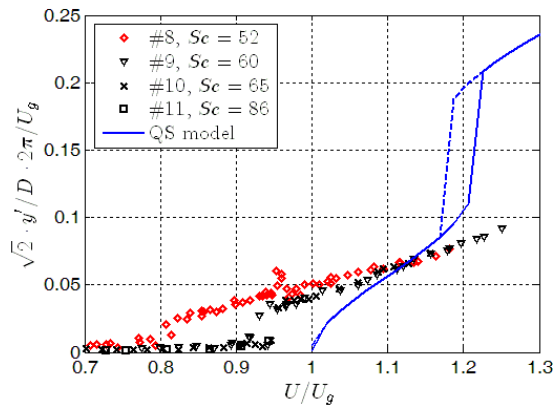


Figure 6: Universal plot of amplitude-velocity curves for high values of the Scruton number.

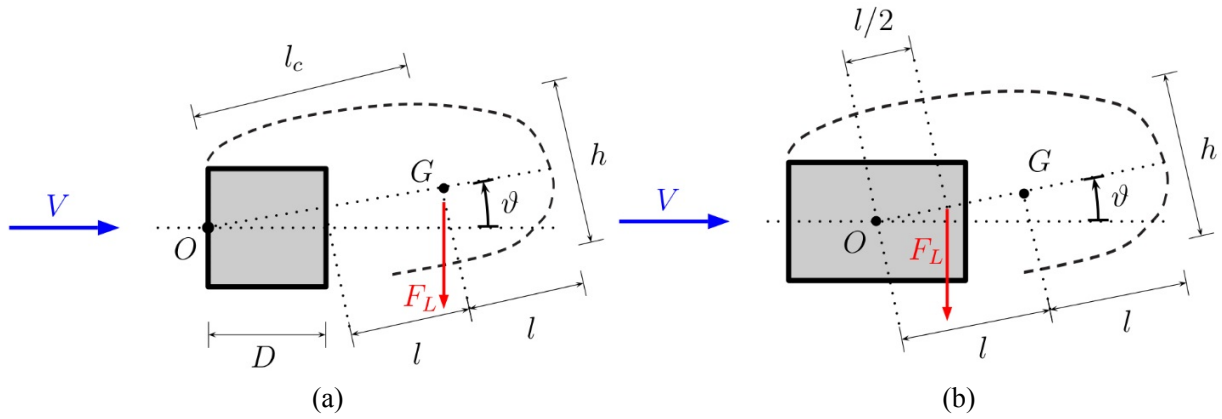


Figure 7: Schematics of the wake-oscillator model in Tamura and Shimada⁸⁾ (a) and in the present work (b).

4. MATHEMATICAL MODEL

In 1987, Tamura and Shimada⁸⁾ proposed a model for the interference of VIV and galloping, obtained by simply adding the quasi-steady forces into the wake-oscillator model equations proposed by Tamura and Matsui¹²⁾. The latter was originally conceived to model the vortex-induced vibration of a circular cylinder. It is based on Birkhoff's oscillator model¹³⁾ for the dead-air region behind a stationary circular cylinder and it assumes the inclination ϑ of the wake (Figure 7) as time-dependent variable. Funakawa¹⁴⁾ had already linearly coupled Birkhoff's model with a structural oscillator, assuming that the wake oscillator is forced by the body motion (velocity and acceleration) and that the force exerted on the cylinder is proportional to the wake angle ϑ . The resulting linear coefficient f had been determined from experimental tests on a rotating cylinder, in analogy to the Magnus effect¹⁴⁻¹⁵⁾. Tamura and Matsui¹²⁾ included in the wake oscillator model the effect of fluctuation of the length of the dead-air region behind the cylinder as a nonlinear contribution to the stiffness of the restoring spring and the effect of the discharged vortices as an equivalent negative linear damping. Finally, they obtained a Van der Pol equation for the wake angle ϑ . Once the quasi-steady forces have been added, the resulting nonlinear system of differential equations reads:

$$Y'' + 2\zeta_0 Y' + Y = -m^* \frac{U^2}{4\pi^2} f \left(\vartheta + \frac{2\pi Y'}{U} \right) + m^* \frac{U^2}{4\pi^2} \left[A_1 \frac{2\pi Y'}{U} + A_3 \left(\frac{2\pi Y'}{U} \right)^3 + \dots \right] \quad (4)$$

$$\vartheta'' - 2\beta \nu \vartheta' \left(1 - \frac{4f^2}{c_{L0}^2} \vartheta^2 \right) + \nu^2 \vartheta = -\lambda Y'' - \nu^2 \frac{2\pi Y'}{U} \quad (5)$$

where, in addition to the variables previously defined, Y denotes the nondimensional steady-state amplitude of body oscillation (normalized with the cross-flow section dimension D); $\nu = St \cdot U = U/U_r$ is the ratio of the flow speed to the vortex resonance velocity (or, alternatively, the ratio of the vortex-shedding frequency to the body natural frequency); $m^* = \rho D^2 L / 2M$ is the mass ratio; c_{L0} is the amplitude of lift fluctuation at the Strouhal frequency measured in the wind tunnel for the stationary cylinder; A_1, A_3, \dots are the coefficients of the polynomial approximation of the quasi-steady transverse force coefficient (Section 3); the prime denotes the derivative with respect to the nondimensional time $\tau = 2\pi n_0 t$.

Herein, Tamura and Shimada's model was slightly modified to account for a pair of inconsistencies introduced by Funakawa¹⁴⁾ with respect to original Birkhoff's model¹³⁾ while coupling it with the mechanical oscillator. The difference between the present formulation and Tamura and Shimada's one is schematized in Figure 7 and it implies a different definition of the coefficients β , λ and l^* in Equations (4)-(5):

$$\beta = \frac{f}{\sqrt{2\pi^2} l^*} \quad (6)$$

$$\lambda = \frac{1}{l^*} \quad (7)$$

$$l^* = \frac{1}{8\pi St^2 h^*} \tag{8}$$

where $h^* = h/D$ is the nondimensional width of the wake.

5. NUMERICAL RESULTS

The 2nd-order differential equations of Tamura and Shimada's model were numerically solved by means of ODE45 Matlab[®] function. Some control parameters, such as relative and absolute tolerances, have been properly tuned beforehand, so to optimize the accuracy of the solution. To highlight possible hysteresis loops in the solutions, initial condition on the normalized amplitude $Y(0)$ was chosen first equal to 0.01 and then to about the maximum value compatibly with the considered reduced flow speed and the available experimental $C_{Fy}(\alpha)$ data, *i.e.* $Y(0) = 15^\circ \cdot \pi/180 \cdot U/2\pi$.

In their analysis of the square-section cylinder, Tamura and Shimada⁸⁾ employed the value of the parameter f determined by Funakawa¹⁴⁾ through the analogy with the Magnus effect for the circular cylinder, that is $f = 1.16$. In the authors' opinion, this analogy is questionable, especially for a sharp-edged body and, in any case, the experimental data are not available. Consequently, the value of f was tuned to obtain the best fit of the experimental data for a high value of the Scruton number ($Sc = 86$), *i.e.* in a pure VIV regime, as shown in Figure 8. By contrast, C_{L0} was set to the value 0.656 measured in the wind tunnel, while it was assumed $h^* = 1.8$, as estimated by Tamura and Shimada⁸⁾ for the square cylinder. It is apparent in Figure 8 that a value of f equal to 9.28, *i.e.* eight times the reference value of 1.16, gives a very good agreement with the experimental data, except for the hysteresis loop, which was not observed in the experiments. In fact, the analytical model correctly predicts the slope of the amplitude-velocity curve, the peak amplitude and the velocity range of excitation.

Figure 9 shows the same type of analysis for a lower value of the Scruton number ($Sc = 28$, $U_g/U_r = 1.63$), for which a full VIV-galloping interaction was observed in the experiments. For low values of the parameter f either a light interference between the two mechanisms of interference was obtained, with a modest reduction of the galloping critical flow speed (for $f = 0.58$), or the behavior already observed by Tamura and Shimada⁸⁾, with the significant overestimation of the response in the resonance region (for $f = 1.16$). By contrast, for higher values of the parameter f , the model is able to predict the nearly linear increase of the response beyond the vortex resonance flow speed observed in the experiments. In particular, if $f = 9.28$ is once again set in the equations, the model's predictions agree reasonably well with the experimental results. It is worth noting that the behavior of the model for such a high value of the coupling parameter has never been explored and therefore the actual potentiality of the model was not clear so far.

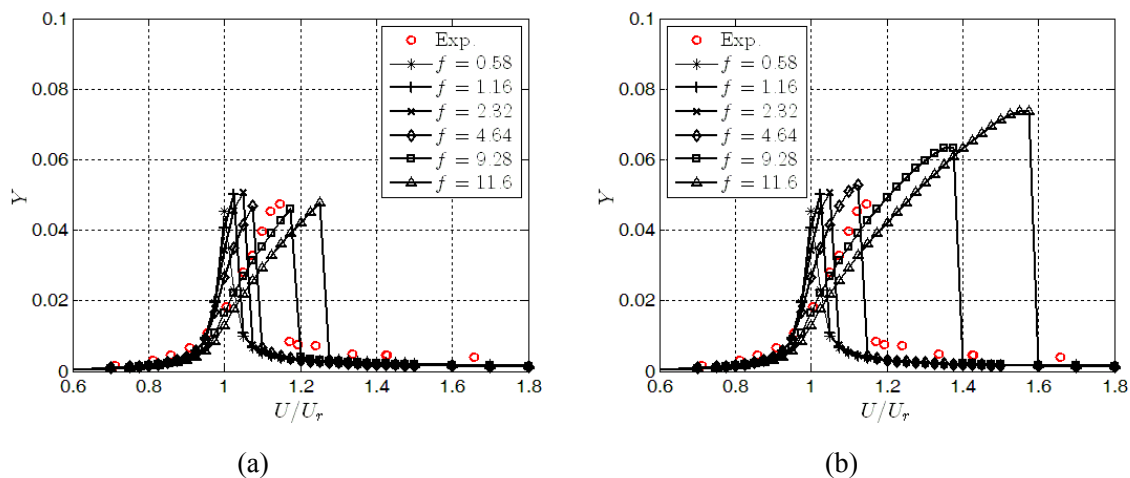


Figure 8: Comparison between the rectangular cylinder response predicted by the analytical model varying the value of the parameter f and the experimental data for a high value of the Scruton number ($Sc = 86$, test case #11). Numerical results obtained for an initial condition $Y(0) = 0.01$ (a) and $Y(0) = 15^\circ \cdot \pi/180 \cdot U/2\pi$ (b).

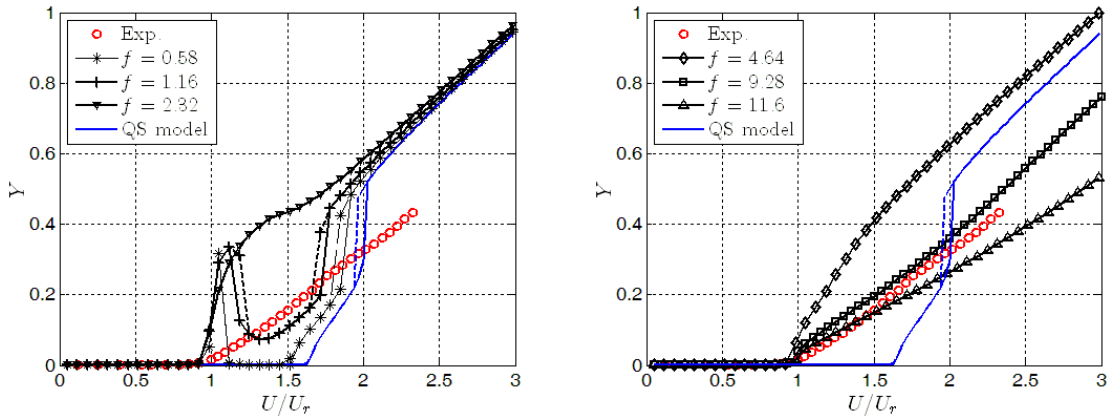


Figure 9: Comparison between the analytical model results obtained varying the value of the parameter f and the experimental data for a value of the Scruton number $Sc = 28$ (test case #4).

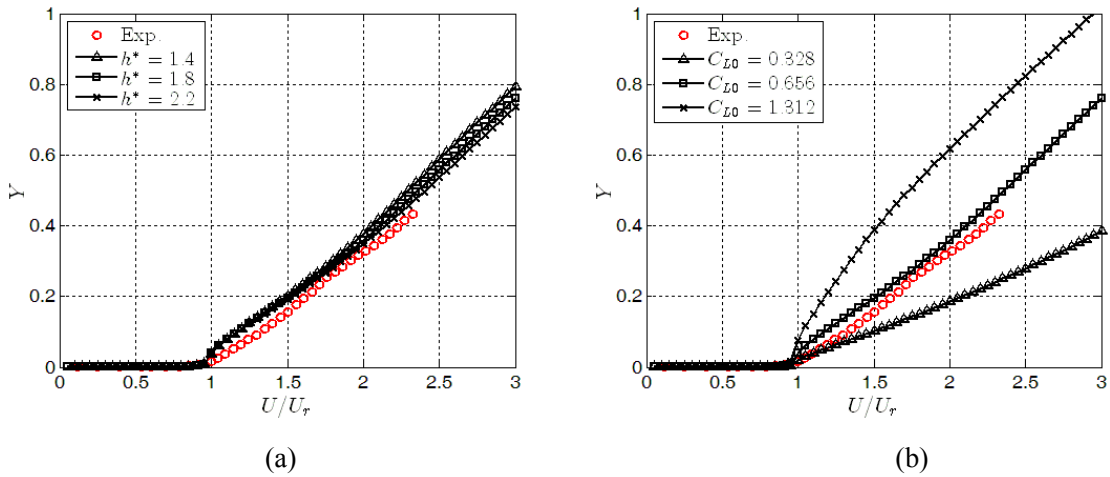


Figure 10: Sensitivity of the analytical model results ($Sc = 28$, test case #4, setting $f = 9.28$) to the variation of the value of the parameter h^* (a) and C_{L0} (b).

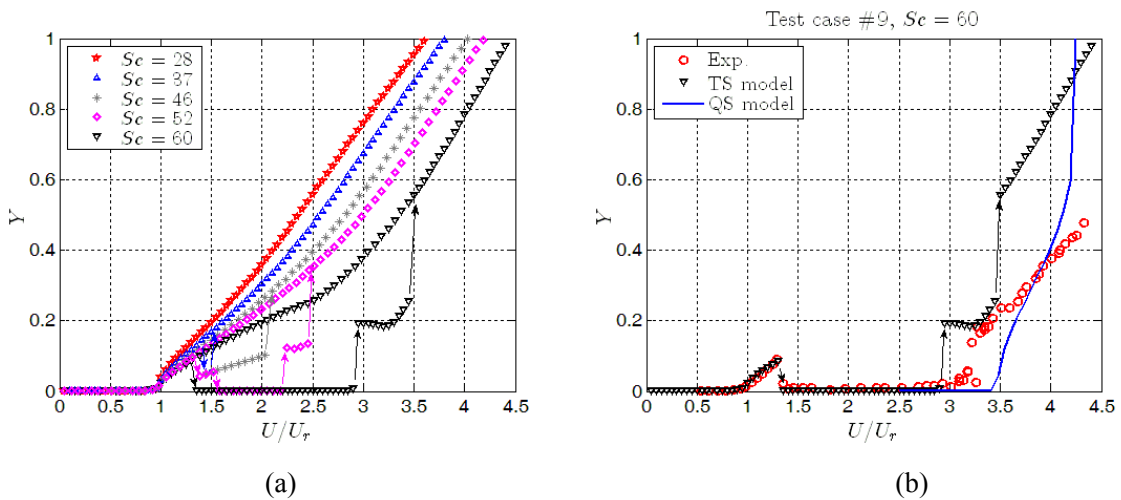


Figure 11: Amplitude-velocity curves obtained with the analytical model (obtained setting $f = 9.28$) in the transitional Scruton number range (a) and comparison with experimental results for $Sc = 60$ (test case #9), considering, for the sake of clarity, only the results relative to the initial condition $Y(0) = 0.01$ (b).

Figure 10 reports the results of the sensitivity study relative to the parameters h^* and C_{L0} . The former is difficult to be determined, as it requires clear flow visualizations or complicated flow velocity measurements, but it is clear that the results are only weakly dependent on its value in the range of interest. By contrast, the solution of the equations is very sensitive to the value of C_{L0} but this parameter can be easily determined through force measurements on the stationary cylinder, although its value is often uncertain. It is interesting to note that in the investigated range of values, an increase of C_{L0} produces the same effect as a proper reduction of f .

Figure 11(a) shows the amplitude-velocity curves predicted by the analytical model in the range of Scruton number wherein transition occurs between various regimes of interaction of vortex-induced vibration and galloping (see Figure 4). The analytical model predicts no discontinuity between VIV and galloping ranges of excitation for $Sc = 37$, although a hysteresis loop appears in a very limited range of reduced flow speed (around $U/U_r = 1.5$). The velocity range of the low-amplitude solution (observed in a similar way also in the experiments, see Figure 4) significantly extends for $Sc = 46$. By contrast, for $Sc = 52$ two hysteresis loops are detected and, for reduced flow speeds approximately in the range $1.5 < U/U_r < 2.2$, the cylinder does not vibrate unless a large initial condition is imposed. Finally, for $Sc = 60$, this intermediate range of stability extends to the left and above all to the right and the hysteresis loop close to the resonance region disappears. In particular, Figure 11(b) compares the numerical results obtained for the initial condition $Y(0) = 0.01$ to experiments for $Sc = 60$, showing reasonable agreement, despite a slight underestimation of the galloping instability threshold. The discrepancy observed for $U/U_r > 3.5$, where the model solution jumps up to a higher branch, is probably due to the inaccurate polynomial approximation of the experimental transverse force coefficient in the zone of the inflection points, which are known to relate to the hysteresis loop in the amplitude-velocity curve¹⁶⁾.

In general, the analytical model captures the main features of VIV-galloping interference but, as compared to experiments, it tends to overestimate the degree of coupling between the two mechanisms of excitation in the intermediate Scruton number range. In addition, the calculated amplitude-velocity curve reduces the slope by increasing the Scruton number, whereas this does not occur in the experiments.

6. CONCLUDING REMARKS

This paper aims at clarifying the phenomenon of interference between vortex-induced vibration and galloping, called here “low-speed galloping”, for a rectangular cylinder with a side ratio of 1.5. First, a wide experimental campaign in the wind tunnel was carried out, reliably changing the mechanical damping of the system in small steps, so to highlight the transition between various levels of VIV-galloping interference.

High values of the Scruton number, say between 50 and 60 (normalized with the cross-section area), are needed to completely decouple the ranges of excitation due to vortex-induced vibration and galloping. This conclusion has an important impact on the engineering practice, since wind-exposed structures can easily be characterized by lower values of the Scruton number. Therefore, sustained vibrations can be encountered where they are not predicted by codes and standards or classical theories of vortex-induced vibration and galloping. These results can also be read in terms of limits of validity of the quasi-steady theory. In fact, the latter correctly predicts the galloping critical flow speed only for Scruton numbers no lower than about 60, *i.e.* for a ratio of the quasi-steady galloping to the vortex resonance critical flow speed no lower than about 3.5.

From both the scientific and the engineering points of view, it is interesting to understand how the aeroelastic behavior of the cylinder modifies due to oncoming turbulence. With this aim, wind tunnel tests in homogeneous turbulent flows are presently underway. One may already conclude that a low incoming turbulence (intensity of about 3%) seems to promote the mechanism of interference between VIV and galloping for intermediate values of the Scruton number (around 40). This result is in line with the findings of Parkinson and co-workers¹⁷⁻¹⁸⁾ and Bearman¹⁹⁾ for the square section and a higher turbulence intensity (from 7% to 10%).

In this work, the modeling of low-speed galloping was also attempted through a slight modification of Tamura and Shimada’s model. It was concluded that this wake-oscillator model, which also incorporates the quasi-steady force contribution, is able to reproduce the main features of the instability promoted by the interference of VIV and galloping, provided that a proper value of the coupling parameter f is set in the equations. This value is much higher than those ever tested in previous modeling efforts.

Finally, it is worth noting that the interference of vortex-induced vibration and galloping can be positively exploited for low-power energy-harvesting systems. In fact, as compared to pure galloping instability²⁰⁾, this phenomenon ensures higher levels of power extraction at low wind speed and therefore improved efficiency, as a consequence of the low onset flow speed and the weak dependency on the Scruton number up to medium values of it.

ACKNOWLEDGMENT

The authors wish to thank Luca Pigolotti for the valuable contribution in the development of the experimental setup.

REFERENCES

- 1) Parkinson G. V., Brooks N. P. H.: On the aeroelastic instability of bluff cylinders, *J. Appl. Mech.*, Vol. 28, pp. 252-258, 1961.
- 2) Parkinson G. V., Smith J. D.: The square prism as an aeroelastic non-linear oscillator, *Q. J. Mech. Appl. Math.*, Vol. 17, pp. 225-239, 1964.
- 3) Mannini C., Marra A. M., Bartoli G.: VIV-galloping instability of rectangular cylinders: Review and new experiments, *J. Wind Eng. Ind. Aerodyn.*, Vol. 132, pp. 109-124, 2014.
- 4) Nakamura Y., Matsukawa T.: Vortex excitation of rectangular cylinders with a long side normal to the flow, *J. Fluid Mech.*, Vol. 180, pp. 171-181, 1987.
- 5) Nakamura Y., Hirata K.: Pressure fluctuations on oscillating rectangular cylinders with the long side normal to the flow, *J. Fluids Struct.*, Vol. 5, pp. 165-183, 1991.
- 6) Matsumoto M.: Aerodynamic damping of prisms, *J. Wind Eng. Ind. Aerodyn.*, Vol. 59, pp. 159-175, 1996.
- 7) Santosham T. V.: *Force measurements on bluff cylinders and aeroelastic galloping of a rectangular cylinder*, Master's thesis, University of British Columbia, Vancouver, Canada, 1966.
- 8) Tamura Y., Shimada K.: A mathematical model for the transverse oscillations of square cylinders, *Proc. First International Conference on Flow Induced Vibrations*, Bownesson-Windermere, UK, 12-14 May 1987, pp. 267-276, 1987.
- 9) Corless R. M., Parkinson G. V.: A model of the combined effects of vortex-induced oscillation and galloping, *J. Fluids Struct.*, Vol. 2, pp. 202-220, 1988.
- 10) Shiraishi N., Matsumoto M.: On classification of vortex-induced oscillation and its application for bridge structures, *J. Wind Eng. Ind. Aerodyn.*, Vol. 14, pp. 419-430, 1983.
- 11) Naudascher E., Wang Y.: Flow-induced vibrations of prismatic bodies and grids of prisms, *J. Fluids Struct.*, Vol. 7, pp. 341-373, 1993.
- 12) Tamura Y., Matsui G.: Wake-oscillator model of vortex-induced oscillation of circular cylinder, *Proc. Fifth International Conference on Wind Engineering*, Forth Collins, US, 8-14 July 1979, pp. 1085-1094, 1979.
- 13) Birkhoff G.: Formation of vortex streets, *J. Appl. Phys.*, Vol. 24, pp. 98-103, 1953.
- 14) Funakawa M.: The vibration of a cylinder caused by wake force in a flow, *Bull. Japan Soc. Mech. Eng.*, Vol. 12, pp. 1003-1010, 1969.
- 15) Marris A. W.: A review on vortex streets, periodic wakes, and induced vibration phenomena, *J. Basic Eng.-T. ASME*, Vol. 86, pp. 185-193, 1964.
- 16) Barrero-Gil A., Sanz-Andres A., Alonso G.: Hysteresis in transverse galloping: The role of inflection points, *J. Fluids Struct.*, Vol. 25, pp. 1007-1020, 2009.
- 17) Parkinson G. V., Sullivan P. P.: Galloping response of towers, *J. Ind. Aerodyn.*, Vol. 4, pp. 253-260, 1979.
- 18) Parkinson G. V., Wawzonek M. A.: Some considerations of combined effects of galloping and vortex resonance, *J. Wind Eng. Ind. Aerodyn.*, Vol. 8, pp. 135-143, 1981.
- 19) Bearman P. W., Gartshore I. S., Maull D. J., Parkinson G. V.: Experiments on fluid-induced vibration of a square-section cylinder, *J. Fluids Struct.*, Vol. 1, pp. 19-34, 1987.
- 20) Barrero-Gil A., Alonso G., Sanz-Andres A.: Energy harvesting from transverse galloping, *J. Sound Vib.*, Vol. 329, pp. 2873-2883, 2010.

LARGE AMPLITUDE AERODYNAMIC VIBRATION OF RECTANGULAR CYLINDER WITH A SIDE RATIO OF TWO

Tomomi Yagi⁺¹, Hisato Matsumiya⁺², Masaaki Hamano⁺³, Yuta Sasaki⁺⁴ and Takashi Nishihara⁺⁵
^{+1,3,4}Department of Civil and Earth Resources Engineering, Kyoto University,
Kyoto 615-8540, Japan

^{+2,5}Civil Engineering Research Laboratory, Central Research Institute of Electric Power Industry,
Chiba 270-1194, Japan

In general, flutter instabilities of bluff bodies are investigated in the very small amplitude region. The main interests of engineers are to know whether the instabilities appear or not, and to evaluate their onset wind velocities. Therefore, the behaviors of self-induced vibrations at the large amplitude region still remain unexplained. It can be supposed that the amplitudes of so-called divergent type vibrations do not continue increasing all the time, even the structures allow to vibrate. Then, in this study, a rectangular cylinder with a side ratio of two is used to investigate its large amplitude vibrations under three DOF condition with various angles of attack. It is well known that this cylinder shows single DOF flutters, such as the galloping and the torsional flutter at the angle of attack 0 degree. Then, the appearance of aerodynamic interferences between these vibrations is expected in three DOF condition. However, to avoid the interference with Kármán vortices, the wind tunnel tests were conducted at comparatively high reduced wind velocity region. To obtain the large amplitudes in the wind tunnel, the model was mounted by an elastic support system, which is used for the models of overhead transmission lines. Then, the various kinds of self-induced vibration with large amplitudes were observed, e.g. vertical 1DOF dominant vibration, torsional 1DOF dominant vibration, coupled 3DOF vibration and so on. It depends on the angle of attack and the initial condition which phenomenon occurs. To understand these complicated responses, the time history analyses using quasi-steady aerodynamic forces are tried. Also, the aerodynamic force, which has in-phase component to torsional velocity, is added to the quasi-steady formulation virtually. Then, the most of large amplitude vibrations can be explained by using the quasi-steady aerodynamic forces and/or the aerodynamic force attributable to torsional velocity.

Keyword: coupled vibration, galloping, torsional flutter, quasi-steady aerodynamic force

1. INTRODUCTION

Flutter phenomena on bluff bodies can be called as divergent type of aerodynamic vibrations due to rapid increase in amplitude. It is needless to say that the appearance of flutter phenomena on a real structure is not acceptable. Therefore, the specifications of their onset wind velocities or the judgments of their stabilities at the verification wind speed are main targets for the engineering considerations. Then, there are very few investigations on the response behavior of bluff bodies during flutter vibrations. However, due to the recent climate change, the behavior of structures under higher wind velocity than the verification wind speed might be necessary to investigate in future. Furthermore, the large amplitude vibrations of flutter phenomena in 3DOF condition must be also interesting topics on the two dimensional bluff body aerodynamics. Then, in this study, the 3DOF flutter vibrations of a rectangular cylinder are investigated by wind tunnel tests and numerical analyses. For the engineering purposes, the flutter behaviors at around the onset wind velocity and also at very low amplitude region must be of some interest. However, it is not an easy task to make researches in these areas due to existence of strong interference from

⁺¹yagi.tomomi.7a@kyoto-u.ac.jp, ⁺²hisato-m@criepi.denken.or.jp

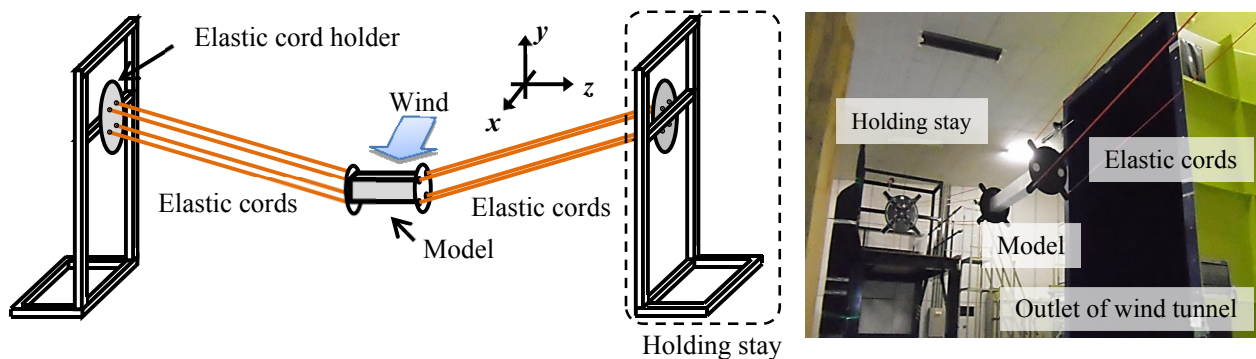


Figure 1: Elastic support system of model in the wind tunnel

vortices shed from the body. To keep the problem simple, the wind tunnel tests were conducted at the comparatively higher reduced wind velocity region and in the larger amplitude region, where the effects of vortex shedding can be avoided.

For a target two dimensional section, a rectangular cylinder with a side ratio two is chosen ($B/D=2$, where B , D denote width and height of the body, respectively). It is well known that this section shows the galloping instability in the case of vertical 1DOF and torsional flutter in the case of torsional 1DOF. Therefore, it can be expected that the aerodynamic interferences between the galloping and torsional flutter must be appeared in 3DOF conditions. Also, the experiments were conducted by this cylinder with various angles of attack from 0 degree to 90 degree, which means the side ratio of the body varies from 2 to 0.5. In the case of side ratio 0.5, both the galloping and the torsional flutter never appear, but the coupling vibration may happen in 3DOF case. The model was supported in the wind tunnel by using elastic cords, which were developed for the sectional tests of transmission lines to allow large amplitudes^{1),2)}. Then, generation mechanisms of each 3DOF responses from the wind tunnel tests are interpreted by the numerical time series analyses applying quasi-steady aerodynamic forces. The galloping originated responses may be simulated by quasi-steady approach, but the torsional flutter originated responses must be difficult to obtain. The previous researches on the unsteady aerodynamic forces on bluff bodies suggest that the torsional velocity terms must be needed to express the torsional flutter, for example A_2^* in the Scanlan's flutter derivatives³⁾. Therefore, contributions of torsional instabilities in these 3DOF responses are considered by applying additional torsional velocity terms on quasi-steady aerodynamic forces.

2. WIND TUNNEL TESTS

A series of wind tunnel tests were conducted by using an Eiffel-type wind tunnel with an axial fan located in Central Research Institute of Electric Power Industry, Japan. The outlet area of the wind tunnel is 1.6 m width x 2.5 m height, and the maximum wind speed is 17 m/s.

(1) Model

The rectangular cylinder of a side ratio $B/D=2$ (B : width, D : height) are considered in this study. The size of model for the wind tunnel tests are width $B=100\text{mm}$, height $D=50\text{mm}$ and length $l=1000\text{mm}$. The model is made of acrylic resin plates and the circular end plates are installed in the both ends of body.

(2) Supporting system

The model was supported by eight elastic cords as shown in Figure 1. These long elastic cords with low rigidity can obtain the significant large of vibration at low natural frequencies. The system can allow the maximum double amplitudes in the both vertical and horizontal directions till $40D$ and one in the torsional rotation till 180 degree. The natural frequencies in vertical, horizontal, and torsional directions can be controlled by chord length, sag, chord's distance and so on¹⁾. Two kinds of structural conditions are considered as follows; the case a) where the vertical and horizontal natural frequencies are set as about 0.5Hz

and the torsional one is set as about 0.9Hz; and the case b) where the all three frequencies are set as about 0.5Hz. In the former case, it is expected that the 1DOF self-induced vibrations such as the galloping or the torsional flutter may easily come out. In the latter case, the 3DOF coupling vibrations must be expected to appear. The wind velocity is fixed as $U=10.2\text{m/s}$ and the initial angles of attack are varied from 0 degree to 90 degree. The each case of angles of attack is adjusted at no wind condition, but it will have static displacement under the wind condition and furthermore the equilibrium position (vibration center) will be depends on the amplitude. Therefore, the experimental results are discussed by the equilibrium torsional position of the body, which is referred as a torsional mean displacement Θ_m . The structural parameters are as shown in Table 1. The displacement coordinates x , y , θ denote horizontal direction, vertical direction and torsional direction, respectively. The 3DOF responses were measured by a video tracking system with a frame rate of 60Hz.

Table 1: Structural parameters for free vibration tests.

Case	Equivalent	Equivalent	Wind velocity	Natural frequencies			Reduced wind velocities		
	Mass	moment of inertia		f_x	f_y	f_θ	$U/f_x B$	$U/f_y B$	$U/f_\theta B$
	m	I	U	[Hz]	[Hz]	[Hz]			
	[kg]	[kg·m ²]	[m/s]						
a)	3.14	0.0355	10.1	0.47	0.52	0.88	214	195	115
b)	3.14	0.0249	10.2	0.47	0.52	0.50	216	196	205

3. AERODYNAMIC FORCES

(1) Steady aerodynamic coefficients

The steady aerodynamic coefficients defined as follows are also measured for the rectangular cylinder of a side ratio $B/D=2$ with various angles of attack, as shown in Figure 2.

$$C_D(\alpha) = \frac{Drag}{\frac{1}{2}\rho U^2 D l}, \quad C_L(\alpha) = \frac{Lift}{\frac{1}{2}\rho U^2 B l}, \quad C_M(\alpha) = \frac{Moment}{\frac{1}{2}\rho U^2 B^2 l} \quad (1)$$

where, C_D , C_L , and C_M are coefficients of drag, lift and pitching-moment, respectively. Also, *Drag*, *Lift*, and *Moment* are the mean values of the measured drag [N], lift [N], and pitching-moment [N·m] on the stationary model and ρ is the air density [kg/m³]. In Figure 3, Den Hartog's criterion⁴⁾ for the galloping 1DOF instability is plotted. At the angles of attack 0-6 degrees and around 70 degree, Den Hartog criterion shows negative values, where the galloping instability may appears. Also slope of aerodynamic pitching-moment coefficient $dC_M/d\alpha$ is shown in Figure 4 for reference, which might be useful to judge the torsional flutter 1DOF instability. As mentioned above, the torsional flutter 1DOF instability can be explained by the Scanlan's flutter derivative A_2^* , which is the torsional velocity term of unsteady pitching-moment, but may have some relationship to $dC_M/d\alpha$. At the angles of attack 0-10 degrees, $dC_M/d\alpha$ shows negative values, and also from the additional experiments for flutter derivatives, A_2^* shows comparative large positive value (which means large negative damping) at the angle of attack 8 degree. Therefore, the torsional flutter can be generated in this region.

(2) Quasi-steady aerodynamic forces

As shown in Figure 5, the quasi-steady aerodynamic forces can be defined as follows. First of all, the relative wind velocity U_r [m/s] and the relative angle of attack α_r [rad.] can be described as follows. The angle Θ_e denotes the static torsional displacement, and this angle is slightly different from the torsional mean displacement Θ_m , which may be called as the equilibrium position or the vibration center as mentioned above.

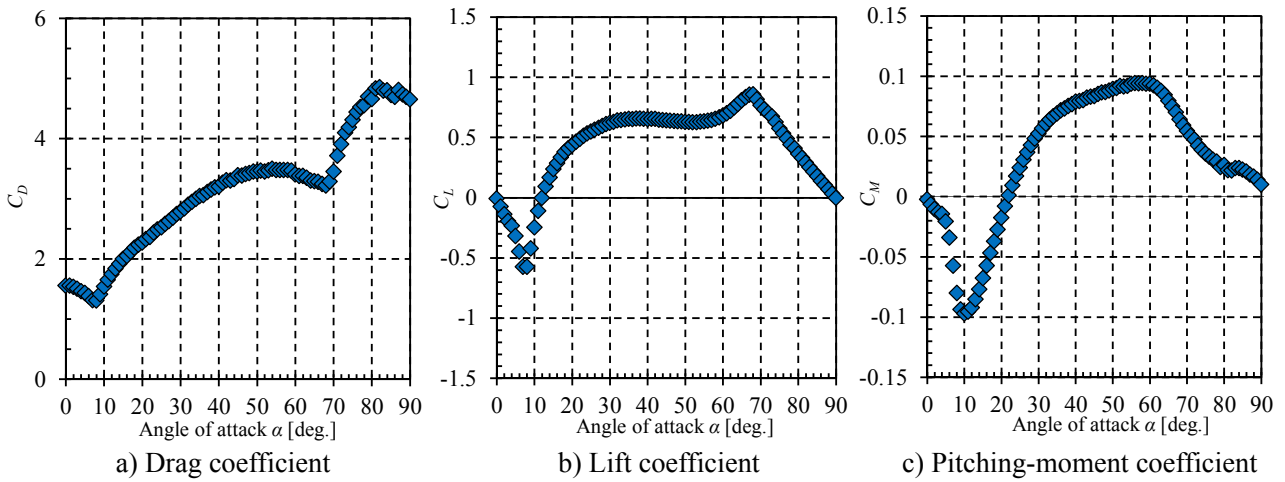


Figure 2: Steady aerodynamic coefficients at various angles of attack

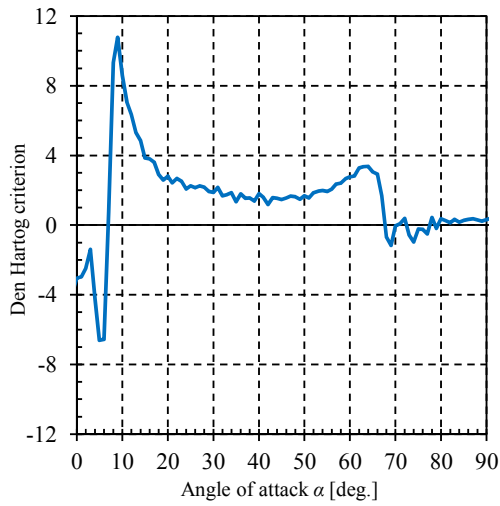


Figure 3: Den Hartog criterion.

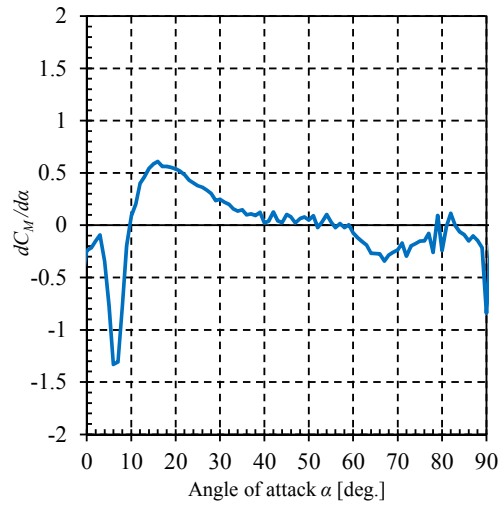


Figure 4: Slope of pitching-moment coefficient.

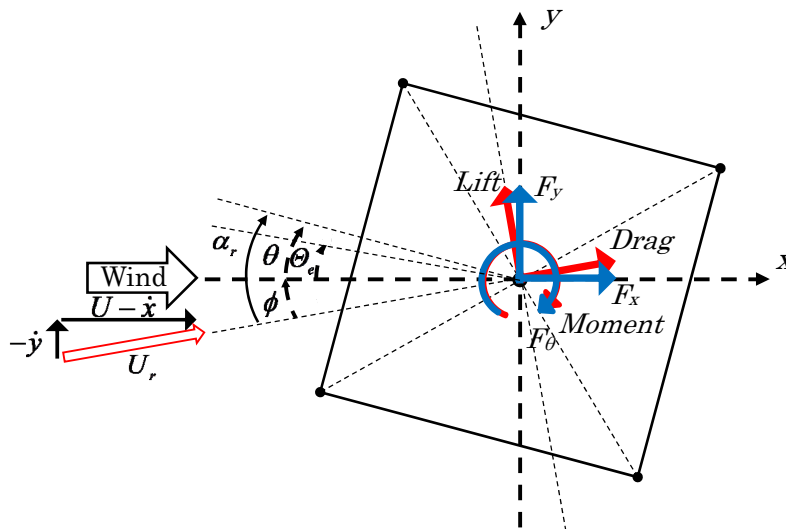


Figure 5: Definition of quasi-steady aerodynamic forces.

$$U_r = \sqrt{(U - \dot{x})^2 + \dot{y}^2} \quad (2)$$

$$\alpha_r = \theta + \phi, \quad \phi = \tan^{-1}\left(\frac{-\dot{y}}{U - \dot{x}}\right) \quad (3)$$

Then, the quasi-steady aerodynamic forces in x, y, θ directions as follows.

$$F_x = \frac{1}{2} \rho U_r^2 l \{DC_D(\alpha_r) \cos \phi - BC_L(\alpha_r) \sin \phi\} \quad (4)$$

$$F_y = \frac{1}{2} \rho U_r^2 l \{DC_D(\alpha_r) \sin \phi + BC_L(\alpha_r) \cos \phi\} \quad (5)$$

$$F_\theta = \frac{1}{2} \rho U_r^2 l \{B^2 C_M(\alpha_r)\} \quad (6)$$

The equations of motions for the body supported by elastic cords in x, y, θ directions are nonlinear equations¹⁾. Then, substituting the quasi-steady aerodynamic forces of Eqs.(4)-(6) to the equations of motion, the response of the body can be simulated using these governing equations. It is very important to notice that the coupling terms exist in the both structural side and aerodynamic side. However, the coupling vibration due to the structural coupling has no interest. It is quite difficult to eliminate the structural coupling effects from the wind tunnel tests. Therefore, the time series analyses using the non-structural coupling equations must be also needed to discuss this matter.

(3) Additional aerodynamic forces attributable to torsional velocity

In general, to express the instability of 1DOF torsional flutter, the torsional velocity terms of the unsteady aerodynamic pitching-moment must be considered. However, those terms never appears on the quasi-steady formulations. To evaluate the contribution of 1DOF torsional flutter to the 3DOF coupling vibrations, the virtual torsional velocity terms of aerodynamic pitching-moment is added to Eq.(6). Then, virtual aerodynamic pitching-moment can be written as follows.

$$F_\theta = \frac{1}{2} \rho U_r^2 B^2 l \left\{ C_M(\alpha_r) + 2\pi G \frac{B \dot{\theta}}{U_r} \right\} \quad (7)$$

where the parameter G can control the aerodynamic damping term in Eq.7. If the flutter derivative A_2^* can be assumed to have linear relation with the reduced wind velocity U/fB , then this parameter G is recognized as the slope of A_2^* against the reduced wind velocity U/fB . Of course, the flutter derivative is defined by the unsteady aerodynamic force, and the direct comparison does not have any physical consistency. Furthermore, the effects of this term to the governing equations are almost same as the structural damping in the torsional motion. Then, the values of virtual parameter G are assumed between 0.02-0.20 in this study.

4. AERODYNAMIC VIBRATIONS IN 3DOF

As mentioned above, there are two kinds of combination of natural frequencies for the free vibration tests, which are the case a) $f_x = f_y = 0.5\text{Hz}$, $f_\theta = 0.9\text{Hz}$ and the case b) $f_x = f_y = f_\theta = 0.5\text{Hz}$, see Table 1. In the both cases, the vibration amplitudes from the wind tunnel tests and from the time series analyses are compared at each angle of attack, and the vibration mechanisms of these 3DOF phenomena are discussed.

(1) In case of no structural coupling with torsional displacement [case a), $f_x = f_y = 0.5\text{Hz}$, $f_\theta = 0.9\text{Hz}$]

In this case, the natural frequency of torsional motion is higher than the vertical one and horizontal one. Therefore, the torsional motion and the vertical motion are difficult to couple each other in this system. The results of vibration double amplitudes in 3DOF from the wind tunnel tests and the time series analyses are shown in Figure 6. The lateral axes denote the torsional mean displacement Θ_m . The blue circle plots are

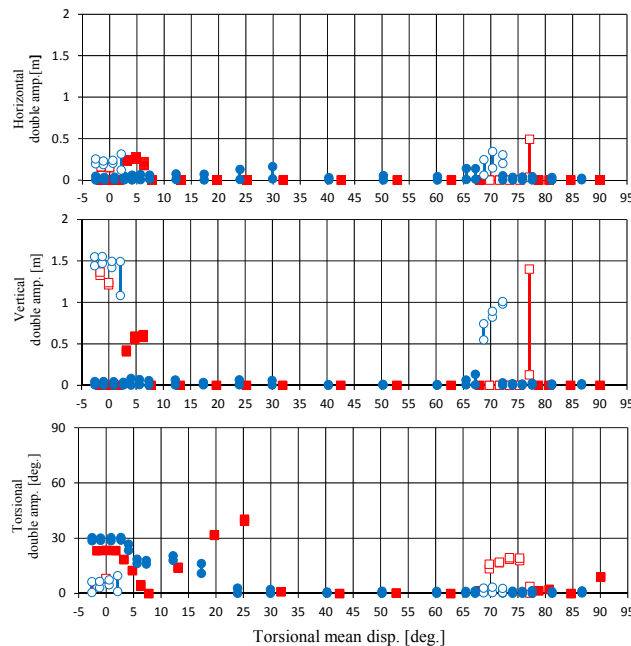
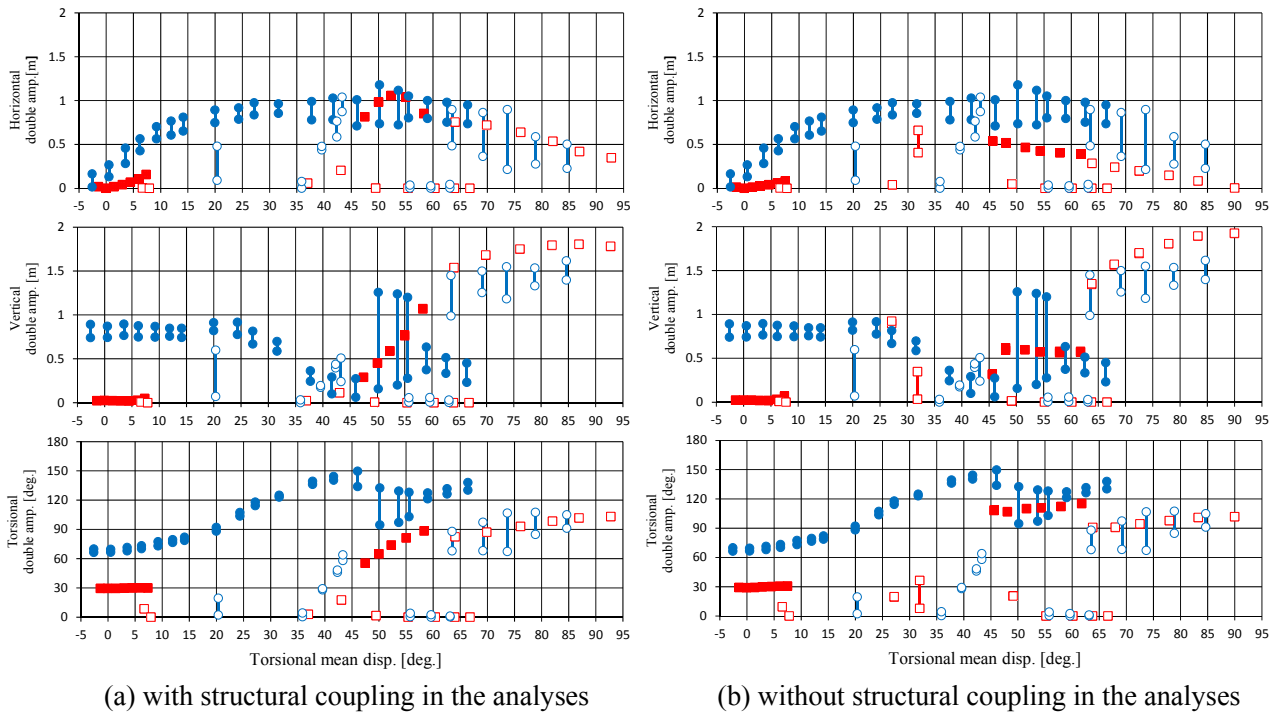


Figure 6: Vibration amplitudes at various torsional mean displacements Θ_m in the case a).
 $f_x=f_y=0.5\text{Hz}$, $f_\theta=0.9\text{Hz}$, Experiments (●: mode1, ○: mode2), Analyses (■: mode1, □: mode2)

results from the wind tunnel tests and the red square plots are from the time series analyses. Also, the open plots and solid plots distinguish the different modes, which depend on the initial conditions. Then the around $\Theta_m=0\text{deg.}$, there are two different modes, one is a large vertical dominant vibration and the other is a large torsional dominant vibration, which never appear in the same time. The blue open circles must be the response due to the galloping at $\Theta_m=-2$ to $+2\text{deg.}$ and around 70deg. , which also correspond to negative values of Den Hartog criterion in Figure 3. On the other hands, the blue solid circles must be the torsional flutter at $\Theta_m=-2$ to around 20deg. , which corresponds to negative values of $dC_M/d\alpha$ (only at $\alpha=0-10\text{deg.}$) and also the positive flutter derivative A_2^* till $\alpha=20\text{deg.}$ (from the other additional tests). Around at $\Theta_m=5\text{deg.}$, the Den Hartog criterion shows negative with comparatively large absolute value, but the galloping never appears in the wind tunnel tests. This might be due to the aerodynamic interferences between the galloping and the torsional flutter.

From the time series analyses using the quasi-steady aerodynamic forces, both of the galloping and the torsional flutter are well simulated around at $\Theta_m=0\text{deg.}$ It is interesting to see that the galloping in 0.5Hz and the torsional flutter in 0.9Hz exist in the same time at around $\Theta_m=5\text{deg.}$ The torsional amplitudes tend to decrease against Θ_m more significantly than the data from experiments. Then, if the positive torsional velocity term is included in the aerodynamic pitching-moment, then the torsional response becomes larger, and furthermore the amplitude of the galloping may be reduced by the aerodynamic interferences. Similarly, an opposite case can be seen at around $\Theta_m=70-75\text{deg.}$ The time series analyses show the torsional response instead of the vertical response. To reduce the torsional responses, the Eq.(7) with negative torsional velocity term $G=-0.1$ is applied in the governing equations, which means increasing total torsional damping. Then, the torsional responses are vanished and the galloping instabilities appear as same as the experimental results. It can be concluded that the aerodynamic interferences between the galloping and the torsional flutter exist. To simulate this interference precisely, the rational introduction of the torsional velocity term in the aerodynamic pitching-moment must be needed. Furthermore, the appearance of vertical vibration at $\Theta_m=77\text{deg.}$ is mainly due to the structural coupling terms in equations of motion and the low aerodynamic damping of the torsional motion.



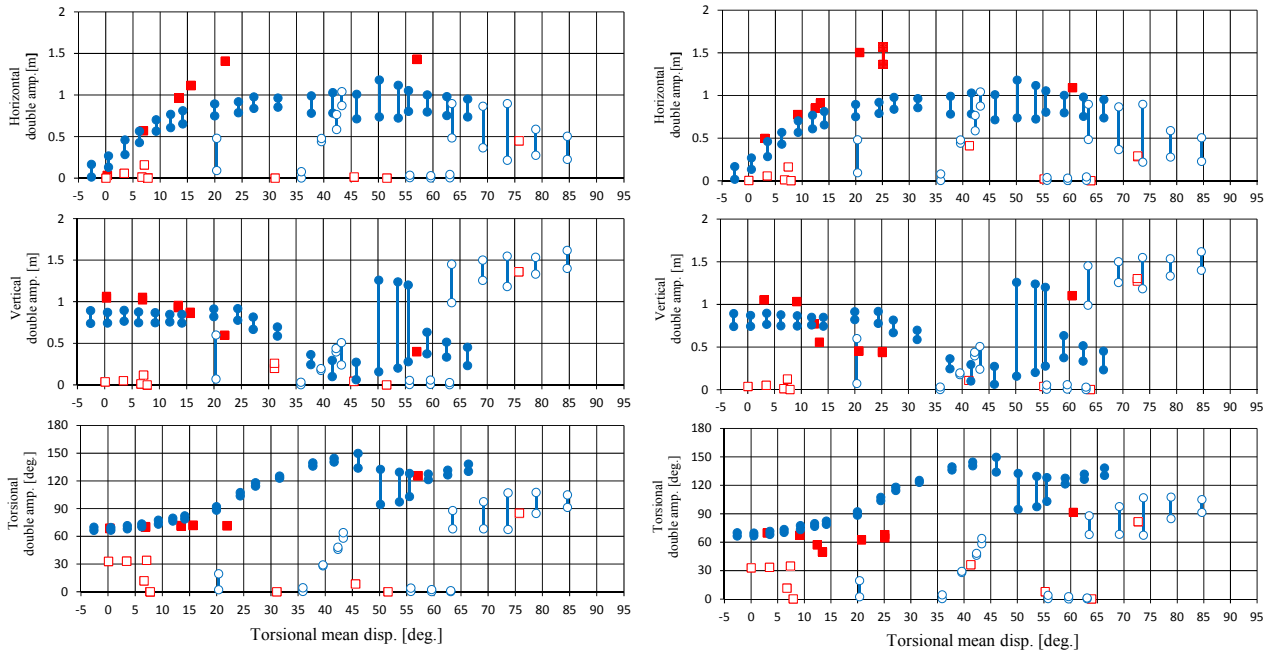
(a) with structural coupling in the analyses (b) without structural coupling in the analyses
 Figure 7: Vibration amplitudes at various torsional mean displacements Θ_m in the case b).
 $f_x = f_y = f_\theta = 0.5\text{Hz}$, Experiments (●: mode1, ○: mode2), Analyses (■: mode1, □: mode2)

(2) In case of fully structural coupling in 3DOF [case b), $f_x = f_y = f_\theta = 0.5\text{Hz}$]

In this case, all of the natural frequencies are almost identical and fully coupling motions in 3DOF are expected. In the same manner as the previous case, the results are shown in Figure 7. To distinguish the 3DOF motions induced by structural coupling or aerodynamically coupling phenomena, the results of time series analyses using the equations of motion without structural coupling terms are also plotted in the Figure 7. Comparing numerical results with the structural coupling and ones without the structural coupling, there are some differences in the amplitudes, but it seems that the 3DOF phenomena due to structural coupling terms are not exist in this case.

From the experimental results, the 3DOF coupled vibration with comparatively large amplitudes are observed through whole range of torsional mean displacement Θ_m . The vibration phenomena can be roughly divided at $\Theta_m = 45\text{deg}$. Furthermore, in the region $\Theta_m > 45\text{deg}$., it seems that the response changes from the torsional dominant type to the vertical dominant type around at $\Theta_m = 65\text{deg}$. Also, the amplitudes of vibrations from the time series analyses coincide well with experimental results at $\Theta_m > 45\text{deg}$. Therefore, the 3DOF coupling vibrations at $\Theta_m > 45\text{deg}$. can be explained by quasi-steady aerodynamic forces. However, at $\Theta_m = -2$ to $+8\text{deg}$., the numerical analyses show only the torsional dominant vibrations and their amplitudes are almost half of the experimental results. In this region, the torsional velocity terms in the aerodynamic pitching-moment might be needed. In the region of $\Theta_m = 10-35\text{deg}$., there is no results from the time series analyses. Even taking into account the static displacements, the vibration center moves to lower angle than $\Theta_m = 10\text{deg}$.

Then, the torsional velocity term in the aerodynamic pitching moment shown in Eq.(7) is applied in this case. The torsional damping parameter G is determined virtually to keep the torsional amplitude almost same as experimental results, as shown in Figure 8. When the torsional displacements are increased by changing the torsional damping, the 3DOF coupling motion appears and the vertical displacements and horizontal displacements are consistent with those from the wind tunnel tests, especially at $\Theta_m = 0-25\text{deg}$. Also, the phase differences between vertical motion and the torsional motion agree with experimental results, see Figure 9. Furthermore, introducing the torsional velocity term, the vibration center never moves to the smaller

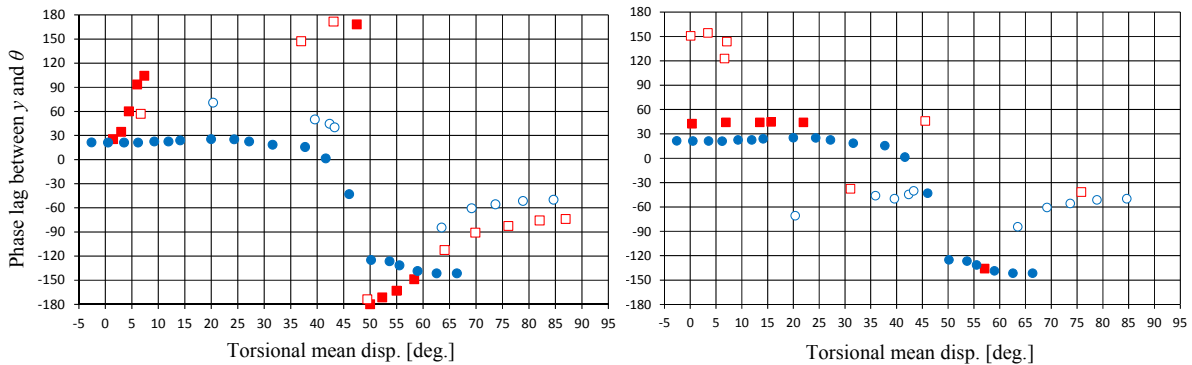


(a) with structural coupling in the analyses

(b) without structural coupling in the analyses

Figure 8: Vibration amplitudes at various torsional mean displacements θ_m in the case b) with additional aerodynamic forces attributable to torsional velocity.

$f_x = f_y = f_\theta = 0.5\text{Hz}$, Experiments (●: mode1, ○: mode2), Analyses (■: mode1, □: mode2)



(a) without torsional velocity terms

(b) with aerodynamic torsional velocity terms

same case as Figure 7(a)

same case as Figure 8(a)

Figure 9: Phase lag between vertical displacement and torsional displacement in the case b)

$f_x = f_y = f_\theta = 0.5\text{Hz}$, Experiments (●: mode1, ○: mode2), Analyses (■: mode1, □: mode2)

angles. Therefore, the 3DOF coupling vibrations in $\theta_m=0-25\text{deg.}$ may be torsional flutter initiated instabilities, and to simulate these vibration, the torsional velocity term in the aerodynamic pitching moment must be needed.

4. CONCLUSIONS

The 3DOF large amplitude vibrations are investigated using the rectangular cylinder of a side ratio two with various angles of attack by both of the wind tunnel tests and the time series analyses. Then, the following conclusions are obtained.

- 1) Both of the 1DOF instabilities such as galloping and torsional flutter with large amplitudes can be simulated by quasi-steady aerodynamic forces in certain extent. However, to discuss the aerodynamic

interference, the additional aerodynamic pitching-moment terms attributable to torsional velocity are needed.

- 2) 3DOF aerodynamically coupling vibrations at the torsional mean displacements more than $\Theta_m = 45$ deg. can be explained by the quasi-steady approach.
- 3) On the other hand, the aerodynamically coupling vibrations at $\Theta_m = 0-25$ deg. must be torsional flutter initiated instabilities, and to simulate these vibration, the torsional velocity terms in the aerodynamic pitching moment are needed.

ACKNOWLEDGMENT

This work was partially supported by the Japan Iron and Steel Federation.

REFERENCES

- 1) Matsumiya, H., Nishihara, T.: Wind tunnel tests for simulating large-amplitude, low-frequency galloping on overhead transmission lines. *Proc. 7th Colloq. Bluff Body Aerodyn. Appl.*, Shanghai, China, 2012.
- 2) Matsumiya, H., Nishihara, T.: validation of two quasi-steady aerodynamic force formulations for galloping simulation of four-bundled conductors. *Proc. Symp. Dynamics Aerodyn. Cables*, Copenhagen, Denmark, 2014.
- 3) Scanlan, R.H., Tomko, J.J. : Airfoil and bridge deck flutter derivatives, *Journal of Engineering Mechanics*, ASCE, Vol.97, No.EM6, pp.1717-1737, 1971.
- 4) Den Hartog, J.P.: Mechanical Vibrations, *McGraw-Hill*, New York, 1956.

VIBRATIONS AND COUNTERMEASURES FOR CABLE STRUCTURE OF HONSHU-SHIKOKU BRIDGES

Shigeki Kusuhara⁺¹

⁺¹ Honshu-Shikoku Bridge Expressway Co., Ltd., Kobe, Japan

The Honshu-Shikoku Bridges are permanent links from Honshu to Shikoku, two of four major islands in Japan, by three routes, which consist of 17 long-span bridges including 10 suspension bridges, 5 cable-stayed bridges. These routes are important parts of the national trunk roads in Japan, and no alternative route exists. Therefore, all bridges are required to be in sound condition for a long time with economical consideration.

Recently, the polyethylene-covered parallel wire strands have been used for the cable system of the long-span bridges in order to reduce the maintenance cost. The polyethylene-covered cables with circular cross-sections are likely to be excited vibration by external turbulences, including winds. Therefore, countermeasures for cable vibration were examined and applied to each bridge during construction stage. However, several cable vibrations were observed during operation stage and the new countermeasures were examined since the cable vibrations are complicated phenomena.

This paper describes the vibration control methods for cable systems of the Honshu-Shikoku Bridges, as well as the current evaluation of these methods.

Keyword: Long-span bridge, Wind-induced vibration, Inclined cable, Suspender rope

1. INTRODUCTION

The Honshu-Shikoku Bridges (HSB) are permanent links from Honshu to Shikoku, two of four major islands in Japan, by three routes, including ten suspension bridges, five cable-stayed bridges, an arch bridge and a truss bridge, as shown in Fig. 1. Especially, the Akashi Kaikyo Bridge was completed in 1998 as the world's longest suspension bridge with the main span of 1991 meters and the Tatara Bridge was completed in 1999 with the main span of 890 meters. The Honshu-Shikoku Bridges are required to be maintained healthy since the three routes are indispensable highway/railway networks. These bridges were constructed and operated by Honshu-Shikoku Bridge Authority (HSBA). In 2005 the Honshu-Shikoku Bridge Expressway Company Limited (HSBE) was founded by the central government and ten local governments in order to take over the HSBA.

Since Japan is located in the Far East Asia, where many typhoons attack the major islands every year, the wind-resistant design is one of the most important technical problems to be solved for long-span bridges. Therefore, various investigations and researches were carried out and the latest technologies were applied to each bridge. Particularly, the large-scale boundary-layer wind tunnel facilities were built for the Akashi Kaikyo Bridge, and the wind tunnel tests were carried out, which verified the aerodynamic stability of the Bridge.

Recently, polyethylene-covered parallel wire strands (PE cables) have been used for cable systems of the long-span bridges to reduce maintenance cost. The PE cables with circular cross-sections are likely to be excited by external turbulences, including winds. Therefore, countermeasures for cable vibrations were examined and applied to each bridge during construction. However, several cable vibrations occurred during operations and the countermeasures were examined since the cable vibrations are complicated phenomena.

This paper describes the vibration control methods for cable systems of long-span bridges at completion and during operation, as well as the current evaluation of these methods.

⁺¹shigeki-kusuhara@jb-honshi.co.jp



Figure 1: Outline of Honshu-Shikoku Bridges

2. COUNTERMEASURE AGAINST CABLE VIBRATION OF HSB

The cable vibration and its countermeasures on the suspension bridges and the cable-stayed bridges of the Honshu-Shikoku Bridges are shown in Tab. 1. Among them, the PE-cables are used for cable systems of the long-span bridges to reduce maintenance cost, and are easy to be excited by winds because of their smooth circular cross section. Therefore, the countermeasures for cable vibrations have been examined and applied to each bridge during construction. On the other hand, the suspenders that use the Center Fit Wire Rope Core (CFRC) have no wind-induced vibrations. In general, the countermeasures are classified to the following three methods:

- 1) Structural improvement by cross tie
- 2) Damping enhancement by damper
- 3) Aerodynamic improvement by surface treatments

We had to select the most appropriate countermeasure against cable vibration, carrying out various examinations. For example, in the case of the Akashi Kaikyo Bridge, the high-damping rubber dampers as an original countermeasure were installed between parallel suspenders against vortex-induced oscillation. The suspenders were widely spaced at 9 times of the diameters, considering the wake galloping. However, the original dampers were damaged by a strong typhoon in September 1999. After an intensive investigation and various examinations, helical wires were wound around suspenders as the alternative countermeasure against a new vibration, called the wake-induced flutter¹⁾. And the Tataru Bridge was installed PE cables with indented surface against rain-induced vibration for the first time around the world²⁾.

The typical countermeasures are shown in Fig. 2. While there were no serious damages for cable structure, some wind-induced vibration of cable structure which has little influence on bridge were found at the cable systems not only as the main structure but also as the sub structure (i.e. the hand rope on main cable for inspection).

Wherein, the field measurement for the stay cables of the Tataru Bridge and new countermeasure for wake galloping of the Hitsuishi-jima Bridge and the Iwakuro-jima Bridge are described in the next chapter.

3. VIBRATIONS AND COUNTERMEASURES FOR LONG STAY CABLES

(1) Profiles of the Tataru Bridge

The Tataru Bridge (shown in Fig. 3) was completed in 1999 as the one of world's longest cable-stayed bridge with the main span of 890 m. This bridge has the multi-fan type stay cables with two planes (168 cables in total), and the longest stay cables are approximately 470 meters long.

Table 1: Cable vibrations and countermeasures on the Honshu-Shikoku Bridges

Bridge name	Main span length (m)	Opened Year	Cable type	Cable vibrations				Countermeasures	
				VIV	RIV	WIF	WG		
Suspension bridge	Akashi Kaikyo	1991	1998	PE-Cable*1	O	/	O	N	Helical wire
	Ohnaruto	876	1986	CFRC	N	/	/	/	-
	Shimotsui Seto	940	1988	CFRC	N	/	/	/	-
	Kita-Bisan Seto	990	1988	CFRC	N	/	/	/	-
	Minami-Bisan Seto	1100	1988	CFRC	N	/	/	/	-
	Innoshima	770	1983	CFRC	N	/	/	/	-
	Ohshima	560	1988	CFRC	N	/	/	/	-
	1 st Kurushima Kaikyo	600	1999	PE-Cable*2	O	/	/	/	Additional damping
	2 nd Kurushima Kaikyo	1020	1999	PE-Cable*2	O	/	/	/	Additional damping
	3 rd Kurushima Kaikyo	1030	1999	PE-Cable*2	O	/	/	/	Additional damping
Cable-stayed bridge	Hitsuishi-jima	420	1988	PE-Cable*1	O	O	N	O	Cross tie & Rigid tie
	Iwakuro-jima	420	1988	PE-Cable*1	O	O	N	O	Cross tie & Rigid tie
	Shin-Onomichi	215	1999	SUS-covered*3,*4	O	O	/	/	Additional damping
	Ikuchi	490	1991	PE-Cable*4	O	O	/	/	Additional damping
	Tatara	890	1999	PE-Cable*4	O	O	/	/	Additional damping & Indent cable

VIV: Vortex-induced vibration

WIF: Wake-induced Flutter

O: Observed

*1: Parallel arrangement

*3: Field assembled PC strand

RIV: Rain-induced Vibration

WG: Wake Galloping

N: Not observed

*2: Additional damping with Butyl rubber

*4: Additional damping with High-damping rubber



(a) Helical wire (Akashi Kaikyo)

(b) Additional damping (Kurushima Kaikyo)

(c) Cross tie & Rigid tie (Hitsuishijima / Iwakurojima)

(d) Indent cable (Tatara)

Figure 2: Cable vibration countermeasure on the Honshu-Shikoku Bridges

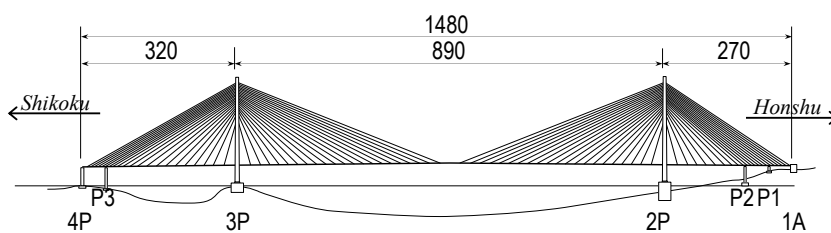


Figure 3: General view of Tatara Bridge

(2) Countermeasure against Rain-induced Vibration

Since the lowest natural frequency of the longest stay cables is 0.26Hz, various investigations were conducted against the wind-induced vibrations.

Various wind tunnel tests for stay cables revealed that an indent PE cable (Fig. 4) was newly developed and the indent cable has a high vibration control performance and a low drag coefficient of 0.7. Eventually, the indent stay cables were applied to the Tataru Bridge for the first time around the world. Currently, no harmful vibration has been observed.



Figure 4: Indent PE cable

(3) Field monitoring of Indent Stay Cables

There is no extraordinary vibration and damage in the stay cable anchors of the Tataru Bridge, which is over 15 years after completion. However, the effect of indent cable is not necessarily evaluated, because the stay cables are not under a long-term observation. In addition, several papers³⁾⁴⁾ reveals that the inclined cable was observed to have an unlimited vibration, called the dry-state galloping.

Considering the latest information, the cable monitoring is required on the Tataru Bridge. The monitoring devices were installed on the Tataru Bridge as follows. The monitoring system is shown in Fig. 5.

- 1) In order to verify the effect of the indent cable against the rain-induced vibration, two accelerometers were installed on the longest stay cables on the main span. The servo-type accelerometers were selected because of the low frequency range.
- 2) In order to observe the possibility of dry-state galloping, two accelerometers were installed on the shortest stay cable near the tower. The strain-gauge-type accelerometers were selected because of the high frequency range.
- 3) In order to observe the wind and rain condition, a propeller-type anemometer and a rainfall-meter were installed at the middle of the main span.

The monitored data were automatically stored in the computer installed in the main girder when the averaged wind speed is exceeded the trigger value of 5 m/s. The monitored data was recorded every 10 minutes, and sampling frequency was 100Hz.

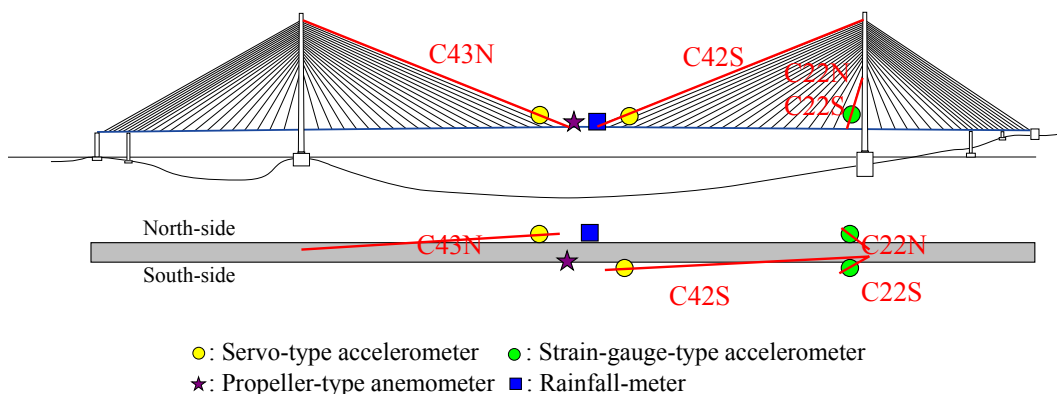


Figure 5: Cable monitoring system for Tataru Bridge

(4) Results of field measurement

The field measurement was started from October 2007, and approximately 50,000 data were recorded until February 2013. The relation between averaged wind speed and direction is shown in Fig. 6. The wind characteristics have a greater tendency to north side transverse direction of this bridge than the other direction.

Fig. 7 shows the relation between the wind speed and standard deviation of acceleration measured by the long cables. The horizontal axis data is plotted by blue mark and the vertical axis data is plotted by red mark. It seems that there are no large amplitudes of wind-induced vibration when the wind speed was increased. Therefore, the indent cable has the effect to suppress the rain-induced vibration from obtained data.

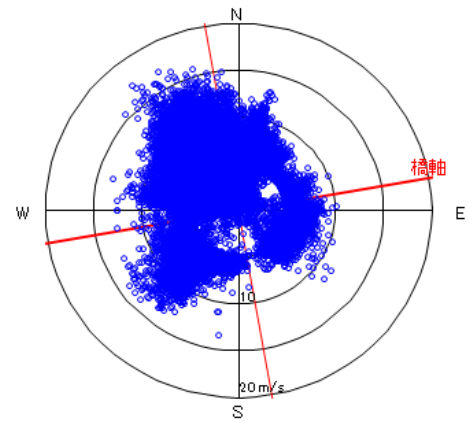


Figure 6: Wind condition of Tataru Bridge

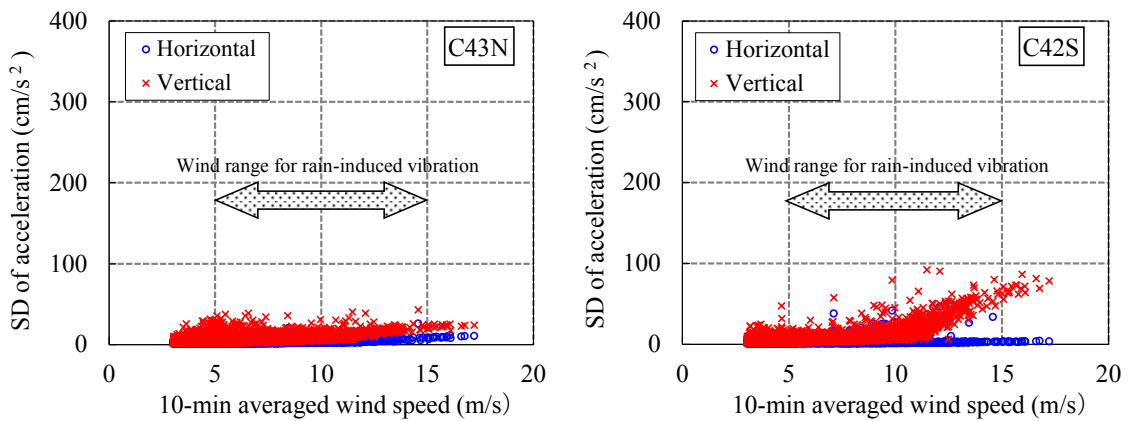


Figure 7: Relation of wind speed and standard deviation of acceleration (C43N, C42S)

On the other hand, those relations for the short cables are shown in Fig. 8. From this figure, it is confirmed that the relatively large accelerations were occurred in the wind speed range of 7 m/s to 15 m/s. In order to clarify the dynamic characteristics caused by wind direction, the observed data were decomposed into 4 directions based on the bridge axis. As a result, it is also confirmed that the large vibrations were occurred in case of the wind from transverse direction of the bridge axis with the rain fall situation (Fig. 9).

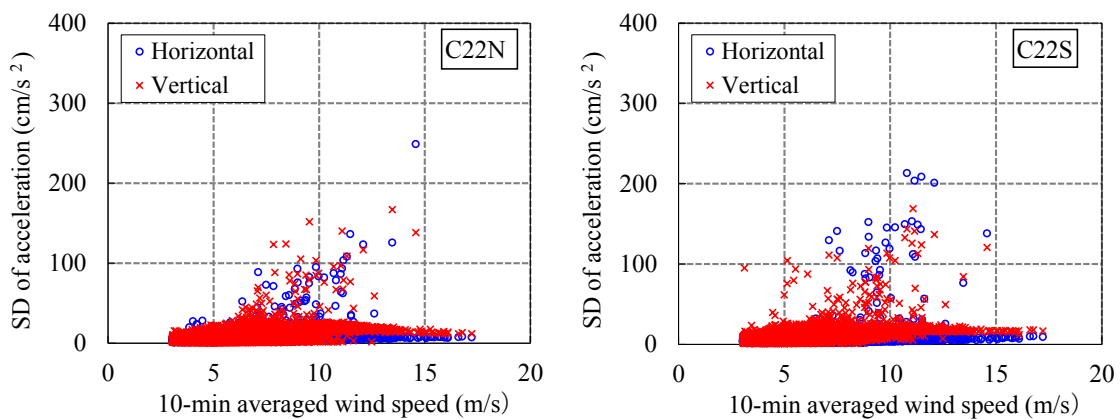


Figure 8: Relation of wind speed and standard deviation of acceleration (C22N, C22S)

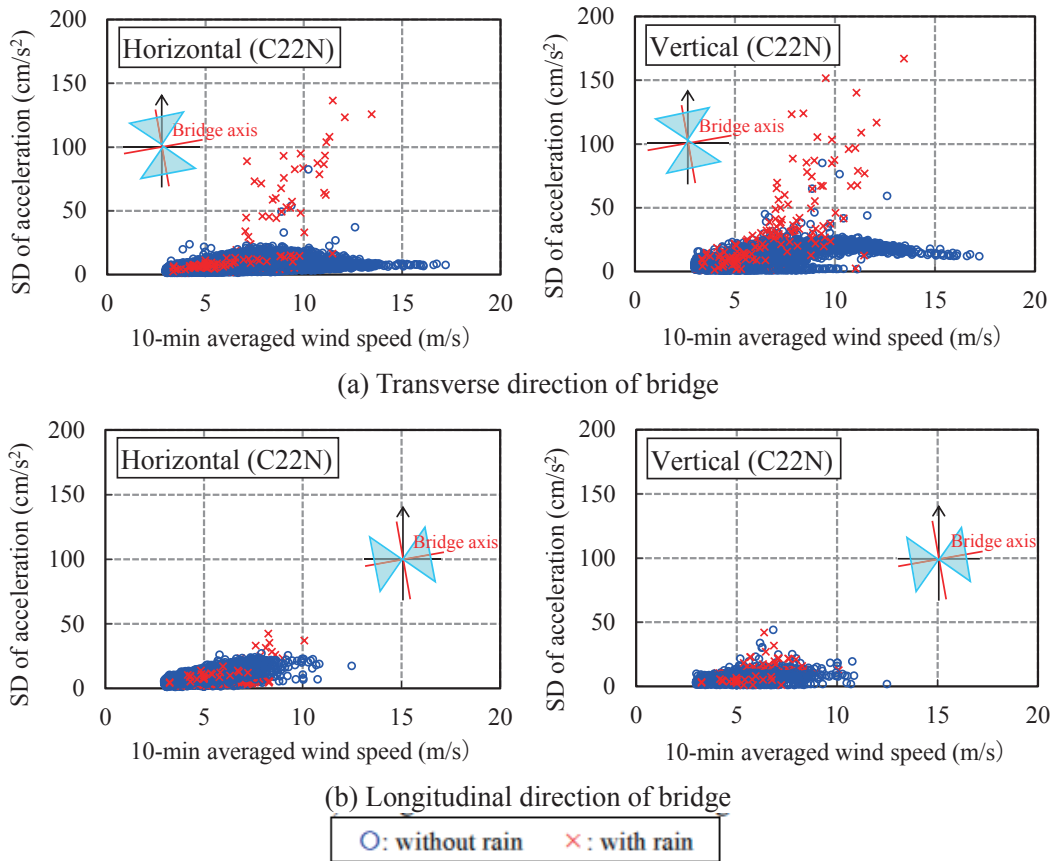


Figure 9: Relation of wind speed and standard deviation of acceleration (C22N)

It is said that the rain-induced vibration is generated when the relative angle (β^*) defined by Eq. 1 is in 17 degrees to 60 degrees⁵⁾.

$$\beta^* = \sin^{-1}(\cos\alpha \cdot \sin\beta) \tag{1}$$

Where α : inclined angle of cable (approx. 75 degrees),
 β : wind direction (-35 degrees from transverse direction)

As the relative angle which shows the largest acceleration is -8.5 degrees, it is thought that the observed vibration is not the rain-induced vibration (Fig. 10). Consequently, the time history of the acceleration which indicated the maximum amplitude was converted into the displacement, in order to confirm the safety of cable structure. The vibration locus at sensor position shows the oval shape (Fig. 11), and the maximum displacement was approximately 2cm. The maximum displacement of this cable was thought to be 7 cm supposing that the cable vibrated in the third sine curve mode. It is confirmed that the structural safety is assured because of the observed amplitude is smaller than the allowable value of 15 cm.

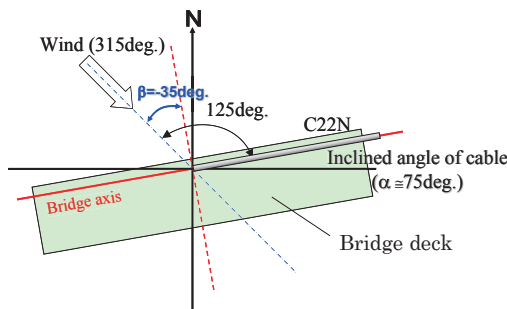


Figure 10: Relative angle of wind

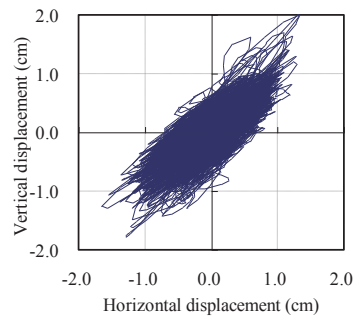


Figure 11: Vibration locus at sensor

However, there still remains that the observed vibration might be the dry-state galloping. Therefore, it is necessary to continue the monitoring to obtain effective data of cable vibrations during strong winds.

4. VIBRATIONS AND COUNTERMEASURES FOR PARALLEL CABLE SYSTEM

(1) Profiles of the Hitsuishi-jima and the Iwakuro-jima Bridge

The Hitsuishi-jima Bridge and the Iwakuro-jima Bridge were designed for highway-railway combined bridges and completed in 1988 as a part of the Seto Chuo Route. The bridges are twin cable-stayed bridges with the similar profiles: the main span of 420 m and the side span of 185 m, as shown in Fig. 12. The bridges have truss-type stiffening girders and H-shape towers and fan-type stay cables with two planes of parallel stay cables. Each stay cable consists of PWS and is covered by PE with in-site grouting.

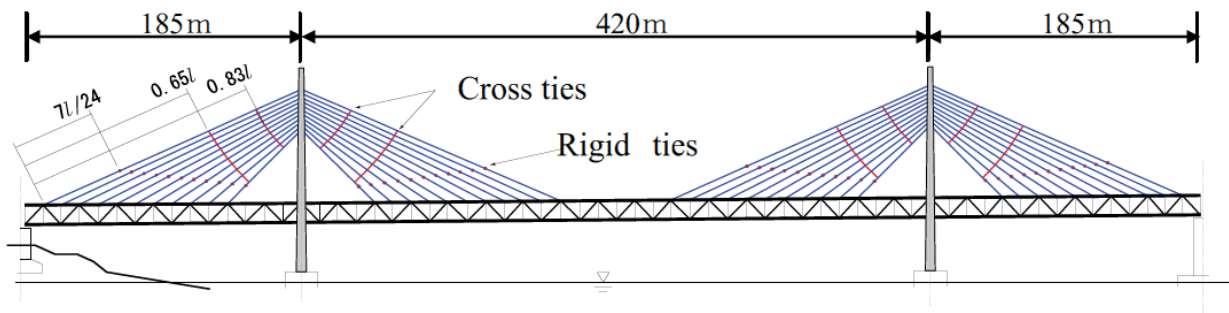


Figure 12: Cable vibration countermeasures for Hitsuishi-jima and Iwakuro-jima Bridge

(2) Original vibration countermeasure for stay cables

Since the wake galloping was considered to occur in the parallel cables like these bridges, rigid ties were installed between parallel stay cables for vibration countermeasure, carrying out various wind tunnel tests. However, the large amplitude occurred during construction, and cross ties were installed for the additional vibration countermeasure, as shown in Fig. 2(c) and Fig. 12.

After installation of rigid ties as well as cross ties, large amplitude vibrations were reduced, but small-amplitude vibrations, called the sub-span vibrations, were observed. The sub-span vibrations were excited in the small range between nodes of rigid ties or cross ties. Furthermore, several cross tie cables were cut off after ten-year operation because of the sub-span vibration. Therefore, countermeasures against the sub-span vibration were studied in order to protect the cross ties and to reduce the maintenance cost.

(3) Alternative vibration countermeasure for stay cables by structural improvement

One of the effective methods to control the cable vibrations is to increase the structural damping. Although the wake galloping is known that the exciting force is large, the required damping to control the wake galloping is not clarified. New rigid ties with dampers, which have the target damping of 0.1, were developed and installed on the cables (Fig. 13).

The field measurement result shows that sub-span vibration was not observed. But the vibration countermeasure by the structural damping needs a periodical maintenance of dampers, including the replacement of viscous-elastic body. Therefore, another method was studied.



Figure 13: Alternative countermeasures by rigid tie with damper

(4) Alternative vibration countermeasure for stay cables by aerodynamic improvement

Another effective method to control the cable vibration is to improve the cable cross-section. As the aerodynamic improvement, the helical wire was applied to the hanger ropes of the Akashi Kaikyo Bridge, and then was studied for the application to the parallel stay cables of the cable-stayed bridges. As shown in the Fig. 14, four cases combining the two kinds of wire diameters and two kinds of winding pitches were examined through wind tunnel test, referring the results of wind tunnel test for the hanger ropes of the Akashi Kaikyo Bridge. The test conditions for the wind tunnel except for the frequency and the weight were the same as real. The test cable was selected from the middle class of stay cables, considering the ability of the testing equipment.

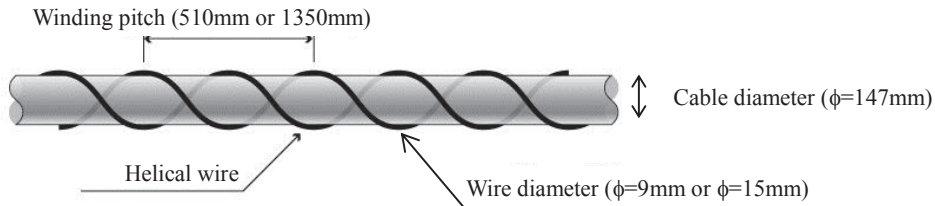


Figure 14: Alternative countermeasure for parallel stay cables by helical wires

Two cases of the wind tunnel test results for parallel inclined cables were shown in Fig. 15. One is the case of the large exciting force (case 1: distance between two cables (c.t.c.) = 2.5D, attack angle (a.a.) = 20 degrees) and the other is the case of the low critical wind speed (case 2: c.t.c. = 3.5D, a.a. =10 degrees). They focus on the depressing effect of helical wires.

In case 1, the critical wind speed of wake galloping reduces drastically with the winding pitch of 1350 mm, and increases slightly with the winding pitch of 510 mm. In addition, the exciting force reduces drastically with the winding pitch of 510 mm in case of c.t.c. = 2.5D, as shown in Fig. 16. In case 2, the critical wind speed of wake flutter increases more than 18 m/sec in every combinations, as compared with the original stay cable, which has a cross section with no helical wire.

Consequently, the test revealed that the combination of the wire diameter of 9 mm and winding pitch of 510 mm was the most effective for the parallel stay cables. More detailed examinations, however, is required to the application of other bridges, because the helical wire is ineffective to the wake galloping in case of other combinations of wire diameters and winding pitches.

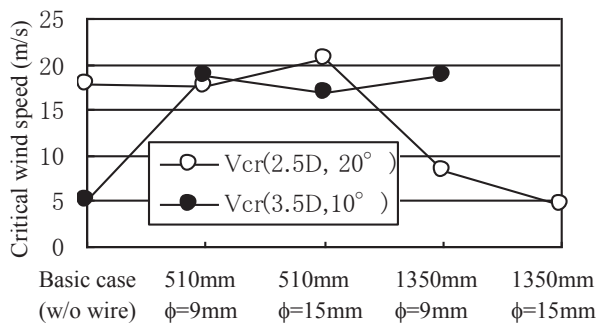


Figure 15: Effect of helical wires in four combinations

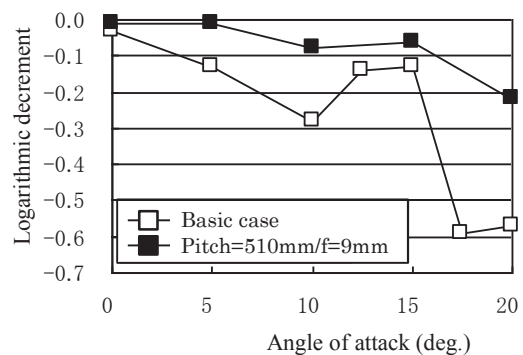


Figure 16: Influence to exciting force (2.5D)

(4) Field measurement of helical wires for stay cables

The wind tunnel tests showed that the helical wires were effective to control the wake galloping and that they had different effects to the distance between parallel stay cables. Since the anchoring distance between parallel stay cables in the real bridges are different at the girder sides and at the tower sides, the results of the wind tunnel tests can not necessarily applied to the real bridges without any consideration.

Therefore, the helical wires were temporarily installed on the stay cable in order to verify the effect on the bridge, and the sub-span vibration was observed for three months. The filed measurement was carried out on the west-side uppermost stay cable (C23) of the Hitsuishi-jima Bridge (Fig. 17, Fig. 18), considering the wind tunnel test. The second uppermost stay cable (C24) with no helical wire was observed at the same time.

Two cases, varying the installation range, were verified in the filed measurement. In range 1, the helical was installed around half of the sub span, i.e., from the girder-side anchoring point to the middle of sub span (35 m in length). In range 2, the helical was installed at range of the sub span, i.e., from the girder-side anchoring point to the Rigid tie (55 m in length). Two accelerometers were arranged at the height of 1.5 meters on the deck both in the vertical direction and the horizontal direction in order to measure the cable vibration. The anemometer was arranged at the nearest light pole in order to observe the wind conditions.

The filed measurement result showed that the helical wire successively controlled the sub-span vibrations and that the cable response was more depressed in range 2 than in range 1 because of the longer installation range, as shown in Fig. 19. In order to enhance the durability and to reduce the maintenance cost, the anchoring points of cross ties were improved in detail. Currently, more observation will be required to the stay cables with no helical wire in order to ensure the detailed improvement.

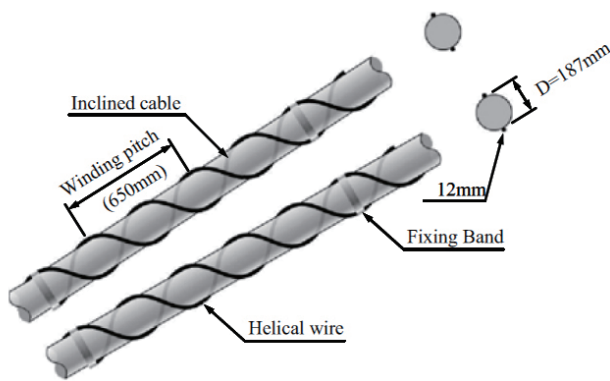


Figure 17: Arrangement of helical wires

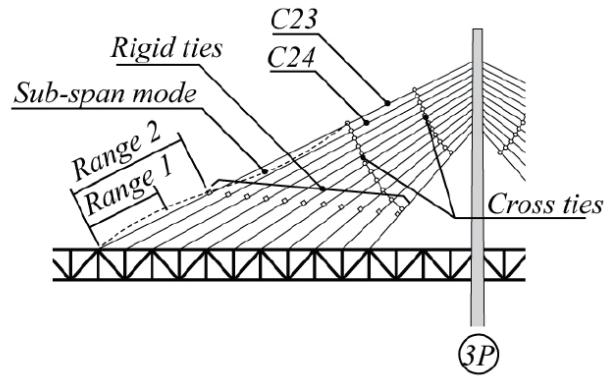


Figure 18: Temporary installation range of helical wires

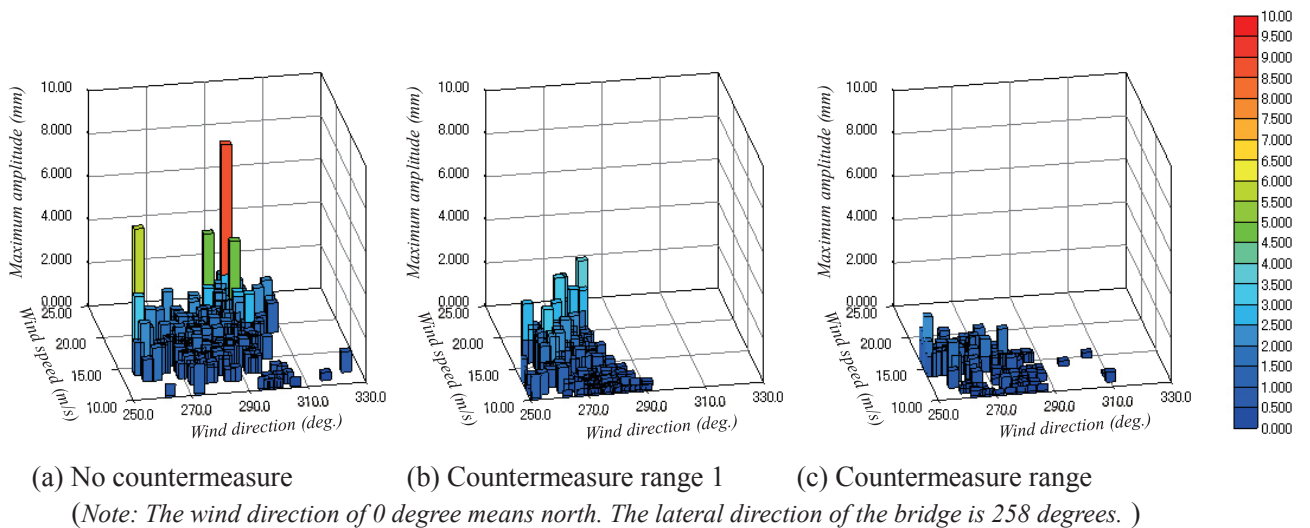


Figure 19: Cable response of with/without countermeasure during field measurement (C23)

5. CONCLUSION

As the results of the field observations for vibration of cable structure on the Tatara Bridge, the conclusions are summarized as follows.

- 1) The indent stay cable has the effect to suppress the rain-induced vibration from obtained data.
- 2) There still remains that the dry-state galloping might be occurred in the indent stay cable.

As the results of the wind tunnel tests and the field measurement, the conclusions of parallel stay cables on the cable-stayed bridge are summarized as follows.

- 1) The wind tunnel tests with a real-scale cable model showed that the wake galloping could occur in the distance of 2.5D-5.5D in the attack angle of 0-20 degrees.
- 2) For the cable with the diameter of 147 mm, the helical wire with the diameter of 9 mm is effective in case of the winding pitch of 510 mm.
- 3) The field measurement showed that the cable with the helical wire was relatively smaller in amplitude than the cable with no wire.

Although the major problem has not occurred in the maintenance of PE cables, the cable structures should be carefully observed and intensively studied because of the cable is an essential member in the cable-supported bridges and the cable vibration is not clarified in aerodynamic instability.

ACKNOWLEDGMENT

The authors would like to express the acknowledgement to Technical Committee of the Honshu-Shikoku Bridges for the technical advice to cable vibration and countermeasures.

REFERENCES

- 1) R. Toriumi, N. Furuya, M. Takeguchi, M. Miyazaki and Y. Saito : A Study on Wind-induced Vibration of Parallel Suspenders observed at the Akashi Kaikyo Bridge, *3rd International Symposium on Cable Dynamics*, 1998
- 2) T. Miyata, T. Fujiwara, H. Yamada, and T. Hojo : Wind-resistant Design of Cables for the Tatara Bridge, *Proceedings of International Association of Bridge and Structural Engineering*, Kobe, Japan, pp.25-30, 1998
- 3) M. Matsumoto, T. Yagi, Q. Liu, T. Oishi and Y. Adachi: "Effects of axial flow and Karman vortex interference on dry-state galloping of inclined stay-cables", *Proceedings of the Sixth International Symposium on Cable Dynamics*, pp.247-254, 2005
- 4) M. Matsumoto, T. Yagi, H. Hatsuda, T. Shima, and M. Tanaka: "Sensitivity of Dry-state Galloping of cable stayed bridges to Scruton number," *Proceedings of the Seventh International Symposium on Cable Dynamics*, 2007
- 5) Japan Road Association: *Wind resistant design manual for highway bridges*, pp.209-216, 2007 (in Japanese)

An observation of dry galloping at critical Reynolds number in normal wind

Qingkuan Liu⁺¹ Wenyong Ma⁺² Xiaobing Liu⁺³

⁺¹⁺²⁺³Wind Engineering Research Center, Shijiazhuang Tiedao University, Shijiazhuang, Hebei 050043, China

⁺¹⁺²⁺³The Key Laboratory for Health Monitoring and Control of Large Structures, Hebei, 050043, China

This paper aims to reproduce dry galloping in the normal wind in the wind tunnel and illustrates the relationship between galloping response and aerodynamic corresponding to it. A vertical dominated large vibration is observed in Reynolds number from 1.7×10^5 to 3.0×10^5 . The aerodynamic force along the axis of the cylinder is not uniform, and some of them input energy to keep large vibration and others work oppositely. A key trait for energy input is that aerodynamic has right phase delay possibly induced by vibration, and these energy input process can be provided by wind pressure distribution without separation bubble.

Keyword: circular cylinder¹, wind tunnel test², dry galloping³, critical Reynolds number⁴

1. INTRODUCTION

The dry galloping, which occurs in the absence of rain or ice accretions, is a large amplitude vibration of stay cables in cable-stay bridges and have recently attracted much interest. This vibration has been observed at a wind speed corresponding to critical Reynolds numbers, between 10^5 and 3.5×10^5 for a circular cylinder. Dry galloping is characterized by the presence of divergent-type vibrations or by limited amplitude vibrations. It has been studied experimentally^{1, 2)} and theoretically³⁻⁵⁾.

The mechanism of dry galloping is still unclear, and the most researchers believe it is associated with the critical Reynolds number. Zdravkovich⁶⁾ categorized the transition occurring in the boundary layer of the cylinder into three different states, depending on the Reynolds number, pre-critical regime which implies that transition occurs at shear layer, the single bubble regime whereby the transition occurs on one side of the cylinder and the tow bubble regime whereby the transition occurs on both sides. When the transition occurs either close to the cylinder or on the cylinder. Flow around the cylinder is easily influenced by a small disturbance when it is transiting, which may lead a significant change of aerodynamic on the cylinder.

For the complicated features of flow characteristic in the critical Reynolds number regime, many arguments are reasonable to explain dry galloping. Matsumoto who first describe dry galloping argues that dry galloping is caused by mitigation of Karman vortex shedding⁷⁻¹⁰⁾. It shares some common features with wind-rain-induced vibration because the formation of upper water rivulet at wind-rain-induced vibration seems to play a similar role with an existence of axial flow at dry inclined cable galloping to mitigate Karman vortex shedding. This can also explain large vibration under normal wind in critical Reynolds number range for the disappearance of regular vortex shedding. In fact, Karman vortex shedding does occur in critical Reynolds number because reattachment interrupts the wake flow communication while the dry galloping may occur. Surface roughness and cross-sectional distortion have already been proved to have significant effects on both aerodynamic force and wind-induced response^{11, 12)}. Another explanation is that vibration in critical Reynolds number range is related an interaction between the cylinder and unsteady flow pattern^{11, 13, 14)}. The mechanism of the interaction is still unclear, but it is sensitive to the condition of circularity-defect and approaching flow. It should be mentioned that although the traditional quasi-steady assumption is not persuasive on explaining dry galloping, it still is a possible reason because of the limitation of using it on a circular cylinder.

Unfortunately, dry galloping has never been fully verified full-scale, and reproducing in the wind tunnel is limited as well and only on inclined cable. This paper aims to reproduce dry galloping in the normal wind in the wind tunnel and illustrates the relationship between galloping response and aerodynamic

⁺¹lqk@stu.edu.cn, ⁺²ma@stdu.edu.cn, ⁺³x_b_liu@126.com

corresponding to it by measuring instantaneous displacement and wind pressure distribution synchronously.

2. WIND TUNNEL TEST

Tests were carried out at Shijiazhuang Tiedao University in the STDU-1 wind tunnel, a closed-circuit wind tunnel having a larger test section with 4 m wide, 3 m high, 24 m long and a smaller one with 2.2 m wide, 2 m high and 5 m long. The model and supporting system were fixed in the larger test section in which the velocity profile was uniform within $\pm 0.5\%$ and the turbulence intensity was approximately 0.5% at 20m/s.

Wind tunnel test setup is shown in Figure 1. The cylinder model had a length L of 2900 mm, a diameter D of 270 mm. The model was made of polyethylene pipe. In each end, an end plate had a length of 2280mm was fixed to keep a uniform flow along the model axis, and end cover with a shape of NACA2420 was connected with endplate to reduce effects of flow around cylinder end and supporting system on aerodynamic forces and vibration. In this arrangement, the supporting system and cylinder ends were surrounded by end plate and end cover, and cylinder could move in the circle hole with a diameter of 300 mm in the center of the end plate. A supporting system, which can provide a three-degree-of-freedom vibration, were consisted by four springs and an end bar at each end. The nature frequencies can be estimated by the following formula

$$f_V = \frac{1}{\pi} \sqrt{\frac{(K_u + K_d) \sin \gamma}{m}}, \quad f_H = \frac{1}{\pi} \sqrt{\frac{(K_u + K_d) \cos \gamma}{m}}, \quad f_T = \frac{1}{\pi} \sqrt{\frac{(K_u + K_d) \sin \gamma L_s}{m_T}} \quad (1)$$

Where f_V , f_H and f_T are vertical, horizontal and torsional frequency respectively; m and m_T are mass and rotational inertia; K_u and K_d are stiffness of upside spring and downside spring; L_s is a distance of two hanging points; γ is the angle between end bar and the axis of spring.

The displacement was measured by two laser displacement sensors (Panasonic HL-G112-A-C5) in each end for the vertical and the torsional and one sensor for the horizontal with a sampling frequency of 500 Hz. The aerodynamic pressure was collected with pressure sensors (ESP-64Hd, Measurement Specialties (formerly PSI), Hampton, VA, USA) and a data acquisition system (DTC Initium, Measurement Specialties) with a sampling frequency of 331.6 Hz. Pressure measuring taps were arranged at four discrete cross-sections (termed Ring A, B, C and D). Each ring has 50 taps. The pressure tubes were in length of 800mm and its effect on data distortion was corrected by using the frequency-response function of each tube.

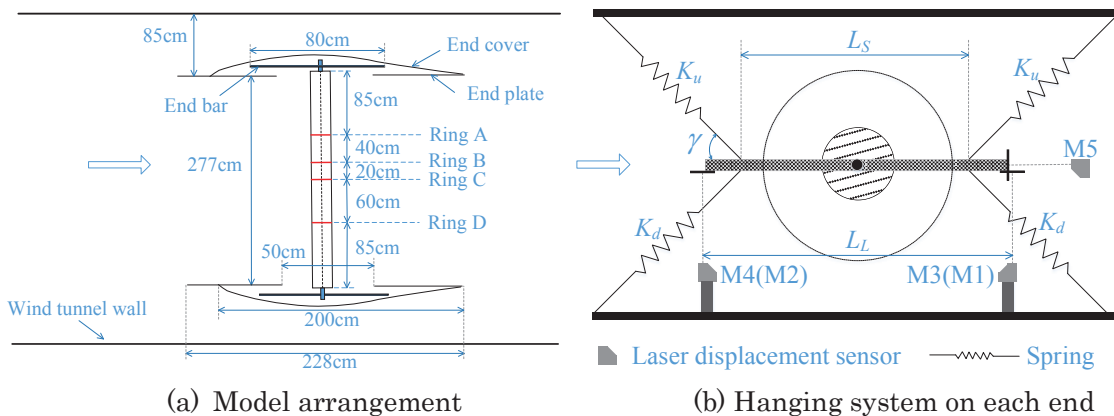
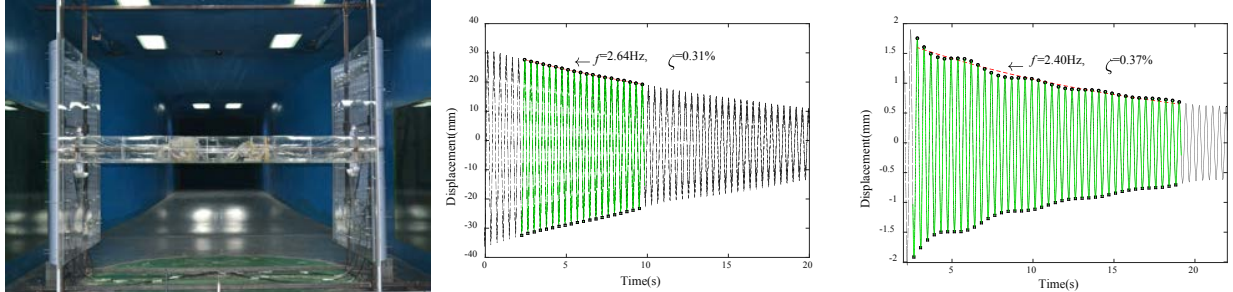


Figure 1: Schematics of wind tunnel arrangement

The wind were speeds from 2m/s to 18m/s corresponding to Reynolds number from 0.37×10^5 - 3.35×10^5 (based on diameter D). In this paper, the pressure coefficient is defined as the ratio of the wind pressure on the cylinder to the velocity pressure. The drag and lift coefficients were calculated from the integral of the pressure coefficients over the perimeter of the cross-section. C_p , C_D , C_L are pressure coefficient, drag coefficient, lift coefficient. The Reynolds number Re is defined as $Re = \rho DU / \mu$, where ρ , μ and U are the air density, mean incoming wind velocity and the dynamic viscosity of the air, respectively.

Figure 2 shows a picture of model arrangement and dynamic parameters given by this arrangement. The vertical and horizontal nature frequency are 2.64Hz and 2.40Hz, and structural damping ratios are 0.31% in vertical and 0.37% in horizontal.



(a) Picture of the model arrangement (b) Vertical dynamic parameter (c) Horizontal dynamic parameter

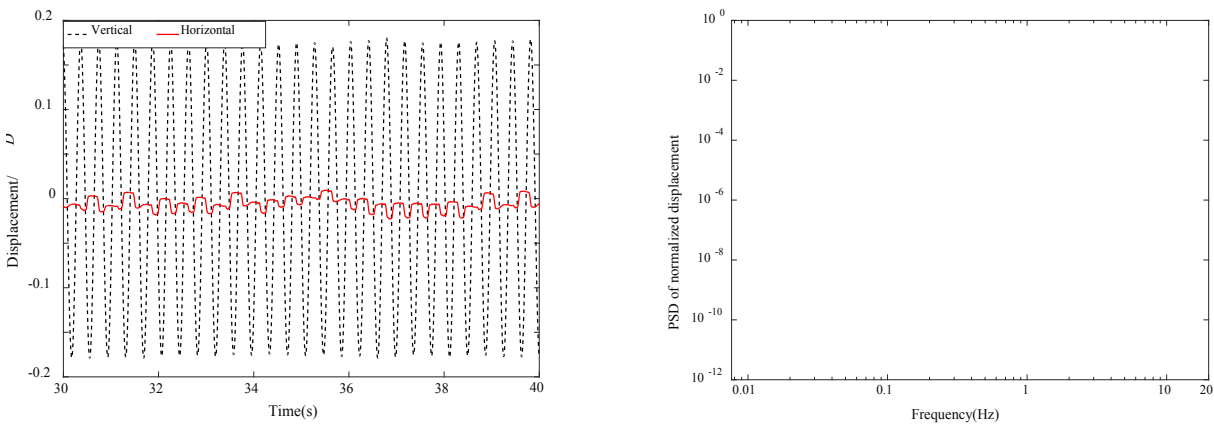
Figure 2: Schematics of wind tunnel arrangement

3. EXPERIMENTAL RESULT

(1) Occurrence of galloping

Figure 3 (a) shows a typical displacement time history observed in this study. The displacement is normalized by dividing by diameter. It presents a steady vertical dominated vibration for its horizontal displacement is approximate 10% of the vertical one. An interesting phenomenon is a jump in horizontal displacement which may be induced by a periodic jump of drag. The power spectrum density in Figure 3 (b) gives a further explanation for this jump. It shows this jump is on vertical nature frequency which means the jump is created by vertical vibration periodically.

In order to quantify the response of this vibration, a displacement history record is divided into cycles based on nature frequency, the amplitude of each cycle is defined as half of peak to peak distance. Figure 4 shows the mean and the RMS of normalized amplitude around 200 cycles in each record. Large vibration observed occurs in Reynolds number from 1.7×10^5 to 3.0×10^5 , which is far from the vortex induced vibration range around 0.66×10^5 , so dry galloping will be used to describe these vibrations for simple. The RMS of normalized amplitude showed in Figure 4 means that the vibration is steady because of the amplitude does not change much with time.



(a) Normalized displacement history (b) PSD of normalized displacement

Figure 3: A typical normalized displacement history and its PSD

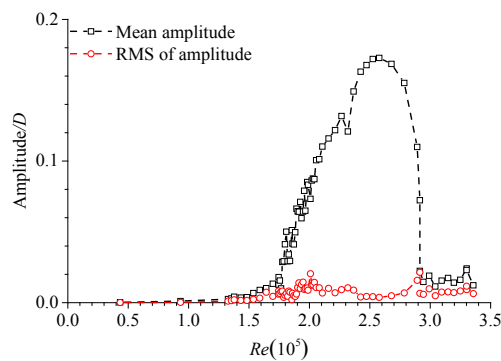


Figure 4: Normalized amplitude against Reynolds number

(2) Aerodynamic force characteristics

Because aerodynamic force distribution along the cylinder axis is not uniform in the critical Reynolds number range, some of them input energy to the motion of cylinder to enlarge or maintain vibration and others dissipate energy. The energy input is defined as the product of lift coefficient and vertical velocity. Figure 5 shows an energy input for vibration at $Re=2.51 \times 10^5$. In this case, aerodynamic on ring C contributes energy to keep the large vibration. It should be highlighted that the aerodynamic force on the four rings measured may not represent the total aerodynamic, but the vibration is attributed to aerodynamic forces like the one on ring C. Meanwhile, dry galloping occurs when energy input by the aerodynamic force on many cross-sections (like on ring C in Figure 5) is larger than that dissipated by structure damping and aerodynamic force on others (like on ring A, B and D in Figure 5).

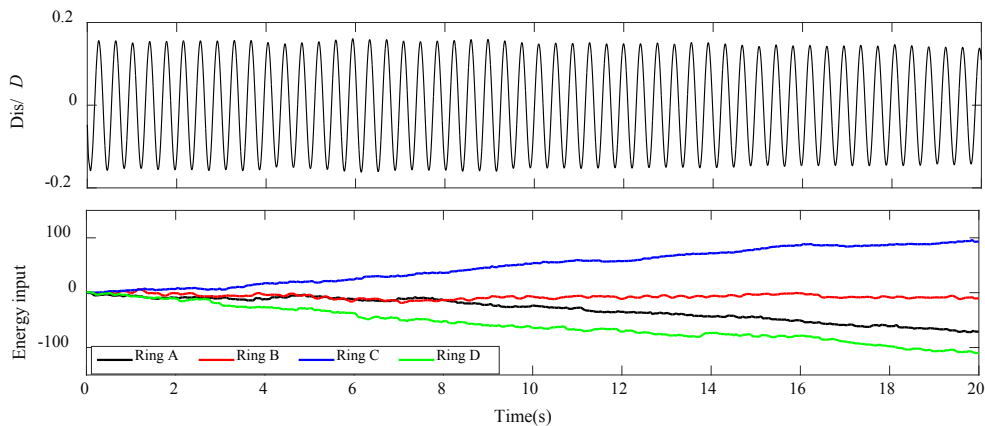


Figure 5: Energy input for vibration at $Re=2.51 \times 10^5$

The power spectrum density (PSD) of lift coefficient on ring A and ring C at $Re=2.51 \times 10^5$ is shown in Figure 6 to compare aerodynamic forces which input and dissipates energy. The Strouhal number St , which defined as fD/U , are presented at $St=0.15$ and 0.20 at $Re=2.51 \times 10^5$ as well to show whether vortex shedding disappears. When dry galloping occurs, PSD of lift coefficient on both ring A and ring C have a peak in nature frequency. That implies an interaction between cylinder and flow around it. However, it seems the PSD of lift coefficient does not show obvious traits of energy input. Between $St=0.15$ and 0.20 , a concentrated energy representing vortex shedding is still shown in Figure 6. This means the flow does not reattach on the cylinder and the wake flow communication still exists even it is weak.

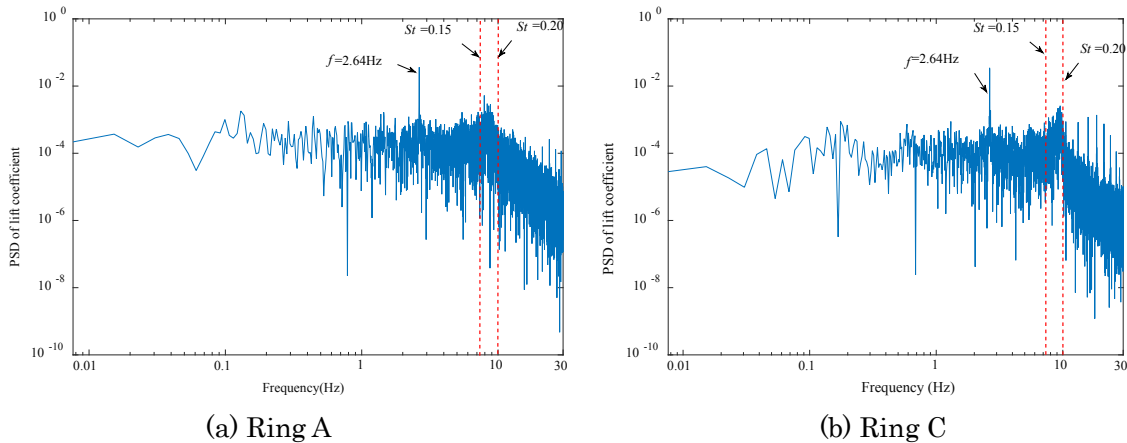


Figure 6: PSD of lift coefficient on Ring A and Ring C at $Re=2.51 \times 10^5$

Figure 7 shows phase averaged vertical displacement, velocity, and corresponding lift coefficient on four rings. The black solid line refers to displacement, and it reaches a maximum at the phase of zero. The red dash line is vertical velocity, and the maximum velocity is at the phase of $3/2\pi$. The lift coefficient on ring C, which inputs energy to the cylinder, is shown in blue. The result shown in Figure 7 can explain the energy input shown in Figure 5. The lift coefficient of ring B in red with an empty circle has a small change in phase and it does not show harmony change with velocity, so the work made by it is close to zero and it does not contribute much to vibration on either increasing or decreasing. The lift on ring D in green changes oppositely with the velocity, and it dissipates energy efficiently. The change of lift coefficient in ring C has similar trends with the velocity, and this is a way to input energy to the cylinder.

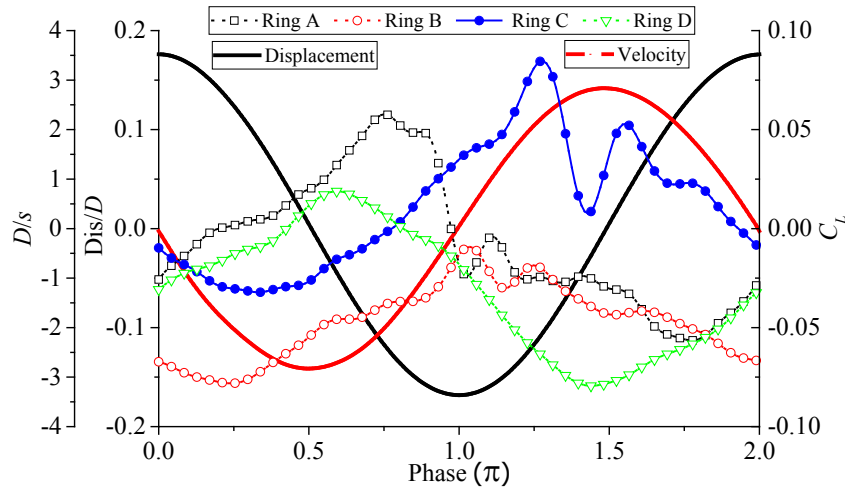


Figure 7: Phase averaged displacement, velocity and lift coefficients on four rings at $Re=2.51 \times 10^5$

Comparing data in Figure 5, Figure 6 and Figure 7, when dry galloping occurs, the cylinder interacts with a flow around it, while aerodynamic force on the part of cylinder input energy to vibration and others dissipate energy. The aerodynamic force which makes a positive contribution to keeping vibration is those who have periodical change similar to velocity. This also can be expressed that an important trait for lift coefficient to input energy is having a right phase delay.

(3) Wind pressure distribution

The variation of phase averaged wind pressure distribution for three cases shown in Figure 8 illustrates

the mean wind pressure distribution on the red line and instantaneous phase averaged pressure in a blue empty circle. The wind pressure distribution in Figure 8 (a) is more likely in pre-critical Reynolds numbers in which reattachment does not occur. The distribution is mainly changed in windward and two flanks with phase, this makes a fluctuating lift which contributes energy to vibration. The similar process in Figure 8 (b) has an unsymmetrical mean pressure distribution which means that the flow on two flanks has already been different. A separation bubble clearly shown in Figure 8 (c) implies that flow reattaches at that side. The wind pressure on a range of separation point to reattachment point fluctuates strongly, but instantaneous phase average pressure has small change with phase when it does not interact with vibration.

To summarize, the energy input which dry galloping depends on can be provided by wind pressure distribution without separation bubble, and on the other hand, the reattachment on one side may not surely induce large vibration.

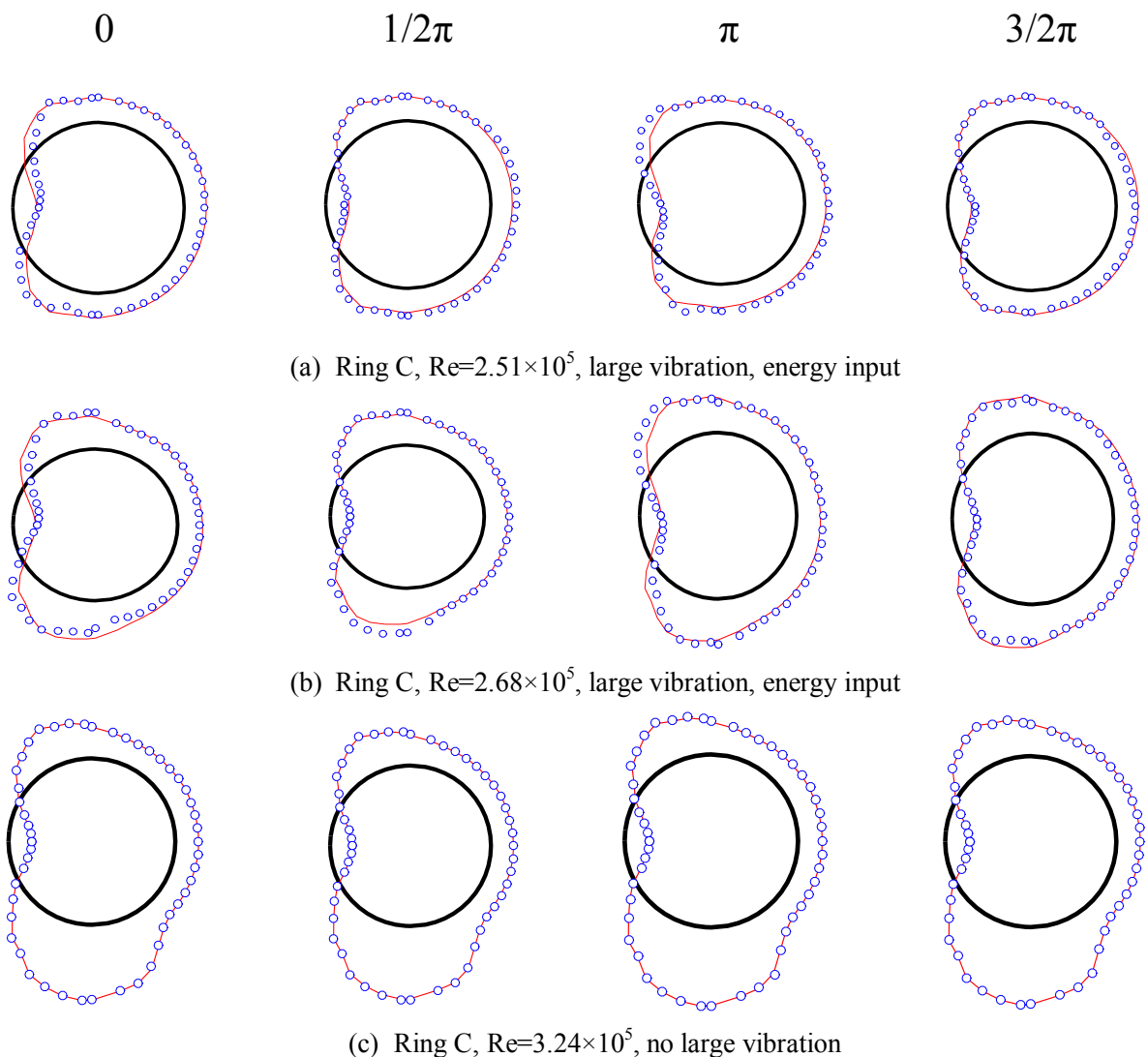


Figure 8: Variation of phase averaged wind pressure distribution for three cases

4. CONCLUSION

A large vibration of a circular cylinder in the normal wind is observed in this study. These vibrations occur at a certain range of Reynolds number from 1.7×10^5 to 3.0×10^5 when the cylinder interacts with the flow around it. The aerodynamic force along the axis of the cylinder is not uniform, and some of them input

energy to keep large vibration and others work oppositely. A key trait for energy input is that aerodynamic has right phase delay possibly induced by vibration, and these energy input process can be provided by wind pressure distribution without separation bubble. That means this vibration may occur at pre-critical Reynolds number.

It should be highlighted that the aerodynamic force on four tested rings may not represent total aerodynamic force on the cylinder. The Reynolds number range in which dry galloping occurs in this study agree well with the result in 11) and 14), but the wind pressure distribution shows the difference. The reason for this needs further analysis.

ACKNOWLEDGMENT

The authors gratefully acknowledge the support of the National Natural Science Foundation of China (Grant Nos. 51378323), National Science foundation for Distinguished Young Scholars of Hebei Province (E2014210138) and the Research Foundation of Education Bureau of Hebei Province (YQ2014039).

REFERENCES

- 1) Cheng, S., et al., Experimental study on the wind-induced vibration of a dry inclined cable--Part I: Phenomena. *Journal of Wind Engineering and Industrial Aerodynamics*, 96(12): p. 2231-2253, 2008.
- 2) Cheng, S., P.A. Irwin, and H. Tanaka, Experimental study on the wind-induced vibration of a dry inclined cable--Part II: Proposed mechanisms. *Journal of Wind Engineering and Industrial Aerodynamics*, 96(12): p. 2254-2272, 2008.
- 3) Raeesi, A., S. Cheng, and D.S.K. Ting, A two-degree-of-freedom aeroelastic model for the vibration of dry cylindrical body along unsteady air flow and its application to aerodynamic response of dry inclined cables. *Journal of Wind Engineering and Industrial Aerodynamics*, 130(0): p. 108-124, 2014.
- 4) Raeesi, A., S. Cheng, and D.S.K. Ting, Aerodynamic damping of an inclined circular cylinder in unsteady flow and its application to the prediction of dry inclined cable galloping. *Journal of Wind Engineering and Industrial Aerodynamics*, 113(0): p. 12-28, 2013.
- 5) Macdonald, J.H.G. and G.L. Larose, A unified approach to aerodynamic damping and drag/lift instabilities, and its application to dry inclined cable galloping. *Journal of Fluids and Structures*, 22(2): p. 229-252, 2006.
- 6) Zdravkovich, M.M., *Flow Around Circular Cylinder Vol. I*. New York: Oxford University Press, 199.
- 7) Matsumoto, M., et al., Dry galloping characteristics and its mechanism of inclined/yawed cables. *Journal of Wind Engineering and Industrial Aerodynamics*, 98(6-7): p. 317-327, 2010.
- 8) Matsumoto, M., et al., Rain-wind-induced vibration of inclined cables at limited high reduced wind velocity region. *Journal of Wind Engineering and Industrial Aerodynamics*, 91(1-2): p. 1-12, 2003.
- 9) Matsumoto, M., et al., Vortex-induced cable vibration of cable-stayed bridges at high reduced wind velocity. *Journal of Wind Engineering and Industrial Aerodynamics*, 89(7-8): p. 633-647, 2001.
- 10) Du, X., M. Gu, and S. Chen, Aerodynamic characteristics of an inclined and yawed circular cylinder with artificial rivulet. *Journal of Fluids and Structures*, 43(0): p. 64-82, 2013.
- 11) Matteoni, G. and C.T. Georgakis, Effects of surface roughness and cross-sectional distortion on the wind-induced response of bridge cables in dry conditions. *Journal of Wind Engineering and Industrial Aerodynamics*, 136(0): p. 89-100, 2015.
- 12) Benidir, A., et al., Impact of roughness and circularity-defect on bridge cables stability. *Journal of Wind Engineering and Industrial Aerodynamics*, 137(0): p. 1-13, 2015.
- 13) Nikitas, N. and J.H.G. Macdonald, Aerodynamic Forcing Characteristics of Dry Cable Galloping at Critical Reynolds Number. *European Journal of Mechanics - B/Fluids*, 49: p. 243-249, 2015.
- 14) Jakobsen, J.B., et al., Wind-induced response and excitation characteristics of an inclined cable model in the critical Reynolds number range. *Journal of Wind Engineering and Industrial Aerodynamics*, 110(0): p. 100-112, 2012.

DRY GALLOPING OF SURFACE MODIFICATION CABLE IN LOW SCRUTON NUMBER RANGE

Duy Hung VO⁺¹, Hiroshi KATSUCHI⁺², Hitoshi YAMADA⁺³

^{+1, +2, +3}Department of Civil Engineering, Yokohama National University, 79-5 Tokiwadai, Hodogaya-ku, Yokohama, 240-8501, Japan

It is pointed out that normal cable can gallop divergently in both rain and dry condition which call rain-wind induced vibration and dry galloping (DG) respectively. For suppression rain wind induced vibration, indented surface and parallel protuberance cables have been applied in Japan and some Asia countries. Nevertheless, it is also figured that those methods are still defective in mitigating cable dry galloping. Moreover, DG characteristics of indented surface and parallel protuberances cable have not fully investigated yet. Therefore, the aim of this study is to figure out comprehensively the aerodynamic performances of indented surface and parallel protuberance in low Scruton number range. In addition, axial flow near the cable-wake will be measured and discussed. Wind tunnel test results elucidated that divergent galloping occurred in specific conditions in case of smooth surface. Similarly, large amplitude vibration still appeared in presence of indented surface and parallel protuberances. Finally, it also reconfirmed the existence of axial flow around cable wake which can excite galloping and this kind of axial flow still remains in for the other surface cables.

Keyword: dry galloping, indented surface, parallel protuberances, low Scruton number, axial flow

1. INTRODUCTION

After the rain-wind induced vibration (RWIV) was figured out as a dangerous vibration which can cause the harmfulness of cable attachment and bridge deck, so wind-resistant design of stay cables always requires a countermeasure versus RWIV. Indented surface and parallel protuberance cables have been developed for this aim. The main purpose of these countermeasures is rain rivulet destruction, leading to the suppression of RWIV. Indented surface was the first applied to Tatara stayed-cable Bridge and later to the Sutong and Stonecutters Bridges. This control method was initially proposed by Miyata et al.¹⁾. In order to eliminate the rain rivulet, dimples were made on the cable surface with a specific scale and arrangement. It has been also found to improve the stabilization of cable under rain-wind interaction with low drag force. In the other scenario, parallel protuberances initially applied in Higashi Kobe Bridge. This countermeasure uses twelve of fillets along cable to control the forming of upper and lower rivulets, and then it can stop RWIVs. Recently, it is also pointed out that circular stay cable can gallop with large amplitude at high reduced wind speed in dry condition which called dry galloping. The characteristic of this phenomenon has attracted many researchers. Dry galloping was observed in wind tunnel tests (WTTs) by Saito et al.²⁾ Honda et al.³⁾ and Vo et al.⁴⁾ in the subcritical Reynolds number regime, and Miyata et al.¹⁾, Cheng et al.⁴⁾, Jacobsen et al.⁵⁾ in the transition and critical Reynolds number regime. Matsumoto et al.⁶⁾ explained the differences between the Saito criterion and FHWA criterion by classifying galloping into divergent-type galloping and unsteady galloping. They also shed light on the role of axial flow for galloping instability by conducting wind tunnel test with and without artificial axial flow along the wake of cable. According to Cheng et al.⁴⁾, both divergent type of motion and limited-amplitude vibration at high reduced wind speed were recorded. However, the characteristics and excitation conditions of these two phenomena are separately different. The former has

⁺¹vo-hung-sc@ynu.jp, ⁺²katsuchi@ynu.ac.jp, ⁺³yamada@ynu.ac.jp

similar response as galloping while the latter occurs only in certain narrow high reduced wind speed ranges and has different onset conditions. When compared the characteristics of dry-galloping between normal and indented cable surface, Katsuchi and Yamada⁷⁾ found that the indented cable could not mitigate the dry-galloping effectively, in which divergent galloping still occurred. This conclusion agreed with the report of Hojo et al⁸⁾. However, the full aerodynamic responses in low Scruton number of these methods have not been clarified yet. Furthermore, due to the defectiveness of current mitigation methods, it is urgent to develop an effective aerodynamic countermeasure not only for RWIV but also for DG.

The aim of this study is to investigate the DG characteristics of indented surface and parallel protuberance in low Scruton number region. Firstly, the WTT will examine smooth surface in various wind attack for the base line. Then, aerodynamic responses of indented surface and parallel protuberances will be recorded with various conditions. Finally, the axial flow in the wake of cables will be measured and discussed.

2. MATERIAL AND METHOD

(1) Wind tunnel

The wind tunnel test were performed at the 1.3mx1.3m² cross-section open-circuit wind tunnel in Yokohama National University, Japan (Figure 1). Cable model was supported by a 1-DOF spring system in vertical plane and small wire system was used in horizontal plane in order to keep cable model unmoved laterally. The flow conditions were measured at cable model position by hot wire anemometer and turbulence intensities of 0.48–0.62% were recorded for 25%/50%/100% of maximum wind speed.



Figure 1: Wind tunnel in Yokohama National University

(2) Models fabrication

Three models were examined, included a plain HDPE smooth cylinder for reference, a HDPE cylinder with parallel protuberances and a HDPE cylinder with indented surface. The model samples were fabricated with same scale to real bridge cables. Cable diameters are 110mm and 158mm with an effective model length of 1.5 m, the aspect ratio is 13.6 and 9.5, respectively. The indented surface was fabricated same pattern of stayed-cables of Tataru stayed cable Bridge while a parallel protuberances cable was fabricated similarly to Higashi Kobe Ohashi Bridge cables by adding the twelve rubber fillets. The detail of surface modification can be seen as Figure 2 and 3.



Figure 2: Indented surface cable

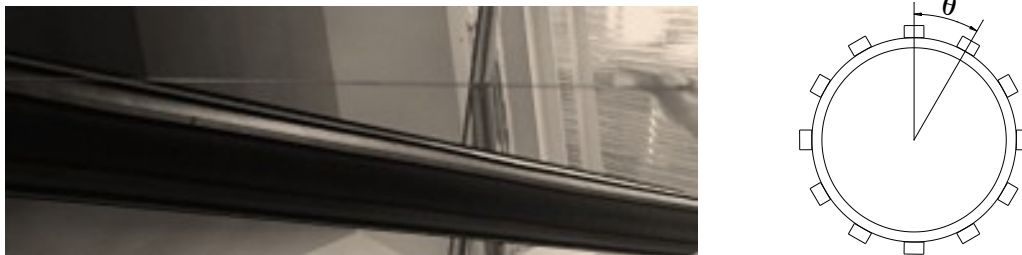


Figure 3: Parallel protuberances cable

(3) Inclined angle and flow angle

Wind attack angle can be created by moving the cable suspended frame by two angles: inclined angle α and flow angle β . Then, wind relative angle β^* , which defines the angle between wind direction and cable axis as shown in Figure 4, can be calculated by below formula:

$$\beta^* = \sin^{-1} (\cos \alpha \cdot \sin \beta) \tag{1}$$

In this WTT, the inclined angle was fixed at 40° and 25° combined with the flow angle of $0^\circ, 15^\circ, 30^\circ, 45^\circ$ and 60° . These inclinations were selected to take into account an inclined angle of stay cables in middle and top section of a normal cable-stayed bridge, respectively.

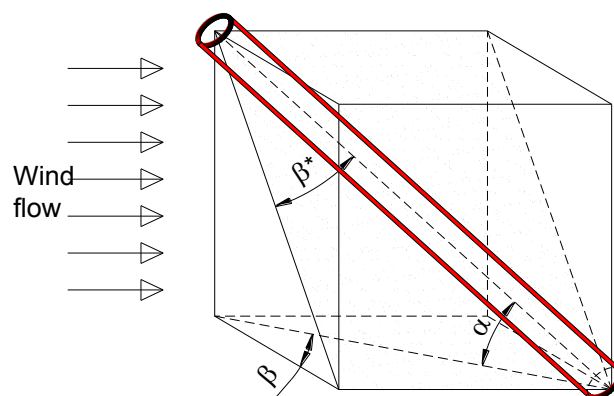


Figure 4: Inclined angle and flow angle

(4) WTT parameters

Table 1 shows the detail of experiment parameters in which cable diameters are 110mm and 158mm. Damping ratio ranges from approximately 0.08% to 0.25% and natural frequency is around 0.77 - 1.02 Hz in considering typical stay cables values. Due to the limitation of wind tunnel capacity, maximum wind speed is

up to 20m/s equivalent to Reynolds number around 2.1×10^5 . Nevertheless, according to previous studies DG of inclined cable could be observed in the subcritical Reynolds number regime as well as in the transition and critical Reynolds number regime. Therefore, above range of Reynolds number enable to reproduce the DG.

Moreover, Scruton number ($2m\delta/\rho D^2$) is a non-dimensional parameter that characterizes the mass and damping properties of a flexible body. In this study, Scruton number range from 5.1 to 15.6.

Table 1: Conditions of WTT

Diameter: D (mm)	110 and 158
Effective length (mm)	1,500
m (kg/m)	11.98 - 13.02 (D110 mm) 14.55 - 16.13 (D158 mm)
Natural frequency (Hz)	0.82 – 1.02
Damping ratio	0.08% - 0.25%
Scruton number ($2m\delta/\rho D^2$)	5.1 – 15.6
Reynolds number	0- 2.1×10^5

3. RESULTS AND DISCUSSIONS

(1) Dry galloping of smooth surface cable

In order to reproduce dry galloping for smooth surface cable, 158mm and 110mm diameters were examined in these tests. WTTs were carried out in a dry condition and results are summarized in Figure 5 and 6. Generally, dry galloping took place in many cases. For 110 mm cable, divergent vibration took place at several attitudes such as the inclined angle (α) 40° with the flow angles (β) 15° , 30° and 45° , and (α) 25° with (β) 30° in the subcritical Reynolds number region ($6 \times 10^4 - 1.2 \times 10^5$). In the case of cable diameter of 158 mm, similar divergent vibration also recorded in most cases. This experimental result is consistent with previous studies that DG can occur at some specific wind attack angles and wind speed range^{10, 11, 12, 13}.

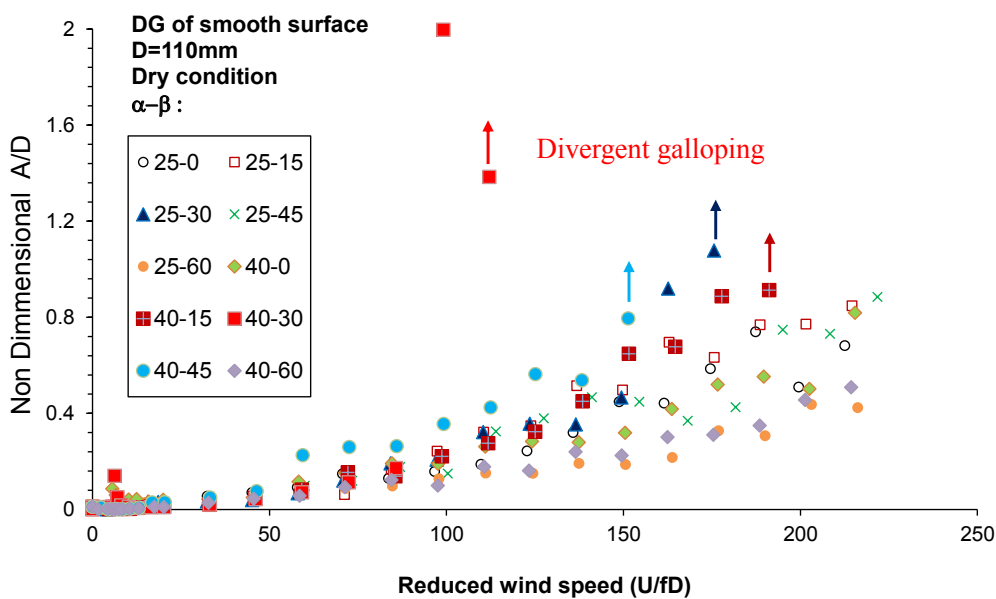


Figure 5: Dry galloping of smooth surface cylinder, D110mm

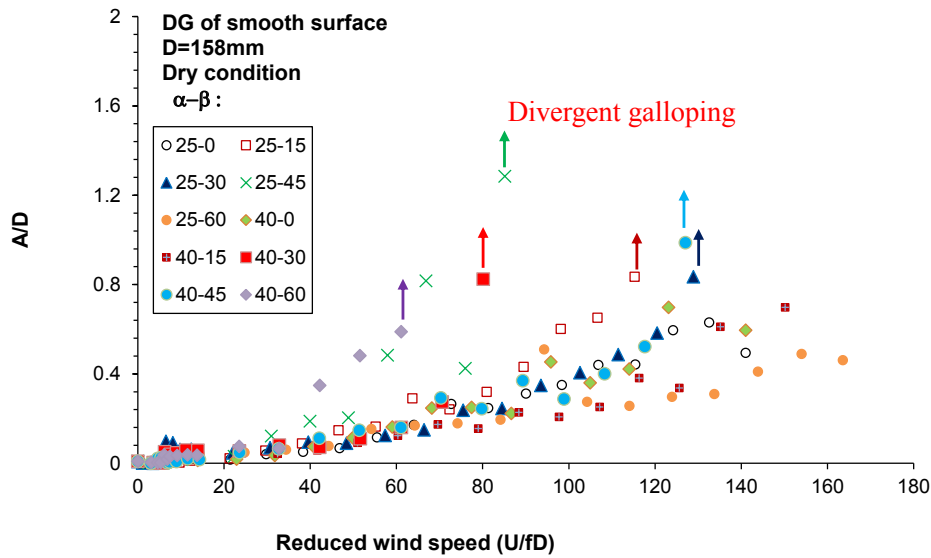


Figure 6: Dry galloping of smooth surface cylinder, D158mm

(2) Effectiveness of indented surface

Indented surface has been applied for some cable-stayed bridges in Japan and East Asia. Tataru Bridge was the first case applying the indented surface cable. Nevertheless, it is pointed out that this modification type could not suppress well DG particularly in a low Scruton number condition³⁾. Hence, the main purpose of the present test is to examine mitigation efficiency for dry galloping. WTT parameters were unchanged to the circular cylinder cases.

Figure 7 illustrate the aerodynamic responses of indented surface in dry condition. Generally, mostly divergent vibration was mitigated, except unexpected cases of the inclined angle (α) 25° with the flow angle (β) 45°. Nevertheless, limited vibration still appeared for many cases. This may be due to the inherent unstable characteristic of stayed cables in small Scruton number range. It is also observed that D158 mm cable tended to be more unstable rather than 110 mm cable. Large vibration mostly started at the reduced wind speed (U/fD) of approximately 70 with amplitude of around 1.2D in case of α 25° and β 45°. In range of Scruton number around 5.1 – 15.6, indented surface is still defective in eliminating DG.

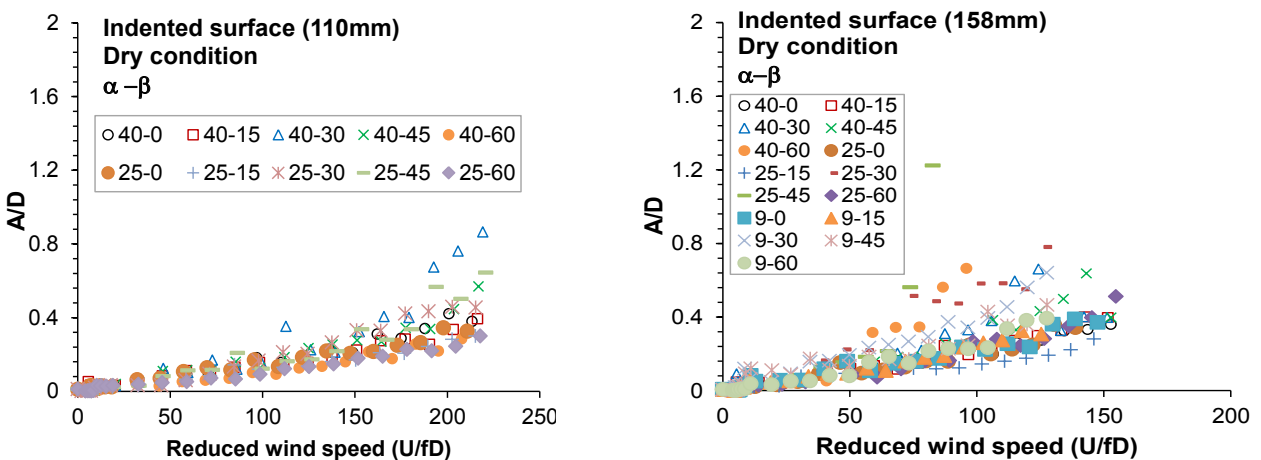


Figure 7: DG of indented surface cable

(3) Effectiveness of parallel protuberance

For comparison with the indented surface cable, same extensive WTTs were carried out for verifying the effectiveness of the parallel-protuberance countermeasure to DG. In dry condition, parallel protuberance can mitigate cable vibration to some extent as shown in Figure 8. Nevertheless, divergent type vibration still appeared. The largest amplitude is approximately $1.4D$ in the case of the inclined angle 25° with the flow angle 15° for 110 mm cable. Large vibration started occurring at reduced wind speed around 100-170 in cases of wind angles 40° - 30° , 25° - 45° and 25° - 15° . In case of D158, divergent galloping appeared at wind angles 25° - 45° and 25° - 45° whereas the remained cases still exhibited the large amplitude vibration.

In addition, when cable model was rotated around its axis to check the effect of protuberances location, vibration response was almost similar. This result totally agreed with the WTT result of Higashi Kobe Ohashi Bridge¹⁰). Above discussions suggest that one should be careful when applying the indented surface and parallel protuberance for suppressing RWIV and DG, especially for the cables with low Scruton number. It is also urgent to propose an innovative cable surface which can mitigate both RWIV and DG more efficiently.

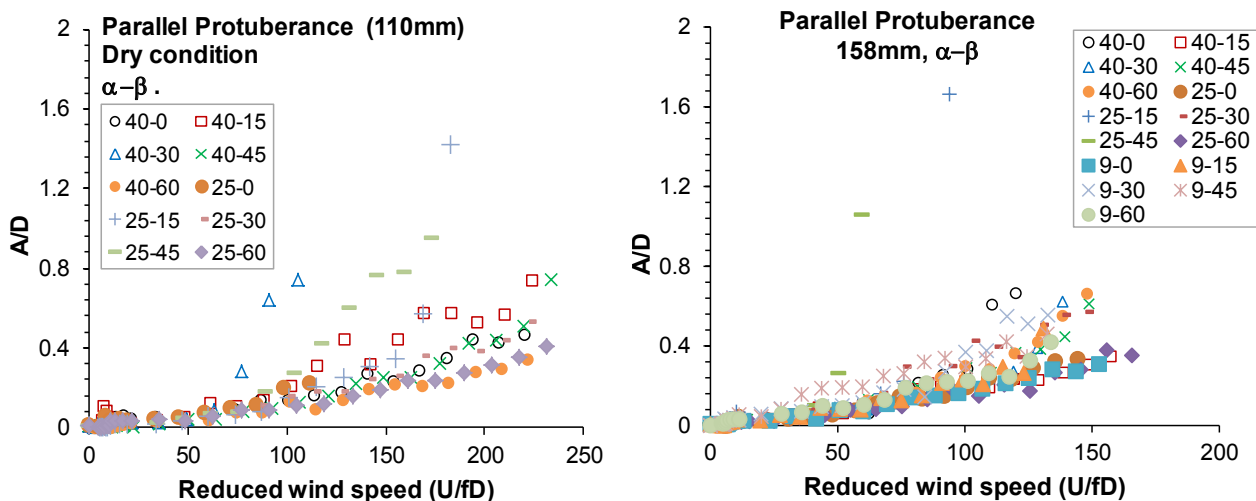


Figure 8: Dry galloping of Parallel protuberance cable

(4) Axial flow near the wake of cable

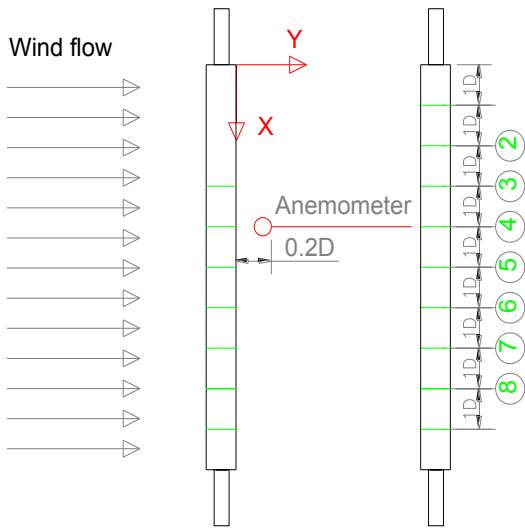
It is pointed out that axial flow in a wake of cable plays significant role for galloping instability in dry condition⁶). To confirm this characteristic, the axial flow was measured by anemometer with smooth surface, indented surface and parallel protuberances. The static model was installed at inclined angle 25° and flow angle 30° . Diameter of 158mm was used in this experiment. The detail of measured results can be seen in below sections.

a) Smooth surface

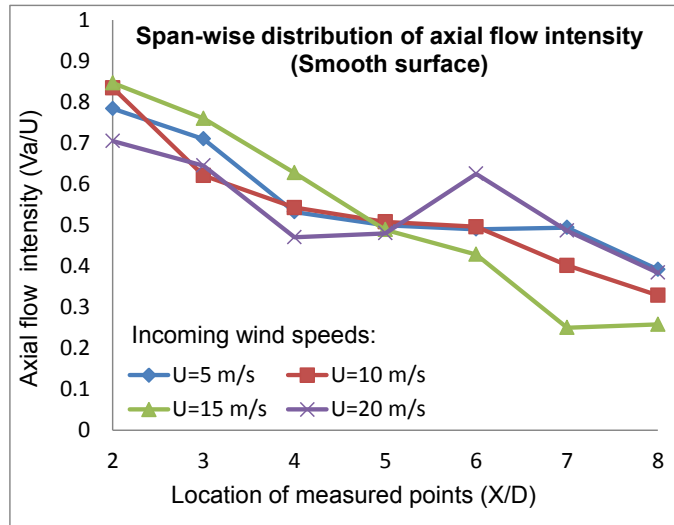
The axial flow velocity was measured in span-wise direction and stream-wise direction. The measurement plan is illustrated in Figure 9a and 10a. For measuring the span-wise axial flow velocity, anemometer was located $0.2D$ from the wake of cable. Figure 9b elucidates that axial flow velocity distributes non-uniformly and decrease gradually from the upstream cable end to the downstream one. In the upstream cable end, axial flow velocity was around 70-85% of incoming velocity whereas it was 30-40% in the downstream cable end. The distribution of axial flow intensity seems to be similar to every incoming velocity as Figure 9b.

In addition, the stream-wise axial flow distribution was also recorded. In this measurement, the anemometer was located at center-line from $0.2D$ to $2D$ with steps as Figure 10. Interestingly, the velocity intensity of axial flow in the range from $0.2D$ to $0.8D$ seems to be unchanged with high intensity around 60-80%. This strong channel can play the role as “splitter plate” which can stop the communication between

upper and lower flows. From that, this can excite galloping. This finding agreed with the conclusion of Matsumoto et al⁽⁶⁾.

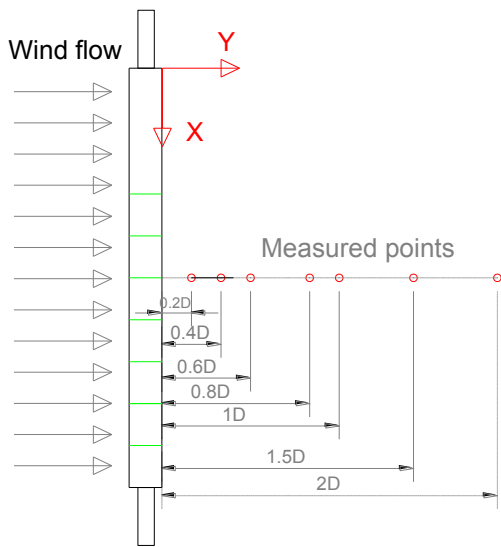


a. Measurement arrangement

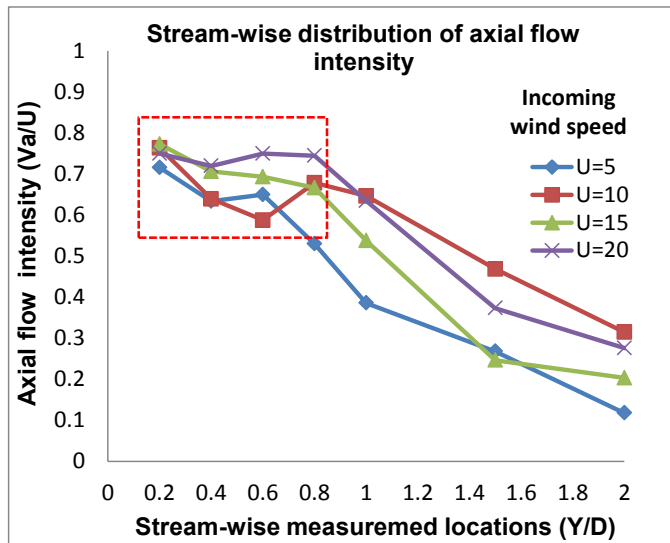


b. axial flow distribution

Figure 9: Span-wise velocity distribution of axial flow



a. Measurement arrangement



b. axial flow distribution

Figure 10: Stream-wise distribution of axial flow velocity

b) Indented surface and parallel protuberances

The distribution of axial flow velocity near wake of indented surface and parallel protuberances cables can be seen in Figure 10 and Figure 11. Obviously, strong channel of axial flow still existed with intensity above 50% of coming flow. Upper cable end still exhibited higher velocity intensity compare to lower side. Axial flow patterns are quite similar for both cable types. However, the difference between upper end and lower ends of cable is smaller compare to smooth surface case. This fact elucidates that why DG appeared with these cables.

In addition, the comparison between smooth surface, indented surface and parallel protuberances can

be seen in Figure 11. In this Figure, incoming wind speed is 15m/s in order to take in to account the occurrence range where DG. Generally, the axial flow distributions of three cables were quite similar for all cases. In the other expression, it seems to be that the axial flow is one of inherent characteristic of inclined cable again wind incoming wind and it does not depends on the cable surface much. Further investigation should be carried out.

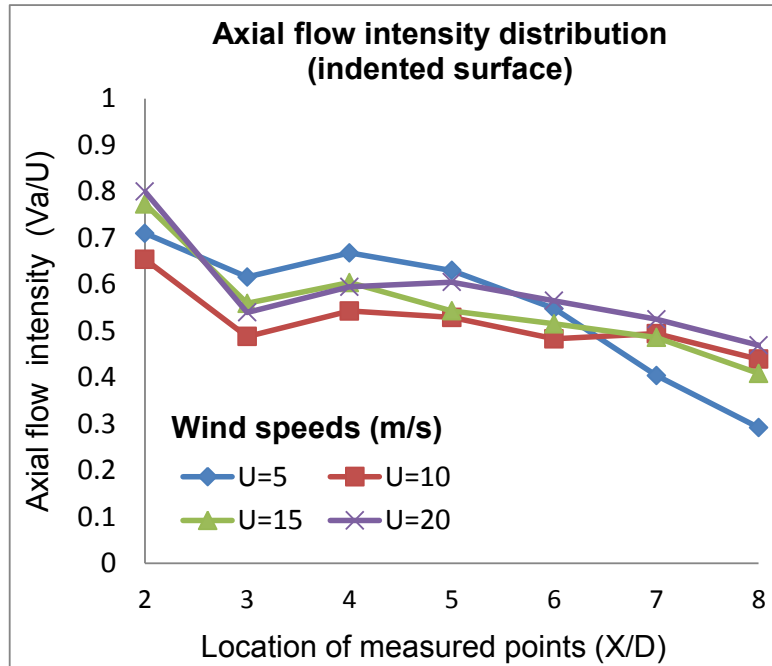


Figure 9: Span-wise distribution of axial flow of indented cable

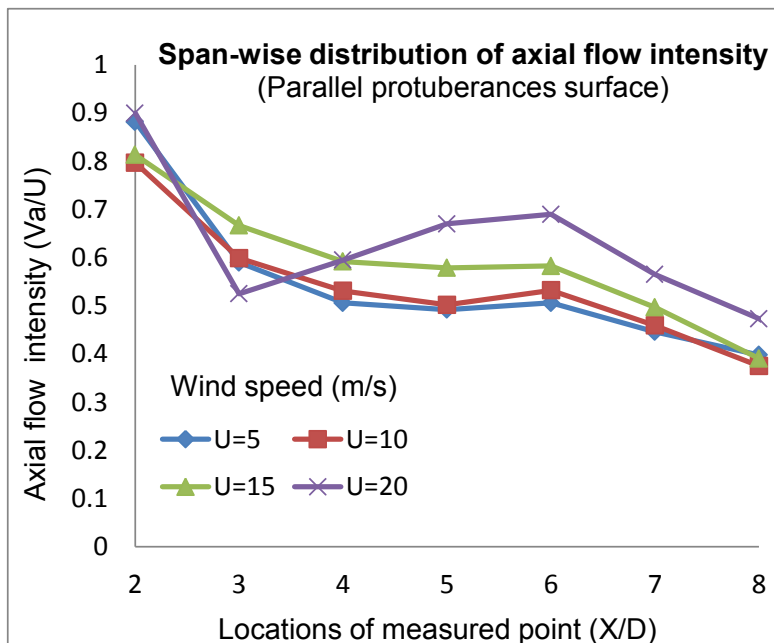


Figure 10: Span-wise distribution of axial flow of parallel protuberances cable

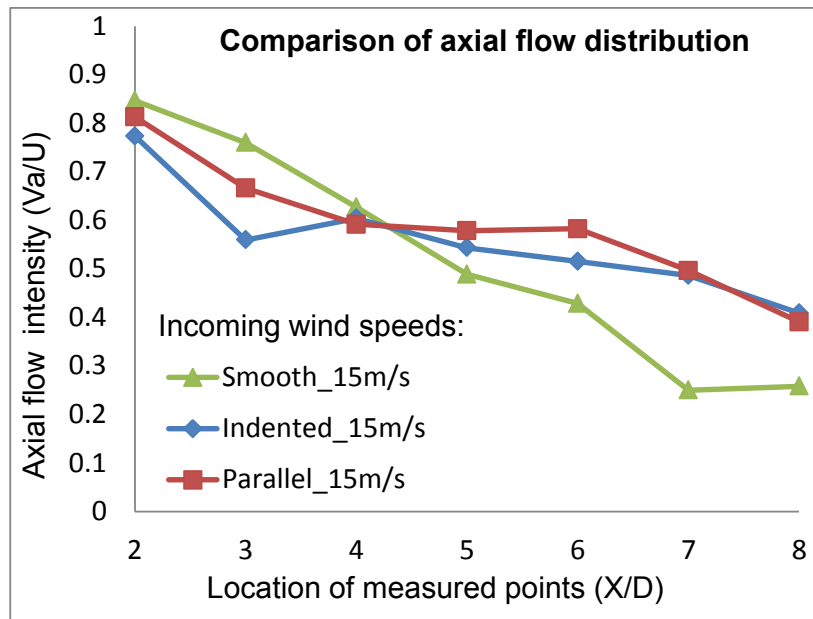


Figure 11: Comparison between smooth surface, indented surface and parallel protuberances cables.

3. CONCLUSIONS AND RECOMMENDATION

The main objectives of this paper are to give the general understanding about the dry-galloping of indented surface and parallel protuberances. Under each case, responses of cable were different and it depended on wind attack angle, surface modification. In addition, the axial flow near the wake of cable was investigated. The present study allows the following conclusions to be drawn:

- 1) Dry galloping is one of large amplitude vibration which can damage the cable attachment.
- 2) Indented surface and parallel protuberances used to apply for RWIV; however, it could not eliminate dry galloping well. Large amplitude vibration still occurred for many cases in low Scruton number range.
- 3) There is existence of axial flow with high intensity around 60-80% located from 0.2D to 0.8D near wake of smooth cable which can excite galloping. These flow channels still remain in case of indented surface and parallel protuberances cable. Therefore, axial flow is one of inherent characteristic of inclined cable again wind incoming wind and it does not depends on the cable surface much.

REFERENCES

- 1) Miyata, T., Yamada, H., Hojo, T., Aerodynamic response of PE stay cables with pattern-indented surface, *Proc. of International Conference on Cable-Stayed and Suspension Bridges (AFPC)*, Deauville, France, Vol. 2, pp. 515–522, 1994.
- 2) Saito, T., Matsumoto, M. and Kitazawa, M., Rain-wind Excitation of Cables on Cable-stayed Higashi-Kobe Bridge and Cable Vibration Control, *Proc. of Cable-stayed and Suspension Bridges*, Vol.2, pp.507-514, 1994.
- 3) Honda, A., Yamanaka, T., Fujiwara, T., Saito, T., Wind tunnel test on rain-induced vibration of the stay cable, *Proceedings of International Symposium on Cable Dynamics*, Lie`ge, Belgium, pp.255–262, 1995.
- 4) Cheng, S., Larose, G.L, Savage, M.G., Tanaka, H., Irwin, P.A., Experimental study on the wind-induced vibration of a dry inclined cable—Part I: Phenomena, *Journal of Wind Engineering and Industrial Aerodynamics*, 96, pp.2231–2253, 2008.

- 5) J.B. Jakobsen, T.L. Andersen, J.H.G. Macdonald, N.Nikitas, G.L. Larose, G.Savage, B.R. McAuliffe, Wind-induced response and excitation, characteristic of an inclined cable model in the critical Reynolds number range, *Journal of Wind Engineering and Industrial Aerodynamics*, 110, pp100–112, 2012.
- 6) Matsumoto, M., Yagi, T., Hatsuda, H., Shima, T., Tanaka, M. and Naito, H., Dry-galloping characteristics and its mechanism of inclined/yawed cables. *Journal of Wind Engineering and Industrial Aerodynamics*, 98, pp.317–327, 2010.
- 7) Katsuchi, H., and Yamada, H., Wind-tunnel Study on Dry-galloping of Indented-surface Stay Cable, *11th Americas conference on wind engineering-* San Jaun, Puerto Rico June pp.22-26, 2009.
- 8) Hojo, T., Yamazaki, S., and Okada, H., Development of low drag aerodynamically stable cable with indented processing, *Nippon Steel Technical Report*, No. 82, July 2000.
- 9) Nakamura, Y., Hirata, K. and Urabe, T., Galloping of rectangular cylinders in the presence of a splitter plate. *Journal of Fluids and Structures*, Vol.5, 1991, 521-549.
- 10) Matsumoto, M., Kitazawa, M. and Kanaji, H. Wind tunnel test for stay cables of Higashi Kobe Ohashi Bridge (part 2) *Proc. Of 44th Annual Conference of JSCE*, pp.802-803, 1989 (in Japanese)

DRY GALLOPING CHARACTERISTIC AND VIBRATION CONTROL OF INCLINED STAY CABLE

Tomo Tanaka⁺¹, Masaru Matsumoto⁺², Hiroshi Ishizaki⁺³, Hiroshi Kibe⁺⁴

⁺¹SE Corporation, Tokyo, Japan

⁺²Kyoto University, Prof. Emeritus, Kyoto, Japan

⁺³SE Corporation, Vice President, Tokyo, Japan

⁺⁴SE Corporation, Tokyo, Japan

The rain and wind induced vibration (RWIV) and the dry galloping (DG) of the stay cables of cable-stayed bridges are greatly concerning issue for their safety. A numerous studies have been carried out to clarify their generation mechanism and to aerodynamically stabilize those. Recently the authors [1] pointed out that extremely complex RWIV and DG might be excited by the unsteady behavior of the separation bubble (SB) on the cable surface, it means its formation and its destruction (burst) at the particular situations, such as the water rivulet location, the intensity of the axial flow in a near wake of an inclined cable and the critical Reynolds number regime, in similar with the airfoil-stall. Their aerodynamic instabilities are called as stall-type galloping (STG). Based upon this scenario on the generation mechanism, the positive promotion of flow separation to interrupt the formation of SB might effectively stabilize RWIV and DG. The wind tunnel tests have been, in consequence, conducted by the use of rigid cable model with the proto-type size in diameter by installing the large size double helical fillets to verify for their aerodynamic stabilization effect. Furthermore, DG mechanism at the critical Reynolds number regime of the non-yawed cable has been investigated in comparison of the stationary and fluctuating lift forces and the stationary drag force with the cross-flow response of the both cases of non-yawed cable and the yawed cable without/with the double helical fillets.

Keyword: stall, dry galloping, double helical fillet, full scale cable model, aerodynamic stabilization

1. INTRODUCTION

The rain and wind induced vibration (RWIV) and the dry galloping (DG) have been widely known to be typical aerodynamic vibrations of the inclined stay cable of the cable stayed bridge. The numerous investigations also have been carried out, however the precise generation mechanism hasn't been clarified, because of their extremely complex and sensitive fluid-structures interaction mechanism in relation to the water-rivulet on cable surface, the axial-flow in a near wake and the Reynolds number.

The authors [1] have recently pointed out the substantial role of an unsteady production/burst of the "Separation Bubble (SB)" which were generated by the separation and reattachment of the flow on a cable surface for excitation of RWIV and DG, similarly with airfoil-stall [2]. They have called it the "Stall-Type Galloping (STG)", since that fluid phenomenon is fundamentally identical to the airfoil stall. Rinoie [2] has pointed out that the definitely essential role of the behaviour of the separation bubble on the airfoil at near the stalling critical angle, in particular, the appearance of the low frequency fluctuation of flows and lift force at the critical stall event related to K-H instability. It should be noted that the low frequency fluctuation of flow and lift force at the critical stall event must be a key issue for the detection of stall events.

Based upon this scenario on the generation mechanism, the positive promotion of flow separation to interrupt the formation of SB might effectively stabilize RWIV and DG. The wind tunnel tests have been, in

⁺¹tomo_tanaka@se-corp.com, ⁺²matsu@brdgeng.gee.kyoto-u.ac.jp, ⁺³hiroshi_ishizaki@se-corp.com, ⁺⁴hiroshi_kibe@se-corp.com

consequence, conducted by the use of rigid cable model with the proto-type size in diameter by installing the large size double helical fillets to verify for their aerodynamic stabilization effect. Furthermore, DG mechanism at the critical Reynolds number regime of the non-yawed cable has been investigated in comparison of the stationary and fluctuating lift forces and the stationary drag force with the cross-flow response of the both cases of non-yawed cable and yawed cable without/with the double helical fillets. In summary it has been clarified that the double helical fillets with big size can sufficiently stabilize DG of the non-yawed and yawed cables without increasing the drag force. Furthermore, the generation mechanism of STG, that is DG at the critical Reynolds number regime, has been investigated in comparison of the stationary and fluctuating lift forces and the stationary drag force with the cross-flow response of the both cases of non-yawed cable and yawed cable without/with the double helical fillets, taking in to account of the low frequency fluctuation of lift force.

2. WIND TUNNEL TESTS

(1) The wind tunnel and the test facilities

This test, in a high velocity wind tunnel of Japan Aerospace Exploration Agency (JAXA) (2m×2m Low Speed Wind Tunnel, H2m×W2m), was carried out in the range of wind velocity up to 36 m/s ($Re=4.8 \times 10^5$ defined by cable diameter D of 0.2m). The tested flow is a uniform flow ($I_u < 0.1\%$).

The test was carried out at the reconstructed part with the ceiling, the floor and both side walls made of woods in the length of 5m as shown in Photo 1.

At the both wooden walls of wind tunnel, a circular opening was provided for non-preventing the axial flow in a near wake referred to the previous study [3]. Both ends of the cable models are arranged to be positioned at the outside of wind tunnel through these openings. The load-cells or the non-contact displacement meter was set up at the both cable ends and upstream end for measurement of the aerodynamic force and for measurement of the cross-flow response, respectively. And, in free vibration tests, all materials such as a coil spring and a fixed piano wire had also been installed at the outside in the same way. The overview of the wind tunnel facility is shown in Photo 1.



Photo 1: JAXA 2m×2m Low Speed Wind Tunnel

a) Aerodynamic force measurement test

In the aerodynamic force measurement test, the drag force and the lift force were separately measured by the load cell (KYOWA: LTZ-100KA) directly connected to the axial rods of cable model at the both ends. (See Photo 2(a))

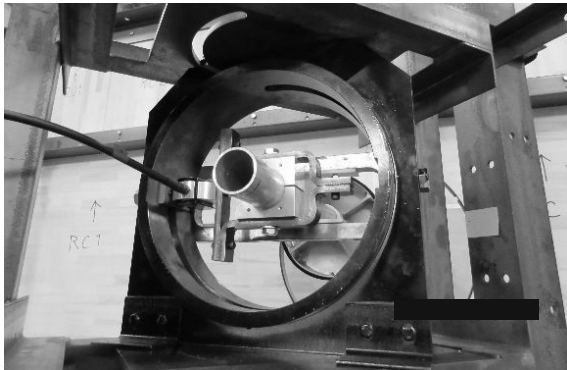
The opening of the both side walls were closed in the case of the yawed angle $\beta=0^\circ$ and opened (3D size circle) in the case of the yawed angle $\beta=45^\circ$, respectively.

b) Free vibration test

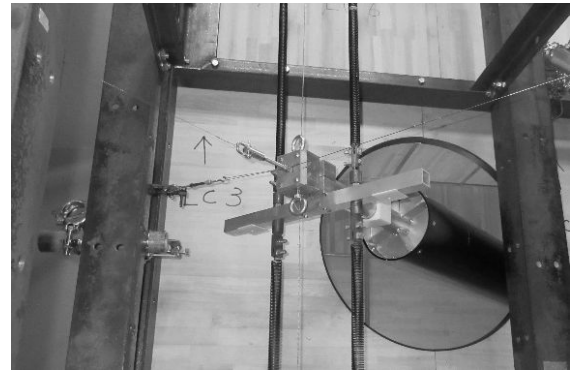
In the vibration test, the rocking system with the one-degree-of-freedom was adopted in order to prevent of mixing of the rolling type vibration and the structural damping was minimized as much as possible. In particular, the cable-end at the downwind side was fixed by five piano wires as a pin support, and the other cable-end at the windward side is supported by upper and lower four springs.

The amplitude of the cross-flow response was measured by the laser displacement meter (Keyence: IL-600) at the free end. The detail of cable specimen end is shown in Photo 2(b).

The opening of the both side walls were closed as much as possible in case of the yawed angle $\beta=0^\circ$. On the other hand, in case of the yawed angle $\beta=45^\circ$, the opening was opened (3D circle) to generate an axial flow in the near wake.



(a) Aerodynamic force measurement tests



(b) Free vibration tests

Photo 2: The detail of cable specimen end

(2) The cable rigid model and the installed large-size fillets

The cable rigid model of an aluminum tube with polyester coating was used (outer diameter 200mm, thickness 5mm, total length 3200mm). By the roughness measurement of the coating surface, roughness of the polyester coatings was confirmed to have a relatively close value as polyethylene.

Fillets used for this verification are the double helical type, the winding pitch was set to 5.44D (D: cable outer diameter, winding angle: 30° to the cable axis). The fillet cross sections are set to three kinds of shapes (I-type, Circular-type and Square-type (see Fig.1)), the basic height were set at 5, 8, and 10% of the cable diameter D.

The yawed angle β of the cable model was changed in two cases of 0° and 45° with respect to a perpendicular direction from the cable-axis to the wind direction. The cross-sectional shape of the 10% fillet is shown in Figure 1 and a cable model set up for measurement with I-type fillet is shown in photo 3.

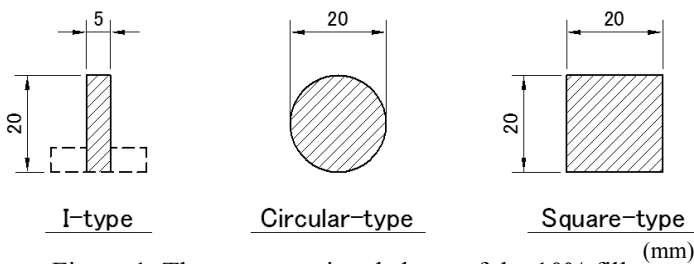


Figure 1: The cross-sectional shape of the 10% fillet (mm)

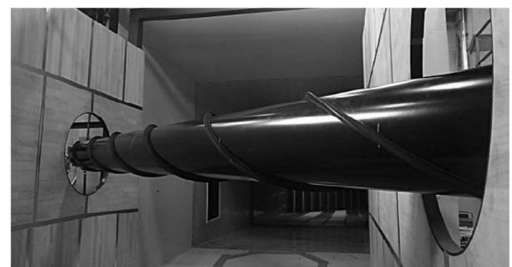


Photo 3: A cable specimen with I-type fillet

(3) Vibration characteristics

The vibration characteristics of 1 DOF locking system, at $V=0$ m/s, (V : Oncoming wind velocity) are as follows: the frequency is approximately 1.3Hz and the logarithmic decrement was approximately $1.2\sim 1.4 \times 10^{-3}$ at the amplitude of 10mm. The mass per unit length of cable model was 25.8 kg/m, the mass rocking inertia was 202.2 kg·m², Scruton number of 1DOF locking system was approximately 70.8 (equivalent corresponding Scruton number of heaving vibration is 1.4).

4. AERODYNAMIC FORCE MEASUREMENT TEST

(1) Drag force measurement

The drag coefficient calculated from results of the drag measurement is shown in Fig. 2. The drag coefficient C_D of all test cases was calculated from the following equation.

$$C_D = \frac{F_D}{0.5 \cdot \rho \cdot V^2 \cdot D}$$

F_D : the drag measured by load-cell per unit length [N/m], ρ : Air density [kg/m^3],

V : Wind velocity [m/sec], D : Cable diameter [m]

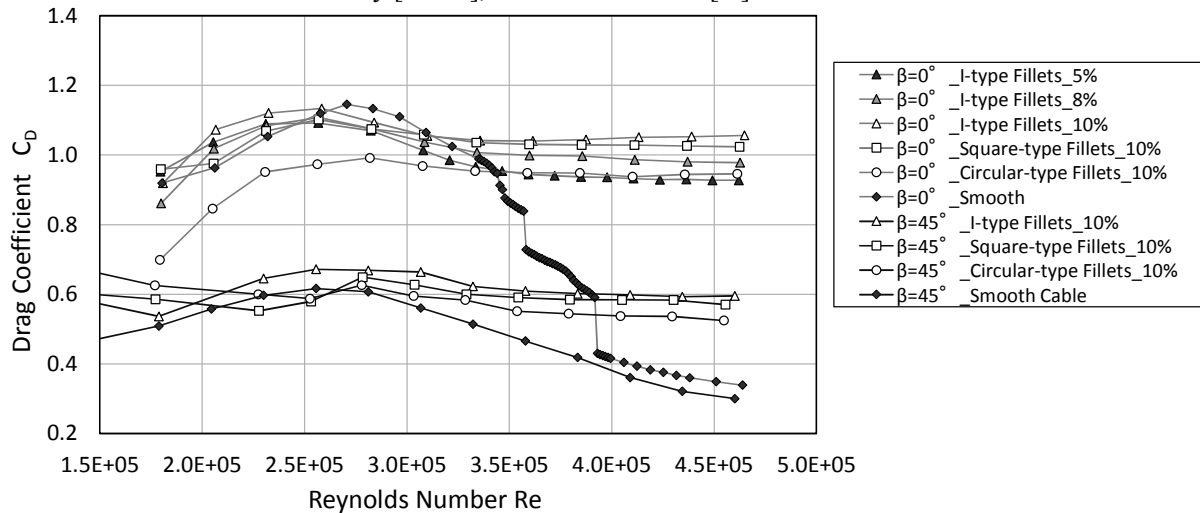


Figure 2: Characteristics of the drag coefficient C_D in terms of the Reynolds number Re

a) Drag coefficient C_D v.s. Reynolds number Re of the Smooth cable at the yawed angle $\beta=0^\circ$

The drag-crisis at around $Re=3 \times 10^5 \sim 4 \times 10^5$ was observed as shown in Fig.2. The characteristics of the drag-Reynolds number show almost similar property reported by Schewe [4]. It should be noted that at the extremely narrow range of the Reynolds number and at the slightly bigger than $Re=3.5 \times 10^5$, the slight discrete change of drag. Describing the details on the drag crisis, in the result of Schewe [4], only one drag-crisis appears, on the other hand, twice or thrice drag-crises are observed at slightly bigger than $Re=3.5 \times 10^5$, and the around $Re=3.7 \times 10^5$ and 4.1×10^5 . This different property is thought to be caused slight change of flow fields caused by various different test conditions. On the other hand, Liu [5] showed the twice drag-crises at near $Re=3.5 \times 10^5$ and at near $Re=4.3 \times 10^5$. As far as the magnitude of C_D , at the prior drag-crisis and at the sub-critical Reynolds number regime, $C_D \approx 1.2$, which almost with agree with the test results by Schewe and Liu. On the other hand, at the post drag-crisis and at the super critical Reynolds number regime, there is discrepancy of C_D . C_D in this study shows a little less than 0.4 and gradually decreasing with increase of the Reynolds number, which might be roughly identical with Liu's result. But Schewe's case shows $C_D \approx 2.5$ and almost constant with increase of the Reynolds number. The reason of this significant difference of C_D at the super-critical Reynolds number is not cleared, so further survey on this point is needed.

b) The fillet effect on C_D of the non-yawed cable ($\beta=0^\circ$)

C_D of I-type 10% fillet and Square-type 10% fillets were $C_D \approx 1.1$ at the maximum at the sub-critical Reynolds number regime. It should be noted that the installation of big size fillets do not increase C_D at the subcritical Reynolds number regime less than 3.25×10^5 . At the Reynolds number regime larger than 3.25×10^5 C_D shows around 0.9 ~ 1.1 in the different cases of different fillet shape and the fillet height. At this higher Reynolds number regime, the fillets increase C_D than the smooth cable, but from the point of view of the wind resistance design of the stay cable, this property is not concerned matter, because of utilization of C_D at the subcritical Reynolds number regime for the evaluation of wind load on the stay cables.

c) Drag coefficient C_D characteristics at the yawed angle $\beta=45^\circ$

In the yawed angle $\beta = 45^\circ$, C_D of the cable without/with fillets remarkably decreased in comparison with the result of $\beta=0^\circ$. C_D is decreased to approximately 0.6 from 1.1 with Re =around 3.0×10^5 .

In the case of the smooth cable, C_D gradually and mildly is decreased at the range of between $Re=2.7 \times 10^5$ and $Re=4.8 \times 10^5$. This C_D mild decreasing property might be a kind of drag-crisis, which would excite STG, that is cross-flow response (Katsuchi [6], Andersen&Jakobsen [7]). The installation of fillets can eliminate the mild drag-crisis as shown in Fig.2, it is, in consequence, expected that the DG would be stabilized.

(2) Lift force measurement

Lift coefficient calculated from results of the lift force measurement is shown in Fig.3. The lift coefficient C_L of all models was calculated from the following equation.

$$C_L = \frac{F_L}{0.5 \cdot \rho \cdot V^2 \cdot D}$$

F_L : the lift measured by load-cell per unit length [N/m], ρ : Air density [kg/m³],
 V : Wind velocity [m/sec], D : Cable diameter [m]

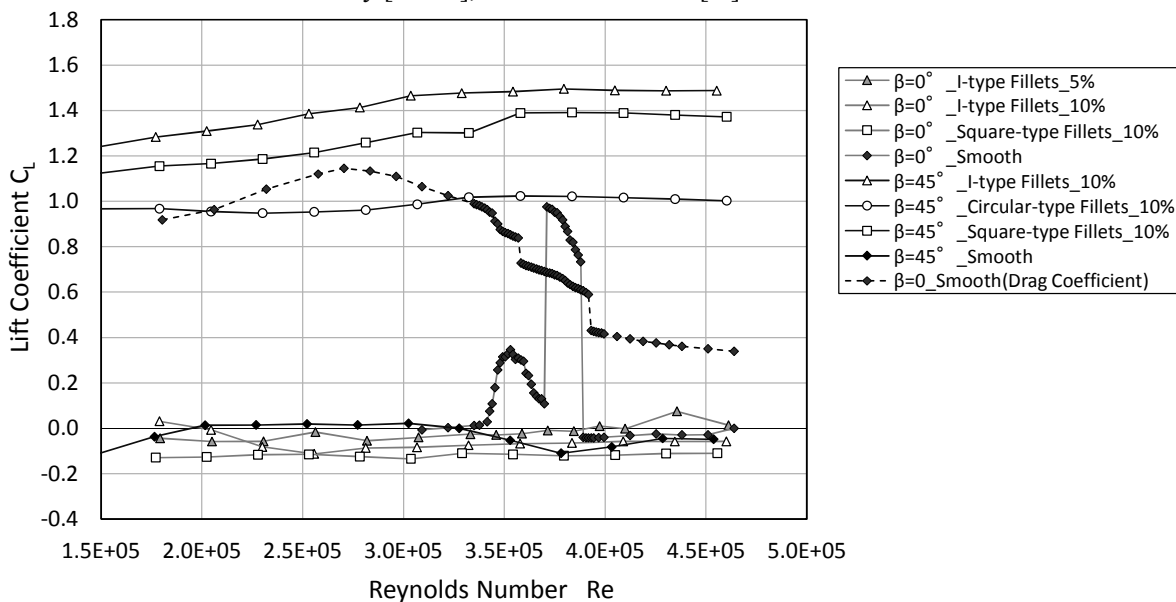


Figure 3: Characteristics of the lift coefficient C_L and the Reynolds number Re

a) Lift coefficient C_L of the non-yawed ($\beta=0^\circ$) smooth cable

Former studies [4], [5], [8], [9], it was verified that steady lift of the non-yawed ($\beta=0^\circ$) smooth cable, was produced at the critical Reynolds number regime. Which must be caused by the formation of the separated bubble on one side face of circular cylinder. Furthermore, it is also known that the generation of the steady lift is highly correlated with the drag crisis at the critical Reynolds number regime. However the particular Reynolds number regime where the steady lift is generated, are different among the related previous literatures, because of the extremely sensitive flow at the particular critical Reynolds number, where the stall might occurs, affected by many test conditions. As far as the peak value of stationary lift coefficient, Schewe [4], Larose [8], Benidir&Flamand [9], Liu [5] reported $C_L \approx 1.1$, 0.8, 1.1~1.4, and 1.6, respectively. This test result shows $C_L \approx 1.1$. The significant different characteristics of the stationary lift at the critical Reynolds number regime from the previous test results are twice or thrice appearances as in shown in Fig.3. As described above, the delicate discrepancy of the force characteristics at the critical Reynolds number regime might be caused by the difference of various tests condition. C_L shows almost zero at the outside of the critical Reynolds number regime where the drag-crises and the stationary non-zero C_L have been observed similarly with the previous test results by Schewe [4], Benidir&Flamand [9], Liu [5].

b) The fillet effects on C_L of the non-yawed($\beta=0^\circ$) cable model

C_L of the non-yawed cable ($\beta=0^\circ$) with fillet seems to be fundamentally almost zero.

c) Lift coefficient C_L characteristics at the yawed ($\beta=45^\circ$) cable without/with fillets

C_L at yawed angle $\beta=45^\circ$ was approximately 1.0~1.6 with gradual decrease with the Reynolds number as shown in Fig.3 because of unsymmetrical geometrical shape caused by the existence of helical fillets associated the cable center in the wind tunnel test section. On the other hand, C_L of the yawed ($\beta=45^\circ$) smooth cable is almost zero at the Reynolds number of $(1.5\sim 5.0) \times 10^5$ as shown in Fig.3.

5. FREE VIBRATION TEST

(1) Cross-flow response characteristics of the non-yawed ($\beta=0^\circ$) cable

a) Smooth cable

The non-yawed ($\beta=0^\circ$) smooth cable without fillets showed velocity restricted response at the multiple velocity ranges as shown in Fig.4 in correspondence to observation of the multiple drag-crises, explained above. It was significantly interesting that those responses were observed at the particular wind velocity range where the drag-crises and the stationary lift force occurred, even though the complete different tests, those are stationary test for force measurement of the stationary cable model and the vibration test in the 1DOF locking system. In the detail, the cross flow response seems to appear at the wind velocity correspondingly to the disappearance of stationary lift caused by the destruction (burst) of the separation bubble. On the other hand, Liu [4] reported the cross flow velocity restricted response appears correspondingly to the both velocity where the of the stationary lift starts disappears.

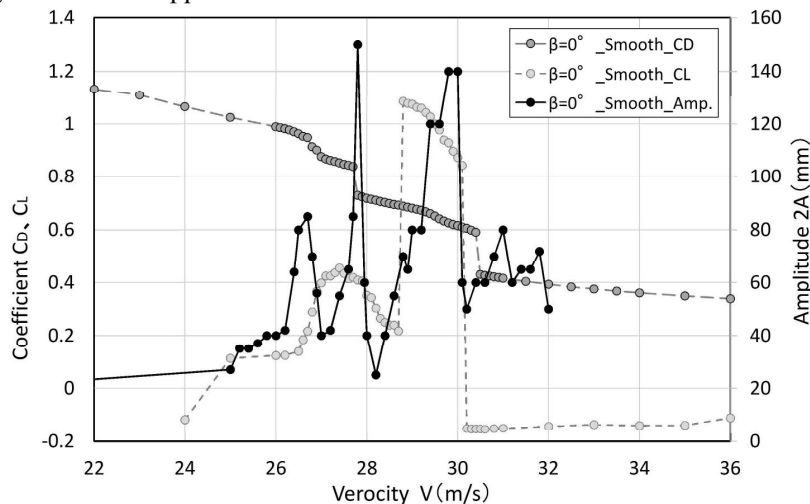


Figure 4: 2A-V diagrams of the smooth cable at the yawed angle $\beta=0^\circ$ with C_D, C_L

b) PSD of the unsteady lift force at the low frequency range of the non-yawed ($\beta=0^\circ$) smooth cable

In order to verify the generation mechanism of these velocity-restricted response of non-yawed ($\beta=0^\circ$) cable, the PSD (Power Spectral Density function) at the low frequency regime, less than 5Hz. As explained before, the stall phenomenon should produce the low frequency fluctuation of velocity around an obstacle, in another expression, the stall phenomenon can be detected by the existence of the low frequency fluctuation of velocity or lift force, therefore PSD of the lift force at the low frequency regime was analyzed at various velocity where cross flow responses were observed as shown in Fig.5. As shown in Fig.5, the typical power characteristics in PSD of the lift force at the low frequency regime were observed at correspondingly to the velocity where the cross-flow response disappears. These PSD properties at the low frequency caused by the stall are similar with those at the stall of a circular cylinder at the particular critical Reynolds number studied by Schewe [4], a circular cylinder with protuberance at the particular position of 50° from the front stagnation point at the subcritical Reynolds number regime studied by the authors [1], yawed ($\beta=45^\circ$) circular cylinder, snow-accreted conductors studied by Matsumiya [10]. At slightly increase of velocity, it is finishing of the cross-

flow response caused by the stall, the low frequency fluctuation of lift force cannot be observed as shown in the left and bottom Fig.5 (velocity of 30.2m/s). In summary, the cross-flow response of the non-yawed cable might be a kind of STG.

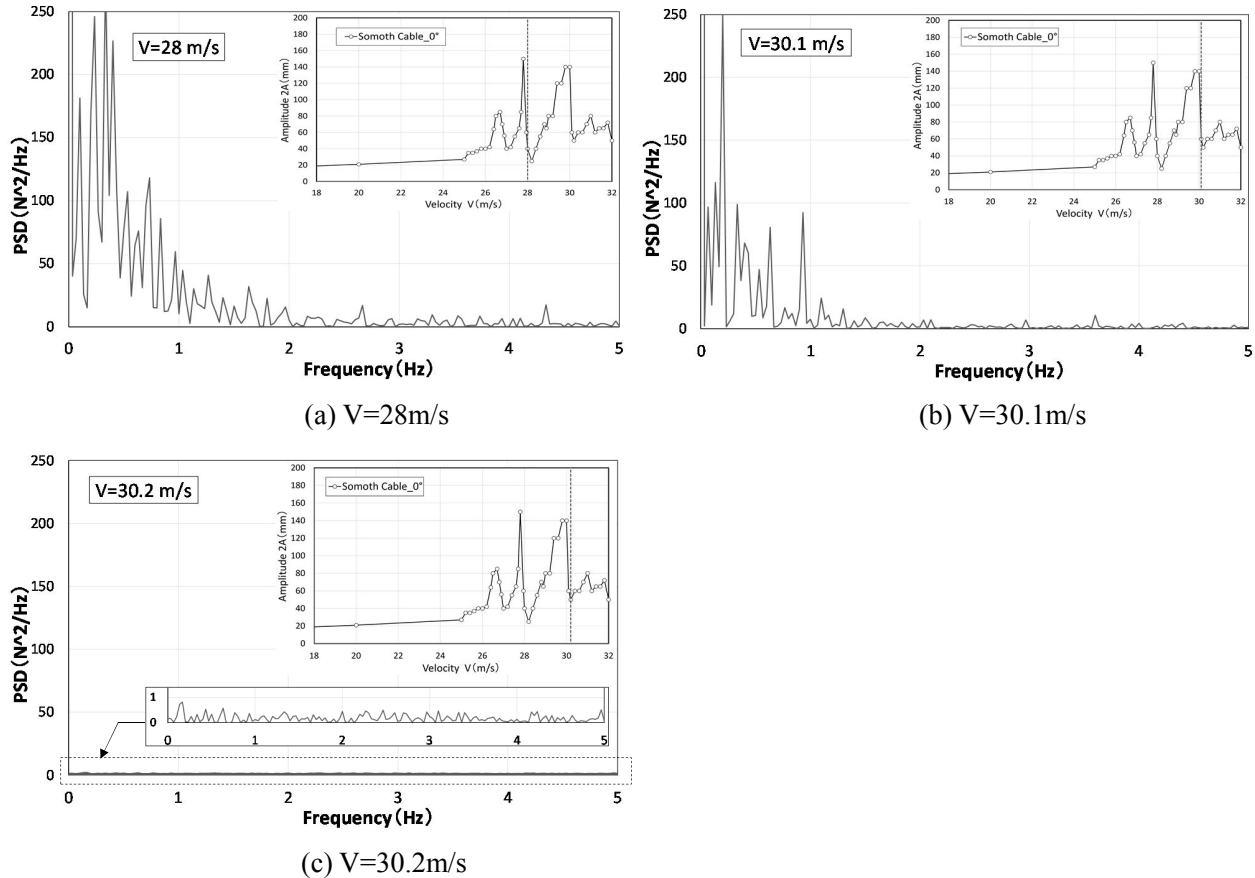


Figure 5: P.S.D of the lift force of the smooth cable at the yawed angle $\beta=0^\circ$

(2) Cross-flow response characteristics of the yawed ($\beta=45^\circ$) cables

a) Smooth cable

Saito [11], Kimura [12] and Matsumoto [3] have reported the cross-flow response of the yawed ($\beta=45^\circ$) circular cylinder, separately. In particular first two studies, the tested Reynolds number was covered in the both regimes of the sub-critical and the critical. All of the responses in three test results started at the reduced velocity $V_r (=V/fD)$ of approximately 40, or 50. However, in the first two test results, the amplitude of cross-flow response becomes small or stabilized at the particular Reynolds number of $Re=1.5 \times 10^5 \sim 2.0 \times 10^5$. At the high Reynolds number, that is the critical Reynolds number, the particular low frequency vortex must be generated by the stall by the axial flow, but the different more intensive vortex might be produced by the critical Reynolds number. On the other hand, the cross-flow response measured in this study continues the divergent-type response after the onset without locally stabilized in the other two tests results, as shown in Fig.6. The authors evaluate that the two sorts of response are excited by the stall caused by the axial flow at the subcritical Reynolds number and the one by the critical Reynolds number, respectively. The locally stabilized response at the particular high Reynolds number might be caused by the intensive interaction of an intensive vortex generated by the low frequency fluctuation of the flows related to the stall. The reason, why the response does not show the locally-stabilized property, is thought to be caused by the extremely small Scruton number of the 1DOF rocking system. The switching property of the stall-mechanism, latently hidden in the divergent-type response diagram shown in Fig 6, can be detected by the analysis of the low frequency property of the PSD of the lift force as lately explained.

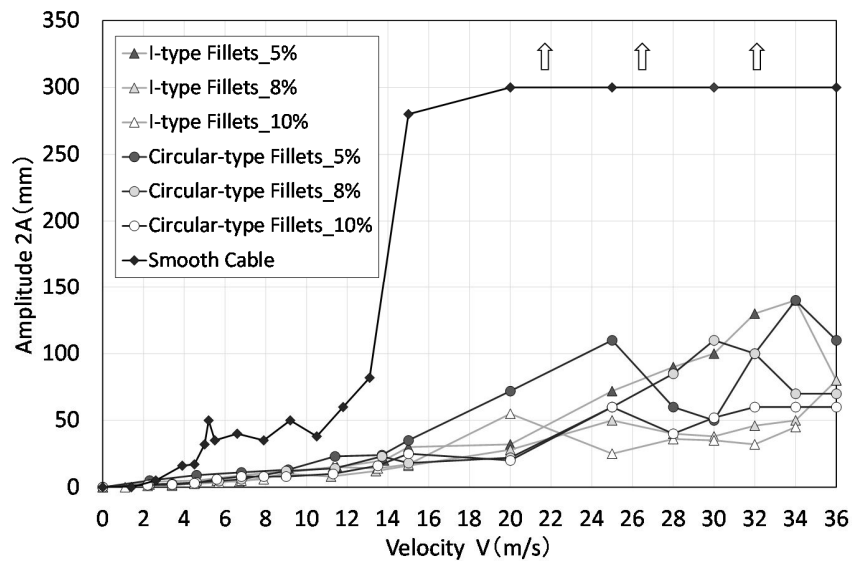


Figure: 6 2A-V diagrams of the smooth cable and the cable with fillet at the yawed angle $\beta=45^\circ$

b) Fillet effect on the yawed ($\beta=45^\circ$) cable

The cross flow response of the yawed ($\beta=45^\circ$) smooth cable can be drastically stabilized by the installation of the proposed large size double helical fillets with various shapes and various size of 5%, 8% and 10% as shown in Fig. 6. The response at the higher velocity shows a random vibration induced by the amplified flow separation by the helical fillets. The proposed large size helical fillets can be significantly stabilize the cross flow vibration, that is the dry galloping as a type of stall galloping (STG) even though under the extremely small Scruton number.

c) PSD of the unsteady lift force at the low frequency regime of the yawed ($\beta=45^\circ$) smooth cable

As described above, to detect the latent switching of the stall mechanism by the axial flow and the critical Reynolds number, the PSD analysis of the unsteady lift force, at the low frequency regime, of the yawed ($\beta=45^\circ$) smooth cable measured by the force-measurement tests at various wind velocities. At the low velocity regime of $V=12\text{m/s}\sim 20\text{m/s}$, where the cross-flow response appeared, significantly small power at the low frequency regime of unsteady lift force were observed, however, at the higher wind velocity than $V=24\text{m/s}$ ($Re=3.2\times 10^5$) approximately, its power drastically becomes large. Fig. 7 shows the examples of their PSDs at $V=18\text{m/s}$, 24m/s and 29.6m/s . Thus, the switching of stall mechanism might be occurred at $V\approx 24\text{m/s}$. The cross flow response at the higher velocity regime than $V\approx 24\text{m/s}$ might be generated by the stall related to the critical Reynolds number.

d) Aerodynamic stabilization by the large-size double helical fillets

Taking into account that the RWIV and DG of the inclined cable, and they must be Stall-type galloping essentially related by the separation behavior characterized unsteady flow change between the separated flow and the reattached flow, the large-size double helical fillets were investigated with the expectation of the mitigation of the stall appearance by the promotion of flow-separation by the large-size object on cable-surface. As in shown in Fig. 6, the cross-flow divergent-type violent response of yawed ($\beta=45^\circ$) was drastically stabilized by the helical fillets. As shown in Fig. 7, in the PSD of lift force at the low frequency of the yawed ($\beta=45^\circ$) cable with the double helical I-type fillets at the all wind velocities regime between $V=12\text{m/s}$ and 36m/s , the significant power at the low frequency regime is not observed. (See the example of the case of $V=30\text{m/s}$ in Fig. 7.) Thus it is verified that the large-size fillets must prevent the stall and stabilize the sequential aerodynamic instability. Furthermore, it is verified that the power-property in the PSD diagram of the lift force at low frequency is a key-property of the stall of various bodied including an airfoil with the critical stalling angle.

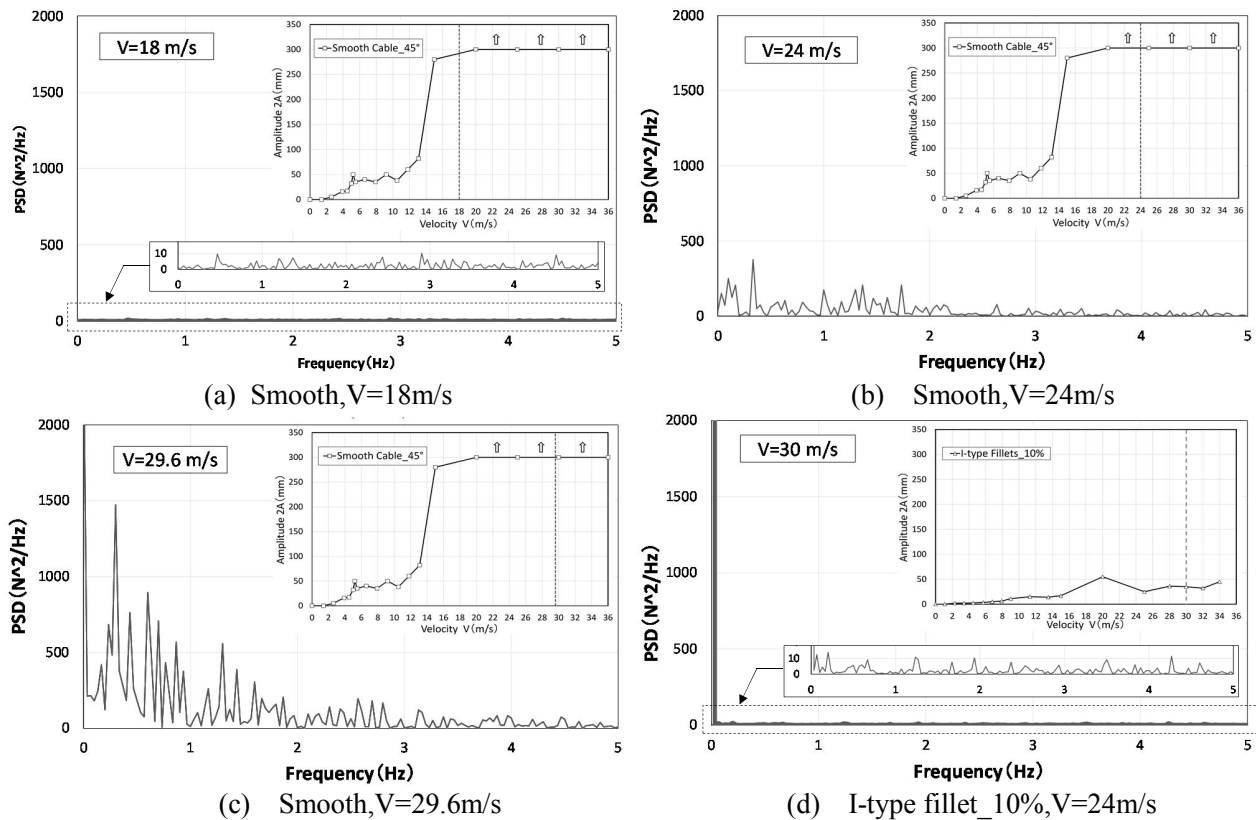


Figure 7: P.S.D of lift force of the smooth cable and the cable with I-type fillet at the yawed angle $\beta=45^\circ$

6. CONCLUSION

The main conclusions obtained in this study are as follows:

(1) Drag force

The drag force of the cable installed of the big-size double helical fillets is almost identical with the smooth cable at the sub-critical Reynolds number of approximately $C_D \approx 1.1$. Furthermore, the drag force of the cable installed of the big-size double helical fillets does not show the drag-crisis, which is observed for the smooth cable at the critical Reynolds number regime, and sustain the almost same value at this high Reynolds number regime. The drag crisis of the non-yawed ($\beta=0^\circ$) smooth cable is observed roughly similar with the result formerly studied by Schewe [4], but in details, the two times or three times multiple drag-crises were observe in this study. On the other hand, in the case of C_D of yawed ($\beta=45^\circ$) smooth cable, the gradual decrease of C_D at the comparatively high Reynolds number regime is thought to be a kind of drag-crisis similarly reported by former studies(Larose [8], Katsuchi [6], Georgakis[13]).

(2) Stationary lift force

The stationary lift force is observed at the particular multiple Reynolds regime in corresponding well to the appearance of the drag-crises in relation to the formation or destruction of the separated bubble on the cable-surface. The maximum value of the stationary lift coefficient, C_L , is $C_L \approx 1.1$, which is roughly identical or smaller than those reported by Flamand [9] and Liu [5], respectively.

(3) The cross-flow response of the non-yawed ($\beta=0^\circ$) smooth cable

The cross-flow response of the non-yawed ($\beta=0^\circ$) smooth cable is observed, in well correspondingly, at the particular wind velocity/Reynolds number regime where the drag-crises appeared. These responses seem to appear when the response disappear.

(4) The cross-flow response of the yawed ($\beta=45^\circ$) smooth cable and the one of the cable with a large-size helical fillets

The yawed ($\beta=45^\circ$) smooth cable showed the violent divergent-type cross-flow response is observed similarly with the former test results. The onset reduced wind velocity, $V_r=V/fD$, was evaluated to be approximately 40~50 in similar with test results by Saitou [11], Kimura [12] and Matsumoto [3]. After installation of the large-size double helical fillets, the violent divergent-type cross-flow response can be drastically stabilized even though the random response with small amplitude remains at higher wind velocity.

(5) The reappearance of the stall-type galloping

It is verified that the stall-appearance of the dry galloping of non-yawed ($\beta=0^\circ$) cable at the critical Reynolds number regime and the one of yawed ($\beta=45^\circ$) at the wide Reynolds number regime including the subcritical and the critical Reynolds number, can be detected by the PSD-property of the unsteady lift force.

(6) The stabilization effect of the large-size double helical fillets

It is verified that the proposed the cable with large-size double helical fillets shows significantly stable against the dry-galloping of stay cable, and also against the rain and wind induced vibration(RWIV) because of the interruption (Ueshima [14]) of the formation of the upper water rivulet without the increase of drag force on the stay cables.

ACKNOWLEDGEMENT

The authors would like to express the deepest appreciation to Mr. H. Inoue (NIPPON KAIJI KYOKAI(ClassNK), ex-MES), Mr. Y. Miyasaka (Miyasaka Co.), Dr. J. Nakamichi (JAXA), Dr. K. Saito (JAXA) and Dr. H. Arizono (JAXA) for their worthy advises on these wind tunnel tests.

REFERENCES

- 1) Matsumoto, M., Ishizaki, H. : Stall-type Galloping and VIV-initiated Galloping of Inclined Stay Cable Aerodynamics and its Aerodynamic Stabilization. Proc. of SDAC, Lyngby Denmark, 2014.
- 2) Rinoue, K. : "Laminar separation bubbles formed on airfoils", NAGARE(Fluid) 22, pp15-22, 2003 (in Japanese)
- 3) Matsumoto, M. : The role of Axial Flow in Near Wake on the Cross-Flow Vibration of the Inclined Cable of Cable-stayed Bridges, Proc. of FIV Symposium, Montreal, 2010.
- 4) Schewe, G. : On the force fluctuations acting on a circular cylinder in crossflow from subcritical up to transcritical Reynolds numbers, JFM, 265-285, 1983.
- 5) Liu, K., Wang, Y., Cheng, Y., Ma, W. : Reynolds Number Effect on Wind-Induced Vibration of Stay-Cables Proc. of the 9th ISCD, Shanghai, China, 2011.
- 6) Katsuti, H., Yamada H. : Dry galloping characteristics of indented stay cables in turbulent flow, Proc of 7th ISCD, Shanghai, 2011
- 7) Andersen, T., Jakobsen, J.B., Macdonald, J., Nikitas, N., J. Larose, G., Sarvage, M., McAuliffe, B.G. : Drag crisis response of an elastic cable model, Proc of 10th ISCD, Paris, 2003.
- 8) Larose, G.L., Savage, M.G., Jakobsen, B.J. : Wind tunnel experiments on an inclined and yawed circular cylinder in the critical Reynolds number range, Proc. of 11th ICWE, Lubbock, Texas, 2003
- 9) Benidir and Flamand, L., Gaillet, G., Dimitriadis "dry galloping on bridge cables: shape effect on an inclined circular cylinder in the wind tunnel" Proc. of the 6th EAWEC, 2013, London,
- 10) Matsumiya : personal communication.
- 11) T. Saito : personal communication.
- 12) Kimura, K., Kato, K., Kubo, K., Ohashi, Y. : An Aeroelastic Wind Tunnel Test of an Inclined Circular Cylinder, Proc. of 8th ISCD, Paris, 2009.
- 13) Matteoni, G., Georgakis, C. : Aerodynamic coefficients of dry inclined cables in smooth flow, Proc. of the 9th ISCD, Shanghai, 2011.
- 14) Yamauchi, K., Uejima, H., Kuroda, S., An investigation of the Aerodynamic Characteristics of Cable with Surf ace Ribs, 9th ISCD, Shanghai, 2011.

COMPARATIVE ANALYSIS OF BRIDGE CABLES WITH CONCAVE FILLETS

1st Celeste Burlina⁺¹, 2nd Christos T. Georgakis⁺², 3rd Søren V. Larsen⁺³ and 4th Philipp Egger⁺⁴
^{+1,2}Technical University of Denmark, Copenhagen, Denmark
⁺³FORCE Technology, Copenhagen, Denmark
⁺⁴VSL International Ltd., Knizö, Switzerland

In this paper the aerodynamic performance of two new cable surfaces with concave fillets are examined and compared to cables with traditional helically filleted, plain and pattern indented surfaces. To this end, an extensive wind-tunnel campaign was undertaken to measure the aerodynamic static force coefficients up to the super-critical Reynolds number range and rain-rivulet suppression ability. Flow visualizations tests were performed to better understand the structure and development of the wake. Both innovations outperform traditional surfaces in terms of rain-rivulet suppression thanks to the ability of the concave shaped fillet to act as a ramp for the incoming rain-rivulet. Furthermore both innovations are able to suppress vortex shedding at low Reynolds numbers, in contrast to the other cable surfaces tested. Moreover the innovation with the staggered surface shows an early reduction of the drag force while maintaining a zero lift up to the super-critical range.

Keyword: cable aerodynamics, concave fillets, rain rivulet suppression, force coefficients, flow visualizations.

1. INTRODUCTION

In order to reduce wind-induced vibrations on bridge stay cables, such as rain wind induced vibrations (RWIV) and dry galloping, bridge cable manufacturers have introduced cable surface modifications on the protective high-density polyethylene (HDPE) pipes. These modifications come mainly in the form of helical fillets, extensively used in Europe and North America, and in the form of dimples, used predominantly in Asia. The main purpose of these modifications is rain-rivulet impedance, since the presence of one or more longitudinally running rivulets on the cable surface is considered one of the major causes of the initiation of RWIV. Nevertheless, the introduction of helical fillets and dimples has not completely eliminated RWIVs, often leading bridge owners to the installation of cable vibration dampers or cross-ties (Kleissl and Georgakis, 2013). Previous research (Yagi, 2011 and Kleissl and Georgakis, 2013) shows that by modifying the shape, alignment and configuration of the protuberances on the HDPE tube, it is possible to eliminate or further reduce the RWIVs, together with a reduction in drag force. Drag force represents more than 50% of the overall horizontal wind load on long span bridges (Gimsing and Georgakis, 2012). In particular, cable surface modifications in the form of a concave fillet, studied by Kleissl and Georgakis (2013), were found to outperform traditional surfaces, showing similar aerodynamic coefficients, compared to a traditional helical fillet and dimpled surface despite a significant increase in the fillet height.

As a result, the objective of the present study is to examine the aerodynamic performance and to further understand the behavior of innovative bridge cable surfaces with concave fillets, and to compare this performance with that of a cable with a traditional helical fillet, dimpled and plain surface. In particular, a better understanding of the flow structure and development of the near wake of the bridge cable makes it possible to investigate the flow mechanisms initiated and to employ further manipulation and improvement of the concave fillet for drag reduction, while at the same time guaranteeing optimal performance in terms of rain-rivulet suppression.

To this end, an extensive wind-tunnel test campaign was performed at the Climatic Wind Tunnel

⁺¹celebur@byg.dtu.dk, ⁺²cg@byg.dtu.k, ⁺³svl@force.dk, ⁺⁴philipp.egger@vsl.com

(CWT) at FORCE Technology (Denmark). A first set of tests was run in static conditions, in order to evaluate aerodynamic coefficients for different cable surfaces from the sub-critical to the post-critical Reynolds number range. In a second stage, rain rivulet suppression and flow visualization tests on the same samples were undertaken at different wind velocities in the sub-critical Reynolds number range. These investigations were performed in order to investigate the dependencies of the shape of the concave fillet on the suppression of the rain-rivulet and on the development of the wake in relation to the resultant drag coefficient and initiation of vortex shedding.

2. MODELS

The models tested were full-scale samples of high density polyethylene (HDPE) tubing with an outer diameter of 160mm (excluding fillet). Different cable surfaces were tested. Two innovative profiles that involve the application of concave protruding fillets were tested. The fillet cross section has a trapezoidal shape with concave sides and a height of 6.5mm. In the first model, which will be subsequently referred as Innovation 1, the fillets replicate the typical arrangement of current stay cables with helical fillets, with a pitch angle of 45° and a spiral distance of 251mm. In the second model, Innovation 2, the fillets are arranged laterally in a staggered helical pattern with a pitch angle of 30° and spacing between the fillets of 20mm. For comparison reasons plain, dimpled and traditional helically filleted cable surfaces were also tested.

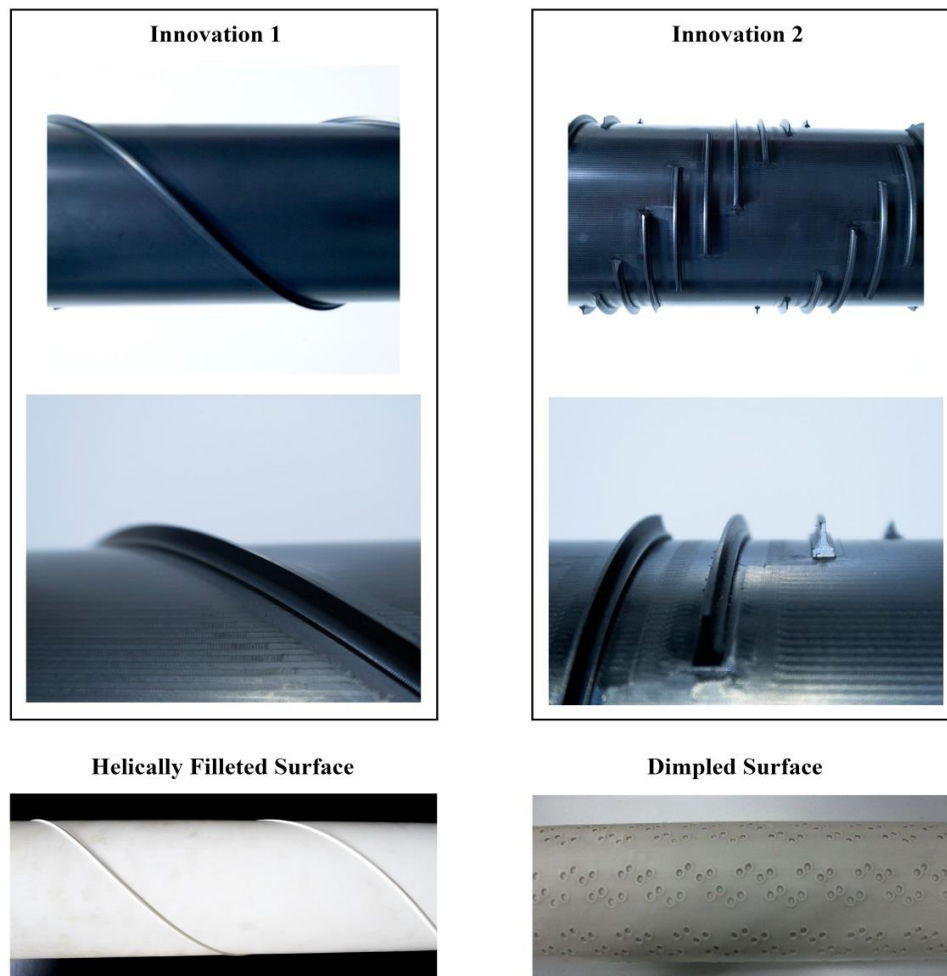


Figure 1: Cable sample models

3. EXPERIMENTAL WORK

The cables section prototypes were placed horizontally in the wind tunnel cross section, resulting in a near two-dimensional flow normal to the cable section, for both static and flow visualization set-ups. The drag and lift forces were measured up to super-critical Reynolds number range, using 6DOF force transducers (AMTI MC3A-500) at either end. The two force transducers were installed between the cable model and supporting cardan joints. The length of the models was 1.42m, resulting in an aspect ratio of 8.9:1. The blockage ratio for the cable model ratio for the cable model was 8% and thus the drag coefficients have been corrected using the Maskel III method, according to Cooper et al. (1999). For each tested configuration, the drag C_D and the lift C_L coefficients were calculate, based on the averaged along-wind and across-wind forces respectively, normalized by the along-wind flow velocity:

$$C_D = \frac{F_D}{\frac{1}{2}\rho U^2 L D} \quad (1)$$

$$C_L = \frac{F_L}{\frac{1}{2}\rho U^2 L D} \quad (2)$$

where F_D is the along-wind force and F_L is the across-wind component, U is the mean wind velocity, L is the effective length of the cable, D the outer diameter and ρ the air density, taken here as 1.25kg/m^3 .

During the flow visualization tests, smoke particles were added into the flow to trace the fluid motion. With smoke particles in the order of $0.2\mu\text{m}$, it can be assumed that the particles follow the streamline of the flow. Due to dispersion of the particles at high wind velocities, tests were run up to the sub-critical Reynolds number range limit. In order to visualize a slice of the fluid flow pattern, the particles were illuminated with sheet of laser light.

Rivulet suppression tests were performed with the cable declining along the wind direction at a relative cable-wind angle of 45° (See Kleissl and Georgakis 2013). A plain surface cable section was used to make up the first top half of the model length, in order to facilitate the formation of the upper and lower rivulet, while the different cable surfaces section were used to make up the second half of the model length. All tests were repeated for 8m/s and 14m/s , which are the representative values for the upper and lower velocity range for RWIV. The dimpled surface was not tested for rivulet suppression due to incompatibility of the set-up.

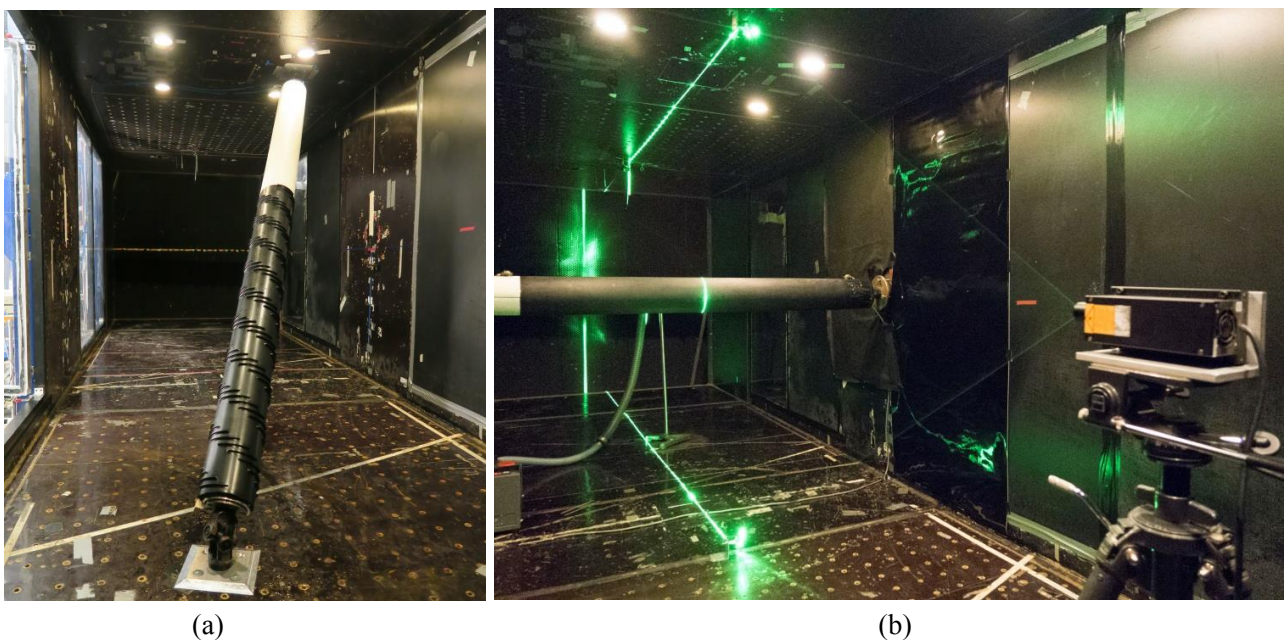


Figure 2: Rivulet suppression Set-up (a) and Static and Flow Visualization Set-Up (b)

4. RESULTS AND DISCUSSION

(1) Force Coefficients

The drag and lift coefficients obtained for each of these tested models are shown in Figure 3. It can be noted that the plain cable's aerodynamic forces are in agreement with the expectations for a smooth cylinder of this kind, entering the critical Reynolds number region for $Re = 2.2 - 2.6 \times 10^5$ and reaching a minimum value of drag coefficient of 0.4 in the supercritical state. In the same interval the lift coefficient shows a relatively large value, due to the formation of a single separation bubble.

The traditional helically filleted surface and Innovation 1 experience the same drag force in the sub-critical Reynolds number range, while after the transition to the post-critical range, the traditional fillet experiences a lower drag force due to a more accentuated drag transition in the Reynolds number range between 2.0 and 2.6×10^5 . Despite the same arrangement of the fillet for the surfaces in question, the higher drag coefficient in the post-critical Reynolds range for Innovation 1 can be attributed to the higher profile of the fillet directly facing the incoming flow, which acts as a fixed ramp and separation point and thus resulting in a wider wake.

On the other hand, Innovation 2 and the dimpled surface show an earlier reduction in the drag force in the sub-critical Reynolds range and exhibit a more smooth and prolonged transition which starts at a lower Reynolds number between $0.8 - 1.0 \times 10^5$ and enters the post-critical state at a Reynolds number of 2.0×10^5 . The early flow transition for the dimpled surface cable agrees well with what has been observed for circular cylinders with uniform high roughness, which easily triggers turbulence ensuring a near constant super-critical drag (Miyata et al. 1994 and Hojo et al. 1995). For Innovation 2, it is hypothesized that the early transition and the subsequent constant super-critical drag is the result of the fact that the circumferential orientation of the fillets reduces the drag penalty, whilst triggering turbulence at the boundary layer and introducing counter rotating vortices.

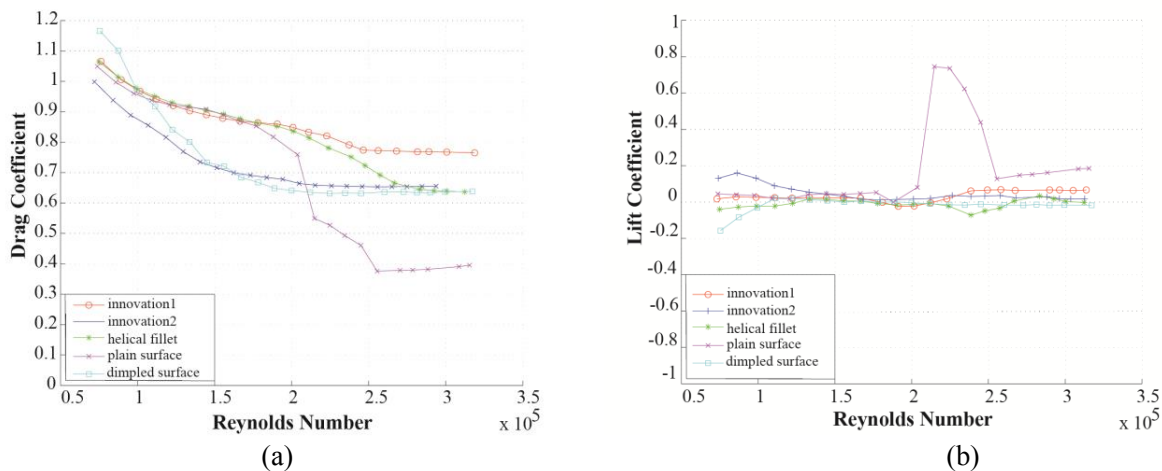


Figure 3: Drag coefficients (a) and Lift coefficients (b) comparison.

Concerning the lift force, apart from the plain cable surface as mentioned before, the other four cable surfaces experience an almost zero lift along the whole range of wind velocities tested (Figure 3b) This is most likely due to the ability of all the surface modifications to generate variations in the flow and separation lines along the length of the cable. These variations, as largely reported in previous studies, are the result of enhanced vorticities and counter rotated vortices for the dimpled surface (Miyata et al., 1994) and of periodic structures in the spanwise direction with localized increased streamwise vorticities and elongations of the vortex formation region for the traditional helical fillet (Nebres and Batill, 1993).

(2) Fluctuating Lift Forces

A frequency analysis of the unsteady cross-stream force (fluctuating lift) was undertaken. With the particular cross flow test set up employed, the fluctuations of the total lift force on the model can be determined. The frequency distributions of the lift force are determined using a Fast Fourier Transformation (FFT) to compute the power spectral density (PSD) of the lift coefficient. The PSD is computed for each of the flow velocities tested. The discrete number of flow velocity-specific spectra is then expanded into a two-dimensional contour plot, as seen in Figure 4, for each of the cable models. The Strouhal number is computed for all five cables ($St = f_s D/U$, where f_s is the frequency of vortex shedding). The increased PSDs at around 30 and 35 Hz can be explained as the incidences of model resonance. The linear trend identifying vortex shedding disappears around a Reynolds number of 2.0 and 2.2×10^5 for the plain cable and the traditional helically filleted cable respectively. These values correspond for both surfaces to the flow transition from sub-critical to the post-critical Reynolds range. The same linear behavior disappears at much lower Reynolds numbers for Innovation 1 and 2. Here this occurs at Reynolds number of 1.5×10^5 for both innovations, which correspond to the smooth and prolonged drag transition for Innovation 1 and the entrance in the super-critical range for Innovation 2. On the other hand, the vortex shedding remains throughout the whole range of tested velocities for the dimpled cable surface, despite the early flow transition at a $Re = 0.8 - 1.0 \times 10^5$, as experienced also by Innovation 2. Furthermore, a significantly higher Strouhal number of 0.28 is determined for the dimpled surface compared to the other samples, which were founded to have a Strouhal number of 0.20.

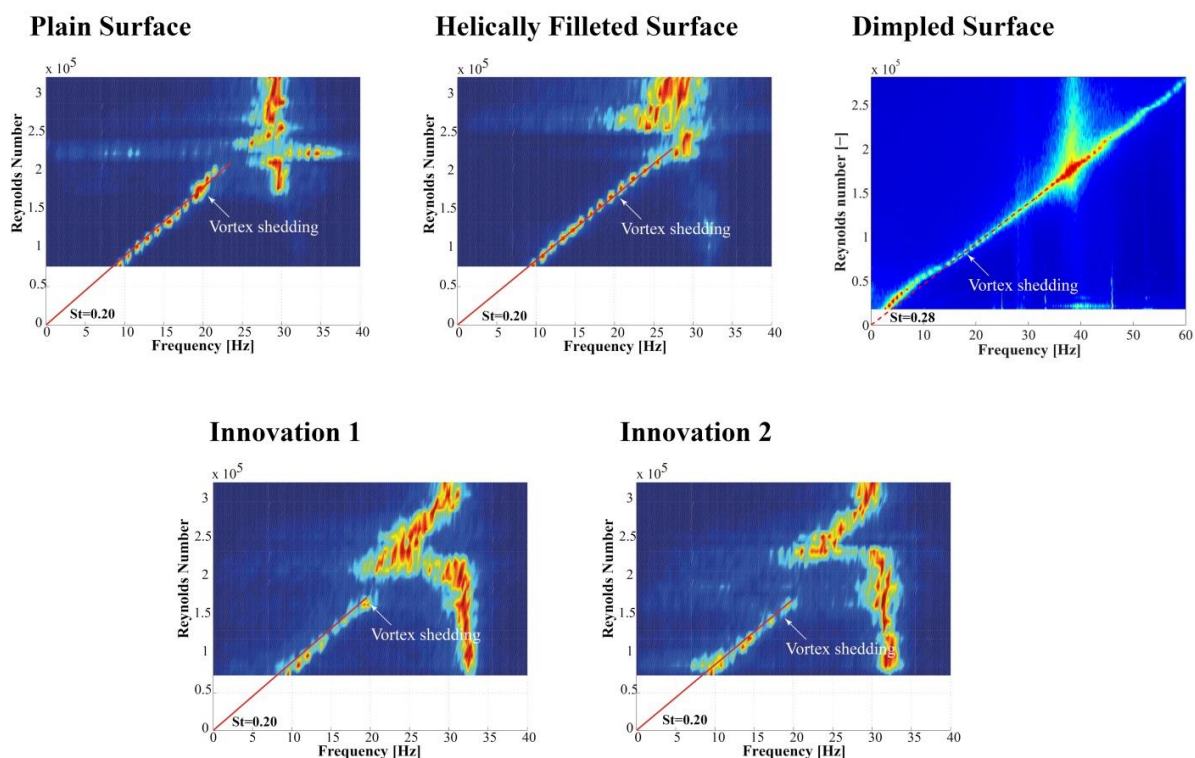


Figure 4: Normal flow lift coefficient PSD for different cable surfaces.

As a result, both Innovation 1 and 2 are able to suppress vortex shedding formation at much lower wind velocities than a traditional helical fillet or dimpled surface. In particular Innovation 2, which experiences the same drag reduction showed by the dimpled surface, is able to suppress vortex shedding in the same range as the transition to the super-critical regime.

(3) Rivulet suppression

As found in by previous studies by Kleissl and Georgakis (2013) the critical range of velocities for the formation of both upper and lower rain-rivulets is between 7 – 15 m/s. Outside this range, the upper rivulet does not form, as either gravity or the wind loading become dominant. As RWIVs typically occur within this range, the presence of the upper rivulet is considered particularly critical for the initiations of these vibrations.

Figure 5 shows the rain rivulet suppression ability of the tested cable surfaces. The traditional helical fillet is able to reduce the size of the rain rivulet along the length of the cable but it is not able to completely suppress. Innovation 1 and Innovation 2 experience a complete suppression of the upper and lower rivulets at both velocities tested. The particular shape of the concave fillet acts as a ramp, blocking the formation of the upper and lower rivulet along the whole length of the cable. In particular it was noticed that this is mainly due to the concavity of the fillet and its sharp top edge.

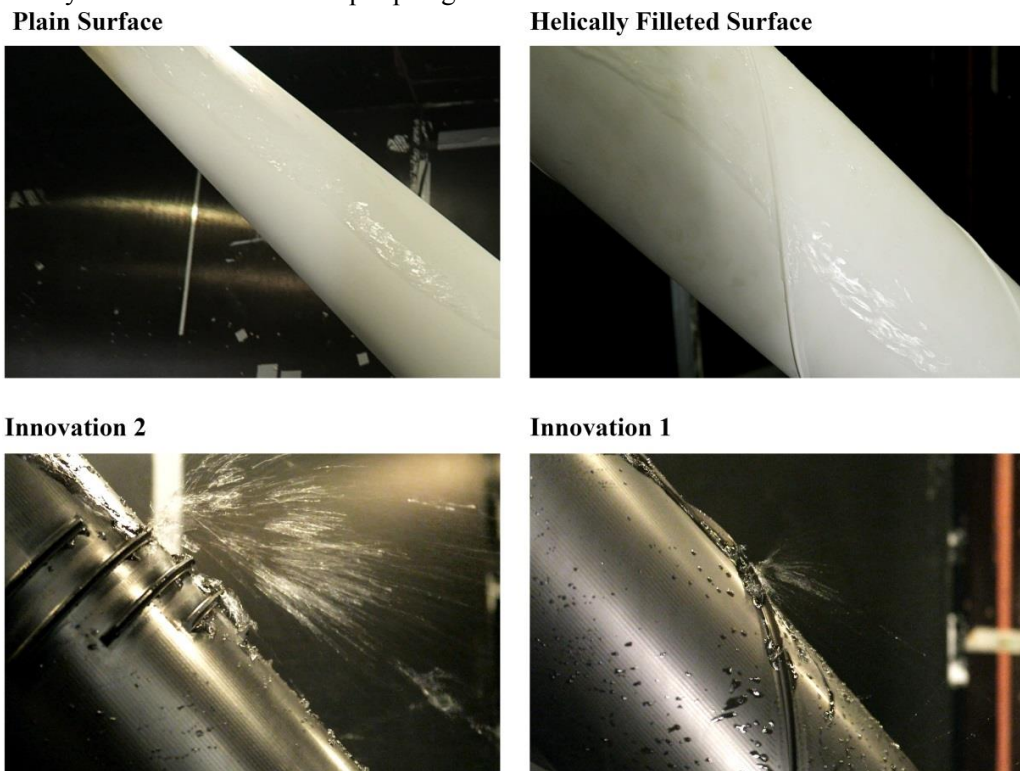


Figure 5: Rivulet suppression ability for different cable surfaces.

(4) Flow Visualization

a) Far-wake flow visualization

The flow visualizations of the far-wake flow structure for all the five cables tested, whilst positioned normal to the flow, are shown in Figure 6. As previously discussed, when analyzing the power spectral density (PSD) of the lift coefficient, at $Re = 0.6 \times 10^5$ all five samples experience the formation of vortex shedding, although this is disturbed in the case of traditional helical fillet, Innovation 1 and Innovation 2, due to the generation of three-dimensional flow structures introduced by the presence of the fillets, as they generate uncorrelated fluctuations along the span of the cylinder (Zdravkovich, 1981 and Nebres and Batill 1993).

At $Re = 1.5 \times 10^5$ all cables exhibits a reduction of the vortex shedding formation, which is particularly reduced for Innovation 1 and 2, due to an increase of the disturbance created by the concave fillet compared to the traditional rounded shape of the helical fillet. This behavior is particularly accentuated in Innovation 2, where the staggered configuration of the fillet around the circumference is able to enhance turbulences at the boundary layer. On the other hand, the dimpled surface, even though showing the same behavior as Innovation 2, is not able to suppress vortex shedding formation even after entering the post-critical regime.

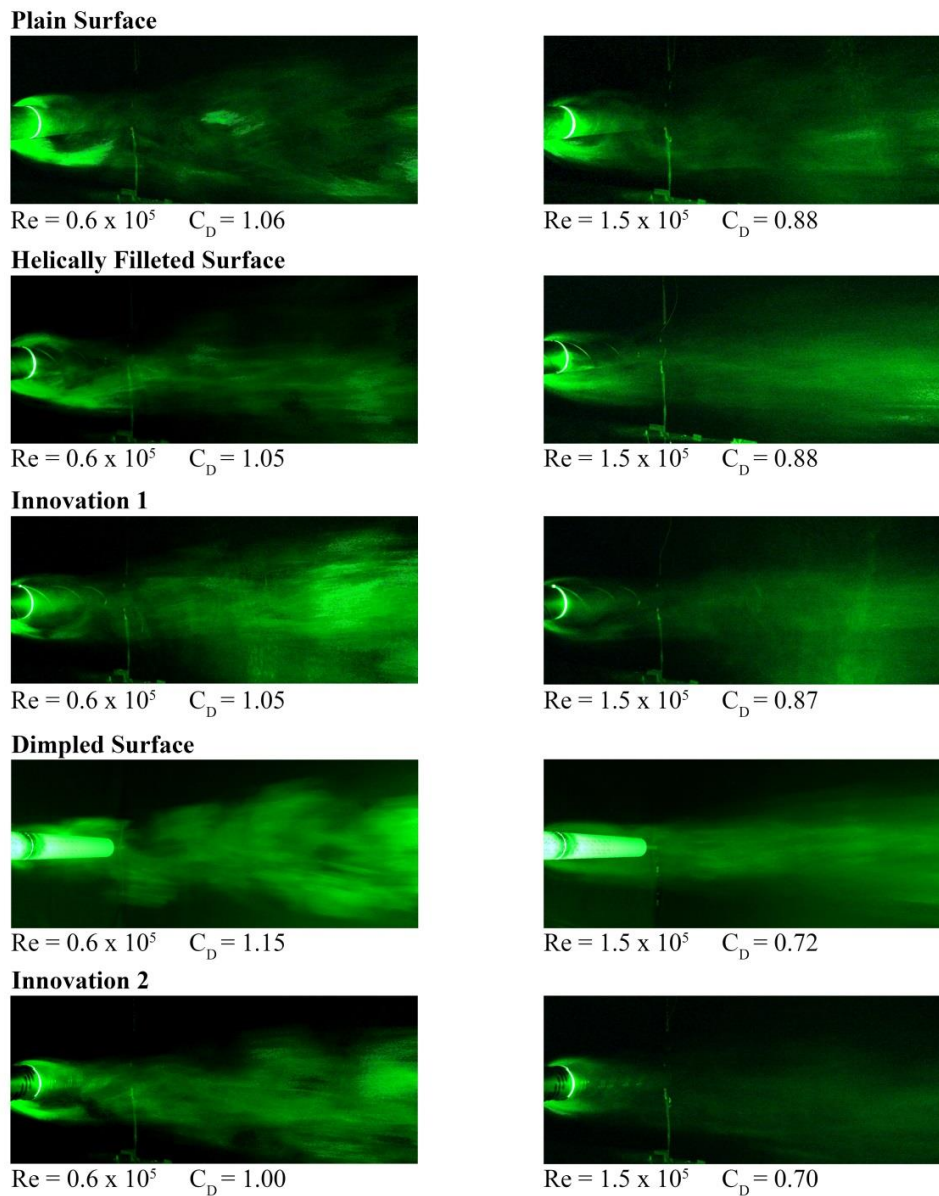


Figure 6: Far-wake flow visualization for different cable surfaces at $Re = 0.6 \times 10^5$ and $Re = 1.5 \times 10^5$

b) Near-wake flow visualization

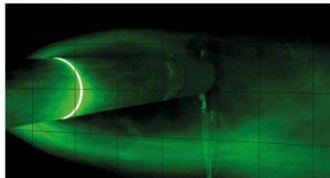
The flow visualizations of the near-wake and separation mechanisms are shown in Figure 7. The near-wake photographs represent the average wake size over a full development and evolution of its structure.

From $Re = 0.6 \times 10^5$ to $Re = 1.5 \times 10^5$ all five samples exhibit a reduced width of their wakes, indicating also a drop in the drag coefficient. When comparing them, this behavior is particularly enhanced for the dimpled surface and Innovation 2. As we can see in Figure 7, both cable surfaces exhibit the same behavior of a plain cable in the supercritical state, where the boundary layer is fully turbulent before the separation line, resulting in a narrow wake and in a drop of the drag coefficient (Zdravkovich, 1997). This mechanism is generated artificially by the dimples in the dimpled surface and by the staggered concave fillets in Innovation 2, which are able to initiate turbulence at the boundary layer at low Reynolds number with an early transition to the post-critical state.

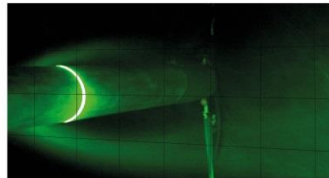
On the other hand, Innovation 1, exhibit a smaller reduction in the wake size and a resulting higher drag coefficient, compared to the other surfaces. The flow is governed by the presence of the concave fillet which acts as a ramp for the incoming flow, creating a fixed separation point and a subsequent enhanced

vorticity. This particular behavior does not allow for a transition in the flow for increased Reynolds numbers, leading to a small reduction of the wake's size and subsequently a small reduction of the drag coefficient also in the supercritical range. It is hypothesized that a reduction of the height of the concave fillet will result in a narrower wake and as a consequence a lower drag coefficient, whilst maintaining optimal performance in terms of rain-rivulet suppression.

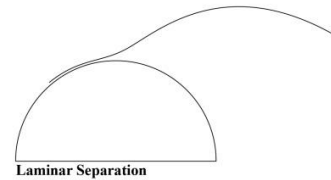
Plain Surface



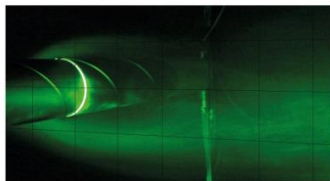
$Re = 0.6 \times 10^5 \quad C_D = 1.06$



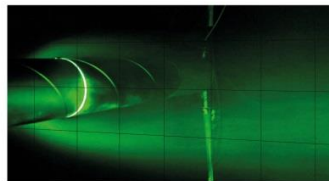
$Re = 1.5 \times 10^5 \quad C_D = 0.88$



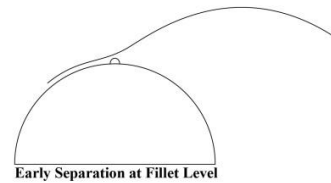
Helically Filleted Surface



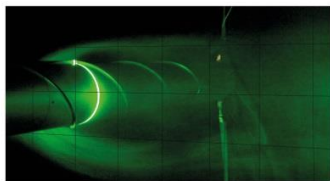
$Re = 0.6 \times 10^5 \quad C_D = 1.05$



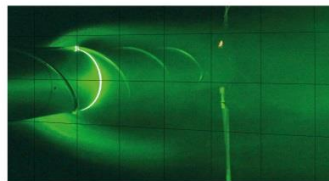
$Re = 1.5 \times 10^5 \quad C_D = 0.88$



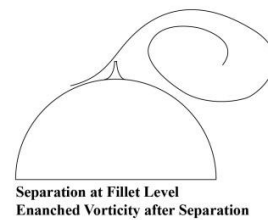
Innovation 1



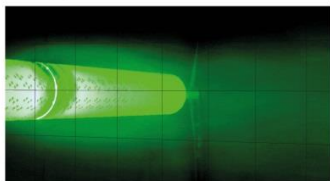
$Re = 0.6 \times 10^5 \quad C_D = 1.05$



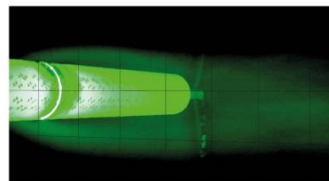
$Re = 1.5 \times 10^5 \quad C_D = 0.87$



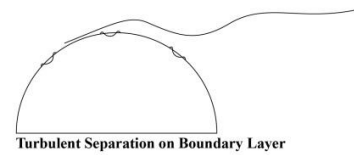
Dimpled Surface



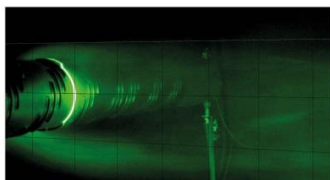
$Re = 0.6 \times 10^5 \quad C_D = 1.15$



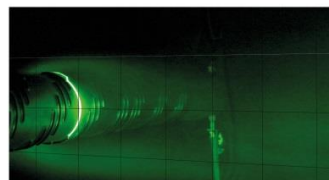
$Re = 1.5 \times 10^5 \quad C_D = 0.72$



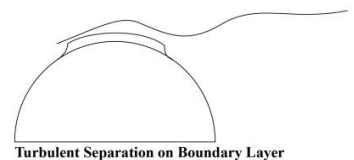
Innovation 2



$Re = 0.6 \times 10^5 \quad C_D = 1.00$



$Re = 1.5 \times 10^5 \quad C_D = 0.70$



100mm

Figure 7: Near-wake flow visualization for different cable surface at $Re = 0.6 \times 10^5$ and $Re = 1.5 \times 10^5$

5. CONCLUSIONS

Two new cable surfaces with concave fillets were wind tunnel tested for the determination of the aerodynamic coefficients, the structure of the flow's near and far-wake and for rain rivulet suppression. The results were compared with plain, dimpled and traditional helically filleted cable surfaces.

Innovation 1 and 2 outperformed in terms of rain-rivulet suppression, with a complete suppression of the upper and lower rain-rivulets at all tested velocities. This is due to the ability of the concave fillet to act as a ramp for the incoming rivulet. Moreover, they are able to suppress vortex shedding at lower Reynolds numbers compared to the other surfaces.

Both innovations maintain optimal performance in terms of aerodynamic coefficients despite a more than 100% increase of the fillet height compared to a traditional helical fillet. In particular, Innovation 2 exhibits the same behavior as a dimpled cable surface in terms of drag coefficient, showing an early transition to the super-critical and a subsequent reduction of the drag force. This is due to the ability of the staggered surface configuration to enhance turbulence at the boundary layer level. Innovation 2 is also able to suppress vortex shedding formation at lower Reynolds numbers compared to the dimpled cable surface, which maintains it up to the critical Reynolds number range.

On the other hand, Innovation 1 shows a higher drag in the super-critical range compared to the other surfaces tested. It is believed that by reducing the height of the fillet it will be possible to reduce the drag force while maintaining optimal performances in terms of rain-rivulet suppression.

ACKNOWLEDGMENT

This work would not have been possible without the generous support of VSL and FORCE Technology.

REFERENCES

- 1) Cooper, K., Mercke, E., Wiedemann, J. : Improved blockage corrections for bluff-bodies in closed and open wind tunnels, In: *10th International Conference Wind Engineering, Copenhagen, June.*, pp. 1627-1634, 1999.
- 2) Flamand, O. : Rain-wind induced vibration of cable, In: *J. of Wind Engineering and Industrial Aerodynamics*, 57 (2-3), 353-340, 1995.
- 3) Flamand, O., Boujard, O. : A comparison between dry cylinder galloping and rain-wind induced excitation, In: *Proceeding of the 5th European & African Conference on Wind Engineering, Florence, 2009*
- 4) Georgakis, C.T., Koss, H.H., Ricciardelli, F. : Design specifications for a novel climatic wind tunnel for the testing of structural cables, In: *8th International Symposium on Cable Dynamics, Paris, France, September*, pp. 333–340, 2009.
- 5) Gimsing, N.J., Georgakis, C.T. : *Cable Supported Bridges: Concept and Design, 3rd ed. John Wiley & Sons Ltd.*, 2011.
- 6) Hojo, T., Yamazaki, S., Okada, H. : Development of Lowdrag Aerodynamically Stable Cable with Indented Processing, Nippon Steel Corporation, *July (Special Issue on Steel Structure 82)*, URL /<http://www.nsc.co.jp/en/tech/report/pdf/8203.pdf>, 2000.
- 7) Hojo, T., Yamazaki, S., Miyata, T., Yamada, H. : Development of aerodynamically stable cables for cable-stayed bridges having low resistance, *Bridges & Foundations Engineering* 6, 27–32, in Japanese, 1995
- 8) Kleissl, K., Georgakis, C.T. : Comparison of the aerodynamics of bridge cables with helical fillets and a pattern-indented surface in normal flow (a), In: *Proceedings of the 13th International Conference on Wind Engineering, Amsterdam*, 2011.
- 9) Kleissl, K., Georgakis, C.T. : Comparison of the aerodynamics of yawed bridge cables with helical fillets and a pattern-indented surface (b), In: *Proceedings of the 9th International Symposium on Cable Dynamics, Shanghai, China*, 2011.

- 10) Matsumoto, M. : Observed behavior of proto type cable vibration and its generation mechanism, In: *Bridge Aerodynamics, Proceedings of the International Symposium on Advances in Bridge Aerodynamics*, pp. 189–211, 1998.
- 11) Matsumoto, M., Daito, Y., Kanamura, T., Shigemura, Y., Sakuma, S., Ishizaki, H. : Wind-induced vibration of cables of cable-stayed bridges, In: *J. of Wind Engineering and Industrial Aerodynamics*, 74-76, 1015 – 1027, 1998.
- 12) Miyata, Y., Yamada, H., Hojo, T. : Experimental study on aerodynamic characteristics of cables with patterned surface, In: *J. of Structural Engineering 40A (March)*, 1065–1076, 1994.
- 13) Miyata, T., Katsuchi, H., Tamura, Y. : Comprehensive discussion on structural control for wind-induced responses of bridges and buildings, In: *Wind Engineering into the 21st Century, Proceedings of the 10th International Conference on Wind Engineering*, vol. 1, pp. 487–494, 1999.
- 14) Nebres, J. V., Batill, S. M. : Flow about cylinders with helical surface protrusions, In: *30th AIAA Aerospace Sciences Meeting and Exhibit, Reno, Nevada 92 (0540)*, 1992.
- 15) Yagi, T., Okamoto, K., Skski, I., Koroyasu, H., Liang, Z., Narita, S., Shirato, H. : Drag force reduction and aerodynamic stabilization of stay cables by modifying surface configurations, In: *The 21th Symposium on Wind Engineering, Tokyo, Japan*. In Japanese, 2010.
- 16) Zdravkovich, M. M. : Review and classification of various aerodynamic and hydrodynamic means for suppressing vortex shedding, In: *Journal of Wind Engineering and Industrial Aerodynamics 7 (2)*, 145 – 189, 1981.
- 17) Zdravkovich, M. M. : Reduction of effectiveness of means for suppressing wind-induced oscillation, In: *Engineering Structures 6 (4)*, 344 – 349, 1984.
- 18) Zdravkovich, M. M. : Flow around circular cylinders vol.1: fundamentals, *Oxford Science Publications*, 1997.

INFLUENCE OF NATURAL WIND TURBULENCE ON VORTEX SHEDDING EXCITATION, FROM REAL STRUCTURE EXPERIENCE

Olivier FLAMAND⁺¹, Akis PANAGIS⁺² and Aris STATHOPOULOS-VLAMIS⁺²
⁺¹CSTB, Nantes ,FRANCE
⁺²GEFYRA, Antirion, GREECE

Vortex shedding is a broadly studied phenomenon, in the well-defined conditions of wind tunnel laboratory. But vortex shedding excitation at is not easy to observe in real life on real structures, as its occurrence depends not only on the instantaneous wind speed, but on the duration of the wind event (stability) and the turbulence of the oncoming flow.

On large bridges especially, because they are often monitored by complete systems, recording vibrations as well as the wind speed, it is possible to follow multiple occurrences of vortex shedding, when the bridge is prone to it, and analyze the conditions of this occurrence. This was done from the data issued by the monitoring system of The Charilaos Trikoupis bridge between Rion and Antirion, in Greece which showed that the actual wind turbulence was lower than supposed at design stage. The full set of data running from 2005 to 2014 was analyzed with the aim to show the correlation between the vortex shedding excitation and the wind speed stability, the duration of wind events, the wind turbulence at the time of VS excitation and other sources of excitation on the bridge. One of the main feature is to highlight the relationship between the wind conditions and the birth and vanishing of the aeroelastic phenomenon.

Keyword: Vortex-shedding, full scale, turbulence.

1. ORIGIN OF THE FULL SCALE DATA

The Charilaos Trikoupis bridge is a 2252m long multi-span cable stayed bridge opened in 2004. It spans the Gulf of Corinth in a windy area, also prone earthquakes. As it was carefully designed to resist natural hazards, it was also equipped with a very complete monitoring system, with the aim to follow up vibration of the deck in flexural bending and torsion as well as vibrations of stays, including measurement of wind speed on top of pylons. This vibration recording system is perfectly maintained, what opens the possibility to follow the bridge behavior all over a period of some years¹⁾.

Records of all accelerometers placed on the viaduct are taken every 2 hours at a 100Hz frequency over 60 seconds duration, what is enough for measuring the vibration amplitude of the third vertical bending mode of the deck initially reckoned at 0.207Hz (Figure 1).

Sometimes the wind direction and speed take the best values for giving way to excitation of the deck in vertical bending by the vortex shedding. This is the kind of events that will be highlighted in the present paper.

Simple methods are used for the detection of these vortex shedding events. One of the most efficient is to take the ratio of vertical acceleration to vertical displacement for calculating an equivalent “resulting frequency” following formula :

$$f_{result} = \sqrt{\frac{A_i}{D_i} * \frac{1}{4\pi^2}} \quad (1)$$

With A_i and D_i acceleration and displacement measured at location i .

⁺¹olivier.flamand@cstb.fr, ⁺²akis.panagis@gefyra.gr

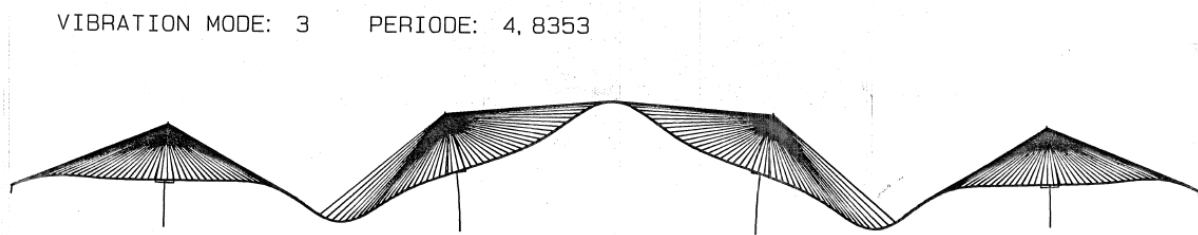


Figure 1: Mode shape of the third vertical bending mode, occasionally excited by vortex shedding

As an example, this criterium calculated for the 39 882 records taken along the period from January 1st 2005 to December 31th 2014 has been plotted on Figure 2 together with the acceleration amplitude. A series of spots is shown on an horizontal line corresponding to many events at a frequency of 0.216 Hz, that is precisely the actual modal frequency of third vertical bending mode. These 458 events, surrounded by an ellipse on the plot, are identified as vortex shedding excitation and will be more deeply analyzed in the following. There is another group of events leading to noticeable acceleration in the vicinity of resulting frequency 0.3Hz, but not corresponding to one well defined frequency (vertical modes 5 and 6 are respectively at 0.25 and 0.28Hz).

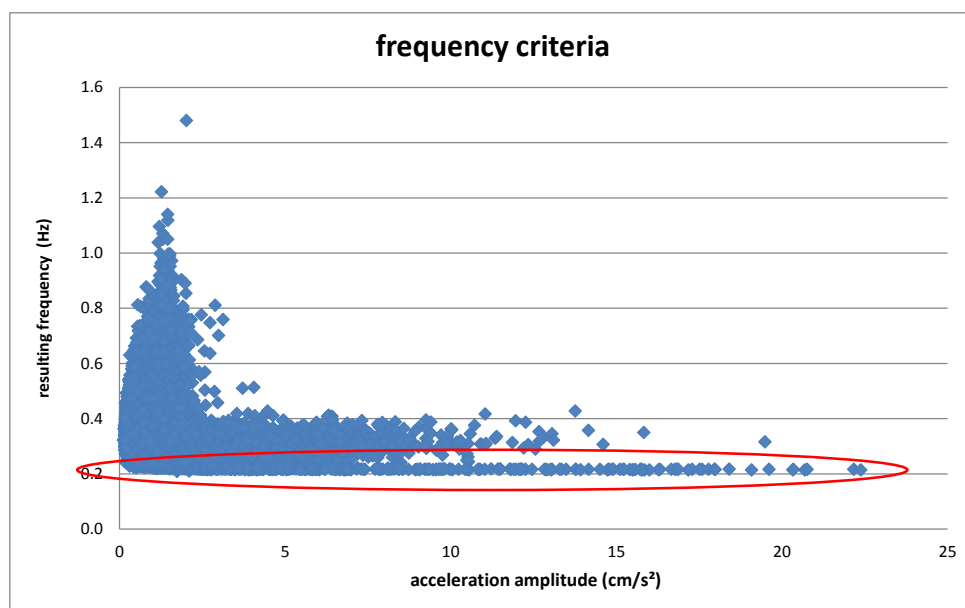


Figure 2: Plotting the resulting frequency criteria for 10 years record

2. ANALYSIS FOCUSED ON VORTEX-SHEDDING EVENTS

Reducing the set of data to the events identified as vibration initiated by vortex shedding, the influence of the oncoming wind direction, of oncoming wind turbulence and of oncoming wind speed was analyzed.

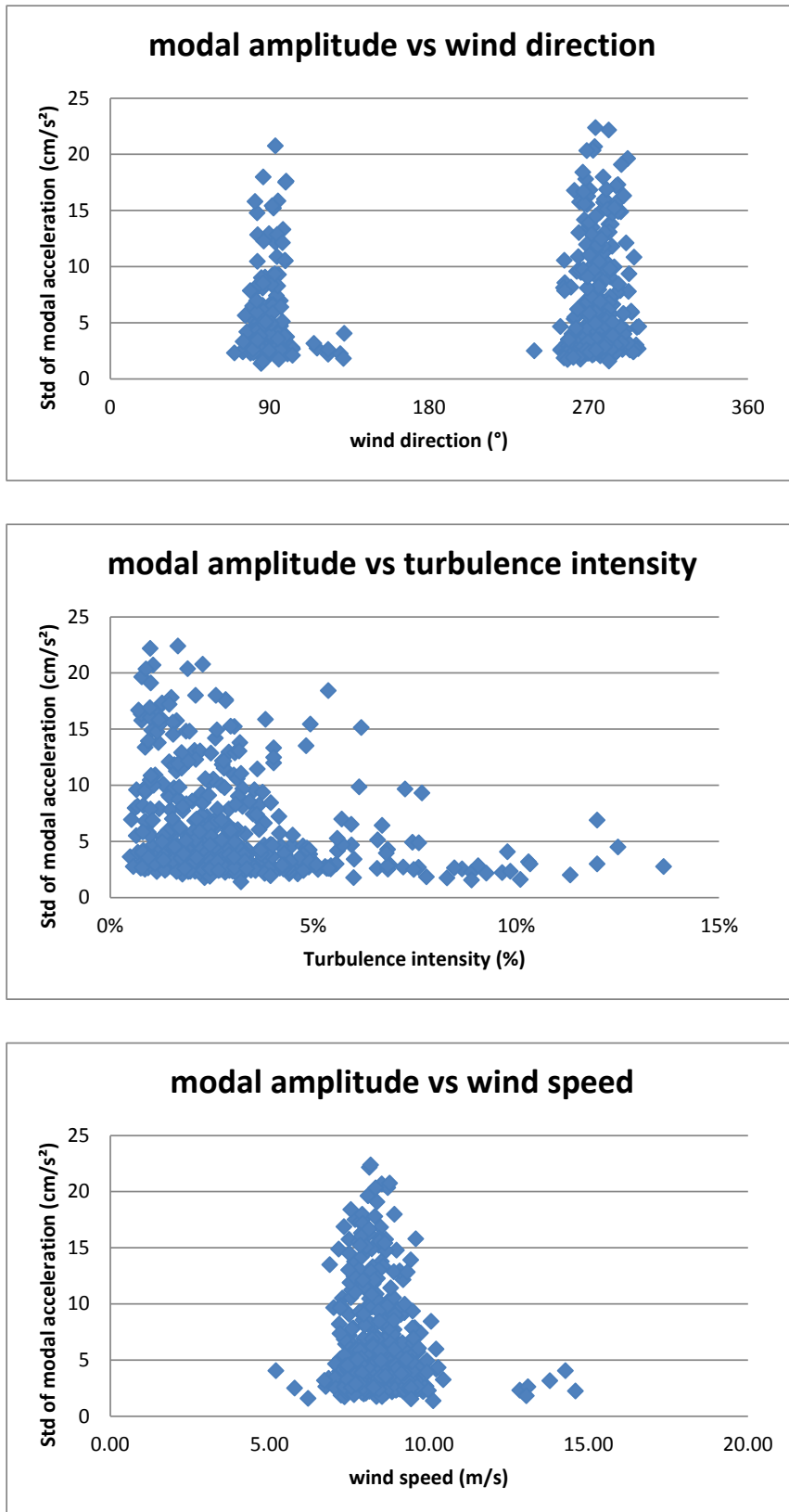


Figure 3: Influence of oncoming wind direction, turbulence and speed on modal amplitude.

It is noticeable that the wind directions corresponding to vortex shedding excitation are in a narrow band around 90° and 270°, what means perfectly perpendicular to the bridge axis. Some events correspond to wind direction between 115° and 130°, that do not yield large amplitude vibration of the deck.

It is clear also that the wind speeds giving way to this excitation of the third vertical bending mode are all in a range 7-10 m/s, with the exception of 6 events giving reduced amplitude vibration for wind speeds ranging between 13m/s and 15m/s. A closer view on these 6 events shows they all correspond to high turbulence winds. This high turbulence level may be the cause of these amplitudes, which are not due in this case to the vortex shedding excitation. Characteristics of these six events summarized in table 1 also show five of them belong to the few (actually six) events that correspond to wind directions apart from 90° and 270° directions.

Table 1: characteristics of the six events with higher wind speed.

Date	WS M1M2 (m/sec)	WD M1M2 (deg)	Turbulence Intensity M1M2 (%)	STDacc D17 (cm/sec ²)
4/9/11 10:00	12.85	70	9.86%	2.30219576
14/11/11 14:00	13.06	132	7.79%	1.79988398
27/9/11 4:00	13.11	123	8.48%	2.62035638
27/8/11 0:00	13.80	115	10.31%	3.14937251
25/10/11 18:00	14.29	132	9.79%	4.04852348
28/9/11 22:00	14.60	130	8.91%	2.22862779

The most interesting feature of these vortex shedding events is the relationship between amplitude and turbulence intensity as illustrated on Figure 3. It seems from this 10 years collection of data that most of the high amplitude vibrations occur for wind turbulence intensity lower than 6% and in addition that a turbulence intensity lower than 4% is the most favorable for this excitation to fully develop. This result is consistent with other observations³⁾. This must be compared to the turbulence intensity used for the design of the bridge, $I_u=12%$ at deck level, that was issued from the Eurocodes rules. Sorting the events by classes of step 1% turbulence intensity and calculating the mean and standard deviation in each class, this trend is confirmed in Figure 4 but the influence of turbulence intensity on the amplitude is not so strong. The mean amplitude of events with high turbulence (9% to 12%) is, broadly speaking, half the mean amplitude for low turbulence winds.

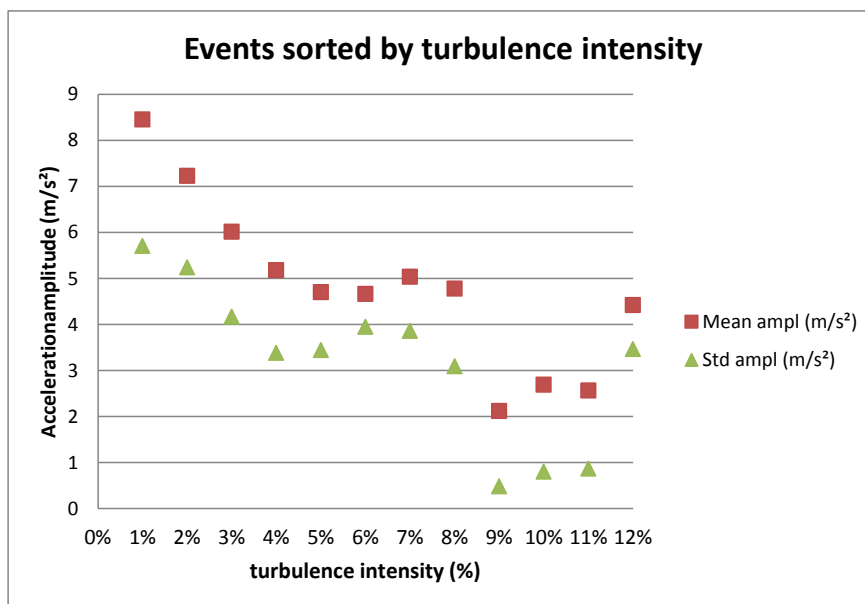


Figure 4: Vortex shedding events sorted by level of turbulence intensity.

Looking at the duration of the vortex shedding events we can find some occurrences when two, three or four records are following each other. There is also two occurrences of five consecutive records, what means the duration of this vibration occasion was, approximately, 10h. From this reduced set of data there is no occurrence of a correlation between the duration of the event and the vibration amplitude reached by the bridge deck, but it must be underlined that we do not have a proper view of the duration of events lesser than 2 hours.

Table 2: vortex shedding events sorted by duration.

duration of events (h)	number of events	Std of acceleration (mean)
2	415	5.95
4	32	7.87
6	7	5.60
8	2	4.08
10	2	5.85

5. CONCLUSIONS

Analysis of full scale data from the monitoring system of Rion-Antirion Bridge shows a correlation between the oncoming wind turbulence and the amplitude of the deck's vibrations due to vortex shedding on the first pure vertical mode, that is the third mode. This correlation is not as strong as the influence of the wind speed and of the wind direction, but it could be retained that low turbulence intensity gives way to amplitude of vibration twice the ones observed for "normal" turbulence intensity, as described by the codes.

ACKNOWLEDGMENT

Acknowledgment are directed with emphasis to GEFYRA company who gave access to its data base for achieving this study.

REFERENCES

- 1) Flamand, O., De Oliveira F., Stathopoulos-Vlavis A., Papanikolas P. : Conditions for occurrence of vortex shedding on a large cable stayed bridge. Full scale data from monitoring system, Journal of Wind Engineering and Industrial Aerodynamics, Volume 135, December 2014, Pages 163-169.
- 2) Li H., Laima S., Zhang Q., Li N., Liu Z. : Field monitoring and validation of vortex-induced vibrations of a long-span suspension bridge, J. Wind Eng. Ind. Aerodyn. 124 (2014), 54–67.
- 3) Owen J.S., Vann A.M., Davies J.P., Blakeborough A.: The prototype testing of Kessock Bridge: response to vortex shedding, Journal of Wind Engineering Industrial Aerodynamics 60 (1996), 91-108

Effects of gap distance on VIV of a parallel cable-stayed bridge

Jin Park⁺¹ and Ho-Kyung Kim⁺²

⁺¹Ph.D. Candidate, Seoul National University, Seoul, Republic of Korea

⁺²Professor, Seoul National University, Seoul, Republic of Korea

The effects of gap distance on vortex-induced vibration of two parallel section models are studied in a wind tunnel. Since two section models have similar cross-section and dynamic properties, the position whether the deck is located in upstream or downstream is the most significant difference between two decks in this study. Wind velocity at the beginning of the vibration of the downstream deck is affected by vortices from upstream deck. This is connected with separation flows from upstream deck through flow field observation.

Keyword: parallel bridge, vortex-induced vibration, particle image velocimetry, gap distance

1. INTRODUCTION

The vibrational vulnerability of bridge deck to vortex critically increases when two decks are located closely in a parallel disposition. This sort of phenomenon is observed and reported in previous researches^{1),2)}. Since one of the critical parameters, which affects the vortex-induced vibration (VIV) of a parallel bridge, is the gap distance between two adjacent bridge decks, this study investigates the effect of gap distance on VIV of the two bridge decks identical to the previous researches with a series of wind tunnel tests.

2. EXPERIMENTAL SETUP

Every experiments were carried out in an Eiffel-type wind tunnel operated by the Department of Civil and Environmental Engineering at Seoul National University.

Since two section models are same with those used in the previous papers^{1),2)}, the detail geometry and dimensions of two sections are omitted in this paper. Two section models have similar shape and aspect ratio. The upstream is referred to B2 and the downstream deck is referred to B1, respectively hereafter.

Figure 1 shows the experimental setup. For the dynamic tests, two section model were mounted on spring-supported systems. The vertical and torsional displacements of both models were measured by 8 (4 for each section model) laser sensors. In this study, the gap distance and wind velocity are used in non-dimensional forms as L/D and V/nD , where L is the open gap distance between two sections, D is the depth of B2, V is the upcoming wind velocity and n is the motional frequency of section. It is noted that n is changed corresponding to the sections or modes of motion.

The setup parameters are summarized in Table 1. As meaningful torsional vibration were not observed during the entire experiments, the torsional setup parameters are omitted. Two bridges have similar vertical frequencies but B2 is slightly lower. The damping ratios were set to a minimum level for a better observation of vibrations. The Struton numbers of two sections are defined with the depths of each section model.

Averaged flow field in specific phase of one entire period³⁾ were obtained by a high-resolution PIV system with a trigger generator which was synchronized with the vertical vibration of B2.

3. RESULTS AND DISCUSSIONS

Vortex-induced vibration (VIV) is well known for its resonance phenomenon with a limited amplitude. Flow crossing a structure alternately rolls up behind the structure with the vortex shedding frequency which is proportional to the mean wind velocity. The shedding vortex tuned to a natural frequency of the structure causes VIV in a specific velocity. For the sake of convenience, the specific velocity in which the vortex

⁺¹az22@snu.ac.kr, ⁺²hokyungk@snu.ac.kr

shedding frequency is identical to the nature frequency of the structure is designated as “resonant velocity”, hereafter. In a different manner, the minimum wind velocity causing VIV on a specific section is designated as “outset velocity”.

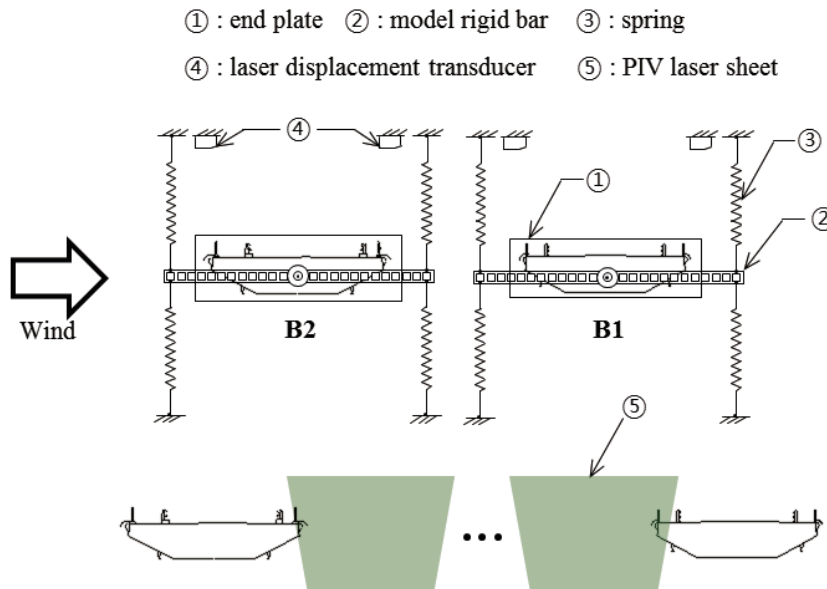


Figure 1: The experimental setup

Table 1: Captions should be centered above tables.

Parameters	B2	B1
Length (m)	0.900	0.900
Breadth (m)	0.353	0.329
Depth (m)	0.076	0.078
Mass (kg/m)	6.874	5.400
Vertical frequency (Hz)	5.096	5.875
Vertical damping ratio (%)	0.1	0.1
Scruton number	12.0	8.9

Figure 2 shows measured resonant velocities and outset velocities with various gap distances. The resonant velocity of B2 marked by black dots is derived by the vortex shedding frequency measured by a hot-wired anemometer while two sections are fixed, i.e. the sections are restrained to vibrate. The outset velocities are naturally obtained while the sections are free to vibrate. VIVs of B2 are observed at the gap distance of 2.1 or more. The outset velocity of B2 marked by squares are well matched with the resonant velocity in all cases.

Interesting points are observed on B1, the downstream deck. Since B1 has a different Strouhal number with B2, outset velocity of B1 should be different with the resonant velocity of B2. According to the results, it is true for only small gap distances. The outset velocities of B1 are also matched with the resonant velocity of B2 for large gap distances. It implies that B1 is affected by the vortices from B2 instead of the Strouhal number of itself. The gap distances of 2.5 to 4.0 seem to be a transient region. At this region, B1 is controlled by its Strouhal number as long as B2 is fixed, but it disappears while B2 is oscillating. PIV results at the transient gap distance show that the separation flows from the windward edge of B2 directly cross over the

gap so re-separation at the windward edge of B1 does not occur as shown in figure 3. As separation flows comes into the gap area for further gap distances, re-separation occurs at the windward edge of B1.

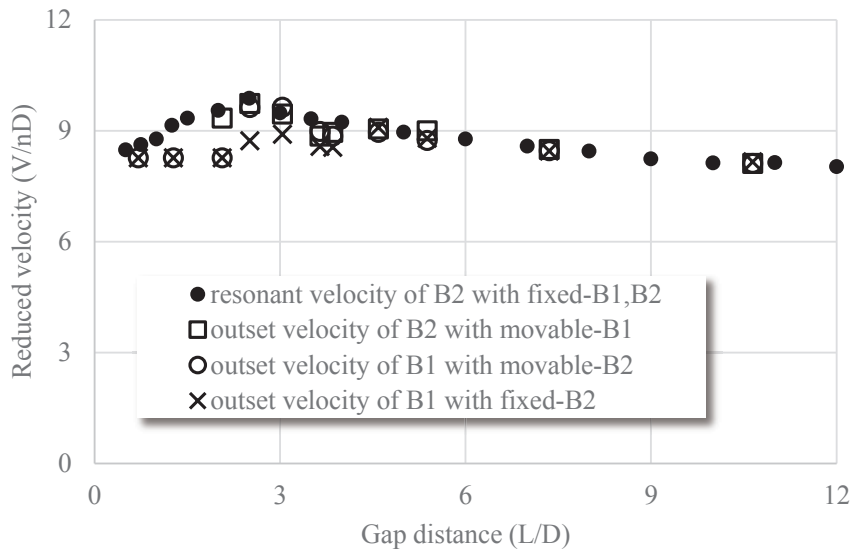


Figure 2: The resonant velocity and the outset velocities according to the gap distances

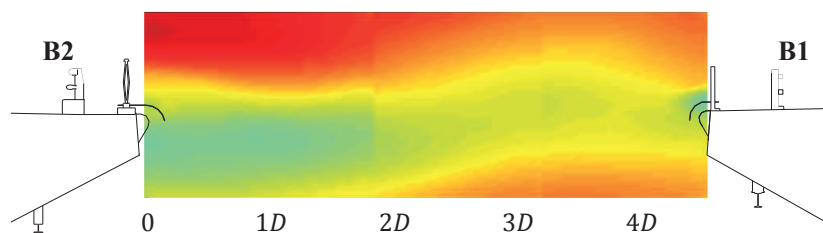


Figure 3: Magnitude of velocity distribution in the gap (red: higher velocity, blue: lower velocity)

4. CONCLUSION

VIV characteristics of two parallel section models with various gap distances are studied. Wind velocities of VIV of both decks are controlled by the vortex shedding frequency of upstream deck as long as the gap distance is larger than $4.6D$. The motion of upstream deck is also important factor for the downstream deck as long as re-separation at the downstream deck does not occur.

ACKNOWLEDGMENT

This research was supported by a grant (09CCTI-A052531-05-000000) from the Ministry of Land, Transport and Maritime Affairs of the Korean government through the Core Research Institute at Seoul National University for Core Engineering Technology Development of Super Long Span Bridge R&D Center and BK21 plus research program.

REFERENCES

- 1) Seo, J.-W., Kim, H.-K., Park, J., Kim, K.-T., Kim, G.-N. : Interference effect on vortex-induced vibration in a parallel twin cable-stayed bridge, *J. Wind Eng Ind Aerod.*, 116, pp. 7-20, 2013.
- 2) Kim, S.-J., Kim, H.-K., Calmer, R., Park, J., Kim, G.S., Lee, D.K. : Operational field monitoring of interactive vortex-induced vibrations between two parallel cable-stayed bridges, *J. Wind Eng Ind Aerod.*, 123, pp. 143-154, 2013.
- 3) Hussain, A.K.M.F., Reynolds, W.C. : The mechanics of an organized wave in turbulent shear flow, *J. Fluid Mechanics*, 41, pp. 241-258

STUDY ON AERODYNAMIC VIBRATIONS OF A BRACING MEMBER WITH A RECTANGULAR CROSS SECTION OF A LONG-SPANDED TRUSS BRIDGE

Kentaro Suda⁺¹, Kazutoshi Matsuda⁺¹, Kusuo Kato⁺¹ and Yusuke Tamai⁺²
⁺¹ Kyushu Institute of Technology, Kitakyushu, Japan
⁺² Hitachi, Ltd., Tokyo, Japan

In 2009, Ikitsuki Bridge, a truss bridge in Nagasaki Prefecture with a center span length of 400 m, was discovered to have a crack in the bracing member of the bridge. As a result of the subsequent vibration measurement at the site, the main cause of the crack was identified as Kármán vortex-induced excitation. However, vibrations were also observed in the wind speed range of 7-8 m/s, which was lower than the resonance wind speed of Kármán vortex-induced excitation. Conventionally, according to the results from a wind tunnel test using a side ratio of $B/D=2-8$ (B: along-wind length, D: cross-wind length), the motion-induced vortex excitation was confirmed. However, the side ratio of the section of the bracing member is $B/D=1.18$, and the motion-induced vortex excitation in the case of this side ratio has not yet to be confirmed by the conventional wind tunnel test. Therefore, in this research, a spring-supported test was carried out targeting a rectangular cross section of $B/D=1.18$. Furthermore, flow visualization was performed and the results of the spring-supported test were discussed. The vibrations in the bracing member with a rectangular cross section ($B/D=1.18$) of Ikitsuki Bridge generated in the wind speed range of lower than Kármán vortex-induced excitation among the aerodynamic vibrations caused by wind were suggested to possibly be motion-induced vortex excitation by experimental results of a spring-supported test and the flow visualization. Further investigation should be undertaken.

Keyword: bracing member, rectangular cross section, motion-induced vortex excitation, Kármán vortex-induced excitation, spring supported test, flow visualization

1. INTRODUCTION

The vortices separated from rectangular cross sections are broadly classified into Kármán vortices and motion-induced vortices (vortices separated from leading edge)^{1, 2)}. The former are those that are accompanied by the interferences of two separated shear layers at both the top and bottom surfaces of the structures. The latter are the ones that are shedding separately from the leading edges of the top and bottom surfaces caused by the separated shear layers at the top and bottom surfaces excited alternately due to the vibration of the rectangular cross section. The vibration caused by the latter vortices was found in the past wind tunnel tests^{3, 4)}. The vibration is known as either motion-induced vortex excitation^{1, 2)} or impinging-shear-layer instability⁵⁻⁸⁾. The onset wind speed of this vibration depends on the side ratio of the rectangular cross section and this relationship is schematically clarified^{1), 8)}. The mechanisms of the motion-induced vortex excitation of the rectangular section and H-shaped section cylinders are also revealed⁹⁻¹²⁾. This research is involved in the motion-induced vortex excitation and Kármán vortex-induced excitation generated in a bracing member of a real truss bridge in Japan.

In 2009, Ikitsuki Bridge, a truss bridge in Nagasaki Prefecture with a center span length of 400 m, was discovered to have a crack in the bracing member of the bridge¹³⁾. As a result of the subsequent vibration measurement at the site, the main cause of the crack was identified as Kármán vortex-induced excitation. However, vibrations were also observed in the wind speed range of 7-8 m/s, which was lower than the resonance wind speed of Kármán vortex-induced excitation. Conventionally, according to the results from a wind tunnel

test using a side ratio of $B/D=2-8$, the motion-induced vortex excitation was confirmed¹⁾. However, the side ratio of the section of the bracing member is $B/D=1.18$, and the motion-induced vortex excitation in the case of this side ratio has not yet to be confirmed by the conventional wind tunnel test. Therefore, in this research, a spring-supported test was carried out targeting a rectangular cross section of $B/D=1.18$. Furthermore, flow visualization was performed and the results of the spring-supported test were discussed. In order to clarify the relationship between the generation of motion-induced vortices and the side ratio of B/D , flow visualization was conducted by changing a side ratio of B/D from 0.5 to 1.5.

2. EXPERIMENTAL SETUPS

(1) Section models

Table 1 shows the scale and dimensional data of the section model, $B/D=1.18$, used in each test. Two cross-sections of a rectangular cross-section and a cross-section with a flange, a reproduction of the cross-section of the cracked bracing member of Ikitsuki Bridge, were used. Table 2 shows the dimensional data of the models used for the flow visualization test. The models used for the flow visualization tests were rectangular section models without flanges, because the spring-supported test results were not influenced by the existence or non-existence of flanges when an angle of attack was 0 degrees. The reason for this will be described later. Table 3 shows the dimensional data of the models used for the 2nd spring-supported tests.

Table 1: Section models ($B/D=1.18$)

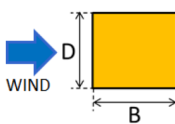
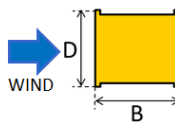
Wind tunnel tests	Model scale				
		B(mm)	D(mm)	B(mm)	D(mm)
1 st spring-supported tests	1/5.6	107	90.0	107	90.0
Flow visualization	1/12.5	47.2	40.0		

Table 2: Section models for flow visualization

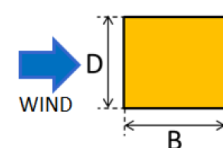
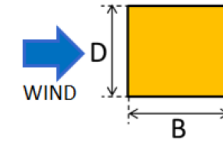
Cross-section	B/D	B(mm)	D(mm)
	2.0	80.0	40.0
	1.5	60.0	
	1.18	47.2	
	1.0	40.0	
	0.75	30.0	
	0.62	24.8	
	0.50	20.0	

Table 3: Section models for 2nd spring-supported tests

Cross-section	B/D	B(mm)	D(mm)
	1.18	212.4	180.0
	1.0	180.0	
	0.75	135.0	
	0.62	111.6	
	0.50	90.0	

(2) 1st spring-supported tests

The spring-supported test for $B/D=1.18$ was conducted in the closed circuit wind tunnel (cross-section: 1.8m high \times 0.9m wide) at Kyushu Institute of Technology. Main experimental conditions for the model were: mass per unit length=3.12 kg/m, natural frequency of heaving vibration=9.13 Hz, logarithmic decrement of structural damping=0.0021 and Scruton number=1.32. Table 4 shows the conditions for the spring-supported test. Figure 1 shows a photo of the section model installed in the wind tunnel.

Table 4: 1st spring-supported test conditions for $B/D=1.18$

Angle of attack, α	0, 10 deg.
Yaw angle, β	0 deg.
Mass per unit length, m	3.12 kg/m
Natural frequency, f	9.13Hz
Structural damping (in logarithmic decrement), δ	0.0021
Scruton number, $Sc=2m\delta/\rho D^2$	1.32
Blockage ratio	5 %

ρ : air density=1.23kg/m³, D: model height =0.090m, L: Model length=0.76m



Figure 1: Section model for spring-supported tests mounted in Kyushu Institute Technology wind tunnel

(3) Flow visualization

The flow visualizations around the model during static and oscillating times were conducted using a small-sized wind tunnel (0.4m high \times 0.4m wide) at Kyushu Institute of Technology. It was considered that the wind speeds in the wind tunnel of $V=0.6$ -1.0 m/s are good for visualization, so that eventually $V=0.6$ m/s and 1.0 m/s were selected at the onset wind speeds of motion-induced vortex excitation and Kármán vortex-induced excitation, respectively. Accordingly, the experimental Reynolds numbers are $Re=VD/\nu=1.6\times 10^3$ and 2.7×10^3 , respectively. As for the forced-oscillating amplitude η , because the peak of aerodynamic response in the range of low wind speed is $2\eta/D=0.12$, the non-dimensional double amplitudes were set up as $2\eta/D=0.10$, 0.05 and 0.025 in accordance with the spring-supported test results. Tables 5 and 6 show the conditions for the flow visualization tests.

Table 5: Flow visualization test conditions at the onset wind speed of motion-induced vortex excitation

B/D	B (mm)	D (mm)	Angle of attack α (deg.)	Reduced wind speed $V_r=V/fD$ ($=1.67B/D$) ¹⁾	Wind speed V(m/s)	Frequency of forced oscillation method f(Hz)
0.50	20.0	40	0	0.8	0.6	18.0
0.62	24.8			1.0		14.5
0.75	30.0			1.3		12.0
1.00	40.0			1.7		9.0
1.18	47.2			2.0		7.6
1.5	60.0			2.5		6.0
2.0	80.0			3.3		4.5

Table 6: Flow visualization test conditions at the onset wind speed of Kármán vortex-induced excitation

B/D	B (mm)	D (mm)	Angle of attack α (deg.)	Strouhal number $St=fD/V$	$V_r=V/fD$ ($=1/St$)	Wind speed V(m/s)	Frequency of forced oscillation method f(Hz)
1.18	47.2	40	0	0.122	8.20	1.0	3.0

(4) 2nd spring-supported tests

Spring-supported tests were conducted on $B/D=0.5-1.18$ based on the results of the flow-visualization experiment. Table 7 shows the 2nd spring-supported test conditions for $B/D=1.18$. Because the cross-sectional side ratio, which was the object of the experiment, was smaller than that of the first spring-supported test, the measured reduced wind-speed range was very low. Therefore, in order to lower the natural frequency of the vibration system to a value which can be experimented, the size of the cross section of the model had to be enlarged. Due to experimental restrictions such as this, the blockage ratio was changed to 10%. Because the blockage ratio in the first spring-supported tests was 5%, it was confirmed at the beginning that, in the case of $B/D=1.18$, the difference in blockage ratio did not influence the response characteristics.

Table 7: 2nd spring-supported test conditions for $B/D=1.18$

Angle of attack, α	0 deg.
Yaw angle, β	0 deg.
Mass per unit length, m	3.76 kg/m
Natural frequency, f	5.70Hz
Structural damping (in logarithmic decrement), δ	0.0085
Scruton number, $Sc=2m\delta/\rho D^2$	1.64
Blockage ratio	10 %

ρ : air density=1.20kg/m³, D: model height =0.180m, L: Model length=0.828m

3. EXPERIMENTAL RESULTS AND DISCUSSION

(1) 1st spring-supported tests

Figure 2 shows the result of the spring-supported test for an angle of attack of 0 degrees¹⁴⁾. Vibrations were confirmed from the neighborhoods of reduced wind speed $V_r=2$ and 8. Because the reduced wind speed at motion-induced vortex excitation is calculated as $V_r=1.67 \times B/D=1.67 \times 1.18=2.0^1)$, vibrations around $V_r=2$ were considered to be motion-induced vortex excitation. The effects of the existence or non-existence of flange on the maximum response amplitude of motion-induced vortex excitation are extremely small. However, Figure 3 shows the result of an experiment separately conducted for an angle of attack of 10 degrees that the maximum response amplitude in the case with flanges was approximately 1.5 times larger than that in the case with no flange. In other words, it turns out that as the angle of attack becomes larger, the existence or non-existence of flange tends to exercise an effect on the patterns of the flows around the cross-section.

The Strouhal number measured on the cross-section with flanges was $St=0.124$. Its inverse number is the critical reduced wind speed of beginning Kármán vortex-induced excitation. In other words, because $V_r=1/St=8.1$, a vibration beginning in the neighborhood of a reduced wind speed of 8 can be judged as Kármán vortex-induced excitation. However, from the fact that the Scruton number in this experiment's case was small at $Sc=1.32$, it was found that Kármán vortex-induced excitation was changed to a galloping along with the increase in wind speed.

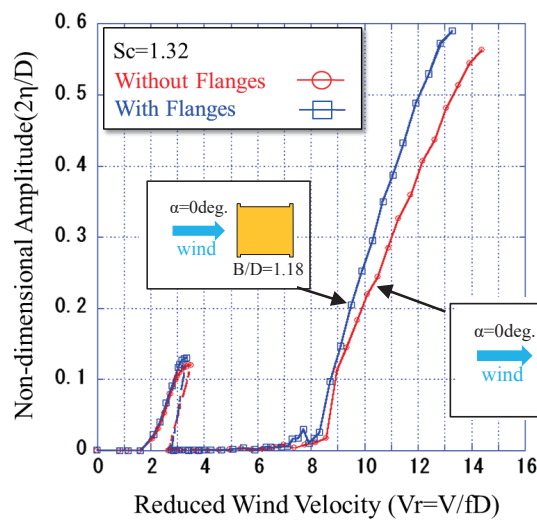


Figure 2: Spring-supported test result (Angle of attack, $\alpha=0$ deg., Yaw angle, $\beta=0$ deg.)¹⁴⁾

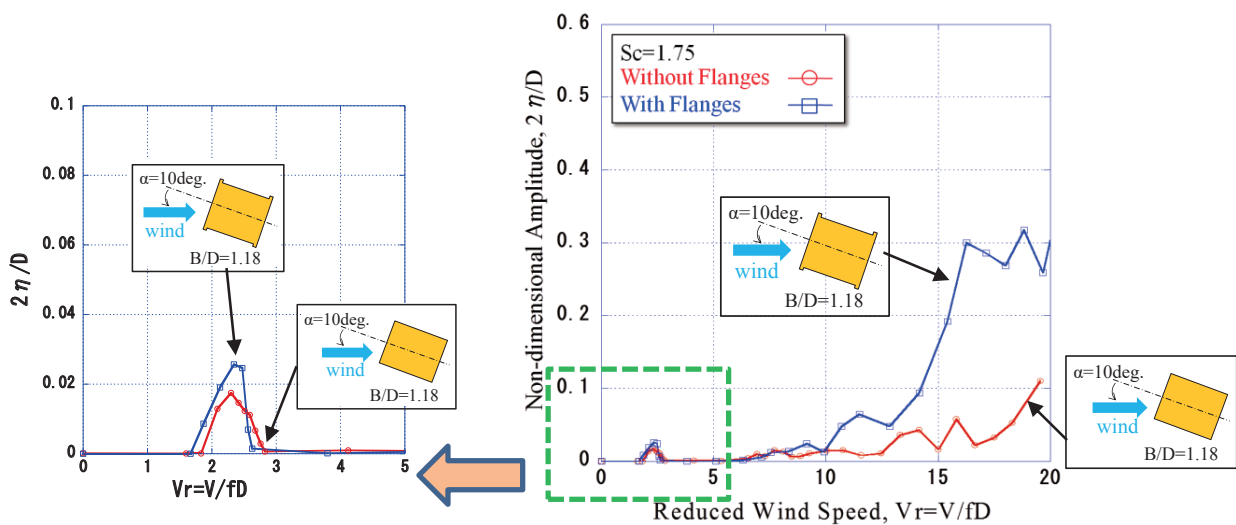


Figure 3: Spring-supported test result (Angle of attack, $\alpha=10$ deg., Yaw angle, $\beta=0$ deg.)¹⁴⁾

(2) Flow visualization

a) B/D=1.18 cross-section of the bracing member of Ikitsuki Bridge

From the response characteristics of Figures 2 and 3, the possibility of the existence of motion-induced vortex excitation at the neighborhood of $V_r=2$ was suggested. The possibility of the existence of motion-induced vortex excitation of $B/D=1.18$ was discussed here from the aspects of the flow visualization.

Table 8 shows the results of the flow visualization of the cross-section of $B/D=1.18$. At static time, only Kármán vortices were formed in the same way as in the case of the experiment at $B/D=2.0$. At the time of oscillation at the onset wind speed of motion-induced vortex excitation, although separated vortices from leading edge were formed, no secondary vortices at trailing edge were formed. Due to the fact that secondary vortices at trailing edge were confirmed at the cross-section of $B/D=2.0$ at the time of oscillation as shown in Figure 4(a) which was carried out to confirm the validity of the experimental method of the research, it was suggested that when the side ratio of B/D becomes small, secondary vortices at trailing edge tend not to be formed.

The generation of motion-induced vortex excitation is considered to be caused by the unification of separated vortices from leading edge and secondary vortices at trailing edge¹⁾. However, according to the spring-supported test results targeting $B/D=1.18$ where the formation of secondary vortices at trailing edge were not observed, aerodynamic vibrations considered to be motion-induced vortex excitation were confirmed as shown in Figures 2 and 3. Although it was suggested that motion-induced vortex excitation would possibly occur at the range of low wind speed even in the case of side ratios where secondary vortices at trailing edge were not confirmed, further investigation should be undertaken to confirm.

Table 8: Results of flow visualization ($B/D=1.18$, Angle of attack, $\alpha=0$ deg.)

	<p style="text-align: center;">$2\eta/D$</p> <p style="text-align: center;">V_r</p> <p style="text-align: center;">(Re=VD/v=1.6 × 10³)</p>	<p style="text-align: center;">$2\eta/D$</p> <p style="text-align: center;">V_r</p> <p style="text-align: center;">(Re=VD/v=2.7 × 10³)</p>
Fixed model		
Forced-oscillating model at the top displacement ($2\eta/D=0.10$)		

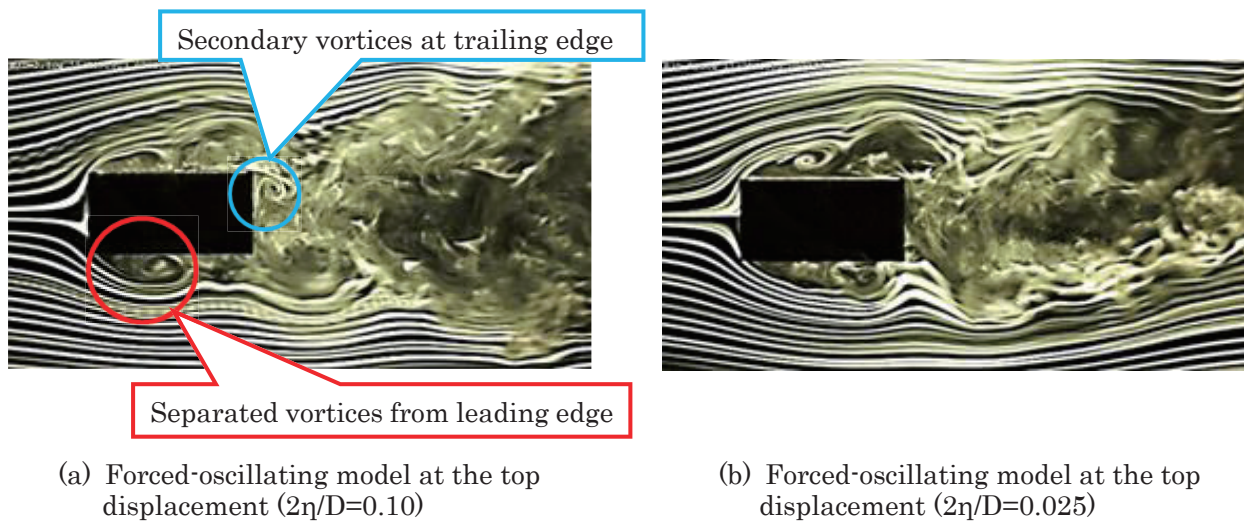


Figure 4: Flow visualization (Validity of experimental method, $B/D=2.0$, Angle of attack, $\alpha=0$ deg., $V_r=3.3$)

b) Rectangular cross-sections of less than $B/D=1.5$

For the purpose of clarifying the relationship between the formations of separated vortices from leading edge and the side ratio of B/D , the flow visualizations around the cross-section were conducted by the side ratio being changed from 0.5 to 1.5. Table 9 shows the experimental results of the flow visualization at the side ratio of $B/D=0.5-1.5$. In the experimental results of non-dimensional double amplitude $2\eta/D=0.050$, the generation of separated vortices from leading edge were confirmed in all B/D s. However, as a result of non-dimensional double amplitude $2\eta/D=0.025$, the vortices that separated from the leading edge were gradually separating from the top and bottom surfaces of the cross-sections of less than $B/D=0.62$ and flowing downward. The generation of secondary vortices at trailing edge was not confirmed clearly in all cross-sections of less than $B/D=1.5$.

(3) 2nd spring-supported tests

Table 10 shows the results of the spring supported test. Motion-induced vortex excitation was confirmed in the three cross sections of $B/D=1.18$, 1.0 and 0.75. The less the side ratio B/D is, the less the maximum amplitude of motion-induced vortex excitation tends to become. It is considered that if the side ratio B/D becomes smaller, the areas of the upper and lower surfaces of the model, on which fluctuating lift acts, gradually reduce and as a result, exciting force becomes smaller. The reason why motion-induced vortex excitation did not generate in $B/D=0.62$ and 0.5 for $Sc=1.6$, it is presumed, is that the separated vortex from the leading edge gradually separate from the upper and lower surfaces of the model and flow down as shown in Table 9, and therefore, fluctuating lift does not fully act on the upper and lower surfaces of the model. However, motion-induced vortex excitation was confirmed in $B/D=0.62$ for $Sc=0.82$.

Then, it turns out that there is a difference between the estimated critical wind speed of Kármán vortex-induced excitation $1/St$ calculated from the inverse number of the measured Strouhal number St and the experimental critical wind speed of Kármán vortex-induced excitation in $B/D=0.62$ and 0.5. As Hirata¹⁷⁾ pointed out, the vibration of the reduced wind speed generated in the neighborhood of 4 is considered to be a low speed galloping in the cases of $B/D=0.62$ and 0.5.

Table 9: Results of flow visualization around forced-oscillating rectangular section models at the top displacement at the onset wind speed of motion-induced vortex excitation (Angle of attack, $\alpha=0$ deg.)

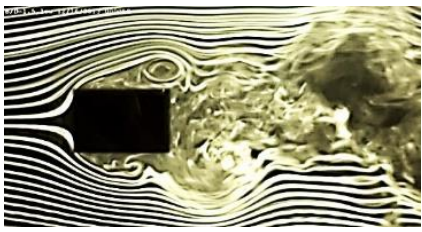
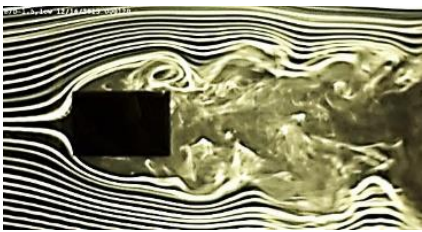
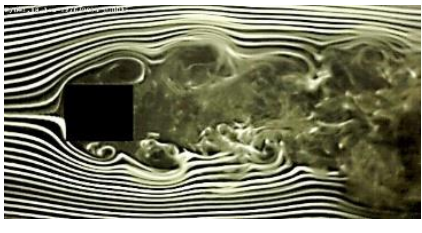
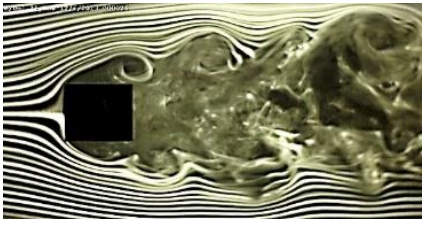
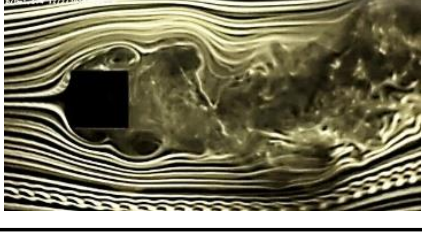
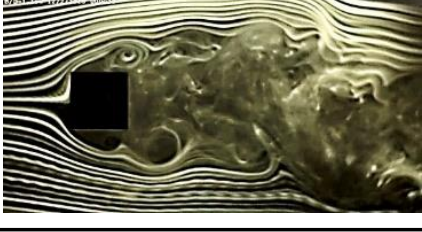
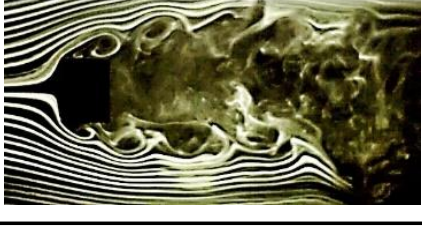
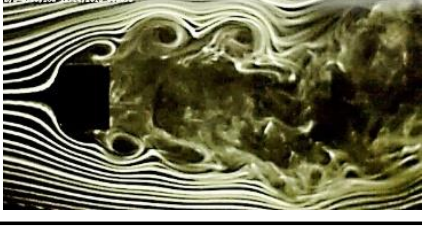
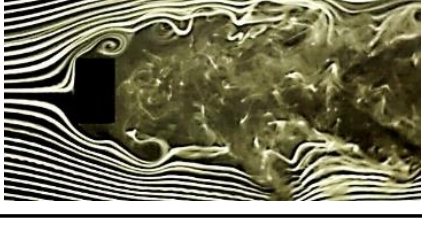
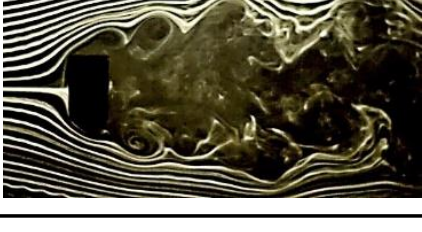
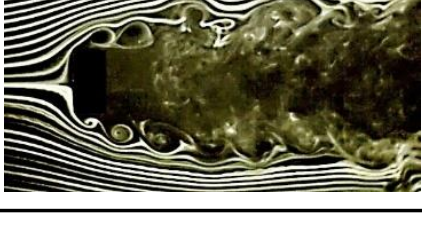
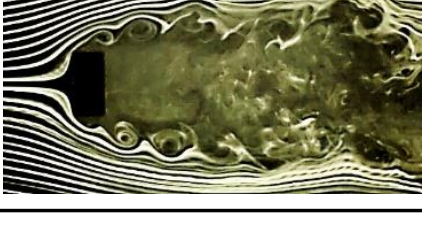
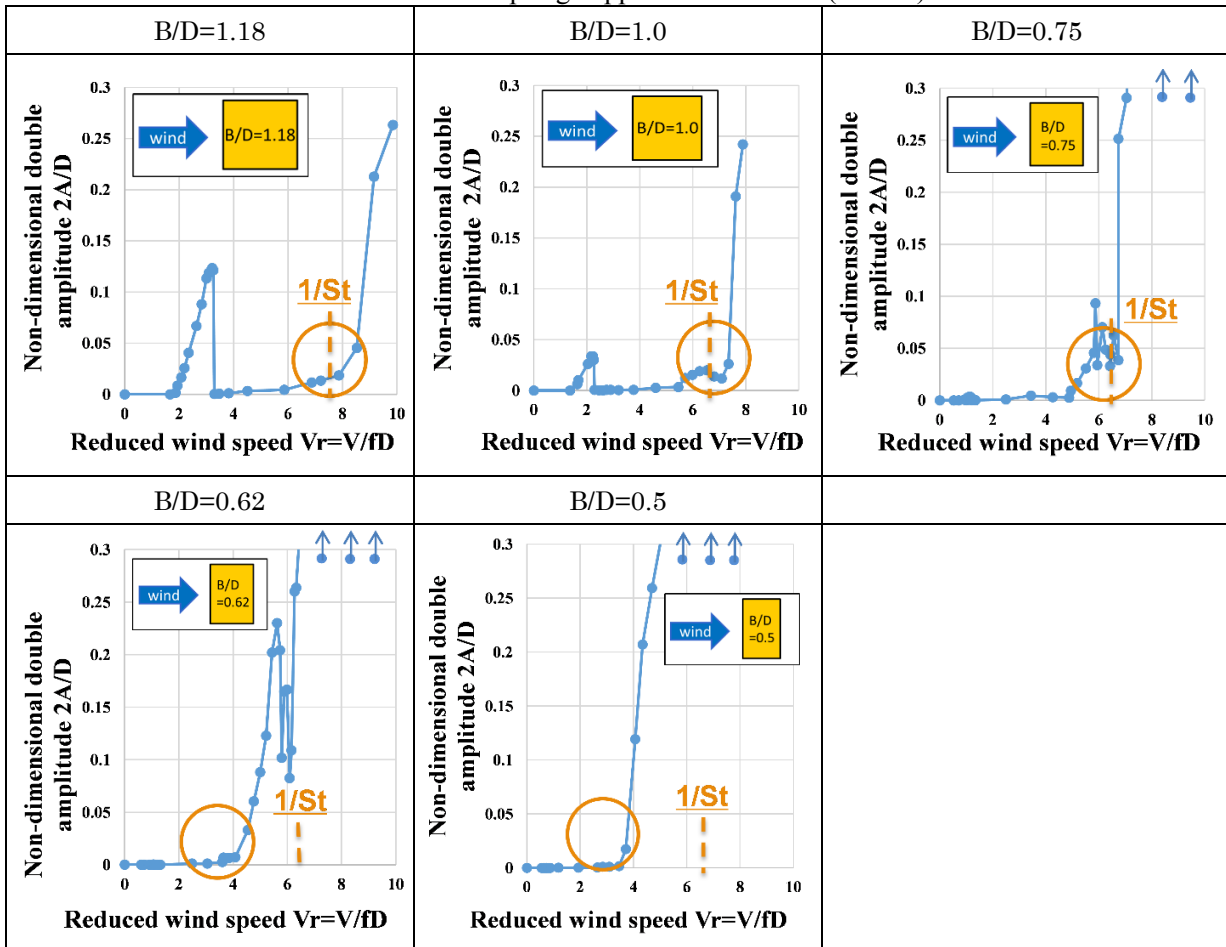
B/D	V_r	$2\eta/D = 0.050$	$2\eta/D = 0.025$
1.50	2.5		
1.18	2.0		
1.0	1.7		
0.75	1.3		
0.62	1.0		
0.50	0.8		

Table 10: 2nd spring-supported test results ($Sc=1.6$)

4. CONCLUSIONS

The findings obtained from this research are as follows:

- (1) The vibrations of the bracing member with a rectangular cross section ($B/D=1.18$) of Ikitsuki Bridge generated in the wind speed range of lower than Kármán vortex-induced excitation among the aerodynamic vibrations caused by wind were suggested to possibly be motion-induced vortex excitation by experimental results of the spring-supported test and the flow visualization test. Further investigation should be undertaken.
- (2) Given that this aerodynamic vibration is motion-induced vortex excitation, the possibility was suggested that motion-induced vortex excitation might be generated even at side ratios of less than $B/D=2.0$ where the generation of secondary vortices at trailing edge was not confirmed.
- (3) Aerodynamic vibration which can be considered to be motion-induced vortex excitation was also confirmed in the three cross sections of $B/D=1.18$, 1.0 and 0.75 . The less the side ratio B/D is, the less the maximum response amplitude of motion-induced vortex excitation tends to become. The reason why motion-induced vortex excitation did not generate in $B/D=0.62$ and 0.5 for $Sc=1.6$, it is presumed, is that the separated vortices from the leading edge gradually separate from the upper and lower surfaces of the model and flow down, and therefore, fluctuating lift does not fully act on the upper and lower surfaces of the model. However, motion-induced vortex excitation was confirmed in $B/D=0.62$ for $Sc=0.82$.

REFERENCES

- 1) N. Shiraishi, M. Matsumoto: On classification of vortex-induced oscillation and its application for bridge structures, *Journal of Wind Engineering and Industrial Aerodynamics*, Vol.14, Nos.1-3, pp.419-430, 1983.
- 2) S. Komatsu and H. Kobayashi: Vortex-induced oscillation of bluff cylinders, *Journal of Wind Engineering and Industrial Aerodynamics*, Vol.6, pp.335-362, 1980.
- 3) M. Novak: Galloping and vortex induced oscillations of structures, *Proceedings of the Third International Conference on Wind Effects on Buildings and Structures*, Tokyo, Japan, pp.799-809, 1971.
- 4) Y. Otsuki, K. Washizu, H. Tomizawa, A. Ohya and K. Fujii: Experiments on the aeroelastic instability of prismatic bars with rectangular sections, *Proceedings of the Third International Conference on Wind Effects on Buildings and Structures*, Tokyo, Japan, pp.891-898, 1971.
- 5) D. Rockwell and E. Naudascher: Review- Self-sustaining oscillations of flow past cavities, *Transactions of the ASME, Journal of Fluids Engineering*, Vol.100, pp.152-165, 1978.
- 6) Y. Nakamura, Y. Ohya and H. Tsuruta: Experiments on vortex shedding from flat plates with square leading and trailing edge, *Journal of Fluid Mechanics*, Vol. 222, pp.437-447, 1991.
- 7) Y. Ohya, Y. Nakamura, S. Ozono, H. Tsuruta and R. Nakayama: A numerical study of vortex shedding from flat plates with square leading and trailing edges, *Journal of Fluid Mechanics*, Vol. 236, pp.445-460, 1992.
- 8) E. Naudascher and Y. Wang: Flow-induced vibrations of prismatic bodies and grids of prisms, *Journal of Fluids and Structures*, Vol.7, pp.341-373, 1993.
- 9) M. Matsumoto, N. Shiraishi, H. Shirato, S. Stoyanoff, and T. Yagi: Mechanism of, and turbulence effect on vortex-induced oscillations for bridge box girders, *Journal of Wind Engineering and Industrial Aerodynamics*, Vol. 49, Issues 1-3, pp.467-476, 1993.
- 10) Y. Kubo, K. Hirata and K. Mikawa: Mechanism of aerodynamic vibrations of shallow bridge girder sections, *Journal of Wind Engineering and Industrial Aerodynamics*, Vol.41-44, pp.1297-1308, 1992.
- 11) R. Mills, J. Sheridan, K. Hourigan and M.C. Welsh: The mechanism controlling vortex shedding from rectangular bluff bodies, *Proceedings of the twelfth Australasian Fluid Mechanics Conference*, Sydney, pp.227-230, 1995.
- 12) R. Mills, J. Sheridan and K. Hourigan: Particle image velocimetry and visualization of natural and forced flow around rectangular cylinders, *Journal of Fluid Mechanics*, Vol. 478, pp.299-323, 2003.
- 13) S. Nakamura, T. Okumatsu, T. Nishikawa and T. Okabayashi: A Fatigue Damage of a Diagonal Member in a Steel Truss Bridge Due to Wind-Induced Vibration, *Developments in International Bridge Engineering - Selected Papers from Istanbul Bridge Conference*, pp.211-220, 2014.
- 14) K. Matsuda, K. Kato, K. Hisadomi and K. Harada: Low speed instability of two-dimensional rectangular prisms, *Proceedings of the ASME 2013 Pressure Vessels and Piping Conference (PVP2013)*, 97353, 2013.
- 15) T. Yagi, K. Shinjo, S. Narita, T. Nakase and H. Shirato: Interferences of vortex sheddings in galloping instability of rectangular cylinders, *Journal of Structural Engineering*, JSCE, Vol.59A, pp.552-561, 2013.(in Japanese)
- 16) Y. Nakamura and T. Mizota: Unsteady lifts and wakes of oscillating rectangular prisms, *Journal of the Engineering Mechanics Division, ASCE*, Vol.101, No.EM6, Proc. Paper 11813, pp.855-871, 1975.
- 17) K. Hirata: Study on Galloping generation mechanism. Doctor Dissertation, Kyushu University, 1993. (in Japanese)

Time-Domain Aeroelastic Loads and Response of Wind Turbine Blades in Gusty Wind: Prediction and Experimental Validation

Heather Scot Sauder⁺¹ and Partha P. Sarkar⁺²

⁺¹Iowa State University, Ames, USA

⁺²Iowa State University, Ames, USA

The traditional method of flutter analysis of wind turbine blades employs a mixed-domain (frequency- and time- domain) formulation for self-excited aerodynamic loads, because flutter derivatives are functions of reduced frequencies. However, a time domain formulation for self-excited and buffeting loads allows the equations of motion to be continuously solved for response time histories of wind turbine blades below flutter speed and captures the transient response in gusty and turbulent winds. The rational function coefficients and buffeting indicial function coefficients that appear in the time domain formulation were previously extracted for the NREL S830 airfoil, a low-noise and high lift to drag ratio airfoil with 21% thickness to chord ratio used in wind turbine blades, using section model tests in a wind tunnel. The objective of the current study is to evaluate how well these experimentally extracted coefficients can predict the aerodynamic loads on a blade in different wind conditions, through a separate set of tests conducted on a much larger (3.3 times) section model of the blade in a larger wind tunnel than originally used. The tests were performed for different upstream wind conditions (stationary, ramp-down gust, low turbulence and high turbulence) and the loads (lift and moment) were validated by simulating them in time domain using the measured displacements and comparing them with the measured ones. The amplitudes and pattern of the simulated aerodynamic loads compared reasonably well with those measured, even in gusty and more turbulent wind environment.

Keyword: Wind Turbine blades¹, Time-domain², Aeroelastic load prediction³, Gusty wind⁴

1. INTRODUCTION

Traditional analysis for calculating response of a slender structure such as a wind turbine blade subject to aerodynamic loads employs a frequency-domain formulation of the loads which works on the assumption that the incident wind is stationary and the response of the blade is sinusoidal or near-sinusoidal, neither of which is true. A frequency-domain formulation of the aerodynamic loads on a wind turbine blade uses Theodorsen functions¹ that are theoretically-derived functions for thin airfoils (thickness to chord ratio less than 10%)^{2),3),4)} or uses experimentally-derived flutter derivatives, both of which are functions of reduced frequency⁵⁾. The dynamic equations of motion for the wind turbine blade then becomes a mixed-domain (frequency- and time- domain) formulation because the aerodynamic loads are formulated in mixed domain. To utilize this formulation, some authors use the pseudo-steady formulation^{6),7),8)} of the flutter derivatives which uses approximate expressions of the flutter derivatives in terms of the static force coefficients for the airfoil sections and their derivatives with respect to angle of attack at zero degree angle of attack. Wind turbine blades consist of thick airfoils operating at non-zero angles of attack, questioning the applicability of these approximations. Alternately and preferably, flutter derivatives of the airfoil sections^{9),10)} of the wind turbine blades can be extracted from wind tunnel tests, however, these frequency-domain formulations cannot be used to continuously predict the response of wind turbine blades in real time. Therefore, time-domain formulations for aerodynamic loads^{11),12),13),14)} were proposed and investigated because these are more suitable for gusty or non-stationary incident wind, finite element modeling, feedback-dependent structural control, and fatigue-life prediction. Cao

⁺¹hsauder@iastate.edu, ⁺²pparkar@iastate.edu

and Sarkar¹⁵⁾ developed an algorithm to experimentally extract time-domain rational function coefficients for a section model while Chang and Sarkar¹⁶⁾ developed a method to experimentally extract the time-domain buffeting indicial functions. A time-domain procedure for predicting the loads and response which uses both the rational function coefficients and the buffeting indicial functions, was also developed and validated¹⁷⁾. Sauder and Sarkar¹⁸⁾ employed these methods to extract the rational function (RF) coefficients and the buffeting indicial functions for a thick, asymmetric wind turbine blade airfoil corresponding to different mean angles of attack. In the current paper, these time-domain RF and buffeting indicial function coefficients are used to predict the total aeroelastic loads acting on an airfoil section model that was subjected to stationary wind, ramp-shaped gusty wind, and turbulent wind. The predictions are compared to the measured loads to validate the procedure.

2. TIME-DOMAIN EQUATIONS FOR AEROELASTIC LOADS

For wind turbine blades, it is sufficient to consider only the vertical and torsional modes of vibration because airfoils are designed to have low drag coefficients. For other structures, it might be necessary to consider the along-wind motion as well. In this paper, only the self-excited and buffeting loads are included because vortex-induced loads are not typically a problem for current wind turbine blades. The equations of motion can be written as

$$m(\ddot{h} + 2\zeta_h\omega_h\dot{h} + \omega_h^2h) = L_{ae} = L_b + L_{se} \quad (1)$$

$$I(\ddot{\alpha} + 2\zeta_\alpha\omega_\alpha\dot{\alpha} + \omega_\alpha^2\alpha) = M_{ae} = M_b + M_{se} \quad (2)$$

where m is the mass per unit length; I is the mass moment of inertia about the centroidal axis per unit length; $h(t,x)$, $\alpha(t,x)$ are the vertical (cross-wind) and torsional displacements, respectively; ζ_h, ω_h are the damping ratio and the natural frequency for the vertical mode; $\zeta_\alpha, \omega_\alpha$ are the damping ratio and the natural frequency for the torsional mode; $(\dot{}) = d()/dt$; $(\ddot{}) = d^2()/dt^2$; L_{ae} is the total aeroelastic lift; M_{ae} is the total aeroelastic moment; L_{se} is the self-excited lift; M_{se} is the self-excited moment; L_b is the buffeting lift component; and M_b is the buffeting moment component.

(1) Self-excited loads

The self-excited lift and moment for a wind turbine blade section in time-domain, as obtained by transforming the rational function formulation from Laplace domain, can be written as

$$L_{se}(t) = \frac{1}{2} \rho U^2 c \left\{ \begin{array}{l} ((\underline{A}_0)_{11} + (\underline{F})_{11}) \frac{h}{c} + (\underline{A}_1)_{11} \frac{\dot{h}}{U} - (\underline{F})_{11} \frac{\lambda_L U}{c^2} \int_0^t e^{-\frac{U}{c} \lambda_L (1-\tau)} h(\tau) d\tau \\ + ((\underline{A}_0)_{12} + (\underline{F})_{12}) \alpha + (\underline{A}_1)_{12} \frac{c}{U} \dot{\alpha} - (\underline{F})_{12} \frac{\lambda_L U}{c} \int_0^t e^{-\frac{U}{c} \lambda_L (1-\tau)} \alpha(\tau) d\tau \end{array} \right\} \quad (3)$$

$$M_{se}(t) = \frac{1}{2} \rho U^2 c^2 \left\{ \begin{array}{l} ((\underline{A}_0)_{21} + (\underline{F})_{21}) \frac{h}{c} + (\underline{A}_1)_{21} \frac{\dot{h}}{U} - (\underline{F})_{21} \frac{\lambda_M U}{c^2} \int_0^t e^{-\frac{U}{c} \lambda_M (1-\tau)} h(\tau) d\tau \\ + ((\underline{A}_0)_{22} + (\underline{F})_{22}) \alpha + (\underline{A}_1)_{22} \frac{c}{U} \dot{\alpha} - (\underline{F})_{22} \frac{\lambda_M U}{c} \int_0^t e^{-\frac{U}{c} \lambda_M (1-\tau)} \alpha(\tau) d\tau \end{array} \right\} \quad (4)$$

where ρ is the air density; U is the mean velocity; c is the chord length; $\underline{A}_0, \underline{A}_1$ are the stiffness and damping matrix, respectively; \underline{F} is the lag matrix, all of order 2×2 , and λ_L and λ_M are the lag coefficients. The elements of $\underline{A}_0, \underline{A}_1$ and \underline{F} matrices and λ_L and λ_M are known as the Rational function coefficients.

(2) Buffeting Loads

In time domain, buffeting lift and moment for a wind turbine blade section can be formulated using the buffeting indicial functions in terms of non-dimensional time, $s = Ut/c$, as follows:

$$L_b(s) = \frac{1}{2} \rho U^2 c^2 \left[\frac{2C_L}{U} \int_0^s u(\sigma) \phi_L'(s-\sigma) d\sigma + \frac{C_D + C_L'}{U} \int_0^s w(\sigma) \phi_L'(s-\sigma) d\sigma \right] \quad (5)$$

$$M_b(s) = \frac{1}{2} \rho U^2 c^2 \left[\frac{2C_M}{U} \int_0^s u(\sigma) \phi_M'(s-\sigma) d\sigma + \frac{C_M'}{U} \int_0^s w(\sigma) \phi_M'(s-\sigma) d\sigma \right] \quad (6)$$

where u and w are the longitudinal and vertical components of wind turbulence fluctuations and ϕ_L' and ϕ_M' are the derivatives of the buffeting indicial functions ϕ_L and ϕ_M with reduced time. C_L , C_D , and C_M are the static force coefficients for lift, drag, and moment, respectively, and C_L' and C_M' are the derivatives with respect to angle of attack.

3. EXPERIMENTAL SET-UP

The experimental tests presented here were performed on a larger section model in order to show that the coefficients extracted on the smaller section model could be used to predict the loads on a model of a larger scale. This allows the functions to reasonably be extended to predict the loads on an actual wind turbine blade.

(1) Description of Wind Tunnel Used

The experiments described here were performed in the Aerodynamic and Atmospheric Boundary Layer (AABL) wind and gust tunnel located in the Wind Simulation and Testing Laboratory (WiST Lab) in the Department of Aerospace Engineering at Iowa State University. This wind tunnel has an aerodynamic test section of 2.44 m (8.0 ft) width \times 1.83 m (6.0 ft) height, an atmospheric boundary layer test section of 2.44 m (8.0 ft) width \times 2.21 m (7.25 ft) height, and a designed maximum wind speed of 53 m/s (173.9 ft/s) in the aerodynamic section. An active gust generator was developed and implemented by Haan et al.¹⁹⁾ in this wind tunnel. The gust generator works by diverting air to and from the main duct to a bypass duct which allows the flow velocity in the test section to be increased or reduced in a short duration.

(2) Model

A profile view of the National Renewable Energy Laboratory (NREL) S830 (21% thickness to chord ratio) airfoil is shown in Fig. 1. This airfoil is part of the S-series family of airfoils that are thick (high thickness to chord ratio), generate low-noise during operations and aerodynamically efficient with high lift-to-drag ratio, for use in 20-25 m wind turbine blades.

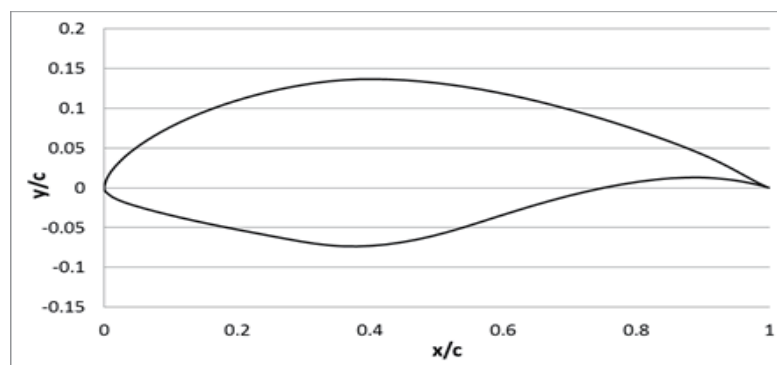


Figure 1: Non-dimensionalized profile of the NREL S830 airfoil.

The section model used for the experiment is shown in Fig. 2. The model is constructed out of a rectangular wooden spar with foam airfoil sections mounted over the top. The length L , chord length c , and thickness t of the model are about 1.52, 0.508, and 0.107m, making this model 3.3 times larger than the section model used to extract the rational function and buffeting indicial function coefficients. The two-DOF model suspension

system used in this experiment is also shown in Fig. 2. The suspension system enables vertical (h) and torsional (α) motions using 12 linear helical springs, six at each end of the model. Free vibration tests were completed prior to the wind tests to determine the two uncoupled stiffness coefficients of the two-DOF system for each DOF, calculated as $K_h = 2,233.5$ N/m and $K_\alpha = 103.72$ Nm/rad, respectively. The natural frequencies

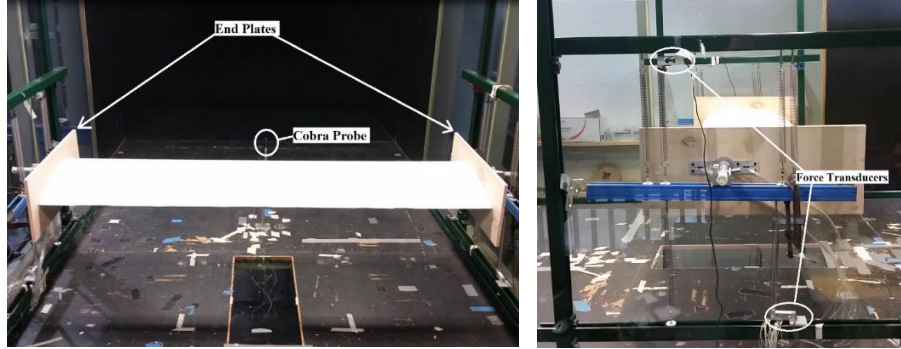


Figure 2: Section model and experimental set up: (left) view from downstream; (right) view from side.

were also measured in the free vibration tests as $f_h = 1.98$ Hz and $f_\alpha = 3.43$ and the mechanical damping ratios of the system as $\zeta_h = 0.24\%$ and $\zeta_\alpha = 0.45\%$. To induce coupling and hence vibration in the model, two C-clamps were added as lumped masses, one on each side of the model span at a distance of 0.25 m downstream of the model shaft. The mass and the mass moment of inertia of the entire dynamic system were $M = 14.88$ kg and $I = 0.0059$ kg/m².

(4) Rational and Indicial Functions for the S830 airfoil

A section model ($c = 152.4$ mm, $t = 32$ mm, $L = 450$ mm) of the NREL S830 airfoil with end plates was placed in the Bill James Wind Tunnel (0.915 m width by 0.762 m height), an open return tunnel in the Wind Simulation and Testing Laboratory at Iowa State University, for the extraction of the rational function coefficients and the buffeting indicial functions with two separate sets of experiments. In these experiments four angles of attack were used (0, 3, 6, 9 deg), but the validation effort presented here corresponds to the 3 degree angle of attack (AOA). The rational function coefficients and the derivatives of the buffeting indicial functions for 3° AOA, as extracted in Sauder and Sarkar¹⁸⁾, are given below:

$$\underline{A}_0 = \begin{bmatrix} -8.2582 & -14.2616 \\ 1.2395 & 5.4781 \end{bmatrix}; \underline{A}_1 = \begin{bmatrix} -7.0203 & -7.4707 \\ 1.2396 & 3.0931 \end{bmatrix}; \underline{F} = \begin{bmatrix} 6.9796 & 8.9027 \\ -0.8657 & -4.9014 \end{bmatrix}$$

$$\lambda_L = 0.0157; \lambda_M = 0.282$$

$$\phi'_L = 0.016 \cdot e^{-0.0367 \cdot s} + 0.088 \cdot e^{-0.167 \cdot s}$$

$$\phi'_M = 0.0031 \cdot e^{-0.0326 \cdot s} + 0.189 \cdot e^{-0.211 \cdot s}$$

In these tests, the static force coefficients were also measured as follow: $C_L = 0.66$, $C_L' = 5.29$, $C_D = 0.02$, $C_M = -0.26$, $C_M' = 1.63$.

(3) Instrumentation

In this experiment, wind velocity time histories were measured by a Cobra Probe (Turbulent Flow Instrumentation) placed immediately upstream of the airfoil section model. The sampling rate was set at 312.5 Hz. The vertical and torsional displacement of the model was measured by measuring the elastic force in each of four helical springs, which are connected to the model at one end and a strain gauge force transducer at the other end, as show in Fig. 2. The LabVIEW program was used for data acquisition and the sampling rate was set to 625 Hz. The aerodynamic pressures were also recorded in the experiment to determine the aeroelastic loads for comparison with those obtained through numerical simulation. The pressures were measured through 24 pressure taps placed along the upper and lower surface at the centerline of the model. A 64-channel pressure module (Scanivalve ZOC33/64 Px) was used to measure the pressures. The sampling rate was 312.5 Hz and

Scanivalve's Scantel was used for data acquisition. Data synchronization was accomplished using an external trigger to begin data acquisition for all three instruments.

4. RESULTS AND DISCUSSION

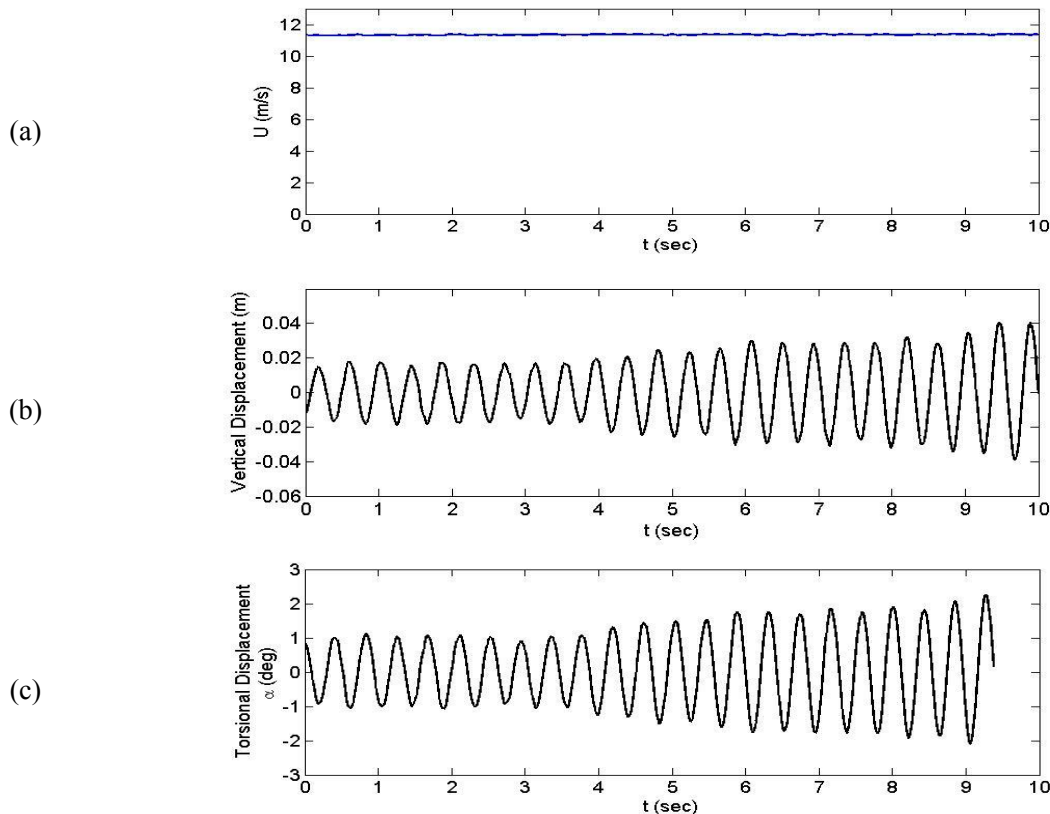
In the wind tunnel tests, the wind speed was increased until the model was on the edge of divergent flutter and both the model displacement and pressures were recorded during the vibration. Tab. 1 shows the predicted flutter speed and the measured flutter speed for this section model. The measured model displacements $[h(t)$ and $\alpha(t)]$, their first derivatives $[\dot{h}(t)$ and $\dot{\alpha}(t)]$ were calculated using finite difference method, and the previously extracted rational function coefficients were input into Eqs. 3 and 4 to simulate the self-excited lift and moment at each time step. Similarly, the time history of the turbulent wind velocity (both u and w) was input into Eqs. 5 and 6 to simulate the buffeting lift and moment at each time step. Four cases were considered: stationary wind (Turbulence Intensity $TI = 0.27\%$), ramp-down gust, low turbulence ($TI = 0.85\%$) and high turbulence ($TI = 11.7\%$) to evaluate the predictions in time-domain.

Table 1: Error in original flutter speed prediction for the airfoil prediction

Predicted Flutter Speed	Measured Flutter Speed	Error
11.42	11.35	0.61%

(1) Load Prediction for Stationary Wind Case

For the stationary wind case, the aeroelastic loads were predicted and measured at a mean wind speed of about 11.35 m/s, as can be seen in the velocity time history show in Fig. 3(a). The measured turbulence intensity by the Cobra Probe was 0.27% and, therefore, this flow condition can be classified as smooth flow which limits the effect of the buffeting loads. Figs. 3(b) and 3(c) show the time histories for the vertical (cross wind, h) and torsional (α) displacements that were used in the prediction of the aeroelastic loads. Finally, Figs. 3(d) and 3(e) show the comparison of the measured and simulated non-dimensionalized lift and moment, respectively.



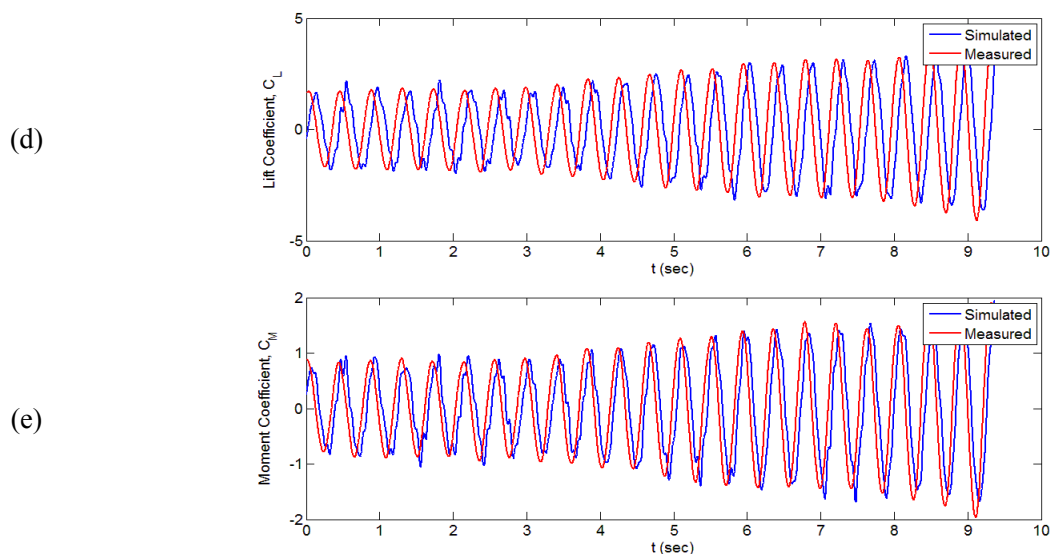
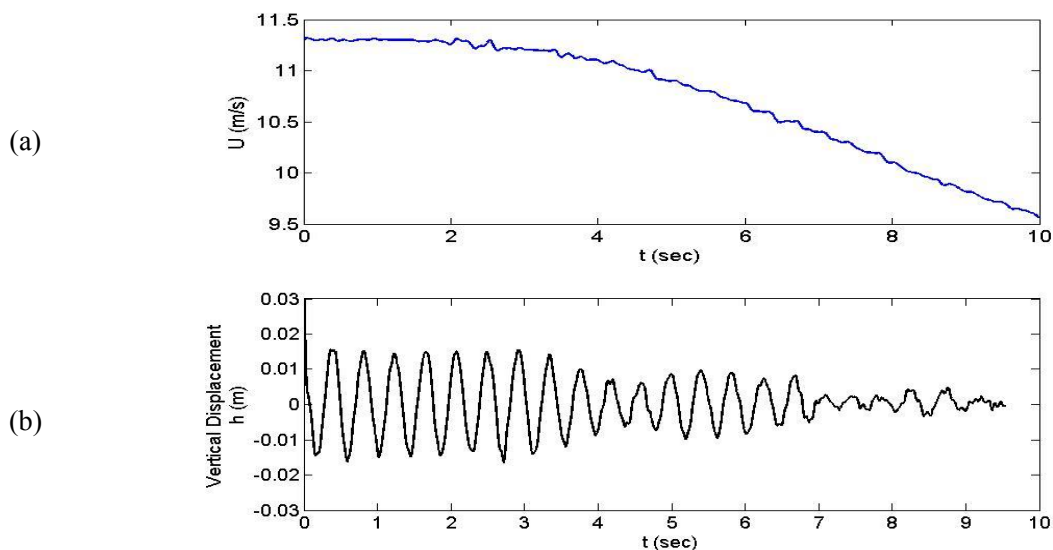


Figure 3: (a) Measured wind speed for stationary wind case; (b) Measured vertical (cross-wind) displacement; (c) Measured torsional displacement; (d) Comparison of the numerically simulated lift with measured; (e) Comparison of numerically simulated moment with measured.

As can be observed from the lift and moment comparison plots, the moment coefficient time history prediction matches well with the experimental results for both amplitude and phase angle. While the amplitude of the lift coefficient was predicted well, the predicted phase angle was slightly different from that of the measurement. Cao and Sarkar¹⁷⁾ saw a similar shift, but in the moment coefficient. It was theorized that it was due to an error in the extracted rational function coefficients that are related to the flutter derivative A_2^* . Another reason for this slight error in the predictions could be attributed to the current formulation that used only one lag term for lift or moment, whereas additional lag term(s) could be used to improve the predictions that will be examined in the future.

(2) Load Prediction for Ramp-Down Gusty Wind Case

To ultimately validate the feasibility of the time domain formulation for this airfoil in a non-stationary wind environment, the wind tunnel tests were carried out in a ramp-down gusty wind. The horizontal wind velocity time history is shown in Fig. 4(a) and the corresponding displacement and force coefficient time histories are plotted in Figs. 4(b) to 4(e).



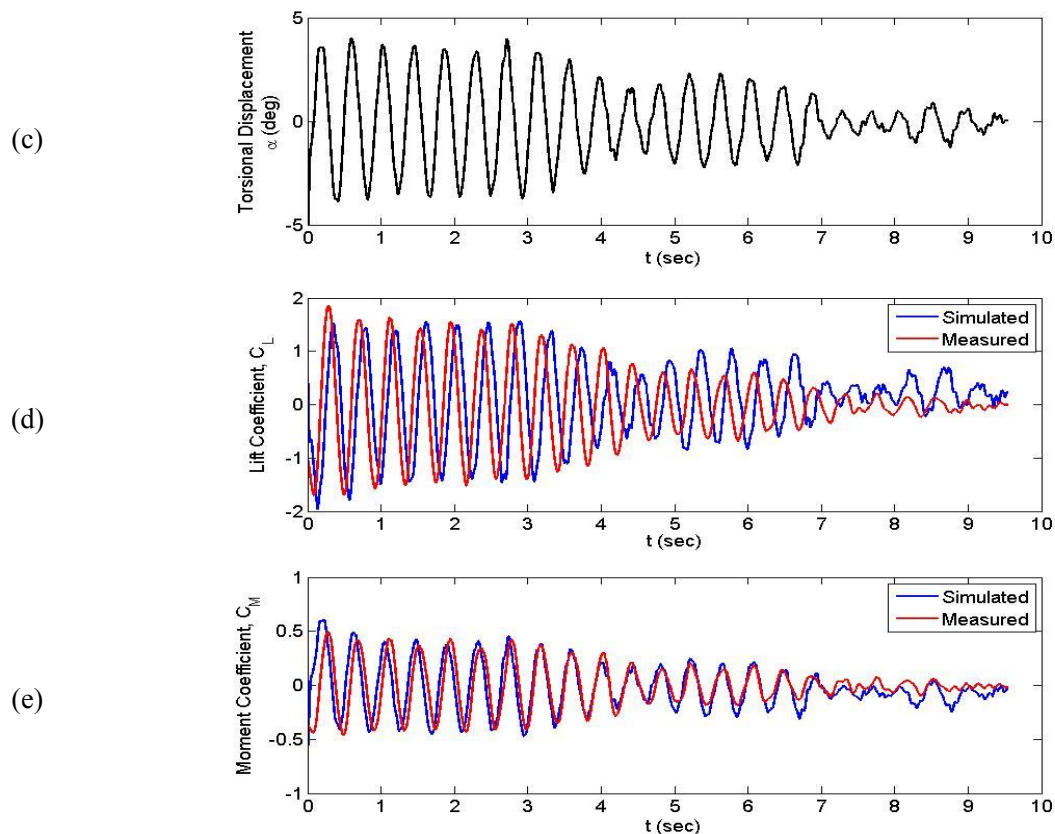


Figure 4: (a) Measured wind speed for gusty wind case; (b) Measured vertical (cross-wind) displacement; (c) Measured torsional displacement; (d) Comparison of the numerically simulated lift with measured; (e) Comparison of numerically simulated moment with measured.

For this gusty wind case, it is observed that the amplitudes of the load coefficients are predicted well for the first half of the time intervals. However, in the later part of the time histories the lift coefficient is over predicted and the moment coefficient is slightly under predicted. Moreover, the phase shift between the simulated and measured results is still present in both lift and moment. Given intrinsic errors in the pressure measurements, errors in extracting the time-domain coefficients and errors in the numerical differentiation and integration procedures used, the comparison seems quite encouraging.

(3) Load Prediction for Turbulent Wind Cases

Two turbulent wind cases were examined to evaluate this prediction procedure in more complex scenarios. The first, or low turbulence, case has a measured turbulence intensity of 0.85%. This turbulence was generated by placing 4in roughness elements in the diffuser section of the wind tunnel (following the fan section). This use of roughness elements resulted in the nearly sinusoidal wind velocity in both the along wind (u) and the vertical (w) components of velocity. Fig. 5(a) shows the along-wind measured velocity. Figs. 5(b) to 5(e) show the measured displacements and comparison of the simulated and the measured lift and moment coefficients. There are slight errors in the predicted amplitudes at certain moments in time, but the overall prediction is quite good given that it was turbulent wind.

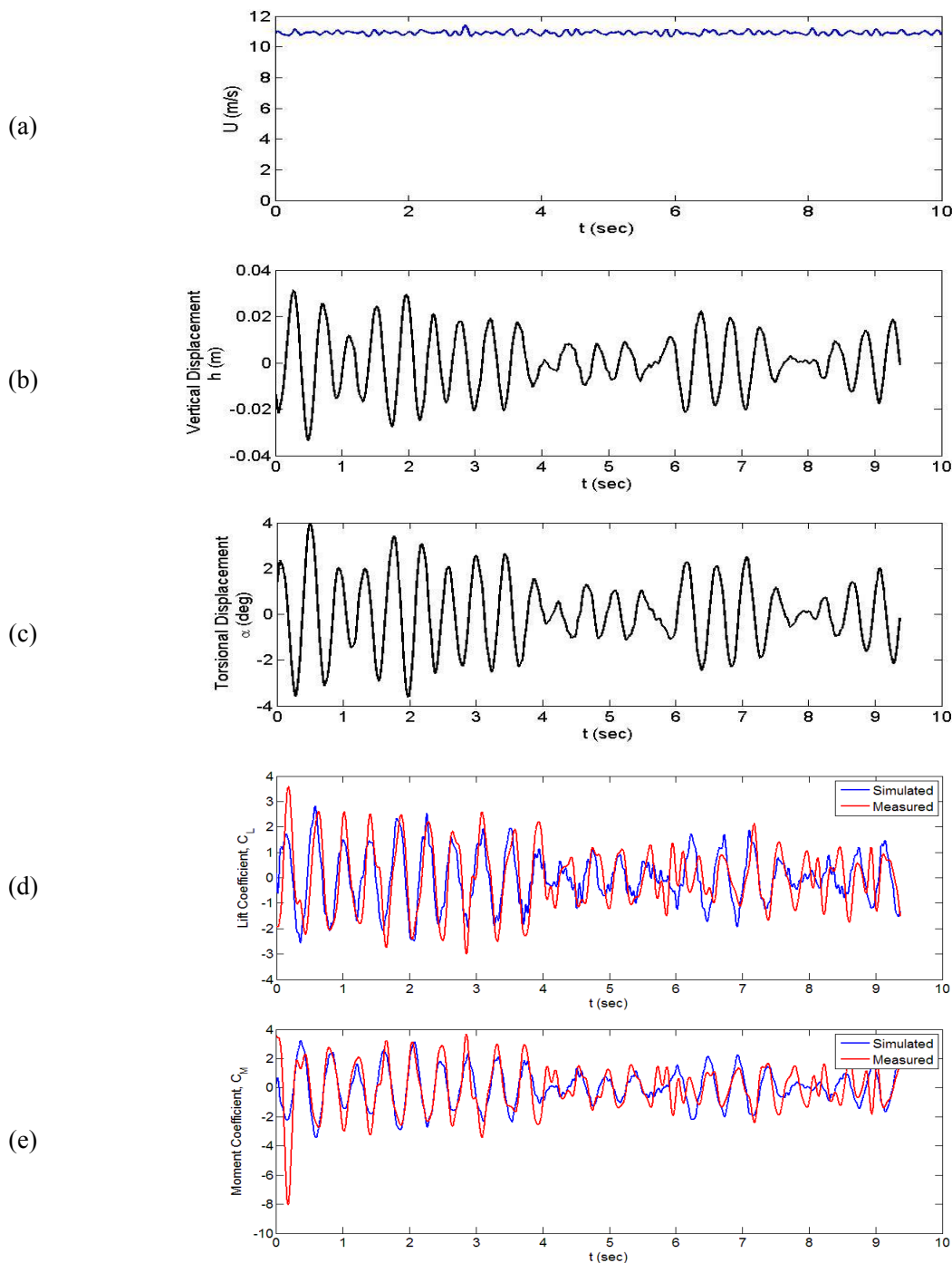


Figure 5: (a) Measured wind speed for low turbulence wind case; (b) Measured vertical (cross-wind) displacement; (c) Measured torsional displacement; (d) Comparison of the numerically simulated lift with measured; (e) Comparison of numerically simulated moment with measured.

The second turbulent wind case that was evaluated is considered a high turbulence case with a turbulence intensity of 11.7%. This turbulence intensity is much lower than the Lower Turbulence wind classes set by the IEC 61400-1²⁰ standard for wind developers, but has a good representation of how this time domain formulation would work for an actual wind turbine operating in the field. The turbulence in this case was generated using 4 spires (0.13m base and 1.17m height). These spires were placed 2.5m upstream of the model.

The horizontal wind velocity generated in this case is shown Fig. 6(a) and the comparison of the measured and the simulated load coefficients are shown in Fig. 6(b) and 6(c). The amplitudes here are

occasionally over predicted or under predicted, however the overall pattern and standard deviation between the two compare well with a 7.3% and a 11.0% error in the standard deviation of the lift and moment coefficients, respectively. Given this information, this procedure seems to hold up even in a high turbulence situation.

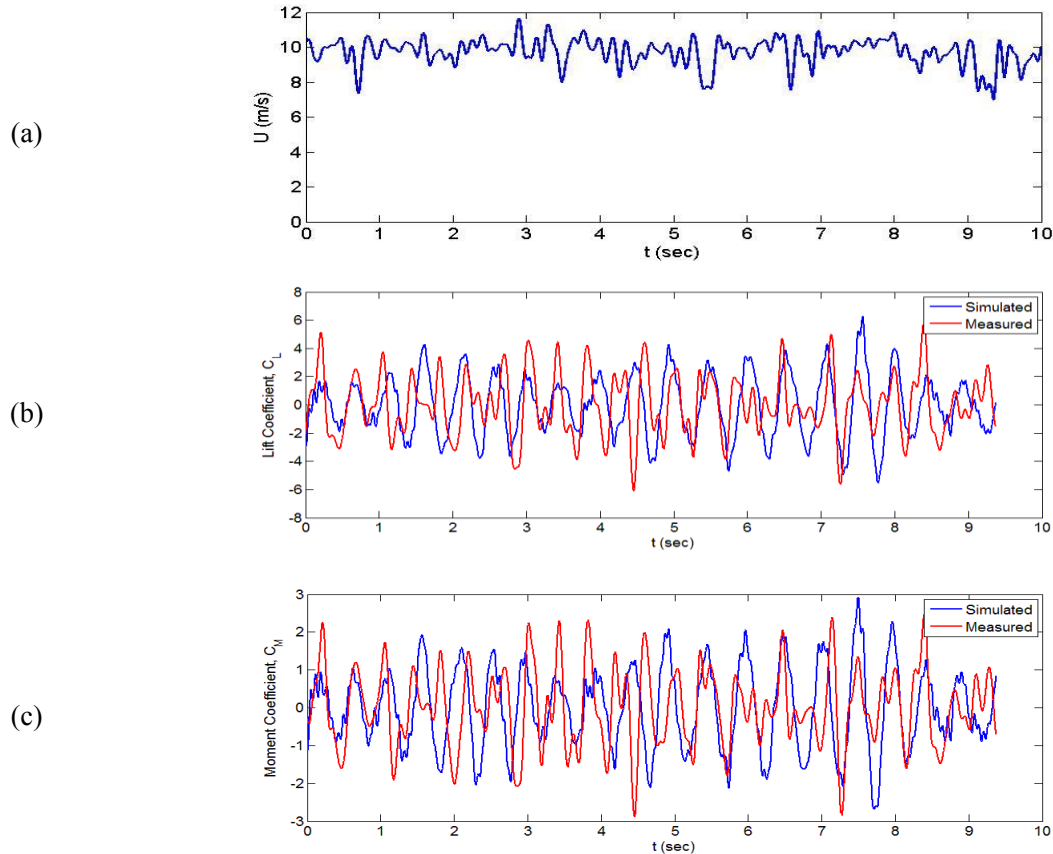


Figure 6: (a) Measured wind speed for the high turbulence wind case; (b) Comparison of the numerically simulated lift with measured; (c) Comparison of numerically simulated moment with measured.

5. CONCLUSIONS AND FUTURE WORK

In order to validate the time domain formulation for predicting aerodynamic loads on a wind turbine blade airfoil at a non-zero angle of attack, experiments were carried out for four different wind inputs (stationary, ramp-down gust, low turbulence and high turbulence). In each case, the amplitudes and pattern of the simulated aerodynamic loads (lift and moment) compared well with those measured, however, there was a slight phase shift in the time histories. This shows that this formulation and procedure to predict aerodynamic loads in real time using the incident wind information will be very useful for structural health monitoring applications and hence preventive maintenance and also for the evaluation of the fatigue life of wind turbine blades. Future work will include a second lag term in the self-excited load formulation using rational function coefficients to improve the phase shift error and evaluate this procedure when blade rotation is added.

ACKNOWLEDGMENTS

This work is supported by Grant # 13-02 from the Iowa Energy Center; their support is gratefully acknowledged. The author⁺¹ is supported under the U.S. National Science Foundation Grant No. 1069283 which supports the activities of the Integrative Graduate Education and Research Traineeship (IGERT) in Wind Energy Science, Engineering and Policy (WESEP) at Iowa State University.

REFERENCES

- 1) Theodorsen, T. : General theory of aerodynamic instability and mechanism of flutter. NACA Report 496, 1935.
- 2) Riziotos, V.A., Voutsinas, S.G., Politis, E.S., Chaviaropoulos, P.K. : Aeroelastic stability of wind turbine airfoils: the problem, the methods, and the issues. *Wind Energy*, Vol. 7, pp. 373-392, 2004.
- 3) Lobitz, D.W. : Aeroelastic stability predictions for MW-sized blades. *Wind Energy*, Vol. 7, pp. 211-224, 2004.
- 4) Jeong, M.S., Lee, I., Yoo, S.J., Park, K.C. : Torsional stiffness effects on the dynamic stability of horizontal axis wind turbine blades. *Energies*, Vol. 6, pp. 2242-2261, 2013.
- 5) Scanlan, R.H., Tomko, J.J. : Airfoil and bridge deck flutter derivatives. *J. Eng. Mech. Div.*, Vol. 97, Pt. 6, pp. 1717-1733, 1971.
- 6) Hansen, M.H. : Improved modal dynamics of wind turbines to avoid stall induced vibrations. *Wind Energy*, Vol. 6, pp. 179-195, 2003.
- 7) Rasmussen, F., Petersen, J.T., Madsen, H.A. : Dynamic stall and aerodynamic damping. *J. of So. Energy Eng.* Vol. 21, Pt. 3, pp. 51-55, 1999.
- 8) Chaviaropoulos, P.K. : Flap/lead-lag aeroelastic stability of wind turbine blade sections. *Wind Energy*, Vol. 2, Pt. 2, pp. 99-112, 1999.
- 9) Gan Chowdhury, A., Sarkar, P.P. : A new technique for identification of eighteen flutter derivatives using a three-degree-of-freedom section model. *Eng. Struct.*, Vol. 25, pp. 1763-1772, 2003.
- 10) Yamada, H., Ichikawa, H. : Measurement of aerodynamic parameters by extended Kalman filter algorithm. *J. Wind Eng. Ind. Aerodyn.*, Vol. 42, pp. 1255-1263, 1992.
- 11) Lin, Y.K., Ariaratnam, S.T. : Stability of bridge motion in turbulent winds. *J. Struct. Mech.*, Vol. 8, Pt. 1, pp. 1-15, 1980.
- 12) Chen, X., Matsumoto, M., Kareem, A. : Time domain flutter and buffeting response analysis of bridges. *J. Eng. Mech.*, Vol. 126, Pt. 1, pp. 7-16, 2000.
- 13) Salvatori, L., Borri, C. : Frequency and time-domain methods for numerical modeling of full-bridge aeroelasticity. *Comp. Struc.*, Vol. 110, Pt. 11-14, pp. 675-687, 2007.
- 14) Zhang, Z., Chen, Z., Cai, Y., Ge, Y. : Indicjal functions for bridge aeroelastic forces and time-domain flutter analysis. *J. Bridge Eng.*, Vol. 16, Pt. 4, pp. 546-557, 2011.
- 15) Cao, B., Sarkar, P.P. : Identification of rational functions using two-degree-of-freedom model by forced vibration method. *Eng. Struct.*, Vol. 43, pp. 21-30, 2012.
- 16) Chang, B., Sarkar, P.P., Phares, B.M. : A time-domain model for predicting aerodynamic loads on a slender support structure for fatigue design. *J. Eng. Mech.*, Vol. 136, Pt. 6, pp. 736-746, 2010.
- 17) Cao, B., Sarkar, P.P. : Time-domain aeroelastic loads and response of flexible bridges in gusty wind: prediction and experimental validation. *J. Eng. Mech.*, Vol. 139, Pt. 3, pp. 359-366, 2013.
- 18) Sauder, H.S., Sarkar, P.P. : Time-domain aeroelastic loads and response of wind turbine blades. *Proc. 14th Int. Conf. on Wind Eng.*, Int. Association for Wind Eng., Porto Alegre, Brazil, 2015.
- 19) Haan, F.L., Sarkar, P.P., Spencer-Bergen, N.J. : Development of an active gust generation mechanism on a wind tunnel of wind engineering and industrial aerodynamics applications. *Wind Struct.*, Vol. 9, Pt. 5, pp. 369-386, 2006.
- 20) IEC 61400-1 third edition 2005-08 Wind turbines – Part 1: Design requirements, International Electrotechnical Commission, IEC, 2005.

PRELIMINARY INVESTIGATION OF A FLAPPING VERTICAL AXIS WIND TURBINE

Yutaka Terao
Tokai University, Sizuoka, Japan

Vertical axis wind turbine (VAWT) is one of the promising wind energy conversion systems and many ideas are proposed to improve this performance. In this paper, newly designed Flapping VAWT (FVAWT) system performance is discussed. We will discuss the efficiency of this system using with a simple two dimensional hydrofoil theory and compare the performance of fixed type VAWT and FVAWT. Numerical calculation shows the FVAWT is 15% higher performance compared with the fixed type VAWT system without any external energy supply.

Keyword: Flapping Foil, Vertical Axis Wind Turbine, Hydrofoil Motion Foil Control

1. INTRODUCTION

Fixed type VAWT such as H type or Darius type wind turbine are simple but rather poor performance is reported compared to the cycloidal one. In the foil azimuth angle is near zero degree, which zone is the maximum relative velocity acting on the foil, both VAWT foil system can't generate trust or foil rotating torque but only generate the drag force or negative turbine driving torque. It is well known that the flow energy is proportional to the cubic of the flow speeds; therefore if we introduce some mechanisms to generate the foil thrust or driving torque with small mechanical loss, this may increase these VAWT performances. In this system, it will distribute the absorbed energy in one foil circular motion to the energy of the foil heaving damping works and acting as the optimization of the total energy gain.

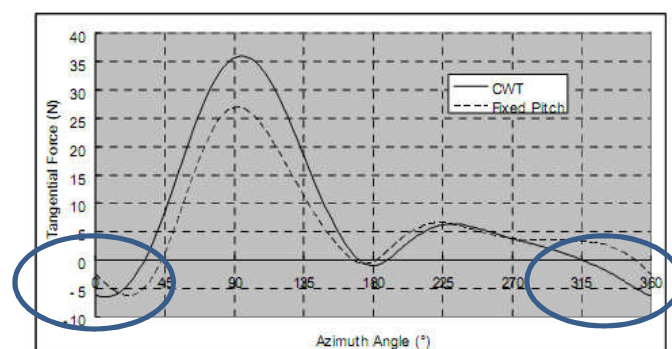


Figure 1. VAWT hydrofoil thrust (tangential) force.

In the azimuth angle 0 and 180 deg., negative thrust force zone appeared.

In a system with a vertical-axis hydrofoil, even a pitch-controlled system that theoretically should be able to achieve optimum efficiency, no torque is produced when the relative flow rate is a maximum. When such a turbine is rotating, right at the point when the wind becomes a head wind, the hydrofoil is simply subject to resistance, so naturally no torque is generated that would cause the hydrofoil to rotate.

However, because the wind flow speed rate relative to the hydrofoil surface at this point is a maximum, if it was possible to have the air strike the hydrofoil at a certain angle, thrust and torque could be generated. A search of the literature for information relating to this idea turned up no results.

Having come this far, the next step was to consider a hydrofoil drive mechanism designed for this purpose. With that in mind, I devised a number of feasible methods and mechanisms. The following describes one of these approaches.

2. FLAPPING VERTICAL AXIS WIND TURBINE MECHANISM

Regardless of what method is used, it should be possible to configure a system to control the heaving motion of the rotor hydrofoil. However, the system can only be put into practical use if it is as straightforward as possible, and is highly robust. I came up with a number of mechanisms that would satisfy these requirements, and here I will describe one that is highly promising in terms of practical use.

Let us consider the performance of a VAWT that rotates while generating a heaving motion in the hydrofoil. One way of controlling the hydrofoil motion would be to have an arm with joints, which would fold to control the heaving motion of the hydrofoil. Hereafter, we will call this the flapping vertical-axis wind turbine (FVAWT). Figure 2 shows a schematic view of the FVAWT with simple link system. Photograph 1 and 2 show functional model of FVAWT, with spur gear and link system, made of ABS materials with 3-D printer. The hydrofoil is set holding and open condition with link system.

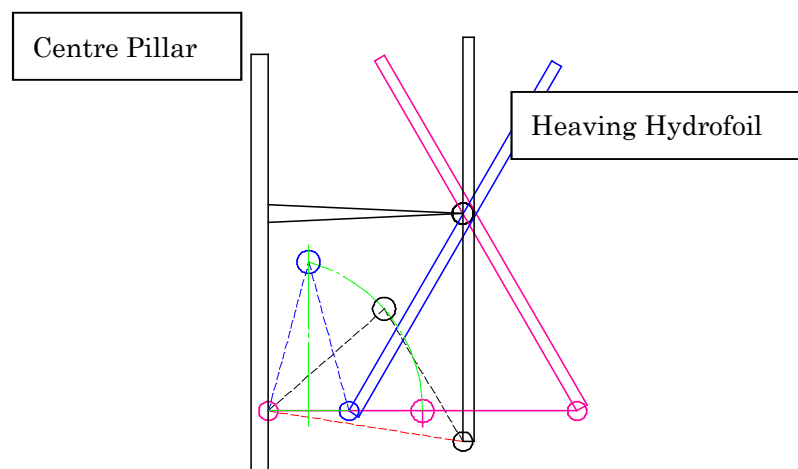


Figure 2. A concept of the foil heave motion controlled VAWT
Schematic view shows the foil's heave motion is controlled by the arms with 3 joints.



Photograph 1. Foil Closed FVAWT with spur gear.



Photograph 2. Foil Opened FVAWT with spur gear.

This method involves a new principle of hydrofoil motion. Even if the hydrofoil is a rotor hydrofoil, it can normally be controlled using two control parameters that increase the hydrofoil performance. One of these is the pitch angle of the hydrofoil, and a method using efficient hydrofoil angle control for VAWTs based on the azimuth angle and relative flow speed is already in practical use. The Voith Schneider propeller uses this method.

In this section, I evaluate the performance of a VAWT, based on the idea of controlling the heaving motion of the rotary hydrofoil and improving the energy absorption efficiency. The reason that I have not previously come across an idea such as this may be because of the centrifugal force generated by the rotor hydrofoil.

However, devices have already been researched and developed in which a hydrofoil is positioned to act in the same way as the tail fin of a fish in a uniform flow such as an ocean or tidal current, causing the hydrofoil to vibrate and absorb the energy of the flow.

3. ENERGY BALANCE

In order to control the heaving motion of a rotating hydrofoil, let us look at the energy balance required. To make the hydrofoil undergo heaving motion, we need to identify where the energy comes from to provide that motion. That is, obtaining this energy from a part of the hydrofoil positive trust azimuth angle zone, and redistributing this kinetic energy to the negative trust azimuth angle zone. Main object is looking for a point at which the rotational energy balance becomes positive during a single rotation of the hydrofoil motion, compared to normal VAWTs as shown in Fig.3. It might be possible to implement a control principle based on this, but the hydrofoil turning trajectory would not be a perfect circle as shown in Fig.4.

Energy flow will be shown as Fig.5, and if the flapping hydrofoil absorbed energy exceed the work done by the hydrofoil, this idea and foil control system will be success.

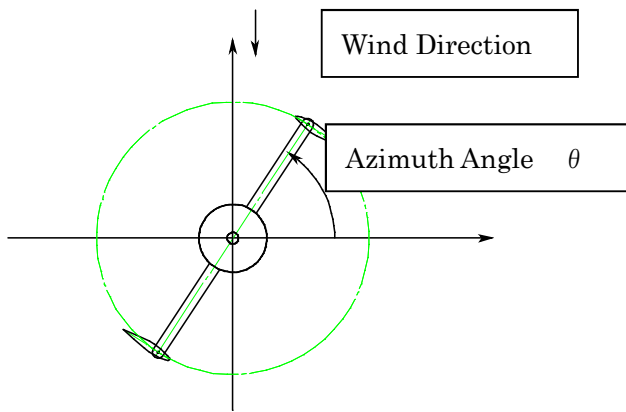


Figure 3. Normal VAWT at operation.

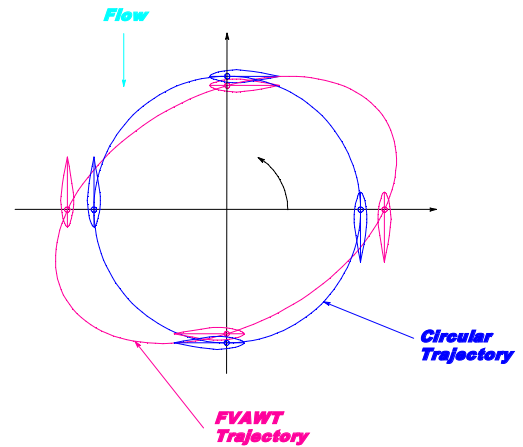


Figure 4. FVAWT foil trajectory.

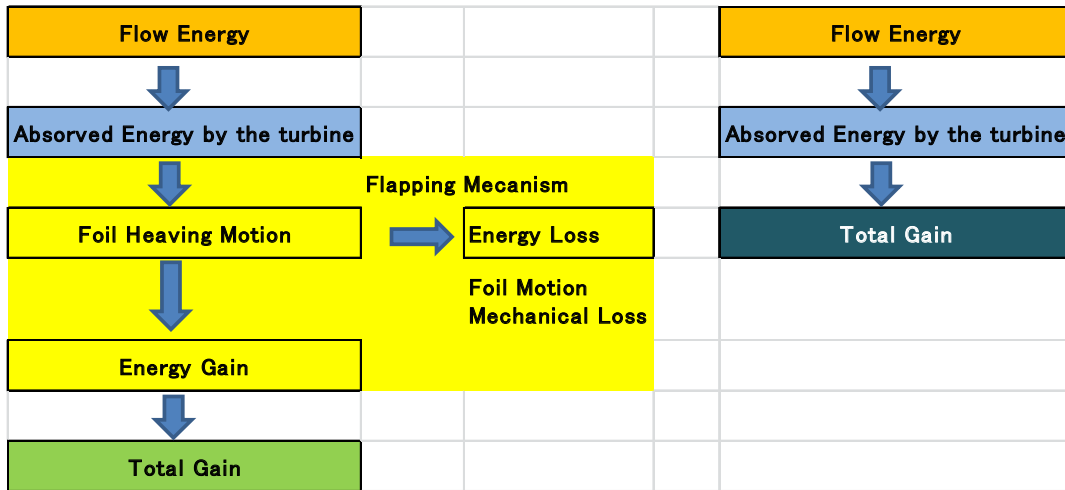


Figure 5. Energy flow diagram (left is FVAWT and right is fixed pitch normal VAWT)
 Yellow zone is newly added function of FVAWT.

We will consider the energy gain about a normal VAWT hydrofoil, which undergoes simple circular motion, and an FVAWT hydrofoil, in which the trajectory changes and no more circular motion. We will carry out some numerical calculations to explore the energy balance for these hydrofoil systems.

Here, denoting the angle for which the hydrofoil is turning at the maximum relative velocity as $\theta=0$.
 The inflow rate is:

$$u = (U + r\dot{\theta}) \tag{1}$$

The velocity of the hydrofoil in the vertical direction was set to be lower than this velocity. U is flow speed, r is rotating arm length and θ is rotating angle.

$$v = \dot{r} \tag{2}$$

The inflow angle is approximated as: $\alpha = \frac{v}{u}$.

Here,

$$u^2 = (U + r\theta)^2 + v^2 \quad (3)$$

$$\cong (U + r\theta)^2 \quad (4)$$

and the lift force generated by the hydrofoil is:

$$L = \frac{1}{2} \rho S u^2 C_L(\alpha) \quad (5)$$

$$T = L \sin \alpha \quad (6)$$

$$\cong L \alpha \quad (7)$$

$$= \frac{1}{2} \rho S u^2 k \alpha^2 \quad (8)$$

S is foil area, ρ is fluid density. And considering the three-dimensional lift force correction parameter k,

$$k = \frac{2\pi\Lambda}{2+\Lambda} \quad (9)$$

Λ : foil aspect ratio

The thrust is given by:

$$T = \frac{1}{2} \rho S (\dot{r})^2 k \quad (10).$$

However, this can be evaluated as increasing the thrust,

$$\varepsilon = 1 + \left\{ \frac{v}{(U+r\theta)} \right\}^2 \quad (11)$$

causing it to double. Here, for purposes of simplification, (10) is used for evaluation.

Also, at the position of the minimum relative flow rate,

$$u^- = (U - r\theta) \quad (12)$$

Carrying out a similar approximation, then

$$T^- = \frac{1}{2} \rho S (\dot{r})^2 k \quad (13)$$

In this case, however, the result will contain a larger error than with the (10) approximation.

Because this thrust will always be positive, it might be possible to overcome a disadvantage of the normal VAWT, which is that the thrust of the VAWT goes from zero to a negative value.

4. NUMERICAL ANALYSIS

An even number of hydrofoils is better in terms of keeping the configuration simple, so here I used two hydrofoils. However, I calculated the hydrodynamic force acting on only one hydrofoil, and did not take hydrofoil interference into consideration. Also, I created the simplest possible hydrofoil analysis model, not taking fluid hysteresis into consideration. The reason for this is that the focal point of interest in this experiment is how the energy balance changes in response to the heaving motion of the hydrofoil.

The parameters necessary for the calculation are the hydrofoil amplitude, frequency and phase. The heaving amplitude r for the FVAWT is added to the rotation radius R for a normal VAWT. The parameter evaluated in the analysis is r/R . The rotating speed of the normal VAWT is ω , and that of the FVAWT is $n\omega$,

where n is set at first as an integer value. The FVAWT system, to decide the hydrofoil heaving motion, motion phase angle must be introduced. After these parameters, the heaving motion of the FVAWT hydrofoil trajectory to be described.

Parametric survey of the dependence of the energy acquisition rate on r/R is examined under the given phase conditions for which the acquired energy is largest.

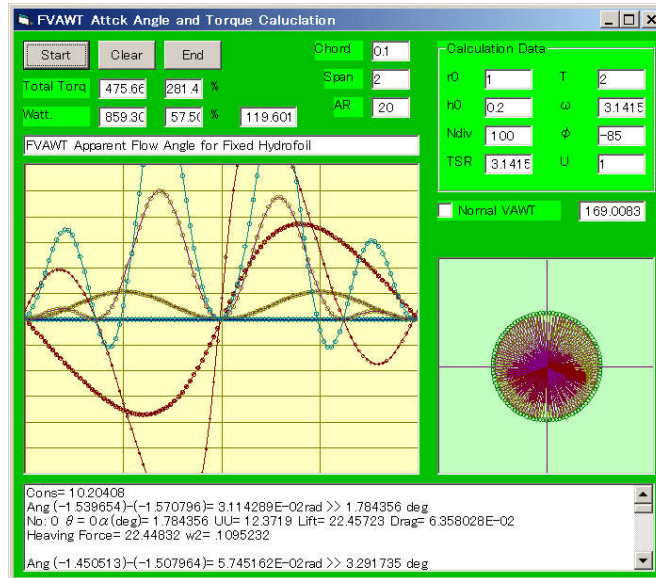


Figure 6. A sample of the FVAWT calculation.

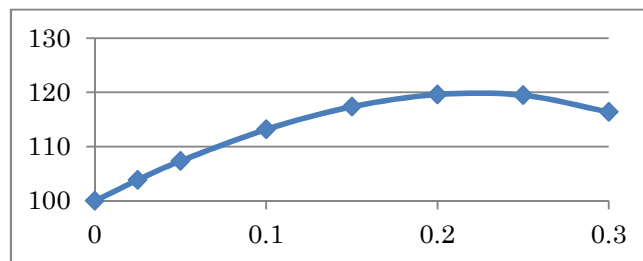


Figure 7. Energy gain (%) vs. heave amplitude/radius.

Fig.6 shows an example when the heaving period is set to twice the rotation period of the hydrofoil, and Fig.7 shows the corresponding gain. From Fig.7, it can be seen that when the heaving amplitude is around 20% of the rotation radius, the maximum energy is obtained. It is also clear, however, taking stalling of the hydrofoil into consideration, that it will not be possible to achieve performance at this level.

The heaving motion at this time is determined as shown below. We call $n\omega$ as the mode is n . Here, the mode is set to 2.

$$h(t) = \sum_{i=1}^n h_i \sin(2i\omega t + \varphi_i) \tag{14}$$

If asymmetrical movement is allowed, then

$$h(t) = \sum_{j=1}^n h_j \sin\{(2j - 1)\omega t + \varphi_j\} \tag{15}$$

φ_j is j -th phase angle. In this case, the centrifugal force due to the rotation of the hydrofoil cannot be canceled, and this causes vibration. If this vibration is not considered a problem, the energy absorption can be

calculated.

Let us calculate this using $j=1$, with mode 1. Fig.8 and Fig.9 shows calculated results. The gain changes significantly as a result of the rotational motion of the hydrofoil and the phase of the hydrofoil heaving motion. Naturally, the point of maximum efficiency is at a phase angle of 90° as shown in Fig.10.

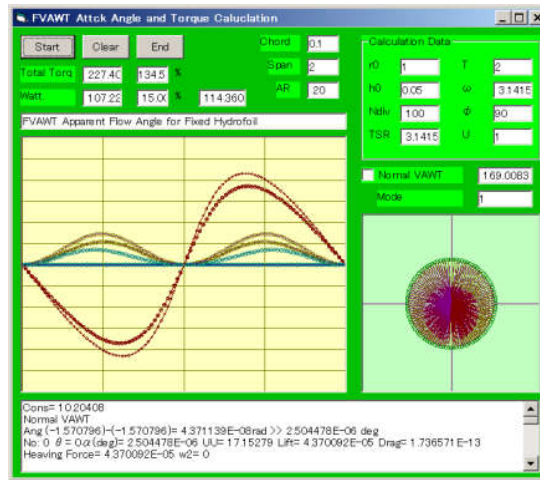


Figure 8. Efficiency of the VAWT and FVAWT at mode=1.

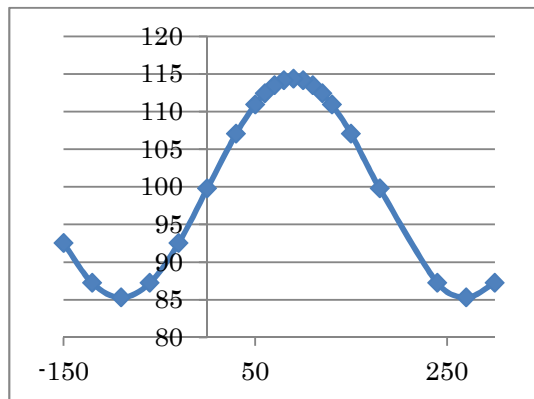


Figure 9. Gain with Mode=1, case with asymmetric heaving motion. Heave amplitude / turning radius=0.05.

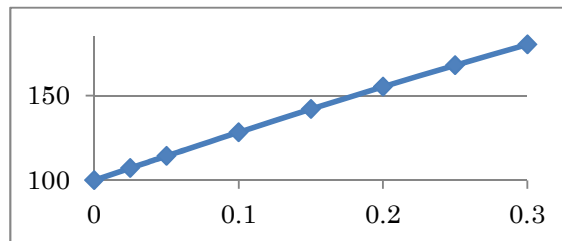


Figure 10. Energy gain(%) vs. heave amplitude/radius asymmetric motion. Mode=1, $\phi = 90^\circ$. I must expect the foil stall phenomena in this case.

Following intuition, the performance is calculated for different modes. The phase of the heaving motion must be correct in relation to the current flow in order to produce sufficient power. If we calculate

another mode, Mode=1.5, this means three foil flapping motions is conducted while two circulating motion. As shown in Fig.11 and Fig.12, zero phase angle is optimum.

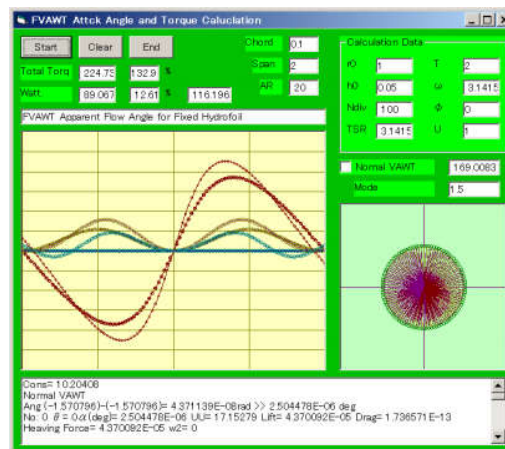


Figure 11. Calculated FVAWT performance at mode=1.5.

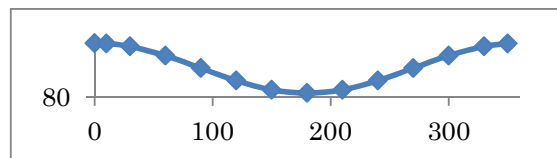


Figure 12. Phase and efficiency of FVAWT at mode=1.5.

5. CONCLUSION

In order to improve the efficiency of the VAWT based on the numeric calculation, the following guidelines were obtained for the FVAWT system.

- a) The energy absorption efficiency is strongly dependent on the flapping frequency, and should be up to three times as high of main rotating frequency.
- b) The amplitude ratio should be 0.2 or less.
- c) In the control scheme, it is necessary to consider the phase difference with respect to the current flow.
- d) For the amplitude characteristics, it is sensitive for stalling performance, has to be taken into consideration.

The calculation described here is an example of FVAWT performance evaluation using the simplest possible model. As a result, this paper describes just one aspect of performance improvement with adding the pure flapping motion of the hydrofoil.

In the future, I plan to perform higher-precision calculations using a hydrodynamic model, and to conduct experiments in a water tank in order to verify the improvement in performance of the VAWT using the new mechanism.

REFERENCE

- 1) Hwang. I.S, etc. 2005; Efficiency improvement of a new vertical axis wind turbine by individual active control of blade motion. <http://cyclocopter.snu.ac.kr/paper/SPIE2006.pdf>

FIELD MEASUREMENT OF THE MAIN SHAFT DYNAMIC LOADINGS ON A FIXED-SPEED ACTIVE STALL CONTROLLED 1MW WIND TURBINE

Sho Oh⁺¹

⁺¹ClassNK, Tokyo, Japan

Deeper understanding of the characteristics of the drive-train dynamic load under natural wind field is important because the failure it causes to wind turbine components will leads to long down time and sometimes serious accidents. In this study, field measurements are carried out on the main shaft of an active-stall controlled wind turbine located at a site where the surrounding ground surface varies from land to sea, and the dynamic characteristics of the bending moment, thrust and torque are evaluated according to the ground surface condition. While little difference could be seen between land wind and sea wind in the mean value of rotor thrust and torque, the mean tilt bending moment showed less value for land wind in higher wind speed compared to sea wind. For shaft tilt bending moment and torque there is a qualitative trend of load fluctuation per 1/3 of the rotation, which may considered to be the effect of each blade passing the tower shadows.

Keyword: low-speed shaft bending moment, torque fluctuation, wind shear

1. INTRODUCTION

Failures in wind turbine drivetrain components, such as bearings and gears, cause high cost for repair and replacement operation¹⁾ and the study of failure mechanisms is an urgent task. Dynamic loadings of the main shaft are important factors for drivetrain components as external excitation forces. As studies have shown that not only torque but also non-torque loadings of the main shaft have a large effect on the component failures²⁾, evaluation of the characteristics of the dynamic loadings, such as bending moment, thrust, and torque acting on the main shaft is necessary for the understanding of the drivetrain behavior.

Meanwhile, the peculiarity of wind turbine loadings is their large variation driven by the fluctuating wind. Therefore a qualitative evaluation of the impacts of wind field parameters on the shaft loadings would help not only to get insights of the mechanism of wind oriented drivetrain behavior, but also to estimate the difference in drivetrain loadings for different sites. Considering that the aerodynamic analysis of wind turbines includes the uncertainties of aerodynamic coefficients and control algorithms, statistical analysis of field measurement data are performed in previous studies. However, previous studies of field measurements on wind turbines focused mainly on towers and shaft fatigue loads³⁾ and studies with a focus on main shaft dynamics is limited. Link et al. ⁴⁾ carried out field tests on the main shaft as well as the planetary gears to determine the characteristic input signal to dynamometer tests, and more detailed information of the characteristics of dynamic loading of the main shaft is required for further study of drivetrain behavior.

The aim of this study is to provide qualitative information of the dynamic loadings of main shaft for future studies of drivetrain behavior. In this study, field measurement is carried out on the main shaft and the tower of a 1MW wind turbine with three-point supporting drivetrain. The measured results for bending moment, estimated thrust and torque of the main shaft is presented and the dependence on ground surface is discussed.

2. OUTLINE OF ON-SITE MEASUREMENT

(1) On-site measurement

The target wind turbine is a fixed-speed, active-stall controlled 1MW Bonus wind turbine. The hub

⁺¹s-oh@classnk.or.jp

height is 45m and the rotor radius is 27m. Outline of the target wind turbine is shown in Figure 1, and details of the wind turbine are shown in Table 1.

For measurement of main shaft loading, pairs of strain gauges are attached at two points; one pair is between main bearing and hub, and the other pair is attached at the middle of the low speed shaft. Another strain gauge is also attached at the end of the shaft to measure the torque. Beside the torque sensor, one pulse sensor is attached to estimate the rotation speed as well as the azimuth angle of the rotor. Details of the devices of the shaft strain measurements are shown in Figure 1(Right). Thrust force of also important for drive-train loading. However, as the axial stiffness of the shaft is extremely high and the deformation will be too little to eliminate the measurement noises, it is difficult to directly measure the thrust force. In this study, tower loading is measured instead for thrust estimation assuming the aerodynamic force acting on tower in negligible compared to those acting on rotor during power generation. Strain gauges are attached for 16 directions separately at 3 heights of tower; 4.62m height, 38.1m height and 38.8m height. Rotor thrust force are evaluated using the average of the result from these three heights.

Table 1: Basic Wind Turbine Properties.

Wind Turbine	Bonus 1MW
Control strategy	Fixed-Speed Active-stall
Hub Height	45m
Rotor Diameter	27m
Cut-in/Cut-out	3m/s/25m/s
Number of main bearing	1
Gearbox	3-stage planetary-helical
Hub-Shaft Coupling	Flange
Shaft-Gearbox Coupling	Shrink

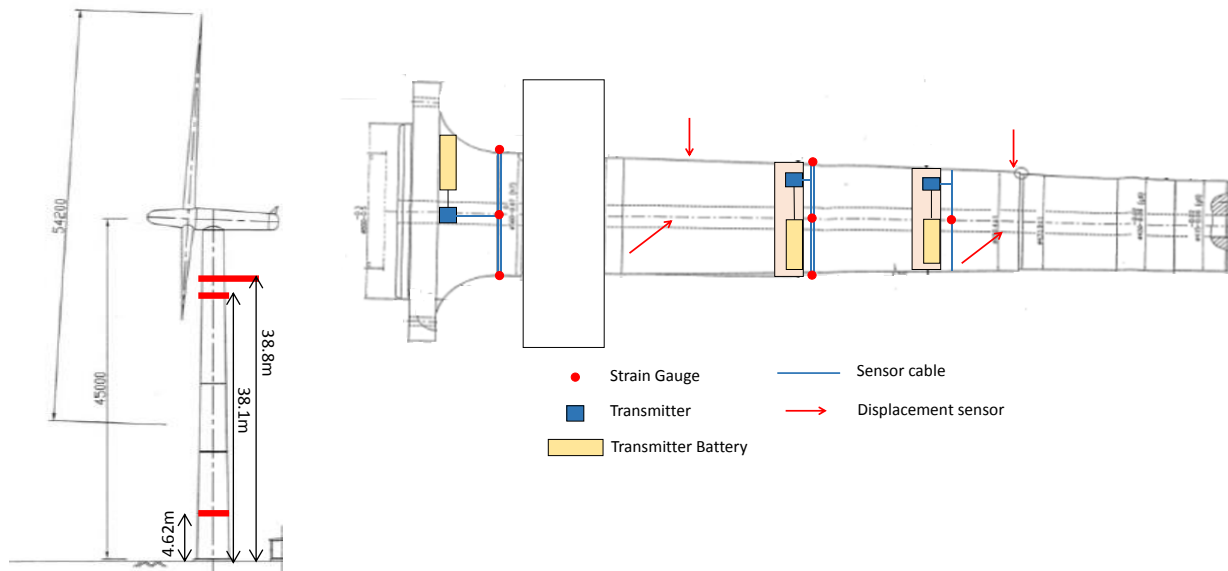


Figure 1: (Left) Outline of the target wind turbine and (Right) Detail of shaft measurement devices

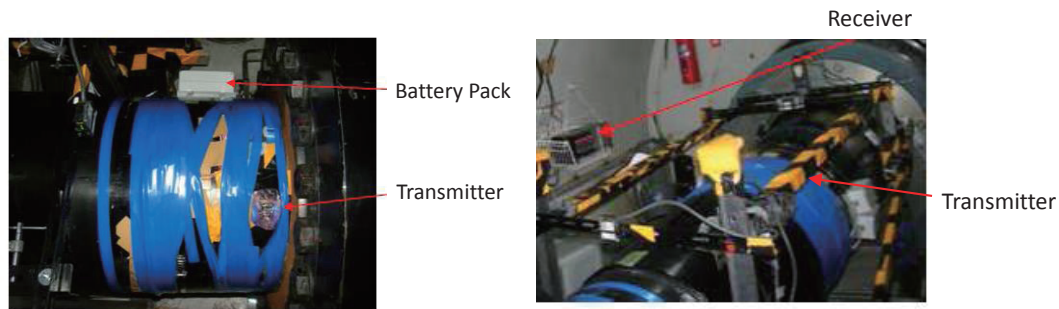


Figure 2: (Left) Transmitters and (Right) receivers used for shaft load measurement

For data acquisition of rotating sensors, telemetry systems are used for data acquisition. Picture of the transmitter and receiver of the system is shown in Figure 2. The transmitter is connected to the gauges and attached to and rotate with the shaft together with the battery pack which will last about several weeks while the receiver is fixed on the nacelle outer shell. All data are filtered with 20Hz low-pass filter, and are recorded with 50Hz sampling frequency.

After attachment of all the sensors, the whole nacelle is rotated slowly in order to evaluate the dead load for wind turbine tower. From the amplitude of the sinusoidal signal of strain during the rotation, tower dead load is estimated as 2876kNm at 4.62m height. Also, for the dead load evaluation of the low-speed shaft, the rotor is rotated slowly by manual under low wind speed condition. From the amplitude of the sinusoidal signal of the strain, the dead load for low-speed shaft is estimated as 212kNm for both bending measurement positions.

(2) Wind Field Measurement

Wind field measurements are carried out near the target wind turbine with Doppler Lidar. The location of Doppler Lidar and the wind turbine is shown in Figure 3. As can be seen from the figure, the surface condition is flat land for wind from east side, while for wind from west side the surface condition is open sea. In this study, wind directions from 170 degree to 350 degree are defined as sea wind and others are defined as land wind. Horizontal wind speeds from 40m to 220m heights are measured at 20m pitch with 1Hz sampling frequency. Figure 4 shows the measured and fitted vertical distribution of wind speed for sea wind and land wind. Figure shows that while the vertical distribution for sea wind is almost uniform due to the low surface roughness, those for land wind has larger shear. Figure 5 shows the turbulence intensity of land wind and sea wind, which took almost same value for reference turbulence intensity I_{ref} . The relationship of Doppler Lidar data and nacelle-mounted cup anemometer is also investigated and the correlation coefficient was 1.007 for 10 minute average wind speed.

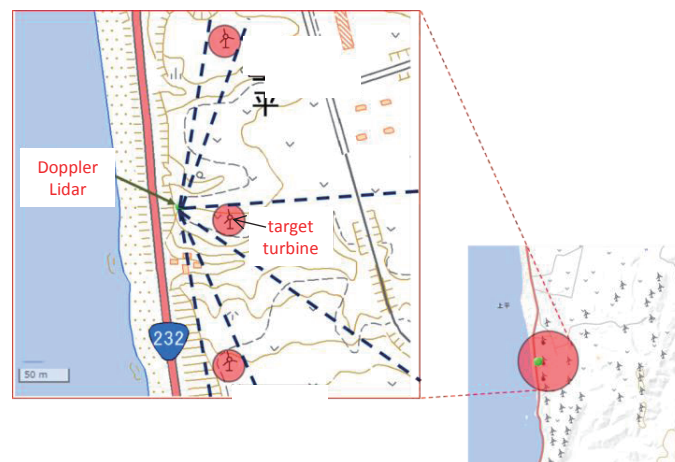


Figure 3: Position of Doppler Lidar and target wind turbine

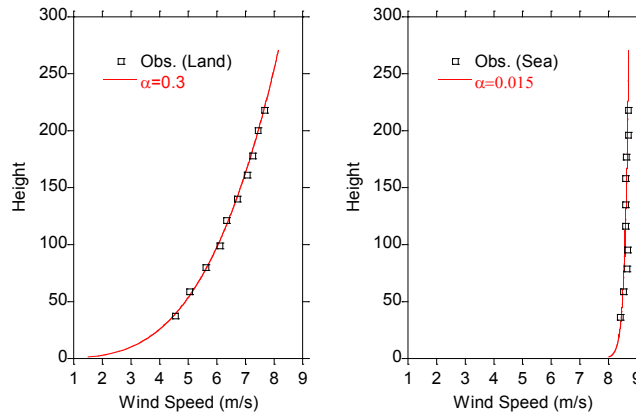


Figure 4: Measured vertical distribution of (a) land wind and (b) sea wind

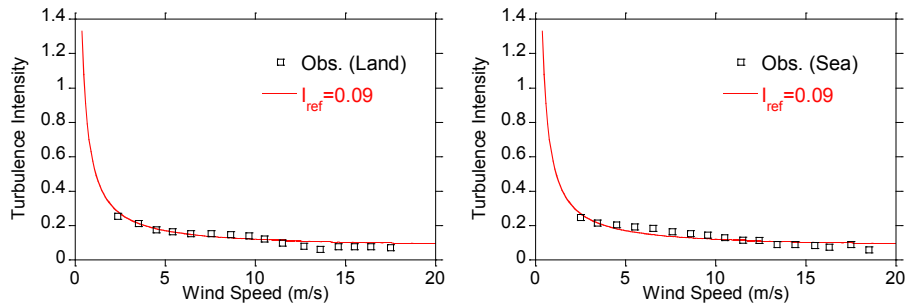


Figure 5: Turbulence intensity at 40m height for (a) land wind and (b) sea wind

3. RESULTS

(1) Shaft Tilt Bending Moment

Results of measured shaft tilt bending moment between hub and main bearing are shown in Figure 6. The left figure is for 10 minute average value, and the right figure is for 10 minute standard deviation. Figure shows that for all wind speed there is large mean bending moment acting on the shaft resulting from the rotor dead load. However, as the wind speed becomes higher, results for land wind and sea wind shows different trend; the mean bending moment remains almost same value for sea wind while those decrease with wind speed for land wind. This may largely due to the difference in wind shear acting on the rotor. For the standard deviations, there is no clear difference in the trend for land wind and sea wind. Results for land wind show slightly larger deviations than those for sea wind, which may be due to the difference in turbulence intensity.

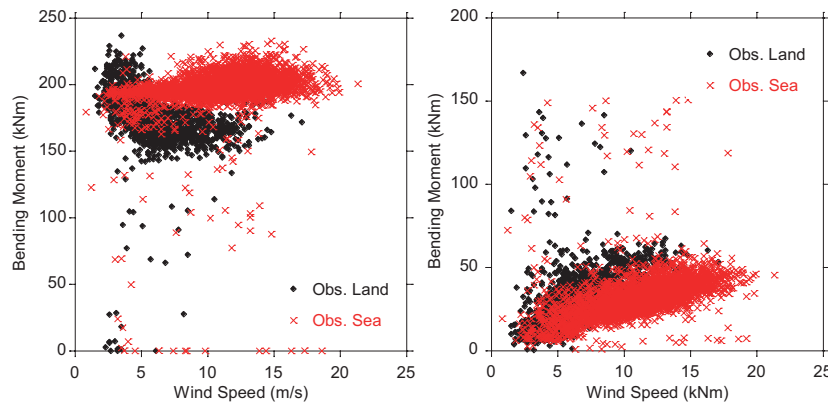


Figure 6: (Left)Mean and (Right)standard deviation of measured shaft tilt moment for land wind and sea wind

Two time-series data sets are chosen for detailed time-series investigation. One is November 24th 15:30-15:40 with the average wind speed 9.95m/s blowing from land and turbulence intensity 15%, the other

is November 22nd 8:50-9:00 with the average wind speed 9.90m/s blowing from sea and turbulence intensity 15%. During both time the wind turbine was operating at regulated rotor speed. 8 rotations were extracted from the data set and the bending moment is plotted against azimuth angle in Figure 7 as an example. Figure shows that there are larger fluctuations per one rotation for results for land wind. However, though there is less fluctuations per one rotation for sea wind, bending moments show almost same low frequency trend.

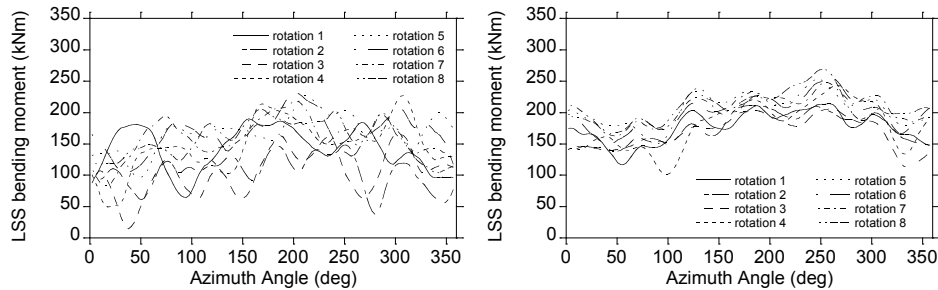


Figure 7: Shaft tilt bending moment vs azimuth angle for (Left) land wind and (Right) sea wind for 8 rotations

Figure 8 shows the average of the bending moment of 200 rotation data extracted from selected data series. As can be seen from the figure, there is certain trend of load decreasing per 1/3 of the rotation, indicating the effect of each blade passing the tower shadows. Result for sea wind shows clearer load variation, which may due to the lesser disturbance from wind.

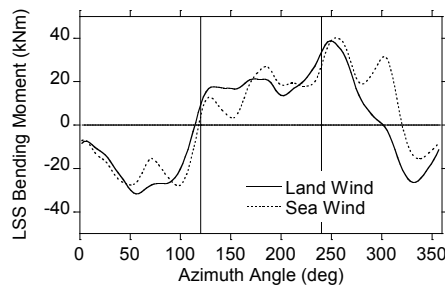


Figure 8: Comparison of averaged shaft tilt bending moment vs azimuth angle for land wind and sea wind

(2) Shaft Yaw Bending Moment

Results of measured shaft yaw bending moment between hub and main bearing are shown in Figure 9. The left figure is for 10 minute average value, and the right figure is for 10 minute standard deviation. Figure shows that for 10 minute average, the value changes from negative value to positive with increase of wind speed, and the effect of wind shear is relatively low. For standard deviation, data of land wind showed larger value than data of sea wind, which is the same trend with shaft tilt bending moment.

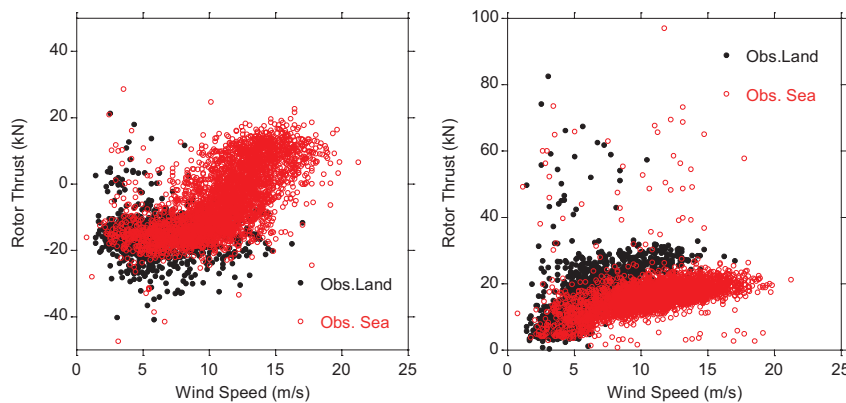


Figure 9: (Left)Mean and (Right) deviation of measured shaft yaw moment for land wind and sea wind

(3) Torque

Results of 10 minutes standard deviation for measured LSS torque are shown in Figure 10. Results show that large fluctuations in LSS torque are seen between the wind speed of 8m/s to 14m/s which may due to the switching of control strategy before and after rated wind speed. The difference between land wind and sea wind seems to be limited.

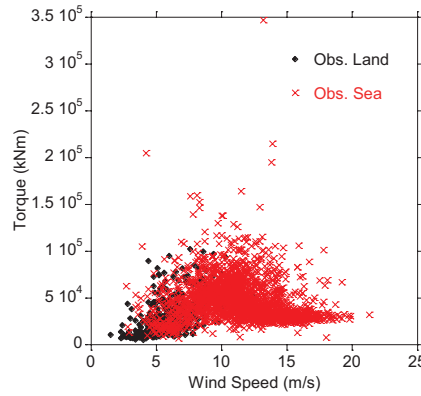


Figure 10: Comparison of measured tower along wind bending moment at 4.62m height from land wind and sea wind for (a) mean and (b) standard deviation

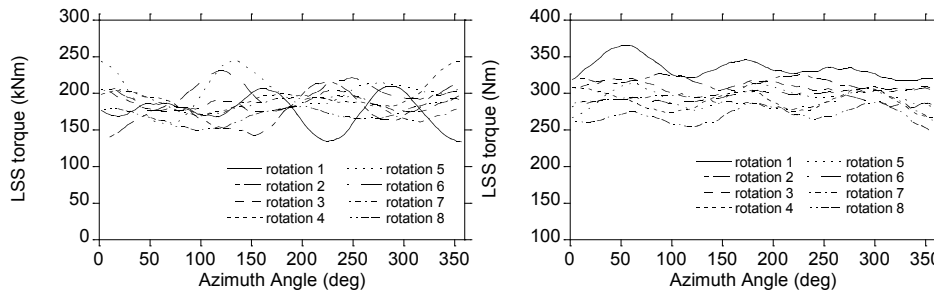


Figure 11: Torque vs azimuth angle for (Left) land wind and (Right) sea wind for 8 rotations

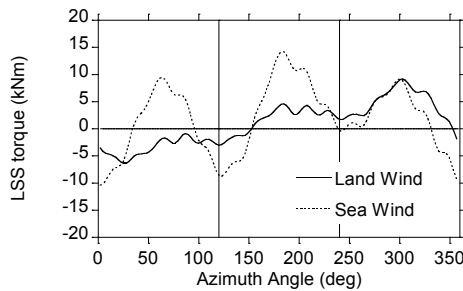


Figure 12: Comparison of averaged torque vs azimuth angle for land wind and sea wind

Variation of torque per one rotation versus azimuth angle is plotted for 8 rotations extracted from the data sets described above in Figure 11. Figure shows that the deviation per one rotation is almost same for land wind and sea wind. However, while some randomness in phase can be seen for land wind, the low frequency trend for sea wind seems almost same. Figure 12 shows the comparison of average of torque of 200 rotations extracted from the two selected data set for land wind and sea wind. Note that the mean torque is subtracted in order to compare the variation. Figure shows that there is periodicity in the torque variation per 1/3 of the rotation, indicating the effect from each blade. Results also show that the variation of averaged torque is lesser for land wind. This may due to the randomness shown in Figure 11 which may be caused from the larger turbulence intensity. Another explanation may be that since the sea wind has larger wind speed below hub height than land wind and the wind speed difference caused by tower shadow is proportional to

wind speed⁶⁾, the fluctuations is larger for sea wind under the condition of same hub-height wind speed.

(4) Estimated Thrust

Since the strain of main shaft due to thrust force is small and the measurement will be easily affected by noise, the thrust forces are estimated by assuming the tower bending moment are induced only by rotor thrust. Results of estimated thrust are shown in Figure 13. The left figure is for 10 minute average value, and the right figure is for 10 minute standard deviation. Measured data are chosen for those with positive power generation and those with regulated rotor speed regarding to SCADA data. Results show that there is no large difference between land wind and sea wind for tower bending moment for both heights and thus for rotor thrust. Results for land wind showed larger fluctuations compared to sea wind, which is may largely due to the larger turbulence intensity in this region.

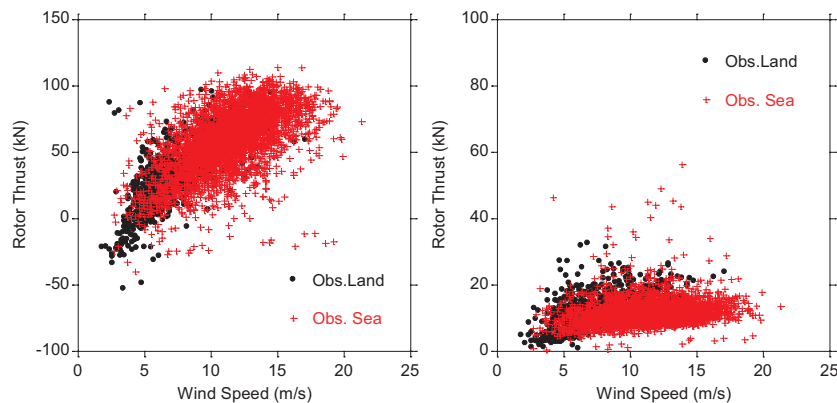


Figure 13: Comparison of estimated rotor thrust for (Left) mean and (Right) standard deviation

4. CONCLUSION

Bending moment and torque of low-speed shaft for an active stall controlled wind turbine is evaluated by direct on-site measurement and the following conclusions are obtained;

1. For all wind speed there is large mean bending moment acting on the shaft resulting from the rotor dead load. However, the mean bending moment remains almost same value for sea wind while those decrease with wind speed for land wind.
2. There is certain trend of load decreasing per 1/3 of the rotation for LSS bending moment, indicating the effect of each blade passing the tower shadow. Result for sea wind shows clearer load variation, which may due to the lesser disturbance from wind.
3. Large fluctuations in LSS torque are seen between the wind speed of 8m/s to 14m/s which may due to the switching of control strategy before and after rated wind speed.
4. Periodicity in the torque variation could be seen per 1/3 of the rotation, indicating the effect of each blade passing tower shadow. Result for sea wind shows clearer load variation, which may due to the lesser disturbance from wind.
5. There is no large difference between land wind and sea wind for mean value of estimated rotor thrust force.

ACKNOWLEDGMENT

This research is carried out as a part of a project funded by The New Energy and Industrial Technology Development Organization (NEDO), Japan. The target wind turbine is provided by Eurus Wind Energy along with its physical and operational information. Measurements were carried out under considerable support of stuffs from Tomamae Branch of Eurus Wind Energy. The author wishes to express the deepest gratitude to the concerned parties for their assistance.

REFERENCES

- 1) Tavner.P.: Offshore Wind Turbines-Reliability, availability & maintenance, The Institute of Engineering and Technology, 2012
- 2) Guo.Y., Keller.J., LaCava.W., Combined effects of gravity, bending moment, bearing clearance, and input torque on wind turbine planetary gear load sharing, NREL Technical Report CP-5000-55968, 2012
- 3) Mouzakis.F., Morfiadakis.E., Dellaportas.P., Fatigue loading parameter identification of a wind turbine operating in complex terrain, Journal of Wind Engineering and Industrial Aerodynamics, 82, 69-88, 1999
- 4) Link.H., LaCava.W., vanDam.J., McNiff.B., Sheng.S., Wallen.R., MacDade.M., Lambert.S., Butterfields.S., Oyague.F., Gearbox reliability collaborative project report; Findings from Phase 1 and Phase 2 testing, NREL Technical Report TP-5000-51885, 2011

AEROELASTIC STABILITY ANALYSIS OF OFFSHORE WIND TURBINE BLADES AT STANDSTILL CONDITION CONSIDERING UNSTEADY AERODYNAMICS

Koji FUKAMI⁺¹, Kai KARIKOMI⁺¹, Akihiro HONDA⁺¹ and Masaaki SHIBATA⁺²
⁺¹ Mitsubishi Heavy Industries, Ltd. (Research & Innovation Center), Nagasaki, Japan
⁺² Mitsubishi Heavy Industries, Ltd. (Energy & Environment Domain), Yokohama, Japan

This paper deals with aeroelastic stability analysis of offshore wind turbine blades at standstill condition considering unsteady aerodynamics focusing on the stall flutter of a coupled flap-and-edgewise bending motion. Taking an example of a 7MW offshore wind turbine, it was investigated that dynamic stall effect on the aeroelastic damping covering the whole regions of angle of attack and direction of blade vibration. To conduct the analysis, state space modeling was applied, which consists of linearized unsteady aerodynamic model as well as 1 DoF blade vibration model. According to the analysis, it was revealed that unsteady aerodynamics could alleviate aeroelastic instabilities to different but great extents for each region defined based on angle of attack and direction of blade vibration.

Keyword: wind turbine, aeroelastic stability, unsteady aerodynamics, stall flutter

1. INTRODUCTION

Wind power is one of the most widely installed renewable energies around the world – in particular, offshore wind is drawing growing interest in recent years as more powerful and boundless energy resources. To reduce the offshore wind cost, there is a clear design trend that offshore wind turbines are getting bigger and bigger in size (rotor diameter) and capacity (rated power) with much longer and even more slender rotor blades, whereby aeroelastic investigation of offshore wind turbine blades is becoming more important.

Aeroelastic instability problems for wind turbine blades can be classified into two types¹⁾. The first is a torsional flutter (or simply called flutter) in rotating condition. In extremely high tip speed region, especially in case of the over speed situation, pitching motion would be coupled with edgewise motion and could become unstable in some cases, however, it is considered that there is still a margin for the flutter speed as long as the turbine is operated within normal tip speed region. The second is a stall-induced flutter at standstill condition. A coupled flap-and-edgewise motion would become unstable when at least one of the blades would be exposed to an oblique strong wind inflow with angles of attack in deep stall region, which could take place during offshore transportation, assembly and maintenance at the site.

This paper deals with aeroelastic stability analysis focusing on the stall-flutter, taking an example of a 7MW offshore wind turbine, MWT167/7.0, which was developed by Mitsubishi Heavy Industries, Ltd., of which blades are the longest (81.6m) among all wind turbines in operation as of now. Unsteady aerodynamic model as well as quasi-steady aerodynamic model was used in order to investigate the dynamic stall effect on the aeroelastic damping, which was required to be investigated covering the whole regions of angle of attack and direction of blade vibration. In this study, state space representation was applied to model unsteady aerodynamics consisting of an effect of shed vorticity from the trailing edge based on Theodorsen's theory²⁾ and an effect of dynamics (time-lag) of separation point based on Leishman's formulation³⁻⁴⁾. According to the analysis, it was revealed that unsteady aerodynamics could alleviate aeroelastic instabilities to different but great extents for each region defined based on angle of attack and direction of blade vibration.

⁺¹koji_fukami@mhi.co.jp, ⁺¹kai_karikomi@mhi.co.jp, ⁺¹akihiro_honda@mhi.co, ⁺²masaaki1_shibata@mhi.co.jp

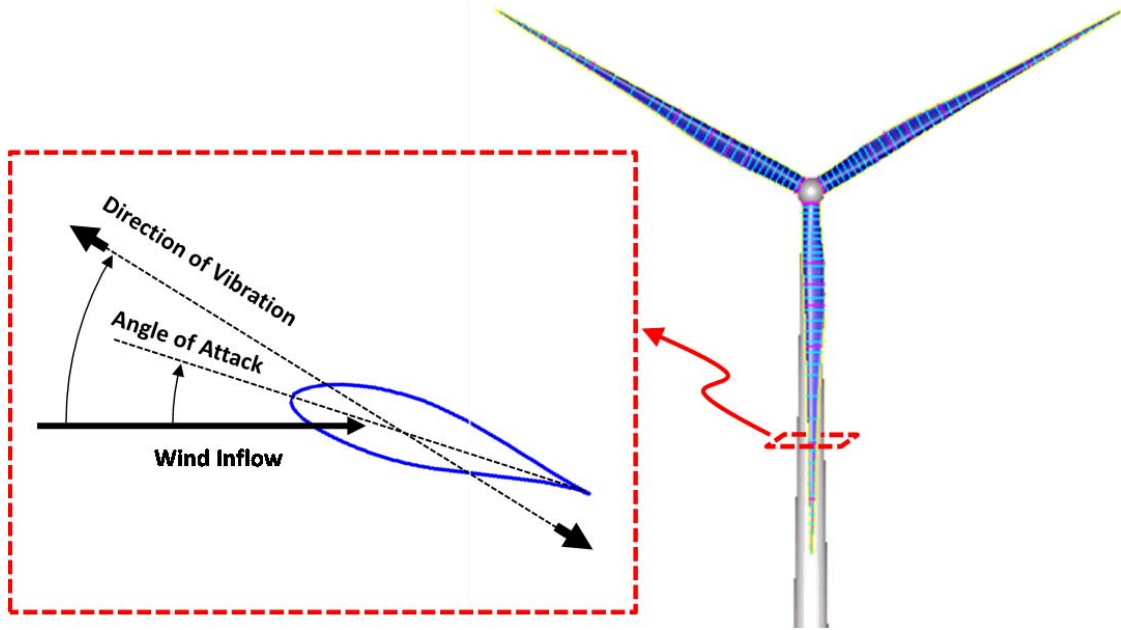


Figure 1: Schematic of the stall-induced flutter analysis of offshore wind turbines

2. UNSTEADY AERODYNAMIC MODEL

Unsteady lift and drag coefficient represented aerodynamic derivatives

$$\Delta C_L^{dyn} = C_{L\alpha}^{dyn} \cdot \Delta\alpha + C_{LX_1}^{dyn} \cdot \Delta x_1 + C_{LX_2}^{dyn} \cdot \Delta x_2 + C_{LX_4}^{dyn} \cdot \Delta x_4 \quad (1)$$

$$\Delta C_D^{dyn} = C_{D\alpha}^{dyn} \cdot \Delta\alpha + C_{DX_1}^{dyn} \cdot \Delta x_1 + C_{DX_2}^{dyn} \cdot \Delta x_2 + C_{DX_4}^{dyn} \cdot \Delta x_4 \quad (2)$$

State space representation of aerodynamic variables by one dimensional displacement of a blade section

$$\begin{bmatrix} 1 & 0 & 0 & 0 \\ 0 & 1 & 0 & 0 \\ 0 & 0 & T_p & 0 \\ 0 & 0 & 0 & T_f \end{bmatrix} \begin{bmatrix} \Delta \dot{x}_1 \\ \Delta \dot{x}_2 \\ \Delta \dot{x}_3 \\ \Delta \dot{x}_4 \end{bmatrix} = \begin{bmatrix} -b_1 \cdot \frac{2u_0}{c} & 0 & 0 & 0 \\ 0 & -b_2 \cdot \frac{2u_0}{c} & 0 & 0 \\ C_{L\alpha}^p & C_{L\alpha}^p & -1 & 0 \\ 0 & 0 & f_{\alpha 0} / C_{L\alpha}^p & -1 \end{bmatrix} \begin{bmatrix} \Delta x_1 \\ \Delta x_2 \\ \Delta x_3 \\ \Delta x_4 \end{bmatrix} + \begin{bmatrix} -A_1 \cdot b_1 \cdot \frac{2}{c} \cdot \sin \theta \\ -A_2 \cdot b_2 \cdot \frac{2}{c} \cdot \sin \theta \\ -C_{L\alpha}^p (1 - A_1 - A_2) \\ 0 \end{bmatrix} \Delta \dot{x} \quad (3)$$

3. EQUATIONS OF MOTION

One dimensional equation of motion

$$m\ddot{x} + 2m\zeta_n\omega_n\dot{x} + m\omega_n^2x = F_X \quad (4)$$

External force represented by lift coefficient and drag coefficient

$$F_X = L \sin(\theta - \Delta\varphi) - D \cos(\theta - \Delta\varphi) = \frac{1}{2} \rho c u^2 \cdot [C_L \sin(\theta - \Delta\varphi) - C_D \cos(\theta - \Delta\varphi)] \quad (5)$$

State space representation

$$\begin{bmatrix} \Delta\dot{x} \\ \Delta\ddot{x} \end{bmatrix} = \begin{bmatrix} 0 & 1 \\ -\omega_n^2 & -2\zeta_n\omega_n \end{bmatrix} \begin{bmatrix} \Delta x \\ \Delta\dot{x} \end{bmatrix} - \begin{bmatrix} 0 \\ \Delta F_X/m \end{bmatrix} \quad (6)$$

$$\Delta F_X = F_{\dot{x}} \cdot \Delta\dot{x} + F_{\ddot{x}} \cdot \Delta\ddot{x} + F_{x_1} \cdot \Delta x_1 + F_{x_2} \cdot \Delta x_2 + F_{x_4} \cdot \Delta x_4 \quad (7)$$

4. AEROELASTIC ANALYSIS

State space representation for equations of motion and unsteady aerodynamic model

$$\begin{bmatrix} 1 & 0 & 0 & 0 & 0 & 0 \\ 0 & 1 & 0 & 0 & 0 & 0 \\ 0 & 0 & 1 & 0 & 0 & 0 \\ 0 & 0 & 0 & 1 & 0 & 0 \\ 0 & 0 & 0 & 0 & T_p & 0 \\ 0 & 0 & 0 & 0 & 0 & T_f \end{bmatrix} \begin{bmatrix} \Delta\dot{x} \\ \Delta\ddot{x} \\ \Delta\dot{x}_1 \\ \Delta\dot{x}_2 \\ \Delta\dot{x}_3 \\ \Delta\dot{x}_4 \end{bmatrix} = \begin{bmatrix} 0 & 1 & 0 & 0 & 0 & 0 \\ -\omega_n^2 & -2 \cdot \left(\zeta_n \omega_n + \frac{\rho c u_0}{4m} \cdot \eta^{dyn} \right) & -F_{x_1}/m & -F_{x_2}/m & 0 & -F_{x_4}/m \\ 0 & -A_1 b_1 \cdot \frac{2}{c} \cdot \sin \theta & -b_1 \cdot \frac{2u_0}{c} & 0 & 0 & 0 \\ 0 & -A_1 b_1 \cdot \frac{2}{c} \cdot \sin \theta & 0 & -b_2 \cdot \frac{2u_0}{c} & 0 & 0 \\ 0 & C_{L\alpha}^p (1 - A_1 - A_2) \cdot \left(-\frac{\sin \theta}{u_0} \right) & C_{L\alpha}^p & C_{L\alpha}^p & -1 & 0 \\ 0 & 0 & 0 & 0 & f_{\alpha 0}/C_{L\alpha}^p & -1 \end{bmatrix} \begin{bmatrix} \Delta x \\ \Delta\dot{x} \\ \Delta x_1 \\ \Delta x_2 \\ \Delta x_3 \\ \Delta x_4 \end{bmatrix} \quad (8)$$

Calculating conditions:

Air density = 1.225kg/m³

Wind speed = 20m/s

Natural frequency = 0.8Hz (1st mode)

Structural damping delta = 0.03

Spanwise station = 0.84Radius

Chord length = 1.447m

Mass per length = 113.5kg/m

Unsteady aerodynamic model parameters:

A1 = 0.165, A2 = 0.335, b1 = 0.0455, b2 = 0.3000, Tp = 0.35, Tf = 0.35

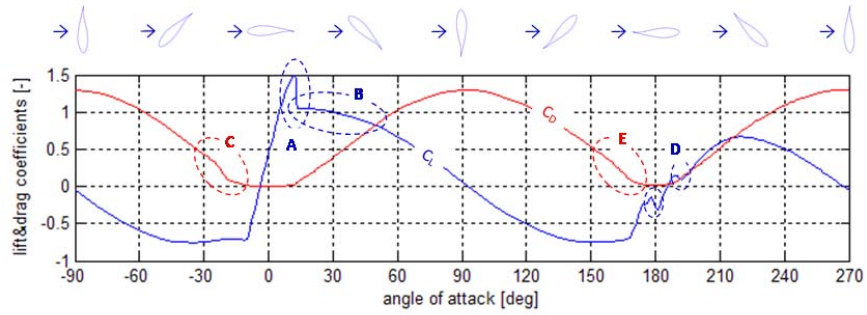


Figure 2: Static (quasi-steady) lift and drag coefficients of representative blade section ($r/R=0.84$) for the whole angle-of-attack range from -90deg to $+270\text{deg}$

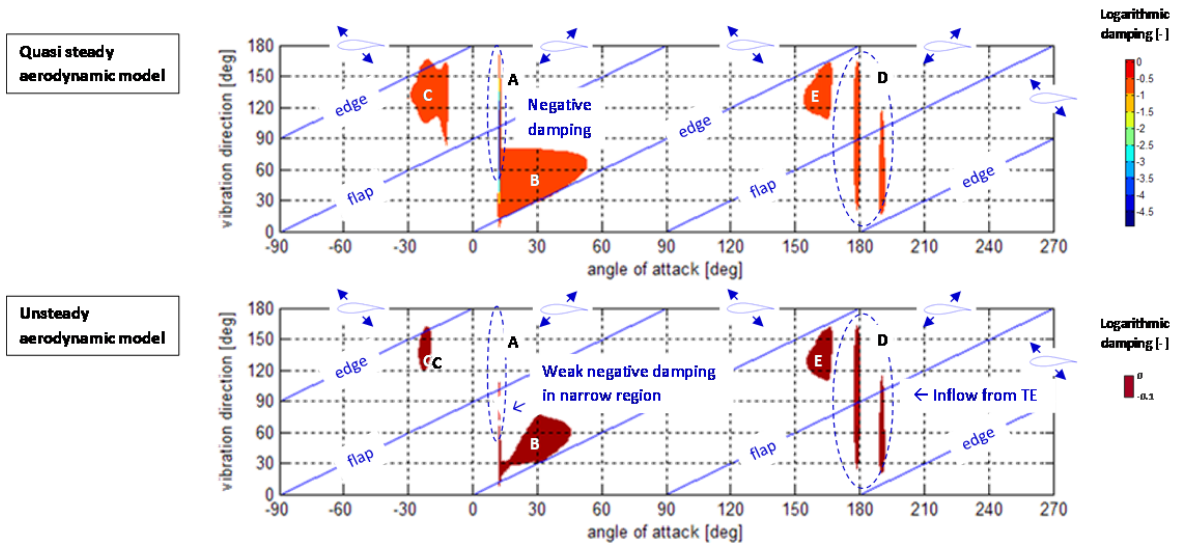


Figure 3: Results of aeroelastic analysis of the representative blade section ($r/R=0.84$) using quasi-steady aerodynamic model (to the top) and unsteady aerodynamic model (to the bottom) for the whole angle-of-attack range from -90deg to $+270\text{deg}$

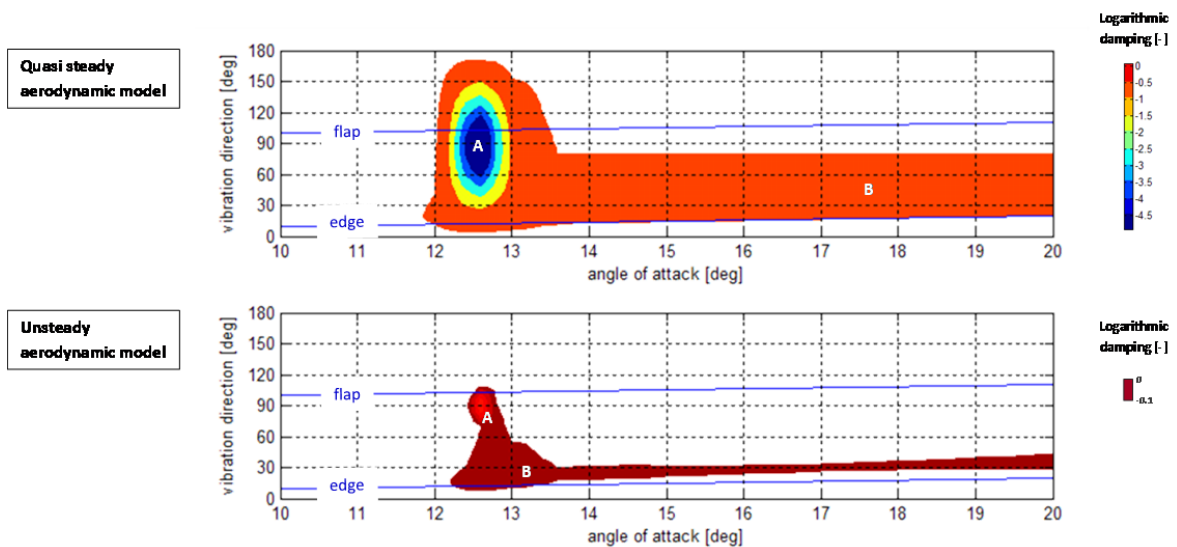


Figure 4: Results of aeroelastic analysis of the representative blade section ($r/R=0.84$) using quasi-steady aerodynamic model (to the top) and unsteady aerodynamic model (to the bottom) at angles of attack in the range of 10deg to 20deg

5. CONCLUSIONS

In this paper, aeroelastic stability analysis of offshore wind turbine blade (81.6m length) at standstill condition was carried out using quasi-steady aerodynamic model and linearized unsteady aerodynamic model, covering the whole regions of angle of attack and direction of blade vibration. According to quasi-steady analysis, it was found that the coupled flap-and-edgewise motion would become unstable when at least one of the blades would be exposed to strong wind inflow with angle of attack in the following five regions; (A) post stall region where flapwise motion would become deeply unstable due to steep negative lift slope, (B) deep stall region where edgewise motion would become slightly unstable for wider angle-of-attack region somewhere between 12deg to 45deg due to gradual negative lift slope, (C) negative angle of attack region of around -20deg where the coupled flap-edgewise motion would become slightly unstable due to negative lift coefficient with negative drag slope, (D) angle of attack from 180deg to 190deg (reverse flow condition) where the flapwise or the coupled flap-edgewise motion would become slightly unstable due to negative lift slope and (E) angle of attack around 160deg where edgewise motion would become unstable due to negative slope of lift and drag curves. Based on the analysis that was subsequently conducted considering unsteady aerodynamics, it was revealed that unsteady aerodynamics could greatly alleviate aeroelastic instabilities for each region, especially, the region A was the region most affected by unsteady dynamics, in other words, dynamic stall in the post stall region. It was finally concluded that the region B should be avoided during offshore transportation, assembly and maintenance at the site because, even when unsteady aerodynamics was considered, the region B would remain unstable for wider angle-of-attack region.

REFERENCES

- 1) Hansen. M. H. : Aeroelastic Instability Problems for Wind Turbines, *Wind Energy*, 10:551-557, 2007
- 2) Theodorsen, T. : General theory of aerodynamic instability and the mechanism of flutter, *NACA Report* 496, pp. 413-433, 1935.
- 3) Leishman, J. G. : *Principle of helicopter aerodynamics*, Cambridge University Press, 2000.
- 4) Hansen, M. H. : A Beddoes-Leishman type dynamic stall model in state-space and indicial formulations, *Riso-R-1354*, 2004.

Dynamic Analysis of the Two-Bladed Horizontal Axis Wind Turbine

Shigemitsu AOKI⁺¹, Tetsuya KOGAKI⁺² and Kenichi SAKURAI ⁺³

⁺¹ AIST Invited Research Scientist, National Institute of Advanced Industrial Science and Technology (AIST) Renewable Energy Research Center (RENRC), 2-2-9 Machiikedai, Koriyama, Fukushima, 963-0298, Japan

⁺² Team Leader, National Institute of Advanced Industrial Science and Technology (AIST)

⁺³ Technical Staff, National Institute of Advanced Industrial Science and Technology (AIST)

ABSTRACTS

In order to make an approach according to the dynamic characteristics of the two-bladed Horizontal axis wind turbine, that is substantially unstable and non-linear motion, the basic equations were derived by Lagrange's method on Eulerian coordinate system.

An aero-elastic simulation model named AIST-RAM (AIST Real-Time Model), that represents characteristics of the motion was developed referring to the basic equations and another factors such as an aerodynamic force acting on the blades that is strongly affected by the motion and elasticity of the blades itself.

Also, a scale model of the multi-megawatt horizontal-axis wind turbine was constructed as well as the specified management system called Hard-wear in the Loop (HIL).

Through the successive evaluation by wind-tunnel testing and field testing accompanied with real-time simulation arranged by the Hard-wear in the Loop System, the credibility of the simulation soft-wear is gradually confirmed along with the clear understanding as to a characteristics of the teetered-hub system that has ever been discussed among the industry.

Keyword: Two-Bladed Horizontal Axis Wind Turbine, Basic Equations, Lagrange's Method, Eulerian coordinate system, Real-time Simulation, Hard-wear in the Loop System.

1. Introduction

Multi-megawatt scale Horizontal-Axis Wind Turbine is getting larger and larger revealing the conceptual design of over 200 meter diameter scale recently.

Whereas, the consideration to apply two-bladed rotor instead of current three-bladed design is under discussion, pros. and cons. of the design is recognized as

Pros.

- a) Possibly reduce the weight of the system.
- b) Design constraint for the increasing gear is relaxed with higher rotational speed.
- c) The aerodynamic load in extreme wind condition could be reduced.

Cons.

- d) There are significant difference of the inertial force and/or aerodynamic force according to the blade-position.
- e) Power coefficient of the rotor is inferior.

Recently, although the studies and researches ⁽¹⁾⁽²⁾ according to the teetered hub is upcoming, there are few which applied current advanced technology of evaluation for the system.

In this study, through the successive evaluation by wind-tunnel testing and field testing accompanied with real-time simulation system arranged by the Hard-wear in the Loop System, the credibility of the simulation

⁺¹s.aoki@aist.go.jp, ⁺²kogaki.t@aist.go.jp, ⁺³kenichi-sakurai@aist.go.jp

soft-wear is gradually confirmed along with the clear understanding as to a characteristics of the teetered-hub system

2. Lagrange's Method

2.1 Coordinate system

In order to introduce the basic equations that ordinate the inertial force acting on the system, "Eulerian coordinate system⁽³⁾" was adopted as a generalized coordinates. Basic attitude of the rotor-blade was conducted with four degree of freedom defined as β , ψ , θ and ϕ , as is shown in Figure 1.

Hence β is defined as the pitch angle that adjust the attack angle around the axis approximately put on the aerodynamic center of each blade section, ψ is defined as the azimuth angle of the blade rotating on the main axis of the rotor, θ is defined as the tilt angle that starts from perpendicular position and ϕ is defined as yaw angle of the main axis according to the directional change.

Furthermore in this study, τ is defined as teeter-angle that allows pendulum like motion between the pitch axis of the blades and the main axis, accompany with delta-three (δ_3) angle for the adjustment between the pitch axis and the teeter axis.

Also in Figure 1, u is the wind speed, a is the distance between the hub-center and the base point of the coordinate system, b is the distance between the gravity-center of the blade and the hub-center, m_1 is mass of the blade, I is moment of inertia around the rotor axis, J is moment of inertia around the pitch axis respectively.

In addition, a small amount of mass m_2 is assumed with the distance c from the hub-center, in order to make the adjustment of mass-balance of the rotor according to the teeter-axis.

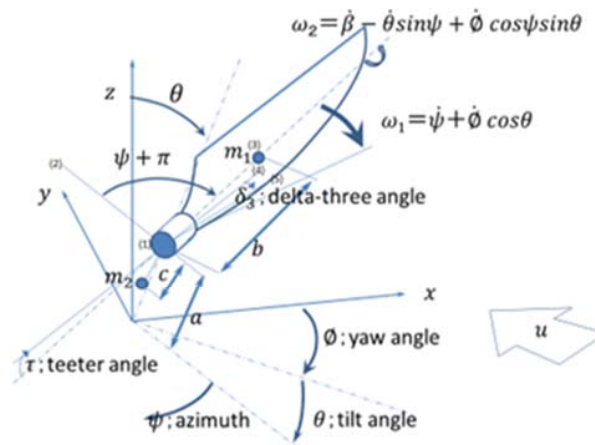


Figure 1: Fundamental coordinate system (Euler)

2.2 Potential energy of the system

Considering the effect of the gravitational acceleration, potential energy related to m_1 is written as equation (1), as to m_2 , equation (2), and as a result, summary of the potential energy according to Lagrange's function is written as equation (3).

$$V_1 = m_1 g [a \cos \theta - b \cos(\psi + \delta_3) \sin \theta - b \sin \tau \cos \theta + b(1 - \cos \tau) \sin \theta \cos(\psi + \delta_3)] \quad (1)$$

$$V_2 = m_2 g [(a - c \cos \tau) \cos \theta + c \sin \tau \cos \psi \sin \theta] \tag{2}$$

$$V = V_1 + V_2 \tag{3}$$

2.3 Kinetic energy of the system

2.3.1 According to yaw axis (ϕ system)

2.3.1.1 as to m_1

Contribution to $\dot{\phi}$, $a \sin \theta \dot{\phi}$,

Similarly, contribution of $\dot{\psi}$ is through $\frac{\partial \psi}{\partial t} [b \sin(\psi + \delta_3)]$ $b \cos(\psi + \delta_3) \dot{\psi}$,

Also, contribution of $\dot{\tau}$ is through $\frac{\partial \tau}{\partial t} [b \sin \tau \sin \theta \sin(\psi + \delta_3)]$ $b \cos \tau \sin \theta \sin(\psi + \delta_3) \dot{\tau}$,

Considering the components above, following equation is derived.

$$E_1 = \frac{1}{2} m_1 [a \sin \theta \dot{\phi} + b \cos(\psi + \delta_3) \dot{\psi} + b \cos \tau \sin \theta \sin(\psi + \delta_3) \dot{\tau}]^2 \tag{4}$$

2.3.1.2 as to m_2

Contribution to $\dot{\phi}$, $[a \sin \theta - c \cos \tau \sin \theta - c \sin \tau \cos \theta + c \sin \tau \cos(\psi + \delta_3) \cos \theta] \dot{\phi}$,

Similarly, of $\dot{\psi}$ is through $\frac{\partial \psi}{\partial t} [c \sin \tau \cos(\psi + \delta_3)]$, $-c \sin \tau \sin(\psi + \delta_3) \dot{\psi}$

Derived equation is written as

$$E_2 = \frac{1}{2} m_2 \{ [a \sin \theta - c \cos \tau \sin \theta - c \sin \tau \cos \theta + c \sin \tau \cos(\psi + \delta_3) \cos \theta] \dot{\phi} - c \sin \tau \sin(\psi + \delta_3) \dot{\psi} \}^2 \tag{5}$$

2.3.1.3 as to I

Projected length of the blade length (R) around yaw axis on the ϕ -plane is, $(R) \sin(\psi + \delta_3)$

Contribution of $\dot{\psi}$ is $\cos(\psi + \delta_3) \dot{\psi}$

Derived equation is written as

$$E_3 = \frac{1}{2} I [\sin(\psi + \delta_3) \dot{\phi} + \cos(\psi + \delta_3) \dot{\psi}]^2 \tag{6}$$

2.3.1.4 as to J

This component seems to be not effective considering that $J/I \ll 1$.

2.3.2 According to tilt axis (θ system)

2.3.2.1 as to m_1

Contribution to $\dot{\theta}$, $a \dot{\theta}$,

As to the contribution of $\dot{\psi}$ is, considering the tangential component as $b \cos(\psi + \delta_3)$,

Through the calculation $\frac{\partial \psi}{\partial t} [b \cos(\psi + \delta_3)]$ $-b \sin(\psi + \delta_3) \dot{\psi}$,

Derived equation is written as

$$E_4 = \frac{1}{2} m_1 [a \dot{\theta} - b \sin(\psi + \delta_3) \dot{\psi}]^2 \tag{7}$$

2.3.2.2 as to m_2

Contribution to $\dot{\theta}$,

$$a\dot{\theta},$$

Contribution of $\dot{\psi}$ is through

$$\frac{\partial \psi}{\partial t} [-c \sin \tau \cos(\psi + \delta_3)] \quad c \sin \tau \sin(\psi + \delta_3) \dot{\psi},$$

Derived equation is written as

$$E_5 = \frac{1}{2} m_2 [a\dot{\theta} + c \sin \tau \sin(\psi + \delta_3) \dot{\psi}]^2 \quad (8)$$

2.3.2.3 as to I

Projected length of the blade length (R) around tilt axis on the θ -plane is,

$$(R) \cos(\psi + \delta_3),$$

Contribution of $\dot{\psi}$ is

$$-\sin(\psi + \delta_3) \dot{\psi}$$

Derived equation is written as

$$E_6 = \frac{1}{2} I [\cos(\psi + \delta_3) \dot{\theta} - \sin(\psi + \delta_3) \dot{\psi}]^2 \quad (9)$$

2.3.2.4 as to J

This component seems also to be not effective considering that $J/I \ll 1$.

2.3.3 According to azimuth (ψ system)

2.3.3.1 as to m_1

Following the definition according to the Eulerian coordinate system, derived equation is

$$E_7 = \frac{1}{2} m_1 b^2 \cos^2 \tau (\dot{\psi} + \cos \theta \dot{\phi})^2 \quad (10)$$

2.3.3.2 as to m_2

Similarly,

$$E_8 = \frac{1}{2} m_2 c^2 \sin^2 \tau (\dot{\psi} + \cos \theta \dot{\phi}) \quad (11)$$

2.3.3.3 as to I

Also,

$$E_9 = \frac{1}{2} I \cos^2 \tau (\dot{\psi} + \cos \theta \dot{\phi})^2 \quad (12)$$

2.3.4 According to pitch axis (β system)

2.3.4.1 as to J

Following the definition according to the Eulerian coordinate system in case that the effect of teetering is negligible, derived equation is,

$$E_{10} = \frac{1}{2} J (\dot{\beta} - \sin \psi \dot{\theta} + \cos \psi \sin \theta \dot{\phi})^2 \quad (13)$$

2.4 Lagrange's function

Summary, the Lagrange's function of the system is calculated by following equation, with the notation of $n ; 1 \sim 9, m ; 2$.

$$L = T - V = \sum E_n - \sum V_m \quad (14)$$

Assuming that each degree of freedom as independent variable q , series of basic equations are derived by following formula.

$$\frac{d}{dt} \left(\frac{\partial L}{\partial \dot{q}} \right) - \frac{\partial L}{\partial q} = 0 \quad (15)$$

3. Basic equations

3.1 Basic equations

Set of differential equation are derived,

As to yaw (ϕ) system,

$$k_{11}\ddot{\phi} + k_{12}\dot{\phi}\dot{\psi} + k_{17}\ddot{\psi} + k_{18}\dot{\psi}^2 + k_{19}\dot{\psi}\dot{\tau} + k_{1a}\ddot{\tau} = 0 \tag{16}$$

As to tilt (θ) system,

$$k_{22}\dot{\phi}\dot{\psi} + k_{24}\dot{\phi}\dot{\theta} + k_{25}\ddot{\theta} + k_{26}\dot{\theta}\dot{\psi} + k_{27}\ddot{\psi} + k_{28}\dot{\psi}^2 + k_{29}\dot{\psi}\dot{\tau} + k_{2a}\ddot{\tau} + k_{2b}g = 0 \tag{17}$$

As to azimuth (ψ) system,

$$k_{31}\ddot{\phi} + k_{32}\dot{\phi}\dot{\psi} + k_{33}\dot{\phi}\dot{\tau} + k_{37}\ddot{\psi} + k_{39}\dot{\psi}\dot{\tau} + k_{3b}g = 0 \tag{18}$$

As to teeter (τ) system,

$$k_{41}\ddot{\phi} + k_{42}\dot{\phi}\dot{\psi} + k_{48}\dot{\psi}^2 + k_{4a}\ddot{\tau} + k_{4b}g = 0 \tag{19}$$

3.2 Coefficients.

Coefficients for each term can be arranged like in Table 1.

Table 1: Coefficients of each term.

	ϕ system	θ system	ψ system	τ system		ϕ system	θ system	ψ system	τ system
$\ddot{\phi}$	k_{11}		k_{31}	k_{41}	$\dot{\theta}\dot{\psi}$		k_{26}		
$\dot{\phi}\dot{\psi}$	k_{12}	k_{22}	k_{32}	k_{42}	$\ddot{\psi}$	k_{17}	k_{27}	k_{37}	
$\dot{\phi}\dot{\tau}$			k_{33}		$\dot{\psi}^2$	k_{18}	k_{28}		k_{48}
$\dot{\phi}\dot{\theta}$		k_{24}			$\dot{\psi}\dot{\tau}$	k_{19}	k_{29}	k_{39}	
$\ddot{\theta}$		k_{25}			$\ddot{\tau}$	k_{1a}	k_{2a}		k_{4a}
$\dot{\theta}\dot{\psi}$		k_{26}			g		k_{2b}	k_{3b}	k_{4b}

Hence, coefficient k_{11} , k_{25} , k_{37} , k_{4a} are principal moment of inertia for ϕ system, θ system, ψ system and τ system

k_{*8} are related to the centrifugal force that causes significant acceleration in general.

k_{*2} , k_{*3} , k_{*4} , k_{*6} , k_{*9} are related to components oriented by coupled angular velocities, and in case, for example, related to k_{22} , k_{33} , k_{29} , the angular acceleration consists of angular velocities of normal axes, it causes gyro-moment.

Coriolis' force is caused in the other cases.

k_{*b} are related to gravitational acceleration.

In this study, influence of the pitch movement for the inertial property was neglected, respectively.

4. Simulation model construction

4.1 Modeling circumstances

A circumstances of time-driven simulation system was prepared to establish the construction of the model shown in Figure 2.

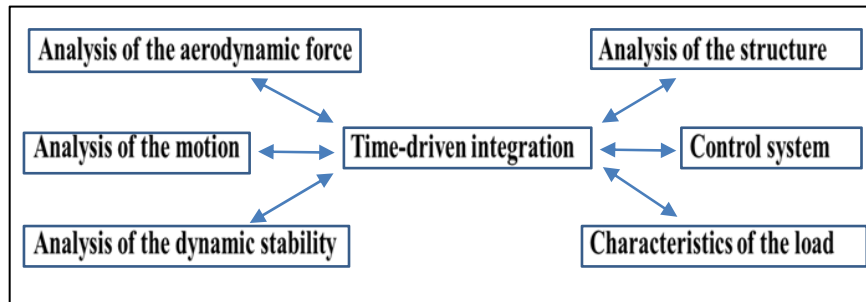


Figure 2 : Structure of the Model

4.2 Inner force implementation

At first, inertial forces derived by consequential basic equations shown as formula (16), (17), (18) and (19) are implemented as inner force of the system.

4.3 Outer force implementation

4.3.1 Effect of the elasticity of the Tower and the Blade(s)

As to the deflection of the tower, following equation of first order bending was applied.

$$\frac{1}{2}\rho(u-\dot{x})^2 AC_T - \frac{3EI}{l^3}x = \left(m_N + \frac{3EI}{l^3} \frac{1}{w^2}\right) \ddot{x} \quad (20)$$

Hence, x is the deflection of the tower at the tower-top, namely the displacement of the main-shaft, ρ is the density of the air, A is the swept area of the rotor, C_T is the thrust coefficient of the rotor, EI is the rigidity of the tower for bending, l is the length of tower, m_N is the mass of tower-top, and w is the mass of tower per unit length.

Similarly, as to the effect of blade-deflection, applying the characteristics of the blade of which used as a scale model for the experiment, result of following equation was used to compensate the teeter motion.

$$2m_1[0.0035\dot{W} + \ddot{x} + 0.53l\ddot{t}] = \frac{1}{2}\rho[u - 0.048\dot{W}]^2 AC_t \quad (21)$$

Hence, W is deflection of the blade-tip, respectively.

4.3.2 Effect of the aerodynamic-force of the rotor-blade(s)

In order to apply the aerodynamic-force of the rotor-blade, aerodynamic torque-coefficient by following equation referring to the characteristics of standard blade design was adopted.

$$C_q = 0.079 + \frac{0.08}{(\beta+2)} - [5.5 + 0.007(\beta + 2)^{2.5}]\lambda \times 10^{-3} \quad (22)$$

4.3.3 Compensation of the effect of aerodynamic-force

Representative factors as follows were considered to be significant and implemented to adjust the torque-coefficient accompany with the variation of λ (tip-speed ratio) and β .

- Δu (variation of hub wind-speed) ; coherent variation of wind-speed around the rotor-disc
- \dot{x} (deflection-speed of tower-head) ; deflection speed of tower-head parallel to the wind speed

- u_{local} (wind-speed distribution) ; effect of the wind speed distribution like wind shear
- $r\dot{t}$ (teetering motion) ; relative variation of wind speed due to the teeter motion
- $r\dot{\phi}$ (yaw movement) ; relative variation of wind speed due to the yaw motion

4.3.4 Effects of another outer force

Effects of actuators like driving-motor of main shaft, that of yawing and that of pitch-axis are implemented to ψ system, ϕ system and β system, based on the D'Alembert's principle as well as the various kind of aerodynamic force as is shown in current Simulation Model⁽⁴⁾.

5. Test facilities for evaluation

5.1 Over view

Figure 3 shows a scale-model of the wind-turbine and a controller, a power source for driving, measurement system with HILS system and Host computer.



Figure 3 Experimental system for Evaluation

Figure 4 shows basic specifications of the wind-tunnel and the model for this study.



- Wind-Tunnel ; RCAST University of Tokyo
 - Type : Goettingen type with open-space measurement area
 - Outlet size : 3 [m] Diameter
 - Maximum wind speed : 60 [m/s]
- Model
 - Rotor diameter : 1.6 [m]
 - Rated speed of revolution : 600 [rpm]
 - Wing section : Avistar
 - Type of Hub : Teetered with adjustable δ_3 angle
- Test-condition
 - Wind speed : 0.1~5 m/s
 - Rotational speed : 300~600 rpm
 - Teeter angle : fix or free(± 4 degree)
- Terms of measurement
 - Wind-speed, Yaw-angle, Power-output
 - Displacement, velocity, acceleration (Yaw, Azimuth, Teeter)
 - Load (Bending-moment at blade-root, torque and thrust of main-shaft)

Figure 4 Basic specifications of the wind tunnel testing

5.2 HILS system

HILS system was invented as a tool for model-base design technology.

As is shown in Figure 5, the main facility of such a system is to exchange the data between one which was measured at hard-wear and the corresponding result of the real-time simulation in order to make a precise and quick comparison.

In order to realize it, the simulation soft-wear is required an ability of real-time simulation.

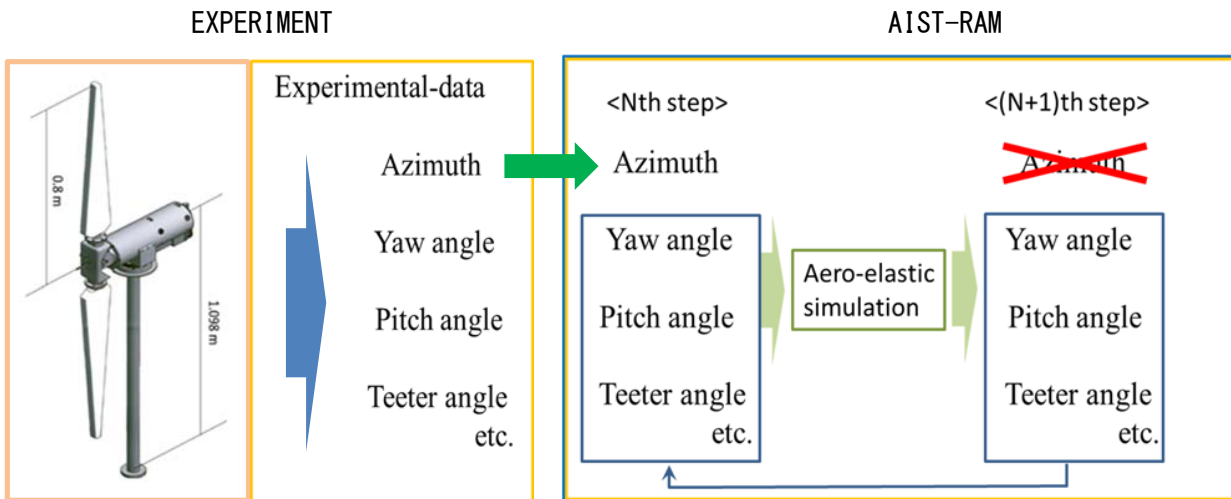


Figure 5 : Main facility of HILS system

As is shown in Figure 5, between the models running parallel, at some step, for example the azimuth datum is exchanged and becomes common in order to make precise and quick comparison between another data.

Through these process, as to the experiment, the preciseness or credibility of the data produced by the sensor and the data-processing can be seen, and for the simulation model very precise identification as well as tuning could be established.

6. Dynamic analyses of the two-bladed teetered rotor

6.1 Teetered-rotor

Teetered-rotor is a kind of technology to support the tail-rotor of the helicopter in order to obtain a dynamic stability.

In 1980th this kind of concept was applied to design prototypes of Megawatt-scale horizontal axis wind turbine, and accordingly, several studies had been conducted.

In this study, referring to the basic equations from (16) to (19), basic characteristics of the motion was investigated.

6.2 Effect of the gravitational acceleration

Figure 6 shows the comparison as to teeter motion between the measurement and simulation result according to the azimuth angle.

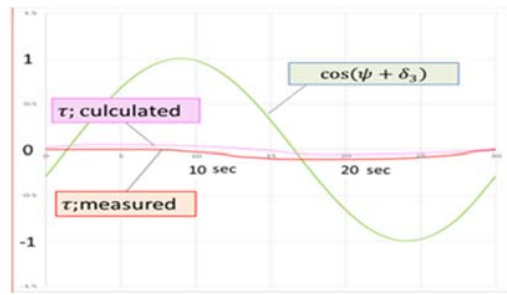


Figure 6 Teeter motion in the case of low-speed by motoring

In this case the rotor is driven by the motor in very low speed of 2 rpm.

According to fifth term of equation (19), effect of the gravity-acceleration is noticeable with a pre-session due to the existence of m_2 and c related to the fifth term of equation (16) and the seventh term of equation (17).

Figure 7 shows the result of wind tunnel test under the condition of wind-speed 5 m/s and rotational speed around 100 rpm.

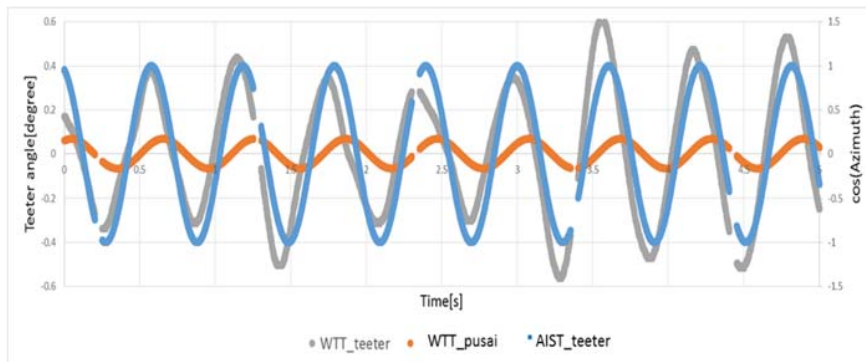


Figure 7 : Comparison between the measurement and simulation as to the teetering motion at wind tunnel test

The result seems identical with the tendency recognized in Figure 6 besides far reduced amplitude of teeter angle due to the effect of centrifugal force by the third term of equation (19).

6.3 Effect of the centrifugal force

Figure 8 shows the comparison as to the amplitude of teetering motion according to the rotational speed of the rotor between the result of simulation and the wind tunnel test.

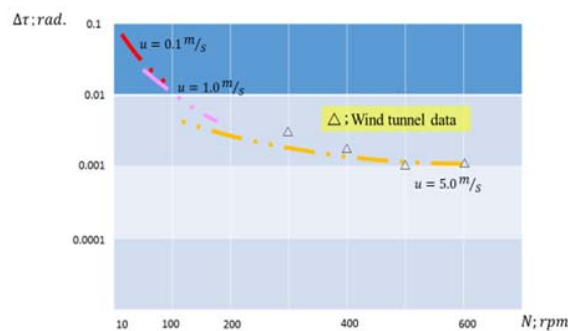


Figure 8 : Comparison of the amplitude of teetered angle according to the rotational speed

6.4 Effect of the wind profile

In order to make a research as to the effect of wind profile, out-door HILS-testing under the natural wind was conducted.

Circumstance of the test was constructed with the measurement of wind-speed not only at hub height but also at the top and foot of the rotor which was implemented to the HILS system.

Figure 9 shows the result.

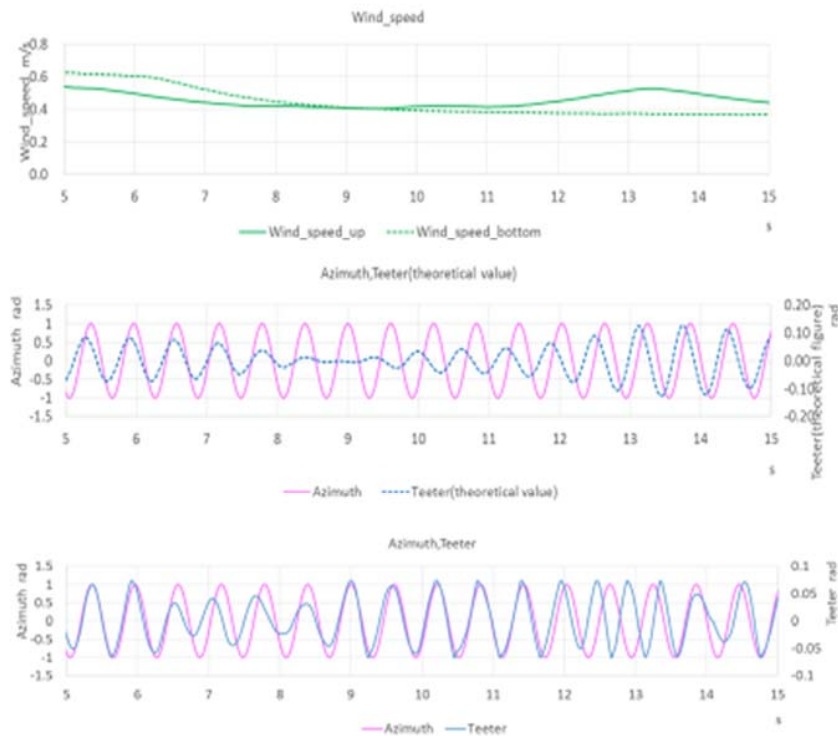


Figure 9 Teetering motion under various wind profile

In this case, at the beginning, wind profile is reverse, namely wind speed at upper area is more weak than that of lower area until 8 second, where the profile begin to change to more normal condition.

Under the normal wind profile condition, the effect of wind speed distribution is similar to the effect of gravitational acceleration by which the peak of teeter motion leads the peak of azimuth as is seen at whole of Figure 7 and at Figure 8 from 8 second to 14 second.

While under the reverse wind profile condition as is seen from 5 second to 8 second in Figure 8, the effect of wind profile weaken the effect of the gravitational acceleration that reduce the lead of teeter-peak to the azimuth-peak.

And when the wind profile is neutral at 9 second, the amplitude of teeter motion becomes minimum, because the effect of centrifugal force becomes dominant in these condition.

There are several point where the result of measurement as to teeter angle has some discrepancy to the result of simulation.

Considering these result, modelling of the wind condition around the rotor seems to be most important to establish the precise and credible simulation.

7. Summary

In order to make an approach according to the dynamic characteristics of the two-bladed Horizontal axis wind turbine, that is substantially unstable and non-linear motion, the basic equations were derived by Lagrange's method on Eulerian coordinate system.

An aero-elastic simulation model named AIST-RAM (AIST Real-Time Model), that represents characteristics of the motion was developed referring to the basic equations and another factors such as an aerodynamic force acting on the blades that is strongly affected by the motion and elasticity of the blades itself.

Also, scale model of the multi-megawatt horizontal-axis wind turbine was constructed as well as the specified management system called Hard-wear in the Loop (HIL).

Through the successive evaluation by wind-tunnel testing and field testing accompanied with real-time simulation arranged by the Hard-wear in the Loop System, the simulation model shows significant credibility and preciseness particularly for the inertial property, while as to the effect of the aerodynamic forces, namely to construct the time-domain detailed characteristics of the wind, there remains a problem with significant difficulty to make and implement it to the real-time simulation model.

8. Acknowledgement

This study was supported by Japanese national project that made a study and research work according to the Multi-Megawatt Large scale Horizontal axis Wind turbine.

I would like to appreciate people who involved to the project on behalf of METI, NEDO, AIST and several Academies and Industries.

REFERENCES

- 1) B.Luhmann, P.W.Cheng
Relevance of aerodynamic modelling for load reduction control strategies of Two-bladed wind turbines
The Science of Making Torque from Wind 2014
- 2) V Schorbach, P Dalhoff, P Gust
Taming the inevitable : significant parameters of teeter end impacts
The Science of Making Torque from Wind 20
- 3)John C. Slater, Nathanael H. Frank
Mechanics
McGraw-Hill Book Company 1947
- 4) J.M.Jonkman and M.L.Buhl, Jr. :
New Development for the NWTTC's FAST Aero-elastic HAWT Simulator.
42nd Aerospace Sciences Meeting and Exhibit Conference, NREL/CP-500-35077,2003.

NUMERICAL ANALYSIS OF THE EFFECTS OF A WIND TURBINE'S ROTATING BLADES ON THE AERODYNAMIC FORCES ON THE TOWER

Takaaki Kono⁺¹, Satoshi Nebucho⁺², Tetsuya Kogaki⁺³,
Takahiro Kiwata⁺⁴, Shigeo Kimura⁺⁵, and Nobuyoshi Komatsu⁺⁶
^{+1,2,4,5,6}Kanazawa University, Kanazawa, 920-1192 JAPAN

⁺²National Institute of Advanced Industrial Science and Technology, Koriyama, 963-0298 Japan

This study investigated the effects of the rotating blades of an upwind-type horizontal-axis wind turbine on the aerodynamic forces of the wind-turbine's tower by conducting computational fluid dynamics (CFD) simulations of the flow around the wind turbine and its tower. The CFD results confirmed that at each height above the lowest point of the rotor, the maximum value of the pressure around the tower shifted in the direction of the rotor rotation; this was caused by the diversion of air flow approaching the tower due to rotation of the blades. It was also confirmed that while a blade was passing upstream of the tower, the pressure fluctuations around the tower at each height above the lowest point of the rotor were greater on the side of the tower where the blade approaches than on the side where the blade moves away, due to the recovery of low pressure on the downstream side of the blade. In addition, it was found out that while a blade was near the tower, the air pressure on the upwind side of the tower was reduced due to interference with the lower-pressure region on the downstream side of the blade. This interference caused a periodic decrease in the drag coefficient of the tower. Moreover, it was recognized that while a blade approached the tower and then moved away, the low-pressure region on the downwind side of the blade caused a drop in the pressure on the side of the tower adjacent to the blade. This pressure drop caused a periodic fluctuation in the side force coefficient of the tower.

Keyword: Horizontal axis wind turbine, CFD, Tower, Aerodynamic force, Blade

1. INTRODUCTION

Accidents due to strong winds or turbulence have resulted in damage and even complete failure of wind turbines (WT) and their towers in recent years. To reduce the occurrence of incidents involving wind turbines, it is essential to design rotors and towers with the proper fatigue strength and shapes by taking into account the vibration characteristics of the tower. However, very few studies have investigated the influence of rotating blades on the aerodynamic forces on towers^{1,2)} and the influence of those forces on tower vibrations, so many aspects of tower behavior remain unclear at this time.

In this study, we investigate the effects of the rotating blades of an upwind-type horizontal-axis wind turbine (HAWT) on the aerodynamic forces of the wind-turbine's tower by conducting computational fluid dynamics (CFD) simulations of the flow around the wind turbine and its tower.

2. NUMERICAL APPROACH

(1) Wind turbine and tower

This analysis was performed on a model of the upwind HAWT used by Krogstad and Eriksen³⁾ in wind tunnel experiments. The diameter of the rotational area of the HAWT was $D = 894$ mm and it had 3 blades based on the NREL S826 airfoil⁴⁾ (Fig. 1). The tower had a uniform diameter in the vertical direction, $d = 61$ mm, and was divided into 5 segments of identical length, $h = 154.4$ mm, to analyze the aerodynamic forces on each segment.

⁺¹t-kono@se.kanazawa-u.ac.jp, ⁺²nebuchou@ryuko.ms.t.kanazawa-u.ac.jp, ⁺³kogaki.t@asit.go.jp, ⁺⁴kiwata@se.kanazawa-u.ac.jp, ⁺⁵skimura@se.kanazawa-u.ac.jp, ⁺⁶komatsu@se.kanazawa-u.ac.jp

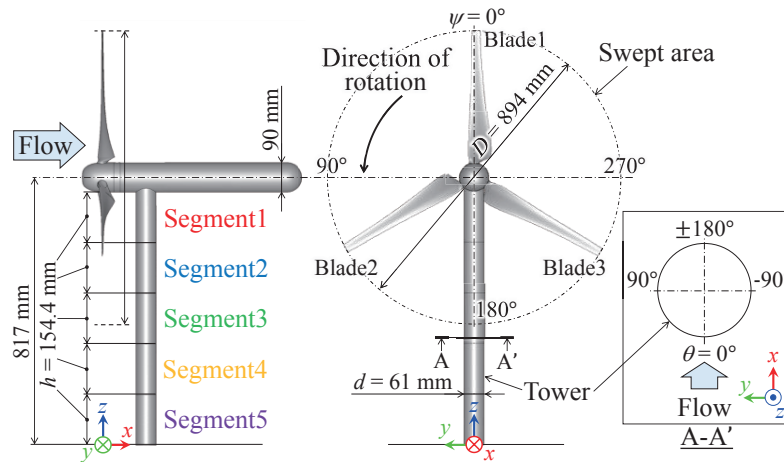


Figure 1: Outline of the wind turbine.

(2) Governing equations and discretization scheme

The CFD package ANSYS Fluent ver. 16.1 was employed. An unsteady incompressible viscous three-dimensional flow field consisting of air at 15 °C was assumed. The governing equations were the Reynolds-averaged continuity equation and Navier-Stokes equations, and were discretized by the finite volume method. The QUICK scheme was used for the advection terms, and the other terms were estimated by the second-order central difference scheme. The Reynolds stresses were computed using the $k-\omega$ shear-stress transport (SST) turbulence model⁵⁾. The time integration was performed by a second-order implicit method. The pressure-based coupled algorithm was used to handle the coupling between pressure and velocity.

(3) Numerical setup

Fig.2 shows the computational domain and the boundary conditions. The size of the computational domain was approximately same as the wind tunnel⁴⁾, $3D \times 12.5D \times 2D$, and consisted of the rotational domain, which included the rotor, and the non-rotating exterior domain. The origin of the coordinate system was defined as the intersection of a vertical line from the center of the rotor with the floor. The total number of cells was approximately 4.5 million. The blades, tower and wind tunnel walls were covered with boundary layer meshes. The first grid node was set at 3×10^{-5} m off the surface of the blades, and was $y^+ < 5$ almost over the blades. On the inlet boundary, a stream-wise wind velocity of $U_{ref} = 10$ m/s with a turbulence intensity of $TI = 0.3\%$ was implemented. On the outlet boundary, outflow boundary condition was imposed. On the surface of the blades and tower and on the wind tunnel walls, no-slip boundary conditions were set. The sliding mesh technique was used to couple the rotational domain and stationary domain. By changing the rotational speed of the rotor ω , three tip speed ratio cases were examined, $\lambda (= D\omega/2U_{ref}) = 3, 6$ and 9 .

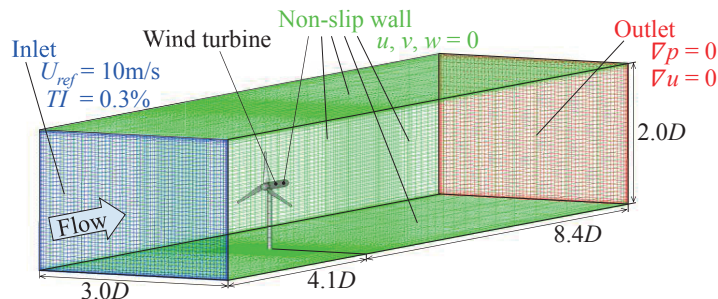


Figure 2: Computational grid and boundary conditions.

3. RESULTS AND DISCUSSION

(1) Validation of numerical approach

Fig.3 shows a comparison of the values of the power coefficient, $C_p (= 2Q\omega/\rho AU_{ref}^3)$ and thrust coefficient $C_T (= 2T/\rho AU_{ref}^2)$, evaluated from the simulations to those from the wind tunnel experiments. Here, Q is the total torque of the WT, ρ is the air density, A is the swept area and T is the total thrust of the blades. The simulations provided a reasonable qualitative and quantitative approximation of the experimentally observed results for both C_p and C_T .

Fig.4 shows comparisons between the simulation and wind tunnel experiment results of the distribution in the y direction of \bar{u} at the hub height in the wind turbine wake at $x/D = 1$ at $\lambda = 6$. The calculated values for \bar{u} matched the experimental results qualitatively and quantitatively well.

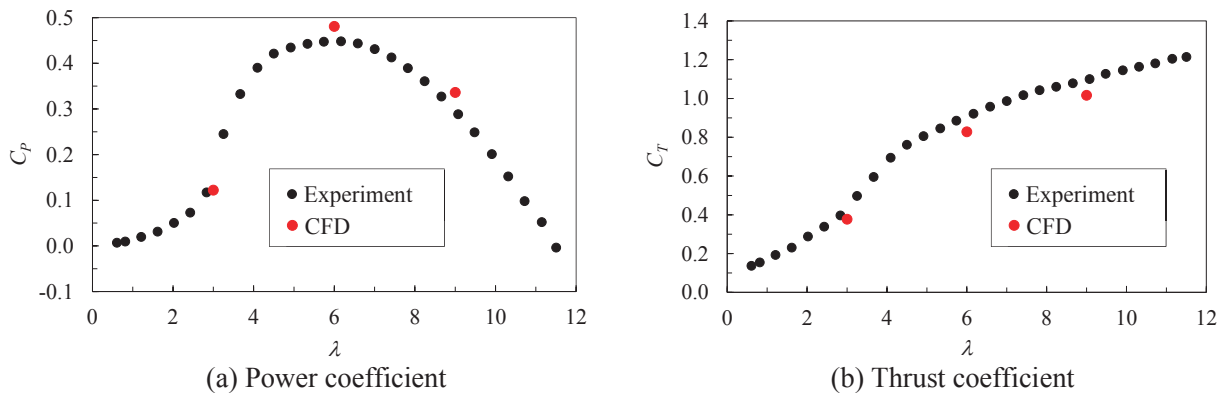


Figure 3: Computational and experimental results of wind turbine performance.

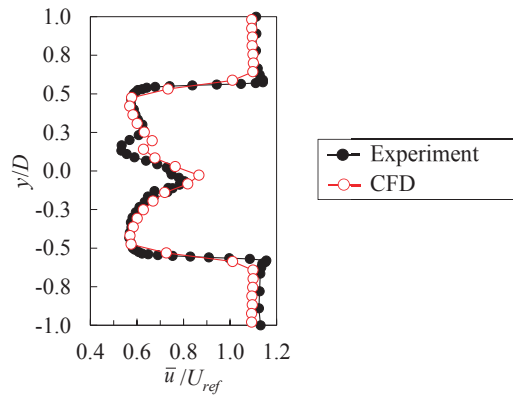


Figure 4: Lateral distribution of the streamwise wind velocity at the hub height in the wind turbine wake ($x/D = 1, \lambda = 6$).

(2) Pressure coefficients on tower

Fig.5 presents the mean pressure coefficients $C_p (= 2(\bar{p} - \bar{p}_{ref})/\rho U_{ref}^2)$ on the tower surface and the rms fluctuating pressure coefficients C_p' in the θ direction at the mid-heights of each tower segment at $\lambda = 6$. Here, \bar{p} and \bar{p}_{ref} are the time-averaged static pressure and the static pressure at the inlet boundary. C_p and C_p' show asymmetric distributions in the $\pm\theta$ directions relative to the stream-wise wind direction at segments 1–3, which are above the lowest point of the rotor. Additionally, with increasing altitude above the lowest point of the rotor, the circumferential location at which C_p reaches a maximum shifts in the $-\theta$ direction, which is the same direction as the rotor rotation. C_p' has high values in the $+\theta$ region, which is the direction from which the blade approaches. The same tendencies were observed at $\lambda = 3$ and $\lambda = 9$.

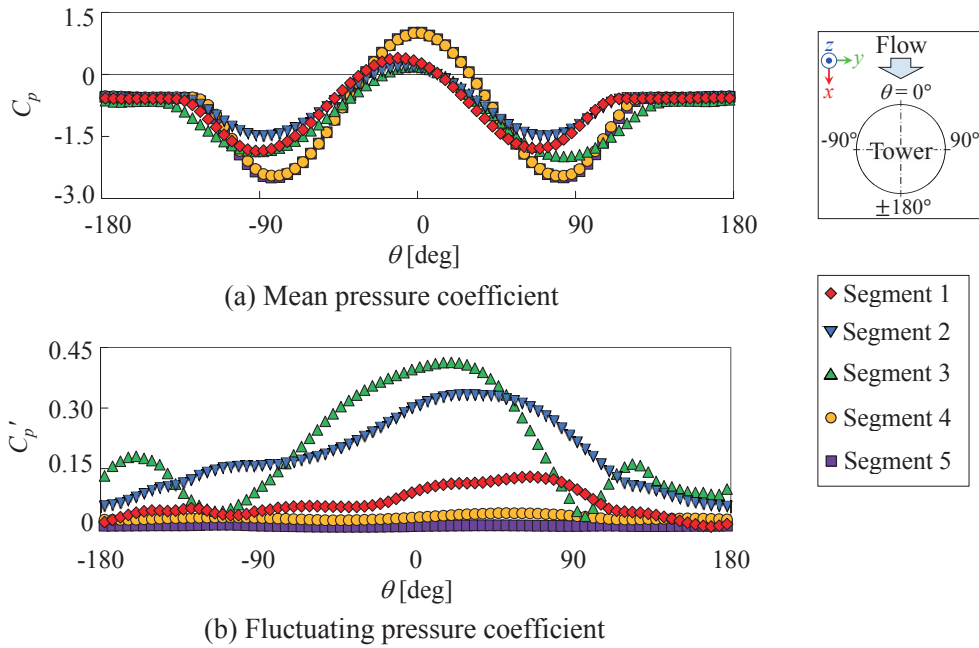


Figure 5: Distributions of mean and fluctuating pressure coefficients around the tower at the mid-heights of each segment ($\lambda=6$).

(3) Characteristic of flow around tower

Figs.6 and 7 show the streamlines and contour plots of static pressure near the tower at the mid-height of segment 2 at $\lambda = 6$. These figures suggest the causes for the asymmetric distributions of C_p and C_p' in the $\pm\theta$ directions. The rotor azimuth ψ is defined as 0° when rotor blade #1 is pointing straight up, parallel to the tower. The positive values follow a counterclockwise direction. Thus, the chords of blades 1, 2 and 3 lie directly upwind of the tower at $\psi = 60^\circ, 180^\circ$ and 300° . As can be seen in Fig. 6, the flows in the vicinity of the tower are diverted at all ψ . However, no such diversion is seen at segments 4 and 5. Thus, the shift of the maximum value for C_p in the $+\theta$ direction at segments 1–3 seen in Fig. 5 appears to be caused by a shift in the stagnation point, which is caused by turning of the flow toward the tower as the rotor rotates; this situation occurs at altitudes above the lowest point of the rotor. In Fig. 7, the low-pressure regions formed on the downwind side of the blade recover as the blade approaches the tower, but the pressures drop again as the blade passes and moves away from the tower. The pressure on the downwind side of the blade is clearly lower at $\psi = 50^\circ$ than at $\psi = 70^\circ$. The pressure at the surface of the tower interferes with the lower-pressure region on the downwind side of the blade on the $+\theta$ side than on the $-\theta$ side, and the C_p' in Fig. 5 is higher on the $+\theta$ side of the tower.

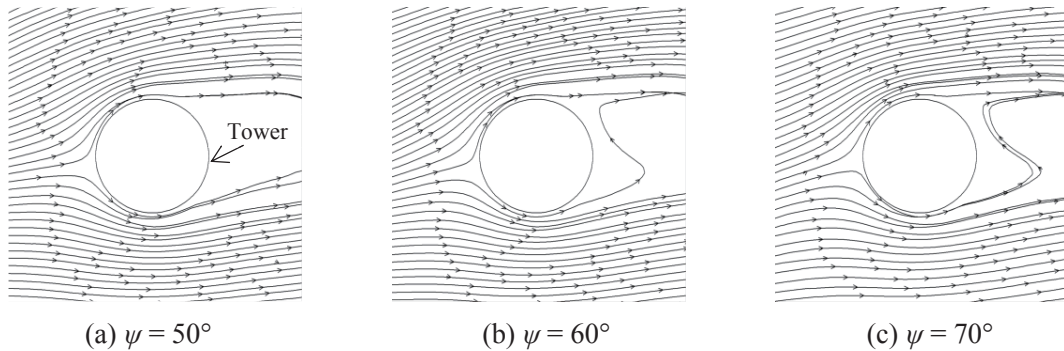


Figure 6: Streamlines near the tower at the mid-height of segment 2 ($\lambda=6$).

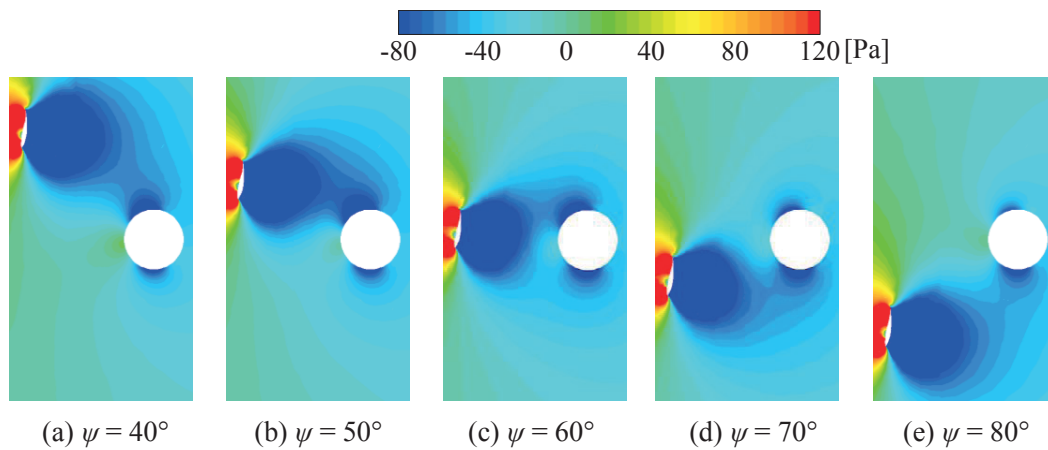


Figure 7: Contour plots of static pressure near the tower at the mid-height of segment 2 ($\lambda=6$).

(4) Drag and lift coefficients of tower

Fig.8 shows the time histories of the drag coefficient C_{Fx} ($= 2F_x/\rho dhU_{ref}^2$) and the lift coefficient C_{Fy} ($= 2F_y/\rho dhU_{ref}^2$) on each segment of the tower at $\lambda = 6$. Here, F_x and F_y are the drag force and the lift force, respectively. The values for C_{Fx} and C_{Fy} fluctuate periodically at time intervals corresponding to when the blade passes upwind of the tower. Segments 1–3, which are affected by the passing of the blades upstream, show particularly high amplitudes of fluctuation. One reason C_{Fx} drops as a blade approaches the tower is the interference from the low-pressure region downwind of the blade, and the resulting drop in air pressure on the upwind side of the tower, as shown in Fig. 7. As also shown in Fig. 7, the reason for the periodic fluctuation in C_{Fy} is the low-pressure region downwind of the blade lowers the pressure on the $+\theta$ side and then on the $-\theta$ side of the tower as the blade approaches and then moves away from the tower.

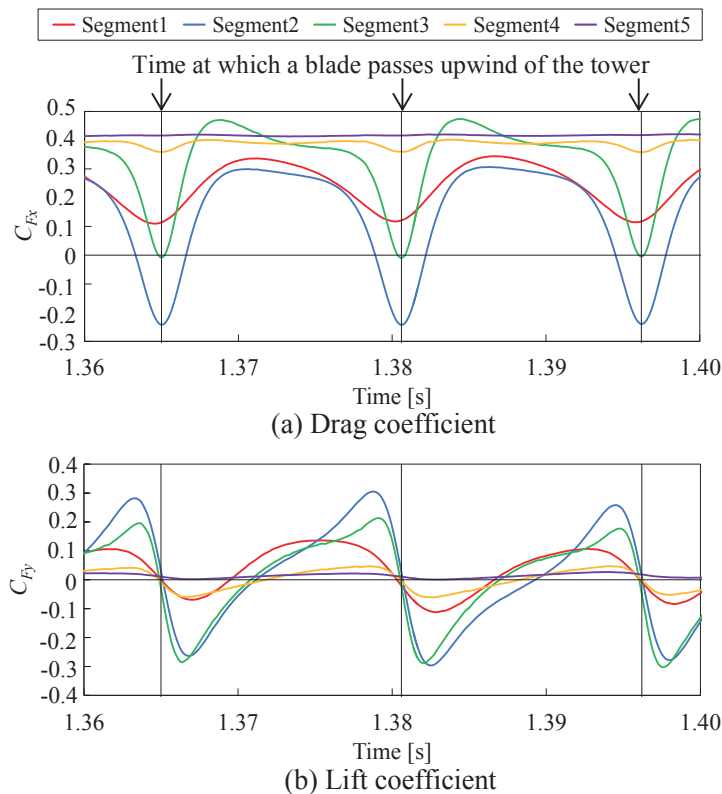


Figure 8: Time-history of the aerodynamic force coefficients on each segment of the tower ($\lambda=6$).

4. CONCLUSIONS

The influence of rotating wind turbine blades on the aerodynamic characteristics of a wind turbine tower was examined by conducting computational fluid dynamics analysis and the following findings were obtained.

- (1) As a result of the diversion of air flow approaching the tower due to rotation of the blades, the maximum value of pressure around the tower at each height above the lowest point of the rotor shifts in the direction of the rotor rotation.
- (2) While a blade is passing upstream of the tower, the pressure fluctuations around the tower at each height above the lowest point of the rotor are greater on the side of the tower where the blade approaches than on the side where the blade moves away, due to the recovery of low pressure on the downstream side of the blade.
- (3) While a blade is near the tower, the air pressure on the upwind side of the tower is reduced due to interference with the lower-pressure region on the downstream side of the blade. This interference causes a periodic decrease in the drag coefficient of the tower.
- (4) While a blade approaches the tower and then moves away, the low-pressure region on the downwind side of the blade causes a drop in the pressure on the side of the tower adjacent to the blade. This pressure drop causes a periodic fluctuation in the lift coefficient of the tower.

ACKNOWLEDGMENT

This research was supported by New Energy and Industrial Technology Development Organization (Project Number: P13010).

REFERENCES

- 1) Gomez-Iradi, S., Steijl, R., Barakos, G. N.: Development and validation of a CFD technique for the aerodynamic analysis of HAWT, *Journal of Solar Energy Engineering*, Vol. 131, 031009.1-031009.13, 2009.
- 2) Wang, Q., Zhou, H., Wan, D.: Numerical simulation of wind turbine blade-tower interaction, *Journal of Marine Science and Application*, Vol. 11, pp. 321-327, 2012.
- 3) Krogstad, P.-Å., Eriksen, P.E., “Blind test” calculations of the performance and wake development for a model wind turbine, *Renewable Energy*, Vol. 50, pp. 325-333, 2013.
- 4) Somers, D.M.: The S825 and S826 Airfoils,” National Renewable Energy Laboratory, NREL/SR-500-36344, 2005.
- 5) Menter, F. R., Langtry, R. B., Likki, S. R., Suzen, Y. B., Huang, P. G., Volker, S.: A correlation-based transition model using local variables—Part I: Model formulation. *Journal of Turbomachinery*, Vol. 128, pp. 413-422, 2006.

EFFECTS OF MULTIDIRECTIONAL SEA STATES AND FLEXIBLE FOUNDATION ON DYNAMIC RESPONSE OF FLOATING OFFSHORE WIND TURBINE SYSTEM

Shining Zhang⁺¹ and Takeshi Ishihara⁺²

^{+1,2}Department of Civil Engineering, School of Engineering, The University of Tokyo, Japan

One reliable simulation tool was developed to be able to predict dynamic response of Floating Offshore Wind Turbines (FOWTs) to various sea states. To represent real environmental condition in field site, multidirectional wave simulation was carried out in this research to investigate effect of wave spreading on dynamic response of FOWT. On the other hand, effect of tower frequency change due to flexible foundation on fatigue load was studied. It was found that unidirectional assumption is conservative in terms of prediction of dynamic motion of platform and multidirectional sea state should be employed to reach cost-effect design. In addition, when wind turbine is supported by flexible foundation, the change of tower natural frequency will result in significant increase of fatigue load. Therefore, Effect of flexible foundation on tower frequency change needs to be taken into consideration in the design of platform and commercial wind turbine.

Keyword: Floating Offshore Wind Turbines, Simulation tool, Multidirectional sea state, Mooring system, Morison equation

1. INTRODUCTION

Development of floating offshore wind turbines is gaining increasing interest because huge wind potential energy is available offshore and less environmental impact is expected. In the design of floating foundation which supports commercial wind turbine, assessment of various load cases associating with sea state are required for safe concern. In IEC-61400-3¹⁾, unidirectional wave propagation is suggested if there is no measured directional information on targeted site. Basically, this unidirectional wave assumption will lead to conservative design since multidirectional wave spreading is expected to dissipate wave energy across wave direction and result in decreased motion of floating platform in dominant wave direction. From economic point of view, however, wave spreading is preferred to be taken into account for cost-effective design of floating platform.

Water tank experiment is thought to be one of popular and reliable ways to investigate performance of platform under hydrodynamic load or to validate developed simulation tool^{2),3),4),5),6)}. Environmental condition in the water tank test, however, is only limited to simple cases, like wind only, wave only (regular or irregular wave), current only and combinations of those individually environmental conditions. Whereas, much more complex and more realistic environmental condition, such as multidirectional wave and misalignment between wind and wave, however, is difficult to carry out in most of water tanks. In real site, wave energy is actually not only function of wave frequency but also the function of angular wave direction. Figure 1 shows typical wave energy distribution at location 20Km offshore from Fukushima, Japan on 17,Sept,2015. One can easily notice that wave energy has a distribution across a specific wave frequency as well as wave direction. It is usually thorny to replicate this kind of complicated environmental sea states in water tank test, simulation tool with consideration of wave spreading function is one alternative way to study effect of multidirectional wave on dynamic response of FOWT. Description of spreading functions can be found in the research by Longuet-Higgins⁷⁾, Mitsuyasu H⁸⁾, T. Duarte et al.⁹⁾ and Kohlmeier M¹⁰⁾.

⁺¹zhang@bridge.t.u-tokyo.ac.jp, ⁺²ishihara@bridge.t.u-tokyo.ac.jp

Another important attention needed to be paid during design of floating platform is elastic impact on evaluation of natural frequency of wind turbine. Figure 2 exhibits variation of dynamic magnification factor versus tower natural frequency¹¹⁾. It can be found that substantial dynamic magnification factor will be experienced and provoke significant fatigue loads in case of the situation that wind turbine natural frequency locates inside of upper and lower blade passing and rotational frequencies. Not like fixed foundation, floating foundation is flexible and will inevitably change the mode shape of wind turbine, which indicates commercial wind turbines might need to be made certain modification to employed in floating platform. Without any modifications, wind turbine which is supported by flexible foundation might encounter significant fatigue load and it might contribute to eventual damage within very short period.

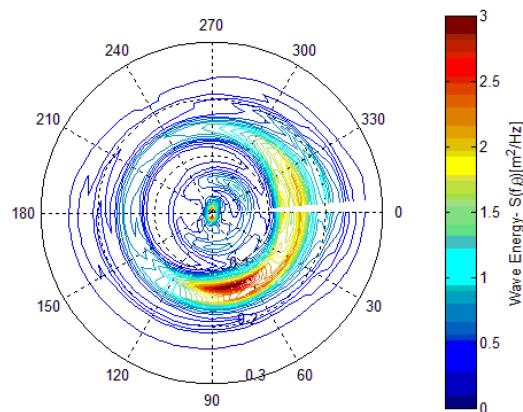


Figure 1: Typical wave energy distribution in Fukushima, Japan on 17, Sept, 2015 22:50-23:10

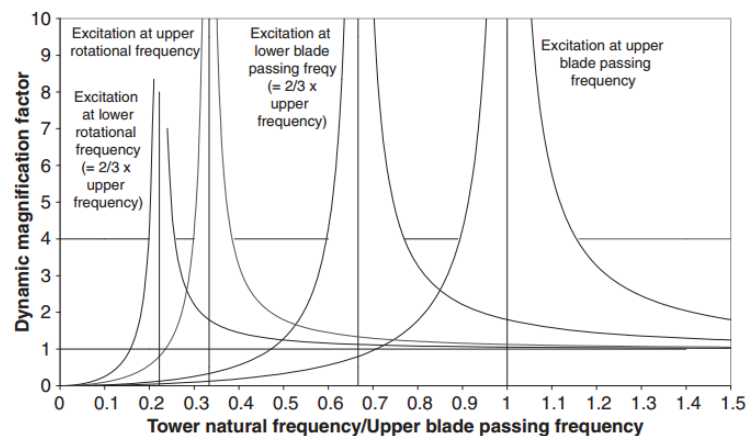


Figure 2: Variation of dynamic magnification factors with tower natural frequency for a two speed, three-bladed

The outline of this paper is as follows. Mathematical model is described in section 2, encompassing hydrodynamic model, wave model and spreading function employed in this research. Section 3 mainly address effect of multidirectional sea states on dynamic response of FOWT. Section 4 aims to discuss impact of change of tower frequency on evaluation of fatigue load. Section 5 gives future work and the paper is finalized with conclusions in Section 6.

2. MATHEMATICAL MODEL

A finite element scheme with beam, truss and spring type elements is developed to calculate dynamic response of full coupled wind turbine, support platform and mooring system. The time domain analysis

enables the FEM to efficiently capture nonlinear characteristics of system in sea states. Morison equation is implemented to evaluate hydrodynamic load on platform. Nonlinear restoring load from mooring system of floating platform is estimated from either quasi-static model¹²⁾.

(1) Hydrodynamic model

Modified Morison equation is utilized to predict hydrodynamic loads on floating structures. Detailed discussion of improved Morison equation could be found in the research by Z. Shining, and T. Ishihara²⁾. Illustration of force acting on segment of slender cylinders and heave plate is shown in Figure 3.

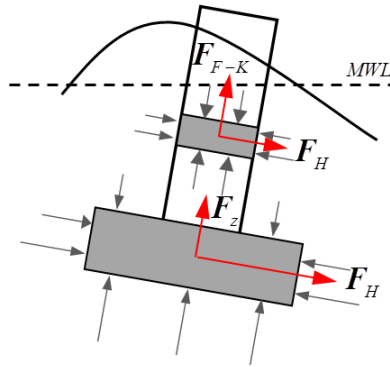


Figure 3: Illustration of hydrodynamic force acting on segment of cylinder and heave plate

a) Normal to axial of segment

The improved Morison equation used in this paper is expressed as following relative form:

$$\{\mathbf{F}_H\} = \underbrace{\rho_w \nabla \dot{\mathbf{u}}}_{\text{Froude-Krylov force}} + \underbrace{\rho_w (C_M - 1) \nabla \dot{\mathbf{u}} - \rho_w (C_M - 1) \nabla \ddot{\mathbf{X}} - [C_{Rdn}] \dot{\mathbf{X}}}_{\text{Diffraction force}} + \underbrace{0.5 \rho_w C_d A (\mathbf{u} - \dot{\mathbf{X}}) |\mathbf{u} - \dot{\mathbf{X}}|}_{\text{Viscous drag force}} \quad (1)$$

Where, first term in right of Eq. (1) accounts for Froude-Krylov force due to undisturbed incident wave and second term represents diffraction force resulting from pressure effects due to presence of structure. The third terms indicates radiation force (hydrodynamic inertia force and radiation damping force) which is caused by motion of structural components in an ideal fluid. Fourth term gives viscous drag force due to the relative velocity between water particle and structural components. ρ_w is density of water; \mathbf{u} and $\dot{\mathbf{u}}$ are vector of undisturbed fluid-particle velocity and acceleration respectively; $\{\mathbf{X}\}$, $\{\dot{\mathbf{X}}\}$ and $\{\ddot{\mathbf{X}}\}$ are vector of support platform displacement and their time derivatives; $[C_{Rdn}]$ is linear radiation damping; ∇ is the displaced volume of fluid by each segment when the support platform is in its undisplaced position; A is cross-sectional area; C_M and C_d are inertia and drag coefficient respectively which depends on Keulegan-Carpenter number $K_C = u_{\max} T / D$, frequency parameter $\beta = D^2 / \nu T$ and surface roughness etc. u_{\max} is the maximum water particle velocity, T is incident wave period, D is diameter of cylinder and ν is the kinematic viscosity of water.

b) Axial of segment

In order to effectively increase the hydrodynamic damping in heave direction and reduce heave response^{13), 14)}, appendage such as a disk (heave plate) are usually added to the keel of a vertical cylinder such as the disk chosen in WindFloat and heave plate employed in Fukushima MIRAI¹⁵⁾. Ishihara et al.¹⁵⁾ proposed Morison like equation to evaluate hydrodynamic force on heave plate in axial direction. Hydrodynamic force for a heave plate is formulated using modified Morison equation as given below

$$\{\mathbf{F}_z\} = \underbrace{0.25\pi D_h^2 p_b^{Hp} - 0.25\pi (D_h^2 - D_c^2) p_t^{Hp}}_{\text{Froude-Krylov force}} + \underbrace{\rho_w (C_{Mz} - 1) \nabla_z \dot{\mathbf{w}}}_{\text{Diffraction force}} - \underbrace{\rho_w (C_{Mz} - 1) \nabla_z \ddot{\mathbf{X}}_3}_{\text{Radiation force}} + \underbrace{0.5 \rho_w C_{dz} A_C (\mathbf{w} - \dot{\mathbf{X}}_3) |\mathbf{w} - \dot{\mathbf{X}}_3|}_{\text{Viscous drag force}} \quad (2)$$

Where, C_{Mz} is the added mass coefficient in the heave direction, ∇_z is volume of heave plate, \dot{w} is the vertical wave particle acceleration, \ddot{X}_3 is acceleration of the heave plate in heave direction, C_{dz} is the drag coefficient in the heave direction, A_c is the cross-sectional area of the heave plate, w is the vertical wave particle velocity, \dot{X}_3 is velocity of the heave plate in heave direction, D_h is the diameter of the heave plate, D_c is the diameter of the upper column (which is placed on top of the heave plate), and p_b^{Hp} and p_t^{Hp} are the dynamic pressure acting on the bottom and top faces of the heave plate. Dynamic pressure at position z in regular wave using Airy theory is expressed as follows

$$P = \frac{\rho g H \cosh k(z+d)}{2 \cosh kd} \cos(kx - \omega t) \quad (3)$$

Where, H is wave height (m), ω is wave frequency(rad/s), k is wave number, d is water depth, z is specified position.

To evaluate axial force on the other segments of elements (such as vertical columns, braces and pontoons), only Froude-Krylove force is taken into consideration by integrating dynamic pressure on member ends as follows,

$$\{F_{F-K}\} = 0.25\pi D_c^2 (p_b - p_t) \quad (4)$$

Where, p_b and p_t are the dynamic pressure acting on the bottom and top faces of segment.

(2) Linear irregular wave theory

As for the dynamic response of FOWT to irregular wave in both unidirectional and multidirectional sea state, JONSWAP wave spectra was used in both simulation tool and water tank experiment. The spectrum is given as

$$S(f) = \alpha_s H_s^2 T_p^{-4} f^{-5} \exp\{-1.25(T_p f)^{-4}\} \gamma^{\exp\left\{\frac{(T_p f - 1)^2}{2\sigma^2}\right\}} \quad (5)$$

$$\alpha_s = \frac{0.0624}{0.230 + 0.0336\gamma - 0.185/(1.9 + \gamma)} \quad (6)$$

Where, f is wave frequency (Hz), H_s is significant wave height, T_p is peak wave period, γ is peak factor ($\gamma = 2$ is used in this paper) and σ is shape factor ($\sigma = 0.07$ for $f \leq (1/T_p)$ and $\sigma = 0.09$ for $f > (1/T_p)$).

(3) Spreading function

The spreading function used in this research is frequency independent cos-2s type implemented in WAFO¹⁶⁾. Total wave spectrum can be defined as

$$S(\omega, \theta) = S(\omega) \cdot D(\theta) \quad (7)$$

Where, $S(\omega)$ is the frequency spectrum, independent of the direction of the waves, and $D(\theta)$ is the directional spectrum.

$$D(\theta) = \frac{\Gamma(s+1)}{2\sqrt{\pi}\Gamma(s+1/2)} \cos^{2s}\left(\frac{\theta - \theta_p}{2}\right) \quad (8)$$

Where, Γ is the gamma function. θ is the spreading angle, θ_p is the energy peak direction and s is the spreading parameter.

After spreading function $D(\theta)$ is determined, equal-energy method⁹⁾ is used to discretize the wave direction. Then wave elevation can be written in following way

$$\eta = \sum_{n=1}^N A_n \cos(k_n (x \cos(\theta_k) + y \sin(\theta_k)) - \omega_n t + \varepsilon_n) \tag{9}$$

Where, $A_n, k_n, \omega_n, \varepsilon_n$ and θ_k are discretized wave height, wave number, wave frequency, random phase and wave direction.

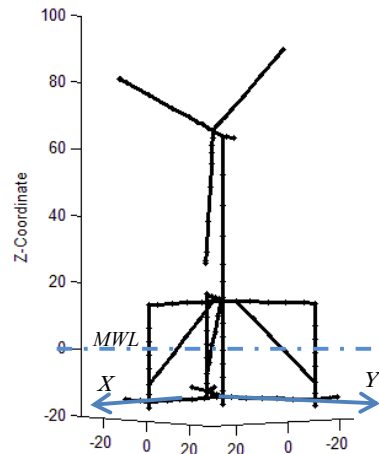
Linear superposition can also be used to compose water particle velocity and acceleration required in Morison equation.

3. DYNAMIC RESPONSE OF FOWT IN MULTIDIRECTIONAL IRREGULAR SEA STATE

In this section, prototype of Fukushima MIRAI 2MW FOWT is established with FEM and dynamic response of floating system is investigated in terms of multidirectional wave spreading effect. Figure 4 shows image of prototype of Fukushima MIRAI and FEM model adopted in numerical simulation. It should be noted that aerodynamic load is excluded in the simulation to classify the solo wave spreading effect. To represent irregular wave, JONSWAP wave spectra with measured significant wave height 3.83m and peak period 8.3sec. is used in this research. Figure 5 illustrates wave spreading function and resulting wave energy distribution across wave frequency and wave direction. Spreading parameter s in Eq.(8) is 13 and dominant wave direction is 0 degree (Y-axis faces to north and wave propagates from west to east). In Figure 5(a), spreading function follows from Eq.(8), it can be concluded that discretized spreading wave direction could represent well for targeted spreading function.

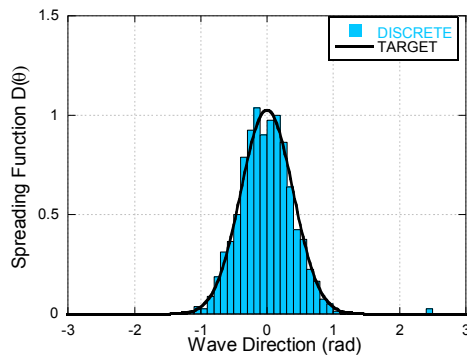


(a) Prototype of Fukushima MARIA

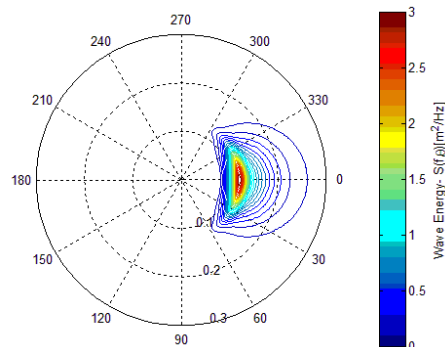


(b) FEM model

Figure 4: Image of prototype of (a) Fukushima MARIA and (b) FEM model



(a) Spreading function



(b) Polar plot of wave energy distribution

Figure 5: Wave spreading function and total wave energy distribution

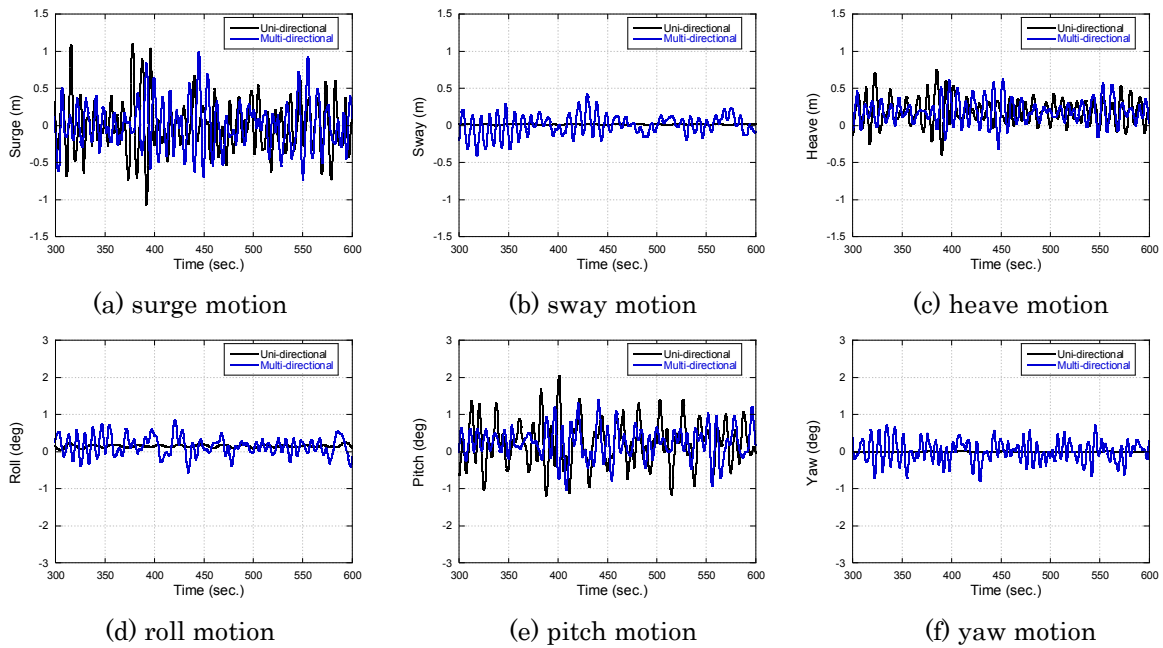


Figure 6: Dynamic motion of platform in unidirectional and multidirectional irregular wave

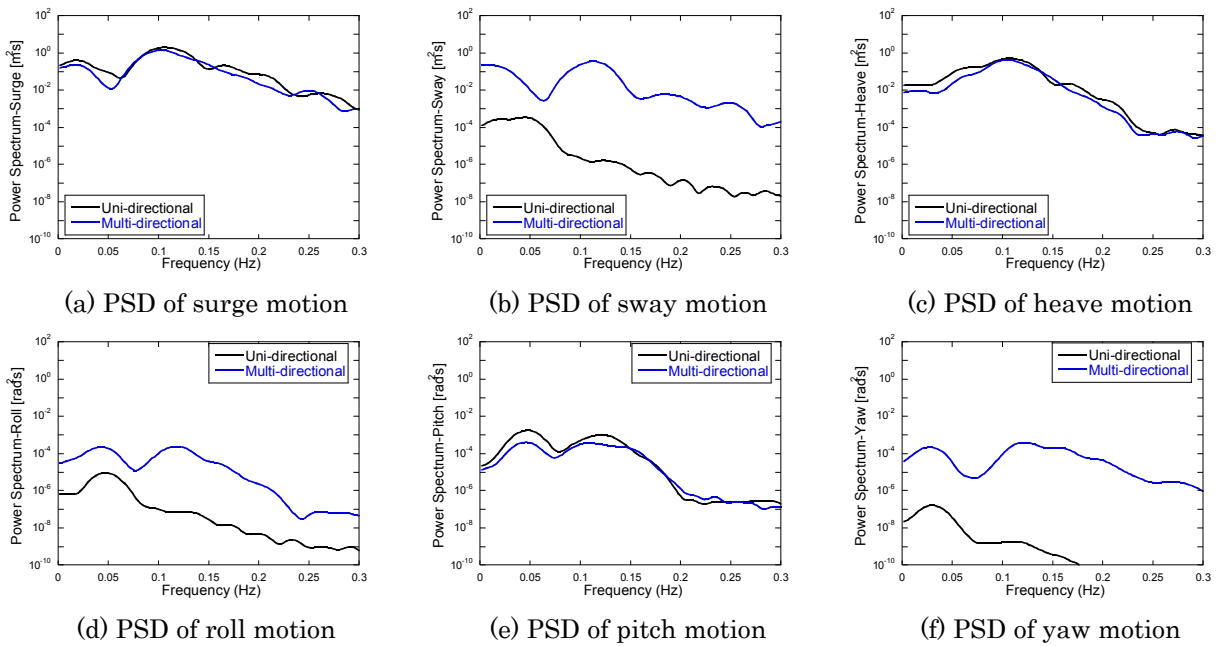
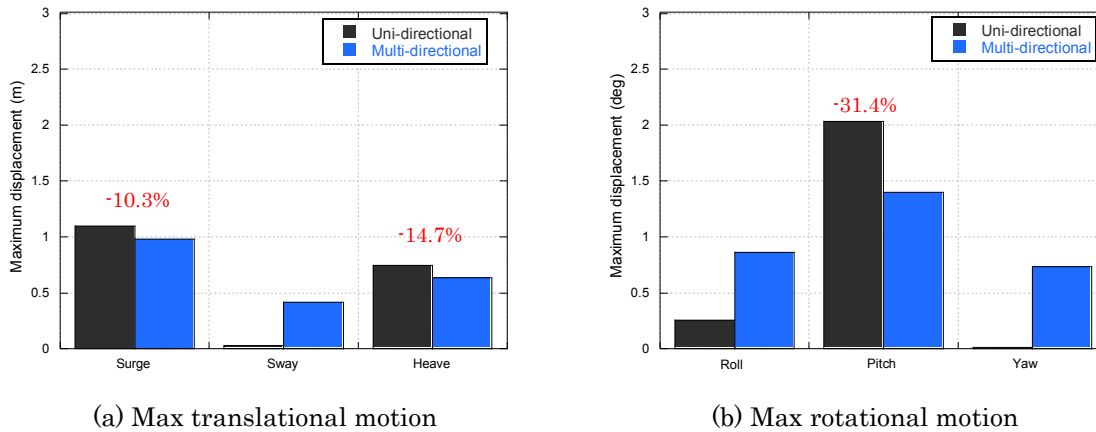


Figure 7: Power spectrum density of dynamic motion of platform in unidirectional and multidirectional irregular wave

Figure 6 provides time history of dynamic motion of platform under unidirectional and multidirectional wave condition within 5mins. It can be found that sway, roll and yaw motion in unidirectional wave condition are almost zero since platform geometry is symmetric about XZ-plane. Significant motion in these three modes, however, are excited in multidirectional sea state since wave is not propagate only in X-axis any more. Dissipation of wave energy over certain angular direction would amplify the motion in sway, roll and pitch direction. At the same time, this wave energy dissipation will decrease surge, heave and pitch motion as expected. Same conclusion can be derived from what shown in PSD of dynamic motion in Figure 7. Two peaks could be found in PSD of the motion, one is same in all modes which corresponds to wave peak

period (0.12Hz) and the other one conforms with to natural period of floating system in each mode.

Figure 8 gives maximum of displacement in mentioned two sets of wave directional condition. Maximum surge, heave and pitch motion decrease by 10.3%, 14.7% and 31.4% respectively when wave spreading is taken into account. Considering the recommendation in IEC-61400-3 in terms of unidirectional wave assumption, appropriate evaluation and consideration of wave spreading will bring about cost-effective design.



(a) Max translational motion (b) Max rotational motion
 Figure 8: Maximum of (a) translational displacement and (b) rotational motion in unidirectional and multidirectional sea state

4. EFFECT OF FLEXIBLE FOUNDATION ON TOWER FATIGUE LOAD

In this section, one 2MW offshore wind turbine will be used to clarify the effect of natural frequency of tower on fatigue load evaluation. One fixed foundation and flexible foundation will be investigated on resulting fatigue load. General characteristics of rotor and turbine are listed in Table 1. Rotor speed is 18rpm and 1P blade passing frequency is 0.3Hz. Information about time dependent wind field is summarized in Table 2. Six 10mins stochastic realizations are conducted to determine the equivalent fatigue load.

Table 1: General characteristics of rotor and turbine

Rotor diameter	80	m
Number of blades	3	
Hub height	61.5	m
Tower height	60	m
Aerodynamic control surfaces	Pitch	
Fixed / Variable speed	Variable	
Cut in wind speed	4	m/s
Cut out wind speed	25	m/s
Rotor speed	18	rpm

Table 2: Time dependent wind field

Wind model type	Turbulent Wind	
Mean wind speed for simulation	21.5	m/s
Wind direction from North	0	deg
Longitudinal turbulence intensity	16.17	%
Lateral turbulence intensity	12.93	%
Vertical turbulence intensity	8.08	%

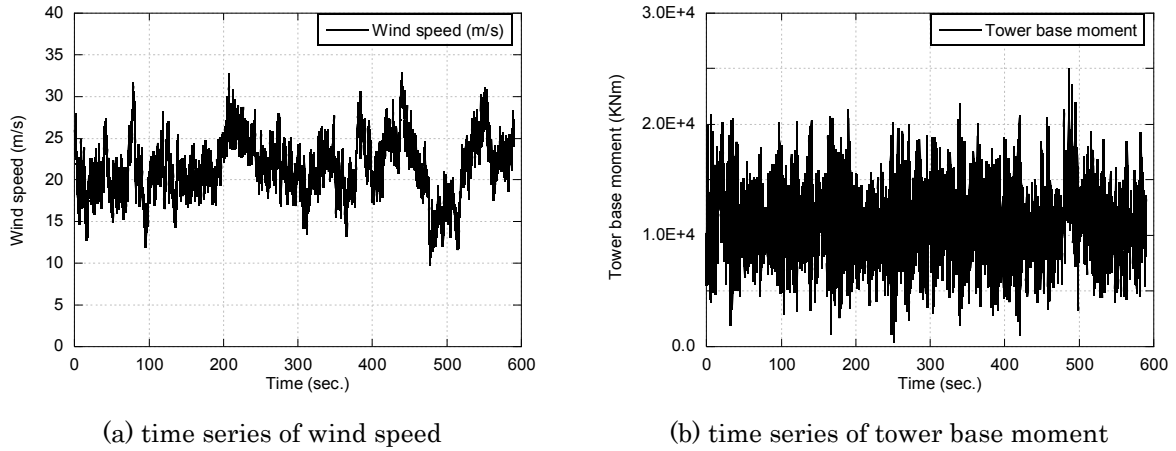


Figure 9: Time series of (a) wind speed and (b) resulting tower base moment in one wind seed

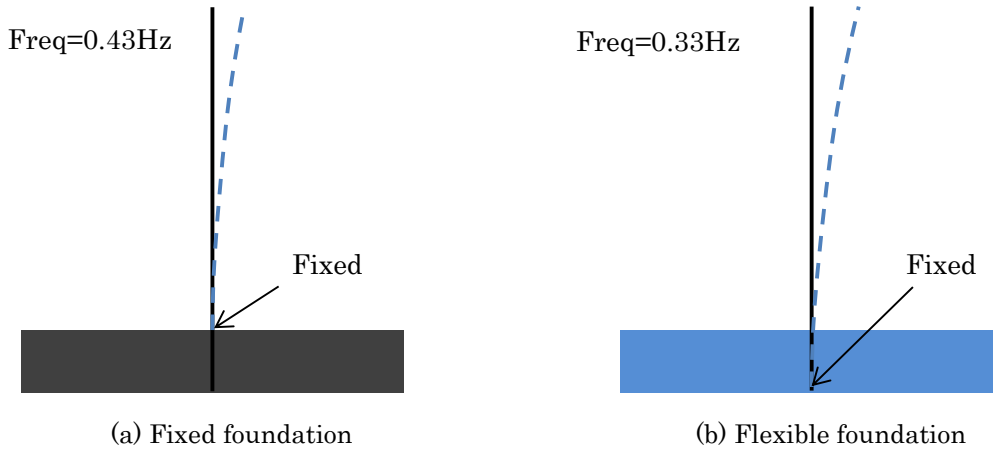


Figure 10: Mode shape of tower in fixed condition and flexible foundation

Figure 9 shows one of simulation results in term of turbulent wind and resulting tower base moment. Rainflow cycle counting is used to deal with time history of tower base moment to determine damage equivalent load which would produce the same fatigue damage as the original signal. The equivalent load M_{eq} is defined as follows,

$$M_{eq} = \left(\frac{\sum_i n_i S_i^m}{Tf} \right)^{\frac{1}{m}} \tag{10}$$

Where, n_i is the number of cycles in load range S_i ; T is the duration of the original time history (10mins); m is inverse S-N slopes and f is frequency of equivalent sinusoidal load.

Two types of foundation are shown in Figure 10. One assumes that wind turbine is supported on rigid foundation and natural frequency is 0.43Hz. The other one assumes foundation is flexible and natural frequency is 0.33Hz as a result. It is noteworthy that rotor speed is 18rpm and 1P blade passing frequency is 0.3Hz. Tower natural frequency under condition of flexible foundation is close to this rotational frequency. Consequently, larger dynamic magnification factor is expected when compared with the wind turbine with fixed foundation.

Figure 11 depicts statistics of tower base moment and evaluated damage equivalent load. In figure (a), one can find maximum and standard deviation of tower base moment increase by 7.1% and 23.7 respectively

in case of flexible foundation. Damage equivalent load in fixed and flexible foundation with respect to various inverse S-N slope m is shown in Figure 11(b). One can conclude that equivalent load increase by at least 10.6% in case of flexible foundation with $m=3$.

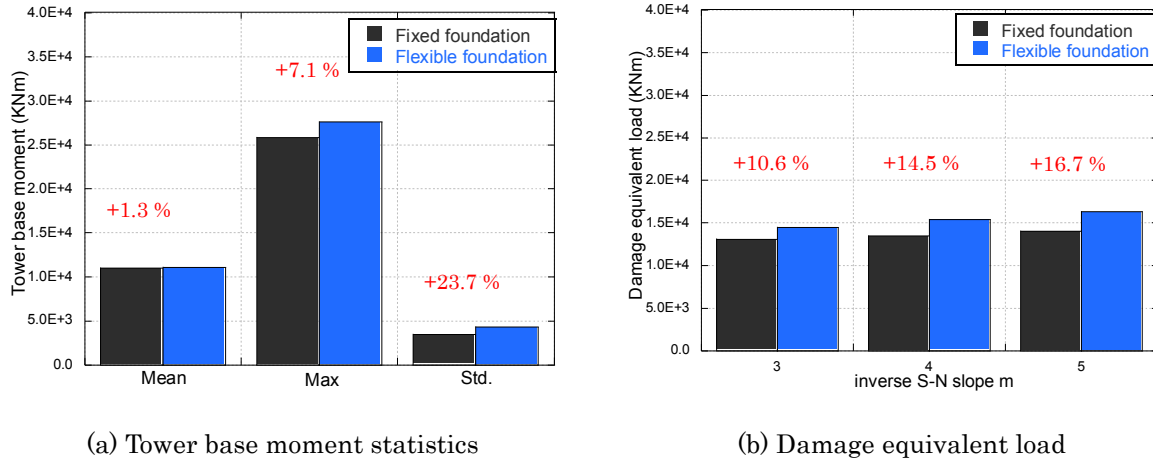


Figure 11: Statistics of tower base moment and damage equivalent load in fixed and flexible foundation

5. FUTURE WORK

The results provided in this research are all based on simulation data. Accurate evaluation in effect of multidirectional sea state and flexible tower frequency will be further validated by field measurement.

6. CONCLUSIONS

Effects of multidirectional sea state on dynamic motion of platform and impact of flexible foundation on damage fatigue load are studied in this research. Main conclusions are as follows,

(1). Recommendation of unidirectional sea state assumption in IEC-61400-3 will lead to conservative design of platform. Multidirectional sea state employment can decrease the motion by 10.3%, 14.7% and 31.4% in surge, heave and pitch respectively which indicate cost-effective design could be reached when introducing reasonable wave spreading function.

(2). Flexible foundation would impact tower natural frequency and could increase damage equivalent load consequently. It means natural frequency of commercial wind turbine should be re-determined when it is supported on flexible platform and impact of flexible foundation on dynamic load on foundation needs to be investigated again. Otherwise, wind turbine will suffer significant fatigue load, which could shorten service time.

ACKNOWLEDGMENT

This research is funded by Ministry of Economy, Trade and Industry, Japan. I wish to express my deepest gratitude to the concerned parties for their assistances and contributions in this research.

REFERENCES

- 1) Quarton D C. An international design standard for offshore wind turbines: IEC 61400-3[J]. Bristol, UK: Garrad Hassan and Partners, Ltd, 2005.
- 2) Shining Zhang and Takeshi Ishihara. Prediction of dynamic response of semi-submersible floating offshore wind turbine using Morison based theory. Proc of EWEA 2015, 17-21
- 3) Latha Sethuraman, Vengatesan Venugopal. Hydrodynamic response of a stepped-spar floating wind turbine: Numerical modelling and tank testing. Renewable Energy 52(2013) 160-174.
- 4) J.R. Browning, J. Jonkman, A. Robertson and A.J. Goupee. Calibration and Validation of a Spar-Type Floating Offshore Wind Turbine Model using the FAST Dynamic Simulation Tool. Conference paper (National Renewable Energy Laboratory (U.S.)); NREL/CP-5000-56138,2012.

- 5) P.V. Phuc, T. Ishihara, A study on the dynamic response of a semi-submersible floating offshore wind system part 2: Numerical simulation, in: Proceedings of the international Conferences of Wind Engineering 12, Cairns, Australia, 2007.
- 6) M. B. Waris and T. Ishihara. Dynamic response analysis of floating offshore wind turbine with different types of heave plates and mooring systems by using a fully nonlinear model. *Coupled Systems Mechanics*, Vol. 1, No. 3 (2012) 247-268.
- 7) Longuet-Higgins M S, Cartwright D E, Smith N D. Observations of the directional spectrum of sea waves using the motions of a floating buoy[J]. 1963.
- 8) Mitsuyasu H, Tasai F, Suhara T, et al. Observations of the directional spectrum of ocean Waves Using a cloverleaf buoy[J]. *Journal of Physical Oceanography*, 1975, 5(4): 750-760.
- 9) Duarte, Tiago, et al. "Computation of Wave Loads under Multidirectional Sea States for Floating Offshore Wind Turbines." ASME 2014 33rd International Conference on Ocean, Offshore and Arctic Engineering. American Society of Mechanical Engineers, 2014.
- 10) Kohlmeier M, Mittendorf K, Kossel T, et al. Wave Load Prediction Methods in Offshore Wind Turbine Modelling and their Influence on Fatigue Load Analysis[C]//European Offshore Wind Conference & Exhibition. 2007.
- 11) Burton T, Sharpe D, Jenkins N, et al. *Wind energy handbook*[M]. John Wiley & Sons, 2011.
- 12) J. M. Jonkman. Dynamics of Offshore Floating Wind Turbines- Model Development and verification. *Wind Energy*. 2009; 12:459-492. DOI 10.1002/we.347
- 13) H.A. Haslum, and O. M. Faltinsen. Alternative Shape of Spar Platforms for Use in Hostile Areas. Offshore Technology Conference, OTC10953, Houston, Texas, 1999.
- 14) L. Tao, K. Y. Lim and K. Thiagarajan. Heave Response of Classic Spar With Variable Geometry. *Journal of Offshore Mechanics and Arctic Engineering*, Vol.126 (2004) 90-95.
- 15) T. Ishihara, K. Kagaya, Y. Kikuchi. Dynamic Analysis of Floating Offshore Wind Turbine System Considering Combined Hydrodynamic Loadings. EWEA OFFSHORE 2013. PO.ID 133.
- 16) Brodtkorb P A, Johannesson P, Lindgren G, et al. WAFO-a Matlab toolbox for analysis of random waves and loads[C]. The Tenth International Offshore and Polar Engineering Conference. International Society of Offshore and Polar Engineers, 2000.

Wind Loads on a Bottom-mounted Offshore Wind Turbine Tower

Kazumasa OKUBO⁺¹, Manabu YAMAMOTO⁺², Yukinari FUKUMOTO⁺³ and Takeshi ISHIHARA⁺⁴
⁺¹⁺²Kajima Technical Research Institute, Tokyo, Japan
⁺³Tokyo Electric Power Company Research & Development Center, Yokohama, Japan
⁺⁴The University of Tokyo, Tokyo, Japan

Having a long coastline, offshore wind energy is one of the most important solutions for the increase of renewable energy in Japan. However, due to the differences in wind, marine and earthquake conditions between Japan and Europe, the safety, the environmental impact and the economic feasibility of offshore wind energy have to be investigated. Since 2009, the authors have started an experimental investigation of NEDO's offshore wind power generation system proving research project on the Pacific Ocean near coast of Japan. This project aims to establish an offshore wind power generation technology which is suitable for Japanese external conditions. This paper describes the characteristics of wind loads on the offshore wind turbine tower. The site is located at 3.1km offshore from Choshi, and the water depth is 11.9m. Proving wind turbine is a propeller-type with three blades (Hub height: 80m, Rated power: 2.4MW, Bottom-mounted). The wind loads were investigated as bending moment at bottom of tower by using strain-gauge data. In this paper, obtained wind loads were compared between operational condition and feathering condition, wind of the landside and of the seaside. As a result, in both condition, the maximum wind loads for the wind of the landside were bigger than those for the wind of the seaside under the influence of the land 3.1 kilometers away from the wind turbine. The gust effect factors in the feathering condition for the wind of the seaside were from 1.8 to 2.0. Furthermore, the gust effect factors for the wind of the landside were more than 2.1 in range of less than 30m/s.

Keyword: offshore wind turbine, field measurement, wind load, gust effect factor

1. Introduction

Most of the wind power generation systems in Japan are sited on land. Offshore wind power generation systems, however, are expected to go into widespread use in the coming years because higher wind speed compared with on-land make it possible to obtain more stable power output and also because large wind turbines and large-scale wind farms can be constructed. In order to establish the technology to build bottom-mounted offshore wind turbine towers capable of withstanding harsh meteorological and oceanographic characteristic of Japan in preparation for the proliferation of offshore wind power generation systems, New Energy and Industrial Technology Development Organization (NEDO) and Tokyo Electric Power Company constructed the first bottom-mounted offshore wind turbine tower¹⁾ in Japan off the coast of Chiba Prefecture under their joint demonstration project. In this paper, the study conducted to estimate bending moments (wind loads) acting on the base of the bottom-mounted wind turbine tower from strain measurement data, and investigate wind load characteristics peculiar to wind turbines and the influence of turbulence on wind loads.

2. Observation System

The structure is a bottom-mounted offshore wind turbine tower constructed 3.1 km to the south of Choshi City, Chiba Prefecture¹⁾ as shown in Figure 1. A wind observation tower has also been built 285m to the east of the wind turbine^{1),2)}. Figure 2 illustrates the offshore wind turbine. Strain gauges were installed to

⁺¹okubokaz@kajima.com, ⁺²yamamoto-ma@kajima.com, ⁺³fukumoto.yukinari@tepcoco.jp, ⁺⁴ishihara@bridge.t.u-tokyo.ac.jp

the internal wall surface of the tower at the three different levels shown in Figure 2. Strain (in the vertical direction) was measured at a sampling frequency of 50Hz. After subtracting the strain under windless conditions (zero-strain point) from the strain under wind loading, the measured strain thus obtained was converted to a combination of an along-wind strain and an across-wind strain by using trigonometric functions based on the 10-minute mean wind direction obtained from the wind vane anemometer installed on top of the nacelle (M.S.L. + approx. 84m). This study turns attention to the along-wind bending moment $M_D(t)$ and the across-wind bending moment $M_L(t)$ at the base of the tower [the top of the foundation + 0.77m (M.S.L. + 10.9m)]. $M_D(t)$ and $M_L(t)$ were calculated by using the following equation:

$$M_D(t) = \frac{EI\{\varepsilon_W(t) - \varepsilon_L(t)\}}{D'}, \quad M_L(t) = \frac{EI\{\varepsilon_{Lr}(t) - \varepsilon_{Ll}(t)\}}{D'} \tag{1}$$

$$I = \frac{(D^4 - D'^4)\pi}{64} \tag{2}$$

where E : Young's modulus for the tower, I : moment of inertia of area of the tower, $\varepsilon_W(t) / \varepsilon_L(t)$: along-wind strain on the windward / leeward side at time t , $\varepsilon_{Lr}(t) / \varepsilon_{Ll}(t)$: across-wind strain on the right / left side at time t , D' : inside diameter of the tower, D : outside diameter of the tower

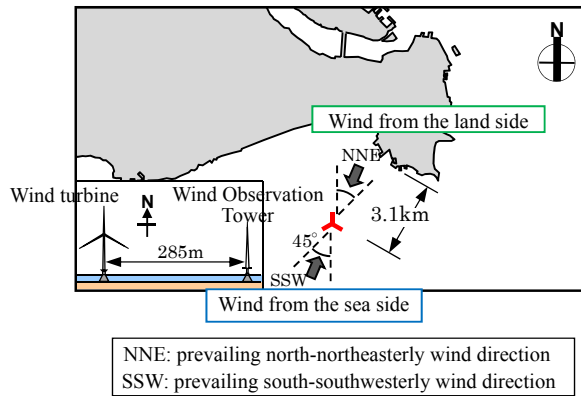


Figure 1: Offshore wind power generation system site

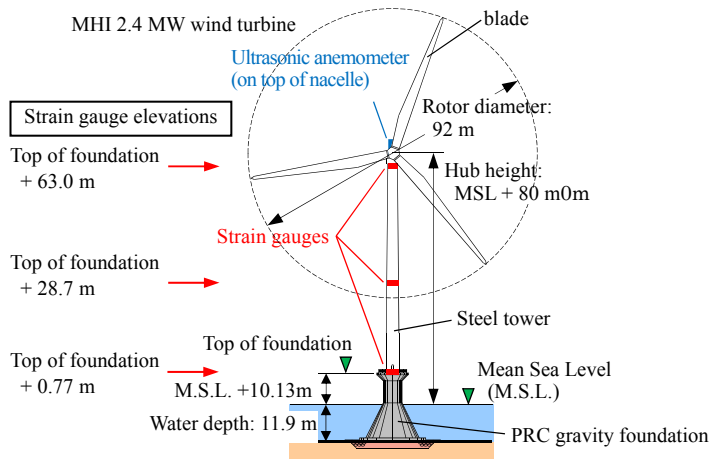


Figure 2: Offshore wind power generation system and strain gauges installed to the wind turbine tower

10-minute mean wind speed was calculated from wind speed obtained on the top of the nacelle. The observed wind speed was corrected to hub-height wind speed (hereinafter referred to simply as "wind speed")

by using the wind speed measurement data obtained from the wind observation tower (M.S.L. + 80m). Figure 3 shows the relationship between the mean wind speeds at the nacelle and the wind observation tower and the wind speed conversion formulas used. Turbulence intensities of wind from the land side and wind from the sea side were about 9% and 5%, respectively²⁾. In the vibration tests conducted by using the excitation system installed in the tower, the first-mode natural frequency and the first-mode damping ratio in the tower main shaft direction (along-wind direction) were 0.35Hz and 0.2%, respectively³⁾.

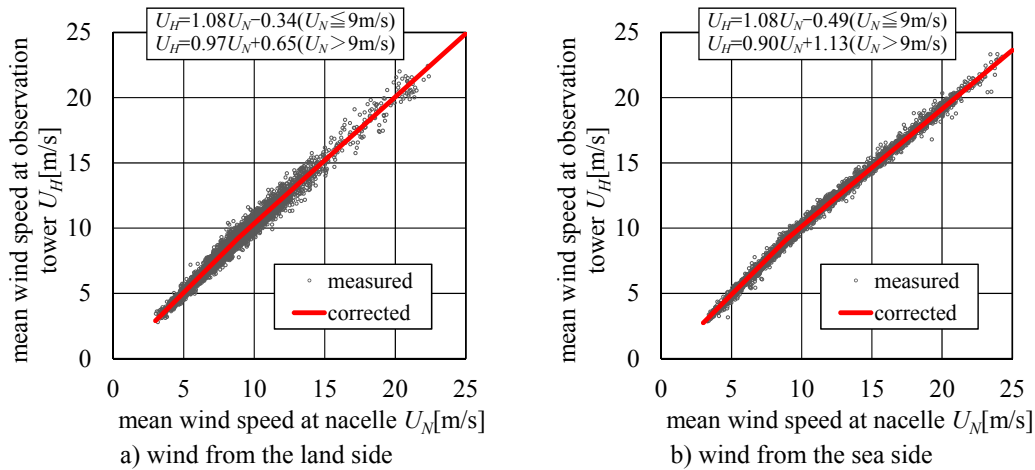


Figure 3: Mean wind speeds at Nacelle and at Wind Observation Tower

3. Observation Results

(1) Test to identify zero-strain point under windless conditions

Since wind turbine yaw control adjusts the turbine blade rotation plane so that it squarely faces the wind, vertical strain changes depending on the direction of the nacelle, which is a heavy component. A test, therefore, was conducted under arbitrarily varied nacelle direction conditions to identify the zero-strain point under windless conditions. The test was conducted under low wind conditions (3 to 5 m/s) and the turbine blades were feathered (so that they did not rotate) during the test so as to minimize the wind force acting on the tower. In order to eliminate the influence of thermally induced elongation due to sunlight on strain, the test was carried out at night. Figure 4 shows an example of the relationship between nacelle direction and the zero-strain point based on the data obtained from the strain gauges on the north side. As shown, the zero-strain point changes depending on nacelle direction: in the case where the nacelle is directed to the north, in which the strain gauge position coincides with the rotor direction, the zero point shifts toward the compression side, and in the case where the nacelle is directed to the south (in the opposite direction), the zero point shifts toward the tension side. Figure 4 also shows nighttime observation data obtained when the wind speed was lower than 1 m/s. As shown, the nighttime observation data show close agreement with the test results. It was decided, therefore, to use those test results to define the zero-strain point under windless conditions.

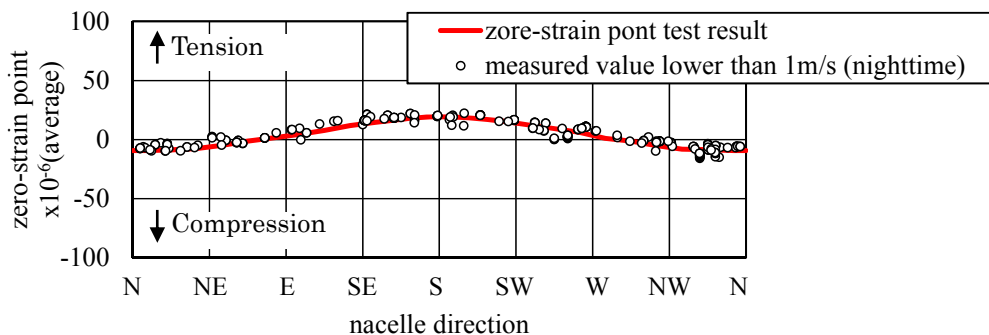


Figure 4: nacelle direction and zero-strain point (example of strain gauge on the north side)

(2) Wind load in operational condition

Figure 5 shows the relationship between wind speed and the along-wind static bending moment (10-minute average) M_D in operational condition. Figure 6 shows the relationship between wind speed and the maximum bending moment (10-minute maximum instantaneous value) M_{Dmax} . To show the differences in the turbulence intensity of approaching flows, Figures 5 to 7 show the values for the wind from the sea side and the wind from the land side defined in Figures 1. The shown values are nighttime observation data that are relatively unaffected by thermally induced elongation due to sunlight. As shown, M_D increases with wind speed when wind speed is not higher than 10m/s. When wind speed exceeds 11m/s, however, M_D begins to decrease. This is a wind load characteristic peculiar to wind turbines. The reason for this is as follows. When wind speed is 10m/s or lower, the blade pitch angle (the angle between the chord line and the rotor plane) is kept small and constant, and at wind speeds of 5 to 8m/s, the rotor speed is increased as wind speed increases. When wind speed is higher than 11m/s, the rotor speed is kept constant and the pitch angle is increased as wind speed increases (pitch control)⁴⁾. Although M_D values show fair agreement between wind from the land side and wind from the sea side, M_{Dmax} values for wind from the land side are greater than those for wind from the sea side, indicating the influence of turbulence intensity. The influence of turbulence intensity was evaluated quantitatively by determining the gust effect factor $G_D (= M_{Dmax}/M_D)$ for along-wind loads. The G_D values shown in Figure 7 are smallest at a wind speed of about 10m/s at which M_D is maximized. At wind

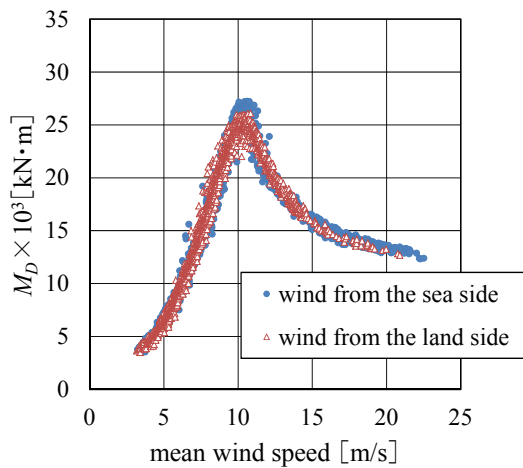


Figure 5: Along-wind static bending moment M_D (operational condition)

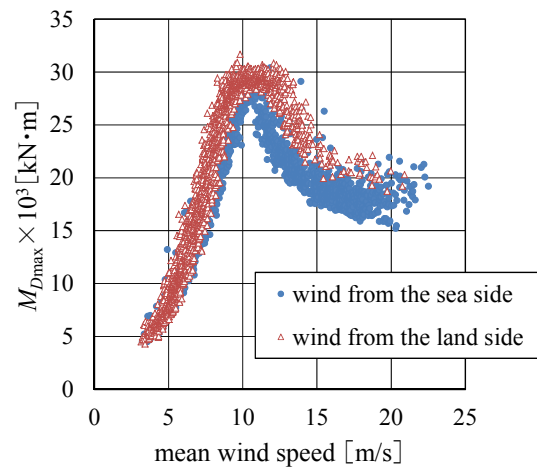
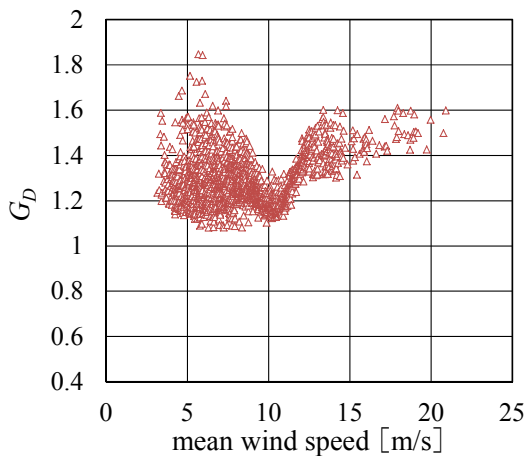
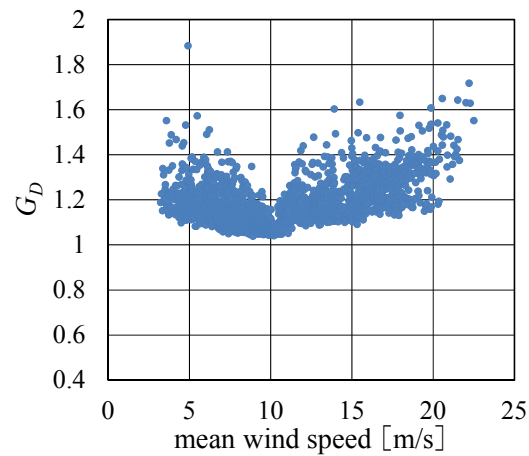


Figure 6: Along-wind maximum bending moment M_{Dmax} (operational condition)



a) wind from the land side



b) wind from the sea side

Figure 7: Along-wind gust effect factor G_D (operational condition)

speeds of 11m/s or higher, G_D tends to increase with wind speed. The values of G_D for wind from the land side tends to be greater than the values for wind from the sea side: G_D values for wind from the land side at a wind speed of 10m/s range from 1.1 to 1.3, and values for wind from the sea side range from 1.05 to 1.1.

(3) Wind load in feathering condition

Figure 8 shows the relationship between wind speed and the along-wind static bending moment M_D in feathering condition. Figure 9 shows the relationship between wind speed and the maximum bending moment M_{Dmax} . Figure 10 shows the relationship between wind speed and the maximum across-wind bending moment M_{Lmax} . To show the differences in the turbulence intensity of approaching flows, Figures 8 to 10 show the values for the wind from the sea side and the wind from the land side defined in Figures 1. The shown values are nighttime observation data that are relatively unaffected by thermally induced elongation due to sunlight. The wind speed range considered in this study is 1 to 29m/s, and the Reynolds numbers range from 3×10^5 to 7×10^6 (the reference length is 3.5m, which is the average width of the tower).

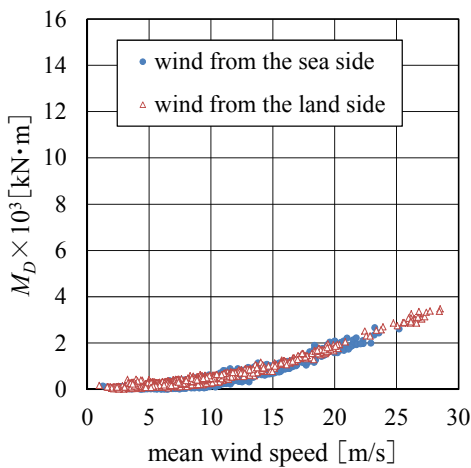


Figure 8: Along-wind static bending moment M_D (feathering condition)

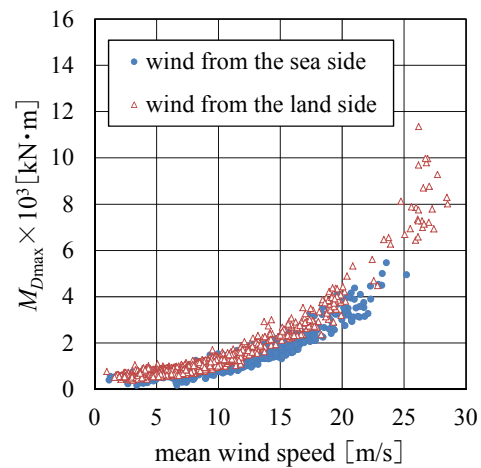


Figure 9: Along-wind maximum bending moment M_{Dmax} (feathering condition)

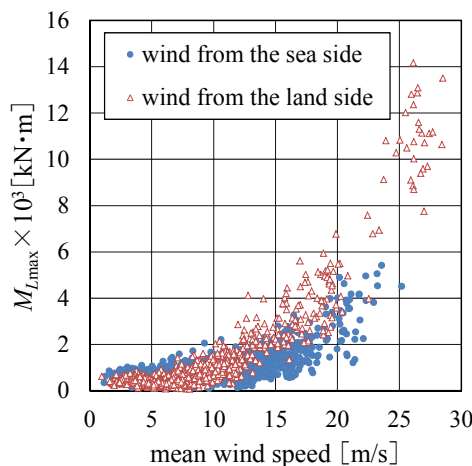


Figure 10: Across-wind maximum bending moment M_{Lmax} (feathering condition)

As shown, M_D increases with wind speed, and the values for wind from the sea side and the values for wind from the land side are similar. The M_{Dmax} and M_{Lmax} values for wind from the land side are greater than those for wind from the sea side, showing the influence of the turbulence intensity of approaching flows. The clear peak of M_{Lmax} which seems vortex induced vibration wasn't seen. Comparison of the values in the

along-wind direction (M_{Dmax}) and the values in the across-wind direction (M_{Lmax}) reveals that M_{Lmax} tends to be greater than M_{Dmax} in the wind speed range higher than 15m/s.

The along-wind static bending moment coefficient C_{MD} was calculated by using the formula shown below. Figure 11 shows the relationship between wind speed and C_{MD} . As shown, C_{MD} gradually approaches approximately 0.42 as wind speed increases.

$$C_{MD} = \frac{M_D}{0.5\rho U_H D H'^2} \tag{3}$$

where ρ : air density, D : average width of the tower, H' : distance between strain measurement height and hub height

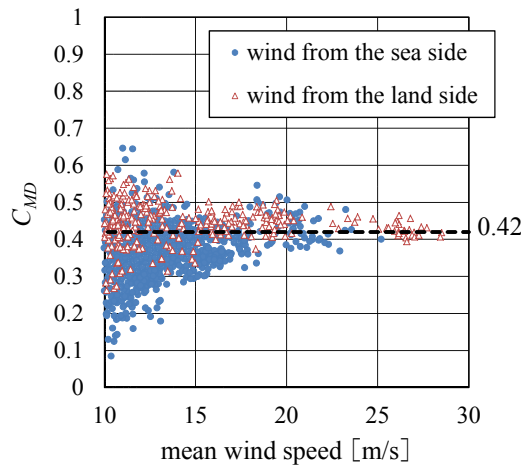


Figure 11: Along-wind static bending moment coefficient C_{MD} (feathering condition)

Figure 12 shows the relationship between wind speed and the gust effect factor G_D . Figure 12 also shows the G_D values specified in the Guidelines for Design of Wind Turbine Support Structures and Foundations⁵⁾. As shown, as wind speed increased, the G_D of wind from the sea side showed values of about 1.8 to 2.0, which correspond to category of surface roughness I or II defined in the Guideline. The G_D of wind from the land side ranged from 2.0 to 3.5 at wind speeds higher than 20m/s, showing values falling into category of surface roughness III or higher. Since the maximum wind speed observed was about 1/2 of the design wind speed, it is necessary to accumulate higher-wind-speed data.

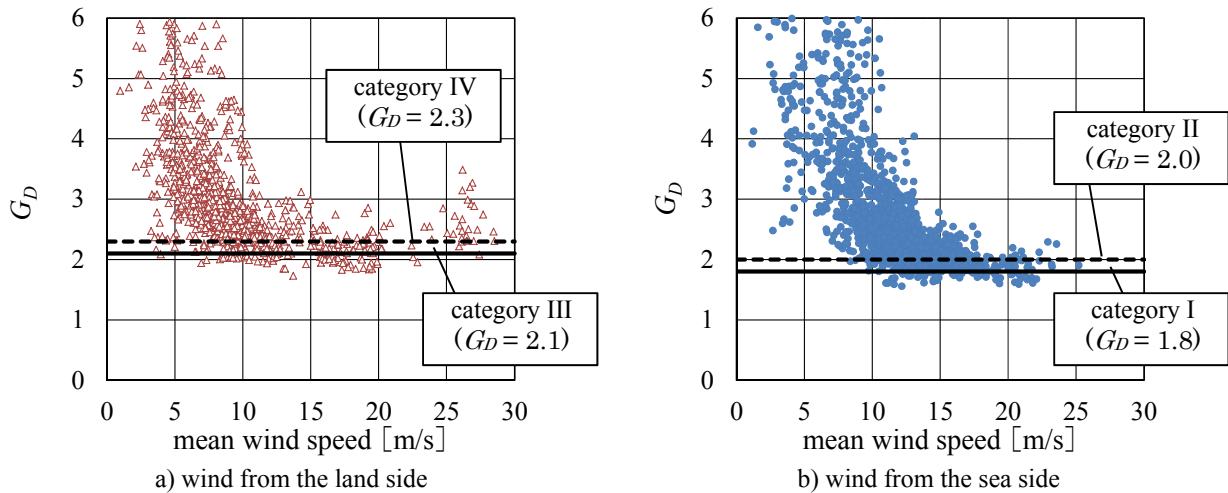


Figure 12: Along-wind gust effect factor G_D (feathering condition)

(4) Comparison between operational condition and feathering condition

M_{Dmax} in operational condition and M_{Dmax} in feathering condition are compared. Figure 13 shows the relationship between wind speed and M_{Dmax} . Figure 13 also shows predicted values in feathering condition calculated by using the C_{MD} values shown in Figure 11 and the G_D values shown in Figure 12. As shown, at wind speeds below the cut-out wind speed, the M_{Dmax} values in feathering condition are substantially smaller than the values in operational condition, but M_{Dmax} is expected to increase as wind speed increases. It is thought likely that at the design wind speed (with a return period of 50 years) shown in Figure 13, M_{Dmax} values in feathering condition will be similar to the values in operational condition.

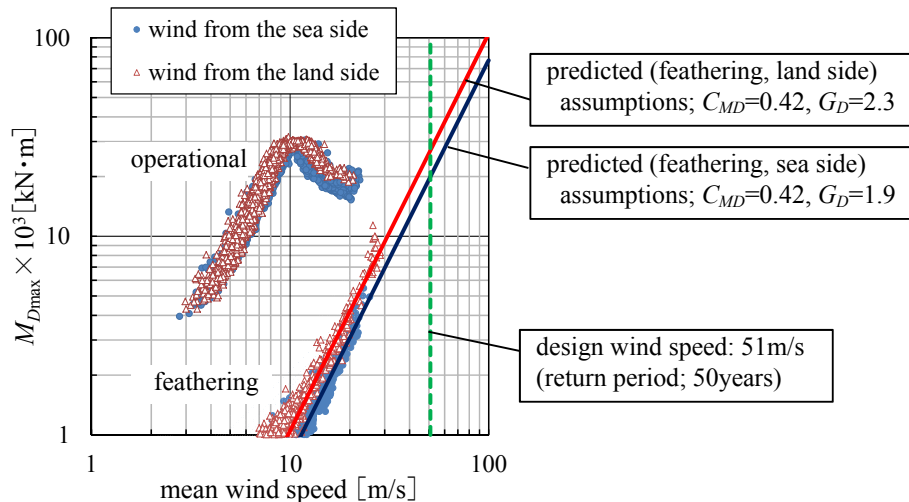


Figure 13: Comparison between operational and feathering condition about M_{Dmax}

4. Conclusion

Focusing on the first bottom-mounted offshore wind turbine tower in Japan, this study investigated wind load characteristics and the influence of turbulence intensity on wind loads. As a result, it has been clarified that the zero-strain point of the tower changes depending on nacelle direction, and that since wind loads are affected by land-induced turbulence even though the tower is located at a distance of 3.1 km from the nearest land, loads induced by wind from the land side are greater than by wind from the sea side. It has also been clarified that the gust effect factor of wind from the sea side in feathering condition ranges from 1.8 to 2.0 (category of surface roughness I or II defined in the JSCE Guideline), and the gust effect factor of wind from the land side shows 2.1 or larger values (category of surface roughness III or higher) at wind speeds lower than 30m/s.

ACKNOWLEDGMENT

The authors would like to gratefully acknowledge that this study was conducted as part of a study commissioned by New Energy and Industrial Technology Development Organization (NEDO).

REFERENCES

- 1) Yukinari Fukumoto, Takeshi Ishihara, Kazumasa Okubo, Koji Hayashida : Empirical Research of Bottom Mounted Offshore Wind Turbine, *Wind Engineers, JAWE*, Vol.36, No.1(No.126), pp.4-8, 2011
- 2) Hiroyuki Sukegawa, Yukinari Fukumoto, Toru Yamanaka, Kazumasa Okubo, Takeshi Ishihara : An Offshore Wind Observation at a Point of 3.1km off Choshi, *Japan Wind Energy Symposium*, Vol. 35, pp.260-263, 2013
- 3) Atsushi Yamaguchi, Sho Oh, Takeshi Ishihara : System identification of an offshore wind turbine based on ambient and forced vibration, *Japan Wind Energy Symposium*, Vol. 35, pp.264-267, 2013
- 4) Manabu Yamamoto, Yukio Naito, Koji Kondo, Takeshi Ohkuma : Wind Loads and External Forces on a

Wind Turbine Tower Based on Field Measurements, *Journal of Structural and Construction Engineering*, No.617, pp.39-46, 2007

- 5) Japan Society of Civil Engineers : Guidelines for Design of Wind Turbine Support Structures and Foundations, 2010

Two-Dimensional Aeroelastic Analysis of a Brimmed-Diffuser Shroud with Composite Material for a Wind Turbine

Taeyoung Kim⁺¹, Hiroto Nagai⁺², Kousei Ono⁺², Nobuhide Uda⁺² and Yuji Ohya⁺³

⁺¹Dept. of Aeronautics and Astronautics, Grad School of Engineering, Kyushu Univ., Fukuoka, Japan

⁺²Dept. of Aeronautics and Astronautics, Faculty of Engineering, Kyushu Univ., Fukuoka, Japan

⁺³Research Institute for Applied Mechanics, Kyushu Univ., Fukuoka, Japan

A brimmed-diffuser shroud also known as a wind-lens is equipment to amplify output power in a wind turbine system by collecting and accelerating wind blowing through its rotor area. A small increase in wind speed accelerated by a wind-lens greatly raises output power from a wind power generator because output power is proportional to wind speed cubed. In spite of this advantage, its thin structure is prone to aeroelastic deformation and vibration. Especially, for a large-sized wind-lens, its wind resistance is also required to improve. In this study, aeroelastic response of the two dimensional brimmed-diffuser shroud for a 100kW wind power generator is computed under uniform wind conditions by using a two-dimensional Navier-Stokes code coupled with the equation of motion for the structure. Three types of material were applied to a diffuser model: aluminum alloy, CFRP laminate and sandwich structure with CFRP layers and PET foam. The density of the sandwich structure is lowest among the three materials. The weight of the three models is kept same by adjusting their thickness for analysis, and the model of the sandwich structure has become thickest. We verified that resonance occurs in the models when a vortex frequency matches a natural frequency of the structure. Besides, we confirmed that vibrating motion in resonance depends on a dominant mode shape. As a result, the sandwich model has the least vibrating motion in resonance because of high rigidity by its thickness. Considering the results, our estimation of critical wind speed using a Strouhal number is found to agree well with the aeroelastic responses.

Keyword: Aeroelasticity, Vortex-induced Vibration, Wind-lens, Wind Turbine, Composite Material

1. INTRODUCTION



Figure 1: A wind generator with a brimmed diffuser

A brimmed diffuser shroud is a ring-like device that amplifies output power in a wind power generator¹⁾. It is installed around a rotor with a few struts that fix it to a nacelle as seen in Fig. 1. It is also known as a wind-lens because it collects and accelerates wind passing through the rotor area. In addition, it helps passive yaw

⁺¹kim-ty@aero.kyushu-u.ac.jp, ⁺²nagai@aero.kyushu-u.ac.jp, ⁺³ohya@riam.kyushu-u.ac.jp

control of a rotor, so the rotor area can always face a wind direction at all times. With wind speed increased by a wind-lens, a rotor is able to rotate fast, which enables a wind turbine system to gain more output power. Even slightly accelerated wind speed can make a large amount of power because output power is proportional to wind speed cubed. In practice, power generated from a wind power generator with a wind-lens is more than twice as large as that from a conventional one²⁾. It is obvious that a brimmed diffuser shroud is advantageous to a wind turbine system in terms of wind energy generation. However, it increases wind load and total weight of a wind power generator by adding it around the rotor. Besides, thin diffuser is exposed to hazardous aeroelastic deformation and vibration in its structure by strong wind. In general, a wind power generator stops its operation over a wind speed of 25 m/s for the safety of a rotor³⁾. Even if a rotor remains at rest under the strong wind condition, a wind-lens around the rotor needs to endure gales. In order to design a large and light brimmed-diffuser shroud which is strong enough to be utilized at fast wind speed, this study investigates the aeroelastic influence on its structure made of composite material under uniform wind conditions.

2. NUMERICAL METHODS

(1) Structural model

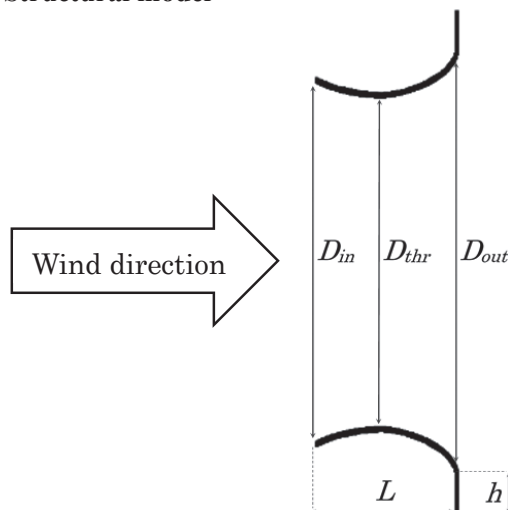


Table 1: Size of the model

Inlet diameter	D_{in}	15.9m
Throat diameter	D_{thr}	15.6m
Outlet diameter	D_{out}	17.0m
Brim height	h	0.78m
Diffuser length	L	2.14m

Figure 2: Schematic diagram of a wind-lens model

A wind-lens for a 100kW generator is the object of this study, illustrated in Fig. 2 and Tab. 1. The brimmed-diffuser named CiB5 consists of a cycloidal curve in the diffuser and a brim with the height of 5% of the throat diameter. The material of a wind-lens in general use is aluminum alloy. We supposed aluminum alloy can be replaced with composite material with CFRP or PET foam to lighten a wind-lens with high stiffness. The material properties of them are as follows.

Table 2: Material properties of CFRP, PET foam, and aluminum alloy

		CFRP ply (0.25mm thick)	PET foam	Aluminum alloy
Young's modulus	E_1	130 GPa	85 MPa	72 GPa
	E_2, E_3	6 GPa		
Poisson' ratio	$\nu_{12}, \nu_{13}, \nu_{23}$	0.33	0.37	0.3
Shear modulus	G_{12}, G_{13}	4 GPa	21 MPa	28 GPa
	G_{23}	2.3 GPa		
Density	ρ	1600 kg/m ³	105 kg/m ³	2700 kg/m ³

Three types of a model were considered by using the three materials above: an aluminum alloy model, a CFRP laminate model, and a model of a sandwich structure which is fabricated as a three-layered structure by attaching

two thin skins to a thick core. In the sandwich model, CFRP laminates are used for both upper and lower faces and PET foam is filled as a core between them. For comparison, the thickness of the diffuser models was adjusted so that all of them can have the same weight.

Table 3: Three types of model

	Material		Total thickness
Aluminum alloy model	Aluminum alloy		6.1mm
CFRP laminate model	CFRP laminate $[(0/90)_{20}/\bar{0}]_s$		10.25mm
Sandwich model	Face: CFRP $[(0/90)_3/0/90]_s$ Thickness: 3.75mm each	Core: PET foam Thickness: 42.5mm	50mm

From the Tab. 3, it is clear that the sandwich model has the lowest density. In the layup sequence of the CFRP laminates, 0° direction heads for the axial direction in the cylindrical coordinate of the brimmed-diffuser and 90° direction corresponds with the circumferential direction of that. It is assumed that a wind-lens is fixed by 3 supports at 120° intervals as shown in Fig. 3. The model focuses on the wind-lens only and excludes other parts such as a rotor and a nacelle. For simplification, a diffuser model is cut in sixths as described in Fig. 4.



Figure 3: A brimmed diffuser shroud fixed by 3 supports

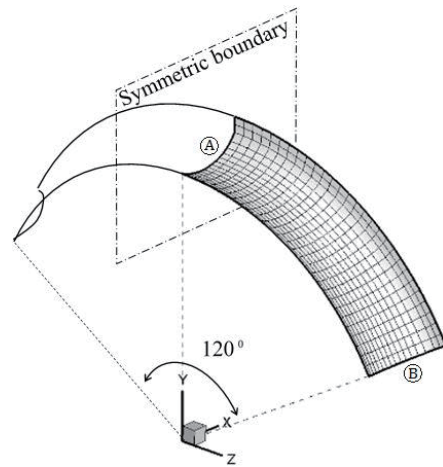


Figure 4: A one-sixth model

(2) Modal analysis

As a first stage, modal analysis of the three abovementioned models was conducted by using a commercial FEM software, ANSYS 15.0, to calculate their mode shapes and natural frequencies. In this FEM analysis, 4-node shell elements were applied for the one-sixth diffuser model. Symmetric boundary conditions were applied at both the sides of A and B in Fig. 4. The side B is additionally fixed and does not move at all in the x-direction (axial direction) since it is supported by a strut. Six modes were obtained in this three-dimensional analysis. Then the 3D mode shapes were reduced to the two-dimensional mode shapes for two-dimensional aeroelastic analysis. Thus, the cross-section of the diffuser model on the symmetric boundary plane (the side A in Fig. 4) is set as the reference cross-section. The first and second mode shapes of the three models are shown in Fig. 5. A natural frequency is a parameter for estimating a resonance phenomenon between a structure and a vortex flow around a diffuser model. In Tab. 4, the sandwich model has the larger natural frequencies than the other models in each mode. In other words, it is most resistant to wind load among them. Figure 5 shows that the first mode of the aluminum alloy model and CFRP laminate model is vibration of the brim, while that for the sandwich model is rotating motion about the circumferential axis at a certain nodal point on the reference cross-section. The second mode shape of the aluminum alloy model and the CFRP laminate

model is vibration of the camber or bending of the shape, while that of the sandwich model is rotating motion about the circumferential axis, which is similar to its first mode shape. The higher-order mode shapes were also obtained, but they do not have a great influence upon aeroelastic responses.

Table 4: The natural frequencies from the first mode to the sixth mode [Unit: Hz]

	f_1	f_2	f_3	f_4	f_5	f_6
Aluminum alloy model	3.38	5.36	6.11	7.46	7.76	9.43
CFRP laminate model	4.33	7.82	9.40	11.91	13.10	14.30
Sandwich model	7.09	13.89	24.56	34.93	40.21	42.22

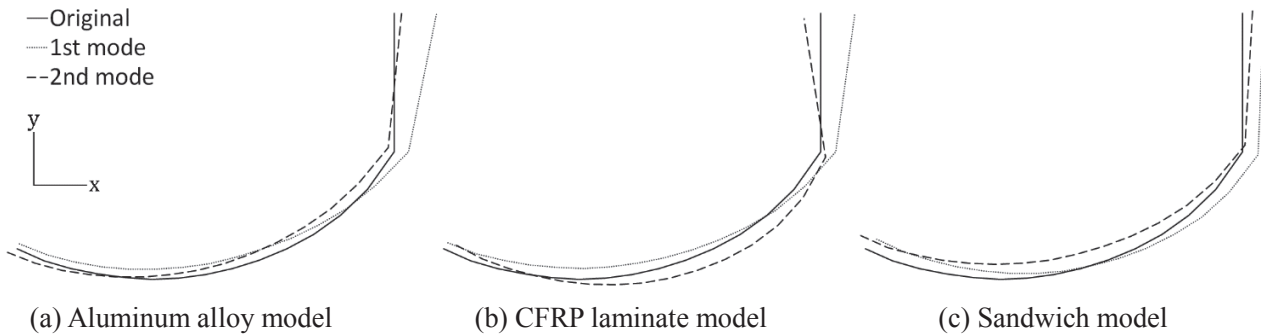


Figure 5: The first and second mode shapes of the cross-section on the symmetric boundary plane

(3) Two-dimensional aeroelastic analysis

We employed a computational fluid dynamics (CFD) developed by Nagai et al. for numerical aeroelastic analysis, which includes a two-dimensional Navier-Stokes code coupled with the equation of motion for the structural model⁴⁾⁵⁾. The modal characteristics from the FEM analysis were used as input data for the CFD program. Based on mode superposition, the displacement vector d_i on the reference cross-section is expressed as

$$d_i(\xi, t) = \sum_{k=1}^N \Phi_{ik}(\xi) q_k(t) \quad (i = 1 \sim 3, k = 1 \sim N) \quad (1)$$

where t is time, ξ is the curvature coordinate along the cross-section, q_k is the generalized coordinate of k -th mode, and Φ_{ik} is the natural mode shapes of k -th mode in i -th coordinate direction. N is the number of modes, which is six as mentioned above. Next, Lagrange's equations of motion give us the ordinary equations of motion for $q_k(t)$ as below.

$$M_k(\ddot{q}_k + g_k \omega_k \dot{q}_k + \omega_k^2 q_k) = \int_{L,E}^{T,E} \Phi_{ik}(\xi) \cdot \Delta P_i(\xi, t) d\xi \quad (i = 1 \sim 3, k = 1 \sim N) \quad (2)$$

In Eq. 2, M_k is the generalized mass, g_k is the modal damping coefficient (= 0.01), ω_k is the natural frequency, and ΔP_i is the pressure difference vector acting on the cross section. ΔP_i is computed at each time step using the 2D Navier-Stokes code absent from turbulence model. If Eq. 2 is solved by numerical time integration, we can gain the generalized coordinate at each time step, and then the deformation of the cross-section using superposition of modes is also determined.

3. RESULTS AND DISCUSSION

(1) Estimation of critical wind speed

The shape of the brimmed-diffuser shroud generates large vortex shedding behind the brim. Although the vortex shedding helps an increase of the flow velocity inside the diffuser, it applies a time-varied aerodynamic load onto the diffuser surface, which may cause severe aeroelastic vibration at a particular wind

speed. The critical wind speed is defined as the wind speed at which the frequency of vortex shedding behind a diffuser model matches one of the natural frequencies of its structure. As the wind speed gets faster, the vortex frequency increases linearly. When the wind speed reaches the critical wind speed, resonance typically arises in an oscillating body by vortices. The Strouhal number St is defined as

$$St = \frac{f_{\omega} l}{U_0} \tag{3}$$

where f_{ω} is the vortex frequency, l is the reference length that is vertical distance from the throat to the top of the brim, and U_0 is the wind speed.

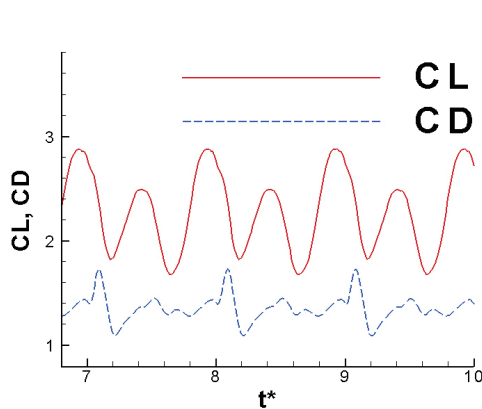


Figure 6: Time history of lift and drag coefficients in the rigid diffuser model

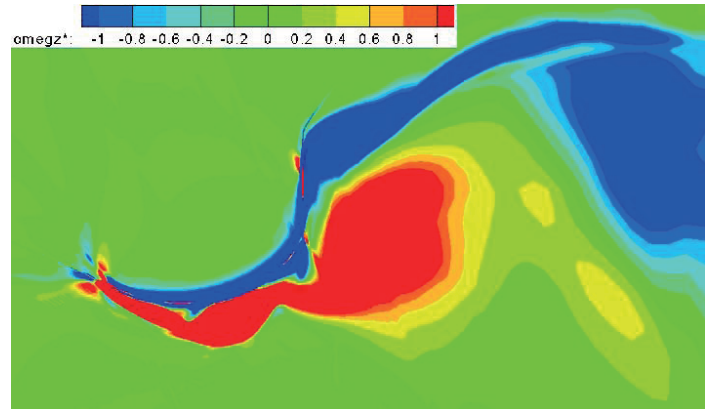


Figure 7: Vortices around the diffuser in the rigid diffuser model

Table 5: Estimated critical wind speeds by the three Strouhal numbers [Unit: Hz]

	Natural frequency [Hz]		Estimated critical wind speed [m/s]		
			$St_1=0.063$	$St_2=0.126$	$St_3=0.189$
Aluminum alloy model	1 st mode	3.38	79.3	39.7	26.4
	2 nd mode	5.36	125.9	62.9	42.0
CFRP laminate model	1 st mode	4.32	101.5	50.8	33.8
	2 nd mode	7.82	183.6	91.8	61.2
Sandwich model	1 st mode	7.09	166.6	83.3	55.5
	2 nd mode	13.89	326.3	163.2	108.8

Firstly, we analyzed a rigid diffuser model at a wind speed of 10m/s with the CFD program to find the Strouhal number for the diffuser shape. The time history of lift and drag coefficients is shown in Fig. 6. Using these waveforms, we calculated the Strouhal number by measuring the wave period. As shown in Fig. 6, the waveform of the aerodynamic force includes some fundamental sinusoidal waves. Each fundamental wave signifies each vortex-shedding frequency as shown in Fig. 7. The Strouhal number calculated by the lowest vortex frequency is denoted by St_1 , which is related to the vortex shedding at the trailing edge of the brim. The Strouhal number St_2 comes from the second lowest vortex frequency which means the vortex shedding inside the diffuser behind the throat. The third Strouhal number St_3 is to do with the vortex shedding around the corner between the diffuser and brim. It possesses a small amplitude and short period within the time history of drag coefficient. In this case, St_1 is 0.063, St_2 is 0.126, twice as much as St_1 , and St_3 is 0.189, triple as much as St_1 . Once St_i is found, we can estimate the vortex frequency $f_{\omega i}$ at each wind speed. The estimated critical wind speed was calculated from the assumption that the resonance occur when the vortex frequency $f_{\omega i}$ is equal to the structural natural frequency $f_{s i}$. Combining the two natural frequencies with the three Strouhal numbers, we

calculated six estimated critical wind speeds tabulated in Tab. 5. The critical wind speed about the third natural frequency is too high to happen in nature. For this reason, the higher-order natural frequencies were not taken into account in the estimation as well. In this study, we are aiming at a diffuser model that satisfies the designed wind speed limit, 70m/s, and the sandwich model is expected to be suitable for that requirement in the estimation of the critical wind speed.

(2) Aeroelastic response for the aluminum alloy model

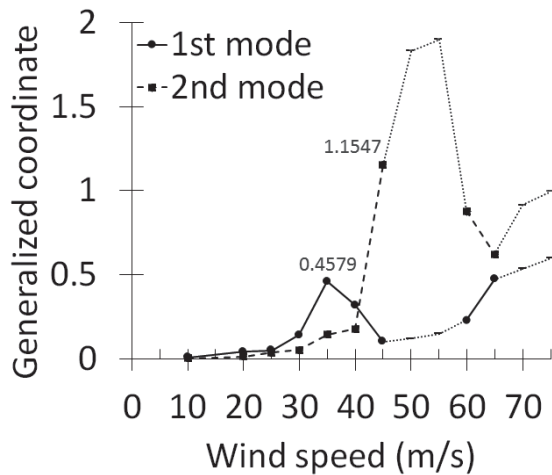


Figure 8: Amplitude of generalized coordinate vs wind speed for the aluminum alloy model

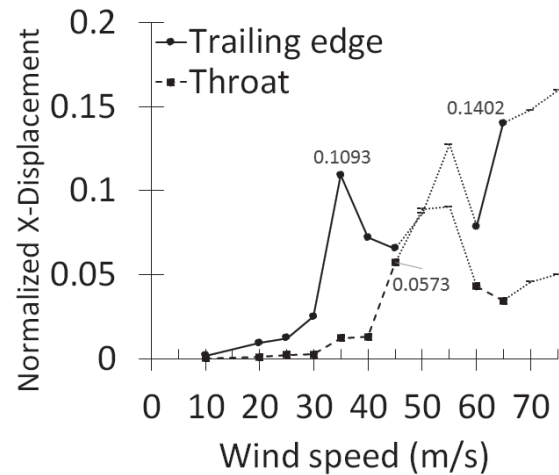


Figure 9: Amplitude of x-displacement vs wind speed for the aluminum alloy model

The aeroelastic responses of the aluminum alloy model were calculated under constant flow conditions. Figure 8 shows the amplitude of the generalized coordinates normalized by the diffuser length, L , for the first and second modes with respect to the wind speed. We could not obtain converged data at 50m/s, 55m/s and more than 70m/s and marked (-) signs because the limitation of the CFD grid system when large deformation occurs. In Fig. 8, the first mode has a peak point at 35m/s, which is close to the estimated critical wind speed of 39.7m/s. At this point, the diffuser model has resonance between the second vortex frequency and the first natural frequency. In the second mode, the largest value lies at 45m/s in the second mode. We guess that the peak point of the second mode would appear at 55m/s without the limitation of computation and it would approximately coincide with the estimated critical wind speed of 62.9m/s. The calculated peak points shown in Fig.8 are slightly different from the estimated critical wind speed shown in Tab. 5. This is because the large deformation of the model affects the flow field around the diffuser considerably, which may lead to the change of the vortex frequencies that have already been estimated. Figure 9 shows the amplitude of the deformation normalized by L at the trailing edge of the brim and the throat. It makes sense that the trailing edge is very easy to move in the x-direction since it is subjected to high wind load and the brim moves in all the modes as shown in Fig. 5. The displacement of the trailing edge has a peak point at 35m/s. At more than 40m/s, the displacement of the throat is sharply increased as the second mode becomes dominant. Meanwhile, we could not observe any peak in Fig. 8 and 9 at around 26.4m/s, the critical wind speed about the first natural frequency and the third Strouhal number. The reason is that the intensity of the third vortex shedding is too small to have an effect on the model at such a low wind speed. However, there is an increasing tendency of the second mode from 30m/s to 40m/s in Fig. 8. It indicates that the third vortex shedding whose frequency is close to the natural frequency of the second mode is effective on the deformation at 42m/s, comparatively high wind speed. Figure 10 and 11 show the time histories of the displacement in the x-direction at the trailing edge and the throat at 35m/s and 55m/s. The response of the model at 35m/s shows the resonance phenomenon between the second vortex frequency and the first natural frequency and forms almost in-phase oscillation between the large displacement of the trailing edge and the small displacement of the throat. It is apparent that they are moving together in the

same direction because of the first mode shape as shown in Fig. 5(a). On the other hand, when the second mode is excited at 55m/s, as shown in Fig. 5, vibration of the camber that bends the shape of the diffuser gives rise to the large displacement of the throat moving in the opposite direction to the trailing edge. That is likely to do harm to the structure due to fatigue by the cyclic load. Therefore, the aluminum alloy model underwent resonance in its structure at a wind speed under 70m/s and its deformation at 70m/s is anticipated to be greatly large.

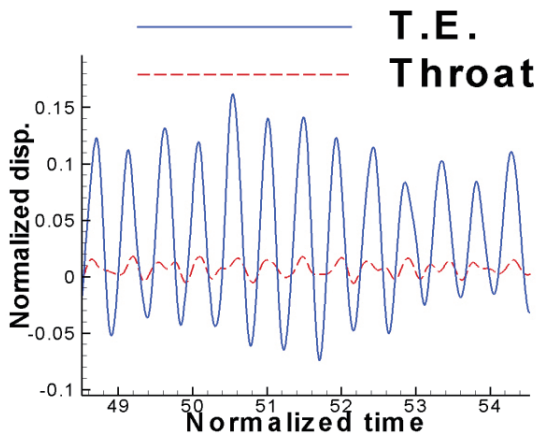


Figure 10: Time history of x-displacement at $U=35\text{m/s}$ for the aluminum alloy model

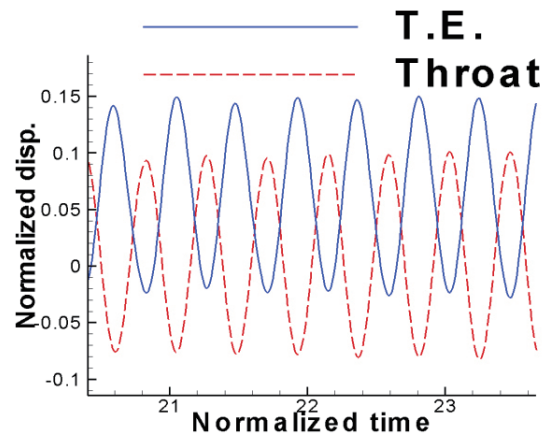


Figure 11: Time history of x-displacement at $U=55\text{m/s}$ for the aluminum alloy model

(3) Aeroelastic response for the CFRP laminate model

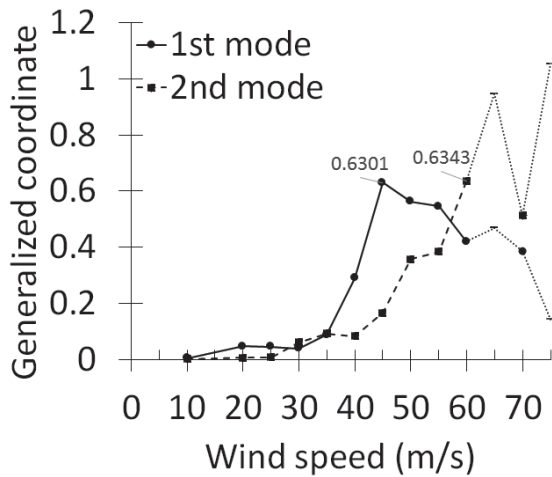


Figure 12: Amplitude of generalized coordinate vs wind speed for the CFRP laminate model

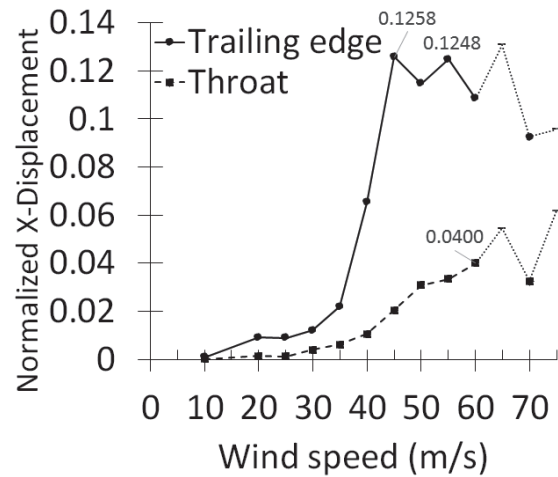


Figure 13: Amplitude of x-displacement vs wind speed for the CFRP laminate model

Figure 12 shows the amplitude of the normalized generalized coordinates for the CFRP laminate model with respect to the wind speed. In this graph, a peak point in the first mode appears at 45m/s and it is located near the estimated critical wind speed by the second vortex frequency in the first mode, 50.8m/s. And the second mode is increasing until 60m/s. The computation of the CFD program at 65m/s which is near to the estimated critical wind speed by St_3 in the second mode, 61.2m/s, could not be completed for the same reason with the case of the aluminum alloy model. Thus, the third vortex frequency quite impacted on the diffuser model in this case. Figure 13 shows two peak points at 45m/s and 55m/s in the displacement of the trailing edge and both have almost the same displacement. We assumed that the peak point at 55m/s was caused by a coupling effect of the first mode and the second mode. As shown in Tab. 5, the estimated critical wind speed by St_2 in the first

mode and that by St_3 in the second mode do not have a great difference. That is, the structure of the model has the high possibility of being simultaneously affected by the two kinds of vortex at between the two critical wind speeds. Figure 14 shows the behavior of resonance between the second vortex frequency and the natural frequency of the first mode at 45m/s. Like Fig. 10, the two wave forms are in-phase oscillation with the very large displacement of the trailing edge and the small displacement of the throat. Irregular patterns in Fig. 15 describe the coupling motion of the first mode and the second mode at 55m/s. Some anti-phase patterns between the trailing edge and the throat demonstrate that the second mode is getting strong as wind speed increases. And then, when the second mode becomes dominant, vibration of the camber comes to be remarkable as shown in Fig. 16, which resembles Fig. 11. Similarly, this sort of movement in a wind-lens may deteriorate its fatigue performance in the structure. Comparing to the aluminum alloy model, the first resonance phenomenon in the CFRP laminate model occurs at relatively high wind speed. However, it proved to have considerable displacement in the model at a wind speed over 45m/s although its thickness is larger than that of the aluminum alloy model.

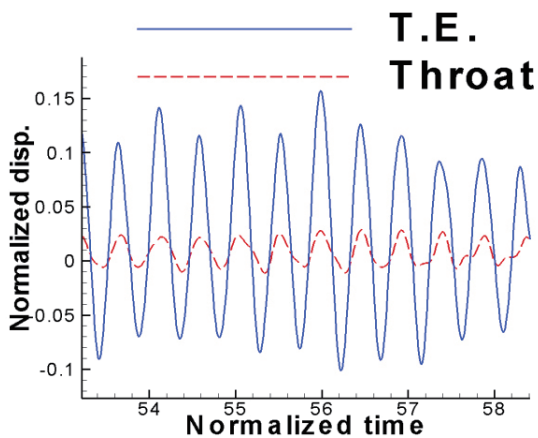


Figure 14: Time history of x-displacement at $U=45\text{m/s}$ for the CFRP laminate model

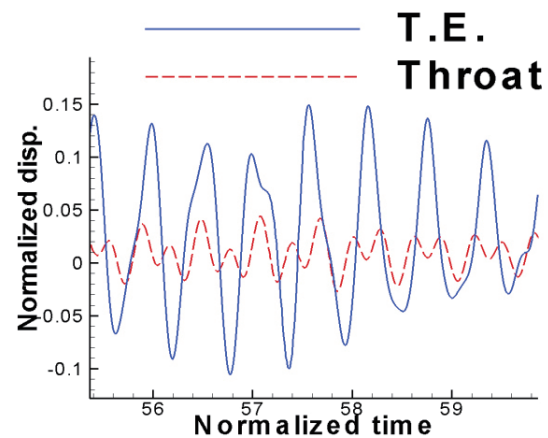


Figure 15: Time history of x-displacement at $U=55\text{m/s}$ for the CFRP laminate model

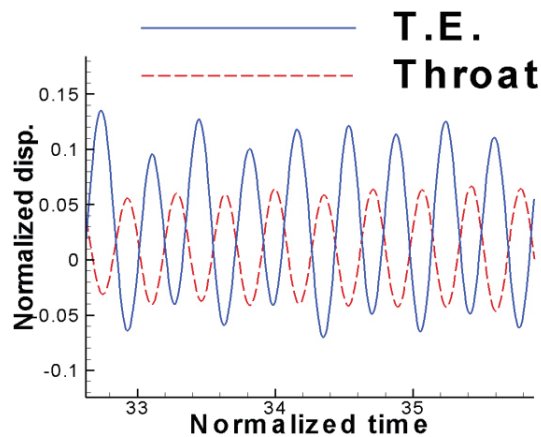


Figure 16: Time history of x-displacement at $U=65\text{m/s}$ for the CFRP laminate model

(4) Aeroelastic response for the Sandwich model

In both Fig. 17 and 18, it is significant that a maximum value of the vertical axis on the two graphs is much smaller than that of the previous models and no calculation failed for all wind speeds until 75m/s. In the sandwich model, as shown in Tab. 5, the critical wind speed by St_3 in the first mode is estimated to be 55.5m/s and the others predicted are over 70m/s, the designed wind speed limit. Accordingly, there is a peak point at

55m/s in the amplitude of generalized coordinate of the first mode. In the second mode, a noticeable peak point is not seen, but it simply tends to gradually increase. Nevertheless, the other peak point in the first mode appear at 40m/s in Fig. 17. The displacement of the trailing edge in Fig. 18 also has two peak points like Fig. 17. We suppose that the increasing curves after 65m/s in both Fig. 17 and 18 is merely on the way to the critical wind speed by St_2 in the first mode, 83.3m/s, and the one at 40m/s might be influenced by the fourth vortex which has not been identified yet in Fig. 6 and 7. In order to figure out vortices in detail at each wind speed, we are going to employ fast Fourier transform afterward.

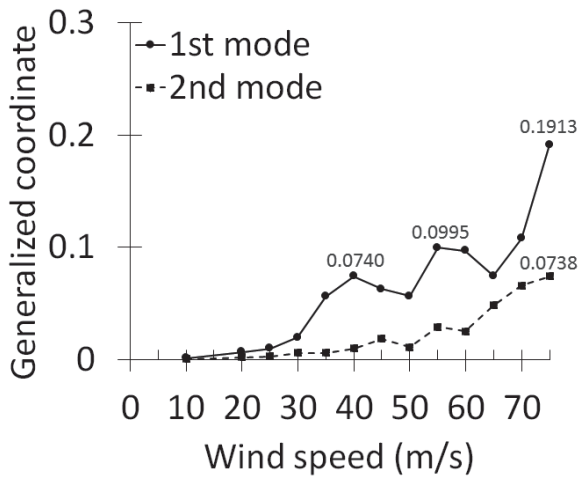


Figure 17: Amplitude of generalized coordinate vs wind speed for the sandwich model

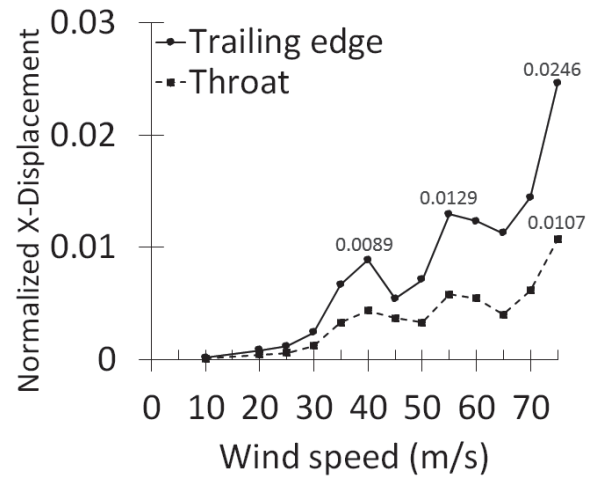


Figure 18: Amplitude of x-displacement vs wind speed for the sandwich model

In the three figures from Fig. 19 to Fig. 21, what has in common is their in-phase oscillation between the trailing edge and the throat because the first mode is more dominant than the second mode at all the wind speeds until 75m/s according to Fig. 17. Furthermore, the second mode does not include bending motion, but has rotating motion like the first mode. In other words, harmful vibration to the structure of the wind-lens hardly occurs in the sandwich model until 75m/s. Most of all, its maximum displacement is far smaller than that of the other models. It is because its bending rigidity became higher by thickening the diffuser model with the use of strong CFRP laminate for the skin and light PET foam for the core. In summary, the sandwich model is considered to nearly satisfy the designed wind speed limit, 70m/s, but the reason why some peak points appeared other than 55m/s needs to be investigated.

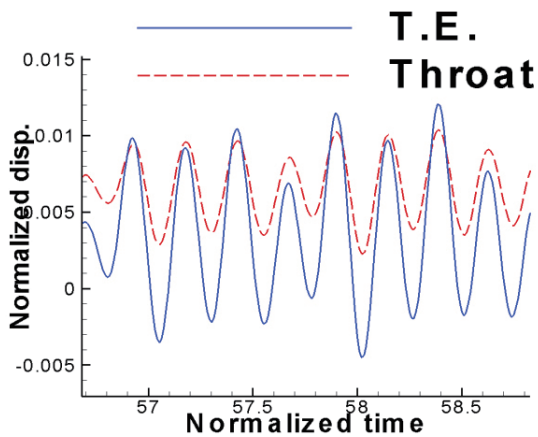


Figure 19: Time history of x-displacement at $U=40m/s$ for the sandwich model

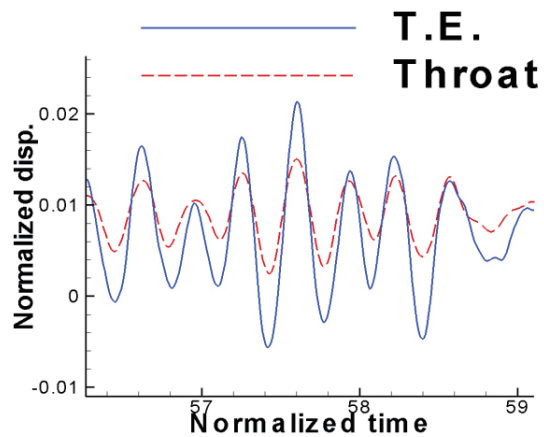


Figure 20: Time history of x-displacement at $U=55m/s$ for the sandwich model

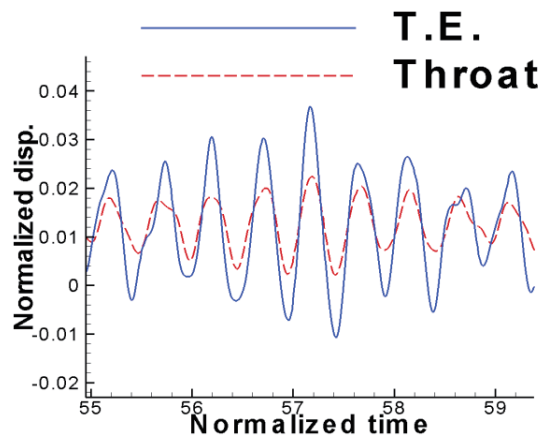


Figure 22: Time history of x-displacement at $U=75\text{m/s}$ for the sandwich model

4. CONCLUSIONS

In this study, two-dimensional aeroelastic analysis of a brimmed-diffuser shroud for a 100kW wind power generator was conducted for the three materials: aluminum alloy, CFRP laminate and sandwich structure. We clarified that the self-excited vibration by the flow around the brimmed-diffuser shroud is amplified due to resonance when the vortex frequency is equal to the structural natural frequencies. It was also found that the dominant mode varies with wind speed. By comparing the three models under a condition of the same weight, we realized that the thickness of the model affects bending rigidity, which is relevant to the displacement of a model. In addition, we estimated the critical wind speed using the Strouhal number calculated from the rigid diffuser model, which is in good agreement with the aeroelastic responses on the whole.

REFERENCES

- 1) Yuji Ohya. Takashi Karasudani : A Shrouded Wind Turbine Generating High Output Power with Wind-lens Technology. *Energies*, 3, 2010, 634-649.
- 2) Yuji Ohya. Takashi Karasudani. Akira Sakurai, Ken-ichi Abe. Masahiro Inoue : Development of a shrouded wind turbine with a flanged diffuser, *Journal of Wind Engineering and Industrial Aerodynamics*, 96, 2008, 524-239
- 3) Peter Jamieson : *INNOVATION IN WIND TURBINE DESIGN*, John Wiley & Sons, Ltd, 2011
- 4) Hiroto Nagai. Koji Isogai. Tatsumi Fujimoto. Toshiyuki Hayase : Experimental and Numerical Study of Forward Flight Aerodynamics of Insect Flapping Wing, *AIAA Journal*, Vol. 47, No. 3, 2009, pp. 730-742
- 5) Hiroto Nagai. Koji Isogai. Masahiko Murozono. Tsutomu Fujishiro : Investigation on Structural and Aerodynamic Characteristics of Resonant Type Elastic Flapping Wing, *ICAS2012*, 2012-9.5.3, 2012

JAXA Special Publication JAXA-SP-16-008E

First International Symposium on Flutter and its Application

Edited and Published by: Japan Aerospace Exploration Agency

7-44-1 Jindaiji-higashimachi, Chofu-shi, Tokyo 182-8522 Japan

URL: <http://www.jaxa.jp/>

Date of Issue: March 15, 2017

Produced by: Matsueda Printing Inc.

©2017 JAXA

Unauthorized copying, replication and storage digital media of the contents of this publication, text and images are strictly prohibited. All Rights Reserved.

